Macromolecules

Perspective

pubs.acs.org/Macromolecules

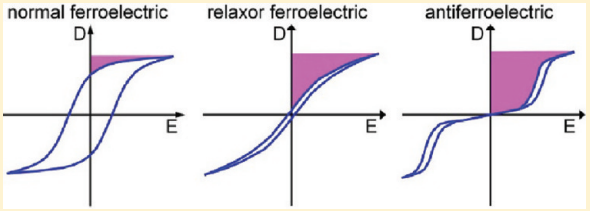
Novel Ferroelectric Polymers for High Energy Density and Low Loss Dielectrics

Lei Zhu*,† and Qing Wang*,‡

†Department of Macromolecular Science and Engineering, Case Western Reserve University, Cleveland, Ohio 44106-7202, United States

‡Department of Materials Science and Engineering, Pennsylvania State University, University Park, Pennsylvania 16802, United States

ABSTRACT: The state-of-the-art polymer dielectrics have been limited to nonpolar polymers with relatively low energy density but ultralow dielectric losses for the past decades. With the fast development of power electronics in pulsed power and power conditioning applications, there is a need for next-generation dielectric capacitors in areas of high energy density/low loss and/or high temperature/low loss polymer dielectrics. Given limitations in further enhancing atomic and electronic polarizations for polymers, this Perspective focuses on a fundamental question: Can orientational polarization in polar polymers be utilized for high energy density and low loss dielectrics? Existing experimental and theoretical results have suggested the following perspectives. For amorphous polar polymers, high energy density and low loss can be achieved below their glass transition temperatures. For liquid crystalline side-chain polymers, dipole mobility is so high that they saturate at relatively low electric fields, and only limited electrical energy can be further stored after dipole saturation. Crystalline polar polymers are promising and can be divided into three categories: normal ferroelectric, paraelectric, and novel ferroelectric. For normal ferroelectric crystalline polymers, switching of a high spontaneous polarization results in a large hysteresis. To reduce the hysteresis, ultrafine crystallites or ferroelectric domains are desired to reduce the spontaneous polarization. For paraelectric crystalline polymers, dipoles have the potential to align in an external electric field. However, a high degree of dipole reversibility is required for the high energy density and low loss application. Novel ferroelectric behaviors include relaxor ferroelectric and antiferroelectric-like behaviors are highly desired because of their high degree of dipole reversibility. To achieve the relaxor ferroelectric behavior, structural defects such as bulky comonomers need to be introduced into the crystalline lattice to expand the lateral unit cell dimensions and speed up the mobility and reversibility of crystalline dipoles. So far, true antiferroelectric crystalline polymers have not yet been discovered. Nevertheless, the antiferroelectric-like behavior has been realized by reducing the compensation polarization via nanoconfinement. In the future, more research is needed to develop new paraelectric and novel ferroelectric polymers for high energy density and low loss dielectrics.



1. ELECTRIC CHARGE STORAGE IN DIELECTRIC POLYMERS

Different from a conductor or a semiconductor, a dielectric is an electric insulator, whose band gap is so large that no electric charges can freely flow through the material. Instead, dielectric polarization is induced by the applied electric field, resulting in accumulations of positive charges on one side of the dielectric toward the field and negative charges on the opposite side.[1] These charge accumulations enabled a direct application, namely, electric charge storage in capacitors. After the success of uniform and large scale metallization of polymers,[2] polymer film capacitors have nearly replaced paper foil and metalized paper capacitors for most applications.[3−5] Among all kinds of polymer films, biaxially oriented polypropylene (BOPP) has remained as the state-of-the-art capacitor film and dominated the market for the past decades because of its high electric breakdown strength (730 MV/m at 63.2% Weibull failure probability and ∼600 MV/m at 1% Weibull failure probability for a test area of 2.0 cm^2),[6] low dielectric loss (tan $\delta \sim 0.0002$ at 1 kHz),[7] excellent self-clearing,[3,4] and low cost. Nevertheless, disadvantages for BOPP films include low energy density and reduced breakdown strength and cycle life above 85 °C.[8] With the fast growth of microelectronics and power electronics worldwide, polymer film capacitors await breakthrough for high energy density while maintaining a low loss in order to meet the stringent requirements for next generation electronics, e.g., dc link capacitors in hybrid electric vehicles,[9] inverters for grid-connected photovoltaics and wind power,[10] and pulsed power systems.[11]

Before proposing any detailed strategies for high energy density and low loss dielectrics, it is necessary for us to understand the fundamentals of dielectric polarization in polymers. As shown in Figure 1, in total five types of polarization can exist in polymers, namely, electronic, atomic, orientational, ionic, and interfacial polarization.[1,12,13] Each type of polarization has its own characteristics. Electronic and atomic polarizations originate from electron cloud and skeletal atom movements deviated away from the equilibrium position as induced by an external field, and thus they occur at very high

Received: October 30, 2011
Revised: January 19, 2012
Published: February 10, 2012

 © 2012 American Chemical Society dx.doi.org/10.1021/ma2024057 | Macromolecules 2012, 45, 2937−2954

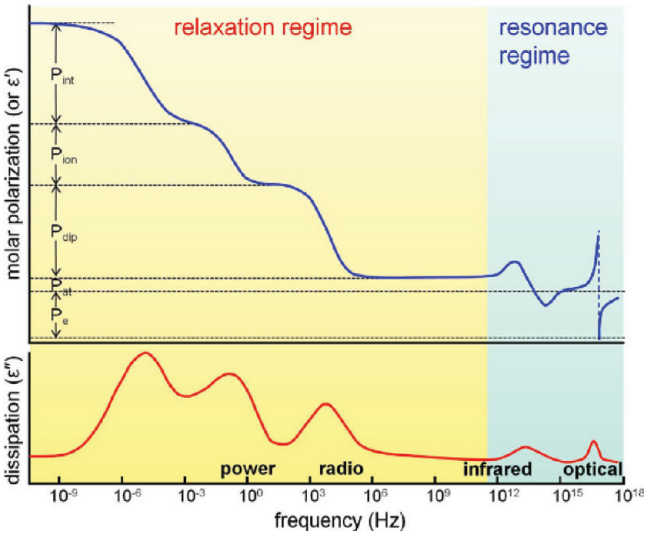


Figure 1. Different types of polarization as a function of frequency in polymers. P_e: electronic polarization; P_{at}: atomic polarization; P_{dip}: (dipolar) orientational polarization; P_{ion}: ionic polarization; P_{int}: interfacial polarization. The top panel shows the molar polarization (or the real part of permittivity), and the bottom panel shows the dissipation factor (the imaginary part of permittivity).

frequencies, i.e., in the infrared and optical range. These two types of polarization exist in all polymers, no matter if they are polar or nonpolar, amorphous or crystalline. If a polymer is polar and contains permanent dipoles, these permanent dipoles may respond to the external field by rotation, resulting in orientational polarization in the polymer. Depending on the nature of these dipoles, amorphous or crystalline, and temperature, they relax between 10 Hz and a few GHz, covering the power and radio frequency ranges. If a polymer contains ionic species, either impurity ions or ions in polymer electrolytes and polyelectrolytes, ionic polarization occurs below a few hundred Hz. Finally, for a multicomponent polymer system, interfaces exist and interfacial polarization takes place due to the Maxwell–Wagner effect.[1,12] The relaxation of these interfacial charges may take from seconds to hours or even years (e.g., charges trapped in polymer electrets).[14] For electric charge storage purpose, the higher the molar polarization, the more the charge storage; however, there will be a greater tendency that the stored charged cannot be quickly released. Obviously, for high voltage power and radio frequency applications, ionic and interfacial polarizations are not suitable due to their high losses.

The remaining types of polarization that can be utilized for high energy density and low loss dielectrics are electronic, atomic, and orientational. It is known that electronic polarization is high for semiconducting conjugated polymers. Although their electronic conductivity is fairly low at low fields, semiconducting polymers are not suitable for high-field applications because the electronic conductivity can dramatically increase under high electric fields.[15] Therefore, there is a trade-off between electron polarization (or electron delocalization) by lowering the band gap and electron conductivity under high electric fields. Unlike ceramic materials,[16] it is difficult to further enhance atomic polarization in polymers because atoms are linked together via covalent bonds with well-defined bond lengths and bond angles, rather than ionic interactions. Therefore, atomic polarization usually contributes less to electric charge storage than other types of polarization for polymers (see Figure 1). Finally, the question remains as: can orientational polarization in polymers be utilized for high energy density (or high K) and low loss dielectric applications?

2. UTILIZING ORIENTATIONAL POLARIZATION FOR HIGH ENERGY DENSITY AND LOW LOSS DIELECTRICS

Whether orientational polarization in polymers can be used for high energy density and low loss dielectrics depends on the frequency where dipole relaxation occurs in addition to the applied electric field. If the dipole relaxation occurs in the frequency range (i.e., 1 kHz to several hundred kHz) and the electric field (e.g., a few tens to several hundreds of MV/m) of power electronics, orientational polarization may not be suitable for high energy density dielectrics because high losses will result in significant dielectric heating due to dipole switching. If the dipole relaxation occurs at high frequencies, i.e., above tens of MHz, orientational polarization shall be suitable for high energy density and low loss dielectrics. Generally speaking, dipole relaxation in polymers depends on temperature and electric field. At low temperatures, dipole motion can be frozen and the corresponding relaxation will be low. At high temperatures, the relaxation frequency of permanent dipoles often increases with increasing the temperature. The temperature effect has been well-studied for polymers in the literature.[17] On the other hand, the external electric field can also significantly affect the dipole relaxation frequency. However, this effect has not been well-investigated for polymers. Under a low electric field (e.g., <0.5 MV/m), mobile amorphous dipoles and certain crystalline dipoles can respond to the external field. The corresponding dipole relaxation under such a low field is often studied by broadband dielectric spectroscopy (e.g., see Figure 1).[1,17] At high fields (e.g., >30 MV/m), nearly all types of crystalline dipoles in polymers can respond to the external field. With increasing the electric field, the dipole relaxation rate will increase and more crystalline dipoles can be polarized. Nonetheless, high-field dielectric spectroscopy has not been widely used to characterize dielectric properties of polymers because high-frequency switching under high fields is difficult to achieve instrumentally. Instead, high-field electric displacement–electric field (D–E) hysteresis loops are commonly used to characterize the dielectric behavior of polymers.[18] Figure 2 shows the unipolar

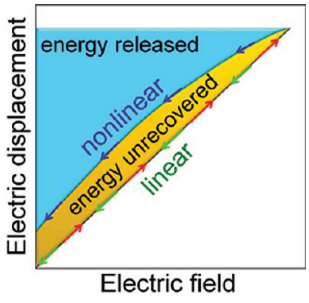


Figure 2. Schematic representation of unipolar electric displacement–electric field (D–E) hysteresis loops for both linear and nonlinear dielectric polymers under high-field switching.

D–E loop for both linear and nonlinear dielectric materials. For linear dielectric materials, the relative dielectric constant is independent of electric field and is defined as $\varepsilon_r = D/\varepsilon_0 E$, where ε_0 is the vacuum permittivity. Typical examples are nonpolar

dx.doi.org/10.1021/ma2024057 | Macromolecules 2012, 45, 2937–2954

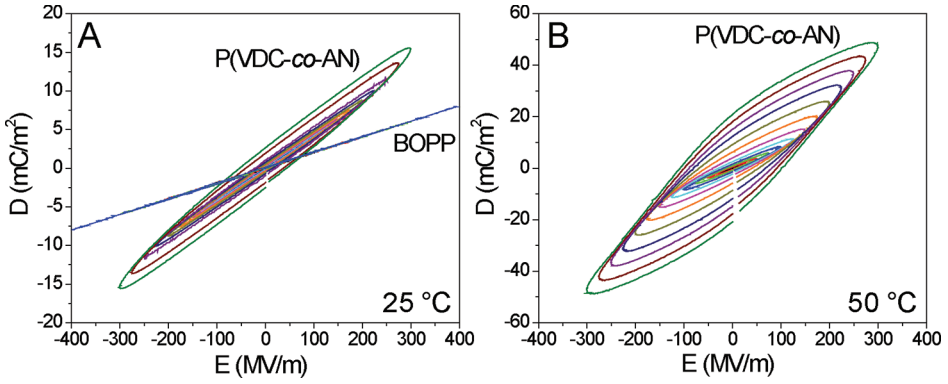


Figure 3. Bipolar $D-E$ hysteresis loops (10 Hz) for P(VDC-*co*-AN) at (A) 25 °C and (B) 50 °C, respectively. For each poling field, the second loop is shown and the field increment is 25 MV/m. $D-E$ loops for a capacitor-grade BOPP film is shown in (A) for comparison.

polymers such as BOPP, polyethylene (PE), polystyrene (PS), etc. The stored energy density is thus $U_{e,stored} = \int E\ dD = 0.5\varepsilon_r\varepsilon_0 E^2$, which is represented by the total (shaded) triangular area in Figure 2. Upon discharge for linear materials, the discharge curve nearly follows the charge curve and there is negligible hysteresis loss. For nonlinear dielectrics, the discharge curve does not follow the charge curve and part of the stored energy is unrecovered, as shown in Figure 2. Typical examples include polar polymers, polymers with impurity ions, and immiscible polymer blends with poor interfaces. The linear part of the dielectric constant, $\varepsilon_r(E)$, becomes electric field dependent and the discharged energy density $U_{e,released} = \int E\ dD \neq 0.5\varepsilon_r(E)\varepsilon_0 E^2$. Both dissipation factor (tan δ) from dielectric spectroscopy and hysteresis from $D-E$ hysteresis loop tests are needed for the evaluation of low- and high-field dielectric properties of polymers. Generally speaking, all relaxation modes observed in the low-field dielectric spectroscopy should also contribute to the hysteresis loss at high fields but at higher frequencies.

On the basis of the above discussion, an ideal high energy density and low loss dielectric requires the following characteristics: (1) high permittivity (or high K), (2) high electric breakdown strength (or field), (3) low dissipation factor at low fields, and (4) low hysteresis at high fields in a frequency range between 10 Hz and a few hundred kHz. The high breakdown field appears more important than high dielectric constant because the stored energy density is a linear function of dielectric constant but square of electric field. Impurity-free polar solvents seem to be good candidates to meet these requirements because they have high dielectric constants and low dielectric loss between 10 Hz and a few hundred kHz.[19−21] However, electrochemical redox reactions often occur for polar solvents on electrodes under high enough electric fields[22,23] and result in low breakdown strength and significant polarization hysteresis (due to the so-called electrode polarization). Therefore, polar liquids are not suitable for high energy density and low loss dielectrics.

On the contrary, polar polymers are much more stable than polar liquids electrochemically. It is known that polar polymers, like nonpolar polymers, can also exhibit high breakdown strengths if the ionic impurity level is very low.[24] Therefore, polar polymers may be good candidates for high energy density and low loss dielectrics. The fundamental question then is: can dipole relaxation in polar polymers take place above tens of MHz in order to minimize the dielectric loss between 10 Hz and a few hundred kHz? Bearing this question in mind, it is necessary to study the dielectric relaxation of different polar polymers as a function of frequency, temperature, and electric field.

Polar polymers can exist in the form of amorphous, liquid crystalline, and crystalline polymers. Examples of polar amorphous polymers include vinylidene cyanide (VDCN) and vinylidene chloride (VDC) containing polymers. Figure 3 shows the $D-E$ hysteresis loops for a poly(vinylidene chloride-*co*-acrylonitrile) [P(VDC-*co*-AN)] random copolymer (Sigma-Aldrich) at different temperatures. The number-average molecular weight (M_n) is 80 000 g/mol, and the polydispersity index is 1.88. This random copolymer has a glass transition temperature (T_g) of 50 °C. When polarized below the T_g (25 °C), nearly linear $D-E$ loops are observed for the poling field below 200 MV/m because permanent dipoles are frozen. Above 300 MV/m, hysteresis loops somewhat open up, possibly due to a small amount of ionic polarization of impurity ions in the polar polymer. It is known that ions can transport in glassy polymers via the free volume.[25−30] It is reasonable that a certain amount of ionic polarization can take place even below the T_g as long as the ions are small enough. From the slopes for the linear loops below 100 MV/m, the relative permittivity for P(VDC-*co*-AN) is calculated to be 4.77, which is higher than that (2.25) for BOPP. However, when the temperature increases to near the T_g (50 °C), significant dipole switching and/or ionic polarization appear above 100 MV/m due to the sluggish motion of molecular dipoles. Above the T_g, the sample breakdown strength dramatically decreases. Therefore, only at temperatures far below the T_g, polar amorphous polymers may be able to store higher energy than nonpolar polymers because of a higher permittivity. We speculate that the hysteresis loss can be low only when impurity ions are absent in the polar polymer. However, complete removal of impurity ions (and moistures) from polar polymers has always been a challenge for industrial practices.

Liquid crystalline polymers often contain polar groups such as cyanobiphenyls or aromatic esters and amides. Because of the liquid crystalline nature, dipole mobility is so high that dipoles are susceptible even to a relatively low electric field. Liquid crystalline dipole switching involves either out-of-plane (for twist nematics) or in-plane (for ferroelectric chiral smectics) large-scale molecular motions, which usually results in a large hysteresis behavior in both electrical and optical properties.[18,31−39] In an electro-optical switching study of a side-chain chiral smectic C (S_C*) liquid crystalline polymer at 115 °C, different switching behaviors are observed.[18] At a low field (7.3 MV/m), the electro-optic response behaves like a

dx.doi.org/10.1021/ma2024057 | *Macromolecules* 2012, 45, 2937−2954

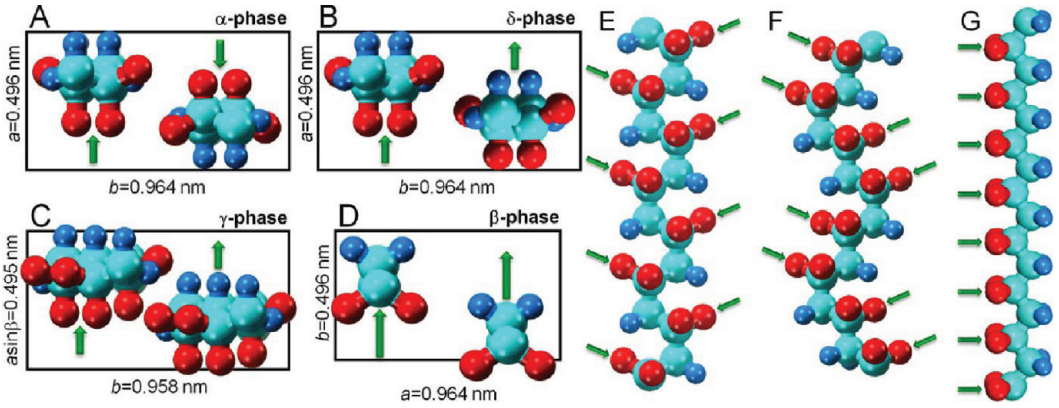


Figure 4. Unit cells of (A) α, (B) δ, (C) γ, and (D) β forms of PVDF crystals viewed along the *c*-axes and schematic chain conformations for (E) TGTG′ (α/δ), (F) TTTGTTTG′ (γ), and (G) all-trans (β) rotational sequences. Red, cyan, and blue spheres represent F, C, and H atoms. The projections of dipole directions are indicated by green arrows.

typical electroclinic effect. At an intermediate electric field (17.7 MV/m), the electro-optic response starts to deviate from the electroclinic effect. Finally, at 24.8 MV/m, a ferroelectric hysteresis switching behavior is observed. From this result, we can see that all the dipoles in ferroelectric liquid crystalline polymers saturate (i.e., aligned along the electric field) at relatively low dielectric fields (i.e., 24.8 MV/m). As we know, early saturation of dipoles at low electric fields will result in low electric energy storage. Therefore, polar liquid crystalline polymers are not suitable for high energy density and low loss dielectrics.

3. NORMAL FERROELECTRIC CRYSTALLINE POLYMERS

Polar crystalline polymers can be divided into three categories: normal ferroelectric, paraelectric, and novel ferroelectric. For ferroelectric crystalline polymers, famous examples include poly(vinylidene fluoride) (PVDF) and its copolymers, odd-numbered nylons, cyanopolymers, polyurea/polythiourea, and biopolymers (e.g., keratin and silk fibroin).[18] Nonetheless, large hysteresis loops are commonly observed for normal ferroelectric crystalline polymers because of the switching of a high spontaneous polarization, and their normal ferroelectricity is intimately dependent upon the crystalline structure and morphology. Before we embark on ferroelectric crystalline polymers for high energy density and low loss dielectrics, it is important for us to understand the nature of normal ferroelectricity and its suitable applications. Since PVDF and its copolymers have been intensively studied in the past, we will focus on these polymers for the discussion.

3.1. Polarization Mechanism in Ferroelectric PVDF. PVDF is a radically polymerized flexible polymer typically with 3−6 mol % head-to-head/tail-to-tail (HHTT) linkages. Because of these structural defects, its crystallinity is often limited to 50−60 wt %. In general, four major crystalline modifications are observed, i.e., α, δ, γ, and β forms, as shown in Figure 4A−D. Among them, the α form is nonpolar and δ, γ, and β forms are ferroelectric. Both α and δ forms have exactly the same unit cell dimensions and the same TGTG′ rational sequence; however, the dipole moments cancel out in the α form, and they point to the same direction in the δ form. The α form can be obtained by cooling from the melt at a normal rate and the δ form is obtained by poling the α form sample under an electric field of 100−200 MV/m at room temperature.[40−42] However, this nonpolar-to-ferroelectric transition is not 100% reversible because the free energies of both forms are fairly similar. As a result, the sample will be trapped in the δ form even after the applied field is removed. Because of the inclination of C−F dipoles at an angle to the molecular axis (Figure 4E), the components of the dipole moment perpendicular and parallel to the chain axis are 1.20 and 1.02 D (D), respectively.[42] The γ form has a TTTGTTTG′ chain conformation and is often obtained by solution-casting from polar solvents at temperatures below 100 °C[18,42,43] or annealing/crystallization at high temperatures.[18,44] Again, since C−F dipoles are inclined (Figure 4F), the components of the dipole moment are perpendicular and parallel to the chain axis, and their values are similar to those for the α/δ phases.[42] The β form is often obtained by mechanical stretching or high field poling (400−500 MV/m) of α or γ form samples and has an all-trans conformation.[18,42] The dipoles are perpendicular to the chain axis (Figure 4G) and have the highest dipole moment per chain per repeat unit, i.e., 2.10 D. Because of the large dipole moment, the β form has the highest spontaneous polarization.

Semicrystalline ferroelectric polymers are different from ferroelectric ceramics (usually 100% crystalline) due to their semicrystalline nature. Let us consider a simple serial capacitor model, as shown in Figure 5A, where a ferroelectric PVDF lamella (in β, γ, or δ forms) is sandwiched between two amorphous PVDF layers. Electrodes are in direct contact with the amorphous layers. The chain direction is perpendicular to the external field (i.e., in the horizontal direction). Upon application of an external electric field (E_0) at room temperature, the amorphous dipoles will be polarized first. However, because of a large thermal fluctuation above the T_g of PVDF (−35 to −40 °C[18]), this polarization is usually small. As the external field increases above the coercive field (E_c), dipoles in the ferroelectric PVDF crystal will align along the field direction, thus creating a local depolarization field (E_{depol}) as shown in Figure 5A:[12,45]

$$E_{depol} = \frac{P_{in}}{\varepsilon_0} \quad (1)$$

where P_{in} is the polarization inside the PVDF crystal induced by aligned dipoles. Because E_{depol} is a local electric field, the relative permittivity of the crystal should not appear in the denominator. In turn, the large P_{in} in the PVDF crystal will induce more polarization of the amorphous PVDF at the

dx.doi.org/10.1021/ma2024057 | Macromolecules 2012, 45, 2937−2954

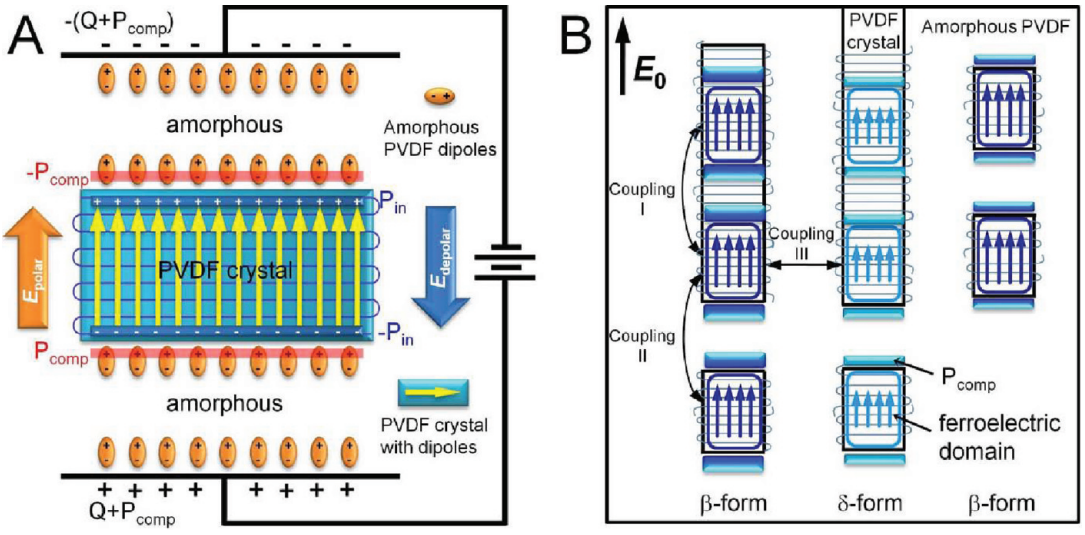


Figure 5. Schematic illustrations of (A) an electrically polarized ferroelectric PVDF crystal sandwiched between two amorphous layers and (B) many electrically polarized ferroelectric PVDF crystals in an amorphous matrix, showing different coupling interactions among ferroelectric domains. The chain direction in the lamellar crystals is perpendicular to the dipole moment or the external electric field E_0.

amorphous−crystalline interface, resulting in an enhanced compensation polarization (P_{comp}) outside the ferroelectric PVDF domain. The P_{comp} in amorphous PVDF is determined by the dipole density in the amorphous phase ($N_{0,am}$), the polarizability for amorphous PVDF (α_{am}), and the local electric field in the amorphous phase ($E_{L,am}$):[12]

$$P_{comp} = N_{0,am}\alpha_{am}E_{L,am} \quad (2)$$

Note that the P_{in} may not equal the P_{comp}, especially during a dynamic poling process. Based on the serial capacitor model in Figure 5A, the local polarization field for the PVDF crystal is imposed from the charges on the electrodes and can be defined as[12,45]

$$E_{pol} = \frac{D}{\varepsilon_0} = \frac{Q + P_{comp}}{\varepsilon_0} \quad (3)$$

where Q is the charge density induced in the vacuum, i.e., $Q = \varepsilon_0 E_0$. Again, E_{pol} is a local electric field, and the relative permittivity should not appear in the denominator.

Dipole switching depends on the local electric field in the crystal ($E_{L,cryst}$), which has at least three sources: (i) E_{pol} (positive), (ii) E_{depol} (negative), and (iii) other contributions from dipoles nearby.[12,13] If we consider that contribution from nearby dipoles can cancel out due to a random orientation, the contribution (iii) may be neglected.[12,13] Then, the local electric field largely depends on the competition between E_{pol} and E_{depol}, which is determined by the relationship between P_{in} and $Q + P_{comp}$. Upon a forward poling, $Q + P_{comp} > P_{in}$ and thus $E_{pol} > E_{depol}$. Crystalline dipoles will be polarized along the external electric field. During a reverse poling process, two scenarios can take place. First, as both E_{depol} and E_{pol} decrease with decreasing the external electric field, at a certain point $P_{in} > Q + P_{comp}$ and then $E_{depol} > E_{pol}$. Fully aligned dipoles will become less stable than they are in a situation where some mobile (or reversible) dipoles revert to the opposite direction, resulting in a minimum (or even net zero) remanent polarization. This behavior is the so-called antiferroelectric-like behavior reported in the literature and will be discussed in detail below (see Figure 11C). Second, when $P_{in} < Q + P_{comp}$ as E_{depol} and E_{pol} decrease with the external field, the E_{depol} turns out to be always lower than the E_{pol}. Therefore, the antiferroelectric-like behavior will not be observed, resulting in normal ferroelectric behavior (see Figure 11A). For ferroelectric polymers, the second scenario is commonly observed and has found numerous practical applications.[18]

When many ferroelectric crystals are polarized by an external electric field, ferroelectric domain coupling[46−48] is realized via induced polarizations (i.e., P_{comp}) from the media (either amorphous or crystalline PVDF) among the domains. Different situations are shown in Figure 5B. First, there are three types of coupling interactions: I (within the ferroelectric crystal), II (between ferroelectric crystals but along the external field direction), and III (between ferroelectric crystals but perpendicular to the external field direction). Note that for the coupling interaction type I the P_{comp} is induced by neighbor domains inside the crystal (i.e., the ferroelectric domain is much smaller than the PVDF crystal; see the top left and top middle panels in Figure 5B), and it may be defined as[12]

$$P_{comp} = N_{0,cryst}\alpha_{cryst}E_{L,cryst} \quad (4)$$

where $N_{0,cryst}$ is the dipole density in the crystalline phase, α_{cryst} the polarizability for crystalline PVDF, and $E_{L,cryst}$ the local electric field in the crystal. Because the coupling interactions are anisotropic,[49] coupling type III is much weaker than coupling types I and II. For ferroelectric polymers, the α_{cryst} is generally higher than the α_{am}, and thus coupling type I is stronger than coupling type II (see the left panel in Figure 5B). Second, dipole moments in β-PVDF crystals are larger than those in δ-PVDF crystals, and thus the local electric field is higher near β domains compared to δ domains. As a result, the P_{comp} induced by β domains is higher than that by δ domains. Therefore, the coupling interactions (types I + II) among β domains are stronger than those among δ domains (see left and middle panels of Figure 5B). Third, when the crystallite size is very small and contains one single ferroelectric domain (right panel of Figure 5B), coupling type I interaction disappears, and thus the overall coupling interaction becomes weaker than the situation where a crystallite contains multiple domains at the same electric field.

From the above discussion, we understand that normal ferroelectricity in ferroelectric polymers originates from high spontaneous polarization (inside the ferroelectric domain) and

dx.doi.org/10.1021/ma2024057 | Macromolecules 2012, 45, 2937−2954

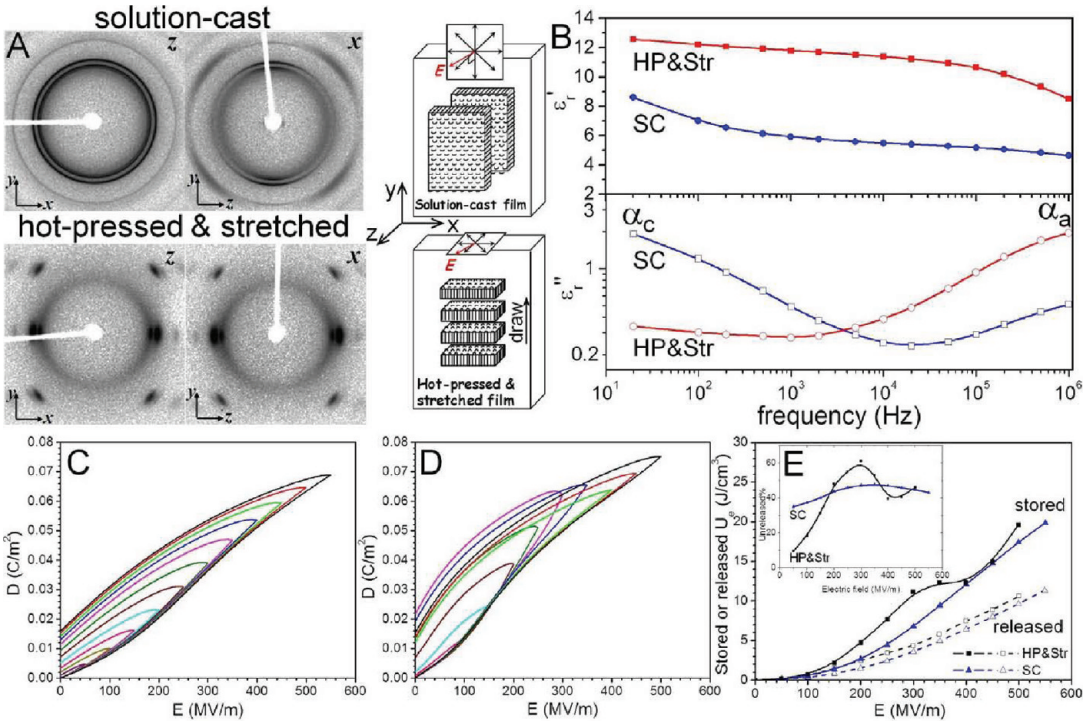


Figure 6. (A) 2D XRD patterns for solution-cast (SC) and hot-pressed/stretched (HP&Str) P(VDF-HFP) 96/4 films along the z and x directions, respectively. Crystal orientations in the SC and HP&Str films are shown in the schematics on the right. (B) Dielectric spectroscopy results: the real part (ε_r') and imaginary part (ε_r'') of relative permittivity as a function of frequency for SC and HP&Str films at room temperature. (C) and (D) show $D-E$ hysteresis loops (10 Hz) at room temperature with a field increment of 50 MV/m. (E) Stored and released energy densities (U_e) and unreleased% (inset) as a function of electric field for SC and HP&Str films. (Reproduced and adapted with permission from ref 65.)

high compensation polarization or interdomain coupling (outside the ferroelectric domain). This high P_{comp} in normal ferroelectric polymers has enabled a number of applications. First, the rectangular-shaped $D-E$ loop (see Figure 11A) enables applications such as nonvolatile capacitor- and transistor-type ferroelectric memories (FeRAMs).[50−54] The advantages of these nonvolatile FeRAMs include fast read/write speed, minimum energy consumption, and long cycle life. P(VDF-*co*-trifluoroethylene) [P(VDF−TrFE)] with a VDF content of 70−75 mol % is usually chosen for polymer FeRAMs because of its large polarization (~0.1 C/m^2), excellent polarization stability, fast switching time (e.g., 20 ns at 840 MV/m for 20 nm thin film[55]), and easy processing.[50,54] In addition, all ferroelectric polymers also possess piezoelectric properties, which have been used for transducers,[18,56] piezo-actuators,[18,57,58] and mechanical energy harvesting devices.[59−61] For these applications, high piezoelectric responses benefit from the large dipolar polarization.

3.2. Crystal Orientation Effect. For high energy density and low loss dielectrics, it is now necessary to understand whether or not normal ferroelectric crystalline polymers are suitable for this application. This is examined by studying effects of crystal orientation, polymorphism, crystallite size (or domain size), and crystallinity for PVDF and its random copolymers. It is known that the dielectric properties of PVDF are anisotropic; namely, the dielectric constants perpendicular and parallel to the chain axes are different.[62−64] In a recent study, this crystal orientation effect is revisited with an emphasis on the charge and discharge behaviors for electric energy storage.[65] Corresponding results are shown in Figure 6. In this study, P(VDF-*co*-hexafluoropropylene) [P(VDF−HFP) 96/4 (mol/mol)] films with chain axes parallel and perpendicular to the film normal direction are obtained by solution-casting (SC) and hot-pressing and stretching (HP&Str), respectively. Two-dimensional (2D) X-ray diffraction (XRD) patterns in Figure 6A prove these different crystal orientations (see the schematics on the right). From analyses of these XRD patterns, the SC film contains 40.8% pure α-form, and the HP&Str film contains 32.9% α-form and 7.3% β-form because of mechanical stretching at 110 °C. Frequency-dependent low-field dielectric spectroscopy results at room temperature are shown in Figure 6B. The HP&Str film exhibits a higher (nearly twice) ε_r' than the SC film because the component dipole moment perpendicular to the chain axis (1.20 D) is higher than that parallel to the chain (1.02 D) for α-form PVDF and a small amount (7.3%) of β-form exists in the HP&Str film. From the ε_r'', two (half) relaxation peaks are observed at both low and high frequencies, respectively. The relaxation peak centered around 10 Hz (the α_c relaxation) is attributed to the dipole relaxation along the chain axes of the α-form,[25,62,66] and the relaxation peak around 1 MHz (the α_a relaxation) is attributed to both amorphous dipoles[66−68] and dipoles at the crystal/amorphous interfaces.[69] Note that the interface between crystalline and amorphous phases for α-form PVDF is not sharp because the TG conformation can exist in both amorphous and crystalline phases. From the loss dielectric constant results in Figure 6B, it is obvious that the SC film with a perpendicular crystal orientation is undesired for high energy density and low loss dielectrics because the α_c relaxation at 10 Hz is within the power frequency range. Instead, the HP&Str film with a parallel crystal orientation may be a better candidate because the α_a relaxation peak is around 1 MHz and can be shifted to higher frequencies with increasing the temperature.[62,67,68] We therefore

dx.doi.org/10.1021/ma2024057 | *Macromolecules* 2012, 45, 2937−2954

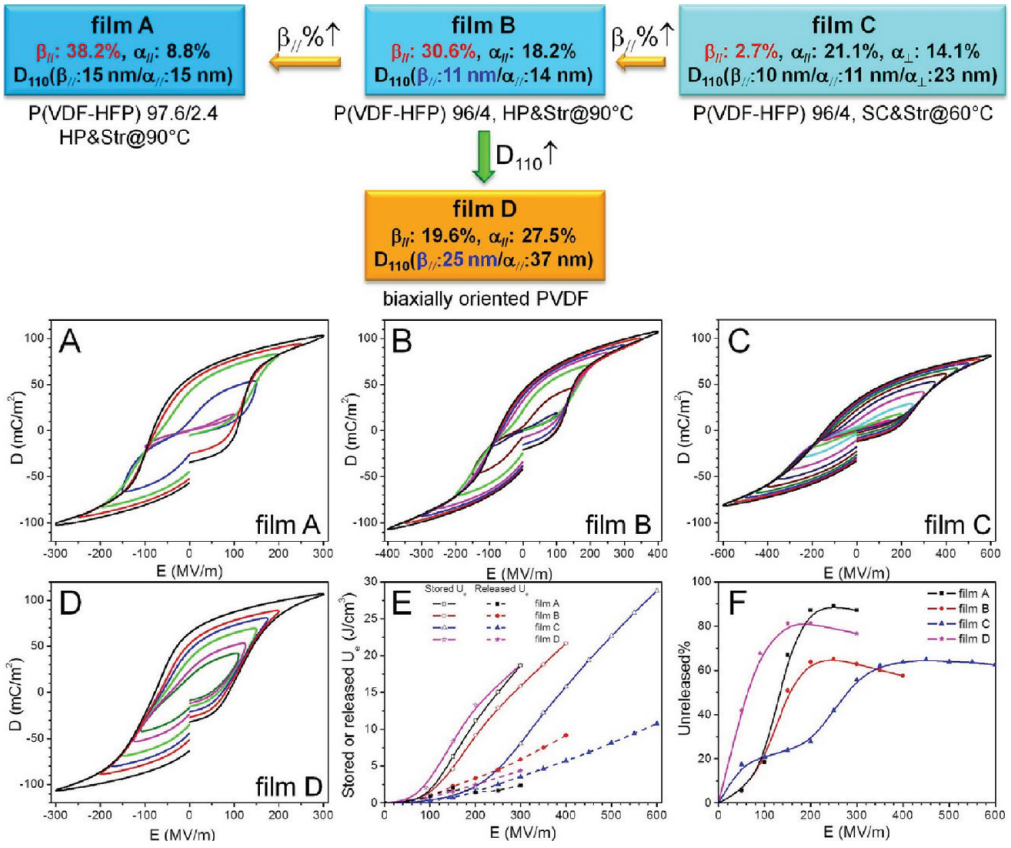


Figure 7. (top) Schematic illustration of PVDF and P(VDF−HFP) films A−D with different β and α contents obtained by different processing conditions. SC&Str and HP&Str stand for "solution-cast and stretched" and "hot-pressed and stretched", respectively. The crystallite size along the [110] direction, the D_{110} for both α and β phases, are estimated by the Scherrer equation. The symbols "||" and "⊥" stand for the chain axes parallel and perpendicular to the film, respectively. (bottom) (A−D) Bipolar $D-E$ hysteresis loops at 10 Hz for films A−D, respectively. (E) Stored and released energy densities and (F) unreleased% as a function of electric field for films A−D, respectively. [Reproduced with permission from refs 70 and 71 (Copyright 2011 IEEE).]

consider that the parallel PVDF crystal orientation may work better at elevated temperatures for the low loss purpose.

The high-field performance is studied by unipolar hysteresis loops shown in Figures 6C and 6D for the SC and HP&Str films, respectively. Corresponding stored and released energy densities are calculated from these polarization loops (see Figure 6E). The unreleased%, defined as $100(1 - U_{e,released}/U_{e,stored})$, is shown as the inset in Figure 6E. In spite of high energy storage (i.e., up to 20 J/cm^3 at 500−550 MV/m), the discharged energy densities are only ~11 J/cm^3 for samples with different crystal orientations. In other words, high values of unreleased% are obtained at high fields. In accordance with the low-field dielectric spectroscopy study, the SC film with a perpendicular crystal orientation shows high unreleased% values from 50 to 600 MV/m; therefore, perpendicular crystal orientation in α-form PVDF indeed is undesired for high energy density and low loss dielectrics. On the other hand, the HP&Str film shows a higher $U_{e,released}$ but a lower unreleased% than the SC film at low fields (<150 MV/m). Therefore, the parallel crystal orientation does appear to be better in terms of low hysteresis loss at low fields. Nonetheless, with increasing the poling field to above 200 MV/m, the unreleased% significantly increases due to the irreversible $\alpha \rightarrow \delta \rightarrow \beta$ phase transformations upon repeated electric poling, as evidenced by the Fourier transform infrared (FTIR) study.[65] Therefore, even though the parallel crystal orientation in α-form PVDF favors high energy storage and low hysteresis loss, the irreversible $\alpha \rightarrow \delta \rightarrow \beta$ phase transformations upon repeated poling at high enough fields prevent it from being suitable for high energy density and low loss dielectrics.

3.3. Polymorphism and Crystallite Size Effects. Effects of polymorphism and crystallite size are studied via a series of PVDF and P(VDF−HFP) films obtained by different processing conditions, as shown in the top panel of Figure 7.[70,71] From film C to films B and A, the β content gradually increases from 2.7% to 38.2%. The crystallite sizes in films A−C are relatively small, ranging from 10 to 15 nm for parallel β crystals. Instead, the biaxially oriented PVDF has an intermediate β content of 19.6% and a large crystallite size of 25 nm for parallel β crystals. Bipolar $D-E$ hysteresis loops for films A−D are shown in Figures 7A−D, respectively. It is obvious that a high β content (film A) and a large crystallite size (film D) favor normal ferroelectric (or rectangular-shaped) loops because of high coupling interactions (or P_{comp}) among large β domains (see discussion for Figure 5B). Although both films A and D exhibit the highest charged energy densities, they have low released energy densities (Figure 7E) and high hysteresis losses (Figure 7F). Different from films A and D, film C with the lowest β content and small parallel crystallite sizes shows a much lower stored energy density but a similar released energy density (Figure 7E). As a result, the unreleased% for film C is much lower than those for films A and D (Figure 7F). This result is consistent with recent reports that parallel α-crystals are favorable for high energy density dielectrics.[72−75] Intriguingly,

dx.doi.org/10.1021/ma2024057 | Macromolecules 2012, 45, 2937−2954

film B with an intermediate β content but a small crystallite size exhibits narrower hysteresis loops (Figure 7B) than films A and D. As a result, its released energy density is the highest among all films (Figure 7E), and its unreleased% is similar to that of film C with the lowest β content. This can be explained by the schematic illustration in the right panel of Figure 5B, where the intracrystal coupling type I interaction is missing for small crystallites, each of which may contain only one ferroelectric domain. From this result, it seems that small crystallites favor narrower hysteresis loops for high energy density and low loss dielectrics. In the future, it is necessary to further decrease the crystallite size of parallel β crystals to be even smaller (e.g., a few nanometers) and examine whether or not the hysteresis loop will decrease.

3.4. Crystallinity Effect. Finally, the crystallinity effect on electric energy storage has not been well-understood in the literature. By using P(VDF-HFP) samples with different HFP contents (see Table 1), the crystallinity effect is studied by unipolar $D-E$ loop tests as shown in Figure 8. Because the HFP comonomer is too large to be included in PVDF crystals, the overall crystallinities for films I, II, and III can be adjusted to 46.4, 31.9, and 25.4 wt % by increasing the HFP content. All films are hot-pressed and uniaxially stretched at 90 °C to a final draw ratio of 450−550%. Both α and β crystals are parallel to the stretching direction as determined by 2D XRD and their contents are shown in Table 1. As the overall crystallinity decreases from film I to film III, the hysteresis loops become continuously slimmer with a gradually decreased maximum electric displacement (D_{max}, see Figure 8A−C). Under relatively low electric fields, D_{max} and remanent electric displacement (D_{rem}) gradually increase with increasing the electric field (Figure 8D). Judging from the D_{max}, dipole saturation for films I and II takes place around 200 MV/m while it occurs around 300 MV/m for film III. After dipole saturation, the further increase in D_{max} with the electric field primarily originates from electronic and atomic polarizations.[76] Assuming the theoretical maximum polarization for β-PVDF is 130 mC/m^2,[77] the percentages of polarized dipoles at 350 MV/m are roughly 77%, 68%, and 47% for films I−III, respectively, much higher than their overall crystallinities. This result indicates that besides crystalline dipoles, part of the amorphous dipoles should also be polarized and contributes to the observed D_{max}. This is consistent with the above discussion for Figure 5A. With decreasing the overall crystallinity, the D_{max} at dipole saturation gradually decreases, indicating that the saturation polarization is dependent on the overall crystallinity in the sample. However, this dependence is not a simple linear relationship. For example, the overall crystallinity drop from film I to film II (14.5 wt %) is much larger than that (6.5 wt %) from film II to film III. However, the decrease in D_{max} from film I to film II is smaller than that from film II to film III. This nonlinearity may be explained using the schematic in Figure 5B. With decreasing the overall crystallinity, PVDF crystals are further separated from one another, and the intercrystal coupling type II interaction will gradually decrease. Similar to the particle−particle interaction, this coupling type II interaction should not be a linear function of the intercrystal distance. Above a certain distance, the coupling type II interaction may disappear, resulting in a much lower P_{comp} or D_{max}. A similar trend as the D_{max} is also observed in the stored energy density results in Figure 8E. With decreasing the overall crystallinity, the D_{rem} also decreases (Figure 8D) and results in a reduced released energy density (Figure 8E). Again, the nonlinear relationships with the overall crystallinity are observed for the D_{rem} and released energy density. From Figure 8F, the unreleased% slightly decreases with decreasing the overall crystallinity. Given only three samples, it is not certain below which overall crystallinity the coupling type II interaction will disappear. In the future, more detailed studies on a series of samples with different overall crystallinities but a similar amorphous phase (e.g., in terms of polarizability) are desired. We speculate that with further decreasing the overall crystallinity to below 15−20 wt % the D_{max} and D_{rem} will further decrease and the hysteresis loops will become even narrower and/or linear.

Table 1. P(VDF−HFP) Films with Different Overall Crystallinities

film	HFP (wt %)	overall x^c (wt %)	normalized x^c (wt %)	T_m (°C)	$\alpha_\parallel$ (%)	$\beta_\parallel$ (%)
I	3.2	46.4	47.9	159	26.2	20.1
II	10.9	31.9	35.8	144	4.0	28.0
III	15.4	25.4	30.0	132	14.3	9.3

4. PARAELECTRIC CRYSTALLINE POLYMERS

By definition, paraelectricity refers to the ability of materials to become polarized under an electric field and upon removal of the applied field the polarization returns to zero.[78] In addition, from a structure point of view, paraelectric polymers should contain polar groups but have a nonpolar crystalline phase. A famous paraelectric polymer is the P(VDF-*co*-trifluoroethylene) [P(VDF−TrFE)] random copolymer at high temperatures. When VDF is copolymerized with TrFE or tetrafluoroethylene (TFE), the lateral dimensions of the unit cell are enlarged by the inclusion of bulky TrFE and TFE comonomers because of isomorphism.[79] Intriguingly, the enlarged lateral dimensions of the unit cell weaken the intermolecular interactions among P(VDF−TrFE) chains and thermodynamically destabilize the ferroelectric phase with all trans zigzag chain conformation. As a result, the ferroelectric-to-paraelectric Curie transition temperature (T_C) decreases from just below the melting temperature (T_m) for β-PVDF to temperatures significantly below the T_m depending on the TrFE content. A typical phase diagram for P(VDF−TrFE) is shown in Figure 9A.[80] At low temperatures, the low-temperature ferroelectric (LTFE) phase is kinetically favored, and the P(VDF−TrFE) samples crystallize exclusively into the LTFE phase (see the left panel in Figure 9B).[81] This is different from PVDF because the α-form is kinetically favored and PVDF exclusively crystallizes into the α-form under a normal cooling condition from the melt. Above the T_C, a high temperature paraelectric (HTPE) phase is observed with further enlarged lateral unit cell dimensions (see the right panel in Figure 9B).[81] After cooling, a cooled ferroelectric (CLFE) phase is obtained with a certain amount of disordered trans−gauche bonds forming the domain boundaries (see the middle panel of Figure 9B).[81] Upon thermal annealing at high temperatures or electric poling, these domain boundaries can be annihilated and the CLFE phase can return to the LTFE phase.[82]

Ferroelectric properties of the LTFE phases in P(VDF−TrFE) have been extensively studied for applications such as nonvolatile FeRAMs and piezoelectric transducers, as described above. In the vicinity of T_C, the dielectric and ferroelectric properties exhibit anomalies; the dielectric constant and heat capacity show a maximum, remanent polarization decreases

dx.doi.org/10.1021/ma2024057 | Macromolecules 2012, 45, 2937−2954

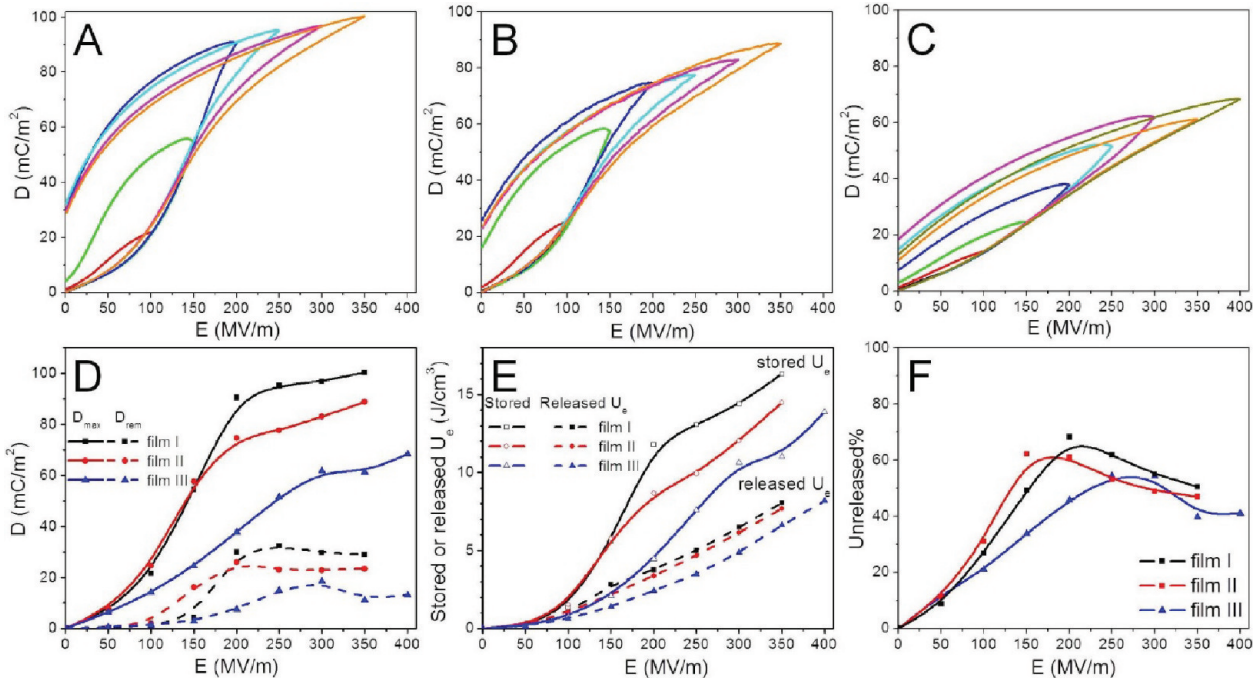


Figure 8. Unipolar $D-E$ hysteresis loops for P(VDF−HFP) films with different overall crystallinities: (A) x^c = 46.4 wt %, (B) x^c = 31.9 wt %, and (C) x^c = 25.4 wt %. (D, E) Stored and released energy densities (U_e) and (F) unreleased% as a function of electric field for P(VDF−HFP) films I, II, and III.

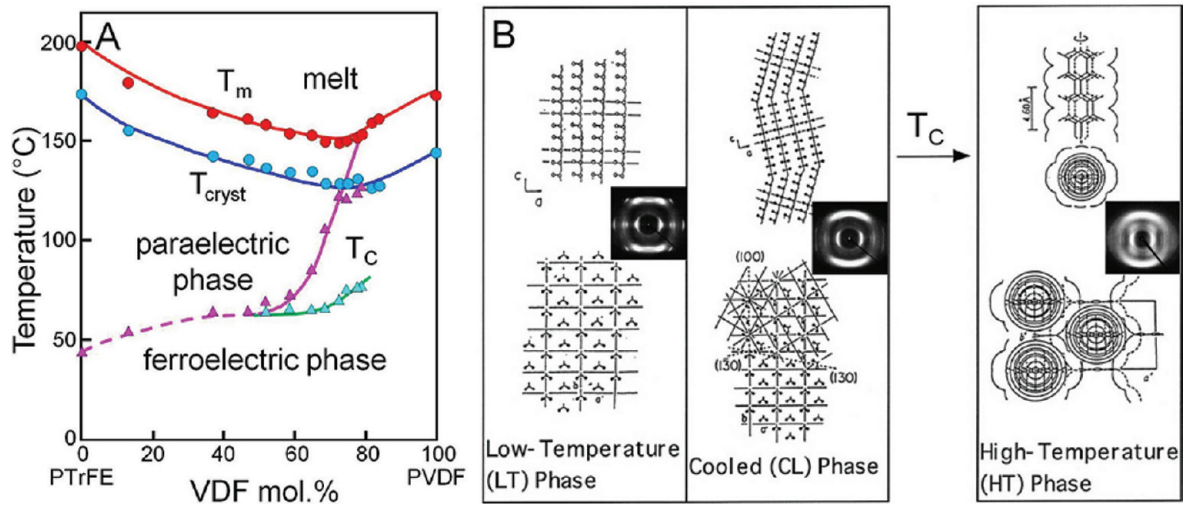


Figure 9. (A) Phase diagram for P(VDF−TrFE) copolymers. T_m: melting temperature; T_{cryst}: crystallization temperature; T_C: Curie temperature (magenta: heating; green: cooling). (Reproduced with permission from ref 80. Copyright 1997 Elsevier.) (B) Crystal structures of P(VDF−TrFE) copolymers. Corresponding XRD patterns are shown as the insets. The vertical axis is parallel to the draw direction. (Reproduced with permission from ref 81. Copyright 2006 Elsevier.)

to zero, and piezoelectric coefficients disappear. All these anomalies can be attributed to the ferroelectric-to-paraelectric phase transition in P(VDF−TrFE) copolymers. Upon heating, the dielectric constant shows a relatively sharp peak, and the peak temperature increases with increasing the applied frequency.

Recently, we have studied the paraelectric properties of a uniaxially oriented P(VDF−TrFE) 50/50 (mol/mol) film by poling the sample at different frequencies in the HTPE phase (at 100 °C, T_C = 64 °C).[83] As shown in Figure 10A, typical paraelectric hysteresis loops are observed when the poling frequency is as high as 1000 Hz. This can be attributed to the high mobility of crystalline dipoles in the HTPE phase. However, when the poling frequency is reduced to 1 Hz, a significant broadening of the hysteresis loops is observed (Figure 10B). Above 100 MV/m, typical ferroelectric polarization loops are observed. These results can be explained using the schematics in the insets of Figure 10. At a high poling frequency (e.g., 1000 Hz), the poling time is short and only small size ferroelectric domains are induced in the paraelectric matrix by the applied electric field. As the poling frequency decreases to 1 Hz, the poling time is long enough to grow the small ferroelectric domains into relatively large domains. As a result, typical ferroelectric hysteresis loops are observed. From this study, we conclude that paraelectric property is poling

dx.doi.org/10.1021/ma2024057 | *Macromolecules* 2012, 45, 2937−2954

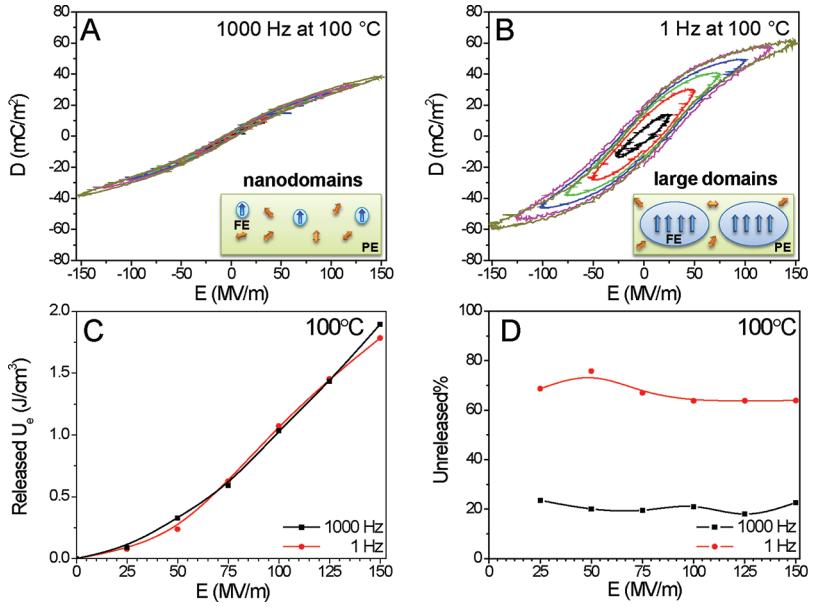


Figure 10. Bipolar *D*–*E* hysteresis loops for a uniaxially oriented P(VDF–TrFE) 50/50 (mol/mol) random copolymer at (A) 1 Hz and (B) 1000 Hz at 100 °C. The Curie temperature (T_C) for P(VDF–TrFE) 50/50 is 64 °C. (C) Released energy density and (D) unreleased% as a function of the electric field. (Reproduced with permission from ref 83. Copyright 2011 Elsevier.)

frequency dependent, similar to our recent report that poling frequency strongly influences the charging behavior of ferroelectric polymers.[84] The released energy densities for the bipolar polarization at 1000 and 1 Hz are nearly the same (Figure 10C). However, the unreleased% for the 1000 Hz bipolar polarization is as low as ca. 20%, much smaller than that (ca. 70%) for the 1 Hz bipolar polarization (Figure 10D).

5. NOVEL FERROELECTRIC POLYMERS TOWARD HIGH ENERGY DENSITY AND LOW LOSS DIELECTRICS

From the above discussion, the normal ferroelectric behavior in polymers (Figure 11A) has not yet met the requirements for high energy density and low loss dielectrics because the unreleased% of 40–60% is too high for real-world applications. Meanwhile, truly reversible paraelectric crystalline polymers so far are quite limited [e.g., only the HTPE phase of P(VDF–TrFE)], and a long time poling will result in normal ferroelectric behavior. Novel ferroelectric behaviors in polymers, such as the relaxor ferroelectric and antiferroelectric behaviors (Figure 11B,C), are thus desirable for high energy density and low loss dielectrics. Both relaxor ferroelectric[46,85] and antiferroelectric[86] phases are well-known for perovskite-type (ABO_3) ceramics. For example, relaxor ferroelectrics belong to a class of disordered crystals with compositional nanodomains. At high temperature, they are in the nonpolar paraelectric phase, which is similar to the cubic perovskite structure. Upon cooling to below the so-called Burns temperature, they transform into the ergodic relaxor state, where nanosized polar (or ferroelectric) domains with randomly distributed dipole directions develop inside the paraelectric matrix. In other words, relaxor ferroelectrics are ferroelectrics with diffuse phase transitions. For ABO_3 perovskites, the disordered arrangement of different ions on the crystallographically equivalent sites is the common feature of relaxors. The difference between relaxor ferroelectrics and paraelectrics is that at zero electric field relaxor ferroelectrics contain ferroelectric nanodomains while paraelectrics do not. Therefore, the advantage of relaxor ferroelectrics is that they may charge and discharge more energy density than paraelectrics but still keep relatively low hysteresis loss.

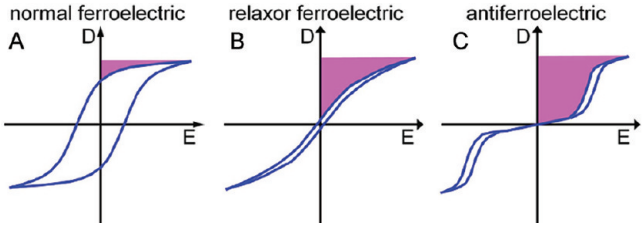


Figure 11. Schematic *D*–*E* hysteresis loops for (A) normal ferroelectric, (B) relaxor ferroelectric, and (C) antiferroelectric behaviors. The shaded areas represent the released energy density.

Antiferroelectric ceramics[86] and liquid crystals[87] belong to a class of ordered structures, which can be considered as being composed of two sublattices polarized spontaneously in antiparallel directions and can be polarized into a ferroelectric phase upon applying an electric field. In other words, antiferroelectricity is defined based on both crystal structures and electrical behavior. For ceramics, the antiferroelectric behavior is often found in lead-containing perovskite-type families such as $PbZrO_3$. The origin of antiferroelectricity in these ceramic oxides is considered to be the small difference in free energy of the ferroelectric and antiferroelectric states, and a sufficient electric field disturbance can induce the antiferroelectric-to-ferroelectric transition. For liquid crystals, the antiferroelectric phase has been observed for both chiral and achiral molecules with a D_2 symmetry (having two C_2-axes with P_x parallel to the tilt plane and P_y perpendicular to the tilt plane). So far, its origin has been attributed to several molecular interaction models, including a dipole pairing model, a P_x–P_x interaction model, and a steric interaction model.[87] Although relaxor ferroelectric and antiferroelectric phases are relatively well-understood for ceramics and liquid crystals, these behaviors are still new for crystalline polymers and their fundamental mechanisms

dx.doi.org/10.1021/ma2024057 | *Macromolecules* 2012, 45, 2937–2954

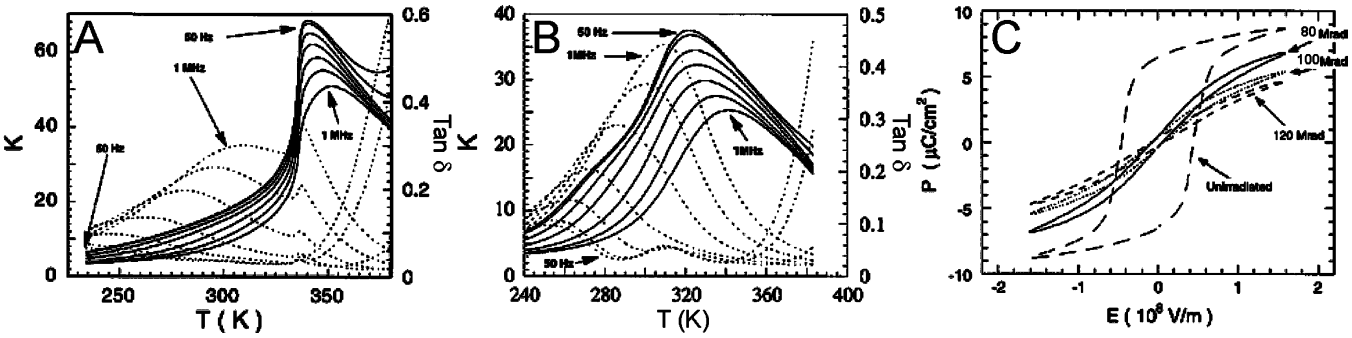


Figure 12. Dielectric spectroscopy results of dielectric constant and dissipation factor (tan δ) as a function of temperature for (A) unirradiated and (B) irradiated (80 Mrad at room temperature) P(VDF−TrFE) 50/50 copolymer. Frequencies are 50 Hz, 100 Hz, 1000 Hz, 100 kHz, 400 kHz, and 1 MHz. (C) Polarization hysteresis loops for P(VDF−TrFE) 50/50 copolymer measured at room temperature before and after electron irradiation. (Reproduced with permission from ref 89. Copyright 1998 Maney Publishing.)

have not yet been fully understood. In the following sections, we will discuss experimental observation and understanding of these novel ferroelectric behaviors in crystalline polymers.

5.1. Relaxor Ferroelectric Behavior in Polymers. The relaxor ferroelectric behavior is first reported for electron-beam-irradiated P(VDF−TrFE) random copolymers.[88] Since then, several methods have been used to achieve the relaxor ferroelectric behavior in polymers. First, ionizing irradiation (electron beam, γ-ray, and proton) is found to induce the ferroelectric-to-paraelectric phase transition by introducing structural defects in the crystalline lattice.[88−101] Similar to the HTPE phase, the irradiation-induced paraelectric phase also has enlarged lateral unit cell dimensions. The ferroelectric-to-paraelectric transition for the irradiated copolymer becomes much broader than that for the unirradiated copolymer (Figure 12A), and the T_C decreases to around room temperature at a high enough irradiation dose (Figure 12B).[89] Intriguingly, slim polarization hysteresis loops, reminiscent of the relaxor ferroelectric behavior in ceramics,[46,85] are obtained for properly irradiated P(VDF−TrFE) films (Figure 12C).[89] These slim polarization hysteresis loops with high maximum polarization can enable practical applications such as electrostriction.[88,89,102−104] However, because of the cross-linking of the amorphous phase in P(VDF−TrFE), structural defects in the crystalline phase are difficult to be identified. Later, solid-state fluorine nuclear magnetic resonance (^{19}F NMR) studies on electron-beam-irradiated P(VDF−TrFE) reveals that a certain amount (2 mol %) of short side groups such as $\rangle$CH−CF$_3$ are introduced into the main chain by electron beam irradiation.[105,106] Although the solid-state ^{19}F NMR gives information mostly from the amorphous phase, we speculate that similar structural defects (i.e., −CF$_3$ side groups) should also be introduced in the crystalline phase. It should be these CF$_3$ side groups that expand the lateral dimensions of the unit cell and result in the formation of the paraelectric phase at room temperature. Similar structural defects in the crystalline phase are also observed in ethylene/α-olefin copolymers, and the corresponding isomorphism is extensively studied.[79,107−109] Nevertheless, further experimental study is needed to understand what structural defects are introduced in the crystalline phase of P(VDF−TrFE) by electron beam irradiation.

In the second method, structural defects can be purposely incorporated into the PVDF main chain to induce room temperature paraelectric phase. For example, with systematically increasing the HHTT content from 3.5 to 6 mol % for PVDF homopolymers to 14.0 mol %, the α-form transforms into the ferroelectric form at room temperature.[110] With further increasing the HHTT content to 15.5 mol % and above, a paraelectric phase with larger lateral unit cell dimensions is observed at room temperature. Later, bulky comonomers such as chlorofluoroethylene (CFE), chlorodifluoroethylene (CDFE), chlorotrifluoroethylene (CTFE), and even HFP are purposely introduced into P(VDF−TrFE) to form defect-modified terpolymers.[111,112] A similar relaxor ferroelectric behavior as that in electron-beam-irradiated P(VDF−TrFE) is observed at room temperature in P(VDF−TrFE−CFE), P(VDF−TrFE−CDFE), and P(VDF−TrFE−CTFE) terpolymers with proper comonomer compositions.[96,102,104,113−124] The narrow hysteresis loops in these terpolymers enable a number of applications such as electric energy storage[72,75,125−127] and electrocaloric refrigeration.[128−131] Compared with the P(VDF−TrFE) copolymer, lateral unit cell dimensions of the terpolymers are further enlarged by the incorporation of bulky CTFE and CFE comonomers in the crystalline phase, as revealed by XRD.[116,127,132] Meanwhile, the T_C decreases to around room temperature, and the ferroelectric-to-paraelectric phase transformation becomes broad. However, P(VDF−TrFE−HFP) copolymer does not show the relaxor ferroelectric behavior because the HFP comonomer is too large to be included in the crystalline lattice.[112,133] As shown in Figure 13A, P(VDF−TrFE−CTFE) terpolymers exhibit a high dielectric constant (~50 at 1 kHz) at an optimal composition at room temperature: VDF% ~ 79 mol %, TrFE% ~ 7 mol %, and CTFE% ~ 14 mol %.[127,134−136] This can be explained by the decreased T_C to room temperature and relaxor ferroelectric behavior for the terpolymers. Figure 13B shows narrow hysteresis loops for a P(VDF−TrFE−CFE) terpolymers at room temperature.[126] The discharged energy densities of different P(VDF−TrFE−CFE) terpolymers are shown in Figure 13C.[126] For a specific terpolymer, the discharged energy density reaches as high as ~10 J/cm^3 at 400 MV/m. Because of the slim hysteresis loops, the unreleased% appears to be fairly low (~20% in Figure 13D). Therefore, P(VDF−TrFE)-based terpolymers are suitable for high energy density and low loss dielectrics. In the future, effects of comonomer type, composition, and temperature on the crystallization behavior as well as dielectric and ferroelectric properties need to be systematically studied to further improve their relaxor ferroelectric property for high energy density and low loss dielectrics.

Recently, the relaxor ferroelectric behavior is reported for a P(VDF−TrFE) 66/34 copolymer synthesized from reductive dechlorination of the corresponding P(VDF−CTFE) 66/34

dx.doi.org/10.1021/ma2024057 | Macromolecules 2012, 45, 2937−2954

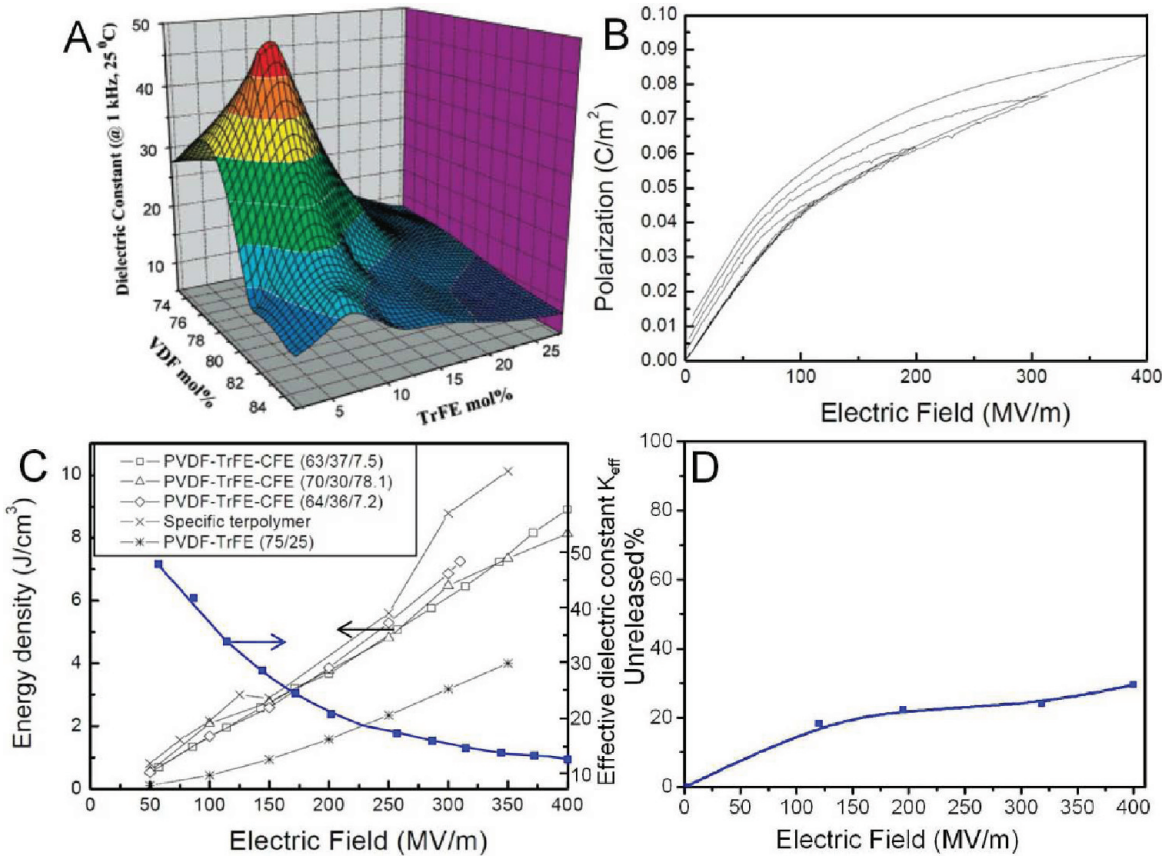


Figure 13. (A) Dielectric constant (at 1 kHz) as a function of VDF and TrFE contents for P(VDF−TrFE−CTFE) terpolymers at room temperature. (Reproduced with permission from ref 134.) (B) Unipolar hysteresis loops (10 Hz) for P(VDF−TrFE−CFE) copolymers at room temperature. (C) Released energy density and (D) unreleased% as a function of electric field at room temperature for different P(VDF−TrFE−CFE) terpolymers. (Reprinted with permission from ref 126. Copyright 2006 IEEE.)

at 100 °C.[137,138] A high content of HHTT defects in the sample is used to explain the high temperature relaxor ferroelectric behavior and a high T_m of ~200 °C. Meanwhile, on the basis of the dielectric spectroscopy study, a relaxor ferroelectric-like behavior is also observed during cooling for a P(VDF−TrFE) 70/30 copolymer at high frequencies (>10^5 Hz)[139,140] because the paraelectric-to-ferroelectric transition is much broader and the observed ε_r' is significantly lower during cooling than during heating. We speculate that structural defects such as the disordered trans−gauche conformation in the cooled ferroelectric phase may be responsible for the observed relaxor-like behavior during cooling under high frequencies.

In spite of numerous reports on the relaxor ferroelectric behavior since its discovery in P(VDF−TrFE)-based ferroelectric polymers,[88,89] the underlying physics is yet to be well-understood. We speculate that the origin for the relaxor ferroelectric behavior in polymers is similar to that for relaxor ferroelectric ceramics,[46,85] i.e., ferroelectric nanodomains dispersed in a compositionally disordered paraelectric matrix. The only difference between ferroelectric polymers and ceramics is that the polarization mechanism is orientational for polymers and atomic for ceramics. The concept of ferroelectric nanodomains and reversible nonpolar−ferroelectric (α−β) phase transitions are used to explain the high energy storage in PVDF copolymers in a recent computer simulation using the density function theory.[141] Currently, there are no effective experimental methods to directly visualize and determine the size of ferroelectric nanodomains in polymers. Our hypothesis will need to wait for experimental and/or theoretical proof in the future. Only after we fully understand the underlying physics of the relaxor ferroelectric behavior can we design new ferroelectric polymers for high energy density and low loss dielectrics.

5.2. Nanoconfined Ferroelectric Behavior in Polymers. Although the relaxor ferroelectric behavior is a good candidate, the antiferroelectric behavior with minimum hysteresis in the antiferroelectric ↔ ferroelectric transitions and a zero D_{rem} appears to be a better choice for high energy density and low loss dielectrics (see Figure 11C). So far, no genuine antiferroelectric crystalline phase has been identified for polymers. In the future, research is needed to discover crystalline polymers with true antiferroelectric phases and study whether or not the antiferroelectric ↔ ferroelectric phase transition is reversible with minimum hysteresis.

However, an antiferroelectric-like behavior with a reduced or minimum remanent polarization (P_r) in the P−E hysteresis loop study has been experimentally observed. Strictly speaking, because of the nonzero P_r, this behavior is more appropriate to be termed as ferrielectric, similar to that for liquid crystals,[142,143] rather than antiferroelectric. However, to be consistent with the literature, we still use the antiferroelectric-like terminology here. The antiferroelectric-like behavior with double hysteresis loops is first reported for β-PVDF at temperatures below −60 °C[144] and P(VDF−TrFE) with the VDF content less than 50 mol %.[145−147] The double hysteresis loop consists of a dipole depolarization step at low fields and a polarization reversal step at high fields, and it only appears in the first a few cycles and eventually transforms into a single

dx.doi.org/10.1021/ma2024057 | Macromolecules 2012, 45, 2937−2954

hysteresis loop upon repeated cycling. Therefore, this behavior is attributed to imperfect P(VDF−TrFE) crystals cooled from the melt with the coexistence of ferroelectric and paraelectric phases.[147] Later, it is attributed to the nonpolar "antiferroelectric-like phase" in P(VDF−TrFE).[54,80,148,149] Recently, we explain the antiferroelectric-like behavior as a rather universal phenomenon for semicrystalline ferroelectric polymers, using the model shown in Figure 5A.[70,150] According to this explanation, double hysteresis loops will take place as long as $Q + P_{comp} < P_{in}$. In other words, when the local E_{depol} becomes higher than the local E_{pol} during discharging, part of aligned dipoles or domains in the poled ferroelectric crystal will depolarize and revert back to their original direction, resulting in a minimum P_r at zero electric field.

There are several methods to achieve the antiferroelectric-like behavior in ferroelectric polymers.[70,150] First, decreasing the polarizability of the amorphous phase at the amorphous/crystal interface can directly result in a lower $Q + P_{comp}$ (or E_{pol}) than P_{in} (or E_{depol}). For example, decreasing the temperature to below the T_g can effectively reduce the polarizability of the amorphous phase due to frozen dipoles. As a result, double hysteresis loops are observed for β-PVDF at temperatures below −60 °C.[144] Second, P_{comp} will be low when the poling field and temperature are relatively low. This is exactly observed for PVDF and P(VDF−HFP) in Figures 6−8. Third, P_{comp} will be low when the dipole moment per repeat unit in a chain is decreased. Several cases could fit into this category. For example, double hysteresis are easily observed in P(VDF−TrFE) copolymers with >50 mol % TrFE, rather than in β-PVDF, because the dipole moments per repeat unit in a chain for TrFE and β-PVDF are 1.05 and 2.1 D, respectively. Double hysteresis loops are also observed in α/δ-PVDF since the component dipole moment perpendicular to the chain axis per chain per repeat unit is only 1.20 D.

To test the above hypothesis that the antiferroelectric-like behavior is a result of a lower $Q + P_{comp}$ (or E_{pol}) than P_{in} (or E_{depol}) during reverse poling, we confined ferroelectric PVDF crystals with a low polarizability polymer such as PS to purposely reduce $Q + P_{comp}$ (see Figure 14F). To achieve this, PS side chains are grafted from a P(VDF−TrFE−CTFE) 88.2/7.7/3.5 terpolymer using atom transfer radical polymerization (ATRP),[150] following an established method in the literature.[151] Dechlorination by n-Bu_3SnH is conducted to avoid cross-linking of the graft copolymer under further thermal treatments. Proton (^{1}H) NMR result shows that the PS content is 14 wt %, corresponding to 3.2 styrene repeating units per PS side chain. A P(VDF−TrFE) 93/7 (mol/mol) copolymer is used as a control to compare with the graft copolymer. P(VDF−TrFE) 93/7 and P(VDF−TrFE−CTFE)-g-PS(14%) films are obtained by hot-pressing at 240 °C followed by uniaxial stretching at 110 °C. The 2D XRD patterns in the insets of Figure 14A,B indicate that the chains in the P(VDF−TrFE) crystals are parallel to the stretching direction. Bipolar D−E hysteresis loops for P(VDF−TrFE) 93/7 and

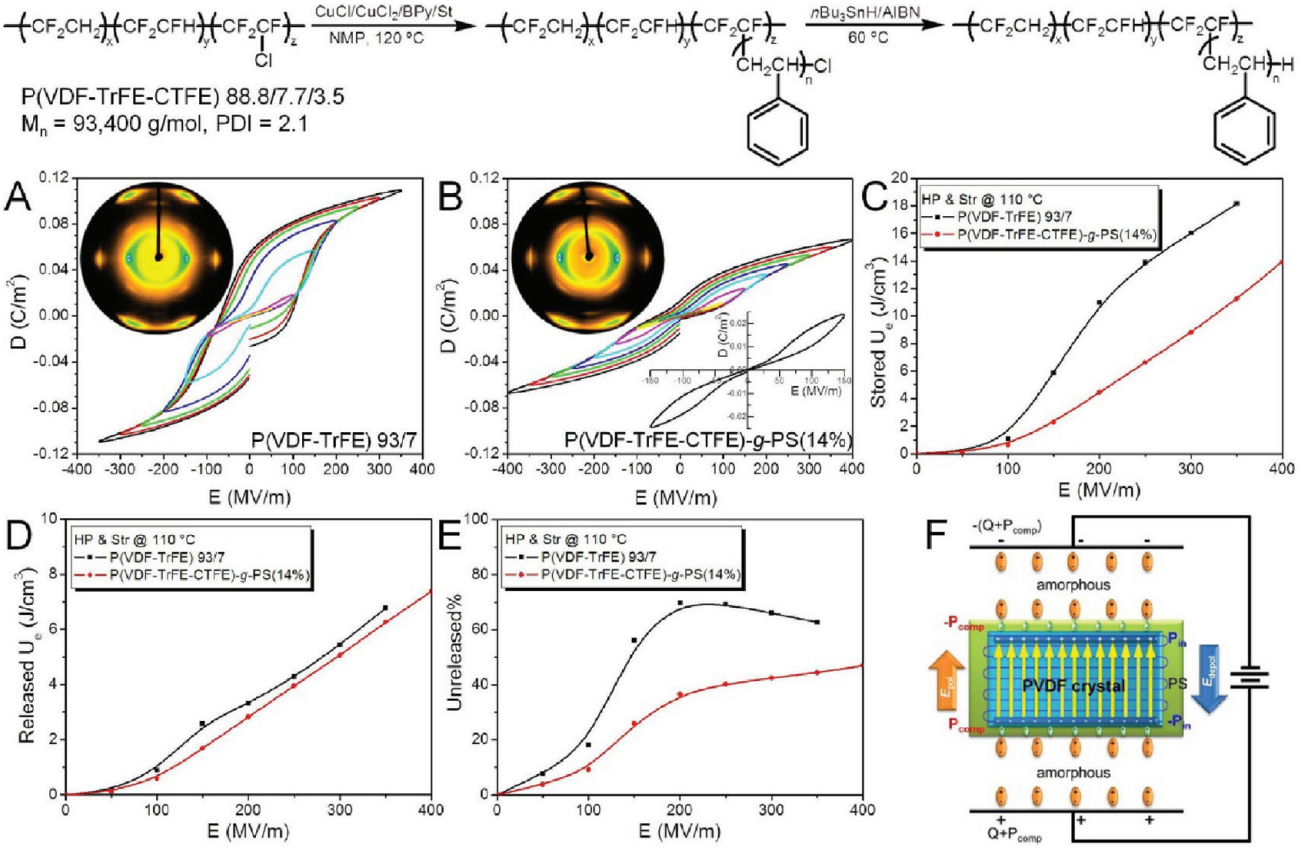


Figure 14. (top) Synthesis of P(VDF−TrFE−CTFE)-g-PS graft copolymer from the P(VDF−TrFE−CTFE) terpolymers using atom transfer radical polymerization followed by dechlorination. (A, B) Bipolar D−E hysteresis loops for uniaxially stretched P(VDF−TrFE) 93/7 and P(VDF−TrFE−CTFE)-g-PS(14%) films. Corresponding 2D XRD patterns are shown as insets. A D−E loop for the graft copolymer at a poling field of 150 MV/m is shown as inset in (B). (C, D) Stored and released energy densities and (E) unreleased% as a function of electric field for P(VDF−TrFE) 93/7 and P(VDF−TrFE−CTFE)-g-PS(14%). (F) Schematic model of a PS-confined ferroelectric P(VDF−TrFE) crystal under a poling electric field. The chain folding direction is perpendicular to the applied electric field. (Reprinted with permission from ref 150.)

dx.doi.org/10.1021/ma2024057 | Macromolecules 2012, 45, 2937−2954

P(VDF−TrFE−CTFE)-*g*-PS(14%) are shown in Figures 14A and 14B, respectively, and a clear difference is seen.[150] For P(VDF−TrFE) 93/7, double hysteresis loops are seen at the poling field below 200 MV/m, above which only normal ferroelectric loops are seen. For P(VDF−TrFE−CTFE)-*g*-PS(14%), double hysteresis loops are seen at the poling field up to 400 MV/m. Especially, a typical antiferroelectric-like behavior with a clear double hysteresis loop ($D_{rem} \sim 0$) at the poling field of 150 MV/m is shown in the inset of Figure 14B. Also, different from the double hysteresis loops in P(VDF−TrFE) with more than 50 mol % TrFE, these double hysteresis loops for P(VDF−TrFE−CTFE)-*g*-PS(14%) do not disappear even after repeated poling processes, indicating that the observed antiferroelectric-like behavior is fairly stable. Comparisons of stored and released energy densities and unreleased% between P(VDF−TrFE) 93/7 and P(VDF−TrFE−CTFE)-*g*-PS(14%) are shown in Figures 14C−E, respectively. Obviously, although P(VDF−TrFE−CTFE)-*g*-PS(14%) stores much less energy than P(VDF−TrFE) 93/7, it discharges a similar energy density as that of P(VDF−TrFE) 93/7. This results in a significant reduction in the unreleased% for P(VDF−TrFE−CTFE)-*g*-PS(14%).

The observed antiferroelectric-like behavior in P(VDF−TrFE−CTFE)-*g*-PS(14%) can be explained using the model in Figure 14F. After the crystallization-induced microphase separation, a low polarizability PS-rich interfacial layer confines (or insulates) the P(VDF−TrFE) crystal. As a result, the P_{comp} in P(VDF−TrFE−CTFE)-*g*-PS(14%) greatly decreases, as compared with that in P(VDF−TrFE). During reverse poling (or discharge), the E_{pol} will be lower than the E_{depol}, and finally the crystalline dipoles aligned at a high electric field will easily revert to the opposite direction, resulting in an antiferroelectric-like behavior at high poling fields with a low D_{rem} and a reduced hysteresis loss. However, as we can see from Figures 14B,E, the dipole switching hysteresis is still significant enough to result in a nearly 40% loss above 200 MV/m. In the future, more research is needed to further reduce the hysteresis for the P(VDF−TrFE−CTFE)-*g*-PS graft copolymers.

A natural extension of the above work is to further increase the PS content in the PVDF copolymer. In a recent study, we grafted different length PS side chains (1.9−7.6 repeat units in each side chain) from P(VDF−CTFE) 93/7 using ATRP followed by dechlorination.[152,153] When the PS graft content is 17 wt %, a similar antiferroelectric-like behavior as that for the P(VDF−TrFE−CTFE)-*g*-PS(14%) in Figure 14B is seen. When the PS graft content is above 30 wt %, linear hysteresis loops are observed for the P(VDF−CTFE)-*g*-PS graft copolymers. It is because of these linear hysteresis loops that P(VDF−CTFE)-*g*-PS graft copolymers exhibit significantly reduced unreleased% at a relatively high PS content. For example, the best performance in terms of high energy density and low loss is observed in P(VDF−CTFE)-*g*-PS(34%): a relatively high released energy density of ∼10 J cm^{-3} at 600 MV m^{-1}, a fairly low dielectric loss (tan δ = 0.006 at 1 kHz), and a low ferroelectric/conduction loss (unreleased% = 17.6% at 550 MV m^{-1}). The energy density for P(VDF−CTFE)-*g*-PS(34%) at 600 MV/m is about 2.8 times that of BOPP. Meanwhile, the P(VDF−CTFE)-*g*-PS graft copolymers exhibit a fast discharge speed down to 8 μs.[152] The higher unreleased% for P(VDF−CTFE)-*g*-PS(34%) may be resulted from the residue metal catalyst during ATRP and subsequent dechlorination. Currently, the reason for the linear hysteresis loops in P(VDF−CTFE)-*g*-PS graft copolymers with the PS content above 30 wt % is still not clear. We consider that after PVDF crystallization PS grafts are rejected out of the PVDF crystal, forming a PS-rich confining layer surrounding the PVDF crystal (similar to the model in Figure 14F but with a much thicker PS-rich layer due to a higher PS content). Because of a large difference in the dielectric constants for the PVDF crystal and the amorphous PS/PVDF phase, electric field distribution must be nonuniform in the crystalline PVDF and amorphous PS/PVDF phases. For example, assuming that the dielectric constant of the PVDF crystal is 12 and that for the amorphous PS/PVDF phase is around 4, the nominal electric field in the PVDF crystal will be 1/3 of that in the amorphous phase. Under such a low nominal electric field in PVDF crystals, no dipole switching is possible and linear hysteresis loops are observed. This will need further investigations to prove our hypothesis.

6. CONCLUDING REMARKS AND OUTLOOK

As we have discussed, there is clearly a need in the pulsed power and power conditioning industry that next generation dielectric capacitors be developed in areas of high energy density/low loss and/or high temperature/low loss dielectrics. In this Perspective, we do not tackle this challenge from the viewpoints of high dielectric constant and high breakdown strength because dielectric constant of a material is a macroscopic quantity and thus does not have a physical meaning at the molecular level, and electric breakdown strength is rather an extrinsic physical property of dielectric materials. Instead, we focus on the concept of polarization because of its clear physical meaning at the molecular level. Meanwhile, the intent of this Perspective is to understand the fundamental physics of orientational polarization in polar polymers and to propose general guidance for molecular/structural design of high energy density and low loss dielectrics, rather than to propose any detailed functional groups or chemical structures of polymers.

For insulating dielectric polymers, opportunity is limited for further increasing the atomic polarization because bond lengths and bond angles are well-defined for covalently linked bonds. There should be some room for enhancing the electronic polarization in dielectric polymers. Because electronic polarization is in the resonance regime (see Figure 1), enhancing electronic polarization seems to be the first choice for high energy density and low loss dielectrics. However, the trade-off between electron delocalization by lowering the band gap and electron conductivity (especially at high electric fields) dictates how much enhancement one can achieve for the electronic polarization. Generally speaking, the band gap should at least be greater than 2 eV in order to be considered as insulating (at least at low fields). In a recent first-principles calculation,[154] the polarizability per unit mass for a −Si(CN)$_2$− homopolymer is nearly twice that of PE or PP, suggesting that −Si(CN)$_2$− may store twice the electric energy that of PE or PP while maintaining a low loss. However, the band gap decreases from ca. 9 eV for PE or PP to slightly below 3 eV for −Si(CN)$_2$−. Therefore, we consider that high (electronic) polarizability and relatively low band gap polymers are only suitable for low-field (e.g., <50 MV/m) applications such as gate dielectrics for thin-film transistors.[155−158]

Polar polymers with permanent dipoles have been discussed for high energy density and low loss dielectrics. Amorphous polar polymers below the T_g show promising results.

dx.doi.org/10.1021/ma2024057 | *Macromolecules* 2012, 45, 2937−2954

Nonetheless, complete removal of ionic impurity and moisture is challenging in practical applications. Meanwhile, the increase in energy density may be limited (e.g., about twice that of BOPP, see Figure 4A) because of frozen dipoles below the T_g. A promising strategy is to utilize the orientational polarization for high energy density and low loss dielectrics. The key issue is to minimize relaxational loss in the power and radio frequencies (100 Hz to a few hundred kHz) at high electric fields. An effective method is to shift high-field dipole relaxation peak to a much higher frequency (e.g., above a few tens of MHz). In other words, the dipole mobility needs to be high under high electric fields. In this sense, liquid crystalline polymer dipoles have a high orientational mobility because of the liquid crystalline nature. However, their mobility is already too high at low electric fields. Dipoles in liquid crystalline polymers saturate at a fairly low field (e.g., 24.8 MV/m), after which limited electric energy can be further stored. Therefore, an optimal situation is that dipole mobility in polymers should be low at low fields and high at high fields and the transition should be gradual (similar to a second order phase transition). This may be achievable for ferroelectric crystalline polymers.

In normal ferroelectric polymers, dipole switching is a first order transition with significant hysteresis (similar to crystallization and melting processes in crystalline polymers). Although the mobility of crystalline dipole is low at low fields and high at high fields, the switching of dipoles happens suddenly as the electric field increases to above a certain threshold (i.e., the E_c). As a result, large hysteresis is observed for normal ferroelectric polymers. From our systematic study of effects of crystal orientation, polymorphism, crystallite size, and crystallinity in PVDF-based polymers, the opportunity for high energy density and low loss dielectric might be realized in the case that the PVDF copolymer has a parallel crystal orientation, an appropriate crystallinity (or a moderate level), an ultrasmall crystallite or domain size (e.g., a few nanometers), and a high β content. The challenge, however, is how to easily and effectively achieve ultrasmall crystallite sizes for PVDF-based polymer films.

For paraelectric crystalline polymers, dipoles have the potential to align in an external electric field. If the polarization can return to zero when the applied electric field is removed, high energy storage and low loss dielectrics can be achieved. In this sense, relatively high dipole mobility is required for complete dipole reversibility. This is observed at high poling frequencies for the HTPE phase in P(VDF−TrFE) copolymers. In the future, more reversible paraelectric crystalline polymers need to be discovered for high energy density and low loss dielectrics.

Opportunity for high energy density and low loss dielectrics may be better found in novel ferroelectric polymers with relaxor ferroelectric and/or antiferroelectric-like behaviors. To achieve relaxor ferroelectricity in polymers, several methods have been used experimentally, including electron beam irradiation of P(VDF−TrFE) copolymers and P(VDF−TrFE)-based terpolymers having a large third comonomer such as CFE, CDFE, or CTFE. The goals are to (1) increase the dipole mobility under high fields by effectively enlarging the lateral unit cell dimensions via inclusion of structural defects (i.e., isomorphism), (2) broaden the dipole switching transition, and (3) make the dipole switching completely reversible. In the future, opportunities exist for further optimizing the crystalline and ferroelectric properties of P(VDF−TrFE)-based terpolymers in terms of comonomer compositions and crystalline morphology.

The best choice for high energy density and low loss dielectrics is the antiferroelectric-like behavior with narrow hysteresis loops and a minimum D_{rem}. Our recent study on a P(VDF−TrFE−CTFE)-*g*-PS(14%) graft copolymer suggest that by nanoconfining PVDF crystals with a low polarizability PS, a delicate balance between the D_{max} (or $Q + P_{comp}$) and the P_{in} can result in the antiferroelectric-like behavior with a minimum D_{rem} (see inset of Figure 14B).[150] However, we can only experimentally determine the D_{max} but not the P_{in}. In the future, computer simulation is needed to understand how the competition between the D_{max} and the P_{in} can result in the antiferroelectric-like behavior in PVDF-based polymers. Further increasing the PS content to beyond 30 wt % results in linear dielectric hysteresis loops,[153] suggesting that crystalline dipole switching is effectively prohibited because of a nonuniform electric field distribution among PVDF crystals and the PVDF/PS amorphous phase. Similar linear dielectric hysteresis loops are also observed in PVDF-based multilayer films,[159] which also exhibit a significantly higher energy density than BOPP and reasonably low losses. In the future, removal of impurity ions in polar crystalline polymers can further reduce the hysteresis loss at high electric fields.

Finally, it is known that all ferroelectrics are also piezoelectric. Therefore, strong electromechanical coupling should be avoided for the capacitor application. To minimize the d_{33} coefficient, the compliance of the polar polymer film should be as low as possible. In other words, rubbery polar polymers must be avoided for dielectric capacitors. More attention should be paid in order to minimize electromechanical coupling in the future. Furthermore, it is still difficult, if not possible, to in situ visualize ferroelectric domains and transformation of domain orientation by experimental methods for polymers. Future research may focus on these topics to further enhance our understanding of ferroelectric switching in polymers.

In summary, novel ferroelectric crystalline polymers exhibiting relaxor ferroelectric and antiferroelectric-like behaviors have demonstrated great potential for high energy density/low loss dielectrics and many other practical applications including electrostriction and solid-state refrigeration. Reasonable success has been achieved for relaxor ferroelectric polymers such as P(VDF−TrFE)-based terpolymers. However, further optimization in terms of comonomer composition and crystalline morphology is still needed to enhance their performance in a specific application. On the other hand, genuine antiferroelectric crystalline polymers have not yet been reported so far. In the future, more research needs to focus on new paraelectric and novel ferroelectric polymers for high energy density and low loss dielectrics.

AUTHOR INFORMATION

Corresponding Author

*E-mail: lxz121@case.edu (L.Z.) and wang@matse.psu.edu (Q.W.).

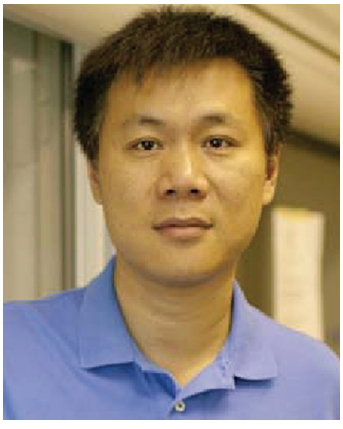
Notes

The authors declare no competing financial interest.

Biographies



Lei Zhu is currently an Associate Professor of Macromolecular Science and Engineering at Case Western Reserve University. He received his B.S. degree in Materials Chemistry in 1993 and M.S. degree in Polymer Chemistry and Physics in 1996 from Fudan University. He earned his Ph.D. degree in Polymer Science in 2000 from the University of Akron. After two-year postdoctoral experience at University of Akron, he joined Institute of Materials Science and Department of Chemical, Materials and Biomolecular Engineering at University of Connecticut, as an Assistant Professor. In 2009, he moved to Case Western Reserve University. He is recipient of National Science Foundation (NSF) Career Award, 3M Nontenured Faculty Award, and DuPont Young Professor Award. His research interests include polymer and polymer−inorganic hybrid materials for electric energy storage, development of artificial antibody as nanomedicines, and supramolecular self-assembly of discotic liquid crystals.



Qing Wang is an Associate Professor of Materials Science and Engineering at the Pennsylvania State University. He received his Ph.D. in Chemistry from the University of Chicago under the supervision of Professor Luping Yu in 2000. Prior to joining the faculty at Penn State in 2002, he was a postdoctoral researcher with Prof. Christopher Ober at Cornell University. Among other awards, he has received the NSF CAREER Award, Rustum and Della Roy Innovation in Materials Research Award and Virginia S. and Philip L. Walker Faculty Fellow. His research interests include the development of ferroelectric polymers, electroactive polymers, polymer nanocomposites, conjugated polymers, and ion-containing polymers for energy storage and conversion applications.

■ ACKNOWLEDGMENTS

L.Z. thanks financial support from Office of Naval Research (ONR, N00014-05-0338, N00014-10-1-0349, and N00014-11-1-0251), NSF (DMR-0907580 and DMR-0423914), and Army Research Office (ARO, W911NF-11-1-0534). Q.W. thanks financial supports from ONR (N00014-08-1-0229 and N00014-11-1-0342) and NSF (DMR-0548146). The authors are indebted to Professors Donald Schuele, Jerome Lando, and Philip Taylor at Case Western Reserve University for helpful discussions. Dr. Fangxiao Guan, Jung-Kai Tseng, Lianyun Yang, and Dr. Elshad Allakhyarov are acknowledged for helping the preparation of the manuscript.

■ REFERENCES

(1) Kao, K.-C. *Dielectric Phenomena in Solids: With Emphasis on Physical Concepts of Electronic Processes*; Elsevier Academic Press: Boston, 2004.
(2) Mittal, K. L. *Metallized Plastics: Fundamentals and Applications*; Marcel Dekker: New York, 1998.
(3) Sarjeant, W. J.; Zirnheld, J.; MacDougall, F. W. *IEEE Trans. Plasm. Sci.* **1998**, *26*, 1368−1392.
(4) Sarjeant, W. J.; Clelland, I. W.; Price, R. A. *Proc. IEEE* **2001**, *89*, 846−855.
(5) Tan, Q.; Irwin, P.; Cao, Y. *IEEJ Trans. Fund. Mater.* **2006**, *126*, 1152−1159.
(6) Ho, J.; Ramprasad, R.; Boggs, S. *IEEE Trans. Dielectr. Electr. Insul.* **2007**, *14*, 1295−1301.
(7) Starkweather, J., H. W.; Avakian, P.; Matheson, R. R.; Fontanella, J. J.; Wintersgill, M. C. *Macromolecules* **1992**, *25*, 6871−6875.
(8) Ho, J.; Jow, T. R. *Characterization of High Temperature Polymer Thin Films for Power Conditioning Capacitors*; Army Research Laboratory: Adelphi, MD, 2009; ARL-TR-4880.
(9) Husain, I. *Electric and Hybrid Vehicles: Design Fundamentals*; CRC Press: Boca Raton, FL, 2010.
(10) Teodorescu, R.; Liserre, M.; Rodríguez, P. *Grid Converters for Photovoltaic and Wind Power Systems*; Wiley: Chichester, 2011.
(11) Bluhm, H.; Rusch, D. *Pulsed Power Systems: Principles and Applications*; Springer: Berlin, 2006.
(12) Blythe, A. R.; Bloor, D. *Electrical Properties of Polymers*, 2nd ed.; Cambridge University Press: Cambridge, 2005.
(13) Riande, E.; Díaz-Calleja, R. *Electrical Properties of Polymers*; Marcel Dekker: New York, 2004.
(14) Sessler, G. H.; Gerhard-Multhaupt, R. *Electrets*, 3rd ed.; Laplacian Press: Morgan Hill, CA, 1998.
(15) Li, L.; Meller, G.; Kosina, H. *Microelectron. J.* **2007**, *38*, 47−51.
(16) Setter, N.; Colla, E. *Ferroelectric Ceramics: Tutorial Reviews, Theory, Processing, and Applications*; Birkhäuser: Basel, 1993.
(17) Kremer, F.; Schönhals, A. *Broadband Dielectric Spectroscopy*; Springer: Berlin, 2003.
(18) Nalwa, H. S. *Ferroelectric Polymers: Chemistry, Physics, and Applications*; Marcel Dekker: New York, 1995.
(19) Kaatze, U.; Behrends, R.; Pottel, R. *J. Non-Cryst. Solids* **2002**, *305*, 19−28.
(20) Barthel, J.; Bachhuber, K.; Buchner, R.; Gill, J. B.; Kleebauer, M. *Chem. Phys. Lett.* **1990**, *167*, 62−66.
(21) Barthel, J.; Bachhuber, K.; Buchner, R.; Hetzenauer, H. *Chem. Phys. Lett.* **1990**, *165*, 369−373.
(22) Orbakh, D. *Nonaqueous Electrochemistry*; Marcel Dekker: New York, 1999.
(23) Izutsu, K. O. *Electrochemistry in Nonaqueous Solutions*; Wiley-VCH: Weinheim, 2002.
(24) Jow, T. R.; Cygan, P. J. *J. Appl. Phys.* **1993**, *73*, 5147−5151.
(25) Miyamoto, T.; Shibayam., K. *J. Appl. Phys.* **1973**, *44*, 5372−5376.
(26) Imrie, C. T.; Ingram, M. D.; McHattie, G. S. *Adv. Mater.* **1999**, *11*, 832−834.
(27) Ingram, M. D.; Imrie, C. T.; McHattie, G. S. *J. Phys. Chem. B* **1999**, *103*, 4132−4138.
(28) Natesan, B.; Karan, N. K.; Rivera, M. B.; Aliev, F. M.; Katiyar, R. S. *J. Non-Cryst. Solids* **2006**, *352*, 5205−5209.
(29) Kawanura, J.; Asayama, R.; Kuwata, N.; Kamishima, O. Ionic transport in glass and polymer: Hierarchical structure and dynamics.

In *Physics of Solid State Ionics*; Sakuma, T., Takahashi, H., Eds.; Research Sighpost: Kerala, India, 2006; pp 193−246.
(30) Ingram, M. D.; Imrie, C. T. *Solid State Ionics* **2011**, *196*, 9−17.
(31) Furukawa, T.; Saito, Y.; Tsutsumi, Y. *7th Int. Symp. Electrets (ISE 7)* **1991**, 421−427.
(32) Svensson, M.; Helgee, B.; Hjertberg, T.; Hermann, D.; Skarp, K. *Polym. Bull.* **1993**, *31*, 167−174.
(33) Soto-Bustamante, E. A.; Yablonskii, S. V.; Ostrovskii, B. I.; Beresnev, L. A.; Blinov, L. M.; Haase, W. *Chem. Phys. Lett.* **1996**, *260*, 447−452.
(34) Soto-Bustamante, E. A.; Yablonskii, S. V.; Ostrovskii, B. I.; Beresnev, L. A.; Blinov, L. M.; Haase, W. *Liq. Cryst.* **1996**, *21*, 829−839.
(35) Gebhard, E.; Zentel, R. *Macromol. Chem. Phys.* **2000**, *201*, 902−910.
(36) Gebhard, E.; Zentel, R. *Macromol. Chem. Phys.* **2000**, *201*, 911−922.
(37) Feller, F.; Geschke, D.; Kozlovsky, M. V. *Mol. Cryst. Liq. Cryst.* **2001**, *357*, 167−175.
(38) Zentel, R. Ferroelectric liquid crystalline elastomers. In *Encyclopedia of Polymer Science and Technology*; Mark, H. F., Ed.; Wiley-Interscience: Hoboken, NJ, 2007; Vol. *6*, pp 251−267.
(39) Suda, K.; Akagi, K. *J. Polym. Sci., Part A: Polym. Chem.* **2008**, *46*, 3591−3610.
(40) Davies, G. R.; Singh, H. *Polymer* **1979**, *20*, 772−774.
(41) Naegele, D.; Yoon, D. Y.; Broadhurst, M. G. *Macromolecules* **1978**, *11*, 1297−1298.
(42) Lovinger, A. J. *Science* **1983**, *220*, 1115−1121.
(43) Kobayashi, M.; Tashiro, K.; Tadokoro, H. *Macromolecules* **1975**, *8*, 158−171.
(44) Lovinger, A. J. *Macromolecules* **1982**, *15*, 40−44.
(45) Black, C. T.; Farrell, C.; Licata, T. J. *Appl. Phys. Lett.* **1997**, *71*, 2041−2043.
(46) Samara, G. A. *J. Phys.: Condens. Matter* **2003**, *15*, R367−R411.
(47) Zhou, Y.; Shin, F. G. *J. Appl. Phys.* **2006**, *100*, 024101.
(48) Stephanovich, V. A.; Luk'yanchuk, I. A.; Karkut, M. G. *Phys. Rev. Lett.* **2005**, *94*, 047601.
(49) Hooton, J. A.; Merz, W. J. *Phys. Rev.* **1955**, *98*, 409−413.
(50) Ducharme, S.; Reece, T. J.; Othon, C. M.; Rannow, R. K. *IEEE Trans. Device Mater. Reliab.* **2005**, *5*, 720−735.
(51) Ling, Q. D.; Liaw, D. J.; Zhu, C.; Chan, D. S. H.; Kang, E. T.; Neoh, K. G. *Prog. Polym. Sci.* **2008**, *33*, 917−978.
(52) Hu, Z.; Tian, M.; Nysten, B.; Jonas, A. M. *Nature Mater.* **2009**, *8*, 62−67.
(53) Naber, R. C. G.; Asadi, K.; Blom, P. W. M.; de Leeuw, D. M.; de Boer, B. *Adv. Mater.* **2010**, *22*, 933−945.
(54) Furukawa, T.; Takahashi, Y.; Nakajima, T. *Curr. Appl. Phys.* **2010**, *10*, E62−E67.
(55) Nakajima, T.; Takahashi, Y.; Okamura, S.; Furukawa, T. *Jpn. J. Appl. Phys.* **2009**, *48*, 09KE04.
(56) Chen, Q. X.; Payne, P. A. *Meas. Sci. Technol.* **1995**, *6*, 249−267.
(57) Zhang, Q. M.; Li, H.; Poh, M.; Xia, F.; Cheng, Z. Y.; Xu, H.; Huang, C. *Nature* **2002**, *419*, 284−287.
(58) Brochu, P.; Pei, Q. *Macromol. Rapid Commun.* **2010**, *31*, 10−36.
(59) Hausler, E.; Stein, L.; Harbauer, G. *Ferroelectrics* **1984**, *60*, 277−282.
(60) Liu, Y.; Tian, G.; Wang, Y.; Lin, J.; Zhang, Q.; Hofmann, H. F. *J. Intell. Mater. Syst. Struct.* **2009**, *20*, 575−585.
(61) Chang, C.; Tran, V. H.; Wang, J.; Fuh, Y. K.; Lin, L. *Nano Lett.* **2010**, *10*, 726−731.
(62) Miyamoto, Y.; Miyaji, H.; Asai, K. *J. Polym. Sci., Part B: Polym. Phys.* **1980**, *18*, 597−606.
(63) Marcus, M. A. *IEEE Trans. Electr. Insul.* **1986**, *EI-21*, 519−523.
(64) Gregorio, R. Jr.; Ueno, E. M. *J. Mater. Sci., Lett.* **1999**, *34*, 4489−4500.
(65) Guan, F.; Pan, J.; Wang, J.; Wang, Q.; Zhu, L. *Macromolecules* **2010**, *43*, 384−392.
(66) Furukawa, T.; Wang, T. Measurements and Properties of Ferroelectric Polymers. In *The Applications of Ferroelectric Polymers*; Wang, T., Herbert, J. M., Glass, A. M., Eds.; Chapman and Hall: New York, 1988; Vol. *5*, pp 66−117.
(67) Furukawa, T.; Johnson, G. E. *J. Appl. Phys.* **1981**, *52*, 940−943.
(68) Mijovic, J.; Sy, J. W.; Kwei, T. K. *Macromolecules* **1997**, *30*, 3042−3050.
(69) Hahn, B.; Wendorff, J.; Yoon, D. Y. *Macromolecules* **1985**, *18*, 718−721.
(70) Guan, F.; Wang, J.; Pan, J.; Wang, Q.; Zhu, L. *Macromolecules* **2010**, *43*, 6739−6748.
(71) Guan, F.; Wang, J.; Pan, J.; Wang, Q.; Zhu, L. *IEEE Dielectr. Electr. Insul.* **2011**, *18*, 1293−1300.
(72) Chu, B.; Zhou, X.; Ren, K.; Neese, B.; Lin, M. R.; Wang, Q.; Bauer, F.; Zhang, Q. M. *Science* **2006**, *313*, 334−336.
(73) Zhou, X.; Chu, B.; Neese, B.; Lin, M.; Zhang, Q. M. *IEEE Trans. Dielectr. Electr. Insul.* **2007**, *14*, 1133−1138.
(74) Zhou, X.; Zhao, X.; Suo, Z.; Zou, C.; Runt, J.; Liu, S.; Zhang, S.; Zhang, Q. M. *Appl. Phys. Lett.* **2009**, *94*, 162901.
(75) Wang, Y.; Zhou, X.; Chen, Q.; Chu, B.; Zhang, Q. M. *IEEE Trans. Dielectr. Electr. Insul.* **2010**, *17*, 1036−1042.
(76) Furukawa, T.; Nakajima, K.; Koizumi, T.; Date, M. *Jpn. J. Appl. Phys.* **1987**, *26*, 1039−1045.
(77) Aljishi, R.; Taylor, P. L. *J. Appl. Phys.* **1985**, *57*, 902−905.
(78) Chiang, Y.-M.; Birnie, D. P.; Kingery, W. D. *Physical Ceramics: Principles for Ceramic Science and Engineering*; J. Wiley: New York, 1997.
(79) Wunderlich, B. *Macromolecular Physics*; Academic Press: New York, 1973; Vol. *1*.
(80) Furukawa, T. *Adv. Colloid Interface Sci.* **1997**, *71*−*2*, 183−208.
(81) Tashiro, K.; Tanaka, R. *Polymer* **2006**, *47*, 5433−5444.
(82) Tashiro, K.; Kobayashi, M. *Polymer* **1986**, *27*, 667−676.
(83) Su, R.; Tseng, J.-K.; Lu, M.-S.; Lin, M.; Fu, Q.; Zhu, L. *Polymer* **2012**, *53*, 728−739.
(84) Guan, F.; Wang, J.; Pan, J.; Wang, Q.; Zhu, L. *Chin. J. Polym. Sci.* **2011**, *29*, 65−80.
(85) Bokov, A. A.; Ye, Z. G. *J. Mater. Sci.* **2006**, *41*, 31−52.
(86) Ohwada, K.; Tomita, Y. *J. Phys. Soc. Jpn.* **2010**, *79*, 011012.
(87) Lagerwall, S. T. *Ferroelectric and Antiferroelectric Liquid Crystals*; Wiley-VCH: Weinheim, 1999.
(88) Zhang, Q. M.; Bharti, V.; Zhao, X. *Science* **1998**, *280*, 2101−2104.
(89) Bharti, V.; Zhao, X. Z.; Zhang, Q. M.; Romotowski, T.; Tito, F.; Ting, R. *Mater. Res. Innovations* **1998**, *2*, 57−63.
(90) Xu, H.; Shanthi, G.; Bharti, V.; Zhang, Q. M.; Ramotowski, T. *Macromolecules* **2000**, *33*, 4125−4131.
(91) Cheng, Z. Y.; Bharti, V.; Mai, T.; Xu, T. B.; Zhang, Q. M.; Ramotowski, T.; Wright, K. A.; Ting, R. *IEEE Trans. Ultrason. Ferroelectr. Freq. Control* **2000**, *47*, 1296−1306.
(92) Bharti, V.; Zhang, Q. M. *Phys. Rev. B* **2001**, *63*, 184103.
(93) Cheng, Z. Y.; Olson, D.; Xu, H.; Xia, F.; Hundal, J. S.; Zhang, Q. M.; Bateman, F. B.; Kavarnos, G. J.; Ramotowski, T. *Macromolecules* **2002**, *35*, 664−672.
(94) Cheng, Z. Y.; Zhang, Q. M.; Bateman, F. B. *J. Appl. Phys.* **2002**, *92*, 6749−6755.
(95) Guo, S. S.; Lau, S. T.; Chan, H. L. W.; Zhao, X. Z.; Choy, C. L. *J. Appl. Phys.* **2003**, *94*, 5566−5573.
(96) Bobnar, V.; Vodopivec, B.; Levstik, A.; Kosec, M.; Hilczer, B.; Zhang, Q. M. *Macromolecules* **2003**, *36*, 4436−4442.
(97) Tang, Y.; Wang, D.; Guo, S.; Zhao, X. Z. *Eur. Polym. J.* **2001**, *37*, 471−474.
(98) Welter, C.; Faria, L. O.; Moreira, R. L. *Phys. Rev. B* **2003**, *67*, 144103.
(99) Lau, S. T.; Leung, K. Y.; Chan, H. L. W.; Choy, C. L.; Sundaravel, B.; Wilson, I. *Ferroelectrics* **2002**, *273*, 2387−2392.
(100) Lau, S. T.; Chan, H. L. W.; Choy, C. L. *Appl. Phys. A: Mater. Sci. Process.* **2005**, *80*, 289−294.
(101) Lam, T. Y.; Lau, S. T.; Chan, H. L. W.; Choy, C. L.; Cheung, W. Y.; Wong, S. P. *J. Polym. Sci., Part B: Polym. Phys.* **2005**, *43*, 2334−2339.

(102) Xia, F.; Cheng, Z.; Xu, H.; Li, H.; Zhang, Q.; Kavarnos, G. J.; Ting, R. Y.; Abdul-Sedat, G.; Belfield, K. D. *Adv. Mater.* **2002**, *14*, 1574−1577.
(103) Guo, S.; Zhao, X. Z.; Zhou, Q.; Chan, H. L. W.; Choy, C. L. *Appl. Phys. Lett.* **2004**, *84*, 3349−3351.
(104) Chen, Q.; Ren, K.; Chu, B.; Liu, Y.; Zhang, Q. M.; Bobnar, V.; Levstik, A. *Ferroelectrics* **2007**, *354*, 178−191.
(105) Mabboux, P. Y.; Gleason, K. K. *J. Fluorine Chem.* **2002**, *113*, 27−35.
(106) Wang, L.; Zhao, X.; Feng, J. *J. Polym. Sci., Part B: Polym. Phys.* **2006**, *44*, 1714−1724.
(107) Seguela, R.; Rietsch, F. *J. Polym. Sci., Part C: Polym. Lett.* **1986**, *24*, 29−33.
(108) Hosoda, S.; Nomura, H.; Gotoh, Y.; Kihara, H. *Polymer* **1990**, *31*, 1999−2005.
(109) Hosoda, S.; Hori, H.; Yada, K.; Nakahara, S.; Tsuji, M. *Polymer* **2002**, *43*, 7451−7460.
(110) Lovinger, A. J.; Davis, D. D.; Cais, R. E.; Kometani, J. M. *Polymer* **1987**, *28*, 617−626.
(111) Chung, T. C.; Petchsuk, A. *Ferroelectr., Lett. Sect.* **2001**, *28*, 135−143.
(112) Chung, T. C.; Petchsuk, A. *Macromolecules* **2002**, *35*, 7678−7684.
(113) Klein, R. J.; Runt, J.; Zhang, Q. M. *Macromolecules* **2003**, *36*, 7220−7226.
(114) Ang, C.; Yu, Z. *Adv. Mater.* **2004**, *16*, 979−982.
(115) Jeong, D. Y.; Wang, Y. K.; Huang, M.; Zhang, Q. M.; Kavarnos, G. J.; Bauer, F. *J. Appl. Phys.* **2004**, *96*, 316−319.
(116) Zhang, S.; Klein, R. J.; Ren, K.; Chu, B.; Zhang, X.; Runt, J.; Zhang, Q. M. *J. Mater. Sci.* **2006**, *41*, 271−280.
(117) Zhang, S.; Chu, B.; Neese, B.; Ren, K.; Zhou, X.; Zhang, Q. M. *J. Appl. Phys.* **2006**, *99*, 044107.
(118) Zhang, S.; Neese, B.; Ren, K.; Chu, B.; Zhang, Q. M. *J. Appl. Phys.* **2006**, *100*, 044113.
(119) Zhen, H.; Ye, H.; Liu, X.; Zhu, D.; Li, H.; Lu, Y.; Wang, Q. *Opt. Express* **2008**, *16*, 9595−9600.
(120) Wang, Y.; Lu, S. G.; Lanagan, M.; Zhang, Q. M. *IEEE Trans. Ultrason. Ferroelectr. Freq. Control* **2009**, *56*, 444−449.
(121) Meng, X. J.; Dkhil, B.; Liu, P. F.; Wang, J. L.; Sun, J. L.; Chu, J. H. *J. Appl. Phys.* **2009**, *106*, 104102.
(122) Meng, X. J.; Wang, J. L.; Xu, H. S.; Sun, J. L.; Chu, J. H. *J. Appl. Phys.* **2009**, *106*, 114106.
(123) Wang, J. L.; Yuan, S. Z.; Tian, L.; Meng, X. J.; Sun, J. L.; Chu, J. H. *Appl. Phys. Lett.* **2011**, *98*, 052906.
(124) Pruvost, S.; Zhu, H.; Cottinet, P. J.; Guyomar, D. *Appl. Phys. Lett.* **2011**, *98*, 222901.
(125) Chu, B.; Zhou, X.; Neese, B.; Zhang, Q. M.; Bauer, F. *Ferroelectrics* **2006**, *331*, 35−42.
(126) Chu, B.; Zhou, X.; Neese, B.; Zhang, Q. M.; Bauer, F. *IEEE Trans. Dielectr. Electr. Insul.* **2006**, *13*, 1162−1169.
(127) Lu, Y.; Claude, J.; Norena-Franco, L. E.; Wang, Q. *J. Phys. Chem. B* **2008**, *112*, 10411−10416.
(128) Neese, B.; Chu, B.; Lu, S. G.; Wang, Y.; Furman, E.; Zhang, Q. M. *Science* **2008**, *321*, 821−823.
(129) Neese, B.; Lu, S. G.; Chu, B.; Zhang, Q. M. *Appl. Phys. Lett.* **2009**, *94*, 042910.
(130) Lu, S. G.; Zhang, Q. M. *Adv. Mater.* **2009**, *21*, 1983−1987.
(131) Li, X.; Qian, X. S.; Lu, S. G.; Cheng, J.; Fang, Z.; Zhang, Q. M. *Appl. Phys. Lett.* **2011**, *99*, 052907.
(132) Zhang, S.; Zhang, N.; Huang, C.; Ren, K.; Zhang, Q. M. *Adv. Mater.* **2005**, *17*, 1897−1901.
(133) Xu, H.; Shen, D.; Zhang, Q. *Polymer* **2007**, *48*, 2124−2129.
(134) Lu, Y.; Claude, J.; Neese, B.; Zhang, Q.; Wang, Q. *J. Am. Chem. Soc.* **2006**, *128*, 8120−8121.
(135) Lu, Y.; Claude, J.; Zhang, Q.; Wang, Q. *Macromolecules* **2006**, *39*, 6962−6968.
(136) Zhao, C.; Guo, M.; Lu, Y.; Wang, Q. *Macromol. Symp.* **2009**, *279*, 52−58.
(137) Bao, H. M.; Jia, C. L.; Wang, C. C.; Shen, Q. D.; Yang, C. Z.; Zhang, Q. M. *Appl. Phys. Lett.* **2008**, *92*, 042903.
(138) Erste, A.; Filipic, C.; Levstik, A.; Bobnar, V.; Chen, X. Z.; Jia, C. L.; Shen, Q. D. *Phys. Rev. B* **2010**, *81*, 214103.
(139) Solnyshkin, A. V.; Wegener, M.; Kunstler, W.; Gerhard-Multhaupt, R. *Phys. Solid State* **2008**, *50*, 562−567.
(140) Solnyshkin, A. V.; Kislova, I. L. *Ferroelectrics* **2010**, *398*, 77−84.
(141) Ranjan, V.; Yu, L.; Nardelli, M. B.; Bernholc, J. *Phys. Rev. Lett.* **2007**, *99*, 047801.
(142) Fukuda, A.; Takanishi, Y.; Isozaki, T.; Ishikawa, K.; Takezoe, H. *J. Mater. Chem.* **1994**, *4*, 997−1016.
(143) Mery, S.; Lotzsch, D.; Heppke, G.; Shashidhar, R. *Liq. Cryst.* **1997**, *23*, 629−644.
(144) Furukawa, T.; Date, M.; Fukada, E. *J. Appl. Phys.* **1980**, 1135−1141.
(145) Yamada, T.; Ueda, T.; Kitayama, T. *J. Appl. Phys.* **1981**, *52*, 948−952.
(146) Furukawa, T.; Lovinger, A. J.; Davis, G. T.; Broadhurst, M. G. *Macromolecules* **1983**, *16*, 1885−1890.
(147) Koizumi, N.; Murata, Y.; Tsunashima, H. *IEEE Trans. Electr. Insul.* **1986**, *21*, 543−548.
(148) Takahashi, Y.; Kodama, H.; Nakamura, M.; Furukawa, T.; Date, M. *Polym. J.* **1999**, *31*, 263−267.
(149) Furukawa, T.; Takahashi, Y. *Ferroelectrics* **2001**, *264*, 1739−1748.
(150) Guan, F.; Wang, J.; Yang, L.; Tseng, J. K.; Han, K.; Wang, Q.; Zhu, L. *Macromolecules* **2011**, *44*, 2190−2199.
(151) Zhang, M.; Russell, T. P. *Macromolecules* **2006**, *39*, 3531−3539.
(152) Guan, F.; Yuan, Z.; Shu, E. W.; Zhu, L. *Appl. Phys. Lett.* **2009**, *94*, 052907.
(153) Guan, F.; Wang, J.; Yang, L.; Guan, B.; Han, K.; Wang, Q.; Zhu, L. *Adv. Funct. Mater.* **2011**, *21*, 3176−3188.
(154) Ramprasad, R., private communication, 2011.
(155) Veres, J.; Ogier, S.; Lloyd, G.; de Leeuw, D. *Chem. Mater.* **2004**, *16*, 4543−4555.
(156) Chua, L. L.; Zaumseil, J.; Chang, J. F.; Ou, E. C. W.; Ho, P. K. H.; Sirringhaus, H.; Friend, R. H. *Nature* **2005**, *434*, 194−199.
(157) Yoon, M. H.; Yan, H.; Facchetti, A.; Marks, T. J. *J. Am. Chem. Soc.* **2005**, *127*, 10388−10395.
(158) Yoon, M. H.; Kim, C.; Facchetti, A.; Marks, T. J. *J. Am. Chem. Soc.* **2006**, *128*, 12851−12869.
(159) Mackey, M.; Schulele, D. E.; Zhu, L.; Flandin, L.; Wolak, M. A.; Shirk, J. S.; Hiltner, A.; Baer, E. *Macromolecules* **2012**, DOI: 10.1021/ma202267r.

NOTE ADDED AFTER ASAP PUBLICATION

This Perspective posted ASAP on February 10, 2012. Equation 3 has been revised. The correct version posted on March 29, 2012.

Macromolecules

Article

pubs.acs.org/Macromolecules

Aryl Amidine and Tertiary Amine Switchable Surfactants and Their Application in the Emulsion Polymerization of Methyl Methacrylate

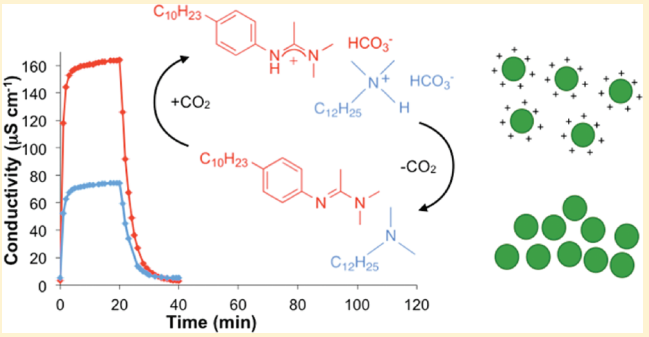
Candace I. Fowler,[†] Philip G. Jessop,*[,†] and Michael F. Cunningham*[,†,‡]

[†]Department of Chemistry, Queen's University, 90 Bader Lane, Kingston, Ontario, Canada K7L 3N6

[‡]Department of Chemical Engineering, Queen's University, 19 Division Street, Kingston, Ontario, Canada K7L 3N6

Supporting Information

ABSTRACT: The switchability and bicarbonate formation of CO_2 triggered aryl amidine and tertiary amine switchable surfactants have been investigated. Despite the lower basicity of these compounds compared to alkylacetamidine switchable surfactants, it was found that amidinium and ammonium bicarbonates could be formed in sufficiently high enough concentrations to perform emulsion polymerization of methyl methacrylate and stabilize the resulting colloidal latexes. Particle sizes ranging from 80 to 470 nm were obtained, and the effects of surfactant concentration, surfactant basicity, initiator type, initiator concentration, and CO_2 pressure on particle size and ζ-potential have been examined. Destabilization of latexes is traditionally achieved by addition of salts, strong acids for anionically stabilized latexes, or alkalis for cationically stabilized latexes. However, with CO_2-triggered switchable surfactants, only air and heat are required to destabilize the latex by removing CO_2 from the system and switching the active amidinium or ammonium bicarbonate surfactant to a surface inactive neutral compound. This process occurs much more rapidly in the case of these less basic aryl amidine and tertiary amine based surfactants compared to previously reported alkyl amidine surfactants.



INTRODUCTION

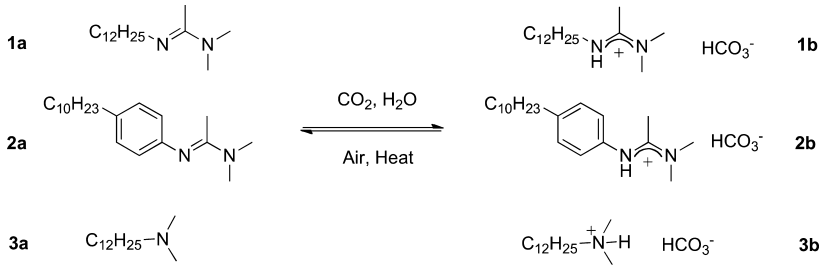
Surfactants are used in many processes to stabilize a dispersion of two immiscible phases. Often, this stabilization is only required for one step of the process, such as in the cases of viscous oil pipelining, metal degreasing, oil sands separations, and emulsion polymerization where the desired product is in the form of a polymer resin.[1] In these processes, subsequent destabilization of the dispersion is required, but this is often a challenging task. Furthermore, the more effective is the surfactant in stabilizing the initial dispersion, the more difficult is the destabilization step. To address this issue, a class of surfactants termed "switchable surfactants" has been developed, whose surface activity can be reversibly altered by the application of a trigger, allowing for reversibly stabilized dispersions. Switchability can be triggered by altering pH,[2−4] adding redox reagents,[5−13] or applying UV light.[14] Surfactants containing ferrocenyl moieties[5,7−12] and "pepfactants"[3,4] (which are switchable surfactants based on a series of amino acids) are expensive, those containing viologen[8] moieties are likely to be toxic, and all of the above rely on the addition of oxidants, reductants, acids, or bases to trigger the switch. Photochemical azobenzene surfactants use only light as a trigger but are limited to nonopaque samples. Switchable surfactants containing amidine[15−18] or guanidine[16,19] headgroups and long chain alkyl or ethoxylated[17,18] tails have recently been developed. These surfactants are charged in the presence of CO_2 due to the formation of bicarbonate salts and become neutral again upon removal of CO_2 (Scheme 1). The basicity of the surfactant headgroup affects the reaction equilibrium and thus the ratio of charged to uncharged forms at a given temperature. Guanidines are generally the most basic and require the most forcing conditions (high temperatures, faster gas flow rates, and/or longer times) to remove the CO_2, whereas CO_2 can be removed from less basic amines at more ambient conditions. This is evidenced by the lower conversions of tertiary amines versus guanidines to bicarbonate salts at a given temperature.[16] The basicity of amidines generally lies between the above two cases.

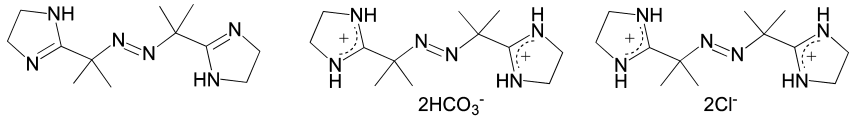
The long chain alkyl amidinium bicarbonate **1b** has been previously shown to be effective for stabilizing emulsions of styrene and methyl methacrylate (MMA) in water and polymer colloids resulting from the emulsion polymerization of those monomers.[20,21] Emulsion polymerization is a widely used chemical process used in the manufacture of synthetic rubbers, paints, adhesives, inks, and sealants, among a variety of other high-quality materials.[22−24] It offers the advantage of being much more rapid than solution or bulk polymerization, yields higher molecular weight polymer, and eliminates the use of potentially hazardous, volatile solvents during synthesis. The product of the emulsion polymerization process is a dispersion

Received: December 20, 2011
Revised: February 16, 2012
Published: March 20, 2012

 © 2012 American Chemical Society dx.doi.org/10.1021/ma2027484 | *Macromolecules* 2012, 45, 2955−2962

Scheme 1. Reaction of Amidines and Amines with CO_2 and Water To Form Bicarbonate Salts





VA-061 4 VA-044

Figure 1. Structures of the initiators used in this paper.

of polymer particles in water, but for many applications the dry solid form of the polymer is desired. Destabilization of the dispersion is carried out industrially using salts or strong acids or bases to alter the electronic environment surrounding the particles, allowing them to form larger particles, or flocs, that can be easily separated from water.[25] In contrast, polymer latexes synthesized using **1b** can be destabilized simply by removal of CO_2 using air or an inert gas and heat.[20,21] While the environmental impact of using air is lower than that of using salt, strong acid, or base, the destabilization times are on the order of hours, which is too slow for practical purposes.[20] Latexes synthesized with small amounts of amidine functionalized comonomer have also been reported.[25] In this case, the authors were not successful in destabilizing the latex simply using air and heat, most likely due to the presence of nonswitchable initiator end groups.

In this paper, the use of less basic amidine and tertiary amine switchable surfactants with more facile switching is described. Emulsion polymerization of MMA was carried out using these surfactants. We hypothesized that more rapid aggregation of the resulting polymer latexes would be possible. The two surfactant precursors chosen were the long chain alkyl tertiary amine, **3a**, and the *p*-alkyl phenyl dimethylacetamidine, **2a** (Scheme 1). These compounds were chosen based on the reported aqueous pK_{aH} (pK_a of the conjugate acid) values of their shorter alkyl chain analogues (10.0 for *N,N*-dimethylbutylamine[26] and 10.8 for *N*′-tolyl-*N,N*-dimethylacetamidine,[27] compared to 12.2 for **1a**).

EXPERIMENTAL SECTION

Reagents. CO_2 (medical grade) was used as received from Praxair. Methyl methacrylate (MMA) (99%) containing monomethyl ether hydroquinone (MEHQ) as a polymerization inhibitor was purchased from Aldrich. MEHQ was removed using an inhibitor removal column, which was also purchased from Aldrich. 2,2′-Azobis[2-(2-imidazolin-2-yl)propane] (VA-061, Figure 1) and 2,2′-azobis[2-(2-imidazolin-2-yl)propane] dihydrochloride (VA-044, Figure 1) were purchased from Wako Pure Chemicals. *N,N*-Dimethyl-*N*-dodecylamine (90%, Alfa Aesar), 4-decylaniline (98%, Alfa Aesar), cetyltrimethylammonium bromide (CTAB, Sigma-Aldrich), and dimethylacetamide dimethyl acetal (90%, TCI) were purchased and used as received. DisponilA 3065 was purchased from Cognis as a 30 wt % solution of linear fatty alcohol ethoxylates in water.

Synthesis and Characterization of 2a. *N*′-(4-Decylphenyl)-*N,N*-dimethylacetamidine (**2a**) was synthesized by a previously developed procedure for related compounds.[15] *N*′-(4-Decylphenyl)-*N,N*-dimethylacetamidine (**2a**) was prepared by mixing 1.0 g (4.2 mmol) of 4-decylaniline with 0.62 g (4.2 mmol) of *N,N*-dimethylacetamide dimethyl acetal in a round-bottom flask equipped with a condenser and heating to 60 °C for 30 min. The methanol was removed by rotary evaporation to yield an orange liquid (1.34 g, 96%). The ^{1}H NMR spectrum shows that the compound is 92% pure, the impurity being the amidate ester.[17] This mixture was not purified before its use as a surfactant. ^{1}H NMR (400 MHz, MeOD-d_4): δ = 0.79 (t, $^3J_{HH}$ = 7.9 Hz, 3 H, CH_2CH_3), 1.18 (m, 14 H, C_7H_{14}), 1.48 (multiplet, $^3J_{HH}$ = 6.8 Hz, 2 H, CH_2CH_2), 1.73 (s, 3 H, CCH_3), 2.44 (t, $^3J_{HH}$ = 6.8 Hz, 2 H, CH_2C), 2.90 (s, 6 H, $N(CH_3)_2$), 6.52 (d, $^3J_{HH}$ = 7.8 Hz, 2 H, C*H*), 6.94 (d, $^3J_{HH}$ = 7.8 Hz, 2 H, C*H*). ^{13}C NMR (100 MHz, $CDCl_3$): δ = 14.2, 14.9, 22.7, 29.3, 29.4, 29.6, 29.7, 31.7, 31.9, 35.4, 38.0, 122.2, 128.6, 135.7, 149.8, 157.4. HRMS (ESI+) calculated *m*/*z* for $[C_{18}H_{34}N_2+H]^+$ = 303.2800, observed = 303.2806. IR (neat, cm^{-1}): 845 (m), 1018 (m), 1188 (m), 1293 (m), 1390 (s), 1466 (m), 1620 (s, ν, (C═N)), 2359 (w), 2853 (s), 2924 (s).

The positions of the ^{1}H NMR peaks correspond to those reported for *N*′-(4-heptylphenyl)-*N,N*-dimethylacetamidine, but the integrations differ due to the different number of protons in the alkyl chain.[18]

Assessing Surfactant Switchability. Conductivity measurements of 20.0 mM solutions of **1b**−**3b** in ethanol (spiked with 200 μL of water) were obtained using a Jenway conductivity meter 4071. CO_2 was bubbled through the solution using a needle at a flow rate of 70 mL min^{-1} (determined using a Varian Intelligent Digital Flowmeter), and the conductivity change over time was measured at room temperature (23 °C) until a constant value was obtained. Air was subsequently bubbled through the solution using a needle at a flow rate of 70 mL min^{-1} . This process was repeated for 3 cycles. As a control, the conductivity of a solution of water (200 μL) in ethanol (20 mL) was determined and changed by less than 5 μS cm^{-1} upon CO_2 addition.

Conversion to Bicarbonate. Because of the potential difficulty in purifying **2a**, a pure sample of the shorter chain analogue *N*′-(4-heptylphenyl)-*N,N*-dimethylacetamidine (**2a**′) was used for this study. The conversion to the bicarbonate salt should not be affected by the alkyl chain length, only by the identity of the headgroup. CO_2 was bubbled through a solution of **2a**′ or **3a** (0.1 mmol) in MeOD-d_4 (0.7 mL) spiked with 50 μL of H_2O for 5 min (one sample at room temperature and one sample at 65 °C), and ^{1}H NMR and ^{13}C NMR spectra were recorded. ^{1}H NMR and ^{13}C NMR spectra of the neutral molecule as well as the hydrochloride salt of each were also recorded. The presence of peaks at 161 ppm (carbon of HCO_3^-) and ~164 ppm (the cationic carbon) in the ^{13}C spectra was taken as evidence of bicarbonate salt formation. Conversion to **2b**′ and **3b** was determined at room temperature and at 65 °C using ^{1}H NMR spectroscopy. Each spectrum (**2a**′, **2a**′**·HCl**, **2b**′, **3a**, **3a·HCl**, and **3b**) was internally

dx.doi.org/10.1021/ma2027484 | *Macromolecules* 2012, 45, 2955−2962

Table 1. Variation in Particle Size and ζ-Potential of PMMA Particles Synthesized Using Different Concentrations of Surfactant 1b, 2b, or 3b and Initiator 4[a]

	surf. choice[b]	mol % surf. precursor added[c]	mol % 4[c]	particle size[d] (nm) (PdI)	ζ-pot.[d] (mV)	conv (%)
1	**1b**	1.0	0.25	46 ± 0.2 (0.07)	67 ± 3	100
2	**1b**	0.25	0.14	83 ± 2 (0.07)	45 ± 4	97
3	**1b**	0.07	0.07	183 ± 2 (0.04)	35 ± 4	99
4	**2b**	1.0	1.0	465 ± 8 (0.05)	56 ± 1	92
5	**2b**	1.0	0.5	334 ± 2 (0.07)	52 ± 2	90
6	**2b**	1.0	0.25	316 ± 3 (0.12)	34 ± 4	96
7	**2b**	0.25	0.25	369 ± 2 (0.04)	41 ± 2	78
8	**2b**	0.07	0.07	852 ± 117 (0.2)	32 ± 2	72
9	**3b**	1.0	1.0	408 ± 9 (0.10)	44 ± 1	91
10	**3b**	1.0	0.5	347 ± 2 (0.06)	44 ± 0.4	93
11	**3b**	1.0	0.25	275 ± 5 (0.14)	35 ± 0.7	94
12	**3b**	0.5	0.5	352 ± 2 (0.09)	32 ± 0.6	85
13	**3b**	0.5	0.25	308 ± 2 (0.07)	45 ± 3	93
14	**3b**	0.25	0.25	397 ± 6 (0.06)	32 ± 1	86

[a]Polymerization was carried out at 65 °C for 2 h at 13.5 wt % MMA. [b]A blank run was also carried out using no surfactant and 0.25 mol % **4**; a stable latex was not formed. [c]With respect to MMA. [d]Ranges indicate the standard deviation in the particle size and ζ-potential measurements using the Zetasizer ZS.

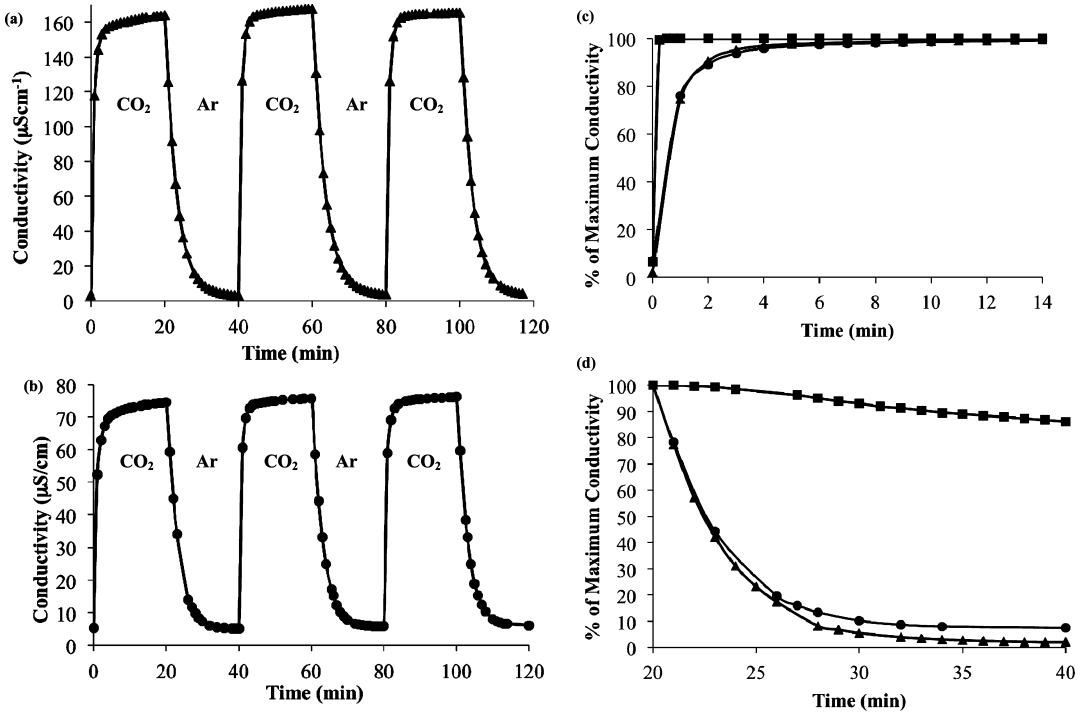


Figure 2. Conductivity of solutions during CO_2/Ar cycles in 20 mL ethanolic solutions containing 200 μL of water and 0.4 mmol of either (a) **2a** or (b) **3a** and the change in conductivity of wet ethanolic solutions of **1a** (■), **2a** (▲), and **3a** (●) at room temperature when (c) CO_2 followed by (d) Ar are bubbled through the solutions.

referenced against the signal for the methyl group at the end of the alkyl chain. The chemical shifts of protons contained close to the headgroup of the surfactant were determined. The HCl salt and neutral compounds were assumed to be converted 100% and 0% to the protonated form, respectively. Equations were developed correlating the chemical shift to % conversion, and using the chemical shift obtained from the spectra of carbonated **2a**′ and **3a**, % conversion to the bicarbonate salt was determined. The data for this experiment can be found in the Supporting Information.

Emulsion Polymerization and Destabilization. **2a** (0.078 mmol, 26 mg) or **3a** (0.078 mmol, 17 mg) was added to MMA (31.3 mmol, 3.13 g) in a 20 mL scintillation vial. This mixture was added to a round-bottom flask containing water (18.0 g) that was presaturated with CO_2 by bubbling the gas into the water using a needle. This mixture was allowed to stir for 30 min. The initiator, VA-061 (20 mg), was added to a separate 20 mL scintillation vial, 2.0 mL of water was added, and the solid was dissolved by adding carbon dioxide to form a water-soluble bicarbonate salt (**4**, Figure 1).[21] In cases where VA-044 was used as the initiator, CO_2 was not added, and the initiator was fully miscible in deionized water. The initiator solution was added to the round-bottom flask, which was equipped with a condenser, and was allowed to stir at 65 °C for 2 h while continuously bubbling CO_2 through the mixture using a needle. To destabilize the polymer latex that was formed, the CO_2 was removed from the system by sparging with air or Ar through a needle at various temperatures while stirring.

Colloid Characterization. Monomer conversion was determined gravimetrically by removing 1−2 g samples from the reaction mixture

dx.doi.org/10.1021/ma2027484 | *Macromolecules* 2012, 45, 2955−2962

Table 2. Variation in Emulsion Polymerization Conditions and Their Effect on the Particle Size and ζ-Potential of the Resulting PMMA Particles[a]

	change in procedure	surf.	particle size[b] (nm) (PdI)	ζ-potential[b] (mV)	conv (%)
1	none	**2b**	316 ± 3 (0.12)	34 ± 4	96
2	hydrochloride surfactant and initiator[c]	**2a**•HCl	34 ± 0.5 (0.18)	70 ± 6	100
3	none	**3b**	275 ± 5 (0.14)	35 ± 0.7	94
4	hydrochloride surfactant and initiator[c]	**3a**•HCl	45 ± 0.3 (0.08)	46 ± 1	100
5	surfactant dissolved in aqueous phase	**3b**	222 ± 7 (0.08)	42 ± 1	92
6	polymerization temperature is 50 °C	**3b**	363 ± 4 (0.04)	45 ± 0.8	85

[a]Polymerization was carried out with 13.5 wt % MMA (with respect to water), 1.0 mol % of **2a** or **3a** and 0.25 mol % of **4** (with respect to MMA), at 65 °C (unless otherwise noted). All reactions were carried out in the presence of CO_2, except in the cases where the hydrochloride versions of the surfactants were used (entries 2 and 4). [b]Ranges indicate the standard deviation in the particle size and ζ-potential measurements using the Zetasizer ZS. [c]VA-044 initiator was used.

using a syringe and allowing them to dry under a flow of air for 24 h and then in the oven for 24 h to determine the solid content of the latex. Plots of conversion versus time of the latexes synthesized according to the conditions in Table 1, entries 7 and 14, are shown in Figure S3. Conversion to polymer reached a maximum after 1 h (see Figure S1). Latex particle sizes were determined using a Malvern Zetasizer Nano ZS (size range of 0.6 nm−6.0 μm) and/or a Malvern Mastersizer 2000 equipped with a Hydro2000S optical unit (size range of 0.05−2000 μm). ζ-potential measurements were obtained using the Zetasizer ZS. To assess the effectiveness of latex destabilization, the Mastersizer 2000 was used to track changes in particle size over time. Measurement with the Mastersizer 2000 requires a large sample dilution with deionized water, which causes quasi-stable particles to aggregate during the measurement, giving irreproducible results. Therefore, the mixture of nonionic surfactants called Disponil A 3065 was added to the sample just prior to its addition to the Mastersizer to prevent particle aggregation and preserve the original particle size distribution during analysis. Samples for ζ-potential measurement were prepared by diluting 1 drop of the latex into ∼1 mL of DI water, and this solution was added to a clear folded capillary cell.

RESULTS AND DISCUSSION

Surfactant Switchability. Formation of solutions of the bicarbonate salts was achieved by purging CO_2 through solutions of **2a** and **3a**, but their isolation as pure solids was unsuccessful. Therefore, bicarbonate formation in solution was confirmed by the presence of a peak at 161 ppm (carbon of HCO_3^-) and ∼164 ppm (the cationic carbon) in the ^{13}C NMR spectra of solutions of **2a** and **3a** in CO_2-saturated MeOD-d_4. It has been shown previously that amidine switchable surfactants form bicarbonate (HCO_3^-) rather than carbonate salts (CO_3^{2-}) when reacted with CO_2 and water.[15] Conversion to **2b** and **3b** was 94% and 98% at room temperature and 47% and 54% at 65 °C, respectively. Since isolation of the bicarbonate salts was unsuccessful, they were formed in situ when used for emulsion polymerization.

The reversibility of the conversion from uncharged base to cationic surfactant was demonstrated by bubbling CO_2 followed by argon through solutions of **2a** and **3a** in wet ethanol and measuring the change in conductivity of the solution. The conductivity increased almost immediately when CO_2 was bubbled through the solution and decreased again when sparged with Ar. The maximum conductivities reached after 20 min of bubbling with CO_2 for **1b**, **2b**, and **3b** were 347, 164, and 75 μS cm^{-1}, respectively. The minimum conductivities reached after 20 min of bubbling with Ar for **2a** and **3a** were 3.0 and 5.1 μS cm^{-1}, respectively. The conductivity of the mixture of **1a**/**1b** after bubbling with Ar for 20 min was still 299 μS cm^{-1}. The CO_2/Ar cycle was performed three times to demonstrate the repeatability of the switching process (Figure 2a,b). The experiment was also carried out using **1a**, and the average results of the three cycles for each surfactant can be seen in Figure 2c,d. The application of Ar to **2b** and **3b** causes a rapid reduction in conductivity, and the original solution conductivity is restored after only 20 min, indicating that the surfactant is fully converted to the uncharged form. In the case of **1b**, after 20 min, the conductivity is only reduced by 14%, indicating that most of the surfactant remains in the charged form when the argon treatment is performed at room temperature. Thus, surfactants **2b** and **3b** would be significantly more effective than **1b** in applications where rapid deactivation of the surfactants is desired.

The extent of switching is related to the enthalpy of protonation of the surfactant. The enthalpies of protonation of the 7-carbon chain analogue of **2a** and the 8-carbon chain analogue of **3a** are 48 and 53 kJ mol^{-1}, respectively.[16] These values are much lower than the enthalpy of protonation of the 8-carbon chain analogue of **1a**, which is 71 kJ mol^{-1}. Therefore, it requires more energy to remove the proton from **1b**, which explains why the conductivity of an ethanolic solution of **1b** is only reduced by 14% versus the complete reduction in conductivity of solutions of **2b** and **3b** when the same destabilization conditions are used.

Initiator Choice. VA-044 (whose 10 h half-life temperature is 44 °C) and VA-061 (whose 10 h half-life temperature is 61 °C) were both used in the emulsion polymerization of MMA. VA-061 was added as an aqueous solution of its bicarbonate salt, **4**. The 10 h half-life temperature of **4** is dramatically decreased compared to that of VA-061 (42 °C vs 61 °C),[28] so **4** should have a similar initiator decomposition rate as VA-044. One significant difference between the VA-044 and **4**, however, is that **4** will revert back to its neutral form simply by heating to remove CO_2 from the system. At high temperatures the ratio of **4** to VA-061 will likely decrease. For this reason, even if the same concentrations of VA-044 and **4** are initially added to the polymerization, at the polymerization temperature the number of radicals produced from initiator decomposition is likely to be higher in cases where VA-044 is used.

Emulsion Polymerization. Bicarbonate salts **2b** and **3b** were formed in situ by bubbling CO_2 through the solution of **2a** or **3a** in MMA prior to emulsification. CO_2 was bubbled continuously through the emulsion while polymerization was being carried out to ensure the maximum amount of the surfactant was maintained in the bicarbonate salt form. Emulsion polymerization was performed using surfactants **2b** and **3b** at an initial concentration of 13.5 wt % MMA to show that stable latexes could be obtained. By investigating the effect of surfactant and initiator concentrations, temperature, and type

dx.doi.org/10.1021/ma2027484 | Macromolecules 2012, 45, 2955−2962

of surfactant on the resultant particle size and ζ-potential of the latex, key aspects of surfactant behavior in emulsion polymerization systems were evaluated (Tables 1 and 2). With the same surfactant type, as the surfactant concentration decreases, the particle size increases, which is expected due to the decrease in the number of particles that can be stabilized. Unexpected, however, is the increase in particle size with increasing initiator concentration which occurs with both **2b** and **3b**, but not **1b**[20] (Table 1, entries 4–6 and 9–11). The most likely explanation is that higher initiator concentrations favor the formation of small water-soluble oligomers containing charged initiator end groups, which increase the ionic strength of the aqueous phase, decreasing colloidal stability and increasing particle size.[29,30]

Greater particle sizes were obtained with surfactants **2b** and **3b** than with **1b** under equivalent conditions (Table 1, entries 1, 6, and 11), which is most likely due to the decreased basicity of these surfactants. The polymerization reactions are carried out at 65 °C, and the ratio of charged to uncharged form of the surfactant will be much less in the case of the **2b** and **3b**, effectively decreasing the amount of active surfactant available for particle stabilization. This hypothesis was tested by carrying out the emulsion polymerization using the hydrochloride salts of **2a** and **3a** (Table 2, entries 2 and 4) because these surfactants should be permanently charged; much smaller particles (45 and 34 nm versus 275 and 316 nm) were produced. This shows that the large particle size (in the cases where surfactants **2b** and **3b** are used) is not due to the decreased ability of the surfactant molecules with these head groups to pack on the particle's surface, but rather due to significant conversion of **2b** and **3b** to **2a** and **3a** under the polymerization conditions. Another possibility is that the neutral tertiary amine **3a** is acting as a chain transfer agent,[31] decreasing the amount available for reaction with CO_2 to form **3b**. This would decrease the amount of active surfactant and increase the particle size. The same conclusion cannot be made for **2a** because it is unknown whether **2a** can act as a chain transfer agent.

The mean particle size of latexes made using **1b** is significantly smaller than latexes made using **2b** or **3b**, indicating a much higher particle number (and thus higher expected polymerization rate) with **1b**. It is therefore curious that conversion in most experiments with **2b** and **3b** is still high within a 2 h reaction time, posing the question of whether the primary particle size with **2b** and **3b** may be small, and whether we are measuring the particle size of aggregates. Although we did not do SEM analyses, we think this is unlikely. While the final conversion in all cases (using surfactants **1b**, **2b**, or **3b**) is typically greater than 90%, the time that it takes to reach these conversions is greater in the cases where **2b** or **3b** are used instead of **1b** (~1 h vs ~20 min). More importantly, all latexes appeared to be colloidally stable with minimal to no coagulum formed. If significant aggregation was occurring with **2b** or **3b**, it would very likely be accompanied by substantial coagulum formation.

In an attempt to make smaller particles using **3b**, polymerization at 50 °C (to ensure a greater ratio of **3b**:**3a**) was attempted (Table 2, entries 3 and 6), but this simply increased reaction time and decreased the number of radicals formed by initiator decomposition, resulting in large particles.

A significant decrease in particle size was noted when **3a** was dissolved in the aqueous phase rather than the monomer phase prior to polymerization (Table 2, entries 3 and 5). This may be due to the greater polarity of the aqueous phase, which would favor greater conversion of **3a** to the ammonium bicarbonate salt. While surfactant **1b** can be used in very low concentrations (0.07 mol % of MMA) and still provide adequate stabilization, such a small concentration of **2b** produces a latex containing very large particles with low conversion of monomer and significant amounts of coagulum (17%) (Table 1, entry 8).

ζ-potential values of all the latexes synthesized were over 30 mV, indicating that the latexes should be stable. It appears that the ζ-potential depends on the basicity of the surfactant, with less basic surfactants producing particles with smaller ζ-potentials (Table 1, entries 1, 6, and 11). This is not surprising in light of the previous discussion concerning the partial conversion of the less basic surfactants **2b** and **3b** to their neutral forms under the polymerization conditions.

Effect of Initiator Type, Additives, and CO_2 Pressure on Particle Size. To broaden the applicability of these surfactants, a wide range of particle sizes must be attainable with slight variations in the polymerization conditions. Three strategies were evaluated for their ability to promote the production of smaller particles: using VA-044 as an initiator, adding CTAB (cetyltrimethylammonium bromide) as an extra stabilizer, and carrying out the reaction under increased CO_2 pressure. While these strategies may lead to smaller particles, as described below and shown in Table 3, the use of VA-044 or CTAB may adversely affect the ability of the product latex to destabilize and aggregate upon removal of the CO_2. For this reason, only a very small amount of VA-044 or CTAB was used. The destabilization will be discussed in the next section.

Table 3. Effect of Modified Conditions for Emulsion Polymerization on the Size and ζ-Potential of the PMMA Particles and the Conversion of Monomer[a]

	change in procedure	mol % **3a** added	mol % initiator[b]	particle size[e] (nm)	ζ-potential[e] (mV)	conv (%)
1	none	1.0	0.25	275 ± 5	35 ± 0.7	94
2	initiator is VA-044	1.0	0.25	167 ± 2	41 ± 2	96
3	initiator is VA-044	1.0	0.10	154 ± 2	39 ± 2	
4	initiator is VA-044	1.0	0.05	161 ± 2	34 ± 2	92
5	CTAB was added[c]	1.0	0.25	78 ± 1	43 ± 4	99
6	CTAB was added[c]	0.25	0.25	126 ± 1	39 ± 2	87
7	increased CO_2 pressure[d]	1.0	0.25	174 ± 1	44 ± 1	88

[a]Polymerization was carried out at 65 °C in the presence of CO_2 when the initiator was **4** and 50 °C when the initiator was VA-044, for 2 h, at 13.5 wt % MMA. [b]Initiator is **4** unless otherwise indicated. [c]6.3 mol % (with respect to **3a**) was used. [d]Pressure was 5 atm. [e]Ranges indicate the standard deviation in the particle size and ζ-potential measurements using the Zetasizer ZS.

The use of VA-044 as an initiator allowed the reaction to be carried out at lower temperatures (50 °C) while maintaining a high rate of initiator decomposition. However, this initiator is a hydrochloride salt, and therefore a polymer prepared with VA-044 cannot be switched to a completely uncharged form by the simple removal of CO_2; the imidazoline·HCl groups from the initiator would either remain charged or, more likely, they would transfer their protons (and chloride counterions) to the more basic amidine group in surfactant **1a** and thereby cause

dx.doi.org/10.1021/ma2027484 | Macromolecules 2012, 45, 2955–2962

the surfactant to be permanently charged. It has been shown that when VA-044 is used with surfactant **1b**, sparging with air and heating does not destabilize the latex.[20,21] However, if VA-044 is used with surfactants **2b** and **3b**, then the situation is slightly different; no transfer of protons will occur from the initiator to the surfactant because the imidazoline fragments are more basic than the tertiary amine or phenyl amidine head groups of **2a** and **3a**; thus, the surfactant would remain switchable while the initiator residues would remain permanently cationic. The results in Table 3 show that the particle size does decrease when this initiator is used and the polymerization is carried out at 50 °C (Table 3, entry 1 vs entries 2–4), which is likely due to the presence of more bicarbonate surfactant, **3b**, at the lower temperature.

The second strategy involved adding CTAB as a cosurfactant to impart extra stability to the emulsion and subsequent latex. This strategy also produced smaller particles (Table 3, entries 5 and 6).

The third strategy involved pressurizing the reaction vessel to ensure that more CO_2 was dissolved in the emulsion in order to increase the amount of surfactant in the charged form. When the polymerization reaction was carried out at a higher pressure (5 atm) in a stainless steel Parr vessel, the particle size decreased compared to the same reaction at atmospheric pressure (Table 3, entry 1 vs entry 7). This is an indication that more bicarbonate surfactant is present in the aqueous phase at higher CO_2 pressures. This makes sense because CO_2 is a reactant in an equilibrium reaction so increasing the CO_2 pressure would increase the ratio of **3b** to **3a** according to the equilibrium expression shown in eq 1, assuming that the equilibrium constant does not change with pressure. The particle size is not as small as it is in the case where **3b•HCl** was used, indicating that some of the switchable surfactant remains in the uncharged form, likely dissolved in the monomer phase where it is not as easily converted to a bicarbonate salt.

$$K = \frac{[\mathbf{3b}][HCO_3^-]}{[\mathbf{3a}]P_{CO_2}} \quad (1)$$

Attempts at making polymer latexes with 24 wt % polymer using surfactant **3a** and initiator **4** failed. The reaction resulted in high amounts of coagulum, high viscosities, and significant aggregation. However, the strategy employed above to make smaller, more stable particles, by using VA-044 as an initiator and lower reaction temperatures, was successfully employed to make 24 wt % latexes. As an example, 1.5 mol % **3b** and 0.05 mol % VA-044 were used at 50 °C to make a latex with 193 ± 3 nm particles (PdI = 0.07) with a ζ-potential of 36 ± 1 mV. There was no coagulum or aggregates formed during the synthesis and the latex could be successfully destabilized using only air at 65 °C.

Long-term stability of the polymer latex synthesized using the conditions in Table 1, entry 7 was assessed by exposing one-half of the latex to air and storing it in a loosely capped vial and storing the other half under an atmosphere of CO_2 in a capped vial with Parafilm. Initial particle size and ζ-potentials were compared to those taken after 3 weeks for both samples, and the data are summarized in Table 4. The particle size of the sample exposed to air dramatically increases and the zeta potential decreases, while no changes are observed in the case of the latex sealed under CO_2. From this data, we conclude that the latexes remain stable as long as they are under an atmosphere of CO_2.

Table 4. Assessment of the Long-Term Stability of a Latex Synthesized According to the Conditions in Table 1, Entry 7 (13.5 wt % MMA, 0.25 mol % 2b, 0.25 mol % 4)[a]

	particle size		
	Zetasizer (nm) (PdI)	Mastersizer (nm)	ζ-potential (mV)
initial	381 ± 5 (0.10)	278	32 ± 1
after 3 weeks (stored under CO_2)	419 ± 3 (0.10)	261	35 ± 1
after 3 weeks (exposed to air and capped)		4500	8.5 ± 0.6

[a]Measurements were taken at room temperature.

Destabilization. Destabilization of the polymer latexes was achieved by sparging the latexes with air or Ar to remove the CO_2. During the destabilization of PMMA latex containing **1b**, a distinct population of particles at ~6 μm forms, creating a bimodal particle size distribution (the other peak in the distribution being the original particle size).[20] This bimodal distribution was also observed during the destabilization of latexes synthesized using **2b** and **3b**. One way to determine the efficiency and rate of the destabilization process is to calculate the volume percentage of each of the particle populations over time. This type of analysis was carried out for the destabilization of latexes formed with **2b** using the conditions of Table 1, entry 7 (Figure 3). After sparging the latex with air

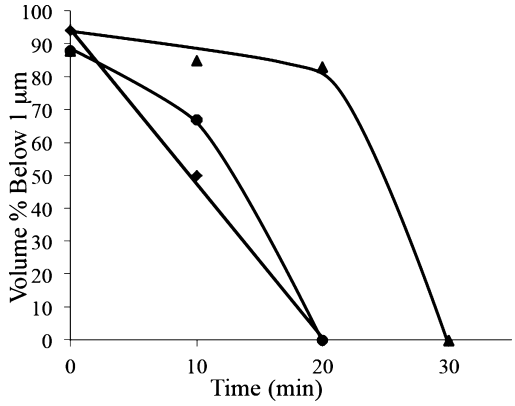


Figure 3. Volume percent of PMMA particles below 1 μm as a function of time during destabilization using air at 65 °C (♦), 40 °C (●), and room temperature (▲) in a latex synthesized using surfactant **2b** according to the conditions in Table 1, entry 7.

at 40 or 65 °C, there are no initial nanometer-sized particles remaining after 20 min. Furthermore, it was found that the destabilization could be carried out to completion after 30 min at room temperature by simply sparging the latex with air with no additional heat supplied. Using surfactant **1b**, higher solid content latexes synthesized under similar conditions required 4 h of sparging with air and heating (65 °C) to be fully destabilized.[20]

In order to determine whether latex destabilization was occurring due to the decreased surface charge on the polymer particles upon CO_2 removal, the ζ-potential was monitored over time during Ar and heat (65 °C) treatment. Figure 4 shows that the ζ-potential decreases more rapidly when sparging with inert gas is combined with heating but that

dx.doi.org/10.1021/ma2027484 | Macromolecules 2012, 45, 2955–2962

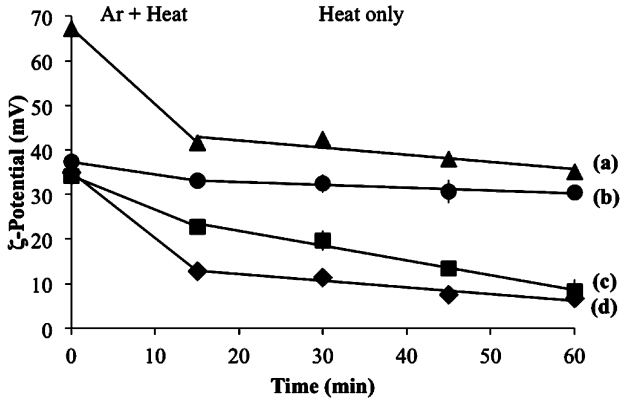


Figure 4. Change in ζ-potential with time of PMMA latexes destabilized using Ar and heat (65 °C) for 15 min followed by 45 min at 65 °C without Ar bubbling. Initial latexes were synthesized using (▲) 1.0 mol % **1b** and 0.25 mol % **4**, (●) 0.07 mol % **1b** and 0.07 mol % **4**, (□) 1.0 mol % **2a** and 0.25 mol % **4**, and (♦) 1.0 mol % **3a** and 0.25 mol % **4**.

simply heating the latex also decreases the ζ-potential, albeit at a slower rate. It has been shown previously for PMMA latexes synthesized using **1b** that the ζ-potential below which destabilization occurs is ~25 mV.[20] Figure 4a,c,d shows that the surface charge of the PMMA particles decreases below the threshold within the first 20 min in the cases where surfactants **2b** and **3b** are used. In contrast, the surface charge of the latex produced using **1b** did not decrease below 25 mV even after 60 min of Ar and heat treatment. Destabilization (appearance of flocs and an increase in latex viscosity) was observed visually in the latexes synthesized using **2b** and **3b** after the first 15 min of destabilization. To ensure that it was not simply a higher starting ζ-potential causing the greater stability of the latex synthesized using **1b** (Figure 4a), another latex was synthesized using less **1b** and **4** (0.07 mol % each) to ensure that the starting ζ-potential matched those in Figure 4c,d. In this case (Figure 4b), the initial ζ-potential was 37 mV, and it was found that Ar and heat treatment caused little change in the ζ-potential. Thus, regardless of the initial ζ-potential, latexes synthesized using **2b** and **3b** destabilized much more rapidly than those synthesized using **1b**.

In the case where nonswitchable initiator VA-044 was used instead of **4** in order to promote the formation of smaller particles, latex destabilization upon exposure to air and heat occurred only when a very small amount of initiator was used (0.05 mol % with respect to monomer). This indicates that the charged initiator end groups contribute greatly to latex stability and that, when a nonswitchable initiator is being used, the initiator concentration must be minimized in order to ensure that the latex can be destabilized. When nonswitchable surfactant CTAB was used as a cosurfactant along with switchable surfactant **3a**, the same phenomenon was observed; latex destabilization was possible as long as the concentration of CTAB was kept sufficiently low. Increased sample viscosity was observed after the first 30 min of treatment when 0.016 mol % was used. This corresponded to a decrease in ζ-potential from 40 to 27 mV (Figure 5), after which the ζ-potential leveled off (which was expected because CTAB should remain in its charged form). The low concentration of CTAB used in this experiment ensures that this leveling off will happen at or below the "threshold of destabilization", which is ~25 mV. In contrast, destabilization of the latex synthesized with 0.063 mol % CTAB

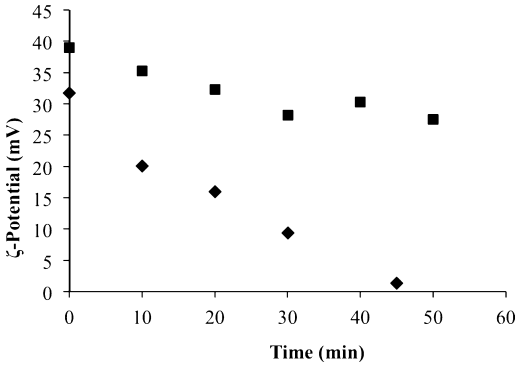


Figure 5. Change in ζ-potential with time during the destabilization of latexes synthesized (♦) with **3a** as the only surfactant (Table 1, entry 14) and (■) with both **3a** and CTAB (0.016 mol % with respect to monomer, Table 3, entry 6).

did not occur in the first 60 min of treatment (determined visually).

■ CONCLUSIONS

In summary, two recently developed, less basic switchable surfactants (where the trigger to go between the uncharged and charged forms is CO_2) have been used in the emulsion polymerization of MMA. The resulting latexes were stable if kept under an atmosphere of CO_2. Upon CO_2 removal using a nonacidic gas, heat, or a combination of both, the surfactant becomes uncharged and the latexes can be destabilized. These less basic surfactants offer a significant advantage over the previously developed switchable surfactants due to their ability to easily and rapidly revert to the uncharged forms, with a much lower zeta potential (approaching zero in some cases) than previously attainable. Both surfactants have similar basicities and yield similar results when used in emulsion polymerization. However, the long chain tertiary amine offers a clear advantage over the aryl amidine due to the lower cost and commercial availability of the amine.

The greatest advantage of using **2b** and **3b** in emulsion polymerization is the ease of postpolymerization latex destabilization compared to **1b**. The rate of formation of micrometer sized aggregates was greater in the case of latexes formed using **2b** and **3b**. Furthermore, final zeta potential values were smaller in the case of these less basic surfactants due to the greater conversion of these surfactants to their neutral forms during the destabilization procedure.

When equal amounts of surfactants were used, particle sizes were always larger in latexes stabilized by **2b** or **3b** than by **1b**. Three strategies (adding a cosurfactant, using a different initiator and increasing the CO_2) were used to promote the formation of smaller particles. Although each method reduced the particle size, destabilization of latexes with nonswitchable cosurfactants was not successful unless the cosurfactant concentration was small. Reducing the initiator concentration also reduces the polymerization rate, making this option not as viable as the addition of a cosurfactant such as CTAB. Furthermore, alteration of the cosurfactant concentration should allow one to obtain latexes with specific particle sizes. Increasing the CO_2 pressure to 5 atm afforded smaller particles, and subsequent latexes were easily destabilized upon addition of air and heat. The limitation of this method is the requirement for vessels designed for use at slightly elevated pressure.

dx.doi.org/10.1021/ma2027484 | *Macromolecules* 2012, 45, 2955−2962

Because these surfactants are not basic enough to remain fully charged under the polymerization conditions, higher concentrations must be used compared to more basic amidine surfactants, although the absolute concentration required is still quite low. The fate of the excess neutral amine or amidine is unknown, but it is likely trapped in the polymer particles, and this could alter the properties of the final product. A possible solution is to find a switchable surfactant with an intermediate pK_{aH} (between 10.8 and 12.2) such that the polymerization can be carried out with lower surfactant concentrations, and yet latex destabilization using air and heat does not take a long time.

■ ASSOCIATED CONTENT

Supporting Information

^{1}H NMR and ^{13}C NMR spectra, experimental data for the conversion of **2a** to **2b** and **3a** to **3b**, and conversion profiles for MMA polymerization. This material is available free of charge via the Internet at http://pubs.acs.org.

■ AUTHOR INFORMATION

Corresponding Author

*E-mail: michael.cunningham@chee.queensu.ca (M.F.C.); jessop@chem.queensu.ca (P.G.J.).

Notes

The authors declare no competing financial interest.

■ ACKNOWLEDGMENTS

We thank Xerox Research Center of Canada for continued support and advice and the National Sciences and Engineering Research Council and the Canada Research Chairs (Jessop) program and the Ontario Research Chairs (Cunningham) program for financial support.

■ REFERENCES

(1) Schramm, L. L. *Emulsions, Foams, and Suspensions: Fundamentals and Applications*; Wiley-VCH: Weinheim, 2005.

(2) Minkenberg, C. B.; Florusse, R. E.; Koper, G. J. M.; van Esch, J. H. *J. Am. Chem. Soc.* **2009**, *131*, 11274−11275.

(3) (a) Dexter, A. F.; Malcolm, A. S.; Middelberg, A. P. *J. Nat. Mater.* **2006**, *5*, 502−506. (b) Minkenberg, C. B.; Florusse, R. E.; Koper, G. J. M.; van Esch, J. H. *J. Am. Chem. Soc.* **2009**, *131*, 11274−11275.

(4) Dexter, A. F.; Middelberg, A. P. J. *Ind. Eng. Chem. Res.* **2008**, *47*, 6391−6398.

(5) Sakai, H.; Abe, M. Control of Molecular Aggregate Formation and Solubilization using Electro- and Photoresponsive Surfactant Mixtures. In *Mixed Surfactant Systems*; Abe, M., Scamehorn, J. F., Eds.; Surfactant Science Series; Marcel Dekker: New York, 2005; Vol. *124*, pp 507−543.

(6) Schmittel, M.; Lal, M.; Graf, K.; Jeschke, G.; Suske, I.; Salbeck, J. *Chem. Commun.* **2005**, 5650−5652.

(7) Saji, T.; Hoshino, K.; Aoyagui, S. *J. Am. Chem. Soc.* **1985**, *107*, 6865−6868.

(8) Anton, P.; Koeberle, P.; Laschewsky, A. *Prog. Colloid Polym. Sci.* **1992**, *89*, 56−59.

(9) Datwani, S. S.; Truskett, V. N.; Rosslee, C. A.; Abbott, N. L.; Stebe, K. J. *Langmuir* **2003**, *19*, 8292−8301.

(10) Aydogan, N.; Abbott, N. L. *Langmuir* **2001**, *17*, 5703−5706.

(11) Cheng, Z.; Ren, B.; Gao, M.; Liu, X.; Tong, Z. *Macromolecules* **2007**, *40*, 7638−7643.

(12) Tsuchiya, K.; Orihara, Y.; Kondo, Y.; Yoshino, N.; Ohkubo, T.; Sakai, H.; Abe, M. *J. Am. Chem. Soc.* **2004**, *126*, 12282−12283.

(13) Ghosh, S.; Irvin, K.; Thayumanavan, S. *Langmuir* **2007**, *23*, 7916−7919.

(14) Sakai, H.; Matsumura, A.; Yokoyama, S.; Saji, T.; Abe, M. *J. Phys. Chem. B* **1999**, *103*, 10737−10740.

(15) Liu, Y.; Jessop, P. G.; Cunningham, M.; Eckert, C. A.; Liotta, C. L. *Science* **2006**, *313*, 958−960.

(16) (a) Scott, L. M. Designing the Head Group of Switchable Surfactants. M.Sc. Dissertation, Queen's University, Kingston, ON, 2009. (b) Scott, L.; Robert, T.; Harjani, J. R.; Jessop, P. G., submitted.

(17) Harjani, J. R.; Liang, C.; Jessop, P. G. *J. Org. Chem.* **2011**, *76*, 1683−1691.

(18) Liang C.; Harjani J. R.; Robert T.; Rogel E.; Kuehne D.; Ovalles C.; Sampath V.; Jessop P. G. *Energy & Fuels* **2012**, *26*, 488−494.

(19) Qin, Y.; Yang, H.; Ji, J.; Yao, S.; Kong, Y.; Wang, Y. *Tenside, Surfactants, Deterg.* **2009**, *46*, 294−297.

(20) Fowler, C. I.; Muchemu, C. M.; Miller, R. E.; Phan, L.; O'Neill, C.; Jessop, P. G.; Cunningham, M. F. *Macromolecules* **2011**, *44*, 2501−2509.

(21) Mihara, M.; Jessop, P.; Cunningham, M. *Macromolecules* **2011**, *44*, 3688−3693.

(22) Blackley, D. C. *High Polymer Latices: Their Science and Technology*; Palmerton Publishing Co. Inc.: New York, 1966.

(23) *Emulsion Polymerization and Emulsion Polymers*; El-Aasser, M., Lovell, P., Eds.; John Wiley & Sons, Inc.: Chichester, NY, 1997.

(24) Gilbert, R. G. *Emulsion Polymerization: A Mechanistic Approach*; Academic Press: London, 1995.

(25) Zhang, Q.; Wang, W.-J.; Lu, Y.; Li, B.-G.; Zhu, S. *Macromolecules* **2011**, *44*, 6539−6545.

(26) Hall, H. Jr. *J. Am. Chem. Soc.* **1957**, *79*, 5441−5444.

(27) Cook, M. J.; Katritzky, A. R.; Nadji, S. *J. Chem. Soc., Perkin Trans. 2* **1976**, 211−214.

(28) Su X.; Jessop P. G.; Cunningham M. F. *Macromolecules* **2012**, *45*, 666−670.

(29) Blackley, D. C. *Polymer Latices: Science and Technology*; Chapman & Hall: London, 1997.

(30) Tanrisever, T.; Okay, O.; Soenmezoğlu, I. C. *J. Appl. Polym. Sci.* **1996**, *61*, 485−493.

(31) Bamford, C. H.; White, E. F. T. *Trans. Faraday Soc.* **1956**, *52*, 716−727.

Macromolecules

Article

pubs.acs.org/Macromolecules

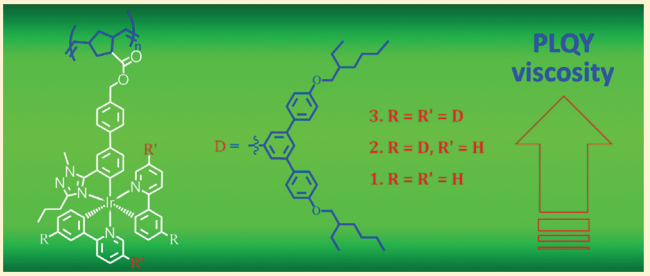
Poly(dendrimers) with Phosphorescent Iridium(III) Complex-Based Side Chains Prepared via Ring-Opening Metathesis Polymerization

Wen-Yong Lai,[†,§] Michael N. Balfour,[†] Jack W. Levell,[‡,∥] Ashu K. Bansal,[‡] Paul L. Burn,*[,†] Shih-Chun Lo,*[,†] and Ifor D. W. Samuel*[,‡]

[†]Centre for Organic Photonics & Electronics (COPE), The University of Queensland, School of Chemistry & Molecular Biosciences, Chemistry Building, Queensland, 4072 Australia

[‡]Organic Semiconductor Centre, SUPA, School of Physics and Astronomy, University of St. Andrews, North Haugh, St Andrews, Fife, KY16 9SS, United Kingdom

ABSTRACT: Phosphorescent poly(dendrimers) with a norbornene-derived backbone have been synthesized using ring-opening metathesis polymerization with the Grubbs III catalyst. The dendrimers are comprised of a heteroleptic iridium(III) complex core with two 2-phenylpyridyl ligands and a phenyltriazolyl ligand, biphenyl-based dendrons, and 2-ethylhexyloxy surface groups. The phenyltriazolyl ligand provides the attachment point to the polymer backbone, and the two poly(dendrimers) differ in the number of dendrons attached to the 2-phenylpyridyl ligands. The poly(dendrimer) with one and two dendrons per ligand are termed mono- and doubly dendronized. The mono- and doubly dendronized poly(dendrimers) were found to have relatively narrow polydispersities, around 1.4, viscosities approaching those required for inkjet printing, and could be solution processed to form thin films. The dendrons played an important role in controlling the photophysical properties of the materials. The parent homopolymer with the same iridium(III) complex but no dendrons attached to the ligands had a solution photoluminescence quantum yield (PLQY) of 48%. The solution PLQY was found to increase with increasing number of dendrons with the mono- and doubly dendronized materials having solution PLQYs of 65% and 71%, respectively. The increase in PLQY is due to decreased intrachain interchromophore interactions. A similar trend was observed in the solid state with the parent, mono-, and doubly dendronized polymers having film PLQYs of 2%, 44%, and 58%, respectively, demonstrating that both intra- and interchain interactions are controlled by the dendrons.



INTRODUCTION

Organic light-emitting diodes (OLEDs) offer a number of important properties for large-area displays and lighting including low driving voltage, high efficiency, light weight, and fast switching times. Tremendous advances have been achieved in OLEDs containing light-emitting small molecules,[1] polymers,[2] and dendrimers.[3,4] Iridium(III) complexes have so far proven to be the most promising candidates as emissive materials in the development of OLEDs because of their high efficiency, relatively short excited state lifetime, and color tunability.[5−7] The strong spin−orbit coupling of the heavy metal allows efficient intersystem crossing that enables harvesting both the singlet and triplet excitons formed in the OLEDs to give internal quantum efficiencies as high as 100%.[5b,c] Small molecules are primarily processed by thermal evaporation, while dendrimers and polymers are generally processed from solution at room temperature. Solution processing of materials is desirable since it can simplify the fabrication of large-area OLEDs and lower the cost. However, the ability to combine the high efficiency of iridium(III) complex emitters with processing by printing techniques has continued to prove challenging. Phosphorescent dendrimers are solution processable and have given rise to very efficient monochrome devices prepared by spin-coating. Inkjet printing is an attractive technique for large area fabrication of pixellated structures on flexible plastic electronics[8] as it allows more than one material to be deposited at a time, thus limiting the number of processing steps, and it is compatible with roll-to-roll production.[9] However, the viscosity of dendrimer solutions used for spin-coating is normally similar to that of the solvent itself at the concentrations used,[10] and is not compatible with large-area inkjet printing.

"Light-emitting inks" for inkjet printed OLEDs require good solution processability and suitable viscosity and should give efficient phosphorescence in the solid state. While there has been some effort on polymeric materials containing iridium(III) side chains the main focus has been on random copolymers with low levels of small molecule iridium(III) complexes attached as side chains.[11−23] The low level of complexes attached to the copolymer is to avoid triplet−triplet annihilation.[24] However, the viscosity of the polymers and their potential for printing has not generally been considered. Our

Received: February 15, 2012
Revised: March 12, 2012
Published: March 22, 2012

ACS Publications © 2012 American Chemical Society

approach to developing "light-emitting" inks has been to combine the excellent photophysical properties of light-emitting dendrimers with the viscosity imparted by a polymer backbone.[25]

In this contribution, we demonstrate that ring-opening metathesis polymerization (ROMP) can be used to form sterically encumbered poly(dendrimers) with a relatively narrow poly(dispersity). The structures of poly(dendrimers) are shown in Figure 1, and they are comprised of a norbornenyl

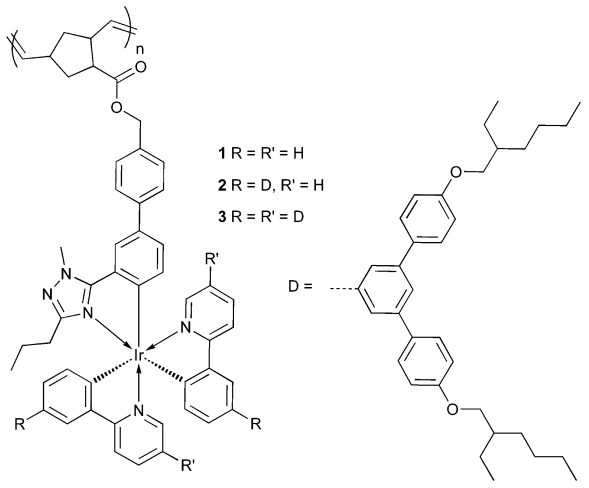


Figure 1. Structures of parent homopolymer **1** and poly(dendrimers) **2** and **3**.

derived backbone and dendrimer "side chains". The dendrimer side chains have a heteroleptic iridium(III) complex core that utilizes a phenyltriazole ligand as the attachment point to the polymer backbone, and the dendrons are attached to the two 2-phenylpyridyl ligands. We compare the physical and optoelectronic properties of the parent polymer that has the simple small molecule complex (no dendrons) attached to each "monomer unit" (**1** in Figure 1) and two poly(dendrimers) (**2** and **3**, Figure 1). **2** has one first generation biphenyl-based dendron with 2-ethylhexyloxy surface groups attached to each ligand while **3** has two.

RESULTS AND DISCUSSION

Synthesis. The synthetic route to all three polymers followed the same three steps as shown in Scheme 1. The "macromonomer" route was chosen to ensure that every monomer unit in the final polymer had a phosphorescent side chain attached. The syntheses all start from the brominated heteroleptic complexes, **4**, **5**, and **6**, which have been previously reported.[27−29] Coupling of the heteroleptic iridium(III) complexes **4**, **5**, and **6** with 4-formylphenylboronic acid under Suzuki conditions[30] gave compounds **7**, **8**, and **9** in yields of 97%, 77%, and 79%, respectively. The aldehyde group of each compound was then reduced to the corresponding alcohol using lithium aluminum hydride, and subsequent esterification with exo-5-norbornene-2-carboxylic acid gave "macromonomers" **10**, **11**, and **12** in excellent yields of 91%, 100%, and 86%, respectively, over the two steps. "Macromonomers" **10**, **11**, and **12** were then polymerized in chloroform (for **10** and THF for **11** and **12**) at room temperature using the Grubbs III catalyst.[31] The polymerizations were left for 20 min and quenched by the addition of ethyl vinyl ether. The target polymers were purified and collected by reprecipitation to give **1**, **2**, and **3** in yields of 94%, 94%, and 94%, respectively.

Physical Properties. The molecular weights of the polymers were determined by gel permeation chromatography (GPC) relative to polystyrene standards. Polymer **1** had an $\bar{M}_w$ of 14 kDa and a polydispersity of 1.5 while poly(dendrimers) **2** and **3** had $\bar{M}_w$s of 74 and 65 kDa and polydispersities of 1.3 and 1.4, respectively. It is worthwhile to note that GPC can underestimate the molecular weights by a factor of around 3−4 as found in our previous work.[10] Nevertheless, the low polydispersity of the polymers indicates good control of the polymerizations under the ROMP conditions. The polymers were soluble in common organic solvents such dichloromethane, chloroform, dichlorobenzene, and tetrahydrofuran, and good-quality films could be formed by spin-coating.

One of the reasons for designing the poly(dendrimers) was to increase their solution viscosity relative to the simple dendrimers. The viscosity of poly(dendrimer) **2** and its corresponding monomer **11** were evaluated at different concentrations in 1,2-dichlorobenzene at 20 °C with deionized freshly distilled water used as the reference[32] (1.00 cSt at 20 °C). 1,2-Dichlorobenzene was determined to have a viscosity of 1.06 cSt. At a concentration of 10 mg/mL "macromonomer" **11** had a viscosity of 1.14 cSt while the viscosity of poly(dendrimer) **2** at the same concentration was 1.30 cSt, a 14% increase. At a concentration of 25 mg/mL, the viscosity of **2** increased to 1.41 cSt. At the same concentration (25 mg/mL), a viscosity of 1.50 cSt was determined for poly(dendrimer) **3** (the doubly dendronized material), which is suitable for inkjet printing.[29]

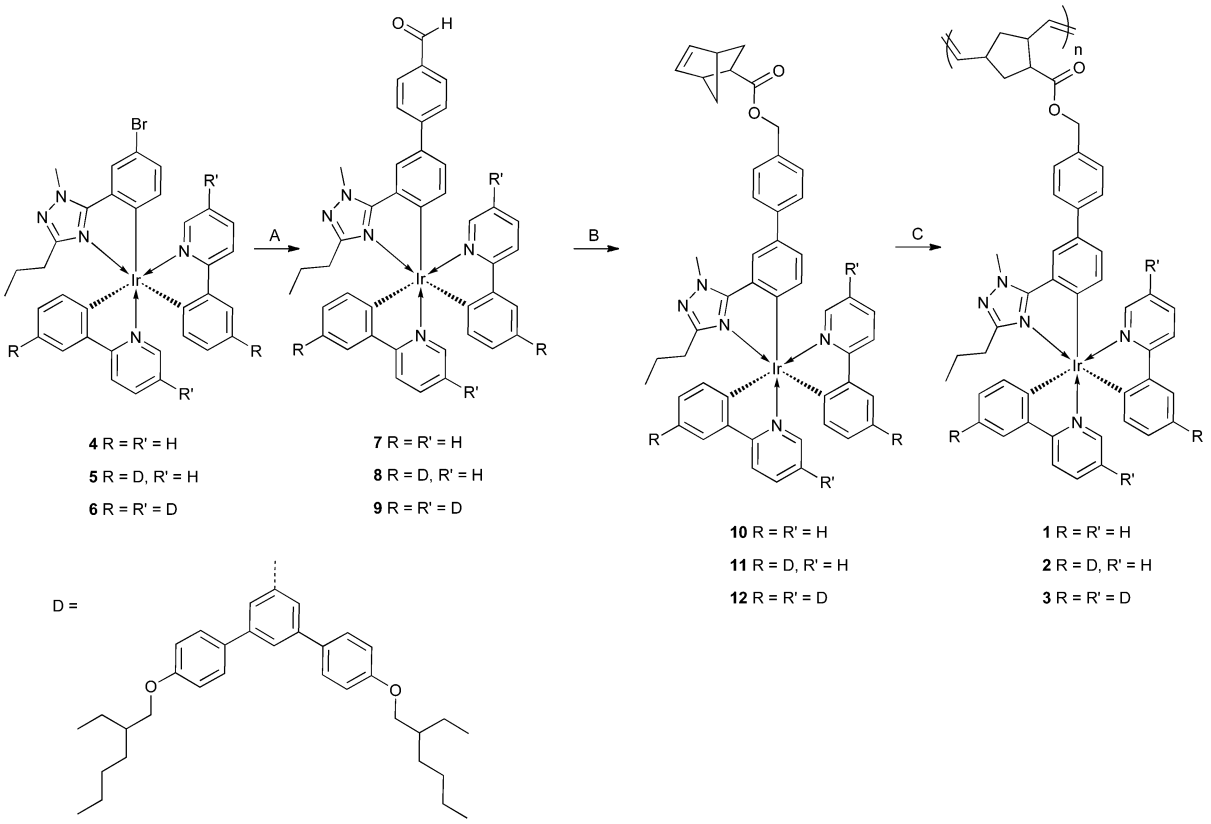
The final step in the analysis of the physical properties of the materials was a study on their thermal properties. Thermal gravimetric analysis of parent polymer **1** showed a 5% weight loss at 365 °C, whereas poly(dendrimers) **2** and **3** were more stable with similar weight losses not seen until 405 and 421 °C, respectively. Thus, dendronization improves the thermal stability. Differential scanning calorimetry of the three polymers showed no thermal transitions, indicating that the materials were amorphous.

Optoelectronic Properties. The first step in studying the optoelectronic properties of the three polymers was determination of their oxidation potentials using cyclic voltammetry. Parent polymer **1** had an oxidation potential of 0.22 V against the ferrocenium/ferrocene couple. As was expected, addition of the dendrons on the phenyl group of the ligand *para* to the phenyl−iridium(III) bond had little effect on the oxidation potential, which was 0.26 V for poly(dendrimer) **2**. Similarly, the oxidation potential for the doubly dendronized poly(dendrimer) **3** was 0.29 V, which again shows a minimal effect of dendronization is small when the $E^{1/2}$(ox) is compared with the parent polymer **1**.

The solution absorption spectra of polymers **1**, **2**, and **3** are shown in Figure 2. Each spectrum is comprised of two main regions: at wavelengths greater than 350 nm the relatively weak absorptions are mainly due to the so-called metal-to-ligand charge transfer (MLCT) transitions,[33] while those at shorter wavelengths are dominated by the $\pi-\pi^*$ transitions of the ligands and in the case of poly(dendrimers) **2** and **3** there is also additional absorption due to the chromophores in the dendrons. For poly(dendrimer) **3**, the onset to the absorption was found at about 544 nm, which is about 30 nm red-shifted compared to those of **1** and **2**. The red shift in the onset of absorption indicates a slightly narrower optical gap in **3**, which

dx.doi.org/10.1021/ma300306d | *Macromolecules* 2012, 45, 2963−2971

Scheme 1[a]



[a]Reagents and conditions: (A) 4-formylphenylboronic acid, $Pd(PPh_3)_4$, 2 M $K_2CO_{3(aq)}$, THF (for **8** and **9**, and EtOH and toluene for **7**), heat, $Ar_{(g)}$; (B) $LiAlH_4$, THF then H_2O, rt, $Ar_{(g)}$, and then *exo*-5-norbornene-2-carboxylic acid, 4-(*N*,*N*-dimethylamino)pyridine, dicyclohexylcarbodiimide, CH_2Cl_2, rt, $Ar_{(g)}$; (C) Grubbs III initiator, $CHCl_3$, rt, $Ar_{(g)}$.

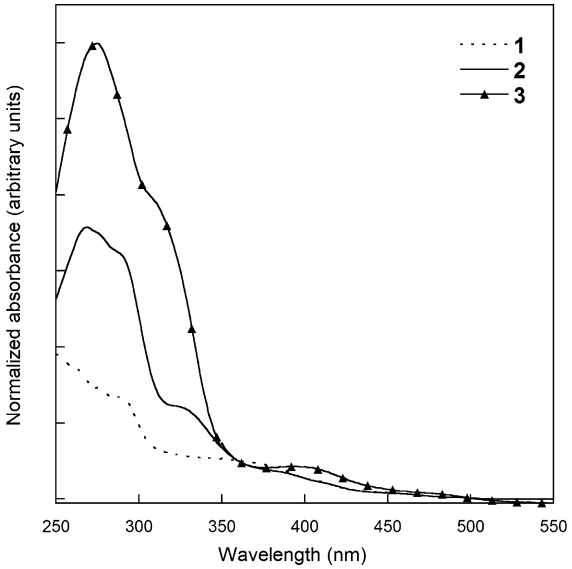


Figure 2. UV−vis absorption spectra of parent polymer **1** and poly(dendrimers) **2** and **3** in dichloromethane, normalized at 360 nm.

is due to the dendron attached to the pyridine moiety of the 2-phenylpyridyl ligand extending the conjugation of the ligand.[7e]

Figure 3a shows the solution spectra for polymers **1**, **2**, and **3**. In solution, the PL spectra of parent polymer **1** and monodendronized polymer **2** are similar with emission maxima at 514 and 517 nm, respectively. This again reflects the fact that when the dendron is attached *para* to the phenyl-iridium bond, the conjugation length of the ligand is not significantly increased. In contrast, the solution PL of the doubly dendronized poly(dendrimer) **3** is red-shifted (with an emission maximum at 550 nm) with respect to **1** and **2**. As discussed for the absorption spectrum, this is because the first phenyl ring of the dendron attached to the pyridyl ring is now in conjugation with the ligand phenyl ring.

The film PL spectra are shown in Figure 3b. For polymers **2** and **3**, the spectra are similar to the solution spectra of the same polymers. However, for small molecule parent polymer **1**, the film spectrum is broader than that in solution with a pronounced shoulder and tail on the long wavelength side of the emission, which is attributed to aggregate or excimer emission arising from interchromophore interactions.

To probe the photophysical properties more closely and the role of interchromophore interactions (both intra- and interchain), we measured the PLQYs and PL lifetimes (Figure 4) in solution and the solid-state for the three polymers with the results summarized in Tables 1 and 2. The solution PLQY of the parent complex (Scheme 1, compound **4** but Br = H)[28] was 82%. In contrast, polymer **1**, which has a complex on every "monomer" unit only has a solution PLQY of 48%. In other systems this has been attributed to intrachain interchromophore interactions.[27] In contrast, poly(dendrimer) **2** had a solution PLQY of 65%, which indicates that the dendrons are significantly reducing the intrachain interchromophore interactions. Doubly dendronizing the ligands led to a slight increase in the solution PLQY for poly(dendrimer) **3** to 71%. On the

dx.doi.org/10.1021/ma300306d | *Macromolecules* 2012, 45, 2963−2971

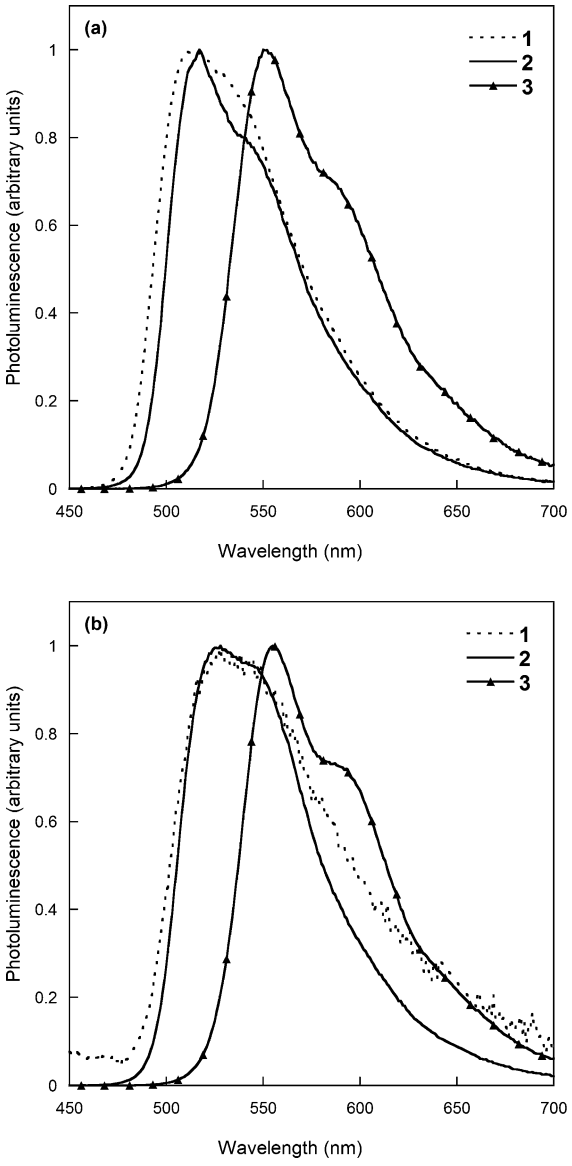


Figure 3. (a) Normalized solution PL spectra of **1**, **2**, and **3**. (b) Normalized film PL spectra of **1**, **2**, and **3**. Excitation wavelength 360 nm for solution and 325 nm for films.

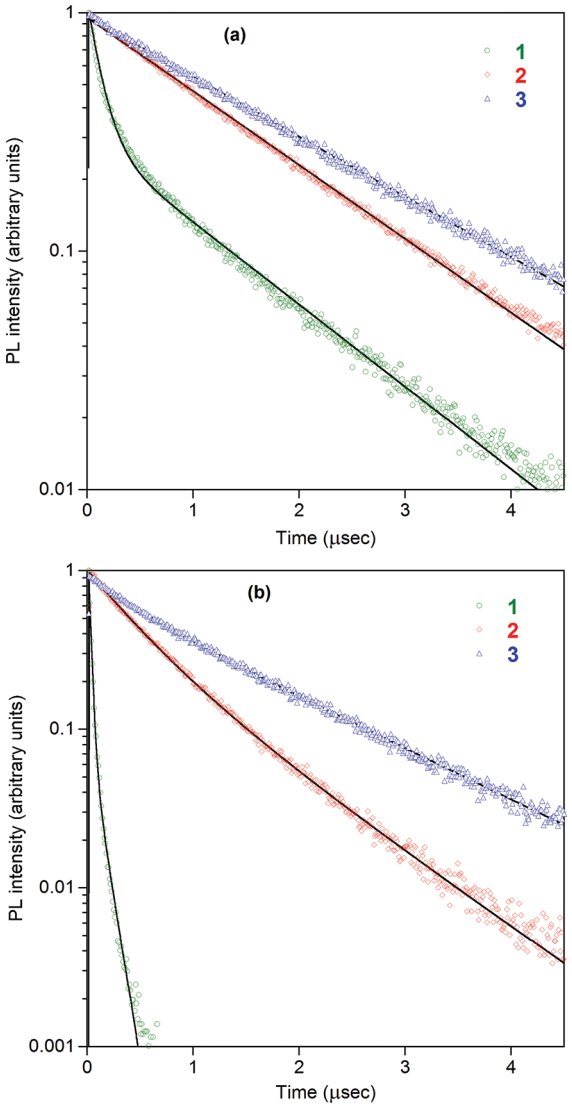


Figure 4. Time-resolved PL intensity of materials **1**, **2**, and **3** in (a) solutions and (b) films. The samples were excited at 393 nm. The emission is collected in each case at the peak of the PL spectra.

basis of the solution PL measurements and spectra, it might be thought that having one dendron per ligand would be sufficient to control the interactions that govern the photophysical properties of the materials. However, in moving from the solution to the solid state, there is an important difference. For polymer **1**, the neat film is almost nonluminescent with a PLQY of only 2%. The low PLQY for **1** is due to strong intra- and interchain interchromophore interactions. That is, in addition to the intrachain interchromophore interactions seen in solution, there are now interchain interchromophore interactions leading to further pathways for PL deactivation. Addition of a dendron to each 2-phenylpyridyl ligand if poly(dendrimer) **2** partially controls the interchain interchromophore interactions. There is a decrease in PLQY in moving from solution (65%) to the film (44%), but it is much smaller decrease than that of polymer **1**. Finally, the film PLQY of poly(dendrimer) **3** was found to be 58%. This is the highest of all three polymers and demonstrates that the double dendron strategy is the best in controlling both intra- and interchain interchromophore interactions.

Similar trends are seen in the time-resolved PL (TRPL) measurements. As the light-emitting chromophores are very similar in the three polymers, differences in lifetime are likely to arise from differences in nonradiative decay rate; i.e., faster decay implies more quenching of PL (as a result of interchromophore interactions). The TRPL results for solutions are shown in Figure 4a. The PL decay of **1** is significantly faster than that of **2**, which decays slightly faster than that of **3**. This is consistent with the observed solution PLQYs of these materials. The single-exponential decay of **2** and **3** indicates a single emitting chromophore. Namely, in solution interchromophore interactions are negligible as a result of the presence of the dendrons. This is not the case for **1**, where the biexponential decay indicates more than one emissive species is present as a result of interchromophore interactions.

The film TRPL data are shown in Figure 4b. It can be seen that the decay of **1** is very much faster than in solution, indicating strong quenching in the solid state for this material.

dx.doi.org/10.1021/ma300306d | *Macromolecules* 2012, 45, 2963−2971

Table 1. Solution PLQYs and PL Lifetime Measurements for the Three Polymers

polymer	detection wavelength (nm)	PLQYs (%)	A_1 (μs)	τ_1	A_2	τ_2 (μs)	radiative lifetime (μs)
1	514	48	0.20	0.12	0.80	1.26	
2	517	65	1	1.40			2.15
3	550	71	1	1.72			2.42

Table 2. Film PLQYs and PL Lifetime Measurements for the Three Polymers

polymer	detection wavelength (nm)	PLQYs (%)	A_1	τ_1 (μs)	A_2	τ_2 (μs)
1	530	2	0.69	0.022	0.31	0.102
2	530	44	0.37	0.415	0.63	0.916
3	550	58	0.10	0.434	0.90	1.34

In fact, for the fast decay component for polymer 1, this is the major part of the PL decay in the film TRPL, which is reflected to the poor film PLQY (2%). The PL decays of **2** and **3** are slightly faster than in solution. However, the very much longer-lived PL than for **1** shows the effectiveness of dendrons for stopping quenching by intermolecular interactions, and the longer lifetime for **3** shows that the double dendron approach is more effective than a single dendron.

Finally, the high film PLQYs of poly(dendrimers) **2** and **3** enable the formation of efficient OLEDs. The detailed OLED study is reported elsewhere but in summary devices with an architecture of indium tin oxide/poly(dendrimer)/1,3,5,-tris(2-*N*-phenylbenzimidazolyl)benzene/LiF/Al achieved 100 cd/m^2 at 4.1 and 5.5 V for **2** and **3**, respectively, with concomitant efficiencies of 11.9% (42 cd/A) and 11.7% (38 cd/A), respectively.[34]

CONCLUSION

Three homopolymers with a norbornene-derived backbone have been prepared using the Grubbs III catalyst. The polymers all contain heteroleptic iridium(III) complex emissive chromophores as side chains. The ROMP conditions enabled polymers of low polydispersity to be formed, and the polymers had higher viscosities compared to the simple "monomer" units. The position and number of dendrons were vital for controlling the optoelectronic properties. By increasing the number of dendrons attached to the ligands of the iridium(III) complex, both intra- and interchain interchromophore interactions could be controlled, leading to high film PLQYs. The homopolymer approach gives control of the intrachain and interchain interchromophore interactions. It also has the advantage over (random) copolymer architectures[35] of being simpler to reproduce and having a well-defined structure. We have therefore achieved our goal of forming highly luminescent materials with increased viscosity as an approach towards inkjet printing phosphorescent materials for OLEDs.

EXPERIMENTAL SECTION

Measurements. All commercial reagents were used as received unless otherwise noted. Tetrahydrofuran was distilled from sodium and benzophenone under a nitrogen atmosphere before use. ^{1}H and ^{13}C NMR spectra were recorded using a 300, 400, or 500 MHz Bruker spectrometer, in deuterated chloroform solution; EH = 2-ethylhexyl, Pr = *n*-propyl, NB = norbornenyl, CP = cyclopentanyl, V = vinyl, LH = ligand phenyl/pyridyl and/or phenyltriazole H, LPH = phenyl H attached to phenyltriazole ligand, G1-BPH = branch phenyl H, SPH = surface phenyl H. All coupling constants (J) are in Hertz and quoted to the nearest 0.5 Hz. Gel permeation chromatography (GPC) was carried out using either a Polymer Laboratories PL-GPC 50 using PLgel Mixed-A columns (600 mm + 300 mm lengths, 7.5 mm diameter) from Polymer Laboratories, calibrated with polystyrene narrow standards ($\bar{M}_p$ = 162 to 6.04 × 10^6 g/mol) (for **10**–**12**) or a 1515 isocratic pump (Waters), a 717 autosampler (Waters), Styragel HT 3 and Styragel HT 6E columns (Waters) (300 mm + 300 mm lengths, 7.8 mm diameter), calibrated with polystyrene standards (Waters) ($\bar{M}_p$ = 1.06 × 10^3 to 1.32 × 10^6 g/mol) (for **1**–**3**) and run in series in tetrahydrofuran with toluene as flow marker. The tetrahydrofuran pumped at a rate of 1 cm^3/min at 40 °C. Microanalyses were carried out at the School of Chemistry & Molecular Biosciences, The University of Queensland. UV–vis absorption measurements were recorded with a Cary Varian 5000 UV–vis–NIR spectrophotometer; sh = shoulder. Melting points were measured in a glass capillary on a BÜCHI melting point B-545 and are uncorrected. Thermogravimetric analysis (TGA) was carried out on a Perkin-Elmer STA6000, and the differential scanning calorimetry was performed using a Perkin-Elmer Diamond DSC. Mass spectra were recorded on an Applied Biosystems Voyager matrix-assisted laser desorption/ionization time-of-flight (MALDI-TOF) from 2-[(2-*E*)-3-(4-*tert*-butylphenyl)-2-methylprop-2-enylidene]malononitrile (DCTB) or 2,5-dihydroxybenzoic acid (DHB) in positive reflection mode.

Viscosities of the poly(dendrimers) at different concentrations in 1,2-dichlorobenzene were determined on a homemade OSTWALD viscometer at a constant temperature of 20 °C. Deionized freshly distilled water with viscosity of 1.00 cSt at 20 °C was used as the reference.[32]

Electrochemistry was performed using a BAS Epsilon electrochemistry station using a glassy carbon working, 0.1 M $AgNO_3$ in acetonitrile reference, and platinum counter electrodes. All measurements were made at room temperature on samples at a 1 mM concentration in dichloromethane (HPLC grade), with 0.1 M tetra-*n*-butylammonium tetrafluoroborate as the electrolyte. The solutions were deoxygenated with argon, and the ferricenium/ferrocene (Fc^+/Fc) couple was used as the standard.[36] The scan rate was 100 mV s^{-1}, and in all cases several scans were carried out to confirm the chemical reversability of the redox processes.

Solution PLQYs were measured by a relative method using quinine sulfate in 0.5 M sulfuric acid, which has a PLQY of 0.546, as the standard.[37] Materials were dissolved in dichloromethane and freeze–pump–thaw degassed. Photoluminescence spectra were recorded in a JY Horiba Fluoromax 2 fluorimeter, with the solutions excited at 360 nm. The optical densities of the standard and sample were similar and small (~0.1). The accuracy of these measurements is estimated to be ±10% of the stated value. Time-resolved luminescence measurements were performed using the time-correlated single photon counting technique, with excitation at 393 nm from a pulsed Picoquant GaN laser diode and an instrument response of 250 ps. The PL decay in each case was measured at a wavelength corresponding to the peak of the emission spectrum. Solid-state PLQY measurements were measured in an integrating sphere under a nitrogen purge[38] using a Hamamatsu C9920-02 luminescence measurement system.

Synthesis of 7. A mixture of **4**[27] (250 mg, 0.321 mmol) and 4-formylphenylboronic acid (120 mg, 0.802 mmol), tetrakis(triphenylphosphine)palladium(0) (56 mg, 0.048 mmol), aqueous potassium carbonate (2 M, 1.6 mL), ethanol (1.6 mL), and toluene (4.8 mL) was deoxygenated (by placing under vacuum and backfilling with argon) before being heated at reflux under argon for 21 h. The mixture was allowed to cool to room temperature, and then water (25 mL) was added. The organic layer was separated, and the aqueous layer was extracted with dichloromethane (4 × 25 mL). The organic portions were combined and dried over anhydrous magnesium sulfate

dx.doi.org/10.1021/ma300306d | Macromolecules 2012, 45, 2963–2971

and filtered. The filtrate was collected, and the solvent was removed. The residue was purified by column chromatography over silica using dichloromethane/hexane (7:3 to 1:0) and then dichloromethane/ethyl acetate (24:1) as eluent to give **7** as a bright yellow solid (251 mg, 97%); mp 322 °C (decomp). Found: C, 60.9; H, 4.2; N, 8.8. $C_{41}H_{34}IrN_5O$ requires C, 61.2; H, 4.3; N, 8.7%. ν_{max}(film)/cm^{-1} 1688 (C═O); λ_{max}(CH_2Cl_2)/nm 248 (log ε/dm^3 mol^{-1} cm^{-1} 4.74), 264 sh (4.70), 279 (4.70), 369 (4.43), 406 sh (4.26), 482 sh (3.01). ^{1}H NMR (400 MHz, $CDCl_3$): δ 0.58 (3H, t, J = 7.5, Pr CH_3), 1.20−1.43 (2H, m, Pr CH_2), 1.79−1.94 (2H, m, Pr CH_2), 4.29 (3H, s, NCH_3), 6.78−7.03 (9H, m, LH), 7.13−7.14 (1H, dd, J = 2 and 8, LH), 7.53−7.59 (2H, m, LH), 7.6−7.720 (3H, m, LH), 7.74 and 7.90 (4H, AA′BB′, LPH), 7.78 (1H, d, J = 2, LH), 7.82−7.96 (3H, m, LH), 10.02 (1H, s, CHO). ^{13}C NMR (100 MHz, $CDCl_3$): δ 13.8, 21.7, 28.7, 38.0, 118.4, 118.9, 119.9, 120.0, 121.4, 122.0, 122.2, 123.9, 124.0, 126.5, 128.5, 129.9, 130.0, 130.4, 130.9, 133.4, 134.2, 135.9, 136.16, 136.20, 136.6, 139.0, 143.5, 143.9, 147.7, 148.1, 159.1, 160.3, 161.3, 163.0, 163.7, 166.5, 167.1, 191.9. m/z (MALDI: DHB): calcd for $C_{41}H_{34}IrN_5O$, 803.2 (56%), 804.2 (27%), 805.2 (100%), 806.2 (46%), 807.2 (11%), 808.2 (2%); found, 803.2 (56%), 804.2 (31%), 805.2 (100%), 806.2 (51%), 807.2 (16%), 808.2 (5%).

Synthesis of 10. Lithium aluminum hydride (5.5 mg, 0.145 mmol) was added to a solution of **7** (90 mg, 0.112 mmol) dissolved in tetrahydrofuran (3.7 mL). The reaction was stirred at ambient temperature for 1.5 h and then quenched with water (25 mL). The mixture was extracted with dichloromethane (7 × 25 mL). The extracts were combined, dried over anhydrous magnesium sulfate, and filtered. The filtrate was collected and the solvent was removed to give the crude alcohol (90 mg), which was used without further purification. A mixture of the crude alcohol (90 mg), *exo*-5-norbornene-2-carboxylic acid (18.5 mg, 0.134 mmol), and (*N*,*N*-dimethylamino)pyridine (7.2 mg, 0.059 mmol) in dichloromethane (4.5 mL) was added to a solution of dicyclohexylcarbodiimide (29 mg, 0.141 mmol) in dichloromethane (0.7 mL). The reaction was stirred under argon at ambient temperature for 24 h. The solvent was evaporated, and the residue was purified by column chromatography over silica using dichloromethane/hexane (2.3:1 to 19:1) as eluent to give **10** as a bright yellow powder (94 mg, 91% for the two steps); mp 163−165 °C. Found: C, 63.3; H, 4.9; N, 7.3. $C_{49}H_{44}IrN_5O_2$ requires C, 63.5; H, 4.8; N, 7.55%; ν_{max}(film)/cm^{-1} 1725 (C═O); λ_{max}(CH_2Cl_2)/nm 247 (log ε/dm^3 mol^{-1} cm^{-1} 4.78), 264 sh (4.71), 275 (4.67), 288 (4.63), 340 sh (4.25), 369 sh (4.18), 406 sh (3.88), 452 sh (3.41), 479 sh (3.00). ^{1}H NMR (400 MHz, $CDCl_3$): δ 0.58 (3H, t, J = 7, Pr CH_3), 1.20−1.48 (3H, m, Pr H_2, NB CH), 1.59−1.60 (2H, m, NB CH_2), 1.75−2.03 (3H, m, Pr H_2, NB CH), 2.30−2.36 (1H, m, NB H), 2.95 (1H, s, NB H), 3.10 (1H, m, NB H), 4.27 (3H, m, NCH_3), 5,17 (2H, s, $COOCH_2$), 6.10−6.19 (2H, m, V H), 6.78−7.03 (9H, m, LH), 7.08−7.12 (1H, m, LH), 7.40 and 7.58 (4H, AA′BB′, LPH), 7.51−7.60 (2H, m, LH), 7.61−7.71 (3H, m, LH), 7.74−7.78 (1H, m, LH), 7.83−7.97 (3H, m, LH). ^{13}C NMR (100 MHz, $CDCl_3$): δ 13.8, 21.7, 28.7, 29.7, 30.4, 38.0, 41.7, 43.2, 46.4, 46.6, 66.2, 118.4, 118.8, 119.8, 119.9, 121.4, 121.9, 122.2, 123.85, 123.9, 126.4, 128.6, 128.7, 129.9, 130.0, 132.0, 133.0, 134.0, 135.7, 136.0, 136.3, 136.6, 138.1, 138.7, 141.9, 143.5, 144.0, 147.7, 159.5, 160.6, 160.9, 161.2, 163.3, 166.5, 167.2, 176.1. m/z (MALDI: DHB): calcd for $C_{49}H_{44}IrN_5O$, 925.3 (54%), 926.3 (31%), 927.3 (100%), 928.3 (53%), 929.3 (15%), 930.3 (3%); found: 925.4 (56%), 926.4 (37%), 927.3 (100%), 928.3 (61%), 929.3 (22%), 930.3 (6%).

Synthesis of 1. A solution of Grubbs III catalyst in chloroform (0.05 M, 11.7 μL) was added to a solution of **10** (27 mg, 0.03 mmol) in chloroform (3 mL). The reaction mixture was stirred at ambient temperature under argon for 20 min. The reaction was quenched by the addition of ethyl vinyl ether (0.3 mL). The mixture was concentrated and precipitated into methanol (20 mL). The resulting solid was collected by filtration, redissolved in dichloromethane (2 mL), and reprecipitated into methanol (20 mL). This procedure was repeated until the methanol solution was clear to yield **1** as a powder (26 mg, 94%); $TGA_{(5\%)}$ 365 °C; Found: C, 63.2; H, 4.6; N, 7.45. $(C_{49}H_{44}IrN_5O_2)_n$ requires C, 63.5; H, 4.8; N, 7.55%; ν_{max}(film)/cm^{-1} 1728 (C═O); λ_{max}(CH_2Cl_2)/nm 248, 263 sh, 276, 290, 386 sh, 405 sh, 446 sh, 484 sh. ^{1}H NMR (400 MHz, $CDCl_3$): δ 0.43−0.59 (br, Pr CH_3), 0.84−1.38 (brm, Pr CH_2, 1/2CP CH_2), 1.65−2.80 (brm, Pr CH_2, 1/2CP CH_2, CP CH_2, CP CH), 2.80−3.24 (brm, OCOCH), 3.80−4.19 (br, NCH_3), 4.83−5.42 (br, $COOCH_2$, V H), 6.64−7.10 (brm, LH), 7.12−7.28 (br, LPH), 7.29−7.65 (brm, LPH, LH), 7.66−7.87 (brm, LH). GPC: $\bar{M}_w$ = 14 185; $\bar{M}_n$ = 9435; polydispersity = 1.5. $E^{1/2}$(ox) = 0.22 V vs Fc^+/Fc.

Synthesis of 8. A mixture of **5**[27] (200 mg, 0.114 mmol) and 4-formylphenylboronic acid (43 mg, 0.287 mmol), tetrakis-(triphenylphosphine)palladium(0) (13 mg, 0.011 mmol), aqueous potassium carbonate (2 M, 0.3 mL), and tetrahydrofuran (2 mL) was deoxygenated (by placing under vacuum and backfilling with argon) before being heated at reflux under argon for 24 h. The mixture was allowed to cool to room temperature, and water (30 mL) was added. The organic layer was separated, and the aqueous layer was extracted with dichloromethane (3 × 10 mL). All the organic portions were combined and dried over anhydrous magnesium sulfate and filtered. The filtrate was collected and the solvent removed. The residue was purified by column chromatography over silica using dichloromethane as eluent to give **8** as a bright yellow solid (157 mg, 77%); mp 148.5−150.5 °C. Found: C, 73.6; H, 6.9; N, 3.8. $C_{109}H_{122}IrN_5O_5$ requires C, 73.8; H, 6.9; N, 3.95%; λ_{max}(solid)/cm^{-1} 1695 (C═O); λ_{max}(CH_2Cl_2)/nm 274 (log ε/dm^3 mol^{-1} cm^{-1} 5.15), 326 (4.63), 391 sh (4.40), 491 sh (2.99). ^{1}H NMR (500 MHz, $CDCl_3$): δ 0.63 (3H, t, J = 7.5, Pr CH_3), 0.94−1.02 (24H, m, EH CH_3), 1.30−1.64 (34H, m, EH CH_2, Pr CH_2), 1.75−1.86 (4H, m, EH CH), 1.89−2.02 (2H, m, Pr CH_2), 3.93−3.95 (8H, m, OCH_2), 4.32 (3H, s, NCH_3), 6.84−6.90 (1H, m, LH), 6.99 (1H, d, J = 8, LH), 7.00−7.08 (10H, m, SPH, LH), 7.13 (1H, d, J = 8, LH), 7.20 (1H, dd, J = 2 and 8, LH), 7.27 (1H, dd, J = 2 and 8, LH), 7.31 (1H, dd, J = 2 and 8, LH), 7.56−7.63 (1H, m, LH), 7.65−7.73 (12H, m, SPH, LH), 7.76 and 7.92 (4H, AA′BB′, LPH), 7.78 (2H, d, J = 1.5, G1-BPH), 7.81 (2H, d, J = 2, G1-BPH), 7.85 (1H, d, J = 2, LH), 7.95 (1H, d, J = 1, LH), 8.01−8.08 (4H, m, G1-BPH, LH), 10.04 (1H, s, CHO). m/z (MALDI: DCTB): calcd for $C_{109}H_{122}IrN_5O_5$, 1771.9 (40%), 1772.9 (50%), 1773.9 (100%), 1774.9 (99%), 1775.9 (58%), 1776.9 (24%), 1777.9 (9%); found, 1771.9 (38%), 1772.9 (44%), 1773.9 (81%), 1774.9 (100%), 1775.8 (38%), 1776.9 (22%), 1777.8 (5%). GPC: $\bar{M}_w$ = 1990; $\bar{M}_n$ = 1984; polydispersity = 1.0.

Synthesis of 11. Lithium aluminum hydride (3.3 mg, 0.087 mmol) was added to a solution of **8** (120 mg, 0.068 mmol) in tetrahydrofuran (5.5 mL). The reaction mixture was stirred at ambient temperature under argon for 45 min and then quenched carefully with water (5 mL). The crude was extracted with dichloromethane (3 × 10 mL), washed with water (30 mL), dried over anhydrous magnesium sulfate, and filtered. The filtrate was collected, and the solvent was removed to give crude alcohol (∼135 mg), which was used without further purification. A solution of dicyclohexylcarbodiimide (20 mg, 0.095 mmol) in dichloromethane (0.5 mL) was added to a solution of the crude alcohol (∼135 mg), *exo*-5-norbornene-2-carboxylic acid (13 mg, 0.091 mmol), and (*N*,*N*-dimethylamino)pyridine (5 mg, 0.04 mmol) in dichloromethane (3 mL). The reaction was stirred at ambient temperature under argon for 24 h. The solvent was removed, and the residue was purified by column chromatography over silica using dichloromethane/hexane (2:1) as eluent to give **11** as a green-yellow powder (128 mg, 100% for the two steps); mp 97−99 °C. Found: C, 73.85; H, 7.0; N, 3.65. $C_{117}H_{132}IrN_5O_6$ requires C, 74.1; H, 7.0; N, 3.7%; ν_{max} (solid)/cm^{-1} 1728 (C═O); λ_{max}(CH_2Cl_2)/nm 269 (log ε/dm^3 mol^{-1} cm^{-1} 5.25), 288 sh (5.22), 325 (4.80), 386 (4.23), 409 (4.03), 494 (2.99); ^{1}H NMR (400 MHz, $CDCl_3$): δ 0.65 (3H, t, J = 7.5, Pr CH_3), 0.97−1.07 (24H, m, EH CH_3), 1.35−1.66 (37H, m, EH CH_2, Pr CH_2, NB CH_2, 1/2NB CH_2), 1.78−2.08 (7H, m, EH CH, Pr CH_2, 1/2NB CH_2), 2.34−2.39 (1H, m, NB CH), 2.99 (1H, s, NB CH), 3.15 (1H, s, NB CH), 3.94−4.03 (8H, m, EH OCH_2), 4.32 (3H, s, NCH_3), 5.22 (2H, s, $COOCH_2$), 6.14−6.25 (2H, m, V H), 6.89 (1H, t, J = 7, LH), 7.03−7.15 (12H, m, SPH, LH), 7.18−7.23 (1H, m, LH), 7.30−7.38 (2H, m, LH), 7.46 and 7.65 (4H, AA′BB′, J = 8, LPH), 7.60 (1H, t, J = 8, LH), 7.56−7.77 (12H, m, SPH, LH), 7.82−7.88 (5H, m, G1-BPH), 7.98−8.10 (5H, m, G1-BPH, LH). m/z (MALDI: DCTB): calcd for $C_{117}H_{132}IrN_5O_6$, 1894.0 (38%), 1895.0 (52%),

1896.0 (97%), 1897.0 (100%), 1898.0 (63%), 1899.0 (29%), 1900.0 (9%); found, 1894.0 (24%), 1895.1 (46%), 1896.0 (78%), 1897.0 (100%), 1898.1 (51%), 1899.0 (22%), 1900.0 (11%). GPC: $\bar{M}_w$ = 2112; $\bar{M}_n$ = 2106; polydispersity = 1.0. $E^{1/2}$(ox) = 0.22 V vs Fc^+/Fc.

Synthesis of 2. Deoxygenated **11** (71 mg, 0.037 mmol) (by placing under high vacuum and backfilling with argon three times) was dissolved in dry tetrahydrofuran (0.35 mL). Grubbs III catalyst (3.8 mM, 100 μL) was rapidly injected. After stirring at ambient temperature under argon for 20 min, the reaction mixture was quenched by the addition of ethyl vinyl ether (0.3 mL). The resulting solution was added to methanol (20 mL) that was being stirred to precipitate the polymer. The precipitate was filtered, washed with methanol (20 mL), and dried under high vacuum to give **2** as a powder (67 mg, 94%); mp > 230 °C; $TGA_{(5\%)}$ 405 °C. Found: C, 73.75; H, 6.9; N, 3.6. $(C_{117}H_{132}IrN_5O_6)_n$ requires C, 74.1; H, 7.0; N, 3.7%; ν_{max}(solid)/cm^{-1} 1732 (C═O); $\lambda_{max}(CH_2Cl_2)$/nm 269, 276 sh, 287 sh, 326 sh, 350 sh, 384 sh, 441 sh, 458 sh, 493 sh. ^{1}H NMR (400 MHz, $CDCl_3$): δ 0.36−0.54 (br, Pr CH_3), 0.75−1.00 (br, EH CH_3), 1.10−1.53 (brm, EH CH_2, 1/2CP CH_2), 1.64−2.55 (brm, EH CH, Pr CH_2, CP CH_2), 2.57−3.25 (br, OCOCH), 3.75−4.20 (brm, OCH_2, NCH_3), 4.56−5.40 (brm, $COOCH_2$, V H), 6.57−6.73 (br, LH), 6.74−6.83 (brm, LH), 6.84−6.97 (br, SPH), 6.98−7.08 (brm, LH), 7.11−7.26 (brm, LPH, LH), 7.32−7.46 (brm, LPH, LH), 7.48−7.62 (brm, SPH, LH), 7.63−7.73 (brm, G1-BPH), 7.74−8.02 (brm, G1-BPH, LH). GPC: $\bar{M}_w$ = 73 663; $\bar{M}_n$ = 57 290; polydispersity = 1.3. $E^{1/2}$(ox) = 0.26 V vs Fc^+/Fc.

Synthesis of 9. A mixture of **6**[29] (200 mg, 0.074 mmol), 4-formylphenylboronic acid (28 mg, 0.184 mmol), tetrakis-(triphenylphosphine)palladium(0) (8.5 mg, 7.36 μmol), aqueous potassium carbonate (2 M, 0.2 mL), and tetrahydrofuran (1 mL) was deoxygenated (by placing under vacuum and backfilling with argon) before being heated at reflux under argon for 24 h. The mixture was allowed to cool to room temperature before water (10 mL) was added. The organic layer was separated. The aqueous layer was extracted with dichloromethane (2 × 10 mL). The organic portions were combined and dried over anhydrous magnesium sulfate and filtered. The filtrate was collected and the solvent removed. The residue was purified by column chromatography over silica using dichloromethane/hexane (1:1) as eluent to give **9** as an orange-yellow solid (159 mg, 79%); mp 158 °C. Found: C, 77.15; H, 7.8; N, 2.6. $C_{177}H_{210}IrN_5O_9$ requires C, 77.5; H, 7.7; N, 2.55%; ν_{max}(solid)/cm^{-1} 1697 (C═O); $\lambda_{max}(CH_2Cl_2)$/nm 276 (log ε/dm^3 mol^{-1} cm^{-1} 5.46), 307 sh (5.26), 397 (4.57), 474 sh (3.77). ^{1}H NMR (500 MHz, $CDCl_3$): δ 0.56 (3H, t, J = 7.0, Pr CH_3), 0.93−1.09 (48H, m, EH CH_3), 1.30−1.68 (66H, m, EH CH_2, Pr CH_2), 1.69−1.78 (2H, m, EH CH), 1.79−1.90 (6H, m, EH CH), 1.99−2.06 (1H, m, 1/2Pr CH_2), 2.07−2.17 (1H, m, 1/2Pr CH_2), 3.75−3.83 (4H, m, OCH_2), 3.90−4.03 (12H, m, OCH_2), 4.32 (3H, s, NCH_3), 6.82 (4H, d, J = 8, SPH), 7.02 (4H, d, J = 8.5, SPH), 7.05 (4H, d, J = 8.5, SPH), 7.09 (4H, d, J = 9, SPH), 7.14 (1H, d, J = 7.5, LH), 7.23−7.28 (1H, m, LH,), 7.28−7.35 (2H, m, LH), 7.35−7.41 (2H, m, LH), 7.42−7.56 (10H, m, G1-BPH, SPH), 7.60 (2H, s, G1-BPH), 7.65−7.77 (12H, m, LH, SPH), 7.80 and 7.95 (4H, AA′BB′, LPH), 7.78−7.92 (6H, m, G1-BPH, LH), 8.00−8.06 (1H, m, LH), 8.07−8.25 (5H, m, G1-BPH, LH), 8.53 (1H, s, G1-BPH), 10.06 (1H, s, CHO). *m/z* (MALDI: DHB): calcd for $C_{177}H_{210}IrN_5O_9$, 2740.6 (22%), 2741.6 (43%), 2742.6 (78%), 2743.6 (100%), 2744.6 (86%), 2745.6 (55%), 2746.6 (27%), 2747.6 (12%), 2748.6 (4%); found, 2740.7 (24%), 2741.7 (43%), 2742.7 (81%), 2743.7 (100%), 2744.7 (83%), 2745.7 (52%), 2746.7 (30%), 2747.7 (13%), 2748.7 (8%). GPC: $\bar{M}_w$ = 2974; $\bar{M}_n$ = 2961; polydispersity = 1.0.

Synthesis of 12. Lithium aluminum hydride (2.7 mg, 0.071 mmol) was added to a solution of **9** (150 mg, 0.055 mmol) in tetrahydrofuran (3.5 mL). The reaction mixture was stirred at ambient temperature under argon for 45 min and then quenched carefully with water (5 mL). The crude mixture was extracted with dichloromethane (3 × 10 mL), dried over anhydrous magnesium sulfate, and filtered. The filtrate was collected, and the solvent was removed to give the crude alcohol (~150 mg), which was used without further purification. A solution of dicyclohexylcarbodiimide (14 mg, 0.068 mmol) in dichloromethane (0.35 mL) was added to a solution of the alcohol (~150 mg), *exo*-5-norbornene-2-carboxylic acid (9 mg, 0.066 mmol), and (*N*,*N*-dimethylamino)pyridine (3.5 mg, 0.029 mmol) in dichloromethane (2 mL). The reaction was stirred under argon at ambient temperature for 24 h. The solvent was removed, and the residue was purified by column chromatography over silica using a dichloromethane/hexane (1:1) as eluent to give **12** as an orange-yellow powder (135 mg, 86% for the two steps); mp 151 °C. Found: C, 77.3; H, 7.9; N, 2.25. $C_{185}H_{220}IrN_5O_{10}$ requires C, 77.5; H, 7.7; N, 2.4%; ν_{max}(solid)/cm^{-1} 1729 (C═O); $\lambda_{max}(CH_2Cl_2)$/nm 275 (log ε/dm^3 mol^{-1} cm^{-1} 5.62), 308 sh (5.46), 393 (4.46), 472 sh (3.89); ^{1}H NMR (300 MHz, $CDCl_3$): δ 0.57 (3H, t, J = 7, Pr CH_3), 0.91−1.09 (48H, m, EH CH_3), 1.29−1.66 (70H, m, EH CH_2, Pr CH_2, NB CH_2), 1.67−1.76 (2H, m, EH CH), 1.77−1.92 (6H, m, EH CH), 1.96−2.16 (2H, m, Pr CH_2), 2.32−2.40 (1H, m, NB CH), 2.99 (1H, s, NB CH), 3.15 (1H, s, NB CH), 3.73−3.86 (4H, m, EH OCH_2), 3.88−4.07 (12H, m, EH OCH_2), 4.32 (3H, s, NCH_3), 5.22 (2H, s, $COOCH_2$), 6.13−6.24 (2H, m, V H), 6.83 (4H, d, J = 8.5, SPH), 6.99−7.17 (14H, m, LH, SPH), 7.23−7.31 (2H, m, LH), 7.34−7.41 (2H, m, LH), 7.42−7.57 (13H, m, LH, LPH, G1-BPH, SPH), 7.58−7.63 (2H, m, G-BPH), 7.66 (2H, 1/2AA′BB′, LPH), 7.68−7.81 (12H, m, LH, SPH), 7.82−7.92 (5H, m, G1-BPH, LH), 8.00−8.27 (6H, m, LH, G1-BPH), 8.51−8.57 (1H, m, G1-BPH). *m/z* (MALDI: DHB): calcd for $C_{185}H_{220}IrN_5O_{10}$, 2862.6 (19%), 2863.6 (41%), 2864.6 (77%), 2865.6 (100%), 2866.6 (91%), 2867.6 (58%), 2868.6 (30%), 2869.6 (13%), 2870.6 (6%), 2871.6 (2%); found, 2862.7 (17%), 2863.7 (37%), 2864.7 (64%), 2865.7 (100%), 2866.7 (97%), 2867.7 (70%), 2868.7 (42%), 2869.7 (20%), 2870.7 (12%), 2871.7 (9%). GPC: $\bar{M}_w$ = 3137; $\bar{M}_n$ = 3124; polydispersity = 1.0. $E^{1/2}$(ox) = 0.28 V vs Fc^+/Fc.

Synthesis of 3. Deoxygenated **12** (97 mg, 0.034 mmol) (by placing under high vacuum and backfilling with argon three times) was dissolved in dry tetrahydrofuran (0.2 mL). Grubbs III catalyst (3.8 mM, 100 μL) was rapidly injected. After stirring at ambient temperature under argon for 1.5 h, the reaction mixture was quenched by the addition of ethyl vinyl ether (0.3 mL). The resulting solution was added to methanol (20 mL) that was being stirred to precipitate the polymer. The precipitate was filtered, washed with methanol (20 mL), and dried under high vacuum to give **3** as a powder (91 mg, 94%); mp > 240 °C. $TGA_{(5\%)}$ 421 °C; Found: C, 77.2; H, 7.6; N, 2.5. $(C_{185}H_{220}IrN_5O_{10})_n$ requires C, 77.5; H, 7.7; N, 2.4%; ν_{max}(solid)/cm^{-1} 1732 (C═O); $\lambda_{max}(CH_2Cl_2)$/nm 270, 308 sh, 398, 482 sh; ^{1}H NMR (400 MHz, $CDCl_3$): δ 0.30−0.48 (br, Pr CH_3), 0.75−0.98 (br, EH CH_3), 1.15−1.50 (brm, EH, Pr CH_2, 1/2CP CH_2), 1.56−1.72 (brm, EH CH), 1.79−2.80 (brm, Pr CH_2, CP CH_2, CP CH), 2.90−3.20 (br, OCOCH), 3.52−4.20 (brm, EH OCH_2, NCH_3), 4.74−5.42 (brm, $COOCH_2$, V H), 6.61−6.98 (brm, SPH, LH), 7.00−7.68 (brm, LPH, G1-BPH, LH), 7.80−8.18 (brm, G1-BPH, LH), 8.30−8.48 (br, G1-BPH). GPC: $\bar{M}_w$ = 64 890; $\bar{M}_n$ = 47 417; polydispersity = 1.4. $E^{1/2}$(ox) = 0.29 V vs Fc^+/Fc.

AUTHOR INFORMATION

Corresponding Author

*E-mail: p.burn2@uq.edu.au (P.L.B.), s.lo@uq.edu.au (S.-C.L.), idws@st-andrews.ac.uk (I.D.W.S.).

Present Addresses

[§]Key Laboratory for Organic Electronics & Information Displays (KLOEID) and Institute of Advanced Materials (IAM), Nanjing University of Posts & Telecommunications (NUPT), 9 Wenyuan Road, Nanjing 210046, China.

[∥]Holst Centre, High Tech Campus 31, 5656 AE, Eindhoven, Netherlands.

Notes

The authors declare no competing financial interest.

ACKNOWLEDGMENTS

P.L.B. is recipient of an Australian Research Council Federation Fellowship (Project No. FF0668728). J.W.L. and I.D.W.S. are

grateful to the Engineering and Physical Sciences Research Council (UK) for financial support. This work was carried out in part at the Queensland node of the Australian National Fabrication Facility, a company established under the national collaborative research infrastructure strategy to provide nano- and microfabrication facilities for Australia's researchers.

REFERENCES

(1) (a) Tang, C. W.; van Slyke, S. A. *Appl. Phys. Lett.* **1987**, *51*, 913. (b) Baldo, M. A.; O'Brien, D. F.; You, Y.; Shoustikov, A.; Sibey, S.; Thompson, M. E.; Forrest, S. R. *Nature* **1998**, *395*, 151. (c) Holder, E.; Langeveld, B. M. W.; Schubert, U. S. *Adv. Mater.* **2005**, *17*, 1109. (d) Huang, Q.; Walzer, K.; Pfeiffer, M.; Lyssenko, V.; He, G.; Leo, K. *Appl. Phys. Lett.* **2006**, *88*, 113515.

(2) (a) Burroughes, J. H.; Bradley, D. D. C.; Brown, A. R.; Marks, R. N.; Mackay, K.; Friend, R. H.; Burn, P. L.; Holmes, A. B. *Nature* **1990**, *347*, 539. (b) Grimsdale, A. C.; Chan, K. L.; Martin, R. E.; Jokisz, P. G.; Holmes, A. B. *Chem. Rev.* **2007**, *107*, 1097. (c) Wang, X.-Y.; Kimyonok, A.; Weck, M. *Chem. Commun.* **2006**, 3933.

(3) (a) Burn, P. L.; Lo, S.-C.; Samuel, I. D. W. *Adv. Mater.* **2007**, *19*, 1675. (b) Lo, S.-C.; Burn, P. L. *Chem. Rev.* **2007**, *107*, 1097. (c) Harding, R. E.; Lo, S.-C.; Burn, P. L.; Samuel, I. D. W. *Org. Electron.* **2008**, *9*, 377. (d) Lo, S.-C.; Harding, R. E.; Brightman, E.; Burn, P. L.; Samuel, I. D. W. *J. Mater. Chem.* **2009**, *19*, 3213.

(4) (a) Tsuzuki, T.; Shirasawa, N.; Suzuki, T.; Tokito, S. *Jpn. J. Appl. Phys.* **2005**, *44*, 4151. (b) Lo, S.-C.; Namdas, E. B.; Shipley, C. P.; Markham, J; Anthopoulos, T. D.; Burn, P. L.; Samuel, I. D. W. *Org. Electron.* **2006**, *7*, 85. (c) Ding, J.; Gao, J.; Cheng, Y.; Xie, Z.; Wang, L.; Ma, D.; Jing, X.; Wong, F. *Adv. Funct. Mater.* **2006**, *16*, 575. (d) Velusamy, M.; Thomas, J. K. R.; Chen, C.-H.; Lin, J. T.; Wen, Y. S.; Hsieh, W.-T.; Lai, C.-H.; Chou, P.-T. *Dalton Trans.* **2007**, 3025. (e) Huang, W.-S.; Lin, J. T.; Lin, H.-C. *Org. Electron.* **2008**, *9*, 557.

(5) (a) Baldo, M. A.; Thompson, M. E.; Forrest, S. R. *Nature* **2000**, *403*, 750. (b) Adachi, C.; Baldo, M. A.; Thompson, M. E.; Forrest, S. R. *J. Appl. Phys.* **2001**, *90*, 5048. (c) Ikai, M.; Tokito, S.; Sakamoto, Y.; Suzuki, T.; Taga, Y. *Appl. Phys. Lett.* **2001**, *79*, 156. (d) Yang, X.; Müller, D. C.; Neher, D.; Meerholz, K. *Adv. Mater.* **2006**, *18*, 948. (e) You, Y.; Park, S.-Y. *Dalton Trans.* **2009**, 1267. (f) Ulbricht, C.; Beyer, B.; Friebe, C.; Winter, A.; Schubert, U. S. *Adv. Mater.* **2009**, *21*, 4418. (g) Chi, Y.; Chou, P.-T. *Chem. Soc. Rev.* **2010**, *39*, 381. (h) Xiao, L.; Chen, Z.; Qu, B.; Luo, J.; Kong, S.; Gong, Q.; Kido, J. *Adv. Mater.* **2011**, *23*, 926.

(6) (a) Nazeeruddin, M. K.; Humphry-Baker, R.; Berner, D.; Rivier, S.; Zuppiroli, L.; Grätzel, M. *J. Am. Chem. Soc.* **2003**, *125*, 8790. (b) Gong, X.; Ma, W. L.; Ostrowski, J. C.; Bazan, G. C.; Moses, D.; Heeger, A. J. *Adv. Mater.* **2004**, *16*, 615. (c) Coppo, P.; Plummer, E. A.; De Cola, L. *Chem. Commun.* **2004**, 1774. (d) Yang, C.-H.; Cheng, Y.-M.; Chi, Y.; Hsu, C.-J.; Fang, F.-C.; Wong, K.-T.; Chou, P.-T.; Chang, C.-H.; Tsai, M.-H.; Wu, C.-C. *Angew. Chem., Int. Ed.* **2007**, *46*, 2418. (e) Chang, C.-F.; Cheng, Y.-M.; Chi, Y.; Chiu, Y.-C.; Lin, C.-C.; Lee, G.-H.; Chou, P.-T.; Chen, C.-C.; Chang, C.-H.; Wu, C.-C. *Angew. Chem., Int. Ed.* **2008**, *47*, 4542.

(7) (a) Lo, S.-C.; Male, N. A. H.; Markham, J; Magennis, S. W.; Burn, P. L.; Salata, O. V.; Samuel, I. D. W. *Adv. Mater.* **2002**, *14*, 975. (b) Frampton, M. J.; Namdas, E. B.; Lo, S.-C.; Burn, P. L.; Samuel, I. D. W. *J. Mater. Chem.* **2004**, *14*, 2881. (c) Lo, S.-C.; Richards, G. J.; Markham, J; Namdas, E. B.; Sharma, S.; Burn, P. L.; Samuel, I. D. W. *Adv. Funct. Mater.* **2005**, *15*, 1451. (d) Lo, S.-C.; Anthopoulos, T. D.; Namdas, E. B.; Burn, P. L.; Samuel, I. D. W. *Adv. Mater.* **2005**, *17*, 1945. (e) Knights, K. A.; Stevenson, S. G.; Shipley, C. P.; Lo, S.-C.; Olsen, S.; Harding, R. E.; Gambion, S.; Burn, P. L.; Samuel, I. D. W. *J. Mater. Chem.* **2008**, *18*, 2121. (f) Lo, S.-C.; Harding, R. E.; Shipley, C. P.; Stevenson, S. G.; Burn, P. L.; Samuel, I. D. W. *J. Am. Chem. Soc.* **2009**, *131*, 16681. (g) Gambino, S.; Lo, S.-C.; Liu, Z. H.; Burn, P. L.; Samuel, I. D. W. *Adv. Funct. Mater.* **2012**, *22*, 157.

(8) Sirringhaus, H.; Kawase, T.; Friend, R. H.; Shimoda, T.; Inbasekaran, M.; Wu, W.; Woo, E. P. *Science* **2000**, *290*, 2123.

(9) De Gans, B. J.; Duineveld, P. C.; Schubert, U. S. *Adv. Mater.* **2004**, *16*, 203.

(10) Gunning, J. P.; Levell, J. W.; Wyatt, M. F.; Burn, P. L.; Robertson, J.; Samuel, I. D. W. *Polym. Chem.* **2010**, *1*, 730.

(11) Sandee, A. J.; Williams, C. K.; Evans, N. R.; Davies, J. E.; Boothby, C.; Kohler, A.; Friend, R. H.; Holmes, A. B. *J. Am. Chem. Soc.* **2004**, *126*, 7041.

(12) (a) Tokito, S.; Suzuki, M.; Sato, F. *Thin Solid Films* **2003**, *445*, 353. (b) Tokito, S.; Suzuki, M.; Sato, F.; Kamachi, M.; Shirane, K. *Org. Electron.* **2003**, *4*, 105. (c) Suzuki, M.; Tokito, S.; Sato, F.; Igarashi, T.; Kondo, K.; Koyama, T.; Yamaguchi, T. *Appl. Phys. Lett.* **2005**, *86*, 103507. (d) Wang, X.-Y.; Prabhu, R. N.; Schmehl, R. H.; Weck, M. *Macromolecules* **2006**, *39*, 3140. (e) Haldi, A.; Kimyonok, A.; Domercq, B.; Hayden, L. E.; Jones, S. C.; Marder, S. R.; Weck, M.; Kippelen, B. *Adv. Funct. Mater.* **2008**, *18*, 3056.

(13) (a) Chen, X.; Liao, J. L.; Liang, Y.; Ahmed, M. O.; Tseng, H.; Chen, S. A. *J. Am. Chem. Soc.* **2003**, *125*, 636. (b) Zhen, H. Y.; Luo, C.; Yang, W.; Song, W. Y.; Du, B.; Jiang, J. X.; Jiang, C. Y.; Zhang, Y.; Cao, Y. *Macromolecules* **2006**, *39*, 1693. (c) Liu, S. J.; Zhao, Q.; Xia, Y. J.; Deng, Y.; Lin, J.; Fan, Q. L.; Wang, L. H.; Huang, W. *J. Phys. Chem. C* **2007**, *111*, 1166. (d) Jiang, J.; Jiang, C.; Yang, W.; Zhen, H.; Huang, F.; Cao, Y. *Macromolecules* **2005**, *38*, 4072. (e) Yang, W.; Zhen, H. Y.; Jiang, C. Y.; Su, L. J.; Jiang, J. X.; Shi, H. H.; Cao, Y. *Synth. Met.* **2005**, *153*, 189.

(14) Liu, S. J.; Zhao, Q.; Chen, R. F.; Deng, Y.; Fan, Q. L.; Li, F. Y.; Wang, L. H.; Huang, C. H.; Huang, W. *Chem.—Eur. J.* **2006**, *12*, 4351.

(15) (a) Deng, L.; Furuta, P. T.; Garon, S.; Li, J.; Kavulak, D.; Thompson, M. E.; Fréchet, J. M. J. *Chem. Mater.* **2006**, *18*, 386. (b) Furuta, P. T.; Deng, L.; Garon, S.; Thompson, M. E.; Fréchet, J. M. J. *J. Am. Chem. Soc.* **2004**, *126*, 15388.

(16) Kimyonok, A.; Domercq, B.; Haldi, A.; Cho, J.-Y.; Carlise, J. R.; Wang, X.-Y.; Hayden, L. E.; Jones, S. C.; Barlow, S.; Marder, S. R.; Kippelen, B.; Weck, M. *Chem. Mater.* **2007**, *19*, 5602.

(17) (a) Marin, V.; Holder, E.; Hoogenboom, R.; Schubert, U. S. *J. Polym. Sci., Part A: Polym. Chem.* **2004**, *42*, 4153. (b) Ito, T.; Suzuki, S.; Kido, J. *Polym. Adv. Technol.* **2005**, *16*, 480.

(18) Carlise, J. R.; Wang, X.-Y.; Weck, M. *Macromolecules* **2005**, *38*, 9000.

(19) Holder, E.; Marin, V.; Alexeev, A.; Schubert, U. S. *J. Polym. Sci., Part A: Polym. Chem.* **2005**, *43*, 2765.

(20) Tekin, E.; Holder, E.; Marin, V.; de Gans, B. J.; Schubert, U. S. *Macromol. Rapid Commun.* **2005**, *26*, 293.

(21) (a) Lee, C. L.; Kang, N. G.; Cho, Y. S.; Lee, J. S.; Kim, J. J. *Opt. Mater.* **2002**, *21*, 119. (b) You, Y.; Kim, S. H.; Jung, H. K.; Park, S. Y. *Macromolecules* **2006**, *39*, 349.

(22) Schulz, G. L.; Chen, X. W.; Chen, S. A.; Holdcroft, S. *Macromolecules* **2006**, *39*, 9157.

(23) (a) Park, M.-J.; Lee, J.; Kwak, J.; Jung, I. H.; Park, J.-H.; Kong, H.; Lee, C.; Hwang, D.-H.; Shim, H.-K. *Macromolecules* **2009**, *42*, 5551. (b) Park, M.-J.; Kwak, J.; Lee, J.; Jung, I. H.; Kong, H.; Lee, C.; Hwang, D.-H.; Shim, H.-K. *Macromolecules* **2010**, *43*, 1379.

(24) Poulsen, D. A.; Kim, B. J.; Ma, B.; Zonte, C. S.; Fréchet, J. M. J. *Adv. Mater.* **2010**, *22*, 77.

(25) (a) Lai, W.-Y.; Levell, J. W.; Burn, P. L.; Lo, S.-C.; Samuel, I. D. W. *J. Mater. Chem.* **2009**, *19*, 4952. (b) Lai, W.-Y.; Cavaye, H.; Wang, X.; Lo, S.-C.; Meredith, P.; Burn, P. L. *Polym. Prepr.* **2009**, *50*, 296.

(26) Furuta, P.; Brooks, J.; Thompson, M. E.; Fréchet, J. M. J. *J. Am. Chem. Soc.* **2003**, *125*, 13165.

(27) Lai, W.-Y.; Levell, J. W.; Jackson, A. C.; Lo, S.-C.; Bernhardt, P. V.; Samuel, I. D. W.; Burn, P. L. *Macromolecules* **2010**, *43*, 6986.

(28) Levell, J. W.; Lai, W.-Y.; Lo, S.-C.; Burn, P. L.; Samuel, I. D. W. *Polym. Prepr.* **2011**, *52*, 884.

(29) Lai, W.-Y.; Levell, J. W.; Balfour, M. N.; Lo, S.-C.; Burn, P. L.; Samuel, I. D. W. *Polym. Chem.* **2012**, *3*, 734.

(30) (a) Lo, S.-C.; Namdas, E. B.; Burn, P. L.; Samuel, I. D. W. *Macromolecules* **2003**, *36*, 9721. (b) Lo, S.-C.; Bera, R. N.; Harding, R. E.; Burn, P. L.; Samuel, I. D. W. *Adv. Funct. Mater.* **2008**, *18*, 3080. (c) Cavaye, H.; Shaw, P. E.; Wang, X.; Burn, P. L.; Lo, S.-C.; Meredith, P. *Macromolecules* **2010**, *43*, 10253.

(31) (a) Love, J. A.; Morgan, J. P.; Trnka, T. M.; Grubbs, R. H. *Angew. Chem., Int. Ed.* **2002**, *41*, 4035. (b) Choi, T.-L.; Grubbs, R. H. *Angew. Chem., Int. Ed.* **2003**, *42*, 1743.
(32) (a) Swindells, J. F.; Coe, J. R.; Godfrey, T. B. *J. Res. Natl. Bur. Std.* **1952**, *48*, RP2279. (b) Korosi, A.; Fabuss, B. M. *Anal. Chem.* **1968**, *40*, 157.
(33) (a) Schmid, B.; Garces, F. O.; Watts, R. J. *Inorg. Chem.* **1994**, *33*, 9. (b) Hofbeck, T.; Yersin, H. *Inorg. Chem.* **2010**, *49*, 9290.
(34) Levell, J. W.; Zhang, S.; Lai, W.-Y.; Lo, S.-C.; Burn, P. L.; Samuel, I. D. W. *Opt. Express* **2012**, *20*, A213.
(35) (a) Levell, J. W.; Lai, W.-Y.; Borthwick, R. J.; Lo, S.-C.; Burn, P. L.; Samuel, I. D. W. *J. Phys. Chem. C* **2011**, *115*, 25464. (b) Levell, J. W.; Lai, W.-Y.; Borthwick, R. J.; Burn, P. L.; Lo, S.-C.; Samuel, I. D. W. *New J. Chem.* **2012**, *36*, 407.
(36) Gritzner, G.; Kuta, J. *Electrochim. Acta* **1984**, *29*, 869.
(37) Demas, J. N.; Crosby, G. A. J. *J. Phys. Chem.* **1971**, *75*, 991.
(38) Greenham, N. C.; Samuel, I. D. W.; Hayes, G. R.; Phillips, R. T.; Kessener, Y.; Moratti, S. C.; Holmes, A. B.; Friend, R. H. *Chem. Phys. Lett.* **1995**, *241*, 89.

Macromolecules

Article

pubs.acs.org/Macromolecules

Efficient Copper-Mediated Surface-Initiated Polymerization from Raw Polymer Latex in Water

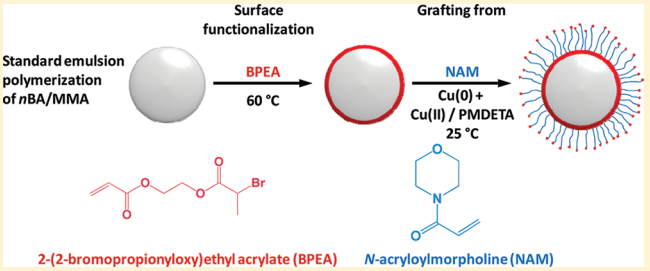
Virginie Chabrol,[†] Didier Léonard,[§] Matthias Zorn,[‡] Bernd Reck,[‡] Franck D'Agosto,[†] and Bernadette Charleux*,[†]

[†]Université de Lyon, Univ Lyon 1, CPE Lyon, CNRS, UMR 5265, C2P2 (Chemistry, Catalysis, Polymers & Processes), Bât. 308F, 43 Bd du 11 Novembre 1918, F-69616 Villeurbanne, France

[‡]BASF SE, Carl-Bosch-Str.38, 67056 Ludwigshafen, Germany

[§]Université de Lyon, F 69622, Lyon, France. Institut des Sciences Analytiques, UMR 5280, Laboratoire des Sciences Analytiques, Bât. J. Raulin, Université Claude Bernard-Lyon 1, F-69622 Villeurbanne, France

ABSTRACT: The copper-mediated radical polymerization of *N*-acryloylmorpholine initiated from the surface of latex particles in water was studied to form hydrophobic core/hydrophilic shell particles. The latexes were synthesized via classical radical emulsion polymerization and were functionalized at their surface by a comonomer bearing a Br-functional group (the so-called inimer). The latter was introduced to initiate the grafting reaction, in the presence of the Cu(0)/$CuBr_2$/PMDETA (1,1,4,7,7-pentamethyldiethylenetriamine) catalytic system. Conditions in which the grafting step could be performed at room temperature, using high particle concentration in the presence of surfactant and initiator remaining from the emulsion polymerization were identified. The success of the functionalization and grafting steps was evaluated by TOF-SIMS (time-of-flight secondary ion mass spectrometry), by FTIR, and by the final properties of the so-formed core−shell particles. It is the first time such grafting conditions have been applied with success from "real latexes".



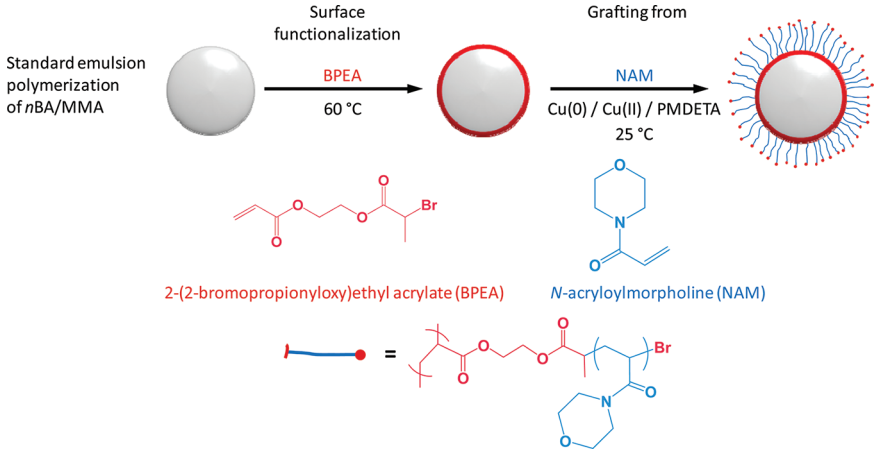
INTRODUCTION

Core−shell particles with a hydrophobic polymer core and a hydrophilic polymer shell have been the subject of many studies[1−3] as they can find a wide range of applications in fields such as coatings, paints, adhesives, impact modifiers, support for biological molecules, etc. Various strategies to incorporate a hydrophilic polymer shell have been employed with the use for instance of an amphiphilic block copolymer as a stabilizer in emulsion polymerization or via emulsion copolymerization of the hydrophobic monomers with a water-soluble (macro)-monomer. There has also been a growing interest in the "grafting from" method[1,3−6] with the development of controlled/living radical polymerization (CRP) techniques.[7] The general principle of the "grafting from" strategy consists in introducing initiating groups at the particle surface and in activating them to grow polymer chains via CRP. Because of fast initiation and simultaneous growth of the chains, CRP allows grafting density and brush thickness to be well-controlled.[1,3−6] Among the various CRP methods, atom transfer radical polymerization (ATRP) has been particularly used on different colloidal substrates, in organic solution, or in water.[8,9,1,3−6] The latter mainly include silica particles, whereas only a few examples are related to the use of polymer latexes,[2] resulting from a free-radical emulsion polymerization recipe. The use of functionalized latexes as support for aqueous surface-initiated ATRP (SI-ATRP) has been reported for the first time by Manuszak-Guerrini et al.[10] in 2000. The grafting strategy was to functionalize a cross-linked polystyrene latex with an inimer (i.e., a monomer bearing an alkyl halide group able to serve as an initiator in ATRP) at the particle surface and to activate it by a Cu(I) complex in the presence of a water-soluble monomer. Following this seminal work, other teams have used the same strategy to prepare core−shell particles by SI-ATRP.[11−15] Mittal et al.[16,17] studied the functionalization process by the inimer so as to find the best conditions for the SI-ATRP of *N*-isopropylacrylamide. To favor the synthesis of functionalized particles and to avoid secondary nucleation, the introduction of the inimer along with a cross-linker had to be performed at 70% conversion of the monomers in the first stage emulsion polymerization. Another method to functionalize a latex by surface halide groups was chloromethylation of polystyrene particles as described by Min et al.[18] More recently, Liu et al.[19] proposed an easier way to immobilize bromide group at the surface of cross-linked poly(methyl methacrylate) (polyMMA) particles using CBr_4 as a chain transfer agent in the emulsion polymerization step. A different approach for SI-ATRP from latex particles was performed without covalently incorporating the initiator at the particle surface.[20] The authors took advantage of the Br functional group at the hydrophilic end of an amphiphilic block copolymer previously prepared via

Received: February 1, 2012
Revised: March 8, 2012
Published: March 22, 2012

 © 2012 American Chemical Society

Scheme 1. General Principle of the Cu-Mediated Surface-Initiated Radical Polymerization Used in This Work



ATRP and used as a stabilizer in the emulsion polymerization process. It was further reacted as the initiating site for the ATRP of a water-soluble monomer, hence leading to the formation of a second hydrophilic shell. In all instances, the grafting reaction by ATRP was carried out with diluted latexes (low solids contents of ∼5 wt %; except in ref 20 in which the solids content was 16.6 wt %) that were carefully cleaned by dialysis and/or by centrifugation to eliminate all traces of low molar mass initiator and surfactant.

In this context, the aim of this work was to incorporate a hydrophilic polymer shell at the surface of submicrometric polymer particles from emulsion polymerization by postsynthesis modification, using a "grafting from" approach based on aqueous CRP. The use of a single type of functionalized particles as a platform to grow any kind of hydrophilic polymers with tailor-made characteristics (see Scheme 1) would allow to target different applications from the same starting latex recipe. It also offers the opportunity to incorporate a polymer shell that cannot be introduced in another way (via the amphiphilic block copolymer strategy for instance) without impacting the features of the grafted particles.

To reach this goal, we considered the following key points: (i) the choice of the CRP method and the possibility to functionalize the latex particles with an inimer suitable for the selected technique; (ii) the ability to perform the grafting reaction from "as-synthesized" concentrated latexes, without elimination of the surfactant and of the remaining initiator. To fulfill both criteria, ATRP was selected as it uses a variety of alkyl halide initiators that can be easily turned into inimers. The latter can be polymerized via classical radical emulsion polymerization without interference with the initiating and propagating radicals. Finally, the method can be performed at room temperature, hence preventing unwanted initiation by the remaining radical initiator. All those criteria impede the use of other CRP methods such as nitroxide-mediated polymerization (performed at elevated temperature) and reversible addition−fragmentation chain transfer (in which the reactive group of the functional monomer will react during the functionalization step). However, a drawback of ATRP is the need for large quantities of catalyst (in particular copper(I) halide), which contaminate the final product and are difficult to remove. The reduction of the amount of copper has been achieved through the use of techniques such as activators (re)generated by electron transfer (A(R)GET).[21] Since a few years, the use of copper metal has been particularly investigated because Cu(0) is easier to handle than Cu(I) or Cu(II) salts. As a reducing agent for Cu(II) in A(R)GET ATRP[22] or as an activator in single electron transfer living radical polymerization (SET-LRP),[23] the role of Cu(0) in the mechanism of copper-mediated polymerization is not fully understood and still under debate[24] but will not be the focus of this work. In all cases, however, it offers a rather easy way to proceed and allows to decrease the amount of catalyst. The couple Cu(0)/Cu(II) was thus employed as a catalyst for our grafting reactions from latex particles in aqueous media at room temperature. The use of AGET ATRP with Cu(II) and ascorbic acid as a reducing agent has been reported in a single article.[25] However, the grafting of polymer chains from latex particles has never been performed with Cu(0) in concentrated latex, in the presence of surfactant and residual initiator ("real" latex). With the aim of studying the efficiency of the reaction, the aqueous SI-ATRP of *N*-acryloylmorpholine (NAM), used as a model of neutral water-soluble monomer, was considered and the effect of the concentrations of both the inimer and the Cu(0)/$CuBr_2$ catalyst (with 1,1,4,7,7-pentamethyldiethylenetriamine, PMDETA, as a ligand) was evaluated.

EXPERIMENTAL PART

Materials. Sodium dodecyl sulfate (DISPONIL SDS, 15 wt % aqueous solution) was purchased from Cognis. Sodium hydrogen carbonate ($NaHCO_3$, 0.07 M aqueous solution), NaOH solution (0.25 M aqueous solution), *n*-butyl acrylate (*n*BA), methyl methacrylate (MMA), and 1,4-butanediol diacrylate (BDDA) were obtained from BASF. 4,4′-Azobis(4-cyanopentanoic acid) (ACPA, >98%), *N*-acryloylmorpholine (NAM, 97%), 1,1,4,7,7-pentamethyldiethylenetriamine (PMDETA, 99%), $CuBr_2$ (>99%), $CuCl_2$ (99.999%) and copper wire (>99.9%; diameter = 1 mm) were used as received from Sigma-Aldrich. Deionized water was employed in all the experiments. The inimer 2-(2-bromopropionyloxy)ethyl acrylate (BPEA) was synthesized by an esterification reaction between 2-hydroxyethyl acrylate (Sigma-Aldrich, 96%) and 2-bromopropionyl bromide (Sigma-Aldrich, 97%), according to a protocol published previously,[26] and briefly described here. A solution of 2-bromopropionyl bromide (79.33 g, 0.38 mol) in 50 mL of CH_2Cl_2 was added dropwise to a stirred solution (cooled in an ice bath) of 2-hydroxyethyl acrylate (40.64 g, 0.35 mol) and triethylamine (38.96 g, 0.38 mol) in 220 mL of CH_2Cl_2, during 3 h under an atmosphere of argon. After complete addition, the reaction was further stirred at room temperature for 24 h. The precipitate was removed by filtration, and the organic phase was washed with water (3 × 50 mL). It was then dried over magnesium sulfate, and CH_2Cl_2 was evaporated under vacuum. The obtained yellow oil was distilled under vacuum in the presence of 0.5 wt % of

dx.doi.org/10.1021/ma300236r | *Macromolecules* 2012, 45, 2972−2980

Table 1. Synthesis[a] of Poly(*n*-butyl acrylate-*co*-methyl methacrylate) (Poly(*n*BA-*co*-MMA)) Latex Particles Cross-Linked with 1,4-Butanediol Diacrylate (BDDA) and Functionalized at the Surface with 2-(2-Bromopropionyloxy)ethyl Acrylate (BPEA) (T = 70 °C)

latex no.	composition of the core *n*BA/MMA/BDDA (wt %)	composition of the shell MMA/BPEA/BDDA (wt %)	shell/core weight ratio (wt %)	BPEA conv (%)	overall BPEA content (mol/g_{Latex})	final diameter D from DLS (nm)
L0	30.7/66.7/2.6				0	112
L1	30.7/66.7/2.6	95.0/1.8/3.2	5.1/94.9	95	1.5×10^{-6}	110
L2	30.7/66.7/2.6	65.0/32.5/2.5	7.5/92.5	95	3.9×10^{-5}	110
L3	30.7/66.7/2.6	48.6/49.0/2.4	9.7/90.3	97	7.3×10^{-5}	116

[a]The experimental procedure is described in the Experimental Part.

hydroquinone to give a colorless liquid. 300 MHz ^{1}H NMR ($CDCl_3$): δ (ppm) = 6.44 (d, 1H, CH_2=), 6.13 (dd, 1H, =CH), 5.87 (d, 1H, CH_2=), 4.41 (m, 5H, H_2C−O and CH−Br), 1.83 (d, 3H, CH_3).

Characterization Techniques. *NMR.* ^{1}H NMR spectroscopy for kinetic analysis (i.e., conversion of the monomer NAM in the surface-initiated aqueous polymerization) was performed in 5 mm diameter tubes in D_2O solution at 25 °C using a Bruker Avance 300 (300 MHz) spectrometer. The chemical shift scale was calibrated on the basis of the solvent peak (δ = 4.79 ppm), and sodium *p*-toluenesulfonate was used as an internal reference (aromatic H peaks).

DLS. The intensity-average diameters of the latex particles and the dispersity factor were measured by dynamic light scattering (DLS) at a temperature of 25 °C using a Zetasizer Nano Series (Nano ZS) from Malvern Instrument using the Zetasizer 6.2 software. The instrument was calibrated with a standard polystyrene latex in water exhibiting a particle size of 220 ± 6 nm. Before measurements, the latex samples were diluted with deionized water.

Gas Chromatography. Gas chromatography (GC) of the polymer dispersions was used to determine the residual amount of BPEA inimer. It was performed with HP6890N equipment from Agilent Technologies with a 30 m column (DB 5, 5% polydiphenylsiloxane/95% polydimethylsiloxane) and a temperature ramp of 8 °C/min from 120 to 280 °C. The injection temperature was 280 °C.

SEM. Scanning electron microscopy (SEM) images were examined on a FEI QUANTA 250 FEG scanning electron microscope, at an acceleration voltage of 15 kV (Centre Technologique des Microstructures (CTμ), Claude Bernard University, Lyon, France). A drop of the particle suspension was placed on a Formvar film on a 200 mesh copper grid, dried, and covered by a thin layer of gold/palladium (sputtering Au/Pd with Baltec MED020-5.9 nm).

DSC. Differential scanning calorimetry was measured in a Q2000 by TA Instruments. The instrument is calibrated with adamantane, water, and indium. For determination of the glass transition temperature, 8−9 mg was placed in an aluminum pan. The sample was rapidly cooled from 150 to −110 °C and afterward scanned with a heating rate of 2 K/min. Glass transition was determined at the half step height (according to ISO 11357-2).

FTIR. Fourier transform infrared analyses were performed on a Nicolet iS10 spectrometer with an ATR diamond crystal and a DTGS KBr detector. The data were measured with a resolution of 4 cm^{-1} from 525 to 4000 cm^{-1}. A background spectrum was collected and subtracted from the spectrum. The latex were dialyzed against water for 2 weeks using a Spectra/Por dialysis membrane (cutoff at 12 000−14 000 Da), dried at room temperature, grinded to powder, and then dissolved in dichloromethane. A drop of the dispersion was deposited onto the diamond crystal, dried, and then analyzed.

ToF SIMS. Time-of-flight secondary ion mass spectrometry (ToF-SIMS) measurements were carried out using a Physical Electronics TRIFT III ToF-SIMS instrument operated with a pulsed 22 keV Au^+ ion gun (ion current of 2 nA) rastered over a 300 μm × 300 μm area. An electron gun was operated in pulsed mode at low electron energy for charge compensation. Ion dose was kept below the static conditions limit. Data were analyzed using the WinCadence software. Mass calibration was performed on hydrocarbon secondary ions. Before the analysis, the latexes were dialyzed in water for 2 weeks using a Spectra/Por dialysis membrane (cutoff at 12 000−14 000 Da), dried at room temperature, and grinded to a powder, and this powder was pressed onto an indium foil. Data were normalized to the total intensity minus $H^{+/-}$ intensity (because of its critical dependence on slight variations in the experimental settings)[27] and minus the intensity of peaks related to ubiquitous contamination or to the sample preparation (i.e., Na^+ and In^+ in the positive mode and F^- in the negative mode). Standard deviations were calculated from measurements performed on three different areas.

Viscosity Measurements. Viscosity measurements were performed at 25 °C using a parallel-plate (25 mm in diameter) geometry fixture on a TA Instruments AR2000ex rheometer. The shear rate was fixed at 50 s^{-1}, and the gap between the upper plate and the Peltier plate was set at a distance of 1000 μm.

Stability Tests. The ionic strength and freeze−thaw stability of the grafted latexes were tested (raw latexes or dialyzed latexes). A drop of latex dispersion was added to 5 mL solutions of $CaCl_2$ with concentrations of 4.5 mM, 9.0 mM, 22.5 mM, 45 mM, 91 mM, 0.18 M, 0.47 M, 1 M, and 2.25 M. The colloidal stability of the dispersion was assessed by a simple visual test. A 2 mL dispersion of grafted particles was frozen for 2 h and then thawn. This cycle was repeated three times. The colloidal stability of the dispersion was assessed by DLS measurements.

Synthesis of Poly(MMA-*co*-*n*BA) Cross-Linked Functionalized Latex Particles. In a first step, functionalized, cross-linked latex particles were synthesized via free-radical emulsion polymerization in an automated reactor at the BASF Laboratories for Advanced Materials and Systems Research. Particles were cross-linked with 1,4-butanediol diacrylate, a divinylic monomer, in order to maintain their shape and integrity for analytical purposes. In a typical example (latex L3 in Table 1), a monomer in water emulsion was first prepared using 260 g of deionized water, 26.5 g of SDS solution, 5.6 g of sodium hydrogen carbonate solution, 88 g of *n*BA, 190 g of MMA, and 7.3 g of BDDA. An aqueous solution of ACPA initiator (6.28 g of the solution prepared with 48 g of deionized water, 3.0 g of ACPA, and 11.7 g of NaOH aqueous solution 0.25 M) was introduced into a 2 L reactor preloaded with 138 g of deionized water, equipped with a thermocouple, a cooling condenser, and a paddle stirrer, and heated at 70 °C. After 15 min, the monomer-in-water emulsion was gradually added to the reactor for a total time of 180 min while 56.5 g of the residual initiator solution was fed during 215 min. After complete addition of the monomer emulsion (achieving 92% conversion), a mixture containing 15 g of the BPEA inimer, 15 g of MMA, and 0.7 g of BDDA was added during 30 min, and the reaction medium was stirred at 70 °C for an additional 60 min and then cooled to room temperature. The final latex had a solids content of 40 wt % (obtained by gravimetric analysis). The particle diameter was determined using DLS. The conversion of BPEA was determined by gas chromatography. All data are summarized in Table 1.

Copper-Mediated Surface-Initiated Polymerization of NAM. The latexes (raw or slightly diluted in water) with a low amount of sodium *p*-toluenesulfonate (4 mg/g_{Latex}) were deoxygenated with a nitrogen flow for 30 min. A deoxygenated mixture of NAM, PMDETA, 0.1 M $CuBr_2$ aqueous solution, and additional water was slowly added under stirring. The reaction medium was heated at 25 °C, and a piece of a copper wire was introduced (0.14 cm/g_{Latex}, i.e., 12.6 cm^2/g_{Latex}). Samples were periodically withdrawn to monitor the

dx.doi.org/10.1021/ma300236r | *Macromolecules* 2012, 45, 2972−2980

Table 2. Surface-Initiated Polymerization of *N*-Acryloylmorpholine (NAM) Performed at 25 °C from Cross-Linked Poly(*n*-butyl acrylate-*co*-methyl methacrylate) Aqueous Latex Particles Functionalized at the Surface with 2-(2-Bromopropionyloxy)ethyl Acrylate (BPEA)

entry	functionalized latex	overall BPEA content (mol/g_{Latex})	NAM ($g/g_{polymer}$)	NAM/BPEA/PMDETA/$CuBr_2$ (molar equiv)	time (h)	conv (%)	*D* from DLS after grafting (nm) /dispersity	final solids content of the grafted latex[a] (wt %)	final viscosity[b] (10^{-3} Pa s)	color[c]
L1G1	L1	1.4×10^{-6}	0.05	97.5/1/0.6/0.10	8	30	120/0.08	38	2.4	*
L1G2	L1	1.1×10^{-6}	0.22	441.5/1/0.8/0.15	1		formation of a gel			*
L2G1	L2	2.1×10^{-5}	0.05	4.1/1/0.5/0.10	7	100	105/0.03	24	1.6	***
L2G2	L2	2.6×10^{-5}	0.26	20.5/1/0.5/0.10	2	40	171/0.09	37	33.3	****
L2G3	L2	2.0×10^{-5}	0.26	20.5/1/0.5/0.10	7	93	210/0.3	30	22.1	***
L2G4	L2	1.9×10^{-5}	0.42	33.3/1/0.5/0.10	7	71	270/0.3	31	287.7	***
L3G0	L3	6.6×10^{-5}	0	0/1/0.5/0.10[d]	6					
L3G1	L3	6.1×10^{-5}	0.125	5.0/1/0.6/0.09	6	96	140/0.04	38	2.6	*****
L3G2	L3	4.9×10^{-5}	0.23	8.9/1/0.5/0.10	4	86	119/0.06	33	1.6	****
L3G3[e]	L3	5.5×10^{-5}	0.25	10.9/1/0.5/0.10	8	79	140/0.03	41	1.7	*****
L3G4	L3	4.7×10^{-5}	0.25	9.9/1/0.2/0.05	5	89	130/0.05	31	5.9	***
L3G5	L3	4.8×10^{-5}	0.25	9.7/1/0.1/0.025	2		formation of a gel			**
L3G6[f]	L3	1.1×10^{-5}	0.40	13.3/1/0.5/0.10	6	88	260/0.2	8.6	2.7	**
				Control Experiments						
L0G1	L0	0	0.13	9.8/0/1/0.5/(Cu(0) wire: 1.5 cm)	5	0				
L3G7	L3	3.4×10^{-5}	0.15	6.3/1/0/0/(Cu(0) wire: 0 cm)	5	0				
L3G8	L3	3.4×10^{-5}	0.15	6.1/1/0/0/(Cu(0) wire: 1 cm)	5	0				
L3G9[g]	L3	3.4×10^{-5}	0.15	6.0/1/0.7/0/(Cu(0) wire: 1 cm)	5	9				
L3G10[g]	L3	3.4×10^{-5}	0.15	6.3/1/0.7/0.15/(Cu(0) wire: 0 cm)	5	11				

[a]Obtained by thermogravimetric analysis—includes the nonreacted NAM, which is nonvolatile. [b]At 20 wt % solids (except latex L3G6 measured at 8 wt %). [c]Color qualitative scale: * (light blue) to ***** (dark blue). [d]$CuCl_2$ instead of $CuBr_2$ [e]Two successive feeds of NAM (feed 1: 81% conversion in 2 h; feed 2: 67% conversion in 8 h − overall conversion = 79%). [f]The latex L3 was dialyzed before the grafting reaction, to remove the initiator and surfactant. [g]Latex destabilization.

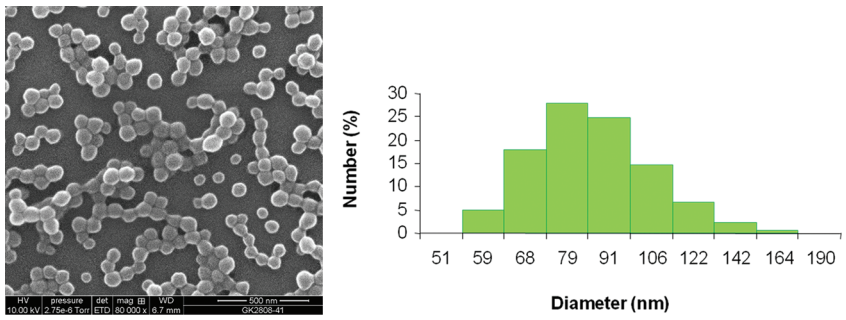


Figure 1. Scanning electron microscopy image and particle size distribution from DLS of the final latex L3.

conversion by ^1H NMR after dilution in D_2O. All reaction details and exact quantities are reported in Table 2.

RESULTS AND DISCUSSION

Surface Functionalization of Latex Particles with the BPEA Inimer. The latex particles were based on methyl methacrylate and *n*-butyl acrylate and were slightly cross-linked with 1,4-butanediol diacrylate to maintain their integrity during the analyses. The experimental conditions are reported in Table 1. The surface functionalization of such latex particles has been already reported in the literature.[16,17] The functional monomer BPEA was used in a very low amount to introduce a thin layer of brominated groups able to initiate the polymerization from the surface. The main requirements that had to be fulfilled are the absence of secondary nucleation and a high conversion of BPEA with a preferential location at the particle surface. BPEA was thus added at the end of the latex synthesis before complete conversion of the core monomers (~90%). During this step, MMA was used as a comonomer, to ensure an efficient anchoring of the adsorbed oligoradicals by fast chain propagation and to avoid their precipitation and the generation of a second crop of particles. The final conversion of BPEA was high as assessed by gas chromatography (see Table 1). On the basis of the scanning electron microscopy and DLS analyses of the final latexes (Figure 1), a monomodal particle size distribution was observed, indicating the absence of secondary nucleation.

Because of the very low amount of BPEA used and due to the remaining core monomers present during the functionalization step, it was important to check the location of the inimer. Burial of the inimer may actually occur during the polymerization, even though the use of additional MMA should lead to a rather polar polymer that remains preferentially at the particle surface. ToF-SIMS has already been used to detect functional groups at the surface of synthetic latex particles[28−30] and was selected for the present analytical purpose. This surface analysis technique is based on the *m*/*z* detection of secondary ions (positively charged and negatively charged as obtained in two

dx.doi.org/10.1021/ma300236r | *Macromolecules* 2012, 45, 2972−2980

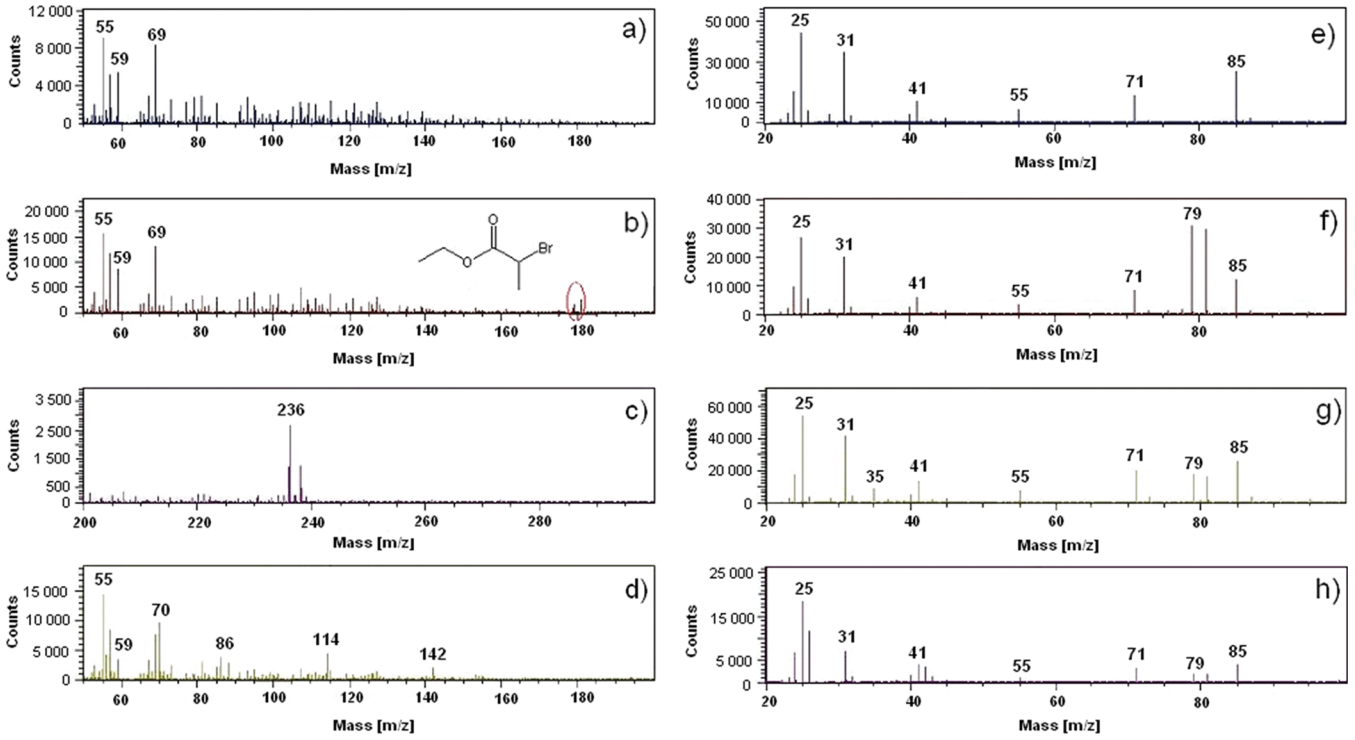


Figure 2. Positive ion mode ToF-SIMS spectrum (m/z = 50−200) for (a) latex L0, (b) latex L3, (c) latex L3G0 (m/z = 200−300), and (d) latex L3G1. Negative ion mode ToF-SIMS spectrum (m/z = 20−100) for (e) latex L0, (f) latex L3, (g) latex L3G0, and (h) latex L3G1.

Table 3. ToF-SIMS Normalized Intensity (in ‰) for Various Characteristic Peaks[a] for Latexes L0, L1, L2, L3, L3G0, L3G1, and L3G3 (see Table 2)

	characteristic signatures for core latex		characteristic signatures for BPEA		characteristic signature for Cl	characteristic signatures for polyNAM		
entry	I^{59+}	I^{85-}	I^{79-}	I^{179+}	I^{35-}	I^{26-}	I^{42-}	I^{142+}
L0	13.7 ± 2.2	21.9 ± 2.6	0.9 ± 0.2	1.2 ± 0.3	0.5 ± 0.5	5.8 ± 0.2	0.4 ± 0.1	1.6 ± 0.2
L1	16.5 ± 1.0	27.3 ± 1.8	3.7 ± 0	1.4 ± 0.2	0.6 ± 0.2	7.4 ± 0.6	0.5 ± 0.1	1.8 ± 0.2
L2	16.0 ± 0.4	18.8 ± 3.1	39.9 ± 3.6	7.4 ± 0.7	0.2 ± 0	4.4 ± 0.2	0.3 ± 0	2.0 ± 0
L3	13.4 ± 3.6	15.5 ± 2.5	39.8 ± 4.7	6.6 ± 1.1	0.2 ± 0	5.7 ± 1.3	0.3 ± 0.1	1.5 ± 0.2
L3G0	14.3 ± 0.6	18.9 ± 1.6	14.1 ± 0.7	2.4 ± 0.2	8.9 ± 1.6	3.7 ± 0.5	0.4 ± 0	1.6 ± 0.1
L3G1	7.0 ± 0.5	9.1 ± 1.3	4.7 ± 0.2	1.1 ± 0.1	0.7 ± 0.1	23.7 ± 2.6	7.5 ± 1.1	8.1 ± 0.8
L3G3[b]	5.4 ± 0.1	7.2 ± 0.5	2.4 ± 0.1	0.9 ± 0	7.0 ± 3.4	29.1 ± 0.4	10.5 ± 0	8.4 ± 0.1

[a]Peaks at: m/z = 59^+ corresponding to $C_2H_3O_2^+$ and m/z = 85^- corresponding to $C_4H_5O_2^-$, characteristic of the core latex; m/z = 79^- corresponding to $^{79}Br^-$ and m/z = 179^+ corresponding to $C_5H_8O_2{}^{79}Br^+$, characteristic of BPEA; m/z = 35^- corresponding to $^{35}Cl^-$, characteristic of the ion exchange reaction between Br and Cl but contribution from Cl ubiquitous contamination cannot be excluded (it is especially the case for L3G3); m/z = 26^- corresponding for a major part to CN^- but contribution from $C_2H_2^-$ cannot be excluded, m/z = 42^- corresponding to CNO^- and m/z = 142^+ corresponding to $C_7O_2H_{12}N^+$. [b]Measurements performed only on two areas and therefore poorly accurate.

separate data acquisitions) emitted following the bombardment of solids using primary ions in the keV range. If a limited number of primary ions are used for this purpose (static conditions), the information depth is limited to a few atomic layers. Moreover, this technique allows the detection of very low amounts[31] (detection limit of ppm to ppb), which is appropriate considering the quantity of BPEA involved for surface modification of the latexes. The latexes were first carefully dialyzed to remove all nonconverted monomers and water-soluble oligomers, and the dried powder was then pressed onto an indium foil at room temperature. The particles being cross-linked and their glass transition temperature being 52 °C (as determined by DSC, i.e., above room temperature) a good shape stability and the absence of film formation by chain interdiffusion is expected. This is an important point when targeting the surface analysis exclusively.

Figure 2 displays ToF-SIMS spectra in the positive and negative modes in selected m/z ranges. It illustrates the main observations at the surface of latexes before and after the various steps of the surface modification (modification with BPEA inimer, test for ion-exchange, surface-initiated polymerization of NAM). Table 3 provides normalized intensity values (in ‰) for secondary ion peaks specific to the latexes and to the various surface modifications. Figures 2a and 2e correspond to the spectra obtained on the latex L0 (nonfunctionalized) in the positive mode (m/z = 50−200) and in the negative mode (m/z = 20−100), respectively. ToF-SIMS spectra display peaks characteristic for polyMMA[28] (as well as other peaks detected in the nonillustrated m/z ranges), i.e., in the displayed m/z range, a peak at m/z = 59.014 (corresponding to $C_2H_3O_2^+$, m/z = 59.013) and those at m/z = 31.016 (corresponding to CH_3O^-, m/z = 31.018), m/z = 55.018 (corresponding to

$C_3H_3O^-$, m/z = 55.018), and m/z = 85.029 (corresponding to $C_4H_5O_2^-$, m/z = 85.029). This confirmed that latexes had the expected chemical structure (see also Table 3) without significant contamination (see e.g. Br and Cl ubiquitous contamination in Table 3).

After surface functionalization with BPEA inimer, both ToF-SIMS spectra of latex L3 in the positive mode (Figure 2b) and in the negative mode (Figure 2f) indicate that the main signatures of the latexes are still detected, which is consistent with the intended limited extent in surface modification. In addition, peaks characteristic for BPEA were detected. The most obvious signature was Br, which was detected in the negative mode with both isotopes (and in the expected isotopic ratio): a peak at m/z = 78.913 (corresponding to $^{79}Br^-$, m/z = 78.918) and a peak at m/z = 80.911 (corresponding to $^{81}Br^-$, m/z = 80.916). However, Br being ubiquitous contamination (see in Table 3 the very slight amount detected for the unmodified latex L0), it was important to confirm that the high relative intensity for $^{79}Br^-$ was a direct signature for BPEA. The detection of peaks in the positive mode at m/z = 178.981 corresponding to $C_5H_8O_2{}^{79}Br^+$, m/z = 178.971—see BPEA chemical structure in Scheme 1) and a peak at m/z = 180.972 (corresponding to $C_5H_8O_2{}^{81}Br^+$, m/z = 180.969) brought this confirmation.

Table 3 (entries L0−L2) indicates that when modifying the BPEA concentration used for surface modification (see entries L0−L2 in Table 1), characteristic signatures for BPEA varied accordingly in normalized intensity. ToF-SIMS data are known to be highly dependent on severe matrix effects, which hinder any absolute quantification from these data. However, when comparing similar samples only varying as a function of the BPEA content, matrix effects can be considered as close enough to allow a semiquantitative comparison of normalized intensities for characteristic signatures of BPEA, i.e., Br^-. In addition, the relative intensity for 179^+ for the latex L0 in Table 3 is not due to $C_5H_8O_2{}^{79}Br^+$ (179^+ is detected at m/z = 179.0975 for L0, excluding any relation to BPEA), but the value was given to allow the reader to identify the relevance of the increase in normalized intensity for that specific signature (thus relevant for L2 and L3 but not for L1). It can then be concluded here that BPEA is significantly less detected for latex L1 compared to latexes L2 and L3. For the latter two latexes, similar values could be related to the very limited information depth of the ToF-SIMS technique. BPEA might be more incorporated in L3 than in L2, but the amount in the sample depth probed by ToF-SIMS was similar. As expected, for latexes L2 and L3, a more significant decrease in normalized intensity was observed for the core polymer characteristic peaks (especially $C_4H_5O_2^-$), which is consistent with the larger introduction of BPEA at the surface of these latexes.

Prior to any polymerization from the surface, and in order to assess the accessibility of the surface anchored Br toward an ion exchange reaction with water-soluble species, the latex L3 was further subjected to a reaction with Cu(0) and $CuCl_2$/PMDETA (entry L3G0, Table 2). The change of Br signature to Cl one should show that activation of the alkyl bromide group of BPEA is possible and further confirm the appropriate location of BPEA. Figure 2g displays the ToF-SIMS spectrum in the negative mode for the latex L3G0, obtained by reacting the latex L3 with $CuCl_2$/PMDETA in the presence of Cu(0). The characteristic signatures for BPEA ($^{79}Br^-$ but as well $C_5H_8O_2{}^{79}Br^+$) are still detected but with a significantly lower normalized intensity (see Table 3). It was expected that peaks similar to $179^+/181^+$, thus possibly $C_5H_8O_2{}^{35}Cl^+$ and $C_5H_8O_2{}^{37}Cl^+$, could be detected, but they were not identified (data not illustrated). It can be due to the low $CuCl_2$ concentration used in this experiment. Still, Cl was detected in the negative mode with both isotopes (and in the expected isotopic ratio): a peak at m/z = 34.970 (corresponding to $^{35}Cl^-$, m/z = 34.969) and a peak at m/z = 36.967 (corresponding to $^{37}Cl^-$, m/z = 36.966) in a higher level than the ubiquitous contamination. This confirmed an exchange reaction, most likely based on the radical process that is required for initiation and controlled propagation (based on the activation/deactivation equilibrium).

Surface-Initiated Polymerization of NAM. The successful introduction of BPEA and the accessibility of the alkyl bromide groups being confirmed, the latexes L1, L2, and L3 were further used as substrates for the surface-initiated polymerization of NAM in the presence of Cu(0), $CuBr_2$, and PMDETA. This monomer was selected as a good model for water-soluble neutral monomer, which can be easily characterized due to the amide group that is not present in the core monomers. The reactions were carried out at room temperature without purification and at high solids content of the initial latexes. The conditions are summarized in Table 2. The reagent concentrations were adapted from solution polymerizations performed in water (nonreported here) to avoid too fast polymerizations. Typically, the $CuBr_2$/BPEA molar ratios were in the 0.025−0.15 range, while the molar ratio PMDETA/$CuBr_2$ was around 5. The conversion of NAM was monitored by ^1H NMR spectroscopy in D_2O. In general, it appeared that most of the polymerizations reached a conversion plateau at rather high conversion values after 2−3 h reaction time (Figure 3).

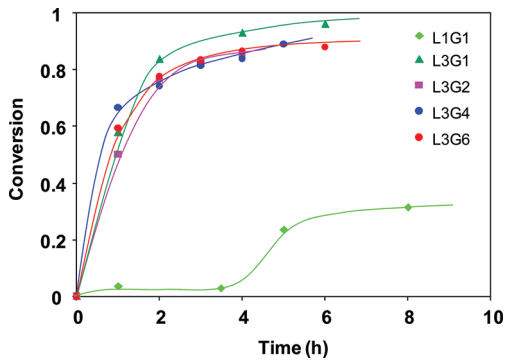


Figure 3. Conversion of NAM measured by ^1H NMR analysis vs time for the Cu-mediated surface-initiated polymerizations of NAM from the latexes L1 and L3.

Even though all control experiments showed that there was no polymerization initiation from residual ACPA, or from other components of the catalytic system (see Table 2, control experiments), we still intended to confirm that the polymerization of NAM was initiated by the surface bromide groups, creating a covalently attached hairy polyNAM layer. For this purpose, the grafted latexes were dialyzed against water, dried, and analyzed first by FTIR and for one of them by ToF-SIMS. Besides the C═O band at 1725 cm^{-1} (ester stretching vibration) that was observed on the FTIR spectra of the analyzed latexes (Figure 4), the band at 1640 cm^{-1} typical of the amide group (amide I stretching vibration) was evidenced for the cleaned latexes L3G6, L3G1, and L3G3. These results

dx.doi.org/10.1021/ma300236r | Macromolecules 2012, 45, 2972−2980

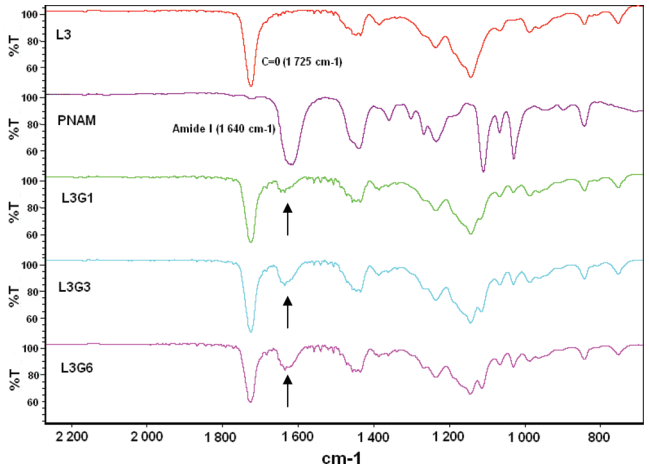


Figure 4. FTIR analysis of the latexes L3, L3G1, L3G3, and L3G6 cleaned by dialysis and dried and of polyNAM.

thus confirm the incorporation of polyNAM in the latex by a covalent bonding. The strong stability provided by the grafting of polyNAM chains (see following section) did not allow us to cleanly centrifuge the final grafted latex to determine the water-soluble content, which appeared to be very small on the basis of the NMR analysis performed on the collected serum.

The experimental conditions and the hydrophilic nature of NAM are in favor of the creation of a hydrophilic shell rather than polyNAM domains engulfed within the polymer core. ToF-SIMS analyses were performed on L3G1 grafted latex to confirm this assumption (see Figure 2 and Table 3). Figures 2d and 2h correspond to the spectra obtained on the latex L3G1 in the positive mode (m/z = 50−200) and in the negative mode (m/z = 20−100), respectively. Peaks characteristic to polyNAM are detected such as those at m/z = 26.004 (corresponding to CN^-, m/z = 26.003), m/z = 42.007 (corresponding to CNO^-, m/z = 41.998), m/z = 114.069 (corresponding to $C_5H_8NO_2^+$, m/z = 114.055), and at m/z = 142.095 (corresponding to $C_7H_{12}NO_2^+$, m/z = 142.087). This is confirmed by normalized intensity values in Table 3. The few N-based signatures already detected for L0, L3, and L3G0 are due to the use of ACPA as an initiator. Peaks characteristic of the core latex and Br are still detected (Figure 2d,h and Table 3). The normalized intensity values for core latex specific peaks significantly decreased, which illustrates a significant grafting of polyNAM at the surface. On the other hand, Br is still detected but not anymore the peaks specific to BPEA, i.e., $C_5H_8O_2{}^{79}Br^+$ and $C_5H_8O_2{}^{81}Br^+$ (see Table 3). The normalized intensity for 179^+ is back to the value previously observed—and not corresponding to $C_5H_8O_2{}^{79}Br^+$—for the latex L0. This result is consistent with the polymerization mechanism in which chains are extended from BPEA units while maintaining a dormant Br end group. If $C_5H_8O_2{}^{79}Br^+$ was as expected not detected anymore, no peak combining polyNAM and Br end group was however detected. The latex L3G1 should contain a low amount of polyNAM (see Figure 4), but this is not apparent in ToF-SIMS data. It should be reminded that the ToF-SIMS information depth is limited to the top surface where NAM polymerization is expected to start while FTIR information depth is larger, allowing the detection of the increase in the amount grafted.

Bulk and surface analyses thus confirmed the efficiency of the grafting reaction. The effect of the experimental conditions on the polymerization yield and kinetics was then examined from the information displayed in Table 2 and in Figure 3. It first appeared that the polymerization was slow and the final NAM conversion was low at the lowest amount of BPEA (core latex L1). For higher BPEA concentrations (latexes L2 and L3), the grafting kinetics were faster but not significantly different from each other (see experiments L2G1 and L3G1 in Table 2). For both core latexes and irrespective of the added concentration of NAM, the final conversion was generally above ∼80% and sometimes higher than 90%. Thus, a minimum BPEA concentration was needed to ensure a high surface concentration (as suggested by the ToF-SIMS results) along with good accessibility of the bromide group at the surface. Upon polymerization of NAM, the hydrodynamic diameter of the particles determined by DLS increased (Table 2). When a narrow particle size distribution (dispersity below 0.1) was maintained, the final diameters reached values as high as 140 nm, corresponding to a maximum hydrodynamic layer thickness of ∼12 nm. In a few examples the final diameter was much higher (above 170 nm), but the dispersity was also high (above 0.1), indicating the presence of aggregates, most likely in very low concentration. In general, the core−shell latexes formed by grafting polyNAM from L2 and L3 remained very stable and became more viscous when the NAM/BPEA molar ratio was increased (see Table 2). Nevertheless, the viscosity values remained acceptable in most cases, i.e., below 6 mPa·s. Moreover, the latexes exhibited a blue color that was more or less intense depending on the experiments (the lower the Cu(II) absolute concentration, the lighter the color; see Table 2). In some examples a gel was obtained within short polymerization time and could not be diluted, indicating interparticle cross-linking via radical termination, which is not surprising at such high substrate concentration (i.e., short interparticle distance).

A series of grafting reactions were performed with the core latex L2 as a substrate and varying concentrations of NAM in the system, exhibiting an average molar ratio with respect to the overall BPEA of 4.1 (entry L2G1, Table 2), 20.5 (entries L2G2 and L2G3, Table 2), and 33.3 (entry L2G4, Table 2). The initiator and catalyst concentrations remained the same in all four experiments. Note that the relative proportion of NAM to BPEA was kept rather low, anticipating that the initiating efficiency of BPEA would not be 100%, as only part of it would be really accessible at the extreme surface. This corresponded to amounts of NAM from 5 up to 42 wt % with respect to the core polymer. Except for entry L2G2 (short reaction time), the final conversion decreased from 100% to 71% when the amount of NAM was increased. The overall amount of grafted polyNAM however increased from 0.05 $g/g_{polymer}$ for entry L2G1 to 0.30 $g/g_{polymer}$ for entry L2G4. The influence of the initial concentration of NAM on the final conversion is not very clear but might possibly be explained by competitive copper ions complexation between monomer and PMDETA.[32] The same trend was also observed for experiment L3G1 with the lowest concentration of NAM in comparison with the other grafting experiments from latex L3 (L3G2 to L3G6). With 0.125 $g/g_{polymer}$ of initial NAM, the final conversion was 96%, whereas it remained below 90% when NAM concentration was increased. The final particle diameter was larger when the amount of NAM was increased, and the particle size distribution became broader, indicating both the formation of a hydrophilic shell and the generation of aggregates via possible interparticle radical coupling reactions.

dx.doi.org/10.1021/ma300236r | *Macromolecules* 2012, 45, 2972−2980

The effect of the concentration of the catalytic system was explored in grafting latex L3 with NAM in the presence of decreasing concentrations of PMDETA and $CuBr_2$ (entries L3G2, L3G4, and L3G5 in Table 2), while keeping a similar molar ratio between both and keeping the same amount of Cu(0) wire. When the PMDETA/$CuBr_2$ molar ratio was 0.5/0.1 (L3G2) or 0.2/0.05 (L3G4), the kinetics and the features of the grafted latex were similar. In contrast, when it was further decreased to 0.1/0.025 (L3G5) the reaction led to a gel. At such low deactivator content, the concentration of propagating radicals would be enhanced and would favor interparticle coupling reaction and the formation of gel. Eventually, the latex L3 was cleaned by dialysis before performing the grafting reaction in experiment L3G6 (Table 2). Although the polymerization of NAM was performed under diluted conditions, the results were very similar to the grafting reactions performed from raw latexes. This last result is a clear indication that residual initiator and surfactant do not interfere with the grafting process.

To conclude this part, robust conditions for an efficient Cu-mediated surface-initiated polymerization at room temperature were found from Br-functionalized latex particles that were not cleaned, i.e., in the presence of remaining radical initiator and SDS surfactant.

Colloidal Stability of the Grafted Latexes. In the previous section, we showed that core−shell latexes were obtained using surface-initiated polymerization of NAM. Such latexes coated by a neutral hydrophilic polymer may exhibit improved stability toward high ionic strength and freeze−thaw cycles. Demonstrating this improved stability would be an additional proof of the success of our grafting procedure. The corresponding data reported in Table 4 showed that, for all grafted latexes, the stability to three freeze−thaw cycles was strongly improved since none of them underwent coagulation, while the nongrafted latex L3 did not remain stable. Similarly, an amazing stability of the grafted latexes under high $CaCl_2$ concentration (2.25 M) was shown (except for L2G1 with the lowest amount of grafted polymer). This is a strong evidence for the presence of the non ionic grafted polyNAM shell that protects the particles from irreversible aggregation.

Table 4. Stability Tests to Freeze−Thaw Cycles and $CaCl_2$ Concentration of the Latexes L2 and L3 Grafted with PolyNAM

entry	*D* from DLS before freezing (nm)/dispersity	*D* from DLS after 3 freeze−thaw cycles (nm)/dispersity	critical $CaCl_2$ conc (M)
L3	101/0.03	783/0.8	<0.0045
L2G1	105/0.03	112/0.06	0.0045
L2G3	210/0.30	193/0.25	>2.25
L2G4	270/0.3	235/0.3	>2.25
L3G1	140/0.04	146/0.05	>2.25
L3G1[a]	145/0.05	150/0.08	>2.25
L3G2	119/0.06	113/0.03	>2.25
L3G3	140/0.03	147/0.002	>2.25
L3G4	130/0.05	180/0.08	>2.25
L3G6	260/0.2	230/0.24	>2.25

[a]Dialyzed latex.

CONCLUSION

This article proposes, for the first time, robust conditions for grafting hydrophilic polymer chains using copper-mediated polymerization from concentrated bromide-functionalized latex particles, used "as synthesized" via classical emulsion polymerization. All steps were assessed very carefully by various analytical techniques, in particular ToF-SIMS. The latter evidenced the consumption of the initiating sites and the presence of a hydrophilic polymer layer at the particle surface. The grafting reaction was shown to be efficient from both the kinetic point of view and the final latex properties. For such a purpose, the main conditions to respect are (i) the need for sufficient Br surface concentration to maintain a fast reaction and high final conversion, (ii) the need for sufficient Cu(II) initial concentration to avoid gel formation, and (iii) the control of monomer/Br ratio to avoid too high viscosities. In the conditions studied, the grafted chains were not isolated, and it is thus impossible to conclude on their living character or on the control over their molar mass, which might be expected from an ATRP reaction. Although this was not the focus of this work, such a conclusion is of interest for fundamental understanding and should be studied further.

AUTHOR INFORMATION

Notes

The authors declare no competing financial interest.

ACKNOWLEDGMENTS

We are grateful to Christina Laue and Antje Polenz from BASF for their technical work in the latex synthesis. Laura Autin and Philippe Cassagnau from the laboratory Ingénierie des Matériaux Polymères (IMP, UMR 5223, Villeurbanne) are acknowledged for their help in viscosity measurements. The electron microscopy analyses were performed at the CTμ (Centre Technologique des Microstructures of the University Claude Bernard Lyon 1), and we wish to thank the team for constant help and fruitful advice.

REFERENCES

(1) Barbey, R.; Lavanant, L.; Paripovic, D.; Schulwer, N.; Sugnaux, C.; Tugulu, S.; Klok, H. A. *Chem. Rev.* **2009**, *109*, 5437−5527.
(2) Charleux, B.; D'Agosto, F.; Delaittre, G. *Adv. Polym. Sci.* **2010**, *233*, 125−183.
(3) Cayre, O.J.; Chagneux, N.; Biggs, S. *Soft Matter* **2011**, *7*, 2211−2234.
(4) Tsujii, Y.; Ohno, K.; Yamamoto, S.; Goto, A.; Fukuda, T. *Adv. Polym. Sci.* **2006**, *197*, 1−45.
(5) Advincula, R. C. Brittain, W. J., Caster, K. C., Rühe, J., Eds. *Polymer Brushes*; Wiley-VCH: Weinheim, Germany, 2004.
(6) Ayres, N. *Polym. Chem.* **2010**, *1*, 769−777.
(7) Matyjaszewski, K., Davis, T., Eds. *Handbook of Radical Polymerization*; John Wiley & Sons: Hoboken, NJ, 2002.
(8) Fristrup, C. J.; Jankova, K.; Hvilsted, S. *Soft Matter* **2009**, *5*, 4623−4634.
(9) Edmondson, S.; Osborne, V. L.; Huck, W. T. S. *Chem. Soc. Rev.* **2004**, *33*, 14−22.
(10) Manuszak-Guerrini, M.; Charleux, B.; Vairon, J. P. *Macromol. Rapid Commun.* **2000**, *21*, 669−674.
(11) Kizhakkedathu, J. N.; Brooks, D. E. *Macromolecules* **2003**, *36*, 591−598.
(12) Kizhakkedathu, J. N.; Kumar, K. R.; Goodman, D.; Brooks, D. E. *Polymer* **2004**, *45*, 7471−7489.
(13) Kizhakkedathu, J. N.; Norris-Jones, R.; Brooks, D. E. *Macromolecules* **2004**, *37*, 734−743.

(14) Zhang, M.; Liu, L.; Wu, C.; Fu, G.; Zhao, H.; He, B. *Polymer* **2007**, *48*, 1989−1997.
(15) Zhang, M.; Liu, L.; Wu, C.; Fu, G.; Zhao, H.; He, B. *J. Colloid Interface Sci.* **2006**, *301*, 85−91.
(16) Mittal, V.; Matsko, N. B.; Butté, A.; Morbidelli, M. *Eur. Polym. J.* **2007**, *43*, 4868−4881.
(17) Mittal, V.; Matsko, N. B.; Butté, A.; Morbidelli, M. *Polymer* **2007**, *48*, 2806−2817.
(18) Min, K.; Hu, J. H.; Wang, C. C.; Elaissari, A. *J. Polym. Sci., Part A: Polym. Chem.* **2002**, *40*, 892−900.
(19) Liu, Y. Y.; Chen, H.; Ishizu, K. *Langmuir* **2011**, *27*, 1168−1174.
(20) Muñoz-Bonilla, A.; van Herk, A. M.; Heuts, J. P. A. *Polym. Chem.* **2010**, *1*, 624−627.
(21) Jakubowski, W.; Matyjaszewski, K. *Macromolecules* **2005**, *38*, 4139−4146.
(22) Magenau, A. J. D.; Kwak, Y.; Matyjaszewski, K. *Macromolecules* **2010**, *43*, 9682−9689.
(23) Rosen, B. M.; Percec, V. *Chem. Rev.* **2009**, *109*, 5069−5119.
(24) Zhang, Y.; Wang, Y.; Peng, C. H.; Zhong, M.; Zhu, W.; Konkolewic,z, D.; Matyjaszewski, K. *Macromolecules* **2012**, *45*, 78−86.
(25) Taniguchi, T.; Kasuya, M.; Kunisada, Y.; Miyai, T.; Nagasawa, H.; Nakahira, T. *Colloids Surf., B* **2009**, *71*, 194−199.
(26) Matyjaszewski, K.; Gaynor, S. K.; Kulfan, A.; Podwika, M. *Macromolecules* **1997**, *30*, 5192−5194.
(27) Poleunis, C.; Médard, N.; Bertrand, P. *Appl. Surf. Sci.* **2004**, *231*, 269−273.
(28) Davies, M. C.; Lynn, R. A. P.; Davis, S. S.; Hearn, J.; Vickerman, J. C.; Paul, A. J. *J. Colloid Interface Sci.* **1993**, *161*, 83−90.
(29) Davies, M. C.; Lynn, R. A. P.; Hearn, J.; Vickerman, J. C.; Paul, A. J.; Watts, J. F. *Langmuir* **1996**, *12*, 3866−3875.
(30) Ihalainen, P.; Backfolk, K.; Sirvio, P.; Peltonen, J. *Colloids Surf., A* **2010**, *354*, 320−330.
(31) Becker, J. S.; Dietze, H.-J. *Int. J. Mass Spectrom.* **2000**, *197*, 1−35.
(32) Tang, W.; Kwak, Y.; Braunecker, W.; Tsarevsky, N. V.; Coote, M. L.; Matyjaszewski, K. *J. Am. Chem. Soc.* **2008**, *130*, 10702−10713.

Macromolecules

Article

pubs.acs.org/Macromolecules

Novel Functional Organic Network Containing Quaternary Phosphonium and Tertiary Phosphorus

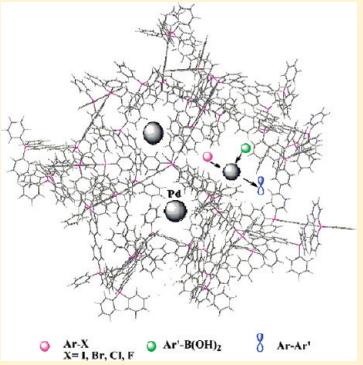
Qiang Zhang,[†,‡] Suobo Zhang,*[,†] and Shenghai Li[†]

[†]Key Laboratory of Polymer Ecomaterials, Changchun Institute of Applied Chemistry, Chinese Academy of Sciences, Changchun 130022, China

[‡]Graduate School of Chinese Academy of Sciences, Beijing 100049, China

Supporting Information

ABSTRACT: A quaternary phosphonium and tertiary phosphorus functionalized microporous polymer was obtained via nickel(0)-catalyzed Yamamoto-type cross-coupling reaction. The integration ratio of signals (quaternary phosphonium to tertiary phosphorus atoms) was close to 3:2. The polymer networks were stable toward water, base, and acid, and indeed no change in surface area was observed even after the material was treated with 10 M HCl. The pore size distribution calculated by the Horvath−Kawazoe method indicated the presence of micropores with a mean width of about 0.7 and 1.4 nm. Their apparent BET specific surface areas can be tuned (from 650 to 980 $m^2 g^{-1}$) by changing the counteranions (Br^- to F^-). It displays high intrinsic catalytic activity for the reaction between epoxide and CO_2 (yield: 98%, 1 atm). Pd nanoparticles supported on the polymer networks were also prepared, which exhibits high catalytic activity for cross-coupling reaction between 1-chlorobenzene and phenylboronic acid (yield: >95.8%).



1. INTRODUCTION

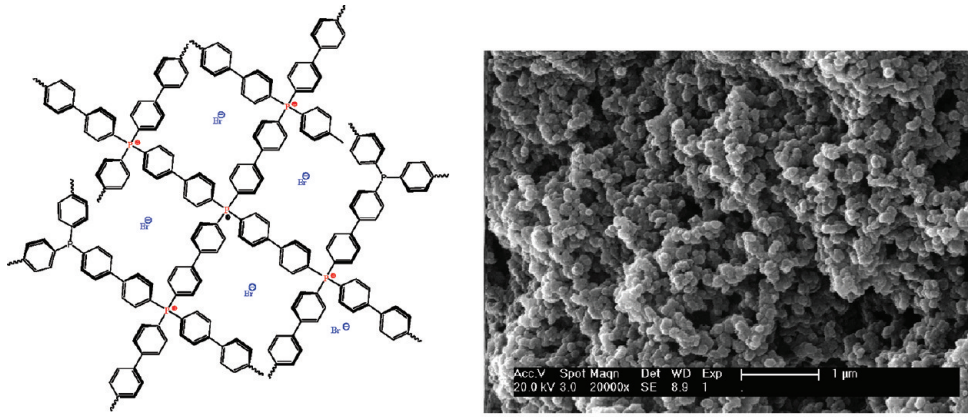
The past decade has witnessed an immense growth in the importance of microporous organic polymers (MOPs) with pore size smaller than 2 nm.[1] They have broad potential applications in the area of molecular storage, separation, delivery, or catalysis.[1] Such applications often rely on the presence of a large permanent surface area. In the past decades, there has been an intense international effort to produce the highly porous materials with large surface areas. However, it is recognized that there is a pressing requirement for porous materials containing functional groups to fulfill a certain task.[2] For example, the incorporation of some functional groups will play a major role in interacting more strongly with a certain compound than others in a mixture or a solution, resulting in excellent performance in the areas of ion exchange, purification, and absorption or separation. For catalysts, catalytically active centers or binding sites have to be incorporated in a porous, heterogeneous material.[2a]

MOPs include polymers of intrinsic microporosity (PIMs),[3] hypercrosslinked polymers (HCPs),[4] covalent organic frameworks (COFs),[5] or in the case where fully aromatic compositions are used, conjugated microporous polymers (CMPs).[6] Because most polymer skeletons do not incorporate any functional groups or active sites, functionalization of MOPs could open up second-generation porous materials with useful combined chemical and physical properties.[1c,2] Functional group containing MOPs combines a robust functional framework together with an open porous structure. The pores provide space for the transmission of molecules, thus promoting the performance of these materials. MOPs functionalized with amines, carboxylic acids, tetrazole, triazine rings, and hydroxyl groups exhibited excellent CO_2 adsorption/separation due to the microporous structures and interaction between these polar groups and CO_2.[3,7] Noble metals have been incorporated into MOPs containing functional units such as bipyridine, metalloporphyrin, and triazine ring, which displayed high catalytic activity for a host of reactions.[8] For example, a recent paper reported a porphyrin-derived MOP that shows high catalytic activity for the oxidation of thiols.[8b] The bipyridine-functionalized precursor networks were prepared and treated with $(DBPP)_2Ir\text{-}(\mu\text{-}Cl)_2\text{-}Ir(DBPP)_2$, which have been studied as heterogeneous catalysts for reductive amination reaction.[1c]

A tetrahedral MOP based on a tetraphenylmethane unit has been synthesized recently, which exhibits high surface area and excellent stability.[9] The high surface area can be attributed to the default diamondoid framework topology imposed by the tetrahedral monomer, which provides wide openings and interconnected pores to eliminate efficiently "dead space".[10] Subsequently, the central carbon in tetrahedral networks was replaced by other quadricovalent building centers such as adamantane, silicon, and germanium atoms.[11] In the present work, the quaternary phosphonium cation has been selected to be the center for the tetrahedral networks (Figure 1a). To the best of our knowledge, this is the first report on ionic microporous polymer prepared by homopolymerization. In comparison with other tetrahedral MOPs containing centers such as carbon, silicon, germanium, and adamantane, it

Received: February 9, 2012
Revised: March 16, 2012
Published: March 29, 2012

 © 2012 American Chemical Society dx.doi.org/10.1021/ma300278d | Macromolecules 2012, 45, 2981−2988



(a) (b)

Figure 1. (a) Structure of PP-Br polymer and (b) SEM image of microporous polymer.

possesses many unique properties, which has been applied in conducting materials,[12a,b] catalyst transfer agents,[12c] ionic liquids,[12d] and flame-proofing agents.[12e] Some of these properties could be easily controlled by varying the counterions. Also, the cationic centers could act as a catalyst in the reaction of CO_2 with epoxides yielding cyclic carbonates. Quaternary phosphonium-containing polymers have been applied as ion exchange materials, which exhibited excellent stability and remarkable ion conductivity[12a,b] It also has potential applications as an ion absorbent due to its high surface area and ion exchange capacity (2.75 mmol/g) or as a scaffold to immobilize noble metal nanoparticles for heterogeneous reactions.

2. EXPERIMENTAL SECTION

Materials. 1-Bromo-4-chlorobenzene, $Pd(OAc)_2$, 1,5-cyclooctadiene, $Ni(cod)_2$, and 2,2′-bipyridyl were purchased from Aldrich and used as received. Anhydrous THF was distilled from its sodium naphthalenide solution under nitrogen. DMF was dried over CaH_2 and distilled under reduced pressure prior to use. Other chemicals were used as received.

Tris(*p*-chlorophenyl)phosphine. Tris(*p*-chlorophenyl)-phosphine was prepared according to the previously reported method.[12f] Yield: 65%; mp: 102.0−102.5 °C. ^{1}H NMR (600 MHz; DMSO) δ: 7.23−7.25 (6 H, t, J = 6.1 Hz), 7.48−7.50 (6 H, d, J = 12.0 Hz). ^{13}C NMR (100 MHz, $CDCl_3$) δ: 135.6 (s), 134.8 (d, J_{C-P} = 21 Hz), 133.3 (s, J_{C-P} = 11 Hz), 129.0 (d, J_{C-P} = 7.2 Hz). ^{31}P NMR (202 MHz, $CDCl_3$) δ: −7.21. Anal. Calcd for $C_{18}H_{12}Cl_3P$: C, 59.15; H, 3.21. Found: C, 59.17; H, 3.02. MS $(M+H)^+$ $C_{18}H_{12}Cl_3P$: calculated, 364.9814; observed, 364.9818.

Tetrakis(*4*-chlorophenyl)phosphonium bromide. 1-Bromo-4-chlorobenzene (1.15 g, 6 mmol), $Pd(OAc)_2$ (0.013 g, 1 mol %) and tris(*p*-chlorophenyl)phosphine (2.19 g, 6 mmol) were mixed together under an inert atmosphere of argon in a dry 50 mL tube. To this mixture was added dry *o*-xylene (2 mL, 3 M) and a magnetic stir bar. The reaction mixture was heated to reflux for 5 h under argon. The phosphonium salts precipitated as the reaction proceeded. After 5 h, the tube was cooled to room temperature, 20 mL of diethyl ether was added, and the resulting suspension was stirred at room temperature for 2 min. The precipitate was filtered and washed with 50 mL of diethyl ether. Yield: 50%. mp: above degradation temperature. ^{1}H NMR (600 MHz; DMSO) δ: 7.71−7.78 (8 H, q, J = 5.4 Hz), 7.84−7.88 (8 H, q, J = 16.8 Hz). ^{13}C NMR (100 MHz, DMSO) δ: 115.4−116.3 (4 C, d, J = 89.6 Hz), 130.6 (8 C, d, J = 12.6 Hz), 136.6 (8 C, d, J = 10.2 Hz), 141.2 (4 C, d, J = 2.6 Hz). ^{31}P NMR (202 MHz, $CDCl_3$) δ: 23.2. Anal. Calcd for $C_{24}H_{16}Cl_4PBr$: C, 51.74; H, 2.89; Found: C, 51.67; H, 2.64. MS $(M+H)^+$ $C_{24}H_{16}Cl_4PBr$: 557.0728, observed 557.0734.

Synthesis of PP-Br. The polymer networks are denoted as PP−X, where X represents the counterions. $Ni(cod)_2$ (2.25 g, 8.18 mmol) was added to a solution of 1,5-cyclooctadiene (1.05 mL, 8.32 mmol) and 2,2′-bipyridyl (1.28 g, 8.18 mmol) in anhydrous DMF (100 mL), and the mixture was heated to 80 °C for 30 min. To the resulting solution was added tetrakis(4-chlorophenyl)phosphonium bromide (0.874 g, 1.57 mmol) at 80 °C, and the mixture was stirred at that temperature for 10 h. After cooling to room temperature, concentrated HCl (5 M, 20 mL) was added to the solution. The solid obtained was filtered, and the residue was successively washed with DMF (5 × 30 mL), THF (5 × 30 mL), H_2O (5 × 30 mL), and propan-2-one (5 × 30 mL). The polymer was then dried in a vacuum oven at 120 °C (Yield: 83%).

Gel fractions (GF = weight of insoluble dried sample/initial sample weight) were determined gravimetrically from samples. The GF content was estimated by weighing the insoluble portion obtained after Soxhlet extraction in tetrahydrofuran (THF) for 24 h.

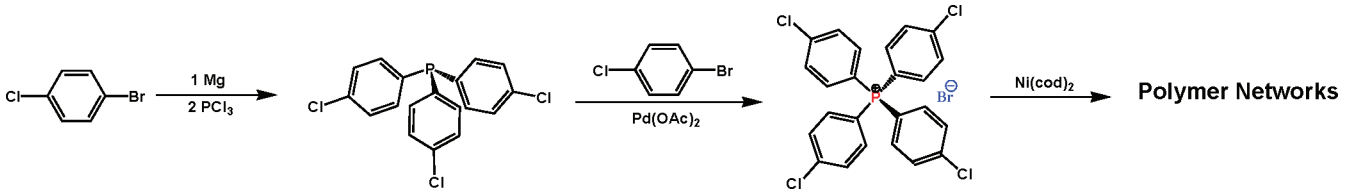
Reaction of 2-Phenoxymethyloxirane with CO_2. The PP-Br (0.042 g) was added to a solution of 2-phenoxymethyloxirane (1.5 g, 10 mmol) in DMF (10 mL), and the mixture was stirred at the given temperature under a slow stream (40 mL/min) of carbon dioxide gas. The catalyst was filtered, and the filtrate was analyzed by GC−MS.

Preparation of PP−Pd^0. The PP-Br polymer (0.1 g) was soaked in aqueous H_2PdCl_4 (20 mL, 5.0 mmol L^{-1}) for 24 h to convert the Br^- form into the $PdCl_4^-$ form and finally washed thoroughly with water (200 mL) to remove any excess H_2PdCl_4. A 10-fold excess of aqueous $NaBH_4$ was added with vigorous stirring; then, the mixture was kept at RT for 12 h. The resultant PP−Pd^0 particles were collected by filtration, washed with water several times, and dried under vacuum at 80 °C for 12 h.

Typical Procedure for the Suzuki Reaction. Phenylboronic acid (1.2 mmol), K_2CO_3 (2.5 mmol), Pd catalyst (1 mol %), aryl halide (1.0 mmol), and H_2O/EtOH (10 mL; 3:1 v/v) were added to a screw−capped vial with a side tube under argon. The mixture was stirred at 80 °C for 6 h and then

dx.doi.org/10.1021/ma300278d | *Macromolecules* 2012, 45, 2981−2988

Scheme 1. Synthesis of Polymer Networks



cooled. The product was extracted from the reaction mixture with diethyl ether, and the organic phase was analyzed by GC–MS.

Ionic Exchange. The PP-Br polymer (0.1 g) was converted to the PP–Cl or PP–F form by immersing the polymer in 1 M NaCl (20 mL) or NaF (20 mL) at 80 °C for 12 h, followed by immersion in deionized water for 24 h. This route was also applied for the preparation of ionic exchange membranes.[13]

3. RESULTS AND DISCUSSION

Synthesis and Characterization. We selected tetrakis(4-chlorophenyl)phosphonium bromide as the building unit. The monomer was obtained through the reaction of tris(*p*-chlorophenyl)phosphine and 1-bromo-4-chlorobenzene in the presence of $Pd(OAc)_2$ as catalyst, and the synthetic route was illustrated in Scheme 1. The yield of the reaction was 50%, and the proposed structure was confirmed by ^{1}H NMR (Figure S1 of the Supporting Information). The signals at 7.86 and 7.74 ppm were assigned to the hydrogen atom in ortho and meta position to quaternary phosphonium atom, respectively. The integration ratio of the two signals is very close to 1:1, as expected for the composition of tetrakis(4-chlorophenyl)-phosphonium bromide. The ^{13}C NMR spectrum also verified the structure of tetrakis(4-chlorophenyl)phosphonium bromide (Figure S2 of the Supporting Information).

The polymer networks were synthesized by the nickel(0)-catalyzed Yamamoto-type cross-coupling reaction. This reaction produced an off-white powdery compound, which had a low density (0.0546 $cm^3\ g^{-1}$) and was not soluble in any common organic solvents. PP-Br was characterized by FT-IR spectroscopy. The spectra clearly indicated the disappearance of the C–Cl stretching resonance around 763 cm^{-1} (Figure S3 of the Supporting Information),[14] thus indicating the completion of the phenyl–phenyl coupling. To confirm further the structure of the polymeric networks, the polymer was characterized at the molecular level by solid-state ^{31}P NMR (Figure 2). Two signals at approximately 23 and −8.8 ppm were observed, corresponding to quaternary phosphonium and tertiary phosphine atoms, respectively. The resonance at −8.8 ppm corresponds to the tertiary phosphine atoms, resulting from P–C-bond cleavage during Yamamoto polymerization. The integration ratio of signals (quaternary phosphonium to phosphine atoms) was close to 3:2. Figure S4 of the Supporting Information gives the assignment of each carbon in polymer networks. X-ray diffraction measurement of the material indicated an amorphous structure (Figure S5 of the Supporting Information), and scanning electron micrograph showed that PP-Br consisted of relatively uniform spheres with a diameter of 100–200 nm (Figure 1b). The gel fraction of PP-Br was examined by Soxhlet extraction in THF for 24 h. The weight loss of PP-Br was negligible after Soxhlet extraction, indicating that the gel fraction was 100%.

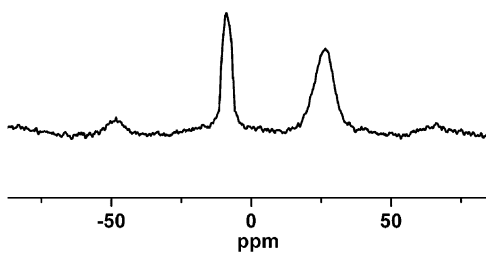


Figure 2. Solid-state ^{31}P NMR spectrum of PP-Br polymer.

The polymer was also stable toward water, base (NaOH 10 M, 1 h), and acid, and indeed no change in surface area was observed even after the material was treated with 10 M HCl for 1 h. As shown in Figure S6 of the Supporting Information, PP-Br displayed 5% weight loss at temperature of 360 °C. The result reveals that it possesses a high thermal stability.

Micropore Size and Surface Area. The porosity parameters of the polymer were studied by sorption analysis using nitrogen as the sorbate molecule. Nitrogen adsorption–desorption isotherms measured at 77 K are shown in Figure 3. The nitrogen isotherm for PP-Br exhibited a combination of type I and II nitrogen sorption isotherms according to the IUPAC classification.[15] Applying the Brunauer–Emmett–Teller (BET) model within the pressure range of P/P_o = 0.05 to 0.3 resulted in an apparent surface area of 650 $m^2\ g^{-1}$, which makes PP-Br the first microporous polymer based on an quaternary phosphonium salt. The high uptake at very low pressures indicates a high microporosity. With increasing pressure, the nitrogen uptake increases too. This indicates a high external surface area due to the presence of very small particles.[16] The isotherm shows a hysteresis extending to low relative pressure. The effect was interpreted as a result of swelling in polymer framework. A further hint in this interpretation is the high loss of volume of the sample, when it is dried after synthesis. The pore size distribution calculated by the Horvath–Kawazoe method indicated the presence of micropores with a mean width of ~0.7 and 1.4 nm (Figure 3b). As the Br^- anion is located inside the micropores, the surface area can be fine-tuned by changing the anion size. For example, their apparent BET specific surface areas increased from 650 to 750 and 980 $m^2\ g^{-1}$, respectively, as the Br^- anion was changed to Cl^- or F^- by ionic exchange due to the decreasing ionic radius of Cl^- and F^-. The amount of counterions was measured by elemental analysis (Table S1 of the Supporting Information), indicating that the Br^- was completely replaced by other counterions. In general, the surface area can only be controlled on varying the monomer structure.[17] We have thus developed a novel approach for the variation of surface area that is more facile than the traditional methods.

Catalytic Performances. Microporous polymers used in heterogeneous catalysis systems usually contain various noble metal complexes.[1c,8a,18,19] However, microporous polymers rarely possess intrinsic catalytic activity due to lack of active sites.[20] It is well known that the addition reaction of oxiranes

dx.doi.org/10.1021/ma300278d | *Macromolecules* 2012, 45, 2981–2988

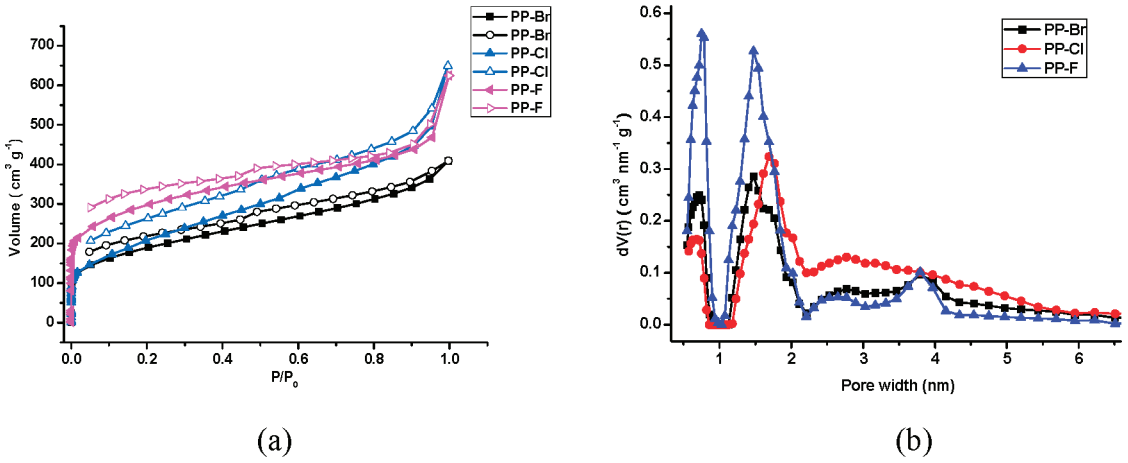
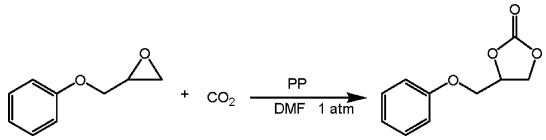


Figure 3. (a) Nitrogen adsorption−desorption isotherms measured at 77 K (the adsorption and desorption branches are labeled with solid and open symbols, respectively) and (b) pore size distribution of the polymer with different anions.

Table 1. PP-Br Catalyzed Conversion of 2-(Phenoxymethyl)oxirane to Cyclic Carbonate in the Presence of CO_2 at 1 atm



entry	catalyst amount (%)	temperature (°C)	time (h)	yield (%)[a]
1	1	90	30	29.5
2	2	90	30	41.3
3	3	90	30	46.2
4	4	90	30	50.0
5	2	90	70	80.4
6	2	100	50	75.3
7	2	110	40	78.7
8	2	120	24	76.9
9	2	130	19	84.2
10	2	140	20	98.5

[a]Yield was determined by GC analysis (internal standard: dodecane).

with CO_2 catalyzed by quaternary phosphonium salts gives the corresponding cyclic carbonates in high yield.[21] Recently, polymeric nanoparticles supported by phosphonium salt were prepared and applied as catalysts for cycloaddition of CO_2 to epoxides.[21d] An 83.7% yield for the cycloaddition reaction of CO_2 to styrene oxide was achieved when the reaction was conducted at 160 °C and 3 MPa for 48 h. The reaction mechanism was reported by Nishikubo and coworkers.[21c] In this work, the PP-Br polymer was applied as a catalyst in the conversion of CO_2 to cyclic carbonates via reaction with epoxides. Table 1 summarizes the catalytic activity of PP-Br in the formation of cyclic carbonate from the reaction between 2-(phenoxymethyl)oxirane and CO_2 in DMF at 1 atm. The yield of 4-(phenoxymethyl)-1,3-dioxolan-2-one increased gradually with reaction time, temperature, and catalyst concentration, and a yield of 98% was obtained at 140 °C after 20 h. According to entries 1−10, it can be concluded that the reaction temperature seems to be a relatively more critical factor than others. Under these reaction conditions, no cyclic carbonate was formed in the absence of PP-Br. Compared with the polymeric nanoparticles system, the high yield (98% within 24 h) of PP-Br system resulted from the large surface area and porosity.[21d]

These studies demonstrate that PP-Br was active only during the reaction and that the reaction proceeded on the heterogeneous surface. The recovered PP-Br showed nearly the same reactivity as the original (Table 2).

Table 2. Activity and Recycling of the PP-Br Catalyst in the Reaction between 2-(Phenoxymethyl)oxirane and CO_2[a]

run	yield (%)
1	98.5
2	94.6
3	93.5
4	91.8
5	92.7

[a]Reaction was carried out with 2 mol % PP-Br at 140 °C for 20 h. The yield was determined by GC analysis (internal standard: dodecane).

Much interest has been directed toward noble-metal nanoparticles captured in microporous materials for use in heterogeneous catalytic systems.[22] Budd and McKeown have reported that microporous polymers act as scaffolds for incorporating various metal nanoparticles such as Cu, Zn, Pd, and Co.[22d−f] For modification with noble metals, several methods have been developed, such as chemical vapor deposition,[23] ionic exchange,[24] in situ generation,[25] and so on. In the present work, PP-Br has been used as a scaffold for

dx.doi.org/10.1021/ma300278d | Macromolecules 2012, 45, 2981−2988

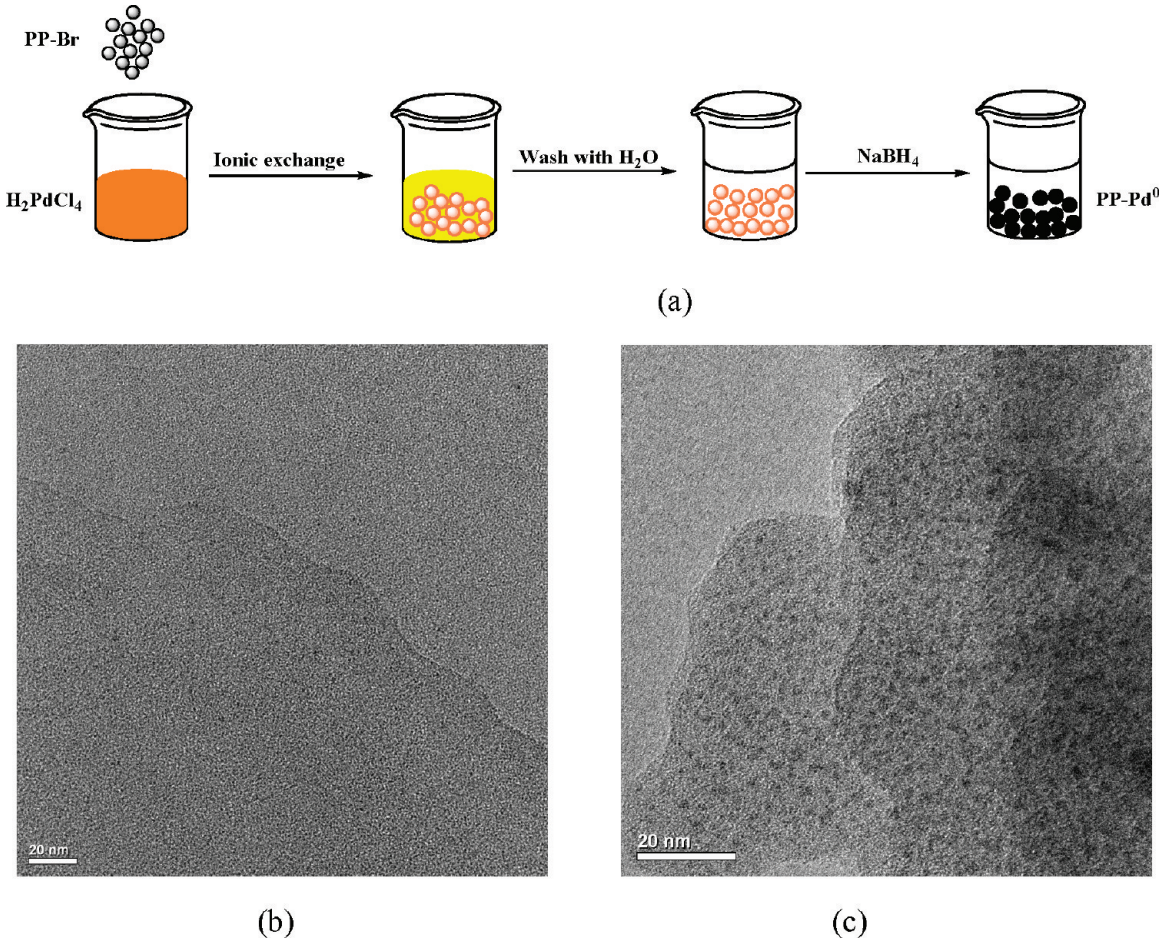


Figure 4. (a) Schematic diagram of Pd^0 nanoparticles immobilization inside PP-Br. TEM images of PP-Br (b) and PP-Pd^0 (c).

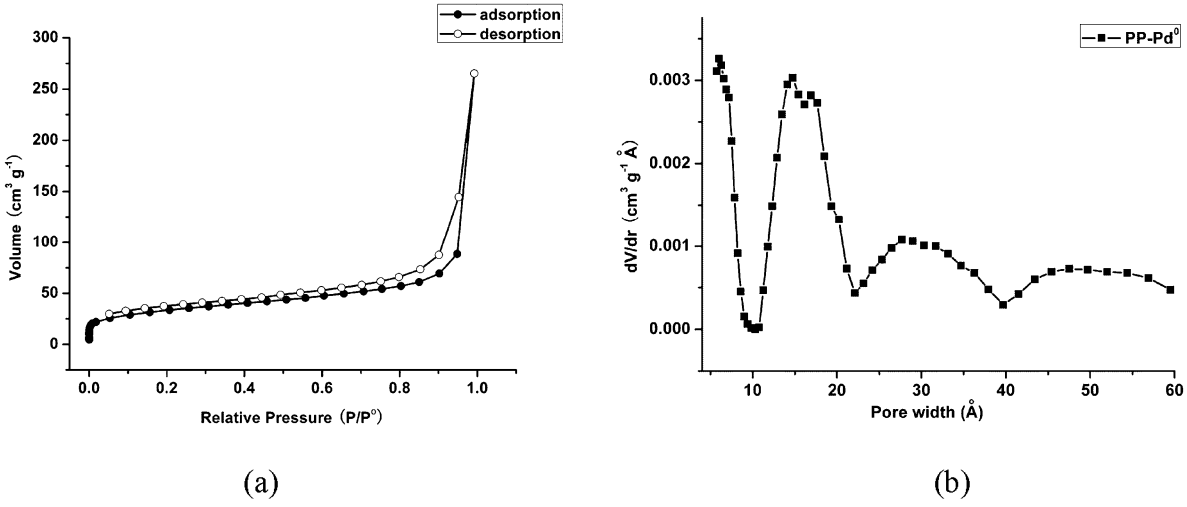
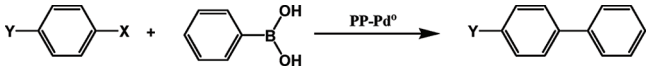


Figure 5. (a) Nitrogen adsorption–desorption isotherms of PP-Pd measured at 77 K. (b) Pore size distribution of PP-Pd.

immobilizing palladium nanoparticles by ionic exchange. As shown in Figure 4, tetrachloropalladate ($PdCl_4^{2-}$) was exchanged with bromide ion, followed by $NaBH_4$ reduction to obtain black PP–Pd^0. Inductively coupled plasma (ICP) analysis confirmed the loading of Pd on polymer networks to be 0.96 mmol g^{-1}; that is, the Pd/P molar ratio was found to be 1:2.2. The nitrogen-adsorption isotherms of PP-Pd^0 were collected at 77 K, and the results are shown in Figure 5. The effect of the Pd on the surface area and pore size distribution was investigated. As expected, the BET surface area decreases from 650 m^2 g^{-1} (PP-Br) to 114 m^2 g^{-1} (PP-Pd). The decrease in specific surface area can be ascribed both to partial pore filling and to simple increase in mass. Also, no significant change in the pore size was observed and the density of micropores decreases before and after the loading of Pd (Figure 5b), which is similar to other works.[18a] Because the Pd^0 was

dx.doi.org/10.1021/ma300278d | Macromolecules 2012, 45, 2981–2988

Table 3. PP−Pd^0-Catalyzed Suzuki Cross-Coupling Reactions of Aryl Halides with Phenylboronic Acid[a]



entry	X	Y	yield (%)
1	Br	CHO	97.4
2	Br	$COCH_3$	98.2
3	Br	H	96.8
4	Br	Me	97.9
5	Br	OMe	96.5
6	I	H	99.8
7	Cl	H	95.8
8	F	H	87.2

[a]Solution of aryl halide (1.0 mmol), phenylboronic acid (1.2 mmol), Pd^0 (0.01 mmol), and K_2CO_3 (2.5 mmol) in H_2O/EtOH (10 mL; 3:1 v/v) was heated at 80 °C under N_2 for 6 h. The yield was determined by GC analysis (internal standard: dodecane).

immobilized in polymeric networks by ionic exchange, it is reasonable to assume that this synthesis route can be applied for loading other classes of transition-metal nanoparticles (e.g., Au, Rh, Ru, and Ir). X-ray photoelectron spectroscopy (XPS) analysis confirmed the presence of Pd^0 nanoparticles within polymer networks (Figure S7 of the Supporting Information). The diffractogram of PP−Pd^0 (Figure S5 of the Supporting Information) showed a signal at 2θ = 39.0° confirming the presence of Pd (1 1 1). The Pd (1 1 1) facets are generally acknowledged to be the best surface for catalytic usage.[25] Transmission electron microscopy (TEM) images were obtained to check the morphology and measure the particle size of Pd^0 nanoparticles. The results presented in Figure 4c show that the Pd^0 particles are uniformly dispersed in the polymer networks, and the average particle size was found to be 2.5 nm. No free Pd^0 aggregates were observed in the PP−Pd^0 even when the weight ratio of Pd to the polymeric scaffold was increased to as high as 10%.

We carried out Suzuki cross-coupling reactions as a model reaction to evaluate the catalytic ability and recyclability of the PP−Pd^0 catalyst. Because of environmental, economic, and safety concerns, the Suzuki reactions were performed in water.[26] A suitable amount of EtOH was used as a cosolvent to increase the solubility of the substrates. The cross-coupling reactions were carried out with 1 mol % Pd catalyst in H_2O/EtOH (3:1 v/v) at 80 °C. After the reaction was complete, the mass was extracted with diethyl ether (10 mL), and the yield of the product was determined by performing GC−MS analysis of the diethyl ether phase with dodecane as the internal standard. Table 3 shows the catalytic activity of PP−Pd^0 for the Suzuki−Miyaura reaction with a range of aryl halides and phenylboronic acid. The reactions proceeded efficiently and gave the desired product in >95% conversion with aryl bromides or aryl chlorides after 6 h. In general, relatively lower yields have been reported for electron-rich aryl bromides. For example, Kato and coworkers have recently shown that palladium nanoparticles captured in polymeric networks gave an 82% conversion yield for the reaction between 1-bromo-4-methoxybenzene and phenylboronic acid.[22a] Using both electron-rich and electron-deficient aryl bromides with the PP−Pd^0 system, the desired coupling products were obtained in high yield (>95%). More importantly, a high yield of 95.8% for the reaction between chlorobenzene and phenylboronic acid was obtained, which is much higher than the 36% yield reported by our group with another catalytic system.[27] It is well known that catalytic C−C cross-coupling reactions of fluoroderivatives are rare because of the strong C−F bond.[28] We obtained a yield of 87% in the reaction between fluorobenzene and phenylboronic acid using this PP−Pd^0 catalyst. For comparison, the coupling of 1-fluoro-4-methylbenzene with phenyl boronic acid was conducted in the presence of $Pd(PPh_3)_4$, and no product was obtained.

We have also examined the recyclability and reusability of the PP−Pd^0 catalyst. The catalyst was recycled in the reaction between 4-bromobenzaldehyde and phenylboronic acid, and the catalytic activity of the preformed PP−Pd^0 catalyst proved to be almost constant with the initial yield of 97.4%, decreasing to 93% after five runs (Table 4). The catalyst was separated from the solution by a simple filtration, and the resultant filtrate was tested for palladium by ICP−MS. The result showed that ~17 ppb of palladium leached into the solution, which corresponds to an original metal loss of 0.00256% and was thus found to be one hundred times lower than the corresponding value (0.27%) reported for Kato's system.[22a] Therefore, PP−Pd^0 was demonstrated to be a durable catalyst.

Table 4. Activity and Recycling of the PP−Pd^0 Catalyst in the Suzuki Coupling of 4-Bromobenzaldehyde and Phenylboronic Acid[a]

run	yield (%)
1	97.4
2	97.6
3	96.5
4	96.4
5	95.2

[a]Solution of 4-bromobenzaldehyde (1.0 mmol), phenylboronic acid (1.2 mmol), Pd^0 (0.01 mmol), and K_2CO_3 (2.5 mmol) in H_2O/EtOH (10 mL; 3:1 v/v) was heated to 80 °C under N_2 for 6 h. The yield was determined by GC analysis (internal standard: dodecane).

A possible explanation for the superior catalytic performance of PP−Pd^0 can be due to the structural features of the composite system. The PP−Pd^0 polymer can draw the reactants into its pore channels by capillary condensation of the micropores, where the catalyst particles are located. The concentration of reagents around the Pd nanoparticles is relatively higher than that in the bulk solution.

The micropores within the PP−Pd^0 polymer can be considered to act as nanoreactors, where they pose a space confinement effect on the reactants, leading to a high catalytic activity.[22c] Furthermore, the highly polar ionic environment allows the electrostatic stabilization of preformed nanoparticles (as for Bu_4N^+ ions in tetrabutylammonium bromide[29]) and

dx.doi.org/10.1021/ma300278d | Macromolecules 2012, 45, 2981−2988

could endow Pd^0 with its high activity in the Suzuki cross-coupling reactions. The Pd^0 nanoparticles inside the networks are very small, which can be another reason for the high activity of the catalyst.

4. CONCLUSIONS

A quaternary phosphonium and tertiary phosphorus functionalized microporous polymer was prepared by Yamamoto coupling reaction. The content ratio of quaternary phosphonium to phosphine atoms was close to 3:2, determined by ^{31}P solid-state NMR. It was also stable toward water, base (1 M NaOH, 24 h), and acid (1 M HCl, 24 h). The polymeric networks display high surface area, and the surface area can be tuned by changing the counteranions. Their apparent BET specific surface areas increased from 650 to 750 and 980 $m^2\ g^{-1}$ respectively, as the Br^- anion was changed to Cl^- or F^- by ionic exchange, due to the decreasing ionic radius of Cl^- and F^-. It displays high intrinsic catalytic activity for the reaction between epoxide and CO_2. An 98% yield of the reaction between epoxide and CO_2 was obtained at 140 °C and 1 atom for 20 h. Pd nanoparticles supported on PP were also prepared, which are uniformly dispersed in the polymeric networks and exhibit high catalytic activity for Suzuki reactions. The coupling reactions between aryl chlorides and phenylboronic acid gave the desired product in >95% conversion in the presence of PP-Pd. More importantly, a yield of 87% was obtained when fluorobenzene was used as reactant. In general, catalytic C−C cross-coupling reactions of fluoroderivatives are rare.

■ ASSOCIATED CONTENT

Supporting Information

^1H and ^{13}C NMR spectra, TGA curves, IR, XPS, and WAXD spectra for polymers and monomers. This material is available free of charge via the Internet at http://pubs.acs.org.

■ AUTHOR INFORMATION

Corresponding Author

*E-mail: sbzhang@ciac.jl.cn.

Notes

The authors declare no competing financial interest.

■ ACKNOWLEDGMENTS

This research was financially supported by the National Basic Research Program of China (nos. 2009CB623401, 2012CB932802) and the National Science Foundation of China (nos. 51133008, 50825302, and 51021003).

■ REFERENCES

(1) (a) McKeown, N. B.; Budd, P. M. *Chem. Soc. Rev.* **2006**, *35*, 675. (b) Morris, R. E.; Wheatley, P. S. *Angew. Chem., Int. Ed.* **2008**, *47*, 4966. (c) Jiang, J. X.; Wang, C.; Laybourn, A.; Hasell, T.; Clowes, R.; Khimyak, Y. Z.; Xiao, J.; Higgins, S. J.; Adams, D. J.; Cooper, A. I. *Angew. Chem., Int. Ed.* **2011**, *50*, 1072.

(2) (a) Thomas, A. *Angew. Chem., Int. Ed.* **2010**, *49*, 8328. (b) Thomas, A.; Driess, M. *Angew. Chem., Int. Ed.* **2009**, *48*, 1890. (c) Weber, J.; Thomas, A. *J. Am. Chem. Soc.* **2008**, *130*, 6334. (d) Cho, H. C.; Lee, H. S.; Chun, J.; Lee, S. M.; Kim, H. J.; Son, S. U. *Chem. Commun.* **2011**, *47*, 917.

(3) (a) Du, N.; Park, H. B.; Robertson, G. P.; Dal-Cin, M. M.; Visser, T.; Scoles, L.; Guiver, M. D. *Nat. Mater.* **2011**, *10*, 372. (b) Weber, J.; Du, N.; Guiver, M. D. *Macromolecules* **2011**, *44*, 1763.

(4) (a) Schwab, M. G.; Lennert, A.; Pahnke, J.; Jonschker, G.; Koch, M.; Senkovska, I.; Rehahn, M.; Kaskel, S. *J. Mater. Chem.* **2011**, *21*, 2131. (b) Martin, C. F.; Stöckel, E.; Clowes, R.; Adams, D. J.; Cooper, A. I.; Pis, J. J.; Rubiera, F.; Pevida, C. *J. Mater. Chem.* **2011**, *21*, 5475. (c) Moon, S. Y.; Bae, J. S.; Jeon, E.; Park, J. W. *Angew. Chem., Int. Ed.* **2010**, *49*, 9504.

(5) (a) Spitler, E. L.; Dichtel, W. R. *Nat. Chem.* **2010**, *2*, 672. (b) Colson, J. W.; Woll, A. R.; Mukherjee, A.; Levendorf, M. P.; Spitler, E. L.; Shields, V. B.; Spencer, M. G.; Park, J.; Dichtel, W. R. *Science* **2011**, *332*, 228.

(6) Dawson, R.; Adams, D. J.; Cooper, A. I. *Chem. Sci.* **2011**, *2*, 1173.

(7) (a) Katsoulidis, A. P.; Kanatzidis, M. G. *Chem. Mater.* **2011**, *23*, 1818. (b) Jiang, J.; Trewin, A.; Su, F.; Wood, C. D.; Niu, H.; Jones, J. T. A.; Khimyak, Y. Z.; Cooper, A. I. *Macromolecules* **2009**, *42*, 2658. (c) Choi, J. H.; Choi, K. M.; Jeon, H. J.; Choi, Y. J.; Lee, Y.; Kang, J. K. *Macromolecules* **2010**, *43*, 5508. (d) Jiang, J.; bourn, A. L.; Clowes, R.; Khimyak, Y. Z.; Bacsa, J. *Macromolecules* **2010**, *43*, 7577.

(8) (a) Xie, Z.; Wang, C.; deKrat, K. E.; Lin, W. *J. Am. Chem. Soc.* **2011**, *133*, 2056. (b) Chen, L.; Yang, Y.; Jiang, D. *J. Am. Chem. Soc.* **2010**, *132*, 9138. (c) Palkovits, R.; Antonietti, M.; Kuhn, P.; Thomas, A.; Schüth, F. *Angew. Chem., Int. Ed.* **2009**, *48*, 6909. (d) Chen, L.; Yang, Y.; Guo, Z.; Jiang, D. *Adv. Mater.* **2011**, *23*, 3149. (e) McKeown, N. B.; Hanif, S.; Msayib, K.; Tattershall, C. E.; Budd, P. M. *Chem. Commun.* **2002**, 2782. (f) McKeown, N. B.; Makhseed, S.; Budd, P. M. *Chem. Commun.* **2002**, 2780. (g) Budd, P. M.; Ghanem, B.; Msayib, K.; McKeown, N. B.; Tattershall, C. *J. Mater. Chem.* **2003**, *13*, 2721.

(9) Ben, T.; Ren, H.; Ma, S.; Cao, D.; Lan, J.; Jing, X.; Wang, W.; Xu, J.; Deng, F.; Simmons, J. M.; Qiu, S.; Zhu, G. *Angew. Chem., Int. Ed.* **2009**, *48*, 9457.

(10) (a) Lu, W. G.; Yuan, D. Q.; Zhao, D.; Schilling, C. I.; Plietzsch, O.; Muller, T.; Brase, S.; Guenther, J.; Blumel, J.; Krishna, R.; Li, Z.; Zhou, H. C. *Chem. Mater.* **2010**, *22*, 5964. (b) Trewin, A.; Cooper, A. I. *Angew. Chem., Int. Ed.* **2010**, *49*, 1533.

(11) Yuan, D.; Lu, W.; Zhao, D.; Zhou, H. *Adv. Mater.* **2011**, *23*, 90.

(12) (a) Gu, S.; Cai, R.; Luo, T.; Chen, Z.; Sun, M.; Liu, Y.; He, G.; Yan, Y. *Angew. Chem., Int. Ed.* **2009**, *48*, 6499. (b) Ghassemi, H.; Riley, D. J.; Curtis, M.; Bonaplata, E.; McGrath, J. E. *Appl. Organomet. Chem.* **1998**, *12*, 781. (c) Sefkow, M.; Borsuk, N.; Wolff, M. O. *Chim. Oggi* **2001**, *19*, 19. (d) Dupont, J.; deSouza, R. F.; Suarez, P. A. Z. *Chem. Rev.* **2002**, *102*, 3667. (e) Sefkow, M.; Borsuk, N.; Wolff, M. O. *Chim. Oggi* **2001**, *19*, 35. (f) Leffler, J. E.; Temple, R. D. *J. Am. Chem. Soc.* **1967**, *89*, 5235.

(13) Clark, T. J.; Robertson, N. J.; Kostalik, H. A. IV; Lobkovsky, E. B.; Mutolo, P. F.; Abruna, H. D.; Coates, G. W. *J. Am. Chem. Soc.* **2009**, *131*, 12888.

(14) Calvo, S.; Castao, F.; Basterretxea, F. J. *J. Mol. Struct.* **2010**, *975*, 190.

(15) Sing, K. S. W.; Everett, D. H.; Haul, R. A. W.; Moscou, L.; Pierotti, R. A.; Rouquérol, J.; Siemieniewska, T. *Pure Appl. Chem.* **1985**, *57*, 603.

(16) Rose, M.; Bohlmann, W.; Sabo, M.; Kaskel, S. *Chem. Commun.* **2008**, *44*, 2462.

(17) Jiang, J. X.; Su, F.; Trewin, A.; Wood, C. D.; Niu, H.; Jones, J. T. A.; Khimyak, Y. Z.; Cooper, A. I. *J. Am. Chem. Soc.* **2008**, *130*, 7710.

(18) (a) Zhu, J.; Kailasam, K.; Xie, X.; Schomaecker, R.; Thomas, A. *Chem. Mater.* **2011**, *23*, 2062. (b) Zhang, Y.; Riduan, S. N.; Ying, J. Y. *Chem.—Eur. J.* **2009**, *15*, 1077.

(19) Chen, L.; Yang, Y.; Jiang, D. *J. Am. Chem. Soc.* **2010**, *132*, 9138.

(20) Chaikittisilp, W.; Kubo, M.; Moteki, T.; Sugawara-Narutaki, A.; Shimojima, A.; Okubo, T. *J. Am. Chem. Soc.* **2011**, *133*, 13832.

(21) (a) Xiong, Y.; Wang, H.; Wang, R.; Yan, Y.; Zheng, B.; Wang, Y. *Chem. Commun.* **2010**, *46*, 3399. (b) Tian, J.; Cai, F.; Wang, J.; Du, Y.; He, L. *Phosphorus, Sulfur Silicon Relat. Elem.* **2008**, *183*, 494. (c) Nishikubo, T.; Kameyama, A.; Yamashita, J.; Tomoi, M.; Fukuda, W. *J. Polym Sci. Part A. Polym. Chem.* **1993**, *31*, 939. (d) Xiong, Y.; Wang, H.; Wang, R.; Yan, Y.; Zheng, B.; Wang, Y. *Chem. Commun.* **2010**, *46*, 3399.

(22) (a) Ogasawara, S.; Kato, S. *J. Am. Chem. Soc.* **2010**, *132*, 4608. (b) Zhu, J.; Xie, X.; Carabineiro, S. A. C.; Tavares, P. B.; Figueiredo, J. L.; Schomäcker, R.; Thomas, A. *Energy Environ. Sci.* **2011**, *4*, 2020. (c) Chen, Z.; Cui, Z.; Niu, F.; Jiang, L.; Song, W. *Chem. Commun.*

2010, *46*, 6524. (d) McKeown, N. B.; Budd, P. M. *Chem. Soc. Rev.* **2006**, *35*, 675. (e) Mackintosh, H. J.; Budd, P. M.; McKeown, N. B. *J. Mater. Chem.* **2008**, *18*, 573. (f) McKeown, N. B.; Budd, P. M.; Msayib, K. J.; Ghanem, B. S. *Chem.—Eur. J.* **2005**, *11*, 2610.

(23) Hermes, S.; Schroter, M. K.; Schmid, R.; Khodeir, L.; Muhler, M.; Tissler, A.; Fischer, R. W.; Fischer, R. A. *Angew. Chem., Int. Ed.* **2005**, *44*, 6237.

(24) Hwang, Y. K.; Hong, D. Y.; Chang, J. S.; Jhung, S. H.; Seo, Y. K.; Kim, J.; Vimont, A.; Daturi, M.; Serre, C.; Férey, G. *Angew. Chem., Int. Ed.* **2008**, *47*, 4144.

(25) Moon, H. R.; Kim, J. H.; Paik Suh, M. *Angew. Chem., Int. Ed.* **2005**, *44*, 1261.

(26) (a) Gentle, T. M.; Muetterties, E. L. *J. Phys. Chem.* **1983**, *87*, 2469. (b) Rucker, T. G.; Logan, M. A.; Gentle, T. M.; Muetterties, E. L.; Somorjai, G. A. *J. Phys. Chem.* **1986**, *90*, 2703.

(27) Li, S.; Wang, J.; Kou, Y.; Zhang, S. *Chem.—Eur. J.* **2010**, *16*, 1812.

(28) (a) Gallon, B. J.; Kojima, R. W.; Kaner, R. B.; Diaconescu, P. L. *Angew. Chem., Int. Ed.* **2007**, *46*, 7251. (b) Kim, Y. M.; Yu, S. *J. Am. Chem. Soc.* **2003**, *125*, 1696.

(29) For representative papers on TBAB-promoted cross-coupling reactions, please see: (a) Li, J.; Liu, W.; Xie, Y. *J. Org. Chem.* **2005**, *70*, 5409. (b) Selvakumar, K.; Zapf, A.; Beller, M. *Org. Lett.* **2002**, *4*, 3031.

Macromolecules

Article

pubs.acs.org/Macromolecules

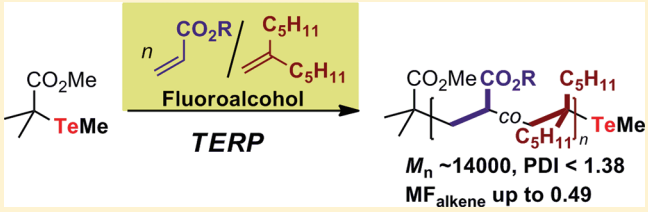
Controlled Copolymerization of Acrylate and 6-Methyleneundecane by Organotellurium-Mediated Living Radical Polymerization (TERP)

Eri Mishima,[†] Tomoki Tamura,[†] and Shigeru Yamago*[,†,‡]

[†]Institute for Chemical Research, Kyoto University, Uji 611-0011, Japan

[‡]CREST, Japan Science and Technology Agency, Tokyo 102-0076, Japan

ABSTRACT: Copolymerization of acrylates, such as methyl acrylates (MAs) and trifluoroethyl acrylates (TFEAs), and 6-methyleneundecane (6MU), under organotellurium-mediated living radical polymerization (TERP) conditions, was investigated. Structurally well-controlled copolymers, poly(MA-*co*-6MU) and poly(TFEA-*co*-6MU), with predetermined number-average molecular weights (M_n = 3000−14000) and low polydispersity indices (PDI = 1.14 to 1.45) were obtained under thermal condition in the presence of an azo-initiator or photoirradiation. The addition of protic acids, such as 1,3-$C_6H_4[C(CF_3)_2OH]_2$ and $(CF_3)_2CHOH$, was effective to increase the insertion of 6MU into the copolymer. The structure of the ω-polymer-end group was analyzed by using labeling experiments, which revealed that the majority of the end groups were derived from 6MU. Although activation of dormant species derived from α-olefin is difficult, the copolymers were successfully reactivated and served as macro-chain-transfer agents for the synthesis of block copolymers. Poly(MA-*co*-6MU)-*block*-styrene and poly(MA-*co*-6MU)-*block*-(*N*-vinylpyrrolidone) with controlled structures were synthesized for the first time.



INTRODUCTION

Living radical polymerization (LRP) has become one of the most powerful polymerization methods for the synthesis of structurally well-controlled macromolecules with rich functionalities because LRP does not require stringent conditions like those required for living anionic, cationic, and coordination polymerizations.[1] Extension of LRP from homopolymerization to copolymerization significantly increases the availability of polymers for macromolecular engineering because copolymerization can finely tailor the properties of polymer materials by changing the composition of the monomers. However, the controlled synthesis of copolymers by LRP has been limited to the combination of monomers having similar reactivities, and application of LRP for the controlled copolymerization of monomers having different reactivities, such as conjugated and nonconjugated monomers, for example, acrylates and α-olefins, has been limited.[2−12] For example, although random copolymerization of methyl acrylate (MA) and α-olefins has already been examined by using reversible addition−fragmentation chain transfer polymerization (RAFT),[13−15] atom-transfer radical polymerization (ATRP),[2,15−19] nitroxide-mediated radical polymerization (NMP),[20] and iodine-mediated LRP,[4] structurally well-controlled copolymers with low polydispersity indices (PDIs) were obtained only with low molecular weights and low α-olefin insertion ratios (mol fraction of α-olefin [MF_{alkene}] < 0.26). When the targeted number-average molecular weight (M_n) was increased to greater than 10 000, PDI was greater than 1.5, which is a theoretical criterion for LRP. This is due to the accumulation of dormant species terminated with α-alkene monomer units, which less efficiently undergo regeneration to form polymer end radicals than those terminated with acrylate monomers do.[17,21] Furthermore, although the addition of Lewis acids, such as $AlCl_3$[15] and $Sc(OTf)_3$,[22] and Brønsted acids, such as $(CF_3)_2CHOH$ and $(CF_3)_3COH$,[4] under RAFT and iodine-mediated LRP conditions significantly increased MF_{alkene} to 0.27 to 0.50, the PDI control decreased (>1.9) upon the addition of acids. This is probably due to the low compatibility of RAFT reagents and organoiodine compounds under acids, whereas acids increase electrophilicity of acrylate and the resulting polymer-end radical species upon coordination. Moreover, there is no report on the use of copolymers as macro-chain-transfer agents (CTAs) for the controlled synthesis of block copolymers.

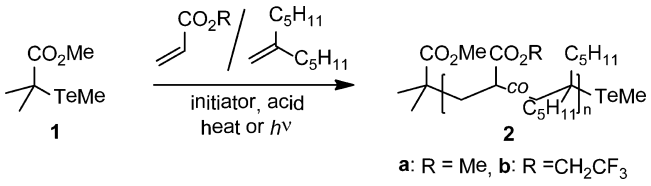
We have already developed organotellurium-, organostibine-, and organobismuthine-mediated LRPs (TERP,[23−29] SBRP,[30−32] and BIRP,[33,34] respectively), which mainly proceed by the degenerative chain transfer mechanism.[35−37] One of the most characteristic features of these methods is their high versatility in polymerizing both conjugated and nonconjugated monomers by using the same CTA. This feature has been exemplified in the first controlled synthesis of a block copolymer of conjugated and nonconjugated monomers[30,31,33,38] and controlled random and alternating copolymerization of (meth)acrylates and vinyl ethers.[39] These results prompted us to investigate controlled random copolymerization of acrylate and α-alkene under TERP conditions with methyl 2-methyl-2-methyltellanylpropionate (**1**) as the CTA

Received: February 19, 2012
Revised: March 15, 2012
Published: April 2, 2012

 © 2012 American Chemical Society dx.doi.org/10.1021/ma300325r | *Macromolecules* 2012, 45, 2989−2994

(Scheme 1). 6-Methyleneundecane (6MU) was used here because tertiary C−Te bond of the dormant species derived

Scheme 1. Controlled Copolymerization of Acrylate and α-Olefin under TERP



from 6MU is weaker and thus easier to regenerate polymer end radicals than secondary C−Te bond derived from monosubstituted α-alkene. We have recently reported that photoirradiation is effective for the activation of organotellurium dormant species possessing stable carbon−tellurium bonds by C−Te bond homolysis.[40−43] Therefore, the effect of photoirradiation on the copolymerization was also examined.[44] In addition, we report the synthesis of new block copolymers starting from random copolymer **2** as a macro-CTA.

EXPERIMENTAL SECTION

Materials. Unless otherwise noted, materials obtained from commercial suppliers were used without purification. Methyl acrylate (MA; >99%), 2,2,2-trifluoroethyl acrylate (TFEA; >98%), stylene (St; >99%), and *N*-vinylpyrrolidone (NVP; >99%) were washed with 5% aqueous sodium hydroxide solution and were distilled over calcium hydride under reduced pressure. Dimethyl 2,2′-azobis(2-methylpropionate) (V-601) was recrystallized from methanol. 1,1,1,3,3,3-Hexafluoro-2-propanol (>99%) and 1,3-$C_6H_4[C(CF_3)_2OH]_2$ (>97%) were distilled over CaH_2 and deaerated by passing anhydrous nitrogen. Toluene and hexane were distilled over CaH_2 and stored over molecular sieves. Methyl 2-methyl-2-methyltellanylpropionate (**1**) was prepared as reported.[45]

Measurements. ^{1}H NMR (400 MHz) and ^{13}C NMR (100 MHz) spectra were measured for a $CDCl_3$ solution of a sample. ^{1}H NMR spectra are reported in parts per million (δ) from internal tetramethylsilane or residual solvent peak and ^{13}C NMR from solvent peak. MALDI-TOF mass spectra were recorded on a spectrometer equipped with a 337 nm N_2 laser in the reflection mode and at 20 kV acceleration voltage. Samples were prepared from a tetrahydrofuran (THF) solution by mixing sample (1 mg/mL), dithranol (10 mg/mL), and sodium trifluoroacetate (1 mg/mL) in a ratio of 5:1:1. Gel permeation chromatography (GPC) was performed on a liquid chromatography equipped with two linearly connected polystyrene (PSt) mixed gel columns (Shodex LF-604), which were calibrated with poly(methyl methacrylate) (PMMA) standards using $CHCl_3$ or DMF containing LiBr (0.1 mol/L) as an eluant. Preparative/recycling GPC was carried out with two linearly connected PSt mixed gel columns using $CHCl_3$ as an eluent.

Synthesis of 6MU. Sodium hydride (4.5 g, 60% dispersion in mineral oil; 0.36 mol) was placed on a three-neck, round-bottomed flask under a nitrogen atmosphere. The mineral oil was washed off with hexane (20 mL × 3) by using hypodermic syringe, and remaining hexane was removed under vacuum. Methyl triphenylphosphonium bromide (81.5 g, 0.23 mol) and 300 mL of toluene were added, and the mixture was heated to 60 °C for 1.5 h. 6-Undecanone (37.5 mL, 0.18 mol) was added, and the mixture was heated to this temperature for 15 h. The reaction mixture was poured into a 300 mL ice bath, and organic phase was extracted twice with hexane. The combined organic layers were dried over $MgSO_4$, filtered, and evapolated. The residue was purified by column chromatography by using hexane as an eluant, followed by distillation (bp = 85 °C/10.4 mmHg) to give 22.9 g (74%) of 6MU as an oil. ^{1}H NMR ($CDCl_3$): 0.89 (t, 6 H), 1.26 (m, 8 H), 1.42 (m, 4 H), 1.99 (t, 4 H), 4.69 (s, 2 H). ^{13}C NMR ($CDCl_3$): 14.30, 22.01, 27.70, 31.89, 36.24, 108.51, 150.70.

Typical Procedure of Copolymerization under Thermal Conditions. Synthesis of Poly(MA-*co*-6MU). A solution of MA (0.26 g, 3.0 mmol), 6MU (0.50 g, 3.0 mmol), V-601 (4.6 mg, 0.020 mmol), and **1** (15.5 μL, 0.10 mmol) was heated to 60 °C for 12 h with stirring under a nitrogen atmosphere in a glovebox. A small portion of the reaction mixture was withdrawn and dissolved in $CDCl_3$. The conversion of the monomer was determined by using ^{1}H NMR spectroscopy (Figure 1). Conversion of MA and 6MU reached to 89 and 23%, respectively, after 12 h. PhSH (12.0 μL, 0.13 mmol) was added to the reaction mixture, and the resulting solution was stirred at 80 °C for 2 h.[46] The mixture was concentrated under reduced pressure to give the crude product (0.64 g). The MF_{6MU} = 0.22 was determined by using ^{1}H NMR spectrometry. The M_n = 3400 and the PDI = 1.26 were determined by GPC calibrated against PMMA standards.

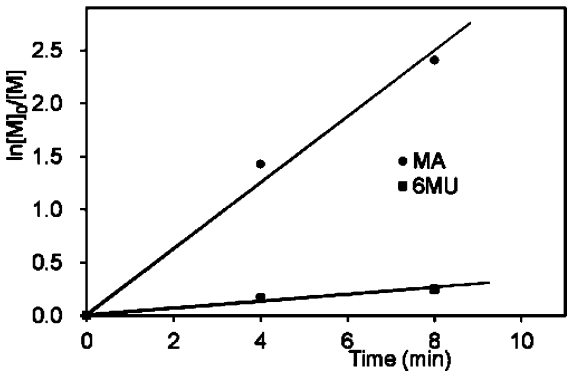


Figure 1. First-order kinetic plot of PMA-*co*-P(6MU).

Typical Procedure for Copolymerization under Photoirradiation Conditions. Synthesis of Poly(MA-*co*-6MU). A solution of MA (0.26 g, 3.0 mmol), 6MU (0.50 g, 3.0 mmol), 1,3-$C_6H_4[C(CF_3)_2OH]_2$ (1.2 g, 3.0 mmol), and **1** (15.5 μL, 0.10 mmol) was irradiated by 500 W high-pressure mercury lamp through a > 470 nm cutoff filter at 60 °C for 6 h. A small portion of the reaction mixture was withdrawn and dissolved in $CDCl_3$. The conversion of the monomer (MA: 93%, 6MU: 46%) was determined by using ^{1}H NMR spectroscopy. PhSH (12.0 μL, 0.13 mmol) was added to the reaction mixture, and the resulting solution was stirred at 80 °C for 2 h. The mixture was concentrated under reduced pressure to give the crude product (0.47 g). The MF_{6MU} = 0.32 was determined by using ^{1}H NMR spectrometry. The M_n = 5100 and the PDI = 1.24 were determined by GPC calibrated against PMMA standards.

Synthesis of Poly[(MA-*co*-6MU)-*block*-St]. A solution of **1** (15.5 μL, 0.10 mmol), MA (0.26 g, 3.0 mmol), 6MU (0.50 g, 3.0 mmol), and 1,1,1,3,3,3-hexafluoro-2-propanol (0.49 g, 2.9 mmol) was irradiated by 500 W high-pressure mercury lamp through a >520 nm cutoff filter at 20 °C for 24 h to give PMA-*co*-P(6MU) with M_n = 5000 and PDI = 1.18. Conversion of MA (95%) and the MF_{6MU} = 0.31 was determined by ^{1}H NMR spectroscopy. St (3.1 g, 30 mmol) and V-601 (4.8 mg, 0.021 mmol) were added, and the resulting solution was heated to 60 °C for 40 h. The monomer was removed under reduced pressure to give the block copolymer (2.7 g, 72% conversion of St) with M_n = 21 900 and PDI = 1.41.

Synthesis of Poly[(MA-*co*-6MU)-*block*-NVP]. A solution of **1** (15.5 μL, 0.10 mmol), MA (0.26 g, 3.0 mmol), 6MU (0.51 g, 3.0 mmol), and 1,1,1,3,3,3-hexafluoro-2-propanol (0.51 g, 3.0 mmol) was irradiated by 60 W black lamp at 20 °C for 60 h to give PMA-*co*-P(6MU) with M_n = 4000 and PDI = 1.22. Conversion of MA (96%) and the MF_{6MU} = 0.31 was determined by ^{1}H NMR spectroscopy. NVP (2.2 g, 20 mmol) was added, and the resulting solution was irradiated by 500 W high-pressure mercury lamp through a filter (>580 nm) at 60 °C for 110 h. The monomer was removed under reduced

dx.doi.org/10.1021/ma300325r | *Macromolecules* 2012, 45, 2989−2994

pressure to give the block copolymer (3.6 g, 82% conversion of NVP) with M_n = 31 000 and PDI = 1.22.

Synthesis of End-Deuterated and Protonated Poly(TFEA-*co*-6MU). A solution of **1** (7.7 μL, 0.050 mmol), TFEA (0.12 g, 0.75 mmol), 6MU (1.3 g, 7.5 mmol), and 1,1,1,3,3,3-hexafluoro-2-propanol (0.13 g, 0.75 mmol) was irradiated by 60 W black lamp at 60 °C for 10 h. A small portion of the reaction mixture was withdrawn and dissolved in $CDCl_3$. The conversion of monomer (TFEA: 80%, 6MU: 8%) was determined by ^{1}H NMR spectroscopy. Volatile materials were removed under vacuum, and tributyltin deuteride (34 μL, 0.13 mmol) and V-601 (2.5 mg, 0.011 mmol) were added. The resulting solution was stirred at 80 °C for 2 h. Volatile materials were removed under reduced pressure, and the crude polymer was purified by preparative GPC to give a product (0.21 g) with M_n = 4800 and PDI = 1.24. The MF_{6MU} = 0.46 determined by using ^{1}H NMR spectroscopy was identical to the MF_{6MU} = 0.47 determined by MALDI TOF MS spectra (Figure 2).

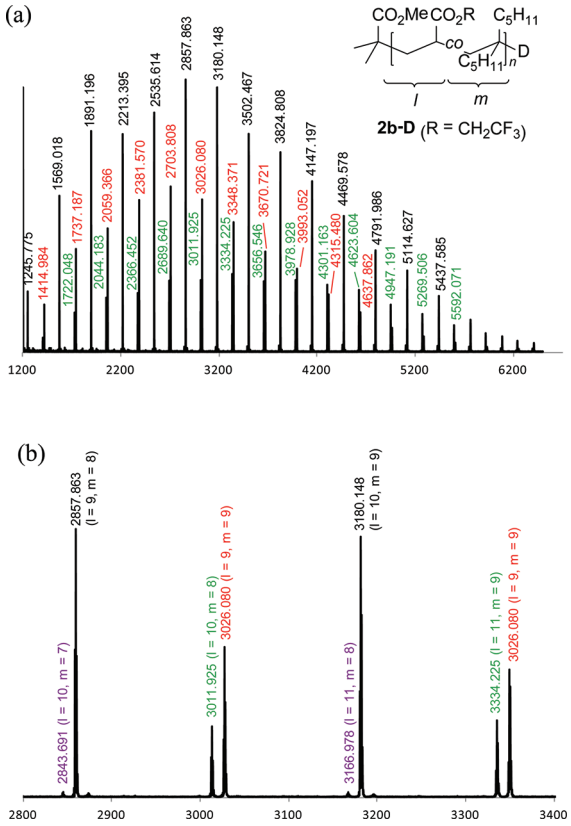


Figure 2. (a) Full and (b) partial MALDI TOF MS spectra of the end deuterated copolymer.

RESULTS AND DISCUSSION

MA (R = CH_3, MA, 30 equiv) and 6MU (30 equiv) were polymerized in the presence of **1** and dimethyl 2,2′-azobis(2-methylpropionate) (V-601, 0.2 equiv) at 60 °C for 12 h. The conversion of MA and 6MU followed first-order kinetics (Figure 1) and reached 89 and 22%, respectively, after 12 h. GPC analysis indicated that structurally well-controlled copolymer **2a** (R = Me) with M_n = 3400 and PDI = 1.26 was formed. The mole fraction of 6MU (MF_{6MU}) in the copolymer was determined to be 0.22 by using ^{1}H NMR analysis after isolation, and the ratio is identical to the one estimated from the monomer conversion.

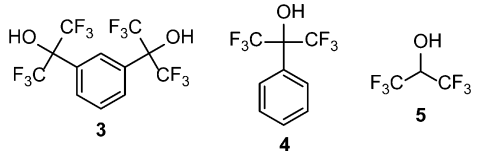
We next examined the effects of acids because they increase MF_{alkene} in the copolymerization of acrylates and α-alkenes.[47−49] TERP was compatible with various inorganic Lewis acids, such as $Mg(OTf)_2$, $Sm(OTf)_3$, $Yb(OTf)_3$, $Lu(OTf)_3$, and $TiO{i}Pr_4$, and copolymerization afforded structurally well-controlled copolymers with M_n values close to the theoretical values calibrated by PMMA standards (M_n = 2800−4100) and low PDIs (PDI = 1.18 to 1.31). However, no significant effects on MF_{6MU} were observed (MF_{6MU} = 0.17to 0.24). This is partially because these Lewis acids coordinate strongly with MA and the copolymers, causing the resulting complexes to phase-separate from the reaction mixture. Next, organic and liquid Brønsted acids **3**, **4**, and **5** (Chart 1), which have recently been used by Kamigaito and coworkers to increase MF_{alkene} in the iodine-mediated copolymerization of acrylate and α-alkene,[4] were examined. Copolymerization in the presence of **3** under otherwise identical conditions proceeded in a controlled manner giving a copolymer with M_n close to the theoretical value (M_n = 4400) and a low PDI of 1.17 (run 2), and MF_{6MU} slightly increased to 0.28. MF_{6MU} further increased to 0.32 and 0.42, when the amount of **3** (30 equiv to **1**) was increased and the use of an excess amount of 6MU over that of MA (runs 3 and 4, respectively) while keeping the low PDIs. A longer reaction period was required as the increase in MF_{6MU} probably due to the low efficiency of regeneration of polymer end radicals from the dormant species derived from 6MU.

Acids **4** and **5** were also effective for increasing MF_{6MU}, and the copolymerization gave the corresponding copolymers in a controlled manner (M_n values = 4800−5600, PDIs = 1.17 to 1.18) with a high MF_{6MU} of 0.32 to 0.34 (runs 5 and 6). Other Brønsted acids, such as phenol and phosphoric acid, did not affect MF_{6MU}, although the copolymerization proceeded in a controlled manner.

We next examined the copolymerization under photoirradiation, which is effective for the activation of organotellurium dormant species having a stable carbon−tellurium bond.[40−43] The copolymerization under photoirradiation with a 500 W high-pressure mercury lamp through a >480 nm cutoff filter or 60 W black lamp proceeded smoothly at 60 °C, and controlled copolymers with M_n close to the theoretical values, narrow PDIs, and high MF_{6MU} (0.30 to 0.32) were obtained in the presence of acid **3** or **5** (runs 7 and 11). The copolymerization in the presence of excess amount of 6MU over that of MA also gave corresponding copolymer with a better MF_{6MU} of 0.38 (run 8). Polymerization proceeded at low temperature, such as 20 °C, under photoirradiation because the generation of radicals from the dormant species does not require heating (run 9). A structurally well-controlled copolymer with a high MF_{6MU} was obtained in the presence of **5**. A copolymer with a high M_n of 13 100 and a low PDI of 1.19 was obtained by increasing the amount of MA and 6MU over that of **1** (run 10), and the result is consistent with the living character of TERP.

TFEA was next employed as an acrylate monomer because the high electrophilic character of the TFEA-polymer end

Chart 1. Structure of Brønsted Acids Used in This Study



dx.doi.org/10.1021/ma300325r | Macromolecules 2012, 45, 2989−2994

Table 1. Random Copolymerization of MA and 6MU in the Presence of 1 and Acid[a]

run	MA/6MU (equiv)	additive (equiv)	condition[b]	time (h)	conv. of MA (%)[c]	M_n(theo)	M_n(exp)[d]	PDI[d]	MF_{6MU}[e]
1	30/30	none	A	12	89	3700	3400	1.26	0.22
2	30/30	**3** (1)	A	24	90	4100	4400	1.17	0.28
3	30/30	**3** (30)	A	8	93	4600	5700	1.14	0.32
4	30/150	**3** (30)	A	26	100	6200	5500	1.32	0.42
5	30/30	**4** (30)	A	6	89	4500	5600	1.17	0.33
6	30/30	**5** (30)	A	6	92	4600	4800	1.18	0.32
7	30/30	**3** (30)	B	6	93	5000	5100	1.24	0.32
8	30/150	**3** (30)	B	13	95	5400	3900	1.38	0.38
9[f]	30/30	**5** (30)	B	18	92	4800	4700	1.20	0.34
10[e]	100/100	**5** (100)	B	83	83	11700	13100	1.19	0.28
11	30/30	**5** (30)	C	32	93	4400	2800	1.32	0.30

[a]**1** (1.0 equiv), MA, and 6MU in the absence of presence of acids **3**–**5** were stirred at 60 °C. [b]A: V-601 (0.2 equiv), B: *hν* (500 W high-pressure Hg lamp through a >470 nm cutoff filter), C: *hν* (60 W black lamp). [c]Determined by using ^{1}H NMR spectroscopy. [d]M_n and PDI determined by GPC calibrated against PMMA standards. [e]Mole fraction of 6MU in the copolymer determined by using ^{1}H NMR spectroscopy. [f]Polymerization was carried out at 20 °C.

Table 2. Photoinduced TERP of TFEA and 6MU Using 1[a]

run	monomer (equiv)	additive (equiv)	time (h)	conv. (%)[b]	M_n(theo)	M_n(exp)[c]	PDI[c]	MF_{6MU}[d]
1	TFEA/6MU (30/30)	none	20	92	6300	4600	1.18	0.31
2	TFEA/6MU (30/30)	**5** (30)	24	98	7800	6400	1.15	0.40
3	TFEA/6MU (30/150)	**5** (30)	24	94	7900	5300	1.19	0.49
4[e]	TFEA/6MU (30/30)	**5** (30)	66	75	5300	2300	1.15	0.35
5[e]	TFEA/6MU (100/100)	**5** (100)	220	80	19800	10100	1.07	0.35
6[e]	TFEA/6MU (200/200)	**5** (200)	384	81	35300	14200	1.14	0.33

[a]**1** (1.0 equiv), TFEA, and 6MU with or without **5** were stirred under irradiation with a 60 W black lamp at 60 °C. [b]Conversion of acrylate determined by using ^{1}H NMR spectroscopy. [c]M_n and PDI obtained by GPC calibrated against PMMA standards. [d]Mole fraction of 6MU in the copolymer determined by using ^{1}H NMR spectroscopy. [e]Polymerization was carried out at 20 °C.

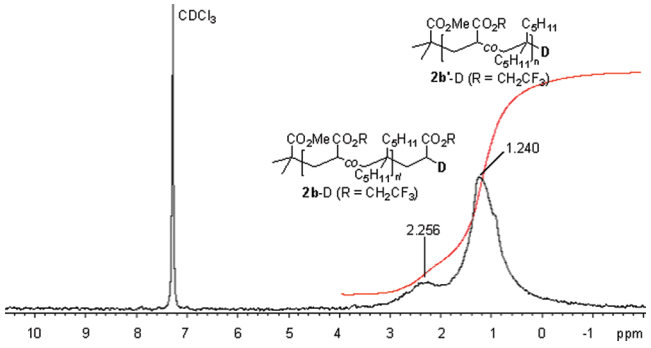
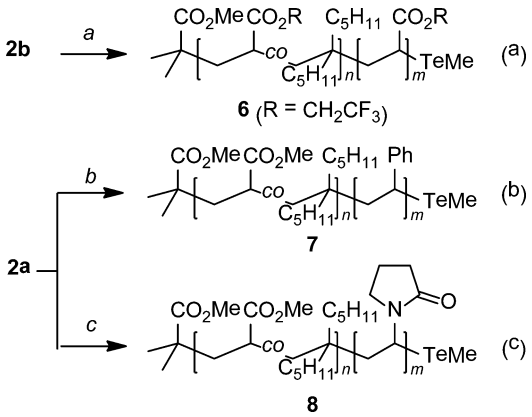


Figure 3. ^{2}H NMR spectra of **2b**-D and **2b**′-D.

radical should increase the insertion of 6MU.[50] When an equimolar amount of TFEA and 6MU (30 equiv each) was polymerized in the presence of **1** without acid under photoirradiation at 60 °C, the polymerization followed first-order kinetics for both TFEA and 6MU and reached 92 and 46% conversion, respectively, after 20 h. The structurally well-controlled copolymer **2b** (R = CH_2CF_3) with M_n = 4600 and PDI = 1.18 was obtained (Table 2, run 1). The value of MF_{6MU} in **2b** was 0.31, which is considerably higher than that in **2a** (Table 1, run 1). The addition of acid **5**, giving the corresponding controlled copolymer with an MF_{6MU} of 0.40 (run 2), was also effective for increasing MF_{6MU}. MF_{6MU} further increased to 0.49 when the 6MU/TFEA ratio was greater than five in the presence of **5**, suggesting that nearly alternating copolymerization occurred (run 3). MF_{6MU} of this copolymer was estimated to be 0.47 by using MALDI TOF mass spectroscopy by comparing the peak intensities (Figure 2),

Scheme 2. Synthesis of Block Copolymers from Copolymer 2[a]



[a]Reaction conditions: (a) **2b** (M_n = 3800, PDI = 1.24, MF_{6MU} = 0.44), TFEA (85 equiv), V-601 (0.2 equiv), 60 °C, 10 h, 98% conv. of TFEA. (b) **2a** (M_n = 5000, PDI = 1.18, MF_{6MU} = 0.31), St (300 equiv), V-601 (0.2 equiv), 60 °C, 40 h, 72% conv. of St. (c) **2a** (M_n = 4000, PDI = 1.22, MF_{6MU} = 0.31), NVP (200 equiv), 500 W high-pressure Hg lamp through a >580 nm cutoff filter, 60 °C, 110 h, 82% conv. of NVP.

and the value was almost identical to the one obtained by using ^{1}H NMR spectroscopy. High-molecular-weight copolymers (M_n > 10 000) with low PDIs (<1.14) and considerably high MF_{6MU} values (0.33 to 0.35) were synthesized by increasing the amount of TFEA and 6MU over that of **1** (runs 5 and 6).

The *ω*-polymer-end structure of the copolymer **2b** was analyzed by using deuterium labeling experiments. After nearly alternating copolymer **2b** was prepared under the conditions in

dx.doi.org/10.1021/ma300325r | *Macromolecules* 2012, 45, 2989–2994

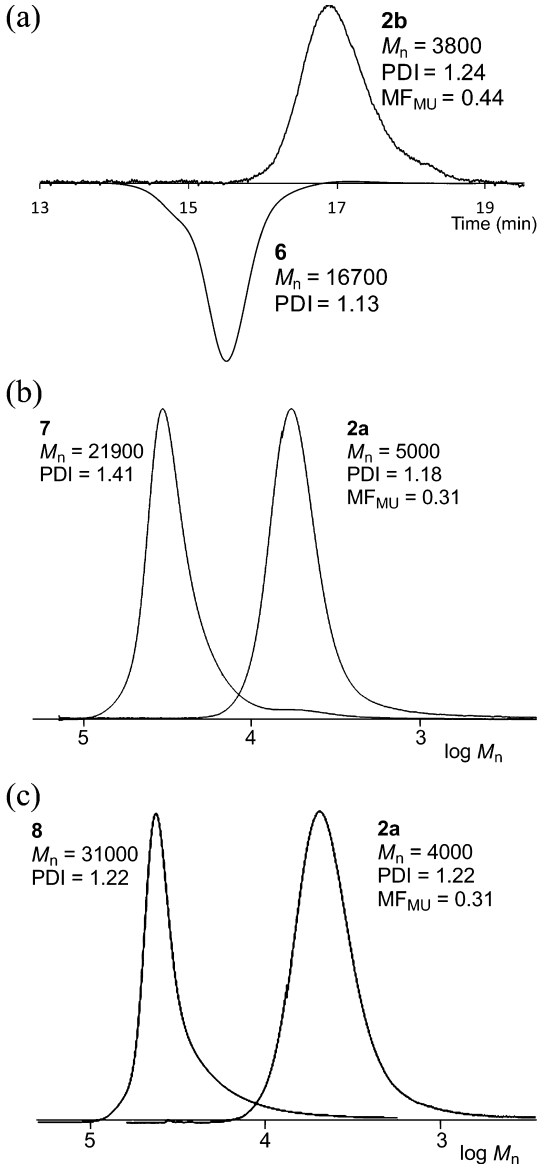


Figure 4. GPC traces before and after the block copolymer synthesis.

Table 2, run 3, it was reduced with Bu_3SnD to afford ω-end deuterated **2b**-D and **2b′**-D. In ^2H NMR spectra, two signals corresponding to **2b**-D and **2b′**-D were observed at 1.2 and 2.3 ppm in a ratio of 85:15, indicating that the polymer-end monomer unit was mainly from 6MU (Figure 3). This is probably due to the use of an excess amount of 6MU over that of TFEA and the stronger polymer end C−Te bond derived from 6MU than that from TFEA.

We next examined the synthesis of block copolymers starting from **2** (Scheme 2). **2b** (M_n = 3800, PDI = 1.24, MF_{6MU} = 0.44), which was prepared from **1**, TFEA (15 equiv), and 6MU (150 equiv) in the presence of **5** (15 equiv), was heated in the presence of TFEA (85 equiv) and V-601 (0.2 equiv) at 60 °C for 10 h. Copolymer **2b** completely disappeared, and the desired structurally well-defined block copolymer poly[(TFEA-*co*-6MU)-*block*-TFEA] (**6**) with M_n = 16 700 and PDI = 1.13 formed, as shown in GPC traces in Figure 4. The result clearly indicates that both polymer-end species having TFEA and 6MU monomer units are activated efficiently to generate the corresponding polymer-end radical species.

Macro-CTA **2a** could be used to synthesize a block copolymer. Treatment of **2a** (M_n = 5000, PDI = 1.18, MF_{6MU} = 0.31) with styrene (St, 300 equiv) in the presence of V-601 (0.2 equiv) at 60 °C for 40 h afforded the desired block copolymer poly[(MA-*co*-6MU)-*block*-St] (**7**) with M_n = 21 900 and PDI = 1.41 (Figure 4b). In GPC traces, macro-CTA **2a** almost completely disappeared, and a new signal corresponding to the block copolymer appeared (Figure 2b). Moreover, *N*-vinylpyrorridone (NVP), which is a non-conjugated monomer, could be used in the block copolymerization, and polymerization of **2a** (M_n = 4000, PDI = 1.22, MF_{6MU} = 0.31) and NVP (200 equiv) under photoirradiation afforded the desired block copolymer poly[(MA-*co*-6MU)-*block*-NVP] (**8**) with M_n = 31 000 and PDI = 1.22 (Figure 4c) on the basis of GPC analysis (Figure 2c).

■ CONCLUSIONS

Controlled copolymerization of acrylates and 6MU was achieved under TERP conditions. Structurally well-controlled copolymers with low to high molecular weights (M_n = 3000−14000) and low PDIs (<1.4) were synthesized. Insertion of 6MU into the copolymer could be increased to nearly 0.5 by adding fluoroalcohols as a Brønsted acid without losing control of the PDI. Deuterium-labeling experiments proved that the ω-polymer end groups were mainly from 6MU rather than from the acrylates. Both polymer-ends were activated simultaneously in the presence of various monomers giving structurally well-defined block copolymers. Poly[(MA-*co*-6MU)-*block*-St], poly-[(MA-*co*-6MU)-*block*-NVP], and poly[(TFEA-*co*-6MU)- *block*-TFEA] were prepared for the first time. These results will make it possible to tune the properties of polymer materials via macromolecular engineering by controlling the polymer structures, monomer sequences, and compositions.

■ AUTHOR INFORMATION

Corresponding Author

*E-mail: yamago@scl.kyoto-u.ac.jp.

Notes

The authors declare no competing financial interest.

■ ACKNOWLEDGMENTS

This work was partially supported by the Core Research for Evolutional Science and Technology (CREST) of the Japan Science and Technology Agency and a Grant-in-Aid for Scientific Research from the Japan Society for the Promotion of Science. E.M. acknowledges receipt of a JSPS Fellowship for Young Scientists.

■ REFERENCES

(1) Matyjaszewski, K.; Davis, T. P. *Handbook of Radical Polymerization*; Wiley-Interscience: New York, 2002.
(2) Liu, S.; Elyashiv, S.; Sen, A. *J. Am. Chem. Soc.* **2001**, *123*, 12738.
(3) Liu, S.; Sen, A. *Macromolecules* **2004**, *37*, 7924.
(4) Koumura, K.; Satoh, K.; Kamigaito, M. *Macromolecules* **2009**, *42*, 2497.
(5) Schmidt-Naake, G.; Butz, S. *Macromol. Rapid Commun.* **1996**, *17*, 661.
(6) Benoit, D.; Hawker, C. J.; Huang, E. E.; Lin, Z.; Russell, T. P. *Macromolecules* **2000**, *33*, 1505.
(7) Chen, G.-Q.; Wu, Z.-Q.; Wu, J.-R.; Li, Z.-C.; Li, F.-M. *Macromolecules* **2000**, *33*, 232.

(8) De Brouwer, H.; Schellekens, M. A. J.; Klumperman, B.; Monteiro, M. J.; German, A. L. *J. Polym. Sci., Part A: Polym. Chem.* **2000**, *38*, 3596.
(9) Zhu, M.-Q.; Wei, L.-H.; Li, M.; Jiang, L.; Du, F.-S.; Li, Z.-C.; Li, F.-M. *Chem. Commun.* **2001**, 365.
(10) Chernikova, E.; Terpugova, P.; Bui, C.; Charleux, B. *Polymer* **2003**, *44*, 4101.
(11) Wu, D.-C.; Hong, C.-Y.; Pan, C.-Y.; He, W.-D. *Polym. Int.* **2003**, *52*, 98.
(12) Daviesa, M. C.; Dawkinsa, J. V.; Hourstonb, D. J. *Polymer* **2005**, *46*, 1739.
(13) Liu, S.; Gu, B.; Rowlands, H. A.; Sen, A. *Macromolecules* **2004**, *37*, 7924.
(14) Venkatesh, R.; Staal, B. B. P.; Klumperman, B. *Chem. Commun.* **2004**, 1554.
(15) Liu, S.; Sen, A. *J. Polym. Sci., Part A: Polym. Chem.* **2004**, *42*, 6175.
(16) Venkatesh, R.; Harrison, S.; Haddleton, D. M.; Klumperman, B. *Macromolecules* **2004**, *37*, 4406.
(17) Venkatesh, R.; Vergouwen, F.; Klumperman, B. *Macromol. Chem. Phys.* **2005**, *206*, 547.
(18) Tanaka, K.; Matyjaszewski, K. *Macromolecules* **2007**, *40*, 5255.
(19) Tanaka, K.; Matyjaszewski, K. *Macromol. Symp.* **2008**, *261*, 1.
(20) Gu, B.; Liu, S.; Leber, J. D.; Sen, A. *Macromolecules* **2004**, *37*, 5142.
(21) Kwak, Y.; Goto, A.; Fukuda, T.; Kobayashi, Y.; Yamago, S. *Macromolecules* **2006**, *39*, 4671.
(22) Nagel, M.; Poli, D.; Sen, A. *Macromolecules* **2005**, *38*, 7262.
(23) Yamago, S.; Iida, K.; Yoshida, J. *J. Am. Chem. Soc.* **2002**, *124*, 2874.
(24) Yamago, S.; Iida, K.; Yoshida, J. *J. Am. Chem. Soc.* **2002**, *124*, 13666.
(25) Yamago, S.; Iida, K.; Nakajima, M.; Yoshida, J. *Macromolecules* **2003**, *36*, 3793.
(26) Goto, A.; Kwak, Y.; Fukuda, T.; Yamago, S.; Iida, K.; Nakajima, M.; Yoshida, J. *J. Am. Chem. Soc.* **2003**, *125*, 8720.
(27) Kayahara, E.; Yamago, S.; Kwak, Y.; Goto, A.; Fukuda, T. *Macromolecules* **2008**, *41*, 527.
(28) Yamago, S.; Ukai, U.; Matsumoto, A.; Nakamura, Y. *J. Am. Chem. Soc.* **2009**, *131*, 2100.
(29) Sugihara, Y.; Kagawa, Y.; Yamago, S.; Okubo, M. *Macromolecules* **2007**, *40*, 9208.
(30) Yamago, S.; Ray, B.; Iida, K.; Yoshida, J.; Tada, T.; Yoshizawa, K.; Kwak, Y.; Goto, A.; Fukuda, T. *J. Am. Chem. Soc.* **2004**, *126*, 13908.
(31) Ray, B.; Kotani, M.; Yamago, S. *Macromolecules* **2006**, *39*, 5259.
(32) Yamago, S.; Yamada, T.; Togai, M.; Ukai, Y.; Kayahara, E.; Pan, N. *Chem.–Eur. J.* **2009**, *15*, 1018.
(33) Yamago, S.; Kayahara, E.; Kotani, M.; Ray, B.; Kwak, Y.; Goto, A.; Fukuda, T. *Angew. Chem., Int. Ed.* **2007**, *46*, 1304.
(34) Kayahara, E.; Yamago, S. *J. Am. Chem. Soc.* **2009**, *131*, 2508.
(35) Yamago, S. *Synlett* **2004**, 1875.
(36) Yamago, S. *J. Polym. Sci., Part A: Polym. Chem.* **2006**, *44*, 1.
(37) Yamago, S. *Chem. Rev.* **2009**, *109*, 5051.
(38) Yusa, S.; Yamago, S.; Sugahara, M.; Morikawa, S.; Yamamoto, T.; Morishima, Y. *Macromolecules* **2007**, *40*, 5907.
(39) Mishima, E.; Yamago, S. *Macromol. Rapid Commun.* **2011**, *32*, 853.
(40) Kayahara, E.; Yamago, S.; Kwak, Y.; Goto, A.; Fukuda, T. *Macromolecules* **2008**, *41*, 527.
(41) Yamago, S.; Ukai, Y.; Matsumoto, A.; Nakamura, Y. *J. Am. Chem. Soc.* **2009**, *131*, 2100.
(42) Sugihara, Y.; Kagawa, Y.; Yamago, S.; Okubo, M. *Macromolecules* **2007**, *40*, 9208.
(43) Yamago, S. *J. Polym. Sci., Part A: Polym. Chem.* **2006**, *44*, 1.
(44) Nakamura, Y.; Kitada, Y.; Kobayashi, Y.; Ray, B.; Yamago, S. *Macromolecules* **2011**, *44*, 8388.
(45) Mishima, E.; Yamada, T.; Watanabe, H.; Yamago, S. *Chem. Asian J.* **2011**, *6*, 445.
(46) Yamago, S.; Matsumoto, A. *J. Org. Chem.* **2008**, *73*, 7300.
(47) Logothetis, A. L.; McKenna, J. M. *J. Polym. Sci.: Polym. Chem. Ed.* **1978**, *16*, 2797.
(48) Logothetis, A. L.; McKenna, J. M. *J. Polym. Sci., Part A: Polym. Chem.* **1977**, *15*, 1431.
(49) Logothetis, A. L.; McKenna, J. M. *J. Polym. Sci., Part A: Polym. Chem.* **1977**, *15*, 1441.
(50) Mishima, E.; Yamago, S. *J. Polym. Sci. Part A: Polym. Chem.* **2012**, in press.

Macromolecules

Article

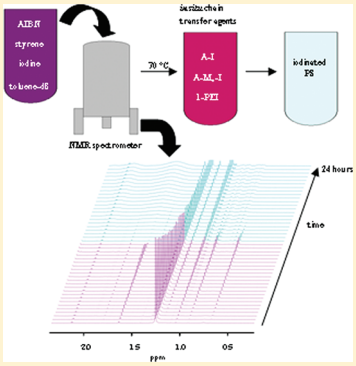
pubs.acs.org/Macromolecules

NMR Studies on the Mechanism of Reverse Iodine Transfer Polymerization of Styrene

Trevor Wright, Helen Chirowodza, and Harald Pasch*

Department of Chemistry and Polymer Science, University of Stellenbosch, Private Bag X1, Matieland 7602, South Africa

ABSTRACT: The evolution of chain transfer agents (CTAs) was studied for the polymerization of styrene by reverse iodine transfer polymerization (RITP). CTAs are formed during an inhibition period where the radical initiator reacts with molecular iondine. These compounds were studied using *in situ* ^{1}H nuclear magnetic resonance (NMR) experiments. The molecular weight of polystyrene was evaluated with size exclusion chromatography (SEC) and ^{1}H NMR. Structural analysis of the resulting polymers was done using ^{1}H NMR spectroscopy and matrix-assisted laser desorption/ionization time-of-flight (MALDI−ToF) mass spectrometry. The inhibition period of styrene polymerized by RITP was much shorter than expected. This is due to the consumption of iodine in the reaction between styrene and iodine which reversibly forms 1,2-diiodoethylbenzene leading to the subsequent formation of 1-phenylethyl iodide (1-PEI). For the first time the formation of 1,2-diiodoethylbenzene as an intermediate structure in RITP of styrene has been proven experimentally. The active role of 1-PEI in the polymerization process is documented through the detection of phenylethyl end groups by MALDI−ToF and ^{1}H NMR.



INTRODUCTION

Reverse iodine transfer polymerization (RITP) is a technique where molecular iodine is reacted with initiator radicals to form alkyl iodide chain transfer agents (CTAs) *in situ*. The basic mechanism of RITP is shown in Scheme 1.[1−3]

RITP is divided into two stages: (1) the inhibition period and (2) the polymerization period. Iodine is a strong inhibitor, and therefore, the inhibition period is ended only once all iodine has been consumed. Throughout the inhibition period, free radicals (A$^\bullet$) generated by the decomposing initiator (AIBN) react directly with iodine to form iodinated CTAs. The CTAs generated are A−I and A−M$_n$−I ($n \geq 0$), where A is a radical from the initiator, M is a monomer unit, n is the average degree of polymerization, and I is the iodine atom. During the inhibition period, iodine can also react with the double bonds of a monomer molecule to form a 1,2-disubstituted olefin. The formation of these compounds is reversible and they tend to be very unstable in UV light.[2,4,5]

The monomer conversion during the inhibition period is insignificant. Thereafter, however, the monomer is converted during the polymerization period, a process that is governed by a degenerative transfer mechanism.

Studies of styrene polymerization by RITP have been reported by Tonnar et al.[3] and Shiman et al.[6] It was observed that the mechanism for RITP of styrene differs significantly from that of acrylates and methacrylates. The experimental inhibition times reported were much shorter than the theoretical times. Although it was speculated that the short inhibition period is attributed to the formation of 1,2-diiodoethylbenzene (Scheme 2), which depletes free iodine, no experimental proof has been reported in the literature of this compound being formed during the inhibition period of RITP. This side reaction does not, however, interfere with the formation of iodinated chain transfer agents, as it is reversible and iodine is liberated from the 1,2-diiodoethylbenzene throughout the polymerization.

The main objectives of this work were to prepare polystyrene by RITP in order to investigate the chemical structures of CTAs formed during the inhibition period. The formation of the CTAs was to be followed by ^{1}H NMR and the polymerization products were to be analyzed by SEC, NMR, and MALDI−ToF.

EXPERIMENTAL SECTION

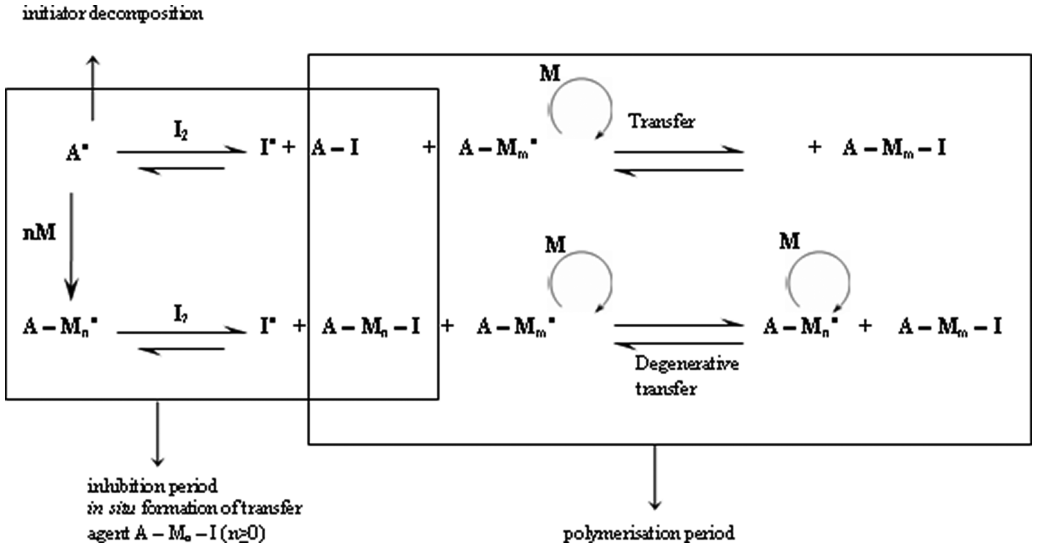
Materials. Styrene (Sigma-Aldrich) was washed with 10% aqueous solution of sodium hydroxide and then washed with distilled, deionized water and dried with anhydrous magnesium sulfate. The monomer was then distilled under reduced pressure and stored at low temperatures. Toluene (Sigma-Aldrich 99%), deuterated toluene (C_7D_8, Sigma-Aldrich 99%), deuterated benzene (C_6D_6, Sigma-Aldrich 99%) and iodine (I_2, ACROS Organics) were used as received. AIBN (Riedel de Haën) was recrystallized from methanol, dried under vacuum and stored at −5 °C.

Polymerization of Styrene. In a typical homopolymerization reaction, styrene (1.00 g, 9.60×10^{-3} mol), toluene (1.25 g, 1.36×10^{-2} mol), AIBN (49.7 mg, 3.03×10^{-4} mol), iodine (45.3 mg, 1.78×10^{-4} mol) and a magnetic stirrer were added into a Schlenk flask and mixed by magnetic stirring. The mixture was then degassed by three successive freeze−pump−thaw cycles and then backfilled with argon.

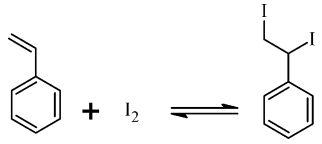
Received: February 27, 2012
Revised: March 8, 2012
Published: March 20, 2012

 © 2012 American Chemical Society dx.doi.org/10.1021/ma3003888 | *Macromolecules* 2012, 45, 2995−3003

Scheme 1. Basic Mechanism of RITP



Scheme 2. Reversible Formation of 1,2-Diiodoethylbenzene



The flask was then immersed in an oil bath that was preheated to 70 °C. The polymerization was carried out with magnetic stirring in the dark. After 24 h, the polymerization was halted by removing the flask from the oil bath and placing the flask in a container of ice. The polymer was dried in a vacuum oven overnight.

***In situ* ^{1}H NMR Monitoring of Styrene Polymerization.** Styrene polymerization was followed by *in situ* ^{1}H NMR at 70 °C in toluene-d_8.

The sample NMR tube was inserted into the NMR spectrometer and a reference spectrum was acquired at 25 °C. The temperature of the NMR spectrometer was then equilibrated at 70 °C for 30 min before the NMR tube was reinserted into the spectrometer. The first spectrum was acquired 8−15 min after the sample was reinserted. Thereafter, spectra were obtained by taking 15 scans every 15 min for 23 h.

In a typical *in situ* ^{1}H NMR polymerization reaction, styrene (2.00 g, 19.2×10^{-3} mol), AIBN (99.5 mg, 6.06×10^{-4} mol), iodine (90.5 mg, 3.57×10^{-4} mol) were weighed carefully and mixed thoroughly in a glass vial. A portion of the mixture (0.25 mL) was introduced into a

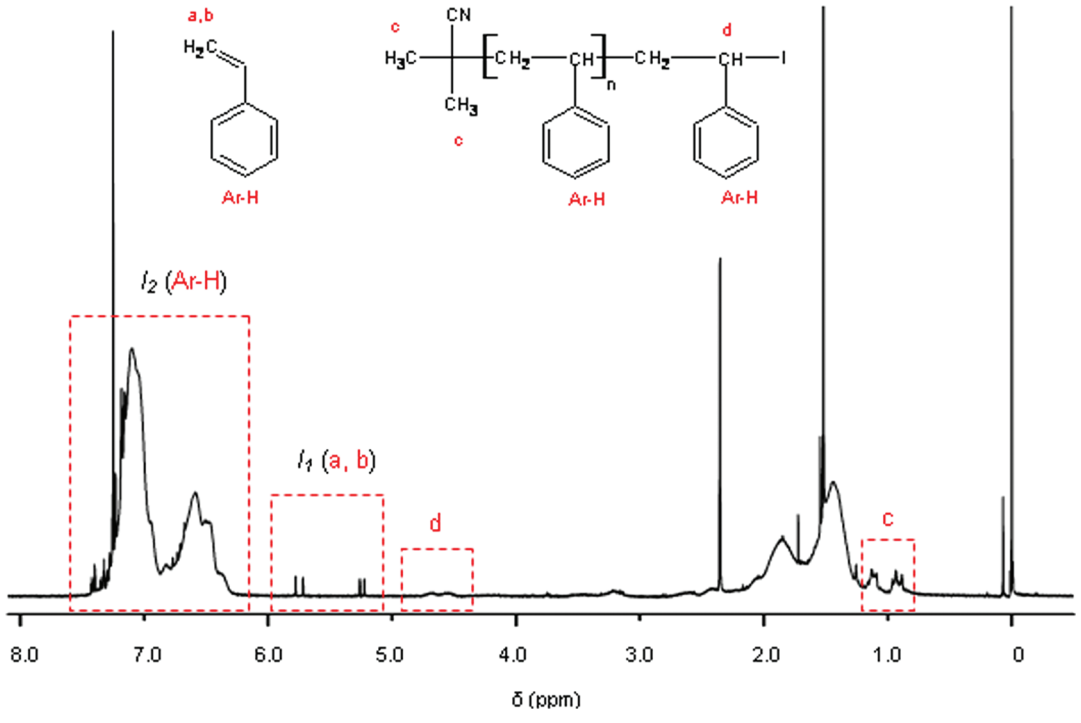


Figure 1. ^{1}H NMR spectrum in $CDCl_3$ of styrene polymerized by RITP at 70 °C ([styrene] = 3.70 M, [toluene] = 5.44 M, [AIBN] = 0.12 M and $[I_2] = 6.86 \times 10^{-2}$ M, conversion = 70%, $M_{n,SEC}$ = 2400 g·mol^{-1}, $M_{n,NMR}$ = 2500 g·mol^{-1}), showing the regions for the integrals I_1 and I_2 respectively.

dx.doi.org/10.1021/ma3003888 | *Macromolecules* 2012, 45, 2995−3003

Table 1. Results of Styrene Polymerization by RITP for 24 h at 70 °C[a]

run	[AIBN]/[I_2]	$M_{n,target}$ (g/mol)	$t_{inh,theory}$ (h)[b]	$t_{inh,exp}$ (h)	convn (%)[c]	$M_{n,theory}$ (g/mol)[d]	$M_{n,SEC}$ (g/mol)[e]	PDI
1	1.5	8000	23	8	63	5100	4600	1.60
2	1.7	1500	14	8	62	900	700	1.53
3	1.7	3000	14	6	70	2150	2400	1.50
4	1.7	5500	14	5	68	3800	3600	1.58
5	1.7	8000	14	4	65	5250	4850	1.74
6	2.0	8000	9	4	72	5700	5300	1.76

[a]Polymerization of styrene ([styrene] = 3.70 M) in toluene ([toluene] = 5.44 M) at 70 °C with AIBN and molecular iodine. [b]Calculated by $t_{inh,theory} = (-\ln((1-[iodine]_0)/f[initiator]_0))/k_d$ where $k_d = 3.71 \times 10^{-5}$ s^{-1} and $f = 0.7$. [c]Determined by ^{1}H NMR in $CDCl_3$ by conversion = $(1 - (I_1/I_2)) \times 100$ where I_1 is the integral of the vinylic protons $((\int CH_2{=}C)/2)$ of styrene at 5.1 and 5.6 ppm, and I_2 is the integral of the aromatic protons $((\int C_6H_5)/5)$ of styrene and polystyrene. [d]Calculated by $M_{n,theory} = ((m_{styrene} \times conversion)/(2n_{iodine})) + M_{chain\ ends}$. [e]Calibrated using polystyrene standard.

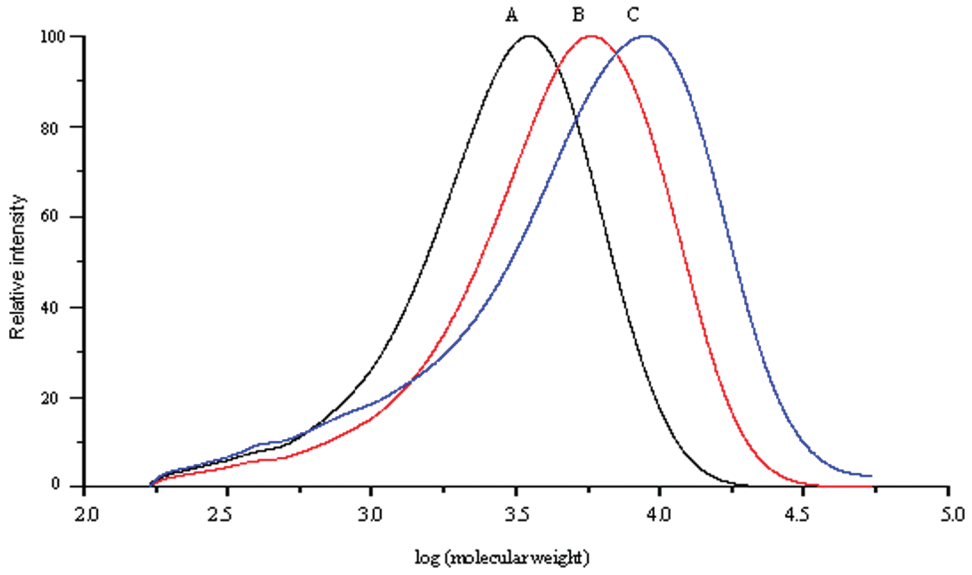


Figure 2. Molecular weight distributions from SEC (RI traces) of polymers prepared by RITP ([styrene] = 3.70 M, [toluene] = 5.44 M) for 24 h at 70 °C: (A) $M_{n,theory}$ = 3000 g·mol^{-1}, [AIBN] = 0.12 M and [I_2] = 6.86 × 10^{-2} M, conversion =70%, $M_{n,SEC}$ = 2400 g·mol^{-1}, PDI = 1.50; (B) $M_{n,theory}$ = 5500 g·mol^{-1}, [AIBN] = 6.16 × 10^{-2} M and [I_2] = 3.63 × 10^{-2} M, conversion =68%, $M_{n,SEC}$ = 3600 g·mol^{-1}, PDI = 1.58; (C) $M_{n,theory}$ = 8000 g·mol^{-1}, [AIBN] = 4.19 × 10^{-2} M and [I_2] = 2.46 × 10^{-2} M, conversion =65%, $M_{n,SEC}$ = 4850 g·mol^{-1}, PDI = 1.74).

J Young NMR tube, followed by the addition of 0.25 mL of toluene-d_8. An internal reference of 20 μL of DMF was inserted into the J Young NMR tube. The sample in the NMR tube was degassed by three successive freeze−pump−thaw cycles and then filled with UHP argon gas.

Analyses. SEC was carried out using a SEC instrument equipped with a Waters 717plus autosampler, Waters 600E system controller and a Waters 610 fluid unit. For detection, a Waters 2414 differential refractometer was used. Two PLgel 5 μm Mixed-C columns and a PLgel 5 μm guard column were used. Polymer samples of 2 mg were dissolved in 2 mL of THF and the sample volume injected into the column was 100 μL, with the oven temperature kept at 30 °C. The eluent that was used was THF (HPLC grade, BHT stabilized) at a flow rate of 1 mL/min. Calibrations were done using narrow polystyrene standards with a molecular range of 800 to 2 × 10^6 g mol^{-1}. Data obtained from SEC were reported as polystyrene equivalents.

The ^{1}H NMR spectra were obtained on a Varian Unity INOVA 400 MHz spectrometer, with a pulse width of 3 μs (40°) and a 4 s acquisition time. The solvent used for crude polystyrene samples was deuterated chloroform ($CDCl_3$), with toluene-d_8 being used for online kinetic ^{1}H NMR experiments. All NMR spectra were processed using ACD Laboratories 10.0 ^{1}H NMR processor. The spectra were phased automatically, whereas baseline correction and integration were done manually. From the processed spectra it was possible to construct concentration profiles relative to an internal DMF reference.

MALDI−ToF analysis was performed using an AximaToF^2 spectrometer (Shimadzu Biotech) equipped with a nitrogen laser (337 nm). The instrument was operating at an accelerating potential of 20 kV. All analyses were carried out in the linear positive mode, with calibrations carried out using a 1450 Da poly(ethylene glycol) (PEG) standard. The mass accuracy of the instrument is ±2 Da. Samples were dissolved in dioxane with a concentration of 2 mg.mL^{-1}. The sample solutions were mixed with a 10 mg mL^{-1} solution of the matrix (dithranol/dioxane) in THF. The salt used to enhance ion formation was copper chloride (CuCl), with a concentration of 2 mg.mL^{-1}. The analyte-to-matrix ratio was 1:2. Here, 1 μL of the mixture was deposited on a stainless steel target, air-dried, and introduced into the spectrometer.

RESULTS AND DISCUSSION

The ^{1}H NMR peaks for AIBN, A−I and A−A were investigated for a solution of AIBN and iodine in deuterated benzene (C_6D_6) at 70 °C. The peak assignments were AIBN (δ = 1.15 ppm), A−I (δ = 1.54 ppm), and A−A (δ = 1.03 ppm), respectively. These assignments are in reasonable agreement with the chemical shifts observed by Lacroix-Desmazes et al.[2] but differ slightly due to NMR analysis operating temperature. The assignments made by Lacroix-Desmazes et al. were made after heating the reaction mixture at 70 °C and

dx.doi.org/10.1021/ma3003888 | Macromolecules 2012, 45, 2995−3003

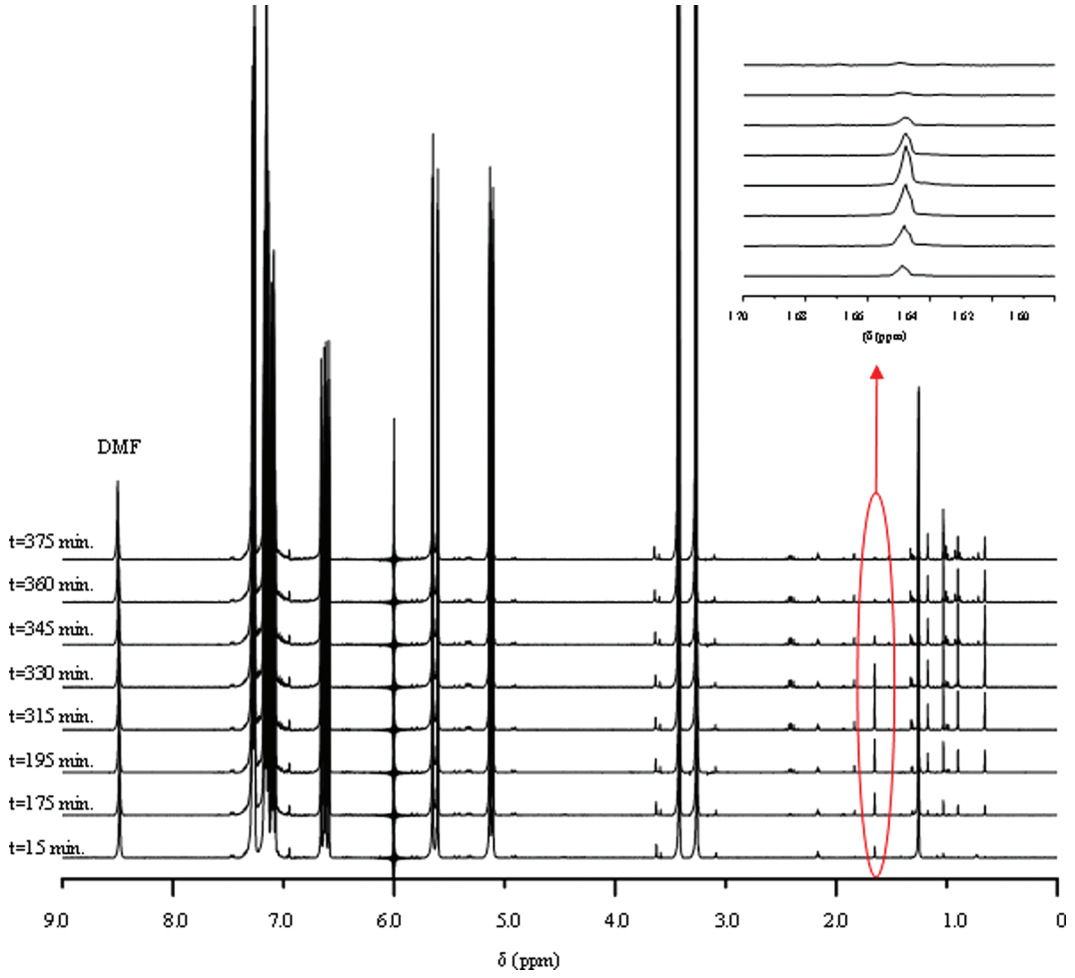


Figure 3. NMR spectrum of reaction medium during RITP of styrene in toluene-d_8 at 70 °C ([styrene] = 4.27 M, [toluene-d_8] = 4.82 M, [AIBN] = 0.13 M and $[I_2] = 7.91 \times 10^{-2}$ M), showing the formation and consumption of the A–I adduct during the inhibition period ($t_{inh,exp} \sim 360$ min).

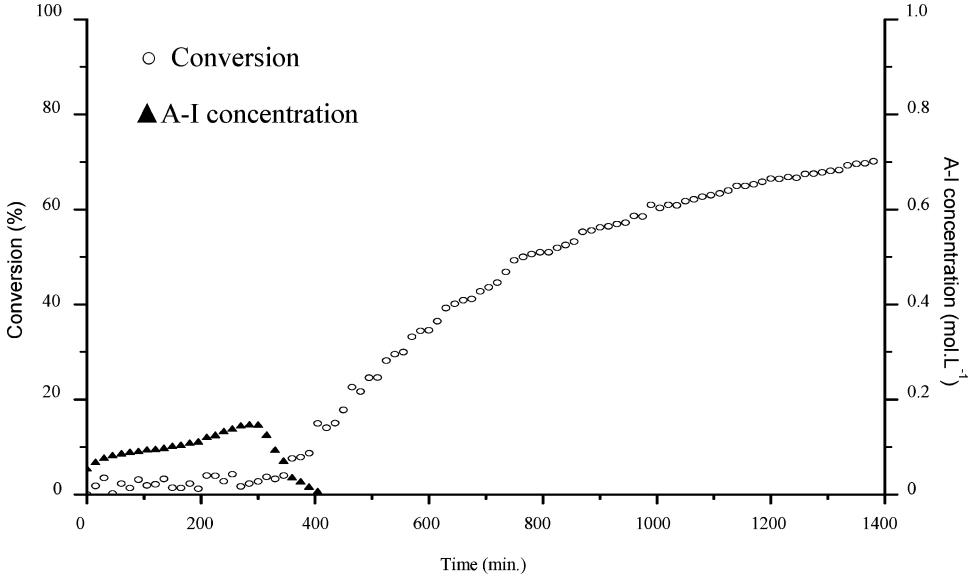
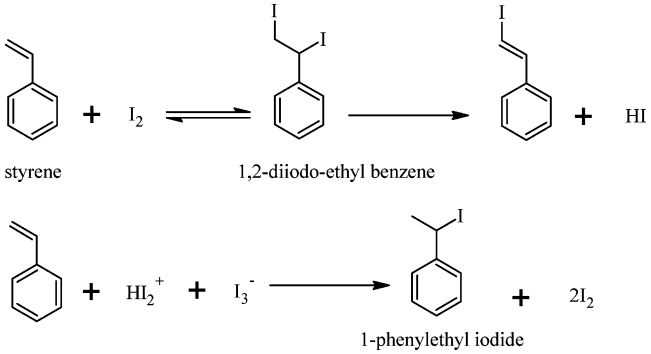


Figure 4. Evolution of styrene conversion and A–I adduct concentration ($t_{inh,exp} \sim 360$ min) as a function of reaction time for the polymerization of styrene by RITP at 70 °C ([styrene] = 4.27 M, [toluene-d_8] = 4.82 M, [AIBN] = 0.13 M, and $[I_2] = 7.91 \times 10^{-2}$ M).

the NMR spectrum measured at room temperature. The assignments made in our study were done with the NMR spectrum measured at 70 °C. The peak assignments change slightly when styrene is added to the reaction mixture: AIBN (δ = 1.25 ppm), A–I (δ = 1.65 ppm), and A–A (δ = 0.90 ppm).

dx.doi.org/10.1021/ma3003888 | *Macromolecules* 2012, 45, 2995–3003

Scheme 3. General Mechanism for the Formation of 1,2-Diiodoethylbenzene and the Subsequent Formation of 1-Phenylethyl Iodide



A study of several alkyl iodides (with a general structure of R−I) used in styrene polymerization is reported in literature by Gaynor et al.[7] Such alkyl iodides include 1-phenylethyl iodide (1-PEI), iodoform, and iodoacetonitrile. The radical formed by the loss of the iodine atom from such CTAs is stabilized by the R group, either by inductive or resonance effects.

In our study, polystyrene was synthesized by RITP at 70 °C, where various [AIBN]/[I_2] ratios were used and molecular weights from 1500−8000 g·mol^{-1} were targeted. The molecular weights and polydispersities of the samples were determined by SEC. The monomer conversion of styrene was determined by ^{1}H NMR analysis of the crude polystyrene samples in deuterated chloroform ($CDCl_3$). Using ^{1}H NMR, the monomer conversion was determined with eq 1

$$\text{conversion} = \left(1 - \frac{I_1}{I_2}\right) \times 100 \tag{1}$$

where I_1 is the integral of the vinylic protons (($\int CH_2{=}C)/2$) of styrene at 5.1 and 5.6 ppm, and I_2 is the integral of the aromatic protons (($\int C_6H_5)/5$) of styrene and the resulting polystyrene (Figure 1).[8] From the conversion the theoretical molecular weight ($M_{n,theory}$) was calculated using eq 2

$$M_{n,theory} = \frac{(m_{styrene} \times \text{conversion})}{(2 \times n_{iodine})} + M_{chain\ ends} \tag{2}$$

where $m_{styrene}$ is the mass of styrene, n_{iodine} is the number of moles of molecular iodine, and $M_{chain\ ends}$ is the combined molecular weight of the cyanoisopropyl and iodine chain ends (195 g·mol^{-1}).[1−3] The results for styrene polymerized by RITP at 70 °C for 24 h are shown in Table 1.

The conversion is not particularly high and is usually in the region of 65%. This may be explained by the low concentration of AIBN near the end of polymerization. This means that there are insufficient numbers of initiator radicals to consume the iodine that is liberated from 1,2-diiodoethylbenzene.[3] The monomer conversion also increases with increasing initiator to iodine ratio. The M_n values calculated from conversion are in reasonable agreement with the values obtained from SEC (Table 1). Figure 2 shows the refractive index (RI) detector traces of runs 3−5 (Table 1).

The distributions are unimodal with some low molecular weight tailing and a shift toward higher molecular weights as would be expected with increasing targeted molecular weights. The PDI values of the polystyrene samples are in an acceptable range (1.5−1.7) for polymers synthesized by an iodine mediated system.[7,9] The relatively low PDI values obtained for the RITP of styrene may be attributed to the formation of 1-PEI during the inhibition period, since this transfer agent has been reported to gives rise to low PDI values for degenerative transfer mediated polymerization of styrene.[7] In addition to this, the polymerization of styrene is quite slow, which leads to low PDI values.[10]

Kinetic experiments followed by ^{1}H NMR were run to investigate the mechanism of RITP of styrene by examining the monomer conversion as well as the inhibition period and the evolution of chain transfer agents therein. The results in Table 1 show the experimental inhibition times ($t_{inh,exp}$) as well as the theoretical inhibition times ($t_{inh,theory}$) for the various experiments. The $t_{inh,theory}$ was calculated using eq 3

$$t_{inh,theory} = \left(-\ln \frac{1 - [\text{iodine}]_0}{f[\text{initiator}]_0}\right)/k_d \tag{3}$$

where $[\text{iodine}]_0$ is the initial concentration of molecular iodine in the reaction medium, f is the initiator efficiency with a value of 0.7,[1,11] $[\text{initiator}]_0$ is the initial concentration of initiator (AIBN), and k_d is its dissociation constant.

During the inhibition period, the initiator decomposes to form radicals that react with molecular iodine to generate CTAs. The end of the inhibition period is marked visually by the change of color of the mixture from brown to colorless. This change in color is due to the complete consumption of iodine. According to the RITP mechanism (Scheme 1), CTAs are formed and consumed during the inhibition period, which is composed of two stages. In the first stage, iodine is consumed to form the A−I adduct, while in the second stage, the A−I adduct is consumed to form oligomers.[1] The decrease in A−I adduct concentration is indicative that the A−I adduct forms oligomers, and polymerization commences once all the A−I adduct has been consumed. The evolution of the A−I adduct over time is shown in Figure 3.

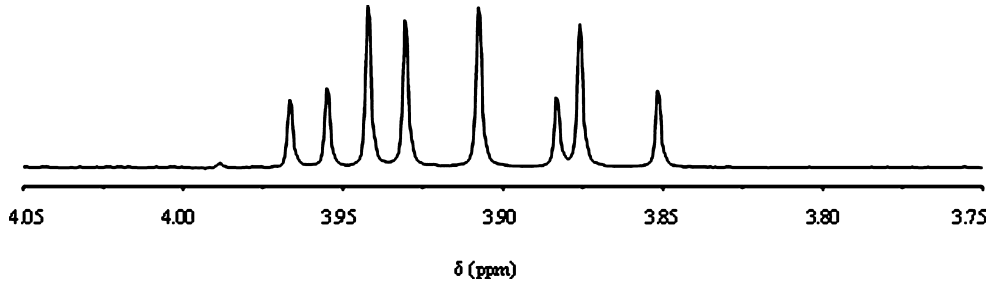


Figure 5. Enlarged portions of the ^{1}H NMR spectrum of 1,2-diiodoethylbenzene formed from a mixture of styrene and iodine in $CDCl_3$, showing the peaks for aliphatic protons of 1,2-diiodoethylbenzene.

dx.doi.org/10.1021/ma3003888 | Macromolecules 2012, 45, 2995−3003

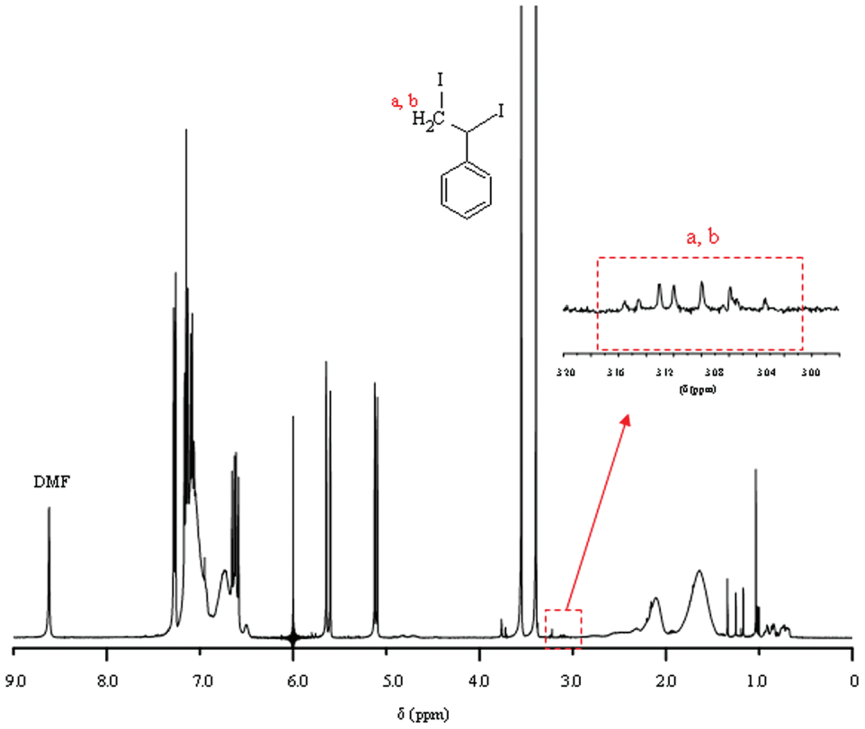


Figure 6. ^{1}H NMR spectrum of styrene polymerized by RITP in toluene-d_8 at 70 °C ([styrene] = 3.70 M, [toluene] = 5.44 M, [AIBN] = 0.12 M and $[I_2] = 6.86 \times 10^{-2}$ M, conversion = 70%, $M_{n,SEC}$ = 2400 g·mol^{-1}, PDI = 1.50), showing the peaks for aliphatic protons of 1,2-diiodoethylbenzene.

The theoretical inhibition time for acrylates and methacrylates is dependent on the temperature and the ratio of initiator to molecular iodine, while being independent of the targeted molecular weight.[1−3] However, for styrene polymerized by RITP, $t_{inh,exp}$ is dependent on the targeted molecular weight.[3] From Table 1 it is evident that $t_{inh,exp}$ is much shorter than that of $t_{inh,theory}$. It can also be seen that $t_{inh,exp}$ decreases with increasing targeted molecular weight.

The inhibition period can be seen clearly by a conversion versus time profile, as shown in Figure 4. The plot shows that the A−I adduct concentration increases over time to a maximum and then decreases. Upon complete consumption of the A−I adduct, one can see the onset of polymerization. Throughout the polymerization period, the monomer is being converted, yet, toward the higher end of monomer conversion (>50%) there is a downward curvature ($t \sim 700$ min). This may indicate a reduction in the rate of polymerization. The half-life ($t_{1/2}$) of AIBN at 70 °C is about 5 h and the reason for this decrease in the rate of polymerization may be due to the low concentration of AIBN at the end of polymerization. This implies that there are insufficient initiator radicals to consume the iodine that is liberated from 1,2-diiodoethylbenzene, hence the limited monomer conversion.[3]

The shorter experimental inhibition time compared to the theoretical can be explained by the complex chemistry between iodine and styrene.[4,5] The most notable reactions between iodine and styrene are as follows: (1) cationic polymerization of styrene by iodine, (2) reversible formation of 1,2-diiodoethylbenzene, and (3) formation of a charge transfer complex. Tonnar et al.[3] suggested that the inhibition time for styrene polymerized by RITP is shortened due to the formation of 1,2-diiodoethylbenzene although this has never been proven experimentally (Scheme 3). When styrene and iodine are reacted with one another, a colorless compound is formed. This colorless compound is 1,2-diiodoethylbenzene. Subsequently, hydrogen iodide is generated and an equilibrium reaction with free iodine gives I_3^- and HI_2^+ respectively. The cation (HI_2^+) is added to the monomer to generate 1-PEI, a commonly used chain transfer agent in ITP.[5,12]

In order to identify 1,2-diiodoethylbenzene in RITP, the ^{1}H NMR spectrum of a mixture of styrene and iodine in $CDCl_3$ (Figure 5) was studied. The proton signals for 1,2-diiodoethylbenzene in this mixture were observed around 3.85−3.97 ppm. The peculiar multiplicity of the CH_2 group is explained as follows; the CH group of 1,2-diiodoethylbenzene is an asymmetric center and thus the CH_2 protons are not in the same chemical environment. The CH_2 protons couple with one another resulting in two doublets. They also couple with the CH proton and the number of signals is doubled, resulting in a total number of eight signals. When an RITP experiment is run at 70 °C using AIBN, iodine and styrene in toluene-d_8, the peak positions are shifted to 3.04−3.16 ppm (Figure 6). Still, the same multiplicity is observed confirming that 1,2-diiodoethylbenzene is formed in the course of the styrene polymerization.

Comparable to 1,2-diiodoethylbenzene is the compound 2-iodo-1-phenylethanol, whose proton signals are observed at 3.25−3.45.[13,14] The presence of 1,2-diiodoethylbenzene in the reaction medium suggests that there should also be 1-PEI (Scheme 3). It is assumed that 1-PEI is a chain transfer agent in RITP of styrene. Therefore, kinetic ^{1}H NMR spectra were examined in order to identify the proton signals of 1-PEI, as well as the subsequent phenylethyl end group protons that could transpire. Figure 7 is a ^{1}H NMR spectrum of styrene polymerized by RITP at 70 °C, showing the proton signals for the methyl protons of 1-PEI and those of the phenylethyl end

dx.doi.org/10.1021/ma3003888 | Macromolecules 2012, 45, 2995−3003

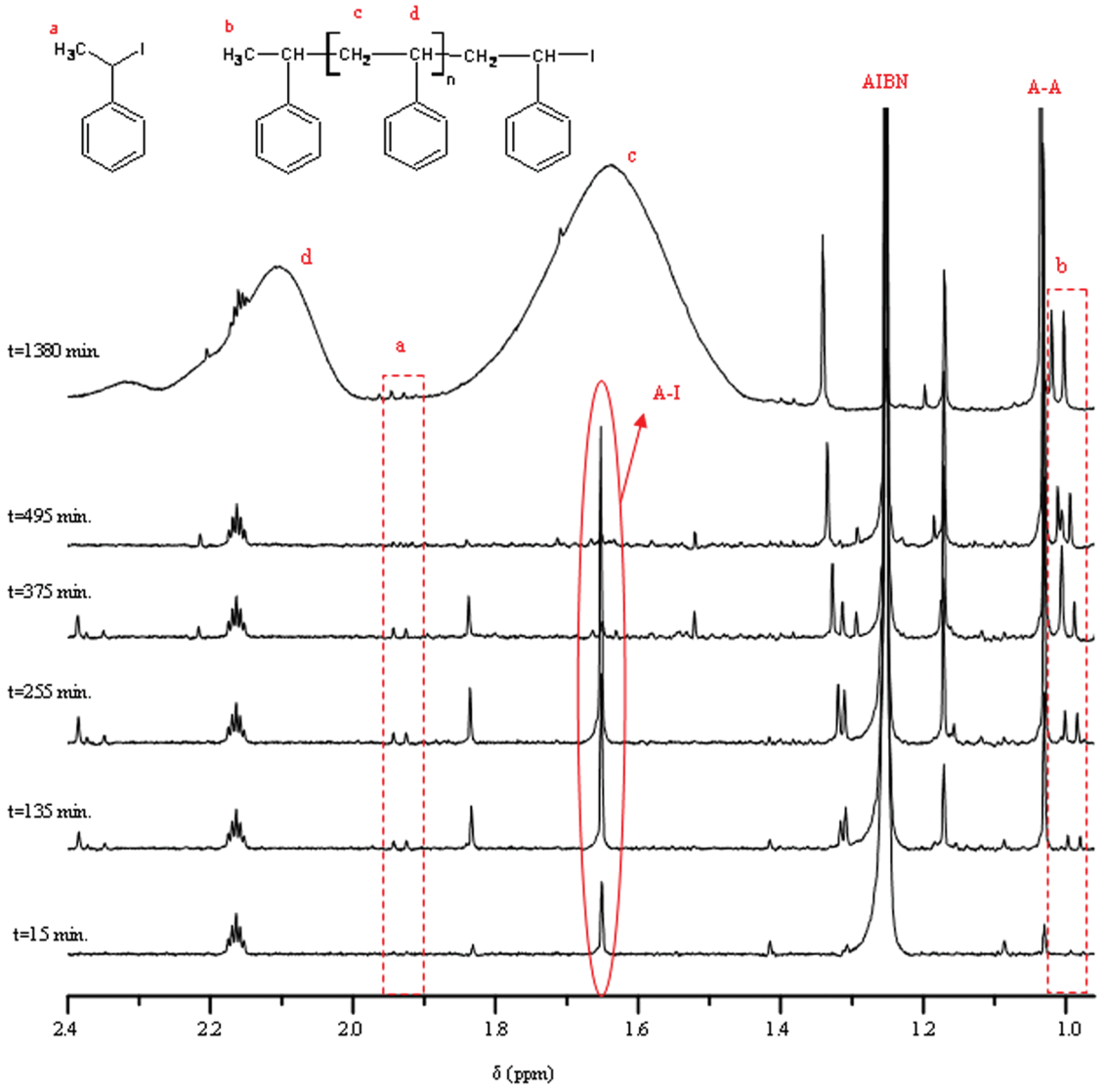


Figure 7. An enlarged portion (0.95–2.05 ppm) of the ^{1}H NMR spectrum in toluene-d$_8$ of styrene polymerized by RITP at 70 °C [styrene] = 4.27 M, [toluene-d_8] = 4.82 M, [AIBN] = 0.13 M and [I_2] = 7.91 × 10^{-2} M), showing the signals for the methyl protons of 1-PEI at 1.94 ppm and for the polymer phenylethyl end group at 0.97 ppm.

group of the polymer. The methyl proton signals in ^{1}H NMR were observed at 1.94 ppm, in reasonable agreement with Gaynor et al.[7] who observed a doublet at 2.2 ppm after isolating 1-PEI. The phenylethyl end group proton signals of the polymer were observed at 0.97 ppm, which is in good agreement with the peak assignments observed by Goto et al.[15]

1-PEI could possibly originate from the autoinitiation of styrene, which entails the formation of the Diels–Alder dimer 1-phenyl-1,2,3,4-tetrahydronaphthalene, followed by the transfer of a hydrogen atom to form a phenylethyl and 1-phenyltetralyl radical.[16−18] However, the ^{1}H NMR spectra for styrene polymerized by RITP showed no proton signals for the 1-phenyltetralyl radical. The use of MALDI–ToF to characterize polystyrene synthesized by various CRP methods has been reported in literature.[19] MALDI–ToF analysis, run in linear mode, was used to substantiate the structures identified from ^{1}H NMR spectra of polystyrene synthesized by RITP. An enlarged portion of a typical MALDI–ToF spectrum is shown in Figure 8. From the spectrum, several populations were identified and shown in Scheme 4 and Figure 8, respectively.

The terminating ends of these structures would be expected to be iodinated. However, during MALDI–ToF analysis the terminating end is fragmented by the cation of the salt. Also, the C–I bond in PS synthesized by RITP is weak and can fragment easily. Therefore, the expected iodine terminated PS was observed in the 1-H NMR spectra, whereas unsaturated structures are observed in in MALDI–ToF.[3]

The major population of polystyrene oligomers is separated by a mass increment of 104 Da, corresponding to the monomer repeat unit. The structures identified in MALDI–ToF are listed in Table 2 with their respective predicted masses. The major population, which appears, e.g., at 2008.59 Da (Table 2), is the structure A–M_{m-1}–CH═C(Ph)H (Scheme 4). A 1-H NMR chemical shift for the unsaturated chain end would be expected at around 6.4–6.6 ppm. However, since the signal was not observed in ^{1}H NMR, the structure is assumed to form during

dx.doi.org/10.1021/ma3003888 | *Macromolecules* 2012, 45, 2995–3003

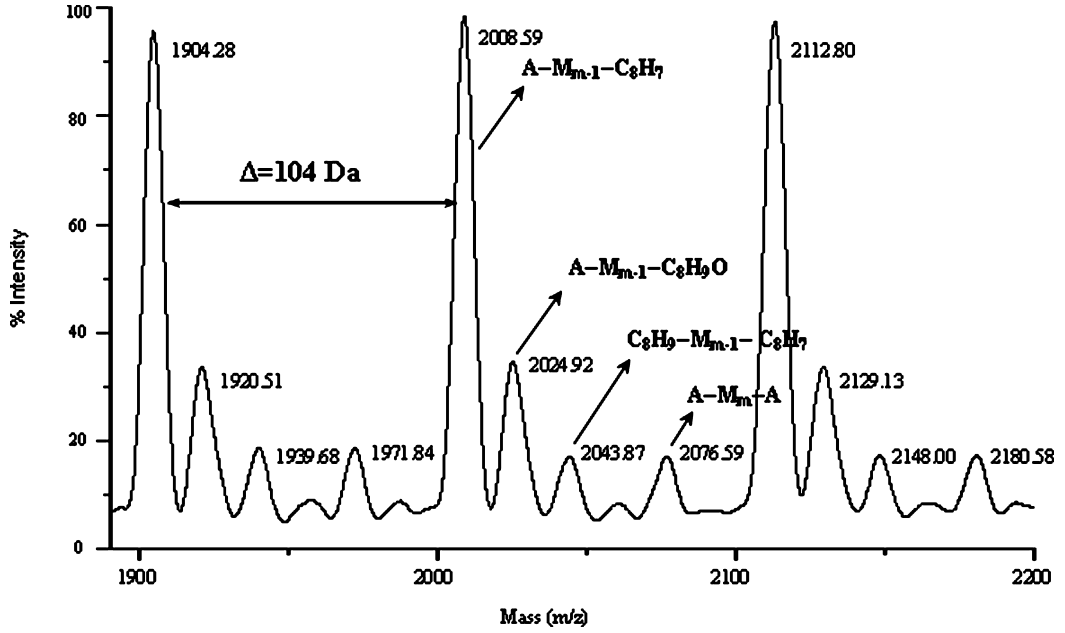


Figure 8. Enlarged portion of the MALDI–ToF spectrum (linear mode) of PS synthesized by RITP at 70 °C for 24 h ([styrene] = 3.70 M, [toluene] = 5.44 M, [AIBN] = 0.12 M and $[I_2] = 6.86 \times 10^{-2}$ M, conversion =70%, $M_{n,SEC}$ = 2400 g·mol^{-1}, $M_{n,NMR}$ = 2500 g·mol^{-1}).

Scheme 4. Structures Identified from the MALDI–ToF Analysis of Polystyrene Synthesised by RITP at 70°C

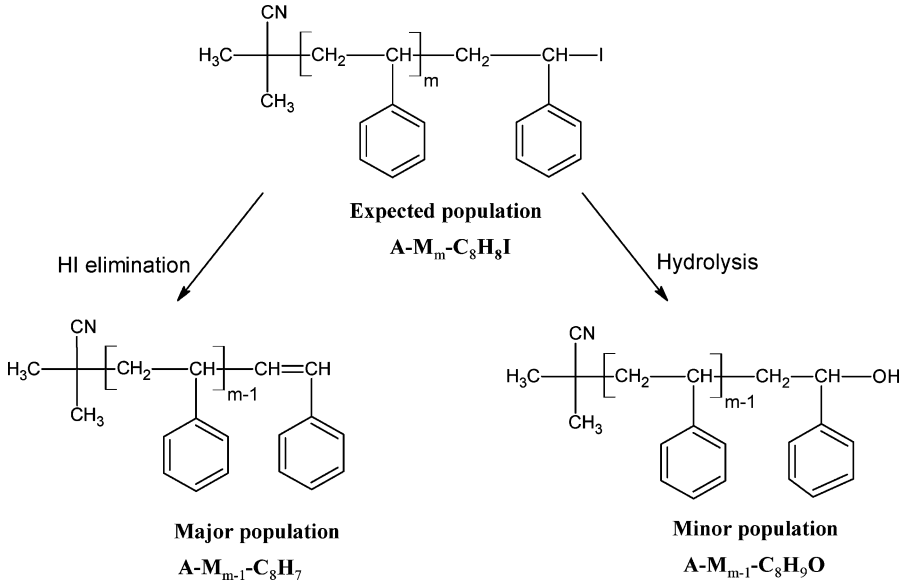


Table 2. Peak Assignments for MALDI–ToF Analysis (Linear Mode) of Styrene Polymerized by RITP for 24 h at 70°C in Toluene

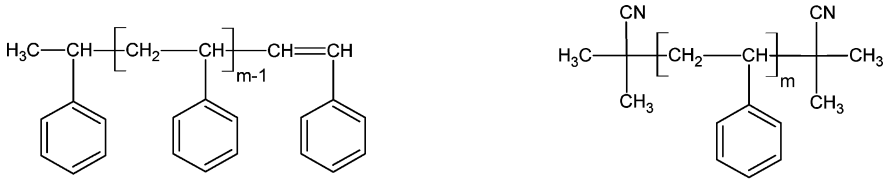
structure	m	experimental mass $(m/z)^a$	theoretical mass $(m/z)^b$
A–M_{m-1}–C_8H_7, –HI (Cu^+)	17	2008.59	2005.10
A–M_{m-1}–C_8H_9O, –HI (Cu^+)	17	2024.92	2023.11
C_8H_9–M_{m-1}–C_8H_7, –HI (Cu^+)	17	2043.87	2042.12
A–M_m–A (Cu^+)	18	2076.59	2074.16

MALDI–ToF analysis where HI is eliminated from A–M_m–I due to Cu^+. The unsaturated population has been observed for the RITP[3] of styrene as well as for metal–catalyzed CRP of styrene.[20]

A minor population (Scheme 4) is observed at 2024.92 Da. A signal for the hydroxyl end group of this population is not observed in ^{1}H NMR, and therefore might form due to hydrolysis of the halogen end group during MALDI ToF analysis.

A second minor population is observed at 2043.87 Da (Table 2 and Figure 9). 1,2-diiodoethylbenzene generates 1-PEI, a good transfer agent for CRP. The minor population contains a phenylethyl end group (C_8H_9–M_{m-1}–C_8H_7), which originates from the reaction between styrene and the alkyl iodide chain transfer agent.[7,15] As was the case with the major population, this structure forms during MALDI–ToF analysis due to the elimination of HI. Another third minor population, appearing at 2076.59 Da, is that of a direct initiation and termination reaction (combination of the initiator and styrene) to form the structure A–M_m–A. These structures have been reported for iodine mediated polymerization.[7,8,15,21]

dx.doi.org/10.1021/ma3003888 | *Macromolecules* 2012, 45, 2995–3003



Minor population

C_8H_9-M_{m-1}-C_8H_7

Minor population

A-M_m-A

Figure 9. Structures identified in MALDI–ToF analysis for the minor populations that do not derive from the A–M_m–I population.

■ CONCLUSIONS

The mechanism of styrene polymerization by RITP is significantly different to that of acrylates and methacrylates.[1,2] The inhibition period is the feature of its mechanism that makes it so different. Throughout the inhibition period, iodine reacts with initiator radicals to form chain transfer agents (A–I and A–M_n–I adducts). Iodine not only reacts with the initiator, but also reacts with styrene to form 1,2-diiodoethylbenzene. The inhibition period is significantly reduced due this side reaction. For RITP, this compound has not been reported. We found evidence of 1,2-diiodoethylbenzene in ^{1}H NMR, which consequently reacted with styrene to form a chain transfer agent, 1-PEI. This compound, commonly used in degenerative transfer mediated polymerization,[7] has not been identified in literature for RITP. The evolution of 1-PEI was followed by *in situ* ^{1}H NMR and the resulting polymer structure containing phenylethyl end group was confirmed by MALDI–ToF analysis. Although iodine is liberated from 1,2-diiodoethylbenzene throughout the polymerization period of RITP, the monomer conversion is often limited (~65%) due to the shortage of initiator radicals toward the end of polymerization.

■ AUTHOR INFORMATION

Corresponding Author

*E-mail: hpasch@sun.ac.za.

Notes

The authors declare no competing financial interest.

■ ACKNOWLEDGMENTS

Mpact Company (South Africa) is acknowledged for funding this research. Lebohang Hlalele is acknowledged for his assistance and advice regarding *in situ* ^{1}H NMR. Karsten Rode (Deutsches Kunststoff-Institut) is acknowledged for performing the MALDI–ToF analysis.

■ REFERENCES

(1) Boyer, C.; Lacroix-Desmazes, P.; Robin, J.-J.; Boutevin, B. *Macromolecules* **2006**, *39*, 4044–4053.
(2) Lacroix-Desmazes, P.; Severac, R.; Boutevin, B. *Macromolecules* **2005**, *38*, 6299–6309.
(3) Tonnar, J.; Severac, R.; Lacroix-Desmazes, P.; Boutevin, B. *Polym. Prepr.* **2008**, *49*, 68–69.
(4) Fraenkel, G.; Bartlett, P. D. *J. Am. Chem. Soc.* **1959**, *81*, 5582–5590.
(5) Trifan, D. S.; Bartlett, P. D. *J. Am. Chem. Soc.* **1959**, *81*, 5573–5581.
(6) Shiman, D. I.; Kostyuk, S. V.; Gaponik, L. V.; Kaputskii, F. N. *Russ. J. Appl. Chem.* **2010**, *83*, 2028–2034.
(7) Gaynor, S. G.; Wang, J.-S.; Matyjaszewski, K. *Macromolecules* **1995**, *28*, 8051–8056.
(8) Valade, D.; Boyer, C.; Ameduri, B.; Boutevin, B. *Macromolecules* **2006**, *39*, 8639–8651.
(9) David, G.; Boyer, C.; Tonnar, J.; Ameduri, B.; Lacroix-Desmazes, P.; Boutevin, B. *Chem. Rev.* **2006**, *106*, 3936–3962.
(10) Matyjaszewski, K. *Curr. Opin. Solid State Mater. Sci.* **1996**, *1*, 769–776.
(11) Moad, G.; Solomon, D. H.; Johns, S. R.; Willing, R. I. *Macromolecules* **1984**, *17*, 1094–1099.
(12) Maschio, G.; Cerrai, P.; Giusti, R. *Polym. Bull.* **1982**, *8*, 147–153.
(13) Cerritelli, S.; Chiarini, M.; Cerichelli, G.; Capone, M.; Marsili, M. *Eur. J. Org. Chem.* **2004**, *3*, 623–630.
(14) Kotsuki, H.; Shimanouchi, T.; Ohshima, R.; Fujiwara, S. *Tetrahedron* **1998**, *54*, 2709–2722.
(15) Goto, A.; Ohno, K.; Fukuda, T. *Macromolecules* **1998**, *31*, 2809–2814.
(16) Matyjaszewski, K. *Controlled/Living Radical Polymerization: Progress in ATRP, NMP, and RAFT*; ACS Symposium Series 768; American Chemical Society: Washington, DC, 2000; pp 122–123.
(17) Pryor, W. A.; Coco, J. H. *Macromolecules* **1970**, *3*, 500–508.
(18) Zammit, M. D.; Davis, T. P.; Haddleton, D. M.; Suddaby, K. G. *Macromolecules* **1997**, *30*, 1915–1920.
(19) Ladaviere, C.; Lacroix-Desmazes, P.; Delolme, F. *Macromolecules* **2009**, *42*, 70–84.
(20) Nonaka, H.; Ouchi, M.; Kamigaito, M.; Sawamoto, M. *Macromolecules* **2001**, *34*, 2083–2088.
(21) Lansalot, M.; Farcet, C.; Charleux, B.; Vairon, J.-P. *Macromolecules* **1999**, *32*, 7354–7360.

Macromolecules

Article

pubs.acs.org/Macromolecules

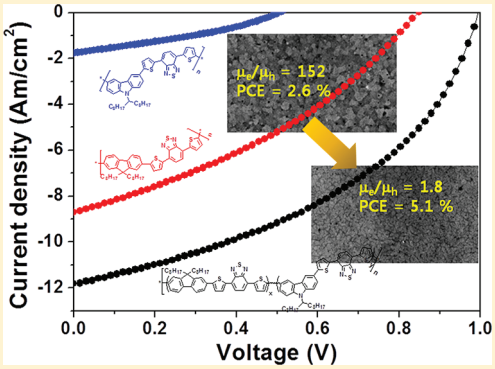
3,6-Carbazole Incorporated into Poly[9,9-dioctylfluorene-*alt*-(bisthienyl)benzothiadiazole]s Improving the Power Conversion Efficiency

Yuanhe Fu,[†] Hyojung Cha,[†] Gang-Young Lee, Byung Joon Moon, Chan Eon Park, and Taiho Park*

Department of Chemical Engineering, Pohang University of Science and Technology, San31, Nam-gu, Pohang, Gyeongbuk, 790-780, Korea

Supporting Information

ABSTRACT: A novel concept of D−A-type copolymers based on fluorene polymer incorporated with 3,6-carbazole unit enhances the device performance for organic photovoltaic cells. **P($F_{45}C_5$-DTBT)**, incorporating 5 mol % 3,6-carbazole into **P(2,7F-DTBT)**, shows an almost 2-fold improvement (5.1%) in power conversion efficiency relative to **P(2,7F-DTBT)** (2.6%). This results is ascribed to the good balance between electron and hole mobilities in the devices ($\mu_e/\mu_h \sim 1.8$ for **P($F_{45}C_5$-DTBT)** vs 152 for **P(2,7F-DTBT)**), and the formation of a nanoscale morphology in the blend of the copolymer and [6,6]-phenyl C71-butyric acid methyl ester ($PC_{71}BM$).



INTRODUCTION

Organic photovoltaic solar cells (OPVs) have been under development for a couple of decades in an effort to capitalize on their low cost, flexibility, tunability with respect to light-harvesting capabilities, lightweight properties, and large-area processability.[1] OPVs could be fabricated from a blend of photoactive conducting polymers and fullerene derivatives, forming bulk heterojunctions.[1,2] Much effort has been applied toward developing a variety of photoactive conducting polymers.[3] Among such polymers, electron donor− (D−) electron acceptor (A) type copolymers show promise and are widely used for harvesting solar energy over a broad spectral range.[4] For instance, poly[4,4-bis(2-ethylhexyl)dithieno(3,2-*b*:2′,3′-*d*)silole-*alt*-*N*-octylthieno(3,4-*c*)pyrrole-4,6-dione],[3a] poly[benzo(1,2-*b*:4,5-*b*′)dithiophene-*alt*-5,6-difluoro-4,7-di-thien-2-yl-2,1,3-benzothiadiazole (PBnDTDTffBT),[3b] poly[4,8-bis-substituted-benzo(1,2-*b*:4,5-*b*′)dithiophene-2,6-diyl-*alt*-4-substituted-thieno(3,4-b)thiophene-2,6-diyl] (PBDTTT),[5] and its fluorinated polymer (PBDTTT-CF)[5] exhibited power conversion efficiencies (PCEs) in the range 7.2−7.7%. An important consideration for developing novel copolymers is cost. With that in mind, easy large-scale synthetic approaches that rely on low-cost materials provide the most attractive commercial opportunities and are, therefore, in high demand.

Dioctylfluorene 2,7-diborate (**1**) is an easily scalable fused-aromatic monomer and has been widely investigated for use in organic light emitting diodes (OLEDs) and organic field effect transistors (OFETs).[6] D−A copolymers employing 2,7-fluorene, poly[9′,9′-dioctyl-2,7-fluorene-*alt*-5,5-(4′,7′-di-2-thien-yl-2′,1′,3′-benzothiadiazole)] (**P(2,7F-DTBT)**) have been used in OPVs, yielding PCEs of 0.75%, which can be improved up to 2.84% by optimizing the film morphology.[7] The short-circuit current density (J_{SC}) can be influenced by several parameters, including the molecular weight of the copolymer, overlap between the absorption spectrum and the solar illumination spectrum, the exciton dissociation rate, the film morphology, and the charge carrier mobility. More importantly, the hole ($\mu_{h,blend}$) and electron ($\mu_{e,blend}$) mobilities in a blend should be well balanced to promote the continuous generation of electrons without recombination reactions or saturation of charges.[8] Apart from the device structures and fabrication processes, an intrinsic limitation of **P(2,7F-DTBT)** is its low hole mobility, 2.7×10^{-6} $cm^2 V^{-1} s^{-1}$, measured using the space charge limited current (SCLC) method[9] (see Table 1). One method for improving Jsc is to increase the hole mobility ($\mu_{h,polymer}$) of **P(2,7F-DTBT)**, leading to a good balance between $\mu_{e,blend}$ and $\mu_{h,blend}$ in a device (e.g., $\mu_e/\mu_h \sim 1$).

Recently, we reported the synthesis of a series of copolymers **P(F_xC_y-DTBT)** prepared from a Suzuki condensation polymerization of fluorene 2,7-diborate, carbazole 3,6-diborate and bis(bromothienyl)benzothiadiazole as shown in Figure 1a. The copolymers included conjugation breaks to the 3,6-linkages in the resulting polymers.[10] As a result, the polymers showed a highly coplanar structure that formed strong intramolecular charge complexes with strong $\pi-\pi$ stacking between conjugation breaks. Thus, inclusion of conjugation breaks in

Received: February 3, 2012
Revised: March 8, 2012
Published: March 23, 2012

 © 2012 American Chemical Society dx.doi.org/10.1021/ma3002438 | *Macromolecules* 2012, 45, 3004−3009

Table 1. Summary of GPC, Spectroscopic, and Hole Mobility Data for the Copolymers[a]

device	$M_n/10^3$ (g/mol)[b]	Tg (°C)[c]	ε_{abs} (dm^3 mol^{-1}cm^{-1})[d]	λ_{max} (nm)[e]	E_{opt} (eV)[f]	HOMO (eV)[g]	$\mu_h/10^{-6}$ (cm^2/(V s))[h]
P(2,7F-DTBT)	18.4(2.2)	113	38 000	564	1.92	−5.50	2.7
P($F_{49}C_1$-DTBT)	11.4(3.8)	119	37 800	558	1.89	−5.56	3.5
P($F_{45}C_5$-DTBT)	14.5(2.9)	120	37 000	549	1.88	−5.51	4.1
P($F_{40}C_{10}$-DTBT)	8.3(1.5)	122	33 300	559	1.88	−5.50	4.3
P(3,6C-DTBT)	4.1(1.1)	161	22 000	551	1.85	−5.18	12.0

[a]Data for the two control polymers [**P(2,7F-DTBT)** and **P(3,6C-DTBT)**], and **P($F_{45}C_5$-DTBT)** were taken from our previous reports[10,11] and **P($F_{49}C_1$-DTBT)** and **P($F_{40}C_{10}$-DTBT)** were synthesized and characterized in this work (see Figures S1 and S2, Supporting Information, for the DSC thermograms and cyclic voltamograms). [b]Number-average molecular weight determined by GPC in chloroform using polystyrene standards. The polydispersity index (M_w/M_n) is given in parentheses. [d]Absorption coefficient measured in a $CHCl_3$ solution (dm^3 mol^{-1}cm^{-1}). [c]DSC curves were in the Supporting Information (Figure S1). [e]Absorption maxima from the intramolecular charge complexes in the film state. [f]Optical band gap in a film. [g]Estimated in the film state (Figure S2, Supporting Information). [h]Extracted and calculated from space charge limited current (SCLC) measurements in hole-only devices.

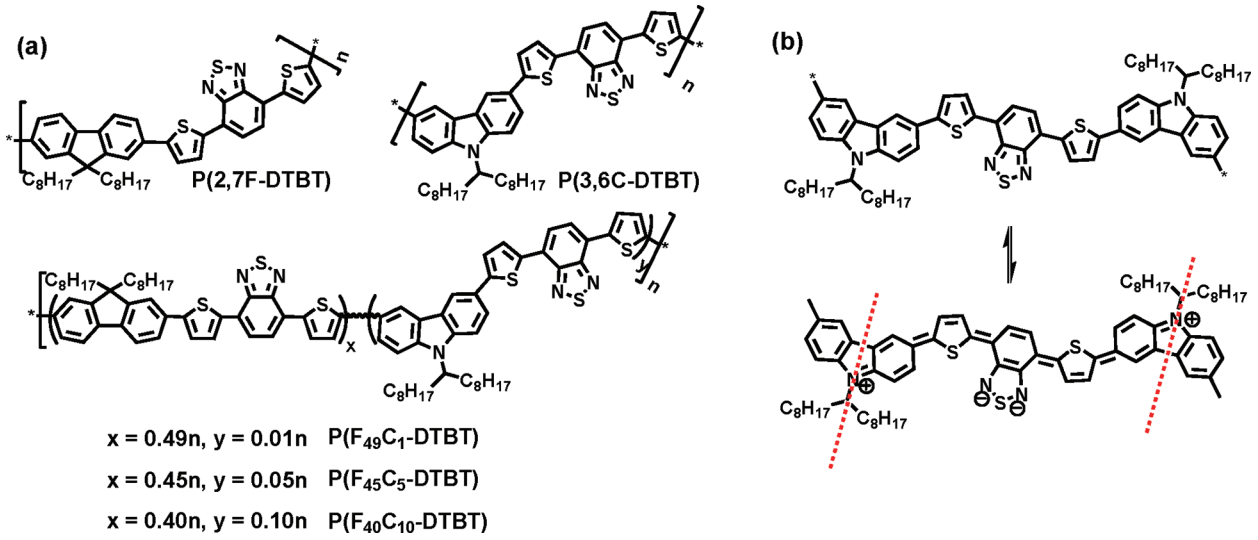


Figure 1. (a) Chemical structures of **P(2,7F-DTBT)**, **P(3,6C-DTBT)**, **P($F_{49}C_1$-DTBT)**, **P($F_{45}C_5$-DTBT)**, and **P($F_{40}C_{10}$-DTBT)**. (b) Equilibria between the aromatic structure and the quinoid structure in **P(3,6C-DTBT)**. The dotted line indicates a conjugation break.

the **P(2,7F-DTBT)** structure improved the hole mobility and $\pi-\pi$ stacking between copolymer chains.[11]

Herein, we report a novel concept to enhance the photovoltaic performance of D−A-type copolymers prepared from easily scalable fused-aromatic monomers (e.g., octylfluorene 2,7-diborate). **P(F_xC_y-DTBT)**, incorporating y mol % 3,6-carbazole into **P(2,7F-DTBT)**, shows a great improvement in PCE relative to **P(2,7F-DTBT)**, due to the good balance between electron and hole mobilities in the devices (e.g., $\mu_e/\mu_h \sim 1.8$ for **P($F_{45}C_5$-DTBT)** and **P($F_{45}C_5$-DTBT)**, vs 152 for **P(2,7F-DTBT)**) and the formation of a nanoscale morphology in the blend of the copolymer and [6,6]-phenyl C71-butyric acid methyl ester ($PC_{71}BM$).

The balance between carrier generation by extraction and carrier losses by recombination leads to a distinct optimum in the carrier mobility with regard to the efficiency of organic solar cells.[12] We have shown that the maximum performance of organic solar cells is governed by the balance between transport and recombination of charge carriers through incorporating a small amount of 3,6-carbazole moiety into **P(2,7F-DTBT)**.

EXPERIMENTAL SECTION

Materials. All chemicals were purchased from Sigma-Aldrich Co, Junsei Co and used without further purification. 2,7-Bis(4′,4′,5′,5′-tetramethyl-1′,3′,2′-dioxaborolan-2′-yl)-9,9-dioctylfluorene and 4,7-bis-(5-bromo-2-thienyl)-2,1,3-benzothiadiazole (**DTBT**) were prepared according to the literature.[13] 3,6-bis(4′,4′,5′,5′-tetramethyl-1′3′2′-dioxaborolan-2′-yl)-*N*-9″-heptadecanylcarbazole was synthesized following the same procedure as we previously reported.[2] Preparation of **P(2,7F-DTBT)**, **P(3,6C-DTBT)**, **P($F_{45}C_5$-DTBT)** were described in our previous reports.[10,11]

Instrumentation. Microwave irradiation experiments were performed using "Monowave 300" single-mode microwave reactor with a maximum of 850 W magnetron output power. ^{1}H and ^{13}C NMR spectra were recorded on a Bruker BioSpin AG system operated at 400 MHz using tetramethylsilane (TMS; $\delta = 0$) as internal standard. Number−average (M_n) and weight-average (M_w) molecular weights were determined by gel permeation chromatography (GPC) using the Shimadzu LC solution, chloroform as the eluent with a flow rate of 1.0 mL/min, and polystyrenes as standards to calibrate. UV−vis absorption and photoluminescence spectra were obtained using a Carry 5000 UV−vis−near-IR double beam spectrophotometer and FR 650, JASCO spectrophotometer, respectively. Cyclic voltammetry (CV) was performed using a PowerLab/AD instrument model system in 0.1 M solution of tetrabutylammonium hexafluorophospate (Bu_4NPF_6) in anhydrous acetonitrile as supporting electrolyte at a scan rate of 50 mV s^{-1}. A glassy carbon disk (~0.05 cm^2) coated with a thin polymer film, an $Ag/AgNO_3$ electrode, and a platinum wire were used as working electrode, reference electrode, and counter electrode, respectively. Differential scanning calorimetric (DSC) measurements of the copolymers were performed using a Seiko DSC 220 CU instrument under a nitrogen atmosphere at a heating cooling rate of 10 °C/min. The atomic force microscope (AFM) (Multimode IIIa, Digital Instruments) was operated in tapping mode to acquire images of the surfaces of polymers films. Films were prepared by dissolving

dx.doi.org/10.1021/ma3002438 | *Macromolecules* 2012, 45, 3004−3009

the copolymer and $PC_{71}BM$ in dichlorobenzene, followed by spin-coating on the top surface of a PEDOT:PSS substrate. The prepared samples were annealed at 120 °C on a hot plate under nitrogen. TEM images were obtained using a HITACHI-7600 operated at 100 kV. The polymers:$PC_{71}BM$ layers were floated from the water-soluble PEDOT:PSS substrate onto the surface of dematerialized water and picked up with 200-mesh copper TEM grids.

Synthesis of P($F_{40}C_{10}$-DTBT). To a microwave reactor vial containing 9-dioctylfluorene-diboronate (180 mg, 0.28 mmol), the 3,6-carbazole diboronate (21 mg, 0.031 mmol) and DTBT (143 mg, 0.31 mmol) in a mixture of degassed toluene (3 mL) and Et_4NOH 20% solution in water (1 mL) was added a catalyst of tetrakis-(triphenylphosphine)palladium(0) (5 mg) and three drops of Aliquat 336. The mixture was allowed to stir for 2 h at 110 °C. After reaction completion and cooling to room temperature, the mixture was poured into methanol (200 mL). The precipitated solid was recovered by filtration in a Soxhlet thimble and extracted with acetone, hexane and chloroform for 24 h each. To the chloroform fraction was added ethylenediaminetetraacetate (EDTA) (150 mg, 0.403 mmol) and stirred for 6 h. Then the organic fraction was washed with demineralized water (200 mL) three times and concentrated under reduced pressure. The residue was precipitated in a vigorously stirred methanol (200 mL) and the desired dark violet polymers were obtained: (130 mg, 61%). M_n = 8300, M_w = 12 800, PDI = 1.54. ^{1}H NMR (400 MHz, $CDCl_3$, ppm): δ 8.16−6.99 (m, 12H); 2.01 (br, 2H); 1.52 (br, 2H); 1.25 (br, 12H); 0.80 (br, 6H).

Synthesis of P($F_{49}C_1$-DTBT). Following the method for the synthesis of **P($F_{40}C_{10}$-DTBT)** procedure, 198 mg (0.31 mmol) of 9-dioctylfluorene-diboronate, 2 mg (0.003 mmol) of 3,6-carbazole diboronate and 143 mg (0.31 mmol) of DTBT afforded the title copolymer as a dark violet solid (130 mg, 61%). M_n = 11 400, M_w = 42 900, PDI = 3.76. ^{1}H NMR (400 MHz, $CDCl_3$, ppm): δ 8.14−7.25 (m, 12H); 2.05 (br, 3H); 1.53 (br, 2H); 1.09 (br, 20H); 0.78 (br, 9H).

Mobility Measurement. Hole-only devices of the polymers were fabricated on top of a prepatterned ITO substrate. After cleaning the ITO with aqueous detergent, deionized water, acetone, and 2-propanol, UV-ozone treatment was applied for 15 min. PEDOT:PSS (Baytron P TP AI 4083, Bayer AG) was spin-coated from an aqueous dispersion phase to a layer 36 nm thick. The coated substrate was then baked at 120 °C for 60 min. After baking, a solution of the copolymer in chloroform was spin-cast on top of the PEDOT:PSS layer to a thickness of ∼50 nm, and the samples were dried for 6 h at room temperature under vacuum conditions. The Pd electrode was deposited by thermal evaporation under a vacuum of ∼10^{-6} Torr. A similar way was employed to measure the hole only mobility of the polymer:$PC_{71}BM$ blend through the space charge-limited current (SCLC) method with a device structure of ITO/PEDOT:PSS/polymer:$PC_{71}BM$/Au. We also fabricated electron-only devices (Al/copolymer:PCBM/Al) and investigated their $J-V$ characteristics in the dark. The SCLC mobilities were estimated using the Mott−Gurney square law.[14]

$$J = \frac{9}{8}\varepsilon_0\varepsilon_r\mu_h\frac{V^2}{L^3}$$

where J is the current density, L is the film thickness of active layer, μ_h is the hole mobility, ε_r is the relative dielectric constant of the transport medium, ε_0 is the permittivity of free space (8.85×10^{-12} Fm^{1-}), V is the internal voltage in the device and $V = V_{appl} - V_r - V_{bi}$, where V_{appl} is the applied voltage to the device, V_r is the voltage drop due to contact resistance and series resistance across the electrodes, and V_{bi} is the built-in voltage due to the relative work function difference of the two electrodes. The V_{bi} can be determined from the transition between the ohmic region and the SCLC region.

Devices Fabrication and Evaluation. The polymer solar cells were fabricated as following: ITO-coated glass substrates were cleaned with detergent, D.I. water, acetone, and isopropyl alcohol. A thin layer (ca. 40 nm) of PEDOT:PSS (Baytron P VP AI 4083) was first spin-coated on the precleaned ITO-coated glass substrates at 4000 rpm and baked at 120 °C for an hour under ambient conditions. The substrates were then transferred into a nitrogen-filled glovebox. Subsequently, the copolymer:$PC_{71}BM$ active layer (ca. 120 nm) was spin-coated on the PEDOT:PSS layer from a homogeneously blended solution. The solution was prepared by dissolving the polymer at various blend weight ratios of 1:1−1:5 in 1,2-dichlorobenzene and filtered with a 0.2 μm PTFE filter. At the final stage, the substrates were pumped down to high vacuum, and LiF (1 nm) topped with aluminum (100 nm) was thermally evaporated onto the active layer through shadow masks to define the active area of the devices. The thickness of films was measured with a Tencor Alpha-Step 500 profilometer. The unencapsulated solar cells were tested under ambient conditions using a Keithley 2400 SMU and an Oriel xenon lamp (450 W) with an AM1.5 filter. A mask was used to define the device illumination area of 0.06 cm^2 to minimize photocurrent generation from the edge of the electrodes. The solar cells (with no protective encapsulation) were then tested in air under AM 1.5G illumination of 100 mW/cm^2 (Oriel 1 kW solar simulator), which was calibrated with a KG5 filter covered silicon photovoltaic solar cell traceable to the National Renewable Energy Laboratory (NREL). The external quantum efficiency (EQE) was performed using a photomodulation spectroscopic setup (model Merlin, Oriel), a calibrated Si UV detector, and an SR570 low noise current amplifier.

RESULTS AND DISCUSSION

The preparation of the two control polymers [**P(2,7F-DTBT)** and **P(3,6C-DTBT)**] and **P($F_{45}C_5$-DTBT)** were described elsewhere[10,11] and **P($F_{49}C_1$-DTBT)** and **P($F_{40}C_{10}$-DTBT)** were synthesized following the literature.[11] The characterization data are summarized in Table 1 (see Figures S1 and S2, Supporting Information, for DSC thermograms and cyclic voltammograms of the polymers, respectively). The hole mobilities of the copolymers were extracted and calculated from space charge limited current (SCLC) measurements in hole-only devices.[9] The dark current characteristics of the device (ITO/PEDOT:PSS (36 nm)/copolymer (50 nm)/Pd) clearly exhibited ohmic behavior at low voltages and trap-free SCLC behavior at high voltages (see Figure S3, Supporting Information). The hole mobilities of the copolymers series **P(F_xC_y-DTBT)** were improved through increasing the content of 3,6-carbazole unit (y). For instance, **P($F_{49}C_1$-DTBT)**, **P($F_{45}C_5$-DTBT)** and **P($F_{40}C_{10}$-DTBT)** exhibited 3.5×10^{-6}, 4.1×10^{-6} and 4.3×10^{-6} $cm^2/(V\ s)$ of the hole mobility, respectively, smaller than that of **P(3,6C-DTBT)** (1.2×10^{-5} $cm^2/(V\ s)$) but greater than that of **P(2,7F-DTBT)** (2.7×10^{-6} $cm^2/(V\ s)$), even though 1−5 mol % of 3,6-carbazole were incorporated into the main backbone of **P(2,7F-DTBT)**. These results indicated that charges were stabilized by delocalization within the conjugation breaks (Figure 1b),[15] and they were intermolecularly transferred to adjacent hopping sites.

In the preliminary investigation, an optimized weight ratio of a blend of **P($F_{45}C_5$-DTBT)** and $PC_{71}BM$ in o-dichlorobenzene (DCB) was found to be 1:4 with a general structure of ITO/PEDOT:PSS (40 nm)/copolymer:$PC_{71}BM$ (120 nm)/LiF/Al (see Figure S4 and Table S1, Supporting Information). In this condition, we investigated the effect of 3,6-carbazole incorporated into the main backbone of **P(2,7F-DTBT)** on the photovoltaic performance (Figure 2). The $J-V$ characteristics of the devices under AM1.5G (100 mW/cm^2) illumination are summarized in Table 2. An optimized **P(2,7F-DTBT)** device after annealing at 120 °C for 15 min provided a V_{OC} of 0.85 V, a J_{SC} of 8.7 mA/cm^2, and a fill factor (FF) of 0.35, resulting in an estimated PCE of 2.6%, consistent with literature.[9] Meanwhile, the device prepared from **P(3,6C-DTBT)** did not yield photovoltaic properties, even when fabricated under identical conditions, probably due to the low molecular weight

dx.doi.org/10.1021/ma3002438 | Macromolecules 2012, 45, 3004−3009

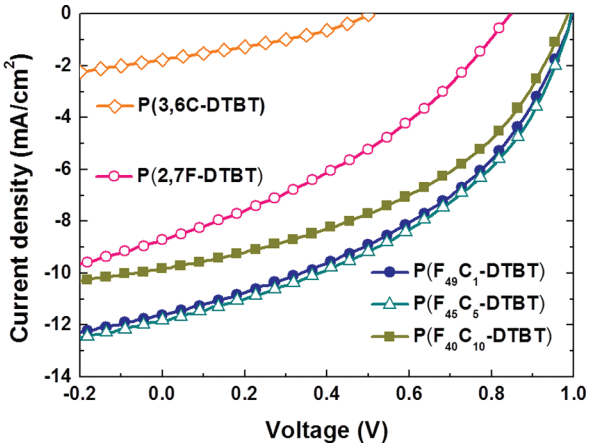


Figure 2. *J*–*V* characteristics for the devices of the blends composed of copolymer:$PC_{71}BM$ (1:4).

Table 2. Photovoltaic Properties of the Copolymer Solar Cells[a]

polymer	V_{OC} [V]	J_{SC} [mA/cm^2]	FF [%]	PCE [%]
P(2,7F-DTBT)	0.85	8.7	35.4	2.6
P($F_{49}C_1$-DTBT)	1.0	11.6	42.4	4.9
P($F_{45}C_5$-DTBT)	1.00	11.8	43.1	5.1
P($F_{40}C_{10}$-DTBT)	0.98	9.8	44.3	4.3
P(3,6C-DTBT)	0.50	1.75	23.6	0.21

[a]A mask was used to define a device illumination area of 0.06 cm^2 to minimize photocurrent generation from the edge of the electrodes. Cell size: 0.06 cm^2 under a mask. Thermal treatment at 120 °C for 15 min. Light intensity: 100 mW/cm^2.

and full conjugation breaks, which shortened the effective conjugation length.[10] On the other hand, incorporation of 3,6-carbazoles into the main backbone of **P(2,7F-DTBT)** greatly improved photovoltaic performance of the devices (2.6% → 4.3–5.1% PCE). The best performance of the device was obtained from **P($F_{45}C_5$-DTBT)** with V_{OC} = 1.00 V, J_{SC} =11.8 mA/cm^2, FF = 0.43, and PCE = 5.1%. The FF (0.43) of the device remained low due to the low hole mobility (4.1×10^{-6} cm^2/(V s))[4b] of the copolymer even though this value was higher than that (FF = 0.35) observed in **P(2,7F-DTBT)**. The V_{OC}s for the optimized devices employing **P(2,7F-DTBT)** and **P($F_{45}C_5$-DTBT)** were 0.85 and 1.00 V, respectively. These values were, respectively, 0.29 and 0.15 V smaller than those estimated from the energy gap (ΔE_{gap} = 1.14 V) between the $LUMO_{PCBM}$ and $HOMO_{copolymer}$.[7] This result indicated that recombination reactions between the photoinduced electrons[8c] and holes were more dominant in **P(2,7F-DTBT)** than in **P($F_{45}C_5$-DTBT)**. Thermal treatment effect was only observed on the copolymers having 3,6-carbazole moiety (see Figure S5 and Table S2, Supporting Information). Device performances employing **P(2,7F-DTBT)** before and after thermal treatments (120 °C for 15 min) were relatively unchanged. In contrast, **P($F_{45}C_5$-DTBT)** exhibited a V_{OC} of 0.98 V, a J_{SC} of 10.8 mA/cm^2, a FF of 0.38, and a PCE of 4.1% prior to thermal treatment. By annealing the device, J_{SC}, FF, and PCE were particularly improved to 11.8 mA/cm^2, 0.43, and 5.1%, respectively (see Figure S6, Supporting Information).

The external quantum efficiency (EQE) and the enhanced EQE spectra for the devices are shown in Figure 3, corresponded to an excellent photocurrent response over the absorption range, covering 300–700 nm. The shapes of the

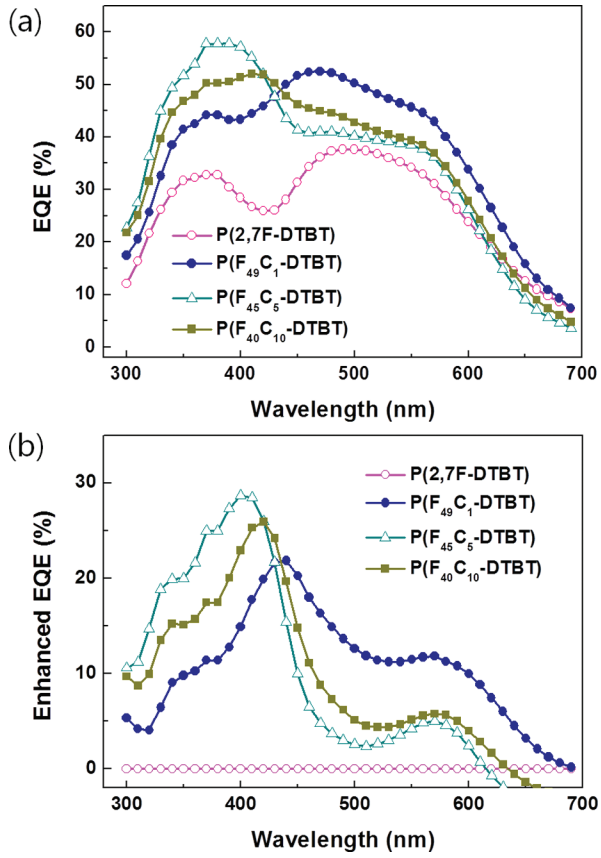


Figure 3. External quantum efficiency (EQE) (a) and enhanced EQE (b) for the devices of the blends composed of copolymer:$PC_{71}BM$ (1:4).

EQE plots for the copolymers are similar to the corresponding absorption spectra (Figure S7, Supporting Information), indicating that all absorption wavelengths of the copolymers contribute to photocurrent generation.

The EQE of the device prepared from **P($F_{49}C_1$-DTBT)** showed a similar shape to **P(2,7F-DTBT)**, but a remarkably enhanced EQE over the absorption range of 300–700 nm was observed (also see Figure S5). The highest EQE value for **P($F_{49}C_1$-DTBT)** approached ca. 54% at 450–500 nm, which was ca. 18% greater than that for **P(2,7F-DTBT)**, despite the slightly lower absorption coefficient in **P($F_{49}C_1$-DTBT)**. For the devices prepared from **P($F_{45}C_5$-DTBT)** and **P($F_{40}C_{10}$-DTBT)**, EQEs were also enhanced, especially in the range of 330–450 nm, probably due to the relatively high content (5–10 mol %) of 3,6-carbazole. 3,6-Carbazole moiety induces conjugation break and reduces the conjugation length in the main backbone of the polymer as we reported previously.[10,16a] These results clearly showed that the enhanced EQEs for **P(F_xC_y-DTBT)s** were consistent with the improved PCEs in the devices.

The maximum J_{SC} of organic BHJ solar cells is governed by the balance between transport and recombination of charge carriers. Imbalanced mobilities of hole and electron could contribute to the large recombination which resulted in a lower J_{SC}.

$$V_{OC} \approx \frac{nkT}{q} \ln\left(\frac{J_{SC}}{J_S}\right)$$

dx.doi.org/10.1021/ma3002438 | *Macromolecules* 2012, 45, 3004–3009

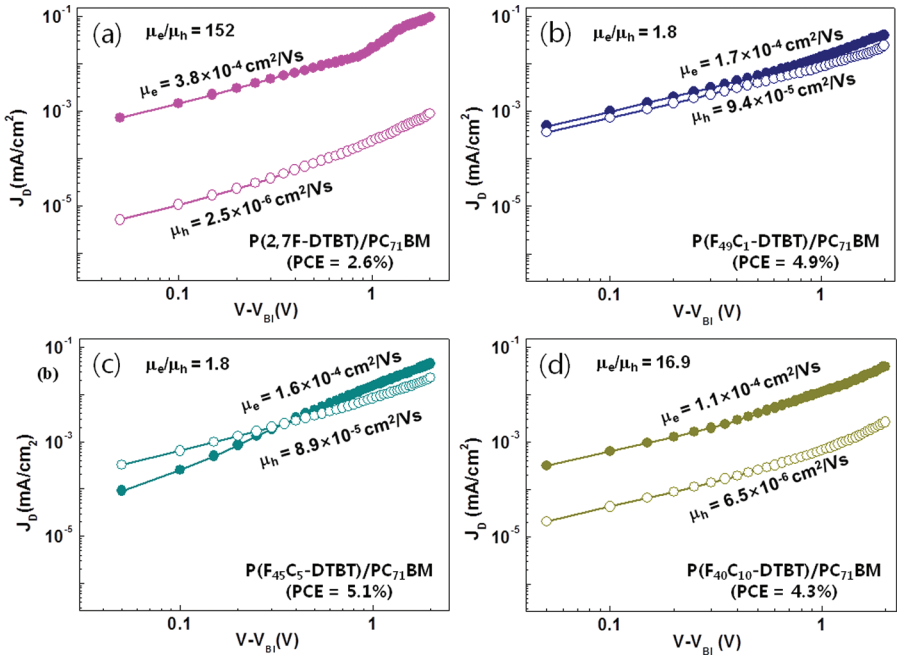


Figure 4. Ratios of electron ($\mu_{e,blend}$, filled circles) and hole ($\mu_{h,blend}$, open circles) mobilities of the blends composed of copolymer:$PC_{71}BM$ (1:4). (a) **P(2,7F-DTBT)**, (b) **P($F_{49}C_1$-DTBT)**, (c) **P($F_{45}C_5$-DTBT)**, and (d) **P($F_{40}C_{10}$-DTBT)**.

Here, n is the diode ideality factor, k is the Boltzmann constant, T is the Kelvin temperature, q is the fundamental charge, J_S is the saturation current density.[16b,c] This equation describes the relationship between V_{OC} and J_{SC}. Therefore, the optimized balance between hole and electron is a key factor for the not only high J_{SC} but also V_{OC}.

We investigated the basis for the improved PCE upon incorporation of 3,6-carbazole. We considered that the imbalance between $\mu_{e,blend}$ and $\mu_{h,blend}$ could contribute to the discrepancy between V_{OC} and $V_{OC,calc}$ due to recombination reactions in the device fabricated with **P(2,7F-DTBT)**, as well as to the greatly improved J_{SC} in the devices fabricated with **P(F_xC_y-DTBT)**s.[8,12]

If the space charges remained in the bulk heterojunction due to a low charge mobility or an imbalance between $\mu_{e,blend}$ and $\mu_{h,blend}$, the photoinduced charge carriers would not be fully extracted and, therefore, would not produce an efficient current under an applied voltage. In this case, the possibility for recombination between holes and electrons at the donor/acceptor interface may increase and J_{SC} and FF may be reduced.

Indeed, large differences were observed between the mobility ratios (μ_e/μ_h) for blends of **P(2,7F-DTBT)**:$PC_{71}BM$, **P($F_{49}C_1$-DTBT)**:$PC_{71}BM$, **P($F_{45}C_5$-DTBT)**:$PC_{71}BM$ and **P($F_{40}C_{10}$-DTBT)**:$PC_{71}BM$ (Figure 4) and the μ_e/μ_hs have a strong relationship with PCEs as seen Figure 4. $\mu_{e,blend}$ and $\mu_{h,blend}$ for a blend of **P(2,7F-DTBT)**:$PC_{71}BM$, calculated using the SCLC model under dark current conditions, were 3.8 × 10^{-4} and 2.5 × 10^{-6} cm^2 V^{-1} s^{-1}, respectively, yielding μ_e/μ_h = 152 (Figure 4(a)). In contrast, μ_e/μ_hs for **P($F_{49}C_1$-DTBT)**:$PC_{71}BM$, **P($F_{45}C_5$-DTBT)**:$PC_{71}BM$ and **P($F_{40}C_{10}$-DTBT)**:$PC_{71}BM$ were 1.8, 1.8, and 16.9, respectively (Figure 4). This result was mainly ascribed to an increase in μ_h (e.g., $\mu_{h,polymer}$ = 4.5 × 10^{-6} (**P($F_{49}C_1$-DTBT)**) → $\mu_{h,blend}$ = 9.4 × 10^{-5} cm^2 V^{-1} s^{-1} (**P($F_{49}C_1$-DTBT)**:$PC_{71}BM$), consistent with Blom's results, who reported an example for the more than 2 orders of magnitude increased hole mobility of a blend ($\mu_{h,blend}$), compared to its polymer value ($\mu_{h,polymer}$).[9,17]

The improvements in the FF and J_{SC} of the device might be related to the morphology of the blends. Figure 5 shows atomic force microscopy (AFM) images for a neat **P(2,7F-DTBT)** and a neat **P($F_{45}C_5$-DTBT)**, and transmission electron microscopy (TEM) images for a blend of **P(2,7F-DTBT)**:$PC_{71}BM$ (1:4) and a blend of **P($F_{45}C_5$-DTBT)**:$PC_{71}BM$ (1:4). The neat **P($F_{45}C_5$-DTBT)** film formed more fibril structure than the neat **P(2,7F-DTBT)** film as seen in the AFM images (compare parts a and b of Figure 5), probably leading to the higher μ_h, polymer (2.7 × 10^{-6} vs 4.1 × 10^{-6} cm^2 V^{-1} s^{-1}). TEM images provide a great difference between two blend films of **P(2,7F-DTBT)**:$PC_{71}BM$ and **P($F_{45}C_5$-DTBT)**:$PC_{71}BM$ (compare parts c and d of Figure 5). The domain size for the blend of

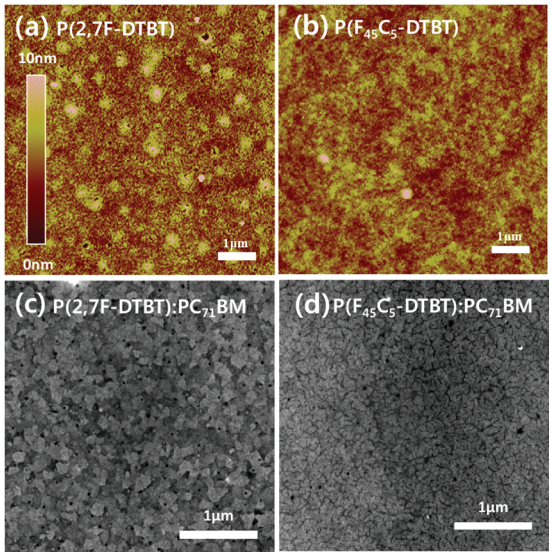


Figure 5. AFM images of neat **P(2,7F-DTBT)** (a), neat **P($F_{45}C_5$-DTBT)** (b). TEM images of a blend of **P(2,7F-DTBT)**:$PC_{71}BM$ (1:4) (c), and a blend of **P($F_{45}C_5$-DTBT)**:$PC_{71}BM$ (1:4) (d).

dx.doi.org/10.1021/ma3002438 | Macromolecules 2012, 45, 3004−3009

P(F$_{45}$C$_5$-DTBT):PC$_{71}$BM is much smaller than that of **P(2,7F-DTBT)**:PC$_{71}$BM. This morphology might be favorable for charge separation and the formation of percolation paths, leading to the improved $\mu_{h,blend}$ and high-efficiency solar cells. Hence, we can speculate that the phase separation can be controlled by the incorporation of 5 mol % 3,6-carbanzole into **P(2,7F-DTBT)**. This led to a good balance between $\mu_{e,blend}$ and $\mu_{h,blend}$ in the device.[12]

In summary, we have demonstrated a novel concept to improve PCE using easily scalable monomers. The incorporation of 3,6-carbazole into **P(2,7F-DTBT)** induced nanoscale morphology of the blends, improving the hole mobility. This result led to a good balance between the electron and hole mobilities in the device (μ_e/μ_h = 152 for **P(2,7F-DTBT)** → μ_e/μ_h = 1.8 for **P(F$_{45}$C$_5$-DTBT)**. The well-balanced mobility almost doubled the PCE (to 5.1%) relative to that of **P(2,7F-DTBT)** (2.6%).

■ ASSOCIATED CONTENT

Ⓢ Supporting Information

J−*V* characteristics for the devices fabricated from various ratios of copolymer PC$_{71}$BM and different annealing temperatures. UV−vis absorption spectra, DSC thermograms, cyclic voltammograms, and the SCLC characteristics of the copolymers. This material is available free of charge via the Internet at http://pubs.acs.org.

■ AUTHOR INFORMATION

Corresponding Author

*E-mail: taihopark@postech.ac.kr.

Author Contributions

†These authors contributed equally.

Notes

The authors declare no competing financial interest.

■ ACKNOWLEDGMENTS

This work was supported by grants from the Energy R&D Program (20093020010040) funded by the MKE, the Basic Science Research Program (No. 2009-0093462), and the Future-based Technology Development Program (Nano Fields, No. 2010-0019119) through the NRF, funded by the MEST (Korea), and by the second stage of a BK21 (Brain Korea 21) grant. Partial support for this work was provided by POSCO.

■ REFERENCES

(1) (a) Chen, J. W.; Cao, Y. *Acc. Chem. Res.* **2009**, *42*, 1709. (b) Gunes, S.; Neugebauer, H.; Sariciftci, N. S. *Chem. Rev.* **2007**, *107*, 1324.

(2) (a) Dennler, G.; Scharber, M. C.; Brabec, C. J. *Adv. Mater.* **2009**, *21*, 1323. (b) Yu, G.; Gao, J.; Hummelen, J. C.; Wudl, F.; Heeger, A. J. *Science* **1995**, *270*, 1789. (c) Rice, A. H.; Giridharagopal, R.; Zheng, S. X.; Ohuchi, F. S.; Ginger, D. S.; Luscombe, C. K. *ACS Nano* **2011**, *5*, 3132.

(3) (a) Chu, T. −Y.; Lu, J.; Beaupré, S.; Zhang, Y.; Pouliot, J. −R. M.; Wakim, S.; Zhou, J.; Leclerc, M.; Li, Z.; Ding, J.; Tao, Y. *J. Am. Chem. Soc.* **2011**, *133*, 4250. (b) Zhou, H.; Yang, L.; Stuart, A. C.; Price, S. C.; Liu, S.; You, W. *Angew. Chem., Int. Ed.* **2011**, *50*, 2995.

(4) (a) Hou, J. H.; Chen, H. Y.; Zhang, S. Q.; Chen, R. I.; Yang, Y.; Wu, Y.; Li, G. *J. Am. Chem. Soc.* **2009**, *131*, 15586. (b) Chen, M. H.; Hou, J.; Hong, Z.; Yang, G.; Sista, S.; Chen, L. M.; Yang, Y. *Adv. Mater.* **2009**, *21*, 4238. (c) Wang, E.; Hou, L.; Wang, Z.; Hellström, S.; Zhang, F.; Inganäs, O.; Andersson, M. R. *Adv. Mater.* **2010**, *22*, 5240.

(5) Chen, H.-Y.; Hou, J.; Zhang, S.; Liang, Y.; Yang, G.; Yang, Y.; Yu, L.; Wu, Y.; Li, G. *Nat. Photonics* **2009**, *3*, 649.

(6) (a) Bernius, M. T.; Inbasekaran, M.; O'Brien, J.; Wu, W. *Adv. Mater.* **2000**, *12*, 1737. (b) Leclerc, M. *J. Polym. Sci., Part A: Polym. Chem.* **2001**, *39*, 2867. (c) Scherf, U.; List, E. J. W. *Adv. Mater.* **2002**, *14*, 477. (d) Cho, S. Y.; Grimsdale, A. C.; Jones, D. J.; Watkins, S. E.; Holmes, A. B. *J. Am. Chem. Soc.* **2007**, *129*, 11910.

(7) (a) Zhang, F.; Kim, G. J.; Bjorström, C.; Scensson, M.; Andersson, M. R.; Sundström, V.; Magnusson, K.; Moons, E.; Yrkady, A.; Inganäs, O. *Adv. Funct. Mater.* **2006**, *16*, 667. (b) Yohannes, T.; Zhang, F.; Scensson, M.; Hummelen, J. C.; Andersson, M. R.; Inganäs, O. *Thin Solid Films* **2004**, *449*, 152.

(8) (a) Berson, S.; Bettignies, R.; Severine, B.; Stephane, G. *Adv. Funct. Mater.* **2007**, *17*, 1377. (b) Kim, J. S.; Lee, J, H.; Park, J. H.; Shim, C.; Sim, M.; Cho, K. *Adv. Funct. Mater.* **2011**, *21*, 480. (c) Deibel, C.; Strobel, T.; Dyakonov, V. *Adv. Mater.* **2010**, *22*, 4097. (d) Chen, S.; Choudhury, K. R.; Subbiah, J.; Amb, C. M.; Reynolds, J. R.; So, F. *Adv. Energy Mater.* **2011**, *1*, 963.

(9) Mihailetchi, V. D.; Xie, H.; de Boer, B.; Koster, L. J. A.; Blom, P.W. M. *Adv. Funct. Mater.* **2004**, *14*, 865.

(10) Kim, J.; Kwon, Y.; Shin, W.; Moon, S.; Park, T. *Macromolecules* **2011**, *44*, 1909.

(11) Fu, Y.; Kim, J.; Siva, A.; Shin, W.; Moon, S.; Park, T. *J. Polym. Sci., Part A: Polym. Chem.* **2011**, *49*, 4368.

(12) Mandoc, M. M.; Koster, L. J. A.; Blom, P. W. M. *Appl. Phys. Lett.* **2007**, *90*, 133504.

(13) Hou, Q.; Xu, Y.; Yang, W.; Yuan, M.; Peng, J.; Cao, Y. *J. Mater. Chem.* **2002**, *12*, 2887.

(14) (a) Park, J. H.; Kim, J. S.; Lee, J. H.; Lee, W. H.; Cho, K. *J. Phys. Chem. C* **2009**, *113*, 17579. (b) Mihailetchi, V. D.; Blom, P. W. M.; Hummelen, J. C.; Rispens, M. T. *J. Appl. Phys.* **2003**, *94*, 6849.

(15) Iraqi, A.; Wataru, I. *J. Polym. Sci., Part A: Polym. Chem.* **2004**, *42*, 6041.

(16) (a) Bijleveld, J. C.; Zoombelt, A. P.; Mathijssen, S. G. J.; Wienk, M. M.; Turbiez, M.; de Leeuw, D. M.; Janssen, R. A. J. *J. Am. Chem. Soc.* **2009**, *131*, 16616. (b) Kumar, A.; Liao, H.-H.; Yang, Y. *Org. Electron.* **2009**, *10*, 1615. (c) Mandoc, M. M.; Koster, L. J. A.; Blom, P. W. M. *Appl. Phys. Lett.* **2007**, *90*, 133504.

(17) Mihailetchi, V. D.; Koster, L. J. A.; Blom, P. W. M.; Melzer, C.; de Boer, B.; van Duren, J. K. J.; Janssen, R. A. J. *Adv. Funct. Mater.* **2005**, *15*, 795.

Macromolecules

Article

pubs.acs.org/Macromolecules

Effect of Ionic Liquid on Structure and Properties of Polysquaraines

Mei-Chan Ho,[†] Ching-Hsun Chao,[‡] Chun-Hua Chen,[†] Ren-Jye Wu,[§] and Wha-Tzong Whang[†,*]

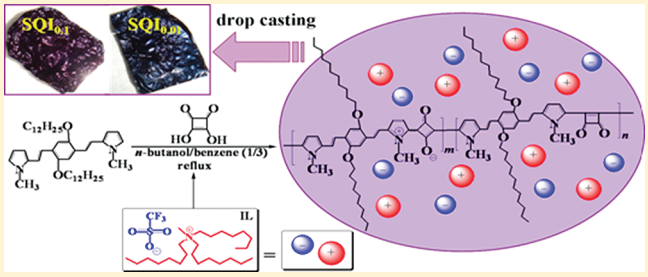
[†]Department of Materials Science and Engineering, National Chiao Tung University, 1001 University Road, Hsinchu, Taiwan, 30010, R.O.C

[‡]Advanced Materials, Electronic Materials, Dow Chemicals, No. 6, Kesi second Road, Jhunan, Miaoli, Science-Based Industrial Park, Taiwan, 35053, R.O.C

[§]Material and Chemical Research Laboratories, Industrial Technology Research Institute, Room 104, Building 67, 195, Sec. 4, Chung Hsing Road, Chutung, Hsinchu, Taiwan, 31040, R.O.C

Supporting Information

ABSTRACT: Polycondensation of 4-bis[2-(1-methylpyrrol-2-yl)vinyl]-2,5-didodecyloxybenzene and squaric acid yielded the polysquaraine **SQ** with two isomeric subunits—1,3-addition (zwitterionic) and 1,2-addition (diketonic) moieties—in the main chain structure. The former featured a C−O/C═O infrared (IR) absorption frequency at 1622 cm^{-1}; the latter, a C═O signal at 1716 cm^{-1}. Traditional synthesis yielded **SQ** as a powder with metallic luster that could not be cast as a polymer film from solution. When the ionic liquid [Oct_3NMe][TfO] (**IL**) was present in the cosolvent of BuOH and benzene (1:3), however, the resulting $\mathbf{SQI}_x$ polymers (x = 0.01−5 wt %) did not precipitate from solution, making it possible to cast continuous free-standing films with a large area (>1 × 1 cm^2). A greater content of **IL** in the solution favored the formation of the 1,3-addition zwitterionic subunits in the $\mathbf{SQI}_x$ polymer main chains, thereby changing the physical and optical properties of the polysquaraine, as evidenced in IR and optical absorption spectra. The features in the UV−Vis−NIR absorption spectra of **SQ** and $\mathbf{SQI}_x$ were dependent on the **IL** concentration and the nature of the solvent. Among our synthesized $\mathbf{SQI}_x$ polymers, $\mathbf{SQI}_{0.01}$ and $\mathbf{SQI}_{0.1}$ formed flexible free-standing films with metallic luster, smooth surfaces, and good semiconductivities (2.27 × 10^{-5} and 4.74 × 10^{-5} S/cm, respectively). X-ray diffraction patterns revealed that the presence of **IL** in the polymerization medium increased the $\mathbf{SQI}_x$ interchain packing distance. $\mathbf{SQI}_{0.01}$ and $\mathbf{SQI}_{0.1}$ possessed thermal stabilities comparable with that of **SQ**. Our successful use of **IL** in the preparation of $\mathbf{SQI}_x$ polymers appears to have great potential for application in ionic liquid−related organic or polymeric preparation and processing.



INTRODUCTION

Squaraines, zwitterionic dyes possessing donor/acceptor-type resonance-stabilized structures, exhibit unique optoelectronic properties.[1−3] The combination of intramolecular charge transfer through S_0−S_1 electronic excitation and extended π-conjugated networks gives rise to squaraine dyes displaying intense absorption bands extending from the visible to the near-infrared (NIR) region.[4,5] In general, larger π-conjugated systems and stronger donor/acceptor interactions endow a polymer with a lower optical band gap (E_g)[6] and intrinsic semiconducting properties.[7] Because of their unique optoelectronic properties and intrinsic conductivity, NIR squaraine dyes are used widely in a variety of electronic and photonic materials, with applications in such fields as optical recording,[8,9] solar cells,[10,11] photodynamic therapy,[12,13] laser printing,[14] and infrared (IR) photography.[15]

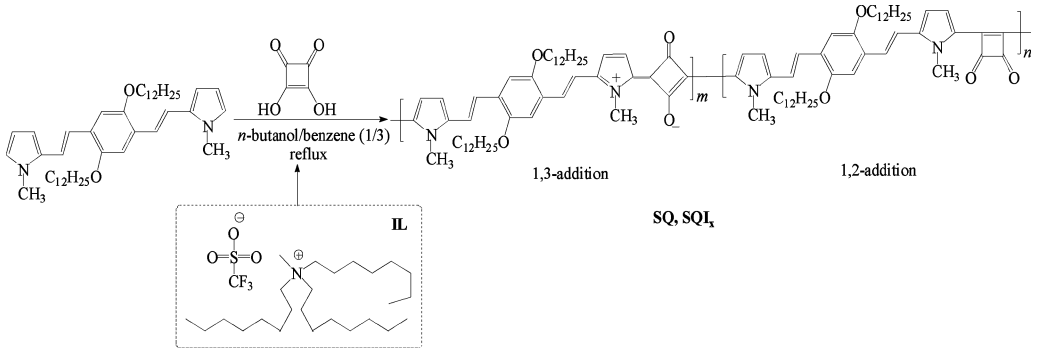
π-Conjugated squaraine dyes are functional materials with tailorable optoelectronic and photophysical properties, which can be tuned through structural modification to achieve optimal performance. The properties of NIR low-E_g squaraines can be modulated by modifying the π-conjugation length, the nature of the donor/acceptor interactions,[16,17] and the polycondensation reaction conditions. The addition of metal ions in the reaction solution can influence the ratio of the two isomeric repeating units in the polysquaraine[18] and the selectivity and sensitivity of squaraine-based sensors.[19−21] Metal ions also can influence the conformations and photoabsorption spectra of polysquaraines through reversible isomerization.[22,23] Unfortunately, the low solubility of polysquaraines (i.e., intrinsic aggregation) limits their practical applications.[24−26]

Ionic liquids (ILs) are organic salts that usually have melting points below 100 °C. Their melting points are much lower than those of traditional inorganic salts because of the asymmetric structures of the cations and the presence of bulky organic groups, resulting in lower charge density and, in turn, weaker ion pairing interactions.[27,28] In addition, ILs also exhibit low vapor pressures, nonvolatility, good thermal stabilities, high ionic conductivities, and good solubilities in many organic and

Received: November 20, 2011
Revised: February 21, 2012
Published: March 21, 2012

 © 2012 American Chemical Society

Scheme 1. Polycondensation of Bispyrrole with Squaric Acid in the Presence of IL (Structure Displayed in the Box)



inorganic solvents.[29,30] The solvation and solubility effects of ILs can have favorable effects during chemical and material processing.[31] ILs have also been employed as key components in dispersion media; for example, as solvents in polymerizations,[32] steric stabilizers in organic dispersions,[33,34] and electrolytes for electrochemical polymerizations.[35,36]

For the purposes of easy processing and good free-standing film quality, the methyltrioctylammonium trifluoromethanesulfonate, [Oct_3NMe][TfO] (**IL**), has been used in the preparation of bispyrrole-based polysquaraines (**SQI$_x$**) and in the casting of **SQI$_x$** films. **IL** does not react with either of the monomers during the polymerization leading to **SQ** polymers. Ion−ion solvation interactions between **IL** and the **SQI$_x$** chains can lead to the stable dispersion of **SQI$_x$** polymer chains in solution, thereby decreasing their intrinsic tendency to aggregate and precipitate. Here, we report the influence of **IL** on the structures and physical properties of **SQI$_x$** chains. We used Fourier transform infrared (FTIR) and UV−vis−NIR optical absorption spectrometry to characterize the **SQI$_x$** polymer chains and a four-point probe electrical measurement device, scanning electron microscopy, X-ray diffraction (XRD), and thermogravimetric analysis (TGA) to study their morphological and physical properties.

EXPERIMENTAL SECTION

Materials and Measurements. All reagents were of analytical reagent grade and used as received without further treatment. Hydroquinone (99%, Sigma−Aldrich), 1-bromododecane (98.0%, T.C.I.), K_2CO_3 (anhydrous, 99%, Alfa Aesar), formaldehyde (37% solution, Tedia), AcOH (99.7%, Showa), HBr (33 wt % solution in glacial AcOH, Acros), triethyl phosphite (97%, Sigma−Aldrich), *N*-methylpyrrol-2-carboxaldehyde (98%, Aldrich), squaric acid (99%, Acros), IL (99%, UR-MATOATS), NaH (60% dispersion in mineral oil, Acros), NaCl (99.5%, Showa), $MgSO_4$ (anhydrous, 99%, Showa), MeCN (99.9%, Tedia), MeOH (99.9%, Echo), hexane (99.8%, Echo), $CHCl_3$ (99%, Sigma−Aldrich), tetrahydrofuran (THF, anhydrous, 99.9%, Tedia), CH_2Cl_2 (99.9%, Echo), butanol (99.9%, Echo), and benzene (99.9%, Echo) were obtained from the indicated suppliers. 2,5-Bis(dodecyloxy)-1,4-dibenzyl phosphonate was prepared from 2,5-bis(dodecyloxy)-1,4-bis(bromomethyl)benzene and triethyl phosphite using a previously reported procedure.[37]

Analysis and Characterization. ^1H and ^{13}C NMR spectra were recorded using a Varian Inova (500 MHz) spectrometer and $CDCl_3$ solutions. Fast atom bombardment (FAB) mass spectra were recorded using a MICROMASS TRIO-2000 mass spectrometer. FTIR spectra were measured using KBr pellets on a Perkin−Elmer Spectrum 100 spectrometer. UV−Vis−NIR spectra were recorded using a Jasco V-670 spectrophotometer. The specimens for UV−vis-NIR are prepared by ultrasonically dissolving the formed films following with filtrating (filter paper: pore size =3 μm). The filtrated solution and the corresponding solubility are shown in Figure S5 and Table S1, Supporting Information, respectively. Elemental analyses were performed using a Heraeus CHN-O-RAPID elemental analyzer. TGA curves are performed using a TGA Q500 analyzer, in N_2 atmosphere (99.99%) and operated at a heating rate of 15 °C/min. Powder XRD patterns were performed on a Bruker NanoStar SAXS system (Cu Kα radiation). The electrical conductivities of the polymers were measured using a four-point probe electrical measurement device.

1,4-Bis[2-(1-methylpyrrol-2-yl)vinyl]-2,5-didodecyloxybenzene (Bispyrrole). A N_2-purged flask equipped with a reflux condenser was charged with anhydrous THF (30 mL), NaH (40 mmol), 2,5-bis(dodecyloxy)-1,4-dibenzyl phosphonate (1.8 mmol), and *N*-methylpyrrole-2-carboxaldehyde (3.6 mmol). The mixture was heated under reflux with stirring at 65 °C for 24 h.[38] The dark-yellow solution was concentrated through vacuum distillation; the residue was poured into water and extracted with CH_2Cl_2. The organic layer was dried ($MgSO_4$) and concentrated to give a crude product, which was purified chromatographically (hexane/EtOAc, 25:1) to yield a bright yellow product (76%). ^1H NMR ($CDCl_3$): δ 7.15 (d, J = 16.5 Hz, 2H), 7.05 (d, J = 16.5 Hz, 2H), 6.98 (s, H), 6.63 (s, 2H), 6.49 (m, 2H), 6.15 (t, J = 2.5 Hz, 2H), 4.01 (t, J = 6.5 Hz, 4H), 3.70 (s, 6H), 1.84 (m, 4H), 1.52 (m, 4H), 1.26 (m, 32H), 0.88 (t, J = 7.0 Hz, 6H). ^{13}C NMR ($CDCl_3$): δ 150.95, 132.88, 126.58, 123.44, 121.45, 117.53, 110.94, 108.24, 106.67, 104.99, 69.51, 34.22, 31.92, 29.68, 29.64, 29.50, 29.35, 26.31, 22.69, 14.12. IR (KBr) ν_{max}: 2921, 2847, 1464, 1392, 1284, 1204, 1049, 966, 721 cm^{-1}. FAB-MS m/z: calcd for $C_{44}H_{68}N_2O_2$ [M]$^+$, 656; found, 657.

Poly(bispyrrole-co-squaric acid) (SQ). A solution of **bispyrrole** (0.08 mmol) and squaric acid (0.08 mmol) in butanol and benzene (1:3, 30 mL) was heated under reflux at 120 °C for 24 h and then cooled to room temperature and filtered. The filtrate was concentrated through vacuum distillation and washed sequentially with hexane, Et_2O, and MeOH. The final product was dried in a vacuum oven at 100 °C for 24 h to yield a dark-green powder (70%). IR (KBr) ν_{max}: 2924, 2853, 1716, 1622, 1439, 1347, 1278, 1088, 942 cm^{-1}. Calcd for $(C_{48}H_{66}N_2O_4{\cdot}H_2O)_n$: C, 76.56; H, 9.10; N, 3.72; Found: C, 76.49; H, 8.85; N, 3.99.

Poly(bispyrrole-co-squaric acid) (SQI$_x$). The polymers **SQI$_x$** were prepared in butanol/benzene mixed solvents in which **IL** was present solvent at concentrations (x) in the range 0.01−5 wt %. **Bispyrrole** (0.08 mmol) and squaric acid (0.08 mmol) in butanol and benzene (1:3, 30 mL) were heated under reflux at 120 °C for 24 h. The reaction mixture was cooled to room temperature and filtered to cast thin film (drop casting method). The **SQI$_x$** films were immersed in MeOH to remove any remaining **IL** and then dried in a vacuum oven at 100 °C for 24 h. **SQI$_5$** (5 wt %): powder film; IR (KBr) ν_{max}: 2923, 2852, 1738, 1623, 1439, 1348, 1279, 1092, 944 cm^{-1}. Anal. Calcd for $(C_{48}H_{66}N_2O_4{\cdot}H_2O)_n$: C, 76.56; H, 9.10; N, 3.72. Found: C, 76.48; H, 9.18; N, 3.24. **SQI$_1$** (1 wt %): powder film; IR (KBr) ν_{max}: 2920, 2850, 1736, 1622, 1438, 1347, 1277, 1089, 942 cm^{-1}. **SQI$_{0.1}$** (0.1 wt %): metallic luster film; IR (KBr) ν_{max}: 2920, 2850, 1736, 1620, 1436, 1345, 1272, 1089, 940 cm^{-1}. **SQI$_{0.01}$** (0.01 wt %): metallic luster film; IR (KBr) ν_{max}: 2920, 2850, 1735, 1620, 1436, 1345, 1274, 1088, 940

dx.doi.org/10.1021/ma202526z | *Macromolecules* 2012, 45, 3010−3016

cm^{-1}. Anal. Calcd for $(C_{48}H_{66}N_2O_4{\cdot}H_2O)_n$: C, 76.56; H, 9.10; N, 3.72. Found: C, 74.37; H, 8.79; N, 3.66.

RESULTS AND DISCUSSION

The monomer **bispyrrole** was synthesized and characterized using ^{1}H and ^{13}C NMR spectroscopy, IR spectroscopy, and mass spectrometry. We then polymerized **bispyrrole** with squaric acid to form **SQ** (Scheme 1), a low−band gap polysquaraine that presumably contained 1,2- and 1,3-addition moieties (the latter zwitterionic) in the polymer main chains. The zwitterionic subunits in the **SQ** main chains should have induced strong intermolecular interactions, implying that the polymer would have a strong tendency for aggregation and precipitation from solution. In general, it is hard to find a proper solvent to make quality films of polysquaraines. Thus, we expected **IL** to solvate the zwitterionic polymers well in solution to ensure the absence of precipitation.

Figure 1 reveals the success of our IL-based polymerization approach. The ion−ion interactions between **IL** and **SQ** resulted in the polymer being dispersed stably in solution without precipitation, overcoming the intrinsic aggregation behavior, and finally enhancing the film formation quality. Figure 1a presents a photograph of the broken tiny pieces of the cast SQ film after drying, which had a metallic luster but could not be dissolved in the reaction solvent or any other organic solvent. Figure 1b−e presents photographs of the thin films of **SQI**$_x$ obtained for values of x (**IL** concentration, wt %) of 5, 1, 0.1, and 0.01 respectively. The **SQI**$_5$ and **SQI**$_1$ films were readily crushed, which might originate from the greater conformational relaxation as more **IL** is extracted out, whereas the **SQI**$_{0.1}$ and **SQI**$_{0.01}$ films were of good quality with a large area (>1 × 1 cm^2) and had metallic luster. The free-standing films can be bended without breaking as shown in Figure 1(f). Thus, the properties of these films were affected by the content of **IL**; in other words, a suitable amount of **IL** in the **SQI**$_x$ polymerization solution can optimize the resulting film quality.

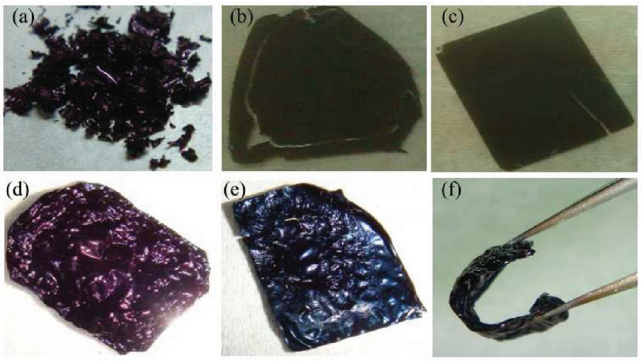


Figure 1. Photographs of (a) the **SQ** powder with metallic luster and (b−e) the **SQI**$_x$ films (b) **SQI**$_5$, (c) **SQI**$_1$, (d) **SQI**$_{0.1}$, (e) **SQI**$_{0.01}$, and (f) flexible **SQI**$_{0.1}$ film.

FTIR Spectroscopic Structural Analysis. The FTIR spectra in Figure 2 reveal structural information regarding the polymer chains of **SQ** and **SQI**$_x$. At first glance, the features in the FTIR spectra of the polymers **SQ** and **SQI**$_x$ in Figure 2a appear similar. Notably, the characteristic absorptions of **IL** were almost completely absent in the spectra of **SQI**$_x$; that is, **IL** was effectively absent in the final polymeric products. Usually, polysquaraines prepared from **bispyrrole** and squaric acid feature two types of repeating units: 1,3-addition (zwitterionic) and 1,2-addition (diketonic) products.[39−42] The FTIR spectroscopic absorptions of the zwitterionic 1,3-addition moieties and weak absorptions at 1716 cm^{-1} for the 1,2-addition (diketonic) moieties. From these FTIR spectra, Table 1 reveals that the 1,3-addition moieties were of the zwitterionic moieties and weak absorptions at 1716 cm^{-1} for the 1,2-addition (diketonic) moieties. The 1,3-addition moieties were more predominant in **SQI**$_x$ than they were in **SQ**. The ratio of 1,3- to 1,2-addition moieties increased upon increasing the **IL** concentration in the polymerization solution. In other words, the formation of zwitterionic 1,3-addition moieties was more favorable (i.e., they were stabilized) in solutions containing higher **IL** concentrations because of the excellent ion solvation capability of **IL** in polar organic solvents.

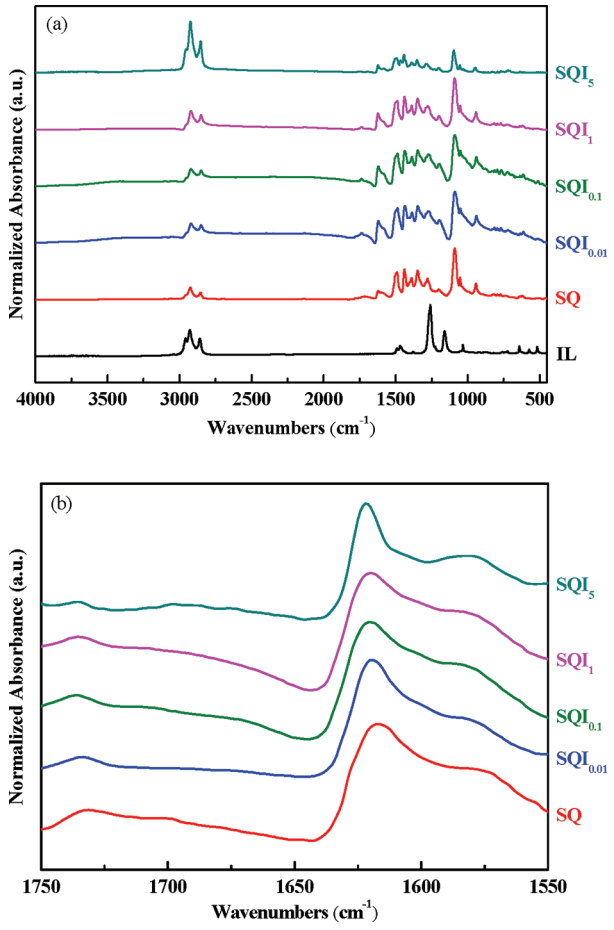


Figure 2. FTIR spectra of neat **IL** and the polysquaraines **SQ** and **SQI**$_x$: (a) 4000−500 cm^{-1}; (b) 1750−1550 cm^{-1}.

Table 1. FTIR Spectroscopic Analysis of the Effect of IL on the Main Chain Structures of SQ Powder and SQI$_x$ Films[a]

SQ dye	ν_{C-O} (cm^{-1}) 1,3-addition	intensity	ν_{C-O} (cm^{-1}) 1,2-addition	intensity	ratio 1,3-/ 1,2-addition
SQ	1622	0.071	1716	0.024	2.96
SQI$_{0.01}$	1619	0.099	1735	0.034	2.91
SQI$_{0.1}$	1620	0.054	1736	0.010	5.40
SQI$_1$	1622	0.232	1736	0.036	6.44
SQI$_5$	1623	0.036	1737	0.005	7.20

[a] **SQI**$_X$:"x" denotes the concentration (wt %) of **IL** relative to the *n*-BuOH/benzene (1:3) reaction solvent.

dx.doi.org/10.1021/ma202526z | *Macromolecules* 2012, 45, 3010−3016

Since the 1,2-addition moieties have a neutral structure compared with the 1,3-addition ones, the stability is relatively low in the presence of **IL** in the polymerization solution. Therefore, the polycondensation of squaric acid with **bispyrrole** in **IL**-containing solutions favored the production of the 1,3-addition configuration.

Electronic Absorption Spectral Properties. Figure 3 displays the UV−vis−NIR absorption spectra of the poly-

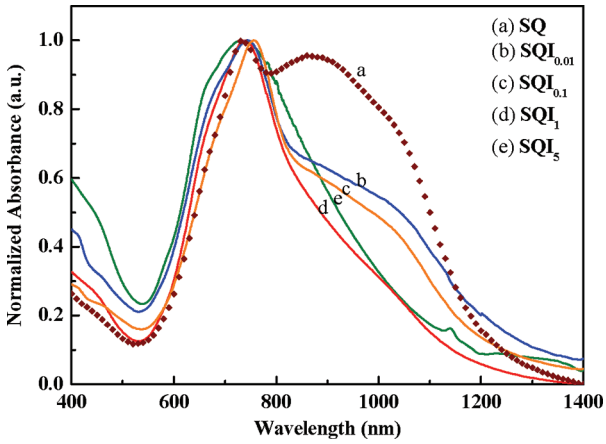


Figure 3. UV−vis−NIR spectra of the polysquaraines **SQ** and $\mathbf{SQI}_x$ in *n*-BuOH/benzene (1:3).

squaraines **SQ** and $\mathbf{SQI}_x$. The spectrum of **SQ** (prepared in the absence of **IL**) featured two intensity maxima at long wavelengths (734 and 874 nm, curve a). $\mathbf{SQ}_{0.01}$ and $\mathbf{SQ}_{0.1}$, which we prepared in the presence of low concentrations of **IL**, featured their maximum intensities at 743−757 nm with a shoulder near 1012 nm (curves b and c, respectively). This feature appears to correlate with the presence of relatively higher ratios of 1,2-addition covalent repeat units. The 1,2-addition structure provides electronic structures of lower symmetry and electronic interactions split into different energy levels, resulting in splitting of the absorption band. Splitting of the absorption bands occurs in the case of mesomeric substituents.[43] Hence, the intensity of the shoulder signal, attributed to the 1,2-addition moieties, decreased upon increasing the ratio of the 1,3-addition moieties. The spectrum of $\mathbf{SQI}_5$, display a maximum absorption at 730 nm, without the shoulder. The absorption peaks at 540−840 nm predominantly represented the electron transitions of the 1,3-addition moieties.

Figure 4 presents the electron absorption spectra of $\mathbf{SQI}_{0.01}$ and $\mathbf{SQI}_5$ prepared in solvents of high (BuOH) and low (benzene) polarity. The spectra of both $\mathbf{SQI}_{0.01}$ and $\mathbf{SQI}_5$ featured broader absorptions when prepared in BuOH than in benzene, with the broadening effect on $\mathbf{SQI}_{0.01}$ being more evident than that on $\mathbf{SQI}_5$. These phenomena are consistent with $\mathbf{SQI}_{0.01}$ featuring a higher ratio of neutral 1,2-diketonic moieties. In the excited state, the 1,2-diketonic structure features significant charge separation,[44,45] with δ^- localized on C═O oxygen atoms and δ^+ accumulated on the pyrrolyl nitrogen atoms, producing a greater change in dipole moment with respect to the ground state than that of the 1,3-moieties, which already possess ionic character. The more highly polar solvent (BuOH) provides greater stabilization of the excited 1,2-moieties, thereby inducing a red−shift of the absorption

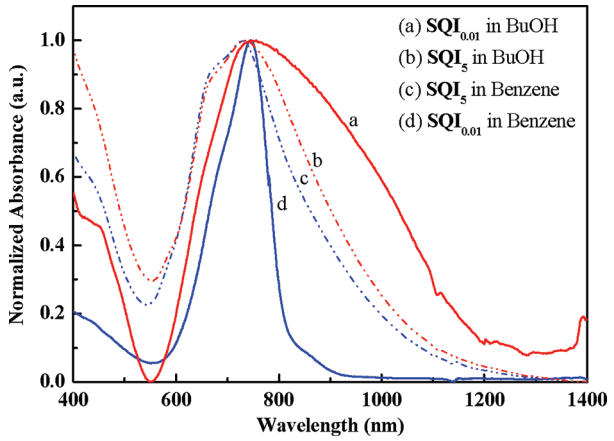


Figure 4. UV−vis−NIR spectra of $\mathbf{SQI}_{0.01}$ (solid line) and $\mathbf{SQI}_5$ (dashed dotted line) in (a, b) *n*-BuOH and (c, d) benzene.

signal. The increase in absorption for $\mathbf{SQI}_{0.01}$ was more evident than that for $\mathbf{SQI}_5$ upon increasing the solvent polarity.

Figure 5 displays the UV−vis−NIR spectra of the polysquaraines $\mathbf{SQI}_{0.01}$ and $\mathbf{SQI}_5$ dissolved in six different solvents. The signals for $\mathbf{SQI}_5$ were relatively unchanged upon increasing the solvent polarity from benzene (lowest polarity) to MeOH (highest polarity). Ionic bonds usually undergo much less of a change in dipole moment upon photon

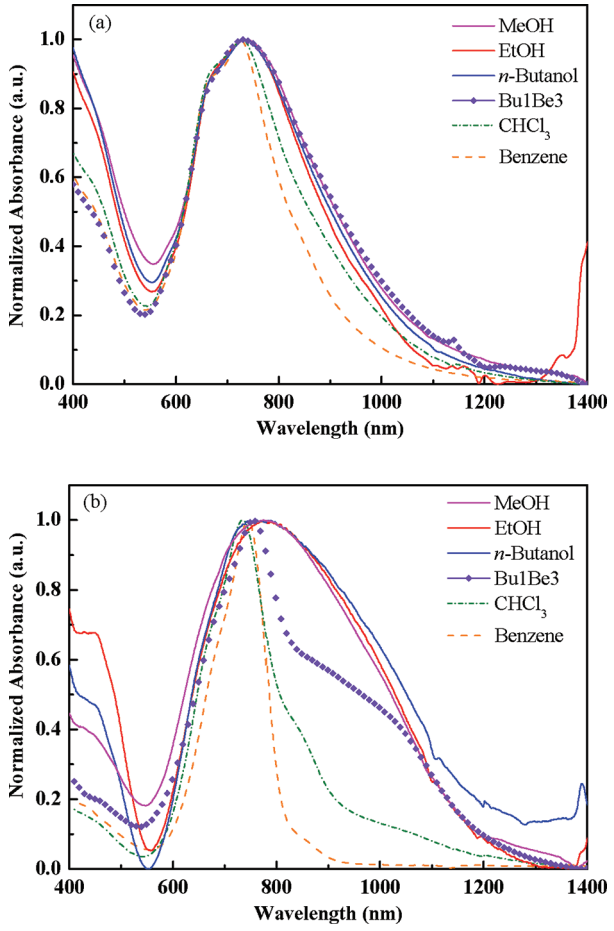


Figure 5. UV−vis−NIR spectra of (a) $\mathbf{SQI}_5$ and (b) $\mathbf{SQI}_{0.01}$ in polar and nonpolar solvents ["Bu1Be3" denotes a mixed solvent of BuOH/benzene (1:3)].

dx.doi.org/10.1021/ma202526z | *Macromolecules* 2012, 45, 3010−3016

absorption than do neutral covalent bonds. Because of its higher content of zwitterionic 1,3-addition moieties, **SQI$_5$** underwent a less significant change in dipole moment upon photon absorption; therefore, the solvent polarity had no significant impact on the photon absorption spectra. In contrast, the spectra of **SQI$_{0.01}$** featured a more noticeable change in absorption upon varying the solvent polarity (Figure 5b). **SQI$_{0.01}$** featured a higher ratio of 1,2-diketone repeat units, which undergo a greater change in dipole moment upon photon absorption. A higher-polarity solvent would better stabilize the dipole moment change upon photon absorption, thereby broadening the absorption spectrum. Hence, the UV–vis–NIR absorption spectrum of **SQI$_{0.01}$** was more sensitive to the solvent polarity.

Surface Morphology and Conductivity. Figure 6 displays the surface morphologies of **SQI$_x$** films prepared

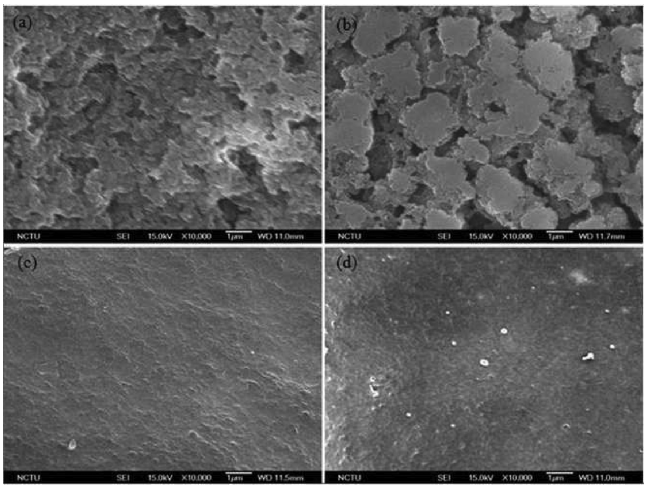


Figure 6. SEM micrographs of the films of (a) **SQI$_5$**, (b) **SQI$_1$**, (c) **SQI$_{0.1}$**, and (d) **SQI$_{0.01}$**.

using the drop casting method. The films of **SQI$_5$** and **SQI$_1$** were readily crushed; their surface morphologies were relatively rough and noncontinuous (Figures 6a and 6b, respectively; cf. Figures 1b and 1c). In contrast, the films of **SQI$_{0.1}$** and **SQI$_{0.01}$** exhibited smooth surfaces, good film quality, and metallic luster (Figure 6, parts c and d; cf. Figure 1, parts d and e). We suspect that this behavior is related to the **IL** content in the drop-casting solution affecting the packing of the polysquaraine chains. A small amount of **IL** in the **SQI$_x$** solution forms a more-stable dispersion of **SQI$_x$**, allowing ready stacking of the chains with less interference from **IL** during the film formation process. In contrast, large amounts of **IL** caused the **SQI$_x$** chains to interact with the; when residual **IL** was removed from the film, the resulting **SQI$_x$** film featured much free space and, therefore, a noncontinuous surface structure.

Table 2 lists the electrical conductivities of the polymers **SQI$_x$**, as measured using the four-point probe method. The conductivities of **SQI$_{0.1}$** and **SQI$_{0.01}$** were 4.74×10^{-5} and 2.27×10^{-5} S/cm, respectively; notably, the former is double the latter. These values are higher than those for **SQI$_1$** and **SQI$_5$**, presumably because of the better molecular close packing and film quality of **SQI$_{0.1}$** and **SQI$_{0.01}$**. Therefore, a low **IL** content in the solution used for polysquaraine preparation enhanced the final polymer film quality, surface morphology, and electrical conductivity.

Table 2. Electrical Conductivities of SQ and SQI$_x$ Films

polymer film	cnductivity (S/cm)
SQ	*a*
SQI$_5$	*b*
SQI$_1$	8.67×10^{-7}
SQI$_{0.1}$	4.74×10^{-5}
SQI$_{0.01}$	2.27×10^{-5}

[a]Powder. [b]not measured.

X-ray Diffraction Studies. The wide-angle X-ray diffraction patterns of solid **SQ** and **SQI$_x$** films (Figure 7) feature

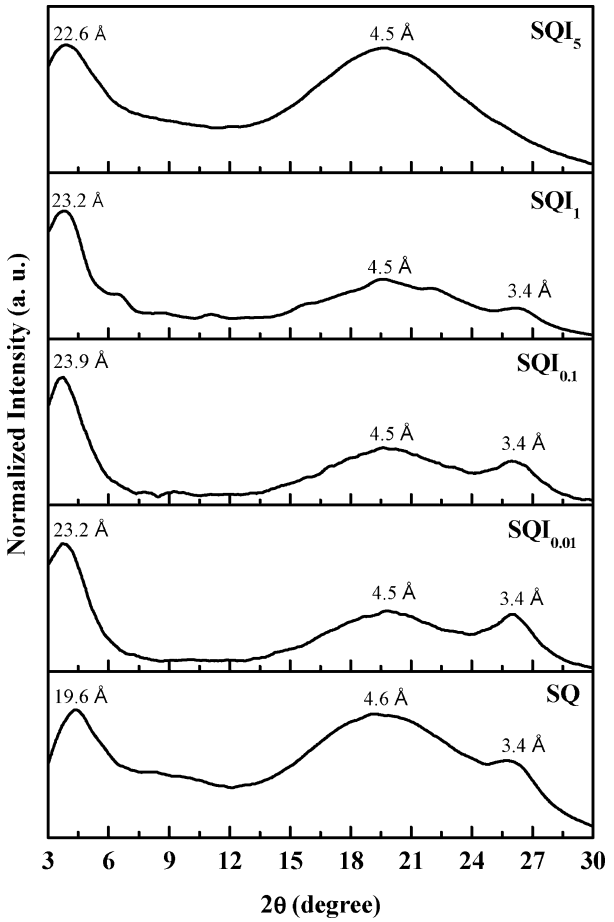


Figure 7. XRD patterns of **SQ** and **SQI$_x$**.

common reflection peaks at angles of 2θ of approximately 4.5 and 3.7–3.9°, corresponding to *d*-spacings of 19.6 and 22.6–23.9 Å, respectively, for the *O*-dodecyl side chains. The interchain packing distance increased from 19.6 Å for **SQ** to 23.9 Å for **SQI$_{0.1}$**, presumably because the presence of **IL** weakened the electrostatic interactions between the **SQ** chains and, thereby, increased the interchain distance. The XRD patterns of the polymers **SQ** and **SQI$_x$** featured broad signals near 19.6–19.2°, corresponding to interlayer spacings of 4.5–4.6 Å. The reflections at values of 2θ near 25.8–26.2° correspond to *d*-spacings of approximately 3.4 Å, consistent with interlayer π-stacking of the **SQ** and **SQI$_x$** chains. The XRD pattern of **SQI$_5$** lacks the signal for π-stacking, presumably because this film possessed a disordered phase associated with more free volume originally occupied by the **IL**. The greater content of **IL** in solution led to more-disordered packing of the

dx.doi.org/10.1021/ma202526z | *Macromolecules* 2012, 45, 3010–3016

polysquaraine layers. Thus, the XRD patterns confirmed the effect of **IL** on the layer packing disorder.

Thermogravimetric Analysis. Figure 8 displays TGA traces of the polymers **SQ** and **SQI**$_x$. These polymers were all

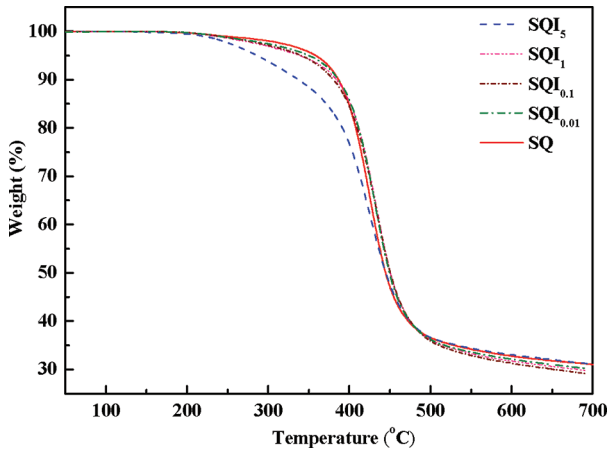


Figure 8. Dynamic thermogravimetric analysis traces of **SQ** and **SQI**$_x$.

very stable at temperatures below 200 °C, exhibiting negligible weight losses. Consistent with a previous report of regarding structural stability, we found that polymer backbones richer in 1,2-addition moieties were more stable than those richer in zwitterionic 1,3-addition moieties.[27] The **SQI**$_x$ polymers featured fewer 1,2-addition moieties than did **SQ**, resulting in their lower thermal degradation temperatures in Figure 8 and Table 3. The dynamic thermal stabilities among the **SQI**$_x$ films

Table 3. Thermal Stabilities of SQ and SQI$_x$ Films

polymer film	T_d[a] (°C)
SQ	357
SQI$_5$	286
SQI$_1$	339
SQI$_{0.1}$	340
SQI$_{0.01}$	349

[a] T_d: Temperature at which 5% weight loss occurred.

followed the trend **SQI$_{0.01}$** > **SQI$_{0.1}$** > **SQI$_1$** > **SQI$_5$**; that is, the greater the content of 1,3-addition moieties on the main chain, the lower the value of T_d. Nevertheless, appropriate control over the **IL** concentration can provide polysquaraines **SQI**$_x$ with thermal stability comparable with that of **SQ**. Therefore, our **SQI**$_x$ polymers that exhibited good film quality has also featured excellent thermally stability, combined with other excellent physical properties.

CONCLUSIONS

The polycondensation of **bispyrrole** with squaric acid results in the formation of polysquaraines featuring both 1,3-addition (zwitterionic) and 1,2-addition (diketonic) moieties. We applied an organic **IL** to the successful preparation of polysquaraine films, because its organic anions and cations solvated the ionic polymer chains effectively in organic solvents. Such solvation induced stable dispersions of the **SQ** chains in solution and decreased the natural tendency for aggregation and precipitation from solution. The polymers **SQI$_{0.01}$** and **SQI$_{0.1}$** provided lustrous semiconductive films exhibiting electron conductivities of 2.27 × 10^{-5} and 4.74 × 10^{-5} S/cm, respectively. The presence of **IL** during the polymerization of **bispyrrole** and squaric acid enhanced the ratio of 1,3- to 1,2-addition moieties in the polymers **SQI**$_x$. We attribute this behavior to ion−ion interactions between **IL** and the **SQ** chain's zwitterionic 1,3-moieties, thereby stabilizing the 1,3-addition structures during polymerization. The changing ratio also influenced the UV−vis−NIR absorption spectra and could be used to determine the influence of the solvent polarity on the absorption signals. The UV−Vis absorption spectrum of **SQI$_{0.01}$** was more sensitive to the solvent polarity than was that of **SQI$_5$**. The presence of **IL** in the reaction solutions not only affected the ratio of the two isomeric moieties in the resultant polymers **SQI**$_x$ but also the *d*-spacings for the packing of the *O*-dodecyl side chains. The interchain packing distance increased from 19.6 Å for **SQ** to 23.9 Å for **SQI$_{0.1}$**, due to weaker electrostatic interactions between **IL** and the latter polymer. A suitable concentration of **IL** in the solution enhances the optical properties, film morphology, polymer chain packing, and electrical conductivity, while maintaining excellent thermal stability. We suspect that the use of **IL** as an additive will also have other applications in organic synthesis and polymer chemistry.

ASSOCIATED CONTENT

Supporting Information

The thermal stability of the **IL**, IR absorption spectra of **SQI$_5$** before and after **IL** removing processes, photographs of flexible **SQI$_{0.1}$** film, and the solubility of **SQI$_{0.01}$**. This material is available free of charge via the Internet at http://pubs.acs.org.

AUTHOR INFORMATION

Corresponding Author

*E-mail: wtwhang@mail.nctu.edu.tw.

Notes

The authors declare no competing financial interest.

ACKNOWLEDGMENTS

The authors would like to thank the National Science Council Republic of China, Taiwan, for financially supporting in this research under Grant NSC100-2221-E009-023-MY3.

REFERENCES

(1) Chung, S. J.; Zheng, S.; Odani, T.; Beverina, L.; Fu, J.; Padilha, L. A. *J. Am. Chem. Soc.* **2006**, *128*, 14444−14445.
(2) Shi, Q.; Chen, W. Q.; Xiang, J.; Duan, X. M.; Zhan, X. *Macromolecules* **2011**, *44*, 3759−3765.
(3) Ajayaghosh, A. *Acc. Chem. Res.* **2005**, *38*, 449−459.
(4) Zhang, T. Q.; Tour, J. M. *J. Am. Chem. Soc.* **1998**, *120*, 5355−5362.
(5) Cornelissen-Gude, C.; Rettig, W.; Lapouyade, R. *J. Phys. Chem. A.* **1997**, *101*, 9673−9677.
(6) Ajayaghosh, A.; Eldo, J. *Org. Lett.* **2001**, *3*, 2595−2598.
(7) Zhang, X.; Jenekhe, S. A. *Macromolecules* **2000**, *33*, 2069−2082.
(8) Emmelius, M.; Pawlowski, G.; Vollmann, H. W. *Angew. Chem., Int. Ed. Engl.* **1989**, *28*, 1445−1471.
(9) Natansohn, A. *Macromolecules* **1994**, *27*, 2580−2585.
(10) Silvestri, F. M.; Irwin, D.; Beverina, L.; Facchetti, A.; Pagani, G. A.; Marks, T. J. *J. Am. Chem. Soc.* **2008**, *130*, 17640−17641.
(11) Hagfeldt, A.; Boschloo, G.; Sun, L.; Kloo, L.; Pettersson, H. *Chem. Rev.* **2010**, *110*, 6595−6663.
(12) Cauchon, N.; Tian, H.; Langlois, R.; Madeleine, C. L.; Martin, S.; Ali, H.; Hunting, D.; Lier, J. E. *Bioconjugate Chem.* **2005**, *16*, 80−89.
(13) Comuzzi, C.; Cogoi, S.; Overhand, M.; Van der Marel, G. A.; Overkleeft, H. S.; Xodo, L. E. *J. Med. Chem.* **2006**, *49*, 196−204.

(14) Law, K. Y. *Chem. Rev.* **1993**, *93*, 449−486.
(15) Fabian, J.; Nakazumi, H.; Matsuoka, M. *Chem. Rev.* **1992**, *92*, 1197−1226.
(16) Cho, H. S.; Jeong, D. H.; Cho, S.; Kim, D.; Matsuzaki, Y.; Tanaka, K.; Tsuda, A.; Osuka, A. *J. Am. Chem. Soc.* **2002**, *124*, 14642−14654.
(17) Sreejith, S.; Carol, P.; Chithra, P.; Ajayaghosh, A. J. *Mater. Chem.* **2008**, *18*, 264−274.
(18) Chenthamarakshan, C. R.; Eldo, J.; Ajayaghosh, A. *Macromolecules* **1999**, *32*, 251−257.
(19) Oguz, U.; Akkaya, E. U. *Tetrahedron Lett.* **1998**, *39*, 5857−5860.
(20) Arunkumar, E.; Chithra, P.; Ajayaghosh, A. *J. Am. Chem. Soc.* **2004**, *126*, 6590−6598.
(21) Chenthamarakshan, C. R.; Eldo, J.; Ajayaghosh, A. *Macromolecules* **1999**, *32*, 5846−5851.
(22) Lu, H. C.; Whang, W. T.; Cheng, B. M. *Chem. Phys. Lett.* **2010**, *500*, 267−271.
(23) Lu, H. C.; Whang, W. T.; Cheng, B. M. *J. Mater. Chem.* **2011**, *21*, 2568−2576.
(24) Eldo, J.; Ajayaghosh, A. *Chem. Mater.* **2002**, *14*, 410−418.
(25) Treibs, A.; Jacob, K. *Angew. Chem., Int. Ed. Engl.* **1965**, *4*, 694−695.
(26) Lu, H. C.; Whang, W. T.; Cheng, B. M. *Synth. Met.* **2010**, *160*, 1002−1007.
(27) Seddon, K. R.; Stark, A.; Torres, M. J. *Pure Appl. Chem.* **2000**, *72*, 2275−2287.
(28) Winterton, N. *J. Mater. Chem.* **2006**, *16*, 4281−4293.
(29) Wilkes, J. S.; Levisky, J. A.; Wilson, R. A.; Hussey, C. L. *Inorg. Chem.* **1982**, *21*, 1263−1264.
(30) Welton, T. *Chem. Rev.* **1999**, *99*, 2071−2083.
(31) Lu, J.; Yan, F. *Prog. Polym. Sci.* **2009**, *34*, 431−448.
(32) Kubisa, P. *Prog. Polym. Sci.* **2004**, *29*, 3−12.
(33) Marcilla, R.; Ochoteco, E.; Pozo-Gonzalo, C.; Grande, H.; Pomposo, J. A.; Mecerreyes, D. *Macromol. Rapid Commun.* **2005**, *26*, 1122−1126.
(34) Guerrero-Sanchez, C.; Erdmenger, T.; Sereda, P.; Wouters, D.; Schubert, U. S. *Chem.—Eur. J.* **2006**, *12*, 9036−9045.
(35) Kubo, W.; Kitamura, T.; Hanabusa, K.; Wada, Y.; Yanagida, S. *Chem. Commun.* **2002**, *4*, 374−375.
(36) Ikeda, A.; Sonoda, K.; Ayabe, M.; Tamaru, S.; Nakashima, T.; Kimizuka, N. *Chem. Lett.* **2001**, *11*, 1154−1155.
(37) Arbuzov, B. A. *Pure Appl. Chem.* **1964**, *9*, 307−335.
(38) Eldo, J.; Arunkumarand, E.; Ajayaghosh, A. *Tet. Lett.* **2000**, *41*, 6241−6244.
(39) Lynch, D. E.; Geissler, U.; Peterson, I. R.; Floersheimer, M.; Terbrack, R.; Chi, L. F.; Fuchs, H.; Calos, N. J.; Wood, B.; Kennard, C. H. L.; Langley, G. J. *J. Chem. Soc., Perkin Trans.* **1997**, *2*, 827−832.
(40) Lynch, D. E.; Geissler, U.; Byriel, K. A. *Synth. Met.* **2001**, *124*, 385−391.
(41) Ashwell, G. J.; Jefferies, G.; Green, A.; Skjonnemand, K.; Rees, N. D.; Bahra, G. S.; Brown, C. R. *Thin Solid Films* **1998**, *327*, 461−464.
(42) Chenthamarakshan, C. R.; Eldo, J.; Ajayaghosh, A. *Macromolecules* **1999**, *32*, 251−257.
(43) Lewis, F. D.; Kalgutkar, R. S.; Yang, J. S. *J. Am. Chem. Soc.* **1999**, *121*, 12045−12053.
(44) Neuse, E. W.; Green, B. R.; Holm, R. *Macromolecules* **1975**, *8*, 730−734.
(45) Neuse, E. W.; Green, B. R. *J. Am. Chem. Soc.* **1975**, *97*, 3987−3991.

Macromolecules

Article

pubs.acs.org/Macromolecules

Spirobifluorene-Based Conjugated Polymers for Polymer Solar Cells with High Open-Circuit Voltage

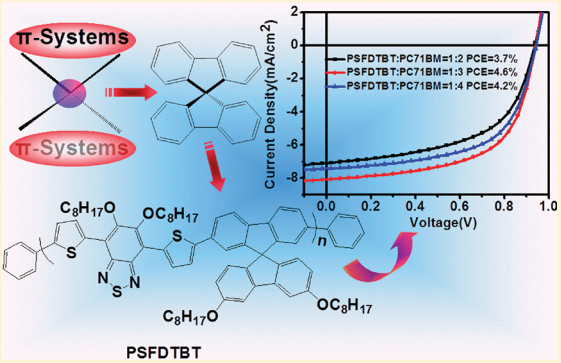
Ming Wang,[†] Cuihong Li,[‡,*] Aifeng Lv,[†] Zhaohui Wang,[†] and Zhishan Bo[‡,†,*]

[†]Institute of Chemistry, Chinese Academy of Sciences, Beijing 100190, China

[‡]College of Chemistry, Beijing Normal University, Beijing 100875, China

Supporting Information

ABSTRACT: A new alternating copolymer (**PSFDTBT**) based on spirobifluorene, thiophene, and benzothiadiazole units has been synthesized. **PSFDTBT** has an optical band gap of 1.97 eV with the low-lying HOMO energy level at −5.4 eV. The hole mobility of the pristine **PSFDTBT** film spin-cast from *o*-dichlorobenzene (DCB) solution is 7.26×10^{-3} cm^2 V^{-1} s^{-1} with on/off ratios in the order of 10^5. Polymer solar cell devices based on the blend films of **PSFDTBT** and $PC_{71}BM$ show a high open-circuit voltage of 0.94 V and a power conversion efficiency of 4.6% without any post-treatment. All the device measurements were performed in air without encapsulation. This is the first report on spirobifluorene-based conjugated polymers used for polymer solar cells, demonstrating the great potential of spirobifluorene moiety as an electron-donating unit for the construction of main chain donor−acceptor alternating conjugated polymers for high performance polymer solar cells.



INTRODUCTION

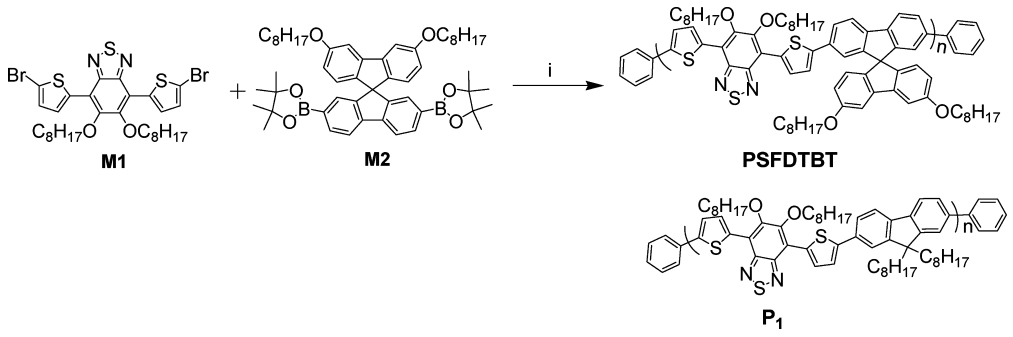
Polymer solar cells (PSCs), as the most promising sustainable energy source alternative to inorganic-based solar cells, have received intensive attention in both academia and industry in recent years.[1] In comparison with inorganic solar cells, PSCs have the potential advantages of lightweight, flexibility, and manufacturing by low cost roll-to-roll process.[2] Up to date, bulk heterojunction (BHJ) structure, in which the active layer consists of an interpenetrating blend of electron donating conjugated polymers and electron accepting fullerene derivatives, is still the most useful active layer structure for high power conversion efficiency (PCE) polymer solar cells.[1,3] Intensive researches worldwide on polymer design and device fabrication have led to a rapid development in the field of PSCs.[1,4] Recently, power conversion efficiency higher than 7% for BHJ polymer solar cells has been achieved by several groups through the developing of new polymer donor materials with the use of [6,6]-phenyl-C_{61}-butyric acid methyl ester ($PC_{61}BM$) or [6,6]-phenyl-C_{71}-butyric acid methyl ester ($PC_{71}BM$) as electron acceptors.[4a−i] For the designing high power conversion efficiency donor polymers, the following three points should be considered:[5] (1) the polymer should have appropriate highest occupied molecular orbital (HOMO) and lowest unoccupied molecular orbital (LUMO) energy levels for harvesting as more photons as possible from solar radiation;[5b] (2) the polymer/PCBM blend films should have high and balanced carrier mobility for generating more free charge carriers and efficiently collecting them at corresponding electrodes;[6] (3) the polymer should be soluble in common organic solvent for solution processing.[7]

Main chain donor−acceptor alternating design is a very efficient way to engineer the band gap of conjugated polymers through the internal charge transfer from donor to acceptor unit.[4a−n,8] Main chain donor−acceptor alternating conjugated polymers with 9,9-dialkylfluorene as donor unit and benzothiadiazole as acceptor unit have been extensively studied as donor components in BHJ PSCs.[9] PCE of polymer solar cells based on 9,9-dialkylfluorene moieties has been improved to 4.5% with an open circuit voltage (V_{oc}) of almost 1 V.[10] Compared with the large number of publications on 9,9-dialkylfluorene based D−A alternating copolymers applied in PSCs, less attention was paid to spirobifluorene-based copolymers. In the past few years, spirobifluorene has been used as an ideal building block in construction of stable blue light-emitting materials.[11] In the spiro-annulated molecules, the two perpendicular conjugated moieties are connected with the sp^3-hybridized carbon atom as the spiro center. This structural feature can minimize the extravagant aggregation of polymers containing spiro-annulated molecules and thus can improve their solubility and processability.[11,12] Furthermore, the spirobifluorene structure can prevent the possible photo/thermal oxidation of the 9-position of the fluorene unit to form the undesired low energy ketonic defect.[13] In theory, stable polymer structures are beneficial for the long lifetime of polymer solar cells. Here, we demonstrate for the first time that spirobifluorene can be a very useful building block to construct

Received: December 20, 2011
Revised: March 8, 2012
Published: March 26, 2012

 © 2012 American Chemical Society dx.doi.org/10.1021/ma202752h | *Macromolecules* 2012, 45, 3017−3022

Scheme 1. Synthetic Route to Polymer PSFDTBT and the Chemical Structure of 9,9-Dialkyl-9*H*-fluorene-Based Polymer P1[a]



[a]Conditions and reagents: (i) $Pd(PPh_3)_4$, Na_2CO_3, toluene−H_2O (v/v, 4:1), and tetra(*n*-butyl)ammonium bromide, reflux.

main chain donor−acceptor alternating conjugated polymer, poly[2,7-(3′,6′-dioctyloxy)-9,9′-spirobifluorene-*alt*-5,5-(4′,7′-di-2-thienyl-5′,6′-dioctyloxy-2′,1′,3′-benzothiadiazole)] (**PSFDTBT**) as shown in Scheme 1, for high efficiency polymer solar cells. The octyloxy chains on spirobifluorene and 2′,1′,3′-benzothiadiazole units can provide **PSFDTBT** with good solubility in common organic solvents. The transport properties of the polymer are investigated by fabricating organic thin film field-effect transistors (OFETs). The pristine **PSFDTBT** film spin-cast from DCB solution exhibited hole mobility of 7.26×10^{-3} cm^2 V^{-1} s^{-1} with on/off ratios in the order of 10^5. The **PSFDTBT**/$PC_{71}BM$ blend films show hole mobility of 1.14×10^{-2} cm^2 V^{-1} s^{-1} and an electron mobility of $2.7 \times 10^{-4}cm^2$ V^{-1} s^{-1}. Under simulated solar illumination of AM 1.5G (100 mW/cm^2), a PCE of 4.6% has been achieved for PSCs composed of **PSFDTBT** and **$PC_{71}BM$** as the active layer in simply processed devices. The devices illustrate a considerably high V_{oc} of 0.94 V, a J_{sc} of 8.0 mA/cm^2, and a comparable fill factor (FF) of 0.60. All device measurements were conducted in air without any encapsulation. Noticeably, **PSFDTBT** exhibits significantly improved PSC performance when compares with the analogous 9,9-dialkyl-9H-fluorene based polymer **P1** (Scheme 1), which showed general PSC performance with PCE of about 3.1% in our previous report.[8]

RESULTS AND DISCUSSION

Material Synthesis. As shown in Scheme 1, **PSFDTBT** is synthesized by Suzuki−Miyaura polycondensation of **M1** and **M2**. The polycondensation was carried out in a biphasic mixture of toluene/aqueous K_2CO_3 solution (4:1) with $Pd(PPh_3)_4$ as the catalyst precursor. After the polymerization proceeded for 72 h, phenylboronic acid and bromobenzene were successively added at a time interval of 4 h to end-cap the polymer. **PSFDTBT** was obtained as a dark red solid in a yield of 86%. The molecular weight and molecular weight distribution were determined by gel permeation chromatography (GPC) using tetrahydrofuran (THF) as an eluent calibrated with polystyrene standards. **PSFDTBT** showed a number-average molecular weight (M_n) of 23 kg/mol, a weight-average molecular weight (M_w) of 78 kg/mol, and a polydispersity index (PDI) of 3.4. Because of the three-dimensional structure of spirobifluorene units, **PSFDTBT** is readily dissolved in common organic solvents such as chloroform, chlorobenzene, toluene, THF, 1,2-dichlorobenzene (DCB), 1,2,4-trichlorobenzene (TCB), etc. at room temperature. Thermogravimetric analysis (TGA) showed that **PSFDTBT** is of good thermal stability with less than 5% weight loss up to 340 °C. No clear glass transition was observed from 25 to 300 °C in its DSC curves of the second heating and cooling runs (20 °C/min).

Optical and Electrochemical Properties. UV−vis absorption spectra of **PSFDTBT** in THF solution and in film are shown in Figure 1. In THF solution, **PSFDTBT** exhibited a broad absorption in the range of ultraviolet to visible region with two peaks located at 395 and 527 nm, respectively. In film, the absorption of **PSFDTBT** became broader and slightly red-shifted with two peaks located at 401 and 562 nm, respectively. In comparison with the absorption spectrum in solution, the absorption spectrum in film became broader and red-shifted for about 35 nm, indicating the aggregation or ordered packing of polymer chains in solid state. Ordered packing of polymer chains is beneficial for improving the charge mobility of resulting films.[14] The optical absorption onset of **PSFDTBT** film is at 629 nm, corresponding to an optical band gap of 1.97 eV. $PC_{71}BM$ was chosen as the acceptor because it has similar electronic properties as $PC_{61}BM$, but a higher absorption coefficient in the visible region with a broad peak from 440 to 530 nm, which compensates the absorption valley of the polymer.[15] As shown in Figure 1, the **PSFDTBT**/$PC_{71}BM$ blending film (1:3 by weight) has a strong absorption over a broad wavelength range of 400 −700 nm. The electrochemical properties of **PSFDTBT** were investigated by cyclic voltammetry (CV). The HOMO energy level of **PSFDTBT** was determined to be −5.40 eV according to the equation $E_{HOMO} = -e(E_{ox} + 4.71)$ (eV), where E_{ox} is the onset oxidation potential in volts vs Ag/Ag^+.[16] Since the open circuit voltage V_{oc} of BHJ

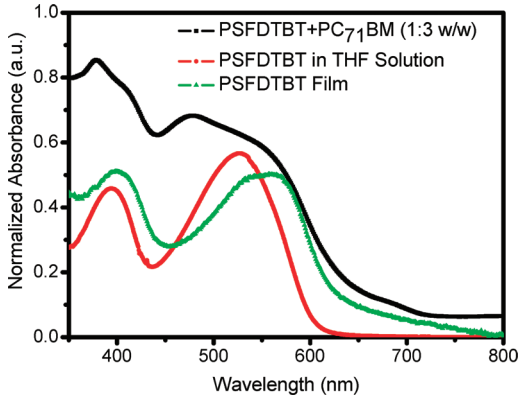


Figure 1. UV−vis absorption spectra of **PSFDTBT** (in THF solution and in film) and **PSFDTBT**/$PC_{71}BM$ blending film (1:3 by weight).

dx.doi.org/10.1021/ma202752h | *Macromolecules* 2012, 45, 3017−3022

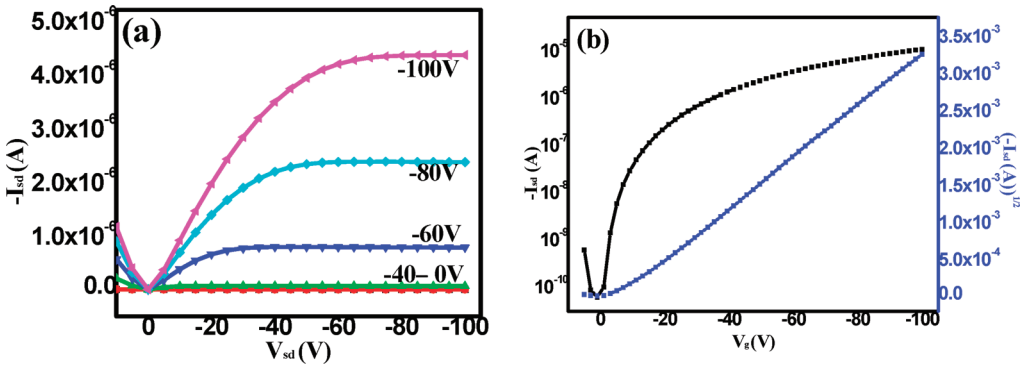


Figure 2. (a) Output and (b) transfer characteristics of the spin-coated film of **PSFDTBT** transistors based on OTS-modified Si/SiO_2 substrate.

Table 1. Summary of Photovoltaic Properties of BHJ PSCs Based on PSFDTBT

active layer	weight ratio (PSFDTBT:$PC_{71}BM$)	thickness (nm)	V_{oc} (V)	J_{sc} (mA/cm^2)	FF	PCE (%)
PSFDTBT:$PC_{71}BM$ DCB	1:2.5	90	0.96	7.6	0.56	4.1
	1:3	85	0.95	7.3	0.57	4.0
	1:3.5	70	0.96	7.6	0.57	4.2
	1:4	75	0.95	7.7	0.56	4.1
PSFDTBT:$PC_{71}BM$ TCB	1:2	75	0.94	7.1	0.56	3.7
	1:3	70	0.94	8.0	0.60	4.6
	1:4	75	0.94	7.4	0.60	4.2
P1:$PC_{71}BM$[a] DCB	1:3	80	0.97	6.7	0.47	3.1

[a]Data from ref 8.

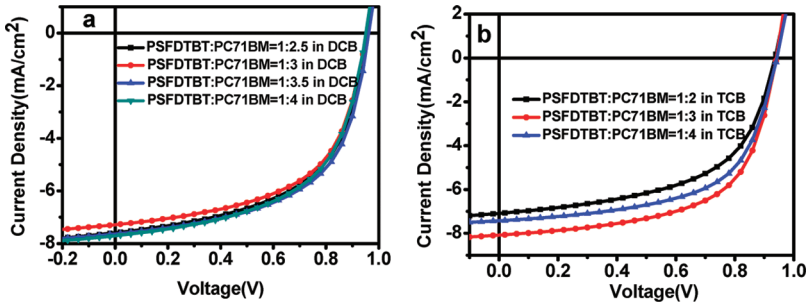


Figure 3. *J*–*V* curves of PSCs fabricated from **PSFDTBT**:$PC_{71}BM$ with different weight ratio in DCB (a) and TCB (b) solutions.

PSCs is correlated to the difference between the LUMO energy level of the acceptor and HOMO energy level of the donor polymer,[5,17] therefore a higher V_{oc} for **PSFDTBT** based polymer solar cells is anticipated due to the low-lying HOMO energy level. According to the equation $E_{LUMO} = E_{HOMO} + E_{g,opt}$, the LUMO energy level of **PSFDTBT** was calculated to be −3.43 eV. The LUMO energy level of **PSFDTBT** is positioned about 0.80 eV above that of $PC_{71}BM$ (4.2 eV, measured under the same condition), which offers enough driving force for charge separation and transfer without too much energy loss.[5,17]

Transport Properties. The transport properties of the polymer were investigated by fabricating organic thin film field-effect transistors (OFETs). Typical *p*-channel field-effect transistor behavior was obtained. The hole mobility (μ) was estimated in the saturated regime from the derivative plots of the square root of source-drain current (I_{SD}) versus gate voltage (V_G) through equation $I_{SD} = (W/2L)C_i\mu(V_G - V_T)^2$ where W is the channel width, L is the channel length, C_i is the capacitance per unit area of the gate dielectric layer (SiO_2, 500 nm, C_i = 7.5 nF/cm^2), and V_T is the threshold voltage. The output (a) and transfer characteristics (b) of the spin-coated **PSFDTBT** films are shown in Figure 2. The hole mobility of the pristine **PSFDTBT** film spin-cast from DCB solution is 7.26×10^{-3} cm^2 V^{-1} s^{-1} with on/off ratios in the order of 10^5, which is almost two orders higher than that of **P1** (the hole mobility of pure **P1** film is 2×10^{-5} cm^2 V^{-1} s^{-1}).[8] Such comparable high mobility is beneficial for charge transfer in the resulting PSCs.[5] For the **PSFDTBT**/$PC_{71}BM$ blend film (in a weight ratio of 1:3, spin-coated from ODCB solutions), hole mobility (μ_{hole}) of 1.14×10^{-2}cm^2 V^{-1} s^{-1} and electron mobility (μ_e) of 2.7×10^{-4}cm^2 V^{-1} s^{-1} were obtained.

Photovoltaic Properties. Broad absorption, appropriate HOMO/LUMO positions, and comparable hole mobility make **PSFDTBT** a promising donor material in BHJ PSCs. Therefore, the photovoltaic performance of **PSFDTBT** was investigated in PSCs. Polymer solar cells with a device configuration of ITO/PEDOT:PSS/polymer:$PC_{71}BM$/LiF/Al were fabricated and characterized under the illumination of AM1.5G (100 mW/cm^2). The weight ratio of **PSFDTBT** to $PC_{71}BM$ and the processing solvent have been carefully optimized. The results are summarized in Table 1. Using DCB as the processing solvent, four polymer solar cells with blends of **PSFDTBT** and $PC_{71}BM$ in weight ratios of 1:2.5, 1:3,

dx.doi.org/10.1021/ma202752h | *Macromolecules* 2012, 45, 3017–3022

1:3.5, and 1:4, respectively, as the active layer were fabricated, and their $J-V$ curves are shown in Figure 3a. In all cases, PCEs of about 4.1% were obtained. The performance of PSCs was insensitive to the ratio of donor to acceptor in range of 1:2.5 to 1:4. With a weight ratio of **PSFDTBT** to $PC_{71}BM$ is 1:3.5, a PCE of 4.2% with a V_{oc} of 0.96 V, a J_{sc} of 7.6 mA/cm^2, and an FF of 0.56 was achieved under illumination from an AM 1.5G solar simulator (100 mW cm^{-2}). Such high V_{oc} of almost 1 V is consistent with the low-lying HOMO energy level of **PSFDTBT**. In comparison with the device performance of **P1** based PSCs,[8] devices based on **PSFDTBT** exhibited almost identical V_{oc}, but higher J_{sc} and much higher FF. As shown in Table 1, the optimized devices based on **P1** showed a PCE of 3.1% with a V_{oc} of 0.97 V, a J_{sc} of 6.7 mA/cm^2, and an FF = 0.47. It is well-known that the processing solvent can dramatically affect the morphology of blend film and thus the photovoltaic performance of devices. When the solvent was changed from DCB to TCB, the photovoltaic performance could be further improved. As shown in Table 1, when the active layer was **PSFDTBT**/$PC_{71}BM$ in a weight ratio of 1:3, the highest PCE of 4.6% with a V_{oc} of 0.94 V, a J_{sc} of 8.0 mA/cm, and an FF of 0.60 was achieved. $J-V$ curves of polymer solar cells fabricated with different weight ratio of **PSFDTBT**:$PC_{71}BM$ in TCB solutions are shown in Figure 3b. It is worth noting that such performance was achieved from simply fabricated devices without using any additive, post-treatment, or extra layers, which is beneficial for preparation of low cost polymer solar cells. To verify the accuracy of the J_{sc} measurement results, external quantum efficiencies (EQEs) of solar cells were measured under illumination of monochromatic light. As shown in Figure 4, solar cells, which were fabricated

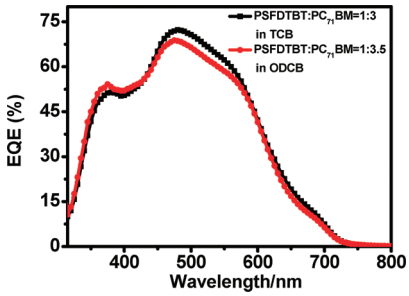


Figure 4. EQE curves of PSCs fabricated from **PSFDTBT**:$PC_{71}BM$ = 1:3.5 (w/w) in DCB and **PSFDTBT**:$PC_{71}BM$ = 1:3 (w/w) in TCB.

from **PSFDTBT**:$PC_{71}BM$ in a ratio of 1:3.5 (w/w) in DCB solutions and **PSFDTBT**:$PC_{71}BM$ in a ratio of 1:3 (w/w) in TCB solutions, both exhibited a broad photoresponse extending from 350 to 700 nm. Especially, the device based on a ratio of **PSFDTBT** to $PC_{71}BM$ of 1:3 (w/w) in TCB solutions exhibited the maximum EQE of 72% at 479 nm. The J_{sc} calculated from integration of the EQE with an AM 1.5G reference spectrum roughly agreed with the J_{sc} obtained from the J-V measurements.

To understand the relationship between device performances and active layer morphology, atomic force microscopy (AFM) measurements were conducted to investigate the surface morphology of **PSFDTBT**/$PC_{71}BM$ blend films. Figure 5 shows the AMF height images of **PSFDTBT**:$PC_{71}BM$ (1:3.5, w/w) blend film spin coated from DCB and **PSFDTBT**:$PC_{71}BM$ (1:3, w/w) blend film spin coated from TCB. In these two cases, AFM height images showed similar surface morphology with fairly small phase separation, and the root-mean-square (rms) values for the blend films from DCB and from TCB are 0.242 and 0.306 nm, respectively. These AFM results are consistent with their photovoltaic device performances (vide supra). The reason for that may be due to both DCB and TCB are good solvents for **PSFDTBT.** It is well-known that balanced electron and hole mobility of the active layer is required for high performance polymer solar cells.[2f] The formation of an interpenetrating bicontinuous network between polymer donor and PCBM with an ideal domain size of 10−20 nm is crucial for charge generation and transportation.[18] For bulk heterojunction polymer solar cells, appreciate phase separation is a practical way to form bicontinuous donor−acceptor network.[19] We believe that the solar cell performance of this type of copolymer can be further improved by the optimization of film morphology and device fabrication conditions.

CONCLUSION

An alternating copolymer **PSFDTBT** of spirobifluorene and 2′,1′,3′-benzothiadiazole unit was designed and synthesized. **PSFDTBT** shows a broad absorption, appropriate HOMO/LUMO positions, and comparable hole mobility. Without using any additive and any post-treatment, polymer solar cells based on **PSFDTBT**/$PC_{71}BM$ demonstrated a PCE of 4.6% with a high open-circuit voltage of 0.94 V. This is the first report on spirobifluorene-based polymers applied in BHJ PSCs. High open-circuit voltage, simple device fabrication process, and easy synthesis make **PSFDTBT** a highly promising donor polymers for high efficiency polymer solar cells. We believe that spirobifluorene as a promising building block for conjugated polymer donor materials warrants further exploration and the performance of **PSFDTBT**-based polymer solar cells can be further improved from the optimization of device fabrication conditions.

EXPERIMENTAL SECTION

Materials and Instruments. Unless otherwise noted, all chemicals were purchased from commercial suppliers and used without further purification. Solvents were dried using standard procedures. **M1**[4j] and **M2**[11g] were synthesized according to literature procedures. The catalyst precursor $Pd(PPh_3)_4$ was prepared according to the literature and stored in a Schlenk tube under nitrogen.[20] Tetrahydrofuran (THF) and diethyl ether (Et_2O) were distilled from sodium with benzophenone as an indicator under nitrogen atmosphere. Hexane and dichloromethane (CH_2Cl_2) were distilled from CaH_2. Chloroform was distilled before use. All reactions were performed under an atmosphere of nitrogen and monitored by thin layer chromatography (TLC) on silica gel 60 F254 (Merck, 0.2 mm). Column chromatography was carried out on silica gel (200−300 mesh). ^1H and ^{13}C NMR spectra were recorded on a Bruker DM 300 or AV 400 spectrometer in $CDCl_3$. UV−vis absorption spectra were obtained on a SHIMADZU UV−visible spectrometer model UV-1601PC. Elemental analyses were performed on a Flash EA 1112 analyzer. Thermal gravimetric analysis (TGA) and differential scanning calorimetry (DSC) measurements were performed on TA2100 and Perkin-Elmer Diamond DSC instrument, respectively, under a nitrogen atmosphere at a heating rate of 10 °C/min to record TGA and DSC curves. Elemental analysis was performed on a Vario EL elemental analysis instrument. Number- (M_n) and weight-average (M_w) molecular weights were measured by gel permeation chromatography (GPC) on a PL-GPC 50 with THF as an eluent and calibrated with polystyrene standards. Atomic force microscopy (AFM) images of blend films were obtained on a Nanoscope IIIa Dimension 3100 operating in the tapping mode. The film thickness

dx.doi.org/10.1021/ma202752h | Macromolecules 2012, 45, 3017−3022

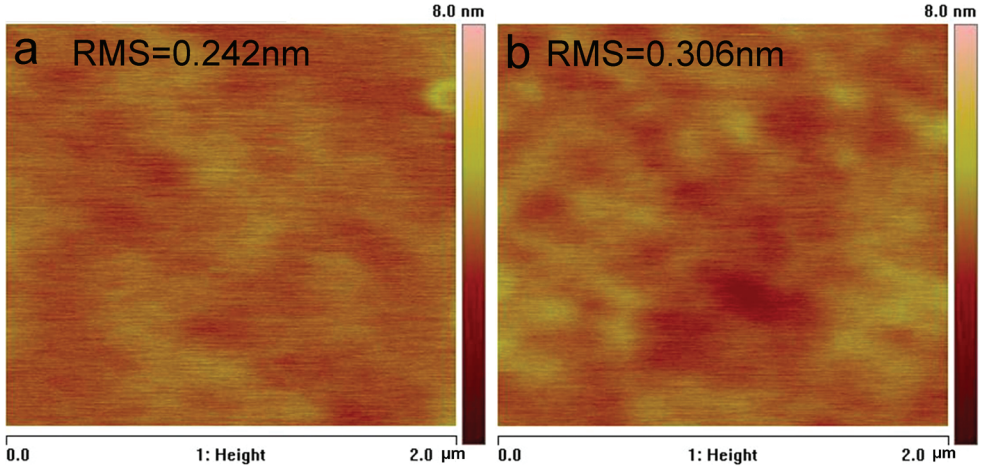


Figure 5. AFM height images ($2 \times 2\ \mu m^2$) of **PSFDTBT**/$PC_{71}BM$ (1:3.5, w/w) blend films spin coated from DCB (a) and **PSFDTBT**/$PC_{71}BM$ (1:3, w/w) blend films spin coated from TCB (b).

was determined by a Dektak 6 M surface profilometer. Electrochemical measurements were performed on a CHI 630A Electrochemical Analyzer with a standard three-electrode electrochemical cell in a 0.1 M tetrabutylammonium tetrafluoroborate solution in CH_3CN at room temperature with a scanning rate of 0.1 V/s^{-1}. A glassy carbon working electrode, a Pt wire counter electrode, and an $Ag/AgNO_3$ (0.01 M in CH_3CN) reference electrode were used. The experiments were calibrated with the standard ferrocene/ferrocenium (Fc) redox system and assumption that the energy level of Fc is 4.8 eV below vacuum.

Synthesis of Poly[2,7-(3′,6′-dioctyloxy)-9,9′-spirobifluorene-*alt*-5,5-(4′,7′-di-2-thienyl-5′,6′-dioctyloxy-2′,1′,3′-benzothiadiazole)] (PSFDTBT). A mixture of **M1** (142 mg, 0.2 mmol), **M2** (165 mg, 0.2 mmol), K_2CO_3 (1.35 g, 10 mmol), tetra(*n*-butyl)-ammonium bromide (200 mg, 0.62 mmol), toluene (20 mL), and H_2O (5 mL) was carefully degassed before $Pd(PPh_3)_4$ (2 mg, 2 μmol) was added. The mixture was refluxed under nitrogen atmosphere with vigorous stirring for 72 h. Then phenylboronic acid and bromobenzene were added to end-cap the polymer. Chloroform and water were added; the organic layer was separated and concentrated; and the residue was poured into methanol. The resulted solid was collected by filtration and washed with acetone to remove oligomers and catalyst residues to afford **PSFDTBT** as a red solid (194 mg, 86%). The resulted polymer was fully soluble in common organic solvents such as THF, chloroform, and chlorobenzene. ^1H NMR (400 MHz, $CDCl_3$): δ 8.34 (s, 2H), 7.38 (m, 6H), 7.06 (m, 10H), 6.71 (m, 10H), 4.05 (s, 8H), 1.84 (m, 16H), 1.31 (m, 32H), 0.90 (s, 12H); ^{13}C NMR (100 MHz, $CDCl_3$): δ 159.6, 151.7, 150.8, 145.7, 143.1, 140.9, 133.6, 131.7, 124.8, 123.0, 120.3, 117.4, 114.6, 106.0, 74.4, 68.4, 64.8, 31.9, 30.4, 29.5, 29.3, 26.2, 26.0, 22.7, 14.1. Anal. Calcd for $C_{71}H_{84}N_2O_4S_3$: C, 75.76; H, 7.52; N, 2.49. Found: C, 75.77; H, 7.56; N, 2.53.

Polymer Solar Cell Fabrication and Characterization. PSCs were fabricated with the device configuration of ITO/PEDOT:PSS/polymer:$PC_{71}BM$/LiF/Al. The conductivity of ITO is 20 Ω/□. PEDOT:PSS is Baytron Al 4083 from H. C. Starck and was filtered with a 0.45 μm PVDF film before use. A thin layer of PEDOT:PSS was spin-coated on top of cleaned ITO substrate at 3000 rpm/s for 60 s and dried subsequently at 130 °C for 15 min on a hot plate before transferred into a glovebox. The active layer was prepared by spin-coating the solution of polymers and $PC_{71}BM$ on the top of ITO/PEDOT:PSS. The top electrode was thermally evaporated, with a 0.6 nm LiF layer, followed by 80 nm of aluminum at a pressure of 10^{-6} Torr through a shadow mask. Four cells were fabricated on one substrate with an effective area between 0.04 and 0.05 cm^2. The measurement of devices was conducted in air. Current−voltage characteristics were recorded using a Keithley 2400 Source Meter under AM 1.5 illumination with an intensity of 100 mW/cm^2 from a solar simulator (Model SS-50A, photo Emission Tech., Inc.). The *J*−*V* curves were recorded at the temperature of about 25 °C.

Fabrication and Characterization of Organic Field-Effect Transistors (OFETs). The thin film organic field-effect transistors (OFET) of all three polymers were investigated by spin-coating method. Each polymer with the concentration of 10 mg/mL in *o*-dichlorobenzene (DCB) was spun on OTS-treated Si/SiO_2 substrates. Au electrodes were thermally deposited through a multiple finger configuration mask with channel length 50 μm and width 2500 μm separately. Measurements were performed in air using a Keithley 4200-SCS semiconductor parameter analyzer and a Micromanipulator 6150 probe station in a clean and shield box.

■ ASSOCIATED CONTENT

Ⓢ Supporting Information

^1H and ^{13}C NMR spectra and plots of hole and electron transport performance. This material is available free of charge via Internet at http://pubs.acs.org.

■ AUTHOR INFORMATION

Corresponding Author

*E-mail: (C.L.) licuihong@bnu.edu.cn; (Z.B.) zsbo@iccas.ac.cn or zsbo@bnu.edu.cn..

Notes

The authors declare no competing financial interest.

■ ACKNOWLEDGMENTS

We express thanks for the financial support by the NSF of China (20834006, 51003006, and 21161160443), the 973 Programs (2011CB935702 and 2009CB623603), and the Fundamental Research Funds for the Central Universities.

■ REFERENCES

(1) (a) Brabec, C. J.; Sariciftci, N. S.; Hummelen, J. C. *Adv. Funct. Mater.* **2001**, *11*, 15. (b) Chen, H. Y.; Hou, J. H.; Zhang, S. Q.; Liang, Y. Y.; Yang, G. W.; Yang, Y.; Yu, L. P.; Wu, Y.; Li, G. *Nat. Photonics* **2009**, *3*, 649. (c) Li, G.; Shrotriya, V.; Huang, J. S.; Yao, Y.; Moriarty, T.; Emery, K.; Yang, Y. *Nat. Mater.* **2005**, *4*, 864. (d) Liang, Y. Y.; Yu, L. P. *Acc. Chem. Res.* **2010**, *43*, 1227. (e) Park, S. H.; Roy, A.; Beaupre, S.; Cho, S.; Coates, N.; Moon, J. S.; Moses, D.; Leclerc, M.; Lee, K.; Heeger, A. J. *Nat. Photonics* **2009**, *3*, 297. (f) Peet, J.; Kim, J. Y.; Coates, N. E.; Ma, W. L.; Moses, D.; Heeger, A. J.; Bazan, G. C. *Nat. Mater.* **2007**, *6*, 497. (g) Thompson, B. C.; Frechet, J. M. J. *Angew. Chem., Int. Ed.* **2008**, *47*, 58.

(2) (a) Li, C.; Liu, M. Y.; Pschirer, N. G.; Baumgarten, M.; Mullen, K. *Chem. Rev.* **2010**, *110*, 6817. (b) Krebs, F. C. *Sol. Energy Mater. Sol. Cells* **2009**, *93*, 394. (c) Po, R.; Maggini, M.; Camaioni, N. *J. Phys. Chem. C* **2010**, *114*, 695. (d) Brabec, C. J.; Padinger, F.; Hummelen, J. C.; Janssen, R. A. J.; Sariciftci, N. S. *Synth. Met.* **1999**, *102*, 861. (e) Cheng, Y. J.; Yang, S. H.; Hsu, C. S. *Chem. Rev.* **2009**, *109*, 5868. (f) Coakley, K. M.; McGehee, M. D. *Chem. Mater.* **2004**, *16*, 4533. (g) Gunes, S.; Neugebauer, H.; Sariciftci, N. S. *Chem. Rev.* **2007**, *107*, 1324. (h) Hadipour, A.; de Boer, B.; Wildeman, J.; Kooistra, F. B.; Hummelen, J. C.; Turbiez, M. G. R.; Wienk, M. M.; Janssen, R. A. J.; Blom, P. W. M. *Adv. Funct. Mater.* **2006**, *16*, 1897. (i) Hoppe, H.; Sariciftci, N. S. *J. Mater. Res.* **2004**, *19*, 1924. (j) Ma, W. L.; Yang, C. Y.; Gong, X.; Lee, K.; Heeger, A. J. *Adv. Funct. Mater.* **2005**, *15*, 1617.

(3) (a) Yu, G.; Gao, J.; Hummelen, J. C.; Wudl, F.; Heeger, A. J. *Science* **1995**, *270*, 1789. (b) Bundgaard, E.; Krebs, F. C. *Sol. Energy Mater. Sol. Cells* **2007**, *91*, 954. (c) Dhanabalan, A.; van Duren, J. K. J.; van Hal, P. A.; van Dongen, J. L. J.; Janssen, R. A. J. *Adv. Funct. Mater.* **2001**, *11*, 255. (d) Janssen, R. A. J.; Hummelen, J. C.; Saricifti, N. S. *MRS Bull.* **2005**, *30*, 33. (e) Padinger, F.; Rittberger, R. S.; Sariciftci, N. S. *Adv. Funct. Mater.* **2003**, *13*, 85. (f) Yang, X. N.; Loos, J.; Veenstra, S. C.; Verhees, W. J. H.; Wienk, M. M.; Kroon, J. M.; Michels, M. A. J.; Janssen, R. A. J. *Nano Lett.* **2005**, *5*, 579.

(4) (a) Amb, C. M.; Chen, S.; Graham, K. R.; Subbiah, J.; Small, C. E.; So, F.; Reynolds, J. R. *J. Am. Chem. Soc.* **2011**, *133*, 10062. (b) Chu, T. Y.; Lu, J. P.; Beaupre, S.; Zhang, Y. G.; Pouliot, J. R.; Wakim, S.; Zhou, J. Y.; Leclerc, M.; Li, Z.; Ding, J. F.; Tao, Y. *J. Am. Chem. Soc.* **2011**, *133*, 4250. (c) Zhou, H. X.; Yang, L. Q.; Stuart, A. C.; Price, S. C.; Liu, S. B.; You, W. *Angew. Chem., Int. Ed.* **2011**, *50*, 2995. (d) He, Z. C.; Zhong, C. M.; Huang, X.; Wong, W. Y.; Wu, H. B.; Chen, L. W.; Su, S. J.; Cao, Y. *Adv. Mater.* **2011**, *23*, 4636. (e) Huo, L. J.; Hou, J. H.; Zhang, S. Q.; Chen, H. Y.; Yang, Y. *Angew. Chem., Int. Ed.* **2010**, *49*, 1500. (f) Liang, Y. Y.; Xu, Z.; Xia, J. B.; Tsai, S. T.; Wu, Y.; Li, G.; Ray, C.; Yu, L. P. *Adv. Mater.* **2010**, *22*, E135. (g) Price, S. C.; Stuart, A. C.; Yang, L. Q.; Zhou, H. X.; You, W. *J. Am. Chem. Soc.* **2011**, *133*, 4625. (h) Son, H. J.; Wang, W.; Xu, T.; Liang, Y. Y.; Wu, Y. E.; Li, G.; Yu, L. P. *J. Am. Chem. Soc.* **2011**, *133*, 1885. (i) Su, M. S.; Kuo, C. Y.; Yuan, M. C.; Jeng, U. S.; Su, C. J.; Wei, K. H. *Adv. Mater.* **2011**, *23*, 3315. (j) Qin, R. P.; Li, W. W.; Li, C. H.; Du, C.; Veit, C.; Schleiermacher, H. F.; Andersson, M.; Bo, Z. S.; Liu, Z. P.; Inganas, O.; Wuerfel, U.; Zhang, F. L. *J. Am. Chem. Soc.* **2009**, *131*, 14612. (k) Seo, J. H.; Gutacker, A.; Sun, Y. M.; Wu, H. B.; Huang, F.; Cao, Y.; Scherf, U.; Heeger, A. J.; Bazan, G. C. *J. Am. Chem. Soc.* **2011**, *133*, 8416. (l) Wang, E. G.; Hou, L. T.; Wang, Z. Q.; Hellstrom, S.; Zhang, F. L.; Inganas, O.; Andersson, M. R. *Adv. Mater.* **2010**, *22*, 5240. (m) Zhang, Y.; Zou, J. Y.; Yip, H. L.; Chen, K. S.; Zeigler, D. F.; Sun, Y.; Jen, A. K. Y. *Chem. Mater.* **2011**, *23*, 2289. (n) He, Z. C.; Zhang, C.; Xu, X. F.; Zhang, L. J.; Huang, L.; Chen, J. W.; Wu, H. B.; Cao, Y. *Adv. Mater.* **2011**, *23*, 3086. (o) Brabec, C. J.; Gowrisanker, S.; Halls, J. J. M.; Laird, D.; Jia, S. J.; Williams, S. P. *Adv. Mater.* **2010**, *22*, 3839. (p) Heremans, P.; Cheyns, D.; Rand, B. P. *Acc. Chem. Res.* **2009**, *42*, 1740. (q) Peet, J.; Senatore, M. L.; Heeger, A. J.; Bazan, G. C. *Adv. Mater.* **2009**, *21*, 1521.

(5) (a) Dennler, G.; Scharber, M. C.; Ameri, T.; Denk, P.; Forberich, K.; Waldauf, C.; Brabec, C. J. *Adv. Mater.* **2008**, *20*, 579. (b) Scharber, M. C.; Wuhlbacher, D.; Koppe, M.; Denk, P.; Waldauf, C.; Heeger, A. J.; Brabec, C. L. *Adv. Mater.* **2006**, *18*, 789.

(6) (a) Mihailetchi, V. D.; Koster, L. J. A.; Blom, P. W. M.; Melzer, C.; de Boer, B.; van Duren, J. K. J.; Janssen, R. A. J. *Adv. Funct. Mater.* **2005**, *15*, 795. (b) Mihailetchi, V. D.; Xie, H. X.; de Boer, B.; Koster, L. J. A.; Blom, P. W. M. *Adv. Funct. Mater.* **2006**, *16*, 699.

(7) Zhou, H. X.; Yang, L. Q.; Xiao, S. Q.; Liu, S. B.; You, W. *Macromolecules* **2010**, *43*, 811.

(8) Li, W. W.; Qin, R. P.; Zhou, Y.; Andersson, M.; Li, F. H.; Zhang, C.; Li, B. S.; Liu, Z. P.; Bo, Z. S.; Zhang, F. L. *Polymer* **2010**, *51*, 3031.

(9) (a) Beaupre, S.; Boudreault, P. L. T.; Leclerc, M. *Adv. Mater.* **2010**, *22*, E6. (b) Gadisa, A.; Zhang, F. L.; Sharma, D.; Svensson, M.; Andersson, M. R.; Inganas, O. *Thin Solid Films* **2007**, *515*, 3126. (c) Inganas, O.; Zhang, F. L.; Andersson, M. R. *Acc. Chem. Res.* **2009**, *42*, 1731. (d) Lee, J. F.; Hsu, S. L. C.; Lee, P. I.; Chuang, H. Y.; Chen, J. S.; Chou, W. Y. *J. Polym. Sci., Part A: Polym. Chem.* **2011**, *49*, 4618. (e) Oh, H. S.; Kim, T. D.; Koh, Y. H.; Lee, K. S.; Cho, S.; Cartwright, A.; Prasad, P. N. *Chem. Commun.* **2011**, *47*, 8931. (f) Svensson, M.; Zhang, F. L.; Veenstra, S. C.; Verhees, W. J. H.; Hummelen, J. C.; Kroon, J. M.; Inganas, O.; Andersson, M. R. *Adv. Mater.* **2003**, *15*, 988. (g) Wang, E. G.; Wang, L.; Lan, L. F.; Luo, C.; Zhuang, W. L.; Peng, J. B.; Cao, Y. *Appl. Phys. Lett.* **2008**, 92.

(10) Chen, M. H.; Hou, J.; Hong, Z.; Yang, G.; Sista, S.; Chen, L. M.; Yang, Y. *Adv. Mater.* **2009**, *21*, 4238.

(11) (a) Kowada, T.; Ohe, K. *Bull. Korean Chem. Soc.* **2010**, *31*, 577. (b) Saragi, T. P. I.; Spehr, T.; Siebert, A.; Fuhrmann-Lieker, T.; Salbeck, J. *Chem. Rev.* **2007**, *107*, 1011. (c) Wu, Y. G.; Li, J.; Fu, Y. Q.; Bo, Z. S. *Org. Lett.* **2004**, *6*, 3485. (d) Yu, W. L.; Pei, J.; Huang, W.; Heeger, A. J. *Adv. Mater.* **2000**, *12*, 828. (e) Tang, S.; Liu, M.; Lu, P.; Xia, H.; Li, M.; Xie, Z. Q.; Shen, T. Z.; Gu, C.; Wang, H. P.; Yang, B.; Ma, Y. G. *Adv. Funct. Mater.* **2007**, *17*, 2869. (f) Wu, C. C.; Lin, Y. T.; Chiang, H. H.; Cho, T. Y.; Chen, C. W.; Wong, K. T.; Liao, Y. L.; Lee, G. H.; Peng, S. M. *Appl. Phys. Lett.* **2002**, *81*, 577. (g) Wu, Y. G.; Zhang, J. Y.; Bo, Z. S. *Org. Lett.* **2007**, *9*, 4435. (h) Wu, Y. G.; Zhang, J. Y.; Fei, Z. P.; Bo, Z. S. *J. Am. Chem. Soc.* **2008**, *130*, 7192.

(12) Chiang, C. L.; Shu, C. F. *Chem. Mater.* **2002**, *14*, 682.

(13) (a) Kadashchuk, A.; Vakhnin, A.; Skryshevski, Y.; Arkhipov, V. I.; Emelianova, E. V.; Bassler, H. *Chem. Phys.* **2003**, *291*, 243. (b) Poriel, C.; Liang, J. J.; Rault-Berthelot, J.; Barriere, F.; Cocherel, N.; Slawin, A. M. Z.; Horhant, D.; Virboul, M.; Alcaraz, G.; Audebrand, N.; Vignau, L.; Huby, N.; Wantz, G.; Hirsch, L. *Chem.—Eur. J.* **2007**, *13*, 10055.

(14) (a) Barche, J.; Janietz, S.; Ahles, M.; Schmechel, R.; von Seggern, H. *Chem. Mater.* **2004**, *16*, 4286. (b) Lan, Y. K.; Huang, C. I. *J. Phys. Chem. B* **2008**, *112*, 14857.

(15) Wienk, M. M.; Kroon, J. M.; Verhees, W. J. H.; Knol, J.; Hummelen, J. C.; van Hal, P. A.; Janssen, R. A. J. *Angew. Chem., Int. Ed.* **2003**, *42*, 3371.

(16) Sun, Q. J.; Wang, H. Q.; Yang, C. H.; Li, Y. F. *J. Mater. Chem.* **2003**, *13*, 800.

(17) Brabec, C. J.; Cravino, A.; Meissner, D.; Sariciftci, N. S.; Fromherz, T.; Rispens, M. T.; Sanchez, L.; Hummelen, J. C. *Adv. Funct. Mater.* **2001**, *11*, 374.

(18) (a) Blom, P. W. M.; Mihailetchi, V. D.; Koster, L. J. A.; Markov, D. E. *Adv. Mater.* **2007**, *19*, 1551. (b) Ruderer, M. A.; Muller-Buschbaum, P. *Soft Matter* **2011**, *7*, 5482. (c) Yao, Y.; Hou, J. H.; Xu, Z.; Li, G.; Yang, Y. *Adv. Funct. Mater.* **2008**, *18*, 1783.

(19) (a) Chen, L. M.; Hong, Z. R.; Li, G.; Yang, Y. *Adv. Mater.* **2009**, *21*, 1434. (b) Maturova, K.; van Bavel, S. S.; Wienk, M. M.; Janssen, R. A. J.; Kemerink, M. *Adv. Funct. Mater.* **2011**, *21*, 261.

(20) Tolman, C. A.; Seidel, W. C.; Gerlach, D. H. *J. Am. Chem. Soc.* **1972**, *94*, 2669.

Macromolecules

Article

pubs.acs.org/Macromolecules

Poly(arylene ether)s with Low Refractive Indices: Poly(biphenylene oxide)s with Trifluoromethyl Pendant Groups via a Meta-Activated Nitro Displacement Reaction

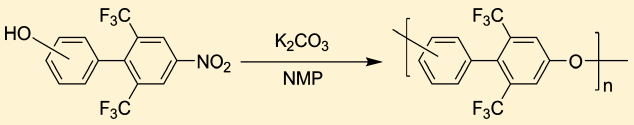
Sun Dal Kim,[†] Duyoun Ka,[†] Im Sik Chung,*[,‡] and Sang Youl Kim*[,†]

[†]Department of Chemistry, KAIST, Daejeon 305-701, Korea

[‡]Immunotherapy Research Center, KRIBB, Daejeon 305-806, Korea

Supporting Information

ABSTRACT: High-molecular-weight poly(biphenylene oxide)s (PBPO) were prepared from AB-type monomers, 4′(3′)-hydroxy-4-nitro-2,6-bis(trifluoromethyl)biphenyl, through a *meta*-activated nitro displacement reaction. The displacement of nitro leaving group activated by the two trifluoromethyl groups at the *meta*-position produced high-molecular-weight polymers, which implies that nucleophilic aromatic substitution reaction of the nitro leaving group proceeded very effectively with two activating groups at the *meta*-position. The obtained polymers have weight-average molecular weight of 20 800−143 300 g/mol and molecular weight distribution of 1.68−2.85. While two homopolymers of 4′- or 3′-hydroxy-4-nitro-2,6-bis(trifluoromethyl)biphenyl, ***p*-PBPO** and ***m*-PBPO**, showed a semicrystalline morphology, copolymers of the two monomers were amorphous and dissolved in a wide range of organic solvents. The PBPOs possessed a high glass transition temperature (T_g) in the range of 169 to 208 °C depending on their structure and high thermal stability with 10% weight loss temperatures from 486 to 542 °C in nitrogen and from 465 to 516 °C in air. Moreover, PBPOs containing two trifluoromethyl groups showed low refractive indices in the range of 1.4979−1.5052 as well as low birefringence values of 0.0095−0.0148.



INTRODUCTION

Fluorine-containing polymers are of considerable interest for optical and electronic applications owing to their low refractive index, optical loss, dielectric constant, surface energy, moisture absorption, and good thermal and chemical stability.[1,2] Although many synthetic methods for fluorine-containing polymers have been reported, a use of the trifluoromethyl group is known as very effective and practical method to incorporate fluorines into the polymer chains.[2] Trifluoromethyl groups provide not only several desirable properties, as above-mentioned, but also good solubility and good optical transparency.[3−10]

Poly(arylene ether)s have been widely used as engineering thermoplastics due to their good mechanical properties, high thermal stability, and excellent resistance to hydrolysis and oxidation reaction.[11] The known approaches for the synthesis of poly(arylene ether)s include electrophilic aromatic substitution, nucleophilic aromatic substitution, and metal catalyzed coupling reactions.[11−13] Among these methods, the nucleophilic aromatic substitution (S_NAr) reaction is the most practical method for the preparation of poly(arylene ether)s despite the fact that it requires some structural features, leaving group activated with electron withdrawing groups.[14,15] Various heterocyclic rings[16] and electron withdrawing groups such as sulfone, ketone, and imide groups have been used as an activating group for S_NAr reactions to produce high-molecular-weight poly(arylene ether)s.[17−19] Trifluoromethyl groups are also useful for S_NAr reactions to activate fluoro or nitro groups for displacement by phenoxides.[20−33]

The activating groups in S_NAr reaction stabilize the negative charge that develops during the transition state largely through conjugation,[34−36] and the electron withdrawing group at the *meta* position of the leaving group is less effective than the same group at the *ortho* or *para* position. Therefore, activating groups at the *ortho* or *para* position are generally required to obtain high-molecular-weight polymers. Since we first succeeded in making linear poly(arylene ether)s via a *meta*-activated S_NAr reaction,[37] some examples of the *meta*-activated S_NAr reaction have been reported to make linear polymers[38−42] as well as hyperbranched polymers.[43,44]

In previous work,[45] we found that trifluoromethyl groups and ether linkages are stable in a nitro displacement reaction, even at 190 °C, and that the displacement reaction occurs quantitatively without side reactions that are frequently observed during the nitro displacement reactions at high temperatures due to the reactive nitrite ion byproduct.[46−52]

In this study, new poly(biphenylene oxide)s containing two trifluoromethyl groups positioned symmetrically on one phenyl ring were prepared from 4′-hydroxy-4-nitro-2,6-bis-(trifluoromethyl)biphenyl and 3′-isomer through a *meta*-activated nucleophilic nitro displacement reaction. The effect

Received: December 30, 2011
Revised: March 14, 2012
Published: March 26, 2012

 © 2012 American Chemical Society dx.doi.org/10.1021/ma2028209 | *Macromolecules* 2012, 45, 3023−3031

of the two trifluoromethyl groups on the reactivity of the *meta*-activated S_NAr reaction and other mechanical and optical properties of the polymers were investigated.

EXPERIMENTAL SECTION

Materials. 4-Bromo-3,5-bis(trifluoromethyl)aniline (**1**, Fluorochem), oxone (Aldrich), 4-methoxyphenylboronic acid (Aldrich), 3-methoxyphenylboronic acid (TCI), tetrakis(triphenylphosphine) palladium(0) ($Pd(PPh_3)_4$, Aldrich), boron tribromide (BBr_3 1 M solution in CH_2Cl_2, Aldrich) were used as received. Potassium carbonate (K_2CO_3) was dried *in vacuo* at 150 °C for 24 h prior to use. *N*-methylpyrrolidone (NMP) was stirred in the presence of CaH_2 overnight and then distilled under reduced pressure. Other commercially available reagent-grade chemicals were used without further purification.

General Measurements. The Fourier-transform infrared (FTIR) spectra of the compounds were obtained with a Bruker EQUINOX-55 spectrophotometer using a KBr pellet. The NMR spectra of the synthesized compounds were recorded on a Bruker Fourier Transform Avance 400 or Avance 300 spectrometer. The chemical shift of the NMR was reported in parts per million (ppm) using tetramethylsilane as an internal reference. Splitting patterns were designated as s (singlet), d (doublet), t (triplet), q (quartet), or m (multiplet). Elemental analyses (EA) of the synthesized compounds were carried out with a CE Instrument EA1110-FISONS analyzer. Gel permeation chromatography (GPC) diagrams were obtained with a Viscotek TDA302 equipped with a triple RI detector array and a packing column (PLgel 10 μm MIXED-B) using tetrahydrofuran (THF) as an eluent at 35 °C. The number and weight-average molecular weight of the polymers were calculated relative to linear polystyrene standards. Thermogravimetric analysis (TGA) and differential scanning calorimetry (DSC) were performed on a TA Instruments TGA Q500 and a DSC Q100 instrument, respectively. The TGA measurements were conducted at a heating rate of 10 °C/min in N_2 and air. The melting points (m.p.) of the synthesized compounds and the T_g and T_m values of the polymers were obtained with DSC instrument at a heating rate of 10 °C/min in N_2. The T_m values were taken from the first heating scan ranging from 0 to 450 °C. T_g values were taken from the second heating scan after cooling to 0 °C from 350 °C. The wide-angle X-ray diffraction (WAXD) patterns were obtained with a Rigaku D/MAX III diffractometer. The refractive indices n_{TE} and n_{TM} for the transverse electric (TE) and transverse magnetic (TM) modes of the polymer films were measured with a Sairon SPA-4000 prism coupler with a gadolinium gallium garnet (GGG) prism at the wavelength of 1310 nm at room temperature. The birefringence values (Δn) were calculated as the difference between n_{TE} and n_{TM}.

Monomer Syntheses. *1-Bromo-4-nitro-2,6-bis-(trifluoromethyl)benzene (**2**).* In a three-neck round-bottom flask fitted with two addition funnels and a pH electrode was placed 50 mL of dichloromethane, 50 mL of acetone, 50 mL of a 0.8 M aqueous solution of sodium phosphate, 170 mg of tetrabutylammonium hydrogen sulfate, and 0.950 g (3.08 mmol) of **1**. In one addition funnel was added a solution of 20.0 g (32.5 mmol) of oxone in 150 mL of water, and in the other addition funnel was placed 100 mL of a 2 N aqueous solution of potassium hydroxide. After cooling the mixture to 0 °C, the aqueous solution of oxone was added dropwise over 30 min while maintaining a pH of 7.5−8.5 with the addition of the aqueous solution of potassium hydroxide. The resulting suspension was filtered off, and the filtrate was partitioned. The organic layer was washed with water, dried over anhydrous magnesium sulfate, filtered, and concentrated under a reduced pressure environment. The solid residue was passed through a silica column using CH_2Cl_2/hexane (v/v = 1/4) as an eluent to give pale yellow 1-bromo-4-nitro-2,6-bis(trifluoromethyl)-benzene (0.860 g, 82.6% yield): mp 56−57 °C. FTIR (KBr, cm^{-1}): 1613, 1598 (aromatic C═C); 1540, 1332 (NO_2); 1125−1197 (C−F). ^1H NMR ($CDCl_3$, 400 MHz, ppm): 8.71(s, 2H). ^{13}C NMR (DMSO-d_6, 100 MHz, ppm): 146.62, 132.48 (q, J = 31.9 Hz), 126.71 (q, J = 5.7 Hz), 125.63, 121.68 (q, J = 272.9 Hz). Anal. Calcd for $C_8H_2BrF_6NO_2$: C, 28.43; H, 0.60; N, 4.14. Found: C, 28.57; H, 0.76; N, 4.03.

*4′-Hydroxy-4-nitro-2,6-bis(trifluoromethyl)biphenyl (**5**).* 4-Methoxyphenylboronic acid (3.37 g, 22.2 mmol) was reacted with **2** (4.98 g, 14.7 mmol) in the presence of $Pd(PPh_3)_4$ (1.00 g). The reaction mixture of 40 mL of toluene, 20 mL of ethanol, and 8.18 g of K_2CO_3 dissolved in 40 mL of water was refluxed for 27 h. The product was extracted with ethyl acetate and passed through a silica column using CH_2Cl_2/hexane (v/v = 1/4) as an eluent to give pale yellow 4′-methoxy-4-nitro-2,6-bis(trifluoromethyl)biphenyl (**3**) (4.16 g, 77.5% yield): mp 94−95 °C. FTIR (KBr, cm^{-1}): 2847 (−OCH_3); 1610 (aromatic C═C); 1536, 1331 (NO_2); 1124−1183 (C−F). ^1H NMR (DMSO-d_6, 400 MHz, ppm): 8.76 (s, 2H), 7.22 (d, 2H, J = 8.52 Hz), 7.02 (d, 2H, J = 8.88 Hz), 3.81(s, 3H, −OCH_3). ^{13}C NMR (DMSO-d_6, 100 MHz, ppm): 159.78, 146.82, 146.07, 131.91(q, J = 30.3 Hz), 130.59, 124.73(q, J = 5.7 Hz), 123.69, 122.16(q, J = 273.5 Hz), 112.73, 55.13. Anal. Calcd for $C_{15}H_9F_6NO_3$: C, 49.33; H, 2.48; N, 3.84. Found: C, 51.15; H, 2.48; N, 3.72.

A solution of **3** (3.00 g, 8.21 mmol) in 60 mL of CH_2Cl_2 was cooled to −78 °C, and 18 mL of 1 M BBr_3 was added slowly. The resulting mixture was stirred at 0 °C for 7 h and quenched by cautiously pouring it into 300 mL of cold water. The mixture was heated until CH_2Cl_2 evaporated completely. The product was extracted with excess CH_2Cl_2 and recrystallized from toluene/*n*-hexane to give pale yellow 4′-hydroxy-4-nitro-2,6-bis(trifluoromethyl)biphenyl (**5**) (2.89 g, 100% yield): mp 139−140 °C. FTIR (KBr, cm^{-1}): 3418 (O−H); 1613 (aromatic C═C); 1538, 1335 (NO_2); 1142−1189 (C−F). ^1H NMR (DMSO-d_6, 400 MHz, ppm): 9.80 (s, 1H, −OH), 8.74 (s, 2H), 7.07 (d, 2H, J = 8.33 Hz), 6.82 (d, 2H, J = 8.56 Hz). ^{13}C NMR (DMSO-d_6, 100 MHz, ppm): 158.06, 146.68, 146.58, 131.90 (q, J = 30.2 Hz), 130.45, 124.70 (q, J = 5.6 Hz), 122.17 (q, J = 273.6 Hz), 121.98, 114.12. Anal. Calcd for $C_{14}H_7F_6NO_3$: C, 47.88; H, 2.01; N, 3.99. Found: C, 49.74; H, 1.54; N, 3.83.

*3′-Hydroxy-4-nitro-2,6-bis(trifluoromethyl)biphenyl (**6**).* 3-Methoxyphenylboronic acid (3.80 g, 25.0 mmol) was reacted with **2** (6.97 g, 20.6 mmol) in the presence of $Pd(PPh_3)_4$ (1.00 g). The reaction mixture of 40 mL of toluene, 40 mL of ethanol, and 8.61 g of K_2CO_3 dissolved in 40 mL of water was refluxed for 31 h. The product was extracted with ethyl acetate and passed through a silica column using CH_2Cl_2/hexane (v/v = 1/4) as an eluent to give pale yellow 3′-methoxy-4-nitro-2,6-bis(trifluoromethyl)biphenyl (**4**) (5.94 g, 78.8% yield). ^1H NMR (DMSO-d_6, 400 MHz, ppm): 8.76 (s, 2H), 7.37(t, 1H, J = 7.96 Hz), 7.06 (m, 1H), 6.86 (s, 1H), 6.85 (d, 1H, J = 12.16 Hz), 3.75 (s, 3H, −OCH_3). ^{13}C NMR (DMSO-d_6, 100 MHz, ppm): 158.03, 146.89, 145.50, 133.06, 131.58 (q, J = 30.8 Hz), 128.42, 124.71 (q, J = 5.7 Hz), 122.09 (q, J = 273.5 Hz), 121.65, 115.49, 114.38, 55.08.

A solution of **4** (3.44 g, 9.42 mmol) in 69 mL of CH_2Cl_2 was cooled to −78 °C, and 21 mL of 1 M BBr_3 was slowly added. The resulting mixture was stirred at 0 °C for 19 h and quenched by cautiously pouring it into 300 mL of cold water. The mixture was heated until the CH_2Cl_2 evaporated completely. The product was extracted with excess CH_2Cl_2 and passed through a silica column using ethyl acetate/*n*-hexane (v/v = 1/3) as an eluent to give pale yellow 3′-hydroxy-4-nitro-2,6-bis(trifluoromethyl)biphenyl (**6**) (3.30 g, 100% yield): mp 84−86 °C. FTIR (KBr, cm^{-1}): 3271 (O−H); 1610 (aromatic C═C); 1539, 1333 (NO_2); 1141−1187 (C−F). ^1H NMR (DMSO-d_6, 400 MHz, ppm): 9.69 (s, 1H, −OH), 8.76 (s, 2H), 7.24 (t, 1H, J = 8.20 Hz), 6.88 (m, 1H), 6.69 (d, 1H, J = 6.98 Hz), 6.68 (s, 1H). ^{13}C NMR (DMSO-d_6, 100 MHz, ppm): 156.10, 146.87, 145.69, 132.94, 131.30 (q, J = 30.5 Hz), 128.36, 124.89 (q, J = 5.7 Hz), 122.14 (q, J = 273.6 Hz), 120.09, 116.35, 116.15. Anal. Calcd for $C_{14}H_7F_6NO_3$: C, 47.88; H, 2.01; N, 3.99. Found: C, 50.29; H, 1.52; N, 3.90.

Model Reactions. *Model Reaction of **3** with Sodium Phenoxide at Room Temperature.* A 25 mL three-necked flask equipped with an N_2 inlet was charged with **3** (500 mg, 1.37 mmol), sodium phenoxide trihydrate (300 mg, 1.77 mmol), and 5 mL of NMP. The reaction mixture was stirred at room

temperature (ca. 25 °C) for 4 days. The major part of the starting compound (**3**) remained intact in TLC.

*Model Reaction of **3** with m-Cresol.* A 25 mL three-necked flask equipped with an N_2 inlet, a Dean–Stark trap, and a condenser was charged with **3** (500 mg, 1.37 mmol), *m*-cresol (190 mg, 1.75 mmol), K_2CO_3 (284 mg, 2.06 mmol), and 3 mL of NMP. The reaction mixture was heated to 90 °C for 31 h. The product was extracted with CH_2Cl_2 to give colorless product **7**. (570 mg, 98.0% yield). The procedure was repeated at 140 °C and at 175 °C. The reaction was complete within 4 and 1 h at 140 and 175 °C, respectively. The isolation yield was almost quantitative in all cases: mp 104–105 °C. FTIR (KBr, cm^{-1}): 1614, 1583 (aromatic C=C); 1295, 1259 (C–O–C); 1133–1185 (C–F). ^{1}H NMR (DMSO-d_6, 400 MHz, ppm): 7.57 (s, 2H), 7,36 (t, 1H, J = 7.84 Hz), 7.15 (d, 2H, J = 8.42 Hz), 7.09 (d, 1H, J = 7.56 Hz), 7.04 (s, 1H), 6.99 (dd, 1H, J = 8.09 Hz, J = 2.11 Hz), 3.79 (s, 3H), 2.32 (s, 3H). ^{13}C NMR (DMSO-d_6, 100 MHz, ppm): 159.19, 156.84, 154.59, 140.52, 133.44, 131.97 (q, J = 29.2 Hz), 131.34, 130.21, 126.03, 124.83, 122.74 (q, J = 273.3 Hz), 120.42, 118.23 (q, J = 5.4 Hz), 116.87, 112.50, 55.00, 20.80. Anal. Calcd for $C_{22}H_{16}F_6O_2$: C, 61.98; H, 3.78; N, 0. Found: C, 63.96; H, 3.69; N, 0.

Polymerizations. All polymerizations were conducted under a dry nitrogen atmosphere.

***p*-PBPO.** A 25 mL three-necked flask equipped with a N_2 inlet, a mechanical stirrer, a Dean–Stark trap, and a condenser was charged with 804 mg (2.29 mmol) of **5**, 470 mg (3.40 mmol) of K_2CO_3, 4 mL of NMP, and 2 mL of toluene. The reaction mixture was heated to 135 °C for 3 h, at which the toluene was brought to reflux. The toluene was periodically removed from the Dean–Stark trap, and fresh dry toluene was added to the reaction mixture to ensure dehydration of the system. After the reaction temperature was raised to 175 °C, precipitation occurred within 1 min. The precipitated product was washed with hot water and methanol repeatedly and dried *in vacuo* at 100 °C for 24 h (654 mg, 93.8% yield).: FTIR (KBr, cm^{-1}): 1603 (aromatic C=C); 1295, 1261, 1235 (C–O–C); 1135–1186 (C–F).

***m*-PBPO.** The same procedure used for ***p*-PBPO** was repeated with 499 mg (1.42 mmol) of **6**, 216 mg (1.57 mmol) of K_2CO_3, and a total of 4.5 mL of NMP. The precipitation also occurred after 1 h at 175 °C. The product was washed with hot water and methanol repeatedly and dried *in vacuo* at 100 °C for 24 h (498 mg, 99.0% yield). The soluble part in THF was collected for characterization.: FTIR (KBr, cm^{-1}): 1610, 1585 (aromatic C=C); 1287, 1268 (C–O–C); 1133–1189 (C–F). ^{1}H NMR (soluble part in THF, THF-d_8, 400 MHz, ppm): 7.62 (s, 2H), 7.51(t, 1H, J = 7.94 Hz), 7.26 (d, 1H, J = 8.17 Hz), 7.19 (d, 1H, J = 7.65 Hz), 7.09 (s, 1H).

***1p3m*-PBPO.** A 25 mL three-necked flask equipped with a N_2 inlet, a mechanical stirrer, a Dean–Stark trap, and a condenser was charged with 201 mg (0.570 mmol) of **5**, 600 mg (1.71 mmol) of **6**, 348 mg (2.52 mmol) of K_2CO_3, and 4 mL of NMP. The reaction mixture was heated to 135 °C for 3 h, at which the toluene was brought to reflux. The toluene was periodically removed from the Dean–Stark trap, and fresh dry toluene was added to the reaction mixture to ensure dehydration of the system. The temperature was raised to 175 °C and the polymerization continued for 14 h. The polymer was precipitated into a 400 mL of vigorously stirred water and then filtered. The precipitated polymer was washed with hot water and methanol repeatedly and dried *in vacuo* at 100 °C for 24 h. Further purification was carried out by dissolving the polymers in THF and then precipitating it into methanol (575 mg, 83.0% yield). FTIR (KBr, cm^{-1}): 1607, 1583 (aromatic C=C); 1293, 1262, 1227 (C–O–C); 1136–1188 (C–F). ^{1}H NMR (THF-d_8, 400 MHz, ppm): 7.70 (m, 2H), 7.62 (m, 6H), 7.52 (m, 3H), 7.37 (m, 2H), 7.28 (m, 3H), 7.19 (m, 5H), 7.10 (m, 3H).

***1p1m*-PBPO.** The same procedure used for ***1p3m*-PBPO** was repeated with 400 mg (1.14 mmol) of **5**, 402 mg (1.14 mmol) of **6**, 348 mg (2.518 mmol) of K_2CO_3, and 4 mL of NMP. (554 mg, 80.0% yield).: FTIR (KBr, cm^{-1}): 1606, 1583 (aromatic C=C); 1294, 1261, 1230 (C–O–C); 1133–1188 (C–F). ^{1}H NMR (THF-d_8, 400 MHz, ppm): 7.71(m, 2H), 7.63 (m, 2H), 7.53 (m, 1H), 7.38 (m, 2H), 7.31 (m, 1H), 7.20 (m, 3H), 7.11 (m, 1H).

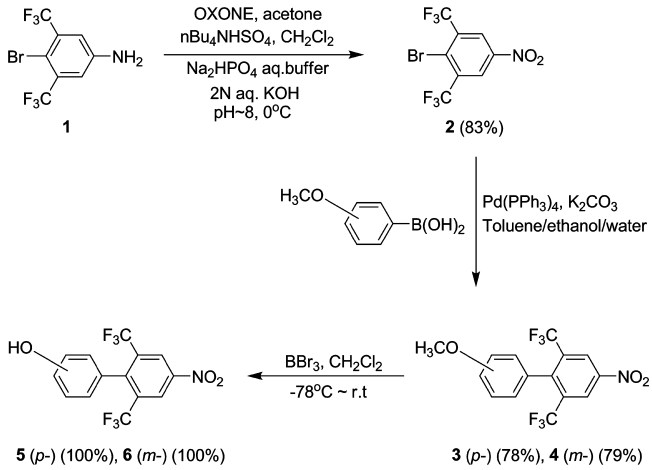
***2p1m*-PBPO.** The same procedure used for ***1p3m*-PBPO** was repeated with 520 mg (1.48 mmol) of **5**, 264 mg (0.750 mmol) of **6**, 348 mg (2.52 mmol) of K_2CO_3, and 4 mL of NMP. (633 mg, 93.2% yield).: FTIR (KBr, cm^{-1}): 1605, 1584 (aromatic C=C); 1294, 1261, 1232 (C–O–C); 1134–1187 (C–F). ^{1}H NMR (THF-d_8, 400 MHz, ppm): 7.72 (m, 4H), 7.64 (m, 2H), 7.54 (m, 1H), 7.39 (m, 4H), 7.30 (m, 1H), 7.20 (m, 5H), 7.12 (m, 1H).

***3p1m*-PBPO.** The same procedure used for ***1p3m*-PBPO** was repeated with 602 mg (1.71 mmol) of **5**, 201 mg (0.750 mmol) of **6**, 346 mg (2.52 mmol) of K_2CO_3, and 4 mL of NMP. (689 mg, 99.4% yield). FTIR (KBr, cm^{-1}): 1605, 1584 (aromatic C=C); 1293, 1261, 1233 (C–O–C); 1136–1186 (C–F). ^{1}H NMR (soluble part in THF, THF-d_8, 400 MHz, ppm): 7.72 (m, 4H), 7.65 (m, 2H), 7.55 (m, 1H), 7.40 (m, 5H), 7.20 (m, 6H).

RESULTS AND DISCUSSION

Monomer Syntheses. The monomers, 4′-hydroxy-4-nitro-2,6-bis(trifluoromethyl)biphenyl (**5**) and 3′-isomer (**6**), were

Scheme 1



Scheme 2

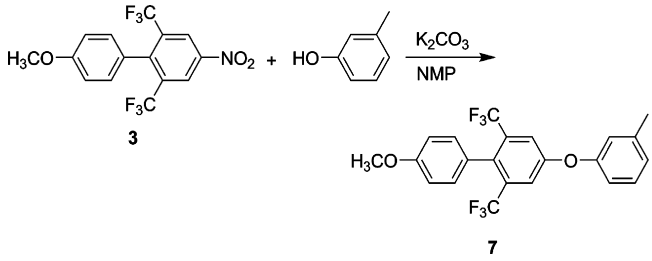
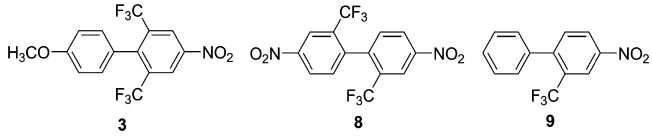


Chart 1



prepared as shown in Scheme 1 with a good yield. 4-Bromo-3,5-bis(trifluoromethyl)aniline (**1**) was oxidized with oxone.[53] The resulting nitro compound (**2**) was reacted with *p*- and *m*-(methoxyphenylbronic acid) through a Suzuki coupling reaction[54] to produce 4′-methoxy-4-nitro-2,6-bis-(trifluoromethyl)biphenyl (**3**) and its 3′-isomer (**4**), respectively. The methoxy compounds were converted to the corresponding monomers by demethylation with BBr_3. The

dx.doi.org/10.1021/ma2028209 | *Macromolecules* 2012, 45, 3023–3031

Scheme 3

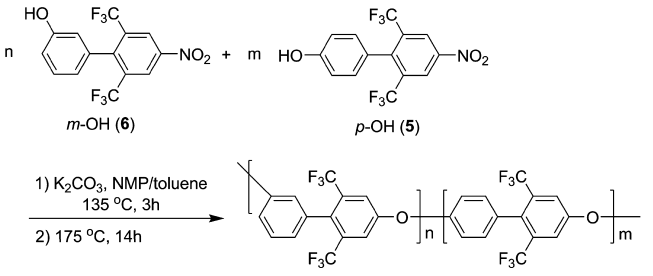


Table 1. Molecular Weight and Polydispersity Index of the Polymers

PBPOs	feed ratio 5/6	M_n[a]/10³	M_w[a]/10³	PDI[b]
***p*-PBPO**[c]	100/0	–	–	–
***3p1m*-PBPO**[d]	75/25 (3/1)	9.3	26.4	2.85
***2p1m*-PBPO**	67/33 (2/1)	34.9	58.6	1.68
***1p1m*-PBPO**	50/50 (1/1)	70.6	143.3	2.03
***1p3m*-PBPO**	25/75 (1/3)	24.6	42.0	1.70
***m*-PBPO**[d]	0/100	9.3	20.8	2.23

[a]Determined by GPC using THF as an eluent at 35 °C with polystyrene standards. [b]Polydispersity Index = M_w/M_n. [c]Insoluble. [d]Soluble part in THF.

monomers were purified by chromatography and recrystallization and were dried *in vacuo* for 24 h prior to polymerization. The structure of the synthesized monomers having both a hydroxyl group and a nitro leaving group activated by two trifluoromethyl groups at the *meta* position was confirmed by spectroscopic data (Experimental Section and Supporting Information, Figures S1 and S2).

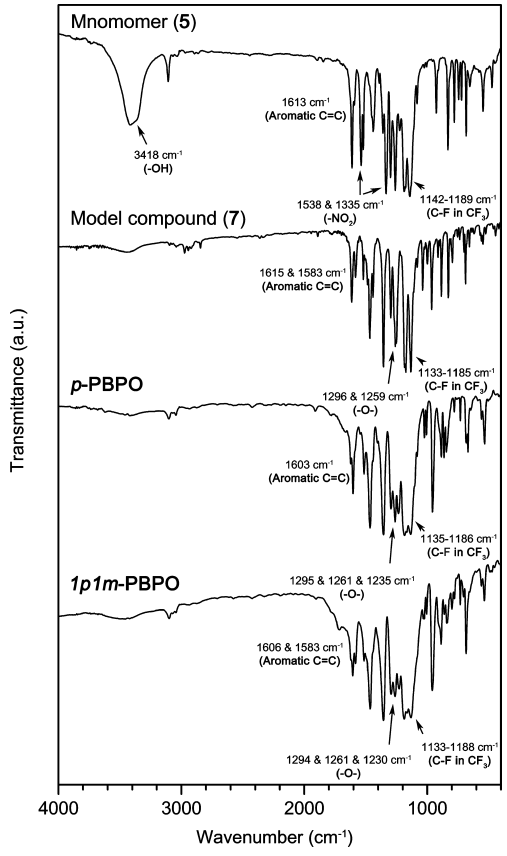


Figure 1. FTIR spectra of monomer **5**, model compound **7**, polymer ***p*-PBPO**, and ***1p1m*-PBPO**.

Model Reactions. To investigate the reactivity of the *meta*-activated nitro displacement, model reactions were conducted with **3** and *m*-cresol in NMP at several temperatures. The model compound containing diary ether linkage (**7**) was obtained as outlined in Scheme 2. The reactions were complete without any detectable side reactions within 31, 4, and 1 h at 90, 140, and 175 °C, respectively, and the yields were quantitative in all cases. The structure of **7** was confirmed by spectroscopic data (Experimental Section and Supporting Information, Figures S3 and S4). On the other hand, the model reaction at room temperature was not effective. The major part of **3** remained intact even after 4 days.

In the previous report,[42] the reactivity of 2,2′-bis-(trifluoromethyl)-4,4′-dinitro-1,1′-biphenyl (**8**) was higher than that of 4-nitro-2-trifluoromethylbiphenyl (**9**) due to the electron withdrawing characteristic of the nitro leaving group and the trifluoromethyl group attached to the other aromatic ring of the biphenyl structure (Chart 1). The reaction of **8** with two equivalents of 4-tert-buthylphenol was complete at 175 °C for 4 h, whereas the reaction of **9** with 4-*tert*-butylphenol was complete at 175 °C for 12 h.[37] Interestingly, the reaction of 4′-methoxy-4-nitro-2,6-bis(trifluoromethyl)biphenyl (**3**) with *m*-cresol was complete at 175 °C for 1 h; even at a reaction temperature of 140 °C, the reaction was complete in 4 h. It appears that the higher reactivity of **3** compared to **8** and **9** is caused by the very strong electron withdrawing characteristic of the two trifluoromethyl groups at the *meta* position of the nitro leaving group in the same phenyl ring. These results imply that activation by the two activating groups at the *meta* position is a very effective strategy for successful S_NAr reactions.

Polymerizations. On the basis of the successful results of the model reaction, we carried out the polymerization process at 175 °C. The monomers were polymerized according to the conventional poly(arylene ether) synthesis method with K_2CO_3 as a base in NMP, as shown in Scheme 3. The initial solid contents were maintained at 20 w/v %, and toluene as an azeotrope was used during the initial stage of polymerization to remove water that formed due to phenoxide generation.

Initially, we tried to obtain the homopolymers (***p*-PBPO** and ***m*-PBPO**) with **5** and **6** as a single monomer. However, the precipitation occurred in 1 h at 175 °C in both cases. It has been known that the incorporation of trifluoromethyl groups in polymer chains improves the solubility of polymers because bulky trifluoromethyl groups disturb the crystal packing between the polymer chains,[55] but the resulting homopolymers, containing numerous trifluoromethyl groups in the main chain, showed limited solubility. It seems that the symmetric incorporation of trifluoromethyl groups cannot effectively hinder the chain packing of poly(arylene ethers). (The details will be discussed later.)

To resolve the unexpected solubility problem, copolymerization, which can hinder chain packing around the diaryl ether by introducing irregular *para*- and *meta*- connections in the main chain, were also conducted. The mixture of **5** and **6** were polymerized to the corresponding copolymers (***1p3m*-PBPO**, ***1p1m*-PBPO**, ***2p1m*-PBPO**, and ***3p1m*-PBPO**). In *italics*, each number indicates the feed ratio of the *para*- and *meta*-monomers. For example, *1p3m* corresponds to the 1 to 3 feed ratio of *para* to *meta* monomers. When the polymerization

dx.doi.org/10.1021/ma2028209 | *Macromolecules* 2012, 45, 3023–3031

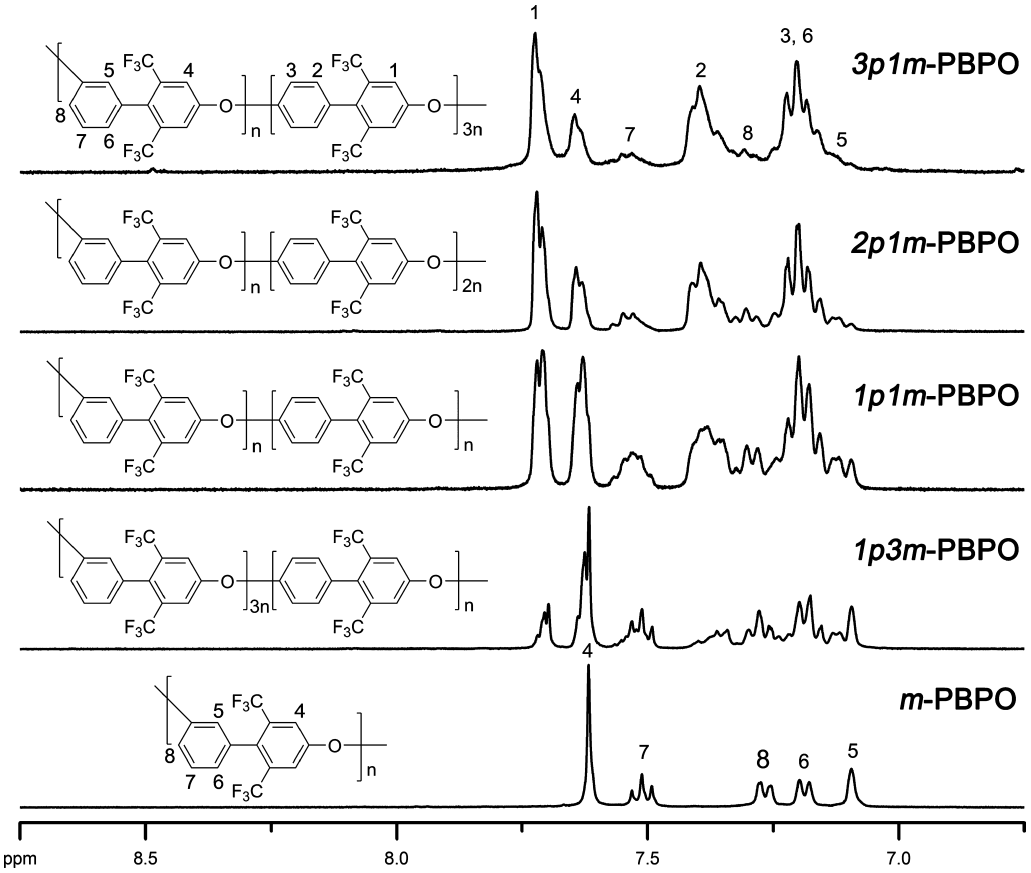


Figure 2. ^{1}H NMR spectra of PBPOs (THF-d_8, 400 MHz, 25 °C).

mixtures reacted for 14 h at 175 °C, precipitation did not occur, contrary to homopolymerization. After the polymerization process, the brown polymers were precipitated in a water/methanol (v/v = 1/1) mixture and washed with hot water and methanol repeatedly, after which they were dried *in vacuo*. Further purification was carried out by dissolving the polymers in THF and then precipitating this mixture into methanol. The molecular weight and polydispersity indices as determined by GPC are listed in Table 1 (Supporting Information, Figure S7). The weight-average molecular weights of the soluble PBPOs (***1p3m*-PBPO**, ***1p1m*-PBPO**, and ***2p1m*-PBPO**) and the partially soluble PBPOs (the soluble part in THF of ***3p1m*-PBPO** and ***m*-PBPO**) were in the range 20800−143000 g/mol based on the polystyrene standard, indicating high-molecular-weight polymers were obtained.

Table 2. Solubility of PBPOs[a]

solvents	*p*-PBPO	*3p1m*-PBPO	*2p1m*-PBPO	*1p1m*-PBPO	*1p3m*-PBPO	*m*-PBPO
NMP	−	+−	++	++	++	+−
DMF	−	+−	++	++	++	+−
DMAc	−	−	+−	++	++	+−
DMPU	−	+−	++	++	++	+−
DMSO	−	−	+−	+−	+−	+−
THF	−	+−	++	++	++	+−
1,4-dioxane	−	+−	++	++	++	+−
cyclohexanone	−	−	++	++	++	+−
acetone	−	−	+−	++	++	−
ODCB	−	+−	++	+−	++	+−
chloroform	−	−	++	+−	++	+−
ethyl acetate	−	−	+−	++	++	−
anisole	−	−	++	+−	+−	+−
toluene	−	−	+−	−	++	−
n-hexane	−	−	−	−	−	−
acetonitrile	−	−	−	−	−	−
methanol	−	−	−	−	−	−

[a]Solubility: ++, soluble at room temperature; +−, partially soluble; −, insoluble. Abbreviations: THF, tetrahydrofuran; DMF, *N*,*N*-dimethylformamide; DMAc, *N*,*N*-dimethylacetamide; DMPU, 1,3-dimethyltetrahydropyrimidin-2(1*H*)-one; DMSO, dimethyl sulfoxide; ODCB, 1,2-dichlorobenzene.

The structures of the synthesized polymers were confirmed by spectroscopic data, which indicated the formation of ether linkages without degradation of their trifluoromethyl groups. The representative FTIR spectra are shown in Figure 1. All of the FTIR spectra of monomer (**5**), model compound (**7**), and ***p*-PBPO** and ***1p1m*-PBPO** show absorption bands at 1130−1190 cm^{-1} corresponding to trifluoromethyl (C−F) stretching. While the FTIR spectrum of monomer (**5**) shows the absorption bands at 3418 cm^{-1} and at 1538 and 1335 cm^{-1} corresponding to hydroxyl (O−H) and nitro (N−O) stretching, respectively, the FTIR spectra of model compound (**7**) and the polymers show a new absorption band around 1250 cm^{-1} corresponding to the diaryl ether (Ph−O−Ph) stretching generated by successful *meta*-activated S_NAr reactions without any trace of nitro or hydroxyl stretching. FTIR spectra of all PBPOs showed similar patterns (Supporting Information, Figure S6). The ^{1}H NMR spectra of the PBPOs are shown in Figure 2. The lack of traces of −OH (9−10 ppm) or $-NO_2$ (8−9 ppm) end groups in the soluble polymers supports the formation of high-molecular-weight polymers. The

dx.doi.org/10.1021/ma2028209 | *Macromolecules* 2012, 45, 3023−3031

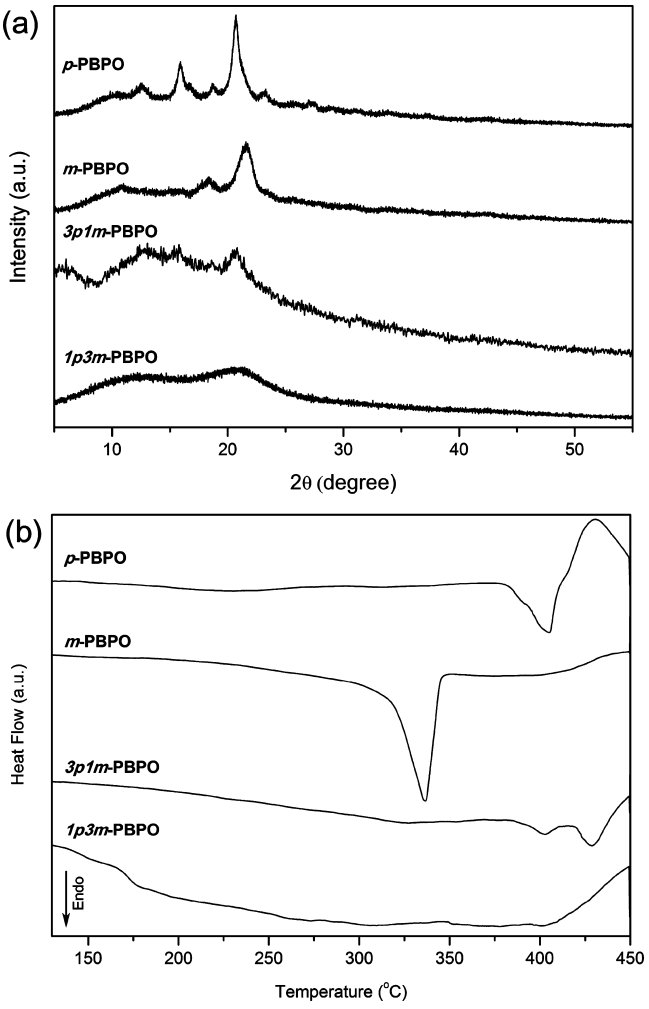


Figure 3. (a) WAXD patterns and (b) DSC curves (the first scan ranging from 0 to 450 °C, Heating rate: 10 °C/min, in N_2) of ***p*-PBPO**, ***m*-PBPO**, ***3p1m*-PBPO**, and ***1p3m*-PBPO**.

Table 3. Thermal Properties of the Polymers

	T_{d5} (°C)[a]		T_{d10} (°C)[a]			
PBPOs	in N_2	in air	in N_2	in air	T_g[b] (°C)	T_m[c] (°C)
***p*-PBPO**	430	398	486	465	*d*	405
***3p1m*-PBPO**	500	457	542	511	208	429 (403)
***2p1m*-PBPO**	432	416	522	499	192	*d*
***1p1m*-PBPO**	505	475	534	516	187	*d*
***1p3m*-PBPO**	463	399	521	480	176	*d*
***m*-PBPO**	394	377	516	474	169	337

[a]5% and 10% weight loss temperature measured by TGA at a heating rate of 10 °C/min. [b]Glass transition temperature measured by DSC (the second scan) in N_2 at a heating rate of 10 °C/min. [c]Crystalline melting temperature measured by DSC (the first scan) in N_2 at a heating rate of 10 °C/min. [d]Not detected.

peaks at 7.7 and 7.6 ppm in the spectra indicate the representative repeating unit of *para*- and *meta*-moieties in the PBPOs, respectively. The integral ratio of the peaks between 7.7 and 7.6 ppm are well matched with the feed ratio of the *para*- and *meta*-monomers, implying that the copolymers contain consistent amounts of the monomers as regards the feed ratio. However, the soluble part of ***3p1m*-PBPO** showed a

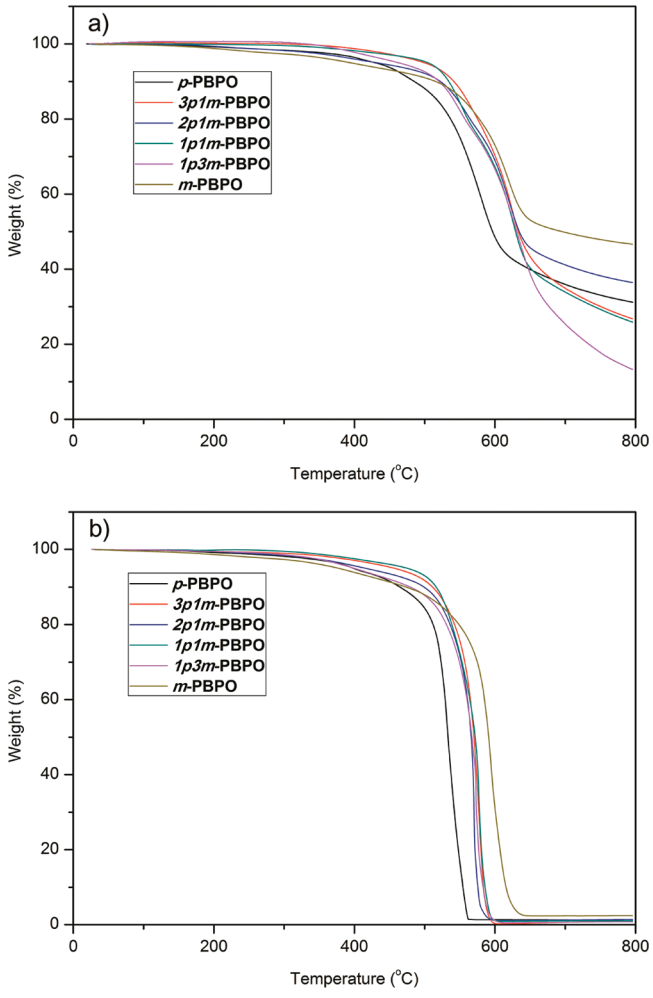


Figure 4. TGA curves of PBPOs in (a) nitrogen and (b) air at a heating rate of 10 °C/min.

2 to 1 integral ratio of *para* to *meta* moieties, indicating that a 2 to 1 ratio is a critical point to obtain good solubility.

Solubility of the Polymer. The solubility of the PBPOs in various solvents is summarized in Table 2. While ***p*-PBPO** and

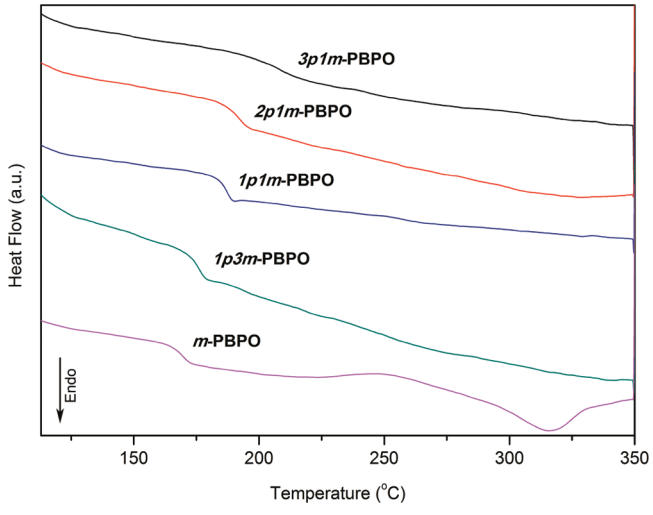


Figure 5. DSC curves (the second scan ranging from 0 to 350 °C, heating rate: 10 °C/min, in N_2) of PBPOs.

dx.doi.org/10.1021/ma2028209 | *Macromolecules* 2012, 45, 3023–3031

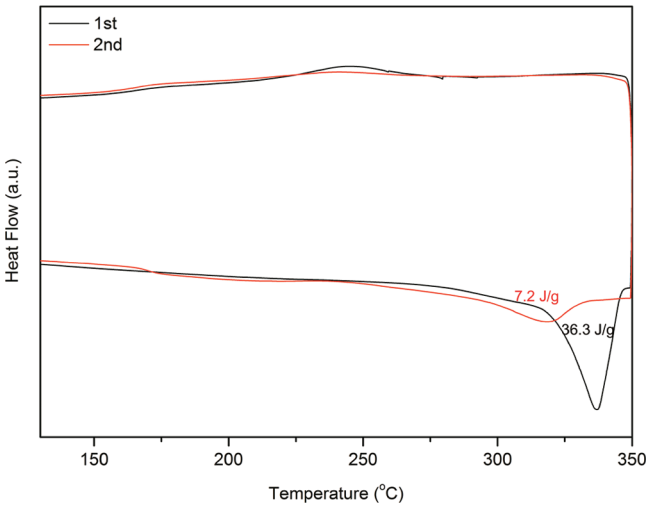


Figure 6. DSC curves (the second scan ranging from 0 to 350 °C, heating rate: 10 °C/min, in N_2) of ***m*-PBPO**.

Table 4. Refractive Indices of the Synthesized Polymers[a]

PBPOs	n_{TE}[b]	n_{TM}[c]	n_{av}[d]	Δn[e]	ε[f]	d[g] (μm)
***2p1m*-PBPO**	1.5084	1.4988	1.5052	0.0096	2.49	4.15
***1p1m*-PBPO**	1.5028	1.4880	1.4979	0.0148	2.47	6.50
***1p3m*-PBPO**	1.5052	1.4957	1.5020	0.0095	2.48	4.51

[a]Measured at a wavelength of 1310 nm at room temperature. [b]n_{TE}: the in-plane refractive index. [c]n_{TM}: the out-of plane refractive index. [d]n_{av}: the average refractive index ($n_{av} = (2n_{TE} + n_{TM})/3$). [e]$\Delta n$: birefringence ($n_{TE} - n_{TM}$). [f]Dielectric constant estimated from the refractive index: $\varepsilon \approx 1.10 n_{av}^2$ [g]Film thickness for the refractive index measured.

***m*-PBPO** have limited solubility, the copolymers were soluble in various organic solvents, including NMP, DMF, DMPU, THF, 1,4-dioxane, and cyclohexanone. Generally, the solubility of the polymers increases as the amount of the *meta*-connected moiety in the polymer backbone increases. The solubility of ***1p1m*-PBPO**, which was soluble in ethyl acetate and acetone, was better than that of ***2p1m*-PBPO** presumably due to its higher *meta*-linkage content. In addition, ***1p3m*-PBPO** was soluble even in toluene. In contrast, ***3p1m*-PBPO** showed poor solubility due to its higher content of the *para*-moiety. All of the polymers were insoluble in *n*-hexane, acetonitrile, and methanol.

It is known that trifluoromethyl pendent groups in rigid polymer chains improve the solubility of polymers because bulky trifluoromethyl groups disturb the crystal packing between the polymer chains.[55] While the PBPOs having one trifluoromethyl group on their repeating unit showed good solubility,[37] three polymers (***p*-PBPO**, ***m*-PBPO**, and ***3p1m*-PBPO**) have limited solubility. ***p*-PBPO** is insoluble in any organic solvents, and less than 10% of ***m*-PBPO** and ***3p1m*-PBPO** are soluble in THF. The unexpected limited solubility behavior was caused by their crystalline characteristics, which indicates that the increased symmetry in the polymer structure overrides the bulkiness of trifluoromethyl groups in their crystal packing structure. The wide-angle X-ray diffraction (WAXD) patterns and the DSC curves of ***p*-PBPO**, ***m*-PBPO**, ***3p1m*-PBPO**, and ***1p3m*-PBPO** are shown in Figure 3, parts a and b, respectively. While the WAXD pattern of ***1p3m*-PBPO** is broad without any obvious peak features, the patterns of ***p*-PBPO**, ***m*-PBPO**, and ***3p1m*-PBPO** show relatively sharp peaks that often appear in crystalline polymers. The WAXD results are consistent with the DSC results. While ***1p3m*-PBPO** shows a glass transition temperature (T_g) at 172 °C, ***p*-PBPO**, ***m*-PBPO**, and ***3p1m*-PBPO** show crystalline melting temperatures (T_m) at 405, 337, and 429 (403) °C, respectively. These WAXD and DSC results show that ***p*-PBPO**, ***m*-PBPO**, and ***3p1m*-PBPO** have crystallinity, leading to its limited solubility.

Thermal Properties. The thermal properties of the polymers were evaluated by TGA and DSC, and the results are summarized in Table 3. They have high thermal stability, as expected for fluoroalkyl-containing poly(arylene ether)s. The TGA and DSC thermograms are shown in Figures 4 and 5, respectively. The dynamic TGA result shows that a 10% weight loss occurred for PBPOs in the range of 486−542 °C in nitrogen and 465−516 °C in air. Although ***p*-PBPO** and ***m*-PBPO**, precipitated during the polymerization process, showed relatively low thermal stability due to the remaining end groups, the main decomposition of ***p*-PBPO** and ***m*-PBPO** starts at above 500 °C in nitrogen. As mentioned above, ***p*-PBPO**, ***m*-PBPO**, and ***3p1m*-PBPO** have T_m values. In the second scan of the DSC measurement in the range of 0 and 350 °C, all of the polymers except ***p*-PBPO** showed a high glass transition temperature (T_g) in the range of 169−208 °C. When increasing the quantity of the *para*-linkage in the main chain, the T_g value of PBPOs increased gradually from 169 to 208 °C. The T_g value of ***3p1m*-PBPO** is comparable to that of PPO™ (T_g = 210 °C)[56] despite the fact that ***3p1m*-PBPO** does not have any pendent group near the ether linkage. ***3p1m*-PBPO** did not show T_m in the second heating scan of DSC from 0 to 350 °C, although they showed a melting peak in the first heating cycle up to 450 °C while the melting peak of ***m*-PBPO** was observed at 337 °C. The first heating, cooling, and second heating traces of ***m*-PBPO** are shown in Figure 6. In the first cooling and the second heating, the trace of T_c and T_m is observed with T_g, respectively. These results imply that a thermal treatment may change the crystalline state of the polymer to an amorphous state in the cases of ***3p1m*-PBPO** and ***m*-PBPO**.

The Refractive Indices of the Polymers. The refractive indices and birefringence of the polymers were measured using a prism coupling method with the laser beam having 1330 nm wavelength. The results are summarized in Table 4. As expected, all of the soluble PBPOs which have two CF_3 groups per biphenyl unit showed very low refractive indices (n_{av}) in the range of 1.4979 to 1.5052 due to the high fluorine content. The refractive indices (n_{av}) of CF_3-substituted poly(arylene ether)s, with one CF_3 group per biphenyl unit of their polymer chains, were reported in the range of 1.5992 to 1.6223.[37,42,45] These values are higher than those of the PBPOs synthesized in this study. The low refractive indices of the PBPOs likely originated from the low molecular polarizability and density caused by the two CF_3 groups of polymeric repeating unit of PBPOs[5,57−61] Moreover, the polymers showed low birefringence (Δn) of less than 0.015, indicating that the linear polarizability and segmental orientation of the amorphous PBPOs are nearly isotropic. The dielectric constant (ε) can be estimated from the refractive index n according to Maxwell's equation, $\varepsilon \approx n^2$. The ε value at 1 MHz was determined to be $\varepsilon \approx 1.10\ n_{av}^2$, including an additional contribution of approximately 10% due to infrared absorption.[62] The ε values of the polymer films estimated from the average refractive indices were in the range of 2.47−2.49. The low dielectric constants may be also attributed to the existence of trifluoromethyl groups in the main chain.

dx.doi.org/10.1021/ma2028209 | *Macromolecules* 2012, 45, 3023−3031

CONCLUSION

In this study, we prepared new aromatic polymers with low refractive indices as well as high temperature resistances. The polymers, poly(biphenylene oxide)s containing two pendent trifluoromethyl groups, were synthesized from 4′-hydroxy-4-nitro-2,6-bis(trifluoromethyl)biphenyl and 3′-isomer through a *meta*-activated nucleophilic aromatic substitution (S_NAr) reaction. The nitro leaving group activated by the two trifluoromethyl groups at the *meta*-position was effectively displaced, resulting in high-molecular-weight polymers. This implies that activation by two activating groups at the *meta*-position is an effective strategy for successful S_NAr reactions. While both the *para*- and *meta*-connected homopolymers were crystalline, the copolymers of the *para*- and *meta*-connected monomers were amorphous and dissolved in a wide range of organic solvents. The polymers were thermally stable and showed very low refractive indices in the range of 1.488−1.508 with low birefringence.

ASSOCIATED CONTENT

Supporting Information

^1H and ^{13}C NMR spectra of the monomers and the model compound, FTIR of polymers, and GPC curves. This material is available free of charge via the Internet at http://pubs.acs.org.

AUTHOR INFORMATION

Corresponding Author

*E-mail: cis123@kribb.re.kr (I.S.C.); kimsy@kaist.ac.kr (S.Y.K.).

Notes

The authors declare no competing financial interest.

ACKNOWLEDGMENTS

This work was supported by a grant from the National Research Foundation of Korea (NRF) funded by the Korean Government (Ministry of Education, Science, and Technology (MEST)), the Basic Science Research Program (2010-07592) and the Nano/Bio Science and Technology Program (2005-01321). This work was also supported by a NRF grant funded by MEST through the NRL (R0A-2008-000-20121-0) and the ERC (R11-2007-050-00000-0) program.

REFERENCES

(1) Hougham, G.; Cassidy, P. E.; Johns, K.; Davidson, T. *Fluoropolymers (Part 2)*; Plenum Press: New York, 1999; pp 233−76.
(2) Dhara, M. G.; Banerjee, S. *Prog. Polym. Sci.* **2010**, *35*, 1022.
(3) Tsuchiya, K.; Shibasaki, Y.; Aoyagi, M.; Ueda, M. *Macromolecules* **2006**, *39*, 3964.
(4) Wan, Y.; Fei, X.; Shi, Z.; Hu, J.; Zhang, X.; Zhao, L.; Chen, C.; Cui, Z.; Zhang, D. *J. Polym. Sci., Part A: Polym. Chem.* **2011**, *49*, 762.
(5) Hougham, G.; Tesoro, G.; Viehbeck, A.; Chapple-Sokol, J. D. *Macromolecules* **1994**, *27*, 5964.
(6) Chung, I. S.; Kim, S. Y. *Macromolecules* **2000**, *33*, 3190.
(7) Chung, I. S.; Park, C. E.; Ree, M.; Kim, S. Y. *Chem. Mater.* **2001**, *13*, 801.
(8) Liu, B.; Hu, W.; Matsumoto, T.; Jiang, Z.; Ando, S. *J. Polym. Sci., Part A: Polym. Chem.* **2005**, *43*, 3018.
(9) Choi, H.; Chung, I. S.; Hong, K.; Park, C. E.; Kim, S. Y. *Polymer* **2008**, *49*, 2644.
(10) Kim, Y. J.; Seo, M.; Kim, S. Y. *J. Polym. Sci., Part A: Polym. Chem.* **2010**, *48*, 1049.
(11) Cotter, R. J. *Engineering Plastics: A Handbook of Polyaryl ethers*; Gordon and Breach Publishers: Amsterdam, 1995.
(12) Rogers, M. E.; Long, T. E. Synthesis of Poly(arylene ether)s. In *Synthetic Methods In Step-Growth Polymers*; John Wiley & Sons, Inc.; Hoboken, NJ, 2003.
(13) Johnson, H. N.; Farnham, A. G.; Clendinning, R. A.; Hale, W. F.; Merriam, C. N. *J. Polym. Sci., Part A: Polym. Chem.* **1967**, *5*, 2375.
(14) Theil, F. *Angew. Chem., Int. Ed.* **1999**, *38*, 2435.
(15) Pitsinos, E. N.; Vidali, V. P.; Couladouros, E. A. *Eur. J. Org. Chem.* **2011**, 1207.
(16) Labadie, J. W.; Hedrick, J. L.; Ueda, M. *Step growth polymers for high-performance materials: New synthetic method*; ACS Symposium Series 624; American Chemical Society: Washington, DC, 1996; pp 210−25.
(17) Kricheldorf, H. R.; *Handbook of polymer synthesis*; CRC Press: New York, 1992; pp 545−615.
(18) Mati, S.; Mandal, B. *Prog. Polym. Sci.* **1986**, *12*, 111.
(19) Chung, I. S.; Eom, H. J.; Kim, S. Y. *Polym. Bull.* **1998**, *41*, 631.
(20) Labadie, J. W.; Hedrick, J. L. *Macromolecules* **1990**, *23*, 5371.
(21) Kim, S. Y.; Labadie, J. W. *Polym. Prepr. (Am. Chem. Soc., Div. Polym. Chem.)* **1991**, *32* (1), 164.
(22) Banerjee, S.; Maier, G.; Burger, M. *Macromolecules* **1999**, *32*, 4279.
(23) Banerjee, S.; Maier, G. *Chem. Mater.* **1999**, *11*, 2179.
(24) Maier, G. *Prog. Polym. Sci.* **2001**, *26*, 3.
(25) Lee, M. S.; Kim, S. Y. *Macromol. Rapid Commun.* **2005**, *26*, 52.
(26) Banerjee, S.; Komber, H.; Häussler, L.; Voit, B. *Macromol. Chem. Phys.* **2009**, *210*, 1272.
(27) Ghosh, A.; Banerjee, S.; Komber, H.; Lederer, A.; Häussler, L.; Voit, B. *Macromolecules* **2010**, *43*, 2846.
(28) Carter, K. R.; Kim, S. Y.; Labadie, J. W. *Polym. Prepr. (Am. Chem. Soc., Div. Polym. Chem.)* **1993**, *34* (1), 415.
(29) Park, S. K.; Kim, S. Y. *Macromolecules* **1998**, *31*, 3385.
(30) Lee, H. S.; Kim, S. Y. *Macromol. Rapid Commun.* **2002**, *23*, 665.
(31) Kim, Y. J.; Chung, I. S.; Kim, S. Y. *Macromolecules* **2003**, *36*, 3809.
(32) Lee, M. S.; Kim, S. Y. *Macromolecules* **2005**, *38*, 5844.
(33) Kim, Y. J.; Kakimoto, M.; Kim, S. Y. *Macromolecules* **2006**, *39*, 7190.
(34) Bunnett, J. F.; Zahler, R. E. *Chem. Rev.* **1951**, *49*, 273.
(35) Bartoli, G.; Todesco, P. E. *Acc. Chem. Res.* **1977**, *10*, 125.
(36) Terrier, F. Nucleophilic aromatic displacement: the influence of the nitro group; VCH Publishers: New York, 1991.
(37) Chung, I. S.; Kim, S. Y. *J. Am. Chem. Soc.* **2001**, *123*, 11071.
(38) Kaiti, S.; Himmelberg, P.; Williams, J.; Abdellatif, M.; Fossum, E. *Macromolecules* **2006**, *39*, 7909.
(39) Beek, D. V.; Fossum, E. *Macromolecules* **2009**, *42*, 4016.
(40) Tienda, K.; Yu, Z.; Constandinidis, F.; Fortney, A.; Feld, W. A.; Fossum, E. *J. Polym. Sci., Part A: Polym. Chem.* **2011**, *49*, 2908.
(41) Rusanov, A. L.; Komarova, L. G. *High Perf. Polym.* **2009**, *21*, 535.
(42) Chung, I. S.; Kim, K. H.; Lee, Y. S.; Kim, S. Y. *Polymer* **2010**, *51*, 4477.
(43) Hawker, C. J.; Chu, F. *Macromolecules* **1996**, *29*, 4370.
(44) Himmelberg, P.; Fossum, E. *J. Polym. Sci., Part A: Polym. Chem.* **2005**, *43*, 3178.
(45) Chung, I. S.; Kim, S. Y. *Macromolecules* **2000**, *33*, 9474.
(46) Williams, F. J.; Donahue, P. E. *J. Org. Chem.* **1977**, *42*, 3414.
(47) Markezich, R. L.; Zamek, O. S.; Donahue, P. E.; Williams, F. J. *J. Org. Chem.* **1977**, *42*, 3435.
(48) Takekoshi, T.; Wirth, J. G.; Heath, D. R.; Kochanowski, J. E.; Manello, J. S.; Webber, M. J. *J. Polym. Sci., Part A: Poym. Chem.* **1980**, *18*, 3069.
(49) White, D. M.; Takekoshi, T.; Williams, F. J.; Relles, H. M.; Donahue, P. E.; Klopfer, H. J.; et al. *J. Polym. Sci., Part A: Poym. Chem.* **1981**, *19*, 1635.
(50) Takekoshi, T. *Polym. J.* **1987**, *19*, 191.
(51) In, I. S.; Eom, H. J.; Kim, S. Y. *Polymer (Korea)* **1998**, *22*, 544.
(52) In, I.; Kim, S. Y. *Polymer* **2006**, *47*, 4549.
(53) Zabrowski, D. L.; Moormann, A. E.; Beck, K. R. *Tetrahedron Lett.* **1988**, *29*, 4501.
(54) Miyaura, N.; Suzuki, A. *Chem. Rev.* **1995**, *95*, 2457.

(55) Qiu, Z.; Wang, J.; Zhang, Q.; Zhang, S.; Ding, M.; Gao, L. *Polymer* **2006**, *47*, 8444.
(56) Hay, A. S. *J. Polym. Sci., Part A: Polym. Chem.* **1998**, *36*, 505.
(57) Lee, K. S.; Kim, J. P.; Lee, J. S. *Polymer* **2010**, *51*, 632.
(58) Yu, H.; Wang, L.; Wang, Z.; Han, X.; Zhao, M. *Polymer* **2010**, *51*, 3269.
(59) Ghim, J.; Shim, H. S.; Shin, B. G.; Park, J. H.; Hwang, J. T.; Chun, C.; Oh, S. H.; Kim, J. J.; Kim, D. Y. *Macromolecules* **2005**, *38*, 8278.
(60) Song, Y.; Wang, J.; Li, G.; Sun, Q.; Jian, X.; Teng, J.; Zhang, H. *Polymer* **2008**, *49*, 724.
(61) Kang, J. W.; Kim, J. P.; Lee, J. S.; Kim, J. J. *J. Lightw. Technol.* **2005**, *23*, 364.
(62) Matsumoto, T. *Macromolecules* **1999**, *32*, 4933.

Macromolecules

Article

pubs.acs.org/Macromolecules

Application of Two-Dimensional Conjugated Benzo[1,2-*b*:4,5-*b*′]dithiophene in Quinoxaline-Based Photovoltaic Polymers

Ruomeng Duan,[†,‡] Long Ye,[‡,§] Xia Guo,[‡,§] Ye Huang,[‡,§] Peng Wang,*[,†] Shaoqing Zhang,[‡] Jianping Zhang,[†] Lijun Huo,[‡] and Jianhui Hou*[,‡]

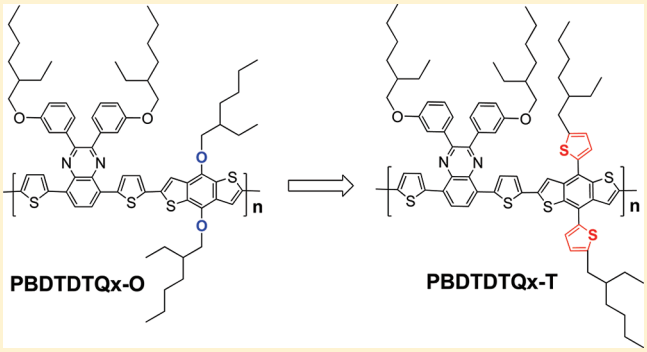
[†]Department of Chemistry, Renmin University of China, Beijing, 100872, China

[‡]State Key Laboratory of Polymer Physics and Chemistry, Institute of Chemistry, Chinese Academy of Sciences, Beijing 100190 China

[§]Graduate University of Chinese Academy of Sciences, Beijing 100049, China

Supporting Information

ABSTRACT: Two new donor−acceptor (D−A) alternative copolymers, PBDTDTQx-T and PBDTDTQx-O, were designed and synthesized to investigate the influence of two-dimensional conjugated structure on photovoltaic properties of conjugated polymers. In these two polymers, PBDTDTQx-O was used as control material, which is an alternative copolymer based on a quinoxaline derivative (DTQx) and alkoxy-substituted benzo[1,2-*b*:4,5-*b*′]dithiophene (BDT-O) unit; PBDTDTQx-T has an identical conjugated backbone as PBDTDTQx-O, but a simple two-dimensional conjugated BDT unit (BDT-T) was used to replace the alkoxy-BDT. The polymers were characterized by TGA, UV−vis absorption, electrochemical cyclic voltammetry, hole mobility of space-charge-limited current (SCLC) model, and photovoltaic measurements. It was found that PBDTDTQx-T exhibits similar molecular energy levels and higher hole mobility than PBDTDTQx-O. The power conversion efficiency (PCE) of the polymer solar cells (PSCs) based on PBDTDTQx-T: [6,6]-phenyl-C-71-butyric acid methyl ester ($PC_{71}BM$) = 1/2 (w/w) reached ∼5%, which is 60% higher than that of PBDTDTQx-O-based PSC. On the basis of these results, it can be concluded that the application of two-dimensional conjugated structure would be a feasible approach to improve photovoltaic properties of conjugated polymers.



INTRODUCTION

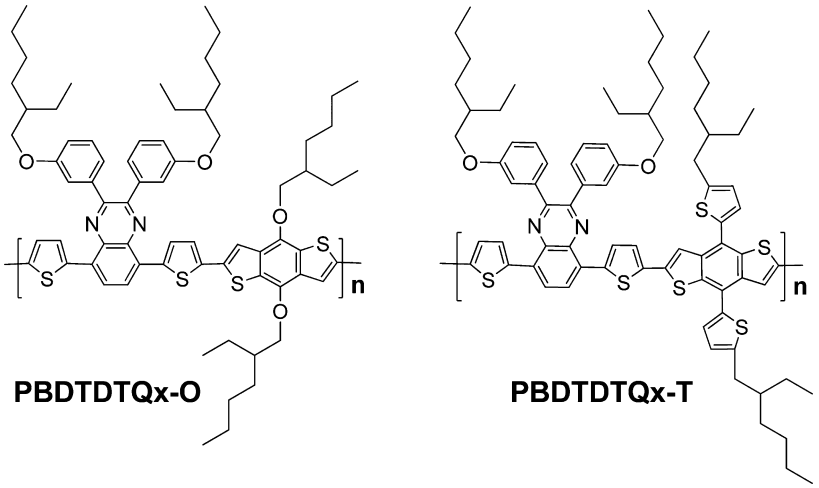
Bulk-heterojunction (BHJ) polymer solar cells (PSCs) have attracted much attention due to its potential applications in making large area, flexible solar panels through roll-to-roll process.[1−6] In a PSC device with BHJ structure, the active layer is consisting of two kinds of key materials: a p-type conjugated polymer donor and a soluble fullerene derivative acceptor. In order to get efficient PSC devices, active layer materials with ideal properties are requisite, and therefore, tremendous efforts have been devoted to tuning the properties of active layer materials through molecular structure design.[7−11]

As electron donor materials in PSC devices, narrow band gap conjugated polymers are much helpful to obtain good harvest of the sunlight, and different strategies of molecular design have been developed. Building a donor−acceptor (D−A) alternating structure has been proved to be an effective way to reduce band gap of conjugated polymer materials.[12−19] For example, PCPDTBT[20,21] and PSBTBT[22] are two representatives with D−A structure, and these two polymers exhibit narrow band gaps (E_g < 1.6 eV) and promising photovoltaic properties (power conversion efficiency, PCE > 5%). Another effective way to reduce band gap of conjugated polymer is to introduce conjugating components with strong quinoid property.[23] For instance, conjugated polymers based on thieno[3,4-*b*]pyrazine (TPZ)[24] and thieno[3,4-*b*]thiophene (TT)[25−27] were designed and these polymers exhibit narrow band gaps and promising photovoltaic properties. Besides band gap control, the modulation of molecular energy levels (HOMO and LUMO) of conjugated polymers is also of great importance for photovoltaic material design. Electron donating or withdrawing functional groups have been used in molecular design for this purpose. For example, the alkoxy-substituted conjugated polymers show much higher HOMO levels than their analogues with alkyl-substituents due to the stronger electron donating ability of the alkoxy groups than the alkyls;[28] the carbonyl-substituted polymer exhibits lower LUMO level than the analogue with carboxylate group, because the carbonyl group has stronger electron withdrawing ability than the

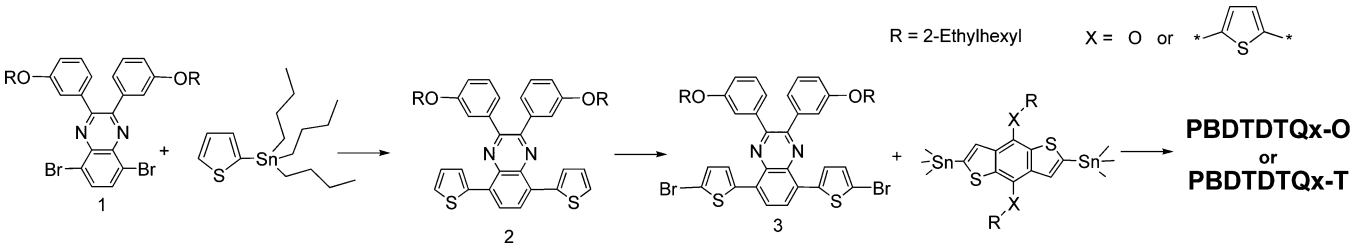
Received: January 10, 2012
Revised: March 6, 2012
Published: March 20, 2012

 © 2012 American Chemical Society dx.doi.org/10.1021/ma300060z | *Macromolecules* 2012, 45, 3032−3038

Scheme 1. Molecular Structures of PBDTDTQx-O and PBDTDTQx-T



Scheme 2. Synthetic Route of PBDTDTQx-O and PBDTDTQx-T



carboxylate;[25] the fluorine-substituted polymers also give excellent examples upon this strategy.[27,29]

Two-dimensional (2-D) conjugated polymers exhibit very interesting properties and promising photovoltaic performance. Representatively, intensive studies about 2-D-conjugated polythiophenes have been done.[30−33] 2-D-conjugated polythiophenes exhibit two main absorption peaks: one originates from the conjugated main chain, and the other is from the conjugated side chain. Consequently, broad and strong absorption band can be achieved in 2-D-conjugated polythiophenes.[30−32] On the other hand, since the 2-D-conjugated polythiophenes have bigger conjugated plane than their one-dimensional conjugated counterparts, better interchain $\pi-\pi$ overlapping can be formed and hence higher charge mobility can be achieved.[33] Recently, we designed and synthesized a new benzo[1,2-*b*:4,5-*b*′]dithiophene (BDT) derivative with 2-D-conjugated structure by introducing alkylthienyl groups to 4 and 8 positions of BDT unit. Initially, a polymer backbone (PBDTTT) was selected to investigate the photovoltaic properties of the 2-D-conjugated BDT-polymer. We found that after introducing 2-D-conjugated structure, broader absorption band, lower HOMO level and higher hole mobility can be achieved, and as a result, better photovoltaic results were recorded. For instance, PCE of the PSC devices based on the 2-D polymers, PBDTTT-E-T and PBDTTT-C-T, are 50% and 20% higher than their analogues with one-dimensional conjugated backbone, respectively.[34]

As known, the backbone of PBDTTT-based polymers has very strong quinoid property, so this kind of polymers exhibit much narrow band gaps.[34] Although it is quite clear that the 2-D-conjugated structure is very helpful to improving the photovoltaic properties of PBDTTT-based polymers, it is still unknown that how does the 2-D-conjugated structure influence photovoltaic properties of the D−A polymers without quinoid characteristic. Quinoxaline (Qx) is a typical electron-deficient conjugated unit due to the strong electronegativity of the two nitrogen atoms. Many conjugated polymers with D−A backbone have been designed by using Qx or its derivatives as electron-withdrawing building blocks in their backbones. These Qx-based polymers generally exhibit interesting photovoltaic behaviors, and ∼6% PCE has been reported in the polymers based on thiophene and quinoxaline.[35−37] Furthermore, since Qx consists of two fused six-member ring, when it was copolymerized with other conjugated components, the target polymer should have much less quinoid property than PBDTTT-polymers. Considering the above reasons, in order to investigate the influence of 2-D-conjugated BDT on photovoltaic properties of D−A conjugated polymers without quinoid property, two polymers based on Qx were designed. In Scheme 1, molecular structures of two D−A polymers based on BDT and the derivative of Qx, PBDTDTQx-O and PBDTDTQx-T, are shown, and these two polymers have identical conjugated backbones (main chain) but different side groups: alkoxy groups and alkylthienyl groups are used on 4 and 8 positions of their BDT units, respectively. Since these two polymers have similar molecular structures, the comparison between them will provide useful information on the influence of 2-D-conjugated structure on photovoltaic properties of D−A polymers.

RESULTS AND DISCUSSION

Synthesis. The general synthetic method of these two polymers is shown in Scheme 2. (2,3-Bis(3-(2-ethylhexyloxy)-phenyl)-5,8-di(thiophen-2-yl)quinoxaline (compound **2**) was synthesized by Stille condensation reaction between 5,8-Dibromo-2,3-bis(3-(2-ethylhexyloxy)phenyl)-quinoxaline

dx.doi.org/10.1021/ma300060z | *Macromolecules* 2012, 45, 3032−3038

(compound **1**) and 2-(tributylstannyl)thiophene with a yield of 60%, and then it was bromided by N-bromosuccininide (NBS) to produce compound **3**. The two target polymers were prepared through Stille polycondensation reaction with a yield of 40−60%. These two polymers exhibit excellent solubility in commonly used solvents, including tetrahydrofuran, chloroform, chlorobenzene, toluene, etc. Molecular weight of the polymers and polydispersity (PDI) was estimated by gel permeation chromatography (GPC) method using monodispersed polystyrene as standard and chloroform as eluent (Table 1). The number-average molecular weight (M_n) of PBDTDTQx-O and PBDTDTQx-T are 84K and 49.5K, respectively.

Table 1. Molecular Weight and Thermal Stability Data of the Polymers

polymer	M_w[a]	M_n[a]	PDI[a]	T_d (°C)
PBDTDTQx-O	186K	84K	2.22	320
PBDTDTQx-T	80.5K	49.5K	1.63	430

[a] M_w, M_n, and PDI of the polymers were estimated by GPC using polystyrene as standards in chloroform.

Thermal Properties. Thermal stability of the two polymers was investigated by thermogravimetric analysis (TGA). As shown in Figure 1, under nitrogen atmosphere, PBDTDTQx-O

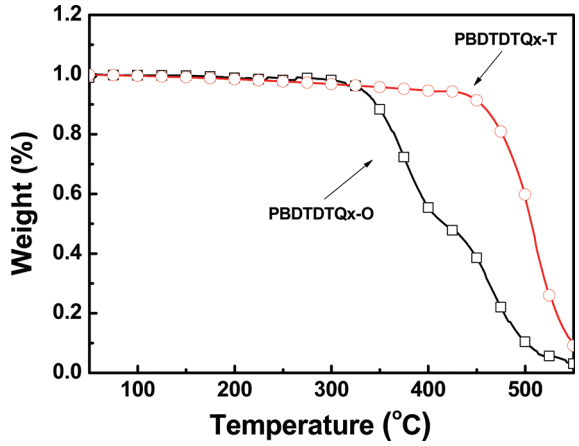


Figure 1. TGA plots of PBDTDTQx-T and PBDTDTQx-O with a heating rate of 10 °C/min under inert atmosphere.

shows an onset decomposition point at about 320 °C; however, PBDTDTQx-T shows an onset decomposition point at about 430 °C. The big difference of their decomposition temperature indicates that the 2-D-structure is much helpful to improving thermal stability of the BDT-based polymers. The difference scanning calorimetry (DSC) measurements for the two polymers have not shown any endothermic or exothermic phases in the temperature range of 25−300 °C. The DSC plots are shown in the Supporting Information (Figure S2).

Absorption Spectra. The absorption spectra of PBDTDTQx-O and PBDTDTQx-T in chloroform solution and of solid films are shown in Figure 2. As listed in Table 2, the absorption peaks of PBDTDTQx-O in solution and of solid film are at ~582 and ~602 nm, respectively; the absorption peaks of PBDTDTQx-T in solution and of solid film are both at ~605 nm. The absorption range of PBDTDTQx-T is red-shifted compared to PBDTDTQx-O. The absorption edges

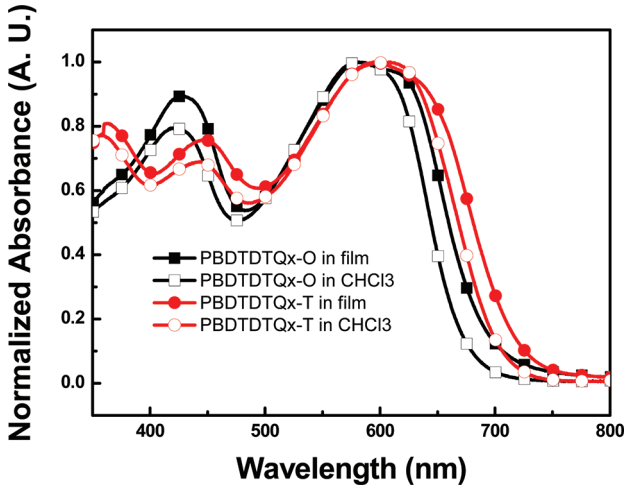


Figure 2. Absorption spectra of PBDTDTQx-T and PBDTDTQx-O in chloroform solution and of solid films.

(λ_{edge}) of PBDTDTQx-O and PBDTDTQx-T are located at 714 and 740 nm, corresponding to band gaps (E_g) of 1.74 and 1.67 eV, respectively; the half peak positions at long wavelength direction of PBDTDTQx-O and PBDTDTQx-T are 658 and 680 nm, respectively. PBDTDTQx-T exhibits a red-shifted absorption spectrum than PBDTDTQx-O indicating that the π-electrons of PBDTDTQx-T can be delocalized more effectively than that of PBDTDTQx-O, which is ascribed to the introduction of the 2-D conjugated structure. Besides of absorption range, absorption coefficient of solid film is also another important parameter to an active layer material in PSCs. As listed in Table 2, PBDTDTQx-O and PBDTDTQx-T exhibit much similar absorption coefficients as solid film, which are 0.60×10^{-2}/nm and 0.61×10^{-2}/nm, respectively. Since the 2-D conjugated polymer exhibits broader absorption band and similar absorption coefficient compared to the control polymer, when PBDTDTQx-T is used as active layer material in PSC, the device will harvest more photons than the PBDTDTQx-O-based device.

Electrochemical Properties. Electrochemical cyclic voltammetry (CV) is performed to evaluate molecular energy levels of conjugated polymers. Figure 3 shows the CV plots of PBDTDTQx-O and PBDTDTQx-T films on glassy carbon electrode. The onset points of *p*-doping process of PBDTDTQx-T and PBDTDTQx-O are both at 0.42 V, corresponding to a HOMO level of −5.12 eV. Since it is very hard to get a sharp n-doping signal for these two polymers, CV curves of p-doping process were only provided here, and the LUMO levels of the polymers were calculated by "LUMO = HOMO + E_g^{opt}". As known, V_{OC} of bulk heterojunction PSCs is directly proportional to the offset between HOMO level of the donor and LUMO level of the acceptor, and it can be concluded that the 2-D conjugated structure has no negative effect on V_{OC} of PSCs.

Photovoltaic Properties. The PSC devices with a structure of ITO/PEDOT−PSS (Clevios 4083)/polymer:$PC_{71}BM$/Ca/Al were fabricated to investigate the photovoltaic properties of these two polymers. *o*-Dichlorobenzene (*o*-DCB) was used to prepare the solution for spin-coating of active layer, and the concentration of the solution used in this work was 10 mg/mL (polymer/*o*-DCB). At first, different donor/acceptor (D/A) ratios, 1:1, 1:2, and 1:3, were scanned. We found that the optimal D/A ratio for both PBDTDTQx-O

dx.doi.org/10.1021/ma300060z | Macromolecules 2012, 45, 3032−3038

Table 2. Optical and Electrochemical Properties of PBDTDTQx-T and PBDTDTQx-O

	λ_{max} [nm]		λ_{edge} [nm]	absorption coefficient			
polymer	solution	film	film	film	E_g^{opt} [eV]	HOMO [eV]	LUMO [eV][a]
PBDTQx-T	443, 605	448, 605	740	0.61×10^{-2}/nm	1.67	−5.12	−3.45
PBDTQx-O	421, 582	428, 602	714	0.60×10^{-2}/nm	1.74	−5.12	−3.38

[a]LUMO = HOMO + E_g^{opt}.

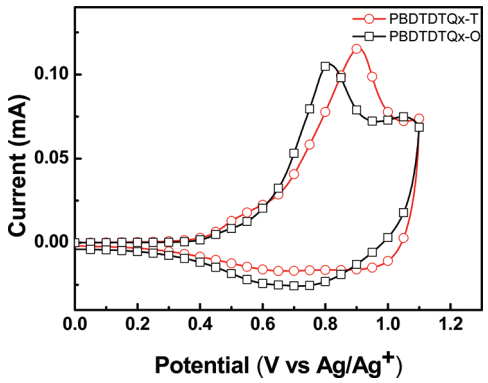


Figure 3. Cyclic voltammograms of PBDTDTQx-T and PBDTDTQx-O film on the glassy carbon electrode in 0.1 mol/L Bu_4NPF_6 in acetonitrile solution at a scan rate of 50 mV/s.

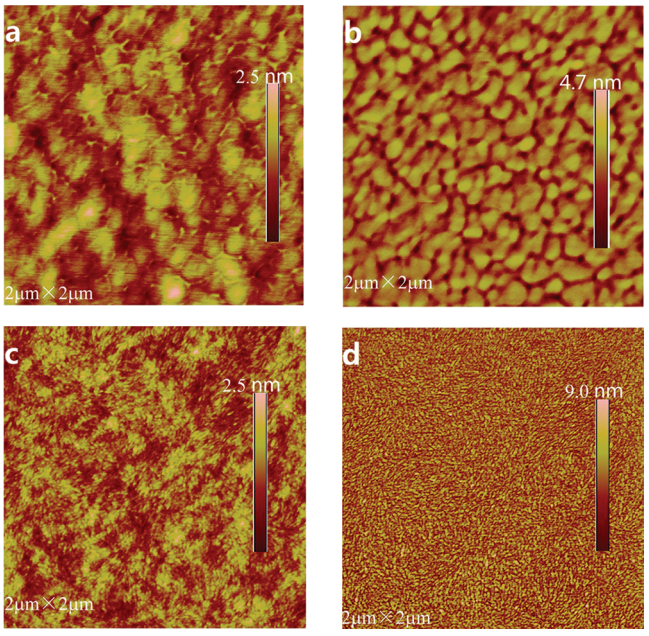


Figure 4. AFM images: (a, b) PBDTDTQX-O topography image and phase constrast image, respectively; (c, d) PBDTDTQX-T topography image and phase constrast image, respectively. All images are 2 μm × 2 μm.

and PBDTDTQx-T-based devices is 1/2, and Figure 5 shows the current−voltage curves (I−V curves) of the PSCs under illumination (AM1.5G 100 mW/cm^2). The detailed photovoltaic data of the optimization process of PBDTDTQx-T-based devices are listed in the Supporting Information as Table S1. It can be seen that the V_{OC} of PBDTDTQx-T-based devices dropped from 0.79 to 0.73 V with increasing $PC_{71}BM$ content in the blends, and the device with a D/A ratio of 1/2 showed the highest short circuit current density (J_{SC}) in these three conditions. As reported, device fabrication process of PSC can be further improved by thermal annealing[38,39] or by using 1,8-

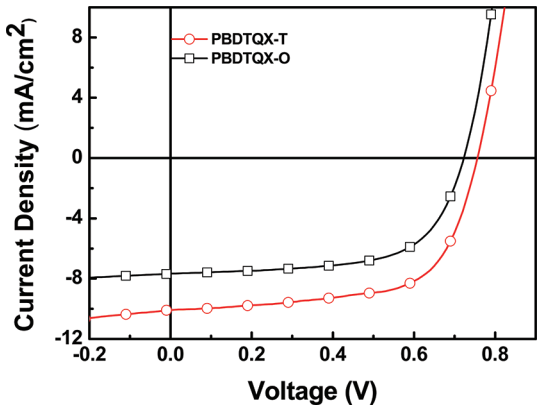


Figure 5. I−V curves of the PSCs based on PBDTDTQx-T and PBDTDTQx-O under the illumination of AM 1.5G, 100 mW/cm^2.

diiodooctane (DIO) as additive during the spin-coating process.[40] In this work, both of these two methods were employed to optimize the device performance. We found that no further improvement can be observed by using DIO as additive. However, after annealing at 120 °C, J_{SC} and fill factor (FF) of the devices can be improved simultaneously without affecting V_{OC}. In the optimized device, the thickness of the PEDOT−PSS layer is about 35 nm, the thicknesses of active layer are 80 and 126 nm for PBDTDTQX-T and PBDTDTQX-O-based devices, respectively. The thicknesses of Ca and Al layers are 20 and 80 nm, respectively. For PBDTDTQx-T-based device, a PCE of 4.95% was recorded with a V_{OC} of 0.76 V, a J_{SC} of 10.13 mA/cm^2 and a FF of 64.3%. Since PBDTDTQx-O has much similar structure as PBDTDTQx-T, the optimal device fabrication conditions of these two polymers are almost the same. However, both the V_{OC} and the J_{SC} of PBDTDTQx-O-based devices are lowered than PBDTDTQx-T-based devices, and therefore, the best PCE of the device of PBDTDTQx-O is only 3.06%. The nanoscale morphology of polymer/$PC_{71}BM$ film was tested by using atomic force microscopy (AFM). The phase graphs are shown in Figure 4. The surface roughness measured from the topograph image was 0.61 and 0.67 for PBDTDTQX-T and PBDTDTQX-O respectively. Although these two kinds of polymer:PCBM films show similar surface roughness, in comparison with the blend of PBDTDTQx-O and PCBM, the blend of PBDTDTQx-T exhibits much smaller domain size.

External Quantum Efficiency. As shown in Figure 6, the external quantum efficiency (EQE) curves of the devices indicate that the PSC devices have good response to the sunlight at the range from 350 to 700 nm, with a peak position at around 500 nm (Table 3). The EQE peak values of the PSC devices of PBDTDTQx-T and PBDTDTQx-O are 58% and 44%, respectively. PBDTDTQx-T-based device shows better EQE to the sunlight in the whole range compared to the PBDTDTQx-O-based device. This result indicates that the replacement of alkoxy group by alkylthienyl group is much

dx.doi.org/10.1021/ma300060z | Macromolecules 2012, 45, 3032−3038

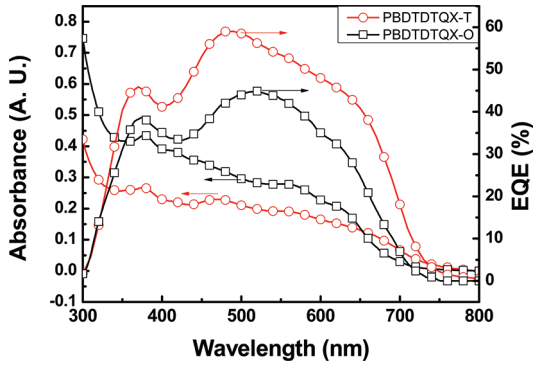


Figure 6. EQE curves of the PSCs based on PBDTDTQx-T or PBDTDTQx-O: $PC_{71}BM$ (1:2 w/w).

Table 3. Photovoltaic Properties of PSCs Based on PBDTDTQx-T and PBDTDTQx-O, under the Illumination of AM1.5G, 100 mW/cm^2

polymer	anneal (120 °C, 10 min)	D/A ratio	V_{OC} (V)	J_{SC} (mA/cm^2)	FF (%)	PCE (%)
PBDTDTQx-T	no	1:1	0.79	7.91	53.3	3.33
PBDTDTQx-T	no	1:2	0.76	8.97	50.5	3.44
PBDDTTQx-T	no	1:3	0.73	7.17	48.4	2.53
PBDTDTQx-T	yes	1:2	0.76	10.13	64.3	5.0
PBDTDTQx-O	yes	1:2	0.71	7.00	61.5	3.06

helpful to improve photovoltaic properties of the polymer. According to the EQE curves and the solar irradiation spectrum, the integral current density value of the PSC devices of PBDTDTQx-T and PBDTDTQx-O are calculated, which are 9.82 mA/cm^2 and 7.0 mA/cm^2, respectively. For both PBDTDTQx-T and PBDTDTQx-O-based devices, the difference between the measured J_{sc} and the integral current density values is within 4%, indicating the accuracy of our photovoltaic measurement is reliable.

Hole Mobility. Furthermore, hole mobilities of the D/A blend films based on these two polymers prepared by the optimal fabrication process were measured by fabricating hole-only device, the device structure as: ITO/PEDOT−PSS/polymer:$PC_{71}BM$/Au, and the results are shown in Figure 7. The hole mobilities of PBDTDTQx-T and PBDTDTQx-O are 1.04×10^{-4} cm^2 V^{-1} s^{-1} and 4×10^{-5} cm^2 V^{-1} s^{-1}, respectively. The higher hole mobility of PBDTDTQx-T than PBDTDTQx-O indicates that the replacement of alkoxy group by alkylthienyl group is an effective way to improve hole transport property of the active layer, and hence, better quantum efficiency can be obtained in the device based on the corresponding polymer with alkylthienyl side chain.

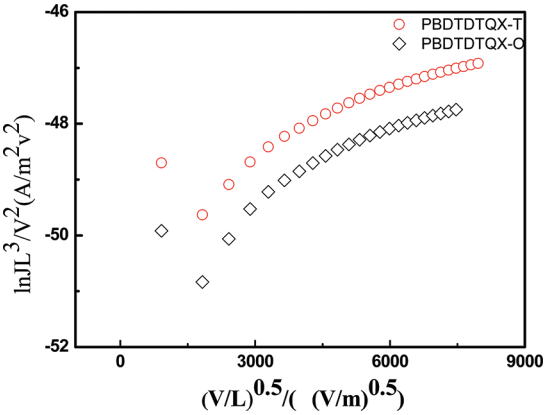


Figure 7. $\ln(JL^3/V^2)$ versus $(V/L)^{0.5}$ plots of the polymers for the measurement of hole mobility by the SCLC method.

CONCLUSION

Two new polymers based on Qx and BDT unit, PBDTDTQx-O and PBDTDTQx-T, were designed, synthesized and characterized. These two polymers exhibit broad absorption bands and appropriate molecular energy levels as electron donor materials in PSCs. Therefore, for the PSC device based on PBDTDTQx-T, a PCE of 5.0% were recorded. More important, two kinds of side groups, alkoxy group and alkylthienyl group, were used as substituents on the BDT units of these two polymers, and the comparison between them provides useful information for molecular design of photovoltaic polymers. The results in this work give solid evidence that the 2-D conjugated structure is beneficial to improve photovoltaic properties of the narrow band gap D/A-polymer system without quinoid properties. Specifically, after introducing the 2-D conjugated structure by replacing alkoxy groups with alkylthienyl groups, higher hole mobility and higher EQE of the PSC device was achieved, and therefore better J_{SC} can be realized; interestingly, although these two polymers exhibit similar HOMO levels, the PSC device based on 2-D conjugated polymer shows higher V_{OC} than the alkoxy-substituted control polymer. As a result, PCE of the device based on PBDTDTQx-T is ~60% higher than that of the device based on PBDTDTQx-O. Considering all the issues mentioned above, it can be concluded that the backbone of PBDTDTQx-T should be a promising molecular structure for photovoltaic polymer and the application of 2-D conjugated structure can be seen as a feasible method in molecular design of photovoltaic polymers.

EXPERIMENTAL SECTION

Materials. 2,6-Bis(trimethyltin)-4,8-bis(5-(2-ethylhexyl)thiophen-2-yl)benzo[1,2-*b*:4,5-*b*′]dithiophene (BDT-T), and 2,6-bis-(trimethyltin)-4,8-bis(2-ethylhexyloxy)benzo[1,2-*b*:4,5-*b*′]dithiophene (BDT-O); and the 5,8-dibromo-2,3-bis(3-(2-ethylhexyloxy)phenyl)-quinoxaline, were purchased from Solarmer Materials Inc. and used without any further purification. The $Pd(PPh_3)_4$ was purchased from Frontier Scientific Inc., and the ultra dry solvents used in device fabrication process are purchased from Aldrich. The other chemicals are commercial available products and used without any further purification.

Measurements. ^{1}H NMR spectra were measured on a Bruker arx-400 spectrometer. Absorption spectra were taken on a Hitachi U-3010 UV−vis spectrophotometer. The molecular weights of polymers were measured by the GPC method, and polystyrene was used as a standard by using chloroform as eluent. TGA measurements were performed on TA Instruments Inc. TGA-2050. Thermograms were obtained on mettle differential scanning calorimeter (DSC). The electrochemical cyclic voltammetry experiments were conducted on Zahner IM6e Eletrochemical workstation, with glassy carbon disk, Pt wire, and a Ag/Ag$^+$ electrode as the working electrode, counter electrode, and reference electrode, respectively, in a 0.1 mol/L tetrabutylammonium hexafluorophosphate (Bu_4NPF_6) in acetonitrile solution.

Synthesis. *2,3-Bis(3-(2-ethylhexyloxy)phenyl)-5,8-di(thiophen-2-yl)quinoxaline (**2**).* 2-(Tributylstannyl)thiophene(2.24 g, 6 mmol), compound **1** (1.40 g, 2 mmol), and 14 mL of toluene were put into a flask. The solution was purge with argon for 10 min, then 100 mg $Pd(PPh_3)_4$ was added. The solution was purge again by argon for 30 min the resulting mixture was

dx.doi.org/10.1021/ma300060z | *Macromolecules* 2012, 45, 3032−3038

heated with stirring at 110 °C for 12 h under argon atmosphere. Then the reactant was cooled to room temperature and then poured into water and extracted by diethyl ether for several times. After removal of the solvent, the crude product was purified by silica gel chromatography with hexane/dichloromethane (v/v, 5/1) mixture as eluent. The pure compound (2) was obtained as red solid (yield 60%). ^{1}H NMR (δ/ppm, $CDCl_3$, 400 MHz): 8.15 (s, 2H), 7.90 (d, 2H), 7.49 (d, 2H), 7.41 (s, 2H), 7.28 (t, 4H), 7.20 (t, 2H), 6.95 (d, 2H), 3.8 (d, 4H), 1.71 (m, 2H), 1.34 (m, 16H), 0.94 (t, 12H).

*2,3-Bis(3-(2-ethylhexyloxy)phenyl)-5,8-bis(5-bromothiophen-2-yl)quinoxaline (**3**).* To a solution of compound **2** (1.16 g, 1.65 mmol) in 10 mL *N*,*N*-dimethylformamide (DMF), a solution of *N*-bromosuccinimide (NBS) (0.60 g, 3.37 mmol) in 10 mL of DMF was added at 0 °C. The reactant was stirred for 30 min and then poured into water and extracted with diethyl ether (50 mL × 3). The organic phase was dried over anhydrous $MgSO_4$. After removal the solvent under reduced pressure, the residues were purified by silica gel column chromatography using hexanes as eluent. The pure product compound **3** was obtained as deep red solid in a yield of 94% (1.33 g). ^{1}H NMR (δ/ppm, $CDCl_3$, 400 MHz): 8.25 (s, 2H) 7.73 (d, 2H), 7.46 (s, 2H), 7.31 (t, 2H), 7.20 (t, 4H), 7.05 (d, 2H), 3.92 (d, 4H), 1.75 (m, 2H), 1.36 (m, 16H), 0.96 (t, 12H).

Synthesis of the Polymers Using Stille Coupling Reaction. Both PBDTDTQx-T and PBDTDTQx-O were prepared by coupling compound **3** with the corresponding bis(trimethylstannyl)-substituted BDT monomer by the same procedure. BDT-T (0.452 g, 0.5 mmol) or BDT-O (0.386 g, 0.5 mmol) and compound **3** (0.430 g, 0.5 mmol) were put into a 50 mL two-neck flask, and 10 mL of degassed toluene was added under the protection of argon. The solution was purge with argon for 10 min, and then 10 mg of $Pd(PPh_3)_4$ was added. After being purged with argon for 20 min, the reaction mixture was heated with stirring at 105 °C for 16 h. Then the reactant was cooled to room temperature, and the polymer was precipitated by adding methanol and then filtered through a Soxhlet thimble, which was then subjected to Soxhlet extraction with methanol, hexane, and chloroform successively. The polymer was recovered from the chloroform fraction by rotary evaporation as solid. The solid was dried under vacuum for 1 day. The yields of the two polymers were both about 40%.

Device Fabrication and Measurements. Polymer solar cell devices were fabricated under conditions as follows: After spin-coating a 35 nm layer of poly(3,4-ethylenedioxythiophene):poly(styrenesulfonate) (PEDOT:PSS) onto a precleaned indium−tin oxide (ITO) coated glass substrates, the polymer/$PC_{71}BM$ blend solution was spin-coated. The concentration of the polymer/$PC_{71}BM$ blend solution for spin-coating was 10 mg/mL (polymer/*o*-dichlorobenzene). The thickness of the active layer was controlled by changing the spin speed during the spin-coating process and measured on profilometer (Ambios Tech. XP-2). The devices were completed by evaporating Ca/Al metal electrodes with an area of 4 mm^2 as defined by masks. The *I*−*V* curves are measured under the illumination of 100 mW· cm^{-2} AM 1.5G using a XES-70S1 (SAN-EI Electric Co., Ltd.) solar simulator (AAA grade, 70 mm ×70 mm photobeam size). The 2 × 2 cm monocrystalline silicon reference cell (SRC-1000-TC-QZ) was purchased from VLSI Standards Inc.

■ ASSOCIATED CONTENT

Ⓢ Supporting Information

Optimizing of PBDTDTQx-base devices, differential scanning calorimetrythermograms, density functional theory calculations, and XRD patterns. This material is available free of charge via the Internet at http://pubs.acs.org.

■ AUTHOR INFORMATION

Corresponding Author

*E-mail: (J.H.) hjhzlz@iccas.ac.cn; (W.P.) wpeng@chem.ruc.edu.cn.

Notes

The authors declare no competing financial interest.

■ ACKNOWLEDGMENTS

The authors would like to acknowledge the financial support from National High Technology Research and Development Program 863, Chinese Academy of Sciences, NSFC (Nos. 2011AA050523, 20874106, 20821120293, 51173189, and 20933010).

■ REFERENCES

(1) Yu, G.; Gao, J.; Hummelen, J. C.; Wudl, F.; Heeger, A. J. *Science* **1995**, *270*, 1789−1791.
(2) Hoth, C. N.; Choulis, S. A.; Schilinsky, P.; Brabec, C. J. *Adv. Mater.* **2007**, *19*, 3973−3974.
(3) Aernouts, T.; Aleksandrov, T.; Girotto, C.; Genoe, J.; Poortmans, J. *Appl. Phys. Lett.* **2008**, *92* (3), 033306.
(4) Brabec, C. J.; Sariciftci, N. S.; Hummelen, J. C. *Adv. Funct. Mater.* **2001**, *11*, 15−26.
(5) Thompson, B. C.; Frechet, J. M. J. *Angew. Chem., Int. Ed.* **2008**, *47*, 58−77.
(6) Park, S. H.; Roy, A.; Beaupre, S.; Cho, S.; Coates, N.; Moon, J. S.; Moses, D.; Leclerc, M.; Lee, K.; Heeger, A. J. *Nat. Photo* **2009**, *3*, 297−U5.
(7) Cheng, Y. J.; Yang, S. H.; Hsu, C. S. *Chem. Rev.* **2009**, *109*, 5868−5923.
(8) Giacalone, F.; Martin, N. *Chem. Rev.* **2006**, *106*, 5136−5190.
(9) Roncali, J. *Chem. Rev.* **1992**, *92*, 711−738.
(10) Li, C.; Liu, M. Y.; Pschirer, N. G.; Baumgarten, M.; Mullen, K. *Chem. Rev.* **2010**, *110*, 6817−6855.
(11) He, Y. J.; Li, Y. F. *Phys. Chem. Chem. Phys.* **2011**, *13*, 1970−1983.
(12) Amb, C. M.; Chen, S.; Graham, K. R.; Subbiah, J.; Small, C. E.; So, F.; Reynolds, J. R. *J. Am. Chem. Soc.* **2011**, *133*, 10062−10065.
(13) Price, S. C.; Stuart, A. C.; Yang, L. Q.; Zhou, H. X.; You, W. *J. Am. Chem. Soc.* **2011**, *133*, 4625−4631.
(14) He, Z. C.; Zhong, C. M.; Huang, X.; Wong, W. Y.; Wu, H. B.; Chen, L. W.; Su, S. J.; Cao, Y. *Adv. Mater.* **2011**, *23*, 4636−4637.
(15) Liang, Y. Y.; Xu, Z.; Xia, J. B.; Tsai, S. T.; Wu, Y.; Li, G.; Ray, C.; Yu, L. P. *Adv. Mater.* **2010**, *22*, E135−136.
(16) Su, M. S.; Kuo, C. Y.; Yuan, M. C.; Jeng, U. S.; Su, C. J.; Wei, K. H. *Adv. Mater.* **2011**, *23*, 3315−3316.
(17) Blouin, N.; Michaud, A.; Gendron, D.; Wakim, S.; Blair, E.; Neagu-Plesu, R.; Belletete, M.; Durocher, G.; Tao, Y.; Leclerc, M. *J. Am. Chem. Soc.* **2008**, *130*, 732−742.
(18) Beaujuge, P. M.; Pisula, W.; Tsao, H. N.; Ellinger, S.; Mullen, K.; Reynolds, J. R. *J. Am. Chem. Soc.* **2009**, *131*, 7514−7515.
(19) Huang, F.; Chen, K. S.; Yip, H. L.; Hau, S. K.; Acton, O.; Zhang, Y.; Luo, J. D.; Jen, A. K. Y. *J. Am. Chem. Soc.* **2009**, *131*, 13886−13887.
(20) Peet, J.; Kim, J. Y.; Coates, N. E.; Ma, W. L.; Moses, D.; Heeger, A. J.; Bazan, G. C. *Nat. Mater.* **2007**, *6*, 497−500.
(21) Muhlbacher, D.; Scharber, M.; Morana, M.; Zhu, Z. G.; Waller, D.; Gaudiana, R.; Brabec, C. *Adv. Mater.* **2006**, *18*, 2884−2889.
(22) Yang, Y.; Hou, J. H.; Chen, H. Y.; Zhang, S. Q.; Li, G. *J. Am. Chem. Soc.* **2008**, *130*, 16144−16145.
(23) Huo, L. J.; Hou, J. H. *Polym. Chem.* **2011**, *2*, 2453−2461.
(24) Zhou, E. J.; Cong, J. Z.; Yamakawa, S.; Wei, Q. S.; Nakamura, M.; Tajima, K.; Yang, C. H.; Hashimoto, K. *Macromolecules* **2010**, *43*, 2873−2879.
(25) Hou, J. H.; Chen, H. Y.; Zhang, S. Q.; Chen, R. I.; Yang, Y.; Wu, Y.; Li, G. *J. Am. Chem. Soc.* **2009**, *131*, 15586−15587.
(26) Liang, Y. Y.; Wu, Y.; Feng, D. Q.; Tsai, S. T.; Son, H. J.; Li, G.; Yu, L. P. *J. Am. Chem. Soc.* **2009**, *131*, 56−57.
(27) Hou, J. H.; Chen, H. Y.; Zhang, S. Q.; Liang, Y. Y.; Yang, G. W.; Yang, Y.; Yu, L. P.; Wu, Y.; Li, G. *Nat. Photo* **2009**, *3*, 649−653.
(28) Shi, C. J.; Yao, Y.; Yang, Y.; Pei, Q. B. *J. Am. Chem. Soc.* **2006**, *128*, 8980−8986.

(29) Zhou, H. X.; Yang, L. Q.; Stuart, A. C.; Price, S. C.; Liu, S. B.; You, W. *Angew. Chem., Int. Ed.* **2011**, *50*, 2995−2998.
(30) Hou, J. H.; Tan, Z. A.; Yan, Y.; He, Y. J.; Yang, C. H.; Li, Y. F. *J. Am. Chem. Soc.* **2006**, *128*, 4911−4916.
(31) Hou, J. H.; Huo, L. J.; He, C.; Yang, C. H.; Li, Y. F. *Macromolecules* **2006**, *39*, 594−603.
(32) Hou, J. H.; Tan, Z.; He, Y. J.; Yang, C. H.; Li, Y. F. *Macromolecules* **2006**, *39*, 4657−4662.
(33) Li, Y. F.; Zou, Y. P. *Adv. Mater.* **2008**, *20*, 2952−2958.
(34) Huo, L. J.; Zhang, S. Q.; Guo, X.; Xu, F.; Li, Y. F.; Hou, J. H. *Angew. Chem., Int. Ed.* **2011**, *50*, 9697−9702.
(35) Wang, E. G.; Hou, L. T.; Wang, Z. Q.; Hellstrom, S.; Zhang, F. L.; Inganas, O.; Andersson, M. R. *Adv. Mater.* **2010**, *22*, 5240−5244.
(36) Gadisa, A.; Mammo, W.; Andersson, L. M.; Admassie, S.; Zhang, F.; Andersson, M. R.; Inganas, O. *Adv. Funct. Mater.* **2007**, *17*, 3836−3842.
(37) Zhou, E.; Cong, J. Z.; Tajima, K.; Hashimoto, K. *Chem. Mater.* **2010**, *22*, 4890−4895.
(38) Zhang, M. J.; Guo, X.; Li, Y. F. *Adv. Energy Mater.* **2011**, *1*, 557−560.
(39) Verploegen, E.; Mondal, R.; Bettinger, C. J.; Sok, S.; Toney, M. F.; Bao, Z. A. *Adv. Funct. Mater.* **2010**, *20*, 3519−3529.
(40) Lee, J. K.; Ma, W. L.; Brabec, C. J.; Yuen, J.; Moon, J. S.; Kim, J. Y.; Lee, K.; Bazan, G. C.; Heeger, A. J. *J. Am. Chem. Soc.* **2008**, *130*, 3619−3623.

Macromolecules

Article

pubs.acs.org/Macromolecules

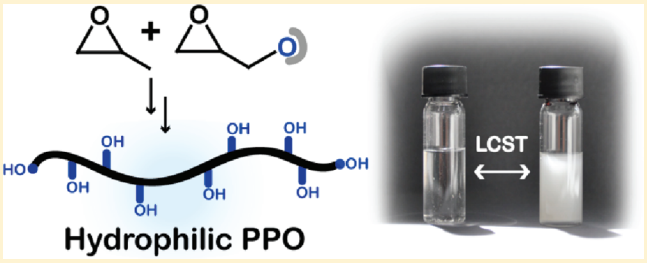
Water-Soluble "Poly(propylene oxide)" by Random Copolymerization of Propylene Oxide with a Protected Glycidol Monomer

Martina Schömer and Holger Frey*

Institute of Organic Chemistry, Johannes Gutenberg-University, Duesbergweg 10-14, D-55099 Mainz, Germany

Supporting Information

ABSTRACT: Hydrophilic, functional poly(propylene oxide) (PPO) copolymers were prepared by anionic random copolymerization of propylene oxide with the protected glycidyl derivative ethoxy ethyl glycidyl ether (EEGE). The monobenzyl-protected ethylene glycol initiator 2-(benzyloxy)-ethanol was used to initiate the polymerization because it allows for the introduction of hydroxyl groups at both ends of the polymer chain. Acidic deprotection permitted selective removal of the acetal protecting groups in the chain or alternatively orthogonal deprotection of the terminal hydroxyl group by catalytic hydrogenation. A series of narrowly distributed hydroxyl-functional PPO copolymers (M_w/M_n < 1.07−1.25 g mol^{-1}) was obtained with varying composition between 2 and 75% glycerol units and molecular weights in the range of 3000 to 8000 g mol^{-1}. Monomer consumption and compositional drift in monomer feed were studied via ^{1}H NMR kinetics, revealing a slightly tapered structure, but confirmed a distribution of EEGE in the polar PPO-based copolymers. Cloud-point measurements showed temperature-dependent water solubility, with LCSTs in the range of 20 to 70 °C. The study demonstrates that an incorporation of 11% of the hydroxyl-functional, linear glycerol units suffices to obtain functional PPO copolymers that are water-soluble at room temperature.



INTRODUCTION

Polyether polyols are important materials that are widely used for the synthesis of polyurethanes (PUs) as a flexible, low glass-transition component. Their preparation via anionic polymerization strategies has been intensively investigated.[1] Poly(propylene oxide) (PPO)-based structures[2] play a key role among them and find application as functional oligomers, copolymers, or star polymer building blocks. Because of its apolar chemical structure, PPO is generally not water-soluble at ambient temperature. Only polymers with low molecular weights have been reported to exhibit solubility below 18 °C.[3] The most widely used copolyethers based on propylene oxide (PO) are random and block copolymers with ethylene oxide (EO),[4,5] also known under their trade names Poloxamer, Pluronics, or Jeffamine. These copolymers are more hydrophilic than PPO homopolymers and may show improved, but still limited solubility in water. Furthermore, copolymers of PO with tetrahydrofuran have been reported[6] that exhibit reduced cold-hardening and improved molding properties when used as a soft segment in PUs.

To increase further polarity or achieve water solubility of PPO copolymers, incorporation of a more hydrophilic comonomer is necessary. This can be achieved via copolymerization of PO with glycidol, which adds one free hydroxyl group to the PPO chain per comonomer unit. However, because of the latent AB_2 character of glycidol, this would lead to branched polymers, unless the hydroxyl group is reversibly protected during the polymerization. Ethoxy ethyl glycidyl ether (EEGE) is an acetal-protected glycidyl ether structure that represents an ideal candidate for this purpose. EEGE can be polymerized in a living manner.[7,8] The use of EEGE as a comonomer for the synthesis of random or block copolymers with other epoxides has attracted increasing attention recently and has been employed in several works.[9−16]

Polyether polyols that are suitable for further functionalization essentially require defined end groups at both termini to react with the surface or an isocyanate component. For example, when using polyols as soft segments in PUs, the presence of monofunctional alcohols in the mixture would lead to termination during the condensation step. Anionic ring-opening polymerization offers the possibility to use a variety of initiators, for example, a protected hydroxyl-functional initiator to generate α,ω-hydroxy-polyether-polyols. Amphiphilic di- and triblock copolymers based on PPO-*b*-PEEGE, PPO-*b*-*lin*PG, and PPO-*b*-*hb*PG were introduced by Tsvetanov et al.[11a,12,17] as well as by our group,[11b] respectively, and were characterized with respect to association and solution properties in aqueous media. Carlotti et al. investigated the copolymerization properties of protected glycidols with PO via monomer-activated polymerization, resulting in copolymers with a

Received: February 5, 2012
Revised: March 12, 2012
Published: March 28, 2012

ACS Publications © 2012 American Chemical Society

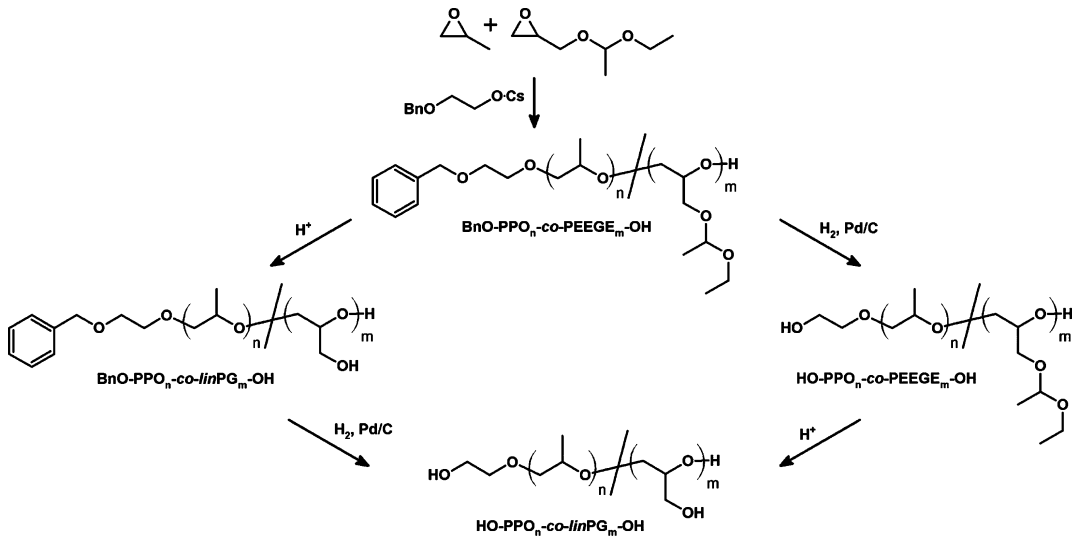


Figure 1. Synthesis of α,ω-hydroxy-poly(propylene oxide)-*co*-poly(glycerol) by copolymerization of PO with EEGE and subsequent cleavage of the acetal protecting groups to release the free hydroxyl groups and hydrogenation of the benzyl end group to generate α,ω-hydroxyl groups.

gradient composition manifest in a predominant incorporation of PO repeat units at the beginning of the chains and EEGE units at the end of the polymerization, however, without hydroxyl end groups.[18] No data on the hydrophilicity and solubility of the respective deprotected polymers were given.

To the best of our knowledge, the introduction of hydroxyl groups into PPO by random anionic copolymerization has not been reported to date. Herein, we describe the synthesis of multi-hydroxyl-functional PPOs via random anionic copolymerization of PO and the protected glycidol monomer EEGE and subsequent cleavage of the protecting groups. By using a suitable hydroxyl-initiator dihydroxy-terminated and in-chain hydroxyl-functional PPOs have been obtained in three steps (Figure 1). The materials were investigated with respect to their solubility in aqueous solution and their LCST behavior.

EXPERIMENTAL SECTION

Reagents. All reagents and solvents were used as received, if not otherwise mentioned. Deuterated DMSO-d_6 and $CDCl_3$ were purchased from Deutero. PO was dried over CaH_2 and distilled under vacuum prior to use. Ethoxyethyl glycidyl ether (EEGE) was prepared as described by Fitton et al.,[19] dried over CaH_2, and freshly distilled before use.

Instrumentation. ^{1}H NMR and ^{13}C NMR spectra were recorded at 300 and 75 MHz, respectively, on a Bruker AC300 and were referenced internally to residual proton signals of the deuterated solvent. For SEC measurements in DMF (containing 0.25 g L^{-1} of lithium bromide as an additive), an Agilent 1100 series was used as an integrated instrument including a PSS HEMA column ($10^6/10^4/10^2$ Å porosity) and both a UV and RI detector. Calibration was achieved with poly(ethylene oxide) (PEO) standards provided by Polymer Standards Service (PSS). Matrix-assisted laser desorption and ionization time-of-flight (MALDI-TOF) measurements were performed on a Shimadzu Axima CFR MALDI-TOF mass spectrometer, using dithranol (1,8,9-trishydroxyanthracene) as matrix. DSC curves were recorded with a Perkin-Elmer DSC 7. Samples were dried for 24 h at 80 °C in vacuum before measurements. Cloud-points were determined in deionized water at varying concentration and observed by optical transmittance of a light beam (λ = 632 nm) through a 1 cm sample quartz cell. The measurements were performed in a Jasco V-630 photospectrometer with a Jasco ETC-717 Peltier element. The intensities of the transmitted light were recorded versus the temperature of the sample cell. The heating/cooling rate was 1 K min^{-1}, and values were recorded every 0.1 K.

^{1}H NMR Kinetics.[20] In a conventional NMR tube, a DMSO-d_6 solution of the initiator and a mixture of PO and EEGE were separately frozen under an argon atmosphere. High vacuum was applied, and the tube was flame-sealed, whereas the solutions were kept frozen. To reduce the necessary time for locking and shimming of the polymerization mixture, we measured a sample of the pure monomer mixture in advance at the relevant temperature. Immediately after melting and mixing, the first spectrum was recorded. Sample spinning was turned off. Intervals between two measurements were 30 s.

Synthesis of BnO-PPO$_n$-*co*-PEEGE$_m$−OH. Here an exemplary synthetic protocol is described for BnO-PPO$_{49}$-*co*-PEEGE$_6$−OH: A two-necked flask equipped with a septum, Teflon seal, and a magnetic stirrer was connected to a vacuum line. 2-(Benzyloxy)ethanol (152 mg, 1 mmol) was deprotonated with 0.9 equiv cesium hydroxide monohydrate in methanol and dried azeotropically with benzene to remove methanol together with formed water and other volatiles. PO (2.61 g, 45 mmol) was transferred to an ampule and subsequently to the reaction flask in vacuo. The flask was sealed, and 730 μL (5 mmol) of freshly distilled EEGE was introduced through the septum via syringe. The reaction mixture was immediately heated to 40 °C and stirred for 18 h. After the addition of an excess of methanol to quench the polymerization, the solution was extracted with sodium carbonate solution to remove remaining salts and dried in vacuo at 80 °C for 24 h to afford the BnO-PPO$_n$-*co*-PEEGE$_m$−OH copolymers in ca. 90% yield.

Synthesis of BnO-PPO$_n$-*co*-*lin*PG$_m$−OH. A 20% solution of the copolymer in ethanol was stirred with the anionic exchange resin DOWEX 50WX8 at 60 °C for 18 h to cleave the acetal protecting group. After filtration and removal of the solvents, the polymer was dried in vacuum at 80 °C for 24 h to afford the BnO-PPO$_n$-*co*-*lin*PG$_m$−OH copolymers in 90−95% yield.

Synthesis of HO-PPO$_n$-*co*-PEEGE$_m$−OH. A 20% solution of the copolymer in ethanol/dichloromethane (1:1) was stirred with palladium on activated charcoal under a hydrogen atmosphere at room temperature for 18 h to cleave the benzyl protecting group. After filtration and removal of the solvent, the polymer was dried in vacuum at 80 °C for 24 h to obtain α,ω-hydroxy-functional copolymers.

RESULTS AND DISCUSSION

Synthesis of Multifunctional Poly(propylene oxide)s. The synthetic strategy developed to obtain the multihydroxy-functional PPO structures with two terminal hydroxyl functionalities is shown in Figure 1. The monobenzyl-protected ethylene glycol initiator 2-(benzyloxy)ethanol (BnO−) was

dx.doi.org/10.1021/ma300249c | *Macromolecules* 2012, 45, 3039−3046

Table 1. Characterization Data for BnO-PPO$_n$-*co*-PEEGE$_m$−OH and BnO-PPO$_n$-*co*-*lin*PG$_m$−OH Copolymers with Varying Monomer Composition

no.	sample	EEGE/mol %[a]	$M_{n,th}$/g mol^{-1}	M_n/g mol^{-1}[a]	M_n/g mol^{-1}[b]	M_w/M_n[b]	T_g/°C	LCST/°C
1a	BnO-PPO$_{50}$−OH	0	3060	3010	1960	1.10	−73	20.0
2a	BnO-PPO$_{62}$-*co*-PEEGE$_1$−OH	2	3280	3970	2450	1.07	−71	13.3
3a	BnO-PPO$_{49}$-*co*-PEEGE$_6$−OH	11	3500	3960	2040	1.12	−69	13.5
4a	BnO-PPO$_{45}$-*co*-PEEGE$_9$−OH	16	3720	4000	2220	1.09	−70	11.4
5a	BnO-PPO$_{38}$-*co*-PEEGE$_{11}$−OH	22	3940	3900	2330	1.16	−69	8.5
6a	BnO-PPO$_{36}$-*co*-PEEGE$_{12}$−OH	25	4160	4000	1440	1.14	−72	n.d.
7a	BnO-PPO$_{17}$-*co*-PEEGE$_{20}$−OH	54	5260	4100	1880	1.13	−67	10.9
8a	BnO-PPO$_{16}$-*co*-PEEGE$_{43}$−OH	74	6360	7400	3710	1.09	−66	4.7
9a	BnO-PEEGE$_{53}$−OH	100	7460	7940	2730	1.15	−67	6.7
2b	BnO-PPO$_{62}$-*co*-*lin*PG$_1$−OH	2	3100	3890	2370	1.07	−69	21.2
3b	BnO-PPO$_{49}$-*co*-*lin*PG$_6$−OH	11	3140	3500	2080	1.14	−63	32.6
4b	BnO-PPO$_{45}$-*co*-*lin*PG$_9$−OH	16	3180	3390	1950	1.12	−61	35.9
5b	BnO-PPO$_{38}$-*co*-*lin*PG$_{11}$−OH	22	3220	3140	2190	1.18	−63	39.3
6b	BnO-PPO$_{36}$-*co*-*lin*PG$_{12}$−OH	25	3260	3020	1350	1.12	−55	79.2
7b	BnO-PPO$_{17}$-*co*-*lin*PG$_{20}$−OH	54	3460	2650	1610	1.21	−31	–
8b	BnO-PPO$_{16}$-*co*-*lin*PG$_{43}$−OH	74	3660	4270	2920	1.22	−29	–
9b	BnO-*lin*PG$_{53}$−OH	100	3860	4100	1910	1.25	−27	–

[a]Calculated from ^{1}H NMR. [b]Calculated from SEC (PEO standards).

used as cesium salt to initiate the copolymerization of PO and EEGE. This initiator was chosen to generate α,ω-hydroxy-poly(propylene oxide)-*co*-poly(glycerol) (HO-PPO$_n$-*co*-*lin*PG$_m$−OH) copolymers in a stepwise deprotection approach (Figure 1). This strategy also permits to only deprotect the functional polymers at the chain end, if required. Cesium alkoxides are known to be efficient initiators for the anionic polymerization of epoxides that also lower the tendency of PO to isomerize to allyl alcohol, which would lead to a substantial amount of terminal double bonds.[11a,12] The ring-opening anionic polymerization of EEGE does not involve any side reactions, and thus copolymers with narrow molecular weight distribution can be obtained in good yields.

The polymerization was quenched with methanol after 18 h, and the cesium salts were extracted with sodium carbonate solution from the polymer solution in chloroform. Subsequent acidic hydrolysis of the acetal protecting groups releases the primary hydroxyl groups and generates the linear glycerol units. The hydrolysis can be conducted without further purification of the polymer obtained. To regenerate the hydroxyl functionality at the α-position, the benzyl protective group was removed by catalytic hydrogenation with palladium on activated charcoal.

The EEGE content in the copolymer was varied between 2 and 74% to adjust systematically the hydrophilicity of the materials. Characterization data for the series of copolymers obtained from the copolymerization of PO and EEGE are given in Table 1. The ratio of monomer to initiator (50:1) was kept constant. Because EEGE exhibits a higher molecular weight than PO, the theoretical molecular weights of the polymers increase with increasing amount of EEGE incorporated, referring to a molecular weight of 3000 g mol^{-1} for the PPO homopolymer and up to 7500 g mol^{-1} for the PEEGE homopolymer. In general, polymers with a slight deviation in molecular weight with respect to the theoretical values based on the ratio of monomers and initiator were obtained. This may be explained by experimental inaccuracies when measuring the monomers volumetrically.

Size exclusion chromatography (SEC) shows narrow molecular weight distributions with M_w/M_n values below 1.15 for all samples (Figure 2). Molecular weights can be determined from SEC and, more accurately, by end group

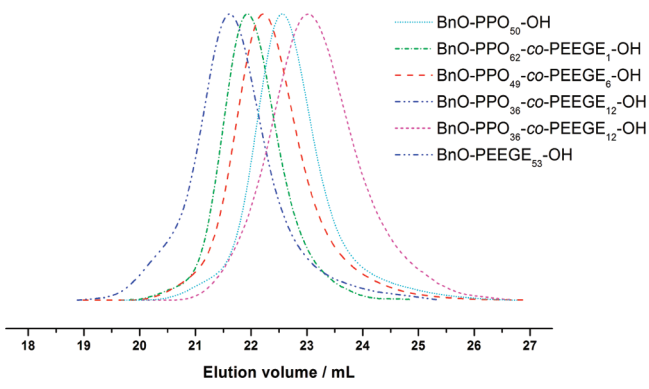


Figure 2. SEC results of several BnO-PPO$_n$-*co*-PEEGE$_m$−OH copolymers.

analysis of the corresponding ^{1}H NMR spectra of the copolymers (Table 1), provided that chain transfer to the monomer does not take place (which would lead to allyl-initiated chains, as will be discussed below). A deviation of the molecular weights calculated from NMR and the values obtained from SEC characterization becomes progressively obvious with increasing amount of EEGE. NMR and MALDI TOF investigations show (see below) that the initiator is incorporated in each polymer chain. Therefore, the molecular weights calculated from NMR are taken as the correct values. The deviation can most likely be explained by the different chemical structure of the polymers investigated in comparison with the calibration standard applied (PEO): The more EEGE units are incorporated, the more side chains are introduced, and the hydrodynamic radius that determines the elution volume changes compared with the PEO standards employed. Therefore, an increasing difference between the values is observed, which was previously reported in one case for other EEGE copolymers.[21]

dx.doi.org/10.1021/ma300249c | *Macromolecules* 2012, 45, 3039−3046

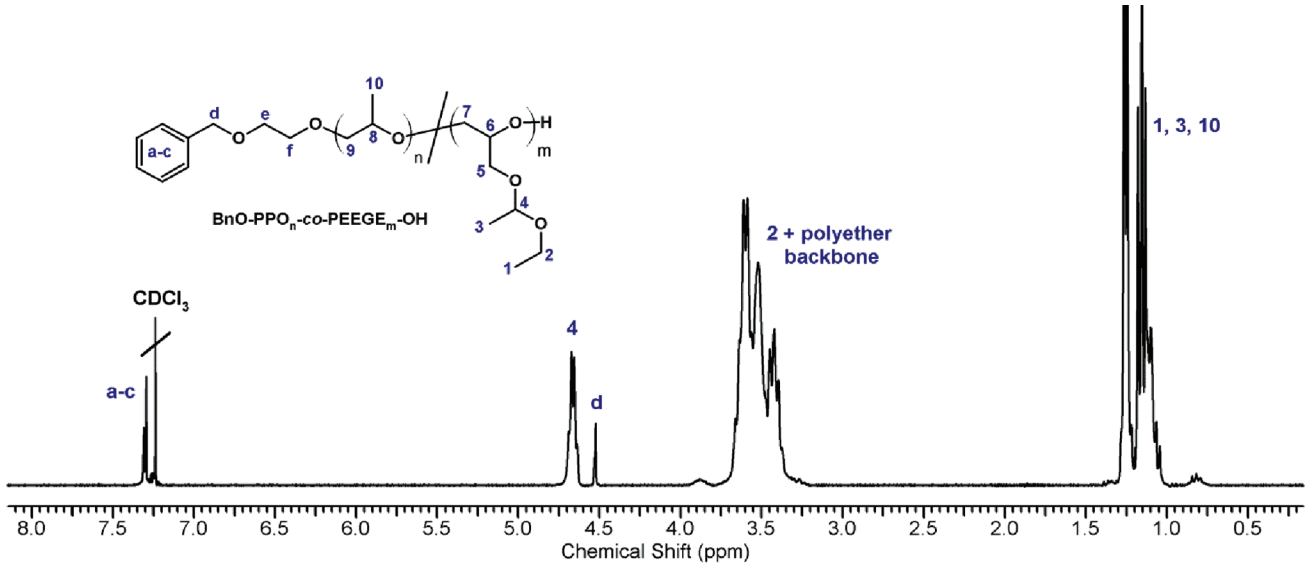


Figure 3. ^{1}H NMR spectrum ($CDCl_3$, 300 MHz) and structural assignment of BnO-PPO_{20}-*co*-$PEEGE_{30}$−OH.

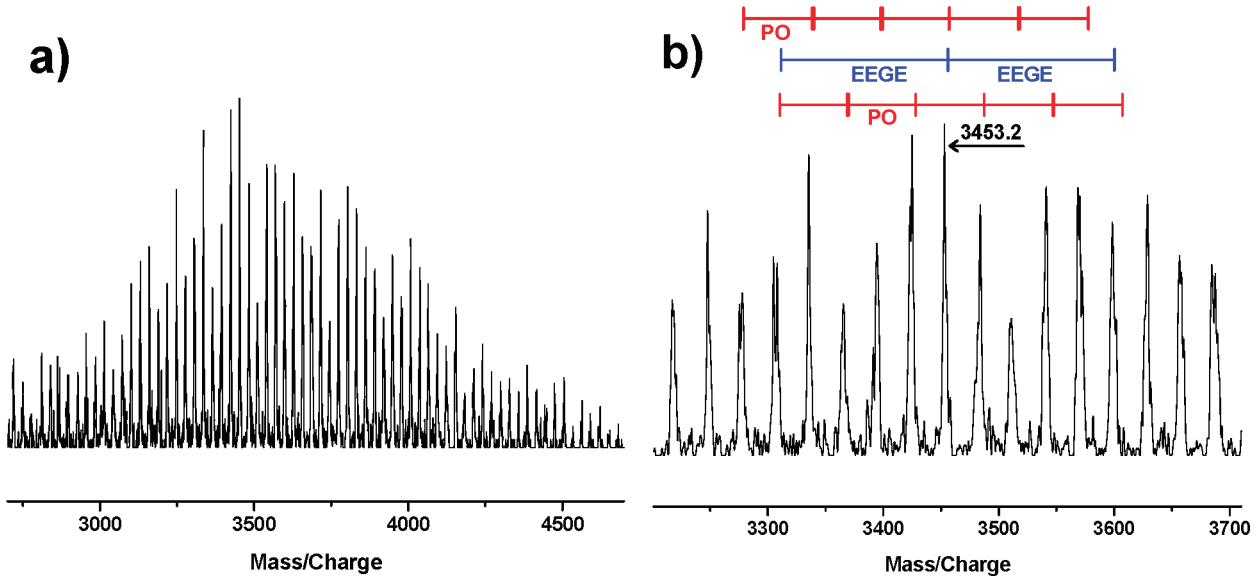


Figure 4. Typical MALDI-TOF mass spectra of BnO-PPO_{49}-*co*-$PEEGE_6$−OH (sample 3a): (a) full spectrum and (b) zoom-in with peak assignment.

Furthermore, NMR analysis permits the calculation of the ratio of comonomers incorporated by determination of the fraction of EEGE units from the intensity of the acetal proton signal (Figure 3). (A detailed description of the calculation is given in the Supporting Information.) The targeted fractions were 5, 10, 15, 20, 25, 50, and 75% for samples 2a to 8a. The incorporated monomer ratios determined by NMR are summarized in Table 1.

Matrix-assisted laser desorption/ionization time-of-flight mass spectrometry (MALDI-TOF MS) as a crucial characterization method for the detailed investigation of end-functional polymers was used to confirm that both comonomers are incorporated in the polymer chain and to demonstrate the absence of homopolymer as well as polymer chains initiated by allyloxy groups resulting from rearranged PO.

The MALDI-TOF spectrum (Figure 4) reveals only one distribution mode, which is unambiguously assigned to 2-(benzyloxy)ethanol-initiated copolymer of PO and EEGE. One representative mass peak at m/z 3453.2 corresponds to the copolymer with 2-(benzyloxy)ethanol as initiator, 47 units of PO, and 3 units of EEGE + Cs^+ (calculated isotopic mass = 3453.4 g mol^{-1}). The multitude of mass peaks results from the different combinations of the two comonomers, but the expected mass difference of both comonomers (PO: 58.1 g mol^{-1}, EEGE: 146.2 g mol^{-1}) can be found between different signals. Furthermore, it has to be emphasized that peaks corresponding to allyloxy-initiated chains that would result from deprotonated, rearranged PO molecules are absent in the mass spectrum, confirming once again that chain transfer to the monomer does not take place.

Copolymerization Kinetics Characterization via ^{1}H NMR. From a comparison with the copolymerization of EO and PO,[22] a higher reactivity of EEGE compared with PO can be expected. A drastic difference of reactivity would lead to gradient or block-like copolymers rather than random copolymers. In a previous study with copolymers of PO and EEGE generated by monomer-activated polymerization, higher reactivity of PO compared with EEGE was reported.[18]

dx.doi.org/10.1021/ma300249c | *Macromolecules* 2012, 45, 3039−3046

To confirm or dispute the random nature of the copolymerization, an investigation of the relative reactivity of EEGE and PO in anionic polymerization with respect to copolymerization kinetics and a detailed analysis of the evolution of the copolymer structure in the course of the polymerization are crucial. An experimental procedure that has recently been developed in our group[20] was used to investigate the copolymerization behavior of EEGE and PO: A DMSO-d_6 solution of the initiator and a mixture of PO and EEGE were separately transferred to an NMR tube under an argon atmosphere and cooled with liquid nitrogen. The cold NMR tube was evacuated and flame-sealed, and the polymerization was subsequently initiated by warming the tube to the respective temperature of the kinetics experiment. Immediately after melting and mixing, the first NMR spectrum was recorded. For experimental reasons, a minimum amount of DMSO-d_6 was used instead of polymerizing the comonomer mixture in bulk.

To examine the copolymerization kinetics, three different temperatures, that is, 25, 40, and 60 °C, with molar fractions of EEGE of 15% were applied. The molecular weight distributions of all samples obtained in these NMR experiments were narrow, with polydispersities around 1.07 (Supporting Information, Figure S2). Incorporation of the two comonomers and the growth of the polyether chain as well as the compositional drift in monomer feed were followed by the decrease in the epoxide signals located at 2.91 ppm for the methine proton of PO and at 3.07 ppm for the methine proton of EEGE, respectively. All signals are referenced to the peak of the methylene group of the initiator at 4.54 ppm, which was set to 2 and remains constant during the reaction.

The temperature dependence of the monomer conversion for 25, 40, and 60 °C is illustrated in Figure 5. Whereas at 60

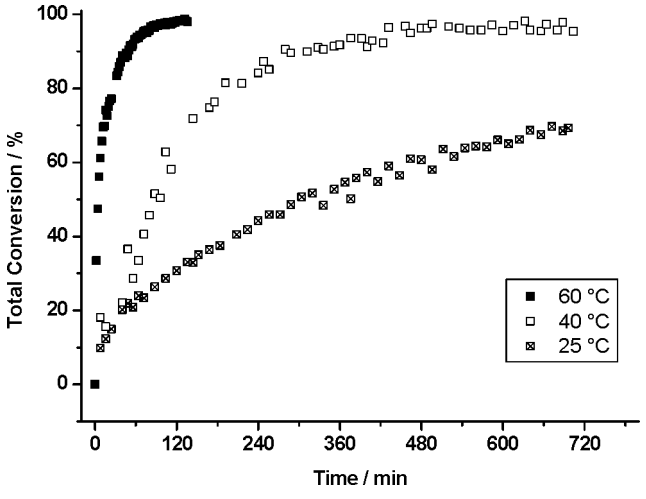


Figure 5. Monomer conversion versus time plots for copolymerization of propylene oxide with ethoxy ethyl glycidyl ether (15%) at 25, 40, and 60 °C, measured in DMSO-d_6.

°C full conversion (>99%) was reached within 100 min, the copolymerization at 40 °C takes about 7 h to complete. At the lowest investigated temperature (25 °C), even after 12 h the overall conversion is only 70%.

Despite the reactivity differences at the temperatures studied that lead to different polymerization rates, our NMR results demonstrate that the relative reactivities of the comonomers remain constant at all investigated temperatures. Figure 6

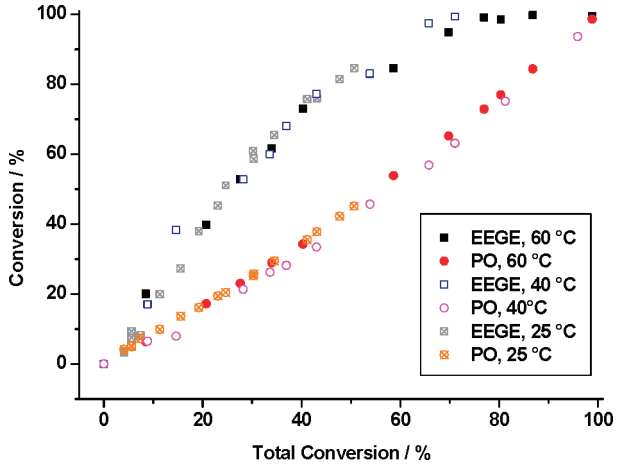


Figure 6. Percentage of monomer conversion of propylene oxide and ethoxy ethyl glycidyl ether (ca. 15% EEGE) versus total monomer conversion for copolymerization at 25, 40, and 60 °C, measured in DMSO-d_6.

illustrates the evolution of monomer feed composition during polymerization, revealing a somewhat faster incorporation of EEGE compared with PO into the growing polymer chain in the initial stage of the polymerization. Throughout the polymerization, the molar ratio of EEGE units in the polymer chain is higher than the initial ratio of the monomer feed. However, toward the end of the copolymerization, the total composition drops to the ratio of the initial feed. This indicates the formation of mainly random copolymers of PO and EEGE by anionic copolymerization, with a tapered structure constituted of more EEGE units at the beginning of the chains and PO units at the end, in contrast with the results found for the monomer-activated mechanism. Most importantly, a strong gradient or even block formation is clearly not observed.

Plotting the polymer molecular weight versus total monomer conversion resulted in a linear graph (Supporting Information, Figure S3).

^{1}H NMR measurements show furthermore that the well-known proton abstraction mechanism in the polymerization of PO can be avoided by adjusting the reaction conditions. First experiments at 60 °C in DMSO solution had shown the occurrence of up to 30% allyl ether initiated polymer chains.[23] This can be completely suppressed by lowering the polymerization temperature to 40 °C and carrying out the polymerization in bulk (Supporting Information, Figure S4).

Upon cleavage of the ethoxy ethyl protecting groups from the glycidol repeat units of the PPO-*co*-PEEGE copolymers by acidic hydrolysis, linear multifunctional PPO copolymers (deprotected samples 2b–9b, Table 1) with free hydroxyl groups at the backbone were obtained. Deprotection was carried out using a strongly acidic ion-exchange resin, such as Dowex 50WX8. SEC measurements show a shift of the distribution mode of the polymer to higher elution volumes that reflects the polarity change of the copolymer upon cleavage of the hydrophobic ethoxy ethyl protective group to the very polar hydroxyl group. The molecular weight distributions remained monomodal and narrow for all samples, confirming the stability of the polyether backbone under the acidic conditions chosen for the removal of the protective groups (Figure 7). The disappearance of the acetal proton signal (4.75 ppm) can also be monitored by ^{1}H and ^{13}C NMR spectroscopy (see Supporting Information, Figure S5 for the ^{13}C NMR

dx.doi.org/10.1021/ma300249c | *Macromolecules* 2012, 45, 3039–3046

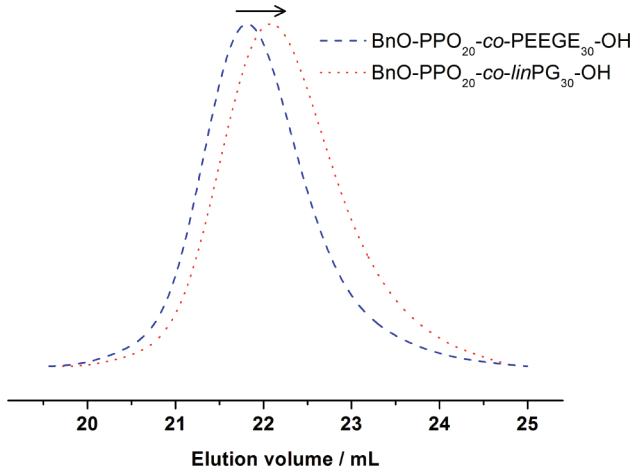


Figure 7. SEC traces showing the molecular weight distribution shift upon cleavage of the acetal protecting groups.

DEPT spectrum). In this manner, full deprotection was confirmed (Figure 8). A broad signal corresponding to the proton of the newly generated primary hydroxyl groups arises between 2.7 and 3.3 ppm (depending on the interaction of the hydrogen bonds in solution; in Figure 8 this resonance can be seen at 3.2 ppm).

To obtain the α-deprotected PPO copolymers with hydroxyl functionalities at both termini and several OH-groups randomly distributed along the PPO chain, we carried out catalytic hydrogenation with palladium on activated charcoal at 60 °C for 18 h with the BnO-PPO$_n$-*co*-PEEGE$_m$−OH copolymer. Deprotection was followed by ^{1}H NMR, monitoring the disappearance of the aromatic protons and the methylene group in benzyl position, as can be seen from Figure 9 from the disappearance of the signals at 4.48 and 7.15 to 7.50 ppm. Subsequent acidic deprotection of the acetal groups (as previously described) yields HO-PPO$_n$-*co*-*lin*PG$_m$−OH.

Thermal Behavior. The thermal behavior of the random copolymers is of interest with respect to the effect of hydroxyl groups on the glass-transition temperature of PPO (Table 1). To the best of our knowledge, the thermal properties of random copolymers of the type PPO-*co*-PEEGE and PPO-*co*-*lin*PG have not been studied to date. Differential scanning calorimetry (DSC) has been used to quantifiy the thermal properties of the materials. Whereas the glass-transition temperature (T_g) of the copolymers PPO-*co*-PEEGE shows only slight variation reflecting the very similar T_g values of the corresponding homopolymers (−73 °C for PPO and −65 °C for PEEGE), the glass-transition temperature increases from −69 °C for BnO-PPO$_{62}$-*co*-*lin*PG$_1$−OH to −31 °C for the copolymer BnO-PPO$_{20}$-*co*-*lin*PG$_{30}$−OH after deprotection, as can also be seen in the Supporting Information (Figure S6). We ascribe this to the additional interaction of the hydroxyl groups via hydrogen-bonding in the copolymers. As both homopolymers are not crystalline, no melting peak is observed for all copolymer samples.

Aqueous Solution Properties and LCST Behavior. From other aliphatic polyether copolymers, temperature-dependent solubility behavior in aqueous solution is known.[24] Therefore, the cloud-points of aqueous copolymer solutions of BnO-PPO$_n$-*co*-*lin*PG$_m$−OH have been investigated by monitoring the transmittance of a laser beam through a sample cell at a heating rate of 1 K min^{-1}. The transition from transparent to opaque solutions was taken as cloud-point and defined as the temperature corresponding to 50% transmission. In the following, we will refer to the LCST of the copolymers in a general sense, although the term LCST in a strict sense corresponds to the lowest cloud-point temperature possible, which is observed only at a certain concentration of a polymer.

Whereas the LCSTs of the BnO-PPO$_n$-*co*-PEEGE$_m$−OH copolymer samples are generally below room temperature (5−13 °C, Table 1), which is in agreement with the PPO-PEEGE block copolymers investigated by Dimitrov et al.,[11a] the

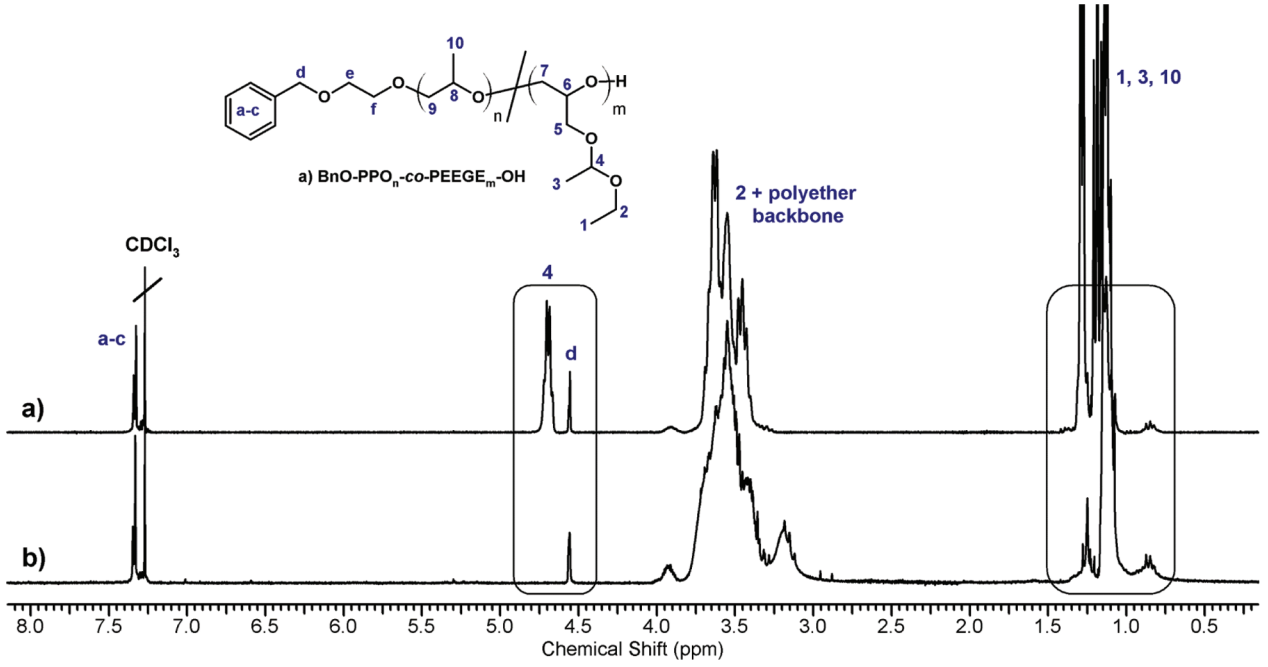


Figure 8. ^{1}H NMR spectra ($CDCl_3$, 300 MHz) showing the cleavage of the acetal protecting groups: (a) BnO-PPO$_n$-*co*-PEEGE$_m$−OH and (b) BnO-PPO$_n$-*co*-*lin*PG$_m$−OH.

dx.doi.org/10.1021/ma300249c | *Macromolecules* 2012, 45, 3039−3046

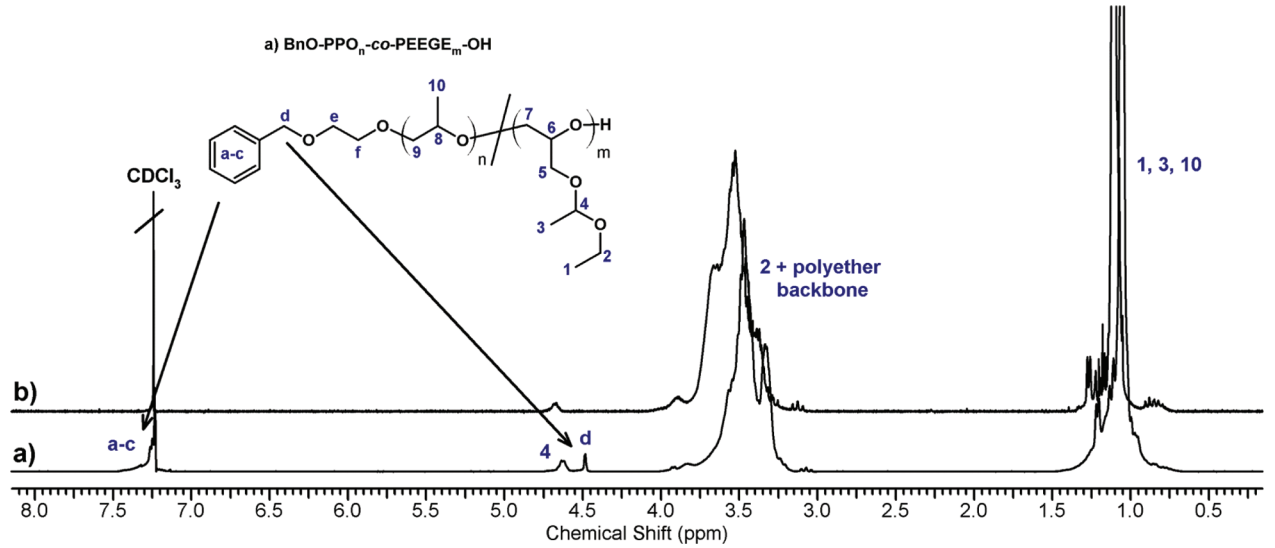


Figure 9. ^{1}H NMR spectra ($CDCl_3$, 300 MHz) of BnO-PPO$_n$-*co*-PEEGE$_m$−OH: (a) and HO-PPO$_n$-*co*-PEEGE$_m$−OH and (b) showing complete cleavage of the benzyl protecting groups.

deprotected BnO-PPO$_n$-*co*-*lin*PG$_m$−OH copolymer samples show considerably higher cloud-points. Samples 2b−5b with 2−22% free glycerol units in the PPO backbone show the typical clouding behavior presented by sigmoidal curves (Figure 10), corresponding to a thermally induced phase separation.

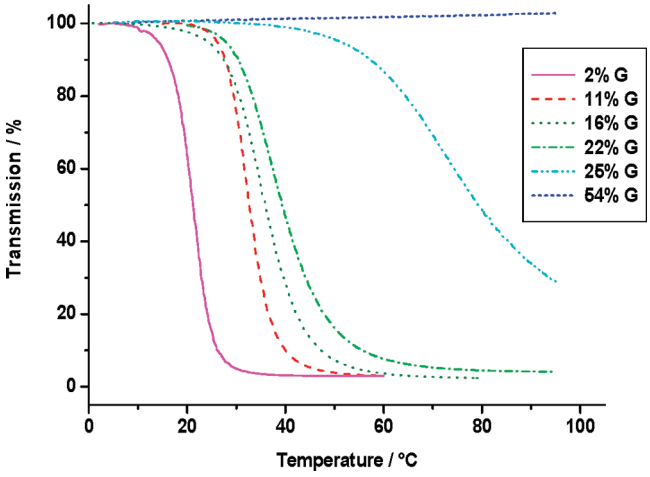


Figure 10. Intensity of transmitted laser light versus the temperature for BnO-PPO$_n$-*co*-*lin*PG$_m$−OH copolymers of varied composition at a concentration of 1 mg mL^{-1} in aqueous solution.

Samples with glycidol content exceeding 54% show no temperature-dependent transmittance and are thus soluble in water over the whole temperature range. Sample 6b with 25% glycidol content is unique for this series of copolymers in that it shows no sharp decrease but only rather slow clouding that does not reach 0% within the investigated temperature range (up to 95 °C). A comparison of the LCSTs of all copolymers with varying comonomer content reveals that with increasing amount of incorporated hydrophilic comonomer (linear glycerol units with a free hydroxyl group), the LCST increases progressively. Remarkably, a glycerol content as low as 11% renders the PPO copolymer completely soluble in water at ambient temperature.

To investigate further the properties of the copolymers, the concentration dependence of the LCST was investigated by comparing solutions with concentrations between 0.1 and 10 mg mL^{-1} of one representative sample. The critical temperatures were found to decrease with increasing copolymer concentration, indicating that the solutions become less translucent at higher concentrations, as also reported for the corresponding block copolymers.[12]

CONCLUSIONS

PPO is generally known as a nonpolar polyether that possesses no in-chain functionalities. In the current work, we have described a convenient synthesis for hydrophilic, functional PPO-based copolymers. The materials were obtained by random copolymerization of PO and EEGE, followed by subsequent cleavage of the protecting groups to release an adjustable number of primary hydroxyl groups randomly distributed in the PPO chain and two hydroxyl functionalities at both chain ends. Selective deprotection of the end group to generate an in-chain protected diol as a telechelic structure has also been demonstrated. It is important to emphasize that carrying out the polymerization at low temperature with Cs counterions permitted to avoid the commonly problematic proton abstraction from PO. ^{1}H NMR kinetic measurements show gradient monomer consumption and incorporation with a faster incorporation of EEGE compared with PO. Temperature-dependent aqueous solubility can be achieved by adjusting the comonomer composition. A glycerol content as low as 11% is sufficient to render the PPO copolymers completely water-soluble at ambient temperature. Precise design of polarity, functionality, and LCST offers intriguing options for the *α*,*ω*-hydroxy-poly(propylene oxide)-*co*-poly(glycerol) structures as functional soft segment in PUs or for biomedical applications, for example, in hydrophilic PUs for wound management as well as generally for functional PUs.[25] Furthermore, a usage as protein repellent surface coating is imaginable. Currently, we are studying toxicity and cell uptake of the copolymers as a potential alternative for poly(ethylene glycol)[26] in biomedical applications. It is obvious that the presented copolymers also offer opportunities for the grafting of other polymers onto the PPO copolymer backbone. We are

dx.doi.org/10.1021/ma300249c | *Macromolecules* 2012, 45, 3039−3046

convinced that our results will inspire further development of other PPO copolymers with functional side chains.

■ ASSOCIATED CONTENT

Supporting Information

Additional spectra and characterization data. This material is available free of charge via the Internet at http://pubs.acs.org.

■ AUTHOR INFORMATION

Corresponding Author

*E-mail: hfrey@uni-mainz.de.

Notes

The authors declare no competing financial interest.

■ ACKNOWLEDGMENTS

We thank Dr. Mihail Mondeshki for NMR measurements, Dr. Elena Berger-Nicoletti for MALDI-TOF measurements, and Sebastian Jäger for technical assistance. M.S. acknowledges financial support by the Max Planck Graduate Center (MPGC) with the Johannes Gutenberg-University.

■ REFERENCES

(1) Price, C. C. *Acc. Chem. Res.* **1974**, *7* (9), 294−301.
(2) Cendejas, G.; Flores-Sandoval, C. A.; Huitrón, N.; Herrera, R.; Zamudio-Rivera, L. S.; Beltrán, H. I.; Vázquez, F. *J. Mol. Struct.* **2008**, *879* (1−3), 40−52.
(3) Mortensen, K.; Schwahn, D.; Janssen, S. *Phys. Rev. Lett.* **1993**, *71* (11), 1728.
(4) Louai, A.; Sarazin, D.; Pollet, G.; François, J.; Moreaux, F. *Polymer* **1991**, *32* (4), 703−712.
(5) Alexandridis, P. *Curr. Opin. Colloid Interface Sci.* **1997**, *2* (5), 478−489.
(6) Blanchard, L. P.; Baijal, M. D. *J. Polym. Sci., Part A: Polym. Chem.* **1967**, *5* (8), 2045−2053.
(7) Taton, D.; Le Borgne, A.; Sepulchre, M.; Spassky, N. *Macromol. Chem. Phys.* **1994**, *195* (1), 139−148.
(8) Keul, H.; Möller, M. *J. Polym. Sci., Part A: Polym. Chem.* **2009**, *47* (13), 3209−3231.
(9) Dimitrov, P.; Utrata-Wesołek, A.; Rangelov, S.; Wałach, W.; Trzebicka, B.; Dworak, A. *Polymer* **2006**, *47* (14), 4905−4915.
(10) Dimitrov, P.; Rangelov, S.; Dworak, A.; Haraguchi, N.; Hirao, A.; Tsvetanov, C. *Macromol. Symp.* **2004**, *215* (1), 127−140.
(11) (a) Dimitrov, P.; Rangelov, S.; Dworak, A.; Tsvetanov, C. B. *Macromolecules* **2004**, *37* (3), 1000−1008. (b) Istratov, V.; Kautz, H.; Kim, Y.-K.; Schubert, R.; Frey, H. *Tetrahedron* **2003**, *59*, 4017−4024.
(12) Halacheva, S.; Rangelov, S.; Tsvetanov, C. *Macromolecules* **2006**, *39* (20), 6845−6852.
(13) Jamróz-Piegza, M.; Wałach, W.; Dworak, A.; Trzebicka, B. *J. Colloid Interface Sci.* **2008**, *325* (1), 141−148.
(14) Dworak, A.; Trzebicka, B.; Wałach, W.; Utrata, A.; Tsvetanov, C. *Macromol. Symp.* **2004**, *210* (1), 419−426.
(15) Erberich, M.; Keul, H.; Möller, M. *Macromolecules* **2007**, *40* (9), 3070−3079.
(16) Dworak, A.; Baran, G.; Trzebicka, B.; Wałach, W. *React. Funct. Polym.* **1999**, *42* (1), 31−36.
(17) Halacheva, S.; Rangelov, S.; Tsvetanov, C.; Garamus, V. M. *Macromolecules* **2010**, *43* (2), 772−781.
(18) Gervais, M.; Brocas, A.-L.; Cendejas, G.; Deffieux, A.; Carlotti, S. *Macromolecules* **2010**, *43* (4), 1778−1784.
(19) Fitton, A. O.; Hill, J.; Jane, D. E.; Millar, R. *Synthesis* **1987**, *1987* (12), 1140−1142.
(20) Obermeier, B.; Wurm, F.; Frey, H. *Macromolecules* **2010**, *43* (5), 2244−2251.
(21) Mangold, C.; Wurm, F.; Obermeier, B.; Frey, H. *Macromol. Rapid Commun.* **2010**, *31* (3), 258−264.
(22) Heatley, F.; Yu, G.-E.; Booth, C.; Blease, T. G. *Eur. Polym. J.* **1991**, *27* (7), 573−579.
(23) Yu, G.-E.; Masters, A. J.; Heatley, F.; Booth, C.; Blease, T. G. *Macromol. Chem. Phys.* **1994**, *195* (5), 1517−1538.
(24) Mangold, C.; Obermeier, B.; Wurm, F.; Frey, H. *Macromol. Rapid Commun.* **2011**, *32* (23), 1930−1934.
(25) Basko, M.; Bednarek, M.; Billiet, L.; Kubisa, P.; Goethals, E.; Du Prez, F. *J. Polym. Sci., Part A: Polym. Chem.* **2011**, *49* (7), 1597−1604.
(26) Dingels, C.; Schömer, M.; Frey, H. *Chem. Unserer Zeit* **2011**, *45* (5), 338−349.

Macromolecules

Article

pubs.acs.org/Macromolecules

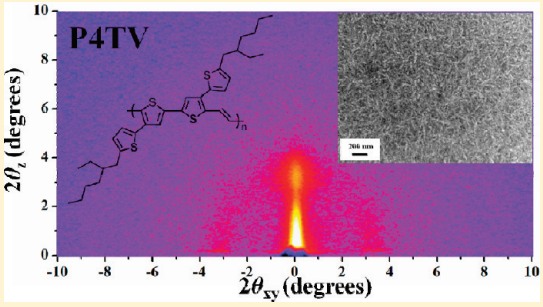
Biaxially Extended Quaterthiophene− and Octithiophene−Vinylene Conjugated Polymers for High Performance Field Effect Transistors and Photovoltaic Cells

Chien Lu,† Hung Chin Wu,† Yu Cheng Chiu, Wen Ya Lee, and Wen Chang Chen*

Department of Chemical Engineering, National Taiwan University, Taipei, Taiwan 10617

Supporting Information

ABSTRACT: We report the synthesis, morphology, and optoelectronic device applications of novel biaxially extended quaterthiophene− (**4T**−) and octithiophene− (**8T**−) vinylene conjugated polymers, **P4TV** and **P8TV**, synthesized via Stille coupling reactions. **P4TV** and **P8TV** exhibited smaller energy band gaps of 1.69 and 1.78 eV than that of parent polythiophenes, respectively, due to the reduced conformation distortion by the vinylene linkage. The HOMO energy levels of **P4TV** and **P8TV** were −5.02 and −5.13 eV, respectively, resulting in air stable device performance. The highest field effect hole mobilities of **P4TV** and **P8TV** were 0.12 and 0.0018 $cm^2\ V^{-1}\ s^{-1}$, respectively, with on/off ratios around 10^4−10^5. The higher carrier mobility of **P4TV** was related to its ordered structure as evidenced from the TEM, AFM, and grazing incidence X-ray diffraction results. The power conversion efficiency (PCE) of the **P4TV**/ $PC_{71}BM$ based photovoltaic cells (PV) under the illumination of AM 1.5G (100 mW/cm^2) was 4.04%, which was significantly higher than that of **P8TV**/$PC_{71}BM$ with 2.69%, due to its superior charge transport ability. However, **P8TV** had a better environmental stability attributed to its low-lying HOMO energy level. These above results demonstrate that biaxially extended thiophene−vinylene conjugated copolymers could be promising materials for high performance organic electronic device applications.



INTRODUCTION

Conjugated polymers have been intensively developed recently for applications in organic electronics such as light-emitting diodes,[1,2] field effect transistors (FETs),[3−8] photovoltaic cells (PVs),[9−17] and memory devices.[18−20] Among these polymers that used in electronic devices, polythiophenes have been attracted large interest due to their essential solubility, processability, and judicious structural flexibility.[21] Regioregular poly(3-hexylthiophene) (P3HT), one of the well-documented conjugated polymers, showed high hole mobilities in range of 0.05−0.2 $cm^2\ V^{-1}\ s^{-1}$[22−24] and PV cells efficiencies around 4−5%.[9,25−27] However, the relatively high HOMO levels obstruct the environmental stability for device applications.[28]

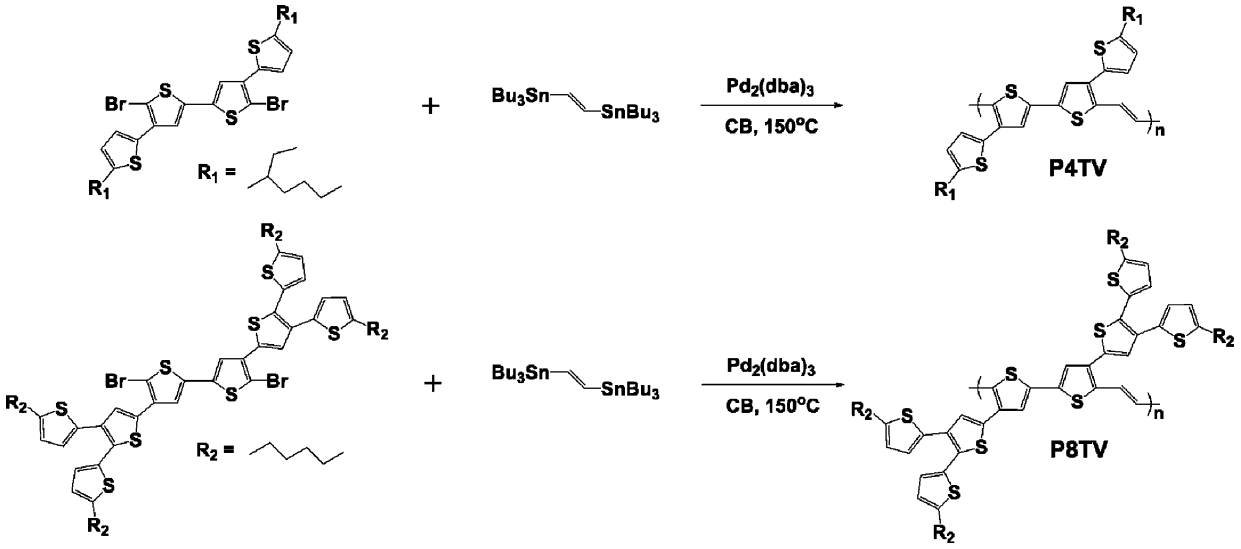
One approach toward high-performance FET or PV devices is the use of highly coplanar conjugated polymers with effective conjugation length and compact molecular packing. Poly(thienylene vinylene)s (PTVs) with a highly coplanar backbone exhibited a low band gap (1.55−1.64 eV) and ordered structure, since the vinylene linkage could reduce the steric hindrance.[29−37] However, the poor solubility of PTV limited their practical device applications.[29,30] Recently, several PTV derivatives were reported for high charge carrier mobility.[31−35] Kim and his co-workers reported low-band gap PC6TV12T with the hole mobility up to 1.05 $cm^2\ V^{-1}\ s^{-1}$, attributed to the coplanar TV unit.[36] However, despite of the low band gaps of PTVs, the power conversion efficiency (PCE) of the PV cells was low (0.24−1.2%).[32−34,37] To further improve the performance of PTV based optoelectronic devices, it is important to design new polymers with high charge carrier mobility, broad absorption in visible region, and optimized morphology.[28,38,39]

Biaxially extended conjugated polymers[40−47] were reported to enhance the absorption range and the carrier mobility for device applications, due to the extension of π-electron delocalization. Li and co-workers reported that the incorporation of conjugated side chains into thiophene backbone facilitated the extension of π-electron delocalization and have broad absorption, such as bi(thienylenevinylene),[38,40] bi(phenylenevinylene),[41] and phenothiazinevinylene.[48] We discovered the biaxial extended conjugated thiopohene-acceptor or fused thiophene copolymers with high unipolar or ambipolar carrier mobility (3×10^{-4} to 0.61 $cm^2\ V^{-1}\ s^{-1}$).[28,41−43] Also, the relatively low-lying HOMO levels (−5.04 to −5.62 eV)[28,43−45] could enhance the open-circuit voltage for high performance PV applications. On the other hand, dendritic and branched thiophenes derivatives were reported to improve charge transport,[49−52] processing solubility,[53,54] or compatibility with PCBM molecules.[39] Thus, conjugated polymers with branched conjugated side chains would be potential candidates for optoelectronic device applications owing to good charge transport, broad absorption, and high air stability.

Received: February 15, 2012
Revised: March 17, 2012
Published: March 26, 2012

ACS Publications © 2012 American Chemical Society

Scheme 1. Synthetic Route on Preparing P4TV and P8TV



In this paper, we report the synthesis, morphology, and device applications of new biaxially extended conjugated (thiophene-vinylene), poly[(*E*)-5,5‴-bis(2-ethylhexyl)-2′-methyl-5″-(prop-1-en-1-yl)-2,3′:5′,2″:4″,2‴-quaterthiophene] (**P4TV**) and poly[(*E*)-5,5⁗-dihexyl-3′,5‴-bis(5-hexylthiophen-2-yl) −5‴-methyl-2″-(prop-1-en-1-yl)-2,2′:5′,3″:5″,2‴:4‴,2⁗:4⁗,2⁗′:4⁗′,2⁗′′-sexithiophene] (**P8TV**). The incorporation of the vinylene unit into the biaxially extended quaterthiophene (**4T**) and octithiophene (**8T**) could enhance the backbone coplanarity to improve charge transport characteristics for device applications. Furthermore, the branched conjugated thiophene side chain may have a broad absorption for enhance PV performance. **P4TV** and **P8TV** were synthesized by Stille coupling reaction under microwave heating, as shown in Scheme 1. The morphology of the prepared conjugated polymers was investigated by transmission electron microscopy (TEM), atomic force microscopy (AFM), and grazing incidence X-ray diffraction (GIXD) analysis. The charge carrier mobility was obtained from the top-contact/bottom-gate field effect transistor device structure. Moreover, the photovoltaic cell with device structure of ITO/PEDOT:PSS/polymer:$PC_{71}BM$/Ca/Al using **P4TV** and **P8TV** were fabricated and characterized.

EXPERIMENTAL SECTION

Materials. Tri(*o*-tolyl)phosphine, tris(dibenzylideneacetone)-dipalladium(0), trimethyl(thiophen-2-yl)stannane, and bromothiophene were purchased from Aldrich (Missouri) and used without further purification. P3HT (M_w ∼ 50 000 g/mol, 90−95% regioregular) was used as received from Reike Metals Inc. (Lincoln, NE). Common organic solvents for synthesis were distilled to keep anhydrous or degassed by nitrogen 0.5 h before using. Ultra-anhydrous *o*-dichlorobenzene for device applications was purchased from Aldrich (Missouri). The monomer of 2′,5″-dibromo-5,5‴-di- (2-ethylhexyl)-[2,3′;5′,2″;4″,2‴]quaterthiophene (**4T-Br$_2$**) was synthesized according to our previous work.[43,45] The synthesis of 2″,5‴-dibromo-5,5⁗-dihexyl-3′,5‴-bis(5-hexylthiophen-2-yl)-2,2′:5′,3″:5″,2‴:4‴,2⁗:4⁗,2⁗′:4⁗′,2⁗′′-sexithiophene (**8T-Br$_2$**) is shown in the Supporting Information. A surface treatment agent of octadecyltrichlorosilane (ODTS) was purchased from Acros (Geel, Belgium) for field-effect transistor characterization. [6,6]-phenyl-C71-butyric acid methyl ester ($PC_{71}BM$) was purchased from Solenne BV (Groningen, The Netherlands) for photovoltaic cell applications.

General Procedures for Polymerization. The general procedure of synthesizing **P4TV** and **P8TV** is shown in Scheme 1. (*E*)-1,2-Bis(tributylstannyl)ethylene (**V-ditin**), dibromomonomers (**4T-Br$_2$** and **8T-Br$_2$**), tri(*o*-tolyl)phosphine (16 mol % with respect to ditin monomer), and tris(dibenzylideneacetone)dipalladium(0) (2 mol % with respect to ditin monomer) were dissolved in chlorobenzene. Then, these copolymers were synthesized by Pd(0)-catalyzed Stille coupling polymerization under microwave heating (150 °C for 30 min). After end-capped with trimethyl(thiophen-2-yl)stannane and bromothiophene (both 1.1 equiv with respect to the monomers and under microwave heating at 160 °C for 10 min on the end-capping), the mixture was cooled and poured into methanol to afford a crude solid. The crude polymer was purified by methanol, acetone and hexane successively using a Soxhlet extraction to remove byproducts, oligomers and catalyst residues.

*Poly[(E)-5,5‴-bis(2-ethylhexyl)-2′-methyl-5″-(prop-1-en-1-yl)-2,3′:5′,2″:4″,2‴ -quaterthiophene] (**P4TV**).* Amounts of 284.02 mg (0.40 mmol) of **4T-Br$_2$**, 242.46 mg (0.40 mmol) of **V-ditin**, and 15 mL of chlorobenzene were used to afford a purple solid (yield, 65%). ^{1}H NMR (CD_2Cl_2), δ (ppm): 7.51−6.19 (m, br, Ar−H and Vin-H, 8H), 2.15−1.72 (br, Ar−CH_2, 4H), 1.49−1.15 (br, −CH and −CH_2, 18H), 1.15−0.46 (br, −CH_3, 12H). Anal. Calcd for [$C_{32}H_{44}S_4$]: C, 70.29; H, 7.63 S, 22.08. Found: C, 68.62; H, 7.01; S, 21.90. Weight-average molecular weight (M_w) and polydispersity index (PDI) estimated from GPC are 87025 g/mol and 2.51, respectively.

*Poly[(E)-5,5⁗-dihexyl-3′,5⁗′-bis(5-hexylthiophen-2-yl)-5‴-methyl-2″-(prop-1-en-1-yl)-2,2′:5′,3″:5″,2‴:4‴,2⁗′:4⁗′,2⁗′′:4⁗′′,2⁗′′′-sexithiophene] (**P8TV**).* Amounts of 460.04 mg (0.40 mmol) of **8T-Br$_2$**, 242.46 mg (0.40 mmol) of **V-ditin**, and 15 mL of chlorobenzene were used to afford a black solid (yield, 68%). ^{1}H NMR (CD_2Cl_2), δ (ppm): 7.61−6.19 (m, br, Ar−H and Vin-H, 14H), 2.90−2.31 (br, Ar−CH_2, 8H), 1.49−0.97 (m, br, −CH_2, 32H), 0.97−0.58 (m, br, −CH_3, 12H). Anal. Calcd for [$C_{58}H_{66}S_8$]: C, 68.18; H, 6.71 S, 25.11. Found: C, 67.76; H, 6.28; S, 25.33. Weight-average molecular weight (M_w) and polydispersity index (PDI) estimated from GPC are 59630 g/mol and 2.33, respectively.

Characterization. Microwave reaction was carried out using a Biotage microwave reactor in sealed vessels. ^{1}H NMR spectra were recorded with a Bruker Avance DRX 400 MHz instrument. Gel permeation chromatographic (GPC) analysis was performed on a Lab Alliance RI2000 instrument (two column, MIXED-C and -D from Polymer Laboratories) which was connected to one refractive index detector from Schambeck SFD Gmbh. All GPC analyses were performed on polymer/THF solution at a flow rate of 1 mL/min at 40 °C and calibrated with polystyrene standards. Thermogravimetric analysis (TGA) and differential scanning calorimetry (DSC) measurements were performed under a nitrogen atmosphere at a heating rate

dx.doi.org/10.1021/ma300313y | *Macromolecules* 2012, 45, 3047−3056

of 10 °C/min by using the TA Instruments Q-50 and Q-100, respectively. X-ray diffraction patterns were collected by X-ray scattering in a grazing-incidence geometry (Nano-Viewer, Rigaku) that includes a two-dimensional (2D) area detector (Rigaku, 100 K PILATUS). The instrument is equipped with a 31 kW mm^{-2} generator (rotating anode X-ray source with a Cu Ka radiation of λ = 0.154 nm). The scattering vector, q ($q = 4\pi/\lambda[\sin\theta]$), along with the scattering angles q in these patterns were calibrated using silver behenate. The thin films were mounted on a z-axis goniometer. UV−visible absorption spectra were recorded using a Hitachi U-4100 spectrophotometer. For the thin film spectra, polymers were first dissolved in o-dichlorobenzene, followed with filtering through a 0.45 μm pore size PTFE membrane syringe filter, and then spin-coated at a speed rate of 800 rpm for 60 s onto quartz substrate. The absorption coefficients were calculated using the Beer's law, and the film thickness was determined with a Microfigure Measuring Instrument (Surfcorder ET3000, Kosaka Laboratory Ltd.). Cyclic voltammetry (CV) was recorded on a CHI 611B electrochemical analyzer using the use of a three-electrode cell in which ITO (polymer films area were about 0.5 × 0.7 cm^2) was used as a working electrode. A platinum wire was used as an auxiliary electrode. All cell potentials were taken with the use of a homemade Ag/AgCl, KCl (sat.) reference electrode. The electrochemical properties of the polymer films were detected under 0.1 M anhydrous acetonitrile solution containing tetrabutylammonium perchlorate (TBAP) as electrolyte. The morphology of polymer film surface was obtained with a Nanoscope 3D Controller atomic force micrographs (AFM, Digital Instruments) operated in the tapping mode at room temperature. Transmission electron microscopy (TEM) images were obtained with a JEOL JEM-1230 instrument operating at a voltage of 100 kV with a Gatam dual vision CCD camera. For the measurements of GIXD, UV, AFM, and TEM, the preparation of polymer samples were the same with that of the device fabrication.

Computational Methodology. Theoretical molecular simulation of the studied polymers was calculated through Gaussian 03 program package.[55] Density functional theory (DFT) method, using Becke's three-parameter functional with the Lee, Yang, and Parr correlation functional method (B3LYP) with 6-31G(d), was used for the optimization of ground-state molecular geometry.

Fabrication and Characterization of Field Effect Transistors. Highly doped n-type Si(100) wafers were used as substrates. A 200 nm SiO_2 layer (capacitance per unit area C_o = 17 nF cm^{-2}) as a gate dielectric was thermally grown onto the Si substrates. These wafers were cleaned in piranha solution (Caution!), a 7:3 (v/v) mixture of H_2SO_4 and H_2O_2, rinsed with deionized water, and then dried by N_2. The octadecyltrichlorosilane (ODTS)-treated surfaces on SiO_2/Si substrates were obtained by the following procedure: a clean SiO_2/Si substrate was immersed into a 10 mM solution of trichlorosilane in toluene at 80 °C for 2 h. Then the substrates were rinsed with toluene and dried with a steam of nitrogen. FET devices were fabricated by spin-coating of the polymer solution in o-dichlorobenzene (12 mg/mL) at a spin rate of 800 rpm for 60 s, and annealed at 100 °C for 60 min. The top-contact source and drain electrodes were defined by 100 nm-thick gold through a regular shadow mask, and the channel length (L) and width (W) were 50 and 1000 μm, respectively. FET transfer and output characteristics were recorded in a N_2-filled glovebox or in ambient by using a Keithley 4200 semiconductor parametric analyzer.

Fabrication and Characterization of Polymer Photovoltaic Cells. All the bulk heterojunction photovoltaic cell was fabricated through the following preparation procedures: The glass−indium tin oxide (ITO) substrate (obtained from Lumtec, (7 Ω/sq)) was first patterned by lithograph, then cleaned with detergent, and ultrasonicated in acetone and isopropyl alcohol, and subsequently dried on a hot plate at 120 °C for 5 min, and finally treated with oxygen plasma for 5 min. Poly(3,4-ethylenedioxy−thiophene):poly(styrene−sulfonate) (PEDOT:PSS, Baytron P VP AI4083) was passed through a 0.45 μm filter and then spin-coated at 5000 rpm on ITO in air and dried at 140 °C for 20 min inside the glovebox. The polymer/$PC_{71}BM$ blend was prepared by dissolving them in anhydrous o-dichlorobenzene (18 mg/mL) followed by spin-coating on the top of the PEDOT:PSS layer. The device was then annealed at 100 °C for 10 min (**P4TV** and **P8TV**) or 140 °C for 20 min (P3HT) in glovebox. Subsequently, the device was deposited with a 30 nm thickness of Ca and a 100 nm thickness of Al by thermal evaporation under high vacuum (<10^{-6} Torr), respectively. The active area of the device is 4 mm^2. The current−voltage (J−V) measurement of the polymer photovoltaic cell was conducted by a computer-controlled Keithley 2400 source measurement unit (SMU) with a Peccell solar simulator under the illumination of AM 1.5 G, 100 mW/cm^2. The illumination intensity was calibrated by a standard Si photodiode detector with KG-5 filter.

RESULTS AND DISCUSSION

Polymer Characterization. The chemical structures of the synthesized polymers were confirmed by ^{1}H NMR and elemental analysis. Figure 1 shows the ^{1}H NMR of **P4TV**

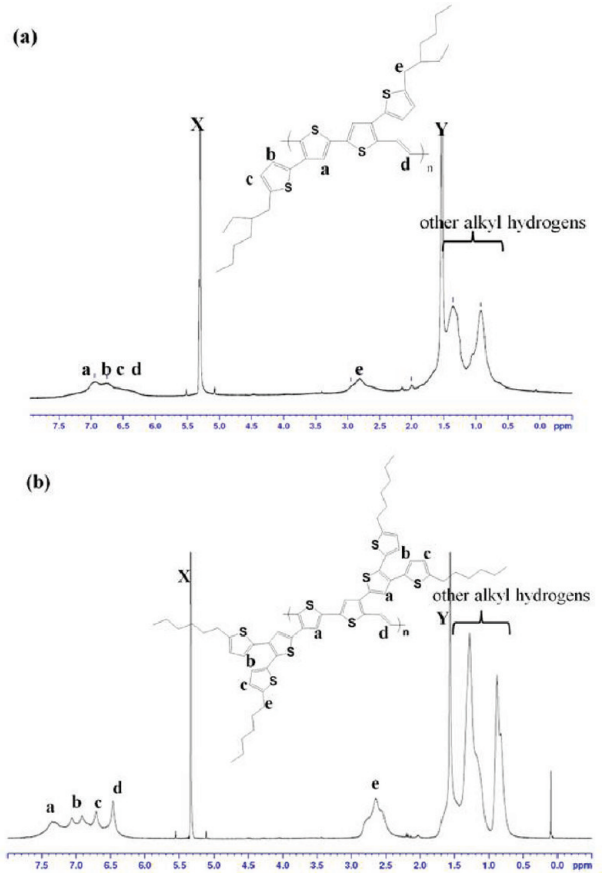


Figure 1. ^{1}H NMR spectra of (a) **P4TV** and (b) **P8TV** in CD_2Cl_2. (X, CD_2Cl_2; Y, H_2O).

and **P8TV** in CD_2Cl_2. For the spectrum of **P4TV**, the three peaks at 7.01 (peak a), 6.75 (peak b), and 6.56 (peak c) ppm are assigned to the aromatic protons on the thiophene rings of the 4T unit, while the peak at 6.32 (peak d) ppm is attributed to the proton on the vinylene segment. Moreover, the peaks at 2.15−1.72 ppm (thiophene−CH_2, peak e), 1.49−1.15 ppm (−CH and −CH_2), and 1.15−0.46 ppm (−CH_3) are attributed to the ethylhexyl group in the 4T unit, respectively. Similarly, the chemical shift and proton numbers in the NMR spectrum of **P8TV** is also consisted with the proposed structure. The elemental carbon, hydrogen, and sulfur contents of the studied polymers are in a good agreement with the theoretical content. The above results suggest the successful preparation of the biaxially extended thiophene−vinylene conjugated polymers.

dx.doi.org/10.1021/ma300313y | Macromolecules 2012, 45, 3047−3056

Both **P4TV** and **P8TV** have good solubility in common chlorinated solvents and thus could be spin-coated into optical quality films for device applications, including chloroform, chlorobenzene, and *o*-dichlorobenzene. The weight-averaged molecular weight and the polydispersity index (M_w, PDI) of **P4TV** and **P8TV** estimated by GPC (Figure S2 of Supporting Information) using polystyrene standards in THF are (87025, 2.51) and (59630, 2.33), respectively.

The thermal properties of **P4TV** and **P8TV** were evaluated by thermo-gravimetric analysis (TGA) and differential scanning calorimetry (DSC) as shown in Figure S3 (Supporting Information). The thermal decomposition temperature (T_d) values of **P4TV** and **P8TV** are 392 and 408 °C, respectively, indicating their good thermal stability. DSC curves were measured up to 250 °C, but no obvious thermal transition in the bulk sample was observed.

Optical Properties. The UV−visible absorption spectra of **P4TV** and **P8TV** thin films are shown in Figure 2a, and

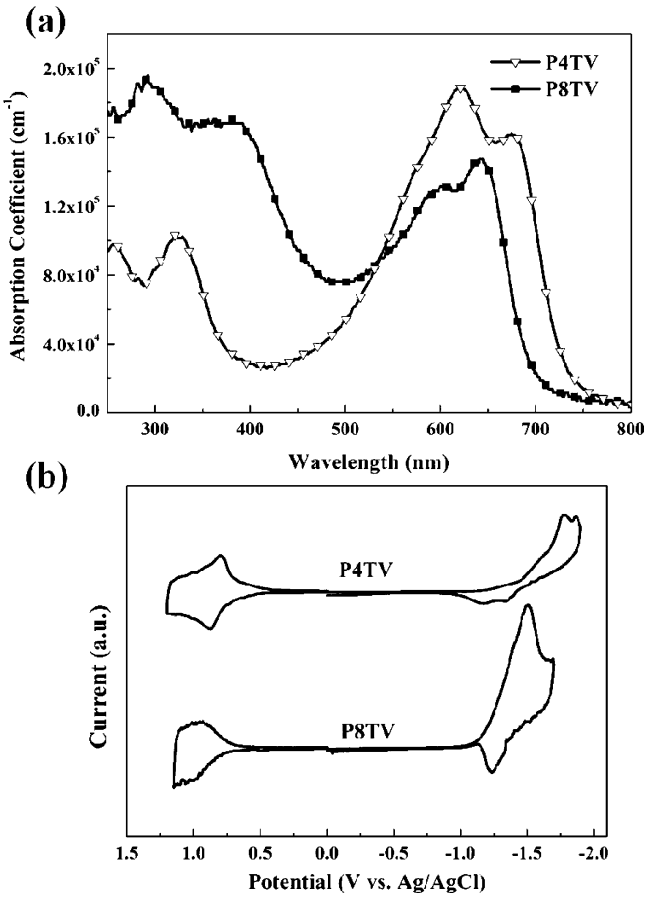


Figure 2. (a) Optical absorption spectra of the **P4TV** and **P8TV** thin films on a quartz plate. (b) Cyclic voltammograms of the **P4TV** and **P8TV** thin film in an acetonitrile solution of 0.1 M TBAP at a scan rate of 100 mV/s.

summarized in Table 1. The absorption maximum wavelength (λ_{max}) in the visible region of the **P4TV** and **P8TV** thin films are observed at 621 and 675 nm for **P4TV** and 603 and 643 nm for **P8TV**, respectively, attributed to the $\pi-\pi^*$ electronic transition. The λ_{max} of the two polymers in dilute *o*-dichlorobenzene (Figure S4 of Supporting Information) are similar to those of the thin films. Both **P4TV** and **P8TV** thin films possess an absorption peak with a clearly observed shoulder, indicating the higher structural organization and ordered packing. The E_g^{opt} of **P4TV** and **P8TV** estimated from the absorption edge are 1.69 and 1.78 eV, respectively, which are smaller than the P3HT with 1.8−2.0 eV. It again suggests the importance of the vinylene linkage affecting the backbone coplanarity and the resulted band gap. **P8TV** has a more branched thiophene side chains and thus provides a higher rotation freedom, leading to reduce the effective conjugation length for a higher E_g than that of **P4TV**.[56] Compare to those P3HT and PTVs, the absorption peaks of **P4TV** (λ_{max} = 325 nm) and **P8TV** (λ_{max} = 291 and 391 nm) located in ultraviolet region arise from the $\pi-\pi^*$ transition of conjugated side chains.[40] Obviously, the relatively branched thiophene of **P8TV** exhibit a higher absorption intensity in the ultraviolet region than that of **P4TV**.

Figure 3 is the optimized geometry on the dimers of **P4TV** and **P8TV**, calculated at the B3LYP/6-31G(d) level through Gaussian 03 program package. θ_α and θ_γ are the torsional angles of the dimers in the main chain, and θ_β and θ_ω are torsional angles of the dimers in the side chains. The small main-chain torsional angles (θ_α, θ_γ) are (1.6°, 4.5°) and (8.5°, 10.2°) for **P4TV** and **P8TV**, respectively, which are smaller than that of P4T (18°, 84°) in our previous work.[45] It indicates that the vinylene moieties inserted into biaxially extended conjugated polythiophene significantly reduces the torsion within the main chain. Besides, **P4TV** exhibit a higher degree of coplanarity than **P8TV**. The side-chain torsional angles (θ_β) are 41.3° and 39.3° for **P4TV** and **P8TV**, respectively. The side-chain torsional angles of branched thiophenes of **P8TV** are 39.6−49.5°, suggesting higher rotational freedom of the branched thiophene side chains. The structural conformation result of **P4TV** and **P8TV** is consistent with the optical band gap described in the previous section. Besides, the optical band gap of **P4TV** is lower compared to other **4T**-based conjugated polymers (1.80−2.65 eV).[37,38] The broad absorption characteristic could also improve the PV cell characteristics and elevate the photocurrent spectrum.

The thin films of **P4TV** (1.89×10^5 cm^{-1} at ca. 621 nm) and **P8TV** (1.47×10^5 cm^{-1} at ca. 643 nm) exhibit moderate absorption coefficients comparable to that of the P3HT film (1.9×10^5 cm^{-1} at ca. 552 nm).[57] The high absorption coefficient of **P4TV** suggests its potential to enhance the PV cells performance.

Electrochemical Properties. The electrochemical characteristics measured in acetonitrile at potential scan rate of 100 mV/s are shown in Figure 2b and summarized in Table 1. The highest occupied molecular orbital (HOMO) energy level, the lowest unoccupied molecular orbital (LUMO) energy level, and the electrochemical band gap (E^{ec}_g) were estimated from the onset oxidation potential (E^{ox}_{onset}) and onset reduction potential (E^{red}_{onset}), based on the following equations: HOMO = $-[E^{ox}_{onset} - E^{ferrocene}_{1/2} + 4.8]$ V; LUMO = $-[E^{red}_{onset} - E^{ferrocene}_{1/2} + 4.8]$ V, where the potential is referred to an Ag/AgCl reference electrode. Apparently, both polymers exhibit both reversible oxidation and reduction processes. The corresponding HOMO energy levels of **P4TV** and **P8TV** are −5.02 and −5.13 eV, respectively, while their LUMO energy levels are −3.15 and −3.16 eV. The corresponding electrochemical band gaps of **P4TV** and **P8TV** are 1.87 and 1.97 eV. The higher HOMO level of **P4TV** than that of **P8TV** is attributed the better backbone coplanarity of the former. Moreover, the HOMO energy levels of **P4TV** and

dx.doi.org/10.1021/ma300313y | *Macromolecules* 2012, 45, 3047−3056

Table 1. Optical and Electrochemical Properties of P4TV and P8TV

	optical absorption				cyclic voltammetry		
polymer	λ_{max}(sol)[a] (nm)	λ_{max}(film)[a] (nm)	α[b] ($\times 10^5$ cm^{-1})	E_g^{opt} (eV)	E^{ox}_{onset}/HOMO (V/eV)	E^{red}_{onset} /LUMO (V/eV)	E_g^{ec} (eV)
P4TV	325, 622, 677	325, 621, 675	1.89	1.69	0.70/−5.02	−1.17/−3.15	1.87
P8TV	380, 592. 638	391, 603, 643	1.47	1.78	0.81/−5.13	−1.16/−3.16	1.97

[a] *o*-dichlorobenzene as processing solvent. [b] Absorption coefficient (α) of the solid thin film at its maximum peak intensity in the visible region (420−700 nm) ($\times 10^{-5}$ cm^{-1}).

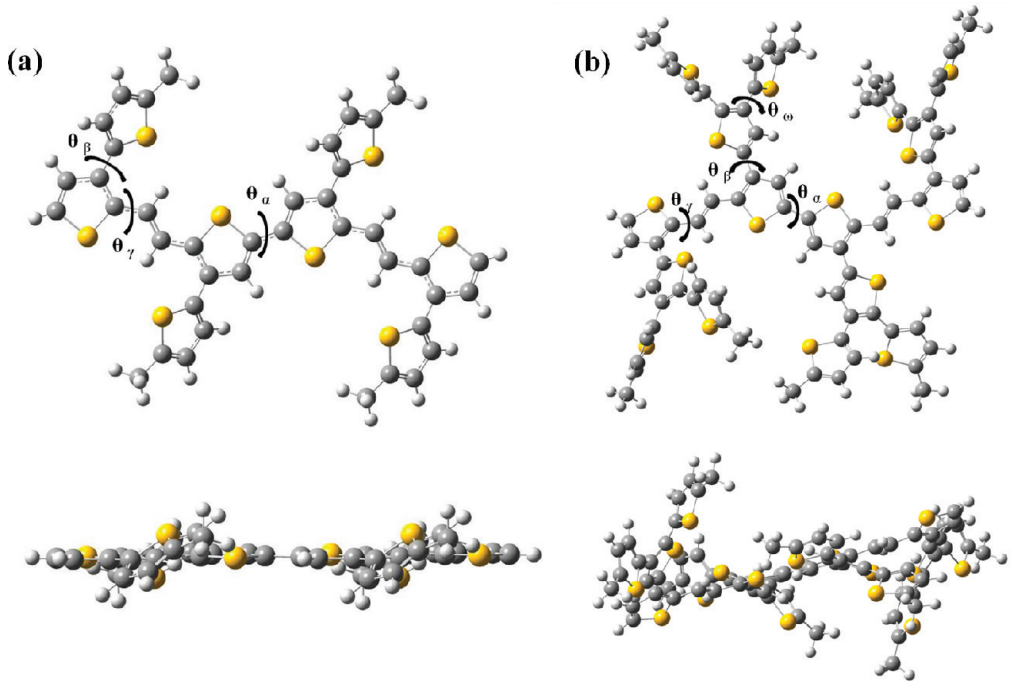


Figure 3. Optimized backbone structure of (a) **P4TV** and (b) **P8TV** in 2 units. The side chains were replaced with the methyl groups to simplify the calculation.

P8TV are lower than P3HT (−4.90 eV), indicating these polymers could have better air stability.

Morphology Characterization. The film morphology of **P4TV** and **P8TV** were examined using Transmission electron microscopy (TEM), atomic force microscopy (AFM), and grazing incidence X-ray diffraction (GIXD) analyses. Figure 4 shows TEM images of the thermal annealed **P4TV** and **P8TV** thin films. The annealed **P4TV** thin film showed a more organized nanofirbrillar structure as compared to **P8TV**. The well-ordered morphology of **P4TV** was expected to result in good charge carrier transporting characteristics. The thin film morphology of **P8TV** was nearly amorphous because the bulky pendent branched thiophene moiety reduces the ordering of polymer backbones. As shown in Figure 5, GIXD analyses of annealed thin films (thickness of 40−50 nm) were carried out to further investigate the structural ordering. The primary diffraction patterns of **P4TV** (Figure 5a) and **P8TV** (Figure 5b) are observed at $2\theta_z$ = 3.66 and 4.06°, respectively, corresponding to the *d*-spacing of 24.14 and 21.76 Å, respectively. The diffraction intensity of **P4TV** is markedly stronger than **P8TV**. It is consistent with the appearance of orderly nanofirbrillar structure of **P4TV** in the TEM images. In Figure 5c, the full width half-maximum (fwhm) of the azimuthal-angle intensity of the first order diffraction is estimated to be 9.49 and 20.25° for **P4TV** and **P8TV**. It suggests that **P4TV** has a significantly concentrative orientation distribution of the crystalline domains with respect to the substrate surface. The alignment of **P4TV** is also more concentrative than that broader orientation distribution of P3HT (fwhm = 14.1° for the best condition).[58] Besides, the *d*-spacing of the studied polymers are slightly larger than that of the other PTVs reported in the literature.[36] Also, P4T also showed a smaller *d*-spacing (16.8 Å) in our previous work.[45] The above results suggest the side chains on the thiophenes and vinylene moieties truly affect the interdigitation of polymer backbones. Furthermore, the nanofirbrillar morphology of **P4TV** was also observed in tapping mode AFM phase images (Figure S5 of Supporting Information)). The ordering nanofirbrillar structure of **P4TV** film with the interconnected networks of the polymer chains may provide the formation of highly efficient pathways for charge carrier transport.[58,59]

Polymer Field-Effect Transistor (FET) Characteristics. Solution-processed top contact FETs based on **P4TV** and **P8TV** were fabricated from *o*-dichlorobenzene. Figure 6 shows the FET transfer characteristics of the copolymer devices on the ODTS-modified SiO_2. In the saturation region ($V_d > V_g - V_t$), I_d can be described by the following equation:[60]

$$I_{ds} = \frac{WC_o\mu}{2L}(V_g - V_t)^2$$

Here W and L are channel width and length, respectively, C_o is the capacitance of gate insulator per unit area (SiO_2, 200 nm, C_0 = 17 nF/cm^2), μ is the hole mobility, and V_t is threshold voltage. The saturation-region mobility of the polymers was

dx.doi.org/10.1021/ma300313y | *Macromolecules* 2012, 45, 3047−3056

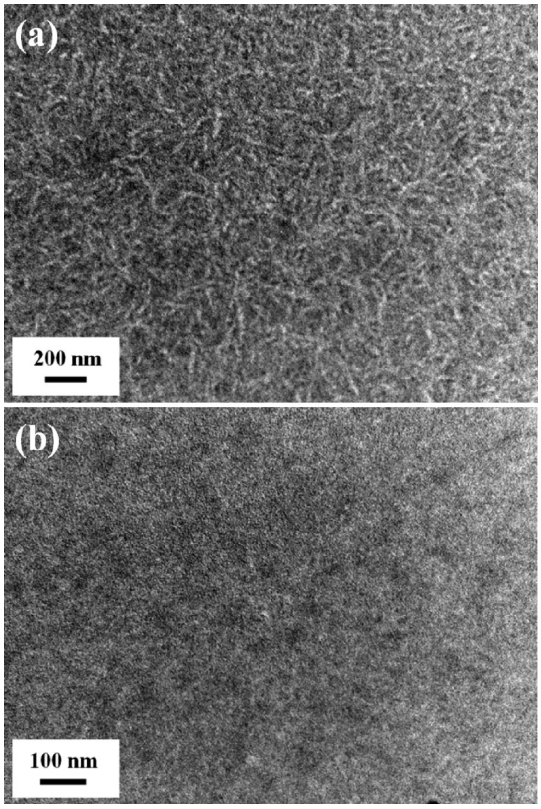


Figure 4. TEM images of (a) **P4TV** and (b) **P8TV** films prepared from *o*-dichlorobenzene solutions and annealed at 100 °C for 60 min.

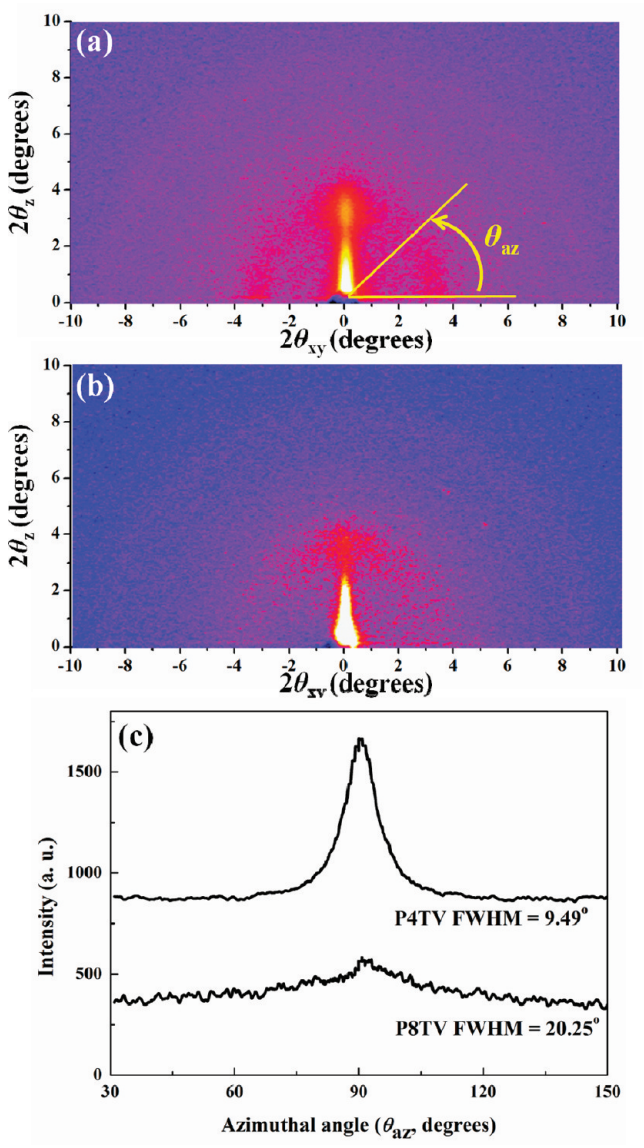


Figure 5. GIXD patterns of (a) **P4TV** film and (b) **P8TV** film prepared by spin coating on the ODTS-treated substrates from *o*-dichlorobenzene solutions and annealed at 100 °C for 60 min. (c) Azimuthal XRD profiles of the films at the first order diffraction in the θ_z direction.

calculated from the transfer characteristics of FET involving plotting $(I_d)^{1/2}$ versus V. As shown in Figure 6, the thermally annealed **P4TV** and **P8TV** reveal typical transfer and output curves. The FET mobilities of the annealed **P4TV** and **P8TV** thin films are $(1.24 \pm 0.20) \times 10^{-1}$ and $(1.79 \pm 0.25) \times 10^{-3}$ $cm^2\ V^{-1}\ s^{-1}$, with the current on-to-off ratio (I_{on}/I_{off}) in the range of 10^4–10^5. **P4TV** has a significantly higher carrier mobility than **P8TV**, due to the superior ordered morphology and more extended π–electron delocalization described previously. The high carrier mobility of **P4TV** is comparable to that of regioregular P3HT[22–24] and the other PTV derivatives (2.1×10^{-4} to 1.05 $cm^2\ V^{-1}\ s^{-1}$).[31–33]

The air stability of the devices were evaluated under ambient by measuring hole mobility (μ_h), on/off ratio (I_{on}/I_{off}), and threshold voltage (V_t) as a function of time, as shown in Figure 7 and Figure S6 (Supporting Information). As shown in the figure, both **P4TV** and **P8TV** exhibited relatively good air-stability. After exposure to air for 1 month, the hole mobility of **P4TV** decreased from 0.18 to 0.062 $cm^2\ V^{-1}\ s^{-1}$, which showed better air stability than P3HT attributed to the lower HOMO energy level. Note that P3HT exhibited a large degradation of charge mobility about 2 orders of magnitude when stored in air.[61] Compared to **P4TV**, the mobility of **P8TV** still kept around 0.0015 $cm^2\ V^{-1}\ s^{-1}$ even after exposure to air for 1 month. The outstanding air-stable performance of the **P8TV** may be correlated to its much low-lying HOMO energy level, avoiding the degradation and the doping of moisture and oxygen.

Polymer Photovoltaic Cell Characteristics. The bulk heterojunction photovoltaic (PV) cells were fabricated with a sandwich configuration of ITO/PEDOT:PSS/polymer:$PC_{71}BM$/Ca (30 nm)/Al (100 nm). The active layers of the studied polymers devices were prepared through thermal annealing at 100 °C for 10 min. The J–V curves of polymer/$PC_{71}BM$ were measured under ambient after encapsulation with UV-curing glue, as shown in Figure 8. The PV characteristics, including open-circuit voltage (V_{oc}), short-circuit current (J_{sc}), fill factor (FF), and power conversion efficiency (PCE), of **P4TV** and **P8TV** devices are summarized in Table 2. The highest PCEs (%) of corresponding polymer-based PV devices are 4.04 (**P4TV**/$PC_{71}BM$ 1:1 w/w) and 2.69 (**P8TV**/$PC_{71}BM$ 1:2 w/w), respectively. The PCE of **P8TV**/$PC_{71}BM$ (1:1) device is only 1.74% relating to a lower FF as well as inferior film quality. The V_{oc} values of the **P4TV** and **P8TV**-based PV cells are 0.642 and 0.814 V, respectively. Obviously, the lower HOMO energy level of **P8TV** leads to a higher V_{oc} because the V_{oc} is related to the energy differences between the HOMO energy levels of the donor (conjugated polymers) and the LUMO energy levels of the acceptor

dx.doi.org/10.1021/ma300313y | *Macromolecules* 2012, 45, 3047–3056

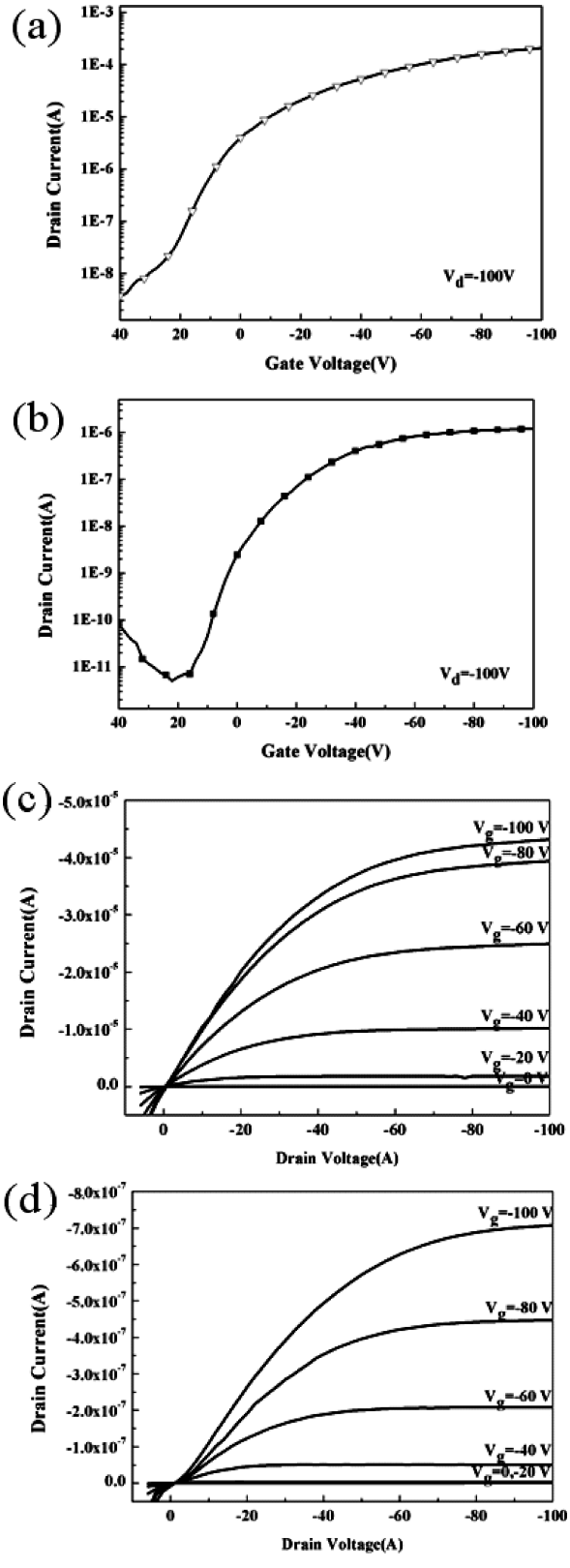


Figure 6. FET transfer characteristics of (a) **P4TV** and (b) **P8TV** thin films and the p-type output characteristics of (c) **P4TV** and (d) **P8TV**.

($PC_{71}BM$).[62] The J_{sc} values of these polymers are 11.689 mA/cm^2 (**P4TV**) and 6.709 mA/cm^2 (**P8TV**), respectively, which has the same trend as the hole FET mobility. Thus, the larger PCE of **P4TV** than **P8TV** is mainly due to the higher hole mobility (higher J_{sc}), and better absorption ability in visible

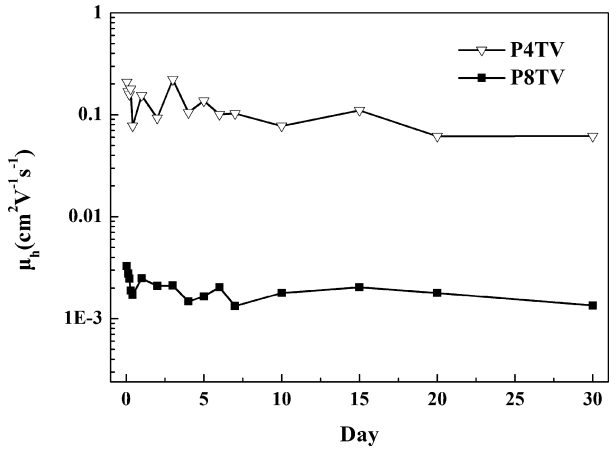


Figure 7. FET air-stability testing on the FET hole mobility of **P4TV** and **P8TV**-based devices. Relative humidity ranges from 41% to 60% in air.

light region. Furthermore, for **P4TV**, the J_{sc} is approximate 1.3 times larger than P3HT (9.097 mA/cm^2) and the smaller band gap increases the light absorption range, leading to better PCE characteristics than P3HT (3.86%) under the same processing condition.

The incident photon conversion efficiency (IPCE) curves of the PV cells based on **P4TV**, **P8TV**, and P3HT are demonstrated in Figure 8b. The IPCE curve of P3HT/$PC_{71}BM$ (1:1 w/w) device covers a wavelength range from 350 to 650 nm with the maximum IPCE value of 55% at ca. 570 nm. As compared to the P3HT device, **P8TV**/$PC_{71}BM$ (1:2) device shows a broader wavelength range from 350 to 700 nm, but the maximum IPCE value is only 41% at ca. 525 nm, thus causing the lower J_{sc} and PCE of **P8TV** device. For **P4TV**/$PC_{71}BM$ (1:1) device, the IPCE curve exhibits maximum IPCE value of 48% at ca. 625 nm, which is slightly lower than that of P3HT; however, it covers the broadest wavelength range from 350 to 750 nm and a platform from 450 to 700 nm. The longer absorption wavelength of **P4TV** device leads to the higher J_{sc} of the PV devices.

For bulk heterojunction PV cells, air stability is an issue as important as PCE. The diffusion of oxygen and moisture into the cells is generally regarded as the dominant source of degradation. It is necessary to extend the lifetime of devices by preventing the degradation from air and humidity. To explore the air stability for the lifetime of PV cells, the prepared devices with encapsulation were stored under an atmosphere with a relative humidity in a range of 60−80% and temperature at approximate 25 °C. As shown in Figure 8c, the PCE decays 22% in the case of P3HT/$PC_{71}BM$ (1:1) device after 40 days similar to our previous work.[26] However, **P4TV** and **P8TV** exhibited the degradation ratio of around 5−18% in the air for 40 days. The significantly enhanced environmental stability could be due to the lower HOMO levels than P3HT. For the blend of **P8TV**/$PC_{71}BM$, the $PC_{71}BM$ aggregations are smaller than 150 nm comparing to **P4TV**/$PC_{71}BM$ (larger than 250 nm) from TEM analysis (Figure S7 of the Supporting Information), which resulted in more stable device performance.[26] Note that the branched thiophene side chains could have better compatibility with $PC_{71}BM$.[39] Therefore, the PCE of the **P8TV**-based cells only decayed 5% after 40 days in air, due to the low-lying HOMO level and small $PC_{71}BM$ aggregation.

dx.doi.org/10.1021/ma300313y | *Macromolecules* 2012, 45, 3047−3056

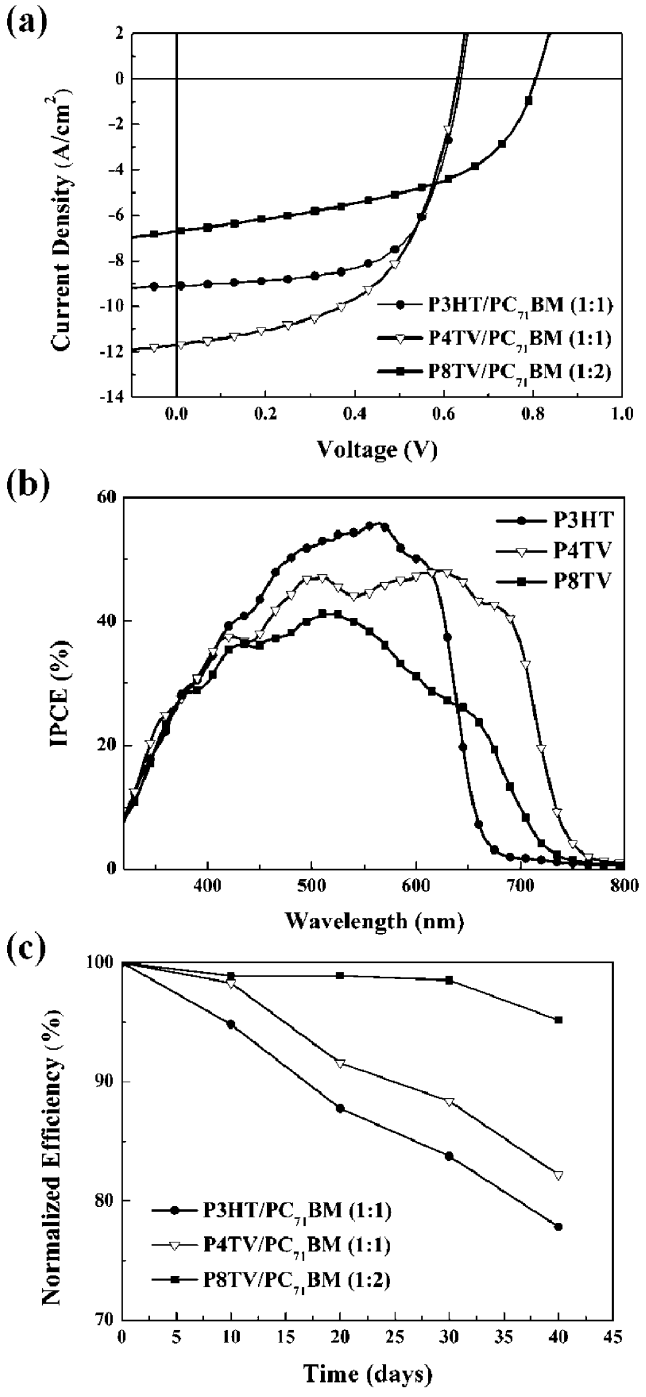


Figure 8. (a) *J*–*V* characteristics, (b) IPCE, and (c) air stability of polymer PV cells with the device structure of ITO/PEDOT:PSS/polymer:$PC_{71}BM$/Ca/Al.

Table 2. PV Characteristics with the Device Structure of ITO/PEDOT:PSS/Polymer:$PC_{71}BM$/Ca/Al Using P4TV, P8TV, and P3HT Processing from the DCB Solvent

polymer	polymer:$PC_{71}BM$	J_{sc} (mA/cm^2)	V_{oc} (V)	FF	PCE[a] (%)
P4TV	1:1	11.689	0.642	0.540	4.04
P8TV	1:1	5.867	0.819	0.362	1.74
P8TV	1:2	6.709	0.814	0.495	2.69
P3HT	1:1	9.097	0.634	0.633	3.68

[a]The average value of PCE is calculated from 4 pixels in the device.

CONCLUSIONS

We have successfully synthesized and characterized two new alternating copolymers containing vinylene moieties and biaxially extended quaterthiophene (**P4TV**) and octithiophene (**P8TV**) by the Pd-catalyzed Stille coupling reaction under microwave heating. The incorporation of vinylene moieties significantly reduced the conformation distortion in the main chain, leading to high coplanarity and the low band gaps of **P4TV** (1.69 eV) and **P8TV** (1.78 eV). Especially in the case of **P4TV**, high structural organization was observed in the GIXD and TEM analysis, mainly due to the reduction of conformation distortions and high coplanarity, resulting in high hole mobility of up to 0.12 cm^2 V^{-1} s^{-1}. **P8TV** with large side-chain torsional angles significantly exhibited the relatively lower mobility of 0.0018 cm^2 V^{-1} s^{-1}. The power conversion efficiencies (PCE) of the copolymers/$PC_{71}BM$ based photovoltaic cells were 4.04% (**P4TV**) and 2.69% (**P8TV**) under the illumination of AM 1.5G (100 mW/cm^2). They showed better PV cell performances than the PTV derivatives on account of their higher photocurrent and low-lying HOMO energy levels. Moreover, the outstanding environmental stability (decays 5% after 40 days in ambient) was observed from the **P8TV**-based PV devices owing to the low-lying HOMO energy level and small $PC_{71}BM$ aggregation. These above results reveal that new biaxially extended thiophene vinylene conjugated copolymers have the backbone coplanarity for increasing charge transport, photovoltaic properties, and air stability.

ASSOCIATED CONTENT

Supporting Information

Synthetic route and ^{1}H NMR spectrum of **8T-Br$_2$**, GPC traces of **P4TV** and **P8TV**, TGA curves and DSC curves of the studied copolymers at the heating rate of 10 °C/min under a nitrogen atmosphere, optical absorption spectra of **P4TV** and **P8TV** in dilute *o*-dichlorobenzene solutions, AFM phase images of **P4TV** and **P8TV** thin films, air-stability testing on the FET performance of **P4TV** and **P8TV**-based devices, including on/off ratio and threshold voltage with relative humidity ranges from 41% to 60% in air, and TEM images of blending films of **P4TV**/$PC_{71}BM$ (1:1, w/w) and **P8TV**/$PC_{71}BM$ (1:2, w/w). This material is available free of charge via the Internet at http://pubs.acs.org.

AUTHOR INFORMATION

Corresponding Author

*Telephone: 886-2-23628398. Fax: 886-2-23623040. E-mail: chenwc@ntu.edu.tw.

Author Contributions

†These authors contributed equally to this work

Notes

The authors declare no competing financial interest.

ACKNOWLEDGMENTS

The financial support from National Science Council of Taiwan is highly appreciated. We also acknowledge the helpful discuss with Prof. Ya-Sen Sun of National Central University of Taiwan.

REFERENCES

(1) Grimsdale, A. C.; Chan, K. L.; Martin, R. E.; Jokisz, P. G.; Holmes, A. B. *Chem. Rev.* **2009**, *109*, 897.
(2) Wu, W. C.; Liu, C. L.; Chen, W. C. *Polymer* **2006**, *47*, 527.

(3) Li, Y. N.; Wu, Y. L.; Liu, P.; Birau, M.; Pan, H. L.; Ong, B. S. *Adv. Mater.* **2006**, *18*, 3029.
(4) I, M.; Heeney, M.; Bailey, C.; Genevicius, K.; I, M.; Shkunov, M.; Sparrowe, D.; Tierney, S.; Wagner, R.; Zhang, W. M.; Chabinyc, M. L.; Kline, R. J.; Mcgehee, M. D.; Toney, M. F. *Nat. Mater.* **2006**, *5*, 328.
(5) Ong, B. S.; Wu, Y. L.; Liu, P.; Gardner, S. *Adv. Mater.* **2005**, *17*, 1141.
(6) Wu, Y. L.; Li, Y. N.; Ong, B. S.; Liu, P.; Gardner, S.; Chiang, B. *Adv. Mater.* **2005**, *17*, 184.
(7) Osaka, I.; McCullough, R. D. *Acc. Chem. Res.* **2008**, *41*, 1202.
(8) Lee, W. Y.; Cheng, K. F.; Wang, T. F.; Chueh, C. C.; Chen, W. C.; Tuan, C. S.; Lin, J. L. *Macromol. Chem. Phys.* **2007**, *208*, 1919.
(9) Li, G.; Shrotriya, V.; Huang, J. S.; Yao, Y.; Moriarty, T.; Emery, K.; Yang, Y. *Nat. Mater.* **2005**, *4*, 864.
(10) Liu, C. L.; Tsai, J. H.; Lee, W. Y.; Chen, W. C.; Jenekhe, S. A. *Macromolecules* **2008**, *41*, 6952.
(11) Thompson, B. C.; Frechet, J. M. J. *Angew. Chem. Inter. Ed.* **2008**, *47*, 58.
(12) Lai, M. H.; Chueh, C. C.; Chen, W. C.; Wu, J. L.; Chen, F. C. *J. Polym. Sci., Part A: Polym. Chem.* **2009**, *47*, 973.
(13) Park, S. H.; Roy, A.; Beaupre, S.; Cho, S.; Coates, N.; Moon, J. S.; Moses, D.; Leclerc, M.; Lee, K.; Heeger, A. J. *Nature Photo.* **2009**, *3*, 297.
(14) Tsai, J. H.; Chueh, C. C.; Lai, M.-H.; Wang, C. F.; Chen, W. C.; Ko, B. T.; Ting, C. *Macromolecules* **2009**, *42*, 1897.
(15) Liang, Y.; Xu, Z.; Xia, J.; Tsai, S.-T.; Wu, Y.; Li, G.; Ray, C.; Yu, L. *Adv.. Mater.* **2010**, *22*, E135.
(16) Tsai, J. H.; Chueh, C. C.; Chen, W. C.; Yu, C. Y.; Hwang, G. W.; Ting, C.; Chen, E. C.; Meng, H. F. *J. Polym. Sci., Part A: Polym. Chem.* **2010**, *48*, 2351.
(17) Brabec, C. J.; Heeney, M.; McCulloch, I.; Nelson, J. *Chem. Soc. Rev.* **2011**, *40*, 1185.
(18) Ling, Q. D.; Liaw, D. J.; Zhu, C.; Chan, D. S. H.; Kang, E. T.; Neoh, K.-G. *Prog. Polym. Sci.* **2008**, *33*, 917.
(19) Fang, Y. K.; Liu, C. L.; Li, C.; Lin, C. J.; Mezzenga, R.; Chen, W. C. *Adv. Funct. Mater.* **2010**, *20*, 3012.
(20) Kuorosawa, T.; Chueh, C. C.; Liu, C. L.; Higashihara, T.; Ueda, M.; Chen, W. C. *Macromolecules* **2010**, *43*, 1236.
(21) Ikegami, R.; Koresawa, A.; Shibata, T.; Takagi, K. *J. Org. Chem.* **2003**, *68*, 2195.
(22) Sirringhaus, H.; Brown, P. J.; Friend, R. H.; Nielsen, M. M.; Bechgaard, K.; Langeveld-Voss, B. M. W.; Spiering, A. J. H.; Janssen, R. A. J.; Meijer, E. W.; Herwig, P.; de Leeuw, D. M. *Nature* **1999**, *401*, 685.
(23) Wang, G. M.; Swensen, J.; Moses, D.; Heeger, A. J. *J. Appl. Phys.* **2003**, *93*, 6137.
(24) Bao, Z.; Dodabalapur, A.; Lovinger, A. J. *Appl. Phys. Lett.* **1996**, *69*, 4108.
(25) Li, G.; Yao, Y.; Yang, H.; Shrotriya, V.; Yang, G.; Yang, Y. *Adv. Funct. Mater.* **2007**, *17*, 1636.
(26) Tsai, J. H.; Lai, Y. C.; Higashihara, T.; Lin, C. J.; Ueda, M.; Chen, W. C. *Macromolecules* **2010**, *43*, 6085.
(27) Yang, X. N.; Loos, J.; Veenstra, S. C.; Verhees, W. J. H.; Wienk, M. M.; Kroon, J. M.; Michels, M. A. J.; Janssen, R. A. J. *Nano Lett.* **2005**, *5*, 579.
(28) Yu, C. Y.; Ko, B. T.; Ting, C.; Chen, C. P. *Sol. Energy Mater. Sol. Cells* **2009**, *93*, 613.
(29) Eckhardt, H.; Shacklette, L. W.; Jen, K. Y.; Elsenbaumer, R. L. *J. Chem. Phys.* **1989**, *91*, 1303.
(30) Henckens, A.; Knipper, M.; Polec, I.; Manca, J.; Lutsen, L.; Vanderzande, D. *Thin Solid Films* **2004**, *451*, 572.
(31) Lim, B.; Baeg, K. J.; Jeong, H. G.; Jo, J.; Kim, H.; Park, J. W.; Noh, Y. Y.; Vak, D.; Park, J. H.; Park, J. W.; Kim, D. Y. *Adv. Mater.* **2009**, *21*, 2808.
(32) He, Y. J.; Wu, W. P.; Zhao, G. J.; Liu, Y. Q.; Li, Y. F. *Macromolecules* **2008**, *41*, 9760.
(33) Jang, S. Y.; Lim, B.; Yu, B. K.; Kim, J.; Baeg, K. J.; Khim, D.; Kim, D. Y. *J. Mater. Chem.* **2011**, *21*, 11822.
(34) Wu, P. T.; Kim, F. S.; Jenekhe, S. A. *Chem. Mater.* **2011**, *23*, 4618.
(35) Chueh, C. C.; Lai, M. H.; Tsai, J. H.; Wang, C. F.; Chen, W. C. *J. Polym. Sci., Part A: Polym. Chem.* **2010**, *48*, 74.
(36) Kim, J.; Lim, B.; Baeg, K. J.; Noh, Y. Y.; Khim, D.; Jeong, H. G.; Yun, J. M.; Kim, D. Y. *Chem. Mater.* **2011**, *23*, 4663.
(37) Smith, A. P.; Smith, R. R.; Taylor, B. E.; Durstock, M. F. *Chem. Mater.* **2004**, *16*, 4687.
(38) Li, Y. F.; Zou, Y. P. *Adv. Mater.* **2008**, *20*, 2952.
(39) Zhou, E. J.; Tan, Z. A.; Huo, L. J.; He, Y. J.; Yang, C. H.; Li, Y. F. *J. Phys. Chem. B* **2006**, *110*, 26062.
(40) Hou, J. H.; Tan, Z. A.; Yan, Y.; He, Y. J.; Yang, C. H.; Li, Y. F. *J. Am. Chem. Soc.* **2006**, *128*, 4911.
(41) Hou, J. H.; Huo, L. J.; He, C.; Yang, C. H.; Li, Y. F. *Macromolecules* **2006**, *39*, 594.
(42) Hou, J. H.; Yang, C. H.; He, C.; Li, Y. F. *Chem. Commun.* **2006**, 871.
(43) Tsai, J. H.; Lee, W. Y.; Chen, W. C.; Yu, C. Y.; Hwang, G. W.; Ting, C. *Chem. Mater.* **2010**, *22*, 3290.
(44) Lin, C. J.; Lee, W. Y.; Lu, C.; Lin, H. W.; Chen, W. C. *Macromolecules* **2011**, *44*, 9565.
(45) Lin, H.-W.; Lee, W.-Y.; Lu, C.; Lin, C.-J.; Wu, H.-C.; Lin, Y.-W.; Ahn, B.; Rho, Y.; Ree, M.; Chen, W.-C. *Polym. Chem.* **2012**, *3*, 767.
(46) Chang, Y. T.; Hsu, S. L.; Chen, G. Y.; Su, M. H.; Singh, T. A.; Diau, E. W. G.; Wei, K. H. *Adv. Funct. Mater.* **2008**, *18*, 2356.
(47) Chang, Y. T.; Hsu, S. L.; Su, M. H.; Wei, K. H. *Adv. Mater.* **2009**, *21*, 2093.
(48) Zou, Y. P.; Wu, W. P.; Sang, G. Y.; Yang, Y.; Liu, Y. Q.; Li, Y. F. *Macromolecules* **2007**, *40*, 7231.
(49) Zen, A.; Bilge, A.; Galbrecht, F.; Alle, R.; Meerholz, K.; Grenzer, J.; Neher, D.; Scherf, U.; Farrell, T. *J. Am. Chem. Soc.* **2006**, *128*, 3914.
(50) Sun, X. B.; Liu, Y. Q.; Chen, S. Y.; Qiu, W. F.; Yu, G.; Ma, Y. Q.; Qi, T.; Zhang, H. J.; Xu, X. J.; Zhu, D. B. *Adv. Funct. Mater.* **2006**, *16*, 917.
(51) Shang, H. X.; Fan, H. J.; Liu, Y.; Hu, W. P.; Li, Y. F.; Zhan, X. W. *J. Mater. Chem.* **2011**, *21*, 9667.
(52) Kanibolotsky, A. L.; Perepichka, I. F.; Skabara, P. J. *Chem. Soc. Rev.* **2010**, *39*, 2695.
(53) Rance, W. L.; Rupert, B. L.; Mitchell, W. J.; Kose, M. E.; Ginley, D. S.; Shaheen, S. E.; Rumbles, G.; Kopidakis, N. *J. Phys. Chem. C* **2010**, *114*, 22269.
(54) Ma, C. Q.; Fonrodona, M.; Schikora, M. C.; Wienk, M. M.; Janssen, R. A. J.; Bauerle, P. *Adv. Funct. Mater.* **2008**, *18*, 3323.
(55) Frisch, M. J.; Trucks, G. W.; Schlegel, H. B.; Scuseria, G. E.; Robb, M. A.; Cheeseman, J. R.; Montgomery, J., J. A.; Vreven, T.; Kudin, K. N.; Burant, J. C.; Millam, J. M.; Iyengar, S. S.; Tomasi, J.; Barone, V.; Mennucci, B.; Cossi, M.; Scalmani, G.; Rega, N.; Petersson, G. A.; Nakatsuji, H.; Hada, M.; Ehara, M.; Toyota, K.; Fukuda, R.; Hasegawa, J.; Ishida, M.; Nakajima, T.; Honda, Y.; Kitao, O.; Nakai, H.; Klene, M.; Li, X.; Knox, J. E.; Hratchian, H. P.; Cross, J. B.; Bakken, V.; Adamo, C.; Jaramillo, J.; Gomperts, R.; Stratmann, R. E.; Yazyev, O.; Austin, A. J.; Cammi, R.; Pomelli, C.; Ochterski, J. W.; Ayala, P. Y.; Morokuma, K.; Voth, G. A.; Salvador, P.; Dannenberg, J. J.; Zakrzewski, V. G.; Dapprich, S.; Daniels, A. D.; Strain, M. C.; Farkas, O.; Malick, D. K.; Rabuck, A. D.; Raghavachari, K.; Foresman, J. B.; Ortiz, J. V.; Cui, Q.; Baboul, A. G.; Clifford, S.; Cioslowski, J.; Stefanov, B. B.; Liu, G.; Liashenko, A.; Piskorz, P.; Komaromi, I.; Martin, R. L.; Fox, D. J.; Keith, T.; Al-Laham, M. A.; Peng, C. Y.; Nanayakkara, A.; Challacombe, M.; Gill, P. M. W.; Johnson, B.; Chen, W.; Wong, M. W.; Gonzalez, C.; Pople, J. A. *Gaussian 03, revision B.04*; Gaussian, Inc.: Wallingford, CT, 2004.
(56) Operamolla, A.; Farinola, G. M. *Eur. J. Org. Chem.* **2011**, *2011*, 423.
(57) Yu, C. Y.; Chen, C. P.; Chan, S. H.; Hwang, G. W.; Ting, C. *Chem. Mater.* **2009**, *21*, 3262.
(58) Yang, H. C.; Shin, T. J.; Yang, L.; Cho, K.; Ryu, C. Y.; Bao, Z. N. *Adv. Funct. Mater.* **2005**, *15*, 671.
(59) Qiu, L.; Lee, W. H.; Wang, X.; Kim, J. S.; Lim, J. A.; Kwak, D.; Lee, S.; Cho, K. *Adv. Mater.* **2009**, *21*, 1349.

(60) Zaumseil, J.; Friend, R. H.; Sirringhaus, H. *Nat. Mater.* **2005**, *5*, 69.
(61) Schafferhans, J.; Baumann, A.; Deibel, C.; Dyakonov, V. *Appl. Phys. Lett.* **2008**, *93*, 093303.
(62) Gadisa, A.; Svensson, M.; Andersson, M. R.; Inganas, O. *Appl. Phys. Lett.* **2004**, *84*, 1609.

Macromolecules

Article

pubs.acs.org/Macromolecules

A Quantitative Correlation between the Mobility and Crystallinity of Photo-Cross-Linkable P3HT

Claire H. Woo,[†,‡,&] Claudia Piliego,[‡,&] Thomas W. Holcombe,[§] Michael F. Toney,[∥] and Jean M. J. Fréchet*[,†,‡,§,⊥]

[†]Department of Chemical and Biomolecular Engineering, University of California, Berkeley, Berkeley, California 94720, United States

[‡]Materials Sciences Division, Lawrence Berkeley National Laboratory, Berkeley, California 94720, United States

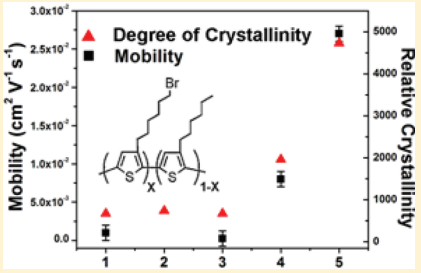
[§]Department of Chemistry, University of California, Berkeley, Berkeley, California 94720, United States

[∥]Stanford Synchrotron Radiation Lightsource, Menlo Park, California 94205, United States

[⊥]King Abdullah University of Science and Technology, Thuwal, Saudi Arabia 23955-6900

Supporting Information

ABSTRACT: The performance of polymer field effect transistors (FETs) can vary by orders of magnitude by applying different processing conditions. Although it is generally believed that a higher degree of crystallinity results in a higher mobility, the correlation is not straightforward. In addition, the effect of cross-linking on polymer thin film microstructural order is relatively unknown. This study investigates the effect of thermal annealing and UV-initiated photo-cross-linking on the FET performance and microstructural order of a photo-cross-linkable P3HT derivative. Our results demonstrate that while cross-linking did not disrupt the overall crystallinity of the polymer thin film, the photo-cross-linking process likely induced doping in the semiconductor layer, leading to the absence of saturation behavior in the FET. Annealing after cross-linking slightly improved the FET performance but only minimally affected the microstructural order of the polymer film since the 3D morphology had been "locked in" during the first cross-linking step. Importantly, annealing and cross-linking simultaneously was a successful method to preserve polymer crystallinity while also achieving effective cross-linking. Using newly developed quantitative X-ray analysis techniques, our study established a quantitative correlation between FET charge mobility and thin film crystallinity.



INTRODUCTION

The performance and reliability of solution-processed organic electronics are rapidly advancing, allowing organic field-effect transistors (OFETs) to become a reality in emerging commercial applications such as printable electronics and flexible optical displays.[1] In the past decade, research efforts have focused on developing new semiconducting polymers for better charge carrier mobility. Despite the progress in synthesizing new p-type[2] and n-type[3] polymers, our understanding on the design criteria that should be followed to obtain high performance remain incomplete. One of the characteristics that has been identified as critical is the ability of the material to self-organize into regular structures.[4] While it is possible to design organic materials that inherently possess a high tendency to self-organize, for example by using a rigid backbone or by choosing appropriate side chains, it is still difficult to control the dependence of self-organized structure and charge transport properties on processing conditions. For instance, the charge carrier mobility of polymer-based field-effect transistors can vary by orders of magnitude by applying different processing conditions such as casting solvent, substrate engineering, or post deposition treatments.[5] However, the mechanism of how each processing step modifies the semiconductor microstructure as well as the properties of the semiconductor/dielectric interface is relatively unknown.

Field effect transistors are not only of great technological interest, but they also can be used as a material characterization tool since the charge carrier transport in thin film transistors is strongly dependent on the microstructure of the semiconducting layer.[6] Transistor measurements therefore allow an indirect and qualitative estimation of the film microstructure at the buried semiconductor/dielectric interface, where charge transport takes place. Up to now, an accurate and quantitative assessment of the degree of crystallinity at this interface has been limited by the lack of appropriate and high-resolution characterization methods. Recent advances in molecular and X-ray characterization techniques,[7] however, have made it possible to quantitatively compare the crystallinity of polymer thin films, thus allowing us to draw a direct correlation between the microstructural order and charge transport properties of a semiconducting polymer film.

In order to explore the potential of these emerging techniques, we investigated a polymer with "tunable" micro-

Received: September 30, 2011
Revised: January 21, 2012
Published: March 20, 2012

 © 2012 American Chemical Society

structural order: a recently developed photo-cross-linkable derivative of poly(3-hexylthiophene) (P3HT).[8] Cross-linking is a valuable technique that has been utilized for the fabrication of multilayered solution processed organic light-emitting diodes,[9] for increasing the thermal stability of organic solar cells,[8,10] for photo patterning,[11] and for the realization of polymeric dielectrics in OFETs.[12]

Here, we use photo-cross-linkable P3HT as a model system to illustrate the effect of cross-linking and thermal annealing on FET performance and to correlate charge mobility with thin film crystallinity. By inserting a bromine as the cross-linkable moiety tethered to the end of the alkyl chains, the functionalized polymer can be easily cross-linked by UV irradiation.[8,10] We chose the P3HT-Br10 derivative, which contains 10% of the bromine functionalized monomer unit in its backbone, to ensure sufficient bromine content for complete cross-linking while minimizing the disruption of the semi-crystalline nature of the P3HT polymer.[8] We tested the OFET performance of the P3HT-Br10 polymer in five different conditions (1: as cast; 2: annealed (AN); 3: cross-linked (XL); 4: cross-linked and then annealed; 5: cross-linked and annealed at the same time). We used quantitative X-ray analysis techniques to compare the degree of crystallinity of all the P3HT-Br10 films. The results of our study show that the different processing conditions affect the device performance and that the mobility trend can be correlated with the evolution of the microstructure. This allowed us to draw an unambiguous correspondence between the degree of crystallinity (DoC) and the FET mobility of a polymer. This is one of the first studies exploring the effects of cross-linking on the microstructural order of a conjugated polymer.

RESULTS AND DISCUSSION

The P3HT-Br10 polymer (Figure 1) was synthesized following the same procedure previously reported.[8] The polymer used in this study had a M_n of 19 000 g/mol, a PDI of 1.2, and regioregularity of ~95%. OFETs were fabricated in a bottom-gate, bottom-contact configuration with highly doped p-type (100) silicon wafers as the gate electrode and 300 nm of SiO_2 as the gate dielectric. Patterned Au electrodes were deposited onto the substrate by lithography. The polymer layer was spun cast from chloroform on octadecyltrichlorosilane (OTS)-treated Si/SiO_2 substrates. Devices were fabricated with typical channel lengths of 10 or 20 μm and channel widths ranging from 200 to 800 μm. Transfer and output curves of the device were measured under vacuum. For each condition, the reported data are averaged over 10−20 devices fabricated in parallel to ensure consistency. The experiments were repeated 4−5 times to ensure reproducibility. Key device performance parameters, including field-effect mobility (μ), threshold voltage (V_{TH}), and on/off current ratio (I_{ON}/I_{OFF}) were extracted following standard procedures (see Supporting Information).[13] The results are summarized in Table 1.

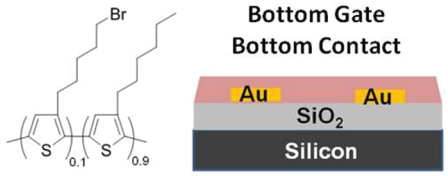


Figure 1. Structure of P3HT-Br10 and the BG-BC FET configuration used.

Table 1. Summary of OFET Performance of P3HT-Br10 Films Processed under Different Conditions

processing condition	μ ($cm^2\ V^{-1}\ s^{-1}$)	I_{ON}/I_{OFF}	V_{TH} (V)
as cast	1.2×10^{-3}	10^2	47
annealed (1 h)	2.7×10^{-2}	10^3	−10
cross-linked (1 h)	–	–	–
cross-linked (1 h) and then annealed (1 h)	2.5×10^{-4}	7×10^3	−5
cross-linked and annealed simultaneously (1 h)	8.5×10^{-3}	10^3	−10

Figure 2 shows two examples of the output and transfer characteristics of devices under two of the five different processing conditions we examined. The remaining $I-V$ plots are shown in the Supporting Information.

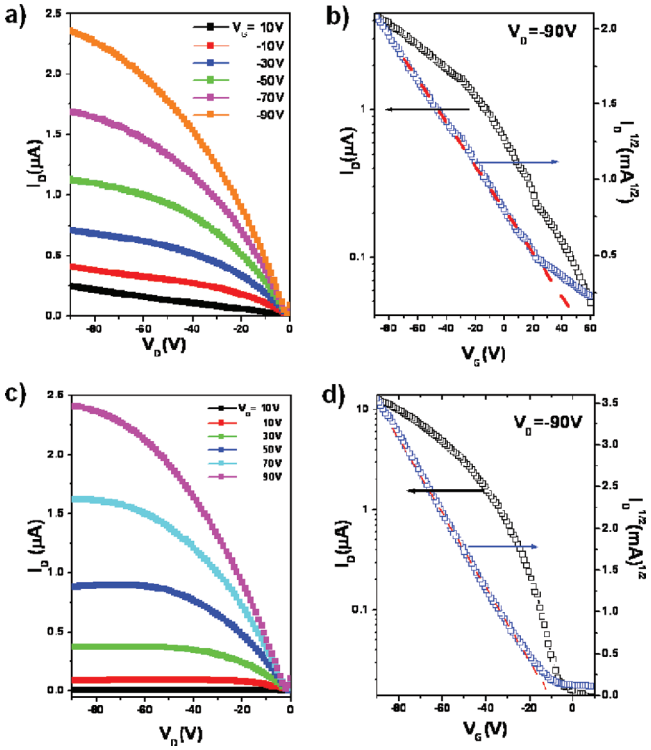


Figure 2. (a) Output and (b) transfer curves of an as cast P3HT-Br10 FET device (L = 20 μm, W = 800 μm). (c) Output and (d) transfer curves of a P3HT-Br10 FET device that has been cross-linked and annealed simultaneously for 1 h (L = 10 μm, W = 400 μm).

Looking at the summary in Table 1, it is clear that the OFET performance is highly dependent on processing conditions. By using five different fabrication procedures with two combinations of cross-linking and annealing sequences, we were able to control the mobility of P3HT-Br10 FET devices over 2 orders of magnitude. For as cast P3HT-Br10 films (see Figure 2a,b for $I-V$ plots), the p-channel FET mobility was measured to be 1.2 $\times 10^{-3}$ $cm^2\ V^{-1}\ s^{-1}$, which is comparable to as cast devices of P3HT from chloroform.[14] The transfer characteristics also indicate that the threshold voltage (V_{TH}) is in the positive V_G region. This implies that the active layer has a sufficient hole concentration to conduct current even if we do not

dx.doi.org/10.1021/ma202203z | Macromolecules 2012, 45, 3057−3062

intentionally accumulate holes in the conduction channel by applying a negative voltage to the gate. We suspect that the origin of the positive threshold voltage is due to the presence of the Br moiety which may be responsible for a doping effect.

A common approach to improving the performance of P3HT-based FETs is by thermal annealing.[15] After annealing at 150 °C for 1 h, the mobility of the P3HT-Br10 device increased by over an order of magnitude to 2.7×10^{-2} cm^2 V^{-1} s^{-1}. The threshold voltage became negative, and the on/off current ratio reached a reasonable value. Annealing of the P3HT-Br10 allows the polymer chains to become mobile and improves the typical lamellar ordering and the π-stacking of the polymer.[5d]

We were interested in probing the effect of cross-linking on the polymer FET performance. The P3HT-Br10 film was photo-cross-linked by illuminating the sample with UV light (λ = 254 nm) from a low-power hand-held lamp (1.9 mW cm^{-2}). After 1 h of photo-cross-linking of the film, the output characteristics of the device did not show any saturation; therefore, an accurate calculation of the mobility from the transfer curve was not possible. A poor saturation behavior suggests that the dominant carrier conduction path is not at the interface between the active layer and the dielectric, as generally assumed for thin film transistors.[16] A possible explanation for this phenomenon is the generation of bromine radicals during cross-linking, which could increase the conductivity of the bulk P3HT layer, leading to the formation of an additional current in the bulk which is not modulated by the field effect. This behavior is usually attributed to the presence of impurities and doping of the semiconductor layer.[17]

Interestingly though, we were able to recover some transistor behavior by subsequently annealing the cross-linked sample. The P3HT-Br10 device that was first photo-cross-linked for 1 h and then annealed at 150 °C for 1 h showed a mobility of 2.5×10^{-4} cm^2 V^{-1} s^{-1}, a threshold voltage of −5 V, and an on/off current ratio of 7×10^3. However, this performance is lower than that of the annealed device, probably because the cross-linking "freezes" the polymer chains and thus making the organization of polymer chains during annealing less effective.

In order to verify this hypothesis, we tested a P3HT-Br10 device that was cross-linked and annealed at the same time with the objective of allowing the polymer chains to reorganize while cross-linking. In this case, the sample was placed on a hot plate at 150 °C while under UV illumination to perform the simultaneous cross-linking and annealing treatment.

Figure 2c and d shows the $I-V$ characteristics of this device, which achieved an FET mobility of 8.5×10^{-3} cm^2 V^{-1} s^{-1}. It is clear that cross-linking and annealing at the same time preserved the favorable electronic properties of the polymer, leading to improved device performance.

The atomic force microscopy (AFM) analysis of the surface morphology of the films treated under the different processing procedures did not show any dramatic difference (Figure S5). All the samples displayed similar features with an average rms roughness of 1 nm, except for the annealed sample that showed slightly more pronounced features with an rms roughness of 3 nm.

To investigate the correlation between charge mobility and microstructural order in the polymer thin films, we performed in-depth X-ray diffraction analysis to quantitatively compare the degree of crystallinity of the P3HT-Br10 samples processed under different conditions. We followed the method developed by Baker et al.[7b,d,e] for quantifying crystallographic information for textured polymer thin films. Because of the anisotropic distribution of crystallite orientations in these semicrystalline polymer thin films, we need to use pole figures to fully capture all the crystallite orientations in order to perform valid quantitative comparisons.[18] A pole figure is a plot that shows the orientation distribution of a particular Bragg reflection and provides information on the texture of the thin film.

The X-ray diffraction samples were prepared under identical conditions as the FET devices. Thin films of P3HT-Br10 (~100 nm) were spin-coated from chloroform onto OTS-treated Si/SiO_2 substrates and subject to the same five processing conditions mentioned above: 1, as cast; 2, cross-linked (XL); 3, cross-linked and then annealed (XL and then AN); 4, cross-linked and annealed at the same time (XL and AN together); 5, annealed (AN). To obtain the complete pole figure, we collected two sets of data: one in grazing incidence geometry (where the sample is horizontal) and the other in local-specular geometry (where the sample is tilted to satisfy the specular geometry for a particular Bragg reflection).[7b] For quantitative comparisons among all the samples, the X-ray data have been corrected for the distortion by the area detector, polarization, X-ray absorption, incident beam intensity, scan duration, and sample thickness.

For the grazing incidence measurement, the angle of incidence (~0.12°) was carefully chosen to allow for complete penetration of the X-rays into the polymer film but not into the Si substrate. Figure 3 shows the 2D grazing incidence X-ray

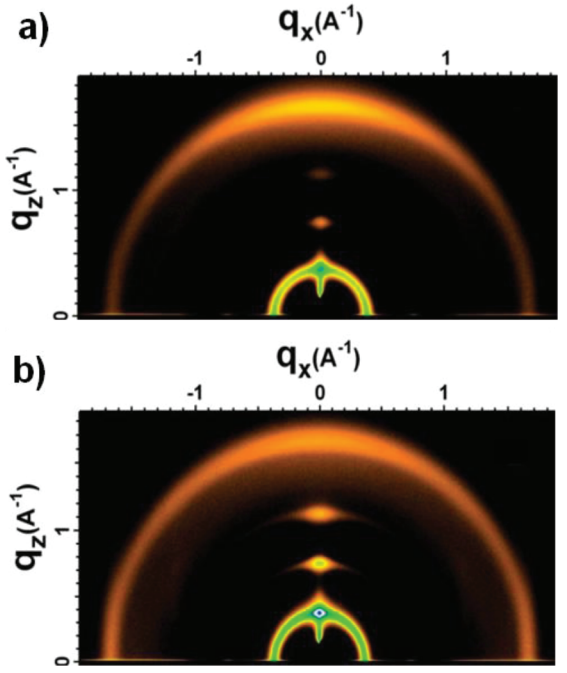


Figure 3. 2D grazing incidence X-ray scattering patterns of (a) as cast and (b) simultaneously cross-linked and annealed P3HT-Br10 films.

scattering (GIXS) patterns of the as cast P3HT-Br10 film and the sample that was cross-linked and annealed simultaneously. The 2D image map can be divided into a component in the plane of the substrate (q_x) and a component perpendicular to the substrate (q_z). Similar to P3HT,[7c,19] P3HT-Br10 samples displayed three strong (h00) peaks, and they exhibited anisotropic orientation with the strongest peak intensity in the out-of-plane (q_z) direction. The (010) peak at q = 1.65 Å^{-1} (d = 3.8 Å) is present in both samples and corresponds to the

dx.doi.org/10.1021/ma202203z | Macromolecules 2012, 45, 3057−3062

π-stacking distance between polymer chains. Qualitatively speaking, the two samples essentially showed similar GIXS patterns. In fact, this was true for all five samples, which showed almost identical GIXS patterns despite being subjected to different processing conditions (see Supporting Information). All the samples contained ordered polymer chains with mixed orientation—some domains of the semicrystalline polymer are oriented with (100) parallel to the substrate and some are oriented perpendicular to the substrate. The mixed texture in the polymer thin film leads to the arcing of the scattering peaks in the GIXS patterns. Importantly, the similarity of all the GIXS patterns indicates that neither cross-linking nor annealing changed the overall crystallite orientation and lattice spacings of the P3HT-Br10 thin film.

However, qualitatively comparing the grazing incidence patterns does not allow us to draw conclusions regarding the relative degree of crystallinity (DoC) of the P3HT-Br10 samples processed under the five different conditions. To do this, it is necessary to collect additional diffraction data in the local-specular geometry. The specular diffraction measurement was performed at both the (100) and (200) Bragg reflections for each sample. The original rectangular detector coordinates (q_x, q_z) were converted to polar coordinates (q_r, χ) so that we could easily extract the signal within an annular region for a selected Bragg diffraction ring. For the (100) reflection, the region selected was from q = 0.2 Å^{-1} to 0.5 Å^{-1}. For the (200) reflection, the signal was integrated from q = 0.7 Å^{-1} to 0.85 Å^{-1}. Therefore, for each Bragg peak, there were two corresponding $I(\chi)$ plots: one from the grazing incidence measurement and one from the local-specular measurement. The two $I(\chi)$ plots were scaled and merged at $\chi \sim 10°$, giving the final pole figure as shown in Figure 4. The intensity near the pole ($\chi < 10°$, i.e., in the out-of-plane direction) came from data collected at the local-specular geometry, whereas the intensity at $\chi > 10°$ came from data in the grazing incidence measurement.

Figure 4 shows the pole figures for the (100) and (200) Bragg reflections of the as cast sample and the sample that was cross-linked and annealed simultaneously. The intensity of the X-ray diffraction signal is plotted in a semilog scale versus χ, which was the polar angle of tilting of the crystallite. First, we observed that for both samples and for both Bragg reflections examined, the signal was strongest near the pole (where χ was small), which indicated that most of the crystalline polymer chains were oriented out-of-plane, perpendicular to the substrate. In the region where $\chi > 15°$, the signal intensity was much smaller and the χ dependence was much weaker. Comparing Figures 4a and 4b, it is clear that the χ dependence of the two samples is similar. The χ dependence was also consistent across the (100) and the (200) Bragg reflections. Second, comparing Figures 4a and 4b, it is clear that the signal-to-noise ratio was higher for the (100) Bragg reflection. However, we note that the pole figure of the (200) Bragg reflection is generally more accurate because of its distance from the direct beam. The intensity of the (100) Bragg peak can be distorted by the beam stop and substrate reflectivity (see Figure 3). For this reason, we chose to use the pole figures from the (200) Bragg reflections of the five samples for quantitative comparison. Nonetheless, the data from the (100) Bragg peak showed a similar trend in all the samples, and the comparison using the (100) reflection is included in the Supporting Information.

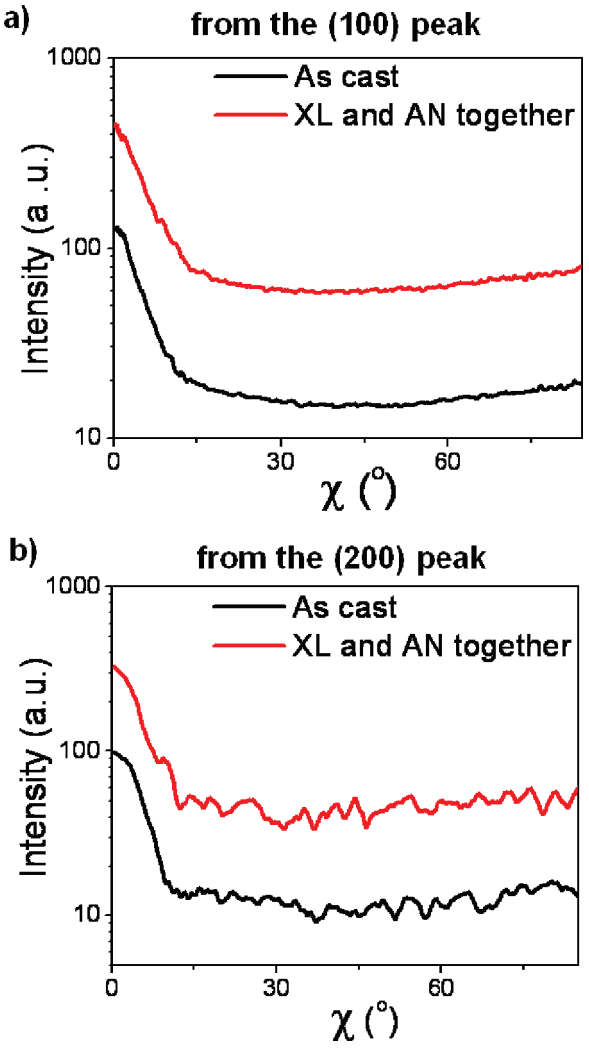


Figure 4. Comparing pole figures of the as cast P3HT-Br10 sample and the sample that was cross-linked and annealed at the same time (XL = cross-linked, AN = annealed). (a) Pole figures from the (100) peak. (b) Pole figures from the (200) peak.

As is apparent in Figure 4, the film that was simultaneously cross-linked and annealed had much higher diffraction intensity across the entire range of χ, which means that this sample had a higher degree of crystallinity than the as cast sample. To obtain the relative DoC for each sample, we integrated the area under the pole figure (corrected for the geometric factor of $\sin(\chi)$)[7b] from $\chi = 0°$ to $\chi = 90°$. Figure 5 shows the DoC results from the five samples. Included in Figure 5 are the corresponding FET mobility values of each sample. This master graph shows the observed correlation between the FET mobility and the relative degree of crystallinity of the films, where a film with a higher degree of crystallinity shows better FET performance. This trend confirms that processing conditions have a huge effect on the microstructural order of the thin film, which in turn determines the charge carrier mobility of the sample. Our results are in agreement with the recent publication by Boudouris et al.[7e] in which the authors correlate the real time crystallization process of poly(3-2′-ethyl)hexylthiophene with the evolution of its optoelectronic properties. In particular, they observe a clear transition in the mobility of the polymer after the film has developed a reasonable DoC due to the formation of a percolating crystalline network. This interpretation is

dx.doi.org/10.1021/ma202203z | Macromolecules 2012, 45, 3057–3062

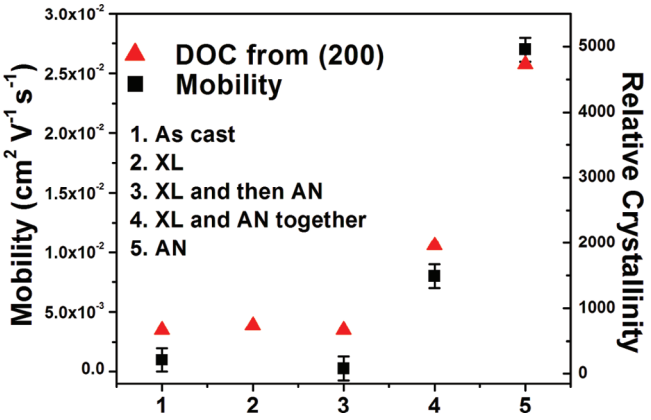


Figure 5. FET mobility (left axis) of P3HT-Br10 thin films processed under five different conditions and their relative degree of crystallinity (DOC) (right axis) obtained from the integration of the corresponding pole figures from the (200) Bragg peak.

consistent with our results: all the samples exhibit a certain degree of crystallinity, but the mobility increases only when the processing induces a more extended crystallization and an even higher DoC.

Our results show that cross-linking did not disrupt the overall degree of crystallinity of the polymer film, as the cross-linked sample had a similar DoC compared to the as cast sample. The lack of FET activity (insufficient current modulation) might have been due to the generation of Br radicals during cross-linking, which could have induced a doping effect. As mentioned above, some FET activity could be recovered by subsequent thermal annealing of the cross-linked sample. However, there was little change in crystallinity upon annealing in a cross-linked sample. This was most likely because the 3D structure of the P3HT-Br10 was "locked in" during cross-linking, and annealing the sample above the glass transition temperature of the polymer did not induce the formation of crystalline domains. We also attempted to first anneal the sample and subsequently perform photo-cross-linking. However, this procedure did not lead to effective cross-linking of polymer chains. Therefore, for effective cross-linking, UV irradiation had to be performed before the polymer chains were organized into regular crystal structures. This result has implications on the cross-linking mechanism of this material, which is currently under investigation.

To circumvent the problem of "locking in" the 3D morphology too early and to achieve effective cross-linking, we simultaneously cross-linked and annealed the P3HT-Br10 film. This processing condition led to effective cross-linking of the polymer film (see Supporting Information for the test of the cross-linking) and afforded FET performance better than that of the as cast devices but not as good as the annealed devices. More importantly, this trend was correlated well with our crystallinity measurements. The sample that was cross-linked and annealed at the same time possessed a degree of crystallinity that was in between that of the as cast sample and the annealed sample. Therefore, this new procedure was able to preserve a high degree of crystallinity in the thin film and was an effective way to achieve good FET mobility.

CONCLUSIONS

In this study, we investigated the effect of thermal annealing and UV-initiated photo-cross-linking on the FET performance and microstructural order of the photo-cross-linkable P3HT-Br10 polymer. Cross-linking did not disrupt the overall crystallinity of the polymer thin film, but the photo-cross-linking process likely induced a doping of the semiconductor layer, leading to the absence of saturation behavior. Annealing after cross-linking partially recovered FET activity but only minimally affected the microstructural order of the polymer film since the 3D morphology had been "locked in" during the first cross-linking step. In addition, we discovered that annealing and cross-linking simultaneously was a successful method to preserve polymer crystallinity while also achieving effective cross-linking. Using a newly developed quantitative X-ray analysis technique, our study established a quantitative correlation between FET mobility and thin film crystallinity.

ASSOCIATED CONTENT

Supporting Information

Synthetic details, FET device fabrication, additional device data, X-ray diffraction data and analysis, atomic force microscopy. This material is available free of charge via the Internet at http://pubs.acs.org.

AUTHOR INFORMATION

Corresponding Author

*E-mail: jean.frechet@kaust.edu.sa, frechet@berkeley.edu.

Author Contributions

[&]These authors contributed equally to this work.

Notes

The authors declare no competing financial interest.

ACKNOWLEDGMENTS

The authors acknowledge financial support by the U.S. Department of Energy, Basic Energy Sciences, under Contract DE-AC03-76SF00098. Partial support from the Frechet "other donors" fund is also acknowledged. C.H.W. and T.W.H. thank the National Science Foundation for Graduate Research Fellowships. Portions of this research were carried out at the Stanford Synchrotron Radiation Laboratory, a national user facility operated by Stanford University on behalf of the U.S. Department of Energy, Office of Basic Energy Sciences. The authors also thank Leslie Jimison and Jonathan Rivnay for helpful discussions.

REFERENCES

(1) (a) Arias, A. C.; MacKenzie, J. D.; McCulloch, I.; Rivnay, J.; Salleo, A. *Chem. Rev.* **2010**, *110*, 3−24. (b) Gelinck, G.; Heremans, P.; Nomoto, K.; Anthopoulos, T. D. *Adv. Mater.* **2010**, *22*, 3778−3798. (c) Sun, J.; Zhang, B.; Katz, H. E. *Adv. Funct. Mater.* **2011**, *21*, 29−45.

(2) (a) Hamadani, B. H.; Gundlach, D. J.; McCulloch, I.; Heeney, M. *Appl. Phys. Lett.* **2007**, *91*, 243512. (b) McCulloch, I.; Heeney, M.; Bailey, C.; Genevicius, K.; MacDonald, I.; Shkunov, M.; Sparrowe, D.; Tierney, S.; Wagner, R.; Zhang, W.; Chabinyc, M. L.; Kline, R. J.; McGehee, M. D.; Toney, M. F. *Nat. Mater.* **2006**, *5*, 328−333. (c) Chabinyc, M. L.; Toney, M. F.; Kline, R. J.; McCulloch, I.; Heeney, M. *J. Am. Chem. Soc.* **2007**, *129*, 3226−3237. (d) Li, Y. N.; Singh, S. P.; Sonar, P. *Adv. Mater.* **2010**, *22*, 4862−4866. (e) Chang, J. F.; Sun, B.; Breiby, D. W.; Nielsen, M. M.; Solling, T. I.; Giles, M.; McCulloch, I.; Sirringhaus, H. *Chem. Mater.* **2004**, *16*, 4772−4776.

(3) (a) Yan, H.; Chen, Z.; Zheng, Y.; Newman, C.; Quinn, J. R.; Dötz, F.; Kastler, M.; Facchetti, A. *Nat. Mater.* **2009**, *457*, 679−686. (b) Rivnay, J.; Toney, M. F.; Zheng, Y.; Kauvar, I. V.; Chen, Z. H.; Wagner, V.; Facchetti, A.; Salleo, A. *Adv. Mater.* **2010**, *22*, 4359−4363. (c) Rivnay, J.; Jimison, L. H.; Northrup, J. E.; Toney, M. F.; Noriega,

R.; Lu, S. F.; Marks, T. J.; Facchetti, A.; Salleo, A. *Nat. Mater.* **2009**, *8*, 952−958.
(4) (a) Salleo, A.; Kline, R. J.; DeLongchamp, D. M.; Chabinyc, M. L. *Adv. Mater.* **2010**, *22*, 3812−3838. (b) Virkar, A. A.; Mannsfeld, S.; Bao, Z.; Stingelin, N. *Adv. Mater.* **2010**, *34*, 3857−3875. (c) Zhang, W. M.; Smith, J.; Watkins, S. E.; Gysel, R.; McGehee, M.; Salleo, A.; Kirkpatrick, J.; Ashraf, S.; Anthopoulos, T.; Heeney, M.; McCulloch, I. *J. Am. Chem. Soc.* **2010**, *132*, 11437−11439. (d) Kline, R. J.; McGehee, M.; Toney, F. M. *Nat. Mater.* **2006**, *5*, 222−228. (e) Tsao, H. N.; Cho, D.; Andreasen, J. W.; Rouhanipour, A.; Breiby, D. W.; Pisula, W.; Müllen, K. *Adv. Mater.* **2009**, *21*, 209−212.
(5) (a) DeLongchamp, D. M.; Vogel, B. M.; Jung, Y.; Gurau, M. C.; Richter, C. A.; Kirillov, O. A.; Obrzut, J.; Fischer, D. A.; Sambasivan, S.; Richter, L. J.; Lin, E. K. *Chem. Mater.* **2005**, *17*, 5610−5612. (b) Salleo, A.; Chabinyc, M. L.; Yang, M. S.; Street, R. A. *Appl. Phys. Lett.* **2002**, *81*, 4383−4385. (c) Kim, D. H.; Park, Y. D.; Jang, Y.; Yang, H.; Kim, Y. H.; Han, J. I.; Moon, D. G.; Park, S.; Chang, T.; Chang, C.; Joo, M.; Ryu, C. Y.; Cho, K. *Adv. Funct. Mater.* **2005**, *15*, 77−82. (d) Salleo, A.; Chen, T. W.; Völkel, A. R.; Wu, Y.; Liu, P.; Ong, B. S.; Street, R. A. *Phys. Rev. B* **2004**, *70*, 115311.
(6) (a) Jimison, L. H.; Salleo, A.; Chabinyc, M. L.; Bernstein, D. P.; Toney, M. F. *Phys. Rev. B* **2008**, *78*, 125319. (b) Labram, J. G.; Domingo, E. B.; Stingelin, N.; Bradley, D. D. C.; Anthopoulos, T. D. *Adv. Funct. Mater.* **2011**, *21*, 356−363.
(7) (a) De Longchamp, D. M.; Kline, R. J.; Fischer, D. A.; Richter, L. J.; Toney, M. F. *Adv. Mater.* **2011**, *23*, 319−337. (b) Baker, J. L.; Jimison, L. H.; Mannsfeld, S.; Volkman, S.; Yin, S.; Subramanian, V.; Salleo, A.; Alivisatos, A. P.; Toney, M. F. *Langmuir* **2010**, *26*, 9146−9151. (c) Verploegen, E.; Mondal, R.; Bettinger, C. J.; Sok, S.; Toney, M. F.; Bao, Z. *Adv. Funct. Mater.* **2010**, *20*, 3519−3529. (d) Jimison, L. H. Understanding microstructure and charge transport in semi crystalline polythiophenes. Ph.D. Thesis, Stanford University, Stanford, CA, 2011. (e) Boudouris, B. W.; Ho, V.; Jimison, L. H.; Toney, M. F.; Salleo, A.; Segalman, R. A. *Macromolecules* **2011**, *44*, 6653−6658.
(8) Kim, B. J.; Miyamoto, Y.; Ma, B.; Fréchet, J. M. J. *Adv. Funct. Mater.* **2009**, *19*, 2273−2281.
(9) (a) Ma, B.; Kim, B. J.; Poulsen, D. A.; Pastine, S.; Fréchet, J. M. J. *Adv. Funct. Mater.* **2009**, *19*, 1024−1031. (b) Zuniga, C. A.; Barlow, S.; Marder, S. R. *Chem. Mater.* **2011**, *23*, 658−681.
(10) Griffini, G.; Douglas, J. D.; Piliego, C.; Holcombe, T. W.; Turri, S.; Fréchet, J. M. J.; Mynar, J. L. *Adv. Mater.* **2011**, *23*, 1660−1664.
(11) (a) Afzali, A.; Dimitrakopoulos, C. D.; Graham, T. O. *Adv. Mater.* **2003**, *15*, 2066−2069. (b) Png, R.-Q.; Chia, P.-J.; Tang, J.-C.; Liu, B.; Sivaramakrishnan, S.; Zhou, M.; Khong, S.-H.; Chan, H. S. O.; Burroughes, J. H.; Chua, L.-L.; Friend, R. H.; Ho, P. K. H. *Nat. Mat.* **2010**, *9*, 152−158. (c) Huh, S.; Kim, S. B. *J. Phys. Chem. C* **2009**, *114*, 2880. (d) Liu, J.; Zheng, R.; Tang, Y.; Haeussler, M.; Lam, J. W. Y.; Qin, A.; Ye, M.; Hong, Y.; Gao, P.; Tang, B. Z. *Macromolecules* **2007**, *40*, 7473.
(12) (a) Kim, C.; Wang, Z. M.; Choi, H. J.; Ha, Y. G.; Facchetti, A.; Marks, T. J. *J. Am. Chem. Soc.* **2008**, *130*, 6867−6878. (b) Cao, Q.; Xia, M. G.; Shim, M.; Rogers, J. A. *Adv. Funct. Mater.* **2006**, *16*, 2355−2362. (c) Yoon, M. H.; Facchetti, A.; Marks, T. J. *Proc. Natl. Acad. Sci. U. S. A.* **2005**, *102*, 4678−4682.
(13) Zaumseil, J.; Sirringhaus, H. *Chem. Rev.* **2007**, *107*, 1296−1323.
(14) Kline, R. J.; McGehee, M. D.; Kadnikova, E. N.; Liu, J.; Fréchet, J. M. J.; Toney, M. F. *Macromolecules* **2005**, *38*, 3312−3319.
(15) Zen, A.; Pflaum, J.; Hirschmann, S.; Zhuang, W.; Jaiser, F.; Asawapirom, U.; Rabe, J. P.; Scherf, U.; Neher, D. *Adv. Funct. Mater.* **2004**, *14*, 757−764.
(16) Sze, S. M. *Physics of Semiconductor Devices*, 2nd ed.; Wiley: New York, 1981.
(17) (a) Rep, D. B. A.; Morpurgo, A. F.; Sloof, W. G.; Klapwijk, T. M. *J. Appl. Phys.* **2003**, *93*, 2082. (b) Meijer, E. J.; Detcheverry, C.; Baesjou, P. J.; van Veenendaal, E.; de Leeuw, D. M.; Klapwijk, T. M. *J. Appl. Phys.* **2003**, *93*, 4831. (c) Street, R. A.; Chabinyc, M. L.; Endicott, F. *Phys. Rev. B* **2007**, *76*, 045208. (d) Maddalena, F.; Meijer, E. J.; Asadi, K.; de Leeuw, D. M.; Blom, P. W. M. *Appl. Phys. Lett.* **2010**, *97*, 043302.
(18) (a) Schwartz, M. *J. Appl. Phys.* **1955**, *26*, 1507−1513. (b) Norton, J. T. *J. Appl. Phys.* **1948**, *19*, 1176−1178.
(19) Woo, C. H.; Thompson, B. C.; Kim, B. J.; Toney, M. F.; Fréchet, J. M. J. *J. Am. Chem. Soc.* **2008**, *130*, 16324−16329.

Macromolecules

Article

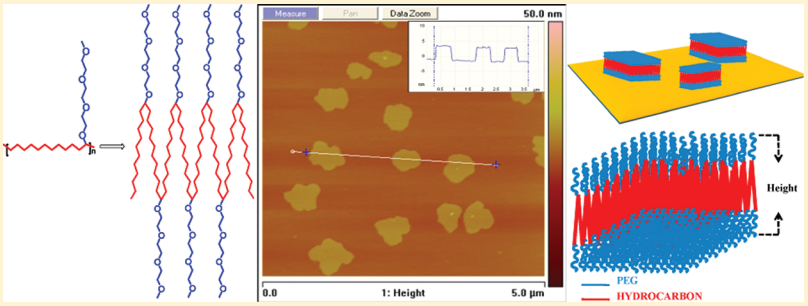
pubs.acs.org/Macromolecules

Periodically Grafted Amphiphilic Copolymers: Nonionic Analogues of Ionenes

Raj Kumar Roy, E. Bhoje Gowd,† and S. Ramakrishnan*

Department of Inorganic and Physical Chemistry, Indian Institute of Science, Bangalore 560012, India

Supporting Information



ABSTRACT: We describe a novel class of periodically grafted amphiphilic copolymers (PGACs) that could serve as nonionic functional mimics of ionenes, the primary difference being that the periodically occurring charged units along the backbone of ionenes are replaced by hydrophilic oligoethylene glycol segments. The synthesis and properties of this new class of segmented polymers that carry a hydrophobic alkylene polyester backone with periodically placed hydrophilic oligo(oxyethylene) pendant units are presented. When the length of the intervening alkylene segment is adequately long, 22-carbons in this case, and the pendant unit is a hexaethylene glycol monomethyl ether (HEG) segment, the polymer chain appears to adopt a folded zigzag conformation, reminiscent of the accordion-type structure formed by cationic ionenes. This transformation is driven by the intrinsic immiscibility of the alkylene and HEG segments and is reinforced by the strong tendency for long chain alkylene segments to crystallize in a paraffinic lattice. Evidence of the formation of such structures comes from the AFM images, which reveal the formation of remarkably flat pancake-like aggregates that are formed by the lateral aggregation of individually collapsed polymer chains; importantly, the heights of these structures match well with the lamellar layer-spacing obtained from SAXS studies of bulk samples. DSC studies further confirm the crystallization of the intervening alkylene segments, especially when they are long (C22), suggesting the formation of the folded zigzag structures. In a suitably designed PGAC that carries diacetylene units symmetrically placed within the alkylene segment, attempts were made to cross-polymerize the diacetylene units and generate PEGylated nanoparticles. However, these attempts were unsuccessful demonstrating the very stringent geometric requirements for the topotactic polymerization of diacetylenes.

INTRODUCTION

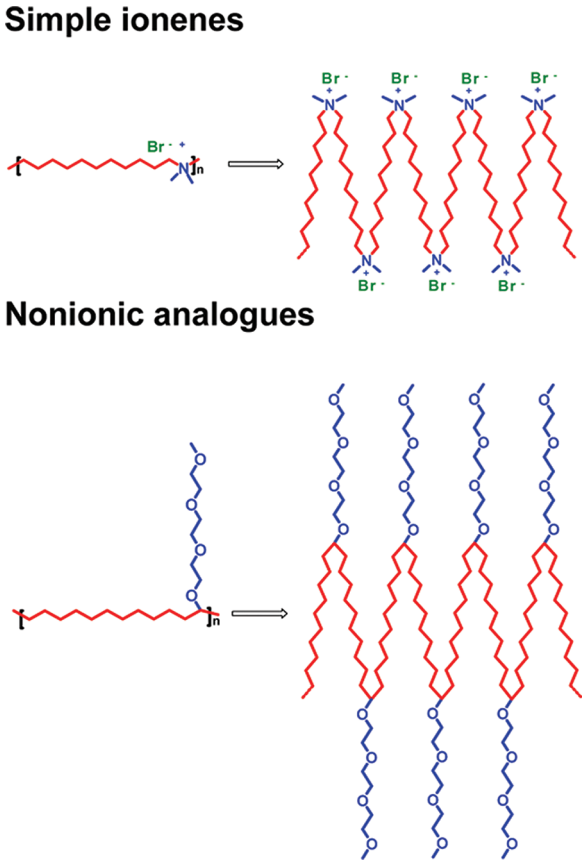
It has been known for several decades, since the early work by Rembaum and coworkers,[1] that cationic ionenes[2] wherein the charges reside directly on the polymer backbone with a regular periodicity exhibit a strong tendency to adopt an accordion-type conformation (Scheme 1) when dissolved in water; this is especially true when the number of intervening carbon atoms are large (>12).[3] Recently, in an effort to reinforce the collapsed zigzag structures, we prepared cationic ionenes wherein alternate alkylene segments carried electron-rich and electron-deficient aromatic units; this, in addition to reinforcing the formation of folded structures in water due to charge-transfer interactions between the donor and acceptor units, also provided a useful spectroscopic tool to follow the folding process.[4]

Just as ionenes may be viewed as polymeric (head-to-tail linked) analogues of ionic surfactants, one can also conceptualize a similar polymeric analogue of nonionic surfactants — these would be polymers wherein hydrophilic oligoethylene glycol segments are periodically placed as pendant groups along a linear hydrophobic polymer backbone, as depicted in Scheme 1. Such periodically grafted amphiphilic copolymers (PGACs) could be viewed as nonionic analogues of ionenes and could also be termed *nonionic ionenes*; as this would help one draw a parallel between the functional similarities that exist between ionic and nonionic surfactants and bring it into the context of their polymeric analogues. As in the case of ionenes, these nonionic analogues may also be expected to form zigzag folded structures (Scheme 1) when the lengths of the alkylene and oxyethylene segments are suitably balanced. In a recent report, Wagener and coworkers described the synthesis of structurally similar systems wherein a long-chain α,ω-diene, carrying a

Received: October 19, 2011
Revised: March 13, 2012
Published: March 26, 2012

 © 2012 American Chemical Society dx.doi.org/10.1021/ma2023414 | *Macromolecules* 2012, 45, 3063–3069

Scheme 1. Schematic Depiction of the Structures and Collapsed Conformations of Ionenes and Their Nonionic Analogues[a]



[a]For simplicity and conceptual clarity, the PEG chains have been shown to adopt an all-*trans* conformation, which in reality would not be the case.

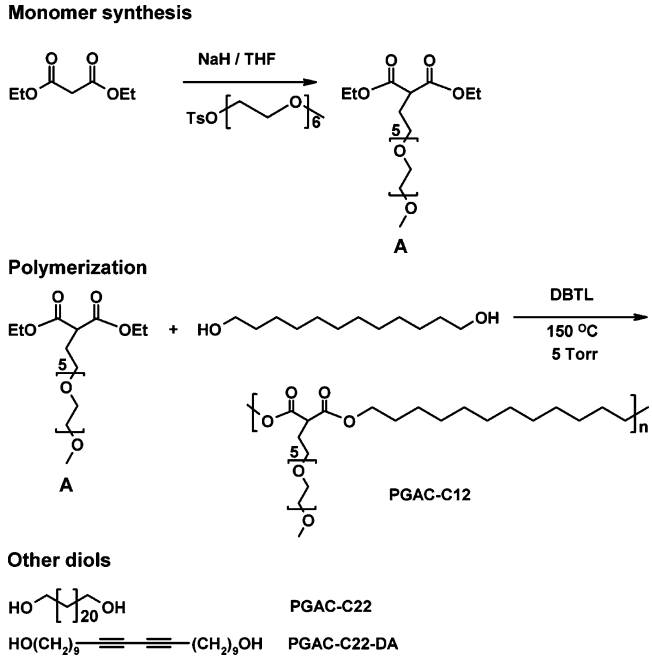
pendant tri- or tetra-ethylene glycol monomethyl ether segment, was polymerized using ADMET to yield periodically grafted copolymers;[5] however, the focus of their investigations was limited to the study of their solid-state properties, in particular, to examine the influence of the lateral substituent on the crystalline morphology of the alkylene segment using WAXS measurements.

In this report, we describe a simple design and synthesis of two novel kinds of PGACs wherein pendant hexaethylene glycol monomethyl ether (HEG) units are periodically placed along a hydrophobic backbone; the nature and length of the hydrophobic alkylene backbone was varied, and in one case a diacetylene unit was incorporated within the alkylene segment to explore the possibility of photoinduced cross-polymerization of the collapsed zigzag structures.

RESULTS AND DISCUSSION

To develop a simple strategy for the synthesis of periodically grafted amphiphilic copolymers (PGACs), we utilized a readily available starting material, such as diethyl malonate; base-catalyzed alkylation of the malonate with hexaethylene glycol monomethyl ether monotosylate[6] yielded the required diester monomer (**A**) carrying the pendant HEG segment (Scheme 2). The proton NMR spectrum of the monomer was in accordance with the expected structure (Figure 1); interestingly, the

Scheme 2. Structure and Synthesis of Monomers and PGACs



presence of a prochiral carbon causes the methylene protons of the ethyl ester group to appear as two distinct quartets. This monomer was first condensed with 1,22-docosane diol[7] under standard trans-esterification conditions at 150 °C using dibutyltin dilaurate as the catalyst to yield PGAC-C22; the polymerization was first done under nitrogen purge, followed by an additional period under reduced pressure to enable formation of higher molecular weight polymer. PGAC-C12 was a highly viscous liquid, whereas the PGAC-C22 was isolated as a white waxy solid. The comparison of the NMR spectra of the monomer and PGAC-C22 clearly reveals the formation of the expected polymer (Figure 1); the explicit disappearance of monomer peaks and formation of new peaks due to the polymer, however, was not clearly evident because of extensive overlap of peaks. For instance, the disappearance of the peaks due to the ethyl ester of monomer, such as the 4.22 ppm peak, is not evident because it is replaced by the methylene ester protons of the polymer; similarly, the methylene proton adjacent to the hydroxyl group in the diol monomer (3.68 ppm) also coincides with the glycol methylene protons in monomer **A**. The ^{13}C NMR spectra, however, clearly revealed the complete disappearance of the ethyl ester peaks in the polymer spectra and the appearance of new peaks corresponding to the polyester formation (Figure S1 of the Supporting Information). Whereas both polymers were soluble in organic solvents, like chloroform and THF, they were insoluble in polar solvents, like water and methanol. In water, they formed a light-blue scattering solution suggesting the formation of aggregated particles. Dynamic light scattering studies indicated that the average size of these particles, in case of PGAC-C22, was ~330 nm.[8]

To examine if these PGACs fold to form the anticipated zigzag structure, we first probed the morphology of the collapsed state using AFM; samples for AFM studies were prepared in two ways – dilute THF solutions (0.05% w/v) of the polymer were spin-coated onto freshly cleaved mica substrates, and these samples were either solvent-annealed in saturated water vapor or thermally annealed at a temperature

dx.doi.org/10.1021/ma2023414 | *Macromolecules* 2012, 45, 3063–3069

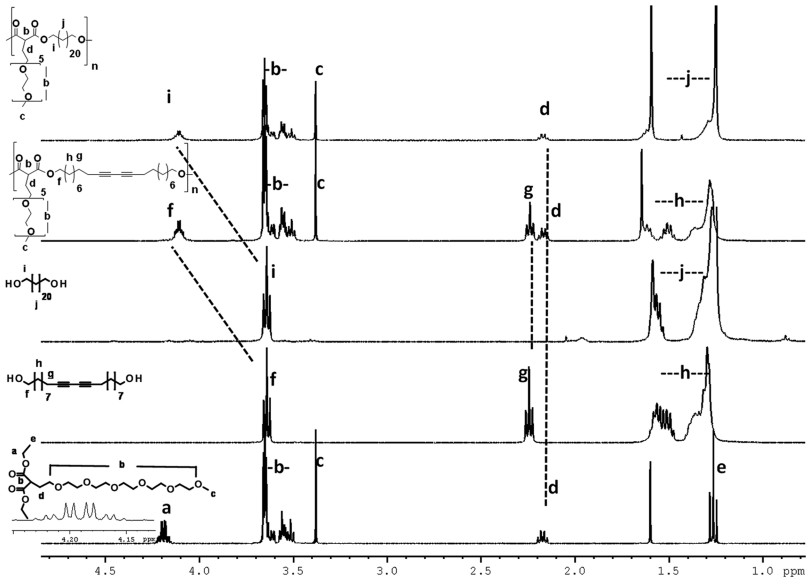


Figure 1. [1]H NMR stack plot of different PGACs along with corresponding monomers.

close to the melting transition (~60 °C) of the polymer; water vapor is expected to swell the PEG domains and enhance the phase separation. Typically, the aggregate features of thermally annealed samples were more uniform than the solvent-annealed samples. A typical AFM image of the PGAC-C22 is shown in Figure 2.

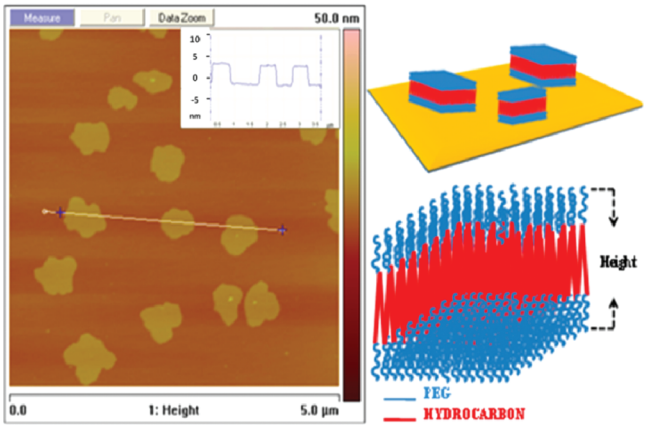


Figure 2. AFM images of PGAC-C22 deposited on mica along with a schematic representation depicting their formation. Inset: line scans depicting the height and lateral dimensions of the flat plate-like aggregates. The coated films were thermally annealed at 60 °C for 8 h prior to scanning.

The line scans (Figure 2; inset) reveal the formation of flat plate-like structures with remarkably uniform heights of ~5 nm; the lateral shape and dimensions, however, varied significantly (in the range 350−650 nm). As seen previously in the case of donor−acceptor ionenes,[4] it appears that these structures are formed when the collapsed zigzag chains of the PGACs laterally aggregate to form large plate-like aggregates, as schematically depicted in Figure 2. Similar structures were also seen when the polymers are deposited on Piranha-treated silicon wafers (Figure S2 of the Supporting Information). An estimate of the height of such a folded zigzag structure was obtained by computing the end-to-end distance of a model compound containing a central C22 alkylene segment flanked by two hexaethylene glycol monomethyl ether units, which was found to be ~6.2 nm. (See the Supporting Information for details.) The slightly lower observed value for the height may reflect the collapsed state of the flexible PEG segments around the relatively rigid alkylene crystallites upon deposition on the hard silicon substrate.

The driving motivation for the formation of these structures arises primarily from two factors: the immiscibility of the alkylene and the HEG segments, which is further reinforced by the strong tendency for the intervening alkylene segments to crystallize in a paraffin-like lattice;[9] the latter effect is known to become dominant when long alkylene segments are present. Therefore, thermal annealing of the sample leads to the effective compaction of the initially formed structures (Figure S2 of the Supporting Information). Although these aggregated structures were formed from THF solutions, the distinctly different solubility parameters of the PEG and the alkylene segments could be expected to lead to their segregation by forming a collapsed zigzag conformation during the evaporation of the THF solvent. In other words, the lower solubility of the alkylene units in THF when compared with the PEG segments would first cause the selective collocation of the alkylene segments as the polymer solution gets concentrated during evaporation; the crystallization of the alkylene segments beyond a certain threshold density could then direct the formation of the proposed collapsed zigzag structures. AFM images of PGAC-C12 (Figure S2 of the Supporting Information) also show similar aggregate structures; however, the aggregates are not perfectly flat and regular. This is clearly due to the fact that at room temperature the C12 alkylene segments are not in a crystalline phase, as will be evident from the DSC studies presented in the following section. AFM studies of light blue aqueous dispersions of PGAC-C22 deposited on mica were also carried out (Figure S2 of the Supporting Information); these images too showed flat plate-like structures with fairly uniform thickness of ~5 nm, thereby confirming that the aggregates formed in water also have similar structures.

To further substantiate our postulate, we carried out DSC studies of both the polymer samples; the PGAC-C22 sample exhibited sharp melting at 61 °C, whereas the PGAC-C12

dx.doi.org/10.1021/ma2023414 | *Macromolecules* 2012, 45, 3063−3069

exhibited a melting peak at −8.8 °C (Figure 3), which is consistent with their respective physical states at room

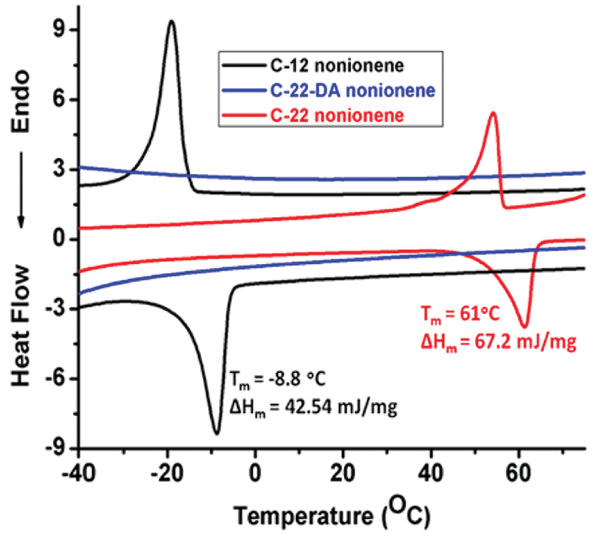


Figure 3. DSC thermograms of the various PGACs; the scans were run at a heating rate of 10 deg/min and are completely reproducible.

temperature. The thermograms were reproducible after the first heating cycle, and the crystallization exotherms were clearly evident during the cooling scans, as seen in the Figure; the enthalpy of melting was significantly higher for PGAC-C22. However, considering the fact that the melting peak is a reflection of the alkylene segments alone, the enthalpies were normalized with respect to the weight-percent of the alkylene segments; the enthalpy values thus obtained were much closer: 150 and 139 mJ/mg for the PGACs, C22, and C12, respectively. These values are roughly in accordance with those seen for *n*-alkane crystals of similar lengths; ΔH_m for docosane is reported to be 157 mJ/mg.[10] Furthermore, we also carried out DSC studies of the aqueous dispersion (the bluish scattering solution) of PGAC-C22 using a nanocalorimeter; the thermogram (Figure S7 of the Supporting Information) clearly reveals a melting transition at 70 °C with a normalized (with respect to the wt-fraction of alkylene segment) enthalpy of 116 mJ/mg. Although the melting temperature is slightly higher and the enthalpy is lower, it provides a clear indication that the aggregates formed in water may possess a similar paraffinic crystalline lattice, which supports the hypothesis that zigzag collapsed chains formed in water laterally aggregated to form larger bundles.

The tendency for intrachain self-segregation of the alkylene and the PEG segments would also be reflected in the bulk morphology of the sample; small-angle X-ray scattering (SAXS) measurements of PGAC-C22 in the q range: 0.005 to 0.2 Å^{-1} (Figure 4) clearly reveal the formation of an ordered structure. The diffraction pattern exhibits a sharp peak at ∼0.1209 Å^{-1} corresponding to a *d*-spacing of 5.2 nm, which is suggestive of the formation of a layered morphology; observation of the higher order reflections reconfirms the lamellar ordering.[11] This *d* spacing is clearly in excellent agreement with the average height of the aggregates seen in the AFM images, suggesting that the layered structure may be formed by an assemblage of the smaller aggregated units. In other words, the final structure is the result of assembly of individually folded molecules − *making this an interesting case of conformational control at a*

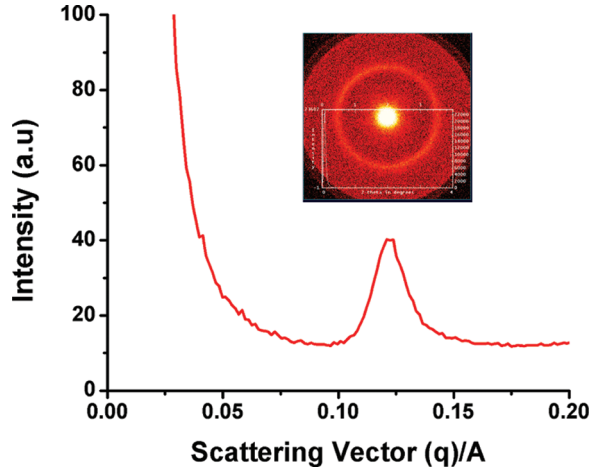


Figure 4. SAXS profiles of PGAC-C22 (red) at room temperature. Inset depicts the complete 2-D scattering patterns.

single-molecule level leading to a predictable organization in the macroscopic sample. No evidence of such layering is seen in the case of PGAC-C12 at ambient temperature; this confirms that the crystallization of the alkylene segments is essential for the formation of such lamellar morphology. (Recall that the melting temperature of PGAC-C12 is −8.8 °C.) At temperatures below its melting point, SAXS measurements of PGAC-C12 may reveal a peak corresponding to a substantially smaller lamellar spacing. It is well known that branching defects along the polyethylene backbone have a strong influence on the lamellar thickness because of the tendency of these defects to exclude from the paraffinic crystal.[12] In a recent study, Alamo et al.[13] showed that polyethylene containing periodic disruptions due to the presence of a pendant chlorine atom exhibited a similar layered morphology, wherein the crystallite thickness showed a clear dependence on the number of intervening methylene units between adjacent chlorine substituents. The formation of such layered morphology in thin solid films, driven segmental immiscibility, was also seen by Ober and coworkers in ionenes that carried pendant semifluoroalkyl groups.[14]

To ascertain the structure of the crystallites formed by the alkylene segments, wide-angle X-ray diffraction (WAXD) measurements were performed on the PGAC-C22 sample (Figure 5), which was annealed at a temperature close to its melting point. The WAXD pattern could be readily deconvoluted into three peaks at: 2θ = 20.8 (d = 4.27 Å), 21.7 (d = 4.08 Å), and 22.6° (d = 3.93 Å), in addition to a broad amorphous halo. The d spacings estimated from the diffraction peaks did not match the predicted values for the orthorhombic form but instead reflected the presence of a crystalline arrangement similar to those reported for periodically branched ADMET polyethylenes that possess a branch on every 21st carbon along the polymer backbone.[15] The peaks at 2θ = 20.8 and 22.6°, which are identical to the results obtained by Hosoda et al.[16] for the ADMET polyethylenes with ethyl branches, possibly originate from a triclinic lattice; the diffraction peak at 2θ = 21.7° suggests the coexistence of a hexagonal phase. Such a coexistence of more than one phase has been previously observed in precise alkyl branched polyethylenes[15] and also when low levels of chlorine are introduced into the polyethylene backbone.[13] Interestingly, the nascent sample does not exhibit this peak (Figure S3 of the

dx.doi.org/10.1021/ma2023414 | *Macromolecules* 2012, 45, 3063−3069

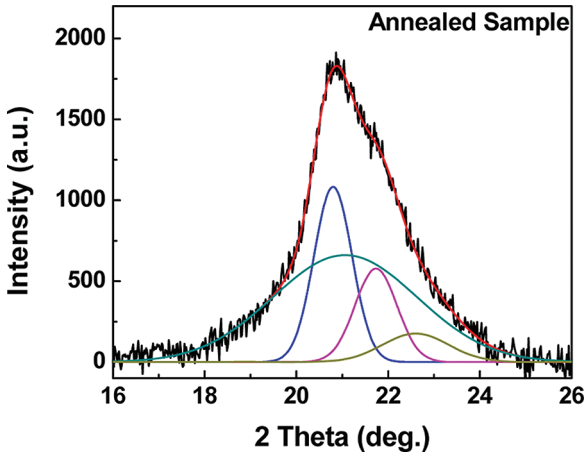


Figure 5. WAXS pattern of annealed PGAC-C22 sample, along with the deconvolution showing the presence of three underlying peaks, along with an amorphous halo.

Supporting Information), but it appears on upon annealing, which appears to introduce this additional hexagonal phase. This suggests that the annealing process causes a partial phase transition from triclinic to hexagonal phase, possibly due to differences in the cross-sectional areas of PEG and alkylene segments.

The formation of a zigzag folded structure with hydrophobic alkylene segments in the center and hydrophilic PEG units on either side suggested the possibility that these single folded chains could also organize to form vesicles in aqueous solutions. Hence, we attempted to prepare vesicles of the PGAC-C22 by the standard sonication method;[16] a drop of the vesicular dispersion was put on a carbon-coated grid, and the TEM measurements were carried out. From the TEM images (Figure S5 of the Supporting Information), it was evident that the PGAC-C22 indeed forms fairly large vesicles; sizes ranging from ∼100 to 200 μm.[17] The presence of biologically benign PEG segments on the outside (and inside) of these vesicular assemblies would be an added advantage for potential applications. In a very recent study, Cho et al. have demonstrated that pendant PEG-grafted hydrocarbon triblock copolymers exhibit anit-fouling properties;[18] this opens up other possible applications of such PGACs.

Finally, in an attempt to transform the collapsed polymer chains into single-chain nanoparticles by an intramolecular cross-linking process, we synthesized another interesting polymer wherein a diol, carrying a diacetylene (DA) unit, was condensed with monomer **A**. (See Scheme 2.) The resulting polyester, PGAC-C22-DA, had a similar amphiphilic nature that, we reasoned, would enable it to form the folded zigzag conformation in water. However, several attempts to cross-stitch the folded structure by photopolymerization of the diacetylene units were unsuccessful, as was evident from the absence of the characteristic absorption peak in the UV−visible spectrum, which is expected from polydiacetylenes.[19] The DSC thermogram of PGAC-C22-DA also revealed that it does not exhibit any melting transition; this suggests that the diacetylene-bearing alkylene segments exhibit a poor tendency to crystallize. This also suggested that the relative disposition of the diacetylene units in the folded polymer was not conducive the topotactic polymerization, which is known to be very sensitive to the interdiacetylene distance and their relative orientation.[20] Evidently the diacetylene units in our collapsed polymeric structures are unable to adopt the required relative geometry to permit easy transformation to polydiacetylenes. Alternate designs that could enhance the interaction between adjacent alkylene segments in the folded form may be needed, which in turn could permit cross-polymerization of the folded structures.

■ CONCLUSIONS

In conclusion, we have developed a simple approach for the preparation of a new class of periodically grafted amphiphilic copolymers (PGAC), wherein hydrophilic pendant HEG units are separated by well-defined hydrophobic alkylene segments. In the case wherein intervening alkylene segment is adequately long, such as 22-carbon chain, the polymer exhibits a strong tendency to adopt a folded zigzag conformation; because of the similarity of this folded structure to those formed by ionenes we suggest a new term, *nonionic ionenes (or nonionenes)*, to describe this class of periodically PEGylated amphiphilic polymers. AFM and SAXS studies of PGAC-C22 suggested the formation of folded zigzag structures; flat pancake-like structures having a thickness of ∼5 nm were seen in the AFM images, whereas the SAXS studies revealed the formation of a lamellar morphology with a similar layer-spacing of ∼5.2 nm. The motivation to form such zigzag folded structures comes from the intrinsic immiscibility of the alkylene and HEG segments, which is strongly reinforced by the crystallization tendency of long alkylene segments to generate paraffinic-type crystals; the importance of crystallization is also confirmed by the absence of a lamellar morphology in amorphous PGAC-C12. The presence of diacetylene units within the alkylene segment also appears to hinder the generation of the critical length of an all-trans alkylene segment that is essential for the formation of a paraffinic crystal; this in turn precluded the possibility of cross-polymerization of the folded chains, which is an interesting objective that still remains to be achieved. The folded form of the PGAC-C22 may be viewed as a single-molecule nanoparticle or more appropriately as a *PEGylated wax nanobundle* because in this case the intervening alkylene segments undergo crystallization to generate a paraffinic-type crystal.[21] Preliminary TEM studies also suggest that large vesicles could also be readily formed from PGAC-C22; the presence of biobenign PEG segments on either side make these assemblies particularly attractive for biological applications. To achieve this, it is essential to impart water solubility to these systems, which should be possible either by increasing the PEG segment length or by developing strategies to place hydroxyl groups at the PEG termini. The simplicity and versatility of the synthetic approach for the preparation this novel class of amphiphilic polymers should open up the possibility of generating several other interesting derivatives that could present some unique application potentials, such as in drug delivery, polar ordering of chromophores, and so on.

■ EXPERIMENTAL SECTION

Materials and Methods. Sodium borohydride, sodium hydride, tosyl chloride, PEG-150, Pd/C (10%), dibutyltin dilaurate (DBTDL), and dodecane diol were purchased from Aldrich Chemical and used as such without further purification. Benzyl chloride, sodium hydroxide, potassium hydroxide, metallic sodium, and tetramethyl ethylene diamine were purchased from Spectrochem Chemical Company and used without further purification. Undecylenic acid was purchased from LEO Chemicals and was distilled before use. All of the solvents were distilled and were dried, if necessary, by the following standard

dx.doi.org/10.1021/ma2023414 | *Macromolecules* 2012, 45, 3063−3069

procedures. 10,11-Dibromoundecanoic acid, 10,11-dibromoundecan-1-ol, undec-10-yn-1-ol, docosa-10,12-diyne-1,22-diol, and docosane 1,22-diol were all synthesized using reported procedures.[22−24] Hexaethylene glycol monomethyl ether monotosylate was synthesized by a previously reported procedure.[25] Structures of all monomers and polymers were confirmed by ^{1}H NMR spectroscopy and by elemental analysis in the case of the final polymers. NMR spectra were recorded on a Bruker AV400 MHz spectrometer using $CDCl_3$ as the solvent and TMS as reference. Small-angle X-ray scattering (SAXS) measurements were performed using a Bruker Nanostar, equipped with a rotating anode generator, operating at 45 kV and 100 mA (copper anode, λ = 1.54 Å), three-pinhole collimation, and a 2-D multiwire Histar detector. The SAXS detector was calibrated using silver behenate. The powdered samples were mounted between thin polymer films during measurements. The exposure time for a single frame was, ∼7200 s. Two-dimensional SAXS images collected were circularly averaged to 1-D formats (intensity versus q) using the Bruker software; the data are presented after background subtraction. Wide-angle X-ray diffraction (WAXD) measurements were performed on a Bruker AXS D8 advance diffractometer operating at 40 kV and 30 mA with a scanning rate 1 deg/min, using Cu K_α radiation (λ = 1.5406 Å). Samples were coated within the cavity of the sample holder made of poly(methyl methacrylate). DSC measurements were carried out on a Mettler Toledo instrument at a heating rate of 10 deg/min; the samples were first heated to melt and cooled, and the subsequent heating and cooling runs were recorded. Gel permeation chromatography (GPC) was carried out with a Viscotek TDA model 300 system and is coupled to refractive-index, differential viscometer, and light-scattering detectors in series. The separation was achieved with two mixed-bed PLgel columns (5 μm, mixed-bed C) maintained at 35 °C using tetrahydrofuran (THF) as the eluent. The molecular weights were determined using a universal calibration curve based on polystyrene standards. AFM measurements of the polymer samples were performed by using Nanoscope IVA multimode AFM (Digital Instrument, Santa Barbara, CA). All of the images presented are tapping mode height images, recorded using a tip of force constant 2.8 N/m and resonance frequency of 75 kHz. Image analysis was performed using the software provided along with the Nanoscope IVA. Either freshly cleaved mica foil or piranha-treated silicon wafer was used as substrate for the measurements.

Monomer (A). Sodium hydride (0.84 g, 60 wt % in mineral oil, 21.2 mmol) was taken in THF, and the solution was cooled to 0 °C. Diethyl malonate (3.51 g, 26.64 mmol) was added dropwise to the ice-cold solution, and the reaction mixture was allowed to stir for 2 h at room temperature. To this solution, hexaethylene glycol monomethyl ether monotosylate (4 g, 8.8 mmol) was added, along with catalytic amount of KI, and the reaction mixture was heated to reflux for 12 h. Subsequently, the reaction mixture was cooled to room temperature and THF was removed under reduced pressure; 30 mL water was added, and the entire solution was extracted with ethyl acetate (3 × 50 mL). The combined organic layer was concentrated under reduced pressure, and the crude product was purified by distillation in Kugelröhr apparatus at 250 °C and 2 Torr; a viscous colorless liquid was obtained in 65% yield. ^{1}H NMR (δ, $CDCl_3$): 1.25 (t, 6H, $-COOCH_2\mathbf{CH_3}$); 2.2 (q, 2H, $-OCH_2\mathbf{CH_2}CH-$); 3.39 (s, 2H, $-O\mathbf{CH_3}$); 3.70−3.50 (m, 22H, $-O\mathbf{CH_2CH_2}O-$); 3.50 (t, 1H, $-\mathbf{CH}COOCH_2CH_3$); 4.2 (m, 4H, $-COO\mathbf{CH_2}CH_3$).

Typical Polymerization. PGAC-C22: 1.0 g (2.28 mmol) of monomer **A**, along with 0.78 g (2.28 mmol) of docosane-1,22-diol and 2 mol % catalyst (dibutyltin dilaurate), was taken in a test tube-shaped polymerization vessel. The mixture was heated to melt under dry N_2 purge, and the contents were stirred for 15 min to ensure homogenization. Subsequently, the reaction mixture was heated to 150 °C for 2 h under N_2 purging. In the second stage, the polymerization vessel was connected to the Kugelröhr apparatus and the polymerization was continued at 150 °C for an additional 1 h under reduced pressure. The resulting polymer was dissolved in THF and filtered; the filtrate was concentrated under reduced pressure to a viscous solution and precipitated in methanol. The polymers were further purified twice by dissolution in THF and reprecipitated into methanol to yield a white waxy solid in 83% yield. ^{1}H NMR (δ, $CDCl_3$): 1.25 (m, 36H, $-OCOCH_2CH_2(\mathbf{CH_2})_{18}CH_2CH_2OCO-$); 1.6 (m, 4H, $-OCOCH_2\mathbf{CH_2}(CH_2)_{18}\mathbf{CH_2}CH_2OCO-$) 2.18 (q, 2H, $-OCH_2\mathbf{CH_2}CHCOO-$); 3.38 (s, 3H, -$O\mathbf{CH_3}$); 3.70−3.50 (m, 22H, $-O\mathbf{CH_2CH_2}O-$); 3.53 (t, 1H, $-OCO\mathbf{CH}CH_2CH_3$); 4.12 (m, 4H, $-OCO\mathbf{CH_2}CH_2(CH_2)_{18}CH_2\mathbf{CH_2}OCO-$). Elemental analysis: C, 64.82%; H, 10.96% (Calculated for $C_{3.8}H_{7.2}O$: C, 66.3%; H, 10.47%).

The other two polymers, namely, PGAC-C12 and PGAC-C22-DA, were prepared using a similar procedure, details of which are available in Supporting Information.

■ ASSOCIATED CONTENT

Ⓢ Supporting Information

Detailed experimental procedures, AFM images of the different polymers, additional X-ray scattering, and DLS data. This material is available free of charge via the Internet at http://pubs.acs.org.

■ AUTHOR INFORMATION

Corresponding Authors

*E-mail: raman@ipc.iisc.ernet.in.

Present Address

†Material Sciences and Technology Division, National Institute for Interdisciplinary Science and Technology (NIIST), Thiruvananthapuram − 695 019 Kerala, India

Notes

The authors declare no competing financial interest.

■ ACKNOWLEDGMENTS

We would like to thank DAE for the ORI award to S.R. and IISc for award of the Centenary Postdoctoral Fellowship to E.B.G.. We thank the Central X-ray facility of IISc and Raman Research Institute for the SAXS measurements and NIIST and Trivandrum for TEM measurements. We would also like to thank Dr V. A. Raghunathan for many valuable discussions regarding the SAXS measurements.

■ REFERENCES

(1) (a) Rembaum, A.; Baumgartner, W.; Eisenberg, A. *J. Polym. Sci., Polym. Lett. Ed.* **1968**, *6*, 159−171. (b) Rembaum, A.; Noguchi, N. *Macromolecules* **1972**, *5*, 261−269. (c) Noguchi, N.; Rembaum, A. *J. Polym. Sci., Polym. Lett. Ed.* **1969**, *7*, 383−394.

(2) For a recent review on ionenes, see: Williams, S. R.; Long, T. E. *Prog. Polym. Sci.* **2009**, *34*, 762−782.

(3) (a) Kunitake, T.; Nakashima, N.; Takarabe, K.; Nagai, M.; Tsuge, A.; Yanagi, H. *J. Am. Chem. Soc.* **1981**, *103*, 5945−5947. (b) Kunitake, T.; Tsuge, A.; Takarabe, K. *Polym. J. (Tokyo, Jpn.)* **1985**, *17*, 633−640.

(4) De, S.; Ramakrishnan, S. *Macromolecules* **2009**, *42*, 8599−8603.

(5) (a) Berda, E. B.; Wagener, K. B. *Macromol. Chem. Phys.* **2008**, *209*, 1601−1611. (b) Berda, E. B.; Lande, R. E.; Wagener, K. B. *Macromolecules* **2007**, *40*, 8547−8552.

(6) Yip, K. T.; Zhu, N. Y.; Yang, D. *Org. Lett.* **2009**, *11*, 1911−1914.

(7) The C-22 diol was synthesized in three steps using reported procedures from 11,12-undecenol; see the Supporting Information for details.

(8) DLS studies (see Supporting Information) were carried out using a dilute aqueous solution of the C22 PGAC. The estimated size using DLS was slightly lower than the estimate (lateral dimension) from AFM, suggesting that the drying process during spin-casting could have led to further aggregation.

(9) (a) Carfagna, C.; Roviello, A.; Sirigu, A. *Mol. Cryst. Liq. Cryst.* **1985**, *122*, 151−160. (b) Kaufman, H. S.; Sacher, A.; Alfrey, T.; Frakuchen, I. *J. Am. Chem. Soc.* **1948**, *76*, 3147−3147.

(10) Dirand, M.; Bouraoukba, M.; Briard, A.-J.; Chevallier, V.; Petitjean, D.; Corriou, J.-P. *J. Chem. Thermodyn.* **2002**, *34*, 1255−1277.
(11) The SAXS data for the PGAC-C22 were also collected in a machine that permitted acquisition over a larger *q*-range; higher order reflections, confirming the formation of uniformly layered morphology, were clearly visible; see Figure S4 of the Supporting Information.
(12) (a) Rees, D. V.; Bassett, D. C. *J. Polym. Sci., Part A-2* **1971**, *9*, 385−406. (b) Prime, R. B.; Wunderlich, R. *J. Polym. Sci., Part A-2* **1969**, *7*, 2061−2072. (c) Reding, F. P.; Lovell, C. M. *J. Polym. Sci.* **1956**, *21*, 157−159. (d) Smith, J. A.; Wagener, K. B. *Colloid Polym. Sci.* **2004**, *282*, 773−781. (e) Smith, J. A.; Brzezinska, K. R.; Valenti, D. J.; Wagener, K. B. *Macromolecules* **2000**, *33*, 3781−3794. (f) Gutzlerand, F.; Wegner, G. *Colloid Polym. Sci.* **1980**, *258*, 776−786. (g) Alamo, R. G.; Mandelkern, L. *Macromolecules* **1989**, *22*, 1273−1277.
(13) Alamo, R. G.; Jean, K.; Smith, R. L.; Boz, E.; Wagener, K. B.; Bockstaller, M. R. *Macromolecules* **2008**, *41*, 7141−7151.
(14) Wang, J.; Ober, C. K. *Macromolecules* **1997**, *30*, 7560−7567.
(15) (a) Qiu, W.; Sworen, J.; Pyda, M.; Nowak-Pyda, E.; Habenschuss, A.; Wagener, K.; Wunderlich, B. *Macromolecules* **2006**, *39*, 204−217. (b) Lieser, G.; Wegner, G.; Smith, J.; Wagener, K. *Colloid Polym. Sci.* **2004**, *282*, 773−781. (c) Sworen, J.; Smith, J.; Wagener, K.; Baugh, L.; Rucker, S. *J. Am. Chem. Soc.* **2003**, *125*, 2228−2240.
(16) Hosoda, S.; Nozue, Y.; Kawashima, Y.; Utsumi, S.; Nagamatsu, T.; Wagener, K.; Berda, E.; Rojas, G.; Baughman, T.; Leonard, J. *Macromol. Symp.* **2009**, *282*, 50−64.
(17) For representative TEM pictures of polymeric vesicles formed by block copolymers, see: (a) Discher, B. M.; Won, Y.-Y.; Ege, D. S.; Lee, J. C-M.; Bates, F. S.; Discher, D. E.; Hammer, D. A. *Science* **1999**, *284*, 1143−1146. (b) Mai, Y.; Eisenberg, A. *J. Am. Chem. Soc.* **2010**, *132*, 10078−10084.
(18) Cho, Y.; Sundaram, H. S.; Weinman, C. J.; Paik, M. Y.; Dimitriou, M. D.; Finlay, J. A.; Callow, M. E.; Callow, J. A.; Kramer, E. J.; Ober, C. K. *Macromolecules* **2011**, *44*, 4783−4792.
(19) (a) Wegner, G. *Makromol. Chem.* **1972**, *154*, 35−48. (b) Enkelmann, V.; Wegner, G. *Angew. Chem., Int. Ed. Engl.* **1977**, *16*, 416−416. (c) Enkelmann, V.; Leyrer, R. J.; Wegner, G. *Makromol. Chem.* **1979**, *180*, 1787−1795.
(20) (a) Wegner, G. *Makromol. Chem.* **1971**, *145*, 85−94. (b) Wegner, G. Z. *Z. Naturforsch., B* **1969**, *24*, 824−832. (c) Xu, R.; Gramlich, V.; Frauenrath, H. *J. Am. Chem. Soc.* **2006**, *128*, 5541−5547.
(21) In a recent study, Yin and Hillmyer similarly implicated the crystallization of long alkylene segments in the formation of disk-like micellar aggregates from amphiphilic diblock copolymers. Yin, L.; Hillmyer, M. A. *Macromolecules* **2011**, *44*, 3021−3028.
(22) Bhanu Prasad, A. S.; Bhaskar Kanth, J. V.; Periasamy, M. *Tetrahedron* **1992**, *48*, 4623−4626.
(23) Narasimhan, S.; Mohan, H.; Madhavan, S. *Indian J. Chem., Sect. B: Org. Chem. Incl. Med. Chem.* **1995**, *34B*, 531−534.
(24) Hay, A. S. *J. Org. Chem.* **1961**, *27*, 3320−3321.
(25) Ramkumar, S. G.; Ramakrishnan, S. *Macromolecules* **2010**, *43*, 2307−2312.

Macromolecules

Article

pubs.acs.org/Macromolecules

Synthesis of Amphiphilic Rod–Coil P3HT-*b*-P4VP Carrying a Long Conjugated Block Using NMRP and Click Chemistry

Ruth H. Lohwasser and Mukundan Thelakkat*

Applied Functional Polymers, Department of Macromolecular Chemistry I, University of Bayreuth, Universitätsstraße 30, 95444 Bayreuth, Germany

Supporting Information

ABSTRACT: We use a combination of click chemistry and nitroxide-mediated radical polymerization (NMRP) for the incorporation of high molecular weight poly(3-hexylthiophenes) (P3HTs) segments into amphiphilic block copolymers. First, a high molecular weight alkyne-terminated P3HT was synthesized using Kumada catalyst transfer polymerization followed by in-situ end-capping with alkyne and by quenching with methanol. We found out that hydrochloric acid, the best quenching agent for nonfunctionalized P3HTs, leads to addition reactions with the alkyne group and therefore is not suitable for alkyne-terminated P3HT. With the use of copper-catalyzed azide–alkyne click reaction, P3HT-alkoxyamine is formed as a macroinitiator for NMRP. This was used to polymerize 4-vinylpyridine to get amphiphilic rod–coil P3HT-*b*-P4VP block copolymers with 55 and 77 wt % of poly(4-vinylpyridine) (P4VP). We investigate how the optical and thermal properties as well as the phase separation behavior depend on the block ratios. These P3HT-*b*-P4VP copolymers are interesting for hybrid organic photovoltaics as well as for studying the colloidal structures of semiconductor amphiphilic systems. The high molecular weight rod influences the rod–rod interaction as described by the Maier–Saupe parameter μ and therefore has consequences in the microphase separation.



INTRODUCTION

Poly(3-hexylthiophene) (P3HT) is one of the widely studied conjugated polymers. It is intensively investigated for applications in organic electronic devices, such as photovoltaics, organic field effect transistors (OFETs), or organic light-emitting diods (OLEDs).[1,2] It has also been incorporated into different types of block copolymers such as P3HT-*b*-polystyrene, P3HT-*b*-poly(perylene bisimide acrylate), P3HT-*b*-fullerene, P3HT-*b*-polylactide, P3HT-*b*-poly(2-vinylpyridine), and others.[3−9] A lot of different methods have been applied for the synthesis of the second block, ranging from anionic polymerization to ring-opening metathesis polymerization (ROMP) and controlled radical polymerization methods.[4,9−12]Also, some work has been done which involved copper-catalyzed azide–alkyne cycloaddition reactions, better known as "click" chemistry.[13−16] Most of these technics used relatively low molecular weight P3HTs (<10000 g/mol) corresponding to less than 40 repeating units.[3,5,7,9,14,15,17,18] Only few reports are known for a high molecular weight P3HT block.[4,12,13,19,20] However, for the application in organic electronic devices high charge carrier mobilities are necessary. From the literature it is known that the charge carrier mobility increases with molecular weight. A better interconnectivity between ordered domains and an increased crystallinity are discussed as the origin for the improved mobility of high molecular weight samples.[21−23] Therefore, it is important to incorporate P3HTs with more than some 40 repeating units into a block copolymer to allow for good charge carrier mobility. Recently, we also showed that the length of the P3HT block plays a major role for the efficiency of block copolymer solar cells. The block copolymers with a P3HT block of 17 000 g/mol showed a much better external quantum efficiency than the blocks with a 8900 g/mol P3HT.[20] However, the direct in-situ synthesis of alkoxyamine macroinitiator resulted in appreciable amounts of difunctionalized derivative in addition to the desired monofunctionalized product when high molecular weight P3HT was used. Jeffries-El et al. have shown that P3HT can be functionalized with different end groups by reacting the active chain end with monofunctionalized Grignard reagents.[24] The π-electron carrying Grignard reagents like ethynylmagnesium chloride lead to predominantly monofunctionalized P3HTs with only a low content of difunctionalized polymers. This alkyne function can be efficiently used in copper-catalyzed azide–alkyne reactions for polymer–polymer click or for the formation of P3HT macroinitiators.[13−15,17] This was exploited earlier to obtain block copolymers containing low molecular weight P3HT segments.[17] Here we adapted this method to prepare high molecular weight rod–coil block copolymers. Additionally, we demonstrate that the choice of the quenching reagent plays an

Received: November 9, 2011
Revised: February 2, 2012
Published: March 20, 2012

 © 2012 American Chemical Society dx.doi.org/10.1021/ma2024733 | *Macromolecules* 2012, 45, 3070–3077

important role in the successful functionalization with alkyne. Hydrochloric acid, which is the best quenching agent for nonfunctionalized P3HTs, leads to addition reactions with the alkyne group and therefore is not suitable. Further, we convert alkyne-functionalized P3HT (P3HT-alkyne) into a high molecular weight macroinitiator for nitroxide-mediated radical polymerization (NMRP) with the help of click chemistry. We use this macroinitiator for the polymerization of 4-vinlypyridine to get P3HT-*b*-P4VP block copolymers. P3HT is a hole conducting material, and P4VP can coordinate electron conducting nanoparticles. Thus, a fully functionalized system for hybrid solar cells could be achieved. It is known that the coordination of P4VP with nanoparticles is stronger than for P2VP because of the smaller steric hindrance of the nitrogen in position 4.[25] To the best of our knowledge, up to now only two reports of P3HT-*b*-P4VP are known in the literature:[18,26] one using anionic polymerization and the other one using reversible addition−fragmentation chain transfer (RAFT) for the synthesis of the second block. However, in both approaches, only small molecular weight P3HT blocks could be incorporated.

Apart from the potential application in organic photovoltaics, these P3HT-*b*-P4VP block copolymers are highly interesting as amphiphilic rod−coil systems for the formation of solution structures such as micelles, vesicles, etc., and for understanding the phase separation and crystallization in such structures.[27−29] Very recently, Lee et al. reported about the change of stiffness of a short P3HT block of 6800 g/mol from a rigid rod to a semirigid chain to a flexible chain depending on the length of the second P2VP block.[30] These changes depend on the balance between the rod−rod interaction as described by the Maier−Saupe parameter μ and the length of the rod in contrast to the enthalpic interaction which depends on the Flory−Huggins interaction parameter χ (between the segments) and the total length of the block copolymer in the case of amorphous systems. Thus, the phase behavior of block copolymers with a longer P3HT block and stronger rod−rod interactions are of high interest.

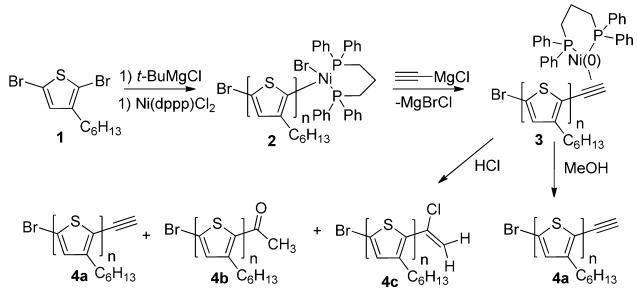
Two different block copolymers with P4VP contents of 55 and 77 wt % were synthesized. Their thermal and optical properties are investigated, and the preliminary bulk and solution structures depending on the different block ratios are shown.

RESULTS AND DISCUSSION

Influence of Quenching Reagent on P3HT-Alkyne. For the synthesis of a P3HT macroinitiator we used an alkyne-functionalized P3HT. Jeffries-El et al. showed that P3HT-alkyne can easily be made by in-situ end-capping of the active chain end with the monofunctionalized Grignard reagent ethynylmagnesium chloride.[24] Recently, Li et al. found that this alkyne-functionalized P3HT is sensitive to homocoupling during purification using a Soxhlet apparatus, which is catalyzed by residual metal traces.[13] We observed similar behavior, but the main reason for the formation of homocoupling seems not to be the residual metal traces but the increased temperature during hot extraction. We also found that when the reaction is quenched with methanol the catalyst remains as a solid, which is no longer soluble in chloroform. Dissolution of the P3HT-alkyne in chloroform, filtration, and precipitation of the polymer in methanol several times at room temperature to remove the remaining catalyst traces yielded a monomodal distributed alkyne-functionalized P3HT. Even though catalyst traces were removed by this cleaning process, we observed homocoupling if the solid polymer is stored at room temperature, indicating that it is a thermally initiated reaction. This could only be avoided by storing at temperatures below 0 °C.[13]

Here, we demonstrate that also the quenching reagent after functionalization plays a major role for the molecular weight distribution and the resulting end groups. Recently, we showed that quenching the Kumada catalyst transfer polymerization (KCTP) of P3HT with methanol causes a small amount of chain−chain coupling by disproportionation.[31] Therefore, hydrochloric acid was the preferred quenching reagent to gain monomodal distributed P3HT with 100% H/Br end groups.[31,32] Generally in KCTP of P3HT, the catalyst is covalently bound to the chain end of the polymer before quenching. After end-capping with an alkyne Grignard reagent the situation is different. For example, the addition of ethynylmagnesium chloride to the active chain end leads to the formation of Ni(0)dppp which is found to form a stable π-complex (Scheme 1).[33] This is used to explain the

Scheme 1. Mechanism for the Formation of P3HT-Alkyne via MeOH Quenching and Side Reactions Due to HCl as Quenching Reagent



predominantly monofunctionalization by capping with unsaturated Grignard agents like allyl, ethynyl, or vinyl.[24]

We found that for the alkyne-functionalized P3HT quenching the reaction with aqueous hydrochloric acid resulted in only very small amounts of the desired alkyne-functionalized product. Instead, it causes hydration and hydrohalogenation of the alkyne group as well as chain−chain coupling. To study this in detail, a small molecular weight sample was analyzed because it allows MALDI-ToF MS measurements in the reflection mode and thus proper end-group analysis. The addition products can be seen in MALDI-ToF MS by the presence of two new peak series (Figure 1a,b). The major peak series belongs to P3HT + C_2H + Br + HCl (e.g., for a 15-mer, 2635 g/mol = 15 × 166.3 g/mol + 25 g/mol + 79.9 g/mol + 36 g/mol) and the two minor ones to P3HT + C_2H + Br + H_2O (2617 g/mol = 15 × 166.3 g/mol + 25 g/mol + 79.9 g/mol + 18 g/mol) and the expected series for P3HT + C_2H + Br (2599 g/mol = 15 × 166.3 g/mol + 25 g/mol + 79.9 g/mol). Further evidence for these addition reactions can be gained from ^{1}H NMR spectrum in Figure 1c.

After quenching with HCl, almost no signal for the alkyne proton is visible at 3.53 ppm; instead, three other end-group signals appear: two doublets at 5.62 and 5.52 ppm as well as a very small singlet at 2.55 ppm (adjacent to the α-CH_2 signal of the alkyl chain at 2.80 ppm and overlapping with the α-CH_2 signal of the end-group unit carrying a bromine at 2.57 ppm). The two doublets belong to the vicinal protons in **4c**, which is formed by the addition of HCl in a Markovnikov manner. The

dx.doi.org/10.1021/ma2024733 | *Macromolecules* 2012, 45, 3070−3077

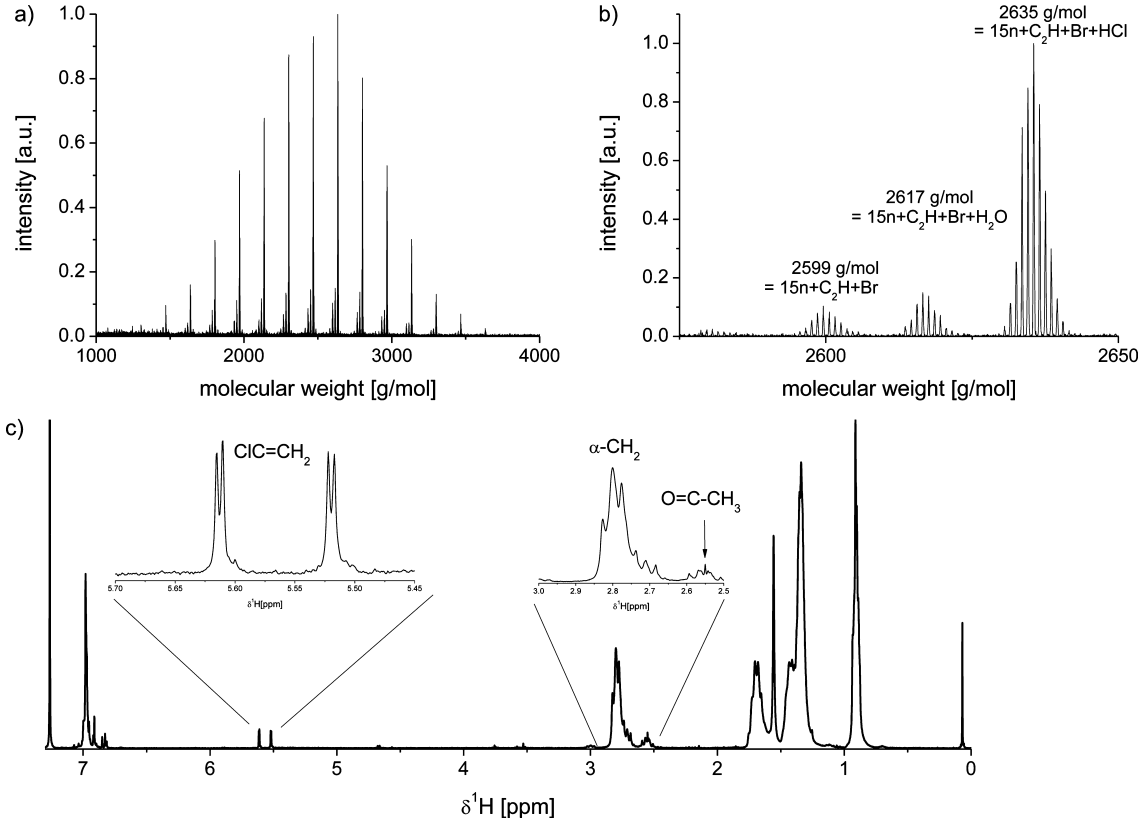
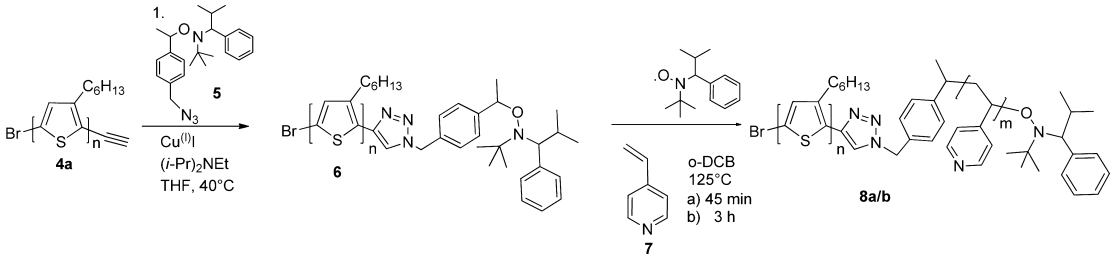


Figure 1. Spectra of P3HT obtained after quenching the end-capping reaction of ethynylmagnesium chloride with hydrochloric acid at 0 °C: (a) MALDI-ToF MS spectra measured in the reflection mode; (b) magnified part in the range of 15 repeating units; (c) ^{1}H NMR spectrum. The respective end groups are indicated.

Scheme 2. Synthesis of P3HT-Alkoxyamine Macroinitiator via Copper-Catalyzed Azide−Alkyne Reaction and of P3HT-*b*-P4VP Using NMRP of 4-Vinylpyridine



singlet at 2.55 ppm belongs to the CH_3 group of the methyl ketone which is formed by hydration resulting in **4b**. Because of keto−enol tautomerism, the enol form transforms into the keto form as the final product. In the shown example, the intensity for the methyl ketone is very low because the main series is that of the hydrohalogenated product **4c** (Supporting Information shows ^{1}H NMR and MALDI-ToF MS spectra of a sample with higher content of methylketone). The alkyne group of P3HT is electron-rich because of the conjugation with the thiophene main chain, and thus an electrophilic addition is promoted. Since aqueous HCl causes these addition reactions, it should not be used as a quenching reagent. Further a small shoulder at double the molecular weight is also observed (Figure SI3, Supporting Information) due to chain−chain coupling.

After end-capping with alkyne, nickel is in a Ni(0) state. On quenching with MeOH, disproportionation which occurred for nonfunctionalized P3HTs is no longer possible for P3HT-alkyne. Thus, methanol can be used as a suitable quenching reagent, and the polymers show a monomodal distribution in size exclusion chromatography (SEC) (see Figure 3a and Figure SI3). Additionally, the MALDI-ToF MS spectrum contains one main peak series belonging to P3HT with one bromine and one alkyne end group (see Figure SI2). The smaller peak series arises due to difunctionalized P3HT. For example, in the sample from the quenching experiments, with a SEC number-average molecular weight of 3200 g/mol, the major peak series corresponds to 90%. The influence of the chain length on the amount of dicapped P3HT was not investigated in detail. However, an even lower content of dicapped P3HT is expected with increasing molecular weight because the diffusion of Ni(0) to the bromine end groups slows with decreasing ratio of end groups to repeating units. For P3HT-alkynes with molecular weights of 20000 g/mol, it was difficult to verify this using MALDI-ToF MS because measuring in the reflection mode, which allows proper end-group analysis, is no longer possible. The MALDI-ToF MS of a

dx.doi.org/10.1021/ma2024733 | *Macromolecules* 2012, 45, 3070−3077

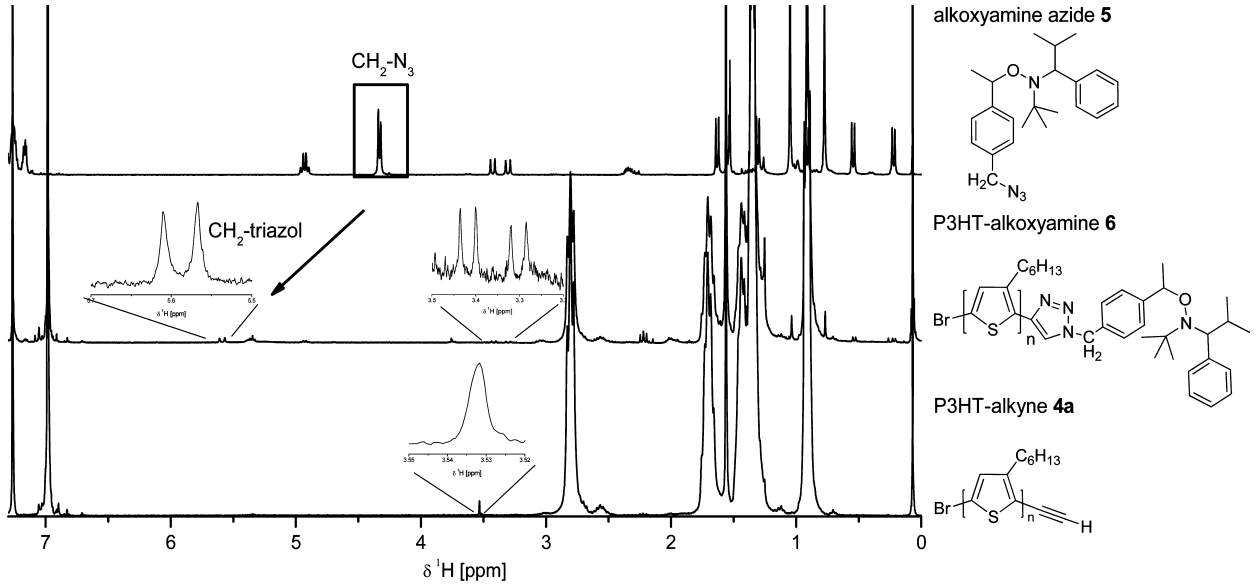


Figure 2. ^{1}H NMR spectra of P3HT-alkyne **4a**, P3HT-alkoxyamine macroinitiator **6**, and 2,2,5-trimethyl-3-(1′-*p*-azidomethylphenylethoxy)-4-phenyl-3-azahexane **5** (alkoxyamine azide). In P3HT-alkyne **4a**, the signal for the alkyne proton at 3.53 ppm is enlarged. P3HT-alkoxyamine macroinitiator **6** shows no more signal for the alkyne proton in the region from 3.20 to 3.60 ppm, but additional signals belonging to the product alkoxyamine macroinitiator **6**. Further the two singlets; belonging to the CH_2 units of the two diastereomers next to the azide of **5**; shift from 4.34 and 4.32 ppm to 5.60 and 5.56 ppm because of the proximity to the triazole unit in P3HT-alkoxyamine **6**. This indicates a quantitative functionalization.

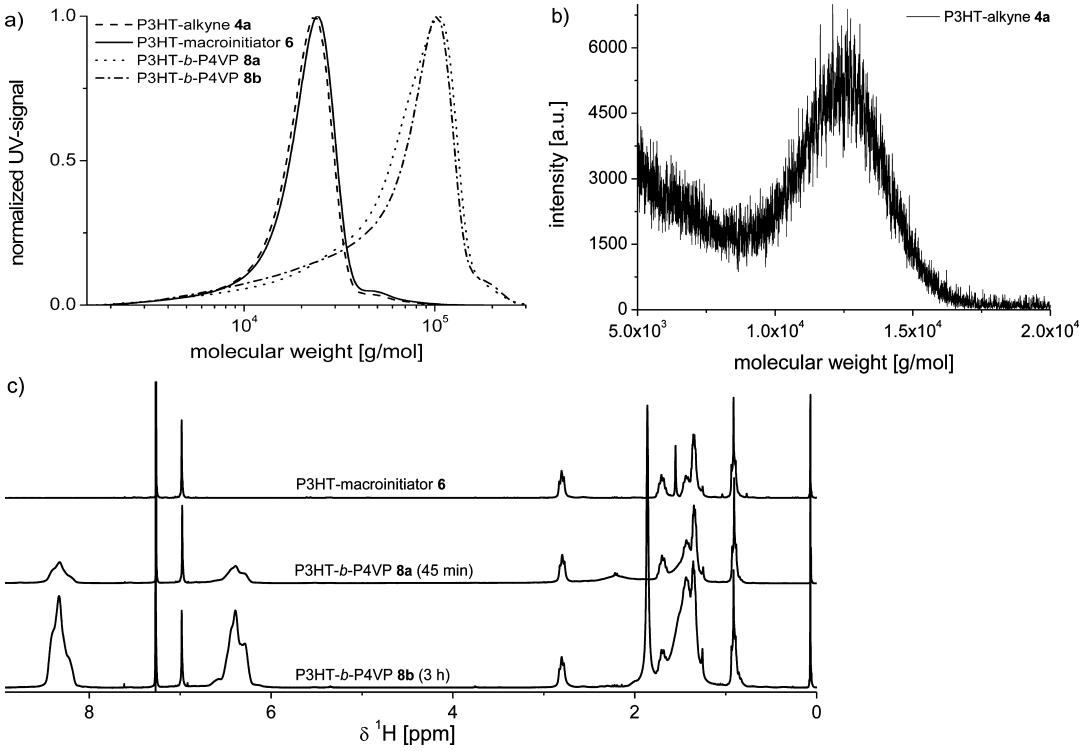


Figure 3. (a) SEC curves of P3HT-alkyne **4a**, P3HT-macroinitiator **6**, and P3HT-*b*-P4VP **8a** and **8b** measured with THF containing 0.25 wt % tetrabutylamonium bromide. (b) MALDI-ToF MS spectra of P3HT-alkyne **4a** measured in the linear mode. (c) ^{1}H NMR spectra of P3HT macroinitiator **6** and P3HT-*b*-P4VP **8a** and **8b**. For comparison, all spectra are normalized to the aromatic proton of P3HT at 6.98 ppm. The intensity of the aromatic protons of P4VP increases with increasing polymerization time from **8a** (45 min) to **8b** (3 h).

high molecular weight P3HT-alkyne, which was measured in the linear mode is shown in Figure 3b.

Synthesis of P3HT-*b*-P4VP. The synthesis route of the block copolymers P3HT-*b*-P4VP is shown in Scheme 2. P3HT-alkyne **4a** with a number-average molecular weight of 19200 g/mol and a PDI of 1.14 was synthesized first, as explained in the section before. Here LiCl was used as an additive for obtaining a higher molecular weight because it speeds up polymerization.[31] According to MALDI-ToF MS, this corresponds to a number-average molecular weight of

dx.doi.org/10.1021/ma2024733 | *Macromolecules* 2012, 45, 3070−3077

Table 1. Overview of the Synthesized Polymers and Block Copolymers Including Data from GPC, ^{1}H NMR, MALDI-TOF MS, and DSC

polymer	M_n(GPC)/ M_n(MALDI-TOF) [kg/mol]	M_p (GPC) [kg/mol]	PDI (GPC)	wt % P4VP (^{1}H NMR)	repeating units P3HT/P4VP	T_g [°C]	T_m [°C]	T_C [°C]	ΔH_m [J/g]
P3HT-alkyne **4a**	19.2/12.3	23.4	1.14	0	74/−				
P3HT-macroinitiator **6**	19.9/−	24.2	1.14	0	74/−		228/238	196	19
P3HT-*b*-P4VP **8a**	57.1/−	104.1	1.43	55	74/144	88	230	193	8
P3HT-*b*-P4VP **8b**	55.3/−	101.8	1.49	77	74/387	145	224	172	2

12300 g/mol and about 74 repeating units. The NMRP-macroinitiator was synthesized by reacting P3HT-alkyne with an alkoxyamine azide. For this, P3HT-alkyne **4a** was coupled with 2,2,5-trimethyl-3-(1′-p-azidomethylphenylethoxy)-4-phenyl-3-azahexane **5** using a copper-catalyzed azide alkyne cycloaddition (Scheme 2). $Cu^{(I)}I$ and *N*,*N*-diisopropylethylamine were used as catalytic system in THF at 40 °C.[34] The completion of this reaction was evidenced by ^{1}H NMR spectroscopy (see Figure 2). The signal of the alkyne proton of P3HT-alkyne (in **4a**) at 3.53 ppm vanishes and the two singlets belonging to the CH_2 units (two diastereomers) next to the azide shifts from 4.34 and 4.32 ppm (in **5**) to 5.60 and 5.56 ppm (in **6**) respectively. This shift in CH_2 signal and the complete disappearance of the alkyne proton signal clearly show a quantitative functionalization. Further, the other signals for the final alkoxyamine product are visible in the ^{1}H NMR spectrum of P3HT macroinitiator **6**. The effect of the alkoxyamine on the hydrodynamic radius of P3HT is low and thus no significant shift was observed in SEC (Figure 3a).

Since the solubilities of the individual segments, P3HT being a hydrophobic block and P4VP a hydrophilic block, are very different, it was important to choose the right solvent mixture for the synthesis of the block copolymers. Further, our earlier kinetic studies of NMRP of 4-vinylpyridine (4VP) indicated the need to avoid a strong dilution of the monomer to allow for a good control of polymerization.[35] Therefore, the 4VP monomer itself was chosen as a solvent for P4VP and *o*-dichlorobenzene (*o*-DCB) as a solvent for P3HT. The volume ratio of 4VP:*o*-DCB was 1:1, and the ratio of monomer to macroinitiator to free nitroxide 3000:1:2. Unfortunately, because this huge excess of monomer was needed for a good solubility, it was not possible to perform kinetic studies. The intensity of the polymer signal in ^{1}H NMR for the reaction mixture was too low in comparison to the monomer signal (due to the presence of 4VP as solvent) to enable the calculation of the percentage of conversion. Nevertheless, the polymerization proceeded quite fast at 125 °C and the amount of incorporated P4VP increased fast with polymerization time. P3HT-*b*-P4VP **8a** was obtained after 45 min and P3HT-*b*-P4VP **8b** after 3 h of polymerization, resulting in two block copolymers with P3HT as the minor block (see Table 1). The initiation of the macroinitiator **6** was not complete as seen in the SEC curves of the raw products in Figure SI4. But because of the amphiphilic nature of P3HT-*b*-P4VP, the remaining macroinitiator could be removed from the block copolymer by extraction with selective solvents for P3HT. First, the block copolymers were washed with 1 N HCl to protonate the P4VP block and to remove homopolymer which might have been formed during polymerization. In a second step, the block copolymer was extracted with toluene in a Soxhlet apparatus until all P3HT macroinitiator **6** was removed.

To recover the pure block copolymer, it was deprotonated with diluted ammonia (NH_3:H_2O, v:v, 1:1) and extracted from the Soxhlet thimble with chloroform. Since P3HT-*b*-P4VP is an amphiphile, performing SEC was difficult. The polymer was no longer soluble in THF, a common solvent for SEC of P3HT. Additionally, the long P3HT block hindered solubility in any P4VP selective solvent. Therefore, THF containing 0.25 wt % tetrabutylamonium bromide was used as an eluent, and the salt allowed for a sufficient solubility of the P4VP block. The SEC curves of the pure block copolymers are shown together with the P3HT-alkyne **4a** and P3HT macroinitiator **6** in Figure 3a. A clear shift of the molecular weight can be observed, and no uninitiated macroinitiator is visible after purification. However, both block copolymers **8a** and **8b** show similar molecular weights in SEC, and tailing is seen in the low molecular weight range. This tailing indicates interaction of the block copolymers with the column material. Therefore, determination of the molecular weights or polydispersities from SEC is not reasonable. The only reliable information, which can be gained, is that no significant amounts of macroinitiator are left after purification. Moreover, the final block copolymers show almost monomodal distributions. Thus, ^{1}H NMR together with MALDI-ToF MS from the P3HT-alkyne was used for the reliable determination of the block length and molecular weight ratios, as seen in Figure 3. The ^{1}H NMR spectra were normalized to the aromatic proton of P3HT at 6.98 ppm. It can be clearly seen that the intensity of the aromatic protons of P4VP increases with polymerization time from **8a** to **8b**. Integration of the P3HT signal of the aromatic proton at 6.98 ppm and a comparison with the integral of the two aromatic protons of P4VP in the range of 6.70−6.00 ppm gives the mole percentage of P4VP as 66 mol % (**8a**) and 84 mol % (**8b**). Taking the molecular weights of the repeating units into account (m_{3HT} = 166.3 g/mol and m_{4VP} = 105.14 g/mol), the weight ratios of P4VP were 55 and 77 wt %, respectively. The block lengths were calculated by using the P3HT repeating units as calculated from MALDI-ToF MS of **4a** together with the molar block ratios from ^{1}H NMR spectroscopy. Both block copolymers had the same macroinitiator with about 74 repeating units for P3HT block and **8a** has about 144 and **8b** 387 repeating units of 4VP (see Table 1).

Thermal and Optical Characterization of P3HT-*b*-P4VP. Both block copolymers and the P3HT-macroinitiator **6** were analyzed with differential scanning calorimetry (DSC) (see Figure 4 and Table 1). The P3HT-macroinitiator **6** has two melting points: a major one at 228 °C and the minor one at 238 °C. Recently, we showed that P3HT adopts a smectic liquid crystalline state between the crystalline and the isotropic phase.[36] This accounts for the observed two melting points.

The melting enthalpy of P3HT is 19 J/g, and on cooling from melt, it recrystallizes at about 196 °C. For the block copolymer **8a** with a P4VP content of 55 wt %, no significant change in the melting (230 °C) and recrystallization (193 °C) temperatures is observed. However, the melting enthalpy is reduced to 8 J/g, and an additional glass transition for the

dx.doi.org/10.1021/ma2024733 | *Macromolecules* 2012, 45, 3070−3077

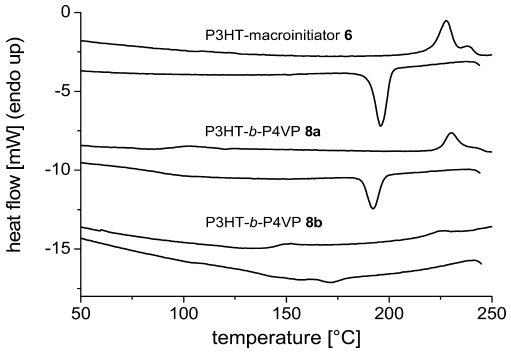


Figure 4. Second heating and first cooling curves from differential scanning calorimetry at a scan rate of 10 °C/min of P3HT-macroinitiator **6** and P3HT-*b*-P4VP **8a** and **8b**.

P4VP block is observed at 88 °C. By further increasing the P4VP block up to 77 wt % for P3HT-*b*-P4VP **8b**, the melting temperature decreases to 224 °C and the recrystallization occurs at 172 °C. Thus, the longer P4VP block (and lesser relative amount of P3HT) slightly decreases the size of the P3HT crystallites. Because of the low content of P3HT in **8b** (23 wt %), the melting enthalpy is also reduced to 2 J/g. Since the chain length of P4VP is higher in **8b** in comparison to **8a**, the glass transition temperature is increased to 145 °C, a typical value for high molecular weight P4VPs. The appearance of individual phase transitions due to each block indicates a possible phase separation in these block copolymers.

Further, these results show that the rod−rod interactions are considerably strong when a high molecular weight P3HT of 19 200 g/mol is used. Thus, for this high molecular weight system, the size of the P3HT crystallites is not influenced up to a coil content of about 55 wt %. Even at a coil content of 77 wt % the shift in the melting temperature and thus the change in crystallite size is small. In contrast, literature reports show that for P3HT-*b*-P2VP with a 6800 g/mol P3HT block a coil content of 46% already causes a shift in the melting temperature of about 60 °C.[30]

The polymers were further characterized with UV−vis spectroscopy in chloroform solution (0.04 mg/mL) and thin films on quartz obtained by spin-coating from 1 wt % chloroform solutions. In solution, the P3HT-macroinitiator **6** and both P3HT-*b*-P4VPs **8a** and **8b** show an absorption band around 449 nm belonging to S_0-S_1 transition due to $\pi \rightarrow \pi^*$ excitations of conjugated P3HT chromophore. The intensity of this band decreases with increasing P4VP content as expected (for solution spectra see Figure SI5). For all aromatic compounds an additional absorption band at 250−270 nm is observed for the nonconjugated aromatic rings due to any $\sigma \rightarrow \pi^*$ absorption common in aromatics. With increasing P4VP content the intensity of this UV band (at 256 nm) increases. For **8b** with 77 wt % P4VP the wavelength of maximum absorption intensity is no longer at 449 nm but at 256 nm.

In thin films the P3HT absorptions are shifted bathochromically in comparison to solution spectra. With decreasing P3HT content from P3HT-macroinitiator **6** to **8a** and **8b** the maximum is slightly shifted from 522 nm over 521 to 514 nm and the intensity of the P3HT absorption decreases. It is known that P3HT thin film absorption arises from weakly interacting H-aggregates.[37,38] Thus, changes in the band structure arise from changes in the crystallinity and conjugation length.[38,39] Apart from the observed shift in absorption maximum the following changes in the band structure are seen (see Figure 5a). While the P3HT-macroinitiator (100 wt

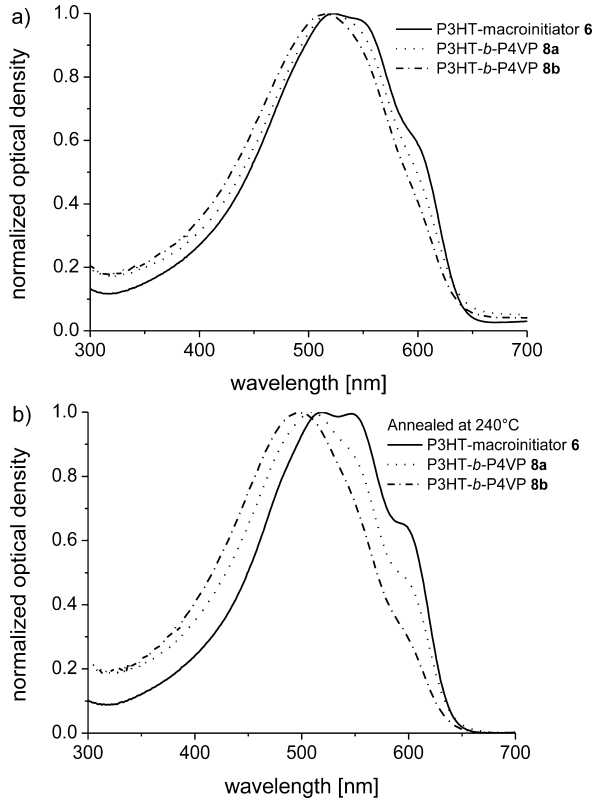


Figure 5. UV−vis spectra of P3HT-macroinitiator **6** as well as P3HT-*b*-P4VP **8a** and **8b** films on quartz obtained by spin-coating from 1 wt % chloroform solution. The spectra are normalized to the P3HT absorption maxima at about 500 nm. (a) As cast and (b) annealed at 240 °C for 5 min and cooled slow from melt.

% P3HT) shows typical vibronic bands of a crystalline P3HT at 550 and 600 nm, the intensity decreases with decreasing P3HT content in the block copolymers.[39] In P3HT-*b*-P4VP **8b** almost no fine structure is visible. Spin-coating from chloroform causes a fast drying of the films, and the polymers are in a nonequilibrium state of less aggregation. Therefore, we annealed the films above the melting temperature and cooled them slowly (cooling from 250 to 50 °C at 2 °C/min) to allow for crystallization of P3HT. After annealing above the melting point (see Figure 5b) the 0−0 transition is clearly enhanced for **8a**, but there is only a weak enhancement for **8b**. This is in accordance with the thermal measurements where the melting enthalpy and thus the crystallinity decrease with increasing P4VP content.

Characterization of the Bulk Structures. We further analyzed the phase separation of the P3HT-*b*-P4VP block copolymers in bulk using transmission electron microscopy (TEM). Figure 6 shows the TEM image of **8a** and **8b**. In both pictures a microphase separation is observed where P4VP appears as dark because of staining with iodine. Because of the higher content of P4VP in **8b**, the extent of dark regions is larger in Figure 6b. The mixed structural features observed in TEM indicate a nonequilibrium state morphology. However, these pictures clearly show microphase separation. Further, optimization of annealing conditions as well as cooling rates may play a role for obtaining equilibrium morphology in

dx.doi.org/10.1021/ma2024733 | *Macromolecules* 2012, 45, 3070−3077

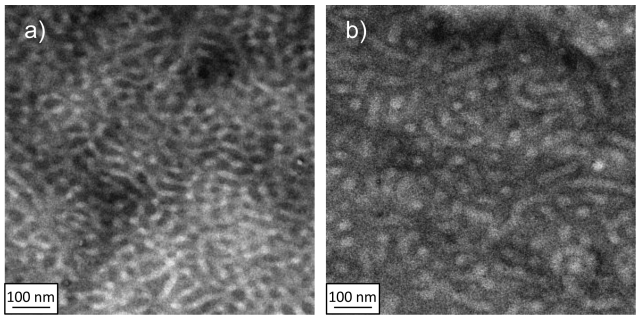


Figure 6. TEM images of P3HT-*b*-P4VP stained with iodine after 20 min annealing at 265 °C and quenching with liquid nitrogen (a) **8a** having 55 wt % P4VP and (b) **8b** with 77 wt % P4VP.

crystalline-amorphous block copolymers such as P3HT-*b*-P4VPs. For better understanding of the buildup of phase separated structures, temperature-dependent small-angle X-ray measurements are underway for bulk and thin film samples.

Characterization of the Solution Structures. Since P3HT-*b*-P4VP is an amphiphile, it should be possible to form colloidal structures in solvents which are selective for either block. Therefore, we dissolved the block copolymers in a nonselective solvent like chloroform and slowly added isopropanol, a selective solvent for the P4VP block. For both block copolymers **8a** and **8b** a color shift from orange to deep purple (indicating colloidal aggregation along with crystallization of P3HT chains) occurred, and the colloidal solutions were stable over time. In contrast, addition of isopropanol to a chloroform solution of P3HT-alkyne **4a** led to a fast precipitation of the polymer. This indicates that in the block copolymer samples the stabilization of the solutions of P3HT-*b*-P4VPs occurs by the formation of self-assembled structures with P4VP in the shell. Dynamic light scattering measurements of the colloidal solutions showed structures with a hydrodynamic radius of 51 nm for **8a** and 44 nm for **8b** and a slightly broader distribution for **8b** than for **8a** (Figure 7a).

Further, UV–vis spectra of these colloidal solutions were measured to obtain preliminary information about the conformation of P3HT within the structures. The normalized UV–vis spectra are given in Figure 8. Both polymers show a broad absorption with distinct vibronic bands of P3HT. The absorption maximum is located at the vibronic band at about

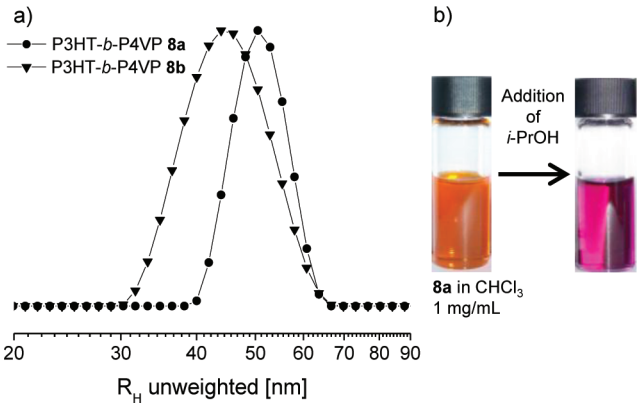


Figure 7. (a) Dynamic light scattering curves of P3HT-*b*-P4VP polymers **8a** and **8b** after addition of isopropanol to a 1 mg/mL solution in $CHCl_3$. (b) Photograph of 1 mg/mL solution of **8a** in $CHCl_3$ and after addition of isopropanol (*i*-PrOH).

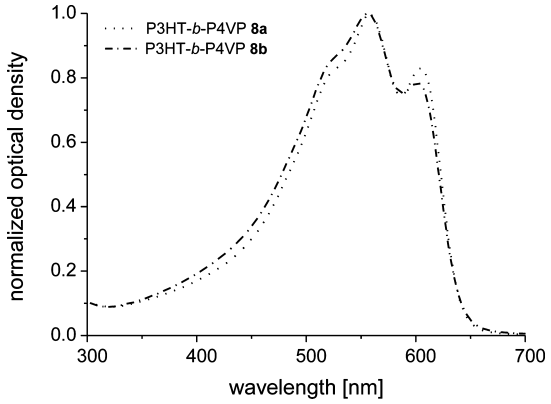


Figure 8. Normalized UV–vis spectra of colloidal solutions of P3HT-*b*-P4VP **8a** and **8b** obtained after addition of isopropanol to a 1 mg/mL solution in $CHCl_3$.

558 nm, and also a strong vibronic band is observed around 600 nm. However in **8a**, with a higher weight percent of P3HT, the intensity of the vibronic band at 600 nm is higher, and thus the packing seems different than in **8b**. In comparison with the spectra of the annealed films in Figure 5b, the vibronic structures of both colloids are much more pronounced than in the film. The high intensity of the vibronic band in the colloidal solution indicates that P3HT is crystalline within the colloidal aggregates. An earlier report correlating the UV–vis absorption spectra and crystallinity in P3HT supports our conclusion.[39] Usually in coil selective solvents, rod–coil block copolymers with a crystalline core tend to form structures with a low curvature like cylindrical micelles, vesicle, or lamella.[40] Further detailed investigations about the structure formation and the type of structures are currently underway.

■ CONCLUSION

We synthesized high molecular weight P3HT-alkyne and optimized the quenching conditions. It is important to choose methanol as a quenching reagent. Hydrochloric acid leads to addition reactions, chain–chain coupling, and a loss of alkyne end groups. From this P3HT-alkyne, by using the copper-catalyzed azide–alkyne "click" reaction, P3HT-alkoxyamine with a high molecular weight of 19 200 g/mol was synthesized as a macroinitiator for NMRP. Further, two block copolymers P3HT-*b*-P4VP with a P4VP content of 55 and 77 wt % were obtained. The thermal and optical properties depend on the P4VP content. However, because of the long P3HT block, the influence of the P4VP segment on the size of the crystallites was small. Microphase separation was observed for both block copolymers. In solution, we observed the formation of colloidal structures which are confirmed to have crystalline cores of P3HT according to UV–vis studies. Because of the amphiphilic nature of P3HT-*b*-P4VP, its semiconducting P3HT rod block, and its nanoparticle coordinating P4VP coil block, it is an interesting system for detailed investigations of structure formation in solution and for organic hybrid devices.

■ ASSOCIATED CONTENT

Ⓢ Supporting Information

Experimental details, additional MALDI-ToF MS spectra, ^1H NMR spectra, SEC curves, and UV–vis spectra. This material is available free of charge via the Internet at http://pubs.acs.org.

dx.doi.org/10.1021/ma2024733 | *Macromolecules* 2012, 45, 3070–3077

AUTHOR INFORMATION

Corresponding Author

*E-mail: mukundan.thelakkat@uni-bayreuth.de.

Notes

The authors declare no competing financial interest.

ACKNOWLEDGMENTS

We acknowledge financial support for this research work from DFG SFB 840. R. H. Lohwasser thanks the Elite network Bavaria for a research stipend. We thank Melanie Förtsch and Annika Pfaffenberger for TEM measurements.

REFERENCES

(1) Sirringhaus, H.; Tessler, N.; Friend, R. H. *Science* **1998**, *280*, 1741−1744.

(2) Ma, W.; Yang, C.; Gong, X.; Lee, K.; Heeger, A. J. *Adv. Funct. Mater.* **2005**, *15*, 1617−1622.

(3) Boudouris, B. W.; Frisbie, C. D.; Hillmyer, M. A. *Macromolecules* **2008**, *41*, 67−75.

(4) Liu, J.; Sheina, E. E.; Kowalewski, T.; McCullough, R. D. *Angew. Chem., Int. Ed.* **2002**, *41*, 329−332.

(5) Richard, F.; Brochon, C.; Leclerc, N.; Eckhardt, D.; Heiser, T.; Hadziioannou, G. *Macromol. Rapid Commun.* **2008**, *29*, 885−891.

(6) Sommer, M.; Lang, A. S.; Thelakkat, M. *Angew. Chem., Int. Ed.* **2008**, *47*, 7901−7904.

(7) Zhang, Q.; Cirpan, A.; Russel, T. P.; Emrick, T. *Macromolecules* **2009**, *42*, 1079−1082.

(8) Dai, C.; Yen, W.; Lee, Y.; Ho, C.; Su, W. *J. Am. Chem. Soc.* **2007**, *129*, 11036−11038.

(9) Moon, H. C.; Anthonysamy, A.; Lee, Y.; Kim, J. K. *Macromolecules* **2010**, *43*, 1747−1752.

(10) Higashihara, T.; Ohshimizu, K.; Hirao, A.; Ueda, M. *Macromolecules* **2008**, *41*, 9505−9507.

(11) Iovu, M. C.; Craley, C. R.; Jeffries-El, M.; Krankowski, A. B.; Zhang, R.; Kowalewski, T.; McCullough, R. D. *Macromolecules* **2007**, *40*, 4733−4735.

(12) Radano, C. P.; Schermen, O. A.; Stingelin-Stutzmann, N.; Müller, C.; Breiby, D. W.; Smith, P.; Janssen, R. A. J.; Mejier, E. W. *J. Am. Chem. Soc.* **2005**, *127*, 12502−12503.

(13) Li, Z.; Ono, R. J.; Wu, Z.; Bielawski, C. W. *Chem. Commun.* **2011**, *47*, 197−199.

(14) Tao, Y.; McCulloch, B.; Kim, S.; Segalman, R. A. *Soft Matter* **2009**, *5*, 4219−4230.

(15) Urien, M.; Erothu, H.; Cloutet, E.; Hiorns, R. C.; Vignau, L.; Cramail, H. *Macromolecules* **2008**, *41*, 7033−7040.

(16) Kolb, H. C.; Finn, M. G.; Sharpless, K. B. *Angew. Chem., Int. Ed.* **2001**, *40*, 2004−2021.

(17) Britze, A.; Möllmann, V.; Grundmeier, G.; Luftmann, H.; Kuckling, D. *Macromol. Chem. Phys.* **2011**, *212*, 679−690.

(18) Sary, N.; Richard, F.; Brochon, C.; Leclerc, M.; Leveque, P.; Audinot, J.; Berson, S.; Heiser, T.; Hadziioannou, G.; Mezzenga, R. *Adv. Mater.* **2009**, *21*, 1−6.

(19) Rajaram, S.; Armstrong, P. B.; Kim, B. J.; Fréchet, J. M. J. *Chem. Mater.* **2009**, *21*, 1775−1777.

(20) Sommer, M.; Hüttner, S.; Steiner, U.; Thelakkat, M. *Appl. Phys. Lett.* **2009**, *95*, 183308.

(21) Kline, R. J.; McGehee, M. D.; Kadnikova, E. N.; Liu, J.; Fréchet, J. M. J. *Adv. Mater.* **2003**, *15*, 1519−1522.

(22) Lan, Y.; Huang, C. *J. Phys. Chem. B* **2009**, *113*, 14555−14564.

(23) Zen, A.; Saphiannikova, M.; Neher, D.; Grenzer, J.; Grigorian, S.; Pietsch, U.; Asawapirom, U.; Janietz, S.; Scherf, U.; Lieberwirth, I.; Wegner, G. *Macromolecules* **2006**, *39*, 2162−2171.

(24) Jeffries-El, M.; Sauve, G.; McCullough, R. D. *Macromolecules* **2005**, *38*, 10346−10352.

(25) Wang, M.; Kumar, S.; Lee, A.; Felorzabihi, N.; Shen, L.; Zhao, F.; Froimowicz, P.; Scholes, Gr. D.; Winnik, M. A. *J. Am. Chem. Soc.* **2008**, *130*, 9481−9491.

(26) Palaniappan, K.; Hundt, N.; Sista, P.; Nguyen, H.; Heo, J.; Bhatt, M. P.; Han, Y.; Schmiedel, E. A.; Sheina, E. E.; Biewer, M. C.; Stefan, M. C. *J. Polym. Sci., Part A: Polym. Chem.* **2011**, *49*, 1802−1808.

(27) Aissou, K.; Pfaff, A.; Giacomelli, C.; Travelet, C.; Müller, A. H. E.; Borsali, R. *Macromol. Rapid Commun.* **2011**, *32*, 912−916.

(28) Huang, K.; Fang, Y.; Hsu, J.; Kuo, C.; Chang, W.; Chen, W. *J. Polym. Sci., Part A: Polym. Chem.* **2011**, *49*, 147−155.

(29) Patra, S. K.; Ahmed, R.; Whittell, G. R.; Lunn, D. J.; Dunphy, E. L.; Manners, I. *J. Am. Chem. Soc.* **2011**, *133*, 8842−8845.

(30) Lee, Y. H.; Yen, W. C.; Su, W. F.; Dai, C. A. *Soft Matter* **2011**, *7*, 10429−10442.

(31) Lohwasser, R. H.; Thelakkat, M. *Macromolecules* **2011**, *44*, 3388−3397.

(32) Miyakoshi, R.; Yokoyama, A.; Yokozawa, T. *Macromol. Rapid Commun.* **2004**, *25*, 1663−1666.

(33) Tolman, C. A.; Seidel, W. C.; Gosser, L. W. *Organometallics* **1983**, *2*, 1391−1396.

(34) Benanti, T. L.; Kalaydjian, A.; Venkataraman, D. *Macromolecules* **2008**, *41*, 8312−8315.

(35) Maria, S.; Susha, S.; Sommer, M.; Talapin, D. V.; Thelakkat, M. *Macromolecules* **2008**, *41*, 6081−6088.

(36) Wu, Z.; Petzold, A.; Henze, T.; Thurn-Albrecht, T.; Lohwasser, R. H.; Sommer, M.; Thelakkat, M. *Macromolecules* **2010**, *43*, 4646−4653.

(37) Clark, J.; Silva, C.; Friend, R. H.; Spano, F. C. *Phys. Rev. Lett.* **2007**, *98*, 206406.

(38) Clark, J.; Chang, J.; Spano, F. C.; Friend, R. H.; Silva, C. *Appl. Phys. Lett.* **2009**, *94*, 163306.

(39) Zhokhavets, U.; Erb, T.; Gobsch, G.; Al-Ibrahim, M.; Ambacher, O. *Chem. Phys. Lett.* **2006**, *419*, 347−350.

(40) Massey, J. A.; Temple, K.; Cao, L.; Rharbi, Y.; Raez, J.; Winnik, M. A.; Manners, I. *J. Am. Chem. Soc.* **2000**, *122*, 11577−11584.

NOTE ADDED AFTER ASAP PUBLICATION

This article posted ASAP on March 20, 2012. The caption of Figure 2 has been revised along with paragraph 1, sentence 6 of the Introduction section, and paragraph 5, sentence 9 of the Results and Discussion section. The correct version posted on March 27, 2012.

Macromolecules

Article

pubs.acs.org/Macromolecules

Luminescent Boron Quinolate Block Copolymers via RAFT Polymerization

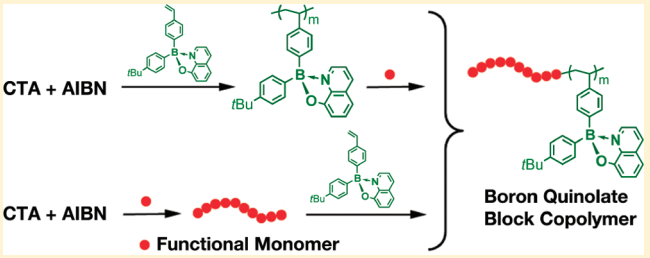
Fei Cheng,[†] Edward M. Bonder,[‡] and Frieder Jäkle[†,*]

[†]Department of Chemistry, Rutgers University—Newark, 73 Warren Street, Newark, New Jersey 07102, United States

[‡]Department of Biological Sciences, Rutgers University—Newark, 195 University Avenue, Newark, New Jersey 07102, United States

Supporting Information

ABSTRACT: The preparation of well-defined luminescent organoboron quinolate block copolymers via sequential RAFT polymerization is reported. Boron-containing block copolymers with PS, P(St-*alt*-MAh), and PNIPAM as the second block were successfully synthesized. The photophysical properties of the block copolymers were studied by UV−vis and fluorescence spectroscopy. Independent of the second block, the boron quinolate block copolymers that contain the parent 8-hydroxyquinolato ligand (PM1-*b*-PS, PM1-*b*-PNIPAM, PM1-*b*-P(St-*alt*-MAh)) are green luminescent, whereas a polymer with 5-(4-dimethylaminophenyl)-8-hydroxyquinolate as the ligand (PM2-*b*-PS) shows red luminescence. The P(St-*alt*-MAh)-based block copolymer was further modified with photoactive azobenzene groups. The self-assembly behavior of the amphiphilic block copolymers was studied by transmission electron microscopy (TEM) and dynamic light scattering (DLS). In water, PM1-*b*-PNIPAM forms spherical micelles. The azobenzene-modified P(St-*alt*-AbMA)-*b*-PM1 exhibits a solvent-dependent self-assembly behavior in basic solutions, and large spindle-shaped aggregates and spherical micelles were observed.



INTRODUCTION

Polymers containing main group elements have developed into a thriving field of research, and many interesting phenomena and new applications have recently emerged.[1] Among this important class of new materials, luminescent organoboron polymers have attracted great attention because of their potential applications as electronic device materials, chemical sensors and biomedical materials.[2] A broad range of synthetic methods, including hydroboration and organometallic condensation polymerization, transition metal-catalyzed polymerization, conventional and controlled free radical polymerization, and postpolymerization modification processes have been developed, and a variety of different boron-containing chromophores have been utilized to functionalize polyolefins.[3] To incorporate these organoborane chromophores into block copolymer structures is a desirable objective, especially when considering the well-known tendency of block copolymers to self-assemble into nanostructured materials and the possibility for realizing stimuli-responsive luminescent behavior in solution.[4]

Much of the early work on boron-containing block copolymers has been directed at borane and carborane-functionalized systems for applications as precursors to nanostructured ceramic materials.[5] The development of boronic acid-functionalized polymers that are responsive to changes in pH and temperature, as well as the presence of sugars and other polyols has also developed into a flourishing research field.[6] However, only recently have the first examples of luminescent boron-containing block copolymers been reported. Chujo and co-workers applied reversible addition−fragmentation chain transfer (RAFT)[7,8] polymerization to synthesize luminescent block copolymers with boron dipyrromethene (BODIPY) dyes in the side chain.[9] In THF, driven by $\pi-\pi$ stacking interactions of the BODIPY groups, the block copolymers form luminescent nanoparticles with enhanced quantum efficiency. Temperature-responsive BODIPY copolymers with dimethylaminoethyl methacrylate (DMAEMA) were introduced by Chujo and copolymers with 2-(2-methoxyethoxy)ethyl methacrylate by Liras and co-workers.[10] Using a difluoroboron dibenzoylmethane chromophore-functionalized initiator for the ring-opening polymerization of lactide and caprolactone, Fraser and co-workers prepared a series of biocompatible luminescent polymers and block copolymers.[11] With increasing molecular weight, the luminescence of the polymers shifts from green to blue in the solid state, which was attributed to reduced excited-state stabilization upon dilution of the chromophore. The polymers were used as bioimaging agents to label living cells and tumor tissues[12] and as a new class of mechano-responsive[13] materials.

In a recent communication, we described the synthesis of the first organoboron quinolate block copolymers by RAFT polymerization using trithiocarbonate-modified PEO as a macro chain transfer agent (macro-CTA).[14] The resulting amphiphilic block copolymers form luminescent micelles in

Received: January 9, 2012
Revised: March 11, 2012
Published: March 28, 2012

 © 2012 American Chemical Society

aqueous solution that show good long-term stability. Another attractive feature is that the luminescence characteristics of boron quinolate chromophores can be readily tuned through modifications in the substitution pattern of the 8-hydroxyquinoline ligand.[15−17] Herein, we describe an alternative, highly versatile approach to these types of materials, in which we use sequential RAFT polymerization to prepare a range of different luminescent organoboron quinolate block copolymers.

EXPERIMENTAL SECTION

General Methods. The 499.9 MHz ^{1}H and 125.7 MHz ^{13}C NMR spectra were recorded on a Varian INOVA 500 MHz spectrometer. The 160.4 MHz ^{11}B NMR spectra were recorded with a boron-free probe using boron-free quartz NMR tubes. The ^{1}H and ^{13}C NMR spectra were referenced internally to the solvent peaks and the ^{11}B NMR spectra externally to $BF_3{\cdot}Et_2O$ (δ = 0) in C_6D_6. Elemental analyses were performed by Quantitative Technologies Inc. (Whitehouse, NJ).

GPC−RI analyses were performed in THF (1.0 mL/min) or DMF with 0.2% w/v of $[Bu_4N]Br$ (0.50 mL/min) using a Waters Empower system equipped with a 717plus autosampler, a 1525 binary HPLC pump, a 2487 dual λ absorbance detector, and a 2414 refractive index detector. Three styragel columns (Polymer Laboratories; two 5 μm Mix-C and one 10 μm Mix-D), which were kept in a column heater at 35 °C (THF), or a set of two polyvinylalcohol columns (Shodex Asahipak; one 5 μm GF-510 HQ and one 9 μm GF-310 HQ) at 65 °C (DMF) were used for separation. The columns were calibrated with polystyrene standards (Polymer Laboratories, Varian Inc.). Multiangle laser light scattering (GPC−MALLS) experiments were performed at 690 nm (30 mW linear polarized GaAs laser) using a Wyatt Dawn EOS instrument in-line with the GPC, using the columns specified above. A Wyatt Optilab refractive index detector operated at 690 nm was used as the concentration detector and differential refractive indices dn/dc were calculated with the Wyatt Astra software assuming 100% mass recovery. The triple detection GPC measurement was preformed using a Viscotek TDA305 Max triple detection SEC system by Malvern. DMF with 30 mM LiBr was used as the eluent at a temperature of 50 °C and a flow rate of 1.0 mL/min. Two Viscotek I-MBHMW-3078 mixed-bed high molecular weight columns with an exclusion limit >10 million g/mol) were used for separation. The dynamic light scattering (DLS) measurement was performed at 25.0 ± 1 °C with a Malver Zetasizer Nano-ZS instrument, equipped with a 4 mW, 633 nm He−Ne laser and an Avalanche photodiode detector at an angle of 173°.

UV−vis absorption data were acquired on a Varian Cary 500 UV−vis NIR spectrophotometer. The mass fraction of the boron quinolate block in the copolymers was determined by preparing solutions of known concentration and measuring the UV−vis absorbance at the absorption maximum of the respective boron chromophore. Assuming that the absorptivity of the individual chromophores is independent of the polymer architecture, we used the molar absorptivity of the homopolymers (ε_{394} = 2460 M^{-1} cm^{-1} per homopolymer repeat unit of PM1 and ε_{440} = 3710 M^{-1} cm^{-1} per homopolymer repeat of PM2) as the reference. The fluorescence data and quantum yields were measured on a Varian Cary Eclipse fluorescence spectrophotometer with optically dilute solutions (A < 0.1). Anthracene was used as the standard, and the quantum yield of anthracene (0.33 in THF) was adopted from ref 18. Sample solutions were prepared using a microbalance (±0.1 mg) and volumetric glassware. The quantum yields were calculated by plotting a graph of integrated fluorescence intensity vs absorbance of at least four solutions with increasing concentration. The gradient of the graph is proportional to the quantum yield.

Transmission electron microscopy (TEM) was conducted on a FEI Tecnai 12 electron microscope operated at 80 kV. One drop of polymer micelle solution was cast on a copper grid with a carbon coating. The water solvent was allowed to evaporate, and then the sample was stained using an aqueous uranyl acetate solution (1% w/w).

Materials. 1,4-Dioxane and THF were distilled from Na/benzophenone prior to use. Azobis(isobutyronitrile) (AIBN) initiator was recrystallized in methanol. Styrene was purified by passing it through a neutral alumina column and then distilled under reduced pressure. Maleic anhydride was purified by recrystallization in toluene, and *N*-isopropylacrylamide (NIPAM) in a hexanes/benzene mixture. All other solvents and chemicals were used without further purification. The chain transfer agents (CTAs) used in this work were synthesized according to literature procedures.[19] The organoboron quinolate monomers (M1, M2) and the corresponding homopolymers (PM1, PM2) were prepared as previously described.[14]

Synthesis of Polystyrene Macro-CTA (PS). To a Schlenk tube, styrene (15.62 g, 150 mmol), benzyl dithiobenzoate (BDTB) (122 mg, 0.500 mmol) and AIBN (20.6 mg, 0.125 mmol) were loaded. After three freeze−pump−thaw cycles, the tube was immersed for 3.5 h in an 80 °C oil bath under stirring. After quenching in liquid nitrogen, the polymer was precipitated three times by dropwise addition of a THF solution of the polymer to a 10-fold volume of methanol. The PS macro-CTA was obtained as a light pink powder after drying in high vacuum. Yield: 4.10 g (26% conversion assuming quantitative recovery). GPC−RI (THF): M_n = 8130 g/mol, PDI = 1.16. GPC−MALLS (THF): M_n = 9470 g/mol, PDI = 1.14, dn/dc = 0.178 mL/g.

Synthesis of Poly(styrene-*alt*-maleic anhydride) (P(St-*alt*-MAh)). A Schlenk tube was loaded with styrene (1.56 g, 15.0 mmol), MAh (1.47 g, 15.0 mmol), BDTB (45.5 mg, 0.167 mmol), AIBN (3.4 mg, 0.021 mmol) and 7.0 mL of dioxane. After three freeze−pump−thaw cycles, the tube was immersed for 3.0 h in a 70 °C oil bath under stirring. After quenching in liquid nitrogen, the polymer was precipitated three times by dropwise addition of a THF solution of the polymer to a 10-fold volume of dry ether. P(St-*alt*-MAh) macro-CTA was obtained as a light pink powder after drying in high vacuum. Yield: 0.69 g (21% conversion assuming quantitative recovery). GPC−RI (DMF, 0.2% $[Bu_4N]Br$): M_n = 10400 g/mol, PDI = 1.28. Triple detection GPC (DMF, 30 mM LiBr): M_n = 4500 g/mol, PDI = 1.26, dn/dc = 0.111 mL/g.

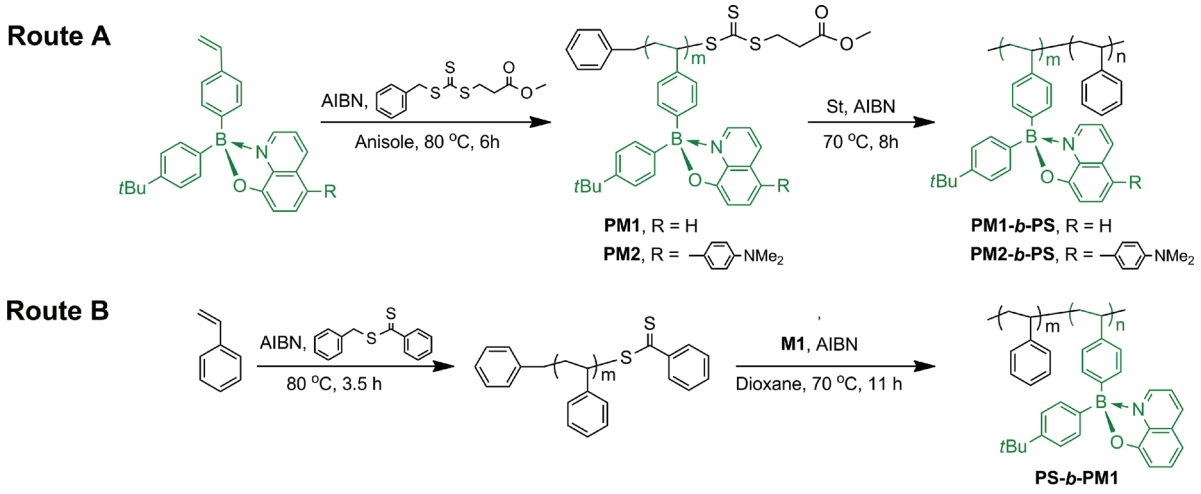
Synthesis of PM1-*b*-PS. A Schlenk tube was loaded with PM1 (25.0 mg, 1.85 μmol; M_n = 13500 g/mol by GPC−MALLS), AIBN (0.10 mg, 0.61 μmol), and styrene (0.70 mL, 6.1 mmol). After three freeze−pump−thaw cycles, the tube was immersed for 8.0 h in a 70 °C oil bath under stirring. After quenching in liquid nitrogen, the polymer was precipitated twice by dropwise addition of a THF solution of the polymer to a 10-fold volume of methanol. PM1-*b*-PS was obtained as a yellow powder after drying in high vacuum. Yield: 80 mg (9% conversion assuming quantitative recovery). GPC−RI (THF): M_n = 32900 g/mol, PDI = 1.27. GPC−MALLS (THF): M_n = 43300 g/mol, PDI = 1.18, dn/dc = 0.201 mL/g. PM1 mass fraction by UV−vis analysis: 0.296.

Synthesis of PM2-*b*-PS. A Schlenk tube was loaded with PM2 (25.0 mg, 1.94 μmol), AIBN (0.13 mg, 0.79 μmol; M_n = 12900 g/mol by GPC−MALLS) and styrene (1.0 mL, 8.7 mmol). After three freeze−pump−thaw cycles, the tube was immersed for 8.0 h in a 70 °C oil bath under stirring. After quenching in liquid nitrogen, the polymer was precipitated twice by dropwise addition of a THF solution of the polymer to a 10-fold volume of methanol. PM2-*b*-PS was obtained as a red powder after drying in high vacuum. Yield: 130 mg (9% conversion assuming quantitative recovery). GPC−RI (THF): M_n = 58400 g/mol, PDI = 1.26. GPC−MALLS (THF): M_n = 64800 g/mol, PDI = 1.24, dn/dc = 0.198 mL/g. PM2 mass fraction by UV−vis analysis: 0.190.

Synthesis of PS-*b*-PM1. A Schlenk tube was loaded with PS macro-CTA (50.0 mg, 6.15 μmol; M_n = 9470 g/mol by GPC−MALLS), AIBN (0.34 mg, 2.1 μmol), M1 (241 mg, 0.615 mmol), and 2.0 mL of dioxane. After 3 freeze−pump−thaw cycles, the tube was immersed for 11 h in a 70 °C oil bath under stirring. After quenching in liquid nitrogen, the polymer was precipitated twice by dropwise addition of a THF solution of the polymer to a 10-fold volume of methanol. PS-*b*-PM1 was obtained as a yellow powder after drying in high vacuum. Yield: 145 mg (39% conversion assuming quantitative recovery). GPC−RI (THF): M_n = 16000 g/mol, PDI = 1.29. GPC−

dx.doi.org/10.1021/ma300063r | *Macromolecules* 2012, 45, 3078−3085

Scheme 1. Synthesis Routes to PS-Based Block Copolymers



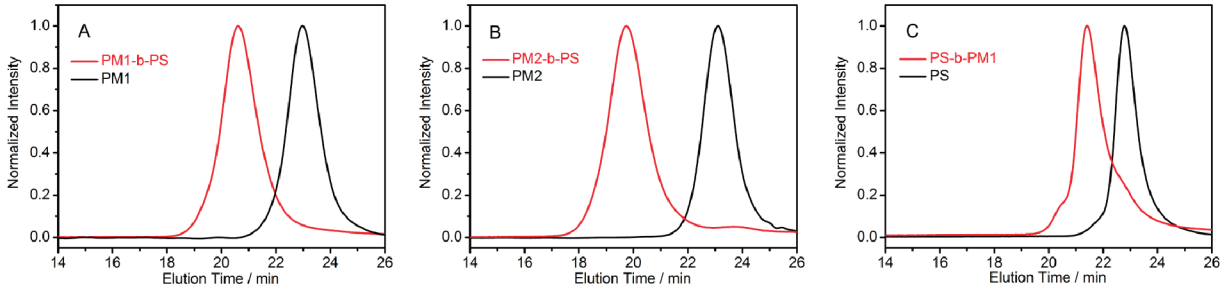


Figure 1. GPC overlays of block copolymers and corresponding macro-CTA precursors: (A) PM1-*b*-PS and PM1; (B) PM2-*b*-PS and PM2; (C) PS-*b*-PM1 and PS. All samples were analyzed in THF at 1.0 mL/min with PS calibration.

MALLS (THF): M_n = 33000 g/mol, PDI = 1.21, d*n*/d*c* = 0.206 mL/g. PM1 mass fraction by UV−vis analysis: 0.670.

Synthesis of PM1-*b*-PNIPAM. In a Schlenk tube, PM1 (45.0 mg, 1.63 μmol; M_n = 27600 g/mol by GPC−MALLS), AIBN (0.12 mg, 0.73 μmol) and NIPAM (600 mg, 5.30 mmol) were dissolved in 0.8 mL of dioxane. After 3 freeze−pump−thaw cycles, the tube was immersed for 8.0 h in a 70 °C oil bath under stirring. After quenching in liquid nitrogen, the polymer was precipitated three times by dropwise addition of a DMF solution of the polymer to a 10-fold volume of diethyl ether. PM1-*b*-PNIPAM was obtained as a yellow powder after drying in high vacuum. Yield: 605 mg (93% conversion assuming quantitative recovery). GPC−RI (DMF with 0.2% [Bu_4N]-Br): M_n = 107200 g/mol, PDI = 1.27. PM1 mass fraction by UV−vis analysis: 0.123.

Synthesis of P(St-*alt*-MAh)-*b*-PM1. A Schlenk tube was loaded with P(St-*alt*-MAh) macro-CTA (30 mg, 6.7 μmol; M_n = 4520 g/mol by triple detection GPC), AIBN (0.38 mg, 2.3 μmol), M1 (226 mg, 0.58 mmol), and 2.0 mL of dioxane. After 3 freeze−pump−thaw cycles, the tube was immersed for 8.0 h in a 70 °C oil bath under stirring. After quenching in liquid nitrogen, the polymer was precipitated twice by dropwise addition of a THF solution of the polymer to a 10-fold volume of diethyl ether. P(St-*alt*-MAh)-*b*-PM1 was obtained as a yellow powder after drying in high vacuum. Yield: 150 mg (53% conversion assuming quantitative recovery). GPC−RI (DMF with 0.2% [Bu_4N]Br): M_n = 22400 g/mol, PDI = 1.34. The absolute molecular weight was determined by UV−vis analysis assuming that M_n = 4520 g/mol for the first block: M_n, = 19500 g/mol. PM1 mass fraction by UV−vis analysis: 0.768.

Synthesis of P(St-*alt*-AbMA)-*b*-PM1 by Postmodification of P(St-*alt*-MAh)-*b*-PM1. In a Schlenk flask, P(St-*alt*-MAh)$_m$-*b*-PM1$_n$ (40 mg, for n = 22, m = 38: 0.19 mmol MAh functional groups) and 4-aminoazobenzene (94 mg, 0.48 mmol) were dissolved in 3.0 mL of dry THF. The mixture was purged with nitrogen for 10 min and then sealed. After stirring at 80 °C for 48 h, the mixture was precipitated twice by dropwise addition of a THF solution of the polymer to a 10-fold volume of diethyl ether. The product was obtained as an orange powder after drying in high vacuum. Yield: 35 mg. GPC−RI (DMF with 0.2% [Bu_4N]Br): M_n = 25500 g/mol, PDI = 1.40.

Photoisomerization Experiments. Solutions of P(St-*alt*-AbMA) and P(St-*alt*-AbMA)-*b*-PM1 (ca. 0.025 mg mL^{-1} in THF), respectively, were irradiated at 330−360 nm using a commercial Hg lamp equipped with appropriate filters and the progress of the isomerization process was monitored by UV−vis spectroscopy.

Self-Assembly of PM1-*b*-PNIPAM in Water. A 2.0 mg sample of block copolymer was dissolved in 10.0 mL of DMF. The block copolymer solution in DMF was loaded in a dialysis tube (cutoff molecular weight = 6−8 kDa) and dialyzed against ∼1 L of deionized water for 3 days. The DMF solvent was completely removed by exchanging with fresh water five times. The resulting block copolymer solution was used for both DLS and TEM analysis.

Self-Assembly of P(St-*alt*-AbMA)-*b*-PM1 in Basic Solution. Two solutions of P(St-*alt*-AbMA)-*b*-PM1 in THF were prepared at a concentration of 0.5 mg/mL. To one of the solutions was added 5% aq. $NaHCO_3$ dropwise under stirring. The final ratio of THF/5% aqueous $NaHCO_3$ was set to be 1:9. The second polymer solution was dialyzed against 5% aqueous $NaHCO_3$ to completely remove the THF solvent. The resulting block copolymer solutions were drop-cast onto a copper grid and examined by TEM.

RESULTS AND DISCUSSION

Two different synthetic routes were studied for the preparation of PS-based block copolymers as shown in Scheme 1. In the first method, we synthesized two organoboron quinolate homopolymers (PM1 and PM2) by RAFT polymerization, which were then used as macro-CTAs to control the polymerization of styrene (route A, Scheme 1). The synthesis of the boron homopolymer precursors with a trithiocarbonate

dx.doi.org/10.1021/ma300063r | *Macromolecules* 2012, 45, 3078−3085

CTA was reported in a prior communication.[14] The polymerization kinetic study and GPC results of the purified polymers demonstrated good polymerization control, and low dispersity macro-CTAs were obtained. The absolute molecular weights of PM1 and PM2 were determined to be 13500 and 12900 g/mol by GPC−MALLS analysis.

To synthesize the block copolymers, bulk polymerization of styrene was conducted at 70 °C with AIBN as the initiator, and PM1 or PM2 as macro-CTA. The conversion was kept relatively low, as the styrene monomer served as the solvent for the resulting block copolymer. The GPC−RI results for the block copolymers and the corresponding precursors are shown in parts A and B of Figure 1. Reasonably narrow and symmetric peaks, at shorter elution times than for the homopolymers, are consistent with chain extension, indicating the effectiveness of PM1 and PM2 as macro-CTAs. Molecular weights of M_n = 32900 g/mol (PDI = 1.27) for PM1-*b*-PS and M_n = 58400 g/mol (PDI = 1.26) for PM2-*b*-PS were determined relative to PS standards. The absolute molecular weights of the block copolymers by GPC−MALLS are higher than the values from GPC−RI relative to PS standards, which is in accord with our previous GPC studies on organoboron quinolate homopolymers.[17]

The ^{1}H and ^{11}B NMR spectra of both block copolymers are shown in Figure 2. In the ^{1}H NMR spectra, the signals of the PS blocks are clearly seen. The signals of the boron quinolate blocks are comparatively very weak, due to the much lower molecular weights relative to those of the PS blocks (Table 1), and they are somewhat obscured by overlap with signals of the PS blocks. Nevertheless, the NMe_2 group of PM2-*b*-PS and the ^{t}Bu group of each of the block copolymers are clearly observed in both the ^{1}H and ^{13}C NMR spectra (Figure 2 and Figure S1, Supporting Information). Moreover, both block copolymers show one single peak at 7.6 ppm in the ^{11}B NMR, further supporting the presence of the boron quinolate blocks. The GPC and NMR analyses thus clearly demonstrate that well-defined PS-based block copolymers of fairly high molecular weight were obtained successfully.

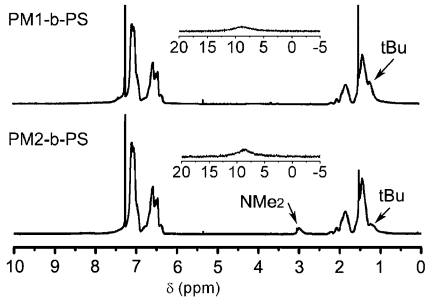


Figure 2. ^{1}H NMR spectra of PM1-*b*-PS and PM2-*b*-PS in $CDCl_3$. The corresponding ^{11}B NMR spectra are shown as insets.

An alternative route to PS-based block copolymers is to use PS as macro-CTA to control the polymerization of boron quinolate monomers as shown in Scheme 1 (route B). A narrow PS macro-CTA (GPC−MALLS: M_n = 9470 g/mol, PDI = 1.14) was synthesized with AIBN and BDTB in bulk at 80 °C. The chain extension of the PS precursor with M1 was conducted in dioxane at 70 °C with AIBN as the initiator. The NMR data for the product are similar to those of PM1-*b*-PS, but the signals for the PM1 block are more readily observed in this case, indicating that the lengths of the blocks are more similar for PS-*b*-PM1 (Figure S1, Supporting Information). This result was confirmed by GPC analysis, which shows apparent chain extension to form a block copolymer (GPC−MALLS: M_n = 33000 g/mol, PDI = 1.21) with an average of 89 styrene and 60 boron quinolate repeat units (Figure 1C). However, small shoulder peaks on both the high and low molecular weight sides are apparent. The high molecular weight shoulder is likely a result of chain−chain coupling at the late stage of polymerization, while the low molecular weight shoulder could be due to incomplete chain extension of the PS precursor or retardation. It is well-known that in the synthesis of block copolymers via RAFT polymerization, the chain transfer constant of the first block should be higher than (or at least comparable to) that of the second block.[20] On the basis of the GPC results (Figure 1, parts A and C), we conclude that the styrene and styryl-type boron quinolate monomers are interchangeable in the block copolymer synthesis via RAFT, but route A is preferable. This could be related to the sterically demanding structure and electron-rich nature of the boron quinolate monomer, which might impact the crossover step from styrene to boron quinolate as a monomer. Another reason for route A to give better results is likely due to the fact that the chain extension of PM1 can be performed in bulk styrene,

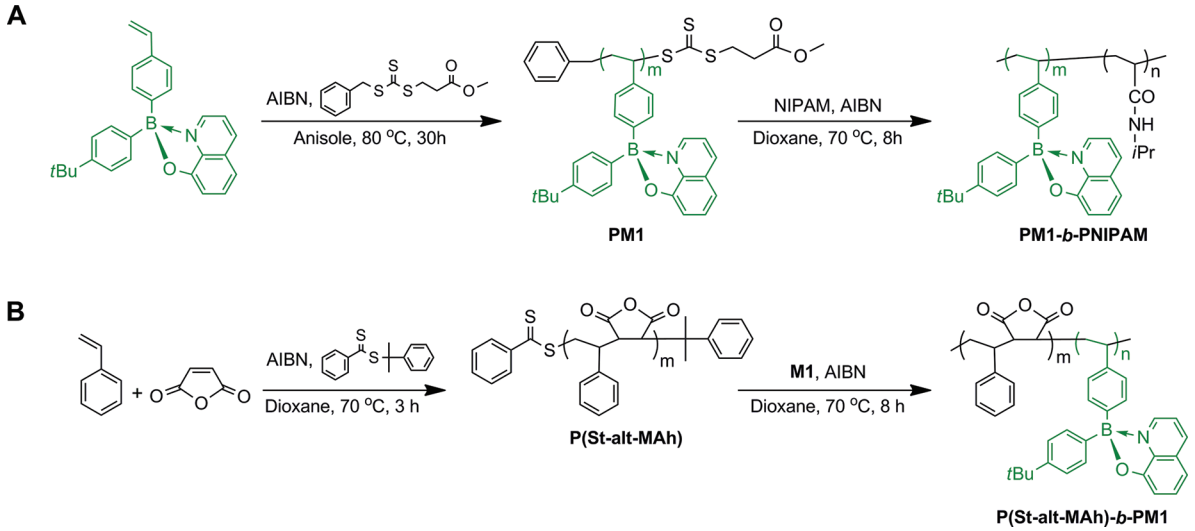
Table 1. Summary of Molecular Weight Data of Organoboron Quinolate Block Copolymers and the Corresponding Macro-CTA Precursors

polymer[a]	$M_{n,GPC}$[b]	PDI_{GPC}[b]	$M_{n,MALLS}$[c]	PDI_{MALLS}[c]	$M_{n,UV}$[b]	m, n_{MALLS}[c,e]	m, n_{UV}[d,e]
$PM1_m$	5800	1.21	13 500	1.23		34	
$PM1_m$-*b*-PS_n	32 900	1.27	43 300	1.18	45 600	34, 290	34, 308
$PM2_m$	4500	1.18	12 900	1.25		25	
$PM2_m$-*b*-PS_n	58 400	1.26	64 800	1.24	67 900	25, 500	25, 528
PS_m	8130	1.16	9470	1.14		89	
PS_m-*b*-$PM1_n$	16 000	1.29	33 000	1.21	28 700	89, 60	89, 49
$PM1_m$	8710	1.28	27 600	1.22		70	
$PM1_m$-*b*-$PNIPAM_n$	107 200	1.27	*f*	*f*	224400[e]	*f*	70, 1740
$P(St\text{-}alt\text{-}MAh)_m$	10 400	1.28	4520	1.26		22	
$P(St\text{-}alt\text{-}MAh)_m$-*b*-$PM1_n$	22 400	1.34	*f*	*f*	19500[e]	*f*	22, 38

[a]For the block copolymers, the block sequence corresponds to the polymerization sequence. [b]Determined by GPC−RI analysis. [c]Determined by GPC−MALLS analysis or triple-detection GPC (for $P(St\text{-}alt\text{-}MAh)_m$). [d]Based on UV−vis analysis and absolute molecular weight data for the homopolymer precursor (ε_{394} = 2460 M^{-1} cm^{-1} per repeat unit of PM1, ε_{440} = 3710 M^{-1} cm^{-1} per repeat unit of PM2). [e]*m* and *n* refer to the degree of polymerization of the first and second block, respectively. [f]Not measured.

dx.doi.org/10.1021/ma300063r | *Macromolecules* 2012, 45, 3078−3085

Scheme 2. Synthesis Routes to PM1-*b*-PNIPAM and P(St-*alt*-MAh)-*b*-PM1



whereas the chain extension of PS with crystalline M1 requires the use of considerable amounts of dioxane as a solvent.

Encouraged by these results, we decided to pursue luminescent boron block copolymers, in which the second block provides additional functionality or responsive properties. PNIPAM and its block copolymers have drawn much interest due to their thermo-responsive behavior in water, which renders them useful as building blocks for self-assembly and smart materials.[21] A PM1-based macro-CTA (GPC−MALLS: M_n = 27600 g/mol, PDI = 1.28) was used to synthesize the block copolymer PM1-*b*-PNIPAM (Scheme 2A). Because DMF phase GPC is not suitable for the PM1 homopolymer, and THF phase GPC is not suitable for the high molecular weight PNIPAM block copolymer, we could not characterize the precursor and the block copolymer under the same GPC conditions. However, by using THF phase GPC for PM1 and DMF phase GPC for PM1-*b*-PNIPAM, and the same PS standards, the molecular weights and distributions were obtained (Table 1). The GPC curve of PM1-*b*-PNIPAM (Figure S2, Supporting Information) indicates well-controlled polymerization and the formation of a narrow, high molecular weight block copolymer. Because the PNIPAM block is much longer than the PM1 precursor block, the ^{1}H and ^{13}C NMR signals of the latter are not easily observed (Figure S3, Supporting Information). However, an ^{11}B NMR signal at the same chemical shift as for the previous block copolymers confirms the presence of the PM1 block, as do the absorption and emission characteristics described *vide infra*.

We explored the self-assembly of the luminescent amphiphilic PM1-*b*-PNIPAM block copolymer in water. A solution of PM1-*b*-PNIPAM in DMF (0.2 mg/mL) was dialyzed against deionized water to remove the DMF solvent. Under these conditions, micelles with a hydrophobic PM1 core and hydrophilic PNIPAM shell are expected to form. The micelle solution was examined by TEM and DLS (Figure 3). The TEM image reveals the formation of quite regular spherical micelles with an average diameter of ca. 25 nm. Some larger structures are also apparent, possibly indicating the presence of higher aggregates. An average $\langle D_h \rangle$ of 45 nm was determined by DLS, which is significantly larger than the size deduced from the TEM image, which is likely because of shrinkage of the PNIPAM corona upon deposition on the TEM substrate. The

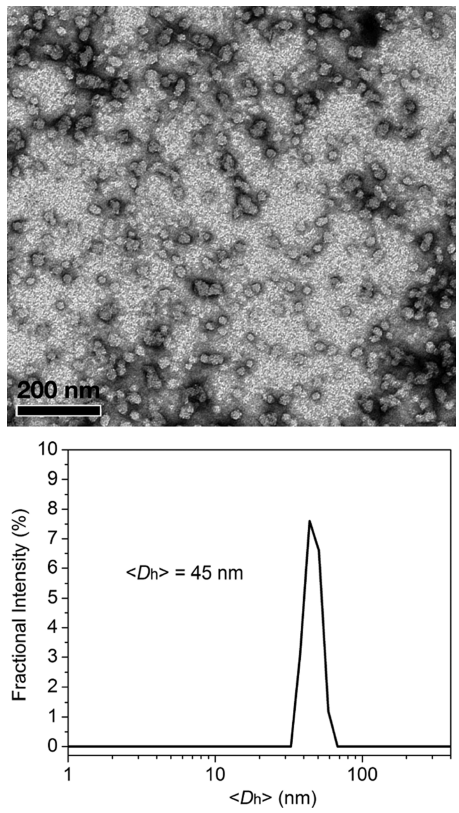


Figure 3. TEM image with uranyl acetate staining (top) and size distribution histogram (bottom) of PM1-*b*-PNIPAM micelles in water.

micelle solution shows good chemical and colloidal stability for at least 3 months.

P(St-*alt*-MAh) is a classic alternating copolymer which can be synthesized by conventional and controlled free radical polymerization. The reactive MAh repeating unit serves as a functional site for facile postmodification of the P(St-*alt*-MAh) polymer. Recently, the synthesis of P(St-*alt*-MAh) based block copolymers via RAFT has been pursued by several groups. Zhu et al. reported a one-pot procedure to synthesize P(St-*alt*-MAh)-*b*-PS using a high St/MAh ratio.[22] In the early stages of polymerization, St and MAh were incorporated in an

dx.doi.org/10.1021/ma300063r | *Macromolecules* 2012, 45, 3078−3085

alternating fashion into the living polymer chain. After the MAh monomer was exhausted, homopolymerization of styrene occurred, leading to a P(St-*alt*-MAh)-*b*-PS block copolymer. The Wooley group used RAFT-polymerized P(St-*alt*-MAh) to control the copolymerization of styrene and other styryl-type monomers.[23]

We decided to pursue the synthesis of a luminescent block copolymer P(St-*alt*-MAh)-*b*-PM1, by RAFT polymerization (Scheme 2B). As discussed above, RAFT-polymerized P(St-*alt*-MAh) is an effective CTA for styrene polymerization. Since our boron quinolate monomer M1 is a derivative of styrene, we chose P(St-*alt*-MAh) as macro-CTA to control the polymerization of M1. First, the copolymerization of styrene and maleic anhydride was carried out in dioxane at 70 °C for 3 h with AIBN as the initiator and cumyl dithiobenzoate as CTA. The P(St-*alt*-MAh) precursor was analyzed by triple-detection GPC in DMF 30 mM LiBr (M_n = 4500 g/mol, PDI = 1.26). The chemical shift of the *ipso*-carbon of the styrene repeating units is known to be sensitive to the sequence distribution of St/MAh copolymers.[24] The observed chemical shift at 140.5–136.5 ppm in the ^{13}C NMR of our P(St-*alt*-MAh) sample is consistent with an alternating sequence (Figure S4, Supporting Information). The block copolymer P(St-*alt*-MAh)-*b*-PM1 (M_n = 22400 g/mol, PDI = 1.34 in DMF with 0.2% [Bu_4N]Br) was then synthesized by AIBN-initiated chain extension with M1 in dioxane at 70 °C for 8 h. The GPC results indicate successful chain extension.

The ^{1}H, ^{11}B, and ^{13}C NMR spectra of P(St-*alt*-MAh)-*b*-PM1 in $CDCl_3$ are shown in Figure 4. In the ^{1}H NMR, the broad

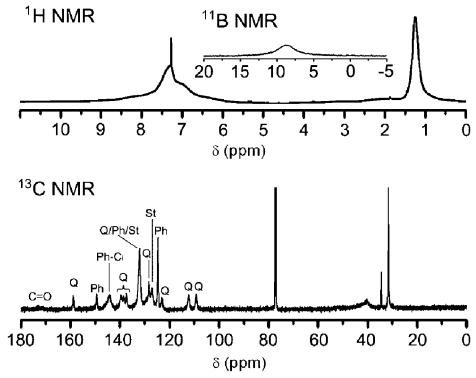


Figure 4. ^{1}H, ^{11}B, and ^{13}C NMR spectra of P(St-*alt*-MAh)-*b*-PM1 in $CDCl_3$; Q = quinolate carbon.

signals of the PM1 block overlap with those of the P(St-*alt*-MAh) block. The ^{11}B NMR shows a single and symmetric peak at a chemical shift of 7.6 ppm, which is identical to that of the PM1-*b*-PS block copolymer. On the basis of the GPC results (Table 1), the PM1 block is relatively longer than the P(St-*alt*-MAh) block, hence the ^{13}C NMR signals of the PM1 block are clearly seen. They match those of the PM1 homopolymer (see Figure S1, Supporting Information). The GPC and NMR characterization suggest that a well-defined P(St-*alt*-MAh)-*b*-PM1 block copolymer was obtained successfully.

The copolymer P(St-*alt*-MAh)-*b*-PM1 lends itself to further functionalization by amidolysis of the maleic anhydride moieties.[25] To explore this possibility, we decided to react the block copolymer with 4-aminoazobenzene, which is expected to lead to decoration with photoresponsive azobenzene chromophores with simultaneous introduction of hydrophilic carboxylate groups. The postmodification was conducted in THF by addition of an excess 4-aminoazobenzene. Unreacted 4-aminoazobenzene was completely removed by precipitation in diethyl ether as confirmed by the absence of any sharp signals in the ^{1}H NMR spectrum. GPC analysis of the product in DMF with 0.2% M [Bu_4N]Br revealed an apparent molecular weight of M_n = 25500 g/mol (PDI = 1.40) for the azobenzene-modified block polymer P(St-*alt*-AbMA)-*b*-PM1, which is slightly larger than that of the precursor P(St-*alt*-MAh)-*b*-PM1 (M_n = 22400 g/mol, Table 1). Because of signal overlap in the aromatic region, ^{1}H NMR did not allow us to clearly identify the polymer-attached azobenzene groups (Figure S5, Supporting Information). However, successful polymer modification is clearly evident from comparison of the IR (Figure S6, Supporting Information) and UV–vis data (vide infra) with those of the respective building blocks and precursor polymers.

The formation of carboxylate groups upon ring-opening of the maleic anhydride moieties is expected to render the block copolymer P(St-*alt*-AbMA)-*b*-PM1 amphiphilic under moderately basic conditions. Thus, the self-assembly behavior of P(St-*alt*-AbMA)-*b*-PM1 was first investigated in aqueous $NaHCO_3$ (5 wt %). Dissolution in THF and subsequent dialysis against 5 wt % aqueous $NaHCO_3$ initially resulted in a turbid solution, from which a precipitate formed within ca. 12 h. A TEM image of the freshly prepared solution revealed micrometer-sized, spindle-like structures (Figure 5A), which is consistent with

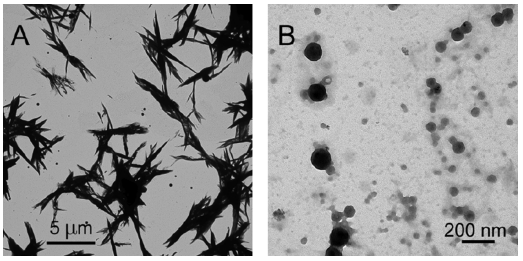


Figure 5. TEM images of P(St-*alt*-AbMA)-*b*-PM1 in (A) 5% aqueous $NaHCO_3$ and (B) THF/5% aqueous $NaHCO_3$ = 1:9.

formation of a semihydrophilic postmodified block P(St-*alt*-AbMA) that does not contain enough carboxylate groups to stabilize the hydrophobic PM1 block in water. To further enhance the solubility of the P(St-*alt*-AbMA) block, a mixture of THF/5% aq $NaHCO_3$ was used as solvent. In THF/5% aqueous $NaHCO_3$ = 1:9, polydispersed spherical structures were observed (Figure 5B).

The photophysical properties of all block copolymers were examined by UV–vis and fluorescence spectroscopy in THF. A comparison of the absorption and emission spectra of the PS-based block copolymers is shown in Figure 6. PM1-*b*-PS shows absorption and emission maxima at 394 and 505 nm, respectively. In contrast, the absorption and emission maxima of PM2-*b*-PS are red-shifted to 440 and 620 nm, respectively, as a result of charge transfer between the $-C_6H_4NMe_2$ substituent and the quinolate moiety.[16,17] The other block copolymers, PS-*b*-PM1, PM1-*b*-PNIPAM, and P(St-*alt*-MAh)-*b*-PM1 show absorption and emission profiles that are almost identical to those of PM1-*b*-PS (Table 2).

The quantum yields of all block copolymers in THF were measured and the data are summarized in Table 2. The quantum yields for the PM1-based block copolymers are in the

dx.doi.org/10.1021/ma300063r | *Macromolecules* 2012, 45, 3078–3085

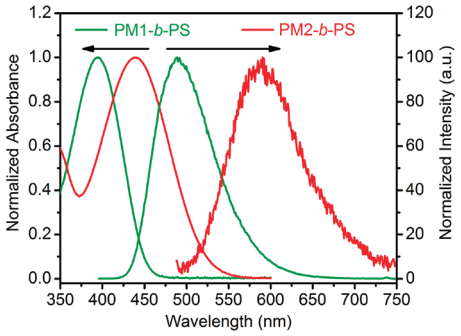


Figure 6. UV−vis and fluorescence spectra of PM1-*b*-PS (green lines, λ_{exc} = 394 nm) and PM2-*b*-PS (red lines, λ_{exc} = 440 nm) in THF.

Table 2. Photophysical Data of Organoboron Quinolate Block Copolymers in THF

block copolymer	λ_{abs} (nm)	λ_{em} (nm)	quantum yield
PM1-*b*-PS	394	505	0.23
PM2-*b*-PS	440	620	0.002
PS-*b*-PM1	394	505	0.19
PM1-*b*-PNIPAM	394	505	0.24
P(St-*alt*-MAh)-*b*-PM1	394	508	0.17
P(St-*alt*-AbMA)-*b*-PM1	355, 394	505	N/A[a]

[a]The P(St-*alt*-AbMA)-*b*-PM1 block copolymer shows almost identical emission at 505 nm when excited at 355 or 394 nm. Because of overlap of the azobenzene and boron quinolate absorptions, the quantum yield of P(St-*alt*-AbMA)-*b*-PM1 was not determined.

range of 0.17−0.24, while that of PM2-*b*-PS is much lower (0.002), which is related to the charge transfer process discussed above. It is noteworthy that the block copolymers with the organic blocks as precursors (PS-*b*-PM1 and P(St-*alt*-MAh)-*b*-PM1) exhibit ∼30% lower quantum yields than polymers with PM1 as precursor block (PM1-*b*-PS and PM1-*b*-PNIPAM). A possible explanation is that the presence of the CTA end group favors nonradiative decay, when M1 is polymerized as the second block.[8]

We further studied the effect of azobenzene modification in P(St-*alt*-MAh)-*b*-PM1. After attachment of the chromophore to the polymer, the absorption maximum of the azobenzene chromophore in THF is blue-shifted from λ_{max} = 389 to 355 nm, as a result of the electron-withdrawing effect of the amide group (Figure 7).[26] The absorption feature of the PM1 block at

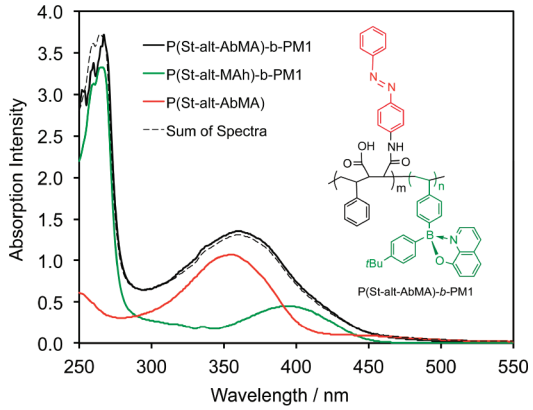


Figure 7. Comparison of the UV−vis spectra of P(St-*alt*-AbMA), P(St-*alt*-MAh)-*b*-PM1, and P(St-*alt*-AbMA)-*b*-PM1 in THF.

394 nm is only seen as a shoulder band due to overlap with the azobenzene absorption, the molar extinction coefficient of which is much larger than that of the boron quinolate chromophore (4-aminoazobenzene: ε_{389} = 14280 M^{-1} cm^{-1}; M1: ε_{394} = 3370 M^{-1} cm^{-1}).

To study the photoisomerization of P(St-*alt*-AbMA)-*b*-PM1, a polymer solution in THF was irradiated at 330−360 nm, and UV−vis spectra were recorded at different irradiation times (Figure S7, Supporting Information). UV irradiation induced a decrease in absorbance at 355 nm due to trans−cis isomerization of the azobenzene chromophore.[27] An equilibrium was reached within ∼15 min, after which no further change in absorbance was observed. Upon gentle heating or irradiation with natural visible light, cis−trans isomerization occurred and the original absorbance was reproduced. For comparison, the photoisomerization of P(St-*alt*-AbMA) was also studied, and a similar trans−cis isomerization process was observed. The relative decrease in absorbance for P(St-*alt*-AbMA)-*b*-PM1 is slightly less pronounced than that of P(St-*alt*-AbMA), possibly due to the relatively long boron quinolate block, whose absorbance overlaps with that of the azobenzene groups. The emission of the boron quinolate block (excited at λ_{exc} = 394 nm) showed no change in position or intensity, which suggests that the two chromophoric systems act fully independently. Even after several hours of irradiation, no decrease in emission intensity was observed, indicating good photostability of the boron quinolate chromophore.

■ CONCLUSIONS

We successfully prepared a series of well-defined luminescent organoboron quinolate block copolymers of high molecular weight and fairly narrow molecular weight distribution via sequential RAFT polymerization. Using boron quinolate-functionalized PS as macro-CTA, we synthesized the block copolymers PM1-*b*-PS and PM1-*b*-PNIPAM with PS and PNIPAM as the second block. In an alternative approach, luminescent block copolymers can also be prepared from an organic polymer as macro-CTA. Using this method we prepared the block copolymers PS-*b*-PM1 and P(St-*alt*-MAh)-*b*-PM1. For the block copolymer with PS, the approach with PM1 as the first block gave better control, possibly because the chain extension can be performed in bulk styrene, whereas extension of PS with M1 requires the use of dioxane to solubilize the crystalline monomer. The photophysical properties of the block copolymers were studied by UV−vis and fluorescence spectroscopy. PM1-based block copolymers exhibit bright green emission, whereas PM2-*b*-PS shows a strongly red-shifted emission as a result of a charge transfer process. The functional copolymer P(St-*alt*-MAh)-*b*-PM1 can be easily further modified by ring-opening of the maleic anhydride moieties with amines. Thus, an azobenzene-decorated polymer, P(St-*alt*-AbMA)-*b*-PM1, was obtained by reaction of P(St-*alt*-MAh)-*b*-PM1 with 4-aminoazobenzene. The latter underwent reversible trans−cis isomerization upon irradiation with UV light without affecting the emission feature of the boron quinolate block. The amphiphilic block copolymers PM1-*b*-PNIPAM and P(St-*alt*-AbMA)-*b*-PM1 self-assemble in aqueous solution; TEM and DLS studies demonstrate that PM1-*b*-PNIPAM aggregates into spherical micelles with good stability. P(St-*alt*-AbMA)-*b*-PM1 shows solvent-dependent self-assembly in basic solutions, and large spindle-shaped and spherical aggregates were observed.

dx.doi.org/10.1021/ma300063r | *Macromolecules* 2012, 45, 3078−3085

■ ASSOCIATED CONTENT

Supporting Information

Additional NMR data and GPC traces, a comparison of IR spectra, and absorption spectra. This material is available free of charge via the Internet at http://pubs.acs.org.

■ AUTHOR INFORMATION

Corresponding Author

* E-mail: fjaekle@rutgers.edu.

Notes

The authors declare no competing financial interest.

■ ACKNOWLEDGMENTS

The National Science Foundation is acknowledged for support of this research. F.J. thanks the Alexander von Humboldt Foundation for a Friedrich Wilhelm Bessel research award and the Alfred P. Sloan foundation for a research fellowship.

■ REFERENCES

(1) Recent examples: Bates, J. I.; Dugal-Tessier, J.; Gates, D. P. *Dalton Trans.* **2010**, *39*, 3151−3159. Ren, L. X.; Hardy, C. G.; Tang, S. F.; Doxie, D. B.; Hamidi, N.; Tang, C. B. *Macromolecules* **2010**, *43*, 9304−9310. Bagh, B.; Gilroy, J. B.; Staubitz, A.; Müller, J. *J. Am. Chem. Soc.* **2010**, *132*, 1794−1795. Nishiyama, H.; Tomita, I. *Macromol. Chem. Phys.* **2010**, *211*, 2248−2253. Liu, J. Z.; Zhong, Y. C.; Lam, J. W. Y.; Lu, P.; Hong, Y. N.; Yu, Y.; Yue, Y. N.; Faisal, M.; Sung, H. H. Y.; Williams, I. D.; Wong, K. S.; Tang, B. Z. *Macromolecules* **2010**, *43*, 4921−4936. Deng, M.; Nair, L. S.; Nukavarapu, S. R.; Jiang, T.; Kanner, W. A.; Li, X. D.; Kumbar, S. G.; Weikel, A. L.; Krogman, N. R.; Allcock, H. R.; Laurencin, C. T. *Biomaterials* **2010**, *31*, 4898−4908. Miles, D.; Burrow, T.; Lough, A.; Foucher, D. *J. Inorg. Organomet. Polym. Mater.* **2010**, *20*, 544−553. Naka, K.; Arita, M.; Shimamoto, T.; Morisaki, Y.; Chujo, Y. *Polym. J.* **2011**, *43*, 358−363. Krüger, R. A.; Gordon, T. J.; Sutherland, T. C.; Baumgartner, T. *J. Polym. Sci. A: Polym. Chem.* **2011**, *49*, 1201−1209. Jung, J. H.; Laine, R. M. *Macromolecules* **2011**, *44*, 7263−7272. Whittell, G. R.; Hager, M. D.; Schubert, U. S.; Manners, I. *Nat. Mater.* **2011**, *10*, 176−188.

(2) Recent examples: Dash, B. P.; Satapathy, R.; Gaillard, E. R.; Maguire, J. A.; Hosmane, N. S. *J. Am. Chem. Soc.* **2010**, *132*, 6578−6587. Juarez-Perez, E. J.; Vinas, C.; Teixidor, F.; Santillan, R.; Farfan, N.; Abreu, A.; Yepez, R.; Nunez, R. *Macromolecules* **2010**, *43*, 150−159. Kim, B.; Ma, B.; Donuru, V. R.; Liu, H.; Fréchet, J. M. J. *Chem. Commun.* **2010**, *46*, 4148−4150. Nagai, A.; Kobayashi, S.; Nagata, Y.; Kokado, K.; Taka, H.; Kita, H.; Suzuri, Y.; Chujo, Y. *J. Mater. Chem.* **2010**, *20*, 5196−5201. Hoven, C. V.; Wang, H. P.; Elbing, M.; Garner, L.; Winkelhaus, D.; Bazan, G. C. *Nat. Mater.* **2010**, *9*, 249−252. Kersey, F. R.; Zhang, G. Q.; Palmer, G. M.; Dewhirst, M. W.; Fraser, C. L. *ACS Nano* **2010**, *4*, 4989−4996. Li, H.; Jäkle, F. *Macromol. Rap. Commun.* **2010**, *31*, 915−920. Kokado, K.; Chujo, Y. *Dalton Trans.* **2011**, *40*, 1919−1923. Peterson, J. J.; Davis, A. R.; Werre, M.; Coughlin, E. B.; Carter, K. R. *ACS Appl. Mater. Interf.* **2011**, *3*, 1796−1799. Jäkle, F. *Chem. Sus. Chem.* **2011**, *4*, 325−326.

(3) Jäkle, F. *Chem. Rev.* **2010**, *110*, 3985−4022. Matsumi, N.; Chujo, Y. *Polym. J.* **2008**, *40*, 77−89.

(4) Cheng, F.; Jäkle, F. *Polym. Chem.* **2011**, *2*, 2011−2121. Manners, I. *Angew. Chem., Int. Ed.* **2007**, *46*, 1565−1568.

(5) Guron, M. M.; Wei, X.; Welna, D.; Krogman, N.; Kim, M. J.; Allcock, H.; Sneddon, L. G. *Chem. Mater.* **2009**, *21*, 1708−1715. Malenfant, P. R. L.; Wan, J. L.; Taylor, S. T.; Manoharan, M. *Nature Nanotechnol.* **2007**, *2*, 43−46. Simon, Y. C.; Ohm, C.; Zimny, M. J.; Coughlin, E. B. *Macromolecules* **2007**, *40*, 5628−5630.

(6) Qin, Y.; Sukul, V.; Pagakos, D.; Cui, C.; Jäkle, F. *Macromolecules* **2005**, *38*, 8987−8990. Cui, C. Z.; Bonder, E. M.; Qin, Y.; Jäkle, F. *J. Polym. Sci. A: Polym. Chem.* **2010**, *48*, 2438−2445. Cambre, J. N.; Roy, D.; Gondi, S. R.; Sumerlin, B. S. *J. Am. Chem. Soc.* **2007**, *129*, 10348−10349. Roy, D.; Cambre, J. N.; Sumerlin, B. S. *Chem. Commun.* **2009**, 2106−2108. Bapat, A. P.; Roy, D.; Ray, J. G.; Savin, D. A.; Sumerlin, B. S. *J. Am. Chem. Soc.* **2011**, *133*, 19832−19838. Kim, K. T.; Cornelissen, J. J. L. M.; Nolte, R. J. M.; van Hest, J. C. M. *Adv. Mater.* **2009**, *21*, 2787−2791. Kim, K. T.; Cornelissen, J. J. L. M.; Nolte, R. J. M.; van Hest, J. C. M. *J. Am. Chem. Soc.* **2009**, *131*, 13908−13909.

(7) Perrier, S.; Pittaya, T. *J. Polym. Sci., Part A: Polym. Chem.* **2005**, *43*, 5347. Moad, G.; Chiefari, J.; Chong, Y. K.; Krstina, J.; Mayadunne, R. T. A.; Postma, A.; Rizzardo, E.; Thang, S. H. *Polym. Int.* **2000**, *49*, 993−1001. Lowe, A. B.; McCormick, C. L. *Prog. Polym. Sci.* **2007**, *32*, 283.

(8) Moad, G.; Chen, M.; Haussler, M.; Postma, A.; Rizzardo, E.; Thang, S. H. *Polym. Chem.* **2011**, *2*, 492−519.

(9) Nagai, A.; Kokado, K.; Miyake, J.; Chujo, Y. *Macromolecules* **2009**, *42*, 5446−5452.

(10) Nagai, A.; Kokado, K.; Miyake, J.; Chujo, Y. *J. Polym. Sci. A: Polym. Chem.* **2010**, *48*, 627−634. Paris, R.; Quijada-Garrido, I.; Garcia, O.; Liras, M. *Macromolecules* **2011**, *44*, 80−86.

(11) Zhang, G.; St. Clair, T. L.; Fraser, C. L. *Macromolecules* **2009**, *42*, 3092−3097. Zhang, G.; Evans, R. E.; Campbell, K. A.; Fraser, C. L. *Macromolecules* **2009**, *42*, 8627−8633.

(12) Zhang, G.; Palmer, G. M.; Dewhirst, M. W.; Fraser, C. L. *Nat. Mater.* **2009**, *8*, 747−751.

(13) Fraser, C. L.; Zhang, G. Q.; Lu, J. W.; Sabat, M. *J. Am. Chem. Soc.* **2010**, *132*, 2160−2162.

(14) Cheng, F.; Jäkle, F. *Chem. Commun.* **2010**, *46*, 3717−3719.

(15) Qin, Y.; Pagba, C.; Piotrowiak, P.; Jäkle, F. *J. Am. Chem. Soc.* **2004**, *126*, 7015−7018. Cui, Y.; Liu, Q.-D.; Bai, D.-R.; Jia, W.-L.; Tao, Y.; Wang, S. *Inorg. Chem.* **2005**, *44*, 601−609. Nagata, Y.; Chujo, Y. *Macromolecules* **2008**, *41*, 2809−2813.

(16) Qin, Y.; Kiburu, I.; Shah, S.; Jäkle, F. *Org. Lett.* **2006**, *8*, 5227−5230.

(17) Qin, Y.; Kiburu, I.; Shah, S.; Jäkle, F. *Macromolecules* **2006**, *39*, 9041−9048.

(18) *Handbook of Photochemistry*, 2nd ed.; Murov, S. L., Carmichael, I., Hug, G. L., Eds.; Marcel Dekker: New York, 1993.

(19) Chong, A. Y. K.; Krstina, J.; Le, T. P. T.; Moad, G.; Postma, A.; Rizzardo, E.; Thang, S. H. *Macromolecules* **2003**, *36*, 2256−2272. Stenzel, M. H.; Davis, T. P.; Fane, A. G. *J. Mater. Chem.* **2003**, *13*, 2090.

(20) Moad, G.; Rizzardo, E.; Thang, S. H. *Aust. J. Chem.* **2005**, *58*, 379−410.

(21) Hu, J.; Ge, Z.; Zhou, Y.; Zhang, Y.; Liu, S. *Macromolecules* **2010**, *43*, 5184−5187.

(22) Zhu, M.-Q.; Wei, L.-H.; Li, M.; Jiang, L.; Du, F.-S.; Li, Z.-C.; Li, F.-M. *Chem. Commun.* **2001**, 365−366.

(23) Ma, J.; Cheng, C.; Sun, G.; Wooley, K. L. *Macromolecules* **2008**, *41*, 9080−9089.

(24) Nguyen, T. H. H. *Polymer* **1999**, *40*, 1081−1086.

(25) Gao, M.; Jia, X.; Kuang, G.; Li, Y.; Liang, D.; Wei, Y. *Macromolecules* **2009**, *42*, 4273−4281.

(26) A similar blue shift from 374 to 350 nm in CH_2Cl_2 was reported in the literature upon amidation of 4-aminoazobenzene with α-lipoic acid; see: Weidner, T.; Bretthauer, F.; Ballav, N.; Motschmann, H.; Orendi, H.; Bruhn, C.; Siemeling, U.; Zharnikov, M. *Langmuir* **2008**, *24*, 11691−11700.

(27) See: Airinei, A.; Rusu, E.; Barboiu, V. *J. Braz. Chem. Soc.* **2010**, *21*, 489−495 and references therein.

Macromolecules

Article

pubs.acs.org/Macromolecules

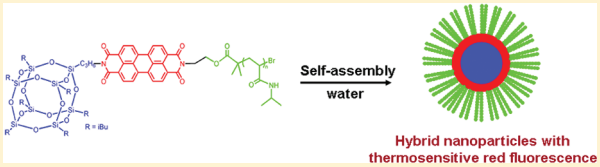
Synthesis and Luminescence of POSS-Containing Perylene Bisimide-Bridged Amphiphilic Polymers

Fanfan Du, Jiao Tian, Hu Wang, Bin Liu, Bangkun Jin, and Ruke Bai*

CAS Key Laboratory of Soft Matter Chemistry, Department of Polymer Science and Engineering, University of Science and Technology of China, Hefei, 230026, People's Republic of China

Supporting Information

ABSTRACT: A novel well-defined amphiphilic fluorescent polymer containing asymmetric perylene bisimide was designed and synthesized by combining reaction of perylene anhydride with amino functional polyhedral oligomeric silsesquioxane (POSS) and atom transfer radical polymerization (ATRP) of *N*-isopropylacrylamide (NIPAM). All the intermediate and final products were characterized by NMR, Fourier transform infrared spectroscopy (FT-IR), elemental analyses, and gel permeation chromatograph (GPC). Self-assembly of the amphiphilic polymers was investigated in aqueous solution and POSS-containing hybrid nanoparticles were obtained and characterized by dynamic laser light scattering (DLS) and transmission electron microscopy (TEM). The novel hybrid nanoparticles exhibit attractive high red fluorescence at 645 nm due to the significant effect of the bulky POSS moieties. Moreover, based on the thermoresponsive PNIPAM coronas, the fluorescence intensity of the self-assembled hybrid nanoparticles can be further enhanced and tuned by changing temperature.



INTRODUCTION

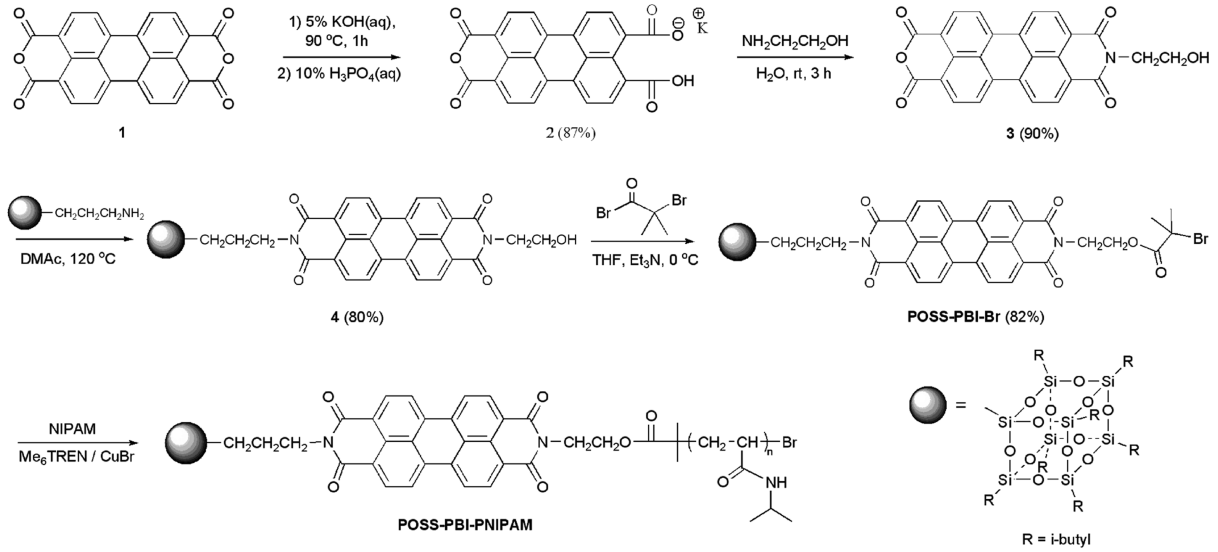
Recently, research on fluorescent nanoparticles has gained considerable attention due to their potential applications as probes and sensors for biological imaging and sensing.[1−3] Such particles are very interesting due to their small size while their fluorescent properties can be tuned by varying their size and composition. Much focus has been placed on the development of efficient, inexpensive, stable, and tunable nanoparticles, such as quantum dots/rods,[4] silica nanoparticles,[5] metal nanoparticles,[6] carbon nanomaterials,[7] and up-converting nanophosphores.[8] However, applications of these robust materials are hampered by the toxicity of the inorganic component and sometimes difficulties with respect to surface modification.[9] In another approach, organic fluorescent particles have been constructed from vesicles and micelles in which fluorescent dyes are incorporated.[10] Such systems can be easily chemically modified to enhance their binding affinity toward specific tissue and analytes. Many organic dyes have been utilized as emitters of light-emitting nanoparticles with various colors.[9,11−14] Among these nanoparticles, red fluorescent organic nanoparticles that emit long enough wavelength (emission maximum wavelength λ_{max} > 610 nm), where the influence of the main tissue absorbing components, oxy- and deoxyhemoglobin (λ_{max} < 600 nm) is minimal,[15] have been dedicated immense attention in biological imaging technologies.[16,17] However, only few red fluorescent organic dyes are suitable for the application. Conventional red fluorescent organic dyes are highly susceptible to concentration quenching and become either weakly emissive or even not emissive at all in aggregate state, due to either attractive dipole−dipole interactions or intermolecular π-stacking caused by their polar or nonpolar but extensively π-conjugated structures.[17−20]

Perylene bisimides (PBIs), the well-known fluorescent dyes, display exceptional chemical, thermal and photochemical stability, strong absorption for visible light, near unity fluorescence quantum yields and low toxicity.[21,22] Red excimer-like emissions are usually observed for weakly interacting π-stacked PBI molecules in solution. However, these attractive red emissions are generally strongly quenched by π-stacking in aggregate state.[23−26] Strong red fluorescence in the aggregate state could be succeeded with the elimination of this self-quenching. The incorporation of sterically demanding groups onto PBIs can reduce the intermolecular interactions and maintain the luminescence in the aggregate state simultaneously. Würthner and co-workers reported a series of amphiphiles based on PBI having different ratios of hydrophobic and hydrophilic coil segments.[27] Aggregation in water of these amphiphile PBIs resulted in the formation of micelles or bilayer vesicles with broad fluorescence band at 600−800 nm.[28] Liu and co-workers demonstrated that the steric hindrance of β-cyclodextrin can increase the $\pi-\pi$ stacking distance of perylene chromophore and reduce the intermolecular interactions.[29] An amphiphilic perylene-cyclodextrin conjugate was synthesized and the resulting aggregates were successfully employed as solid-state fluorescence sensing for organic amines.[30]

Received: January 15, 2012
Revised: March 9, 2012
Published: March 26, 2012

ACS Publications © 2012 American Chemical Society

Scheme 1. Synthesis Procedure of the PBI-Bridged Amphiphilic Polymer



Polyhedral oligomeric silsesquioxane (POSS) has attracted a great deal of attention in the materials field because of the unique nanoscale cage-shaped structure and good solubility in organic solvents.[31] It has been incorporated into conjugated organic/polymer luminescent materials to improve solubility and maintain the luminescence in the aggregate state simultaneously.[32−41] Furthermore, according to the previous works, POSS shows high stability under biological environment and little cytotoxicity.[42,43] Thus, POSS is a suitable scaffold to realize the multifunctional materials for biological applications.[44−46] Incorporation of POSS group into PBI should not only enhance the fluorescence quantum yields of the aggregate state, but also endow novel biological applications of corresponding assemblies. However, much less attention has been paid to this aspect,[47] and to the best of our knowledge, there is no report on the successful preparation and applications of fluorescent polymers based on POSS-containing PBI dyes.

In this work, we report on the synthesis of well-defined amphiphilic polymer possessing an asymmetric PBI as a bridge between a POSS moiety and a PNIPAM chain. The preparation procedure is shown in Scheme 1. All the intermediate and final products were characterized by NMR, Fourier transform infrared spectroscopy (FT-IR), elemental analyses, and gel permeation chromatograph (GPC). The optical properties of the polymer in solution were measured by UV−vis spectroscopy and photoluminescence (PL) spectroscopy. Water-dispersible hybrid nanoparticles were then prepared by self-assembly of the amphiphilic polymers and characterized by dynamic laser light scattering (DLS) and transmission electron microscopy (TEM). It was found that the nanoparticles exhibit strong red fluorescence with a maximum at 645 nm. Moreover, further experimental results show that the fluorescence intensity of the self-assembled hybrid nanoparticles can be further enhanced and tuned by changing temperature owing to the incorporation of a thermal responsive PNIPAM chain in the amphiphilic polymer.

EXPERIMENTAL SECTION

Materials. Perylene-3,4:9,10-tetracarboxylic dianhydride and 2-bromoisobutyryl bromide were obtained from J&K. Aminopropylheptakis (isobutyl) POSS (POSS-NH_2, Hybrid Plastics, 97%) was used as received. Tetrahydrofuran (THF, Shanghai Chemical Reagent Co., >99%) was purified by refluxing over sodium and distillation prior to use. Triethylamine (NEt_3, Shanghai Chemical Reagent Co., >99%) was distilled over potassium. *N*-Isopropylacrylamide (NIPAM) was purified by recrystallization from a mixture of benzene and *n*-hexane (1/3, v/v). Copper(I) bromide (CuBr) was purified by stirring overnight over CH_3COOH at room temperature followed by washing the solid with ethanol, acetone, and diethyl ether, and drying at 40 °C in vacuo for 1 day. Tris(2-aminoethyl) amine (TAEN) was purchased from Fluka and used as received. Tris(2-(dimethylamino)ethyl)amine (Me_6TREN) was prepared according to literature procedures.[48] All other chemical agents were used as received unless otherwise noted.

*Synthesis of N-Hydroxyethyl-3,4:9,10-perylenetetracarboxylic-3,4-anhydride-9,10-imide (**3**).* Perylene-3,4:9,10-tetracarboxylic acid monoanhydride monopotassium carboxylate **2** (0.9 g, 2 mmol), prepared according to the procedure reported by Tröster,[49] was suspended in water (30 mL) at room temperature. 2-Aminoethanol (0.6 g, 10 mmol) dissolved in 5 mL of water, was added dropwise to the suspension of **2**. The mixture was stirred for 3 h at room temperature. Acetone (100 mL) was added into the resulting red solution to induce precipitation. The mixture was allowed to stand overnight, and the resulting brick red precipitate was obtained by vacuum filtration and washed with acetone. The filter residue was resuspended in hydrochloric acid (10%), heated to 90 °C, kept at this temperature for 1 h. The product was then isolated by vacuum filtration, washed with water, and dried under vacuum at 60 °C overnight to yield 0.9 g (1.8 mmol, 90%) of **3** as a brick red solid. IR (KBr): ν = 3500, 1764, 1717, 1693, 1653, 1591, 1504, 1403, 1374, 1321, 1236, 1171, 1152, 1013, 851, 807, 736, 635 (Figure S1, Supporting Information). Anal. Calcd for $C_{26}H_{13}NO_6$: C, 71.72; H, 3.00; N, 3.22. Found: C, 68.87; H, 3.31; N, 3.09.

*Synthesis of N-Hydroxyethyl-N′-propylheptakis(isobutyl) POSS-3,4:9,10-Perylenetetracarboxylic Bisimide (**4**).* To a stirred suspension of **3** (0.34 g, 0.75 mmol) and imidazole (1 g, 15 mmol) in 50 mL of dimethylacetamide (DMAc) was added POSS-NH_2 (1.75 g, 2 mmol). The reaction mixture was stirred at 120 °C under nitrogen for 8 h. After cooling to room temperature, diethyl ether (100 mL) was added, followed by washing with hydrochloric acid (10%, 100 mL × 3). The organic layer was dried over anhydrous Na_2SO_4 and filtered. After removing all the solvents, the residues were further purified on a silica gel column using chloroform as eluent, affording **4**. The product was obtained as a bright red solid (0.78 g, yield: 80%). ^{1}H NMR ($CDCl_3$, δ, ppm): 8.61 (*d*, 2H, *Ar*−*H*), 8.54 (*d*, 2H, *Ar*−*H*), 8.42 (*m*, 4H, *Ar*−*H*), 4.50 (*t*, 2H, β-CH_2), 4.20 (*t*, 2H, α-CH_2), 4.08 (*t*, 2H, α-CH_2), 1.85 (*m*, 7H, $SiCH_2CH$), 1.66 (*m*, 2H, $SiCH_2CH_2$), 0.95 (*m*, 42H, $CH(CH_3)_2$), 0.59 (*m*, 16H, $SiCH_2$) (Figure S2, Supporting

dx.doi.org/10.1021/ma300100s | *Macromolecules* 2012, 45, 3086−3093

Information). ^{13}C NMR ($CDCl_3$, δ, ppm): 164.2, 163.2, 134.8, 134.2, 131.6, 131.2, 129.4, 129.2, 126.2, 126.1, 123.4, 123.3, 123.0, 61.5, 43.1, 40.5, 25.8, 24.0, 22.6, 9.9 (Figure S3, Supporting Information). IR (KBr): ν = 3443, 2957, 2871, 1693, 1660, 1464, 1344, 1234, 1111, 837, 744, 482 (Figure S1, Supporting Information). Anal. Calcd for $C_{57}H_{82}N_2O_{17}Si_8$: C, 53.02; H, 6.35; N, 2.17. Found: C, 52.89; H, 6.40; N, 2.14.

Synthesis of POSS-PBI-Br. NEt_3 (0.2 g, 2 mmol) and **4** (0.65 g, 0.5 mmol) dissolved in anhydrous THF (30 mL) were respectively added into a flask, then 2-bromoisobutyryl bromide (1.0 g, 2 mmol) was added dropwise at 0 °C. The mixture was warmed to room temperature and stirred overnight. After being filtered, diethyl ether (100 mL) was added, followed by washing with distilled water three times. The organic solution was dried over anhydrous Na_2SO_4 and filtered. After removing all the solvents, the residues were further purified on a silica gel column using chloroform as eluent to afford POSS-PBI-Br. The product was obtained as a bright red solid (0.59 g, yield: 82%). ^1H NMR ($CDCl_3$, δ, ppm): 8.67 (*d*, 4H, *Ar*−*H*), 8.58 (*d*, 4H, *Ar*−*H*), 4.59 (*m*, 4H, α-CH_2, β-CH_2), 4.20 (*t*, 2H, α-CH_2), 1.85 (*m*, 7H, $SiCH_2CH$), 1.66 (*m*, 2H, $SiCH_2CH_2$), 0.95 (*m*, 42H, $CH(CH_3)_2$), 0.59 (*m*, 16H, $SiCH_2$) (Figure S4, Supporting Information). ^{13}C NMR ($CDCl_3$, δ, ppm): 171.6, 163.4, 163.1, 134.9, 134.4, 131.5, 131.3, 129.5, 129.3, 126.5, 126.4, 126.0, 123.5, 123.2, 123.0, 122.9, 63.2, 55.8, 39.0, 30.7, 23.8, 22.5, 22.4, 9.8 (Figure S5, Supporting Information). IR (KBr): ν = 3443, 2955, 2871, 1730, 1699, 1660, 1594, 1556, 1464, 1441, 1402, 1345, 1229, 1110, 836, 810, 744, 484 (Figure S1, Supporting Information). Anal. Calcd for $C_{61}H_{87}N_2BrO_{18}Si_8$: C, 50.87; H, 6.05; N, 1.95. Found: C, 50.77; H, 6.06; N, 1.94.

Synthesis of POSS-PBI-PNIPAM. POSS-PBI-PNIPAM was prepared by ATRP. Polymerization of NIPAM was performed using POSS-PBI-Br as an initiator, CuBr as a catalyst and Me_6TREN as a ligand. Typically, CuBr (14 mg, 0.1 mmol) and POSS-PBI-Br (144 mg, 0.1 mmol) were added to a round-bottom flask fitted with a rubber septum and pump-filled with nitrogen three times. The mixture was subsequently deoxygenated, and inhibitor-free NIPAM (3.40 g, 30 mmol), DMF (3 mL), 2-propanol (1 mL), THF (2 mL), and Me_6TREN (23 mg, 0.1 mmol) were added to the round-bottom flask under nitrogen. The solution was further deoxygenated by three freeze−pump−thaw cycles before being kept in 25 °C, and the solution was maintained at this temperature for 7 h. After the polymerization was stopped, the reaction mixture was diluted with THF, and exposed to air. The reaction mixture was passed through a basic alumina column to remove the copper catalyst. After removing the solvents by a rotary evaporator, the residues were dissolved in THF and precipitated into an excess of ethyl ether. The above dissolution−precipitation cycle was repeated twice. The final product as a red solid was dried in a vacuum oven at room temperature in a yield of 1.70 g (58%). $M_{n,GPC}$ = 11.1 kDa, M_w/M_n = 1.31). The DP of PNIPAM block was determined to be 245 by ^1H NMR analysis in $CDCl_3$ (Figure 1). The product was denoted as POSS-PBI-PNIPAM245.

N,N′-Propylheptakis (isobutyl) POSS-perylene Tetracarboxylic Acid Bisimides (POSS-PBI-POSS). POSS-NH_2 (2.36 g, 2.7 mmol), 3,4:9,10-perylenetetracarboxylic dianhydride (0.47 g, 1.2 mmol), imidazole (1.0 g) and *N,N*-dimethylacetamide (25 mL) were vigorously stirred under nitrogen at 140 °C for 6 h. After the reaction, CH_2Cl_2 (100 mL) was added, and the mixture was washed by dilute hydrochloric acid for three times. The organic solution was dried with sodium sulfate and the salts were subsequently filtered off. The filtrate was rotary concentrated and further purified on a silica gel column using $CHCl_3$ as eluent to afford POSS-PBI-POSS as bright-red solid (2.24 g, yield:89%). ^1H NMR ($CDCl_3$, δ, ppm): 8.69 (*d*, 4H, *Ar*−*H*), 8.63 (*d*, 4H, *Ar*−*H*), 4.21 (*t*, 4H, α-CH_2), 1.84 (*m*, 18H, $SiCH_2CH$, $SiCH_2CH_2$), 0.95 (*m*, 84H, $CH(CH_3)_2$), 0.59 (*m*, 32H, $SiCH_2$) (Figure S6, Supporting Information). ^{13}C NMR ($CDCl_3$, δ, ppm): 163.3, 140.8, 134.6, 131.4, 129.4, 126.5, 123.4, 123.0, 42.9, 25.7, 23.9, 22.5, 22.4, 9.8 (Figure S7, Supporting Information). IR (KBr): ν = 2956, 2873, 1700, 1660, 1595, 1464, 1443, 1403, 1346, 1252, 1230, 1113, 837, 809, 744, 564, 482, and 433 (Figure S8, Supporting Information).

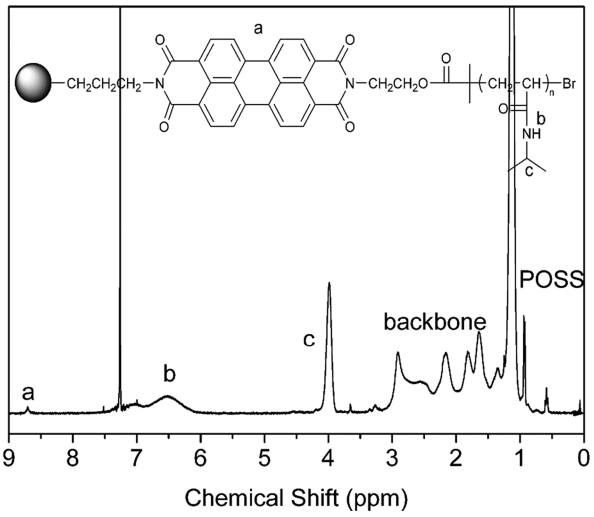


Figure 1. ^1H NMR spectrum of POSS-PBI-PNIPAM245 in $CDCl_3$.

Self-Assembly of POSS-PBI-PNIPAM. Typically a solution of POSS-PBI-PNIPAM (5 mg) in THF (0.5 mL) was rapidly injecting into water (50 mL) under ultrasonic condition at 25 °C and a micellar solution was obtained by further ultrasonic treatment for 5 min.

Characterization. *Nuclear Magnetic Resonance Spectroscopy (NMR).* All NMR spectra were recorded on a Bruker AVANCE II spectrometer (resonance frequency of 400 MHz for ^1H) operated in the Fourier transform mode. $CDCl_3$ and TMS were used as the solvent and internal standard, respectively.

Fourier Transform Infrared Spectroscopy (FT-IR). Fourier transform infrared (FT-IR) spectra were recorded on a Bruker VECTOR-22 IR spectrometer and were collected at 64 scans with a spectral resolution of 4 cm^{-1}.

Elemental Analyses. Elemental analyses were performed on a VARIO ELIII C, H, and N analyzer.

Gel Permeation Chromatography (GPC). Molecular weights and molecular weight distributions were determined by gel permeation chromatography (GPC) equipped with a Waters 1515 pump, a Waters 2414 RI detector, and Waters UV/RI detectors (set at 30 °C). It used a series of three linear Styragel columns HR3, HR4, and HR6 at an oven temperature of 45 °C. The eluent was THF at a flow rate of 1.0 mL/min. A series of low-polydispersity polystyrene (PS) standards were employed for the GPC calibration.

Ultraviolet−Visible Spectroscopy (UV−Vis). UV−vis spectra of solutions were recorded with a UV−vis TU-1901 spectrometer.

Photoluminescence (PL) Spectroscopy. Emission spectra of solutions were measured by an F-4600 PL Spectrophotometer. Quantum yields in solution were determined twice using Rhodamine B in ethanol (5.0 μg/mL) as the standard and the measurements were averaged. Temperature-dependent fluorescence spectra were acquired on a LS 55 luminescence spectrometer. The PL quantum yield of POSS-PBI-POSS in the solid state was determined as absolute values in an integrating sphere.

Transmission Electron Microscopy (TEM). TEM observations were conducted on an H-7650 transmission electron microscope at an acceleration voltage of 100 kV. The sample for TEM observations was prepared by placing 10 μL of micellar solution on copper grids.

Dynamic Laser Light Scattering (DLS). A commercial spectrometer (ALV/DLS/SLS-5022F) equipped with a multitau digital time correlator (ALV5000) and a cylindrical 22 mW UNIPHASE He−Ne laser (λ_0 = 632 nm) as the light source was employed for DLS measurements. Scattered light was collected at a fixed angle of 90° for duration of 10 min.

Table 1. ATRP Results of NIPAM Initiated by POSS-PBI-Br[a]

polymer	time (h)	conversion[b] (%)	$M_{n,th}$[c] (KDa)	$M_{n,NMR}$[d] (KDa)	$M_{n,GPC}$[e] (KDa)	PDI[e]
POSS-PBI-PNIPAM58[f]	3	26	10.2	8.0	3.2	1.39
POSS-PBI-PNIPAM145[g]	5	40	15.0	17.8	8.6	1.32
POSS-PBI-PNIPAM254[g]	7	67	24.1	29.1	11.1	1.31

[a]Polymerization conditions: $[NIPAM]_0/[POSS\text{-}PBI\text{-}Br]_0/[CuBr]_0/[Me_6TREN]_0 = 300/1/1/1$, $[NIPAM]_0 = 5$ M in DMF/2-propanol/THF (3/1/2, v/v/v), temperature = 25 °C. [b]Determined by ^{1}H NMR. [c]Calculated from the equation: $M_{n,th}$ = Conversion ×300 × 113 + 1439. [d]Calculated from the equation: $M_{n,NMR} = 113\times 16A_{3.92}/A_{0.52} + 1439$, where $A_{3.92}$ and $A_{0.52}$ are the integral values of the peaks at 3.92 and 0.52 ppm. [e]Determined by GPC. [f]POSS-PBI-PNIPAM58 was purified by dialysis in water. [g]Purified by precipitated into an excess of ethyl ether.

RESULTS AND DISCUSSION

Synthesis and Characterization of the Amphiphilic Polymers. Scheme 1 illustrates the synthetic route of the amphiphilic polymer comprising of one perylene bisimide moiety, one POSS moiety, and one PNIPAM chain. The synthesis of POSS-containing ATRP initiator includes mainly three steps: first, synthesis of *N*-hydroxyethyl-3,4:9,10-perylenetetracarboxylic monoanhydride monoimide **3** was achieved from the reaction of 2 with 2-aminoethanol; second, POSS-containing asymmetric PBI **4** with a hydroxy functional group was prepared by incorporating POSS moiety into **3**; third, esterification of compound **4** with 2-bromoisobutyryl bromide was carried out to produce the ATRP initiator (POSS-PBI-Br). The products were characterized by FT-IR spectra. As shown in Figure S1, Supporting Information, the successful synthesis of **3** can be confirmed by the sharp band at 1764 cm^{-1} of anhydride and 1693 cm^{-1} of imide,[50] as well as the corresponding hydroxy band at 3500 cm^{-1}. After the reaction of **3** with POSS-NH_2, the complete consumption of anhydride can be confirmed by the disappearance of the characteristic anhydride absorption peak at 1764 cm^{-1} in the spectrum of **4**. Moreover, the bands at 2800−3000 cm^{-1} of C−H vibration stretching on the eight pendant alkyl arms of POSS, and the Si−O−C stretching band of the cubic cores of POSS at 1111 cm^{-1} both indicate that the POSS moiety is incorporated into perylene chromophore.[41] The esterification of **4** with an excess of 2-bromoisobutyryl bromide affords POSS-PBI-Br and typical absorption peak of ester at 1730 cm^{-1} can be observed in the spectrum of POSS-PBI-Br.

We noticed that PBI **3** has poor solubility, however, both PBI **4** and POSS-PBI-Br show good solubilities in common organic solvents due to the incorporation of POSS group. Thus, the structures of PBI **4** and POSS-PBI-Br can be well determined by NMR spectroscopy. ^{1}H NMR and ^{13}C NMR spectra of **4** and POSS-PBI-Br are shown in Figures S2−S4 (Supporting Information), and all the peaks have been well designated. The PBI protons of both **4** and POSS-PBI-Br present a simple pattern of sharp signals located in the region of 8.67−8.39 ppm in $CDCl_3$, indicating that PBI groups exist in the monomeric form (or at most a very low aggregated form) at a high concentration of 1.0×10^{-2} M.[29]

In order to obtain well-defined amphiphilic polymers, ATRP of NIPAM was carried out using POSS-PBI-Br as initiator in the presence of CuBr/Me_6TREN catalyst in ternary mixed solvents of DMF, 2-propanol, and THF at 25 °C. The ternary mixed solvent was chosen as the solvent for ATRP based on the following reasons. First, 2-propanol can form hydrogen bonds with the amide groups of the monomers and the polymers to reduce the interaction between the catalyst and the propagating chain ends.[51] Second, THF can enhance the solubility of POSS-PBI-Br and increase the initiator efficiency. From the polymerization results listed in Table 1, we can see that the molecular weights of POSS-PBI-PNIPAM are well-controlled and the molecular weight distributions are relatively narrow. The structure and molecular weight of the polymers were characterized by ^{1}H NMR spectroscopy and GPC. In Figure 1, aromatic proton peaks of PBI appear at about 8.6 ppm and methine and methylene proton peaks at 1.5−2.8 ppm are ascribed to the backbone of PNIPAM. The signal at 3.92 ppm belongs to the protons of pendant groups of PNIPAM, and the characteristic peaks of POSS moieties appear at 0.87 and 0.52 ppm. The GPC of the polymers depicts monomodal distributions of polymeric species and a clear shift to higher molecular weight with increasing conversion (Figure 2).

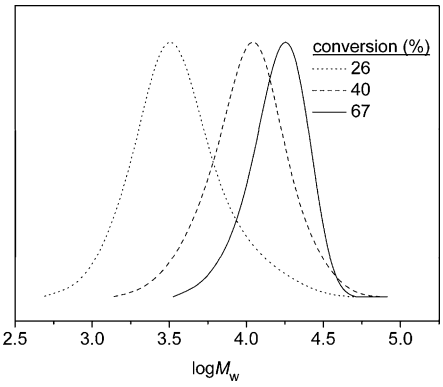


Figure 2. Evolution of molecular weight with monomer conversion measured by GPC.

The absorption and PL spectra of POSS-PBI-PNAPAM245 in THF solution (0.1 g/L) are shown in Figure 3. In the visible region, three pronounced absorptions are observed respectively

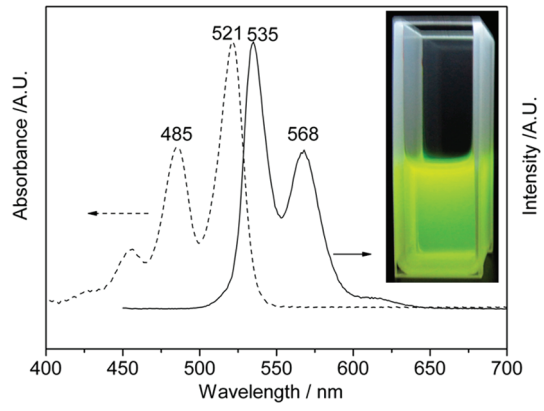


Figure 3. UV−vis absorption and fluorescence spectra ($\lambda_{excit.}$ = 455 nm) of POSS-PBI-PNIPAM245 in THF (0.1 g/L) at 20 °C. Inset: Picture of THF solution of POSS-PBI-PNIPAM245 (0.1 g/L) under a hand-held UV lamp ($\lambda_{excit.}$ = 365 nm).

dx.doi.org/10.1021/ma300100s | Macromolecules 2012, 45, 3086−3093

at 455, 485, and 521 nm, corresponding to the 0−2, 0−1, and 0−0 electronic transitions of the PBI units. Notably, the intensity of the 0−0 band is higher than that of the 0−1 band, this phenomenon indicates that the Franck−Condon factors favor the lower (0−0) excited vibronic state, and implies the absence of significant interaction between the PBI units.[52−54] The fluorescence spectrum of POSS-PBI-PNIPAM245 displays three bands at 535, 568, and 620 nm. They match well with the absorption spectra and there was good mirror-image symmetry between the absorption and fluorescence spectra. These results demonstrate that the PBI fluorophores are in a nonaggregated state.[21] The PL quantum yield of POSS-PBI-PNIPAM245 in dilute THF solution was determined to be above 95%.

Morphology and Fluorescence of Hybrid Nanoparticles Self-Assembled from POSS-PBI-PNIPAM in Aqueous Solution. The newly synthesized amphiphilic polymers contain highly hydrophobic POSS units and PBI species as well as thermoresponsive water-soluble PNIPAM segments.[55,56] In aqueous solution, the amphiphilic nature causes them self-assemble into core−shell micellar structures consisting of hydrophobic POSS cores and hydrophilic PNIPAM coronas at room temperature. Stable micellar solution of POSS-PBI-PNIPAM245 in aqueous solution was successfully prepared by rapidly injecting a solution of POSS-PBI-PNIPAM245 in THF (0.5 mL, 10 g/L) into 50 mL water under ultrasonic condition at room temperature. However, at the same condition, POSS-PBI-PNIPAM58 and POSS-PBI-PNIPAM145 precipitated in water due to their shorter hydrophilic PNIPAM chains. This result indicates that design of polymer structures is very important for the fromation of stable polymer particles.

Figure 4 shows typical plots of the hydrodynamic radius distribution, $f(R_h)$, for the hybrid nanoparticles self-assembled

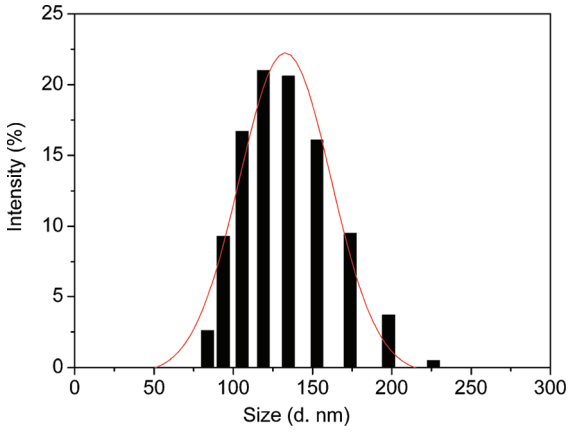


Figure 4. Hydrodynamic radius distributions obtained for hybrid nanoparticles self-assembled from 0.1 g/L aqueous solution of POSS-PBI-PNIPAM245 at 25 °C.

from 0.1 g/L aqueous solution of POSS-PBI-PNIPAM245 at 25 °C. The intensity-average hydrodynamic radius was evaluated to be about 130 nm. TEM observations were performed to examine the actual morphologies of micellar aggregates formed from the same solution at 25 °C. Figure 5 clearly reveals that spherical hybrid nanoparticles are formed in water with diameters of around 10 nm. We noticed that there are huge differences in micelles sizes measured through DLS and TEM. In consideration of the soft nature of PNIPAM segments, TEM actually revealed the core dimensions of the micelles in the dry

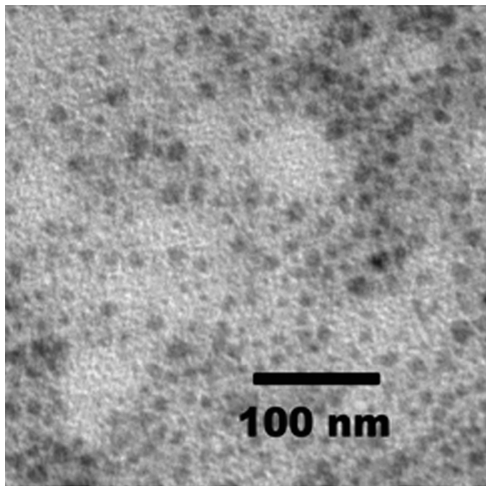


Figure 5. TEM image obtained for hybrid nanoparticles self-assembled from 0.1 g/L aqueous solution of POSS-PBI-PNIPAM245 at 25 °C.

state. Moreover, since DLS reports the intensity-average dimensions of nanoparticles in solution, it contains considerable contribution from the hydrophilic PNIPAM coronas. Therefore, the micelles sizes measured by DLS is often bigger than that measured by TEM.[57,58] In addition, compared with the similar tadpole-shaped POSS-containing PNIAPM reported in literature,[57] POSS-PBI-PNIPAM is more prone to aggregation due to the highly hydrophobic property and effective intermolecular π-stacking of the PBI linkers. As a result, a nanoparticle self-assembled from POSS-PBI-PNIPAM245 contains much more polymer chains, this leads to the larger value of R_h. On the other hand, the cores of POSS-PBI-PNIPAM nanoparticles should be more compact due to the strong $\pi-\pi$ interaction of PBI groups. Thus, a huge difference in micelles sizes was observed in the measurements of DLS and TEM. The theoretical length of POSS-PBI-PNIPAM could be calculated according to the molecular weight. For example, the calculated result shows that the theoretical length of POSS-PBI-PNIPAM245 in the unperturbed state is 65 nm (per repeat unit of PNIPAM is about 0.25 nm,[59] the diameter of POSS molecule is 1.5 nm), which is much smaller than the value of R_h measured by DLS.

As shown in Figure 6, the aqueous suspensions of POSS-PBI-PNIPAM245 exhibit a strong excimer-like emission at 645 nm under UV illumination. The emission is very similar to the excimer-like emissions usually observed for weakly interacting π-stacked perylene molecules in solution. Compared with the emission in dilute solution, a redshift can be observed for the hybrid nanoparticles due to energy transfer to low-energy sites in the packed PBI moieties.[25−27] The red shift is accompanied by reduced PL intensity but affords a relatively large stokes shift of 150 nm, which is useful to decrease the measurement error by excitation light and scattered light for a ideal probe.[16,60,61] A few studies have been reported on the fluorescence properties of PBI aggregates to support the general rule-of-thumb that PBI aggregates tend to emit red fluorescence when separated by sterically demanding groups.[27−30,62] However, the aggregate state emission ability of these examples remains a challenge and the quantum yields are relatively low. In the present case, the PL quantum yield for the assemblies in water was determined to be 27% at 20 °C, which did not provide in the literature. POSS is the vital component to realize the high fluorescence efficiency, because the steric hindrance of POSS prevents the

dx.doi.org/10.1021/ma300100s | Macromolecules 2012, 45, 3086−3093

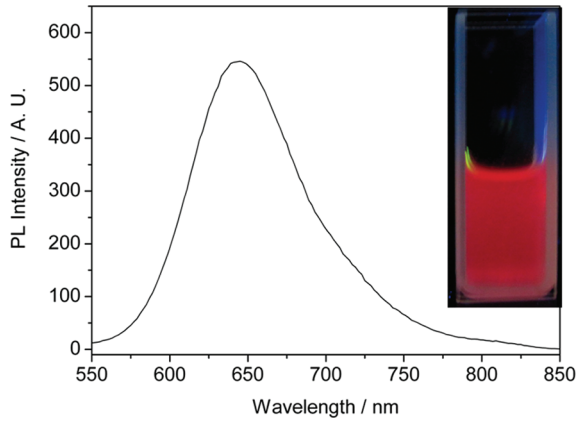


Figure 6. Emission ($\lambda_{excit.}$ = 495 nm) spectra of hybrid nanoparticles self-assembled from 0.1 g/L aqueous solution of POSS-PBI-PNIPAM245 at 20 °C. Inset: Picture of POSS-PBI-PNIPAM245 hybrid nanoparticles in pure water (0.1 g/L) under a hand-held UV lamp ($\lambda_{excit.}$ = 365 nm).

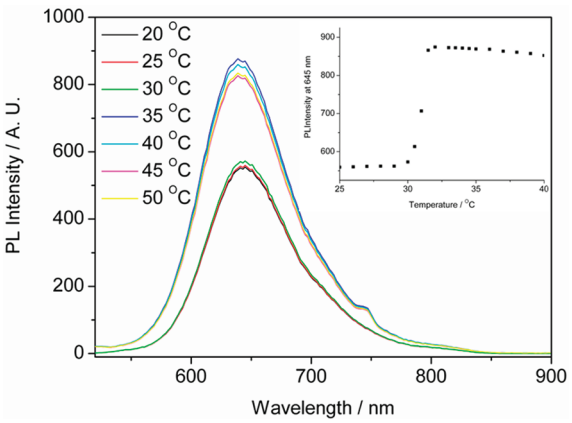


Figure 7. Temperature-dependent fluorescence spectra obtained for 0.1 g/L aqueous solution of POSS-PBI-PNIPAM245 ($\lambda_{excit.}$ = 495 nm). Inset: Temperature dependence fluorescence intensity at 645 nm.

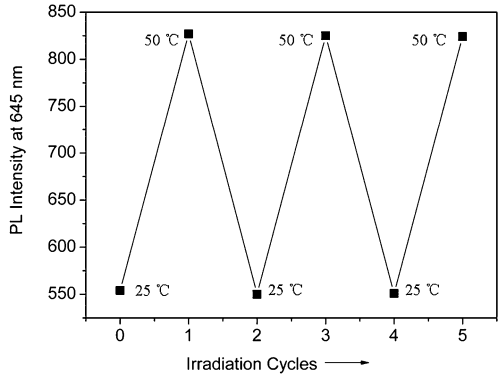


Figure 8. Fluorescent cycling of the hybrid nanoparticles (0.1 g/L in aqueous solution) at various temperature between 25 and 50 °C($\lambda_{excit.}$ = 495 nm).

aromatic ring of PBI from close packing and reduces the intermolecular interactions.

It is necessary to point out that a soft and nonchromogenic propylidene linkage between POSS and PBI is important to generate the strong red fluorescence for the hybrid nanoparticles. Recently, Cheng and co-workers reported a hybrid with two POSSs covalently attached to PBI via a rigid 1,4-phenylene linkage (Figure S9, Supporting Information).[47] The introduction of POSS seems to be ineffective in maintaining the aggregate state fluorescence. We consider that the quenching effect may be attributed to the rigid and electron-rich 1,4-phenylene groups in the molecule.[21] In order to confirm this assumption, we synthesized a similar compound, POSS-PBI-POSS (Figure S9, Supporting Information), with a propylidene linkage instead of 1,4-phenylene linkage between POSS and PBI. It was found that the fluorescence of POSS-PBI-POSS was not quenched in solution, or even in solid state and the solid-state PL quantum yield is about 46%. This result indicates that it is very important to design the structure of organic compounds and polymers for fluorescent materials.

PNIPAM chain can undergo coil-to-globule phase transition upon its lower critical solution temperature (LCST).[55,56] As shown in Figure S10, Supporting Information, with the increase of temperature from 20 to 50 °C, the stretching PNIPAM chains shrink and collapse on the surface of the nanoparticle core, leading to the decrease of R_h from 130 to 87 nm with the critical transition temperature at 31 °C. The temperature-dependent fluorescence spectra obtained for 0.1 g/L aqueous solution of POSS-PBI-PNIPAM245 are shown in Figure 7. With the temperature increasing from 20 to 50 °C, the PL quantum yields of the hybrid nanoparticles increase from ~27% (20 °C) to ~43% (50 °C) while the emission peaks remain almost unchanged. The LCST of the POSS-PBI-PNIPAM245 has been also determined in these experiments, and the lower aggregation temperature (~31 °C) is similar to that of pure PNIPAM (32 °C).[63] Moreover, the PNIPAM coronas display a well reversible coil-to-globule phase transition, and the change of fluorescence intensity of the hybrid nanoparticles is completely reversible (Figure 8).

A mechanism was proposed for the reversible change of fluorescence intensity. In aqueous solution, POSS-PBI-PNIPAM245 self-assemble into micelles with POSS as the core and PNIPAM as the shell with PBI groups located in the middle layer between the core and the shell. Below the LCST, all PNIPAM chains in the shell of the micelles are stretched out and compact PBI aggregates with lower fluorescence form in the middle layer.[27] However, above the LCST, the shrinking and collapsing of PNIPAM chains extend the space between the PBI groups, resulting in weaker $\pi-\pi$ stacking interaction and higher fluorescence.[64] Besides the thermoresponsive PNIPAM chain, the location of PBI in the polymer also contributes to the temperature-dependent fluorescence intensity. Because the size of POSS unit is comparable to the dimensions of a polymer segment in the solid or molten phase,[43] the structure of POSS-PBI-PNIPAM is analogous to that of diblock copolymers with a fluorescent group at the junction between two blocks.[64] Fluorescence response of amphiphilic polymers with a single fluorescent group at the middle of the polymer chains is quite different from that of polymers with a fluorescent group at the polymer chain end.[65−67] Self-assembly of the latter forms micelles with fluorescent groups in the cores, and fluorescence intensity of the polymer solution has little dependence on environment temperature.[64]

CONCLUSION

In this paper, we present the design and synthesis of a novel amphiphilic polymer possessing a perylene bisimide bridge

dx.doi.org/10.1021/ma300100s | Macromolecules 2012, 45, 3086−3093

between a POSS moiety and a PNIPAM chain. The target polymers were efficiently synthesized by ATRP with controlled molecular weight and low polydispersity, as characterized by ^{1}H NMR spectroscopy and GPC. Hybrid nanoparticles were then fabricated via the self-assembly of the polymers in aqueous solution. Because of the incorporation of POSS moieties, the hybrid nanoparticles retain the luminescence in its aggregate state and show red emission with the PL peak at 645 nm and quantum yield of 27%. Moreover, based on the thermoresponsive PNIPAM coronas, the fluorescence intensity of the self-assembled hybrid nanoparticles can be further enhanced and tuned by changing temperature. This work provides a new strategy for design and preparation of red fluorescent nanoparticles with environmental responsiveness, which can find use in many applications such as biosensors, diagnostic nanoprobes, and targeted drug delivery.

■ ASSOCIATED CONTENT

Supporting Information

Additional FT-IR, ^{1}H NMR, and ^{13}C NMR spectra, molecular structures, and hydrodynamic radius vs. temperature results. This material is available free of charge via the Internet at http://pubs.acs.org.

■ AUTHOR INFORMATION

Corresponding Author

*E-mail: bairk@ustc.edu.cn.

Notes

The authors declare no competing financial interest.

■ ACKNOWLEDGMENTS

We express thanks for the financial support from the National Natural Science Foundation (NNSF) of China (No. 20974104 and No. 21074120) and the Ministry of Science and Technology of China (NO. 2007CB936401).

■ REFERENCES

(1) Rosi, N. L.; Mirkin, C. A. *Chem. Rev.* **2005**, *105*, 1547−1562.
(2) Mulder, W. J. M.; Strijkers, G. J.; van Tilborg, G. A. F.; Cormode, D. P.; Fayad, Z. A.; Nicolay, K. *Acc. Chem. Res.* **2009**, *42*, 904−914.
(3) Liong, M.; Angelos, S.; Choi, E.; Patel, K.; Stoddart, J. F.; Zink, J. I. *J. Mater. Chem.* **2009**, *19*, 6251−6257.
(4) Michalet, X.; Pinaud, F. F.; Bentolila, L. A.; Tsay, J. M.; Doose, S.; Li, J. J.; Sundaresan, G.; Wu, A. M.; Gambhir, S. S.; Weiss, S. *Science* **2005**, *307*, 538−544.
(5) Burns, A.; Ow, H.; Wiesner, U. *Chem. Soc. Rev.* **2006**, *35*, 1028−1042.
(6) Green, M. *Angew. Chem., Int. Ed.* **2004**, *43*, 4129−4131.
(7) Amiot, C. L.; Xu, S. P.; Liang, S.; Pan, L. Y.; Zhao, J. X. J. *Sensors* **2008**, *8*, 3082−3105.
(8) Xiong, L. Q.; Chen, Z. G.; Yu, M. X.; Li, F. Y.; Liu, C.; Huang, C. H. *Biomaterials* **2009**, *30*, 5592−5600.
(9) Kaeser, A.; Schenning, A. P. H. J. *Adv. Mater.* **2010**, *22*, 2985−2997.
(10) Mailänder, V.; Landfester, K. *Biomacromolecules* **2009**, *10*, 2379−2400.
(11) Petkau, K.; Kaeser, A.; Fischer, I.; Brunsveld, L.; Schenning, A. P. H. J. *J. Am. Chem. Soc.* **2011**, *133*, 17063−17071.
(12) Patra, A.; Koenen, J. M.; Scherf, U. *Chem. Commun.* **2011**, *47*, 9612−9614.
(13) Kumar, M.; George, S. J. *Nanoscale* **2011**, *3*, 2130−2133.
(14) An, B. K.; Kwon, S. K.; Jung, S. D.; Park, S. Y. *J. Am. Chem. Soc.* **2002**, *124*, 14410−14415.
(15) Stefflova, K.; Chen, J.; Zheng, G. *Front. Biosci.* **2007**, *12*, 4709−4721.
(16) Luo, S.; Zhang, E.; Su, Y.; Cheng, T.; Shi, C. *Biomaterials* **2011**, *32*, 7127−7138.
(17) Zhou, K.; Wang, Y.; Huang, X.; Luby-Phelps, K.; Sumer, B. D.; Gao, J. *Angew. Chem., Int. Ed.* **2011**, *50*, 6109−6114.
(18) Chen, C. *Chem. Mater.* **2004**, *16*, 4389−4400.
(19) Ferrer, M. L.; del Monte, F. *J. Phys. Chem. B* **2005**, *109*, 80−86.
(20) Li, B.; Li, J.; Fu, Y.; Bo, Z. *J. Am. Chem. Soc.* **2004**, *126*, 3430−3431.
(21) Würthner, F. *Chem. Commun.* **2004**, 1564−1579.
(22) Demmig, S.; Langhals, H. *Chem. Ber.* **1988**, *121*, 225−230.
(23) Kaiser, T. E.; Wang, H.; Stepanenko, V.; Würthner, F. *Angew. Chem., Int. Ed.* **2007**, *46*, 5541−5544.
(24) Würthner, F.; Bauer, C.; Stepanenko, V.; Yagai, S. *Adv. Mater.* **2008**, *20*, 1695−1698.
(25) Chen, Z.; Stepanenko, V.; Dehm, V.; Prins, P.; Siebbeles, L. D. A.; Seibt, J.; Marquetand, P.; Engel, V.; Würthner, F. *Chem.—Eur. J.* **2007**, *13*, 436−449.
(26) Chen, Z.; Baumeister, U.; Tschierske, C.; Würthner, F. *Chem.—Eur. J.* **2007**, *13*, 450−465.
(27) Zhang, X.; Chen, Z.; Würthner, F. *J. Am. Chem. Soc.* **2007**, *129*, 4886−4887.
(28) Zhang, X.; Rehm, S.; Safont-Sempere, M. M.; Würthner, F. *Nat. Chem.* **2009**, *1*, 623−629.
(29) Liu, Y.; Wang, K.; Guo, D.; Jiang, B. *Adv. Funct. Mater.* **2009**, *19*, 2230−2235.
(30) Jiang, B.; Guo, D.; Liu, Y. *J. Org. Chem.* **2010**, *75*, 7258−7264.
(31) Cordes, D. B.; Lickiss, P. D.; Rataboul, F. *Chem. Rev.* **2010**, *110*, 2081−2173.
(32) Chan, K. L.; Sonar, P.; Sellinger, A. *J. Mater. Chem.* **2009**, *19*, 9103−9120.
(33) Wang, F.; Lu, X.; He, C. *J. Mater. Chem.* **2011**, *21*, 2775−2782.
(34) He, C.; Xiao, Y.; Huang, J.; Lin, T.; Mya, K. Y.; Zhang, X. *J. Am. Chem. Soc.* **2004**, *126*, 7792−7793.
(35) Xiao, S.; Nguyen, M.; Gong, X.; Cao, Y.; Wu, H.; Moses, D.; Heeger, A. J. *Adv. Funct. Mater.* **2003**, *13*, 25−29.
(36) Chou, C. H.; Hsu, S. L.; Yeh, S. W.; Wang, H. S.; Wei, K. H. *Macromolecules* **2005**, *38*, 9117−9123.
(37) Chou, C. H.; Hsu, S. L.; Dinakaran, K.; Chiu, M. Y.; Wei, K. H. *Macromolecules* **2005**, *38*, 745−751.
(38) Kang, J. M.; Cho, H. J.; Lee, J.; Lee, J. I.; Lee, S. K.; Cho, N. S.; Hwang, D. H.; Shim, H. K. *Macromolecules* **2006**, *39*, 4999−5008.
(39) Lee, J.; Cho, H. J.; Jung, B. J.; Cho, N. S.; Shim, H. K. *Macromolecules* **2004**, *37*, 8523−8529.
(40) Miyake, J.; Chujo, Y. *Macromol. Rapid Commun.* **2008**, *29*, 86−92.
(41) Du, F.; Wang, H.; Bao, Y.; Liu, B.; Zheng, H.; Bai, R. *J. Mater. Chem.* **2011**, *21*, 10859−10864.
(42) Ghanbari, H.; Cousins, B. G.; Seifalian, A. M. *Macromol. Rapid Commun.* **2011**, *32*, 1032−1046.
(43) Wu, J.; Mather, P. T. *Polym. Rev.* **2009**, *49*, 25−63.
(44) Pu, K. Y.; Li, K.; Liu, B. *Adv. Mater.* **2010**, *22*, 643−646.
(45) Pu, K. Y.; Luo, Z. T.; Li, K.; Xie, J. P.; Liu, B. *J. Phys. Chem. C* **2011**, *115*, 13069−13075.
(46) Mi, Y.; Li, K.; Liu, Y.; Pu, K. Y.; Liu, B.; Feng, S. S. *Biomaterials* **2011**, *32*, 8226−8233.
(47) Ren, X.; Sun, B.; Tsai, C.; Tu, Y.; Leng, S.; Li, K.; Kang, Z.; Horn, R. M. V.; Li, X.; Zhu, M.; Wesdemiotis, C.; Zhang, W.; Cheng, S. Z. D. *J. Phys. Chem. B* **2010**, *114*, 4802−4810.
(48) Hong, S. W.; Ahn, C. H.; Huh, J.; Jo, W. H. *Macromolecules* **2006**, *39*, 7694−7700.
(49) Tröster, H. *Dyes Pigm.* **1983**, *4*, 171−177.
(50) Nagao, Y.; Misono, T. *Bull. Chem. Soc. Jpn.* **1981**, *54*, 1191−1194.
(51) Lu, X.; Zhang, L.; Meng, L.; Liu, Y. *Polym. Bull.* **2007**, *59*, 195−206.
(52) Wang, W.; Li, L.; Helms, G.; Zhou, H.; Li, A. D. Q. *J. Am. Chem. Soc.* **2003**, *125*, 1120−1121.
(53) Rybtchinski, B.; Sinks, L. E.; Wasielewski, M. R. *J. Am. Chem. Soc.* **2004**, *126*, 12268−12269.

(54) Yagai, S.; Seki, T.; Karatsu, T.; Kitamura, A.; Würthner, F. *Angew. Chem., Int. Ed.* **2008**, *47*, 3367−3371.
(55) Schild, H. G. *Prog. Polym. Sci.* **1992**, *17*, 163−249.
(56) Kubota, K.; Fujishige, S.; Ando, I. *J. Phys. Chem.* **1990**, *94*, 5154−5158.
(57) Zhang, W.; Liu, L.; Zhuang, X.; Li, X.; Bai, J.; Chen, Y. *J. Polym. Sci., Part A: Polym. Chem.* **2008**, *46*, 7049−7061.
(58) Li, C.; Hu, J.; Yin, J.; Liu, S. *Macromolecules* **2009**, *42*, 5007−5016.
(59) Tricot, M. *Macromolecules* **1986**, *19*, 1268−1270.
(60) Zhang, Z.; Achilefu, S. *Org. Lett.* **2004**, *6*, 2067−2070.
(61) Peng, X.; Song, F.; Lu, E.; Wang, Y.; Zhou, W.; Fan, J.; Gao, Y. *J. Am. Chem. Soc.* **2005**, *127*, 4170−4171.
(62) Amiralaei, S.; Uzun, D.; Icil, H. *Photochem. Photobiol. Sci.* **2008**, *7*, 936−947.
(63) Xia, Y.; Burke, N. A. D.; Stover, H. D. H. *Macromolecules* **2006**, *39*, 2275−2283.
(64) Yan, Q.; Yuan, J.; Yuan, W.; Zhou, M.; Yin, Y.; Pan, C. *Chem. Commun.* **2008**, 6188−6190.
(65) Wang, S. M.; Cheng, Z. P.; Zhu, J.; Zhang, Z. B.; Zhu, X. L. *J. Polym. Sci., Part A: Polym. Chem.* **2007**, *45*, 5318−5328.
(66) Zhang, J. Y.; Li, Y. T.; Armes, S. P.; Liu, S. Y. *J. Phys. Chem. B* **2007**, *111*, 12111−12118.
(67) Ding, H.; Prodinger, W. M.; Kopecek, J. *Biomacromolecules* **2006**, *7*, 3037−3046.

Macromolecules

Article

pubs.acs.org/Macromolecules

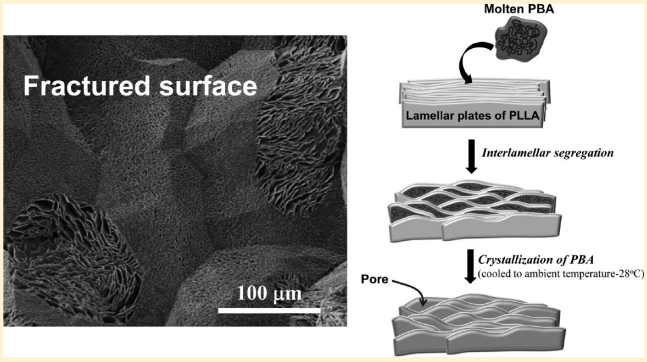
Phase Separation and Lamellae Assembly below UCST in Poly(L-lactic acid)/Poly(1,4-butylene adipate) Blend Induced by Crystallization

Siti Nurkhamidah[†,‡] and Eamor M. Woo*[,†]

[†]Department of Chemical Engineering, National Cheng Kung University, Tainan 701-01, Taiwan

[‡]Department of Chemical Engineering, Faculty of Industrial Technology, Sepuluh Nopember Institute of Technology, Kampus ITS Sukolilo, Surabaya 60111, Indonesia

ABSTRACT: The crystalline/crystalline poly(L-lactic acid)/poly(1,4-butylene adipate) (PLLA/PBA) blend system exhibits upper critical solution temperature (UCST) behavior below the melting temperature of PLLA. When the PLLA/PBA (50/50) blend is cooled to crystallize below UCST, phase-separated domains appear prior to crystallization of PLLA, resulting in PLLA spherulites being overlapped with the phase-separated domains. However, phase-separated domains only appear in blends when they are crystallized after being subjected to maximum melting temperature (T_{max}) for a short melting time (Δt_{max} < 3 min); oppositely, the phase domains in blends become invisible when held for longer times (>5 min). When PLLA/PBA (50/50) blend is melted for short Δt_{max}, the chain entanglement density is less; thus, the PBA chains are easy to be mutually expelled from the PLLA chains during crystallization of PLLA, resulting in PLLA-rich and PBA-rich separate domains. Apparently, phase separation in the PLLA/PBA blends is initiated by the crystallization of PLLA below UCST. Fractured surfaces of bulk blend samples show crystals of a polygonal shape, which is due to impingement between neighboring spherulites growing in 3D interior. For short Δt_{max}, the polygonal crystal is porous with two different sizes. Small and large pore sizes correspond to the PLLA-rich and PBA-rich domains, respectively. The formation of porous-structure lamellae in the PBA-rich domains is due to combined factors: (a) preformed PLLA spherulites acting as a growth template of PBA, leading to preferential orientation of PBA along PLLA lamellae, and (2) densification of PBA upon crystallization at ambient temperature. Detailed analyses were focused on the lamellar assembly leading to various pore sizes in the phase domains and dependence of the assembly patterns and pore sizes on the parameters governing the phase separation.



INTRODUCTION

Lamellar assembly in crystalline/crystalline blends may be influenced by mutual crystals of two constituents in the blends. Furthermore, if phase separation takes place either during, prior to, or after crystallization of one of the two constituents, the lamellar patterns are governed by two competing processes. Upper critical solution temperature (UCST) behavior, though much rarer than the lower critical solution temperature (LCST) phenomenon, can be occasionally observed above the melting points of the crystalline constituents, such as in the blend systems of isotactic polypropylene/ethylene−propylene (iPP/EPR) random copolymer,[1] poly(ε-caprolactone)/polystyrene (PCL/PS),[2,3] poly(ethylene-*co*-hexene)/poly(ethylene-*co*-butene) (PEH/PEB),[4,5] polystyrene/poly(α-methylstyrene) (PS/PαMS),[6,7] polystyrene/poly(4-methylstyrene) (PS/P4MS),[8] and poly(methyl methacrylate) (PMMA)/polyester blend systems.[9] However, there are even fewer blend systems that may exhibit UCST below the melting points of one or both constituents. When amorphous/crystalline polymer blends are quenched from a homogeneous state to a temperature below the UCST that is located below the melting point, liquid−liquid phase separation (LLPS) and crystallization occur spontaneously,[10] and the final blend morphology can be determined by kinetic competition between the crystallization and phase separation processes and if crystallization is too dominant and much faster than phase separation, phase domains may be hardly observed.[11] Recently, a blend of relatively low weight-average molecular weight (M_w) poly(L-lactic acid) (PLLA) with poly(butylene adipate) (PBA) is proven to exhibit UCST behavior below the melting temperature (T_m) of PLLA and above PBA's T_m.[12]

Simultaneous LLPS and crystallization in blends of semicrystalline/amorphous polymers has been less studied because LLPS cannot be determined easily due to its competition with crystallization. Some semicrystalline/semicrystalline blend systems, such as poly(vinylidene fluoride)/poly(1,4-butylene adipate) (PVDF/PBA), also exhibit a complicated behavior.[13−16] The phase diagram of this blend system exhibits a

Received: February 10, 2012
Revised: March 22, 2012
Published: March 28, 2012

 © 2012 American Chemical Society

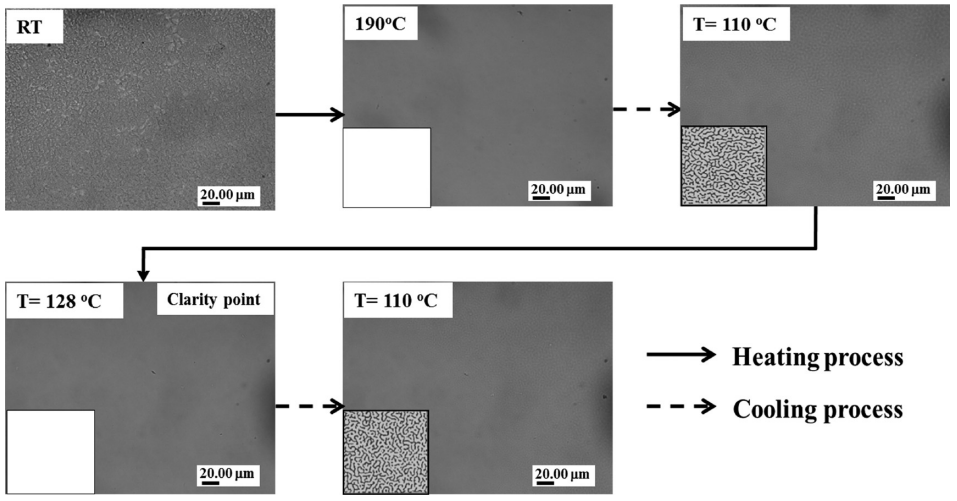


Figure 1. OM graphs showing phase reversibility upon cooling → heating → cooling cycles for PLLA/PBA (50/50) blend.

single glass transition temperature over the entire composition range; two distinct melting temperatures and a thermally reversible lower critical solution temperature (LCST) are observed. By holding at temperature above the melting point of the lower melt constituent, a semicrystalline/semicrystalline blend turns into a semicrystalline/amorphous one. A few other binary systems such as poly(ethylene terephthalate)/poly(ether imide) (PET/PEI)[17,18] and poly(vinylidene fluoride)/poly(methyl methacrylate) (PVDF/PMMA)[19,20] also reportedly exhibit UCST below the respective melting points and upon cooling, and their kinetics of phase separation is coupled with crystallization. In PET/PEI blend, the drastic increase in nucleation or a significant reduction in spherulite size due to the coupling of LLPS with crystallization has been observed.[17] A similar morphological feature is observed in poly(ε-caprolactone)/poly(ethyl glycol) (PCL/PEG) by Chuang et al.,[21] who have reported that when PCL/PEG blend crystallized at 48 °C (below the melting temperature of PCL = 62 °C), LLPS occurs prior to crystallization. They have suggested that this result is thermodynamically favored due to the fact that PCL supercooled below the melting temperature is short of free energy to overcome the energy barrier of the formation of stable nuclei. Thus, the spontaneous spinodal decomposition usually precedes the polymeric crystallization. For this reason, the liquid−liquid phase boundary can still affect the crystalline morphology during a kinetic process, although the final crystal−liquid equilibrium structure below the melting temperature is eventually determined by thermodynamics. Depending on structures of polymers, PBA exhibit different phase behavior in blends with other polymers. For examples, PBA is thermodynamically miscible with PVDF with LCST, but PBA blended with poly(3-chloropropyl methacrylate) (PCPMA) or poly(2-iodoethyl methacrylate) (PIEMA) is miscible. On the other hand, phase behavior of blend of PBA with PLLA, both being polyesters, is not so straightforward.

Blends of two polymers of not too different structures often show UCST behavior. Biodegradable polyesters are increasingly modified with other polyesters for enhancing their properties of balancing biodegradability. For these reasons, it is critical to understand the phase behavior and correlation between phase separation and crystallization for better patterning the crystalline morphology and for enhancing properties. Poly(L-lactic acid) (PLLA), a biodegradable polyesters with relatively higher T_m and PBA, an aliphatic polyester with relatively low T_m are ideally suited for such investigations. In this study, phase behavior of PLLA/PBA blends upon melt crystallization was investigated. PLLA and PBA are both semicrystalline polymers and both exhibit polymorphism behavior.[22−25] Upon heating and cooling, PLLA/PBA blends may exhibit complex combination of UCST, phase domains, dual crystalline spherulites, polymorphic crystal cells, etc. Phase behavior of blends with UCST may be influenced by some subtle factors to lead to distinct crystalline/crystalline phase separation upon cooling from UCST. Morphology of resultant phase separation and crystallization-induced lamellar assembly was analyzed to reveal influences from these two competing processes. Both morphologies of phase domains and lamellar structures in the domains might be influenced by the competing processes of these two kinds of kinetics in crystalline/crystalline blends of two biodedegradable polymers, as modeled by PLLA/PBA mixtures showing UCST, which constituted the objectives of this study.

EXPERIMENTAL SECTION

Materials and Preparation. Poly(L-lactic acid) (PLLA) was purchased from Polysciences, Inc., with a relatively low weight-average molecular weight. The PLLA material was characterized in-house using gel permeation chromatography (GPC, Waters) to reveal M_w = 11 000 g/mol (PDI = 1.1), which differs from the supplier-provided data using solution viscosity measurement. For this grade of PLLA, T_g = 45.3 °C and T_m = 155 °C. Poly(1,4-butylene adipate) (PBA) was purchased from Aldrich Co. with weight-average molecular weight of 12 000 g/mol, PDI = 1.30, T_g = −68 °C, T_m = 54 °C, and T_d = 250 °C. PLLA of a low-M_w grade was chosen for blending with PBA for balancing the phase behavior and faster crystallization rate of PLLA in the blends.

Samples of PLLA/PBA blends were prepared by solution casting using chloroform as solvent with concentration of 4 wt %. A drop of solution of the polymer was deposited and uniformly spread on a micro glass slide at 45 °C, and the solvent was allowed to fully evaporate in an atmosphere. The dried film on the micro glass slide was crystallized with top cover glass. Samples were heated on a hot stage to a maximum melting temperature (T_{max} = 190 °C) and held for different times (Δt_{max}) ranging from 1 to 10 min for erasing the prior residual crystals or nuclei, then rapidly removed to another hot stage preset at a designated isothermal T_c = 110 °C, and subsequently cooled to ambient.

Apparatus and Procedures. A polarized optical microscope (POM, Nikon Optiphot-2), equipped with a digital camera charge-

dx.doi.org/10.1021/ma300288v | Macromolecules 2012, 45, 3094−3103

coupled device (CCD) and a microscopic hot stage (Linkam THMS-600 with TP-92 temperature programmer), was used for characterizing optical homogeneity and crystalline morphology of the blends.

Atomic force microscopy (AFM, *di*Caliber, Veeco Corp., Santa Barbara, CA) investigations were made in intermittent tapping mode with a silicon tip (f_0 = 70 kHz, r = 10 nm) installed. The largest scan range was 150 × 150 μm but could be zoomed-in to 5 × 5 μm, and the scan was kept at 0.5 Hz for zoom regions (5 × 5 μm). Thin films were deposited on substrates of glass slides, with an open face for AFM characterization. AFM samples, sandwiched between two glass slides for fully crystallization, were quenched into liquid nitrogen for easy removal of the top cover. AFM measurements were also carried out to determine the height difference between the inside and outside areas of phase domain in PLLA/PBA (50/50) blend.

Samples of solution-cast films and bulk forms of PLLA/PBA blends were examined using a scanning electron microscope (FEI Quanta-400F, SEM) for revealing the lamellar pattern in the surface of spherulites and morphology in the interior of bulk sample. The top surface or fractured surface of sample is coated with gold by vacuum-sputtering prior to SEM characterization.

PLLA/PBA (50/50) blend samples in thicker bulk forms were characterized using wide-angle X-ray instrument (Shimadzu/XRD-6000) with a Cu Kα radiation (30 kV and 40 mA). The scanning angle (2θ) covered a range between 10° and 30° at a rate of 2°/min.

Melt viscosity of PLLA/PBA blend was measured by using Thermo Scientific HAAKE RheoStress 600 instrument in oscillation time curve mode with shear stress and frequency of 0.001 Pa and 0.1 Hz, respectively. Viscosity of this blend was measured at temperature of 190 ± 0.5 °C (T_{max}) as a function of time.

RESULTS AND DISCUSSION

Figure 1 shows OM graphs of phase reversibility upon cooling → heating → cooling cycles for PLLA/PBA (50/50) blend. As reported in a previous work,[12] the PLLA/PBA blend system exhibits UCST behavior below the melting temperature of PLLA. When samples were heated from ambient temperature (as cast sample) to higher temperature above melting temperature of PBA and PLLA, the PLLA/PBA blend showed homogeneous phase (one phase). However, after being cooled to a lower temperature, below PLLA melting temperature but above PBA melting temperature, the blend system transformed from the homogeneous phase to a heterogeneous phase (two-phase domains). After reaching the homogeneous phase at higher temperatures (i.e., 190 °C), the PLLA/PBA (50/50) blend could be returned to a heterogeneous phase at 110 °C upon cooling to ambient. However, after being heated back again to higher temperatures, the heterogeneous phase became homogeneous phase again at 128 °C. This temperature of clarity point (homogeneous state) is defined as temperature transition from heterogeneous to homogeneous phase upon heating. Reversibility in the cycle is seen as the heterogeneous phase can be obtained again after the sample is cooled from 128 °C to lower temperature, 110 °C. It is quite unusual that UCST is located below the melting points of the two constituents (below PLLA's T_m and above PBA's T_m). That is, above PLLA's T_m only a single molten mixture of PLLA/PBA exists, between T_m and UCST, the crystal and amorphous phases coexist in equilibrium; further down below UCST (but still above PBA melting), a PLLA crystal phase coexists with the amorphous PLLA and PBA domains in the blend within this temperature window. The UCST phase diagram with clarity points for PLLA/PBA blends as a function of composition has been shown in the previous study.[12]

For the PLLA/PBA (50/50) blend melted at 190 °C for 2 min and then crystallized at 110 °C, phase separation occurred in the early stage of initiation of crystallization. Eventually, PLLA was fully crystallized and the PLLA spherulites were seen to overlap with the crystal-induced phase domains. Such transitions are depicted by in-situ POM graphs. Figure 2 shows

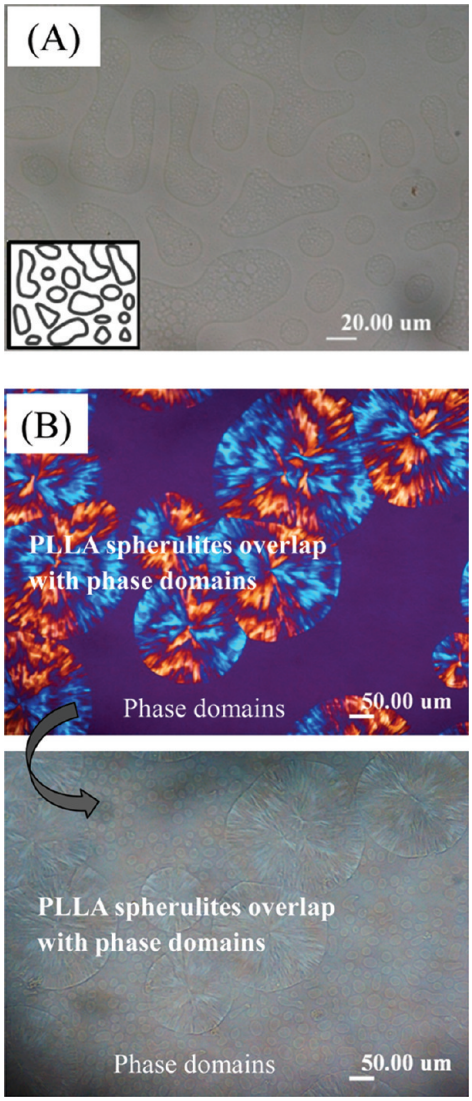


Figure 2. (A) OM graph showing phase separation for PLLA/PBA (50/50) blend. (B) POM graph showing PLLA spherulites overlapped with the phase domains. Graphs A and B taken at T_c = 110 °C.

(A) OM graph showing phase separation for PLLA/PBA (50/50) blend in the early stage of crystallization and (B) POM and OM graphs showing PLLA spherulites overlapped with the phase domains. Size of phase domains increases with increasing annealing time at T_c. As shown earlier in Figure 1 for the blend at T = 110 °C, the size of phase domain is small and irregular, wormlike structure. With increasing annealing time (a few seconds), those wormlike structure aggregates and form larger size of phase domain which is dominated by sphere shapes with diameter ≥15 μm (Figure 2A). After achieving equilibrium state, the size of phase domain is constant with increasing annealing time at T_c and PLLA crystals crystallized. PLLA forms ring-banded spherulites as shown in Figure 2B. PLLA has been reported shows ring-banded spherulites at T_c ranging from 125 to 130 °C.[26] Apparently, the crystallization temperature of PLLA to form ring-banded spherulites decreases by adding PBA as same as PLLA blended with PHB.[27] The OM

dx.doi.org/10.1021/ma300288v | *Macromolecules* 2012, 45, 3094−3103

graph in Figure 2B shows the phase-separated domain clearly, and those domains overlap with ring-banded spherulites of PLLA.

Figure 3 shows the holding time at maximum melting temperature (Δt_{max}) is the influencing factor for initiation of phase domains in PLLA/PBA (50/50) blend system upon crystallization. Phase-separated domains only appear in the short Δt_{max} (2 min). With increasing Δt_{max}, the nucleation density decreases, which leads to large size of spherulites. Not only nucleation density but also spherulites growth rate decreases with the increase of Δt_{max} as shown in Figure 3B. The growth rate of PLLA spherulites for Δt_{max} = 2 and 10 min is 1.65 and 1.18 μm/s, respectively. For short and long Δt_{max}, the difference is not only in the existence of phase domain, nuclei density, size, and growth of spherulites but also on regularity of PLLA ring-banded spherulites. Irregular ring-banded spherulites are associated with PLLA spherulites crystallized by quenching from T_{max} for short Δt_{max} (2 min). However, for blends subjected to long t_{max} and similarly crystallized, the ring bands become regular owing to more severe impingement between spherulites.

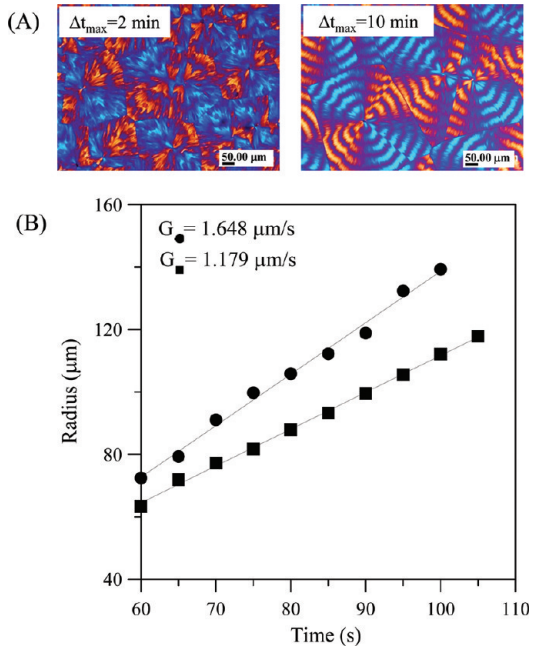


Figure 3. (A) Effect of Δt_{max} to the formation of phase domains in PLLA/PBA (50/50) blend system. (B) Growth rates of PLLA/PBA (50/50) blend crystallized at 110 °C at different Δt_{max}: (●) 2 min and (■) 10 min.

Those phenomena can be explained based on the number of entanglement density (ν_e) during the melting process. The number of entanglement density in blends usually increases with increasing melting time held at maximum melting temperature.[28,29] Figure 4 shows a scheme for illustrating the effect of Δt_{max} on the formation of phase separation in the PLLA/PBA (50/50) blend system. For short Δt_{max}, the number of entanglement density is less or almost zero; thus, PBA chains are easy to be expelled from PLLA chains during crystallization of PLLA, resulting in PLLA-rich and PBA-rich domains and exhibiting crystallization of PLLA spherulites overlap with phase-separated domains as shown in Figure 2B. In contrast, for long Δt_{max}, there is no phase-separated domain because the number of entanglement density is more; thus, most of the PBA chains are entangled with PLLA chains which lead to larger spherulites size with slower growth rate.

Morphology of crystallized blend samples by quenching from T_{max} (190 °C) for Δt_{max} ranging from 1 to 10 min was monitored in situ with time evolution by POM (not shown here for brevity). For shorter Δt_{max} (1 and 2 min), phase domains in crystallized blends with size ≥15 μm appear, and the PLLA spherulites are small and irregular. Tiny phase domains and regular ring-banded spherulites are resulted for intermediate Δt_{max} = 5 min. In contrast, there are no phase

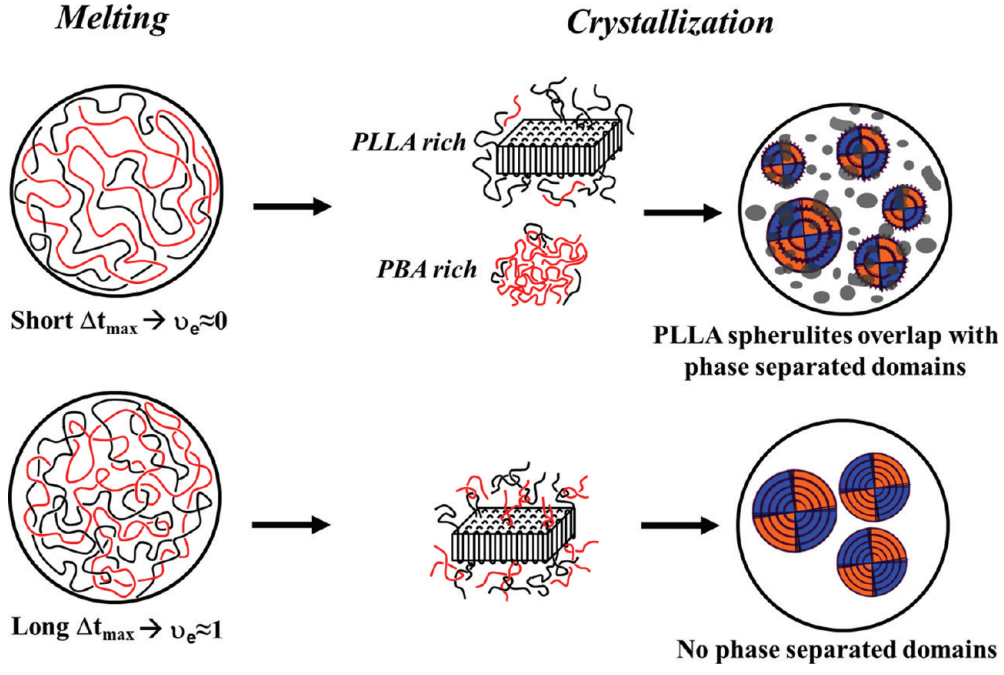


Figure 4. Scheme showing the effect of Δt_{max} on formation of phase separation in PLLA/PBA (50/50) blend system.

dx.doi.org/10.1021/ma300288v | Macromolecules 2012, 45, 3094−3103

domains, and the size of PLLA ring bands becomes greater in spacing and more regular for longer Δt_{max} (7 and 10 min). In the early discussion, with increasing Δt_{max}, the number of entanglement density increases which leads to large size of spherulites. From the thermogravimetry analisys (TGA), the degradation temperature of PLLA and PBA in nitrogen was determined to be 310 and 250 °C, respectively. TGA results proved no degradation at T_{max} = 190 °C. Evidence of thermal stability at 190 °C could be used to rule out possibility of decreasing molecular weight due to thermal degradation.

The original M_w's (11 000 and 12 000 g/mol) of these two polymers, albeit not particular high, could be expected to generate sufficient number of chains entanglement to influence the phase behavior. The classical polymer theory points out that a polymer generally should have M_w = 25 000 g/mol to be an onset of sufficient entanglement for good mechanical properties of polymers. It should be emphasized that it is not the mechanical properties but phase separate kinetic process of the blend that is the issue here. That is, it does not take extremely high M_w to achieve the onset of chain entanglement for influencing the kinetics of phase separation, which ultimately influences the solidified morphology when later cooled to crystallize.

To further show evidence whether the number of entanglement density or thermal degradation is correlated or attributed to the phase behavior in the PLLA/PBA (50/50) blend at T_{max}, the melt viscosity of this blend as a function of melting time (from 0 up to 60 min) was measured, as shown in Figure 5. The result shows that the complex melt viscosity of

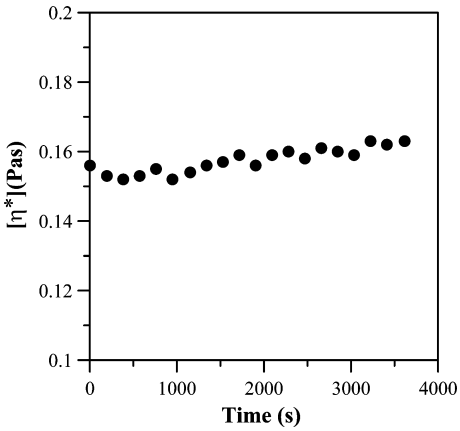


Figure 5. Melt viscosity of PLLA/PBA (50/50) blend as a function of time at T_{max} = 190 °C.

PLLA/PBA (50/50) blend remains almost stable but slightly increases with longer time at T_{max} = 190 °C. It should be commented here that the measured complex viscosity of the PLLA/PBA (50/50) blend is relatively low at 190 °C. This is quite expected because (1) PLLA is mixed with PBA at 50 wt %, (2) the complex viscosity of polymers typically follows the Arrhenius relationship $[\eta^* = \eta^{*\circ} \exp(-E/RT)]$, and T_{max} = 190 °C is substantially above PLLA's T_m = 155 °C and much above PBT's T_m = 54 °C. Additionally and more importantly, this melt-viscosity result also shows that there is no thermal degradation during polymer melt holding at T_{max} = 190 °C, as thermal degradation, if taking place, would have rendered chain cessation and thus a decrease in the viscosity. Thus, both TGA and viscosity measurements are in mutual agreement, proving none or very little degree of thermally induced chemical changes in the blend system. The stable with minor increase of melt viscosity indicates (1) no thermal degradation and (2) minor increase of chain entanglement density.[30]

In-situ growth of PBA at ambient temperature in the presence of PLLA ring-banded spherulites is shown in Figure 6.

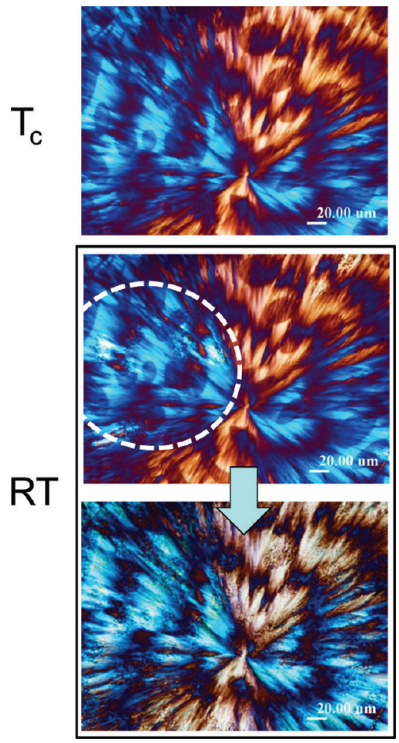


Figure 6. POM images observing in-situ growth of PBA at ambient temperature.

PBA does not crystallize at T_c = 110 °C but only crystallizes at temperature near or below ambient temperature (30 °C or lower). In the early stage of crystallization at this temperature, some part of PBA crystallizes as indicated by circle dashed line and finally fully crystallized in the whole sample. The pattern of PBA crystals cannot be distinguished; apparently, crystallization of PBA follows the pattern of PLLA ring-banded spherulites. The later-stage PBA crystallization on or within PLLA does not disturb or change the ring-band pattern of PLLA, but it only enhances the optical birefringence of PLLA ring-banded spherulites. PBA does not crystallize only inside of phase-separated domains but also extents to the whole crystalline PLLA domains. As shown in the previous scheme in Figure 4, there are two separated phases, PLLA-rich and PBA-rich phases, for shorter Δt_{max}. Thus, it can be expected that PBA crystallizes in the whole PLLA spherulites and not only inside the phase-separated domains.

AFM analysis was carried out to investigate the detailed morphology of phase domains in the crystallized PLLA/PBA (50/50) blend. Figure 7 shows AFM images of PLLA/PBA (50/50) blend melt-crystallized at 110 °C by quenching from T_{max} = 190 °C for 2 min. After being fully crystallized, the sample was quenched into liquid nitrogen to remove the top cover easily and then scanned by using AFM. The phase domain is indicated by black arrow in Figure 7A. Figure 7B shows zoom-in of square-marked region in Figure 7A on the phase domains to see more clearly where the ridge region of spherulites overlaps with phase domains. Morphology of the

dx.doi.org/10.1021/ma300288v | Macromolecules 2012, 45, 3094−3103

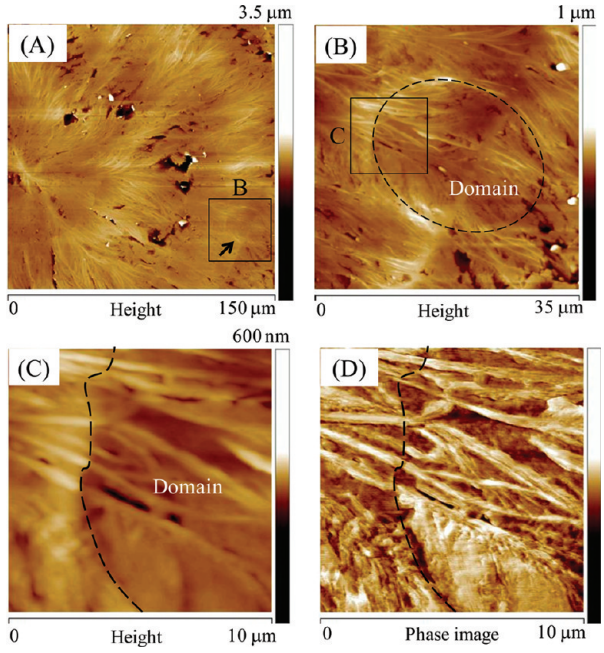


Figure 7. AFM images of PLLA/PBA (50/50) blend melt-crystallized at 110 °C by quenching from T_{max} = 190 °C for 2 min. (A) Height image at 150 × 150 μm, (B) zoom-in of square-marked regions in images (A), (C) further zoom-in of squared region in (B), and (D) phase image of (C).

area inside and outside of phase domain is the same as shown in Figure 7C,D. The boundary between interior and exterior of phase domain is marked by a dashed line. The difference between inside and outside area of phase domain is the brightness, reflecting the differing height of the regions in AFM height images. It means that the inside and outside areas of the phase domain have some height difference. By further measuring the height profiles of these two areas, it was found that the outside area of phase domain is about 40 nm higher than the inside area of phase domain. The AFM phase image (Figure 7D) shows that the lamellar patterns of these two different areas are the same. Obviously, the inside and outside areas of phase domain are only different in height, but the lamellar pattern remains unchanged. This result shows that the phase domains do not affect the morphology of PLLA spherulites in PLLA/PBA blend. During crystallization, the PLLA crystals penetrate into the phase-separated domain, resulting in PLLA ring-banded spherulites overlapping with the phase-separated domains. Apparently, PLLA ring-banded spherulites serve as the growth template for PBA crystals to later grow onto them. The stronger birefringence of the PLLA/PBA (50/50) sample crystallized at ambient temperature after being quenched from T_c is apparently resulted from the additional PBA crystal birefringence imposed onto the PLLA spherulites.

Phase domains have been shown to appear in thin-film PLLA/PBA blend samples. PLLA/PBA bulk samples were also characterized by monitoring the thermal behavior using hot stage. First, more details of phase separation morphology of fractured samples were analyzed by using SEM. Figure 8 shows SEM graphs of PLLA/PBA (50/50) bulk samples melt crystallized at 110 °C by quenching from T_{max} = 190 °C for 2 min: (A) top surface, (B) fractured surface, (C) zoom-in of fractured surface in graph (B), and (D) underneath the top surface in correlation with fractured surface. As shown in SEM graph (A), the morphology of top surface is ringless spherulites, or at most, it can be called a ringed spherulite with only one wide band (50 μm wide). The size of the spherulites in bulk blend is smaller; apparently, about 100 μm in diameter; however, by contrast, the spherulites size in thin films is much

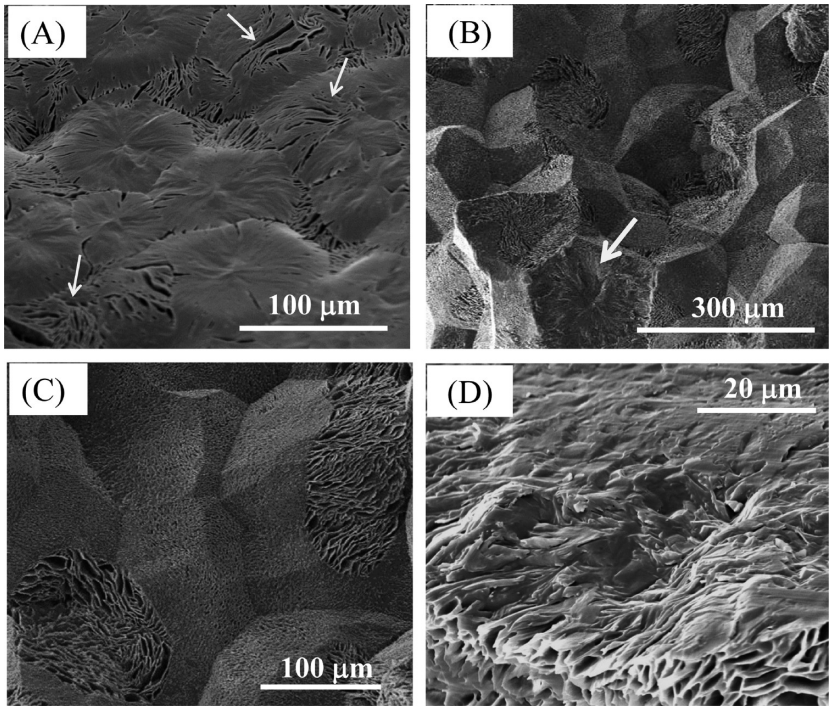


Figure 8. SEM graphs of PLLA/PBA (50/50) blend bulk samples melt crystallized at 110 °C by quenching from T_{max} = 190 °C for 2 min: (A) top surface, (B) fractured surface, (C) zoom-in of fractured surface in graph B, and (D) underneath the top surface in correlation with fractured surface.

dx.doi.org/10.1021/ma300288v | *Macromolecules* 2012, 45, 3094−3103

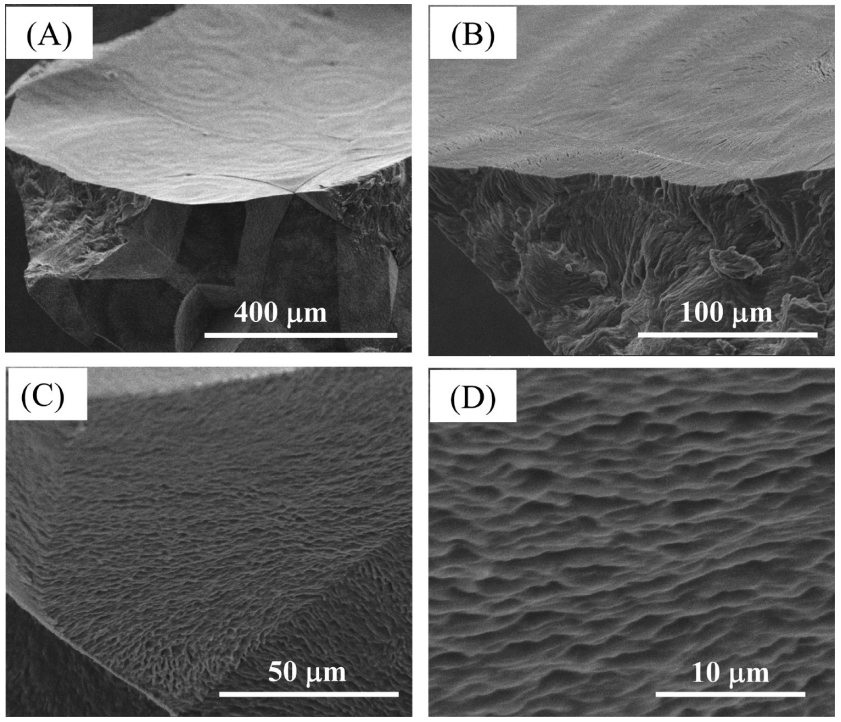


Figure 9. SEM graphs of PLLA/PBA (50/50) blend bulk samples melt crystallized at 110 °C by quenching from T_{max} = 190 °C for 10 min: (A) top surface in correlation with fractured surface, (B) zoom-in of graph A, (C) zoom-in of fractured surface in graph A, and (D) detailed morphology of fractured surface.

larger, about 300−400 μm in diameter. With 100 μm in diameter, it only forms center of spherulites and one band of ring-banded spherulites in the bulk PLLA/PBA blend sample. The number of nuclei in the bulk sample is greater; that may be the reason why it exhibits small size of spherulites. There is no phase-separated domain discernible on the top surface, but there are many voids/pores on the top surface, especially in the impingement region between two spherulites, forming interfaces of two crystal types. Actually, pores on the top surface of bulk sample also appear in the center or in the whole spherulite as shown by the arrow mark in SEM graph A.

Owing to interspherulite impingement among the neighboring 3D spherulites, the fractured surface morphology of bulk PLLA/PBA blend samples exhibits polygonal shapes with rough cleaved lamellae. Apparently, the polygonal-shape boundary in the fractured surface of PLLA/PBA bulk sample is caused by the impingement between spherulites. When the growth rates between two spherulites are the same and the two primary nuclei appear simultaneously, a straight impingement line will be formed.[31] In the 3D bulk forms, the impingement of spherulites with equal growth rate should form a planar surface instead of straight impingement line which is usually formed in 2-D. In the bulk sample, spherulites are easy to grow in 3D. Spherulites grow almost simultaneously and impinge to each other from any directions when they crystallize in 3D; thus, polygonal shape could be formed instead of a well-rounded sphere. Graph B shows the morphology of fractured surface in the bulk sample is heterogeneous, which is indicated by the presence of two types of surface pattern in the polygonal. These two types of surface pattern can be seen clearly in graph C. The detailed surface pattern of fractured surface is similar to a porous structure. For PLLA/PBA blend held with short Δt_{max} = 2 min, there are two different pore sizes on the top of polygonal crystals, small and large pores. Large pore size is minority, and its shape is similar to the phase-separated domain that is observed in the surface of thin films, sphere shape. The correlation between pores and interiors of polygonal shape can be observed clearly in graph D. Pores only form in the surface of polygonal crystals (spherulites); they do not go through the interior of polygonal. As indicated by arrow in graph B, the interior of polygonal crystals is not porous. The length of pore is ca. 20 μm from the polygonal surface as shown in graph D.

In comparison, the detailed morphology of PLLA/PBA (50/50) bulk sample for Δt_{max} = 10 min with no phase separation is shown in Figure 9. As shown in graph A, the morphology on the top and fractured surface is ring-banded spherulites and polygonal shape, respectively. The morphology on the top surface of bulk is in agreement with that in thin film, large and regular ring-banded spherulites. Zoom-in of the left side of graph A is shown in graph B. The detailed morphology inside the polygonal crystals can be seen clearly, and it does not show a porous structure. Graph C shows the surface of polygonal is similar to a porous structure. However, the detailed morphology of polygonal surface is not of a porous structure as shown in graph D.

In addition, two additional PLLA/PBA blend compositions nearby 50/50 were examined. Figure 10 shows fractured surfaces of phase separation morphology of PLLA/PBA blend (40/60 and 60/40 in comparison to 50/50) crystallized at 110 °C by quenching from T_{max} = 190 °C (2 min). The PLLA/PBA blend (40/60) composition shows a greater volume fraction of the PBA constituent than either (50/50) or (60/40) blend compositions and result in large pore size. However, with a less fraction of the PBA constituent, the PLLA/PBA (60/40) blend shows small pore size. Apparently, the size of porous structure depends on the fraction of PBA in the PLLA/PBA blend system. By comparing the morphology patterns of blends of various compositions, it is apparent that the large and small

dx.doi.org/10.1021/ma300288v | *Macromolecules* 2012, 45, 3094−3103

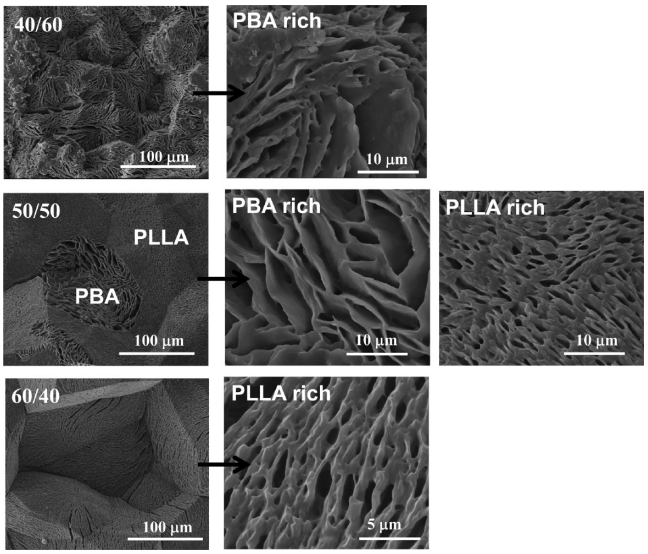


Figure 10. SEM graphs for fractured surfaces of PLLA/PBA blend (40/60 and 60/40 in comparison to 50/50) crystallized at 110 °C by quenching from T_{max} = 190 °C for 2 min and then cooled to ambient (28 °C).

pore sizes in PLLA/PBA (50/50) blend with short Δt_{max} can be attributed to the separated domains of the PBA-rich and PLLA-rich constituents, respectively. By contrast, phase-separated domains in the fractured surface of PLLA/PBA of either 60/40 or 40/60 composition cannot be observed, which may be due to the size of phase-separated domain being too small to be discerned. Additional morphology characterization on thin film samples (instead of bulk) revealed that phase-separated domains with 1−2 μm in diameter can be observed in the thin films after being crystallized at 110 °C for PLLA/PBA (60/40) and (40/60) (for brevity, morphology results for thin films not shown here). The PBA lamellae in the domain assume all edge-on orientation (perpendicular to fracture plane), with weblike interconnection between lamellar plates. The pores in PBA-rich domains have micrometer-scale sizes, while those in the PLLA-rich domains are averaged in the hundreds of nanometers (submicrometers). The nano- or micrometer-size pores in the phase-separated domains of PLLA/PBA (50/50) blend are apparently created by solidification and densification of PBA lamellae upon crystallization at ambient temperature.

Such pores and their lamellar patterns in the UCST-crystallized crystalline/crystalline PBA/PLLA blend resemble the phase-separation patterns in many commercially available polymer membranes. Materials with a porous structure of controlled porosity sizes are usually used in membranes or scaffolds, which are fabricated by using thermally induced phase separation (TIPS) method.[32−39] In the TIPS method,[35] a solution of polymer in an appropriate solvent is cast in a mold at an elevated temperature and then quenched to temperature below the freezing point of the solvent; then, the sample is subsequently freeze-dried to produce a desired porous structure. PLLA is commonly used for biodegradable polymer membranes or porous biodegradable polymeric scaffolds.[36−39] The blend of PLLA/PCL has been used to fabricate polymer membrane via TIPS by using mixed diluent, 1,4-dioxane and water.[40] However, in the PLLA/PBA blend system, porous structure can be obtained from crystallization below UCST without using solvent as diluents. The polygonal shape with porous structure in the fractured surfaces of PLLA/PBA blend is similar to that in fractured surface of poly(vinylidene fluoride) (PVDF) membranes.[31,32] Large pore size in the PLLA/PBA blend system is also similar to that of porous chitosan scaffolds prepared by freeze-drying.[34] Apparently, the crystalline/crystalline PLLA/PBA blend with UCST-phase separation can be considered as a potential candidate to fabricate into either polymer membranes or polymeric scaffolds.

In summary, the PLLA/PBA blend exhibits UCST and a borderline phase behavior between miscibility and immiscibility, whose miscibility or phase separation is dependent on holding time at T_{max} and T_c at which crystallization takes place. The PBA/PLLA blend is miscible when kept in melt above UCST but exhibits simultaneous phase separation prior to crystallization when cooled down and crystallized below UCST. With increasing annealing time at T_c, phase domain transforms from a wormlike structure to sphere with diameter ≥15 μm. The phase domains within a few seconds reach an equilibrium state, as indicated by phase domains stoping to grow. After that, PLLA crystallized and overlapped with those phase domains. Phase-separated domain only appears in PLLA/PBA blends held for short Δt_{max} due to the number of entanglement density for short Δt_{max} is less than that for long Δt_{max}. Thus, the PBA chains are easy to be rejected from the growth front during crystallization of PLLA and form a PBA-rich domain. Phase domains not only can be observed in the thin films but also in the bulk samples. Phase domains in the fractured surface of PLLA/PBA (50/50) bulk sample with short Δt_{max} appear with large pores. Fractured surface of bulk sample is polygonal with porous structure and the size of pore is affected by the fraction of PBA in the blend system. The regions of large and small pore sizes are the characteristic of the PBA-rich and PLLA-rich domains, respectively. Scheme for the formation of porous structures in the PLLA/PBA blend is shown in Figure 11. The scheme illustrates that most of PBA chains are rejected from the growth front of PLLA during crystallization of PLLA in the blend, which initially leads to formation of PLLA-rich and PBA-rich domains. When the PLLA crystal continues to grow, PLLA penetrates/overlaps with PBA-rich domain and amorphous liquid (molten) PBA segregates in the interlamellar region of PLLA. After being cooled to ambient temperature, PBA crystallizes on or within PLLA lamellae and PLLA crystal as its growth template. Thus, crystallization of PBA does not disturb or change the morphology of PLLA spherulites. Apparently, later crystallization of PBA at ambient enhances the crystalline birefringence of spherulites and the larger porous structure in the PBA-rich domain can be formed due to the crystal densification upon crystallization of PBA.

The crystal cell types in the PLLA/PBA blend were verified, in addition to the spherulite morphology and pores created by lamellar assembly in the crystalline/crystalline PLLA/PBA blend. Both PLLA and PBA constituents in the blend have been known to have polymorphism behavior. To investigate the crystal cells in the blends, characterization using WAXD analysis was done. PLLA/PBA blends were crystallized by using two-step crystallizations, at 110 °C for 1 h to first crystallize PLLA constituent and then quenched to 28 or 35 °C, respectively, to crystallize the PBA constituent. Figure 12 shows WAXD patterns of PLLA/PBA (50/50) blend melted at 190 °C for different t_{max} (2 and 10 min), first crystallized at 110 °C and then crystallized at different T_c (28 and 35 °C). When crystallized at 28 and 35 °C, PBA is known to be packed in polymorphic α + β- or solely α-form crystals, respectively.[25] When crystallized at T_c = 28 °C, PBA shows multiple

dx.doi.org/10.1021/ma300288v | Macromolecules 2012, 45, 3094−3103

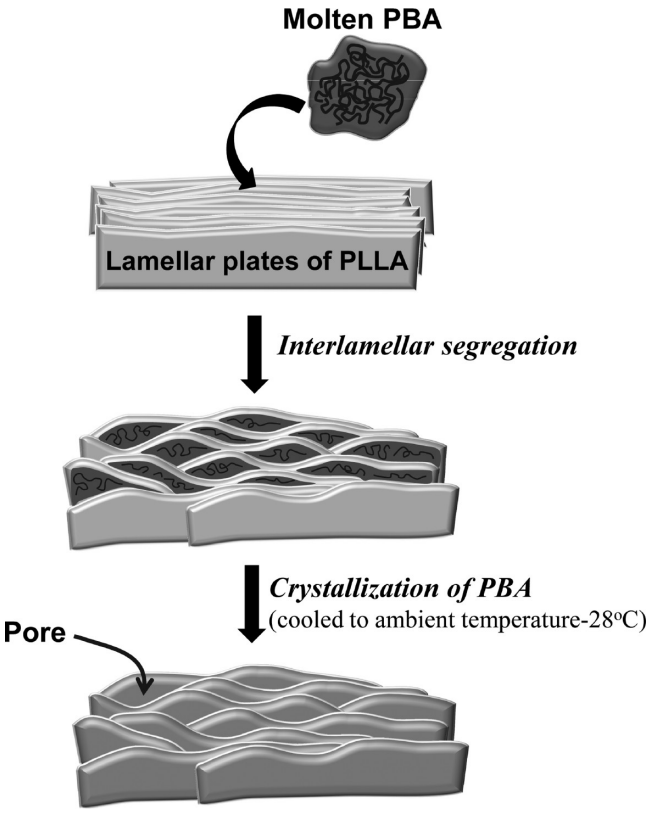


Figure 11. Scheme of the formation of pore structure on the surface of fractured bulk sample in the PLLA/PBA blend system.

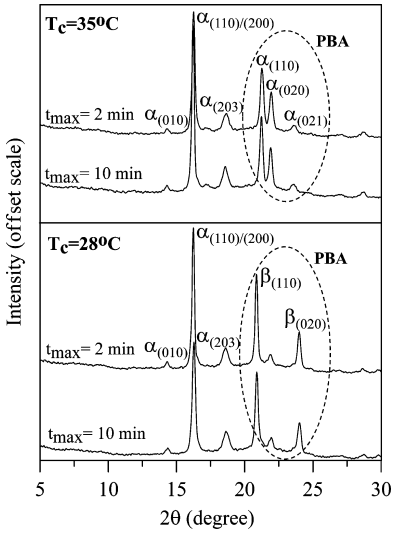


Figure 12. WAXD intensity profiles of PLLA/PBA (50/50) blend melted at 190 °C for different Δt_{max} (2 and 10 min), first crystallized at 110 °C and then crystallized at different T_c (28 and 35 °C).

diffraction peaks, attributed to existence of α- or β-form crystal cells (polymorphism). For PLLA crystallized at 110 °C, its crystal cell is α-form. The facts of WAXD analysis reveals that the crystal cells of PLLA and PBA remain the same after blending and after thermal treatment at different Δt_{max}.

CONCLUSION

The PLLA/PBA blend system exhibits upper critical solution temperature (UCST) behavior below the melting temperature of PLLA. When the PLLA/PBA (50/50) blend crystallized below UCST, phase-separated domains appear prior to crystallization of PLLA, resulting in the PLLA spherulites which are seen to overlap with the phase-separated domains. However, phase-separated domains only appear when the sample is melted for a short maximum melting time (Δt_{max} = 2 min). For longer Δt_{max} (10 min), there is no phase-separated domain. Apparently, when PLLA/PBA (50/50) blend is melted for short Δt_{max}, the number of entanglement density is less; thus, PBA chains are easy to be expelled from PLLA chains during crystallization of PLLA, resulting in PLLA-rich and PBA-rich domains. Because the entanglement density is less, the number of nucleation density is more, resulting in smaller size of spherulites, and the spherulites growth is fast. However, for long Δt_{max}, the number of entanglement density is more; thus, PBA chains remain entangle with PLLA chains during crystallization of PLLA, resulting in smaller nucleation density, larger size of spherulites, and slow growth rate of PLLA spherulite. Apparently, phase separation in the PLLA/PBA blends is initiated by the crystallization of PLLA. The later-stage crystallization of PBA at ambient temperature on or within PLLA does not disturb or change the earlier morphology of PLLA; however, it enhances the birefringence of PLLA spherulites. Apparently, PLLA spherulites is the growth template of the later-stage crystallization of PBA. The crystal cells of PLLA and PBA remain the same after blending and after thermal treatment at different Δt_{max} as shown by WAXD pattern of the PLLA/PBA blend.

Interiors of bulk PLLA/PBA blends with crystallization-induced phase separation below UCST were examined. Lamellar assembly in the phase domains exhibits interesting patterns depending on kinetic process of phase separation. Fractured surface of PLLA/PBA blend exhibits polygonal shape due to the interspherulite impingement among the neighboring 3D spherulites. The surface pattern of polygonal is porous structure, and pore size is affected by the fraction of PBA in PLLA/PBA blend. Large and small pores (cavities) can be obtained from PBA-rich and PLLA-rich domains, respectively. Porous structures are formed due to densification of PBA upon crystallization at ambient temperature. It has been shown that the PLLA/PBA blend exhibits dual-distribution porous structures in both domains; thus, this kind of blend system can be considered as potential candidate materials to fabricate membranes or scaffolds based on biodegradable polymers and their mixtures of controlled compositions.

AUTHOR INFORMATION

Corresponding Author

*E-mail: emwoo@mail.ncku.edu.tw; Fax: +886 6 234-4496; Tel: +886 6 275-7575 ext 62670.

Notes

The authors declare no competing financial interest.

ACKNOWLEDGMENTS

This work has been financially supported by basic research grants (NSC 99-2221-E-006-014-MY3) in three consecutive years from Taiwan's National Science Council (NSC), to which the authors express their gratitude. Melt viscosity of PLLA/PBA blend was measured with instrument and technical help provided by Mr. Chao-Shun Chang of R&D Center of Formosa Plastics Corp. (Kaohsiung, Taiwan), to which the authors express their sincerest thanks.

REFERENCES

(1) Inaba, N.; Sato, K.; Suzuki, S.; Hashimoto, T. *Macromolecules* **1986**, *19*, 1690−1695.
(2) Tanaka, H.; Nishi, T. *Phys. Rev. Lett.* **1985**, *55*, 1102−1105.
(3) Tanaka, H.; Nishi, T. *Phys. Rev. A* **1989**, *39*, 783−794.
(4) Shimizu, K.; Wang, H.; Wang, Z.; Matsuba, G.; Kim, H.; Han, C. C. *Polymer* **2004**, *45*, 7061−7069.
(5) Wang, H.; Shimizu, K.; Hobbie, E. K.; Wang, Z. G.; Meredith, J. C.; Karim, A.; Amis, E. J.; Hsiao, B. J.; Hsieh, E. T.; Han, C. C. *Macromolecules* **2002**, *35*, 1072−1078.
(6) Rameau, A.; Gallot, Y.; Marie, P.; Farnoux, B. *Polymer* **1989**, *30*, 386−392.
(7) Callaghan, T. A.; Paul, D. R. *Macromolecules* **1993**, *26*, 2439−2450.
(8) Chang, L. L.; Woo, E. M. *Macromol. Chem. Phys.* **2001**, *202*, 636−644.
(9) Li, S. H.; Woo, E. M. *Colloid Polym. Sci.* **2008**, *286*, 253−265.
(10) Chen, H. L.; Hwang, J. C.; Yang, J. M.; Wang, R. C. *Polymer* **1998**, *39*, 6983−6989.
(11) Burghardt, W. R. *Macromolecules* **1989**, *22*, 2482−2486.
(12) Nurkhamidah, S.; Woo, E. M. *J. Phys. Chem. B* **2011**, *115*, 13127−13138.
(13) Penning, J. P.; Manley, R. J. *Macromolecules* **1996**, *29*, 77−83.
(14) Fujita, K.; Kyu, T.; Manley, S. J. *Macromolecules* **1996**, *29*, 91−96.
(15) Liu, L. Z.; Chu, B.; Penning, J. P.; Manley, R. J. *Macromolecules* **1997**, *30*, 4398−4404.
(16) Isayeva, I.; Kyu, T.; Manley, R. J. *Polymer* **1998**, *39*, 4599−4608.
(17) Chen, H. L. *Macromolecules* **1995**, *28*, 2845−2851.
(18) Chen, H. L.; Hwang, J. C.; Yang, J. M.; Wang, R. C. *Polymer* **1998**, *39*, 6983−6989.
(19) Tomura, H.; Saito, H.; Inoue, T. *Macromolecules* **1992**, *25*, 1611−1614.
(20) Lee, J. S.; Prabu, A. A.; Kim, K. J. *Macromolecules* **2009**, *42*, 5660−5669.
(21) Chuang, W. T.; Jeng, U. S.; Sheu, H. S. *Macromol. Res.* **2006**, *14*, 45−51.
(22) Minke, R.; Blackwell, J. *J. Macromol. Sci., Phys.* **1979**, *B16*, 407−417.
(23) Minke, R.; Blackwell, J. *J. Macromol. Sci., Phys.* **1980**, *B18*, 233−255.
(24) Gan, Z.; Abe, H.; Doi, Y. *Macromol. Chem. Phys.* **2002**, *203*, 2369−2374.
(25) Wu, M. C.; Woo, E. M. *Polym. Int.* **2005**, *54*, 1681−1688.
(26) Nurkhamidah, S.; Woo, E. M. *Colloid Polym. Sci.* **2011**, *290*, 275−288.
(27) Nurkhamidah, S.; Woo, E. M. *Ind. Eng. Chem. Res.* **2011**, *50*, 4494−4503.
(28) Yamazaki, S.; Hikosaka, M.; Toda, A.; Wataoka, I.; Gu, F. *Polymer* **2002**, *43*, 6585−6593.
(29) Yamazaki, S.; Gu, F.; Watanabe, K.; Okada, K.; Toda, A.; Hikosaka, M. *Polymer* **2006**, *47*, 6422−6428.
(30) Peacock, A.; Calhoun, A. *Polymer Chemistry: Properties and Applications*, 1st ed.; Hanser Gardner Publications: Cincinnati, OH, 2006; Chapter 6, p 110.
(31) Singfield, K. L.; Chisholm, R. A.; King, T. L. *J. Chem. Educ.* **2012**, *89*, 159−162.
(32) Yang, J.; Li, D. W.; Lin, Y. K.; Wang, X. L.; Tian, F.; Wang, Z. *J. Appl. Polym. Sci.* **2008**, *110*, 341−347.
(33) Yang, J.; Wang, X. L.; Tian, Y.; Lin, Y.; Tian, F. *J. Polym. Sci., Part B: Polym. Phys.* **2010**, *48*, 2468−2475.
(34) Madihally, S. V.; Matthew, H. W. T. *Biomaterials* **1999**, *20*, 1133−1142.
(35) Lloyd, D. R.; Kinzer, K. E.; Tseng, H. S. *J. Membr. Sci.* **1990**, *52*, 239−261.
(36) Nam, Y. S.; Park, T. G. *J. Biomed. Mater. Res.* **1999**, *47*, 8−17.
(37) Tanaka, T.; Tsuchiya, T.; Takahashi, H.; Taniguchi, M.; Ohara, H.; Lloyd, D. R. *J. Chem. Eng. Jpn.* **2006**, *39*, 144−153.
(38) Goh, Y. Q.; Ooi, C. P. *J. Mater. Sci.: Mater. Med.* **2008**, *19*, 2445−2452.
(39) Budyanto, L.; Goh, Y. Q.; Ooi, C. P. *J. Mater. Sci.: Mater. Med.* **2009**, *20*, 105−111.
(40) Tanaka, T.; Tsuchiya, T.; Takahashi, H.; Taniguchi, M.; Lloyd, D. R. *Desalination* **2006**, *193*, 367−374.

Macromolecules

Article

pubs.acs.org/Macromolecules

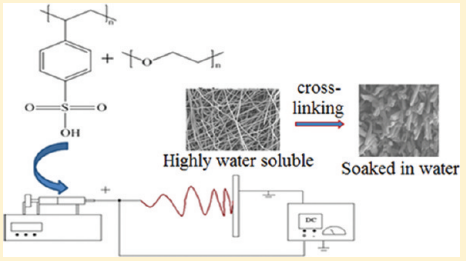
Chemical Cross-Linking of Highly Sulfonated Polystyrene Electrospun Fibers

Chitrabala Subramanian,*[,†] Marcus Giotto,[†] R. A. Weiss,[‡] and Montgomery T. Shaw[†]

[†]Polymer Program, Institute of Materials Science, University of Connecticut, Storrs, Connecticut 06269, United States

[‡]Department of Polymer Engineering, University of Akron, Akron, Ohio 44325, United States

ABSTRACT: Electrospun nanofibers of highly sulfonated polystyrene (IEC ~ 4.8 mequiv/g) might be good candidates for use in ion exchange applications because of their ability to form continuous, highly conducting pathways for cation transport. However, such fibers suffer in terms of dimensional stability due to high water uptake at elevated humidity. To improve the stability of the electrospun nanofiber mats in water, the polyelectrolyte was coelectrospun in the presence of a high molecular weight poly(ethylene oxide) (PEO). Addition of PEO to the spinning dope helped improve the spinnability of the polyelectrolyte and subsequent heat treatment improved the stability of the fiber mats in water. Increasing PEO concentration in the fiber mats reduced the solubility of the heat-treated fiber mats in water; suggesting that the fibers were cross-linked by or in the presence of the PEO. To understand the chemistry of this apparent cross-linking reaction, the electrospun fiber mats were heated in a solid state ^{1}H NMR rotor and changes in the spectrum were monitored as the reaction progressed. The hypothesis is that at higher temperatures, the two polymers react with each other to form sulfonic acid esters that form water-resistant cross-links. An alternative hypothesis of a free-radical cross-linking reaction was not supported by the observations.



1. INTRODUCTION

Perfluorinated ionic membranes such as Nafion are the dominant transport media used for proton exchange membrane (PEM) fuel cells, primarily because of their high proton conductivity and exceptional oxidative stability.[1] Nafion is a random copolymer composed of a hydrophobic backbone with acid-containing side groups. One limitation of the random-copolymer PEM is that the transport and mechanical properties are coupled, so that optimizing one usually degrades the other. Hence, there has been a renewed effort to develop new PEM materials, especially composite materials that allow separation of the transport and mechanical properties. Some of the approaches that have been investigated are block copolymers,[2] nanofiber-based networks[3] and filled systems using particles of high ion exchange capacity (IEC).[4]

Sulfonated polystyrene (SPS), either as a pure polymer or in blends, has been explored for PEM fuel cells. One limitation with using sulfonated polymeric membranes is to strike a balance between proton conductivity and dimensional stability in water at high sulfonation levels. A high degree of sulfonation helps attain high proton conductivity; but, at the same time, high sulfonation levels lead to water solubility. Hence the membranes swell excessively and have poor dimensional stability. In the past, researchers have investigated different cross-linking methods, particularly ionic and covalent cross-linking, to improve the mechanical stability of sulfonated polymeric membranes.

Mikhailenko et al.[5] successfully cross-linked sulfonated poly(ether ether ketone) (SPEEK) with polyatomic alcohols via a condensation reaction between the sulfonic acid groups. Helmer-Metzmann et al.[6] cross-linked SPEEK by reacting the sulfonic acid groups with aromatic or aliphatic amines. Gu et al.[7] covalently cross-linked sulfonated poly(phthalazinone ether sulfone ketone) with poly(vinyl alcohol) by heat treating the films at 120 °C. The hypothesis was that cross-linking involved sulfonic acid ester groups generated by condensation of −OH and $-SO_3H$ from the two polymers. Kerres et al.[8] have described covalent cross-linking of ionomeric membranes by alkylation of sulfinate groups with α,ω-dihalogenoalkanes. These cross-linked membranes exhibited good thermal stability but became brittle on drying. A review paper by Kerres et al.[9] describes both covalently and ionically cross-linked ionomeric membranes and their advantages. Ionic cross-linking was demonstrated by Gasa et al.,[10] who used barium cations to form water-resistant ionic clusters in sulfonated poly(ether ketone ketone). The membranes could be cross-linked to varying degrees by varying the sulfonation level and/or the extent of neutralization with Ba^{2+}.

Specific interactions, e.g., hydrogen bonding, have been used to improve miscibility in polymeric blends. However, Lee et al.[11] observed that binary blends of poly(ethylene oxide), PEO, and SPS were miscible only at the lower PEO concentrations (10 wt % PEO at 3 mol % sulfonation of SPS). The composition range at which the blends were miscible increased with increasing sulfonation of the SPS (20 wt % PEO at 8.8 mol % sulfonation of SPS). Addition of PEO to SPS also reduced

Received: October 25, 2011
Revised: February 28, 2012
Published: March 20, 2012

 © 2012 American Chemical Society dx.doi.org/10.1021/ma202385g | *Macromolecules* 2012, 45, 3104−3111

the intensity of the SAXS peak due to ionic clusters, indicating that the PEO suppressed microphase separation of the ionic species in the ionomer due to interaction of highly polar ether linkages present in PEO with the ionic domains groups. Cross-linked polystyrenesulfonic acid (SXLPS) particles have been used to improve the compatibility of polystyrene and PEO.[4] According to Hong et al.[4] in the SPS + PEO + PS system, SXLPS particles physically cross-link with PEO and the polystyrene chains entangle in this cross-linked network formed thus inhibiting the phase separation. Yamanis et al.[12] reported that Amberlyst 15, a cation-exchange resin used as a catalyst for the reaction of ethylene oxide with ethanol, lost its catalytic activity in a short period. They showed that ethylene oxide reacts with sulfonic acid groups to form esters. This process in turn decreases catalytic activity simply due to the drop in the number of active protons.

Robertson et al. reported that there was strong interaction of amidic solvents like dimethylformamide (DMF) and dimethylacetamide (DMAc) with sulfonated polymers. The interaction adversely influences the PEM performance of membranes cast from those solvents. They showed that the amide group of DMF forms strong hydrogen bonds with the sulfonic acid groups of the polymer at about 60 °C. Researchers have shown in the past that conversion of sulfonic acid to sulfonamides was possible by dissolution of highly acidic polyelectrolytes in amidic solvents such as formamide.[14,15]

In this work, we cross-linked electrospun fiber mats of fully sulfonated polystyrene using low- and high-molecular-weight glycols. Addition of high-molecular-weight PEO improved the electrospinnability of the polyelectrolyte, and subsequent heat treatment of the fiber mats improved the stability in water. In view of the latter observation, we have attempted to understand the chemistry of this apparent cross-linking reaction.

2. EXPERIMENTAL SECTION

2.1. Materials. Poly(ethylene oxide) (PEO) with M_w = 100 000 g/mol was obtained from Polysciences Inc. and used as received. The sodium salt of sulfonated polystyrene with M_w = 500 000 g/mol (Na-SPS-500) was obtained from Scientific Polymer Products. *N,N*-dimethylformamide (DMF) was obtained from Acros Organics and used as received.

2.2. SPS-PEO Blend Electrospinning. The Na-SPS was first converted to the acid form by passing a 5 wt % solution of the polymer in distilled water through an ion-exchange column of Dowex Marathon C. The ion exchange capacity of resulting polystyrenesulfonic acid (SPS) was 4.8 mequiv/g as determined by titration with 0.01 N NaOH.

The electrospinning solutions were prepared by dissolving SPS and PEO in varying ratios in DMF while stirring at room temperature and then heating at ~40 °C for 30 min. Blends of SPS-PEO were electrospun at room temperature using the setup shown schematically in Figure 1. The electrospinning system used a 1-mL Norm-Ject syringe with the tip of the syringe needle (20 Gauge, 12.7 mm length) connected to the positive terminal of a high-voltage DC source (Gamma High Voltage Research, Inc., ES 30R/DDPM). The flow rate at which the solution was dispensed from the syringe was controlled using a syringe pump (KD Scientific, model number 780212). The electrospun web was collected onto a grounded collector (Figure 1) and stored in a desiccator. The collector was a grounded drum; but, to generate sufficiently thick mats, the drum was not rotated.

The spinning distance between the needle and collector was 12 cm, the flow rate at which the polymer solution was dispensed from the syringe was 0.35 mL/h and the applied voltage was 23.5 kV. The solution used for spinning had a polymer concentration of 20 wt %. The relative humidity in the spinning chamber was decreased and held at ~20% because highly sulfonated PS is extremely sensitive to humidity.

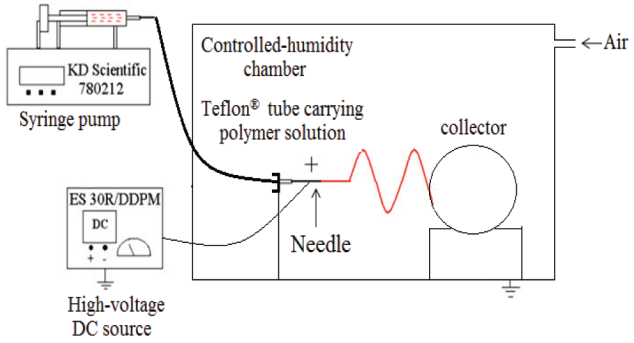


Figure 1. Schematic of the electrospinning setup.

2.3. Curing of SPS-PEO Fiber Mats. The electrospun fiber mat was dried in a vacuum oven at 50 °C overnight to remove most of the solvent. For the heat treatment, the temperature in the vacuum oven was gradually raised over an 8-h period to the 130 °C, and the fiber mat was then heated under vacuum for ~12 h. To avoid shrinkage during drying and heat treatment, the fiber mat was fixed to an aluminum plate by clips on all four sides.

2.4. NMR Analysis of the Curing Process. To investigate the cross-linking reaction, ~ 0.1 g of electrospun mat was heated in the rotor of a solid state NMR, and changes of the spectrum with temperature were monitored. Solid-state magic angle spinning (MAS) ^{1}H NMR spectra were acquired using a 4-mm double-resonance MAS probe with a Bruker DMX 300 NMR spectrometer operating at 300 MHz . The samples were packed in a zirconia rotor with a polyimide (Vespel) cap and spun at 9 kHz at room temperature. Lorentzian line broadening of 10 Hz was applied to all the NMR data. ^{1}H MAS NMR spectra were acquired with a 90° pulse width of 4.0 μs, a delay time of 5 s and 100 kHz of spectral width. The ^{1}H chemical shifts were calibrated by using tetrakis(trimethylsilyl)silane (TTMS) as an external reference.

The electrospun fiber mats were dried overnight in the vacuum oven at room temperature and packed in the rotor. The temperature was increased from 25 to 130 °C in steps of 20 °C and held isothermally at each intermediate temperature for 15 min to equilibrate. At the final temperature of 130 °C, the sample was held for 2 h and then cooled back to room temperature in a similar manner as it was heated. The spectra shown represent an average of 64 scans.

2.5. Gas Chromatography–Mass Spectrometer (GC–MS). The electrospun fiber mats were analyzed by GC–MS (HP 6890 GC and HP 5972 MS) to measure the amount of residual solvent in the dried mats. The reason for this is that DMF may interfere with the curing process, details of which will be covered in the Results and Discussion section. The GC column used was a Restek Rxi-1 ms with a 30-m length, 0.25-mm inside diameter and 1-μm film thickness. The injection port was set to 150 °C. The GC column was held isothermally at 35 °C for 2 min and then ramped to 300 °C at a rate of 15 °C/min. Both the as-spun fiber mat and fiber mat heated in the vacuum oven overnight at ~50 °C were analyzed. A small section of the mat was then heated to 150 °C for 5 min and the volatiles were trapped using liquid nitrogen. Known concentrations (0.01, 0.05, 0.1, 0.5, 1 wt %) of DMF in acetone were run in a similar fashion to calibrate the solvent measurements.

2.6. Characterization of Electrospun Mats. *2.6.1. Microscopy.* Small sections of the electrospun fiber mat before and after curing were analyzed using a field-emission scanning electron microscope (JEOL JSM-6335F) to determine the fiber size and morphology. The samples were first sputter coated with gold for 1 min.

In a separate test, heat-treated fiber mats were exposed to distilled water and analyzed by FESEM to determine if the fiber structure was retained on exposure to water. For this test, a ~0.5-mg sample of the heat-treated fiber mat was immersed in 3 mL distilled water for 15 h.

dx.doi.org/10.1021/ma202385g | *Macromolecules* 2012, 45, 3104–3111

The fiber mat was then dried in the vacuum oven and mounted onto a stub to be analyzed using FESEM. The diameters of the fibers were determined using Image J software.

2.6.2. Ion Exchange Capacity (IEC). The IEC of electrospun fiber mats was determined by titration. Approximately 0.5 mg of the dried fiber mat was treated with 5 mL of 20% NaCl solution for 1 day to exchange the H^+ with Na^+. The HCl formed as a result of the ion exchange was titrated against 0.005 N NaOH using phenolphthalein as an indicator.

2.6.3. X-ray Diffraction. X-ray diffraction patterns of the as-spun and heat treated electrospun fiber mats were collected using an Oxford diffraction, XCalibur PX Ultra with an Onyx areal detector. The diffraction patterns were obtained using Cu Kα X-ray radiation with 1.5418 Å wavelength. The samples were held at room temperature.

3. RESULTS AND DISCUSSION

3.1. Electrospinning of SPS-PEO Fiber Mats. Previously, we reported the successful electrospinning of highly sulfonated polystyrene (IEC ~ 4.5 mequiv/g) nanofibers from solution.[16] Although the high sulfonation level is advantageous in achieving high ion exchange capacity, the as-spun fiber mats dissolved when exposed to water. That problem can be resolved by chemically cross-linking the nanofibers, which was achieved in the present work by adding a second polymer, PEO, to the spinning dope (Table 1). PEO has been added to the spinning dope in the past to spin polyelectrolyte like Nafion that has a very low solution viscosity to sufficiently entangle and form continuous fibers.[16,17] In our experiments too, the addition of PEO to the SPS–DMF solution improved the spinnability of the polyelectrolyte and reduced the polymer concentration needed to generate bead-free fiber mats. With increase in concentration of PEO the morphology changed from beads to bead-on-string and finally bead-free fiber mats.

Table 1. Stoichiometry of Sulfonic Acid Groups from SPS to Ethylene Oxide Units of PEO in the Spinning Solution

SPS:PEO (w/w)	moles (SO_3H)/moles (CH_2CH_2O)
80:20	0.84
70:30	0.49
60:40	0.31

Subjecting the electrospun SPS-PEO fiber mats to heat treatment, as described in the Experimental Section, improved the dimensional stability of the fiber mats when immersed in water. Whereas, neat SPS fiber mats exhibited no shrinkage upon heating, the SPS-PEO fiber mats shrunk when heated due to the melting of the PEO at ~60 °C. However, the heating also produced cross-linking of the mat, which was evident from the retention of the fiber structure upon exposure to water following the heat treatment. Figure 2 shows how the addition of PEO and heating and soaking in water affected the morphology of the fiber mats. While most of the fiber structure in the neat SPS mat disappeared when exposed to water, the fibrous structure in the SPS-PEO mats is still evident in the films after immersion in water. The heat-treated neat SPS fiber mats swelled considerably in water at room temperature to form a hydrogel. As a result of the swelling, a homogeneous film formed and the fibrous structure was destroyed; see Figure 2(e).

Heating the SPS-PEO fiber mats to the curing temperature (130 °C) melted the PEO component of the fibers. For samples with ≤30 wt % PEO, the integrity of the fibers was retained through the curing process. However, for the 60–40 w/w SPS-PEO mats, the fibers fused upon heating and formed a nearly void-free film, although a fibrous component of the film was still evident; see Figure 2d. Note also that some of the fibers coalesced into large (>3 μm) globules, a morphology that was not observed in the other samples. Although the phase structure of the fibers was not evaluated in this study, the results for the 60–40 w/w SPS-PEO sample suggest that a phase inversion may have occurred at this composition, where the PEO became either a cocontinuous or continuous phase in the fibers. This would account for the morphology change of the fibers upon melting the PEO component.

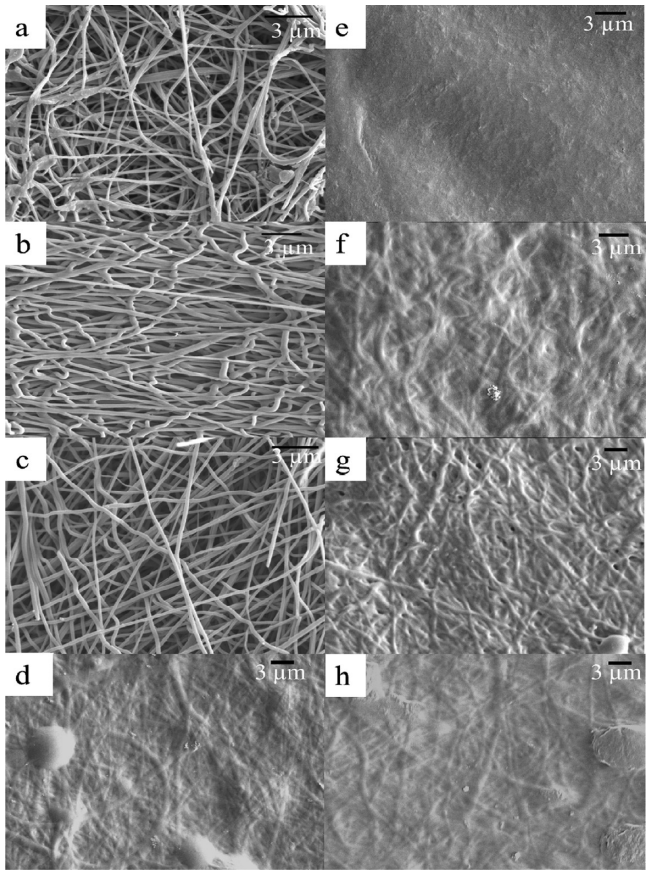


Figure 2. Electrospun fiber mats (a) SPS (b) SPS-PEO 80–20 w/w (c) SPS-PEO 70–30 w/w (d) SPS-PEO 60–40 w/w, all the samples (a–d) were heat treated at 130 °C. Images on the right (e–h) correspond to fibers mats (a–d), respectively, after soaking in water and drying.

In the case of fiber mats containing less than 30% or less PEO, the heating step did not substantially change the fiber structure of the mat, as shown in Figure 2b,c. Exposure of these heat-treated fiber mats to water, however, did fuse the fibers into a film, though part of the individual fibers can still be observed in Figure 2f–h. The diameter statistics for the fibers are reported in Table 2. These are based on 50 measurements made on random sections of the fiber mat.

Unlike the unexposed fiber mats, the fiber boundaries in the case of heat-treated fiber mats exposed to water were not very distinct. Hence the fiber diameters were not compared because picking fibers with sharper boundaries for the measurements would undoubtedly bias the result. In the presence of PEO, the fiber structure was retained in the heat-treated fiber mats, even after long exposure to water, as shown in Figure 3.

dx.doi.org/10.1021/ma202385g | *Macromolecules* 2012, 45, 3104–3111

Table 2. Fiber Diameters of As-Spun and Heat-Treated Fiber Mats

sample SPS-PEO (w/w)	IEC of SPS-PEO fibers[a], meq/g	average diameter of as-spun fibers, nm	average diameter of heat treated fibers, nm	evidence of fiber structure retained after exposure to water
100–0	4.1 ± 0.5[b]	150 ± 28[c]	175 ± 60	no
80–20	2.2 ± 0.3	271 ± 48	322 ± 86	yes
70–30	2.6 ± 0.07	245 ± 40	228 ± 42	yes
60–40	2.4 ± 0.2	306 ± 68	550 ± 159	yes

[a]On the basis of mass of the blend. [b]Standard deviation of the mean based on three determinations. [c]Standard deviation of the mean based on 50 measurements.

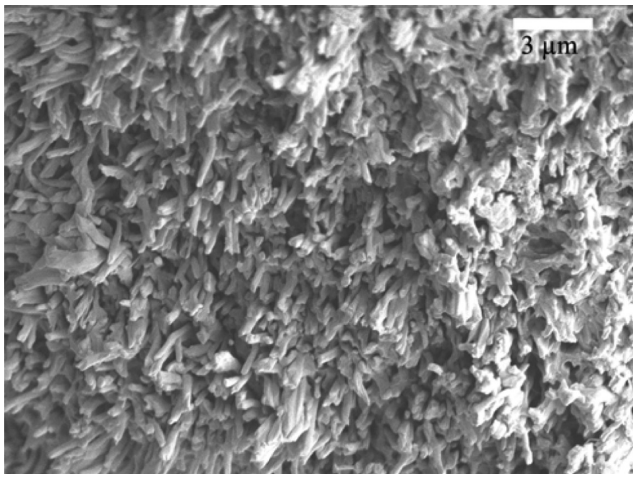


Figure 3. FESEM image of a break surface of heat-treated SPS-PEO (70/30 w/w) fiber mat after soaking in water and drying.

3.2. NMR Analysis of the Fiber Mats. *3.2.1. ^{1}H NMR Analysis of As-Spun and Heat-Treated SPS-PEO Fiber Mat.* Solution ^{1}H NMR spectra were obtained for the as-spun and heat-treated SPS-PEO fiber mats in D_2O, in which the as-spun fiber mat readily dissolved. Not surprisingly, the liquid-state ^{1}H NMR showed the standard resonances for polystyrenesulfonic acid [broad band at 0.8–2 ppm from aliphatic chain protons (3 H's), 6.5 and 7.5 ppm from the aromatic protons (4 H's) from positions 3,4 as shown in the schematic in Figure 4a],[18] water (4.7 ppm) and PEO (3.6 ppm from the methylene groups, 4 H's).[19] Relative area of aromatic proton (labeled as 3 in Figure 4a) to the aliphatic broad band at 0.8–2 ppm of SPS was 0.69. This value is similar to that reported by Baigl et al., who observed a ratio of 2/3 at all sulfonation levels investigated by these authors.[18] Composition of the two polymers was calculated by comparing areas of the aromatic protons closest to the sulfonic acid groups at 7.39 ppm (2 H's) to protons from the methylene groups of PEO (4 H's). The molar ratio of as-spun SPS/PEO fibers by NMR was calculated to be 0.29 and was close to the molar ratio of SPS/PEO in the spinning dope (0.34); the variability may be due to error during weighing the polymer, since SPS is very sensitive to humidity.

Residual DMF shows up in the ^{1}H NMR spectrum at 2.8 and 2.9 ppm[13] and a singlet at 2.54 ppm. For the hydrogen bonded DMF, the aldehyde proton appears at ~8 ppm.[13] Robertson et al.[13] have reported similar resonances for sulfonated poly(ether ether ketone) films cast from DMF and DMAc. The different chemical environments around two CH_3 groups in DMF results in two different peaks at 2.8 and 2.9 ppm for the free DMF. According to Robertson et al.[13] when the sulfonic acid groups from the polymer hydrogen bonds with the electron pair of the nitrogen, free rotation about the C–N bond becomes possible. Hence, the methyl groups average out to give a single resonance at 2.54 ppm.[13]

In the case of the heat-treated fibers (SPS:PEO 80:20, 70:30, 60:40 w/w), the mats swelled to form hydrogels instead of dissolving. The gel fraction and sol fraction after exposing the heat-treated fiber mat in D_2O for 48 h were separated and analyzed by solid-state and liquid-state ^{1}H NMR respectively. The insoluble (gel) fraction showed sulfonation peaks (Figure 4b), while the solution containing the extracted polymer did not (Figure 4c). This result indicates that the water-soluble fraction was PEO and that was substantially free of DMF. The swollen, insoluble fraction was analyzed by solid state ^{1}H NMR (Figure 4b). The insoluble fraction showed all the resonances for SPS, including a resonance at 3.6 ppm corresponding to the methylene protons and sharp peaks at ~2.6 ppm from the residual DMF in the system.[20] The suppression of solubility of SPS component in the heat-treated fibers indicates that cross-linking had occurred.

3.2.2. Interaction of Sulfonic Acid Groups with DMF. Although the heat-treated SPS fibers did not retain their fibrous structure on exposure to water, the fiber mats swelled to form gels. A hypothesis to explain this behavior is that the fibers reacted with residual DMF to form weak cross-links. To further confirm the interaction of SPS with DMF, the polymer was reacted with excess DMF, similar to the procedure reported by Robertson et al.[13] for SPEEK. The reaction was attempted on Dowex Marathon C (cross-linked sulfonated polystyrene resin). Since the resin beads were cross-linked, it was easy to separate them from the liquid after the reaction. The resin was first washed to remove free acids. After drying, the resin was exposed to excess DMF (20 wt % of resin in DMF) at two different temperatures, for 6 h at room temperature and at 60 °C. The resin was then washed repeatedly to remove unreacted DMF. The IEC of the resin was determined by titration against 0.01 N NaOH. The IEC of the resin (treated with DMF at 60 °C) dropped from 4.6 mequiv/g (untreated resin and resin treated with DMF at room temperature) to 0.4 mequiv/g, which suggests that the sulfonic acid groups from SPS were reacting with DMF at higher temperatures. To confirm that the drop in IEC was not due to desulfonation, the resin was analyzed by TGA. Desulfonation did not occur until 200 °C, much higher than our reaction temperatures. Dragan et al.[24] have reported amidation of poly(2-acrylamido-2-methylpropoanesulfonic acid) using DMF. The sharp drop in IEC could be due to reaction of SPS and DMF to form sulfonamides, as shown in Figure 5.

By way of discussion of the DMF interaction or reaction with $-SO_3H$, Dragan et al.[24] have reported amidation of sulfonic acid groups of poly(2-acrylamido-2-methylpropanesulfonic acid) to sulfonamides on reacting the polymer with DMF and DMAc. They also reported that higher temperatures were avoided because partial gelation of the products occurred at 70 °C with longer reaction times. Above 100 °C slight cross-linking was observed, although the cross-linking mechanism was not reported. Thus, the poorly soluble electrospun mats of SPS may be due to the mild cross-linking as reported by Daragan et al.[24] Although a reaction mechanism to form chemical cross-links is hard to imagine, it is possible that the sulfonamides, if sufficiently plentiful, could microphase separate and physically cross-link the polymer.

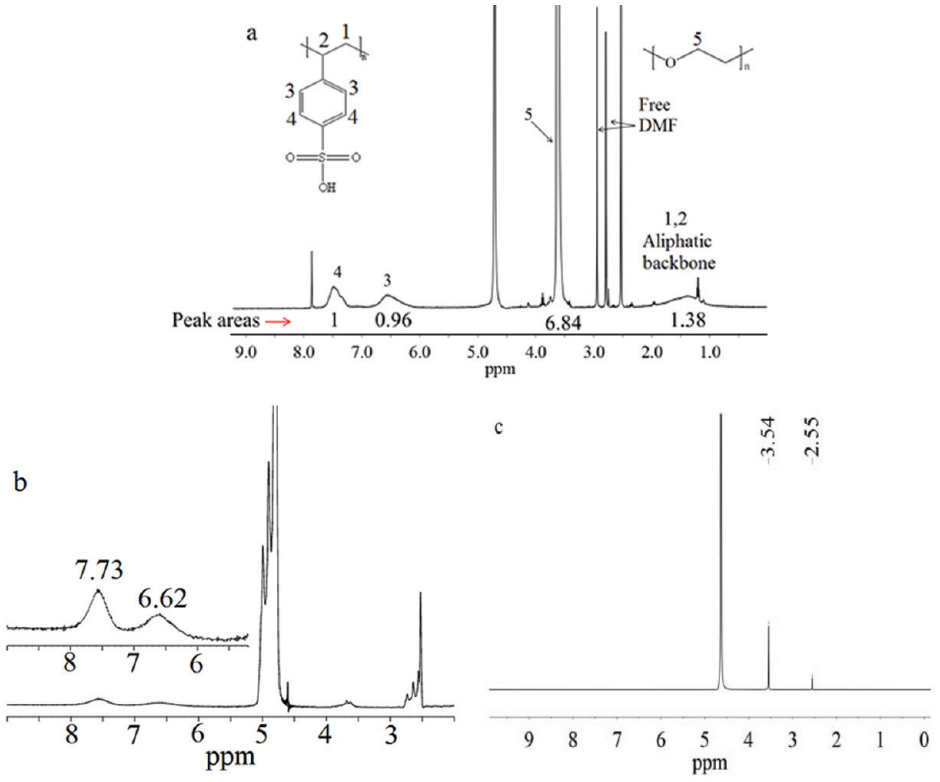


Figure 4. ^{1}H NMR spectra of SPS-PEO (70−30 w/w) in D_2O: (a) dissolved as-spun fibers; (b) insoluble fraction of heat-treated fibers; (c) water-soluble fraction of heat-treated fibers.

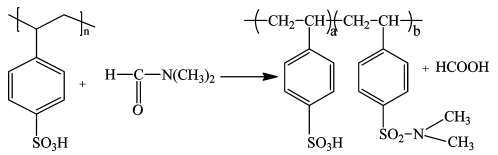


Figure 5. Reaction mechanism for formation of sulfonamides.

From these experiments, it is clear that DMF indeed can interact with the sulfonic acid groups of the polymer, although, it must be noted that this experiment was done in excess DMF; hence, the influence would be much more pronounced than for the real system. Thus, as an additional check, the fiber mats were analyzed by GC−MS to determine the residual solvent present in the fiber mats before cross-linking. As shown in Table 3, the DMF content of the fiber mats was low (molar ratio of DMF/SO_3H = ∼ 0.15). The residual DMF present in the fiber mats heated overnight at 50 °C in the vacuum oven was even lower than in the as-spun fiber mats, an expected result since the sulfonic acid groups from SPS will have a tendency to hydrogen bond to DMF and retain the solvent in the fiber mat. Hence, before cross-linking, all the electrospun fiber mats were left overnight in the vacuum oven at 50 °C to remove the majority of the residual DMF, thus avoiding or substantially reducing DMF-related reactions during the final heat treatment.

Table 3. GC−MS Analysis of Electrospun Fiber Mats for DMF

sample	DMF content (wt %)
as-spun neat SPS	4.5 ± 5.2[a]
neat SPS heated at 50 °C overnight	1.5 ± 0.8
as-spun SPS-PEO (70−30 w/w)	1.6 ± 1.7
SPS-PEO 70−30 heated at 50 °C overnight	0.02 ± 0.02

[a]Estimated standard deviation based on three observations.

3.2.3. Heat-Treatment of Electrospun Fiber Mats in Solid-State ^{1}H NMR Rotor. To understand the chemistry of the cross-linking reaction between the two polymers, the as-spun fiber mats were subjected to the heating cycle in the solid-state NMR rotor to monitor the progressive changes in spectrum. Ćanovas et al.[20] showed that solid-state NMR spectrum of anhydrous polystyrenesulfonic acid features a resonance at ∼10 ppm corresponding to the acid OH from sulfonic acid groups. Solid-state NMR spectra of dry sulfonated polymers like SPEEK and Nafion have been reported in the past.[21,22] Ye et al.[21] observed that the proton mobility depends both on the temperature and water content; a broad peak at ∼9.7 ppm corresponds to protons from sulfonic acid in dry acidified Nafion. Heating Nafion to temperatures as high as 170 °C shifts the peak to ∼13 ppm.[22]

The neat SPS fiber mats from this study showed a peak at 10.7 ppm corresponding to sulfonic acid groups, Figure 6 The two broad peaks at ∼8.3 and 2.9 ppm[13,23] in the NMR spectrum can be assigned to residual solvent (DMF) present in the fiber mats. On heating the fiber mat in the rotor, the sulfonic acid peak shifted upfield to 9.2 ppm. This shift could possibly be due to the interaction of sulfonic acid from the polymer with amide groups of the residual DMF present in the fiber mats[24] and/or due to increased mobility of the protons in sulfonic acid groups at higher temperatures. As the temperature increases, segmental mobility also increases, leading to faster

dx.doi.org/10.1021/ma202385g | Macromolecules 2012, 45, 3104−3111

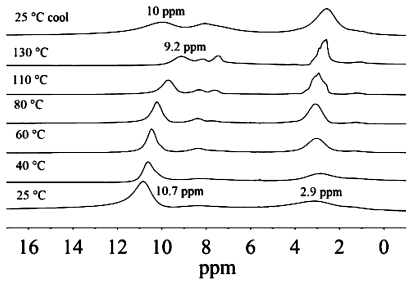


Figure 6. Temperature-resolved solid-state NMR of SPS fibers heated in the rotor.

exchange of protons from sulfonic acid groups. As a result, variations in chemical shifts of these protons are observed.

On cooling after a 2-h hold at 130 °C, the sulfonic acid peak shifted back downfield to ∼10 ppm, as shown in Figure 6. In short, changes observed in the NMR spectrum on heating were reversed on cooling, suggesting there were no permanent changes in the chemical environment. The resonances from aromatic and aliphatic protons were clearly resolved for higher number of scans (512), but the number of scans for the temperature-resolved experiments was set lower to control the total time of exposure of the polymer to high temperatures. Also, since the resonances from residual DMF are broad in the solid state NMR spectrum, the peaks overlap and the signals for other protons resonating in the affected region do not resolve distinctly.

The neat PEO fiber mats showed a broad peak at 3.6 ppm corresponding to the methylene groups (Figure 7). At the

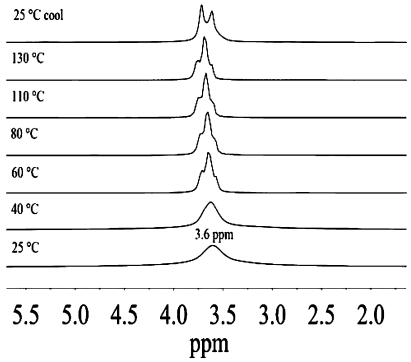


Figure 7. Temperature-resolved solid-state NMR of PEO fibers heated in the rotor.

melting temperature of the polymer, the resonance splits. Above the melting temperature of the polymer, there will be conformational changes which can cause the resonance to split.[25,26]

On heating SPS-PEO fiber mats, the sulfonic acid peak shifted upfield from 9 to 8.4 ppm. This shift was most pronounced above 60 °C, corresponding to the melting temperature of PEO. Additionally the peaks at ∼3.5 ppm due to the CH_2 groups of PEO split above 60 °C, as observed for neat PEO, due to the polymer chains gaining mobility on melting. In contrast to neat fiber mats, the sulfonic acid peak from SPS-PEO fibers did not shift back downfield on cooling, and splitting of methylene peaks from PEO was not reversible. Both of these observations are consistent with permanent changes in the chemical environment (Figure 8), i.e., a reaction

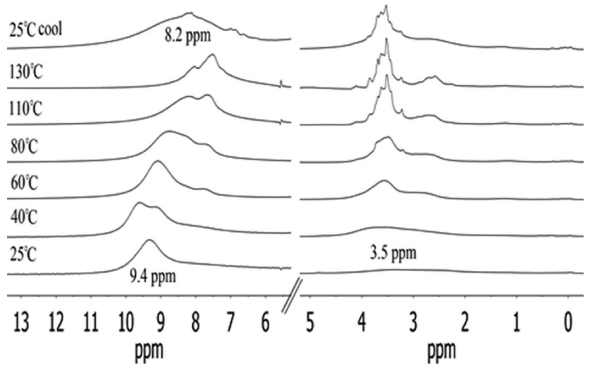


Figure 8. Temperature-resolved solid-state ^{1}H NMR of SPS-PEO 70−30 w/w fibers curing in the rotor.

between PEO and SPS. Splitting of resonances has been reported for the PEO−*p*-nitrophenol complex.[27] According to Spevacek et al.[27] the most probable explanation for the splitting is a conformational change in PEO in a complex. The hypothesis is that the two polymers react at higher temperatures to form sulfonic acid esters, as described in Figure 10.

Another possible route for cross-linking could be due to the free radicals generated at higher temperatures due to the oxidation of PEO. To test this hypothesis, a number of classical experiments were conducted that are known to influence the rate of free-radical reactions. In one, the SPS-PEO fiber mats were heated in a DSC pan to 130 °C in an inert atmosphere of N_2. The experiment was repeated with an O_2 atmosphere. In both the cases the fibers cross-linked, as confirmed by checking the solubility of heat treated fibers in water. Solutions of SPS-PEO in water with varying concentrations of ascorbic acid (a free-radical inhibitor) were cast into films and these films were dried in the vacuum oven followed by heat treatment. Even in the presence of a radical inhibitor, the films cross-linked. In a third trial, cross-linking was attempted using Na-SPS and PEO films. If oxidative cross-linking were active, some cross-linking would be expected; however, the heat-treated films did not exhibit cross-linking. These trials favor the hypothesis of ionic reactions to form sulfonic acid esters, wherein the acid form of the polymer is essential for the cross-linking reaction to take place.

3.3. WAXS of As-Spun and Heat Treated Fiber Mats. WAXD patterns of the as-spun and heat-treated electrospun fiber mats are shown in Figure 9. In the as-spun and heat-treated mats, a broad peak appears at ∼17−18° which corresponds to the amorphous polymer (SPS). When the weight fraction of PEO in the fiber mats was ≥30 wt %, the as-spun fiber mats showed two sharp crystalline peaks at 19 and 23° corresponding to PEO, in addition to the broad amorphous peak from SPS. This is in-line with what has been reported in the literature for electrospun PEO fibers.[28] Unlike the as-spun fiber mats, heat-treated SPS-PEO fiber mats did not show any signs of crystallinity over the investigated concentration range (Figure 9a−d). Although the heat-treated, neat PEO electrospun fiber mat (control) lost its fiber morphology completely on heating, the crystalline peaks in the WAXD pattern were not lost.

3.4. Gas Chromatography−Mass Spectrometer (GC−MS). In addition to the DMF peak discussed earlier, SPS-PEO mats showed a distinct peak for dioxane, which was practically absent for both neat SPS and PEO. Dioxane is undoubtedly a PEO degradation product (Table 4).[29]

dx.doi.org/10.1021/ma202385g | *Macromolecules* 2012, 45, 3104−3111

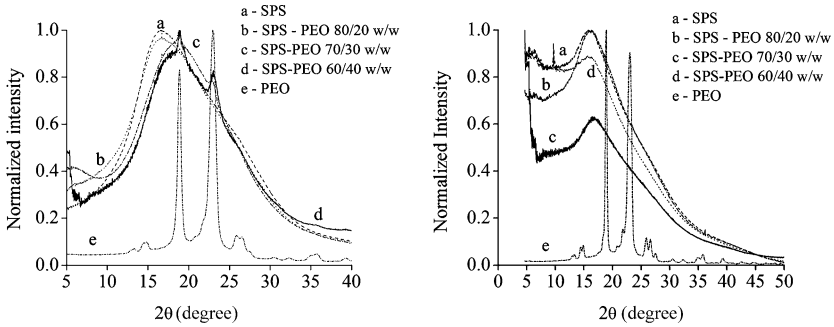


Figure 9. WAXD of as-spun (L) and heat-treated at 130 °C (R) fiber mats.

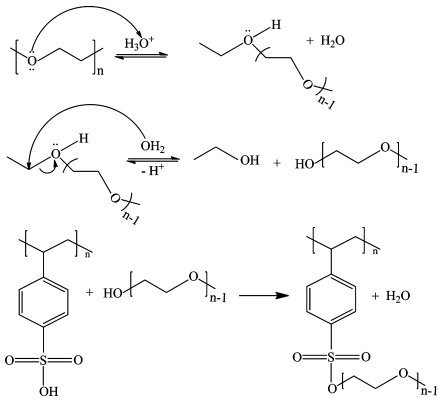


Figure 10. Hypothesized reaction mechanism for formation of sulfonic acid esters.

Table 4. GC−MS Analysis of Electrospun Fiber Mats for Dioxane Content[a]

sample	dioxane content (%)
neat SPS	0
SPS-PEO (80−20 w/w)	0.009
SPS-PEO (70−30 w/w)	0.047
SPS-PEO (60−40 w/w)	1.37
neat PEO	0

[a]Fiber mats were heated overnight at 50 °C in a vacuum oven before analysis.

Choi et al.[29] have reported that PEO can undergo degradation in an acidic environment to form dioxane; a volatile compound. In fact, dioxane has been synthesized by acid-catalyzed dehydration of poly(ethylene glycol) in the presence of cation exchange resin as catalyst.[30] Yamanis et al.[12] observed that in the reaction of ethylene oxide with ethanol catalyzed by cation exchange resin, the high activity of the cation-exchange resin disappeared quickly due to formation of sulfonic acid esters. Their paper explains in detail the various reactions occurring at high temperatures, and one of the byproducts formed was dioxane. They reported that dioxane is formed by a backbiting mechanism after esters of sulfonic acid are formed, which is in-line with what we observed for SPS-PEO fiber mats. In the presence of a strong acid, the ether linkages can be cleaved.[31] The oxygen in the ether can be protonated to form corresponding glycols. These glycols in-turn can react with the sulfonic acid of the SPS to form sulfonic acid esters.

On the basis of all the observations, the most probable hypothesis for the cross-linking reaction mechanism in our system is depicted in Figure 10.

4. CONCLUSIONS

At high sulfonation levels (IEC ~ 4.8 mequiv/g), sulfonated PS fibers can be electrospun, but the fibers are very moisture sensitive and tend to lose their structure when exposed to water or even humid air. To overcome this problem, a method was sought to chemically cross-link the polymer to improve stability of the electrospun mats in water. It was found that addition of PEO to the spinning dope not only helped to improve spinnability of the polyelectrolyte; but, also, with subsequent heat-treatment, the PEO improved the stability of fiber mats in water. As-spun SPS-PEO mats readily dissolved in water and ^{1}H NMR spectrum of the as-spun SPS-PEO fiber mats in D_2O showed sulfonic acid peaks. With increase in PEO concentration in the fiber mats, the heat-treated fiber mats swelled less on exposure to water, suggesting that the fibers were cross-linking in the presence of PEO. ^{1}H NMR spectra of the sol and gel portion of the cross-linked fiber mats showed sulfonic acid peaks in the gel portion but not in solution containing the extracted polymer (sol). The ^{1}H NMR spectra of the sol fraction confirmed that the extracted material was PEO. These results strongly suggest that the PEO is cross-linking the SPS. To further understand this cross-linking reaction, the electrospun fiber mats were heated in a solid state NMR rotor to track changes in the spectrum as the reaction progressed. The hypothesis resulting from the observations is that the PEO is hydrolyzed at higher temperatures to form PEO oligomers with hydroxyl end groups. In turn, these react with the sulfonic acid groups to form esters. Multiple reactions lead to cross-linking, which reduces the solubility of the fiber mats in water.

AUTHOR INFORMATION

Notes

The authors declare no competing financial interest.

ACKNOWLEDGMENTS

The authors acknowledge the financial support provided by Civil, Mechanical and Manufacturing Innovation Program (Directorate of Engineering) of the National Science Foundation, Grant CMMI Grant No. 0727545.

REFERENCES

(1) Dimitrova, P.; Friedrich, K. A.; Stimming, U.; Vogt, B. *Solid State Ionics* **2002**, *150*, 115−122.
(2) Ehrenberg, S. G.; Wnek, G. E. U. S. Pat 6,383,391, 2002.
(3) Choi, J.; Lee, K. M.; Wycisk, R.; Pintauro, P. N.; Mather, P. T. *Macromolecules* **2008**, *41*, 4569−4572.
(4) Hong, L.; Chen, N. *J. Polym. Sci.* **2000**, *38*, 1530−1538.
(5) Mikhailenko, S. D.; Wang, K.; Kaliaguine, S.; Xing, P.; Robertson, G. P.; Guiver, M. D. *J. Membr. Sci.* **2004**, *233*, 93−99.

(6) Helmer-Metzmann, F.; Osan, F.; Schneller, A.; Ritter, H.; Ledjeff, K.; Nolte, R.; Thorwirth, R. U.S. Pat 5,438,082, 1995.
(7) Gu, S.; He, G.; Wu, X.; Guo, Y.; Liu, H.; Peng, L.; Xiao, G. *J. Membr. Sci.* **2008**, *312*, 48−58.
(8) Kerres, J. A.; Cui, W.; Junginger, M. *J. Membr. Sci.* **1998**, *139*, 227−241.
(9) Kerres, J. A. *J. Membr. Sci.* **2001**, *185*, 3−27.
(10) Gasa, J. V.; Weiss, R. A.; Shaw, M. T. *J. Membr. Sci.* **2007**, *304*, 173−180.
(11) Lee, S. C.; Lee, M. S.; Jo, W. H. *J. Polym. Sci., Part B: Polym. Phys.* **1991**, *29*, 759−764.
(12) Yamanis, J.; Patton, B. D. *Can. J. Chem. Eng.* **1979**, *57*, 297−303.
(13) Robertson, G. P.; Mikhailenko, S. D.; Wang, K.; Xing, P.; Guiver, M. D.; Kaliaguine, S. *J. Membr. Sci.* **2003**, *219*, 113−121.
(14) Gooda, S. R.; Huglin, M. B. *J. Polym. Sci., Part A: Polym. Chem.* **1992**, *30*, 1549−1547.
(15) Dragan, D.; Mihai, D.; Mocanu, G.; Carpov, A. *React. Funct. Polym.* **1997**, *34*, 79−90.
(16) Subramanian, C.; Weiss, R. A.; Shaw, M. T. *Polymer* **2010**, *51*, 1983−1989.
(17) Laforgue, A.; Robitaille, L.; Mokrini, A.; Ajji, A. *Macromol. Mater. Eng.* **2007**, *292*, 1229−1236.
(18) Baigl, D.; Seery, T. A. P.; Williams, C. E. *Macromolecules* **2002**, *35*, 2318−2326.
(19) Cong, R.; Bain, A. D.; Pelton, R. *J. Polym. Sci., Part B: Polym. Phys.* **2000**, *38*, 1276−1284.
(20) Ćanovas, M. J.; Sobrados, I.; Sanz, J.; Acosta, J. L.; Linares, A. *J. Membr. Sci.* **2006**, *280*, 461−469.
(21) Ye, G.; Janzen, N.; Goward, G. R. *Macromolecules* **2006**, *39*, 3283−3290.
(22) Zhang, J.; Giotto, M. V.; Wen, W. Y.; Jones, A. A. *J. Membr. Sci.* **2006**, *269*, 118−125.
(23) Kaliaguine, S.; Mikhailenko, S. D.; Wang, K. P.; Xing, P.; Robertson, G.; Guiver, M. *Catal. Today* **2003**, *82*, 213−222.
(24) Drăgan, D. *Angew. Makromol. Chem.* **2003**, *236*, 85−95.
(25) Johansson, A.; Tegenfeldt, J. *Macromolecules* **1992**, *25*, 4712−4715.
(26) Hikichi, K.; Furuichi, J. *J. Polym. Sci., Part A* **1965**, *3*, 3003−3013.
(27) Spevacek, J.; Suchoparek, M. *Macromol. Symp.* **1997**, *114*, 23−34.
(28) Uyar, T.; Besenbacher, F. *Eur. Polym. J.* **2009**, *45*, 1032−37.
(29) Choi, J.; Lee, K. M.; Wycisk, R.; Pintauro, P. N.; Mather, P. T. *J. Mater. Chem.* **2010**, *20*, 6282−6290.
(30) Godfrey, N. B. *Preparation of dioxane and by co-products*. U.S. Patent 4,283,339, 1981.
(31) Peter, K.; Vollhardt, C.; Schore, N. E. *Organic Chemistry: Structure and Function*, 5th ed.; W.H. Freeman and Company: New York, 2005; p 356.

Macromolecules

Article

pubs.acs.org/Macromolecules

Effect of Confinement on Proton Transport Mechanisms in Block Copolymer/Ionic Liquid Membranes

Megan L. Hoarfrost,*[,†,‡] Madhu S. Tyagi,[§,∥] Rachel A. Segalman,[†,⊥] and Jeffrey A. Reimer[†,‡]

[†]Department of Chemical and Biomolecular Engineering, University of California, Berkeley, Berkeley, California 94720, United States

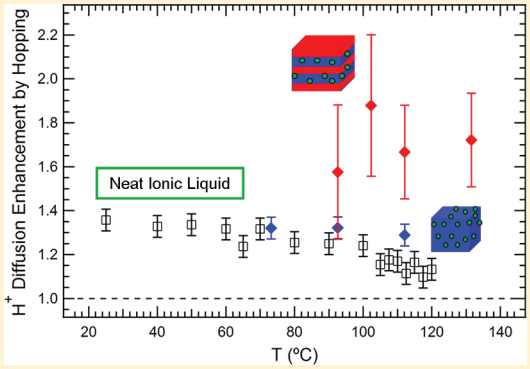
[‡]Energy and Environmental Technologies Division and [⊥]Materials Sciences Division, Lawrence Berkeley National Laboratory, Berkeley, California 94720, United States

[§]NIST Center for Neutron Research, Gaithersburg, Maryland 20899, United States

[∥]Department of Materials Science and Engineering, University of Maryland, College Park, Maryland 20742, United States

Supporting Information

ABSTRACT: Nanostructured membranes containing structural and proton-conducting domains are of great interest for a wide range of applications requiring high conductivity coupled to high thermal stability. Understanding the effect of nanodomain confinement on proton-conducting properties in such materials is essential for designing new, improved membranes. This relationship has been investigated for a lamellae-forming mixture of poly(styrene-*b*-2-vinyl pyridine) (PS-*b*-P2VP) with ionic liquid composed of imidazole and bis(trifluoromethylsulfonyl)-imide, where the ionic liquid selectively resides in the P2VP domains of the block copolymer. Quasi-elastic neutron scattering and NMR diffusion measurements reveal increased prevalence of a fast proton hopping transport mechanism, which we hypothesize is due to changes in the hydrogen bond structure of the ionic liquid under confinement. This, in combination with unique ion aggregation behavior, leads to a lower activation energy for macroscopic ion transport compared with that in a mixture of ionic liquid with P2VP homopolymer. The proton transference number in both samples is significantly higher than that in the neat ionic liquid, which could be taken advantage of for applications such as proton exchange membrane fuel cells and actuators. These results portend the rational design of nanostructured membranes having improved mechanical properties and conductivity.



INTRODUCTION

Nanostructured membranes containing structural and ion-conducting phases are of great interest for a wide variety of applications requiring high ionic conductivity coupled to mechanical durability. Such membranes may be designed to exhibit continuous ion-conducting channels that lead to enhanced conductivity compared with nonordered materials. For instance, Nafion (Dupont) is currently the industry standard proton-conducting polymer membrane for many applications because of its exceptional conductivity and mechanical properties that have been attributed to its nanoscale phase separation into conducting, water-filled domains and structural, hydrophobic domains.[1] Furthermore, materials designed to have well-ordered, continuous nanostructures have significantly higher conductivities than comparable nonordered materials.[2,3] Understanding the effect of morphology on conductivity has become increasingly important in recent years as a tool for designing new, improved membranes.[4−9]

Of the many factors contributing to improved conductivity in nanostructured membranes (including conducting phase continuity and increased contrast between conducting and structural phases[4,8,9]), we expect differences in the local charge carrier environment near the "walls" of conducting phases to have a significant impact on the mechanism of conductivity. It has been shown, for example, that hydrogen bonding is significantly different at the walls of confined water domains[10−13] and that such effects have significant implications for proton transport in hydrated Nafion.[14−18] A few studies of nanostructured materials with ion carriers other than water have also identified wall effects on the mechanism of conductivity.[19,20] These effects were deduced largely based on bulk conductivity measurements. In one case, NMR experiments also provided clues as to how the local dynamics change,[20] but determining exactly how confinement affects the molecular mechanisms of conductivity remains difficult.

Mixing a block copolymer with an ionic liquid is one route to obtaining nanostructured, ion-conducting membranes having high ionic conductivity coupled to favorable mechanical durability. Ionic liquids have been selectively incorporated

Received: December 19, 2011
Revised: March 13, 2012
Published: March 23, 2012

 © 2012 American Chemical Society

into one phase of a diblock copolymer, where the second phase imparts mechanical durability to the membrane.[21−26] Such membranes self-assemble into well-defined nanostructures, making them ideal materials for studying the relationship between structure and conductivity. In this work, the effect of confinement on the mechanism of conductivity has been investigated for mixtures of the diblock copolymer poly(styrene-*b*-2-vinyl pyridine) (PS-*b*-P2VP) with the proton-conducting ionic liquid, imidazolium:bis(trifluoromethylsulfonyl)imide ([Im][TFSI]) having an excess of imidazole, in which the ionic liquid is selective for the P2VP phase of the block copolymer.

Nonstoichiometric [Im][TFSI] containing excess imidazole conducts protons via two mechanisms: a vehicle mechanism whereby protons are carried by imidazolium cations and a proton-hopping mechanism whereby protons are transferred between hydrogen bonded imidazole molecules.[27] Excess imidazole molecules act as proton "acceptors" that facilitate proton hopping, increasing proton conduction vis-à-vis conduction by vehicle diffusion alone.[28,29] Because the proton-hopping mechanism is strongly related to the hydrogen bond network of imidazole and hydrogen bonding is known to be affected by confinement, we surmise that proton hopping in imidazole will also be affected by confinement (i.e., to block copolymer nanodomains).

Previous studies of block copolymer/ionic liquid membranes have focused on bulk conductivity measurements.[7,21,26,30,31] These measurements have provided insight into the relationship between structure and conductivity but afford limited information regarding the mechanism of ionic liquid conductivity. Combined conductivity and NMR studies of mixtures of ionic liquids with homopolymers and random copolymers have shown that specific interactions between the ionic liquid and polymers greatly affect the prevalence of ion aggregation and the number of effective charge carriers,[32,33] yet there have been no similar studies on mixtures containing protic ionic liquids or having well-defined nanostructures. In this work, we employ a combination of experimental techniques that together probe the dynamics of a variety of molecular and atomic species on length scales ranging from tenths of nanometers to micrometers to millimeters to determine the effect of confinement on the mechanisms of proton transport in a self-assembled mixture of PS-*b*-P2VP block copolymer with nonstoichiometric [Im][TFSI] ionic liquid, where the ionic liquid is confined to P2VP domains. A mixture of nonstoichiometric [Im][TFSI] with P2VP homopolymer has been studied in addition to the block copolymer mixture to discriminate effects of confinement from effects of mixing with P2VP. We show that combining the ionic liquid with both P2VP and PS-*b*-P2VP has significant effects on ion aggregation and the proton transference number and, most strikingly, that the amount of proton hopping compared with vehicle diffusion is greatly increased in the nanostructured membrane. These results portend the rational design of nanostructured membranes having improved mechanical properties and conductivity.

EXPERIMENTAL SECTION

Polymer Synthesis and Characterization. Hydrogenated and deuterated poly(2-vinyl pyridine) (P2VP and *d*P2VP) and poly(styrene-*b*-2-vinyl pyridine) (PS-*b*-P2VP and *d*PS-*b*-*d*P2VP) were synthesized via anionic polymerization as previously described.[34] d_8-Styrene monomer (Polymer Source) and d_7-2-vinyl pyridine monomer (Isotec) were used to synthesize deuterated polymers. The molecular weights of the polystyrene blocks (PS or *d*PS) were determined using gel permeation chromatography (GPC), and the total molecular weights of the block copolymers were determined using ^{1}H NMR (Bruker AVB 300 MHz). The molecular weight of P2VP was determined using ^{1}H NMR end-group analysis, and the molecular weight of *d*P2VP was determined using GPC. GPC was used to assess the polydispersity of each polymer. The degree of polymerization of the P2VP or *d*P2VP block, N_{P2VP}, the volume fraction of PS or *d*PS, f_{PS}, and the polydispersity index (PDI) of each polymer are given in Table 1.

Table 1. Degree of Polymerization, Volume Fraction, and PDI of Polymers Studied

polymer	N_{P2VP}	f_{PS}	PDI
*d*P2VP	82	0.00	1.07
*d*PS-*b*-P2VP	72	0.71	1.04
P2VP	118	0.00	1.07
PS-*b*-P2VP	101	0.72	1.04

Ionic Liquid Purification and Preparation. Imidazole (≥95%), d_4-imidazole (≥98% deuteration), and bis(trifluoromethylsulfonyl)-imide (HTFSI, ≥95%) were purchased from Sigma Aldrich and purified by sublimation under vacuum. The final purity of each starting material was assessed using differential scanning calorimetry (DSC) and ^{1}H NMR. Purified imidazole or d_4-imidazole and HTFSI were combined in a 4:1 molar ratio and heated to 100 °C for 2 to 3 h. The compositions of the resulting nonstoichiometric [Im][TFSI] and [*d*Im][TFSI] ionic liquids were confirmed by comparing the measured melting points and ^{1}H NMR profiles to literature.[28] The structures of the ionic liquid molecules are shown in Figure 1. Because of their hygroscopic nature, the ionic liquids and their starting materials were handled in an argon atmosphere glovebox and sealed sample holders at all times.

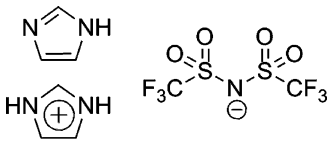


Figure 1. Chemical structure of nonstoichiometric [Im][TFSI] molecules.

Preparation of Polymer/Ionic Liquid Mixtures. Dichloromethane and tetrahydrofuran were degassed using three freeze, pump, thaw cycles, dried by stirring over CaH_2 overnight, and stored on molecular sieves in an argon atmosphere glovebox. All further sample preparation was performed within the glovebox. Predetermined masses of ionic liquids and polymers were added to glass vials. Ca. 5 wt % solutions were prepared by dissolving in dichloromethane (block copolymer mixtures) or tetrahydrofuran (homopolymer mixtures), and the solutions were stirred overnight. Samples were cast one drop at a time into sample holders for DSC, small-angle X-ray scattering (SAXS), quasi-elastic neutron scattering (QENS), and AC impedance spectroscopy. Samples were cast onto pieces of Kapton for NMR. Solvent was removed carefully so as not to remove simultaneously excess imidazole. Block copolymer samples were heated to 65 °C for precisely 30 min. Homopolymer samples were dried at 35 °C for 3 days. Complete solvent removal and negligible imidazole loss were confirmed by ^{1}H NMR. After solvent removal, DSC, SAXS, QENS, and conductivity sample holders were sealed shut, whereas NMR samples were scraped off of the Kapton and into sealable NMR tubes (for diffusion measurements) or 4 mm (outer diameter) magic-angle spinning (MAS) rotors. Samples were sealed in jars containing desiccant for transportation to experimental apparatuses. The exclusion of water from samples was confirmed by ^{1}H NMR.

dx.doi.org/10.1021/ma202741g | *Macromolecules* 2012, 45, 3112−3120

Both homopolymer and block copolymer samples were prepared and studied to distinguish the effects of mixing the ionic liquid with P2VP from the effects of confining the ionic liquid to nanodomains. The ratio of imidazole molecules to 2VP monomer units was held constant at 1.16:1 for all samples, which translates into 30 mass percent ionic liquid in the block copolymer samples and 59 mass percent ionic liquid in the homopolymer samples. This ensured that the glass-transition temperature of the P2VP/ionic liquid phase, $T_{g,P2VP}$, was constant at ~4 °C for each sample. The specific ionic liquid loading was chosen to maximize the number of ionic liquid protons so as to maximize the signal-to-noise ratio in NMR and QENS experiments while limiting the ionic liquid concentration to the range in which the block copolymer mixtures form lamellar nanostructures. Deuterated polymers were used for NMR experiments so that the ionic liquid protons could be easily resolved in NMR spectra. Deuterated polymers as well as deuterated imidazole were used for QENS experiments so that the dynamics studied were dominated by the acidic proton. Hydrogenated materials were used for AC impedance ionic conductivity measurements.

Differential Scanning Calorimetry. DSC samples were crimped in an argon atmosphere glovebox using hermetically sealed pans and placed inside a container with desiccant for transfer to the DSC. DSC was performed on a TA Instruments DSC Q20. Indium and dodecane were used as calibration standards. Samples underwent three heating and cooling cycles with a scan rate of 10 °C/min, and thermal transition temperatures from the second heating scan were recorded.

Morphology Characterization. Mixture morphologies were determined using SAXS. Samples of ca. 1 mm thickness were cast in an argon atmosphere glovebox into sample cells formed by an aluminum spacer sealed onto a Kapton window on one side. After heating to remove solvent, a second Kapton window was glued to seal the sample cells, and the cells were sealed in jars containing desiccant for transportation to the beamline. SAXS was performed on beamline 7.3.3 of the Advanced Light Source (ALS) and beamline 1−4 of the Stanford Synchrotron Radiation Lightsource (SSRL). Samples were equilibrated within the beamline at 145 °C for 30−45 min before data were gathered. At the ALS, the X-ray beam was focused to a 50 by 300 μm spot, and the X-ray wavelength was λ = 1.240 Å. Full 2-D scattering patterns were collected on an ADSC CCD detector with an active area of 188 by 188 mm. The scattering patterns were radially averaged, and the scattering intensity was corrected with the postion chamber intensity using Nika version 1.18. At the SSRL, the X-ray beam was focused to a 0.5 mm diameter spot, and the X-ray wavelength was λ = 1.488 Å. A single quadrant of a 2-D scattering pattern was collected on a CCD detector with an active area of 25.4 by 25.4 mm. The scattering patterns were radially averaged and corrected for detector null signal, dark current, and empty cell scattering.

The block copolymer mixtures in this study have lamellar morphologies. Scattering patterns are shown in Figures S1a and S1b in the Supporting Information. The deuterated mixture used for NMR and QENS experiments has a lamellar domain size, d, of 37 nm, calculated as $2\pi/q^*$, where q^* is the primary scattering peak from SAXS data. The size of the dP2VP/ionic liquid channel, then, is 17 nm, assuming complete segregation of the ionic liquid to the dP2VP domains, ideal mixing, and the density of the ionic liquid to be 1.4 g/mL (based on volumetric measurements). The assumption of complete ionic liquid segregation is justified based on the strong selectivity of the ionic liquid for P2VP. The strong selectivity of stoichiometric [Im][TFSI] has been previously demonstrated based on the scaling behavior of d with mixture composition.[25] Non-stoichiometric [Im][TFSI] is also very selective for P2VP, as evidenced by an increase in d with increased ionic liquid composition (see Figure S1c in the Supporting Information) as well as negligible change in the glass-transition temperature of the PS phase upon ionic liquid addition. The hydrogenated PS-*b*-P2VP block copolymer used for bulk ionic conductivity measurements has a slightly larger molecular weight than the deuterated version, leading to a larger lamellar domain size of the PS-*b*-P2VP/ionic liquid mixture of d = 43 nm (P2VP/ionic liquid channel size equal to 19 nm).

Ionic Conductivity Measurements. Bulk ionic conductivity was measured using four-point probe AC impedance spectroscopy. Samples were cast in an argon atmosphere glovebox into a homemade, airtight, poly(ether ether ketone) cell equipped with rubber o-rings and four stainless-steel electrodes. The working and reference electrodes were 1.7 cm long and placed 0.6 to 0.7 cm apart, and the samples were cast to be ~0.05 cm thick (measured after AC impedance measurements). After solvent removal, the sample cell was screwed shut, removed from the glovebox, and heated to 150 °C for 12 h before measurements were made. AC impedance measurements were performed using a Gamry Reference 600 potentiostat at descending temperatures. An alternating current signal with an amplitude of 5 mV was applied in the frequency range of 0.1 to 65 000 Hz. The nonzero x intercept in the Nyquist plot of the negative imaginary part of the impedance versus the real part of the impedance was taken as the sample resistance, R. The ionic conductivity, σ, was calculated as t/AR, where t and A are the thickness and area of the sample (with respect to electrode placement), respectively, measured after the AC impedance measurements.

Diffusion Coefficient Measurements. Self-diffusion coefficients were measured with pulsed-field gradient spin echo (PGSE) and pulsed-field gradient stimulated echo (PGStE) NMR experiments using a Doty Scientific single-axis diffusion probe with temperature control. The applied gradients were calibrated using water[35] and glycerol[36] standards and were found to reach 1.7 T/m. ^{1}H diffusion coefficients were measured in a 7 T superconducting magnet with a 300 MHz Tecmag Apollo spectrometer and gradient control, and ^{19}F diffusion coefficients were measured in a 1.5 T superconducting magnet with a 61.2 MHz Tecmag LapNMR spectrometer and gradient control. Experiments were performed between 25 and 132 °C, where the temperature was calibrated[37] using an ethylene glycol standard between 24 and 83 °C and extrapolation to higher temperatures.

The NMR signal attenuation for Fickian diffusion in both PGSE and PGStE experiments is described by

$$I = I_0 \exp(-D\gamma^2 g^2 \delta^2(\Delta - \delta/3)) \quad (1)$$

where I is the spin−echo signal intensity, I_0 is the signal intensity with zero gradient, γ is the magnetogyric ratio of the probe nucleus, g is the magnitude of the gradient pulse, δ is the duration of the gradient pulse, Δ is the duration of time between the leading edges of the two gradient pulses, and D is the self-diffusion coefficient of the probe nucleus. I was measured as a function of g, and eq 1 was used to determine D. Example plots of I/I_0 as a function of $\gamma^2 g^2 \delta^2(\Delta - \delta/3)$ are shown in Figure S2 in the Supporting Information. Experiments were repeated on the block copolymer sample using values of Δ ranging from 0.02 to 0.11 s, corresponding to root-mean-squared diffusion path lengths of ionic liquid ions ranging from 0.2 to 2.2 μm, resulting in consistent measurements of D. (See, for example, Figure S3 in the Supporting Information.) PGSE and PGStE experiments performed on each sample also resulted in consistent measurements of D.

Spectroscopic resolution of ionic liquid protons was possible in ^{1}H experiments because the polymers were deuterated. Thus, the diffusion coefficients for protons covalently bound to the carbon atoms on the imidazole (involved only in vehicle diffusion), D_{C-H}, and protons bound to nitrogen atoms on imidazole (involved in vehicle diffusion and proton hopping), D_{N-H}, were measured separately. For ^{19}F experiments, a single peak was observed corresponding to fluorine atoms on the TFSI anion, and a single diffusion coefficient measured, D_{TFSI}.

Magic-Angle Spinning NMR. High-resolution ^{1}H NMR spectra were obtained for ionic liquid/polymer mixtures using MAS NMR. MAS experiments were performed in a 7 T superconducting magnet using a Doty Scientific MAS probe and 300 MHz Tecmag Apollo spectrometer. Samples were annealed in sealed 4 mm (outer diameter) MAS rotors at 150 °C for 12 h before MAS experiments. During MAS experiments, samples were spun at 13 kHz. Spectra were acquired between 93 and 132 °C, where the temperature was calibrated in the same manner as they were for diffusion measurements. Samples equilibrated slowly at each temperature due to fast spinning, so

samples were annealed at each temperature for 1−9 h until the spectra did not change between consecutive acquisitions.

Quasi-Elastic Neutron Scattering. QENS experiments were performed at the National Institute for Standards and Technology (NIST) Center for Neutron Research (NCNR) on the high flux backscattering spectrometer (HFBS). An incident neutron wavelength of λ = 6.271 Å and an energy resolution of ~0.8 μeV were used. Data from all 16 detectors were used to probe a q range from 0.25 to 1.75 Å^{-1}. Polymer/ionic liquid samples were loaded into sample cans with an annular geometry, and the sample transmission was set to ~90% to minimize multiple scattering. All experiments were performed at 140 °C. The acquired data were corrected for detector efficiencies (determined using a vanadium standard), and the resolution function of the instrument was determined by measuring scattering from the *d*P2VP/[*d*Im][TFSI] mixture at 15 K where all of the signal is expected to be elastic.

Elastic and quasi-elastic scattering contribute to the observed scattering profiles, $S(q,\omega)$. Quasi-elastic scattering in $S(q,\omega)$ reflects self-correlated motion and appears as broad signal over a sharp, elastic scattering peak centered around ω = 0. Reduction, visualization, and analysis of HFBS data were performed using the DAVE software package developed at NCNR.[38] The elastic scattering contributions were modeled using a Delta function convoluted with the resolution function of the instrument. The quasi-elastic scattering contributions were modeled using two Lorentzian functions, one for the high-energy background signal and one for the main quasi-elastic contribution in the energy range of the instruments. The full width at half-maximum (fwhm) values of the high-energy background signals were found to be essentially constant at 30 μeV for all q. Fitted fwhm's of the main quasi-elastic contributions in HFBS profiles were reported, with the standard deviation of the fits reported as the error.

RESULTS AND DISCUSSION

Relative cation and anion diffusion in nonstoichiometric [Im][TFSI] was found to be dramatically affected both by combining the ionic liquid with polymer as well as confining it to lamellar block copolymer nanodomains. Whereas the anion and cation diffuse at similar rates in the neat ionic liquid,[28,39] the cation diffuses much more quickly than the anion when the ionic liquid is added to the homopolymer or block copolymer, as shown in Figure 2. Faster cation diffusion can be attributed to the prevalence of anionic aggregates in the membrane or to specific interactions between the TFSI anions and the 2VP repeat units. The presence of anionic aggregates has been shown to cause relatively fast cation diffusion in ionic liquid-impregnated Nafion at low hydration levels.[32] Alternatively, specific polymer/anion interactions may slow anion diffusion. This effect has been previously observed in mixtures of 1-ethyl-3-methylimidazolium/TFSI with poly(methyl methacrylate) (PMMA).[33] The 2VP repeat unit is basic, so this type of specific interaction with TFSI is not anticipated. It is possible, however, that some 2VP moieties are protonated by imidazolium, leading to interactions between protonated 2VP moieties and the TFSI anion.

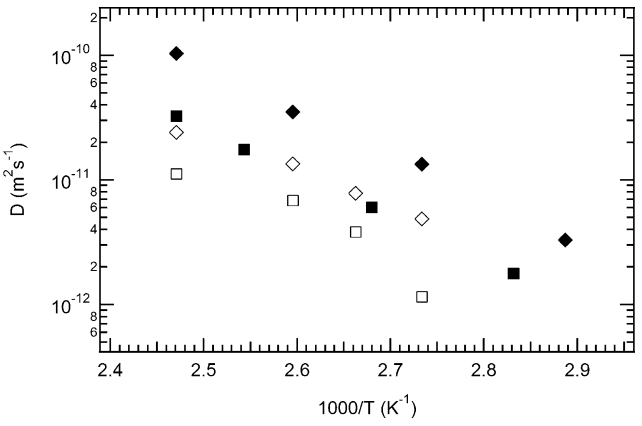


Figure 2. D_{C-H} (diamonds) and D_{TFSI} (squares) as a function of temperature for *d*P2VP/nonstoichiometric [Im][TFSI] (solid symbols) and *d*PS-*b*-*d*P2VP/nonstoichiometric [Im][TFSI] (open symbols).

Cation diffusion is deduced from D_{C-H}, which is actually a molar-weighted average of the diffusion coefficients of imidazolium cations and neutral imidazole.[28] It is possible, then, that an increase in ion aggregation upon mixing the ionic liquid with the lower dielectric polymer could lead to a larger decrease in D_{TFSI} than D_{C-H} and explain the results in Figure 2. $D_{TFSI,St}$ and $D_{C-H,St}$ were also measured for mixtures of stoichiometric [Im][TFSI] with *d*P2VP and *d*PS-*b*-*d*P2VP, in which the ratio of Im/*d*2VP was held constant to that in the nonstoichiometric mixtures. When a stoichiometric ionic liquid is used, diffusion is dominated by the diffusion of ions. At high temperatures, the difference in the diffusion rate of the anion and cation is similar to that in the nonstoichiometric mixtures (Figure S4 in the Supporting Information), confirming that the high cation diffusion in the nonstoichiometric mixtures is real and not due to fast diffusion of neutral imidazole.

The discrepancy between anion and cation diffusion is smaller in the block copolymer mixture than in the homopolymer mixture. For instance, at 132 °C, D_{C-H}/D_{TFSI} = 3.2 for the homopolymer mixed with ionic liquid compared with D_{C-H}/D_{TFSI} = 2.3 for the analogous block copolymer mixture. This is not surprising given that in the block copolymer portions of the *d*P2VP block close to the block copolymer interface are highly stretched, which appears to affect ion coordination.[19] Similarly, coordination of P2VP with metal chlorides has also been shown to be intimately related to chain conformation.[40] Both D_{C-H} and D_{TFSI} are smaller in the block copolymer mixture than in the homopolymer mixture due to the confinement of the ionic liquid diffusion path to interconnected, isotropically oriented lamellar domains with long-range order defects on the length scale of the NMR experiments, including point defects and grain boundaries.[41]

The most striking difference between the mechanism of proton conductivity in mixtures of nonstoichiometric [Im][TFSI] with homopolymer and block copolymer is the greatly increased amount of proton hopping that occurs in the block copolymer sample. The amount of proton hopping was probed by measuring the ratio of the diffusion coefficient of the acidic ionic liquid proton, D_{H^+}, to cation diffusion (D_{C-H}), where D_{H^+} was calculated by assuming D_{N-H} is a molar weighted average of the diffusion of protons bound to nitrogen atoms on charged imidazolium and neutral imidazole

$$D_{N-H} = xD_{H^+} + (1 - x)D_{C-H} \quad (2)$$

where x is the mole fraction of imidazolium.[28] As shown in Figure 3, the fact that the proton diffusion coefficient is much larger than D_{C-H} suggests there is a significant amount of proton hopping in the neat nonstoichiometric ionic liquid over the entire experimental temperature range (25 to 120 °C). The amount of proton hopping decreases with increasing temperature. This decrease may be related to a number of mechanisms, including increased hydrogen bond length or shortened average lifetime or decreased number of imidazole hydrogen bonds accompanying an increase in temperature.[42,43]

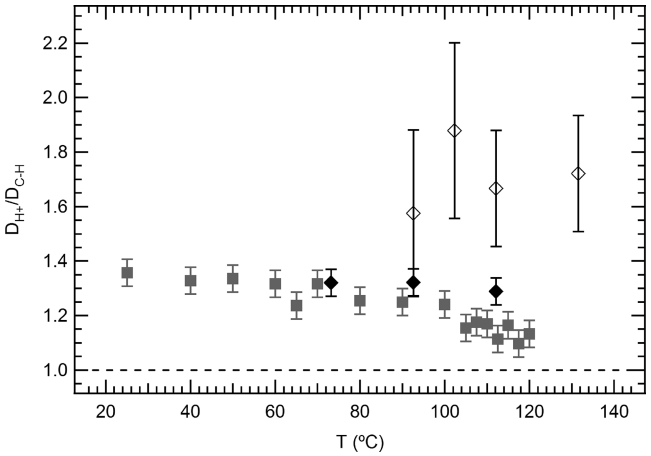


Figure 3. Ratio of acidic proton diffusion to cation diffusion as a function of temperature for *d*P2VP/nonstoichiometric [Im][TFSI] (solid diamonds), *d*PS-*b*-*d*P2VP/nonstoichiometric [Im][TFSI] (open diamonds), and neat nonstoichiometric [Im][TFSI] (gray squares). The degree of proton hopping is greatly enhanced in the nanostructured sample. Error bars on data for the neat ionic liquid and the *d*P2VP mixture represent a reasonable estimate based on the reproducibility of experiments, and error bars on data for the *d*PS-*b*-*d*P2VP mixture represent one standard deviation of the mean obtained from many experiments.

Mixing the ionic liquid with *d*P2VP homopolymer does not appear to affect proton-hopping mechanisms. However, the ratio of D_{H^+}/D_{C-H} is considerably greater for the block copolymer mixture, suggesting the influence of confinement on the mechanism of proton transport. Despite the larger error bars for the block copolymer sample (which reflect a decrease in signal following the decrease in proton concentration in these samples), the significant enhancement of acidic proton diffusion is clear.

Further evidence of increased proton hopping in the block copolymer sample comes from QENS experiments. QENS is an ideal tool for studying proton-transport mechanisms because the relatively large incoherent neutron scattering cross section of ^{1}H compared with that of other atoms leads to the selective observation of self-correlated hydrogen motion (i.e., diffusion). Motion is probed on the length scale of tenths of nanometers to nanometers, so the local information derived from these experiments compliments NMR diffusion measurements, which are on the micrometer length scale, and bulk ionic conductivity measurements, which are on the millimeter length scale. Representative QENS scattering profiles for mixtures of nonstoichiometric [*d*Im][TFSI] with *d*P2VP homopolymer and *d*PS-*b*-*d*P2VP block copolymer are shown in Figure 4. As the scattering vector q increases, the elastic scattering contribution decreases and the fwhm of the quasi-elastic scattering contribution increases, indicating diffusive motion.[44] This is clearly seen in Figure 4a for the homopolymer sample. The trends are less obvious for the block copolymer sample scattering profiles (Figure 4b) due to a combination of increased q-dependent elastic scattering resulting from increased order as well as increased influence of q-dependent coherent scattering resulting from a higher concentration of deuterium atoms.[44] The quasi-elastic contributions were modeled to quantify their dependence on q. Example fits of

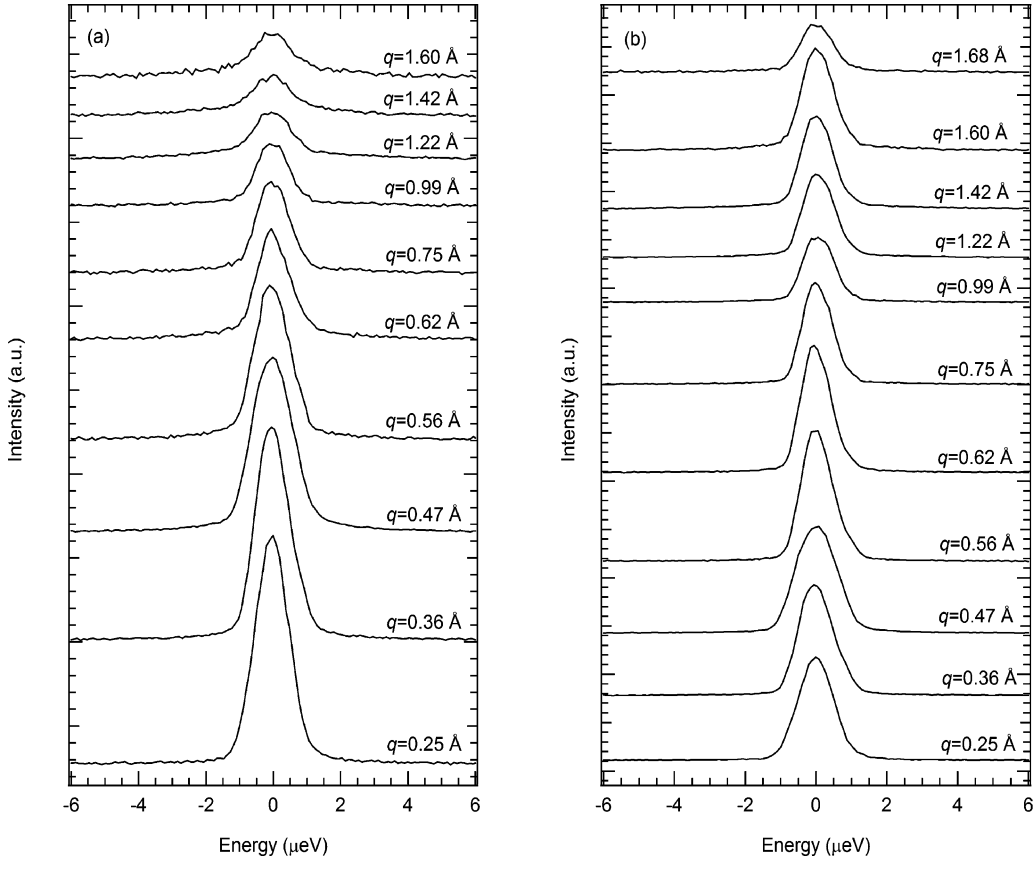


Figure 4. QENS scattering profiles of (a) *d*P2VP/nonstoichiometric [*d*Im][TFSI] and (b) *d*PS-*b*-*d*P2VP/nonstoichiometric [*d*Im][TFSI] at 140 °C.

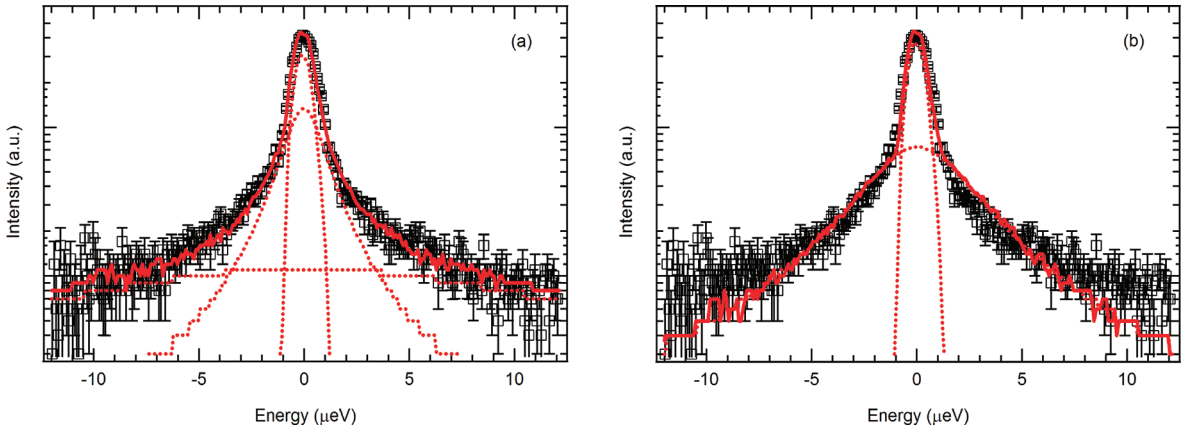


Figure 5. QENS profiles of *d*P2VP/nonstoichiometric [*d*Im][TFSI] at T = 140 °C and q = 0.99 Å^{-1}. The solid lines are the total fits to the data, whereas the dotted lines are the component fits. The fit using two Lorentzians in addition to a delta function convoluted with the resolution function that captures elastic scattering (a) is clearly better than the fit using a single Lorentzian (b).

the homopolymer sample are shown in Figure 5, where it is clear that two Lorentzian functions are necessary to capture fully the scattering profile: one to describe the main quasi-elastic scattering contribution stemming from diffusive motion and one to describe the high-energy background signal. Similar plots of data and fits for the block copolymer sample are shown in Figure S5 in the Supporting Information.

The q dependence of the fwhm of the main quasi-elastic scattering contribution, Γ, provides information regarding the mechanism of proton diffusion. When there is purely Fickian diffusion, Γ is expected to vary linearly with q^2 according to[44]

$$\Gamma/2 = \hbar D q^2 \tag{3}$$

Equation 3 adequately describes simple liquids such as argon[45] and even some more complex liquids such as the ionic liquid 1-butyl-3-methylimidazolium:chloride.[46] When molecular interactions are significant, for instance, in the case of the ionic liquids 1-ethyl-3-methylimidazolium:bromide[47] and *N*,*N*,*N*′,*N*′-tetramethylguanidinium:bis(perfluoroethylsulfonyl)imide,[48] deviations from eq 3 have been observed at high values of q corresponding to length scales smaller than the interaction distance. In these cases, the jump-diffusion model[49] has been used to describe the variation of Γ with q^2 as

$$\Gamma/2 = \frac{\hbar D q^2}{1 + D q^2 \tau_0} \tag{4}$$

where τ_0 is the residence time between jumps or the molecular interaction time. Specifically, the jump-diffusion model describes the complex dynamics of protons in supercooled water, which are dominated by Grotthuss proton transfer between water molecules through hydrogen bonds.[50,51] τ_0 in this case is the time between proton-transfer events. Similarly, eq 4 is a good model for describing quasi-elastic scattering from the combination of diffusion and proton hopping in non-stoichiometric [*d*Im][TFSI], where the interpretation of τ_0 is complex because of significant contributions of both molecular interactions and proton hopping to the deviation from Fickian behavior.[39] Therefore, it is expected that the ionic liquid/polymer mixtures in this study also exhibit non-Fickian behavior that can be estimated by eq 4 and that the magnitude of the departure from Fickian behavior is related to the amount of proton hopping. Figure 6 demonstrates that the acidic protons in mixtures of nonstoichiometric [*d*Im][TFSI] with

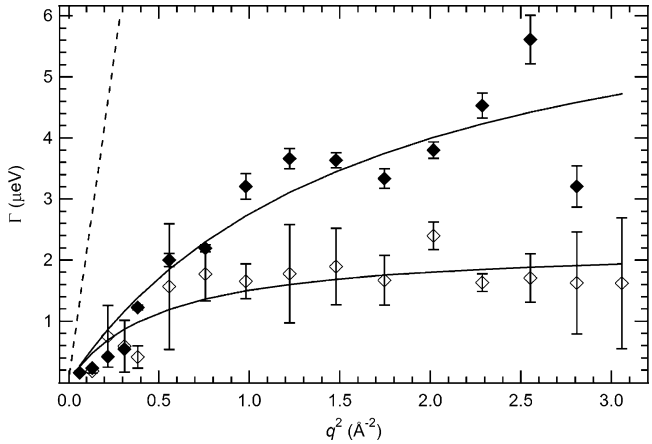


Figure 6. Γ of the main Lorentzian peak fit to QENS scattering profiles as a function of q^2 for *d*P2VP/nonstoichiometric [*d*Im][TFSI] (solid symbols) and *d*PS-*b*-*d*P2VP/nonstoichiometric [*d*Im][TFSI] (open symbols) at 140 °C. Error bars represent one standard deviation of the fits. Solid curves are fits to the data using eq 4, and the dashed line is the Fickian diffusion curve (eq 3) using D_{N-H} in the homopolymer sample from NMR.

*d*P2VP homopolymer and *d*PS-*b*-*d*P2VP block copolymer undergo non-Fickian diffusion, adequately captured by eq 4. The block copolymer sample shows a greater departure from Fickian diffusion than the homopolymer sample, indicating increased proton hopping in agreement with NMR diffusion experiments.

It is anticipated that increased proton hopping in the block copolymer sample is related to a difference in the imidazole hydrogen bond structure under confinement. The ^{1}H MAS NMR chemical shifts of the protons covalently bound to imidazole/imidazolium nitrogens, δ_{N-H}, are strongly dependent on hydrogen bonding.[28] In qualitative similarity with the neat ionic liquid,[39] δ_{N-H} shifts to lower ppm as the temperature is increased (Figure 7a,7b). The temperature dependence of δ_{N-H} is steeper for the block copolymer mixture than for the neat ionic liquid sample and the homopolymer mixture (Figure 7c), suggesting unique hydrogen-bonding behavior. Furthermore, the absolute values of the chemical shifts for the block copolymer sample are unexpected. The higher values for the homopolymer sample compared with those for the neat ionic liquid are unsurprising due to the greater number of molecules

dx.doi.org/10.1021/ma202741g | *Macromolecules* 2012, 45, 3112–3120

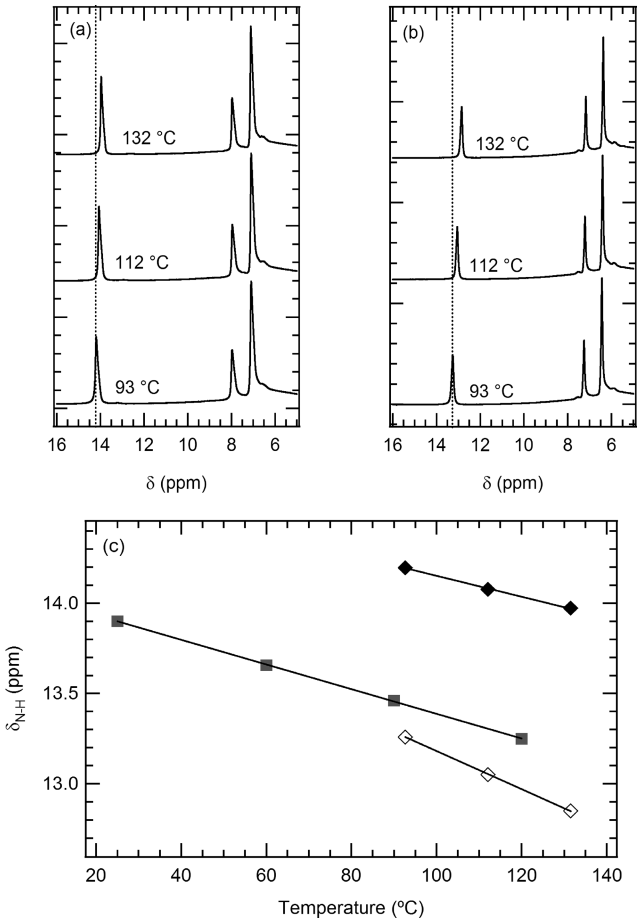


Figure 7. MAS ^{1}H NMR spectra of (a) *d*P2VP/nonstoichiometric [Im][TFSI] and (b) *d*PS-*b*-*d*P2VP/nonstoichiometric [Im][TFSI] as well as (c) δ_{N-H} as a function of temperature for the *d*P2VP mixture (solid diamonds), *d*PS-*b*-*d*P2VP mixture (open diamonds), and neat nonstoichiometric [Im][TFSI] (gray squares). Lines of best linear fit connect the data points.

that can participate in hydrogen bonding. The same phenomena is observed when excess imidazole is added to stoichiometric ionic liquid.[28] The block copolymer sample has lower values of δ_{N-H} despite containing the same number of molecules that can participate in hydrogen bonding as the homopolymer sample. These unexpected trends indicate that a different hydrogen bond network exists in the ionic liquid when confined to block copolymer domains, which affects the amount of proton hopping that occurs.

Polymer chain stretching near the block copolymer interface likely affects how *d*2VP units interact with the imidazole hydrogen bond network. Previous studies have already demonstrated the relationship between polymer chain conformation and ion and metal chloride coordination.[19,40] Additionally, the presence of the interface itself likely alters the near-interface hydrogen bond structure, the effects of which could propagate several nanometers into either side of the 17 nm *d*P2VP/ionic liquid channels. Such confinement effects on hydrogen bonding in water are well-documented.[10−13]

The mechanistic differences in proton transport in the nanostructured and nonordered samples lead to differences in bulk ionic conductivity, σ. In Figure 8, σ is plotted as a function of temperature for mixtures of nonstoichiometric [Im][TFSI] with homopolymer and block copolymer. The conductivity of

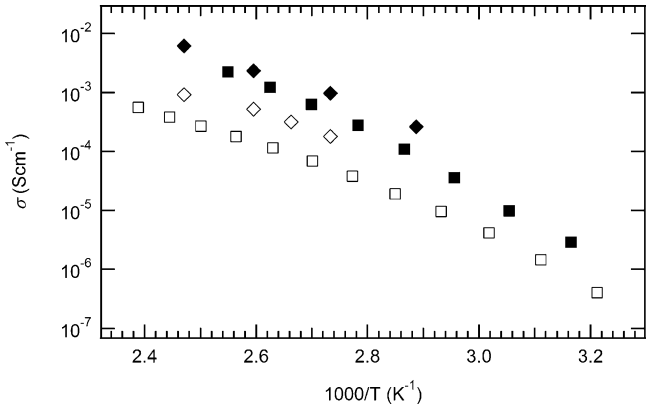


Figure 8. Measured σ (squares) and σ calculated from NMR diffusion coefficients and the Nernst−Einstein equation (diamonds) for mixtures of nonstoichiometric [Im][TFSI] with P2VP (solid symbols) and PS-*b*-P2VP (open symbols).

the block copolymer sample is lower than that of the homopolymer sample due to the overall lower ion concentration in the block copolymer membrane, in addition to the lack of long-range order characterizing its lamellar domains. Ion aggregation in each sample is investigated by comparing the measured conductivity to the conductivity predicted by the Nernst−Einstein equation using ion diffusion coefficients measured by NMR. The Nernst−Einstein equation is given by

$$\sigma = \frac{F^2}{RT}(c_{m,H^+}D_{H^+} + c_{m,TFSI}D_{TFSI}) \quad (5)$$

where c_{m,H^+} and $c_{m,TFSI}$ are the molar concentrations of acidic protons and TFSI anions, respectively. The predicted conductivities for both samples are plotted along with the measured bulk conductivities as a function of temperature in Figure 8. Equation 5 overpredicts the measured ionic conductivity of the block copolymer sample by a factor of 3 to 4 while predicting the homopolymer conductivity relatively well. Because NMR measures diffusion over micrometer length scales and bulk conductivity measurements probe a millimeter dimension, the large discrepancy for the block copolymer sample is likely attributed to a combination of ion aggregation and differences in long-range order. The increasing overprediction of the conductivity of the homopolymer sample at lower temperatures suggests an increase in the degree of ion aggregation with decreasing temperature. The strong temperature dependence suggests that anionic aggregates are not the major cause of faster relative cation diffusion in the homopolymer sample. (If the ion aggregates were anionic aggregates, the temperature dependence would be reflected in Figure 2.) In the block copolymer sample, no temperature dependence is observed, so anionic aggregates in this sample are still a possibility.

The result of different ion aggregation behavior as well as different amounts of proton hopping in the homopolymer and block copolymer samples is that the activation energy for bulk ionic conductivity is lower in the block copolymer sample. This is clearly observed in Figure 8, where the temperature dependence for the measured conductivity is much less steep.

■ CONCLUSIONS

Proton transport in ionic liquids is clearly affected when the ionic liquid is mixed with a polymer and especially when the

ionic liquid is confined to block copolymer nanodomains. Several specific mechanistic changes have been illuminated in this work using a combination of transport measurements that together probe a variety of length scales and a variety of molecular and atomic species. The relative amount of cation and anion diffusion, for example, has been found to change drastically upon incorporation of ionic liquid into a homopolymer and block copolymer. In the case presented here of nonstoichiometric [Im][TFSI] mixed with *d*P2VP and *d*PS-*b*-*d*P2VP, specific interactions between TFSI and *d*2VP moieties or the prevalence of anionic aggregates cause the cation to diffuse significantly faster than the anion, which is in stark contrast with the neat ionic liquid. This asymmetric charge transport could be taken advantage of for a variety of applications, including proton exchange membrane fuel cells or actuators.

The temperature dependence of ion aggregation has been found to be significantly different in the homopolymer and block copolymer samples, contributing to a lower activation energy for ion transport in the block copolymer sample. Determining the degree of ion aggregation in the block copolymer sample as well as understanding the source of its temperature independence could lead to the design of nanostructured membranes with increased conductivity.

The most striking change in proton transport upon incorporation of nonstoichiometric [Im][TFSI] into a block copolymer is that the amount of diffusion-enhancing proton-hopping drastically increases. We propose that block copolymer chain stretching or confinement affect the hydrogen-bond structure of the ionic liquid, leading to this increase. Long-range proton diffusion in the block copolymer/ionic liquid membrane is still not as high as in the homopolymer/ionic liquid membrane because of the lack of long-range order characterizing the lamellar domains. However, highly conductive, mechanically durable membranes could be designed by combining the enhancement of acidic proton diffusion due to block copolymer self-assembly with increased long-range order obtained using one of many channel-aligning techniques.[52]

■ ASSOCIATED CONTENT

Supporting Information

SAXS morphological characterization of block copolymer/ionic liquid mixtures, representative PGSE NMR data, diffusion data as a function of experimental diffusion time, representative QENS fits, and diffusion data for control mixtures of polymer with stoichiometric [Im][TFSI]. This material is available free of charge via the Internet at http://pubs.acs.org.

■ AUTHOR INFORMATION

Corresponding Author

*E-mail: mhoarfrost@berkeley.edu.

Notes

The authors declare no competing financial interest.

■ ACKNOWLEDGMENTS

We gratefully acknowledge support from the Assistant Secretary for Energy Efficiency and Renewable Energy, Office of Hydrogen, Fuel Cell, and Infrastructure Technologies of the U.S. Department of Energy under contract DE-AC02-05CH11231. M.L.H. acknowledges support from an NSF Graduate Research Fellowship. SAXS experiments were performed at the ALS and the SSRL. Both are national user facilities supported by the Department of Energy, Office of Basic Sciences. We gratefully acknowledge Dr. Alexander Hexemer, Dr. Cheng Wang, and Dr. Eric Schaible for experimental assistance at the ALS and Dr. John Pople for experimental assistance at the SSRL. This work also utilized facilities at the NCNR partially supported by the National Science Foundation under agreement no. DMR-0944772. We gratefully acknowledge Dr. Timothy Jenkins for experimental assistance at the NCNR. Finally, we thank Dr. Joel Stettler for technical assistance with NMR experiments. Certain commercial equipment, instruments, materials or material suppliers are identified in this Article to foster understanding. Such identification does not imply recommendation or endorsement by the National Institute of Standards and Technology, nor does it imply that the materials or equipment identified are necessarily the best available for the purpose.

■ REFERENCES

(1) Mauritz, K. A.; Moore, R. B. *Chem. Rev.* **2004**, *104* (10), 4535–4585.
(2) Chen, Y. B.; Thorn, M.; Christensen, S.; Versek, C.; Poe, A.; Hayward, R. C.; Tuominen, M. T.; Thayumanavan, S. *Nat. Chem.* **2010**, *2* (6), 503–508.
(3) Ichikawa, T.; Yoshio, M.; Hamasaki, A.; Mukai, T.; Ohno, H.; Kato, T. *J. Am. Chem. Soc.* **2007**, *129* (35), 10662–10663.
(4) Wanakule, N. S.; Panday, A.; Mullin, S. A.; Gann, E.; Hexemer, A.; Balsara, N. P. *Macromolecules* **2009**, *42* (15), 5642–5651.
(5) Rubatat, L.; Li, C. X.; Dietsch, H.; Nykanen, A.; Ruokolainen, J.; Mezzenga, R. *Macromolecules* **2008**, *41* (21), 8130–8137.
(6) Ruzette, A. V. G.; Soo, P. P.; Sadoway, D. R.; Mayes, A. M. *J. Electrochem. Soc.* **2001**, *148* (6), A537–A543.
(7) Hoarfrost, M. L.; Segalman, R. A. *Macromolecules* **2011**, *44* (13), 5281–5288.
(8) Cho, B. K.; Jain, A.; Gruner, S. M.; Wiesner, U. *Science* **2004**, *305* (5690), 1598–1601.
(9) Kim, Y. S.; Pivovar, B. S. *Annu. Rev. Chem. Biomol. Eng.* **2010**, *1*, 123–148.
(10) Scatena, L. F.; Brown, M. G.; Richmond, G. L. *Science* **2001**, *292* (5518), 908–912.
(11) Piletic, I. R.; Moilanen, D. E.; Spry, D. B.; Levinger, N. E.; Fayer, M. D. *J. Phys. Chem. A* **2006**, *110* (34), 10369–10369.
(12) Moilanen, D. E.; Levinger, N. E.; Spry, D. B.; Fayer, M. D. *J. Am. Chem. Soc.* **2007**, *129* (46), 14311–14318.
(13) Guegan, R. *J. Colloid Interface Sci.* **2011**, *358* (2), 485–490.
(14) Moilanen, D. E.; Piletic, I. R.; Fayer, M. D. *J. Phys. Chem. C* **2007**, *111* (25), 8884–8891.
(15) Choi, P.; Jalani, N. H.; Datta, R. *J. Electrochem. Soc.* **2005**, *152* (3), E123–E130.
(16) Eikerling, M.; Kornyshev, A. A.; Kuznetsov, A. M.; Ulstrup, J.; Walbran, S. *J. Phys. Chem. B* **2001**, *105* (17), 3646–3662.
(17) Mafe, S.; Manzanares, J. A.; Ramirez, P. *Phys. Chem. Chem. Phys.* **2003**, *5* (2), 376–383.
(18) Paddison, S. J.; Paul, R. *Phys. Chem. Chem. Phys.* **2002**, *4* (7), 1158–1163.
(19) Singh, M.; Odusanya, O.; Wilmes, G. M.; Eitouni, H. B.; Gomez, E. D.; Patel, A. J.; Chen, V. L.; Park, M. J.; Fragouli, P.; Iatrou, H.; Hadjichristidis, N.; Cookson, D.; Balsara, N. P. *Macromolecules* **2007**, *40* (13), 4578–4585.
(20) Bureekaew, S.; Horike, S.; Higuchi, M.; Mizuno, M.; Kawamura, T.; Tanaka, D.; Yanai, N.; Kitagawa, S. *Nat. Mater.* **2009**, *8* (10), 831–836.
(21) Simone, P. M.; Lodge, T. P. *ACS Appl. Mater. Interfaces* **2009**, *1* (12), 2812–2820.
(22) Simone, P. M.; Lodge, T. P. *Macromolecules* **2008**, *41* (5), 1753–1759.
(23) Virgili, J. M.; Hexemer, A.; Pople, J. A.; Segalman, R. A.; Balsara, N. P. *Macromolecules* **2009**, *42* (13), 4604–4613.

(24) Virgili, J. M.; Nedoma, A. J.; Segalman, R. A.; Balsara, N. P. *Macromolecules* **2010**, *43* (8), 3750−3756.
(25) Virgili, J. M.; Hoarfrost, M. L.; Segalman, R. A. *Macromolecules* **2010**, *43* (12), 5417−5423.
(26) Gwee, L.; Choi, J. H.; Winey, K. I.; Elabd, Y. A. *Polymer* **2010**, *51* (23), 5516−5524.
(27) Munch, W.; Kreuer, K. D.; Silvestri, W.; Maier, J.; Seifert, G. *Solid State Ionics* **2001**, *145* (1−4), 437−443.
(28) Noda, A.; Susan, A. B.; Kudo, K.; Mitsushima, S.; Hayamizu, K.; Watanabe, M. *J. Phys. Chem. B* **2003**, *107* (17), 4024−4033.
(29) Kreuer, K. D.; Fuchs, A.; Ise, M.; Spaeth, M.; Maier, J. *Electrochim. Acta* **1998**, *43* (10−11), 1281−1288.
(30) Kim, S. Y.; Kim, S.; Park, M. J. *Nat. Commun.* **2010**, *1*, 88.
(31) Kim, S. Y.; Yoon, E.; Joo, T.; Park, M. J. *Macromolecules* **2011**, *44* (13), 5289−5298.
(32) Hou, J. B.; Zhang, Z. Y.; Madsen, L. A. *J. Phys. Chem. B* **2011**, *115* (16), 4576−4582.
(33) Susan, M. A.; Kaneko, T.; Noda, A.; Watanabe, M. *J. Am. Chem. Soc.* **2005**, *127* (13), 4976−4983.
(34) Yokoyama, H.; Mates, T. E.; Kramer, E. J. *Macromolecules* **2000**, *33* (5), 1888−1898.
(35) Price, W. S. *Concepts Magn. Reson.* **1998**, *10* (4), 197−237.
(36) Stejskal, E. O.; Tanner, J. E. *J. Chem. Phys.* **1965**, *42* (1), 288−292.
(37) Raiford, D. S.; Fisk, C. L.; Becker, E. D. *Anal. Chem.* **1979**, *51* (12), 2050−2051.
(38) Azuah, R. T.; Kneller, L. R.; Qiu, Y. M.; Tregenna-Piggott, P. L. W.; Brown, C. M.; Copley, J. R. D.; Dimeo, R. M. *J. Res. Natl. Inst. Stand. Technol.* **2009**, *114* (6), 341−358.
(39) Hoarfrost, M. L.; Tyagi, M. S.; Segalman, R. A.; Reimer, J. A., in preparation.
(40) Lee, D. H.; Kim, H. Y.; Kim, J. K.; Huh, J.; Ryu, D. Y. *Macromolecules* **2006**, *39* (6), 2027−2030.
(41) Hou, J. B.; Li, J.; Madsen, L. A. *Macromolecules* **2010**, *43* (1), 347−353.
(42) Kanaskov, Yd; Sukhoruk, Bi; Pentin, Y. A.; Komarovs, Gv. *Izv. Akad. Nauk SSSR, Ser. Khim.* **1970**, *8*, 1735.
(43) Cavalcanti, W. L.; Portaluppi, D. F.; Joswig, J. O. *J. Chem. Phys.* **2010**, *133* (10), 104703.
(44) Bée, M. *Quasielastic Neutron Scattering: Principles and Applications in Solid State Chemistry, Biology and Materials Science* IOP Publishing Ltd: Bristol, U.K., 1988.
(45) Dasannacharya, B. A.; Rao, K. R. *Phys. Rev.* **1965**, *137* (2A), A417−A427.
(46) Inamura, Y.; Yamamuro, O.; Hayashi, S.; Hamaguchi, H. O. *Phys. B* **2006**, *385*, 732−734.
(47) Aoun, B.; Gonzalez, M. A.; Ollivier, J.; Russina, M.; Izaola, Z.; Price, D. L.; Saboungi, M. L. *J. Phys. Chem. Lett.* **2010**, *1* (17), 2503−2507.
(48) Mamontov, E.; Luo, H. M.; Dai, S. *J. Phys. Chem. B* **2009**, *113* (1), 159−169.
(49) Chudley, C. T.; Elliott, R. J. *Proc. Phys. Soc., London* **1961**, *77* (494), 353−361.
(50) Chen, S. H.; Teixeira, J.; Nicklow, R. *Phys. Rev. A* **1982**, *26* (6), 3477−3482.
(51) Teixeira, J.; Bellissentfunel, M. C.; Chen, S. H.; Dianoux, A. J. *Phys. Rev. A* **1985**, *31* (3), 1913−1917.
(52) Li, J.; Park, J. K.; Moore, R. B.; Madsen, L. A. *Nat. Mater.* **2011**, *10* (7), 507−511.

Macromolecules

Article

pubs.acs.org/Macromolecules

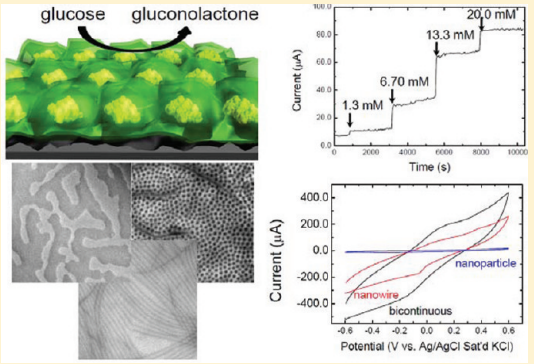
Enhanced Charge Transport in Enzyme-Wired Organometallic Block Copolymers for Bioenergy and Biosensors

Joungphil Lee,[†] Hyungmin Ahn,[†] Ilyoung Choi,[‡] Markus Boese,[§] and Moon Jeong Park*[,†,‡]

[†]Department of Chemistry and [‡]Division of Advanced Materials Science (WCU), Pohang University of Science and Technology (POSTECH), Pohang, Korea 790-784

[§]National Center for Electron Microscopy, Lawrence Berkeley National Laboratory, University of California, Berkeley, Berkeley, California 94720, United States

ABSTRACT: Wiring of glucose oxidase (GOx) onto electrode surface was successfully achieved by cross-linked networks of organometallic block copolymers comprising electroactive ferrocene moieties and chemically cross-linkable diene groups, poly(ferrocenyldimethylsilane-*b*-isoprene)s (PFS−PIs). Different nanoscale morphologies of PFS−PIs, i.e., bicontinuous structure, nanowires, and nanoparticles, have been derived by varying molecular weights and casting solvents. Upon examining catalytic current responses of the GOx integrated PFS−PI systems, notably, the morphology of PFS−PI is found out to be a crucial parameter in determining the efficiency of electron transfer. For example, the use of bicontinuous PFS−PI confirms 2−50 times improved catalytic current densities, compared with the values of other morphologies; the maximum catalytic current of glucose oxidation was 0.7 mA/cm^2 at 70 mM glucose concentration. The biosensing ability of the fabricated electrode with structural optimization was also exploited, and good sensitivity is obtained at the physiological concentration of glucose in blood.



INTRODUCTION

The development of efficient enzymatic biofuel cells is a subject of considerable studies in past decades for potential applications such as biomedical devices,[1−3] microchip systems,[4,5] and portable electronics.[6] Since biofuel cells produce electrical power upon consuming ranges of biomass such as alcohols and glucose, their renewable nature has been highlighted. One of the key challenges in advancing the technology lies in power densities of biofuel cells. Limitations have been arisen from the buried redox active sites within enzyme structures, which result in poor interplay between redox reactions and electron transfer. In fact, the low power density of enzymatic biofuel cells significantly hinders the development of power systems for miniaturized biomedical devices.[7]

Several different approaches to enhance the power density of biofuel cells are proposed.[8,9] One of widely studied methodology is the use of electron mediators to help electron transfer in the systems by shuttling electrons between enzyme catalytic centers and the current collector. Various materials possessing the ability of electron mediation have been extensively reported in recent years.[9−18] Example includes nanocarbons,[10−12] redox active polymers,[13−15] cofactor relay,[16] and metal nanoparticles.[17,18]

To attain more stable and higher current densities of biofuel cells in the presence of electron mediators, the essential requirement is the immobilization of enzymes to the electrodes. Consequently, significant amounts of studies on the electron mediators are concerned with the electrical contact of enzymes to the electrode surfaces with covalently attached mediators.[19,20] With "wiring" point of view, carbon nanotubes (CNTs) have been received great interests[21,22] owing to their large specific surface area[23,24] and excellent electrochemical properties.[25−27] One drawback of applying CNTs to the large area electrodes is the difficulty in preventing CNT aggregations if chemical modification of the CNTs or preorganization of CNT arrays is not carried out.[12,21]

Concurrently with the development of the CNT-based mediator systems, substantial efforts have been also paid to redox-active polymers. A number of organometallic polymers were identified as effective materials transferring the electrons as a result of redox reactions.[28,29] However, although the kinds of redox polymers and their electrochemical properties are well-established,[7,13,30,31] there is an open question about how the morphology of redox polymers makes effect on the electron-mediating properties. Herein, we have explored the electrochemical properties of enzyme integrated redox polymers by varying the self-assembled structures of the redox polymers in nanometer scales.

In present study, a glucose oxidase (GOx) is employed as a model enzyme[29] and ferrocene (Fc)-containing organometallic block copolymers with Os-reactive diene groups, poly(ferrocenyldimethylsilane-*b*-isoprene) (PFS−PI) copolymers, are used as electron mediators. Our efforts are inspired by

Received: January 19, 2012
Revised: March 6, 2012
Published: March 21, 2012

 © 2012 American Chemical Society dx.doi.org/10.1021/ma300155u | *Macromolecules* 2012, 45, 3121−3128

the pioneering studies of Manners et al.[32,33] where the synthesis and self-assembly nature of Fc containing block copolymers are discovered. The Fc moieties packed within the self-assembled structures are particularly aimed at improving the electron transfer rate between the flavin adenine dinucleotide (FAD) cofactor in GOx and an electrode surface.[34]

EXPERIMENTAL SECTION

Synthesis of Organometallic Block Copolymers. A ferrocene-containing monomer, 1,1′-dimethylsilylferrocenophane monomer, was first synthesized by coupling lithiated ferrocene with silane according to the methods described by Manners et al.[33] The synthesized monomer was purified by repeated sublime/recrystallization processes under vacuum. Poly(ferrocenyldimethylsilane-*b*-isoprene) (PFS−PI) copolymers with different molecular weights were synthesized by sequential anionic polymerization.[35] The PI precursor synthesis was performed in purified benzene as a solvent and *sec*-butyllithium as an initiator. An aliquot of the living PI precursor was isolated in the glovebox for molecular weight determination. The aliquot was terminated using methanol. If the molecular weights of the PI precursor were close to target values, a preweighed amount of the purified 1,1′-dimethylsilylferrocenophane monomer was added to the reactor in the glovebox. The reactor was then returned to the vacuum line and was thoroughly degassed. A small quantity of purified THF was distilled into the reactors to speed up the polymerization of the 1,1′-dimethylsilylferrocenophane monomer. As the 1,1′-dimethylsilylferrocenophane monomer polymerized, the color of the reaction solution changed from red to brown. The polymerization proceeded for at least 6 h and then was terminated in the glovebox with isopropanol. Upon termination, the color of the solution changed from brown to red. The PFS−PI copolymers were isolated by precipitation in hexane. The molecular weights and molecular weight distribution of PFS−PI copolymers were characterized by combining ^{1}H nuclear magnetic resonance (NMR, Bruker AVB-300) spectroscopy and gel permeation chromatography (GPC, Waters Breeze 2 HPLC). The ^{1}H NMR spectra were taken by dissolving the copolymers in deuterated choloroform. For GPC experiments, THF was used as an eluent, and the results were calibrated with respect to polystyrene standards (Polymer Standard Service). Molecular weights of the PFS−PI coplymers were determined as 10.4−8.0 and 69.0−92.0 kg/mol where the polydispersity indices were less than 1.08. The molecular structure of PFS−PI copolymers is shown in Figure 1a.

Electrode Preparation. Glucose oxidase from *Aspergillus niger* (~200 units/mg, Lot # 001330219) is purchased from Sigma-Aldrich. GOx is deposited on porous carbon electrode by dropping aliquots of 60 μM GOx stock solution until targeted mass of 2 mg is attained. The GOx-deposited electrode is then completely dried under Ar blanket for 2 days. Homogeneous 0.1 wt % PFS−PI solutions prepared by different solvent mixtures are immediately drop-coated onto the dried electrode by varying the thickness of the PFS−PI layer. The thickness of electrode comprising the GOx and PFS−PI was determined using a XL30S FEG Philips scanning electron microscope (SEM). After complete evaporation of solvents in vacuum oven, the electrodes were exposed to OsO_4 vapor for 3 h. Note that the OsO_4 staining procedures are dangerous, and careful cautions are required. After Os decoration, the electrodes were stored in PBS buffer solution before use.

FT-IR Spectroscopy. Infrared spectra were recorded at room temperature using a Vertex 70 FT-IR spectrometer. Before the measurements, 30 min of equilibration time was allowed under N_2 gas purge, and 32 accumulations were signal-averaged at a resolution of 1 cm^{-1}. Baseline corrected infrared spectra were obtained for the PFS−PI copolymers on silicon wafers in transmission mode.

Morphology Characterization. Surface morphologies of fabricated electrodes were determined by AFM (Digital Instruments, Nanoscope III) in tapping mode. All measurements were made with a phase contrast value of 10°. Samples for transmission electron microscopy (TEM) experiments were prepared by drop-coating of 0.1 wt % PFS−PI copolymers in various solvent mixtures. All imaging have been performed before OsO_4 decoration due to the enough electron contrast between Fe-rich domains and PI domains using a Zeiss LIBRA 200FE microscope operating at 200 kV equipped with a cold stage (−160 °C) and an Omega energy filter. Fe elemental mapping was obtained using energy filtered imaging with the three-window method at the Fe L edge of 709 eV energy loss. Focused ion beam etched TEM (cross-sectional FIB-TEM) samples were prepared with a FEI Strata 235 dual beam FIB system operated at 30 kV. For the FIB-TEM imaging, surface protection of samples was accomplished by exposure to RuO_4 vapor for 10 h. Imaging of etched samples was performed with a JEOL 3010 microscope operated at 200 kV.

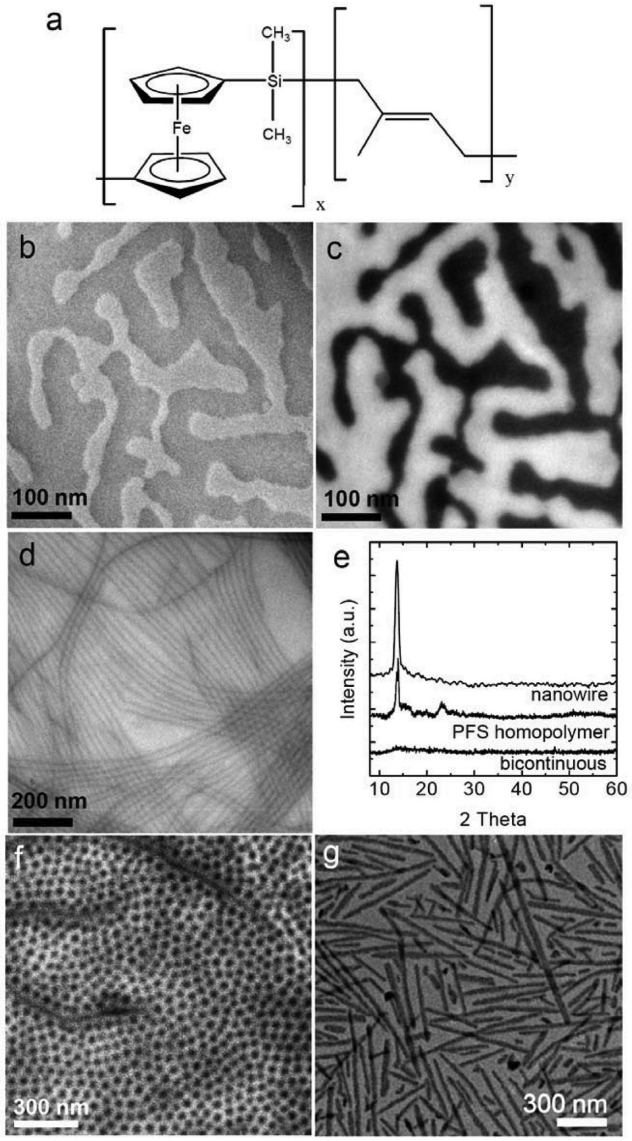


Figure 1. (a) Molecular structure of PFS−PI. TEM images of PFS−PI (10.4−8.0 kg/mol); (b) in toluene/hexane (20/80 vol %), (c) EELS image of (b), and (d) in THF/hexane (20/80 vol %). (e) X-ray diffraction patterns of bicontinuous, nanowire PFS−PI copolymers and PFS homopolymer. TEM images of PFS−PI (69.0−92.0 kg/mol); (f) in THF/hexane (20/80 vol %) and (g) in THF/hexane (25/75 vol %). All TEM samples are prepared by drop-coating on Formvar-coated Cu grids.

Catalytic Activity Characterization. Cyclic voltammetry (CV) measurements were recorded using a EG&G PAR 273A in a three-electrode cell with a platinum gauze as counter electrode and Ag/AgCl/(KCl saturated) as reference electrode. The working electrode was a porous carbon electrode. All measurements were performed in phosphate buffered saline (PBS) (1× PBS in 1 L of deionized water; 137 mM NaCl, 2.7 mM KCl, 10 mM $Na_2HPO_4{\cdot}2H_2O$, 2.0 mM

dx.doi.org/10.1021/ma300155u | Macromolecules 2012, 45, 3121−3128

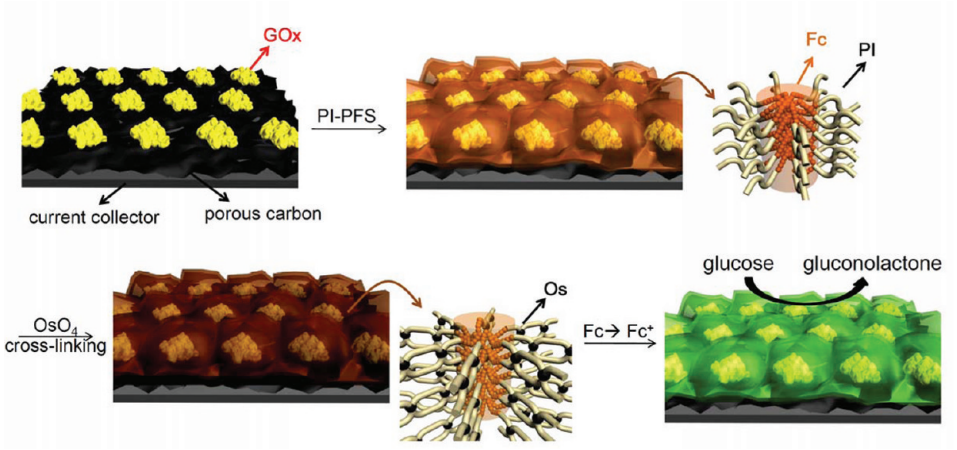


Figure 2. Fabrication process of functional electrodes comprised of GOx and PFS−PI mediators. For brevity, we only show representative graphics for the case of nanowire morphology.

KH_2PO_4, adjusted to pH 7.4) at 25 °C and ambient atmosphere. The conductivities of PFS−PI films were measured using ac impedance spectroscopy in the presence of PBS buffer solution using a home-built two-electrode cell with 1 cm × 1 cm Pt working/counter electrodes. Data were collected using a 1260 Solatron impedance analyzer operating over a frequency range of 1−100 000 Hz.

RESULTS

Nanoscale Morphologies of PFS−PI Redox Polymers. Figure 1a shows the chemical structure of PFS−PI copolymers where x and y indicate degree of polymerization of each blocks. We begin by describing the morphologies of PFS−PI copolymers. Figures 1b−d,f,g show the representative TEM images obtained from solution-cast PFS−PI copolymers. We found that PFS−PI copolymers offer various nanostructures when molecular weights and/or solvent compositions are altered. For example, a low molecular weight PFS−PI (10.4−8.0 kg/mol) in toluene/hexane (20/80 vol %) mixtures yields a bicontinuous structure with spacings of ca. 100 nm, as shown in Figures 1b,c. Figure 1c is obtained by Fe elemental map to confirm that the dark region in Figure 1b is Fc-rich area. When THF/hexane (20/80 vol %) mixture is employed, in contrast, distinctly different morphology of nanowires with the lengths of several micrometers is seen, as shown in Figure 1d. The diameter of the nanowires is 20 nm, which only reflects the size of PFS domains. It should be noted here that the solubility parameter of PFS (18.6 $MPa^{1/2}$) is quite close to the values of toluene (18.3 $MPa^{1/2}$) and THF (18.5 $MPa^{1/2}$) while the values of n-hexane (14.9 $MPa^{1/2}$) and PI chains (16.2 $MPa^{1/2}$) are relatively close.[36] This implies that the dissimilar morphologies depending on the choice of solvents are not originated from the solubility issues. Instead, it is found that the crystalline characteristics of PFS are significantly affected by the choice of the core-filling solvents. In Figure 1e, we compared X-ray diffraction (XRD) patterns of bicontinuous PFS−PI (toluene, amorphous) and nanowire PFS−PI (THF, crystalline). For a reference, a XRD profile of PFS homopolymer (melt processed) with molecular weight of 8.1 kg/mol is also given in the Figure 1e.

While keeping the THF/hexane (20/80 vol %) mixtures, the use of large molecular weight PFS−PI (69.0−92.0 kg/mol) results in fairly monodisperse nanoparticles with size of 55 nm (the darker phase is corresponding to core PFS domains and PI shell was not visible), as shown in Figure 1f. We note in passing that slight increase in THF amounts to 25 vol % results in short and relatively nonuniform nanowires, as given in Figure 1g. This implies that the nanoparticle morphology is only stable at the narrow window of THF/hexane compositions. It is worthwhile to mention here that the nanowire morphology of PFS−PI block copolymers is well-discovered by Manners et al.[32] while the bicontinuous and nanoparticle morphologies were first discovered in the present study.

The nanostructured PFS−PI organometallic polymers are then utilized to transfer electrons from redox reactions of GOx/glucose to electrodes. Figure 2 illustrates the fabrication process of the electrode comprised of GOx and PFS−PI mediators. GOx is deposited on porous carbon electrode by dropping aliquots of 60 μM GOx stock solution until targeted mass (2 mg) is attained. The GOx deposited electrode is then completely dried under Ar blanket for 2 days, followed by drop-coating of homogeneous 0.1 wt % PFS−PI solutions onto the dried electrode by varying the thickness of the PFS−PI layer. The maximum catalytic current is observed for GOx concentration of 30 wt %. At very high enzyme contents above 40 wt %, strong precipitation of GOx was observed.

In present study, PI was particularly chosen as a supporting matrix since the diene groups in PI chains allow us to introduce cross-linking points. The chemical cross-linking has been carried out by exposing the electrodes to OsO_4 vapor for 3 h in which the OsO_4 moieties simultaneously form covalent bonds to hydrocarbon groups in close proximity; hereafter, the OsO_4 cross-linked PFS−PI is referred to as PFS−PI_{OS}. It should be noted here that no noticeable changes in GOx activity owing to the exposure to OsO_4 vapor was confirmed by monitoring the catalytic activity of GOx as a function of exposure time. In addition, without Os decoration, the film becomes unstable within the physiological environments. As a final step, activation of Fc moieties is carried out by applying anodic potential sweep. The activation process prior to the addition of glucose helps to obtain improved current values when glucose is added. Because the Fc moieties will be positively charged after activation, it is expected to enhance association with the negatively charged GOx.

The covalent cross-linking reaction between OsO_4 and PI chains and the chemical stability of the PFS−PI_{OS} electrode under various solution conditions are confirmed by FT-IR experiments. As shown in Figure 3a, the IR peak intensities from 2800 to 3100 cm^{-1} corresponding to characteristic peaks

dx.doi.org/10.1021/ma300155u | Macromolecules 2012, 45, 3121−3128

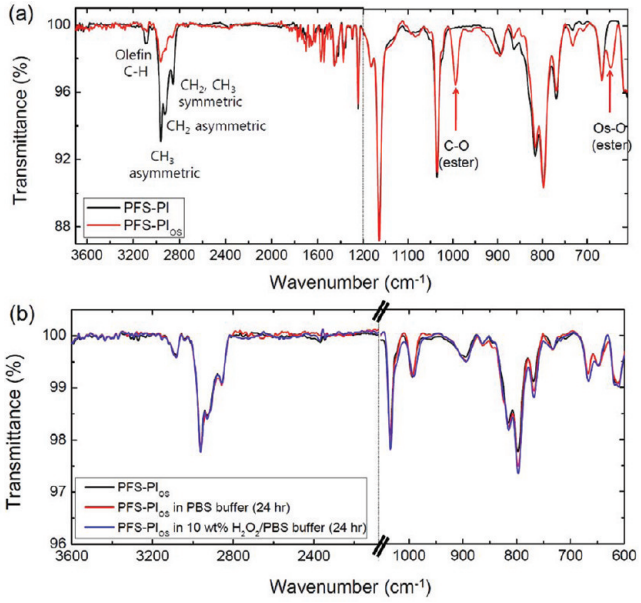


Figure 3. FT-IR data of PFS−PI electrodes (a) before/after OsO_4 staining and (b) under various experimental conditions.

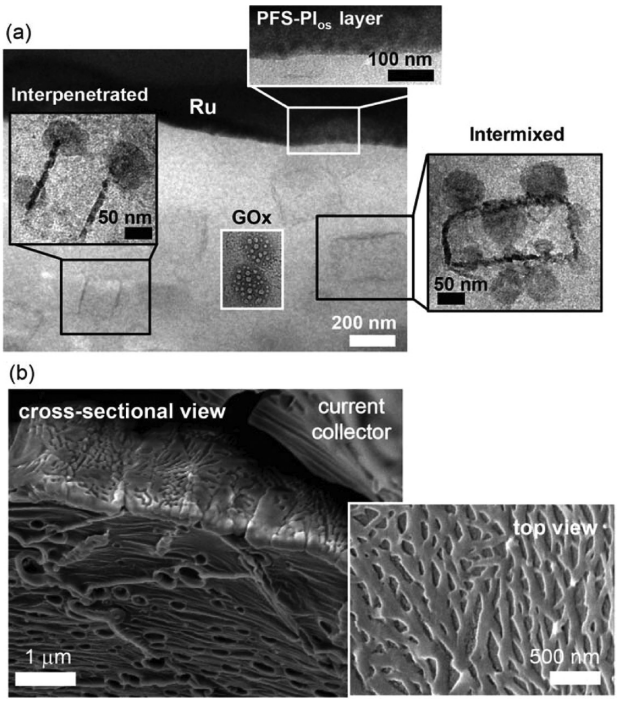


Figure 4. (a) FIB-TEM images of the GOx integrated PFS−PI_{OS} nanowire electrode and (b) SEM images of the GOx incorporated bicontinuous PFS−PI_{OS} electrode; cross-sectional view and top view.

of polyisoprene were significantly reduced, as a result of Os staining. The reaction yield was ∼70% at ca. 200 nm thick PFS−PI film. By examining the low wavenumber region, we found the appearance of new peaks at 993 and 645 cm^{-1}, owing to the development of C−O and Os−O bonds, respectively.[37] The absence of Os═O peaks signals that most OsO_4 takes part in cross-linking reaction, which is in good agreement with the results in ref 38. Upon exposing the PFS−PI_{OS} to various experimental conditions, the IR data given in Figure 3b indicate no detectable degradation of the PFS−PI_{OS} electrodes in both PBS buffer solutions (our experimental condition) and 10 wt % H_2O_2 containing PBS buffer solutions (severe condition). Note that all IR measurements were carried out under N_2-filled conditions, and the low wavenumber regions of Figures 3a,b are intentionally magnified to clarify the ester peaks.

The structural analysis of the fabricated electrodes is elucidated by combining focused ion beam technique (FIB), TEM, and SEM. Figure 4a presents the FIB-TEM images of the GOx integrated PFS−PI_{OS} nanowire electrode. To minimize the sample damage during milling process, Ru is deposited on the surface of the electrode. As clearly seen from Figure 4a, the electrode comprises layers of PFS−PI_{OS} mediators and GOx with some intermixing and interpenetration of these materials. The thickness of PFS−PI_{OS} layer at the top surface of the electrode is ∼100 nm. The cross-sectional view of nanowires with 20 nm diameter is shown in the upper right inset image. The intermixed/interpenetrated layers are also revealed, as shown in the inset boxes, where the GOx is detected as 40−80 nm sized aggregates. It should be noted here that the GOx was extremely unstable under the electron beam even in the presence of cold stage (−160 °C). Typical example of GOx degradation is shown inside the inset box with different contrast, as indicated in the Figure 4a.

The structure of GOx integrated bicontinuous PFS−PI_{OS} electrode was investigated by SEM experiments. As shown in Figure 4b, the top view of the fabricated electrode is well agreed with the TEM image seen in Figure 1b. Upon examining the cross-sectional structure of the electrode, it is found that the electrode is porous that glucose has access to the enzymes, yet it provides a protective cage for immobilizing the GOx without affecting biological function. Note that the current collector is intentionally delaminated with an aid of liquid nitrogen to examine the topology of bottom side of the electrode. As can be seen from Figure 4b, the bicontinuous morphology was again revealed, which leads us to conclude that PFS−PI_{OS} mediators exist at both air surface and the substrate.

Morphology-Sensitive Redox Properties of the GOx Integrated PFS−PI_{OS} Electrodes. To demonstrate the efficiency of GOx wiring onto the electrode, assisted by the networks of PFS−PI_{OS} mediators, we first carried out cyclic voltammetry (CV) measurements of the fabricated electrode. The concentration of the Fc moiety was fixed as 2 mM and a low scan rate of 20 mV was used. As shown in Figure 5a, in the absence of GOx, well-defined current responses upon electrochemical cycling of the Fc moieties are detected at 420 and 550 mV. Note that the standard reduction potential of Fc^+ (versus SHE) is known as E° = 400 mV. When GOx is incorporated into PFS−PI_{OS} nanowires, however, distinctly difference redox responses are seen. New anodic and cathodic waves at 390 and −80 mV were detected. The shift of oxidation peak from 550 to 390 mV reflects the change in solvation of the Fc moieties due to the polar environment provided by GOx.[39] The disappearance of Fc reduction peak at 420 mV implies that Fc^+ is clearly used up in the catalytic regeneration of GO(FAD):

$$GO(FADH_2) + 2Fc^+ \rightarrow GO(FAD) + 2Fc^\circ + 2H^+ \quad (1)$$

where Fc regenerated in the catalytic cycle is again oxidized to Fc^+ at the anode. In the absence of glucose, the NaH_2PO_4 in PBS buffer solution presumably acts as proton donor, as described in the literature.[40,41] Such characteristic change in electrochemical response of the electrode indicates that catalytically active GOx has

dx.doi.org/10.1021/ma300155u | Macromolecules 2012, 45, 3121−3128

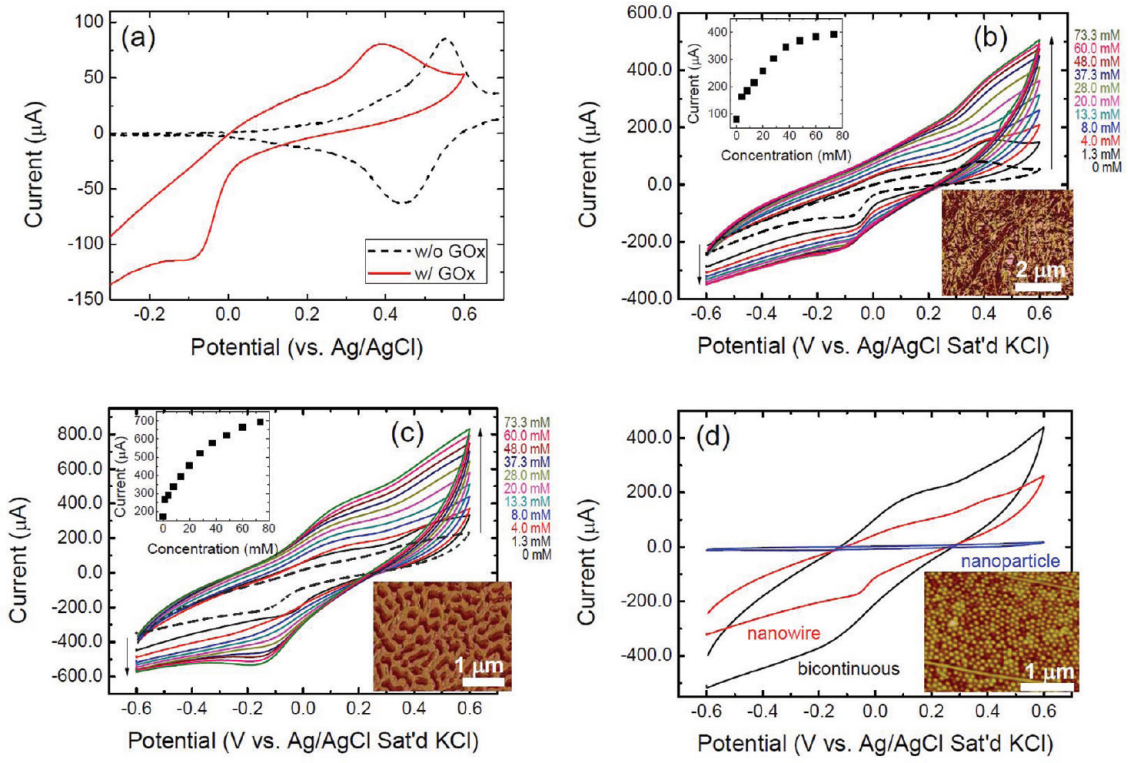
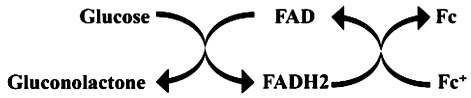


Figure 5. (a) CVs of electrodes with PFS−PI_{OS} nanowires in the absence/presence of GOx. CVs of electrodes with (b) GOx/PFS−PI_{OS} nanowires and (c) GOx/bicontinuous PFS−PI_{OS} as a function of glucose concentration. The inset plots in (b) and (c) show the current values at anodic peaks. (d) CVs of the electrodes with various PFS−PI_{OS} morphologies at 8 mM glucose. The inset AFM images show the surface topology of the electrodes. A scan rate of 20 mV/s is used.

been successfully embedded into the network of PFS−PI_{OS}, yielding the effective communication with Fc sites.

To explore the morphology effects on catalytic responses of the electrodes, CVs of electrodes with different morphologies were recorded as a function of glucose concentration. As given in eq2, FAD is reduced to FADH2 by glucose and Fc^+ is reduced to Fc° in the catalytic regeneration of GO(FAD).



(2)

When the PFS−PI_{OS} nanowire is utilized, as shown in Figure 5b, even with 1.3 mM of glucose, 40% increment in peak currents is seen, reflecting Fc-mediated catalysis of glucose. With the increase in the amount of glucose, catalytic currents gradually increase until the values level off at 60 mM of glucose. In the inset figure of Figure 5b, we plot the anodic current at 390 mV as a function of glucose concentration. The inset AFM image shows the surface topology of the fabricated electrode.

What is surprising is that the redox process of the electrodes appears to be dependent on the morphology of PFS−PI_{OS} copolymers. When the morphology of PFS−PI_{OS} is switched to bicontinuous structure, as shown in Figure 5c, analogous redox waves to the case of nanowire are seen. However, almost 2 times increase in the peak current is detected at the same level of glucose concentration, and the current at 390 mV reaches to high and stable value of 700 $\mu A/cm^2$ at 70 mM glucose, as shown in the inset plot of Figure 5c. The inset AFM image shows the surface topology of the electrode. It should be noted here that the electrodes were very stable regardless of morphologies of PFS−PI_{OS} mediators so that less than 2% of the peak current was lost over 75 consecutive redox cycles. This implies that no considerable leaching of GOx occurs from the fabricated anodes.

Interestingly, when the morphology effect was further exploited by employing nanoparticle-forming PFS−PI_{OS}, fairly negligible redox activity is seen, signaling insufficient communication between Fc moieties and GOx due to the isolated spherical PFS domains. On the basis of the insignificant catalytic responses of PFS−PI_{OS} nanoparticles, we can infer that the Os moieties in PI chains do not play a role in electron mediation due to the loosely packed characteristics. Figure 5d summaries the morphology effects on the current density of GOx/PFS−PI_{OS} electrodes. We plotted only one representative set of CV data at glucose concentration of 8 mM. Among nanowire, nanoparticle, and bicontinuous morphology, the GOx confined by bicontinuous PFS exhibits the best activity for the catalytic reactions. This was also demonstrated from the lower potential (−150 mV) for the regeneration of FAD with bicontinuous PFS−PI_{OS} than the value (−80 mV) of PFS−PI_{OS} nanowire.

In Figure 6, we provided schematic diagram summarizing Fc-mediated catalysis of glucose. The morphology of PFS−PI electron mediators (drawn as a green layer in the scheme) was varied as bicontinuous, nanowire, and nanoparticle, as confirmed by AFM experiments on the electrodes in tapping mode. Typical examples of AFM images representing the surface topology of fabricated electrodes are given in Figure 6. It has been revealed that the morphology of PFS−PI electron mediators is an important parameter in determining the charge transfer rate of GOx-wired electrodes.

It is worthwhile to compare the catalytic properties of GOx integrated nanostructured PFS−PI_{OS} polymers with those of

dx.doi.org/10.1021/ma300155u | *Macromolecules* 2012, 45, 3121−3128

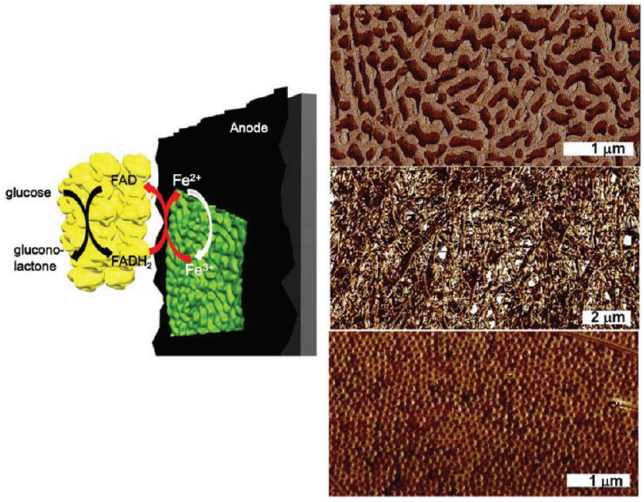


Figure 6. Schematic diagram illustrating Fc-mediated catalysis of glucose and AFM results of electrodes in tapping mode representing nanostructures of PFS−PI electron mediators (drawn as a green layer in the scheme).

GOx-wired other redox polymers reported widely in the literature. In Table 1, we listed anodic current densities of other systems by focusing on Os- and Fc-based redox polymers. All polymers in the literature possess the redox active sites in pendant groups, and self-assembled morphologies were not identified. As seen from the table, the anode comprising bicontinuous PFS−PI_{OS} indicates considerably improved current densities despite rather small amounts of GOx in the electrode. This could be intimately related to the enhanced charge transport rate in the nanostructured PFS−PI_{OS}.

Table 1. Anodic Current Densities of GOx Integrated Redox Polymers Reported in the Literature and Observed in Present Study

redox polymer[a]	GOx activity (U)	GOx amounts applied (mg)	glucose concn (mM)	pH	max current density	ref
Os	*b*	*b*	15	5	360 $\mu A/cm^2$	42
Os	150	4	15	7	200 $\mu A/cm^2$	43
Os	*b*	*b*	15	7	11 $\mu A/mm^2$	44
Fc	150	150	100	7	3000 $\mu A/cm^2$	45
Fc/CNT	150	*b*	40	5	40 μA[c]	46
Fc	200	2	60	7	664 $\mu A/cm^2$ [d]	present study
			15		455 $\mu A/cm^2$ [d]	

[a]Only redox active moieties are marked. [b]The information is unknown in the literature. [c]Area of the electrode is unknown. [d]Current densities were obtained with bicontinuous PFS−PI_{OS}.

DISCUSSION

Then, what would be the origin of the higher current values with bicontinuous PFS−PI_{OS} than those with other morphologies? The conductivities of PFS−PI_{OS} films with different morphologies were measured at 25 °C in PBS buffer solution to elucidate the morphology effects, which should be a key ingredient in modeling how electron transfer reactions couple to GOx and substrate. Interestingly, the conductivities of activated PFS−PI_{OS} films diverge as 1.34×10^{-5} (bicontinuous) and 4.03×10^{-6} S/cm (nanowire). Consequently, the enhanced catalytic response of GOx integrated bicontinuous PFS−PI_{OS} electrode can be rationalized by the better connectivity of the bicontinuous structure as well as larger contact area between PFS domains and entrapped GOx. From the data obtained so far, there is no doubt about the role of morphologies of the redox copolymers on determining the electron-mediating ability of functional electrodes. Our results are intriguing since while a number of publications described the successful use of Fc-based redox polymers,[28−31] none of them demonstrated that the electrode properties are strongly affected by self-assembled nanostructures of the redox polymers.

We hope to conclude our paper by exploring the biosensing ability of the electrodes. The biocatalytic activity of the electrodes was evaluated upon the injection of glucose with different concentrations. Because the physiological concentration of glucose in blood is between 5 and 10 mM, it is essential to obtain sufficient electrical signal at low amount of glucose. The electrode prepared with the bicontinuous PFS−PI_{OS} was tested and the significantly decreased amount of GOx (0.2 mg) was employed to evaluate the sensitivity of the fabricated electrodes. The current responses at anodic wave around 400 mV vs Ag/AgCl were recorded with time. As shown in Figure 7, the addition of glucose to the physiological

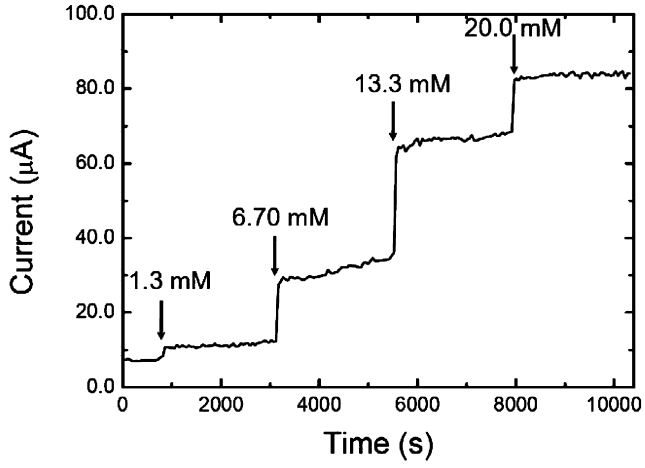


Figure 7. Current responses of a glucose sensor composed of GOx and bicontinuous PFS−PI_{OS} with the injection of glucose; the arrows indicate the injections of glucose.

environments causes a step changes in the observed current with a final steady state value proportional to the concentration of glucose, as a result of continuous electron transfer from the enzyme to the Fc units. In particular, even with fairly small amount of glucose, 1.3 mM, a rapid and obvious current response was revealed by a discontinuous increase in peak current from 7 to 11 μA. Approximately 35 min of equilibrium is allowed at each glucose concentration and the electrode exhibited excellent stability.

The strategy demonstrated here is believed to be generally applicable for the development of other kinds of enzymatic

dx.doi.org/10.1021/ma300155u | *Macromolecules* 2012, 45, 3121−3128

biofuel cells and could prove to be a new and facile route to nanostructured enzymatic biofuel cells. In particular, efficient electron transfer between enzymes and redox polymers as a result of structural optimization will open the way to design sensors for other biomass such as alcohol and amino acids. The investigation on the power density of biofuel cell by combining cathode enzyme is currently under way.

CONCLUSIONS

The catalytic activities of functional electrodes comprising glucose oxidase and cross-linkable, nanostructured ferrocene-containing organometallic block copolymers were investigated. Unlike non-microphase-separated redox polymers, the use of nanostructured PFS−PI block copolymers allow us to control electron transfer rate. The improved stability of the enzyme integrated electrode by osmium decoration is found out where dienes in PI chains are selectively cross-linked. We have demonstrated that morphologies of organometallic polymers play a key role in determining the electrochemical properties of enzyme integrated electrodes. In other words, the different morphologies of the same organometallic polymer yield significant discrepancy in current densities of the fabricated electrodes at the same glucose concentration. The utilization of bicontinuous structure forming PFS-*b*-PI_{OS} reveals remarkable enhancement in catalytic currents and good glucose sensitivities at low glucose concentrations. These results were rationalized by better connectivity in bicontinuous structure than other morphologies as well as large contact area of PFS domains with glucose oxidase. Our results are the first experimental evidence on the adjustable catalytic current densities of enzyme-wired organometallic polymer electrodes with the successive tuning of their morphologies.

AUTHOR INFORMATION

Corresponding Author

*E-mail: moonpark@postech.edu.

Notes

The authors declare no competing financial interest.

ACKNOWLEDGMENTS

This research was supported by Basic Science Research Program (Project No. 2011-0004375) and Midcareer Researcher Program (Project No. 2011-0015343) through the National Research Foundation of Korea (NRF) funded by the Ministry of Education, Science and Technology. We also acknowledge WCU (World Class University) program through the Korea Science and Engineering Foundation funded by the Ministry of Education, Science and Technology (Project No. R31-10059). XRD measurements were conducted on the beamline 1W1A under the approval of the Beijing Synchrotron Radiation Facility and the support of PAL through the abroad beamtime program of Synchrotron Radiation Facility Project under MEST. We gratefully acknowledge Prof. Andrew M. Minor for providing access to the TEM instrument of the National Center for Electron Microscopy, Lawrence Berkeley Lab, which is supported by the U.S. Department of Energy under Contract DE-AC02-05CH11231. Prof. M. J. Park acknowledges a Chong-Am Science Fellowship.

REFERENCES

(1) Willner, I. *Science* **2002**, *298*, 2407.
(2) Barton, S. C.; Gallaway, J.; Atanassov, P. *Chem. Rev.* **2004**, *104*, 4867.
(3) Hansen, B. J.; Liu, Y.; Yang, R.; Wang, Z. L. *ACS Nano* **2010**, *4* (7), 3647.
(4) Chen, T.; Barton, S. C.; Binyamin, G.; Gao, Z.; Zhang, Y.; Kim, H. H.; Heller. *J. Am. Chem. Soc.* **2001**, *123*, 8630.
(5) Moore, C. M.; Minteer, S. D.; Martin, R. S. *Lab Chip* **2005**, *5* (2), 218.
(6) Heller, A. *Phys. Chem. Chem. Phys.* **2004**, *6* (2), 209.
(7) Mano, N.; Soukharev, V.; Heller, A. *J. Phys. Chem. B* **2006**, *110* (23), 11180.
(8) Blanford, C. F.; Heath, R. S.; Armstrong, F. A. *Chem. Commun.* **2007**, *17*, 1710.
(9) Deng, L.; Wang, F.; Chen, H.; Shang, L.; Wang, L.; Wang, T.; Dong, S. *Biosens. Bioelectron.* **2008**, *24*, 329.
(10) Yan, Y.; Zheng, W.; Su, L.; Mao, L. *Adv. Mater.* **2006**, *18* (19), 2639.
(11) Zeng, G.; Xing, Y.; Gao, J.; Wang, Z.; Zhang, X. *Langmuir* **2010**, *26* (18), 15022.
(12) Miyake, T.; Yoshino, S.; Yamada, T.; Hata, K.; Nishizawa, M. *J. Am. Chem. Soc.* **2011**, *133* (13), 5129.
(13) Gallaway, J. W.; Barton, S. C. *J. Am. Chem. Soc.* **2008**, *130* (26), 8527.
(14) Scodeller, P.; Carballo, R.; Szamocki, R.; Levin, L.; Forchiassin, F.; Calvo, E. J. *J. Am. Chem. Soc.* **2010**, *132* (32), 11132/.
(15) Mao, F.; Mano, N.; Heller, A. *J. Am. Chem. Soc.* **2003**, *125*, 4951.
(16) Zayats, M.; Katz, E.; Willner, I. *J. Am. Chem. Soc.* **2002**, *124* (10), 2120.
(17) Scodeller, P.; Flexer, V.; Szamocki, R.; Calvo, E. J.; Tognalli, N.; Troiani, H.; Fainstein. *J. Am. Chem. Soc.* **2008**, *130* (38), 12690.
(18) Yehezkeli, O.; Tel-Vered, R.; Raichlin, S.; Willner, I. *ACS Nano* **2011**, *5* (3), 2385.
(19) Carturan, G.; Toso, R. D.; Boninsegna, S.; Monte, R. D. *J. Mater. Chem.* **2004**, *14*, 2087.
(20) Lim, J.; Malati, P.; Bonet, F.; Dunn, B. *J. Electrochem. Soc.* **2007**, *154*, A140.
(21) Gao, F.; Viry, L.; Maugey, M.; Poulin, P.; Mano, N. *Nat. Commun.* **2010**, *1*, 2.
(22) Yan, Y.; Zheng, W.; Zhang, M.; Wang, L.; Su, L.; Mao, L. *Langmuir* **2005**, *21*, 6560.
(23) Girishkumar, G.; Vinodgopal, K.; Kamat, P. V. *J. Phys. Chem. B* **2004**, *108*, 19960.
(24) Ning, J. W.; Zhang, J. J.; Pan, Y. B.; Guo, J. K. *J. Mater. Sci. Lett.* **2003**, *22*, 1019.
(25) Lyons, M. E. G.; Keeley, G. P. *Chem. Commun.* **2008**, *22*, 2529.
(26) Gallaway, J.; Wheeldon, I.; Rincon, R.; Atanassov, P.; Banta, S.; Barton, S. C. *Biosens. Bioelectron.* **2008**, *23*, 1229.
(27) Hirsch, A. *Angew. Chem., Int. Ed.* **2002**, *41*, 1853.
(28) Abd-EI-Aziz, A. S.; Manners, I. *Frontiers in Transition Metal-Containing Polymers*; John Wiley & Sons, Inc.: Hoboken, NJ, 2007.
(29) Wang, J. *Chem. Rev.* **2008**, *108* (2), 814.
(30) Ammam, M.; Fransaer, J. *Biosens. Bioelectron.* **2010**, *25*, 1474.
(31) Barton, S. C.; Kim, H. H.; Binyamin, G.; Zhang, Y. C.; Heller, A. *J. Phys. Chem. B* **2001**, *105*, 11917.
(32) Wang, X.; Liu, K.; Arsenault, A. C.; Rider, D. A.; Ozin, G. A.; Winnik, M. A.; Manners, I. *J. Am. Chem. Soc.* **2007**, *129* (17), 5630.
(33) Ni, Y. Z.; Rulkens, R.; Manners, I. *J. Am. Chem. Soc.* **1996**, *118* (17), 4102.
(34) Gallardo, B. S.; Gupta, V. K.; Eagerton, F. D.; Jong, L. I.; Craig, V. S.; Shah, R. R.; Abbott, N. L. *Science* **1999**, *283*, 57.
(35) Rulkens, R.; Lough, A. J.; Manners, I. *J. Am. Chem. Soc.* **1994**, *116*, 797.
(36) Muthukumar, M.; Ober, C. K.; Thomas, E. L. *Science* **1997**, *277*, 1225.
(37) Brumley, W. C.; Hinkcley, C. C. *J. Inorg. Nucl. Chem* **1980**, *42*, 1277−1284.
(38) Ribbe, A. E.; Bodycomb, J.; Hashimoto, T. *Macromolecules* **1999**, *32* (9), 3154−3156.
(39) Ju, H.; Leech, D. *Phys. Chem. Chem. Phys.* **1999**, *1* (7), 1549.
(40) Ma, M.; Bong, D. *Langmuir* **2011**, *27*, 8841−8853.

(41) Alvarez-Pez, J. M.; Ballesteros, L.; Talavera, E.; Yguerabide, J. *J. Phys. Chem. A* **2001**, *105*, 6320−6332.
(42) Mano, N.; Mao, F.; Shin, W.; Chena, T.; Heller, A. *Chem. Commun.* **2003**, 518.
(43) Kim, H. H.; Mano, N.; Zhang, X. C.; Heller, A. *J. Electrochem. Soc.* **2003**, *150*, A209.
(44) Mano, N.; Mao, F.; Heller, A. *J. Am. Chem. Soc.* **2002**, *124*, 12962.
(45) Tamaki, T.; Yamaguchi, T. *Ind. Eng. Chem. Res.* **2006**, *45*, 3050.
(46) Tan, Y. M.; Xie, Q. J.; Huang, J. H.; Duan, W. S.; Ma, M.; Yao, S. Z. *Electroanalysis* **2008**, *20*, 1599.

Macromolecules

Article

pubs.acs.org/Macromolecules

Stress–Structure Correlation in PS–PMMA Mixed Polymer Brushes

Jannis W. Ochsmann,[†,‡] Sebastian Lenz,[†] Philipp Lellig,[†,‡] Sebastian G.J. Emmerling,[†] Ali A. Golriz,[†,‡] Peter Reichert,[†] Jichun You,[†] Jan Perlich,[§] Stephan V. Roth,[§] Rüdiger Berger,[†] and Jochen S. Gutmann*[,†,‡,⊥]

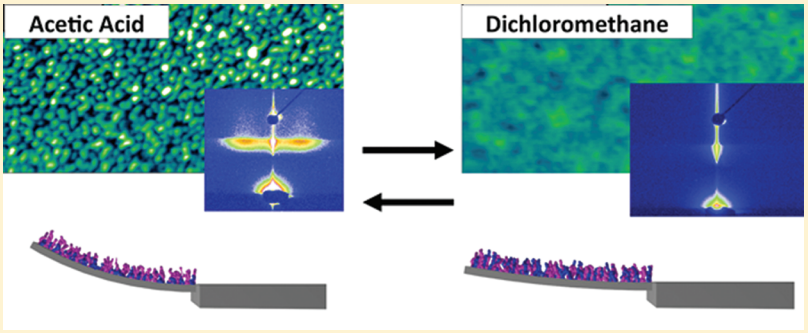
[†]Max Planck Institute for Polymer Research, Experimental physics of interfaces, Ackermannweg 10, D-55128 Mainz, Germany

[‡]Department of Chemistry and Center for Nanointegration Duisburg-Essen (CeNIDE), University Duisburg-Essen, Universitätsstr. 5, D-45117 Essen, Germany

[§]HASYLAB at DESY, Notkestr. 85, D-22603 Hamburg, Germany

[⊥]Deutsches Textilforschungszentrum Nord-West e.V., Adlerstr. 1, D-47798 Krefeld, Germany

Supporting Information



ABSTRACT: The ability to alter surface properties such as morphology and surface energy upon external stimuli makes switchable polymer surfaces a promising field of research. Mixed polymer brushes consisting of two different homopolymers covalently attached to a surface are one system in which surface properties can be switched. In this work the correlation between the change in structure and the resulting surface stress in thin poly(methyl methacrylate)–polystyrene mixed polymer brush film upon exposure to selective solvents is investigated. By measuring the forces acting inside the film, we are able to achieve a deeper understanding of the observed structural changes. To obtain a thorough understanding of the film's morphology, the structure is analyzed by scanning probe microscopy, X-ray reflectivity, and grazing incidence small-angle X-ray scattering (GISAXS). Upon exposure to acetic acid, a selective solvent for PMMA, the film showed a dimple-like structure. This is linked to collapsed domains of polystyrene covered by PMMA chains. Bending experiments resulted in tensile stress, pointing to attractive forces acting inside the polymer film. After exposure to dichloromethane, a good solvent for both polymers, bending experiments revealed a decreased but still high tensile stress, indicating that the microdomains are still present. The results of the experiments enable us to further explain the domain memory effect typically found in these kinds of mixed polymer brush systems.

INTRODUCTION

Switchable polymer surfaces are a promising field of research.[1] The ability to switch surface characteristic such as morphology and surface energy upon external stimuli make them an interesting research topic. In addition, the possibility to move nano-objects on top of a surface by reversible switching of the polymer surface is a subject of current research.[2] Mixed polymer brushes consisting of two different homopolymers covantly attached to a surface are one candidate for these types of polymer surfaces.[3−9] Extensive theoretical research has been done in the past couple of years.[10] Studying the film morphology in relation to the polymer incompatibilities,[11] solvent selectivity,[12] composition,[11] and chain length asymmetry.[13] Fluctuations in local grafting-point positions and its correlations have been investigated. With the help of "single-chain-in-mean-field" simulations it was shown that small fluctuations in grafting point positions influence domain locations and prevent long-range order.[14,15] Although these simulations resemble the experimental findings,[16] the applied mean-field approach neglects chain conformation. Microphase separation of chemical bond polymer chain requires a large amount of stretching of indivual chains. These conformational restrains and the resulting stress inside the polymer film are not accounted for in the mean-field approach.

The stress inside the polymer film is transduced into the substrate. To measure such forces, nanomechanical cantilever sensors (NCS) have become a valuable tool in recent years.[17−21,22] By this means surface stress changes due to

Received: November 18, 2011
Revised: February 11, 2012
Published: March 20, 2012

 © 2012 American Chemical Society

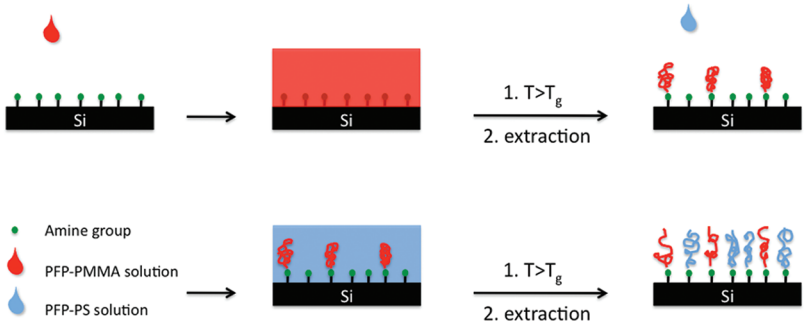


Figure 1. Schematic diagram of the steps necessary for the preparation of PS−PMMA mixed polymer brushes on the amine-functionalized silica surface. First a thin film of PFP−PMMA is applied to an amine-functionalized surface. By heating the film above the glass transition temperature of PMMA, the active ester function at the end of the polymer react with the amine groups. The PMMA is therefore covalently bound to the surface. After extraction of excess polymer, a thin film of PFP−PS is applied to the same surface. By heating the system above the glass transition temperature of the PS, the polystyrene reacts with the vacant amine groups.

polymer brush swelling,[23−26] polyelectrolyte adsorption,[27] and stress upon thermal treatment[18−20,28] could be measured at extremely high resolution.

Mixed polymer brushes can be obtained by the "grafting-from" as well as "grafting-to" technique. The "grafting-from" approach usually involves the preparation of a layer containing two different kinds of initiators (e.g., ATRP-, NMRP-initiator).[7] By this means mixed polymer brushes with high grafting densities may be obtained. In the "grafting-to" approach the two homopolymers are attached to the same surface subsequently. Stamm et al. utilized a reaction in melt to graft acid-functionalized polymers to an epoxide-functionalized surface. Variation of the temperature and duration of the "grafting-to" reaction allowed Stamm et al. to alter the composition of the mixed polymer brushes.[3,29−31]

Both "grafting-from" and "grafting-to" mixed polymer brushes could be switched between different morphologies by exposing them either to selective solvents for one of the polymers, good solvents for both polymers, or thermal annealing.[4,8]

In recent years a domain memory effect has been experimentally observed in mixed polymer brush films. Santer et al. introduced a quantified measurement for domains forming at the same position, size, and shape upon cyclical change.[16,32,33] The effects of chemical structure and fluctuations of the grafting points have been investigated. The authors attribute the domain memory effect to small fluctuation on grafting points, nucleating the domains in the mixed brush. While this explains the static structure formation, the reason for the domain stability over time remains unsolved.

In this paper we use an amine-functionalized silica surface, active ester-functionalized polystyrene, and poly(methyl methacrylate) to obtain PS−PMMA mixed polymer brushes. We investigate the switching behavior of the mixed polymer brushes after they have been immersed in a good solvent for both polymers (dichloromethane) and a selective solvent for only the PMMA (acidic acid). The change in structure between the two equilibrium states is investigated by X-ray reflectivity (XRR), scanning probe microscopy (SPM), contact angle measurement, and μ-focused grazing incidence small-angle X-ray scattering (μ-GISAXS). Using these methods enables us to obtain a comprehensive picture about the change in polymer confirmation before and after switching. Via bending experiments on NCS coated with the PS−PMMA mixed brushes, the change in surface stress was measured. With the help of a phase shifting interferometer[36] (PSI) the 3d topography of the NCS is determined. This allows us to obtain the bending profile of each individual cantilever, enabling us to calculate the absolute values of surface stress acting inside the film. Measuring these forces gives a deeper understanding of the network inside the polymer brush and the surface memory effect.

MATERIALS AND METHODS

Polymer Synthesis. *Active Ester-Functionalized Chain Transfer Agent.* Pentafluorophenyl-(4-phenylthiocarbonylthio-4-cyanovalerate) was synthesized according to a literature procedure.[34] The required di(thiobenzoyl) disulfide was synthesizes according to a different route because no red solid could be obtained after the reaction of dithiobenzoic acid with iodine. The di(thiobenzoyl) disulfide was therefore obtained by dissolving dithiobenzoic acid (5 g, 0.032 mol) and sodium hydroxid (1.28 g, 0,032 mol) in 100 mL of deionized water. Potassium ferricyanide(III) (10.67 g, 0.032 mol) dissolved in 50 mL of deionized water was added dropwise and stirred for several minutes. The violet precipitate was filtered and washed. The product was recrystallized from ethanol.[35]

Pentafluorophenol−Poly(methyl methacrylate) (PFP−PMMA). The polymer was synthesized as described here.[34] The reaction yielded 2.8 g (69%) of pink polymer with a molecular weight M_n(GPC) = 16 196 g/mol with a PDI (GPC) = 1.08.

Pentafluorophenol−Polystyrene (PFP−PS). 5.63 mL (48.8 mmol) of freshly distilled styrene, 11.1 mg of AIBN, 3 mL of toluene, and 120.8 mg of pentafluorophenyl (4-phenylthiocarbonylthio-4-cyanovalerate) were added to a Schlenk tube under an argon atmosphere. The mixture was degassed by three freeze−pump−thaw cycles. The polymerization was carried out at 110 °C for 4 days. The polymer was precipitated three times in methanol from THF. The reaction yielded 2.2 g (40%) of pink polymer with a molecular weight M_n(GPC) = 13 477 g/mol with a PDI (GPC) = 1.15. Altering the experimental conditions did not result in higher molecular weight polymer with reduced PDIs.

Nanomechanical Cantilever Arrays (NCS) and Silicon Wafers. NCS arrays (Octosensis) were purchased from Micromotive Mikrotechnik, Germany. Each array consisted of eight individual cantilevers with an area of 750 × 90 μm^2, a thickness of 2 μm, and a pitch of 250 μm.

Silicon wafers were obtained from Si-Mat Silicon Materials, Germany. The polished silicium wafers with an (100) orientation were cut into 2.5 × 2.5 cm^2 large substrates for sample preparation.

Wafer Preparation. The schematic diagram of the preparation route can be found in Figure 1. Silicon wafer substrates were put in dichloromethane and placed in an ultrasonic bath for 15 min and dried in a stream of nitrogen. The wafers were immersed in a solution of ammonia, hydrogen peroxide, and distilled water (1:1:5) and heated to

dx.doi.org/10.1021/ma2025286 | Macromolecules 2012, 45, 3129−3136

70 °C for 20 min. The wafer were then rinsed with distilled water and dried in a stream of nitrogen.

The cleaned wafers were put into a Schlenk tube filled with argon gas. Two drops of (3-aminopropyl)dimethylethoxysilane (APDES) were added, and the Schlenk tube was evacuated for ∼1 s. The Schlenk tube was placed into a vacuum oven at 120 °C for 14 h. Subsequently, the wafers were extracted with dichloromethane in a Soxhlet extractor for at least 5 h.

A 2 wt % toluene solution of PFP−PMMA was spin-coated on to the before prepared wafer for 30 s at 1000 rpm. Afterward, the film was heated to 120 °C for 90 min. The wafers were cooled down to room temperature and extracted with dichloromethane for at least 5 h.

A 2 wt % toluene solution of PFP−PS was spin-coated on to the PMMA film for 30 s at 1000 rpm. The film was afterward heated to 120 °C for 12 h. The wafers were cooled down to room temperature and extracted with dichloromethane for at least 5 h.

Cantilever Preparation. The cantilever arrays were immersed into a solution of ammonia, hydrogen peroxide, and distilled water (1:1:5) and heated to 70 °C for 20 min. Afterward, the NCS were rinsed with distilled water and carefully dried in a stream of nitrogen. To ensure one-sided coatings of the cantilever, the backside of the NCS was passivated by evaporation of a 30 nm layer of gold via thermal evaporation (0.1 nm/s, $p \approx 2 \times 10^{-5}$ mbar) (BALTEC MED 020, BALTEC, Balzers, Lichtenstein). The NCS were put into an argon gas filled Schlenk tube. Two drops of (3-aminopropyl)-dimethylethoxysilane were added, and the Schlenk tube was then evacuated for ∼1 s. The tube was placed into a vacuum oven and heated to 120 °C for 14 h. The NCS were cooled to room temperature and extracted in dichloromethane for at least 5 h.

A 2 wt % toluene solution of PFP−PMMA were selectively applied to a single cantilever. The solution was deposited using a piezo-controlled nanoliter pipet using a Nano-Plotter NP 2.0 device (GeSim mbH, Germany). The cantilevers were printed by the array dispense procedure (ADP), dispensing a column of 15 drops 150 μm apart from each other. Using the program SpotFrontEnd, the cantilevers were aligned properly and a high reproducibility was obtained.

Usually four cantilevers were functionalized using this printing technique. Next the NCS was heated to 120 °C for 90 min, cooled down to room temperature, and extracted in dichloromethane for at least 5 h. Afterward, a 2 wt % toluene solution of PFP−PS was printed onto two cantilevers previously coated with PFP−PMMA and two cantilevers with no previously deposited polymer. The cantilever array was subsequently heated to 120 °C for 12 h, cooled to room temperature, and extracted in dichloromethane for at least 5 h. By this means we obtained a cantilever array containing two cantilevers coated with mixed PS−PMMA brushes, two cantilevers coated with polystyrene and poly(methyl methacrylate) for comparison, and two cantilevers with no polymer brushes as reference (Figure 2). At the end immersion of the cantilever in a KI/I_2 solution and rinsing with Millipore water removed the protective gold layer.

Switching. For the selective solvent treatment, the wafers/cantilever were immersed into concentrated acetic acid and heated to 45 °C for 30 min. The sample was then quickly rinsed with distilled water several times and dried in a stream of nitrogen gas. The procedure was repeated three times. For the nonselective treatment the wafers/cantilever arrays were immersed in dichloromethane for at least 90 min at 45 °C and subsequently dried in a nitrogen stream. As reported in the literature,[13] switching of the morphology takes several minutes; also, separate tests using solvent vapors showed a fast brush response (see Supporting Information). Since the solvent concentration is even higher in liquids, the chosen experimental conditions should guarantee a complete switching of the brushes. Evaporation of the solvent on the other hand only takes several seconds due to the nanometer film thickness. The brush morphology is therefore frozen during the drying process. After sample preparation the sample are stored under ambient conditions. For both polymers this is well below its glass transition, preserving the film morphology over time.

Methods. *X-ray Reflectivity.* X-ray reflectivity (XRR) measurements on wafers were conducted on a XRD 3003 TT, Seifert Ltd. GB diffraction system. Monochromatic and collimated X-rays were obtained from a Cu anode with a wavelength of $\lambda = 0.154$ nm. The obtained curves were fitted using PARRATT32. The starting values for scattering length densities used in the fit as well as the densities obtained by the fitted scattering length densities were calculated using the scattering length density calculator provided by NIST.[37]

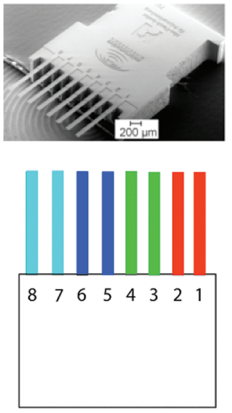


Figure 2. SEM Image of a nanomechanical cantilever sensor array (top) and schematic representation of the used cantilever design (bottom). Two cantilevers are coated with PMMA brushes, two with PMMA−PS mixed brushes, two with PS brushes, and two cantilevers with no polymers as references.

Scanning Probe Microscopy. Scanning probe microscopy images were obtained in tapping mode using an Dimension 3100 scanning probe microscope, Veeco Instruments GmbH. OMCL AC 160 TS (Olympus, Japan) cantilevers were used with a resonance frequency of ∼300 kHz and a spring constant of 42 N/m as specified by the manufacturer.

Contact Angle. Contact angle measurements were conducted on a Krüss, DSA10-MK2. The static contact angle was measured in air under ambient conditions using Milli-Q water.

μ-GISAXS. The μ-GISAXS measurements were conducted at the beamline BW4, HASYLAB at DESY, Hamburg, Germany. The beam had a wavelength of $\lambda = 0.138$ nm. The used beam had a size of 32 × 17 μm^2 (horizontal × vertical). The schematic representation of the used μ-GISAXS geometry can be found in Figure 3.

To obtain transverse q_{II} scans at the Yoneda maximum, the 2D images were cut vertically at the Yoneda maximum ($\alpha_f = \alpha_c$). The q_{II} scans were fitted with the unified fit model.[38] The model allows the analysis of q_{II} scans for lateral structural information on thin films containing weakly correlated and polydisperse structural components.[28,39,40] It uses structural levels, which allows the modeling of scattering from small ($d \approx 10$ nm) up to larger structures ($d \approx 350$ nm). The model allows size and structural determination with an error of less than 20%. Further details can be found here.[41]

Initially, the incident angle (α_i) was set to $\alpha_i = 0.4°$. This avoids the overlap of specular and off-specular scattering in the Yoneda peak regime, which is necessary for the previously described analysis.

NCS Bending Experiments. A home-built interferometric setup was used to determine the bending of each nanomechanical cantilever. The setup consists of a laser with a wavelength of $\lambda = 785$ nm. The recorded image had an area of 1.5 × 1.5 mm^2. All eight cantilevers and part of the supporting chip were simultaneously measured. Custom-made software allowed the simultaneous recording of different interferometric images and its analysis. To obtain curvature data from each individual cantilever, five images at different mirror positions were taken. From these images a 3D profile was calculated. For each cantilever four topography profiles were taken along its x-axis. These profiles were averaged to obtain a mean length/height profile of each cantilever. The averaged profile was then fitted with a parabolic function.[42]

$$z(x) = a_0 + a_1 x + \frac{\kappa}{2} x^2 \quad (1)$$

dx.doi.org/10.1021/ma2025286 | Macromolecules 2012, 45, 3129−3136

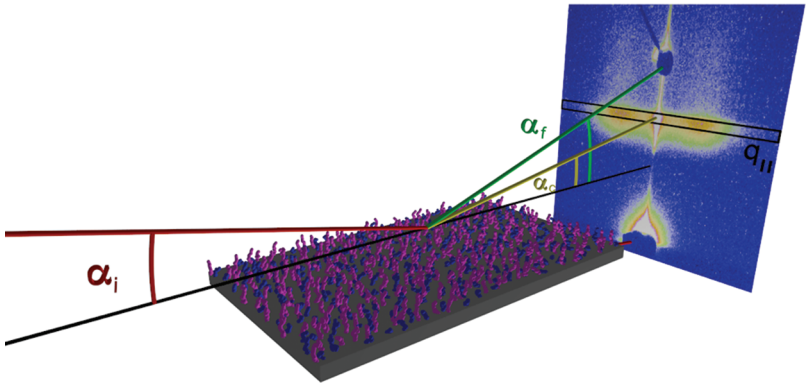


Figure 3. μ-GISAXS geometry.

Under the assumption that the cantilever is bend uniformly, we can calculate the absolute curvature κ

$$\kappa = \frac{d^2z(x)}{(dx^2)} \quad (2)$$

For a typical measurement 100 averaged profiles were recorded over time (0.33 measurements/s) and analyzed. The surface stress σ was calculated with Stoney's formula.[43]

$$\sigma = \frac{E_{Si}t_{NCS}^2}{6(1-\nu_{Si})}\kappa \quad (3)$$

For the calculations E_{Si} = 165 GPa, t_{NCS} = 2 μm, and a Poisson ratio of ν_{Si} = 0.28 were used.

RESULTS AND DISCUSSION

Film Preparation. To obtain mixed polymer brushes on top of the amine-functionalized silicium surface, a "grafting-to" approach was selected. The amine-functionalized surface was obtained by the self-assembling gas phase reaction of (3-aminopropyl)dimethylethoxysilane.

A thin film of PMMA carrying an active ester end group was deposited on top of the functionalized silicium surface. By heating the sample above the glass temperature (T_g) of the polymer, the active ester end groups increase their mobility and react with the amine end groups on the surface. After this solid-state reaction the polymer is covalently bound to the surface. By varying the temperature and time of heating partial saturation of the amine groups can be achieved. After extraction of the excess polymer, a thin PS film is deposited on the sample. Heating the sample above the T_g allows the active ester groups at the end of the polystyrene to react with the remaining free amine groups. In the end the excess polystyrene is again extracted.

The preparation of the mixed polymer brush film was followed by X-ray reflectivity (XRR) to verify the proposed mechanism. The obtained reflectivity curves are shown in Figure 4. The treatment of the freshly cleaned siliceous wafer with (3-aminopropyl)dimethylethoxysilane leads to the formation of a 0.8 nm thick film. This corresponds nicely to the formation of a monolayer of (3-aminopropyl)-dimethylethoxysilane covalently bond to the silica surface.

The analysis of the first prepared PMMA film yielded a 3.6 nm thick film with a relative low roughness of σ_{rms} = 0.3 nm. The following spin-coating of the polystyrene solution led to an increase in thickness. The resulting film yielded a thickness of 5.1 nm and an increase in roughness to σ_{rms} = 0.5 nm. These consecutive increase in film thickness supports the proposed mechanism of step-by-step "grafting-to" of polymer chains to the same functionalized surface. The SPM images (Figure 5 bottom) at the end of the assembling process also supports the formation of a continuous and smooth polymer film.

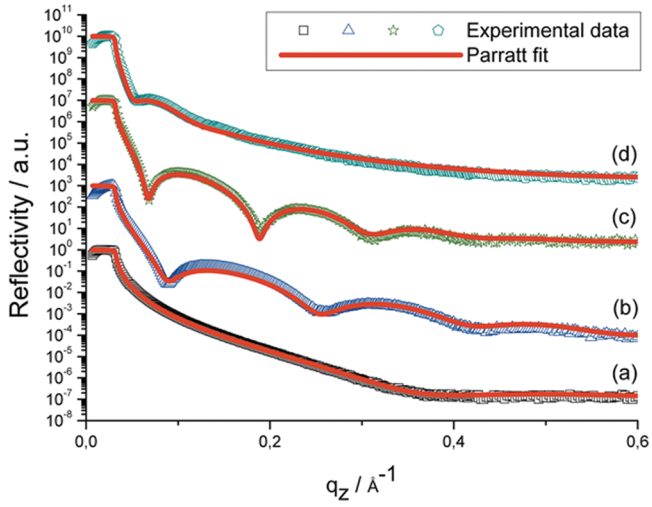


Figure 4. X-ray reflectivity curves of the monolayer of APDES (a), APDES/PMMA (b), and APDES/PMMA–PS after treatment with dichloromethane (c) and acetic acid (d). Hollow symbols represent the experimental data. Straight lines represent the Parratt fit. The curves are shifted along the vertical axis for improved visualization.

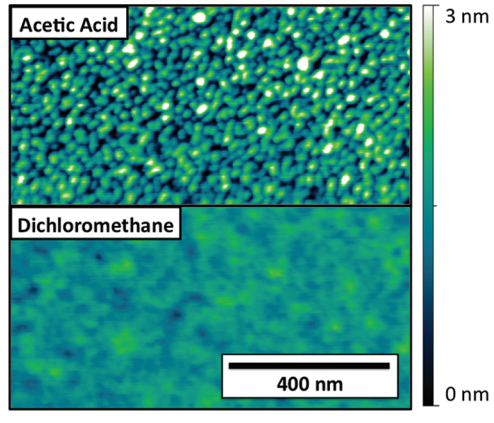


Figure 5. SPM topography images of the PMMA–PS mixed polymer brush film after acetic acid and dichloromethane treatment.

dx.doi.org/10.1021/ma2025286 | *Macromolecules* 2012, 45, 3129–3136

From the measured film thickness d and the molecular weight M_n of the unbound homopolymer measured by GPC the grafting density was calculated using the formula

$$\Gamma = \frac{d\rho}{M_n} N_A$$

The density ρ of the PMMA and the mixed PMMA−PS brushes was determined by the fit of the X-ray reflectivity. For the PMMA brush the value was 1.19 g/cm^{-3} equal to the literature[44] value of an unbound chain. For the PMMA−PS mixed brush case the value was 1.25 g/cm^{-3}, slightly above the literature values of PMMA and PS.[45] The resulting grafting densities are Γ_{PMMA} = 0.16 chains/nm^2 and $\Gamma_{PMMA-PS}$ = 0.26 chains/nm^2.

From the measured film thicknesses the brush composition can be estimated. If we neglect small differences in density, the composition of the mixed polymer brush can be calculated by dividing the film thickness of the PMMA film by the value of the PMMA−PS film. To account for the APDES layer, 0.8 nm is subtracted from both film thicknesses. The PMMA−PS brush films has a composition of ∼65% PMMA and ∼35% PS.

Switching. First the change in structure caused by the switching upon different solvent exposure of the PS−PMMA mixed brushes was examined. Therefore, mixed polymer samples were prepared on silicum wafers and investigated before and after exposition to acetic acid, a selective solvent for PS, and dichloromethane, a good solvent for PS and PMMA, respectively.

Figure 5 shows an SPM height image of the same dichloromethane and acidic acid treated film. The immersion of the polymer film in acetic acid leads to the formation of nanodomains, showing a dimple-like structure. This change in structure is accompanied by a large increase in roughness from σ_{rms} = 0.23 nm to σ_{rms} = 0.65 nm (1 × 1 μm^2). Multiple line cuts were performed to measure the distance between nanodomains. The analysis resulted in an average center-to-center distance of 27.5 ± 8.8 nm of the nanodomains.

The change in structure can also be seen by XRR (Figure 4). The fitted reflectivity curve also confirmed the increase in roughness by a factor of ∼3, which is also clearly visible by vanishing of all but one of the Kiessig fringes. The change in structure also leads to an increase in overall thickness from 5.1 to 6.7 nm.

To investigate the composition at the surface of the polymer film, contact angle measurements were performed on acidic acid as well as dichloromethane treated films. The dichloromethane treated film showed a contact angle of 76°. Treating the film with acetic acid led to a decrease in contact angle to 67°, when compared to the dichloromethane film. The decrease in water contact angle can be attributed to enrichment of the more hydrophilic PMMA at the film−air interface.

Grazing incidence small-angle X-ray scattering was performed to obtain a more averaged and quantified information on the films morphology. The incident angle was set to α = 0.4°, which is above the critical angle of both the polymer film and the silicon substrate. Therefore, structural information from the surface as well as beneath was obtained. The horizontal GISAXS data (Figure 6) obtained from the acetic acid treated film showed a large and broad interference peak. Fitting of the data resulted in domains with an R_g = 6.5 ± 1.3 nm and a center-to-center distance of 19.4 ± 3.9 nm. These results can be related to the domains observed from the SPM images.

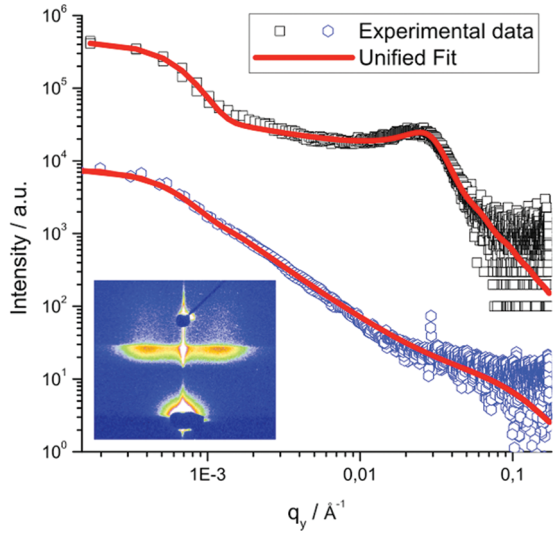


Figure 6. μ-GISAXS horizontal detector cuts of the PS−PMMA mixed polymer brush films after dichloromethane (bottom) and acidic acid (top) treatment. Hollow symbols represent the experimental data. Straight lines represent the unified fit. The upper curve is shifted along the vertical axis for improved visualization. Inset shows the 2D scattering image of the acetic acid treated film.

The morphology obtained after exposure to the selective solvent acetic acid is in good agreement with theoretical studies done by Müller et al.[15] Using self-chain in mean-field (SCMF), they predicted structures for different solvent qualities and brush compositions. In their calculations a dimple conformation is expected for mixed brushes exposed to a solvent, which is a good solvent for the polymer majority component in the film. As calculated by XRR the majority component of the prepared layer is PMMA (∼65%), which has a good solubility in acetic acid. Lateral microphase separation results in the formation of different domains, mainly depending on the brush composition. Highly asymtretric brushes form dimple-like structures. The effect is amplified by the acetic acid, which causes the polystyrene to collapse and migrate to the substrate. After the collapse the dimples are covered by PMMA. From the center-to-center distance and the extracted radius of gyration and average number of chain per domain can be estimated. As visible from the wide peak in the GISAXS scan, the domains have a broad size distribution. A single domain consists of roughly 40−70 single polymer chains. The broad size distribution is probably caused by the preparation method. Each step of the "grafting-to" process is a complete statistical process. A statistical distribution of the different polymer and a large variance in dimple size is therefore anticipated. The large error in the center−center distance extracted from the line cuts of the SPM images is another evidence of this. Also, the composition of the mixed brushes might play a role. Theoretical calculation predicts a transition between dimples to ripple morphology for an increase in the minor component. Mixed morphology would lead to an increase in polydispersity and uncertainty in the radius of gyration. The fitted power law exponent of P = 2.4 is also another evidence of a mixed morphology, proposing an particle arrangement in a arbitrary three-dimensional mass fractal.[41] The GISAXS image also reveals a lag of long-range order in case of the acetic acid treated film. As reported in the literature, this is caused by

dx.doi.org/10.1021/ma2025286 | Macromolecules 2012, 45, 3129−3136

fluctuations in the grafting point positions caused by the step by step preparation method.[14]

Theoretical SCMF calculations suggest that microphase separation is still present after the film has been exposed to a good solvent for both polymers. The increase in the contact angle to 76° suggests that both PMMA and PS are at the polymer−air interface. The previously collapsed PS chain swell due to the osmotic pressure, causing the polystyrene domains to rise to the surface. The SPM images show no contrast in phase mode. This is probably due to the small difference in elastic modulus between PS and PMMA. The horizontal GISAXS analysis also shows no structural peak at an incidence angle of α = 0.4°. Above the critical angle of both PS and PMMA, the beam penetrates the whole film, giving raise to structural information on the whole film. Since each polymer chain is chemically bound to the substrate, microphase separation can only occur at the surface, with a mixed PS/PMMA layer underneath it. Because of the low contrast in electron density between PMMA and PS, no peak is visible in the GISAXS image. In the SPM images no phase differences is visible due to the similarities in elastic modulus.

NCS Analysis. For surface stress analysis of the PS−PMMA brushes NCS bending experiments were conducted. One NCS array possessing eight independent cantilevers was single-sided coated with three different polymer films. Two cantilevers were coated with PS−PMMA mixed brush films, two cantilevers with a homo-PMMA brush film, and two cantilevers with a homo-PS brush film. The other two cantilevers were left uncoated and used as references (Figure 2). The reference cantilevers allow us to deduct and account for all nonspecific effects on the cantilever. The cantilevers only coated with PMMA and PS, on the other hand, allow us to take any polymer specific forces into account.

NCS bending experiment were conducted before and after with dichloromethane and acetic acid, respectively. Figure 7

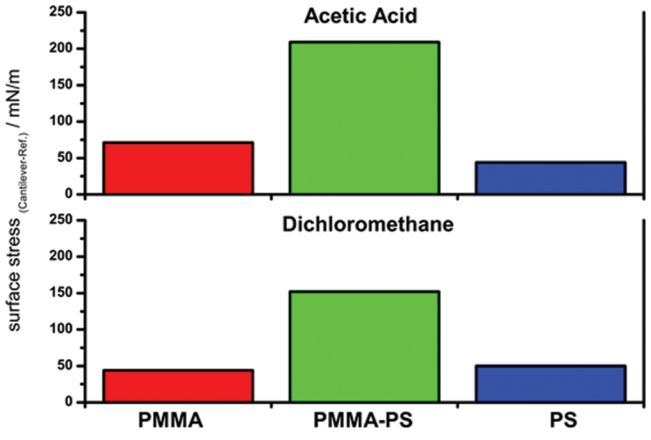


Figure 7. Absolute values of surface stress corrected by reference cantilever.

displays the absolute surface stress values for PMMA−PS mixed polymer brush coated cantilever and the cantilever only coated with one of the homopolymers. Both cantilevers coated with homopolymer brushes as well as the one coated with mixed polymer brushes show a tensile stress upon the exposure with the selective solvent acetic acid. Bending experiments give information about forces acting laterally inside the polymer brush. For the homopolymer case, the tensile stress can therefore be attributed to attractive polymer−polymer interaction. These attractive forces are commonly attributed to interchain entanglements.[46,47] For interchain entanglements to be present, the brushes have to be close enough with respect to the radius of gyration of an unperturbed polymer chain. The PMMA brushes have a grafting density of d = 0.31 chains/nm^2 and the PS brushes of d = 0.45 chains/nm^2. If we calculate the interchain distance from these values and compare them to the radii of gyration of the unperturbed chain, one can see that an overlap is present.

For the mixed polymer brushes much higher tensile stress was measured. Structural information suggests that for the acetic acid treat film microphase separation is the reason for this. As discussed earlier, the polystyrene chain collapses and forms dimple close to the substrate surface. Multiple chains have to stretch and migrate to a common location. Since they are chemical bound to the surface, this happens under loss of entropy. Additional stress is induced through the PMMA covering the PS coil. To cover the coil each chain has to stretch out of their natural configuration. This induces a tensile stress, i.e., the cantilever bends toward the polymer layer.

After treatment with the good solvent dichloromethane the tensile stress in the cantilever coated with the mixed brushes decreases. However, compared to the homopolymer brush films, the tensile stress is higher. The contact angle measurement suggests an increase in PS at the surface of the film. The measured tensile stress indicates that microphase separation is still present inside the mixed brush layer. This means that the PS and PMMA domains are still present in its previous composition. Treatment with dichloromethane causes the polystyrene to swell, increasing its surface coverage. At the same time, stress caused by PMMA bending over the PS is released. The additional surface stress in the acetic acid treated film is mainly a result of an increased stretching of the chains caused by the collapse of the PS brushes and the forced reshaping of the PMMA brush domains.

In summary, the change in stress and structure can be described as follows (Figure 8). Microphase separation inside the mixed polymer brush film induces tensile stress in both acetic acid and dichloromethane treated films. The therefore required stretching of the chain induces a force causing the cantilever to bend upward. Treatment with acetic acid collapses the polystyrene domains; the therefore increased stretching of the PS and PMMA chains covering the polystyrene domains causes the increase in tensile stress.

With our results, the domain memory effect as reported by Santer et al.[16,32,33] can be explained. The fluctuations in local composition and grafting density results in domain formation at specific places. Since domain formation involves a high amount of stretching PS and PMMA domains form most likely at relatively high local grafting densities of their respective species, minimizing the amount of stretching. As measured by the bending experiments, treatment with the good solvent dichloromethane does change the surface structure from a dimple to a flat but does not dissolve the domains itself. The flattening of the surface is due to the swelling of the polystyrene domain caused by the exposure to the good solvent. Treatment with acetic acid causes the polystyrene domain to collapse, leading to the reappearence of the dimple structure. Since no PS and PMMA domains are dissolved during the switching, the domains are formed at the same place and in the same size as before. The change in surface structure from flat to dimple structure is mainly caused by the collapsed and swelling of the polystyrene domains and the therefore necessary rearrange-

dx.doi.org/10.1021/ma2025286 | Macromolecules 2012, 45, 3129−3136

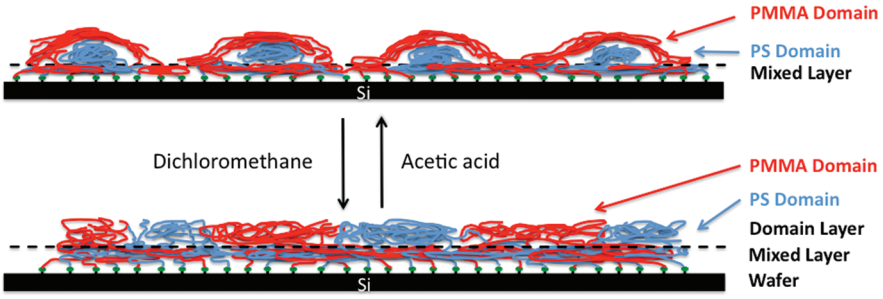


Figure 8. Schematic representation of the proposed structural change of the PMMA–PS mixed polymer brush film upon exposure to dichloromethane and acetic acid, respectively. Upon exposure to acetic acid the polystyrene collapses to the surface and gets covered by poly(methyl methacrylate) in an attempt to maximize the favorable PMMA–PMMA contacts. Upon treatment with dichloromethane the polystyrene microdomains swell.

ment of the surrounding PMMA. Even under optimal conditions only a surface reconstruction of <80% is reported. The incomplete reconstruction of the dimple structure is caused by difference in rearrangements of the PMMA domains after collapse of the PS domains. Partial reconstruction of energetic unfavorable domains in favor of a more stable conformation is also a possibility.

CONCLUSION

Our results show that microphase separation of the grafted polymer chains combined with the chemical fixation to the surfaces induces a large tensile stress when compared to the homopolymer case. Structural analyses of both the acetic acid and dichloromethane treated film concluded microphase separation, in good agreement with theoretical calculations. This allowed us to explain the phenomenon of the domain memory effect. The change in structure is mainly caused by swelling and collapsing of the PS domains. Since the majority of the domains do not dissolve during the switching procedure, the structure is recovered.

Our findings emphasize the importance of chain conformation and the resulting stress in thin polymer brush systems. Bending experiments conducted on nanomechanical cantilever sensors are a useful tool to measure such stress. The utilization of phase shifting interferometry to obtain absolute stress values allows an even deeper understanding when compared to relative values.

ASSOCIATED CONTENT

Supporting Information

Figure S1. This material is available free of charge via the Internet at http://pubs.acs.org.

AUTHOR INFORMATION

Corresponding Author

*E-mail: jochen.gutmann@uni-due.de.

Notes

The authors declare no competing financial interest.

ACKNOWLEDGMENTS

Beamtime provision by the HASYLAB at DESY is gratefully acknowledged. We grateful acknowledge the help of Uwe Rietzler during SPM measurements, Gunnar Kircher with polymerization, and Michael Bach during interferometer construction. Allessandro Cavaliere and Roberto Raitieri effort in programming the software for the PSI are gratefully acknowledged. This research was supported by the Max Planck Society (Institutsübergreifende Forschungsinitiative FRM II), the DFG (SPP-1369 GU 771/3-1, BE 3286/1-1; SPP-1181 GU 771/2, GU 771/6), the graduate school MAINZ, and the Chinese Academy of Science.

REFERENCES

(1) Luzinov, I.; Minko, S.; Tsukruk, V. V. *Prog. Polym. Sci.* **2004**, *29* (7), 635–698.
(2) Prokhorova, S. A.; Kopyshev, A.; Ramakrishnan, A.; Zhang, H. N.; Ruhe, J. *Nanotechnology* **2003**, *14* (10), 1098–1108.
(3) Draper, J.; Luzinov, I.; Minko, S.; Tokarev, I.; Stamm, M. *Langmuir* **2004**, *20* (10), 4064–4075.
(4) Minko, S.; Usov, D.; Goreshnik, E.; Stamm, M. *Macromol. Rapid Commun.* **2001**, *22* (3), 206–211.
(5) Sidorenko, A.; Minko, S.; Schenk-Meuser, K.; Duschner, H.; Stamm, M. *Langmuir* **1999**, *15* (24), 8349–8355.
(6) Zhao, B. *Polymer* **2003**, *44* (15), 4079–4083.
(7) Zhao, B.; He, T. *Macromolecules* **2003**, *36* (23), 8599–8602.
(8) Zhao, B.; Haasch, R. T.; MacLaren, S. *Polymer* **2004**, *45* (23), 7979–7988.
(9) Zhao, B.; Haasch, R. T.; MacLaren, S. *J. Am. Chem. Soc.* **2004**, *126* (19), 6124–6134.
(10) Marko, J. F.; Witten, T. A. *Phys. Rev. Lett.* **1991**, *66* (11), 1541–1544.
(11) Muller, M. *Phys. Rev. E* **2002**, *65* (3), 030802.
(12) Soga, K. G.; Zuckermann, M. J.; Guo, H. *Macromolecules* **1996**, *29* (6), 1998–2005.
(13) Minko, S.; Luzinov, I.; Luchnikov, V.; Muller, M.; Patil, S.; Stamm, M. *Macromolecules* **2003**, *36* (19), 7268–7279.
(14) Wenning, L.; Muller, M.; Binder, K. *Europhys. Lett.* **2005**, *71* (4), 639–645.
(15) Wang, J.; Mueller, M. *J. Phys. Chem. B* **2009**, *113* (33), 11384–11402.
(16) Santer, S.; Kopyshev, A.; Donges, J.; Ruehe, J.; Jiang, X.; Zhao, B.; Mueller, M. *Langmuir* **2007**, *23* (1), 279–285.
(17) Butt, H. J. *J. Colloid Interface Sci.* **1996**, *180* (1), 251–260.
(18) Jun, Z.; Berger, R.; Gutmann, J. S. *Appl. Phys. Lett.* **2006**, *89* (3), 33110–1-33110–33110–3.
(19) Jung, N.; Jeon, S. *Macromolecules* **2008**, *41* (24), 9819–9822.
(20) Jung, N.; Seo, H.; Lee, D.; Ryu, C. Y.; Jeon, S. *Macromolecules* **2008**, *41* (19), 6873–6875.
(21) Toda, M.; Joseph, Y.; Berger, R. *J. Phys. Chem. C* **2010**, *114* (5), 2012–2017.
(22) Liu, T.; Pihan, S.; Roth, M.; Retsch, M.; Jonas, U.; Gutmann, J. S.; Koynov, K.; Butt, H.; Berger, R. *Macromolecules* **2012**, *45* (2), 862––871.
(23) Bumbu, G. G.; Wolkenhauer, M.; Kircher, G.; Gutmann, J. S.; Berger, R. *Langmuir* **2007**, *23* (4), 2203–2207.
(24) Zhou, F.; Shu, W. M.; Welland, M. E.; Huck, W. T. S. *J. Am. Chem. Soc.* **2006**, *128* (16), 5326–5327.

(25) Bradley, C.; Jalili, N.; Nett, S. K.; Chu, L.; Foerch, R.; Gutmann, J. S.; Berger, R. *Macromol. Chem. Phys.* **2009**, *210* (16), 1339−1345.
(26) Chen, T.; Chang, D. P.; Liu, T.; Desikan, R.; Datar, R.; Thundat, T.; Berger, R.; Zauscher, S. *J. Mater. Chem.* **2010**, *20* (17), 3391−3395.
(27) Toda, M.; Itakura, A. N.; Igarashi, S.; Buscher, K.; Gutmann, J. S.; Graf, K.; Berger, R. *Langmuir* **2008**, *24* (7), 3191−3198.
(28) Lenz, S.; Nett, S. K.; Memesa, M.; Roskamp, R. F.; Timmann, A.; Roth, S. V.; Berger, R.; Gutmann, J. S. *Macromolecules* **2010**, *43* (2), 1108−1116.
(29) Minko, S.; Muller, M.; Motornov, M.; Nitschke, M.; Grundke, K.; Stamm, M. *J. Am. Chem. Soc.* **2003**, *125* (13), 3896−3900.
(30) Minko, S.; Patil, S.; Datsyuk, V.; Simon, F.; Eichhorn, K. J.; Motornov, M.; Usov, D.; Tokarev, I.; Stamm, M. *Langmuir* **2002**, *18* (1), 289−296.
(31) Ionov, L.; Sidorenko, A.; Stamm, M.; Minko, S.; Zdyrko, B.; Klep, V.; Luzinov, I. *Macromolecules* **2004**, *37* (19), 7421−7423.
(32) Santer, S.; Kopyshev, A.; Donges, J.; Yang, H. K.; Ruhe, J. *Langmuir* **2006**, *22* (10), 4660−4667.
(33) Santer, S.; Kopyshev, A.; Yang, H. K.; Ruhe, J. *Macromolecules* **2006**, *39* (8), 3056−3064.
(34) Roth, P. J.; Wiss, K. T.; Zentel, R.; Theato, P. *Macromolecules* **2008**, *41* (22), 8513−8519.
(35) Mitsukami, Y.; Donovan, M. S.; Lowe, A. B.; McCormick, C. L. *Macromolecules* **2001**, *34* (7), 2248−2256.
(36) Helm, M.; Servant, J. J.; Saurenbach, F.; Berger, R. *Appl. Phys. Lett.* **2005**, *87* (6), 3.
(37) http://www.ncnr.nist.gov/resources/sldcalc.html.
(38) Beaucage, G. *J. Appl. Crystallogr.* **1995**, *28*, 717−728.
(39) Memesa, M.; Weber, S.; Lenz, S.; Perlich, J.; Berger, R.; Mueller-Buschbaum, P.; Gutmann, J. S. *Energy Environ. Sci.* **2009**, *2* (7), 783−790.
(40) Ochsmann, J. W.; Lenz, S.; Emmerling, S. G. J.; Kappes, R. S.; Nett, S. K.; Lechmann, M. C.; Roth, S. V.; Gutmann, J. S. *J. Polym. Sci., Part B: Polym. Phys.* **2010**, *48* (14), 1569−1573.
(41) Lenz, S.; Bonini, M.; Nett, S. K.; Lechmann, M. C.; Emmerling, S. G. J.; Kappes, R. S.; Memesa, M.; Timmann, A.; Roth, S. V.; Gutmann, J. S. *Eur. Phys. J.: Appl. Phys.* **2010**, *51* (1), 10601.
(42) Korsunsky, A. M.; Cherian, S.; Raiteri, R.; Berger, R. *Sens. Actuators, A* **2007**, *139* (1−2), 70−77.
(43) Stoney, G. G. *Proc. R. Soc. London, Ser. A* **1909**, *82* (553), 172−175.
(44) Gall, W. G.; McCrum, N. G. *J. Polym. Sci.* **1961**, *50* (154), 489−&.
(45) Natta, G. *J. Polym. Sci.* **1955**, *16* (82), 143−154.
(46) Edwards, S. F.; Vilgis, T. *Polymer* **1986**, *27* (4), 483−492.
(47) Urayama, K.; Yamamoto, S.; Tsujii, Y.; Fukuda, T.; Neher, D. *Macromolecules* **2002**, *35* (25), 9459−9465.

Macromolecules

Article

pubs.acs.org/Macromolecules

Two-Dimensional Subnanometer Confinement of Ethylene Glycol and Poly(ethylene oxide) by Neutron Spectroscopy: Molecular Size Effects

Fabienne Barroso-Bujans,*[,†] Felix Fernandez-Alonso,[‡,∥] Silvina Cerveny,[†] Silvia Arrese-Igor,[†] Angel Alegría,[†,§] and Juan Colmenero[†,§,⊥]

[†]Centro de Física de Materiales-Material Physics Center (CSIC-UPV/EHU), Paseo Manuel Lardizábal 5, 20018 San Sebastián, Spain

[‡]ISIS Facility, Rutherford Appleton Laboratory, Chilton, Didcot, Oxfordshire OX11 0QX, U.K.

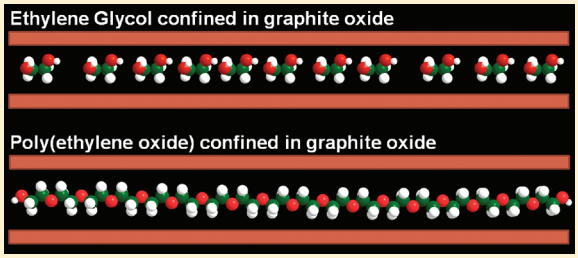
[§]Departamento de Física de Materiales, Universidad del País Vasco (UPV/EHU), Apartado 1072, 20080 San Sebastián, Spain

[⊥]Donostia International Physics Center, Paseo Manuel Lardizábal 4, 20018 San Sebastián, Spain

[∥]Department of Physics and Astronomy, University College London, Gower Street, London, WC1E 6BT, U.K.

Supporting Information

ABSTRACT: We explore the effects of chain size on the structure and dynamics of ethylene glycol (EG) and poly(ethylene oxide) (PEO) intercalated in graphite oxide (GO). To this end, EG as well as a PEO series of increasing chain length have been studied by means of high-resolution inelastic neutron spectroscopy. The neutron experiments are complemented by X-ray diffraction, differential scanning calorimetry, Fourier-transform infrared spectroscopy, and Raman scattering. We find that EG is accommodated in a layer of thickness ∼3 Å within the GO substrate and adopts a preferential, yet largely disordered, gauche conformation. Longer PEO chains give rise to a layer thickness in the range ∼3.0−3.4 Å characterized by planar zigzag (trans−trans−trans) conformations. Moreover, we observe a strong reduction of vibrational motions for the confined EG and polymer phases, as clearly evidenced by the disappearance, shift, and/or broadening of mode-specific inelastic neutron scattering spectral features, as well as by the complete suppression of crystallization. All of these effects are surprisingly insensitive to the length of the PEO chains.



INTRODUCTION

Following the seminal works of McKenna and co-workers,[1,2] many studies on the dynamics of glass-forming liquids subjected to nanoscale confinement have noted a size-dependent reduction in glass-transition temperatures (T_g) which could not be readily explained by conventional theories. Subsequent work has shown that T_g can also increase, remain the same, or even disappear upon confinement.[3] In spite of a plethora of experimental and theoretical studies over the past 2 decades, the influence of spatial confinement on polymer dynamics is still poorly understood and a matter of heated debate. A major obstacle to further progress lies in the difficulties associated with the synthesis of materials with well-defined confining geometries. In this context, graphite oxide (GO) offers a novel means of studying the structure and dynamics of intercalated molecules and macromolecules confined within well-defined two-dimensional (2D) layers of subnanometer dimensions. Pristine GO provides a layered structure characterized by an interlayer spacing of 5.7 Å and it is highly hydrophilic. It can accommodate water[4] as well as other solvent molecules (including methanol, 1-propanol, 1-pentanol, 1-hexanol, benzene, toluene, *p*-xylene, chlorobenzene, CH_2Cl_2, $CHCl_3$)[5,6] between its layers with a surprisingly high degree of interplanar long-range order along the crystallographic *c*-axis.

In a recent study on the intercalation of high-molecular-weight (∼10^5 g/mol) poly(ethylene oxide) (PEO) in GO, we have shown intriguing effects on the structure and dynamics of the confined PEO phase.[7] In essence, we found no evidence of crystallization or glass-transition associated with the confined polymer. For the first time, high-resolution inelastic neutron scattering (INS) provided a direct link between these stark changes in macroscopic behavior and the underlying conformation of the 2D organic phase. Certainly, the conformational changes experienced by PEO as a function of surrounding conditions (i.e., salt addition, pore size, temperature, etc.) have been reported in previous studies using solid-state nuclear magnetic resonance (NMR) as well as Fourier-transform infrared (FTIR) spectroscopy and Raman scattering.[8−17] However, these spectroscopic techniques typically suffer from a strong interference from the substrate. Owing to the strong neutron−proton incoherent cross section, INS

Received: December 7, 2011
Revised: March 12, 2012
Published: March 26, 2012

 © 2012 American Chemical Society

circumvents these difficulties in the characterization of the confined hydrogeneous phase, with minimal interference from the graphitic substrate.[18] Additionally, INS provides access to a broad range of energy transfers, from those associated with stochastic and intermolecular modes in the hard-to-reach terahertz frequency range (1 THz = 33 cm^{-1}), to those characteristic of strong chemical bonds all the way up to 4000 cm^{-1}.

The conformation adopted by PEO upon 2D confinement depends quite critically on the chemical nature of the substrate. For example, PEO intercalated in smectic clays has been hypothesized to form helices capable of accommodating interlayer cations in their cores.[12] However, subsequent computer simulations strongly suggested that such a helical conformation is highly distorted and that the cations reside next to the silicate surface rather than being coordinated to the confined polymer.[19] Likewise, preferential planar conformations have been suggested for PEO and its smaller molecular-weight analogue poly(ethylene glycol) (PEG) confined in kaolinite,[11] V_3O_8,[20] and V_2O_5 interlayers.[21] A bilayer PEO arrangement of thickness 8.3 Å has also been suggested for confinement in the inorganic layered material MoS_2,[22] whereas a more detailed study by means of solid-state NMR has estimated that most of the PEO chains are accommodated with a large fraction of OC−CO bonds (~90%) in a gauche conformation.[8] On the basis of these results, helical conformations are still expected to be the preferential structure of the confined polymer, as it is the case in the bulk material. Furthermore, the strong electrostatic interactions with mobile cations such as K^+, Li^+, and Na^+ ubiquitous in clays and other layered minerals are likely to dictate both the structural and dynamical behavior of the confined polymer phase.[8−10,19,23,24] This is not the case of GO, as it is ion-free and its simple chemical composition (only involving C, O, and H) translates into a far better-defined composite material for fundamental studies of direct relevance to the development of novel technologies.

As mentioned above, high-molecular-weight PEO chains (~10^5 g/mol) intercalate into GO layers giving rise to a well-defined polymer layer of thickness ~3.4 Å and bulk-like areal densities.[7] In this extremely restricted planar geometry, INS has established that the confined macromolecule adopts a preferential planar zigzag conformation, signifying a strong departure from the intramolecular structure of the bulk. Motivated by these new results, the present work explores how macromolecular structure evolves in PEO/GO intercalates as a function of intercalant size. To this end, we have synthesized a series of PEO/GO samples of increasing PEO chain length [HO−$(CH_2CH_2O)_n$−H], where n = 3, 5, 13, 104, 795, and 2135 (hereafter we will use the term "nPEO" to identify the "n" chain length of each PEO used). Note also that we have used the term PEO indistinctly from PEG because it is difficult to establish at which point PEG becomes PEO or vice versa. To complete this chemical series, ethylene glycol (EG, n = 1) was also studied. INS provided access to the entire vibrational density of states (VDOS) of the confined organic phase as a function of chain length over a wide energy-transfer range. The INS data were collected on the TOSCA spectrometer[25] located at the ISIS Facility, Rutherford Appleton Laboratory, U.K. These data were complemented by further measurements using X-ray diffraction (XRD), thermogravimetric analysis (TGA), differential scanning calorimetry (DSC), Fourier-transform infrared spectroscopy (FTIR), and Raman scattering. The experimental results reveal a strong reduction of vibrational motions of the chain for the confined EG and polymer phases, as clearly evidenced by the disappearance, shift, and/or broadening of mode-specific INS bands, as well as by the complete suppression of crystallization. The INS data also account for profound conformational changes taking place in the confined phase, including a preferential gauche conformation for EG in contrast to the characteristic trans conformation favored by longer PEO chains.

EXPERIMENTAL SECTION

Materials. *Synthesis of Graphite Oxide.* Graphite oxide was produced using natural graphite from Alfa Aesar (universal grade, 200-mesh, 99.9995% metal basis, reference number 40799). The starting graphite material was oxidized using a modified Brodie method.[4,26] Briefly, a reaction flask containing 200 mL of fuming nitric acid (Fluka) was cooled to 0 °C for 20 min using a cryostat bath, followed by the immersion of 10 g of graphite. Next, 80 g of potassium chlorate (Fluka) was slowly added over a period of 1 h in order to avoid sudden increases in temperature. The reaction mixture was stirred for 21 h at 0 °C. The mixture was then diluted in distilled water and filtered until the supernatant had a nitrate content below 1 mg/L (AQUANAL-plus nitrate (NO_3) 1−50 mg/L). The resulting GO slurry was dried at 80 °C for 24 h in a vacuum oven (P < 0.1 mbar) and stored in this oven at room temperature until further use. Elemental analysis of the so-obtained GO showed an atomic composition of stoichiometry $C_8H_{1.3}O_{2.6}$. Additional compositional information can be found in ref 4.

Preparation of Graphite−Oxide Intercalates. Triethylene glycol (3PEO) and pentaethylene glycol (5PEO) were purchased from Fluka, whereas EG and nPEO (with n = 13, 104, 795, and 2135) were supplied by Aldrich. nPEO/GO samples with $n \geq 13$ were prepared from aqueous solution by stirring a total of 0.5 g of PEO previously dissolved in 20 mL of water with 0.5 g of GO for 15 days. Any PEO excess was removed by filtration and thorough aqueous washings. The resulting PEO/GO specimen was then dried at 80 °C for 24 h in a vacuum oven (P < 0.1 mbar) connected to a dry scroll rotatory pump. PEO/GO, GO, and PEO were kept dry in the vacuum oven at room temperature prior to their physicochemical characterization. The intercalation of EG, 3PEO, and 5PEO (all of them are liquids at ambient temperature) was performed by direct mixing with GO in the absence of solvent. To remove any remaining liquid, the adduct was carefully rinsed with water and dried at 80 °C under vacuum. As precautionary measure, all samples were analyzed by TGA, DSC, and XRD to identify the presence of excess liquid. The drying procedure explained earlier was performed repeatedly to achieve the complete removal of the nonintercalated fraction. A final composition of ca. 22 ± 2 wt % EG(PEO) in the EG(PEO)/GO samples was ascertained by means of TGA and further corroborated by the INS measurements.

Characterization. *X-ray Diffraction.* XRD patterns were measured using both a Philips X'Pert Pro and a Bruker D8 Advance powder diffractometer. The first one is equipped with a secondary monochromator, Cu Kα radiation (λ = 1.54 Å) and a PIXcel solid-state detector. The second one is equipped with a Cu Kα radiation source (λ = 1.54 Å), a LynxEye detector and an Anton-Paar TTK450 temperature stage. The radiation source in both equipments was operated at a generator voltage of 40 kV and a current of 40 mA. XRD data were collected at 25 °C over the angular range 2θ = 5−60° with a stepsize of 0.026° in Bragg−Brentano parafocousing geometry.

Thermogravimetry. Thermogravimetry was carried out on a TA Instruments Q500 thermogravimetric analyzer. Samples were heated from room temperature to 600 at 1 °C/min under a constant N_2 flow of 60 mL/min. The amount of EG(PEO) in EG(PEO)/GO was calculated from sample-residue analysis at 450 °C, temperature at which the intercalated EG(PEO) undergoes decomposition (see the Supporting Information of ref 7). In this work, intercalated PEO in

GO was shown to decompose in two distinct stages at 214 and 295 °C by means of TGA/mass spectrometry. On the basis of this protocol, the amount of PEO in PEO/GO is given by $W_{PEO/GO} = f_{GO}W_{GO} + f_{PEO}W_{PEO}$, where $W_{PEO/GO}$, W_{GO}, and W_{PEO} are the weight percent of PEO/GO, GO, and PEO residues at 450 °C, respectively, and f_{GO} and f_{PEO} are the mass fractions of GO and PEO in PEO/GO, respectively. Since $f_{PEO} = 1 - f_{GO}$, we can write $f_{PEO} = (W_{GO} - W_{PEO/GO})/(W_{GO} - W_{PEO})$. The mass fraction of EG (f_{EG}) in EG/GO was calculated in a similar fashion via substitution of $W_{PEO/GO}(W_{PEO})$ by $W_{EG/GO}(W_{EG})$ in the last equation above.

Inelastic Neutron Scattering. INS data were collected on the TOSCA spectrometer[25] located at the ISIS Facility, Rutherford Appleton Laboratory, U.K. TOSCA is a so-called indirect geometry time-of-flight neutron spectrometer spanning an energy-transfer range up to 4000 cm^{-1} in neutron energy loss with a spectral resolution of ~1.5%. INS time-of-flight spectra were collected in both back- and forward-scattering geometries, and then added together to obtain hydrogen-projected VDOS's. Typical run times varied between 2 and 8 h depending on the hydrogen content of the sample. All samples were contained in flat aluminum cells of thickness 1−4 mm and cooled to temperatures below 30 K. On the basis of the thermal behavior of EG and *n*PEO observed by DSC, EG and *n*PEO with $n \geq 13$ cannot be obtained in an amorphous state, whereas the quenching of molten 3PEO and 5PEO in liquid nitrogen can prevent their crystallization. Thus, amorphous 3PEO and 5PEO were produced by direct immersion (quenching) in the TOSCA cryostat ($T < 30$ K). Crash cooling to cryogenic temperatures ($T < 100$ K) was optimized by placing the samples at the bottom of the cryostat and exposing them directly to a stream of liquid helium. To prepare a crystalline sample of 5PEO, the sample was first crystallized in a freezer at 240 K prior to its immersion in the low-temperature cryostat. INS data of GO, EG, and PEO were normalized to sample mass and those of EG(PEO)/GO were normalized to the amount of EG(PEO) content (about 22% of EG(PEO)/GO sample mass, as determined by TGA).

Differential Scanning Calorimetry. DSC measurements were carried out on ~12 mg specimens using a Q2000 TA Instruments in both standard and temperature-modulated (TM) modes. Standard DSC measurements were performed by placing the samples in sealed aluminum pans, holding the temperature for 10 min at 353 K, and cooling to 100 K at the highest attainable cooling rate. Bulk liquid samples at room temperature were quenched by immersing the sample in liquid nitrogen and then inserted into the DSC cell at 100 K. Bulk solid samples at room temperature were previously melted on a hot plate at 353 K before quenching. After the cooling run, all samples were heated back to 353 K in TM mode with a 0.48 K temperature amplitude, 60 s modulation period, and 3 K/min underlying heating rate. A helium flow rate of 25 mL/min was used all throughout.

Fourier Transform Infrared Spectroscopy. FTIR spectra were measured at room temperature over the range 700−4000 cm^{-1} with a JASCO 6500 spectrometer using an attenuated-total-reflectance (ATR) stage. Each spectrum was collected with a resolution of 4 cm^{-1} and an average of 200 repetitive scans. The spectra were neither baseline-corrected nor smoothed.

Raman Scattering. Unpolarised Raman scattering measurements were performed at room temperature in backscattering geometry over the energy-transfer range 100−3200 cm^{-1} (Stokes scattering). The Raman setup consisted of a bespoke Renishaw inVia Raman spectrometer equipped with a purpose-built fiber-coupled head to enable both offline as well as simultaneous neutron-Raman measurements. A 300 mW Toptica diode laser operating at a wavelength of 785 nm was used as excitation source. Raman spectra of EG, 3PEO, and 5PEO were recorded offline at room temperature. For more details of the experimental setup and measurement protocols, the reader is referred to ref 27.

RESULTS AND DISCUSSION

Effects of Molecular Size on Intercalate Structure. Owing to the hydrophilic character of the GO substrate, both EG and PEO intercalate into the GO galleries by diffusion either from aqueous solution or the bulk liquid. Moreover, *n*PEO chains with $n \geq 13$ were strongly retained by GO and further PEO recovery was not feasible by rinsing with water. A different behavior was observed for EG as well as the shorter 3PEO and 5PEO chains, which required careful control of sample-preparation conditions to avoid deintercalation. The amount of intercalated species ca. 22 ± 2 wt % was largely independent of molecular weight.

Graphite oxide is a paracrystalline material characterized by turbostratic layer stacking, i.e., irregular shifts and/or rotations of individual planes along the crystallographic *c*-axis. The layers are also irregular since the epoxide and hydroxyl groups and the remaining C=C double bonds are not distributed in a regular fashion within a given two-dimensional layer. As a result, the XRD data (see Figure 1a) typically display a prominent (001)

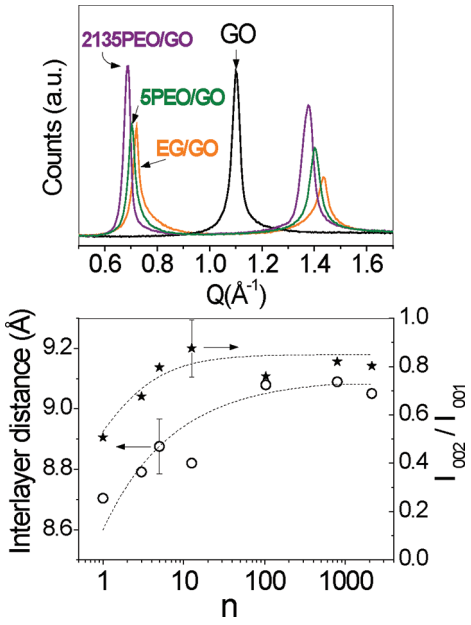


Figure 1. (a) XRD of GO as well as confined EG and *n*PEO with $n = 5$ and 2135 recorded on a Bruker D8 Advance powder diffractometer. (b) Left axis: Dependence of interlayer distance on the chain length of the intercalant (n). Right axis: 002 to 001 peak intensity ratio (I_{002}/I_{001}). The included error bars are a measure of the experimental uncertainties estimated from separate measurements by using different instruments and sample batches. Dashed lines are a guide to the eye.

reflection at 1.10 $Å^{-1}$ followed by a much weaker Bragg reflection (not shown) at 2.23 $Å^{-1}$ (002 line) indicative of in-plane ordering.[5] Representative XRD patterns of EG/GO, 5PEO/GO and 2135PEO/GO are also included in Figure 1a. The XRD patterns of EG/GO and *n*PEO/GO show two well-defined (001) and (002) reflections at 0.69−0.72 $Å^{-1}$ and 1.38−1.43 $Å^{-1}$, respectively, which account for the significant expansion of the GO interlayer along the crystallographic *c*-axis upon intercalation, from 5.7 Å to about 8.7−9.1 Å. After subtracting the 5.7 Å basal spacing of GO, the lattice expansion in (EG)PEO/GO corresponds to a space of approximately 3.0−3.4 Å, which suggests that both oligomers and long-chain polymers are arranged in a single molecular layer. For low-molecular-weight intercalants, the relative intensity of the 002 reflection was found to depend on chain length (see Figure 1b), as these species are more susceptible to adopt different spatial orientations within the GO interlayer. Thus, the observed increase in the intensity of the 002 relative to 001 peaks in

dx.doi.org/10.1021/ma202655f | *Macromolecules* 2012, 45, 3137−3144

going from EG/GO to 13PEO/GO suggests a higher degree of order within the stacks[28] as a function of the molecular weight. This effect was not observed for chain lengths higher than n = 13.

Figure 1b also shows how the interlayer distance varies with chain length. As shown in the figure, the interlayer distance of the EG(PEO)/GO samples does not depend strongly on the chain length of the intercalate, further reinforcing the notion that the oligomer and polymer chains are forced to adopt a planar conformation in a monolayer arrangement, i.e., well-defined and extreme 2D confinement. The readily observable yet relatively small (~0.4 Å) variation in layer thickness from EG to the longest polymer with n = 2135 can be explained by the tendency of the smaller oligomers to adopt the same low-energy conformation as in the bulk, a condition that is harder to achieve for longer polymer chains. In this picture, the free-energy cost associated with achieving a perfectly (higher free-energy) planar conformation becomes significantly higher the longer the polymer chain, and, as result, the underlying GO substrate is forced to undergo a slight expansion.

Thermal Behavior. Figure 2 shows representative DSC profiles corresponding to EG, 3PEO, 5PEO, EG/GO, 3PEO/GO, and 5PEO/GO. Bulk 3PEO and 5PEO exhibit a step at 181 and 192 K, respectively, corresponding to the glass transition of the amorphous phases. Note that amorphous 3PEO and 5PEO can be readily obtained upon quenching, whereas EG crystallizes readily and its glass transition is hard to observe. These DSC thermograms also exhibit large exothermic and endothermic peaks at 224 (234) and 274 (262) K for 3PEO (5PEO), corresponding to the cold crystallization and further melting of crystalline domains in these oligomers. On the other hand, the DSC data for EG shows the presence of small and large endothermic peaks at 210 and 258 K, respectively, corresponding to the melting of two distinct crystalline phases in EG. However, EG/GO, 3PEO/GO, and 5PEO/GO do not show any signs of crystallization, melting, or glass transition. Instead, we only observe small deviations in heat flow compared to pristine GO, which arise from the contribution of the oligomeric species to the total heat flow. The absence of a distinct melting transition in these samples clearly indicates the impossibility of EG and PEO chains to crystallize when intercalated into GO, in agreement with previous studies on PEO intercalated in montmorillonite[24] and fluoromica-based clays.[9] No thermal events were detected for nPEO-mers with longer chain lengths (n = 13–2135), indicating that the organic phase is effectively accommodated in two dimensions irrespective of chain length.

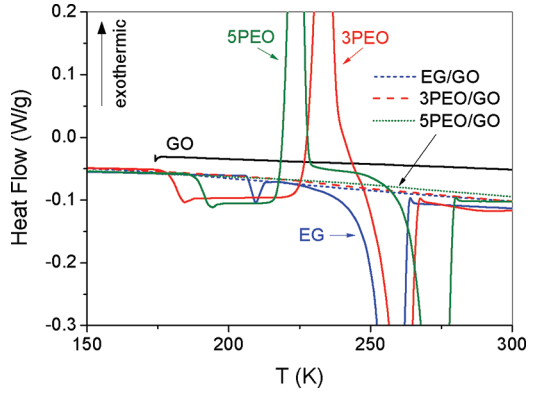


Figure 2. DSC profiles of GO, bulk EG, 3PEO, 5PEO as well as intercalated EG/GO, 3PEO/GO, and 5PEO/GO measured during heating at a rate of 3 K/min. Bulk materials were previously quenched by fast cooling to 100 K. For further details see the text.

Vibrational Spectroscopy. To investigate changes in molecular structure and macromolecular conformation upon confinement, INS measurements were performed on the TOSCA spectrometer on bulk EG(PEO) and EG(PEO)/GO at temperatures below 30 K. Since the most notable differences in the INS data were found for short-chain-length species, we will describe in detail the results for EG, 3PEO, and 5PEO. One of the primary advantages of INS spectroscopy is that there are no hard selection rules and mode intensities can be related to the underlying VDOS. Therefore, spectral assignments can be performed on the basis of our current knowledge and understanding of the vibrational spectrum of the bulk polymer obtained from optical spectroscopy[14,15,29] and computer simulation.[30] Another advantage of INS spectroscopy to characterize confined hydrogenous materials in GO stems from the strong neutron–proton incoherent cross section which dominates the INS response with minimal interference from the GO substrate. Last but not least, INS spectroscopy allows access to very low energy transfers below ~200 cm^{-1}, difficult to access with conventional infrared and Raman techniques.

Ethylene Glycol. INS spectra for GO, bulk EG, and EG/GO spanning the energy-transfer range 24–1600 cm^{-1} are shown in the lower panel of Figure 3. The GO spectrum exhibits a very weak and featureless INS response, which enables a clear identification of EG bands in the EG/GO sample. At higher energy transfers, the spectra only display a broad band associated with C–H stretching vibrations centered at 2935 cm^{-1} (see the Supporting Information). The integrated intensity of this high-energy feature corresponding to C–H stretch modes serves to validate the amount of EG in the sample (ca. 20 wt %), as detailed previously in ref 7 for the case of high-molecular-weight PEO/GO intercalates. Moreover, we find that this spectral feature does not suffer any changes in intensity or line shape upon confinement and can, therefore, be used as a reliable fingerprint of the total concentration of hydrogen in a given sample. On the basis of these observations,

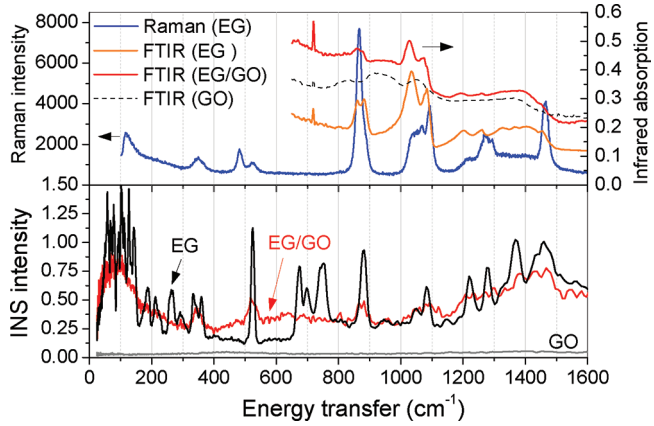


Figure 3. Top: Vibrational spectra of bulk EG, GO, and EG/GO obtained by FTIR spectroscopy and Raman scattering at room temperature. At this temperature, bulk EG is a liquid. Bottom: Mass-normalized INS spectra of GO, bulk crystalline EG, and confined EG/GO measured on the TOSCA spectrometer at 30 K.

dx.doi.org/10.1021/ma202655f | Macromolecules 2012, 45, 3137–3144

intensity changes at lower energy transfers can then be linked to changes in the vibrational dynamics of the intercalate upon confinement.

The most significant differences between bulk and confined EG are observed at energy transfers below 1600 cm^{-1}. The INS data are characterized by the disappearance, shifting, and/or broadening of spectral bands in confined EG compared to the bulk. We can rationalize these results in terms of restricted EG motions within the 2D GO interlayer. Earlier spectroscopic studies have also examined the equilibrium between gauche and trans EG conformers in the bulk liquid and solid,[31,32] as well as confined in silica-glass pores of radii 3−7 nm.[33] These optical studies showed that the Raman bands at 522(480) cm^{-1} could be attributed to the gauche(trans) conformers (see also the Raman and FTIR spectra of liquid EG in the top panel of Figure 3). On the basis of the reported data, the band at 523 cm^{-1} in the INS spectrum of crystalline EG can be then attributed to the asymmetric CCO bending mode of the OCCO skeleton of the gauche conformer. Moreover, the absence of INS features centered around 482 cm^{-1} signals the absence of trans conformers in the crystalline state, in agreement with previous Raman studies on solid EG.[31] Therefore, the presence of a broad INS peak at 521 cm^{-1}, as well as the absence of a peak at 482 cm^{-1} for EG/GO suggests that EG is in a disordered gauche conformation in the confined state. This result is at odds with ref 33, where it was found that confinement of EG in silica-glass nanopores led to an increase of trans EG conformers. It is likely that the geometry as well as the chemical makeup of the silica pores play an important role in dictating the intramolecular structure of EG, as further corroborated in ref 33 after coating the silanol groups on the silica surface with hydrophobic molecules. In that case, the aforementioned changes in gauche−trans isomerism disappeared.

We also observe a decrease in INS peak intensities associated with CH_2 bends (1462 cm^{-1}), O−H in-plane bends (1430, 1369 cm^{-1}), CH_2 twisting modes coupled to wagging motions (1222, 1280 cm^{-1}), symmetric and antisymmetric CH_2−CH_2 rocking vibrations (1085 and 881 cm^{-1}, respectively), coupled vibrations of the C−C and C−O stretching modes (862 cm^{-1}, observed only in the FTIR spectrum), symmetric CCO bending modes (332, 360 cm^{-1}), as well as the absence of features associated with OH torsional modes and internal C−O rotations at 650−780 cm^{-1}.[31] These spectral changes qualitatively account for a strong reduction of EG vibrational motions upon confinement owing to an effective increase in proton effective mass and a concomitant redistribution of INS intensity away from the kinematic trajectories accessible on the TOSCA spectrometer. Such an overall decrease in proton mean-square displacements necessarily arises from a distinctly different local environment in the intercalated case and is amenable to further experimental verification as well as more detailed scrutiny as a function of temperature by quasielastic neutron scattering techniques. The broad INS signals below 300 cm^{-1} for confined EG also account for the suppression of complex collective modes, where the broad response below 160 cm^{-1} closely resembles the vibrational density of states of a disordered amorphous system. These results are also consistent with the DSC data reported in Figure 2, showing a clear suppression of crystalline phases upon confinement.

In the above context, the information offered by the FTIR data of confined EG (top panel in Figure 3) is rather limited due to the extensive overlap of EG and GO contributions in the composite system. Nonetheless, a comparison of the FTIR spectrum of EG/GO with that of liquid EG indicates a red shift of symmetric CH_2−CH_2 rocking vibrations (1085 cm^{-1}) and C−C stretch modes (1034 cm^{-1}), which can be related to conformational changes in the confined EG phase. Figure 4 highlights the spectral region of the FTIR data where the most significant changes occur. These correspond to the OH-stretch region at ca. 3000−3650 cm^{-1}, associated with the presence of OH groups in both EG and GO substrate. The red shift observed in going from pristine GO to EG/GO indicates the formation of intermolecular hydrogen-bonds between OH groups in GO and EG, and are associated with an overall weakening of GO O−H bonds. A similar behavior is found in the 3PEO/GO and 5PEO/GO samples, indicating that 3PEO and 5PEO are also able to form hydrogen bonds with the substrate. Moreover, the presence of a shoulder at 3540 cm^{-1} in EG/GO hints at the rupture of intermolecular hydrogen bonds in EG and the formation of new intramolecular hydrogen bonds or free OH groups in the composite material. This spectral assignment is based on a previous study of OH stretch vibrations for EG in CCl_4 solutions.[31] It is noteworthy that the shoulder at 3540 cm^{-1} disappears as the chain length increases to 3PEO and 5PEO. This result indicates that accessibility to the oxygen-containing functional groups in GO, capable of forming hydrogen bonds with the intercalant (e.g., OH, epoxy, carbonyl, carboxyl, etc.), is favored for longer molecular chains than for a small molecule. As a result, some terminal OH groups in EG cannot bind to the GO substrate and appear as free or as intramolecular OH bonds. On the basis of our spectroscopic observations, Figure 5 depicts several hydrogen-bonding scenarios applicable to EG/GO, including the possibility of free OH groups in intercalated EG. The

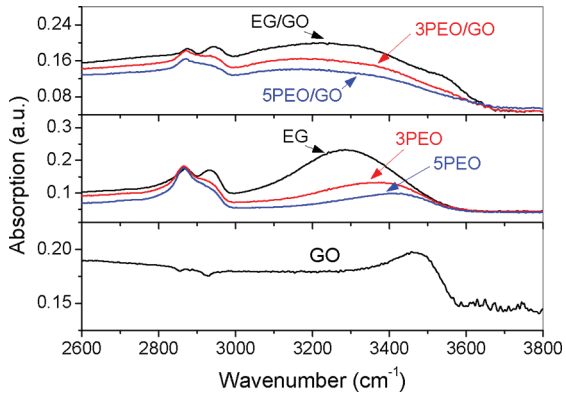


Figure 4. ATR-FTIR spectra of GO as well as of bulk and intercalated EG, 3PEO, and 5PEO at 298 K.

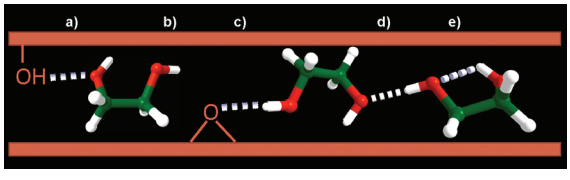


Figure 5. Schematic diagram of hydrogen-bond interactions in EG/GO inferred from the spectroscopic data: (a, c) intermolecular bonds between EG and GO; (d) intermolecular bonds between two EG molecules; and (e) intramolecular EG bonds. Part b signifies the presence of dangling OH groups.

dx.doi.org/10.1021/ma202655f | *Macromolecules* 2012, 45, 3137−3144

concentration of these dangling OH groups must in turn be related to the degree of oxidation and chemical topology of the underlying GO substrate. This observation alone suggests yet another relatively unexplored means of controlling intra- and intermolecular intercalant geometry in this family of composite materials.

Poly(ethylene oxide). The vibrational spectra for 3PEO, 5PEO, and their confined counterparts are shown in Figure 6

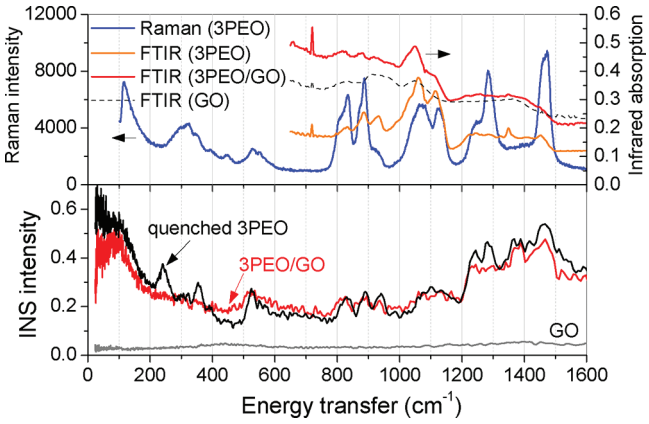


Figure 6. Top: Vibrational spectra of bulk 3PEO, GO, and 3PEO/GO obtained by FTIR spectroscopy and Raman scattering at room temperature. At this temperature, 3PEO is a liquid. Bottom: Mass-normalized INS spectra of GO, crystalline 3PEO, and 3PEO/GO measured on the TOSCA spectrometer at 30 K.

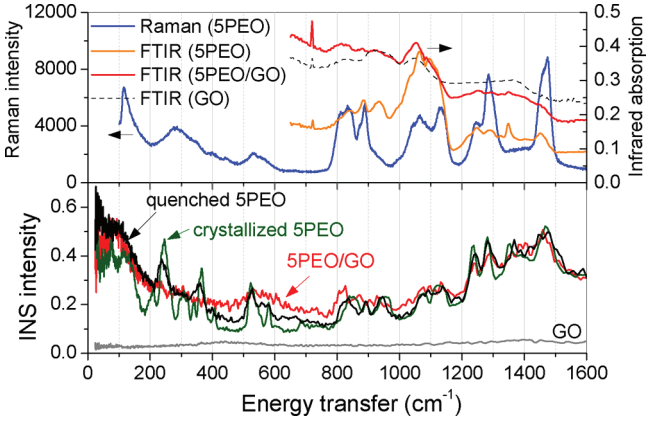


Figure 7. Top: Vibrational spectra of bulk 5PEO, GO, and 5PEO/GO obtained by FTIR spectroscopy and Raman scattering at room temperature. At this temperature, 5PEO is a liquid. Bottom: Mass-normalized INS spectra of GO, quenched 5PEO, crystalline 5PEO, and 5PEO/GO measured on the TOSCA spectrometer at 30 K.

and Figure 7. Similarly to EG/GO, not much information about the structure of 3PEO(5PEO) can be extracted from the FTIR data of 3PEO/GO(5PEO/GO) due to the strong infrared absorption of GO and the limited energy range of our FTIR equipment. The most significant feature in the FTIR spectra is the red shift of C−O−C stretching vibrations from ∼1061 cm^{-1}[29] (bulk 3PEO and 5PEO) to ∼1050 cm^{-1} (3PEO/GO and 5PEO/GO), associated with the formation of hydrogen bonds between PEO chains and the substrate.

The INS spectra of Figure 6 show striking similarities in terms of relative intensities in quenched bulk 3PEO and 3PEO/GO, although some peaks in 3PEO/GO are shifted, absent, or broadened. All of these findings suggest an amorphous-like confined phase for 3PEO as well. In contrast to the sharp peaks observed in the INS spectrum of EG (cf. Figure 3), the vibrational bands of bulk 3PEO are clearly broader and of lower intensity owing to the fact that 3PEO was effectively quenched during the insertion of the liquid sample into the TOSCA cryostat. As mentioned earlier, the strong tendency of EG to crystallize, even upon quenching, did not allow a measurement of amorphous EG using the experimental protocol described in previous sections. Instead, Figure 7 shows the results of a further INS experiment to explore differences in vibrational spectra between the amorphous and crystalline states of 5PEO. The most noticeable changes when comparing the bulk and confined PEO samples, or the amorphous and crystalline 5PEO bulk, lie in the region below 1000 cm^{-1}. The intensity and peak position of the bands observed in this region are particularly sensitive to chain conformation (i.e., trans and gauche conformers) which, in turn, are also affected by temperature, dilution, metal coordination, and geometrical constraints.[7,13−16,29]

At lower energy transfers, the region around 780−970 cm^{-1} is dominated by the presence of CH_2 rocking modes. Amorphous 3PEO and 5PEO show three bands at 831, 890, and 943 cm^{-1} in the INS spectra at nearly the same energies as in the FTIR and Raman spectra of liquid 3PEO and 5PEO, a result that is consistent with the liquid (amorphous) bulk-like behavior of quenched 3PEO and 5PEO. The bands at 831 cm^{-1} show a characteristic blue/red shift for the crystalline/confined 5PEO sample (cf. Figure 7). These spectral shifts are directly related to the appearance of new conformational structures in the different phases. In crystalline PEO, the band at 846 cm^{-1} has been assigned to trans−gauche−trans (*tgt*) conformations of CCOC, OCCO, and COCC groups.[14] For the amorphous phase, there appears to be a sensible increase in the population of trans conformers, reaching a maximum in the confined PEO phase. The band at 816 cm^{-1} appearing in 3PEO/GO and 5PEO/GO has been assigned to CH_2 rocking modes associated with trans−trans−trans (*ttt*) geometries.[14] This assignment is further corroborated by the red shift and intensity suppression of the peak at 953 cm^{-1} in crystalline 5PEO, corresponding to trans−gauche−trans (*tgt*) conformations in the crystal. These results are firm evidence that confined 5PEO is in a different arrangement than that found in the liquid or crystalline bulk phases.

In addition to the above, the INS and Raman band at 890 cm^{-1} decreases in intensity with increasing chain length from n = 3−5 (see Figure 6 and Figure 7) and disappears for $n \geq 13$ (Figure 8). Moreover, the INS band intensity at 890 cm^{-1} does not change in going from the amorphous to the crystalline state in bulk 5PEO. This band has been assigned to CH_2 rocking modes of *tgg* and *ggg* conformations.[14] However, on the basis of the present results, this band could also be associated with the chain end groups. Previous studies have assigned the chain end groups to be a peak at either 811[16] or 830 cm^{-1},[14,30] both of them being very sensitive to the crystalline or amorphous state of the polymer.

The changes in the longitudinal-acoustic-mode (LAM) region (200−400 cm^{-1})[30] reported in Figure 7 provide more evident signatures of changes in macromolecular conformation. These bands correspond to complex modes associated with collective vibrations along the polymer chain. Crystalline 5PEO shows several well-defined spectral features in this region

dx.doi.org/10.1021/ma202655f | *Macromolecules* 2012, 45, 3137−3144

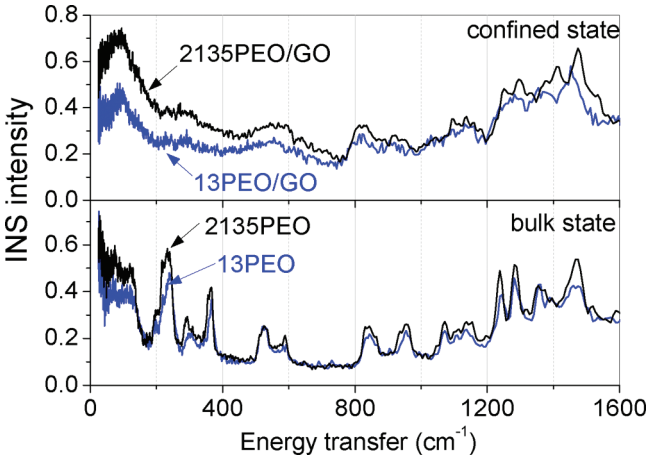


Figure 8. Comparison of mass-normalized INS spectra for bulk and confined *n*PEO with n = 13 and 2135, measured on the TOSCA spectrometer at 30 K.

centered at 210, 246, 308, 340, 364, and 405 cm^{-1}, whereas in the amorphous bulk material only the peaks at 240 and 358 cm^{-1} can be discerned. Earlier experimental and theoretical Raman studies have explained these changes as a result of distinct conformational distributions of the PEO chain.[30] These authors obtained simulated Raman spectra for different combination sequences involving nine rotameric states (i.e., *tgt*−*tgg*−*ttt*, *ttt*−*ttt*−*ttt*, etc.) and observed distinct patterns for each configuration, which were strongly dependent on the exact sequence of rotameric states rather than on the fractional content of *t*, *g*, and *g*′ states. They also determined that the *tgg*′ conformer was favored in molten PEO and that it displayed characteristic bands at 350 and 830 cm^{-1}. Indeed, our INS spectrum of amorphous 5PEO shows the presence of these two bands, the first barely discernible in the Raman data of liquid 5PEO in Figure 7. It is noteworthy that most of the experimental and theoretical studies of the vibrational density of states of PEO are related to *n*PEO with $n \geq 13$, with the notable exception of EG which has been the subject of numerous studies as well. For shorter chain lengths, it is rather difficult to assign the peaks observed in the LAM region without detailed theoretical models. For instance, by comparing the INS spectra of crystalline 5PEO in Figure 7 to those corresponding to *n*PEO with n = 13 and 2135 in Figure 8, it becomes apparent that vibrational modes in the LAM region depend quite sensitively on chain length. The first one shows 6 LAM bands whereas the latter two show only 4. Moreover, the LAM-mode region as well as the entire spectrum for *n*PEO with n = 13 and 2135 are identical except for overall intensity changes arising from differences in hydrogen content for each sample. These results account for the relative importance of the chain ends to the overall configurational structure of the PEO chains, which become less relevant for chain lengths larger than $n \geq 13$.

In the confined state, the absence of peaks in the LAM region for all PEO chains as compared to their bulk counterparts is quite apparent (cf. Figures 6−8). Such a result is largely insensitive to molecular size and suggests the emergence of a new set of chain length scales primarily dictated by the presence of anchoring points on the GO substrate upon intercalation. In the case of confined EG, the persistence of the band at 344 cm^{-1}, which has been found to be independent(dependent) of temperature in the confined (bulk) phase,[34] could be associated with end-group vibrations. These results are a firm indication of a local reduction of vibrational motions of PEO chains within the GO interlayer. A detailed theoretical model taking proper account of the presence of an essentially disordered array of intercalant-substrate hydrogen bonds is, however, required to further quantify the observed and rather stark changes to polymer properties, including a conspicuous absence of LAM-like features in the INS data as well as a sensible reduction in vibrational motion upon intercalation.

CONCLUSIONS

The present work has shown that confinement of EG and *n*PEO (n = 3, 5, 13, 104, 795, and 2135) in GO interlayers induces profound changes to the dynamics and structure of the confined organic phase. Both crystallization and calorimetric glass transition in EG and PEO are inhibited as a result of strong geometric restrictions. Likewise, the INS data unequivocally show that chain conformations are distinctly different from those characteristic of their crystalline and amorphous bulk counterparts. These findings can be related to the extreme 2D confinement (3−3.4 Å), as well as to the role of hydrogen-bonding interactions between intercalant and GO substrate. INS spectroscopy has provided unique insights into the vibrational and conformational properties of the confined phase, and served to confirm the presence of ca. 22 ± 2 wt % intercalant in these composite materials. The disappearance of LAM-like modes in all confined PEO chains and the persistence of a well-defined band at 340 cm^{-1} for confined EG suggest that further control of polymer properties may be achieved via a judicious tuning of the chemical composition and topology of the underlying GO substrate.

ASSOCIATED CONTENT

Supporting Information

Inelastic neutron scattering results at high energy transfer and resume of the INS bands for bulk and confined EG and *n*PEO materials. This material is available free of charge via the Internet at http://pubs.acs.org/

AUTHOR INFORMATION

Corresponding Author

*E-mail: fbarroso@ehu.es. Telephone: +34 94301 8803. Fax: +34 94301 5800.

Notes

The authors declare no competing financial interest.

ACKNOWLEDGMENTS

The authors gratefully acknowledge the support of the Spanish Ministry of Education (MAT2007-63681), the Basque Government (IT-436-07), and the U.K. Science and Technology Facilities Council for beamtime on the TOSCA spectrometer and access to the Raman spectrometer in the ISIS Sample Characterisation Laboratory. F.B.-B. acknowledges a JAE-Doc contract from CSIC. F.F.-A. acknowledges financial support from the U.K. Science and Technology Facilities Council. We thank Dr. A. Larrañaga from SGIker UPV/EHU for the XRD measurements on the Philips X'Pert Pro powder diffractometer.

REFERENCES

(1) Jackson, C. L.; McKenna, G. B. *J. Chem. Phys.* **1990**, *93*, 9002−9011.

(2) Jackson, C. L.; McKenna, G. B. *J. Non-Cryst. Solids* **1991**, *131*−*133*, 221−224.
(3) Alcoutlabi, M.; McKenna, G. B. *J. Phys.-Condes. Matter* **2005**, *17*, R461−R524.
(4) Cerveny, S.; Barroso-Bujans, F.; Alegría, A.; Colmenero, J. *J. Phys. Chem. C* **2010**, *114*, 2604−2612.
(5) Barroso-Bujans, F.; Cerveny, S.; Alegría, A.; Colmenero, J. *Carbon* **2010**, *48*, 3277.
(6) Barroso-Bujans, F.; Cerveny, S.; Verdejo, R.; del Val, J.; Alberdi, J.; Alegría, A.; Colmenero, J. *Carbon* **2010**, *48*, 1079−1087.
(7) Barroso-Bujans, F.; Fernandez-Alonso, F.; Cerveny, S.; Parker, S. F.; Alegría, A.; Colmenero, J. *Soft Matter* **2011**, *7*, 7173−7176.
(8) Harris, D. J.; Bonagamba, T. J.; Schmidt-Rohr, K. *Macromolecules* **1999**, *32*, 6718.
(9) Miwa, Y.; Drews, A. R.; Schlick, S. *Macromolecules* **2008**, *41*, 4701−4708.
(10) Jeevanandam, P.; Vasudevan, S. *Chem. Mater.* **1998**, *10*, 1276−1285.
(11) Tunney, J. J.; Detellier, C. *Chem. Mater.* **1996**, *8*, 927−935.
(12) Aranda, P.; Ruiz-Hitzky, E. *Chem. Mater.* **1992**, *4*, 1395−1403.
(13) Papke, B. L.; Ratner, M. A.; Shriver, D. F. *J. Phys. Chem. Solids* **1981**, *42*, 493−500.
(14) Maxfield, J.; Shepherd, I. W. *Polymer* **1975**, *16*, 505−509.
(15) Matsuura, H.; Miyazawa, T. *J. Polym. Sci., Part A2: Polym. Phys.* **1969**, *7*, 1735−1744.
(16) Koenig, J. L.; Angood, A. C. *J. Polym. Sci., Part A2: Polym. Phys.* **1970**, *8*, 1787−1796.
(17) Wong, S.; Zax, D. B. *Electrochim. Acta* **1997**, *42*, 3513−3518.
(18) Mitchell, P. C. H.; Parker, S. F.; Ramirez-Cuesta, A. J.; Tomkinson, J. *Series on Neutron Techniques and Applications. Vibrational Spectroscopy with Neutrons: with Applications in Chemistry, Biology, Materials Science and Catalysis*; World Scientific: London, 2005.
(19) Hackett, E.; Manias, E.; Giannelis, E. P. *Chem. Mater.* **2000**, *12*, 2161−2167.
(20) Yang, G.; Hou, W.; Sun, Z.; Yan, Q. *J. Mater. Chem.* **2005**, *15*, 1369−1374.
(21) Liu, Y. J.; DeGroot, D. C.; Schindler, J. L.; Kannewurf, C. R.; Kanatzidis, M. G. *Chem. Mater.* **1991**, *3*, 992−994.
(22) Lemmon, J. P.; Lerner, M. M. *Chem. Mater.* **1994**, *6*, 207−210.
(23) Elmahdy, M. M.; Chrissopoulou, K.; Afratis, A.; Floudas, G.; Anastasiadis, S. H. *Macromolecules* **2006**, *39*, 5170.
(24) Vaia, R. A.; Sauer, B. B.; Tse, O. K.; Giannelis, E. P. *J. Polym. Sci., Part B: Polym. Phys.* **1997**, *35*, 59−67.
(25) Colognesi, D.; Celli, M.; Cilloco, F.; Newport, R. J.; Parker, S. F.; Rossi-Albertini, V.; Sacchetti, F.; Tomkinson, J.; Zoppi, M. *Appl. Phys. A—Mater. Sci. Process* **2002**, *74*, s64.
(26) Barroso-Bujans, F.; Alegría, A.; Colmenero, J. *J. Phys. Chem. C* **2010**, *114*, 21645−21651.
(27) Adams, M. A.; Parker, S. F.; Fernandez-Alonso, F.; Cutler, D. J.; Hodges, C.; King, A. *Appl. Spectrosc.* **2009**, *63*, 727−732.
(28) Vaia, R. A.; Liu, W. *J. Polym. Sci., Part B: Polym. Phys.* **2002**, *40*, 1590−1600.
(29) Yoshihara, T.; Tadokoro, H.; Murahashi, S. *J. Chem. Phys.* **1964**, *41*, 2902−2911.
(30) Yang, X.; Su, Z.; Wu, D.; Hsu, S. L.; Stidham, H. D. *Macromolecules* **1997**, *30*, 3796−3802.
(31) Matsuura, H.; Miyazawa, T. *Bull. Chem. Soc. Jpn.* **1967**, *40*, 85−94.
(32) Matsuura, H.; Hiraishi, M.; Miyazawa, T. *Spectrochim. Acta, Part A* **1972**, *28*, 2299−2304.
(33) Luo, R.; Jonas, J. *J. Raman Spectrosc.* **2001**, *32*, 975−978.
(34) Crupi, V.; Majolino, D.; Migliardo, P.; Venuti, V. *J. Chem. Phys.* **2003**, *118*, 5971−5978.

Macromolecules

Article

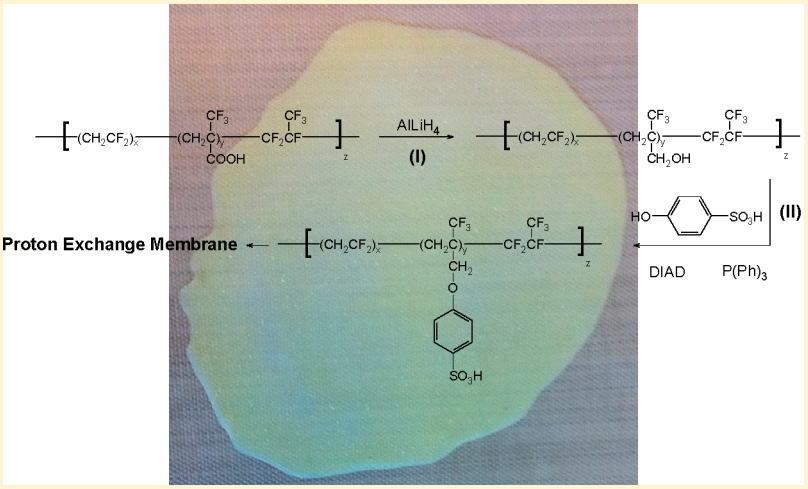
pubs.acs.org/Macromolecules

Synthesis and Characterizations of Novel Proton-Conducting Fluoropolymer Electrolyte Membranes Based on Poly(vinylidene fluoride-*ter*-hexafluoropropylene-*ter*-α-trifluoromethacrylic acid) Terpolymers Grafted by Aryl Sulfonic Acids†

Renaud Souzy, Bernard Boutevin, and Bruno Ameduri*

Ingénierie et Architectures Macromoléculaires, Institut Charles Gerhardt, UMR (CNRS) 5253, Ecole Nationale Supérieure de Chimie de Montpellier, 8 Rue Ecole Normale, 34296 Montpellier Cedex 5, France

Supporting Information



ABSTRACT: The synthesis and the characterization of new polymer electrolyte membranes made of fluorinated copolymers based on vinylidene fluoride (VDF) and hexafluoropropylene (HFP) and grafted by aryl sulfonic acids are presented. They were obtained in a three-step process. First, the conventional batch radical terpolymerization of α-trifluoromethacrylic acid (TFMAA), VDF and HFP, initiated by 2,5-bis(*tert*-butylperoxy)-2,5-dimethylhexane led to original fluorinated functional terpolymers bearing carboxylic acid side groups in fair to good yields (>55%). The microstructure and the thermal properties of these macromolecules were studied. Interestingly, poly[(VDF-*alt*-TFMAA)-*co*-HFP)] random terpolymers that contained alternated microblock structures based on VDF and TFMAA units separated by one HFP unit were evidenced by ^{19}F nuclear magnetic resonance (NMR) spectroscopy. That technique also enabled us to assess the termonomer contents. Average molecular weights, glass transition temperatures, and decomposition temperatures (under air), determined by size exclusion chromatography (SEC), differential scanning calorimetry (DSC), and thermogravimetric analysis (TGA), ranged between 10 000 and 21 400 g mol^{-1}, from −27 to −18 °C and from 140 to 275 °C, respectively. Indeed, the higher the TFMAA content, the lower the thermostability of the terpolymer that arised from decarboxylation. This degradation could be overcome by the reduction of the carboxylic acid dangling functions into hydroxyl ones. The third step concerned an etherification (Mitsunobu) reaction of such resulting primary hydroxyl groups with 4-sulfonic acid phenol. Both these reactions did not affect the contents of fluorinated termonomeric units as evidenced by ^{1}H, ^{19}F, and ^{13}C NMR characterization. The microstructures, physicochemical, and thermal properties of the grafted materials were evaluated by NMR and infrared spectroscopies, SEC and DSC, and TGA. Membranes incorporating these functional fluoropolymers were processed by casting, and their preliminary electrochemical properties (ionic exchange capacity, proton conductivity, and swelling rates that reached 1.2 mequiv mol^{-1}, 9 mS cm^{-1}, and 58%, respectively) were studied, discussed, and compared to those of Nafion and to other fluorinated aromatic membranes of different architectures.

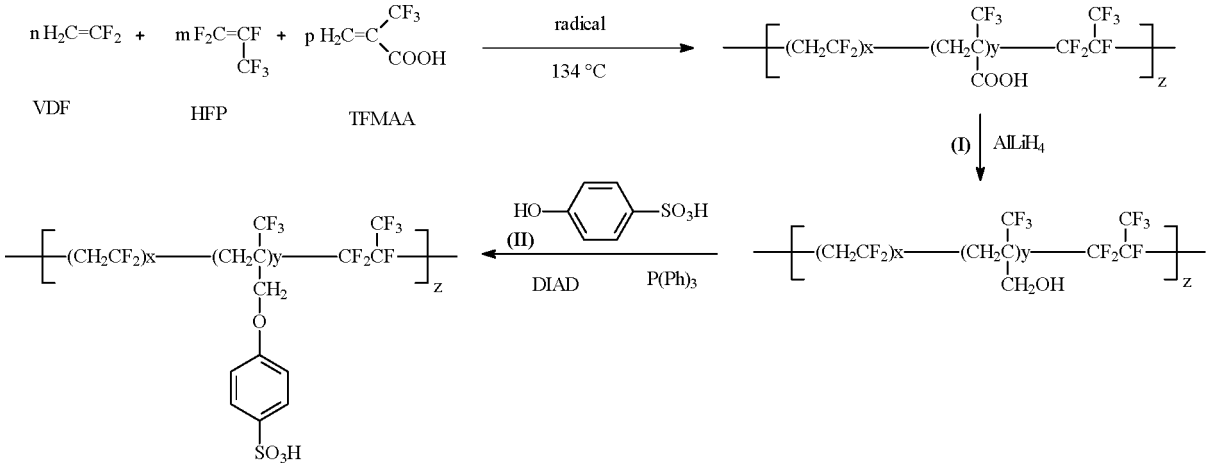
1. INTRODUCTION

The development of new alternative energy conversion technologies has become increasingly important for various applications which today are dependent on fossil fuels. Among them, fuel cell technology offers an attractive combination of high energy conversion efficiency and a potential for large reductions in power source emissions, including CO_2.[1−5]

Received: January 24, 2012
Revised: March 7, 2012
Published: March 23, 2012

ACS Publications © 2012 American Chemical Society

Scheme 1. Synthesis of Poly(VDF-*ter*-HFP-*ter*-TFMAA) Terpolymers, Reduction of Carboxylic Acid into Primary Alcohols, and Grafting of Aryl Sulfonic Acid[a]



[a]VDF, HFP, and TFMAA stand for vinylidene fluoride, hexafluoropropylene, and α-trifluoromethacrylic acid, respectively.

In that context, efforts to find out alternatives to the most widely used perfluorosulfonic acid Nafion (DuPont) as proton exchange membrane fuel cell (PEMFC) have been investigated by many research groups for several decades.[2,3] The preparation and characterization of polymeric materials for PEMFC continues to evolve.[6] Indeed, PEMFCs can be classified according to their fluorine content: perfluorinated,[3,7−9] partially fluorinated,[10−12] and nonfluorinated[13−15] membranes. During the past decade, significant research efforts have been aimed at developing new alternative membrane materials with improved properties and lower cost.

For the most part, these materials have been based on various durable hydrocarbon polymers—mainly on aromatic polymers with the ionic sulfonic acid groups distributed along the backbone. The nonfluorinated ionomer membranes like hydrocarbon polymers[2] exhibit the least resistance to autooxidation but offer the best likelihood of developing a membrane in the \$100−150/m^2 price range. Partially fluorinated and perfluorinated membranes are outstanding materials[16] and are commercially available under the names of Nafion,[2,3] Flemion, 3MIonomer,[17] Aquivion[18] (formerly Hyflon[19]), or Aciplex.[20]

Fluorine-containing PEMFC can be synthesized form fluoropolymers obtained by direct radical (co)polymerization of aliphatic[21−24] or aromatic[8,25−28] perfluorovinyl monomers functionalized by acids (sulfonic, phosphonic,[29,30] or carboxylic) with tetrafluoroethylene[18−21] (TFE) or vinylidene fluoride (VDF).[22,23]

Other well-designed fluorocopolymers (i.e., block[31−33] and graft[36] copolymers) have also increasingly been developed. More recently, Holdcroft's group,[31−34] as well as other teams, have synthesized and made detailed studies of several different graft copolymers where sulfonated polymeric side chains are attached to hydrophobic hydrocarbon or fluorocarbon backbones (Scheme 1d) with the aim being to establish relationships between polymer microstructure, water uptake, and proton conductivity.[15,24,34−38]

Other PEMFCs have been prepared by radio-grafting various monomers onto activated fluoropolymers (such as PTFE, poly(tetrafluoroethylene-*co*-hexafluoropropylene) (FEP), poly(ethylene-*alt*-tetrafluoroethylene) (ETFE), poly(vinylidene fluoride) (PVDF), and poly(TFE-*co*-perfluoropropylvinyl ether) copolymers (PFA).[16] This activation can be achieved by different techniques of irradiation such as thermally, by ozonization, from swift heavy ions, electron beam, or by γ-rays that were reviewed in a book.[39] Afterward, the nonconducting hydrophobic films were sulfonated by chlorosulfonic acid.

Another interesting approach deals with the chemical modification of polyparaphenylene bearing 4-fluoroaromatic side groups able to react onto HO−C_6H_4−$CF_2CF_2SO_3H$, hence leading to original aromatic polymers with $C_2F_4SO_3H$ side groups.[40] This function is made more acidic by the electron-withdrawing difluoromethylene group adjacent to the sulfonic acid. Consequently, membranes prepared from these polymers exhibit high conductivity values and have found applications in fuel cells.[18−20,29,30,40]

As a matter of fact, quite a few articles[41] report the use of PVDF to yield original fuel cell membranes: Prakash et al.[42] synthesized PSSA embedded in PVDF by simple mixing of divinylbenzene and styrene followed by a photopolymerization leading to semi-interpenetrated polymer network (sIPN) that was further sulfonated. Then, Niepceron et al.[43] processed original membranes based on heterogeneous PVDF/nanosilica containing poly(styrenesulfonic acid) by the "grafting from" process. More recently, Zapata et al.[44] produced original PEMFCs by IPN with satisfactory conductivities.

However, mixing highly hydrophobic PVDF with other derivatives sometimes does not achieve homogeneous materials. Hence, other strategies to develop fluorosulfonic membranes based on PVDF were reported by radical copolymerization of VDF with perfluoro(4-methyl-3,6-dioxaoct-7-ene)sulfonyl fluoride either at Dupont[22] or in our group.[23] But, the obtained conductivities were low even when a cross-linked membrane[45] was produced from using a cure site monomer.

Actually, aromatic sulfonic acid functions born by fluorinated (co)polymer have attracted many researchers whatever radio-grafting membranes (well-summarized in an interesting review[46]) or by sulfonation of poly(VDF-*co*-HFP)-*b*-PS block copolymers[31] or poly(VDF-*co*-CTFE)-*g*-PSSA graft copolymers,[36] considering that several precursors of such above block[6,47] and graft[48] copolymers were also produced. Linking PVDF and aryl sulfonic acid is still a challenge, and the objectives of this present article are to synthesize terpolymers based on fluorinated monomers (including VDF and HFP),

dx.doi.org/10.1021/ma3001912 | Macromolecules 2012, 45, 3145−3160

Table 1. Determination of the Monomer/Terpolymer Composition of Poly(VDF-*ter*-HFP-*ter*-TFMAA) Terpolymers versus the Reaction Conditions in the Radical Terpolymerization of VDF, HFP with TFMAA[a]

expt no.	mol % of VDF in feed	mol % of HFP in feed	mol % of TFMAA in feed	mol % of VDF in the terpolymer	mol % of HFP in the terpolymer	mol % of TFMAA in the terpolymer	mass yields (%)	T_g (°C)	M_n (g mol^{-1})	M_w (g mol^{-1})	PDI
1	69.2	17.1	13.7	56.8	3.5	39.7	54	−18	10 100	16 100	1.6
2	74.1	16.8	9.1	57.7	5.4	36.9	54	−19	11 100	18 800	1.7
3	72.7	21.2	6.1	59.5	5.1	35.4	55	−19	11 500	20 700	1.8
4	71.4	23.2	5.4	80.4	12.4	7.2	61	−21	14 000	25 200	1.8
5	77.9	18.9	3.2	86.2	10.4	3.4	65	−26	19 500	31 200	1.6
6	83.9	14.6	1.5	88.8	10.1	1.1	64	−27	21 400	34 200	1.6

[a]Terpolymerization conditions: [2,5-bis(*tert*-butylperoxy)-2,5-dimethylhexane]$_0$/([VDF]$_0$ + [HFP]$_0$ + [TFMAA]$_0$) = 0.9 mol %, 134 °C, 10 h. Average molecular weights, M_n and M_w, assessed from SEC with poly(methyl methacrylate) standards. T_g (glass transition temperature) values were measured by DSC (VDF, HFP, TFMAA, and T_g stand for vinylidene fluoride, hexafluoropropylene, α-trifluoromethacrylic acid, and glass transition temperature, respectively).

one of them being chemically modified to bring aryl sulfonic acid side groups randomly distributed in the fluorinated polymeric backbone. Actually, the radical terpolymerization of VDF with α-trifluoromethacrylic acid (TFMAA) and hexafluoropropylene (HFP) was carried out either in solvent (solution)[49] or in water[50] in the absence[49] or presence[50] of 1,6-diiodoperfluorohexane. In this present study, it is of interest to avoid any chain transfer agent that usually leads to lower molecular weights.[51−53]

Our choice was to use such a methodology and then to graft onto a fluorinated backbone based on VDF, HFP, and TFMAA, which to the best of our knowledge has never been reported. Hence, the objective of this paper concerns first the synthesis and the characterization of poly(VDF-*ter*-HFP-*ter*-TFMAA) terpolymers, followed by the grafting reaction of 4-sulfonic acid phenol onto these terpolymers. Finally, preliminary physicochemical and electrochemical characterizations of the resulting materials were assessed and discussed.

2. EXPERIMENTAL SECTION

2.1. Materials. Vinylidene fluoride (or 1,1-difluoroethylene, VDF), hexafluoropropylene (HFP), and 1,1,1,3,3-pentafluorobutane were kindly offered by Solvay S.A., Tavaux, France, and Brussels, Belgium. α- Trifluoromethacrylic acid (TFMAA) was kindly supplied by Tosoh F-Tech Co. (Shunan, Japan). 2,5-Bis(*tert*-butylperoxy)-2,5-dimethylhexane, tech, 90% (Luperox 101), was kindly supplied by Akzo Nobel, 60540 Compiegne, France, while $AlLiH_4$, diisopropylazodicarboxylate (DIAD), and 4-phenolsulfonic acid were purchased at Aldrich Chimie, 38299 Saint Quentin-Fallavier, France, and were used as supplied. *N*-Methyl pyrolidinone (NMP) and tetrahydrofuran of analytical grade (Aldrich Chimie, 38299 Saint Quentin-Fallavier, France) were distilled over calcium hydride prior to use. Deuterated solvents for recording the NMR were purchased from Euriso-top (Grenoble, France) (purity >99.8%).

2.2. Analyses. The compositions of the terpolymers (i.e., the assessment of the molar contents of VDF, HFP, and TFMAA monomeric units in the resulting terpolymers) were assessed by ^{1}H, ^{19}F, and ^{13}C NMR spectroscopy. The NMR spectra were recorded on Bruker AC 400 and AC 250 spectrometers (400 MHz for ^{1}H, 376 MHz for ^{19}F, and 100 MHz for ^{13}C) at room temperature, using deuterated acetone or DMF as the solvents and TMS (or $CFCl_3$) as the references for ^{1}H (or ^{19}F) nuclei. Coupling constants and chemical shifts are given in Hz and ppm, respectively. The experimental conditions for ^{1}H (or ^{19}F) NMR spectra were the following: flip angle 90° (30°), acquisition time 4.5 s (0.7 s), pulse delay 2 s (5 s), number of scans 16 (64), and a pulse width of 5 μs for ^{19}F NMR spectroscopy.

Infrared spectra were recorded on a Nicolet 510P Fourier transform spectrometer from KBr pellets, and the intensities of the absorption bands were noted as s (strong), m (medium) and w (weak), given in cm^{-1}, with an accuracy of 2 cm^{-1}.

Molecular weights and molecular weight distributions were assessed by size exclusion chromatography (SEC) at 40 °C, carried out in dimethylacetamide (DMAc) that contained 0.2% LiBr, at a flow rate of 0.8 mL min^{-1}, by means of a Spectra Physics Winner Station, a Waters Associate R 401 differential refractometer, and a set of four columns connected in series: PolarGel L PL1117-6830 (Agilent Technologies) 5 μm, PolarGel L Gel 100 Å. Monodispersed poly(methyl methacrylate) standards were used for calibration. Aliquots were sampled from the purified polymers, diluted with DMAc up to a known concentration (4 wt %), filtered through a 20 μm PTFE Chromafil membrane, and finally analyzed by SEC under the conditions described above.

Differential scanning calorimetry (DSC) measurements were conducted using a Perkin-Elmer Pyris 1 instrument connected to a microcomputer. The apparatus was calibrated with indium and *n*-decane. After its insertion into the DSC apparatus, the sample was initially cooled to −105 °C for 15 min. Then, the first scan was made at a heating rate of 40 °C min^{-1} up to 100 °C, where it remained for 2 min. It was then cooled to −105 °C at a rate of 320 °C min^{-1} and left for 10 min at that temperature before a second scan was started at a heating rate of 20 °C min^{-1}. Finally, another cycle was performed and a third scan at a heating rate of 20 °C min^{-1} was initiated, giving the values of T_g reported herein, taken at the half-height in the heat capacity jump of the glass transition.

Thermogravimetric analyses were performed with a Texas Instruments TGA 51-133 apparatus in air at a heating rate of 10 °C min^{-1} from room temperature up to a maximum of 600 °C. The sample size varied between 10 and 15 mg.

2.3. Synthesis of Fluorinated Terpolymers. *2.3.1. Synthesis of Poly(VDF-ter-HFP-ter-TFMAA) Terpolymers by Radical Terpolymerization.* The batch terpolymerizations of VDF, HFP, and TFMAA were carried out in a 160 mL Hastelloy (HC 276) autoclave, equipped with a manometer, a rupture disk, an inlet valve left closed for 20 min, purged with 20 bar of nitrogen pressure to prevent any leakage, and degassed afterward. An electronic device regulated and controlled both the stirring and heating of the autoclave. Prior to reaction, the autoclave was pressurized with 30 bar (ca. 430 psi) of nitrogen to check for leaks. The autoclave was then conditioned for the reaction with several nitrogen/vacuum cycles (10^{-2} mbar) to remove any trace of oxygen. Then, under vacuum, the initiator (2,5-bis(*tert*-butylperoxy)-2,5-dimethylhexane) and TFMAA dissolved 1,1,1,3,3-pentafluorobutane were successively introduced via a funnel tightly connected to the introduction valve. Next, HFP and then VDF were respectively transferred into the vessel by the difference of weight before and after filling the autoclave with the gases. The autoclave was then heated up to 134 °C for 8 h. According to the content of the three monomers, the maximum pressures reached 60−120 bar followed by a decrease of pressure as soon as the gaseous alkenes were consumed. After reaction, the autoclave was weighed immediately after the radical terpolymerization (m_1) and placed in an ice bath for ca.

dx.doi.org/10.1021/ma3001912 | Macromolecules 2012, 45, 3145−3160

30 min. Subsequently, the unreacted VDF and HFP were carefully released, and the autoclave was weighed again (m_2). The conversion of gaseous fluoroalkenes was $[m_0 - (m_1 - m_2)]/m_0 \times 100$, where m_0 stands for the initial VDF and HFP weights transferred into the autoclave. The solvent was distilled and the total product mixture was solubilized in DMF and then precipitated from cold water. The precipitate was filtered off and dried over P_2O_5 at room temperature under a 20 mmHg vacuum for 48 h and then characterized by ^{19}F and ^{13}C NMR spectroscopy. All the resulting poly[(VDF-*alt*-TFMAA)-*co*-HFP] terpolymers were yellow-orange powders whatever their compositions.

2.3.2. Chemical Modification of Carboxylic Acid Functions in Poly(VDF-ter-HFP-ter-TFMAA) Terpolymers. The reduction of carboxylic acid side groups of TFMAA units of the terpolymers was achieved after introducing 4*n* moles of $LiAlH_4$ and 6*n* moles of anhydrous THF in a three necked round-bottom flask fitted with a reflux condenser, a nitrogen inlet, a magnetic stirrer, and a dropping funnel. Then, *n* moles of poly[(VDF-*alt*-TFMAA)-*co*-HFP] terpolymer dissolved in anhydrous THF were dropwise added, and then the reaction temperature was slowly increased up to 90 °C. After 3 h, the excess of $LiAlH_4$ was neutralized by an excess of HCl (10% in water) leading to a solid complex. The mixture was then filtered off, which enabled to separate the complex of residual lithine. After evaporation of the solvent, the reduced fluorinated terpolymers were precipitated from cold pentane, filtered, and then dried at 60 °C under 20 mmHg vacuum until constant weight. The conversion rates of that reduction reaction were ranging between 70 and 98%.

2.3.3. Etherification of the Fluorinated Terpolymers Bearing Hydroxyl Side Groups. The etherification of above terpolymer (that contained primary alcohol side functions) by 4-sulfonic acid phenol was achieved according to the Mitsunobu reaction.[55] A solution containing 12.50 g (0.048 mol) of triphenylphosphine and 10.11 g (0.058 mol) of 4-phenolsulfonic acid (previously dried over $MgSO_4$) in dried THF (60 mL) was dropwise added into a solution composed of 10.10 g (0.051 mol) of diisopropylazodicarboxylate and 8.13 g of reduced terpolymers (containing 56.8 mol % VDF, 3.5 mol % HFP, and 39.7 mol % TFMAA, expt 1, Table 1) at room temperature. A white precipitate of triphenylphosphine oxide and diisopropylhydrazinedicarboxylate quickly appeared. The mixture was stirred at room temperature for 24 h, and the precipitate was removed by filtration. The filtrate was evaporated, the residue was solubilized in acetonitrile, and the triphenylphosphine oxide was completely eliminated using a continuous liquid/liquid extraction involving hexane as the solvent. Then, the terpolymers were precipitated from cold pentane and dried over P_2O_5 at 50 °C under vacuum (20 mmHg) for 48 h. The massic yields of the resulting aromatic sulfonic acid fluorinated terpolymers were ranging from 50 to 75%. All modified terpolymers that bore sulfonic acid side function were orange powders.

2.4. Preparation of the Membranes. Poly(VDF-*ter*-HFP-*ter*-TFMAA) terpolymers that contained aryl sulfonic acid side groups (80−90 wt %) and a commercially available poly(VDF-*co*-HFP) copolymer (kindly supplied by 3M/Dyneon and composed of 80 mol % of VDF and 20 mol % of HFP assessed by ^{19}F NMR spectroscopy) (10−20 wt %) were placed in a 50 mL flask and stirred with NMP (60/40: solvent/terpolymer—commercially available poly(VDF-*co*-HFP) copolymer blend) for 1 h at 65 °C. It was spread onto a PTFE substrate (Teflon), and a thermal cycle was used to evaporate NMP: 50 °C for 2 h, then 80 °C for 4 h, and finally 120 °C for 10 h. Then, the film was peeled off from the substrate. Slightly hazy films were obtained from such a solvent-casting process.

2.5. Electrochemical Properties. *2.5.1. Determination of Water Uptake and Hydration Number.* To assess the water uptake (W_{water}) at 25 °C, the membranes (2.5 × 2.5 cm^2) were first dried under vacuum at 90 °C for 48 h to obtain their dry weights (W_{dry}) and then placed for 3 h in a climate chamber from Binder APT Line KBF equipped with an electronically controlled preheating chamber, a humidification, and dehumidification system with capacitive humidity sensor suitable for stability tests according to ICH guideline Q1A (R2). The weights of the water-swollen membranes (W_{wet}) were obtained. The water uptake was measured at 98% RH and 28 °C and then calculated as follows:

$$W_{water} = [(W_{wet} - W_{dry})/W_{dry}] \times 100\%$$

The experimental IECs of fluorinated terpolymeric ionomers were assessed using a titration method. Membranes were equilibrated in 2 M NaCl solution at room temperature for 2 days before titration. The protons released into the aqueous solution were titrated with 0.025 M NaOH solution using phenolphthalein as the indicator. The experimental IEC values of the grafted terpolymer membranes were determined according to the equation

$$\text{IEC (mequiv/g)} = (M_{NaOH} \times V_{NaOH})/W_{dry}$$

where M_{NaOH} and V_{NaOH} stand for the molar concentration and volume (mL) of the aqueous NaOH solution used in titration and W_{dry} (g) is the weight of dry membrane.

The hydration number (λ) was assessed as follows:

$$\lambda = [(W_{wet} - W_{dry})/18.01] \times 1000/(W_{dry} \times \text{IEC})$$

where the symbols are defined above.

2.5.2. Proton Conductivity Measurements. The proton conductivity (σ) was assessed by electrochemical impedance spectroscopy[54] using a HP 4192 apparatus. Membrane samples (2 × 2 cm^2) were clamped between two stainless steel electrodes of the temperature-controlled conductivity cell. In-plane (four-electrode) resistance measurements were also carried out at ambient temperature and at 95−100% relative humidity. The conductivity was assessed from the following relationship: $\sigma = (1/R_e) \times (e/s)$, where e, R_e, and S are the thickness, the resistance of the membrane, and its surface, respectively. In all the cases, R was derived from the low intercept of the high-frequency semicircle on a complex impedance plane with Re(Z) axis.

3. RESULTS AND DISCUSSION

Novel fluorinated arylsulfonic acid membranes were processed from functional fluoropolymers in a four-step process. The first one consists in the synthesis and the properties of poly(VDF-*ter*-HFP-*ter*-TFMAA) terpolymers obtained by radical terpolymerization of vinylidene fluoride (VDF), hexafluoropropylene (HFP), and α-trifluoromethacrylic acid (TFMAA) initiated by peroxides in 1,1,1,3,3-pentafluorobutane as the solvent. The second step deals with the chemical reduction of carboxylic acid side function in the terpolymers into corresponding hydroxyl dangling groups.

The third part describes the etherification reaction of these fluorinated terpolymers that bear primary hydroxyl groups with 4-phenol sulfonic acid in the presence of diisopropylazodicarboxylate (DIAD) (Scheme 1). Finally, the fourth action consisted in processing membranes from these original fluorinated graft terpolymers and to characterize their physicochemical and electrochemical properties. All these steps are detailed below.

3.1. Synthesis and Characterization of Poly(VDF-*ter*-HFP-*ter*-TFMAA) Terpolymers. *3.1.1. Radical Copolymerization of VDF with TFMAA.*[49] α-Trifluoromethacrylic acid (TFMAA), synthesized from several routes,[56] has found interesting applications in the coating and photoresist materials industries.[57,58] However, TFMAA monomer exhibits a poor behavior in radical homopolymerization leading to oligomers in low yields.[59,60] Nevertheless, TFMAA was successfully copolymerized with various comonomers[61] such as vinyl ethers, MMA, 1-decene-2-methyl-1-hexene, norbornene, and styrenic derivatives, well-summarized in an excellent review.[58] Its radical copolymerization with vinylidene fluoride[49,50] enabled us to

assess their reactivity ratios (r_{TFMAA} = 0 and r_{VDF} = 0.33 ± 0.09 at 55 °C), hence confirming the difficult propagation of TFMAA. Interestingly, the synthesized poly(VDF-*co*-TFMAA) copolymers showed a tendency of alternating structures which is quite unusual for copolymers of VDF,[16] except for hexafluoroisobutylene,[62] hexafluoroacetone,[41] and methyl α,β,β-trifluoroacrylate.[63]

3.1.2. Radical Terpolymerization of VDF with HFP and TFMAA. To enhance both the reactivity of VDF and the physicochemical and thermal properties of the resulting terpolymers, hexafluoropropylene (HFP) was inserted as a termonomer in the copolymerization. The radical terpolymerization of VDF, HFP, and TFMAA was carried out in 1,1,1,3,3-pentafluorobutane solution at 134 °C and initiated by 2,5-bis(*tert*-butylperoxy)-2,5-dimethylhexane, as depicted in Scheme 1.

A series of six terpolymerizations were carried out at 134 °C (at that temperature, the initiator's half-life is 1 h) for 6 h using an initial $[initiator]_0/([VDF]_0 + [HFP]_0 + [TFMAA]_0)$ initial molar ratio, C_0, of 0.9% (Table 1). Below this value (i.e., C_0 = 0.5 mol %), a low olefin consumption was noted (i.e., a low drop of pressure in the autoclave was observed) as well as a poor terpolymerization massic yield (ca. 20%). After precipitation from cold pentane and drying, the synthesized poly(VDF-*ter*-HFP-*ter*-TFMAA) terpolymers were characterized by ^{1}H, ^{13}C, and ^{19}F NMR spectroscopy. All ^{1}H NMR spectra (Figure 1) exhibit the expected signals assigned to

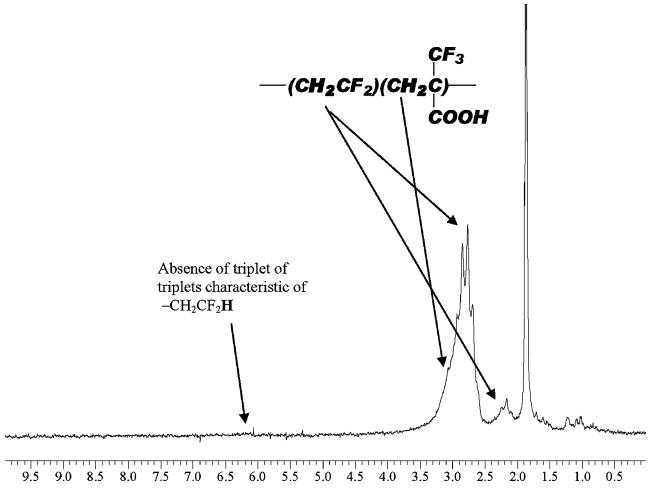


Figure 1. ^{1}H NMR spectrum of poly(VDF-*ter*-HFP-*ter*-TFMAA) terpolymer, recorded in deuterated acetone at 23 °C. Terpolymerization conditions: $[2,5\text{-bis}(tert\text{-butylperoxy})\text{-}2,5\text{-dimethylhexane}]_0/([VDF]_0 + [HFP]_0 + [TFMAA]_0)$ = 0.9%, 134 °C, 6 h, and VDF:HFP:TFMAA initial molar ratio in the feed = 77.1:18.9:3.2 (expt 5, Table 1) where VDF, HFP, and TFMAA stand for vinylidene fluoride, hexafluoropropylene, and α-trifluoromethacrylic acid, respectively.

methylene groups of VDF[49,63,64] (normal VDF−VDF addition) and TFMAA units in the 3.0−3.4 ppm range, and also the multiplet (of small intensity or even absent when alternated VDF−TFMAA dyads were favored[49,50]) attributed to the tail-to-tail VDF reversed addition centered at 2.4 ppm.[64,65] Interestingly, the absence of the characteristic triplet of triplets centered at 6.3 ppm, assigned to the terminal proton in $-(CH_2CF_2)-CH_2CF_2\mathbf{H}$ end group, evidences that the transfer reaction to the terpolymer did not occur.[64,65]

Both these statements above were confirmed by the ^{19}F NMR spectra (Figure 2) that do not exhibit any doublet of

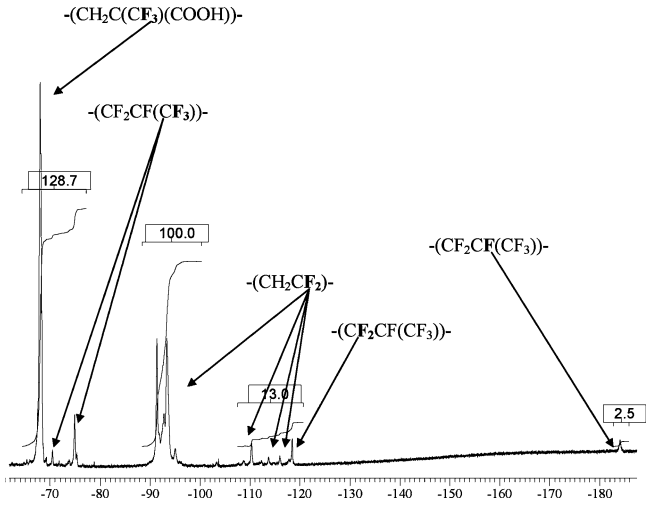


Figure 2. ^{19}F NMR spectrum of poly(VDF-*ter*-HFP-*ter*-TFMAA) terpolymer, recorded in deuterated acetone. Terpolymerization conditions: $[2,5\text{-bis}(tert\text{-butylperoxy})\text{-}2,5\text{-dimethylhexane}]/([VDF]_0 + [HFP]_0 + [TFMAA]_0)$ = 0.9%, 134 °C, 6 h, and VDF:HFP:TFMAA initial molar ratio in the feed = 69.2:17.1:13.7 (expt 1, Table 1) where VDF, HFP, and TFMAA stand for vinylidene fluoride, hexafluoropropylene, and α-trifluoromethacrylic acid, respectively.

multiplets centered at −114.8 ppm[64] but display a signal located at −93.8 ($I_{-93.8}$) assigned to the difluoromethylene groups in VDF units adjacent to a TFMAA unit (i.e., VDF−TFMAA dyad).[49,50] Furthermore, the ^{19}F NMR spectra show the characteristic signal[49,63−66] centered at about −91.1 ppm (named $I_{-91.1}$) assigned to the difluoromethylene groups located in the head-to-tail VDF chaining (i.e., normal VDF addition). In addition, a series of other signals (of lower intensities) were noted at −113.4 ($I_{-113.4}$), −115.7 ($I_{-115.7}$) and −92.8 ppm ($I_{-92.8}$), attributed to CF_2 groups in $(CH_2-\mathbf{CF_2})-(CF_2-CH_2)-(CH_2-CF_2)$, $(CH_2-CF_2)-(\mathbf{CF_2}-CH_2)-(CH_2-CF_2)$, and $(CH_2-CF_2)-(CF_2-CH_2)-(CH_2-\mathbf{CF_2})-(CH_2-CF_2)-$ sequences (i.e., reversed head-to-head VDF additions), respectively (Table 2). Moreover, the signal located

Table 2. ^{19}F NMR Assignments of Poly(VDF-*ter*-HFP-*ter*-TFMAA) Terpolymers Recorded in Deuterated Acetone[a]

chemical shift (ppm)	structure	integrals in eq 1
−68.1	$-CH_2CF_2-[CH_2C(C\underline{F_3})COOH]-$	$I_{-68.1}$
−71.2	$-CH_2CF_2-CF_2CF(CF_3)-CF_2CH_2-$	$I_{-71.2}$
−74.8	$-CH_2CF_2-CF_2CF(CF_3)-CH_2CF_2-$	$I_{-74.8}$
−91.1	$-CF_2-CH_2\mathbf{CF_2}-CH_2CF_2-$	$I_{-91.1}$
−92.8	$(CH_2CF_2)-(CF_2CH_2)-(CH_2C\underline{F_2})-(CH_2CF_2)$	$I_{-92.8}$
−93.8	$-(CH_2\mathbf{CF_2})-[CH_2C(CF_3)(COOH)]-$	$I_{-93.8}$
−110.1	$-CH_2\mathbf{CF_2}-CF_2CF(CF_3)-$	$I_{-110.1}$
−113.4	$-(CH_2C\underline{F_2})-(CF_2CH_2)-(CH_2CF_2)-$	$I_{-113.4}$
−115.7	$-(CH_2CF_2)-(C\underline{F_2}CH_2)-(CH_2CF_2)-$	$I_{-115.7}$
−118.9	$-CH_2CF_2-\mathbf{CF_2}CF(CF_3)-$	$I_{-118.9}$
−183.8	$-CH_2CF_2-CF_2\mathbf{C}F(CF_3)-$	$I_{-183.8}$

[a]VDF, HFP, and TFMAA stand for vinylidene fluoride, hexafluoropropylene, and α-trifluoromethacrylic acid, respectively.

dx.doi.org/10.1021/ma3001912 | *Macromolecules* 2012, 45, 3145−3160

at −110.1 ppm ($I_{-110.1}$) is assigned to the difluoromethylene group of VDF units adjacent to a HFP unit (VDF-HFP dyad). Surprisingly, the experiments that yielded terpolymers with a high amount of TFMAA (runs 1−3) led to intense integral of the signal centered at −93.8 ppm and evidence a high alternation of VDF and TFMAA. In a concomitant way, the integrals of both signals at −113.4 and −115.7 ppm of reversed VDF-VDF dyads were consequently minimized as noted in radical copolymerization.[49,50]

In addition, the ^{13}C NMR spectra (Figure S1 in Supporting Information) of the poly(VDF-*ter*-HFP-*ter*-TFMAA) terpolymers exhibited the following features: (i) a singlet centered at 169 ppm assigned to the carbonyl group in $-(CH_2C(CF_3)\mathbf{C}OOH)$, (ii) triplets ($^1J_{CF}$ = 250 Hz) centered at 121 ppm characteristic of the $\mathbf{C}F_2$ groups, and finally (iii) quintets ($^2J_{CF}$ = 32 Hz) centered at 44 ppm assigned to the $\mathbf{C}H_2$ groups in VDF units.

Furthermore, the chemical shifts centered at −71.2 ($I_{-71.2}$), −74.8 ($I_{-74.8}$) are assigned to the trifluoromethyl side group arising from HFP in the terpolymer: $-CH_2CF_2-CF_2CF(C\mathbf{F}_3)-CF_2CH_2-$, $-CH_2CF_2-CF_2CF(C\mathbf{F}_3)-CH_2CF_2-$, respectively, while that centered at −68.1 ($I_{-68.1}$) is attributed to the trifluoromethyl group of TFMAA in the terpolymer, i.e., $-(CH_2C(C\mathbf{F}_3)(COOH)-$. In comparison, that of nonreacted free monomer is centered at −67.1 ppm[49] as a sharp singlet. In all experiments, the TFMAA conversion rates were quantitative when C_0 = 0.9%, and this monomer exhibited a high reactivity, reaching a high incorporation in the terpolymers (up to ca. 40 mol %) from only ca. 6−14 mol % in the feed (Figure S2). In addition, the signals centered at −118.9 ($I_{-118.9}$) and −183.8 ppm ($I_{-183.8}$) are assigned to the difluoromethylene group in $-CH_2CF_2-C\mathbf{F}_2CF(CF_3)-$ dyad and to the tertiary fluorine in $CF_2C\mathbf{F}(CF_3)$ of HFP, respectively.

From the integrals of these signals in the ^{19}F NMR spectra, the assessments of the molar fractions of VDF, HFP, and TFMAA base units in the terpolymers are given by the following equations (eqs 1a−1c):

$$\text{mol \% of VDF in the terpolymer} = x_{VDF} = \frac{I_A}{I_A + I_B + I_C} \times 100 \quad (1a)$$

$$\text{mol \% of HFP in the terpolymer} = x_{HFP} = \frac{I_B}{I_A + I_B + I_C} \times 100 \quad (1b)$$

$$\text{mol \% of TFMAA in the terpolymer} = x_{TFMAA} = \frac{I_C}{I_A + I_B + I_C} \times 100 \quad (1c)$$

with

$$I_A = \frac{I_{-91.1} + I_{-92.8} + I_{-93.8} + I_{-110.1} + I_{-113.4} + I_{-115.7}}{2}$$

$$I_B = \frac{I_{-71.2} + I_{-74.8}}{3}$$

$$I_C = \frac{I_{-68.1}}{3}$$

All ^1H, ^{13}C, and ^{19}F NMR spectra (Figures 1 and 2, Figure S1) enabled us to characterize the microstructures of these terpolymers without ambiguity and indicate a random structure composed of poly(VDF-*alt*-TFMAA) blocks separated by one HFP unit.

3.1.3. Molecular Weights and Thermal Properties of Poly[(VDF-alt-TFMAA)-co-HFP] Terpolymers. Although there is a lack of standards for fluoropolymers, the values of the average molecular weights (determined by size exclusion chromatography, SEC, with poly(methyl methacrylate) standards) of the poly[(VDF-*alt*-TFMAA)-*co*-HFP)] terpolymers were ranging from 10 000 to 21 400 g mol^{-1} (Table 1). It was noted that the lower the initial mol % of TFMAA, the higher the average molecular weights of the resulting terpolymers. Nevertheless, these values seem low although no transfer reaction was observed as evidenced by the absence of signals centered at 6.3 and −114.8 ppm in ^1H and ^{19}F NMR spectra,[49] respectively. This may arise from solution terpolymerization in contrast to an aqueous process that led to higher molecular weight terpolymers.[50]

The thermal properties of these terpolymers were characterized by assessing the glass transition, T_g, and decomposition, T_{dec}, temperatures from differential scanning calorimetry (DSC) and thermogravimetric analysis (TGA), respectively.

The T_g values were ranging between −27 and −18 °C, but no endothermal peak was observed. Hence, these terpolymers exhibit elastomeric behaviors. These T_g values also confirmed that (i) when the final mol % of VDF in the terpolymer increased, the T_g decreased[66] (as expected because of the low T_g value of PVDF, ca. −40 °C[41]) and (ii) the higher the final mol % of TFMAA in the terpolymer, the higher the T_g[68] and the lower the elastomeric behavior of the material (i.e., TFMAA comonomer brings some hardness since both CF_3 and CO_2H side groups stiffen the terpolymers).

The thermogravimetry (TGA) thermograms, carried out under air (Figure 3), evidenced that these terpolymers exhibit

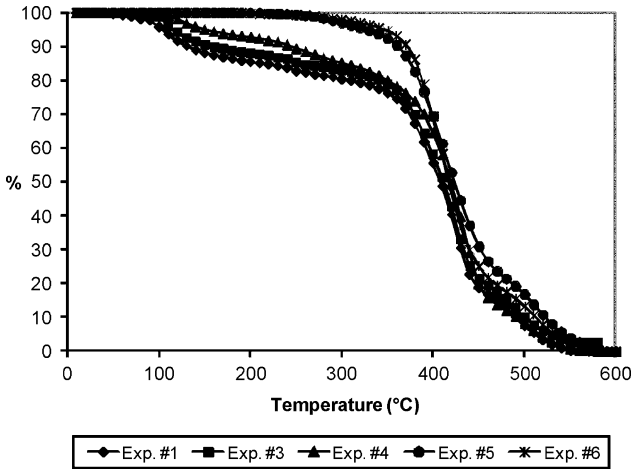


Figure 3. TGA thermograms under air of poly[(VDF-*alt*-TFMAA)-*co*-HFP] terpolymers (56.8:3.5:39.7 in expt 1), (59.5:5.1:35.4 in expt 3), (80.4:12.4:7.2 in expt 4), (86.2:10.4:3.2 in expt 5), and (88.8:10.1:1.1 in expt 6).

fair to suitable thermal stabilities: their decomposition started from 160 to 320 °C with respect to the TFMAA content. Actually, these TGA thermograms indicate that the higher the TFMAA molar percentage in the terpolymers, the lower the thermostability. Indeed, such a degradation was induced from a decarboxylation reaction of CO_2H side functions in TFMAA

dx.doi.org/10.1021/ma3001912 | *Macromolecules* 2012, 45, 3145−3160

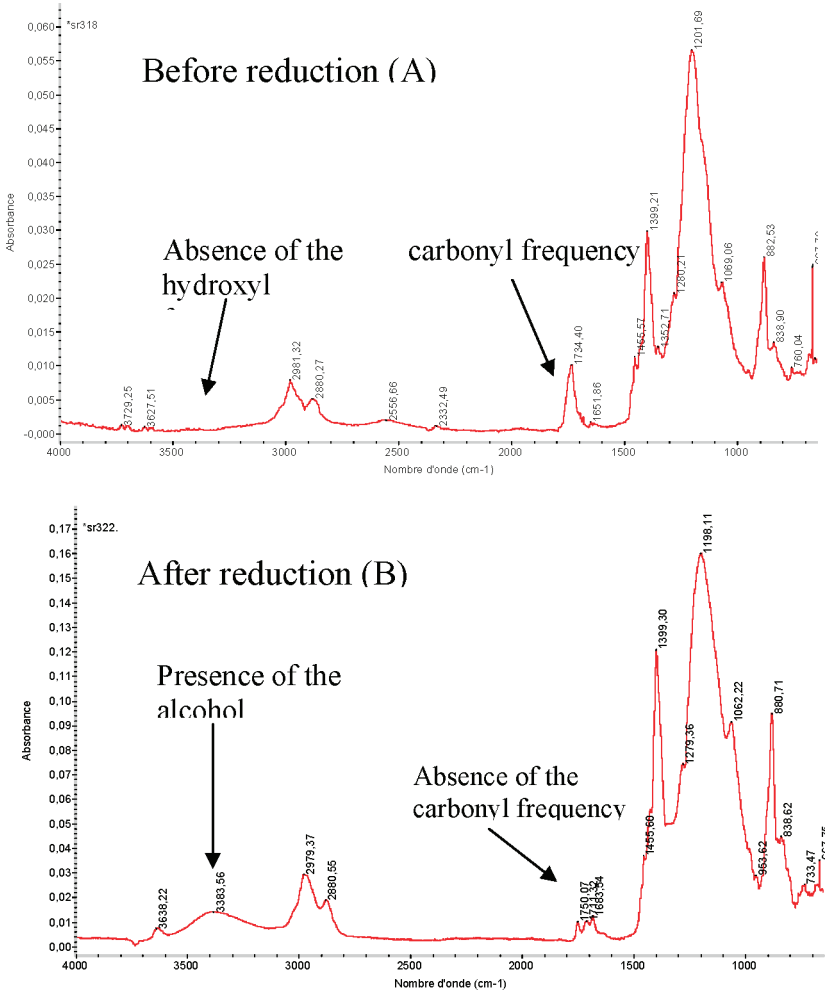


Figure 4. IR spectra of a nonreduced (A) (expt 1, Table 1) and a reduced (B) poly[(VDF-*alt*-TFMAA)-*co*-HFP] terpolymer (achieved from terpolymer prepared in expt 1).

units. Hence, it was of interest to chemically modify such functions and our choice was to favor a reduction to get hydroxyl pendant groups.

3.2. Chemical Reduction of the Carboxylic Acid Functions in TFMAA of Poly[(VDF-*alt*-TFMAA)-*co*-HFP] Terpolymers. Several methods are known to allow the reduction of carboxylic groups into hydroxyl functions, and the reduction in the presence of $LiAlH_4$ was chosen (step I, Scheme 1).

This reaction occurred in the presence of a 4-fold mole excess of $LiAlH_4$ about the poly[(VDF-*alt*-TFMAA)-*co*-HFP] terpolymer. After reaction and work-up, the reduced terpolymers were obtained in 95 mass % yield. The conversion rates ranged between 70 mol % (experiments 1−3) and 100 mol % (experiments 4−6). These resulting hydroxyl terpolymers were characterized by IR and NMR spectroscopies and by SEC, and the thermal properties were assessed by DSC and TGA. After reduction of the carboxylic acid functions, IR spectra display the absence of the bands at 1734 cm^{-1}, assigned to the carbonyl frequency, showing that the reduction of carboxylic end groups was complete (Figure 4). The other frequencies bands were not modified by the reduction of carboxylic end group, except the formation of the broad bands at 3380 cm^{-1} which are characteristic of the formation of alcohol function. Interestingly, the IR spectra of these terpolymers did not exhibit any vibration frequency at 1660 cm^{-1}, attributed to −CF═CH− which could be generated by undesirable dehydrofluorination reactions of VDF−HFP dyads in the presence of $AlLiH_4$.

The successful reduction of the carboxylic acids into hydroxyl functions was confirmed by ^1H NMR spectra (Figure 5) which

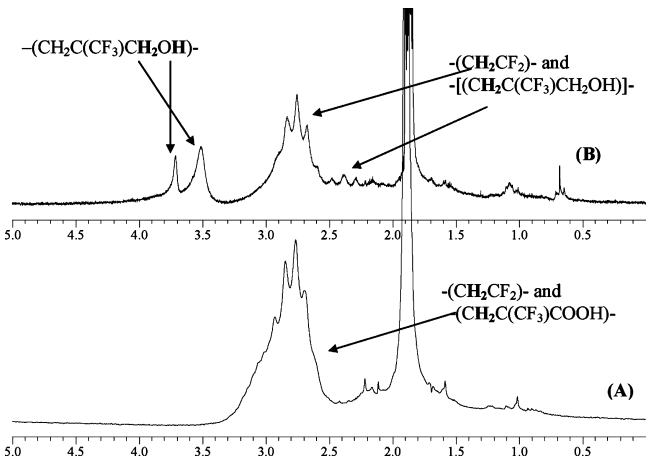


Figure 5. ^1H NMR spectra of a non modified poly[(VDF-*alt*-TFMAA)-*co*-HFP] terpolymer (A) (expt 3, Table 1) and a reduced terpolymer (B), recorded in deuterated acetone (terpolymer prepared in expt 3); a 0.2 ppm high field shift is noted.

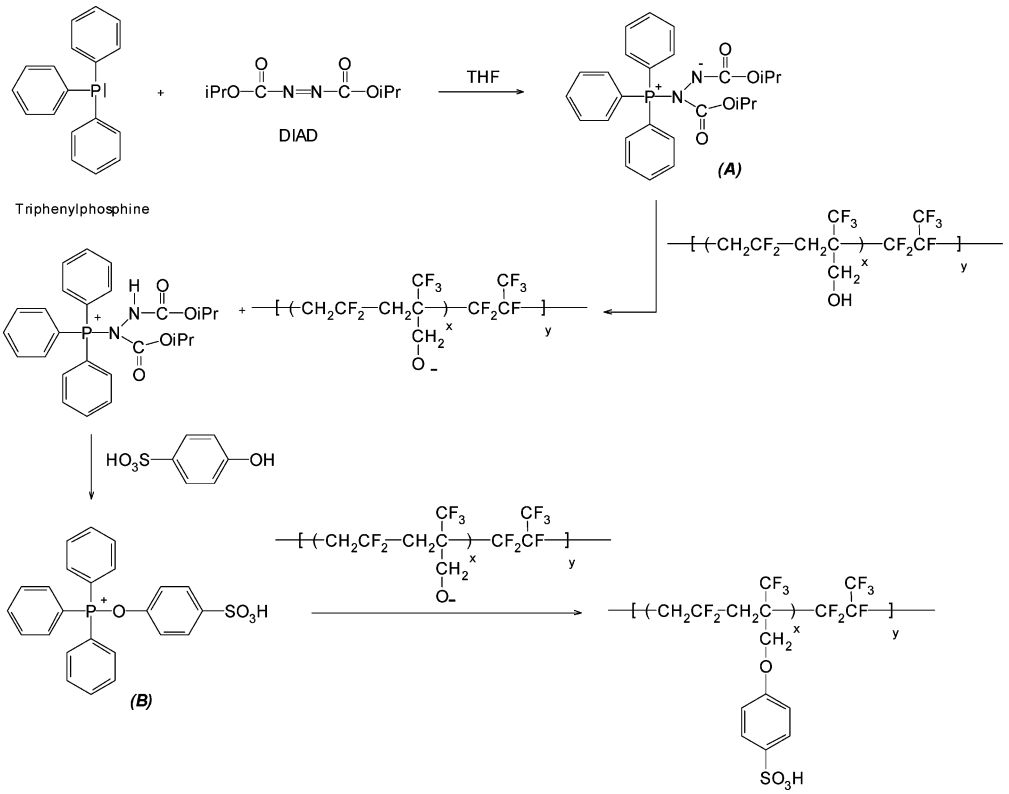
dx.doi.org/10.1021/ma3001912 | *Macromolecules* 2012, 45, 3145−3160

Table 3. Determination of the Compositions of the Grafted Poly[(VDF-*alt*-TFMAA)-*co*-HFP] Terpolymer by 4-Phenolsulfonic Acid[a]

ionomers	mol % of VDF in the terpolymer	mol % of HFP in the terpolymer	mol % of grafted TFMAA in the terpolymer	mol % of TFMAA in the terpolymer	grafting conv rates (%)	T_g (°C)	T_d (°C) Δm (10%) under air	M_n (g mol^{-1})	M_w (g mol^{-1})
A (expt 1)	76	8	12.0	4.0	75	6	170	10 800	17 300
B (expt 3)	82	3	8.0	7.0	53	2	190	12 000	21 700
C (expt 4)	86	5	6.0	3.0	66	−2	210	14 900	26 800
D (expt 6)	94	3	1.5	1.5	50	−17	230	22 000	35 200

[a]Average molecular weights, M_n and M_w, assessed from SEC with poly(methyl methacrylate) standards. T_g and T_d were determined by DSC and TGA, respectively. VDF, HFP, TFMAA, T_g, and T_d stand for vinylidene fluoride, hexafluoropropylene, α-trifluoromethacrylic acid, glass transition temperature, and decomposition temperature, respectively.

Scheme 2. Etherification Reaction between Reduced Poly[(VDF-*alt*-TFMAA)-*co*-HFP] Terpolymers and 4-Phenolsulfonic Acid According to a Mitsunobu Synthesis[55]



do not display any signal in the 5−6.5 ppm range, but they exhibit signals centered at 3.5 and 3.7 ppm attributed to the three protons in −C**H**$_2$OH and −CH$_2$O**H** groups, respectively. The addition of one drop of CCl_3NCO in the NMR tube induced a low field shift from 3.5 (C(CF$_3$)C**H**$_2$OH) to 4.9 ppm (−CH$_2$OC(O)NHCCl$_3$) −(Figure S3), as an expected behavior characteristic of protons adjacent to a hydroxyl group.[67] Furthermore, the addition of trifluoroacetic acid to the reduced poly[(VDF-*alt*-TFMAA)-*co*-HFP] terpolymers produced a chemical shift from 3.7 (CH$_2$C(CF$_3$)CH$_2$O**H**) to 11.5 ppm, which confirmed the attribution of the broad singlet centered at 3.7 ppm to the proton of hydroxyl group. Interestingly, the signal assigned of the C**H**$_2$ in TFMAA in the nonreduced poly[(VDF-*alt*-TFMAA)-*co*-HFP] (δ = 3.4 ppm) underwent a high field shift to 2.4 ppm: C**H**$_2$C(CF$_3$)-(CH$_2$OH). The ^{19}F NMR spectra exhibited the characteristic signals of VDF, HFP, and TFMAA units in poly[(VDF-*alt*-TFMAA)]-*co*-HFP) terpolymers although it did not show any change in the chemical shifts of the signals assigned to the trifluoromethyl and the difluoromethylene groups of TFMAA and VDF, respectively.

In addition, the ^{13}C NMR spectra of these reduced terpolymers display the same characteristic doublets or triplets or quartets of carbon atoms in the poly[(VDF-*alt*-TFMAA)-*co*-HFP] (i.e., at 115−130 ppm for **C**F, **C**F$_2$, **C**F$_3$ and ca. 37−48 ppm for **C**H$_2$) with, however, a decrease or quasi-vanishing of the singlet centered at 169 ppm, assigned to −(C(CF$_3$)**C**OOH). The partially or the complete absence of this signal confirms the reduction of these carboxylic acid functions into hydroxyl groups.

Furthermore, SEC showed that the average molecular weights in number (M_n) of the terpolymers were not modified by that reduction since they were ranging from 10 000 to 21 400 g mol^{-1} (Tables 1−3). These values are relative and not absolute as recently reported from poly(VDF-*co*-*tert*-butyl α-trifluoromethyl acrylate) copolymers bearing CF$_3$ end groups.[49b] M_n values assessed from ^{19}F NMR spectroscopy showed a discrepancy with those assessed by SEC. Differential

dx.doi.org/10.1021/ma3001912 | *Macromolecules* 2012, 45, 3145−3160

scanning calorimetry and thermogravimetric analyses also demonstrated that the reduction of carboxylic end groups did not produce any drastic modifications on the T_g values of the terpolymers. Furthermore, the thermal stabilities of such reduced poly[(VDF-*alt*-TFMAA)-*co*-HFP] terpolymers were assessed by TGA. The thermogravimetric curves showed an increase of the thermal stability and of the decomposition temperature (Figure S4). This better stability can be explained by the decrease of the content of carboxylic functions noted after reduction that hence decreased the decarboxylation reaction. Nevertheless, the reduced or poly[(VDF-*alt*-TFMAA)-*co*-HFP] terpolymers showed a thermogravimetric loss 10 wt % between 90 and 180 °C assigned to the elimination of water (present within the alcohol functions) and the dehydration of the hydroxyl groups (Figure S4).

3.3. Chemical Etherification of the Hydroxyl Functions of the Poly[(VDF-*alt*-TFMAA)-*co*-HFP)] Terpolymers: Grafting Reaction. This intermolecular etherification reaction, via a Mitsunobu reaction,[55] occurred between 4-phenolsulfonic acid and hydroxyl functions of the reduced poly[(VDF-*alt*-TFMAA)-*co*-HFP] components on work up with diisopropyl azodicarboxylate (DIAD) and triphenylphosphine (Scheme 2) and is concomitant with the oxidation of the phosphorus atom. This etherification reaction is regarded to proceed through four steps as reported in the Supporting Information.

This reaction was performed in anhydrous THF under an inert atmosphere and was monitored by IR spectroscopy. Besides the characteristic absorption of C−F bond noted in the 900−1200 cm^{-1} range, the IR spectra of grafted materials exhibited frequencies at 3360 and 1023 cm^{-1} assigned to the SO_2OH stretching vibrations of the sulfonic acid groups. The triphenylphosphine oxide was removed from the reactional mixture by a continuous liquid/liquid extraction in the presence of hexane. The complete extraction of $P(O)(Ph)_3$ was identified by ^{31}P NMR spectroscopy (i.e., absence of the signal centered at 31.6 ppm).

The successful grafting of 4-phenolsulfonic acid was confirmed by the ^1H NMR spectra (Figure 6 and Figure S5)

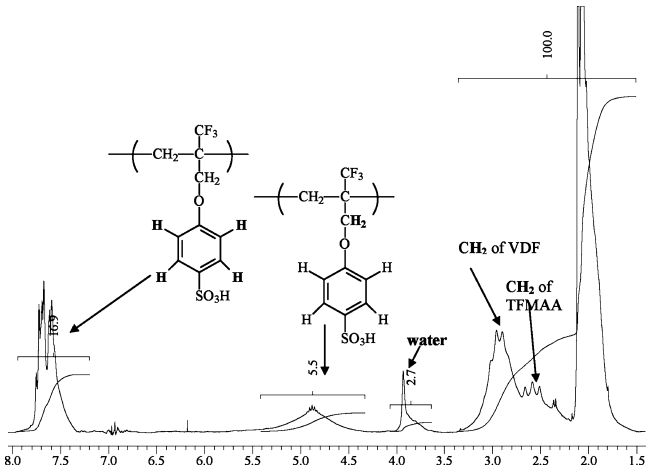


Figure 6. ^1H NMR spectrum of a hydroxyl-containing poly[(VDF-*alt*-TFMAA)-*co*-HFP] terpolymer (ionomer B, Table 3) grafted by 4-phenolsulfonic acid, recorded in deuterated acetone at room temperature, where VDF, HFP, and TFMAA stand for vinylidene fluoride, hexafluoropropylene, and α-trifluoromethacrylic acid, respectively.

which exhibit (i) an A_2B_2 system ranging between 7.3 and 7.8 ppm ($I_{7.5}$) assigned to the aromatic protons of the aryl sulfonic acid grafted onto the terpolymers, (ii) a complex system centered at 4.9 ppm ($I_{4.9}$) that corresponds to $-CH_2-O-C_6H_4-SO_3H$ (the signal that corresponds to CH_2OH underwent a low field shift of 1 ppm), (iii) a signal at 3.9 ppm ($I_{3.9}$) attributed to water absorbed by the sulfonic acid functions, (iv) a small to negligible signal at 3.8 ppm ($I_{3.8}$) overlapping with that of water assigned to $-CH_2OH$ residue, (v) a broad multiplet centered at ca. 3 ppm ($I_{3.0}$) corresponding to methylene in CH_2-CF_2 units (VDF), and finally (vi) a multiplet at 2.6 ppm ($I_{2.6}$) characteristic of the methylene groups of TFMAA in the terpolymers (i.e., $-(CH_2C(CF_3)-(CH_2-O-Ph-SO_3H))-$. The comparison of both ^{19}F NMR spectra of poly[(VDF-*alt*-TFMAA)-*co*-HFP] terpolymers with those of the reduced and grafted ones (Figure 6) led to an additional proof on the successful reduction and grafting. The overlapping of both methylene groups in VDF and TFMAA units is clearly observed in Figure 1, but those of the reduced and grafted with phenylsulfonic acid (i.e., CH_2OR where R stands for H or $C_6H_4SO_3H$) did not display such an overlapping. Indeed, a high field shift of CH_2 of TFMAA is noted in both last spectra, hence making clearer the difference of the multiplets assigned to both methylene groups. This arises from the lower electron-withdrawing effect of CH_2OR versus CO_2H.

The ^{19}F NMR spectrum (Figure S6) exhibits the expected signals centered at the same following chemical shifts as above, i.e., (i) at −91.1 ($I_{-91.1}$), −92.8 ($I_{-92.8}$), −93.8 ($I_{-93.8}$), −110.1 ($I_{-110.1}$) (and in certain cases: −113.4 ($I_{-113.4}$), −115.7 ppm ($I_{-115.7}$)), characteristic of CF_2 of VDF units in the head-to-tail, head-to-head additions, and adjacent to TFMAA and HFP monomers; (ii) a signal centered at −68.1 ppm ($I_{-68.1}$) assigned to CF_3 arising from the TFMAA (actually, no difference in the chemical shifts of that signal was observed between the nonmodified and the grafted terpolymers); (iii) and finally multiplets at −71.2 ($I_{-71.2}$), −74.8 ($I_{-74.8}$) assigned to the trifluoromethyl side group of HFP, −118.9 ($I_{-118.9}$) and −183.8 ppm ($I_{-183.8}$) corresponding to the CF_2 and to the tertiary fluorine of HFP, respectively.

Hence, the molar percentages of VDF (eq 1a), HFP (eq 1b), and TFMAA (grafted and nongrafted, eq 1c) in the terpolymers can be assessed from eqs 1a, 1b, and 1c described above. The molar percentages of grafted groups in the terpolymers can be calculated from ^1H NMR as follows:

$$\text{total mol \% of TFMAA in the terpolymer} = x_{\text{TFMAA}} \quad (2a)$$

$$\text{mol \% of grafted TFMAA} = \frac{I_D}{I_E} \times x_{\text{TFMAA}} \times 100 \quad (2b)$$

where $I_D = I_{7.5}$ and $I_E = I_{3.0} + I_{2.6} + I_{2.4}$

Table 3 shows the molar percentages of VDF, HFP, TFMAA, and grafted TFMAA in the resulting terpolymers and also their average molecular weights (M_n) and thermal properties. The conversion rates of this reaction ranged from 50 to 75%. After grafting, the M_n values were slightly higher than those of the reduced terpolymers and also indicated that the chemical modification occurred. They ranged from 10 800 g mol^{-1} (ionomer A) to 22 000 g mol^{-1} (ionomer D) with reference to PMMA standards. Furthermore, glass transition temperatures of the grafted terpolymers (Table 3) showed that the incorporation of aryl sulfonic acid dangling function led to a significant increase of the T_g (ca. 20 °C), reaching values up

dx.doi.org/10.1021/ma3001912 | *Macromolecules* 2012, 45, 3145−3160

Table 4. Characteristics of Membranes Prepared from A, B, C, and D Ionomers: Poly(VDF-*co*-HFP) Copolymer (from NMP)[a]

ionomers	mass % of ionomer in the formulation	mass % of commercial poly-(VDF-co-HPF)copolymer in the formulation	film thickness (μm)	IEC (mequiv/mol)	water uptake (%)	λ	proton conductivity (mS cm^{-1})	T_g (°C)
A	80	20	88	1.2	67	3.1	9.1	4
B	80	20	88	0.9	54	3.3	5.2	2
C	80	20	99	0.7	51	4.0	2.9	−5
D	90	10	94	0.2	42	11.6	0.5	−19

[a]IEC, λ, and T_g stand for ionic exchange capacity, hydration number, and glass transition temperature, respectively.

to +6 °C. A further evidence to justify the successful grafting of 4-phenolsulfonic acid onto hydroxyl-containing fluorinated terpolymers stems from the presence of both CF_3 and especially $C_6H_4SO_3H$ dangling groups that stiffen the terpolymer, just like hydrogen bonding which thus increased the T_g value.

Finally, the study of the TGA thermograms (under oxidative conditions) enabled us to observe four characteristic steps: (i) combination of water elimination and dehydration of free hydroxyl functions (between 90 and 150 °C), (ii) desulfonation reaction (160 < T < 330 °C), (iii) the dehydrofluorination of the backbone[41] (340 < T < 450 °C), and (iv) finally degradation of the backbone (from 500 °C[68]). From these curves, the characteristic thermogravimetric loss at 10% was assessed. These ionomers exhibit fair to satisfactory thermal stabilities since their decompositions occurred from 170, 190, 210, and 230 °C, for A, B, C, and D ionomers under air, respectively. These results can be explained by different features: (i) the higher the mol % of grafted 4-phenolsulfonic acid onto TFMAA (i.e., the higher the mol % of sulfonic acid), the higher the mol % of water in the terpolymer, and the faster the desulfonation; (ii) the higher the molar percentages of VDF in the terpolymer, the higher the thermal stability.

3.4. Processing and Characterization of Membranes Incorporating Poly[(VDF-*alt*-TFMAA)-*co*-HFP] Terpolymers That Bear Sulfonic Acid Side Functions. Membranes were processed from blends of A, B, C, and D ionomers with commercially available poly(VDF-*co*-HFP) copolymers. Their preparation was achieved using *N*-methylpyrrolidone (NMP) as the solvent and a weight ratio ranging between 80:20 and 90:10 (ionomer:commercially available poly(VDF-*co*-HFP) copolymer). Those containing 80:20 led to the best film-forming membrane properties (homogeneous, color, and state). The characteristics of these obtained membranes (ratio, thickness, ionic exchange capacities, water uptake, hydration number, conductivities, and T_gs) are gathered in Table 4.

Various properties of these membranes based on A, B, C, and D ionomers were investigated such as ionic exchange capacity (IEC), thermal stability, water uptake, hydration number, and proton conductivity.

The molar percentages of sulfonic acid function of A, B, C, and D ionomers were assessed by ^{1}H NMR spectroscopy (Table 3). The information combined with the ratio of monomers in the terpolymer (using ^{19}F NMR spectroscopy; Table 3) enabled us to assess the ionic exchange capacity (IEC, mequiv H^+/mol). The IEC can be determined from eq 3, and the results are gathered in Table 4.

α = mol % of VDF in the graft poly[(VDF-*alt*-TFMAA)-*co*-HFP]), assessed by eq 1a; Table 3.

β = mol % of HFP in the graft poly[(VDF-*alt*-TFMAA)-*co*-HFP], assessed by eq 1b; Table 3.

γ = mol % of grafted TFMAA in the graft poly[(VDF-*alt*-TFMAA)-*co*-HFP], assessed by eq 2a; Table 3.

δ = mol % of nonmodified TFMAA in the graft poly[(VDF-*alt*-TFMAA)-*co*-HFP], assessed by eq 2b; Table 3.

For a graft poly[(VDF-*alt*-TFMAA)-*co*-HFP] terpolymer:

$$\text{IEC (equiv/g)} = \frac{1}{\frac{\alpha}{\gamma} \times 64 + \frac{\beta}{\gamma} \times 150 + \frac{\delta}{\gamma} \times 140 + 282} \quad (3)$$

where 64, 150, 140, and 282 represent the molecular weights of VDF, HFP, TFMAA, and $CH_2C(CF_3)CH_2OC_6H_4SO_3H$, respectively.

Their values were ranging between 0.2 and 1.2 mequiv g^{-1} and matched well with those assessed by titration. As expected, the higher the molar percentages of sulfonic functions in the graft terpolymer, the higher the IEC. The highest values were achieved for a higher grafting rate of the terpolymer that contained the highest TFMAA percentage (Table 4). The hydration number was ranging between 3.1 and 11.6 (considering that of Nafion 112 was 9.6[74]).

Furthermore, the DSC characterization showed only one glass transition temperature. This provides evidence for homogeneous membranes that exhibit a good miscibility between the grafted terpolymers and the commercially available poly(VDF-*co*-HFP) copolymer. Nevertheless, because of the presence of that commercial poly(VDF-*co*-HFP) elastomers (T_g = −31 °C), the T_gs were lower than those of the ionomers. Actually, the T_g values of these membranes were ranging from −19 to +4 °C.

Moreover, several properties of thin films achieved at ambient temperature and for ca. 100% relative humidity were investigated and compared in Table 4. First, the water uptakes of the ionomer membranes were also assessed after immersing the membranes into water for 16 h. These values ranged between 42 and 67% for D and A ionomers, respectively. They confirmed the presence of the sulfonic acid functions in the material that hence increased the IEC values. As expected, the higher the sulfonic acid content, the higher the water uptake.

Second, the corresponding proton conductivity values (σ) were assessed by complex impedance measurements.[54] Conductivity values (eq 4) ranged between 0.5 and 9.1 mS cm^{-1}, and as expected, they increased with the IEC value.

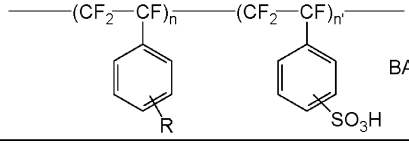
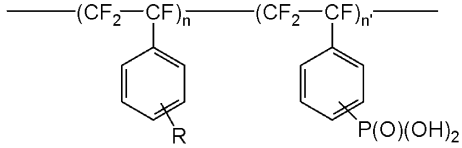
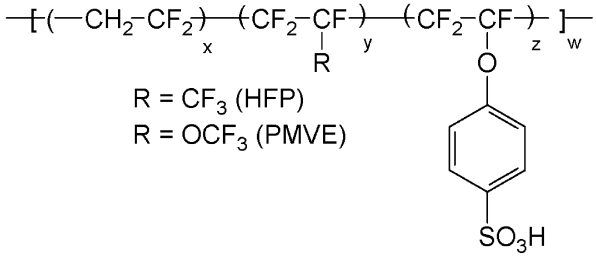
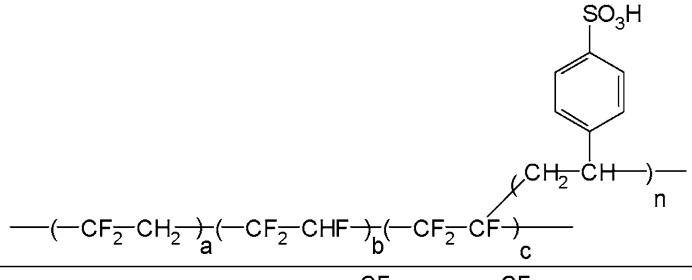
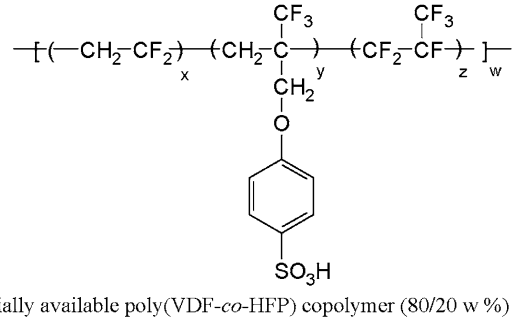
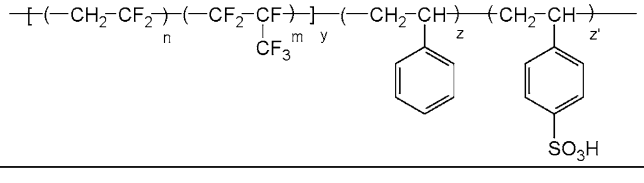
$$\sigma = \frac{1}{R_e} \times \frac{e}{S} \quad (4)$$

where R_e, e, and S stand for the electrolyte resistance, the thickness, and the electrode/membrane−surface, respectively.

It was of interest to compare the electrochemical parameters (IEC, σ) of such membranes processed from these original fluorofunctional terpolymers with those reported on other PEMFCs (Table 5[71−81]). First, the proton conductivities of

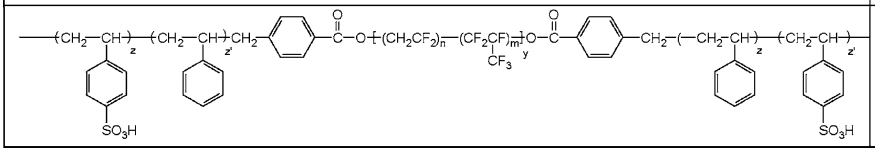
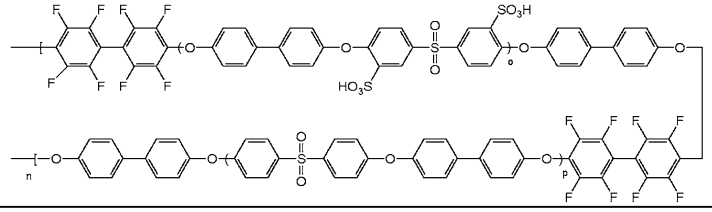
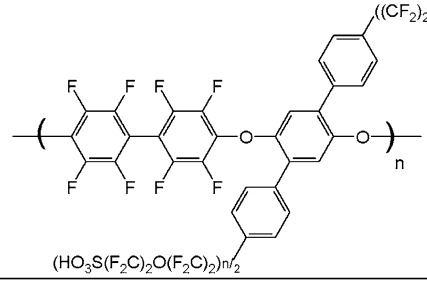
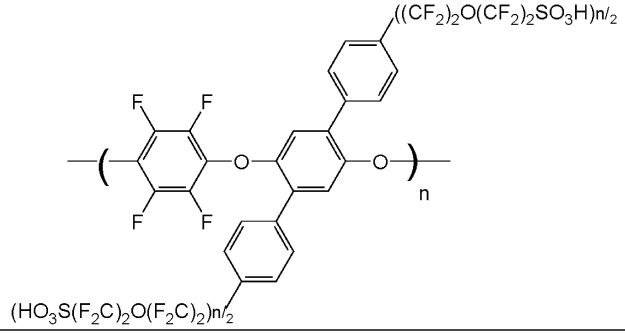
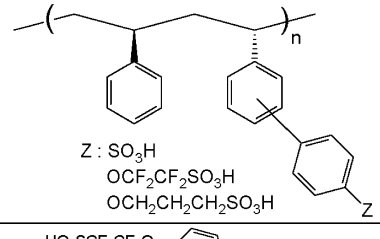
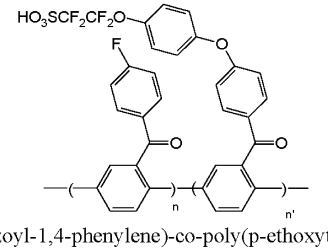
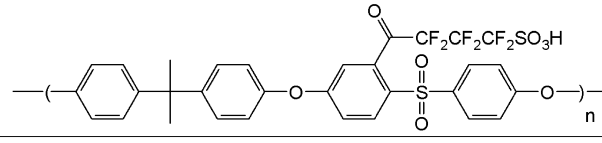
dx.doi.org/10.1021/ma3001912 | Macromolecules 2012, 45, 3145−3160

Table 5. Thickness, Ionic Exchange Capacities, and Proton Conductivities of Different Proton-Conducting Membranes (ns Stands for Not Supplied)

Membrane	Film Thickness (μm)	IEC (mequiv / mol)	Proton conductivity (mS / cm)	Ref.
$-\{(CF_2CF_2)_x[CF_2CF(OCF_2CF(CF_3)OCF_2CF_2SO_3H)]\}_n$ Nafion ® 117	175	0.9	60-100	1-3
Crosslinked $-\{(CH_2CF_2)_y[CF_2CF(OCF_2CF(CF_3)OCF_2CF_2SO_3H)]\}_p$	80	0.8	23	12
 BAM 3G	75	1.1 - 2.6	2 - 10	26a
	90	1.5	0.10	26b
 blend of commercially available poly(VDF-*co*-HFP) copolymer (80/20 w %) with poly(VDF-*ter*-HFP- or PMVE-*ter*-[trifluorovinyloxy]benzene sulfonic acid] terpolymers	71 95 51	0.4 0.5 0.6	0.04 0.06 0.08	28,69,
	ns	1.32-2.75	50-175	33,36
 blend of commercially available poly(VDF-*co*-HFP) copolymer (80/20 w %) with graft (4-sulfonic acid phenoxy) poly[(VDF-*alt*-TFMAA)-*co*-HFP] terpolymers	88 88 99 94	1.2 0.9 0.7 0.2	9 5 3 0.5	70 This work
	100	0.9-1.2	10-80	32

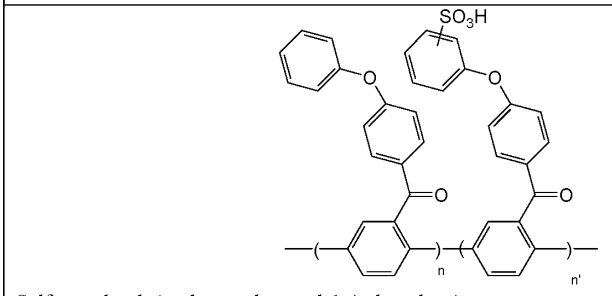
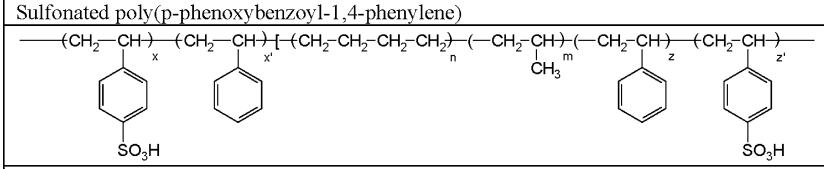
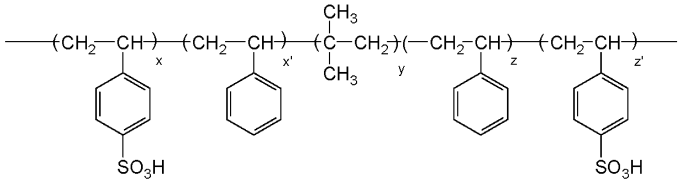
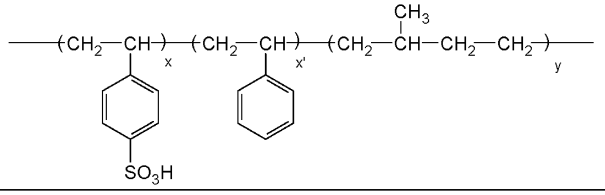
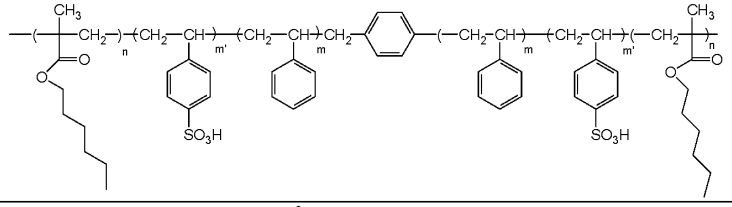
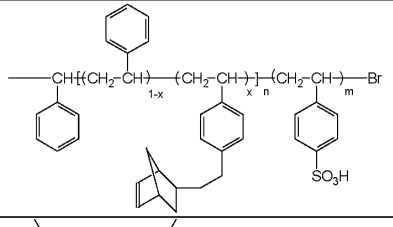
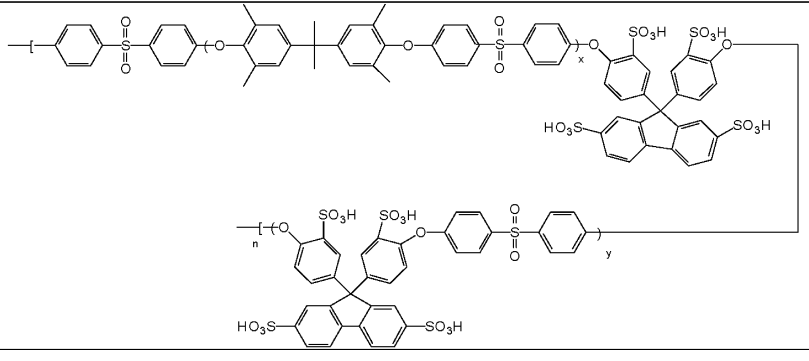
dx.doi.org/10.1021/ma3001912 | *Macromolecules* 2012, 45, 3145−3160

Table 5. continued

Membrane	Film Thickness (μm)	IEC (mequiv / mol)	Proton conductivity (mS / cm)	Ref.
	60-85	0.5-1.7	20-95	71
	ns	1.42-2.08	65-160	72
	ns	1.17-1.60	100	73
	ns	1.83	110	73
	ns	1.64-2.29	60-110	74
 Sulfonated poly(p-fluorobenzoyl-1,4-phenylene)-co-poly(p-ethoxytetrafluoro-p-phenoxybenzoyl-1,4-phenylene)	40	1.3	8	40
	ns	0.45 - 1.17	91	75

dx.doi.org/10.1021/ma3001912 | Macromolecules 2012, 45, 3145−3160

Table 5. continued

Membrane	Film Thickness (μm)	IEC (mequiv / mol)	Proton conductivity (mS / cm)	Ref.
 Sulfonated poly(p-phenoxybenzoyl-1,4-phenylene)	110	1.3	2	40
	212-300	0.9-1.2	13-45	76
	200 - 300	0.11 – 0.96	3 - 25	77
	180	0.8-2.6	75-140	78
	ns	ns	80-85	79
	ns	1.86 – 2.06	15 - 38	80
	50	0.91 – 2.45	70 - 120	81

A–D membranes are lower than those of Nafion considered as the reference for perfluorosulfonic acid PEMFC and regarded as one of the best proton conductivity values (IEC = 0.9 mequiv g^{-1} and σ = 82 mS cm^{-1} assessed in the same conditions as our membranes). This arises from the order of the proton conductivities that follows the same order of the acidities of

dx.doi.org/10.1021/ma3001912 | *Macromolecules* 2012, 45, 3145–3160

the pendant sulfonic acid groups: $-CF_2CF_2SO_3H$ for Nafion (estimated $pK_a = -14$)[82,83] > $-C_6H_4-SO_3H$ (estimated $pK_a = -2.5$)[84,85] > $CH_2P(O)(OH)_2$ (estimated $pK_a = 2.5$ for the first acidity[86]). Second, the conductivity values supplied in this article are better than those reported by Stone et al.[26] from poly[trifluorostyrene-*co*-(4-phosphonic acid)trifluorostyrene] copolymers. This result can be expected when the acidity of phosphonic acid and aryl sulfonic acid are compared. As a matter of fact, for a lower IEC value of our membranes (e.g., 0.2 with respect to that of Stone et al.,[26] i.e. 1.5 mequiv g^{-1}) the conductivity value of our ionomer is higher than that obtained by these authors (i.e., 0.10 mS cm^{-1}). Third, our results are in the same range as those claimed for BAM3G materials[26a] (from the Ballard Co.) and higher than polyparaphenylene bearing a perfluorosulfonic acid side group reported by Balland-Longeau et al.[40] (Table 5). Actually, for the same IEC value (1.2 mequiv g^{-1}), the assessed conductivity of our membranes (σ = 9.1 mS cm^{-1}) is higher than those above (equal to 2 or 8.5 mS cm^{-1}).[40]

Although these results are encouraging, they are a bit far from those reported by various groups, nonexhaustively summarized in Table 5. Two main series can be proposed regarding the architectures of the (co)polymers: (i) those dealing with the grafting of polystyrene by ATRP from aliphatic poly(VDF-*co*-CTFE) polymers further modified into poly(styrenesulfonic acid).[33,36] The conductivity of the resulting membranes reached 175 mS cm^{-1}. This high value arises from the phase separation between the aliphatic fluorinated backbone and the aromatic grafts (that contain hydrophilic sulfonic acid groups). Actually, Holdcroft's group[36] reported that a preferential order was observed in such graft copolymers that induced cocontinuous conducting phases (from gyroid structures) rather than in block polymeric structures (that led to lamellar structures[32,71]); (ii) the polyaromatic structures containing either fluorinated groups (block[72,73] and random[74,75] morphologies) and even without any fluorine group (in block[76−78] or random[79−81] architectures) that also led to high conductivity values (Table 5).

Yet, much work is required to better understand the "structure of the copolymers/IEC value/conductivity value" relationship. In fact, the nature and the length of the spacer located between the sulfonic acid and the polymeric backbone are crucial.[2,3,10,12,15] As mentioned above, the pK_a value of the sulfonic acid in $-CF_2SO_3H$ is higher than that of aryl sulfonic acid.[82−85]

This original process[70] of membrane synthesis allowed us to improve the incorporation of sulfonic acids into the materials endowed with IEC values up to 1.2 mequiv g^{-1} and transverse proton conductivities that reached 9.1 mS cm^{-1}. These encouraging results require optimization (such as (i) to avoid any blending with poly(VDF-*co*-HFP) copolymer that obviously decreases the proton conductivities and thus (ii) to utilize an aqueous process of terpolymerization known to lead to higher molecular weights (or to use perfluorinated branched persistent radical as recently reported[49b]) and (iii) grafting phenol bearing perfluorosulfonic acid functions) and is under investigation.

4. CONCLUSION

For the first time, the synthesis and the chemical modification of original fluorinated terpolymers that contain vinylidene fluoride (VDF), hexafluoropropylene (HFP), and α-trifluoromethacrylic acid (TFMAA) processed into proton-exchange membranes are reported. First, the poly[(VDF-*alt*-TFMAA)-*co*-HFP] terpolymers were produced in good yields, and their microstructures, i.e., the molar contents of these three comonomers in the terpolymer, were assessed by ^1H, ^{13}C, and ^{19}F NMR spectroscopy. Interestingly, TFMAA conversions were quantitative and the resulting terpolymers showed a tendency to an alternating poly(VDF-*alt*-TFMAA) microblock separated by one HFP unit, which is unusual for VDF copolymers. Though TFMAA did not disturb the radical copolymerization of VDF with HFP, it was noted that the lower its molar percentage in the terpolymers, the higher the average molecular weight, the better the thermostability, and the lower the T_g. In a second step, the chemical reduction of carboxylic acid into hydroxyl dangling groups was achieved, leading to original fluorinated polyols in good yields. The experimental parameters of such a reduction were tuned to get optimal conversion rates. Afterward, these original fluorinated polyols were modified using an intermolecular dehydration (etherification or grafting reaction with 4-phenolsulfonic acid). Interestingly, the average molecular weights were slightly increased. As expected, the T_g values of the resulting terpolymers increased significantly as well, just like their thermogravimetric decomposition. Then, membranes, achieved from such grafted poly[(VDF-*alt*-TFMAA)-*co*-HFP] terpolymers/commercially available poly(VDF-*co*-HFP) copolymer blends, exhibited IECs that ranged between 0.2 and 1.2 mequiv g^{-1}. Their corresponding protonic conductivities reached 9.1 mS cm^{-1} while the average swelling rates of the membranes were about 55% and hydration numbers were in the 3.1−11.6 range compared to that of Nafion 112 (λ = 9.6).[74] These preliminary electrochemical results are encouraging. Further works involving 4-phenolperfluorosulfonic acid derivatives are under progress, just like the reduction of the amount of commercially available poly(VDF-*co*-HFP) copolymer to increase the conductivities. Such a way of grafting terpolymers[70] allowed us to prepare original proton exchange materials. Current investigations also involve the characterizations of these membranes such as the oxidative stability (evaluated in Fenton's reagent), the dimensional changes (changes in thickness, width, and length), the investigation of the phase separation between hydrophobic and hydrophilic domains by transmission electron (TEM) and atom force (AFM) microscopies, and by SAXS scattering (for any ordered morphologies), self-diffusion coefficients for water in those membranes versus the water content, and proton conductivity versus relative humidity and temperature, and also on the "structure−property" relationship.

■ ASSOCIATED CONTENT

Supporting Information

Percentages of TFMAA in terpolymers versus those in the feed, ^1H, ^{13}C, and ^{19}F NMR spectra of the different terpolymers, TGA thermograms. This material is available free of charge via the Internet at http://pubs.acs.org.

■ AUTHOR INFORMATION

Corresponding Author

*Tel: +33-467-144-368; fax: +33-467-147-220; e-mail: bruno.ameduri@enscm.fr.

Notes

The authors declare no competing financial interest.

†Presented at the 242nd ACS National Meeting & Exposition, Aug 28−Sept 1, 2011, Denver, CO.

■ ACKNOWLEDGMENTS

The authors acknowledge the Centre National de la Recherche Scientifique (CNRS), Groupement de Recherche (GDR PACEM 2479, PACTE, and PACS), and the Commissariat á l'Energie Atomique et aux Energies Renouvelables (CEA) for the financial support of the PhD grant (to R.S.). The authors also thank the Solvay S.A. (Tavaux in France and Brussels in Belgium) for the generous gifts of vinylidene fluoride, hexafluoropropylene, and 1,1,1,3,3-pentafluorobutane, Dr. K. Kawada and Tosoh F-Tech (Shunan, Japan) for supplying TFMAA monomer as a free sample, Dr. S. Corvely (3M/Dyneon, Antwerept, Belgium) for giving poly(VDF-*co*-HFP) copolymer, and Dr. Ph. Capron and G. Gebel (CEA and SRAM, Grenoble) for their technical assistance in the impedance measurements for the conductivity assessments.

■ REFERENCES

(1) (a) Alberti, G.; Casciola, M.; Massinelli, L.; Bauer, B. *J. Membr. Sci.* **2001**, *185*, 73−81. (b) Kreuer, K. D. *J. Membr. Sci.* **2001**, *185*, 29−39. (c) Curtin, D. E.; Lousenberg, R. D.; Henry, T. J.; Tangeman, P. C.; Tisack, M. E. *J. Power Sources* **2004**, *131*, 41−48.

(2) Hickner, M. A.; Ghassemi, H.; Kim, Y. S.; Einsla, B. R.; McGrath, J. E. *Chem. Rev.* **2004**, *104*, 4587−4611.

(3) Mauritz, K. A.; Moore, R. B. *Chem. Rev.* **2004**, *104*, 4535−85.

(4) De Bruijn, F. *Green Chem.* **2005**, *7*, 132−150.

(5) Zhang, J. L.; Xie, Z.; Zhang, J. J.; Tanga, Y. H.; Song, C. J.; Navessin, T.; Shi, Z. Q.; Song, D. T.; Wang, H. J.; Wilkinson, D. P.; Liu, Z. S.; Holdcroft, S. *J. Power Sources* **2006**, *160*, 872−891.

(6) Yang, Y. S.; Siu, A.; Peckham, T. J.; Holdcroft, S. *Adv. Polym. Sci.* **2008**, *215*, 55−126.

(7) Li, Q. F.; He, R. H.; Jensen, J. O.; Bjerrum, N. J. *Chem. Mater.* **2003**, *15*, 4896−4915.

(8) Souzy, R.; Ameduri, B.; Boutevin, B. *Prog. Polym. Sci.* **2004**, *29*, 75−106.

(9) Yoshitake, M.; Watakabe, A. *Adv. Polym. Sci.* **2008**, *215* (Fuel Cells I), 127−155.

(10) (a) Ghassemi, H.; McGrath, J. E.; Zawodzinski, T. A. *Polymer* **2006**, *47*, 4133−4139. (b) Iacono, S.; Budy, S. M.; Jin, J.; Smith, D. W. *J. Polym. Sci., Part A: Polym. Chem.* **2007**, *45*, 5705−5721. (c) Qian, G.; Smith, D. W.; Bernicewicz, B. *Polymer* **2009**, *56*, 3911−3916.

(11) Higashihara, T.; Matsumoto, K.; Ueda, M. *Polymer* **2009**, *50*, 5341−5357.

(12) (a) Xu, K.; Chanthad, C.; Gadinski, M. R.; Hickner, M. A.; Wang, Q. *ACS Appl. Mater. Interfaces* **2009**, *1*, 2573−2584. (b) Xu, K.; Li, K.; Ewing, C. S.; Hickner, M. A.; Wang, Q. *Macromolecules* **2010**, *43*, 1692−1694. (c) Xu, K.; Chanthad, C.; Hickner, M. A.; Wang, Q. *Chem. Mater.* **2010**, *20*, 6291−6298.

(13) Rozière, J.; Jones, D. J. *Annu. Rev. Mater. Res.* **2003**, *33*, 503−555.

(14) Maier, G.; Meier-Haack, J. *Adv. Polym. Sci.* **2008**, *216*, 1−62.

(15) (a) Parvole, J.; Jannasch, P. *Macromolecules* **2008**, *41*, 3893−3903. (b) Ingratta, M.; Persson Jutemar, E.; Jannasch, P. *Macromolecules* **2011**, *44*, 2074−2083.

(16) Ameduri, B.; Boutevin, B. Synthesis and applications of graft fluoropolymers. In *Well Architectured Fluoropolymers: Synthesis, Properties and Applications*; Elsevier: Amsterdam, 2004; Chapter 5, pp 347−454.

(17) (a) Hamrock, S. J.; Yandrasits, M. A. *Polym. Rev.* **2006**, *46*, 219−244. (b) Aieta, N. V.; Stanis, R. J.; Horan, J. L.; Yandrasits, M. A.; Cookson, D. J.; Ingham, B.; Toney, M. F.; Hamrock, S. J.; Herring, A. M. *Macromolecules* **2009**, *42*, 5774−5780.

(18) Arico, A.; Diblasi, A.; Brunacinni, D.; Sergi, F.; Dispenza, G.; Andaloro, L.; Ferraro, M.; Antonucci, V.; Asher, P.; Buche, S.; Fongolland, D.; Hards, G.; Sharman, J.; Bayer, A.; Heinz, G.; Zandona, N.; Zuber, R.; Gebert, M.; Corasiniti, M.; Ghielmi, A.; Jones, D. *Fuel Cells* **2010**, *10*, 1013−1023.

(19) (a) Arcella, V.; Ghielmi, A.; Tommasi, G. *Ann. N.Y. Acad. Sci.* **2003**, *984*, 226−244. (b) Ghielmi, A.; Vaccarono, P.; Troglia, C.; Arcella, V. *J. Power Sources* **2005**, *145*, 108−115. (c) Arcella, V.; Troglia, C.; Ghielmi, A. *Ind. Eng. Chem. Res.* **2005**, *44*, 7646−7651. (d) Arcella, V.; Ghielmi, A.; Merlo, L.; Gebert, M. *Desalination* **2006**, *199*, 6−8.

(20) Doyle, M.; Rajendran, G.; Vielstich, W.; Gasteiger, H. A.; Lamm, A. Perfluorinated Membranes. In *Handbook of Fuel Cells - Fundamentals, Technology and Applications*; Wiley: New York, 2003; Vol. *3*, pp 351−395.

(21) (a) DesMarteau, D. D. US Patent 1995/5,463,005 assigned to Gas Research Institute. (b) Kotov, S. V.; Pedersen, S. D.; Qiu, W.; Qiu, Z. M.; Burton, D. J. *J. Fluorine Chem.* **1996**, *82*, 13−21.

(22) (a) Feiring, A. E.; Doyle, C. M.; Roelofs, M. G.; Farnham, W. B.; Bekiaran P. G.; Blair H. A. K. WO 1999/45048 (assigned to Du Pont). (b) Bekiarian, P. G.; Doyle, C. M.; Farnham, W. B.; Feiring, A. E.; Morken, P.; Roelofs, M. G. *J. Fluorine Chem.* **2004**, *125*, 187−204.

(23) (a) Ameduri, B.; Armand, M.; Boucher, M.; Manseri, A. US 2007/185293 (assigned to Hydro-Quebec). (b) Sauguet, L.; Ameduri, B.; Boutevin, B. *J. Polym. Sci., Part A: Polym. Chem.* **2007**, *45*, 1814−1834.

(24) (a) Eikerling, M.; Kornyshev, A. A.; Spohr, E. *Adv. Polym. Sci.* **2008**, *215*, 15−54. (b) Elabd, Y. A.; Hickner, M. A. *Macromolecules* **2011**, *44*, 1−11.

(25) Heinze, P. L.; Burton, D. J. *J. Org. Chem.* **1988**, *53*, 2714−2720.

(26) (a) Stone, C.; Steck, A. E.; Lousenberg, R. D. US 1997/5602185 (assigned to Ballard Power Systems Inc.). (b) Stone, C.; Daynard, T. S.; Hu, L. Q.; Mah, C.; Steck, A. E. *J. New Mater. Electrochem. Syst.* **2000**, *3*, 43−50.

(27) DesMarteau, D. D.; Martin, C. W.; Ford, L. A.; Xie, Y. US 2001/6268532 (assigned to 3M Innovative Properties Co.).

(28) Pineri, M.; Marsacq, D.; Ameduri, B.; Souzy, R. French Patent 2004/2,843,398 (assigned to Commissariat à l'Energie Atomique).

(29) (a) Rusanov, A. L.; Kostoglodov, P. V.; Abadie, M. J. M.; Voytekunas, V. Yu.; Likhachev, D. Yu *Adv. Polym. Sci.* **2008**, *216*, 125−155. (b) Ingratta, M.; Elomaa, M.; Jannasch, P. *Polym. Chem.* **2010**, *5*, 739−746. (c) Tayouo, R.; David, G.; Ameduri, B.; Roualdes, S.; Roziere, J. *Macromolecules* **2010**, *43*, 5269−5276.

(30) Jin, L. M.; Hickman, T.; Sharif, I.; Creager, S.; DesMarteau, D. Presented at the 19th International Symposium in Fluorine Chemistry, Jackson Hole, Aug, 23−28, 2009. (b) Herath, M. B.; Creager, S. E.; Kitaygorodskii, A.; DesMarteau, D. D. *J. Phys. Chem. B* **2010**, *114*, 14972−14976. (c) Herath, M. B.; Creager, S. E.; Kitaygorodskii, A.; DesMarteau, D. D. *ChemPhysChem* **2010**, *11*, 2871−2878.

(31) Shi, Z.; Holdcroft, S. *Macromolecules* **2004**, *37*, 2084−2089.

(32) Shi, Z.; Holdcroft, S. *Macromolecules* **2005**, *38*, 4193−4201.

(33) Zhang, Z.; Chalkova, E.; Fedkin, M.; Wang, C.; Lvov, S. N.; Komarneni, S.; Chung, T. C. M. *Macromolecules* **2008**, *41*, 9130−9139.

(34) Ding, J. F.; Chuy, C.; Holdcroft, S. *Adv. Funct. Mater.* **2002**, *12*, 389−394.

(35) Norsten, T. B.; Guiver, M. D.; Murphy, J.; Astill, T.; Navessin, T.; Holdcroft, S.; Frankamp, B. L.; Rotello, V. M.; Ding, J. F. *Adv. Funct. Mater.* **2006**, *16*, 1814−1822.

(36) (a) Tsang, E. M. W.; Zhang, Z.; Shi, Z.; Soboleva, T.; Holdcroft, S. *J. Am. Chem. Soc.* **2007**, *129*, 15106−15107. (b) Tsang, E. M. W.; Zhang, Z. B.; Yang, A. C. C.; Shi, Z. Q.; Peckham, T. J.; Narimani, R.; Frisken, B. J.; Holdcroft, S. *Macromolecules* **2009**, *42*, 9467−9480.

(37) Ding, J. F.; Chuy, C.; Holdcroft, S. *Chem. Mater.* **2001**, *13*, 2231−2233.

(38) Cho, C. G.; Jang, H. Y.; You, Y. G.; Li, G. H.; An, S. G. *High Perform. Polym.* **2006**, *18*, 579−591.

(39) Souzy, R.; Ameduri, B. Fluorofunctional polymers for Fuel Cell Membranes. In *Fluorinated Materials for Energy Conversion*; Nakajima, T., Groult, H., Eds.; Elsevier: Amsterdam, 2005; Chapter 21, pp 469−485.

(40) Balland-Longeau, A.; Pereira, F.; Capron, P.; Mercier, R. Fr Patent 2002/0,210,008 (assigned to CEA).

(41) Ameduri, B. *Chem. Rev.* **2009**, *109*, 6632−6686.

(42) Surya Prakash, G. K.; Smart, M. C.; Wang, Q.-J.; Atti, A.; Pleynet, V.; Yang, B.; McGrath, K.; Olah, G. A.; Narayanan, S. R.; Chun, W.; Valdez, T.; Surampudi, S. *J. Fluorine Chem.* **2004**, *125*, 1217−1230.
(43) (a) Niepceron, F.; Galiano, G.; Tassin, J. F. French Patent FR 2007/55957 (assigned to CEA). (b) Niepceron, F.; Laffitte, B.; Nicol, E.; Galiano, G.; Tassin, J. F. *J. Membr. Sci.* **2009**, *338*, 100−110.
(44) Zapata, P.; Mountz, D.; Meredith, J. C. *Macromolecules* **2010**, *43*, 7625−7636.
(45) Sauguet, L.; Ameduri, B.; Boutevin, B. *J. Polym. Sci., Part A: Polym. Chem.* **2006**, *44*, 4566−4578.
(46) Gubler, L.; Scherer, G. G. *Adv. Polym. Sci.* **2008**, *215*, 1−14.
(47) (a) Silverman, M.; Destarac, M.; Matjyasweski, K.; Ameduri, B.; Boutevin, B. *Macromolecules* **2000**, *33*, 4613−4615. (b) Valade, D.; Boyer, C.; Ameduri, B.; Boutevin, B. *Macromolecules* **2006**, *39*, 8639−8651. (c) Kim, Y. W.; Lee, D. K.; Lee, K. J.; Kim, J. H. *Eur. Polym. J.* **2008**, *44*, 932−939.
(48) Sauguet, L.; Boyer, C.; Ameduri, B.; Boutevin, B. *Macromolecules* **2006**, *39*, 9087−9101.
(49) (a) Souzy, R.; Ameduri, B.; Boutevin, B. *Macromol. Chem. Phys.* **2004**, *205*, 476−485. (b) Patil, Y.; Ameduri, B. *ACS Macro Lett.* **2012**, *1*, 315−320.
(50) Boyer, C.; Ameduri, B. *J. Polym. Sci., Part A: Polym. Chem.* **2009**, *47*, 4710−4722.
(51) Sawada, H.; Tashima, T.; Nishiyama, Y.; Kikuchi, M.; Goto, S.; Kostov, G.; Ameduri, B. *Macromolecules* **2011**, *44*, 1114−1124.
(52) Ameduri, B. *Macromolecules* **2010**, *43*, 10163−10184.
(53) Sanchez, J.-Y.; Iojoiu, C.; Mercier, R.; El Kissi, N.; Salomon, J.; Chabert, F. FR 2005/11807 (assigned to Institut Polytechnique de Grenoble).
(54) (a) Meshechkov, A. I.; Demina, O. A.; Gnusin, N. P. *Electrokhimiya* **1987**, *23*, 1452−1454. (b) Pourcelly, G.; Sistat, P.; Chapotot, A.; Gavach, C.; Nikonenko, V. *J. Membr. Sci.* **1996**, *110*, 69−78.
(55) Mitsunobu, O. *Synthesis* **1981**, *1*, 1−28.
(56) (a) Fuchikami, T.; Yamanouchi, A.; Ojima, I. *Synthesis* **1984**, *9*, 766−768. (b) Patil, Y.; Ameduri, B. *Prog. Polym. Sci.* **2012**, in press.
(57) (a) Yilmaz, E.; Haupt, K.; Mosbach, K. *Angew. Chem., Int. Ed.* **2000**, *39*, 2115−2118. (b) Takeuchi, T.; Matsui, J. *J. High Resolut. Chromatogr.* **2000**, *23*, 44−46. (c) Ito, H.; Wallraff, G. M.; Fender, N.; Brock, P. J.; Larson, C. E.; Truong, H. D.; Breyta, G.; Miller, D. C.; Sherwood, M. H.; Allen, R. D. *J. Photopolym. Sci. Technol.* **2001**, *14*, 583−594. (d) Ito, H.; Brock, P. J.; Wallraff, G. M. US Patent 2002/102,490. (e) Ito, H.; Truong, H. D.; Okazaki, M.; Miller, D. C.; Fender, N.; Brock, P. J.; Wallraff, G. M.; Larson, C. E.; Allen, R. D. *J. Photopolym. Sci. Technol.* **2002**, *15*, 591−602. (f) King, C.-S.; Kanega, A.; Enokida, T.; Nakamura, S. JP Patent 2002/249,522.
(58) Ito, H. *Adv. Polym. Sci.* **2005**, *172*, 37−245.
(59) Aglietto, M.; Passaglia, E.; Montagni di Mirabello, L. *Macromol. Chem. Phys.* **1995**, *196*, 2843−2853.
(60) Ito, H.; Miller, D. C. *J. Polym. Sci., Part A: Polym. Chem.* **2004**, *42*, 1468−1477.
(61) (a) Ito, H.; Miller, D. C.; Willson, C. G. *Macromolecules* **1982**, *15*, 915−920. (b) Ito, H.; Okasaki, M.; Miller, D. C. *J. Polym. Sci., Part A: Polym. Chem.* **2004**, *42*, 1478−1505. (c) Ito, H.; Okasaki, M.; Miller, D. C. *J. Polym. Sci., Part A: Polym. Chem.* **2004**, *42*, 1506−1527.
(62) Minhas, P. S.; Petrucelli, F. *Plast. Eng.* **1977**, *33*, 60−71.
(63) Souzy, R.; Guiot, J.; Ameduri, B.; Boutevin, B.; Paleta, O. *Macromolecules* **2003**, *36*, 9390−9395.
(64) Guiot, J.; Ameduri, B.; Boutevin, B. *Macromolecules* **2002**, *35*, 8694−8707.
(65) Boschet, F.; Cracowski, J. M.; Montembault, V.; Ameduri, B. *Macromolecules* **2010**, *43*, 4879−4888.
(66) (a) Moggi, G.; Bonardelli, P.; Bart, J. C. J. *J. Polym. Sci., Part A: Polym. Chem.* **1984**, *22*, 357−365. (b) Bonardelli, P.; Moggi, G.; Turturro, A. *Polymer* **1986**, *27*, 905−909. (c) Russo, S.; Behari, K.; Chengji, S.; Pianca, M.; Barchiesi, E.; Moggi, G. *Polymer* **1993**, *34*, 4777−4781.
(67) Duc, M.; Ameduri, B.; Boutevin, B.; Kharroubi, M.; Sage, J. M. *Macromol. Chem. Phys.* **1998**, *199*, 1271−1289.
(68) (a) Nguyen, T. *J. Macromol. Sci., Macromol. Chem. Phys.* **1985**, *C25*, 227−275. (b) Zulfiqar, S.; Zulfiqar, M.; Rizvi, M.; Munir, A.; McNeill, I. C. *Polym. Degrad. Stab.* **1994**, *43*, 423−30. (c) Zulfiqar, S.; Rizvi, M.; Munir, A.; Ghaffar, A.; McNeill, I. C. *Polym. Degrad. Stab.* **1996**, *52*, 341−8.
(69) Souzy, R.; Ameduri, B.; Boutevin, B.; Capron, P.; Marsacq, D.; Gebel, G. *Fuel Cells* **2005**, *5*, 383−397.
(70) Souzy, R.; Ameduri, B.; Boutevin, B.; Capron, P. US Patent 2008/0,051,479 (assigned to CEA).
(71) Xu, K.; Li, K.; Khanchaitit, P.; Wang, Q. *Chem. Mater.* **2007**, *19*, 5937−5945.
(72) Lee, H.-S.; Roy, A.; Lane, O.; Dunn, S.; McGrath, J. E. *Polymer* **2008**, *49*, 715−723.
(73) Nakabayashi, K.; Higashihara, T.; Ueda, M. *Macromolecules* **2011**, *44*, 1603−1609.
(74) Ying, C. Y.; Brunello, G. F.; Fuller, J.; Hawley, M.; Kim, Y. S.; Disabb-Miller, M.; Hickner, M. A.; Jang, S. S.; Bae, C. *Macromolecules* **2011**, *44*, 8458−8469.
(75) Ghassemi, H.; Shiraldi, D. A.; Zawodzinski, T. A.; Hamrock, S. *Macromol. Chem. Phys.* **2011**, *212*, 673−678.
(76) Kim, J.; Kim, B.; Jung, B. *J. Membr. Sci.* **2002**, *207*, 129−137.
(77) Elabd, Y. A.; Napadensky, E.; Sloan, J. M.; Crawford, D. M.; Walker, C. W. *J. Membr. Sci.* **2003**, *217*, 227−242.
(78) Park, M. J.; Downing, K. H.; Jackson, A.; Gomez, E. D.; Minor, A. M.; Cookson, D.; Weber, A. Z.; Balsara, N. P. *Nano Lett.* **2007**, *7*, 3547−3552.
(79) Saito, T.; Moore, H. D.; Hickner, M. A. *Macromolecules* **2010**, *43*, 599−601.
(80) Chen, L.; Hallinan, D. T. Jr.; Elabd, Y. A.; Hillmyer, M. A. *Macromolecules* **2009**, *42*, 6075−6085.
(81) Bae, B.; Miyatake, K.; Watanabe, M. *Macromolecules* **2010**, *43*, 2684−2691.
(82) Kim, Y. S.; Pivovar, B. S. *Annu. Rev. Chem. Biomol. Eng.* **2010**, *1*, 123−148.
(83) Bordwell, F. G. *Acc. Chem. Res.* **1988**, *21*, 456−463.
(84) Mikami, T.; Miyatake, K.; Watanabe, M. *ACS Appl. Mater. Interfaces* **2010**, *2*, 1714−1721.
(85) Guthrie, J. P. *Can. J. Chem.* **1978**, *56*, 2342−2354.
(86) Freedman, L. D.; Doak, G. O. *Chem. Rev.* **1957**, *57*, 479−523.

Macromolecules

Article

pubs.acs.org/Macromolecules

Rapid Modular Synthesis and Processing of Thiol–Ene Functionalized Styrene–Butadiene Block Copolymers

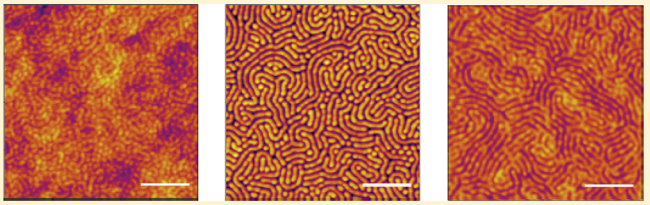
Joshua S. Silverstein,[†,‡] Brendan J. Casey,[‡] Mary E. Natoli,[†] Benita J. Dair,[‡] and Peter Kofinas*[,†]

[†]Fischell Department of Bioengineering, University of Maryland, College Park, Maryland 20742, United States

[‡]Center for Devices and Radiological Health, Office of Science and Engineering Laboratories, Division of Chemistry and Materials Science, Food and Drug Administration, Silver Spring, Maryland 20993, United States

Supporting Information

ABSTRACT: Diblock and triblock copolymers of poly(styrene)-*block*-poly(1,2-butadiene) (PS/PB) and PS/PB/PS were modified by photochemical thiol–ene chemistry to process selected functional nanopatterned polymers, with reaction completion in 1 h. PB molecular weight (MW) and thiol–ene ratios were systematically varied based on a model monomer, boc-cysteamine, to determine the efficiency of the reaction. The results demonstrate the polydispersity index (PDI) of modified block copolymers significantly increased when low thiol–ene ratios were employed and sometimes induced gelation of the reacted polymers. Using a 10-fold excess of thiol, functionalizations between 60% and 90% were obtained for amines, carboxylic acids, amides, and a pharmaceutical with a pendant thiol. Differential scanning calorimetry showed a 30–60 °C increase in the glass transition temperature of the daughter polymers. Subsequently, these polymers were spin-coated from solvents found suitable to form self-assembled block copolymer films. The microstructure domain spacing for each polymer was consistent with those originating from the parent polymer. This technique described allows for the formation of nanopatterned block copolymer films with controlled chemistries from a single source material.



INTRODUCTION

The need for polymers with tailored properties has increased recently with applications ranging from optoelectronics to biomedical.[1] Anionic polymerization is the predominant synthetic scheme for producing monodisperse and well-defined polymer architectures.[2] However, the sensitivity of anionic polymerization to polar and acidic groups makes the synthesis of functional polymers difficult. Therefore, the development of facile and effective postpolymerization modification techniques which maintain monodispersity and architectural integrity of the parent polymer would be beneficial. Commodity polymers such as those containing poly(butadiene) or poly(isoprene) are ideal candidates for backbone modifications due to their widespread commercial availability.

Sulfur's reactivity with poly(isoprene) was discovered in the 19th century by Goodyear to enhance the mechanical integrity of natural rubber.[3] More recently, thiol–ene chemistry was explored by several groups to synthesize polymer networks, block copolymers, dendrimers, liquid crystals, end-functional, and backbone-modified polymers.[4−8] Thiol–ene reactions are directed by the attack of radically initiated ω-functional thiols on unsaturated bonds.[9] Thiol–ene chemistry can be employed for interfacial modifications, including solvent dispersed nanoparticles or thin film surfaces.[10−12] Low-intensity ultraviolet sources are capable of generating radicals including renewable resources like sunlight.[13]

Photochemical and thermal initiation may be used to generate sulfenyl radicals, although photochemical strategies were more effective.[14] Some limitations of thiol–ene chemistry were observed by several research groups, including reduced efficiency and higher side product formation when using low thiol–ene ratios.[7] Compared to low molecular weight compounds, polymeric starting materials exhibited large decreases in reactivity.

Previous research confirmed the pendant vinyl groups of poly(1,2-butadiene) (PB) were over 10-fold more reactive to thiols when compared to the backbone double bonds in poly(1,4-butadiene).[15] The modular capability of thiol–ene chemistry was demonstrated for the synthesis of low molecular weight (MW) ionomers without functional group limitations, including alcohols, amines, amino acids, carbohydrates, carboxylic acids, and fluorinated compounds.[16−19] The thiol–ene reaction on PB is limited by the formation of cyclic groups when intermediate radicals react with adjacent unreacted double bonds, schematically depicted in Figure 1. Possible reaction products are no reaction, thiol addition, and thiol addition followed by cyclic group formation. These studies confirmed that six-membered rings reduce the thiol addition yield despite full conversion of double bonds.[16] In spite of cyclic formation in the thiol–ene reaction of PB, high yields were reported in the range of 75% modification, with near-quantitative conversion of double bonds.

Received: February 13, 2012
Revised: March 18, 2012
Published: March 28, 2012

 © 2012 American Chemical Society

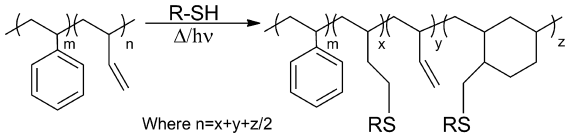


Figure 1. Reaction scheme of the thiol−ene reaction on PS/PB block copolymers. Possible reaction routes include thiol addition, no reaction, and cyclic group formation.

The low molecular weight polymer systems previously investigated for the thiol−ene reaction cannot be used for coating applications that require thin and bulk film processing. Styrene−butadiene block copolymers synthesized by numerous manufacturers have molecular weights in the range of 100−150 kDa, whose mechanical properties and solution viscosity are optimal for film applications. Few studies have examined thiol−ene addition on high molecular weight PB copolymers. Passaglia and Donati found significant issues with cross-linking and low functionalization using thermal initiation on styrene−butadiene random copolymers.[20] In order to decrease cross-linking, lower concentrations of initiator were used at the expense of reduced functionalization. More recently, David and Kornfield were able to graft thiol groups to high molecular weight PB using thermal initiation with a controlled range of yields within 2−6 h.[21] These polymers could be further reacted to create functionalities with potential optoelectronic or liquid crystalline properties.

In this study, modification of styrene−butadiene block copolymers of varying molecular weight by radical thiol addition is reported using a photochemical strategy that allows reaction completion within 1 h. While alkylation of PB was shown to control the orientation of self-assembled butadiene−ethylene oxide block copolymers,[22] this study seeks to synthesize and process a modular collection of highly functionalized BCP nanostructured films with similar morphologies. Low thiol−ene ratios increased the polydispersity index and in some cases induced gelation of the modified or "daughter" polymers. Increased thiol concentrations allowed for efficient grafting of various functional groups, including amines, acids, amides, and a pharmaceutical with a pendant thiol. Various characterization methods are shown and support the efficiency of the thiol−ene reaction. Additionally, microphase separation of the modified polymers into nanostructured domains from solution film casting is described. This work demonstrates the versatility of the thiol−ene reaction in creating a novel class of patterned block copolymers with tunable chemistry.

EXPERIMENTAL SECTION

Materials and Methods. Captopril, thioglycolic acid, boc-cysteamine, thiosalicylic acid, 2-(diethylamino)ethanethiol hydrochloride (DAET), anhydrous tetrahydrofuran (THF), phenylbis(2,4,6-trimethylbenzoyl)phosphine oxide (BAPO), propylene glycol monomethyl ether acetate, dimethylformamide, and chloroform were all purchased from Sigma-Aldrich (St. Louis, MO) and used as received. Deuterated chloroform and tetrahydrofuran were purchased from Cambridge Isotopes (Andover, MA). EasiVial poly(styrene) standards for gel permeation chromatography (GPC) calibration were purchased from Agilent Technologies (Santa Clara, CA). Various poly(styrene)-*block*-poly(1,2-butadiene) diblock and poly(styrene)-*block*-poly(1,2-butadiene)-*block*-poly(styrene) triblock copolymers (PS/PB) were purchased from Polymer Source (Montreal, Canada). The molecular weights and relative molar percentages, as determined by GPC and ^{1}H nuclear magnetic resonance (NMR) spectroscopy, are summarized in Table 1.

Table 1. Summary of the Poly(styrene)-*block*-poly(1,2-butadiene) Diblock and Triblock Copolymers Used in This Study[a]

mol wt (kDa)[b]	PDI[c]	mol % PB[d]
8.5-*b*-8.0	1.08	65
19.3-*b*-18.9	1.06	65
63.5-*b*-33.0	1.13	53
14.1-*b*-67.0-*b*-24.0	1.13	71

[a]Mole percentages were used to determine the thiol−ene ratio for reactions. [b]As described by the manufacturer. [c]Determined by GPC. [d]Determined by NMR.

Synthesis. PS/PB and PS/PB/PS were modified with various thiol compounds radically initiated using BAPO and UV irradiation. The thiol compounds investigated in this study are summarized in Figure 2.

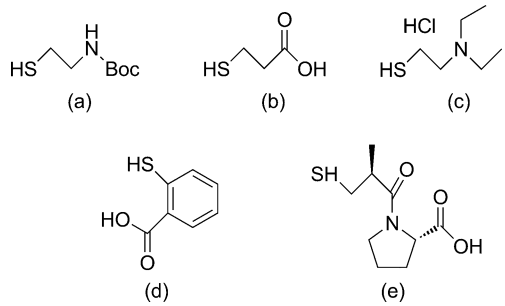


Figure 2. Summary of thiols investigated in this study: (a) boc-cysteamine; (b) thioglycolic acid; (c) 2-(diethylamino)ethanethiol hydrochloride; (d) thiosalicylic acid; (e) captopril.

50 mg of each respective block copolymer (BCP), 25 mg of BAPO photoinitiator, and thiol were preweighed into vials with Teflon septa and purged with nitrogen for 10 min. During the purging process, a minimal amount of anhydrous THF was added via syringe, yielding an ∼5 wt % solution with respect to polymer. Because of the low solubility of captopril and 2-(diethylamino)ethanethiol hydrochloride (DAET) in THF, a minimal amount of chloroform was used. After purging, the vials were placed into an UltraLum photo-cross-linking oven (λ = 365 nm) and irradiated for 60 min to generate sulfenyl radicals. The distance between the UV lamps and the base of the vials was ∼15 cm. After UV irradiation, the polymers were concentrated and precipitated three times in hexane or acetone, followed by redissolution in THF or chloroform each time. Finally, they were dried under vacuum at room temperature until reaching constant mass. It is vital to note that applying heat during vacuum drying often yielded an insoluble product.

For determination of the effects of PB molecular weight on the functionalization and/or gelation of styrene−butadiene BCPs, molar ratios of thiol to double bonds were systematically varied from 1:1 to 10:1. The results reported were calculated from ^{1}H NMR spectra. After recognizing that excess amounts of thiols were required, 10-fold excess of thiol monomers were used to synthesize modified PS/PB block copolymers for calorimetry and thin film analysis.

Characterization. Gel permeation chromatography (GPC) confirmed molecular weight distribution and polydispersity of the stock and modified polymers using a Waters 515 HPLC pump, in-line degasser, a Waters 2410 refractive index detector, and PolyPore columns in series. PS/PB block copolymers were dissolved at 2 mg/mL in THF. THF was used as the eluent at a flow rate of 1 mL/min, and the poly(styrene) equivalent molecular weights reported were determined by constructing a multipoint calibration curve using EasiVial standards (Agilent).

^{1}H NMR spectra were recorded with a Bruker AV-400 high-resolution NMR operating at 400 MHz to assess reaction completion. The stock polymers as received and modified polymers were scanned

dx.doi.org/10.1021/ma300304h | *Macromolecules* 2012, 45, 3161−3167

using deuterated chloroform (d-chloroform), with the exception of the thioglycolic acid and captopril modified polymers, which required the use of deuterated tetrahydrofuran (d-THF). Typically, polymers were dissolved at ~2 wt % and scanned 64 times.

Differential scanning calorimetry (DSC) was used to determine the glass transition temperature of the polymers with a TA Instruments Q100 system. The polymers were analyzed using a heat/cool/heat method to erase thermal history with heating rates of 10 °C/min followed by cooling at 5 °C/min. The glass transition temperatures reported are the midpoint of the slope change as determined by the Universal Analysis software package provided by TA Instruments. Prior to conducting DSC measurements, the calorimeter was calibrated with an indium standard.

Block copolymer solutions were prepared at 0.5 wt % and spin-coated at 2000 rpm onto silicon wafers with a native oxide layer. Prior to spin-coating, silicon wafers were cleaned with isopropyl alcohol, acetone, and dried with a nitrogen stream. Tapping mode atomic force microscopy (AFM) was used to image the surface topography of spin-coated block copolymer films using an Asylum MFP-3D system. VistaProbe AFM tips were purchased from Nanoscience Instruments with a nominal tip radius less than 10 nm, spring constant of 48 N/m, and resonant frequency of 190 kHz. 2 × 2 μm scans were completed at 1 Hz with a resolution of 512 × 512 pixels. Image analysis was performed using ImageJ, which is freeware offered by the National Institutes of Health. Average domain sizes were determined in ImageJ with a minimum of 20 measurements on three different areas, and the error reported is the standard error of the mean.

RESULTS AND DISCUSSION

Influence of Molecular Weight on Polydispersity and Functionalization. The molecular weight and polydispersity index (PDI) of the stock polymers, as purchased, are summarized in Table 1. NMR integrations were calibrated to the aromatic hydrogens of poly(styrene) to determine the relative block ratios. The mole percentage of the butadiene block was determined by ^{1}H NMR spectroscopy (NMR) and was further applied to calculate thiol−ene ratios for all subsequently described reactions. The reaction of boc-cysteamine with various butadiene molecular weights was employed as a model reaction to determine the efficiency of the thiol−ene reaction. Radical addition of boc-cysteamine to the pendant vinyl groups of PS/PB block copolymers generally occurred in an efficient manner. Modifications between approximately 50% and 90% were possible with the lowest molecular weight block copolymer. However, the range of functionalization narrowed to between approximately 70% and 90% when starting from higher molecular weight parent polymers. Less than quantitative thiol addition derives from the cyclic reaction between active radicals and adjacent, unreacted double bonds. This reaction is confirmed by the lack of remaining double bonds in the modified polymers without quantitative thiol addition. The cyclic reaction is unique to the thiol−ene reaction of PB and is thoroughly discussed in the literature.[18]

After UV irradiation, several of the higher molecular weight polymer products showed visible viscosity increases. Despite the solubility of reaction stocks from equimolar concentrations of thiol and vinyl groups during purification, some of these polymers formed an insoluble gel with the exception of the lowest molecular weight PS/PB polymer. Thus, determinations of the PDI and functionalization degree were not possible for these polymers and are described in Table 2 as "gel". GPC determination for the 8.5-*b*-8.0 and 19.3-*b*-18.9 kDa with equimolar thiol−ene concentrations show slight PDI increases on the order of 0.2−0.3 compared to their parent polymers. The PDI of polymer products generally decreases when higher excess of thiol are applied in the polymer modifications, regardless of molecular weight. Specifically, a 10-fold excess of boc-cysteamine increased the PDIs of daughter polymer by ~0.1, when compared to the high molecular weight parent polymer. In contrast, equimolar and 5-fold excess concentations of thiol led to gelation or a 1.41 PDI, respectively. This indicated that the PDI of modified polymers increased due to low thiol−ene ratios; when using equimolar concentrations, this induced gelation of the daughter polymers.

Table 2. Effects of Boc-cysteamine Concentration on the Polydispersity Index and Functionalization Degree[a]

mol wt (kDa)	thiol:ene	PDI ± SEM[b]	f ± SEM (%)[c]
8.5-*b*-8	stock	1.08	N/A
	1	1.45	51 ± 1
	5	1.19	70 ± 3
	10	1.12	87 ± 3
19.3-*b*-18.9	stock	1.06	N/A
	1	1.23	58 ± 2
	5	1.20	82 ± 2
	10	1.16	93 ± 3
63.3-*b*-33	stock	1.13	N/A
	1	gel	gel
	5	1.32	70 ± 2
	10	1.25	79 ± 1
14.1-*b*-67-*b*-24	stock	1.13	N/A
	1	gel	gel
	5	1.41	83 ± 2
	10	1.28	88 ± 2

[a]The errors presented are the standard error of the mean (n = 3). [b]Determined by GPC. [c]Determined by NMR.

As shown in Table 2, the functionalization degree increased with higher thiol−ene ratios and saturated near 90% for the lowest molecular weight polymer. As the molecular weight of the polymers increased, the efficiency of the thiol−ene reaction slightly decreased and resulted in modifications around 80%. Despite the ability to control functionalization on low molecular weight PS/PB block copolymers, low thiol−ene ratios generally increased the PDI of high molecular weight polymers and in some cases induced gelation. Additionally, the potential range of functionalization was narrowed with high molecular weight BCPs. Assuming that all chains within a relatively monodisperse polymer solution have equal reactivity toward thiols, the PDI increase suggests a low density of cross-links.

Radicals remain active after thiol addition, and there are several possibilities for their fate. The active radical can undergo chain transfer and initiate another sulfenyl radical.[7] Radicals can also react with adjacent and unreacted double bonds to form cyclic groups.[16] Finally, two radicals can cause recombination termination by intrachain or interchain cross-linking.[7] A combination of these processes may occur; however, recombination termination is most likely the culprit in increased PDIs and gelation products since neither chain transfer nor cyclic group formation would result in gelation.

The observed results from PS/PB modification at low thiol−ene ratios with different molecular weights are supported by theory, where the critical cross-link density for gelation scales inversely with the degree of polymerization (DP).[23] Thus, higher molecular weight polymers are more susceptible to forming infinite networks. The DP of the butadiene block of the BCPs investigated range from approximately 150 to 1240 repeat units. The critical cross-link densities for these molecular

dx.doi.org/10.1021/ma300304h | Macromolecules 2012, 45, 3161−3167

weights are approximately 0.6% and 0.08% of mer units, respectively. For the highest molecular weight polymer, this corresponds approximately to one cross-linked mer unit per 1000 inducing gelation. These theoretical numbers support the observed experimental in Table 2, which shows that higher molecular weight polymers have a higher propensity for gel formation.

When the thiol−ene ratio was systematically increased, a trend of decreased polydispersity was observed. The chromatogram for the 63 kDa-*block*-33 kDa parent polymer and the daughter polymer with a 10-fold excess of boc-cysteamine is shown in Figure 3. The chromatogram shows a modest shift in the peak elution volume toward a higher molecular weight range when comparing the modified polymer to that of the stock. Additionally, a similar narrow molecular weight distribution is conserved between the stock and modified polymers.

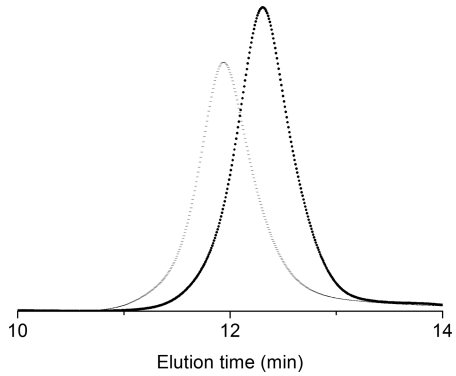


Figure 3. Gel permeation chromatography of 14.1 kDa-*b*-67.0 kDa-*b*-24.0 kDa PS/PB/PS triblock copolymer and another modified with a 10:1 thiol−ene ratio of boc-cysteamine (stock: dark dots; modified: light dashes).

Various applications, including those for biomedical devices, require materials that can withstand cyclical loading. High molecular weight polymers are typically used for coatings due to their advantageous mechanical properties. The experimental observations indicate a large excess of thiol is required to maintain narrow PS/PB molecular weight distribution and inhibit gelation. While lower degrees of functionality were not presented in this study, perhaps the use of thiolated alkanes as comonomers may allow for modifications of PS/PB BCPs on the order of 20−70%. Despite these issues, the photoinitiated thiol−ene reaction presents an effective and facile route for rapid functionalization of butadiene BCPs.

Synthesis of Functional Block Copolymers. After investigating the molecular weight effects of thiol addition, block copolymers were synthesized with a wide set of functionalities. The monomers used in this study were boc-cysteamine, thioglycolic acid, thiosalicylic acid, captopril, and 2-(diethylamino)ethanethiol hydrochloride (DAET), whose structures are depicted in Figure 2. Modified polymers were easily produced and obtained in yields of ∼70%, with the exception of thiosalicyclic acid. The PS/PB BCPs reacted with thiosalicylic acid contained a similar amount of vinyl groups as the parent polymer. Thus, thiol addition did not occur and was confirmed by NMR. The steric constraints from the carboxylic acid group ortho to the thiol group may inhibit thiosalicyclic acid's reactivity with the pendant vinyl groups on PB.[24]

The results from the reaction of the 63.5-*block*-33.0 kDa stock BCP with various thiolated monomers are described in Table 3. Additionally, NMR spectra from a typical thiol−ene reaction are shown in Figure 4. NMR spectra with raw integrations, peak assignments, and sample calculations are included in the Supporting Information. Similar to previous studies, wide functional group tolerance was observed using a photochemical strategy for grafting various groups onto PS/PB block copolymers. With the exception of thiosalicylic acid, PS/PB BCPs thiol addition yields were obtained in the range of 70−90%. Despite variable functionalizations, all products show full conversion of vinyl groups between 4.9 and 5.7 ppm in NMR spectra.

Table 3. Functionalization Degree of 63.5 kDa-*b*-33.0 kDa PS/PB Polymers Modified Using 10:1 Thiol−Ene Ratios on the Monomers Studied[a]

monomer	thiol:ene	$f \pm$ SEM (%)[b]
boc-cysteamine	10	79 ± 1
thioglycolic acid	10	78 ± 3
2-(diethylamino)ethanethiol hydrochloride	10	93 ± 2
captopril	10	69 ± 3
thiosalicyclic acid	10	0

[a]The errors presented are the standard error of the mean (n = 3). [b]Determined by NMR.

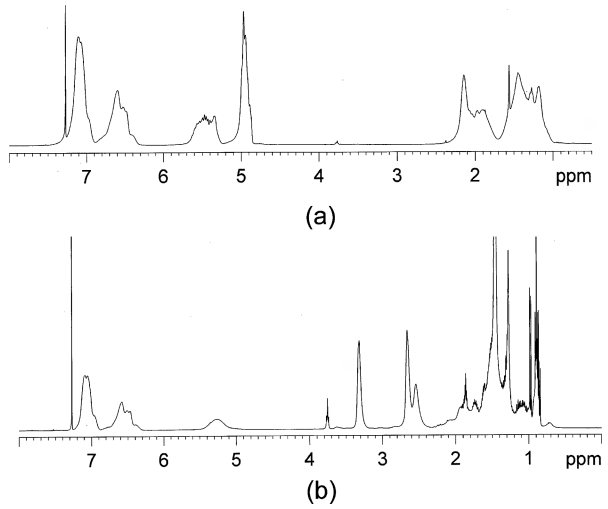


Figure 4. ^{1}H NMR spectroscopy of stock and typical functionalized block copolymer obtained from radical thiol additions: (a) stock polymer; (b) boc-cysteamine.

The lowest yield was 69 ± 3% from captopril. As the bulkiness of the group increased, such as with captopril, the functionalization degree decreased. The experimental conditions approach the solubility limit of captopril; thus, steric hindrance cannot be explicitly confirmed as the cause of reduced functionalization. However, experiments completed on low MW PB demonstrated that larger R groups resulted in lower modification degrees, despite full conversion of double bonds.[13] Because of the cyclic reaction between active radicals on the PB backbone and adjacent, unreacted double bonds, less than quantitative addition occurred. The appearance of a broad peak at 2.5−2.7 ppm, corresponding to the four protons at the thioether linkage, shows the successful addition of thiols to the polymer side chains.

Thermal Characterization. Maintenance of elastomeric behavior is a vital property of styrene−butadiene block

dx.doi.org/10.1021/ma300304h | *Macromolecules* 2012, 45, 3161−3167

copolymers, which are used in a variety of applications, ranging from tires to biomedical devices. The glass transition temperature (T_g) is a key material property to determine whether a polymer conforms to the requirements of a thermoplastic elastomer. Using a heat/cool/heat method to erase thermal history, the T_g's reported are from the PB block only, since the poly(styrene) T_g remained unmodified during the thiol−ene reactions.

The results from the second differential scanning calorimetry (DSC) heating cycle are shown in Figure 5. The glass transition temperature of the PS/PB parent polymer, 63 kDa-*block*-33.5 kDa, was determined to be −15 °C. The daughter polymers' T_g's increased between 30 and 60 °C, depending on the specific monomer modification. The glass transition temperatures for the polymers modified with boc-cysteamine, thioglycolic acid, DAET, and captopril were determined to be 15, 33, 43, and 46 °C, respectively.

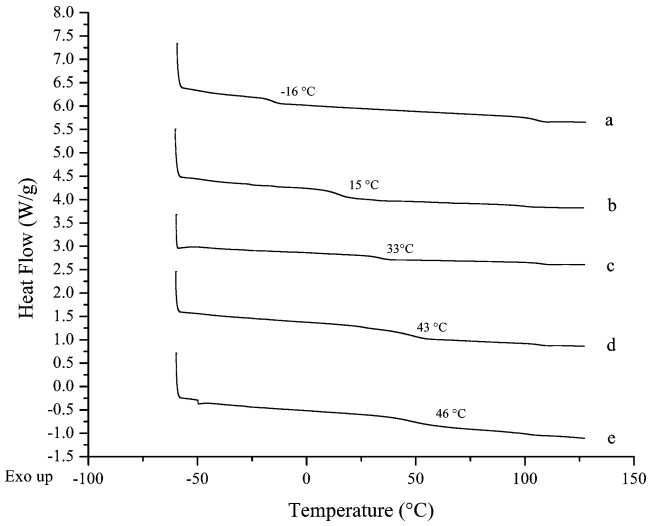


Figure 5. Differential scanning calorimetry of monomer dependency of glass transition temperature of functionalized block copolymers using a thiol−ene ratio of 10:1 on PS/PB with a molecular weight of 63.5 kDa-*b*-33.0 kDa: (a) parent polymer, as received; (b) boc-cysteamine; (c) thioglycolic acid; (d) 2-(diethylamino)ethanethiol hydrochloride; (e) captopril.

An increase in T_g is believed to result from the modification process, which leads to increased steric bulk on the side chains of the PB block. Additionally, the cyclic groups inherent in the thiol−ene reaction of PB led to an elevated T_g; it was previously shown that lower configurational entropy in cyclic systems effectively increases the T_g when compared to linear analogues.[25] These two compounding factors account for the large increase in T_g after thiol−ene-based modification of the PS/PB block copolymers.

Thin Film Processing. After NMR, GPC, and DSC characterization, optimal conditions for processing the grafted block copolymers were determined. Common solvents used for PS/PB BCPs such as chlorinated solvents, tetrahydrofuran, and toluene yielded opaque solutions or dispersions which suggested micellar self-assembly. Dynamic light scattering analysis (DLS) indicated the formation of sub micrometer particles and was confirmed by film spin-coating and AFM analysis.

Various solvents were used to process nanopatterns from each daughter polymer. Generally, the daughter polymers exhibited solubility in dimethylformamide (DMF), propylene glycol monomethyl ether acetate (PGMEA), or dimethyl sulfoxide (DMSO) and were insoluble in water. Thin films were spin-coated from low humidity conditions (<40% RH) from a 0.5% solution at 2000 rpm. The stock 63-*block*-33 kDa PS/PB diblock copolymer was processed from dichloroethane and formed disordered cylindrical nanostructures after spin-coating. Both parallel and perpendicular cylindrical domains existed at the surface from AFM measurements.

Typical results for AFM images are shown in Figure 6. The average center-to-center distance of the stock polymer microstructures was determined to be 65.7 ± 1.5 nm. An iterative method was used to process similar nanopatterns from

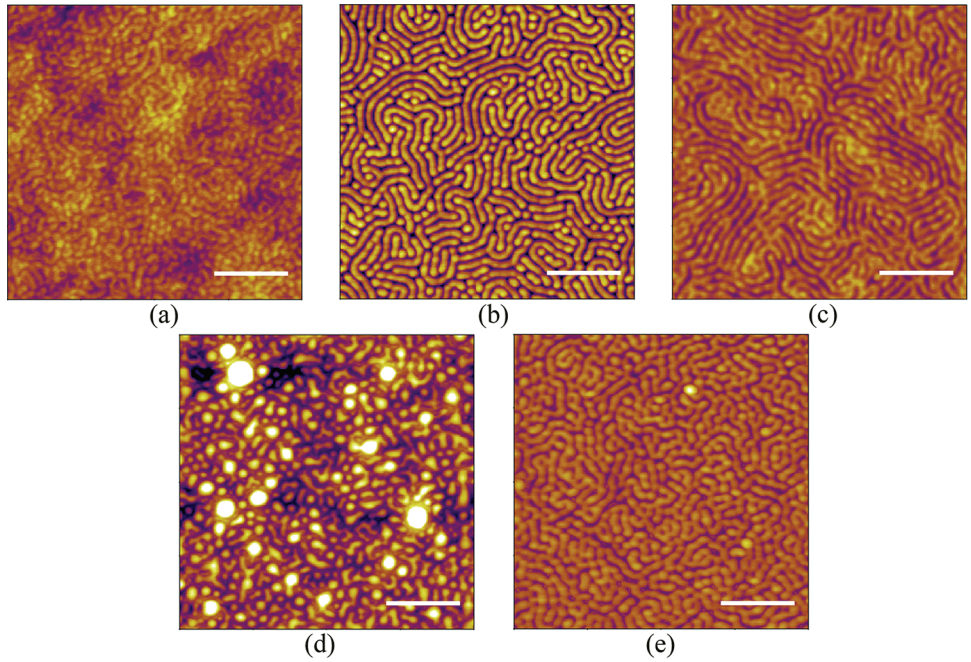


Figure 6. Atomic force micrographs of 63 kDa-*block*-33.5 kDa stock and modified PS/PB block copolymers: (a) parent polymer, as received; (b) boc-cysteamine; (c) thioglycolic acid; (d) 2-(diethylamino)ethanethiol hydrochloride; (e) captopril. Scale bars: 500 nm.

dx.doi.org/10.1021/ma300304h | *Macromolecules* 2012, 45, 3161−3167

each daughter polymer using the solvents resulting in optically clear solutions, which were typically DMF, PGMEA, or DMSO. The boiling point of DMSO was too high for evaporation to occur during spin-coating, even after longer times. The center-to-center domain sizes are tabulated in Table 4. Spin-coating

Table 4. Domain Size Summary of 63 kDa-*block*-33.5 kDa Stock and Modified PS/PB Block Copolymers[a]

monomer	center-to-center spacing ± SEM (nm)
stock	65.7 ± 1.5
boc-cysteamine	66.3 ± 1.5
thioglycolic acid	74.1 ± 1.9
2-(diethylamino)ethanethiol hydrochloride	80.7 ± 2.7
captopril	74.5 ± 2.1

[a]The results were calculated from AFM images, and the error presented is the standard error of the mean.

yielded cylindrical microstructures from the boc-cysteamine, thioglycolic acid, and captopril modified polymers with center-to-center domain sizes of 66.3 ± 1.5, 74.1 ± 1.9, and 74.5 ± 2.13 nm, respectively. The captopril-modified polymer required the addition of ~25% (v/v) THF for solubility in PGMEA. The DAET-modified polymer was spin-coated from PGMEA/DMF (90/10 v/v %) due to insolubility in pure PGMEA. The center-to-center domain sizes of the DAET modified polymer were 80.72 ± 2.72 nm.

DLS showed monodisperse micelles on the order of 20−40 nm for the polymers in PGMEA (not shown). It is postulated that during spin-coating the micelles shear open and reveal the core of the micelle, resulting in a microphase-separated film. This phenomena was observed in other amphiphilic block copolymer systems with aromatic blocks, such as poly(2-vinylnaphthalene)-*block*-poly(acrylic acid).[26] Reasonably ordered nanostructures resulting from PGMEA spin-coating make it an exceptional solvent choice for amphiphilic block copolymers.

Despite the high modification degree of the daughter polymers, there was no visible shift into the lamellar region of the block copolymer phase diagram for symmetric block copolymers. This may be due to the micellar template from solution. Seemingly, as the functionalization degree increased, the level of parallel cylindrical domain formation also increased, most notably in the boc-cysteamine modified BCP films. The parallel orientation of quasi-cylindrical domain is in agreement with studies detailing alkylation of PB side chains.[22] An additional factor in parallel domain orientation may be due to the nature of thin films. When film thicknesses are less than the equilibrium domain size of the block copolymers, parallel domains can form, as validated by theory and experimental data in other systems.[27]

CONCLUSION

We have described a photochemical thiol−ene strategy for creating a versatile set of functional styrene−butadiene block copolymers. The polymers synthesized and characterized confer the ability to control chemistry at the nanoscale and contain precursors that are readily available as commodity polymers. Amine, carboxylic acid, amide, and pharmaceutical compounds were successfully grafted onto the block copolymers in reasonable yields. Although the polydispersity index increased with higher molecular weight polymers, high grafting yields were possible with excess thiol.

These novel functional block copolymers maintained glass transition temperatures near or below room temperature, allowing for their application as elastomeric materials. Despite the amphoteric nature of the daughter polymers, microphase separation of the individual polymer blocks was observed when the casting solvent used was polar with a high boiling point. The highly functional polymers described can be used to make modular nanopatterns.

ASSOCIATED CONTENT

Supporting Information

^{1}H NMR spectra with peak assignments of modified polymers, integrations, and sample calculations for the functionalization degree. This material is available free of charge via the Internet at http://pubs.acs.org.

AUTHOR INFORMATION

Corresponding Author

*E-mail: kofinas@umd.edu.

Notes

The authors declare no competing financial interest.

ACKNOWLEDGMENTS

This project was supported by an appointment to the University Participation Program at the Center for Devices and Radiological Health administered by the Oak Ridge Institute for Science and Education through an interagency agreement between the U.S. Department of Energy and the U.S. Food and Drug Administration. NMR Spectroscopy was performed at the University of Maryland Analytical NMR Service & Research Center. The authors acknowledge technical advice from Dr. H. Schlaad.

REFERENCES

(1) Nie, Z. H.; Kumacheva, E. *Nat. Mater.* **2008**, *7* (4), 277−290.
(2) Hsieh, H. L.; Quirk, R. P. *Anionic Polymerization: Principles and Practical Applications*; Marcel Dekker: New York, 1996; p *viii*, 727 pp.
(3) Goodyear, C. Improvement in the Manufacture of Caoutchouc. 3633, June 15, 1844.
(4) Campos, L. M.; Killops, K. L.; Sakai, R.; Paulusse, J. M. J.; Damiron, D.; Drockenmuller, E.; Messmore, B. W.; Hawker, C. J. *Macromolecules* **2008**, *41* (19), 7063−7070.
(5) Cramer, N. B.; Bowman, C. N. *J. Polym. Sci., Part A: Polym. Chem.* **2001**, *39* (19), 3311−3319.
(6) Killops, K. L.; Campos, L. M.; Hawker, C. J. *J. Am. Chem. Soc.* **2008**, *130* (15), 5062−+.
(7) Koo, S. P. S.; Stamenovic, M. M.; Prasath, R. A.; Inglis, A. J.; Du Prez, F. E.; Barner-Kowollik, C.; Van Camp, W.; Junkers, T. *J. Polym. Sci., Part A: Polym. Chem.* **2010**, *48* (8), 1699−1713.
(8) Yang, H.; Jia, L.; Zhu, C. H.; Di-Cicco, A.; Levy, D.; Albouy, P. A.; Li, M. H.; Keller, P. *Macromolecules* **2010**, *43* (24), 10442−10451.
(9) Kade, M. J.; Burke, D. J.; Hawker, C. J. *J. Polym. Sci., Part A: Polym. Chem.* **2010**, *48* (4), 743−750.
(10) Bertin, A.; Schlaad, H. *Chem. Mater.* **2009**, *21* (24), 5698−5700.
(11) Korthals, B.; Morant-Minana, M. C.; Schmid, M.; Mecking, S. *Macromolecules* **2010**, *43* (19), 8071−8078.
(12) Wickard, T. D.; Nelsen, E.; Madaan, N.; ten Brummelhuis, N.; Diehl, C.; Schlaad, H.; Davis, R. C.; Linford, M. R. *Langmuir* **2010**, *26* (3), 1923−1928.
(13) ten Brummelhuis, N.; Diehl, C.; Schlaad, H. *Macromolecules* **2008**, *41* (24), 9946−9947.
(14) Uygun, M.; Tasdelen, M. A.; Yagci, Y. *Macromol. Chem. Phys.* **2010**, *211* (1), 103−110.

(15) Decker, C.; Viet, T. N. T. *Polymer* **2000**, *41* (11), 3905−3912.
(16) Justynska, J.; Hordyjewicz, Z.; Schlaad, H. *Polymer* **2005**, *46* (26), 12057−12064.
(17) Justynska, J.; Hordyjewicz, Z.; Schlaad, H. *Macromol. Symp.* **2006**, *240*, 41−46.
(18) Justynska, J.; Schlaad, H. *Macromol. Rapid Commun.* **2004**, *25* (16), 1478−1481.
(19) Lotti, L.; Coiai, S.; Ciardelli, F.; Galimberti, M.; Passaglia, E. *Macromol. Chem. Phys.* **2009**, *210* (18), 1471−1483.
(20) Passaglia, E.; Donati, F. *Polymer* **2007**, *48* (1), 35−42.
(21) David, R. L. A.; Kornfield, J. A. *Macromolecules* **2008**, *41* (4), 1151−1161.
(22) Demirel, A. L.; Schlaad, H. *Polymer* **2008**, *49* (16), 3470−3476.
(23) Flory, P. J. *Principles of Polymer Chemistry*; Cornell University Press: Ithaca, NY, 1953; p 672.
(24) Tedder, J. M. *Angew. Chem., Int. Ed. Engl.* **1982**, *21* (6), 401−410.
(25) Dimarzio, E. A.; Guttman, C. M. *Macromolecules* **1987**, *20* (6), 1403−1407.
(26) Zhang, X.; Metting, C. J.; Briber, R. M.; Weilnboeck, F.; Shin, S. H.; Jones, B. G.; Oehrlein, G. S. *Macromol. Chem. Phys.* **2011**, *212* (16), 1735−1741.
(27) Fasolka, M. J.; Banerjee, P.; Mayes, A. M.; Pickett, G.; Balazs, A. C. *Macromolecules* **2000**, *33* (15), 5702−5712.

Macromolecules

Article

pubs.acs.org/Macromolecules

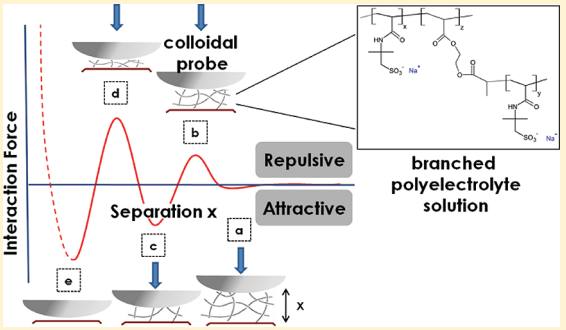
Effect of Molecular Architecture on the Polyelectrolyte Structuring under Confinement

Cagri Üzüm,[†] Ricardas Makuska,[‡] and Regine von Klitzing*,[†]

[†]Stranski-Laboratorium, Institut für Chemie, Technische Universität Berlin, Strasse des 17. Juni 124, D-10623 Berlin, Germany

[‡]Department of Polymer Chemistry, Vilnius University, LT-03225 Vilnius, Lithuania

ABSTRACT: The paper addresses the structuring and rheology of semidilute polyelectrolyte solutions with varied concentration and degree of polymer branching. The used polymer is constituted of the units of sodium 2-acrylamido-2-methylpropanesulfonate (NaPAMPS) with the branching inserts of 2-(2-bromopropionyloxy)ethyl acrylate (BPEA). The content of the branching units of BPEA in the polyelectrolytes was 6, 17, and 24%. Comparison of data obtained by small-angle X-ray scattering (SAXS) and colloidal probe atomic force microscope (CP-AFM) was used to study the effects of a solid−solid confinement on the structuring. Scattering peaks from SAXS and oscillatory force curves from CP-AFM indicate a transient network of polyelectrolyte chains with structural parameters such as interchain distance, correlation length, and interaction strength. The interchain distance and the correlation length obtained by SAXS (bulk) and CP-AFM (confinement) are in the same range, suggesting no compression of the network in the confined geometry. The interchain distance is not affected by the degree of branching at a fixed monomeric unit concentration. The correlation length (the range of ordering), the strength of the interchain interactions, and the solution viscosity, on the other hand, depend slightly on the degree of branching. The electrostatic correlation length and the interaction strength are smaller for 17% and 24% branched chains, reflecting a more disordered network.



1. INTRODUCTION

Polyelectrolytes are defined as polymers with ionizable groups.[1] In contrast to neutral polymers, small-angle scattering techniques (SAXS or SANS) give structural peaks of dilute or semidilute polyelectrolyte solutions.[2] The peak position, q_{max}, can be used to determine the interchain distance d in bulk, using the Bragg equation $d = 2\pi/q_{max}$. Under confinement, structural forces arise in polyelectrolyte systems which are strongly related to the structuring in bulk.[3−6] Force vs confinement thickness profile shows oscillatory behavior as the confinement interfaces come as close as a few times of the interchain distance, which is interpreted as a mesh-by-mesh expulsion of the polyelectrolytes from the slit pore, i.e., the film. The oscillation period gives therefore the interchain distance under confinement. Depending on this fact, structuring, i.e., ordering, under confinement can be studied by surface force apparatus (SFA),[7] total internal reflection microscopy (TIRM),[7,8] optical tweezers,[7] thin film pressure balance (TFPB),[3,9−14] or atomic force microscopy (AFM).[4−6,14−21] There are several reviews discussing the determination of structural forces.[7,22−24] An outstanding observation in the past 10 years is that the bulk and the thin-film structuring differ only slightly in polyelectrolyte systems, restricted that there is no surface adsorption.[4,5,12,17] As an exception, a 20% compression of the interchain distance in confined geometry was reported for dilute and semidilute NaPSS solutions.[25]

Analyzing small-angle scattering patterns or structural forces, the scaling of interchain distance with the concentration can be gathered. This scaling gives information about the structuring in a polyelectrolyte solution, since the conformation of polyelectrolyte chains in the solution depends mainly on their concentration.[2,26−29] At low polyelectrolyte concentrations, i.e., in the dilute regime, the chains form coils and the interchain distance in dilute regime scales with the concentration as $c^{-1/3}$ as was reported for spherical hard particles.[30−34] The mean intercoil distance can be approximated from particle number density.[25] At the overlap concentration c^*, polyelectrolyte chains can no longer exist as individual coils and they start to overlap. Overlapping leads to a transient network in the unentangled-semidilute regime.[26,29] Milling and Kendall,[16] Thedoly et al.,[17] and Jönsson et al.[35] proposed a parallel aligned lateral layers instead of a network structure. Rapoport et al. recently reported that a transition may occur between a lateral layer structure and a network structure.[36] In both cases, the interchain distance in semidilute regime ($c > c^*$) scales with the concentration[2,26,27,29,37−41] as $c^{-1/2}$, and it corresponds to the mesh size of the transient network.

Briefly, a transition from semidilute to dilute regime causes a change in the scaling law[4,42,43] from $c^{-1/2}$ to $c^{-1/3}$. Besides

Received: December 21, 2011
Revised: February 28, 2012
Published: March 23, 2012

ACS Publications © 2012 American Chemical Society

decreasing the concentration, this transition can be induced by charge reduction and increasing the chain hydrophobicity.[4,42] Still, it was reported that there is a charge fraction above which Manning condensation occurs, and the polyelectrolyte structuring becomes independent of the charge fraction.[5] If a hydrophilic neutral monomer is chosen, the scaling law remains as $c^{-1/2}$ even for lower charge fractions,[5,44] and the network structure is preserved.

In addition to the charge fraction, polyelectrolyte chain length and molecular architecture play an important role for the structuring of polyelectrolytes. Previously, the impacts of chain length on the structuring under confinement was discussed in detail.[3,16,19,20,25,45,46] It was shown that the interchain distance scaling changes from $c^{-1/3}$ to $c^{-1/2}$ with increasing chain length at a fixed monomer concentration range. As for the effects of architecture, the structure of the (mostly individual) branched or star-shaped polymers have been studied recently by experiments, simulations, or theory in bulk[47−53] and in confined geometry.[54−63] Because of the very different nature of the studied chains, different types of structuring were observed. For example, the interchain distance d was shown to scale as $c^{-1/3}$ for confined PEI (38% secondary N atoms) dendrimers, and d increased with increasing molecular weight at a fixed concentration, indicating a spherelike ordering.[54] Star-shaped NaPSS, on the other hand, has a scaling of $d \sim c^{-1/2}$ above the overlap concentration and resembles the linear chains at even higher concentrations.[64] It was found that the viscosity of randomly branched polymers is smaller compared to linear ones with the same molecular weight.[65] The viscosity depends also less on the molecular weight for branched polymers.[66]

Despite the number of studies focusing on the effects of confinement on branched polyelectrolytes, most of these studies involve isolated, individual, and highly branched dendrimers or star-shaped chains. A systematic investigation of the polyelectrolyte structuring under confinement as a function of (relatively low) degree of molecular branching is not reported yet. In the current study, the degree of branching of a hydrophilic polyelectrolyte PAMPS was tuned by using 6, 17, and 24% branching monomer-initiator BPEA, as it was previously characterized and studied in the dilute regime.[67] The impacts of the architectural change on the interchain distance, correlation length, and interaction strength were studied in semidilute regime. CP-AFM and SAXS were used to study the structuring in thin-film (confinement) and bulk, respectively. The dependence of conductivity and viscosity on the monomeric unit concentration is discussed in order to correlate the microscopic structuring to macroscopic solution properties.

2. EXPERIMENTAL SECTION

2.1. Materials. Randomly branched poly(sodium 2-acrylamido-2-methylpropanesulfonates) (NaPAMPS) were synthesized via self-condensing AGET ATRP of sodium 2-acrylamido-2-methylpropanesulfonate (NaAMPS) in the presence of 2-(2-bromopropionyloxy)-ethyl acrylate (BPEA) as a branching monomer-initiator (inimer), as the details are given somewhere else.[67] The average fractal dimension is 1.43. Linear LPAMPS was synthesized by homopolymerization of NaAMPS under the same conditions. Composition of the branched NaPAMPS (BPEA content), molecular weight M_w, and polydispersity index M_w/M_n of the branched polymers are presented in Table 1. According to the data of ^{1}H NMR spectroscopy, the content of BPEA units in the branched PAMPS varied as 6, 17, and 24 mol %, namely BPAMPS-6, BPAMPS-17, and BPAMPS-24. The content of branching units (branching degree) in the copolymers was expected to be somewhat less since a part of BPEA units were terminal. Branching degree of BPAMPS-24 was obviously much higher than that of BPAMPS-6. Chemical structures of LPAMPS and branched BPAMPS are presented in Figure 1. The solutions were prepared in Milli-Q (Millipore) water without any further purification or additives.

Table 1. Characteristic Properties of Studied Branched PAMPS Samples Taken from Ref 67

sample	BPEA content, mol %	M_w	M_w/M_n
LPAMPS	0	858 000	2.07
BPAMPS-6	6	112 000	1.99
BPAMPS-17	17	95 000	1.98
BPAMPS-24	24	119 000	2.47

2.2. Colloidal Probe Atomic Force Microscopy (CP-AFM). The colloidal probe technique developed by Ducker et al.[68] was used to study the effect of confinement on the polyelectrolyte structuring. A silica particle was glued with epoxy to a tipless cantilever with a given spring constant of 0.03−0.08 N/m (Ultrasharp Contact Silicon Cantilevers, CSC12, Micromasch). Silica particles with a radius R of about 3.35 μm were purchased from Bangs Laboratories, Inc. The cantilevers carrying the colloidal probes were exposed to air plasma cleaning for 20 min to remove all organic components on their surface. The substrate was a silicon wafer with a native SiO_2 top layer, cleaned with the RCA method,[69] and stored in Milli-Q water. Just before each experiment, the substrate was taken out of the water and dried in a nitrogen stream. Then a drop of the polyelectrolyte solution was put onto the substrate, and the probing head is fully immersed in the solution. Force−separation curves were collected via a commercial atomic force microscope MFP3D (Asylum Research, Inc.). The forces between the silica probe and the substrate were assumed to occur between two flat surfaces, considering that the separation between the probe and the substrate is much smaller than the size of the probe (Derjaguin approximation). No adsorption of the PAMPS is expected as both the polymer chains and the SiO_2 surfaces are negatively charged in the experimental conditions. 15 to 25 force−distance curves were taken at different positions on the same substrate as well as on different substrates with different cantilevers for better statistics. For the analysis, the oscillatory force−separation curves obtained by colloidal probe AFM were fitted with the formula[4−6]

$$F(x)/2\pi R = A^{-\lambda x} \cos[2\pi(x/d) + \varphi] + \text{offset} \quad (1)$$

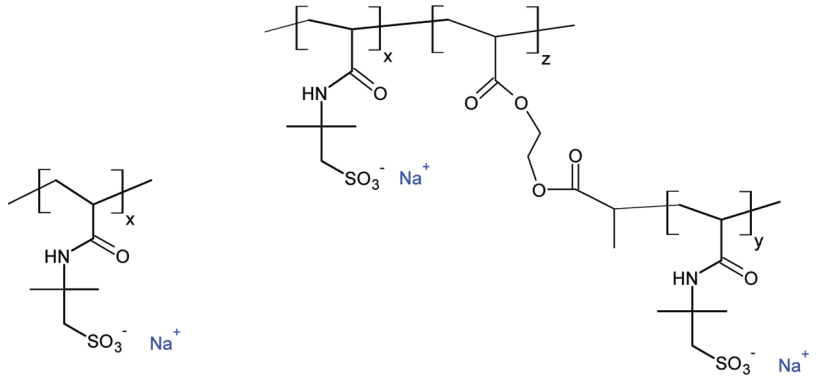
Here, $F(x)$ is the force as a function of the separation between the two confining walls x. R is the radius of the colloidal probe, A is the amplitude, and λ is the decay length of the oscillation. d corresponds to the period of the oscillation while φ and offset are nonessential correction parameters. It should be noted that while fitting the force data, the region very close to hard contact ($x < 10$ nm) should not be included due to additional contribution of the nonstructural forces.

2.3. Small-Angle X-ray Scattering (SAXS). The SAXS measurements were performed using a SAXSess mc^2 system (Anton Paar KG, Graz, Austria) equipped with a sealed tube microsource and a line collimation. Cu Kα radiation having a wavelength of 0.154 nm was produced at 40 kV and 50 mA. Data analysis was done using SAXSquant 3.5 (Anton Paar, Austria) and Igor Pro (Wavemetrics) software packages, for $q < 4$ nm^{-1}. The background subtracted data were desmeared against the beam length profile of the source. All measurements were performed in a 1 mm quartz capillary at 25 °C.

2.4. Conductivity and Viscosity Measurements. The conductivity of the solutions was measured at ambient conditions by a InoLab Cond 720 instrument (WTW GmbH, Weilheim, Germany).

The viscosity of the solutions were measured at 25 °C by a commercial Processor Viscosity System PVS1 (Lauda, Germany) using a micro-Ubbelohde glass capillary viscometer (Schott, Germany) with a viscometer constant of 0.010 05 mm^2 s^2. The flow time was detected by two infrared sensors, and the analysis was made by the relevant Lauda software.

dx.doi.org/10.1021/ma202763m | Macromolecules 2012, 45, 3168−3176



(a) (b)

Figure 1. Chemical structures of (a) LPAMPS and (b) BPAMPS.

3. RESULTS AND DISCUSSION

Understanding the structuring is the first step to clarify the chain conformation and ion distribution in a branched polymer system. In this study, the chain architecture (degree of branching) was systematically changed for a better understanding of its effects in a confined geometry. Four P(AMPS) derivatives with different degrees of branching, namely from the linear to the most densely branched:[67] LPAMPS, BPAMPS-6, BPAMPS-17, and BPAMPS-24 were compared in terms of their conductivity, viscosity, and structuring (via CP-AFM and SAXS). The samples have a fractal dimension of 1.43, so the chain architecture is between rod-like and arborescent.[67] The corresponding charge fractions were calculated as LPAMPS = 100%, BPAMPS-6 = 94%, BPAMPS-17 = 83%, and BPAMPS-24 = 76%. Considering the Manning condensation concept,[5,70] the effective charge fraction is expected to be the same for all four samples at around 45%.[5,71] Figure 2 confirms this

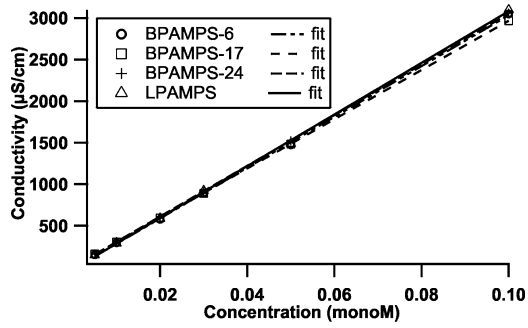
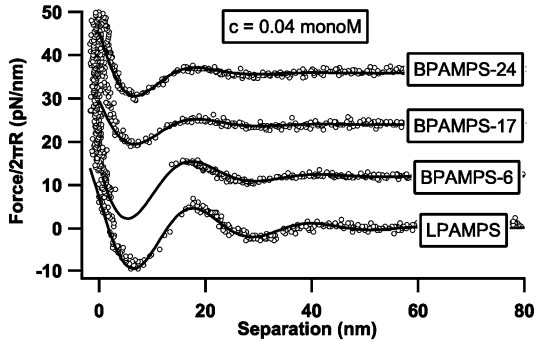


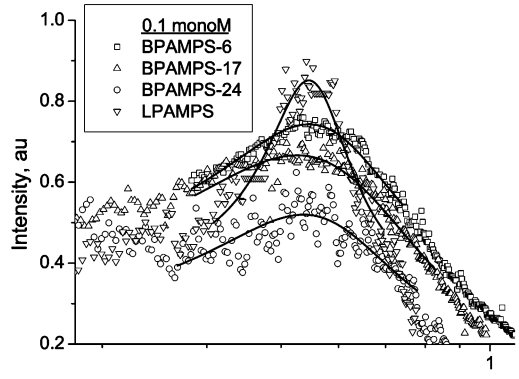
Figure 2. Concentration dependence of the conductivity for P(AMPS) derivatives with different density of branching. The lines present the linear fits. The exact agreement of the conductivities suggest same amount of charge on the chains regardless of the architecture.

assumption by showing the same conductivity values for all samples at a same polymer concentration (expressed in concentration of monomeric units: mol monomer/L or monoM). Keeping in mind that the nominal degree of charge is the same for all systems at a fixed monomeric unit concentration, and assuming that the branched chains in this study have similar molecular weights, any difference in the structuring can be attributed to the different degrees of branching.

CP-AFM force−distance curves and SAXS spectra for all samples at a fixed monomeric unit concentration of 0.04 and 0.1 M, respectively, are shown in Figure 3. Oscillatory force curves from CP-AFM indicate the existence of structural forces,



(a)

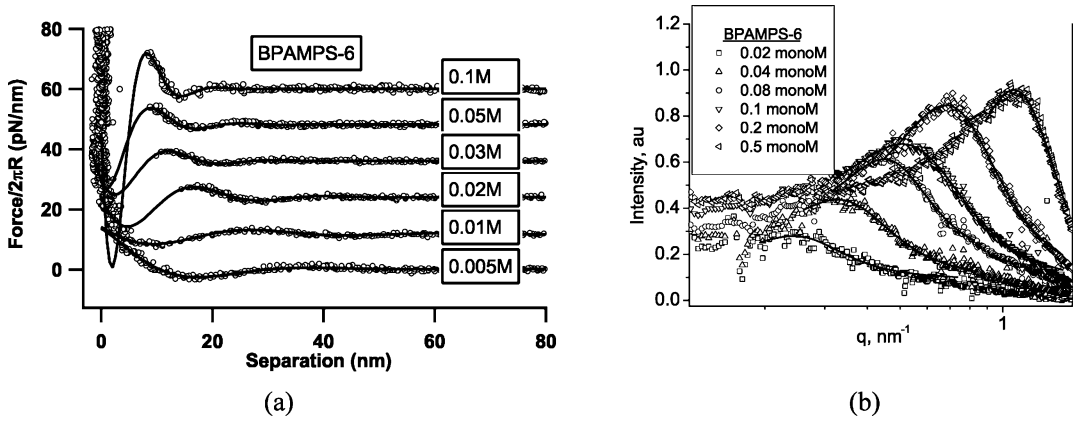


(b)

Figure 3. (a) CP-AFM force-separation curves (shifted in *y*-axis for better visualization) and (b) SAXS patterns for LPAMPS, BPAMPS-6, BPAMPS-17, and BPAMPS-24 at a fixed polymer concentration of 0.04 and 0.1 M, respectively. The solid lines correspond to (a) the extrapolated fits with eq 1 and (b) the Lorentzian fits around the peak.

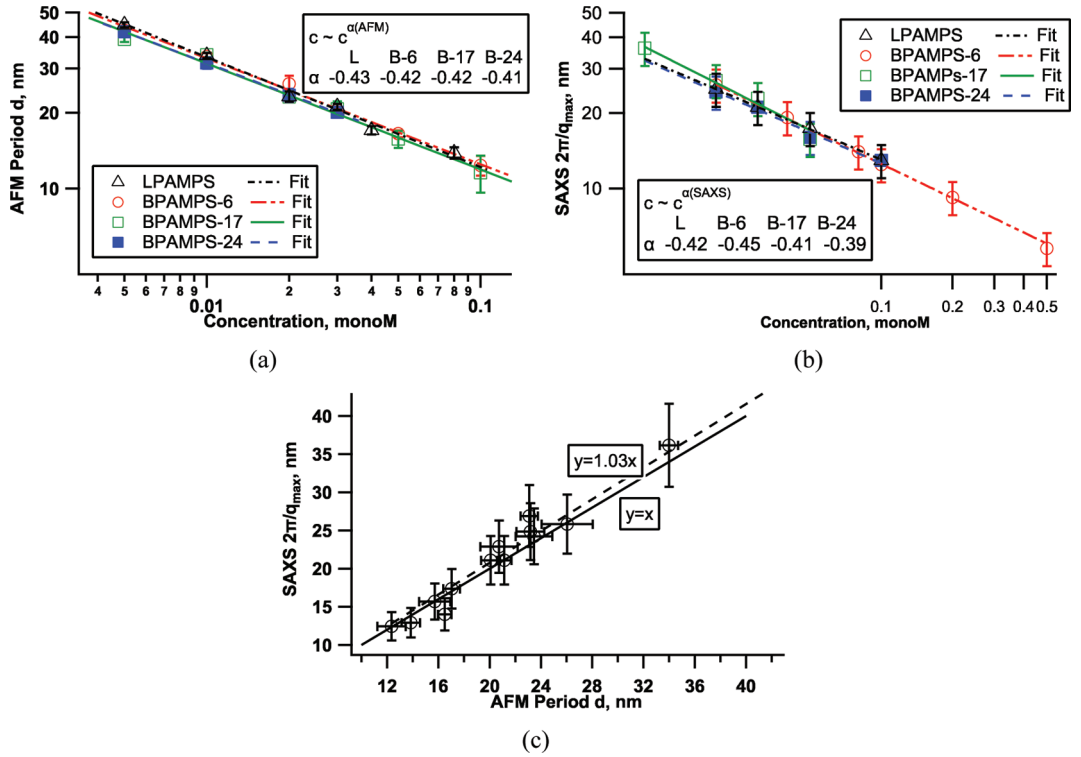
i.e., some layering of the polyelectrolyte chains. The broad peaks in SAXS also indicate at least a near range structuring. The solid lines in the CP-AFM graph are the fits of the force−separation curves according to eq 1, and the ones on the SAXS spectra are the Lorentzian fits.[5,72] Equation 1 defines the asymptotic pair correlation function in bulk, for infinite

dx.doi.org/10.1021/ma202763m | *Macromolecules* 2012, 45, 3168−3176



(a) (b)

Figure 4. (a) CP-AFM force−separation curves (shifted in *y*-axis for better visualization) and (b) SAXS patterns for BPAMPS-6 at different polymer concentrations. The solid lines show (a) the extrapolated fits of the force data according to eq 1 and on (b) the Lorentzian fits.



(a) (b)

(c)

Figure 5. Concentration dependence of (a) CP-AFM periods d obtained from oscillatory force−distance curves by eq 1 and (b) $2\pi/q_{max}$ obtained from SAXS. Samples with different degrees of branching were considered. Both parameters correspond to the interchain distance (mesh size) in the semidilute network. Lines show the linear fits in the log scale. (c) A comparison of all the d and $2\pi/q_{max}$ values. The solid line is the $2\pi/q_{max} = d$ reference, and the dashed line is the actual linear fit of the data showing $2\pi/q_{max} = 1.03d$.

distance.[31,73] However, it was found to be valid in nanoparticle systems under confinement as well.[30,31]

At a fixed c, CP-AFM oscillatory forces become more pronounced and SAXS maximum scattering intensity increases with decreasing degree of branching. The period of the oscillatory forces and the position of the maximum scattering in SAXS seem to be unaffected by the branching. This observation is valid for all studied concentrations.

Figure 4 presents the same plots for various c at a fixed degree of branching (BPAMPS-6). CP-AFM force curves become more pronounced, and they oscillate with a smaller period with increasing concentration. In SAXS spectra scattering intensity of the maximum increases, and its position is shifted to higher q (momentum transfer) values with increasing polymer concentration. This behavior applies to all studied degrees of branching. Interchain distance, correlation length, and interaction strength as measured by CP-AFM and SAXS are discussed in the following sections.

3.1. Interchain Distance: CP-AFM Period d vs SAXS $2\pi/q_{max}$. The concentration dependence of the period of the oscillatory CP-AFM force−distance curves is shown in Figure 5a. The period d is nearly the same for all the samples at a fixed c, and it decreases with increasing c. A concentration regime at which the size of a star-shaped polyelectrolyte is equal to the size of a linear polyelectrolyte was already reported.[52] Apparently, this behavior applies also to the branched BPAMPS at the studied concentration range.

dx.doi.org/10.1021/ma202763m | *Macromolecules* 2012, 45, 3168−3176

Table 2. α and β Values in the Relations d or $2\pi/q_{max} \sim c^{\alpha}$ and λ or $1/\Delta q \sim c^{\beta}$ As Obtained by CP-AFM and SAXS Measurements on Polyelectrolytes with Different Degrees of Branching

sample	degree of branching	α_{AFM}	α_{SAXS}	β_{AFM}	β_{AFM}
LPAMPS	0	−0.43 ± 0.02	−0.42 ± 0.02	−0.66 ± 0.07	−0.64 ± 0.08
BPAMPS-6	6	−0.42 ± 0.02	−0.45 ± 0.02	−0.54 ± 0.04	−0.44 ± 0.06
BPAMPS-17	17	−0.42 ± 0.03	−0.41 ± 0.02	−0.35 ± 0.04	−0.38 ± 0.06
BPAMPS-24	24	−0.41 ± 0.01	−0.39 ± 0.02	−0.31 ± 0.06	−0.34 ± 0.04

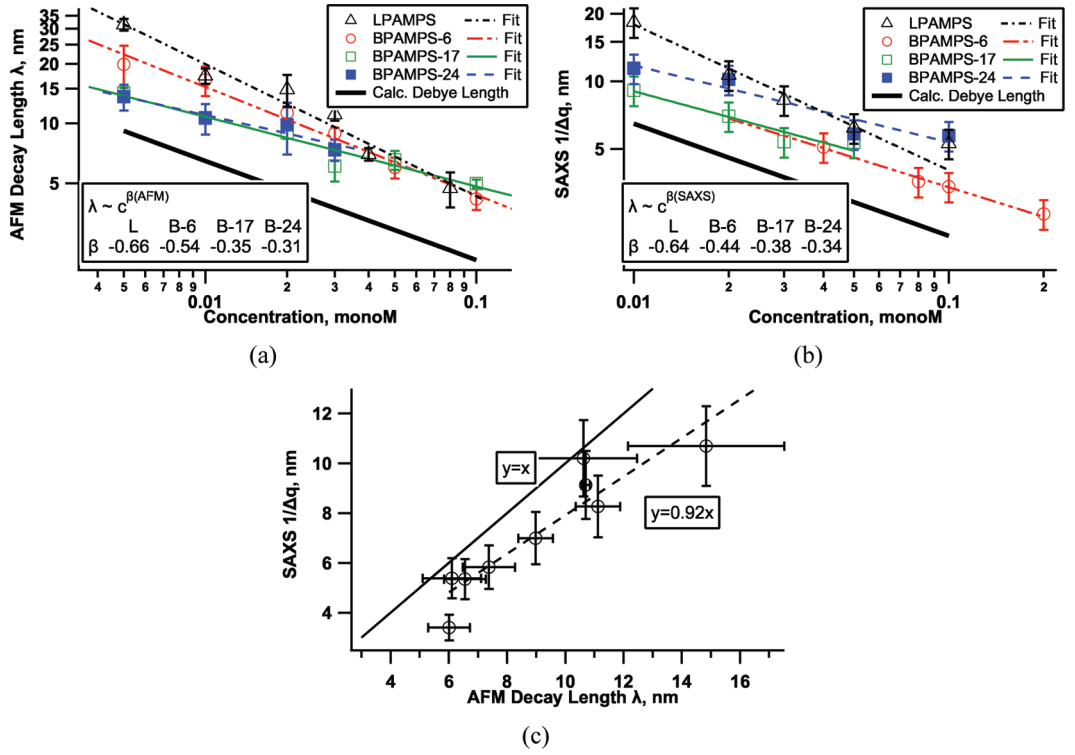


Figure 6. Concentration dependence of (a) CP-AFM decay length λ obtained from oscillatory force−distance curves by eq 1 and (b) reciprocal peak width $1/\Delta q$ obtained from SAXS for samples with different degrees of branching. Both parameters give the range of ordering in the semidilute network. The lines present the linear fits in the log scale. The calculated Debye lengths are shown as a thick solid line. (c) A comparison of λ vs $1/\Delta q$. The solid line is the $1/\Delta q = \lambda$ reference, and the dashed line is the actual linear fit with $1/\Delta q = 0.92\lambda$.

For all four samples, the concentration dependence of the period d was defined as $d \sim c^{\alpha_{AFM}}$, where α_{AFM} is the scaling exponent. $\alpha_{AFM} = -0.42 \pm 0.03$ was found independent of the degree of branching, which lies between the theoretical values −0.5 (transient network) or −0.33 (coils). Noting that the typical experimental scaling exponent for a semidilute polyelectrolyte system is not exactly −0.5 but ≈−0.45, $\alpha_{AFM} = -0.42$ indicates a network structuring rather than layering of individual coils.[5,25] If the chains are long enough, roughly saying when they are made of more than 300 monomeric units, the solution already passes the overlap concentration c^* in the studied concentration regime (>0.005 M) as has been proposed by theory[2,29] and observed experimentally by small-angle scattering techniques (SAXS and SANS),[3−5,17,25,43,44,74,75] dynamic light scattering (DLS),[76−79] thin film pressure balance (TFPB),[3,9−14] and colloidal probe AFM.[4−6,14,18−21,25] Once c^* is reached, only the total number of charged groups determines the interchain distance in the salt-free solutions of linear polyelectrolytes. This behavior was reported previously for different charge fractions[5] and different chain lengths.[25]

In order to compare the thin film (confined) structuring with the bulk one, interchain distance in the solution bulk was determined by SAXS. The interchain distance is given as $2\pi/q_{max}$, where q_{max} is the momentum transfer at the position of maximum scattering intensity. The $2\pi/q_{max}$−c dependence for all four degrees of branching is shown in Figure 5b. As in the case of CP-AFM d, $2\pi/q_{max}$ is also unchanged for all degrees of branching at a fixed concentration. $2\pi/q_{max}$ decreases with increasing c as $2\pi/q_{max} \sim c^{\alpha_{SAXS}}$. α_{SAXS} values for all four samples were calculated from a linear fit of the $2\pi/q_{max}$ vs c data in the log scale (shown as various lines in Figure 5b). $\alpha_{SAXS} = -0.41 \pm 0.04$ for all degrees of branching, indicating a network-like structuring in the semidilute regime. Table 2 shows the scaling exponent α in the relations $d \sim c^{\alpha_{AFM}}$ and $2\pi/q_{max} \sim c^{\alpha_{SAXS}}$ for CP-AFM and SAXS, respectively. The two scaling exponents coincide well within the error range.

A similar scaling law of $2\pi/q_{max} \sim c^{-1/2}$ was previously reported[64] for star-shaped NaPSS above c^*. On the other hand, branched PEI (38% secondary N atoms) was reported to have a particle-like scaling of $d \sim c^{-1/3}$, and d increased with increasing molecular weight.[54]

In order to compare the absolute interchain distances in bulk and in thin film, CP-AFM d is plotted against SAXS $2\pi/q_{max}$ Figure in 5c. The solid line is the reference $2\pi/q_{max} = d$ line, and the dashed line is the actual fit showing that $2\pi/q_{max} = 1.03d$. It should be noted again that these branched chains were

dx.doi.org/10.1021/ma202763m | Macromolecules 2012, 45, 3168−3176

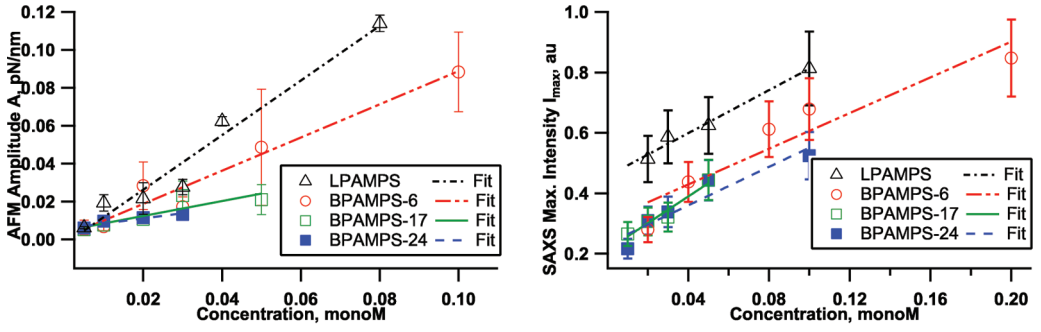


Figure 7. Concentration dependence of (a) CP-AFM amplitude A obtained from fitting the oscillatory force data with eq 1 and (b) maximum SAXS intensity I_{max} for the linear and the branched polyelectrolytes. The lines present the linear fits.

reported to be in the intermediate region between rod-like and arborescent structure.[67] The results above suggest that, first, the rod-like character dominates the interchain distance, at least for $c > c^*$. This is the only explanation for the fact that the more branched samples have similar interchain distance as their less-branched and even linear equivalents. Second, confinement leads to stratification for all degrees of branching and changes the bulk interchain distance only slightly if none, in analogy with the previous reports.[4,5,43] However, NaPSS systems were reported to show a 20% compression under confinement.[25] Note that simulations also predicted a slight compression of star-shaped polyelectrolytes near the walls.[62,63]

3.2. Correlation Length: CP-AFM Decay Length λ vs SAXS $1/\Delta q$. The decay length of the oscillatory force−distance curves is a measure of the correlation length, i.e., the range of ordering in a system, and it can be extracted from eq 1.[4,5] The dependence of the CP-AFM decay length (correlation length) λ on c is presented in Figure 6a for the branched BPAMPS-6, BPAMPS-17, and BPAMPS-24 and the linear LPAMPS. λ decreases with increasing c for all four degrees of branching as in the case of d. Since LPAMPS has a much higher molecular weight than the branched BPAMPS (Table 1), no direct comparison of its decay length with that of branched ones was performed as the molecular weight might affect this parameter.[25]

Figure 6 shows that the more branched samples BPAMPS-17 and BPAMPS-24 have smaller decay lengths than the less branched BPAMPS-6. Under the assumption that the decay length is correlated to the distribution of counterions, it is concluded that the two more branched chains (BPAMPS-17 and BPAMPS-24) have a higher counterion density within the network than the less branched BPAMPS-6. At this point, it is worth recalling the results from the previous part that the interchain distance d remains the same at a fixed monomeric unit concentration irrespective of the degree of branching. A similar behavior was obtained for other branched or linear chains so that the increase in the charge fraction[5,6] or in the ionic strength[3,54] resulted in a decrease in the correlation length while the interchain distance remained the same. BPAMPS-17 and BPAMPS-24, however, have very close correlation lengths which make a quantitative conclusion about degree of branching dependence of λ impossible.

Although the polyelectrolytes addressed in the current study are far from being star-shaped, they are also not purely rod-like. As a comparison, for the star-shaped NaPSS ($d \sim c^{-1/2}$) it was reported that the counterion distribution between the arms has a complex nature and depends on the length and density of the arms as well as the distance from the core of the star.[64] Moreover, simulations suggested two types of counterion capturing between the brushes of the star-shaped polyelectrolytes: A strong Manning condensation and a weak trapping which allows the counterions to move within the arms but restrict them from leaving the brush interior.[62] It should be noted that different backbone[25,54] or branch[64] lengths can also result in slightly different correlation lengths, which might explain the difference of BPAMPS-6, BPAMPS-17, and BPAMPS-24 in the current study.

Some studies[4,5] correlated λ with the theoretical Debye length λ_D; therefore, also for the studied branched systems, the experimental λ values were compared to the theoretical Debye length ($\lambda_D = 1/(4\pi l_b f_{eff} c)^{1/2}$, where f_{eff} is the effective charge fraction under the assumption that Manning condensation takes place and l_b = 7.1 Å is the Bjerrum length[4,5]). This equation suggests that λ_D scales as $\lambda_D \sim c^{-0.5}$, which is not valid for λ of the studied polymers (see Table 2). The calculated λ_D is shown in Figure 6a (thick line) for comparison with the experimental λ. In analogy with the literature,[4,5,43] λ is much larger than λ_D. Of course, the calculation of λ_D is based on many assumptions which might explain the deviation; however, there are strong indications that not only electrostatics but also entropy (steric interactions) determine the correlation length.[4−6,25]

The reciprocal width at half-maximum of a SAXS pattern $1/\Delta q$ is a bulk property and gives also information about the correlation length of the system.[4,5,72] Figure 6b shows $1/\Delta q$ as a function of c for all degrees of branching. Determining Δq is not as straightforward as determining q_{max} due to the low contrast of the SAXS data, and the possible errors are larger, up to ±15%. But $1/\Delta q$ clearly decreases with c with a dependence of $[1/\Delta q] \sim c^{\beta_{SAXS}}$ where β_{SAXS} is in the same range as β_{AFM}.

To summarize, although the correlation length or the counterion distribution within the network depends slightly on the degree of branching, no quantitative trend could be obtained. The agreement between λ and $1/\Delta q$ as well as between β_{AFM} and β_{SAXS} suggests that ion distribution around the chains or the range of ordering in the network system does not depend on the existence of a confinement, in agreement with previous reports.[4,5,43]

3.3. CP-AFM Amplitude A and SAXS Intensity I_{max}. Figure 7a shows how the CP-AFM oscillatory force amplitude A depends on the concentration and on the degree of branching. A increases with increasing polymer concentration for all the linear and the branched polyelectrolytes. This behavior was observed in other studies for several polyelec-

dx.doi.org/10.1021/ma202763m | Macromolecules 2012, 45, 3168−3176

trolyte systems,[3−6,15,16,18,25,45,80] and it is an outcome of the increasing total chain charge in the system and decreasing translational entropy of a single chain. The chains therefore repel each other more strongly before one of the layers is pressed out of the confinement. However, in force measurements, a high solution viscosity was observed to affect the amplitude of the oscillatory curves as well, suppressing the oscillation peaks and giving a significant increase in the hydrodynamic drag force. The dramatic effect of the confinement velocity has been already reported for CP-AFM and thin film pressure balance (TFPB) techniques.[7] According to that, a sufficient relaxation time has to be provided for the ordered layers to rebuild their formation. In the case of TFPB measurements, this can be achieved by increasing the viscosity of the system so that the thinning of the film is slower. In CP-AFM force measurements, the velocity of the piezo extension can be easily lowered to an optimum value. In the current study, a measurement velocity of 20−100 nm/s was used, and it was observed that within this velocity range the peaks are more pronounced. For lower velocities (<20 nm/s), the noise and the signal drift make the analysis of the force curves impossible. For higher piezo extension velocities (>1000 nm/s), the soft cantilever is exposed to a strong hydrodynamic drag and the force curves do not give any detectable oscillations.

An important parameter that was observed to affect the oscillation amplitude in force measurements is the polymer chain length. Longer chains give more pronounced oscillatory force profiles[16,25] and scattering peaks[25,81] due to an entropy penalty. The studied branched samples have comparable chain lengths, but it should be noted that the linear sample LPAMPS has a larger contour length compared to the branched ones, which might explain its larger A shown in Figure 7a.

Figure 7a also shows that the least branched BPAMPS-6 presents higher A as compared to BPAMPS-17 and BPAMPS-24. This trend is the same as for the correlation lengths λ and $1/\Delta q$ discussed in the previous section. This similarity is not surprising considering that a smaller correlation length means a more disordered structure in which the translational entropy of a single chain is increased. Therefore, less work is required in branched systems to exclude the chains out of the confinement, resulting in a decrease in the amplitude A of the structural forces.

The SAXS maximum scattering intensity I_{max} is a measure of the interchain interaction strength and the translational entropy of a single chain in the polyelectrolyte solution bulk. I_{max} as a function of polymer concentration is presented in Figure 7b. The trend under confinement and in solution bulk is the same: A and I_{max} increase with increasing concentration for a fixed degree of branching and decrease with increasing density of branching at a fixed concentration. It is not possible to quantitatively compare A (CP-AFM) and I_{max} (SAXS) and to reveal the effect of confinement on the interaction strength; however, simulations for star-branched polymers show that their mobility decreases with increasing degree of confinement,[58,59] which in turn should result in enhanced interactions in the confined geometry due to entropic reasons explained above.

3.4. Viscosity. Rheological properties of polyelectrolyte solutions are determined by their configuration relative to each other[82] and are highly concentration dependent. It was suggested that the overlap concentration, c^*, is reached when $\eta \approx 2\eta_s$, i.e., $(\eta - \eta_s)/\eta_s = 1$, where η is the measured viscosity and η_s is the solvent viscosity.[82,83] Figure 8 shows the concentration dependence of the specific viscosity for all four degrees of branching. The horizontal dashed line represents the dilute−semidilute transition viscosity. As it was found in section 3.1 from interchain distance vs concentration scaling, viscosity measurements also indicate a semidilute structuring for all the samples, except for very low concentrations of the three branched samples. There is no systematic increase/decrease in the viscosity with respect to the degree of branching. The viscosity increases with increasing concentration and in the order BPAMPS-17 < BPAMPS-24 < BPAMPS-6 < LPAMPS at a fixed monomeric unit concentration. This order is different than that of the microscopic parameters discussed in the sections above. It has been already reported that viscosity of linear polyelectrolytes increases with increasing chain length.[25,29,82,83] This fact explains the much higher viscosity of LPAMPS compared to the BPAMPS samples (see Table 1). The slightly lower viscosity of BPAMPS-17 can be also explained by its ≈10% lower M_w compared to BPAMPS-6 and BPAMPS-24, in agreement with previous reports discussing the viscosity of branched polymers.[84,85]

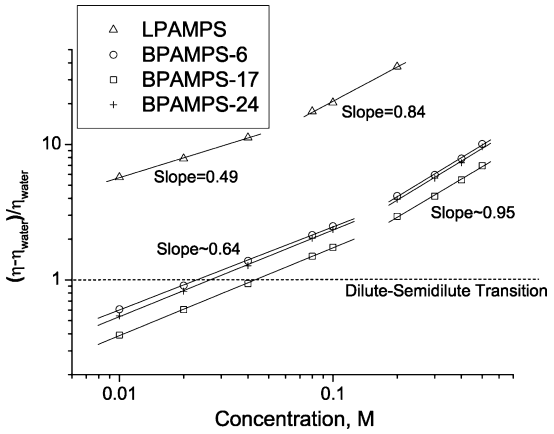


Figure 8. Specific viscosities of PAMPS with different degrees of branching. The dashed line corresponds to the estimated viscosity where concentration regime changes from dilute to semidilute. Error bars are smaller than ±5% and not shown.

For the linear sample, LPAMPS, the dependence of the viscosity is $\sim c^{0.5}$ for c < 0.1 M and $\sim c^{0.84}$ for c > 0.1 M. The scaling of specific viscosity with $\sim c^{0.5}$ up to a polymer concentration of 0.1 M is predicted by theory[29,83] and shown experimentally[25,82,86] for various linear polyelectrolytes. The theoretical scaling for c > 0.1 M is predicted as 3/2,[29,83] not explaining the scaling exponent of 0.84 found in this study for LPAMPS. Nevertheless, a scaling lower than 3/2 in this regime was observed previously.[25,82,83] Presumably, the scaling between the unentangled- and entangled-semidilute regimes is not sharp and around the transition concentration, it starts to increase starting from 1/2 and reaches to 3/2 at a higher concentration.[25]

An interesting result for the branched samples is that the concentration dependence of the specific viscosity is the same for BPAMPS-6, BPAMPS-17, and BPAMPS-24: $(\eta - \eta_s)/\eta_s \sim c^{0.65}$ for c < 0.1 M and $\sim c^{0.95}$ for c > 0.1 M. The lower scaling exponent compared to linear polymers can be explained by the effect of branching[66] so that interdigitation of neighboring chains is less probable for branched polymer chains, but more theoretical effort is needed to clarify why samples with different degrees of branching would have the same viscosity−concentration dependence.

Finally, it should be noted that viscosity measurements suggest a dilute structuring of BPAMPS samples for $c \leq 0.02$ M which could not be observed with CP-AFM or SAXS measurements ($d \approx 2\pi/q_{max} \sim c^{-1/2}$ was observed instead of $\sim c^{-1/3}$). This difference can be attributed to the narrow concentration range (0.01−0.02 M) measured in this region, which is not enough to show a distinguishable dilute solution trend. It should also be reminded that the dilute−semidilute transition line in Figure 8 is only a rough estimation.

4. CONCLUSION

The effect of degree of branching (chain architecture) on polyelectrolyte structuring in salt-free aqueous solutions was studied. In order to better understand the effects of physical confinement, structural parameters such as the interchain distance, the correlation length, and the interchain interaction strength were extracted from CP-AFM (in confined geometry) and SAXS (in bulk). Randomly branched polyelectrolyte chains (with a structure between rod-like and arborescent[67]), with a similar molecular weight but different degrees of branching were compared. CP-AFM, SAXS, and viscosity measurements indicate that the solutions are in the semidilute regime and consist of transient networks. The interchain distance of the polyelectrolyte network is insensitive to the degree of branching, suggesting that it is dominated by chain's rod-like character. The electrostatic correlation length of the least branched chain is, however, larger than that of the other two, indicating a longer range of ordering. Interaction strength between the polyelectrolyte chains depends slightly on the degree of branching by similar means as the correlation length. A direct comparison of the experimental interaction strength under confinement and in bulk is not possible, but theory suggests a decrease in entropy and in turn an increase in the interaction strength under confinement. The interchain distance and correlation length in the thin film (confinement) and bulk are the same regardless of the degree of branching, showing that there is no compression of the chains or counterions even under strong confinement. All branched samples have the same specific viscosity−concentration scaling, which is lower compared to linear polymers. The independence of this scaling from the degree of branching is still to be clarified by theory.

AUTHOR INFORMATION

Corresponding Author

*E-mail: klitzing@mailbox.TU-Berlin.de; Ph: +49 (30) 314 23476; Fax: +49 (30) 314 26602.

Notes

The authors declare no competing financial interest.

ACKNOWLEDGMENTS

We thank Stephanie Christau for her valuable help with the viscosity measurements (financing: DFG IGRTG 1524). Technical University of Berlin, Research Council of Lithuania (Contract MIP-50/2010), and European Union Marie Curie Network SOCON (MCRTN-CT-2004-512331) are acknowledged for the financial support.

REFERENCES

(1) Liao, Q.; Dobrynin, A. V.; Rubinstein, M. *Macromolecules* **2003**, *36*, 3386−3398.
(2) Dobrynin, A.; Rubinstein, M. *Prog. Polym. Sci.* **2005**, *30*, 1049−1118.
(3) von Klitzing, R.; Kolaric, B.; Jaeger, W.; Brandt, A. *Phys. Chem. Chem. Phys.* **2002**, *4*, 1907−1914.
(4) Qu, D.; Baigl, D.; Williams, C.; Mohwald, H.; Fery, A. *Macromolecules* **2003**, *36*, 6878−6883.
(5) Qu, D.; Pedersen, J. S.; Garnier, S.; Laschewsky, A.; Moehwald, H.; von Klitzing, R. *Macromolecules* **2006**, *39*, 7364−7371.
(6) Qu, D.; Brotons, G.; Bosio, V.; Fery, A.; Salditt, T.; Langevin, D.; von Klitzing, R. *Colloids Surf., A* **2007**, *303*, 97−109.
(7) Kleshchanok, D.; Tuinier, R.; Lang, P. R. *J. Phys.: Condens. Matter* **2008**, *20*, 073101.
(8) Biggs, S.; Prieve, D.; Dagastine, R. *Langmuir* **2005**, *21*, 5421−5428.
(9) Asnacios, A.; Espert, A.; Colin, A.; Langevin, D. *Phys. Rev. Lett.* **1997**, *78*, 4974−4977.
(10) Kolaric, B.; Jaeger, W.; von Klitzing, R. *J. Phys. Chem. B* **2000**, *104*, 5096−5101.
(11) von Klitzing, R.; Espert, A.; Asnacios, A.; Hellweg, T.; Colin, A.; Langevin, D. *Colloids Surf., A* **1999**, *149*, 131−140.
(12) von Klitzing, R.; Espert, A.; Colin, A.; Langevin, D. *Colloids Surf., A* **2001**, *176*, 109−116.
(13) Langevin, D. *Eur. Phys. J. E* **2001**, *5*, 81−85.
(14) Kleinschmidt, F.; Stubenrauch, C.; Delacotte, J.; von Klitzing, R.; Langevin, D. *J. Phys. Chem. B* **2009**, *113*, 3972−3980.
(15) Milling, A. *J. Phys. Chem.* **1996**, *100*, 8986−8993.
(16) Milling, A.; Kendall, K. *Langmuir* **2000**, *16*, 5106−5115.
(17) Theodoly, O.; Tan, J.; Ober, R.; Williams, C.; Bergeron, V. *Langmuir* **2001**, *17*, 4910−4918.
(18) Biggs, S.; Dagastine, R.; Prieve, D. *J. Phys. Chem. B* **2002**, *106*, 11557−11564.
(19) Knoben, W.; Besseling, N. A. M.; Stuart, M. A. C. *Phys. Rev. Lett.* **2006**, *97*, 068301.
(20) Knoben, W.; Besseling, N. A. M.; Stuart, M. A. C. *Langmuir* **2007**, *23*, 6095−6105.
(21) Ribeiro, W.; Orfao, M.; Mata, J. L.; Saramago, B. *J. Colloid Interface Sci.* **2008**, *317*, 536−543.
(22) Stubenrauch, C.; von Klitzing, R. *J. Phys.: Condens. Matter* **2003**, *15*, R1197−R1232.
(23) Bonaccurso, E.; Kappl, M.; Butt, H.-J. *Curr. Opin. Colloid Interface Sci.* **2008**, *13*, 107−119.
(24) Üzüm, C.; Kristen, N.; von Klitzing, R. *Curr. Opin. Colloid Interface Sci.* **2010**, *15*, 303−314.
(25) Üzüm, C.; Christau, S.; von Klitzing, R. *Macromolecules* **2011**, *44*, 7782−7791.
(26) Degennes, P.; Pincus, P.; Velasco, R.; Brochard, F. *J. Phys. (Paris)* **1976**, *37*, 1461−1473.
(27) Odijk, T. *Macromolecules* **1979**, *12*, 688−693.
(28) Barrat, J.; Joanny, J. *Europhys. Lett.* **1993**, *24*, 333−338.
(29) Dobrynin, A.; Colby, R.; Rubinstein, M. *Macromolecules* **1995**, *28*, 1859−1871.
(30) Klapp, S. H. L.; Zeng, Y.; Qu, D.; von Klitzing, R. *Phys. Rev. Lett.* **2008**, *100*, 118303.
(31) Klapp, S. H. L.; Grandner, S.; Zeng, Y.; von Klitzing, R. *J. Phys.: Condens. Matter* **2008**, *20*, 494232.
(32) Grandner, S.; Zeng, Y.; von Klitzing, R.; Klapp, S. H. L. *J. Chem. Phys.* **2009**, *131*, 154702.
(33) Klapp, S. H. L.; Grandner, S.; Zeng, Y.; von Klitzing, R. *Soft Matter* **2010**, *6*, 2330−2336.
(34) Zeng, Y.; von Klitzing, R. *Soft Matter* **2011**, *7*, 5329−5338.
(35) Jonsson, B.; Broukhno, A.; Forsman, J.; Akesson, T. *Langmuir* **2003**, *19*, 9914−9922.
(36) Rapoport, D. H.; Anghel, D. F.; Hedicke, G.; Moehwald, H.; von Klitzing, R. *J. Phys. Chem. C* **2007**, *111*, 5726−5734.
(37) Degennes, P. *Macromolecules* **1981**, *14*, 1637−1644.
(38) Khokhlov, A.; Khachaturian, K. *Polymer* **1982**, *23*, 1742−1750.
(39) Yethiraj, A.; Shew, C. *Phys. Rev. Lett.* **1996**, *77*, 3937−3940.
(40) Yethiraj, A. *J. Chem. Phys.* **1999**, *111*, 1797−1800.
(41) Netz, R.; Andelman, D. *Phys. Rep.* **2003**, *380*, 1−95.

(42) Limbach, H.; Holm, C.; Kremer, K. *Europhys. Lett.* **2002**, *60*, 566−572.
(43) Baigl, D.; Ober, R.; Qu, D.; Fery, A.; Williams, C. *Europhys. Lett.* **2003**, *62*, 588−594.
(44) Nishida, K.; Kaji, K.; Kanaya, T. *Macromolecules* **1995**, *28*, 2472−2475.
(45) Biggs, S.; Burns, J.; Yan, Y.; Jameson, G.; Jenkins, P. *Langmuir* **2000**, *16*, 9242−9248.
(46) Biggs, S. *Phys. Chem. Chem. Phys.* **2010**, *12*, 4172−4177.
(47) Charmuszko, K.; Sikorski, A. *J. Non-Cryst. Solids* **2009**, *355*, 1408−1413.
(48) Gray-Weale, A.; Gilbert, R. G. *J. Polym. Sci., Part A1* **2009**, *47*, 3914−3930.
(49) Moeller, D.; Munstedt, H.; Kaspar, H. *Rheol. Acta* **2009**, *48*, 509−516.
(50) Bosko, J. T.; Prakash, J. R. *Macromolecules* **2011**, *44*, 660−670.
(51) Knaapila, M.; Stepanyan, R.; Torkkeli, M.; Lyons, B.; Ikonen, T.; Almasy, L.; Foreman, J.; Serimaa, R.; Guntner, R.; Scherf, U.; Monkman, A. *Phys. Rev. E: Stat., Nonlinear, Soft Matter Phys.* **2005**, *71*, 041802.
(52) Shusharina, N. P.; Rubinstein, M. *Macromolecules* **2008**, *41*, 203−217.
(53) Jusufi, A.; Likos, C. N. *Rev. Mod. Phys.* **2009**, *81*, 1753−1772.
(54) von Klitzing, R.; Kolaric, B. *Aqueous Polym.-Cosolute Syst.* **2003**, *122*, 122−129.
(55) Knaapila, M.; Stepanyan, R.; Lyons, B.; Torkkeli, M.; Hase, T.; Serimaa, R.; Guntner, R.; Seeck, O.; Scherf, U.; Monkman, A. *Macromolecules* **2005**, *38*, 2744−2753.
(56) Cordeiro, C.; Molisana, M.; Thirumalai, D. *J. Phys. II* **1997**, *7*, 433−447.
(57) Chen, Z.; Escobedo, F. *Phys. Rev. E: Stat., Nonlinear, Soft Matter Phys.* **2004**, *69*, 021802.
(58) Sikorski, A.; Romiszowski, P. *J. Chem. Phys.* **2004**, *120*, 7206−7211.
(59) Romiszowski, P.; Sikorski, A. *J. Chem. Phys.* **2002**, *116*, 1731−1736.
(60) Romiszowski, P.; Sikorski, A. *J. Chem. Phys.* **2005**, *123*, 104905.
(61) Romiszowski, P.; Sikorski, A. *Monatsh. Chem.* **2006**, *137*, 969−976.
(62) Konieczny, M.; Likos, C. N. *Macromol. Symp.* **2006**, *245*, 276−286.
(63) Konieczny, M.; Likos, C. N. *J. Chem. Phys.* **2006**, *124*, 214904.
(64) Heinrich, M.; Rawiso, M.; Zilliox, J.; Lesieur, P.; Simon, J. *Eur. Phys. J. E* **2001**, *4*, 131−142.
(65) Graessle, W.; Mittelha, H. *J. Polym. Sci.* **1967**, *5*, 431.
(66) Valles, E.; Macosko, C. *Macromolecules* **1979**, *12*, 521−526.
(67) Gromadzki, D.; Tereshchenko, A.; Makuska, R. *Polymer* **2010**, *51*, 5680−5687.
(68) Ducker, W.; Senden, T.; Pashley, R. *Nature* **1991**, *353*, 239−241.
(69) Riegler, H.; Engel, M. *Ber. Bunsen. Phys. Chem.* **1991**, *95*, 1424−1430.
(70) Manning, G. *J. Chem. Phys.* **1969**, *51*, 924−933.
(71) Essafi, W. Structure des polyelectrolytes fortement charges. Ph.D. Thesis, University of Paris VI, 1996.
(72) Helm, C. A.; Möhwald, H.; Kjaer, K.; Als-Nielsen, J. *Biophys. J.* **1987**, *52*, 381−390.
(73) Evans, R.; Henderson, J.; Hoyle, D.; Parry, A.; Sabeur, Z. *Mol. Phys.* **1993**, *80*, 755−775.
(74) Nierlich, M.; Williams, C.; Boue, F.; Cotton, J.; Daoud, M.; Farnoux, B.; Jannink, G.; Picot, C.; Moan, M.; Wolff, C.; Rinaudo, M.; Gennes, P. *J. Phys. (Paris)* **1979**, *40*, 701−704.
(75) Nierlich, M.; Boue, F.; Lapp, A.; Oberthur, R. *J. Phys. (Paris)* **1985**, *46*, 649−655.
(76) Koene, R.; Mandel, M. *Macromolecules* **1983**, *16*, 220−227.
(77) Drifford, M.; Dalbiez, J. *J. Phys. Chem.* **1984**, *88*, 5368−5375.
(78) Sedlak, M.; Amis, E. *J. Chem. Phys.* **1992**, *96*, 826−834.
(79) Sedlak, M.; Amis, E. *J. Chem. Phys.* **1992**, *96*, 817−825.
(80) Milling, A.; Vincent, B. *J. Chem. Soc., Faraday Trans.* **1997**, *93*, 3179−3183.
(81) Kaji, K.; Urakawa, H.; Kanaya, T.; Kitamiru, R. *J. Phys. (Paris)* **1988**, *49*, 993−1000.
(82) Boris, D.; Colby, R. *Macromolecules* **1998**, *31*, 5746−5755.
(83) Colby, R. H. *Rheol. Acta* **2010**, *49*, 425−442.
(84) Graessle, W.; Prentice, J. *J. Polym. Sci.* **1968**, *6*, 1887.
(85) Claesson, H.; Malmstrom, E.; Johansson, M.; Hult, A. *Polymer* **2002**, *43*, 3511−3518.
(86) Prini, R.; Lagos, A. *J. Polym. Sci., Part A* **1964**, *2*, 2917.

Macromolecules

Article

pubs.acs.org/Macromolecules

SANS Investigation of Global and Segmental Structures of Hyperbranched Aliphatic−Aromatic Polyesters

W. Burchard,*[,†] A. Khalyavina,[‡] P. Lindner,[§] R. Schweins,[§] P. Friedel,[‡] M. Wiemann,[⊥] and A. Lederer*[,‡]

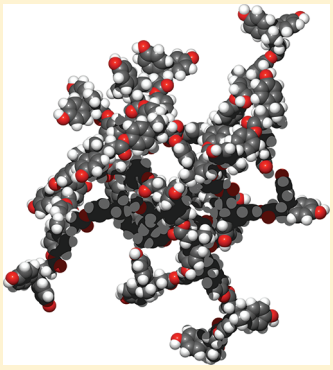
[†]Institute of Macromolecular Chemistry, University of Freiburg, Stefan-Meier-Strasse 31a, 79104 Freiburg, Germany

[‡]Leibniz Institute of Polymer Research, Hohe Strasse 6, D-1069 Dresden, Germany

[§]Institut Laue-Langevin (ILL), 6 rue Jules Horowitz, F-38042 Grenoble, France

[⊥]Insitute of Physical Chemistry, University of Freiburg, Stefan-Meier-Strasse 31a, 70104 Freiburg. Germany

ABSTRACT: SANS measurements in THF-d_6 were carried out at the D11 instrument at ILL, Grenoble with two aliphatic aromatic hyper-branched (hb) samples with nearly the same degree of polymerization (DP ≈ 90), containing hydroxyl (OH) and silyl-ether (SY) terminal groups. The choice of a large region of momentum transfer q permitted probing the global shape and the local structure. The scattering of both samples showed pronounced concentration dependence. Using Zimm's well-known scattering equation the true size and shape of the macromolecules at finite concentration were derived. Agreement of the data and curves at finite concentration with those at c = 0 was obtained. The scattering curves were analyzed on the basis of the Sinha et al.'s refinement of fractals. Complete agreement with the experimental scattering curves was achieved. The apparent anomalous behavior at very large q-values was shown to arise from the monomer and segmental contributions. Molecular dynamics (MD) simulation of an uniform hb sample (DP 35) revealed the monomer contribution in agreement with the experiment. The discrepancy of the experimental curve at small q-values is shown to arise from the broad molar mass distribution. When Flory's molar mass distribution was combined with the MD simulation data, the experimental results were described well.



INTRODUCTION

Hyperbranched (hb) polymers are nowadays not only of academic interest but are rapidly being commercialized especially as additives. They possess dendritic structures leading to special features as for instance globular shape and extremely large number of end-functionalities.[1] Still, improvement of the properties by change in the reaction mechanism would be a welcomed feature. In order to establish a reliable correlation between the chemical structure and the bulk properties, a detailed knowledge of the internal molecular parameters is imperative. Determination of size and shape of these molecules will give valuable insight into the molecular geometry and segmental order. Such a study will be a first step to the understanding of the material properties, and it will give rise to new ideas for tuning the properties by molecular design. A straightforward procedure has been very successful in the field of dendrimers, where stepwise controlled synthesis led to uniform macromolecules, identical in size and a well-defined branching topology for every single molecule. In contrast, hb polymers are fairly easily synthesized, but they are challenging when it comes to their specific characterization. Difficulties arise from the statistical nature of this poly-reaction, which is not fully random but follows a stringent chemical constraint due to the existence of the focal end group A, which can only react with one of the (two or $f \geq 2$) counter-functional groups B, but not with itself. In Flory's nomenclature,[2] the hb samples are denoted as AB_f polymers.[3]

An essential feature of random statistics in polymer reactions is the formation of a broad molar mass distribution which is significantly reduced by the mentioned constraint of hyperbranching reaction.[2] It is still too broad in view of industrial application. Furthermore, the statistical nature includes a not yet fully explored isomer distribution, i.e. samples of the same molar mass still vary in their degree of branching and the sequence of linear and dendritic repeat units, and in the amount of terminal groups. The, perhaps unrealistic, desire is the preparation of homogeneously branched species with a narrow isomer distribution, i.e., the different molecules in the ensemble should be very similar in the sequence of linear and dendritic repeat units.

The present contribution is part of a comprehensive project in which new techniques are developed to find the requirements for the desired efficiency of suitable utility. A first approach was already achieved by increasing the amount of linear elements, still keeping the hb-structural characteristics. It was possible to prepare hb samples with degree of branching (DB) varied between 0% and 50%.[4] A detailed characterization of the macromolecules was already made by static and dynamic light scattering (SLS and DLS) and viscosity measurements and by size exclusion chromatography (SEC) in combination with a multiangle laser light scattering (MALLS) and an online

Received: January 5, 2012
Revised: March 6, 2012
Published: March 20, 2012

ACS Publications © 2012 American Chemical Society

viscosity detection. However, the radius of gyration could not be measured, since the size of the particles was below the detection limit of SLS, namely a particle diameter smaller than $\lambda/20$. Therefore, small angle neutron scattering (SANS) was chosen as the suitable method to close the gap of information. The wavelength of cold neutrons in SANS provides us with the valuable additional information on the shape of the macromolecules, and it will give us insight into the segmental arrangement.

In contrast to microscopy the shape of the particles is not directly seen but appears in a Fourier-transformed reciprocal space. The development of theories with special model structures proved to be considerably simpler than in the Euclidean space. Finally, inversed Fourier transformation leads back to real space, and a radial distance distribution between the various scattering centers in the particles is obtained, a result that cannot be obtained by microscopy.

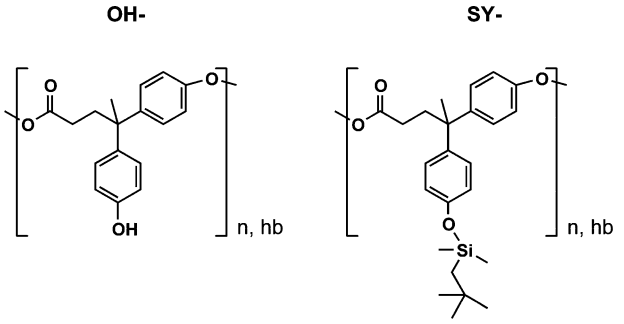
Pioneering work on hb-macromolecules was made by Flory in 1952,[3] who, on the basis of probability theory, derived the molar mass distribution $w(x)$, the number and weight averages of the molar mass (M_n and M_w) and the corresponding polydispersity index PDI = M_w/M_n. His motivation was to develop an appropriate theory for the Meyer model[5] for branched amylopectin. This natural polymer, indeed, is a hyperbranched polymer with a degree of branching (DB) of about 4−5% but extremely high molar mass. More recent research realized that the enzymatic synthesis led to a far more complex structure[6] and Flory's results remained disregarded for a longer period of time. In the past 15 years several hb samples could now be synthesized corresponding to the Flory's model.[3,7−11] Then, 20 years after Flory's work, the theory on hb polymers was extended to the calculation of the static[12] and dynamic light scattering[13] by using a new technique that was introduced by Gordon[14] in 1962 to polymer science. The corresponding model described the unperturbed conformations (i.e., by Gaussian statistics) and was not accepted as a realistic description.[15] Further development was made 1984 by Sinha et al,[16] who included the excluded volume effect of the segments, and via the conception of fractals he succeeded to describe the corresponding angular dependence of randomly branched samples. The same method can be applied to the hb polymers, but now the knowledge of the unperturbed scattering behavior is required as a basis for this treatment. This will be demonstrated in the course of this paper.

SANS and small-angle X-ray scattering (SAXS) were applied earlier to a few types of hb polymers. Analysis of different molar masses of hb polyesters was made by De Luca et al.,[17] with polyglycerols by Garamus et al.[18] and polyester amides by Geladé et al.[19] All these studies revealed similar behavior and gave the desired information on the dimensions of the radius of gyration for the hb structures, but the analysis was limited to relatively small values of the momentum transfer $q = (4\pi/\lambda)\sin(\theta/2)$. The authors failed to give a satisfying description of the experimental curve since it was based on unperturbed conformations. The present study is a successful attempt to quantitatively describe the scattering curve in the full q-range, up to q = 0.5 Å^{-1}. This includes the scattering from the local structure, which concerns mainly the monomer repeat unit. This local structure was found to have a pronounced influence on the scattering behavior of small hb polymers, which has been much underestimated in the literature. Our analysis led to a better outcome due to the significant improvement in the detection of SANS intensities offering improved new possibilities of very accurate detection over the large q region.[20]

Another aspect may be worth mentioning. Dendrimers were found to develop a marked structure factor $S(q)$ at moderately concentrated solutions, similar to hard sphere behavior as it was detected by Prosa et al.[21] This observation gives rise to the question whether similar colloidal properties, though weaker, may be obtained with hyperbranched samples of high segment density. This point appears of interest in the application of hb polymers, since the high amount of terminal functional groups may have a favored influence on significant properties, i.e., on film formation.

In this study, we focused our investigations onto well-defined, statistically branched aromatic−aliphatic polyesters (Scheme 1).[4]

Scheme 1. Chemical Structure of the Hyperbranched Polymers with Different End Functionalities



These hyperbranched polymers were synthesized by polycondensation in solution leading to a significantly reduced polydispersity in comparison to their synthesis in melt.[22] A degree of branching of 50%, according to the definition of Frey,[23] was confirmed for the two investigated samples.

THEORY

In the present project on hyperbranched samples the results from static light scattering (SLS) and small angle neutron scattering (SANS) are combined.[24] The evaluation of data is largely the same in both techniques. A detailed comparison of these two different techniques is given in ref 25. Nonetheless, the outline of a few corresponding features may be helpful, and they are recalled here.

Some Basic Comments on the Scattering Equation. In both methods intensities are recorded, in SLS these intensities are related to visible light or number of photons, in SANS it is the number of neutrons. In light scattering, the intensity can be expressed by the Rayleigh ratio

$$R_\theta = \frac{I(q)}{I_0} r^2 \tag{1}$$

where θ is the scattering angle and r is the distance of the detector from the scattering samples, $I(q)$ is the scattering intensity in arbitrary units which is compared to the scattering intensity I_0 of the primary beam of light or neutrons. The q-parameter depends on the scattering angle θ and is defined as

$$q = \left(\frac{4\pi n_0}{\lambda}\right) \sin(\theta/2) \tag{2}$$

dx.doi.org/10.1021/ma300031g | Macromolecules 2012, 45, 3177−3187

and is denoted as the magnitude of the scattering vector, but in SANS it is more frequently called the momentum transfer of the neutrons caused by the scattering. λ is the wavelength of visible light or that of neutrons. n_0 is the refractive index of the solvent used, which in neutron scattering is unity.

The scattering intensity from samples dissolved in a solvent is related to the particle volume or, equivalently, to the molar mass of the particle. The former result is obtained if the volume fraction of the dissolved sample is used, and the molar mass is obtained if the weight concentration c in mg/mL is used. Using the weight concentration c, the scattering intensity can be expressed by the Debye equation

$$\frac{R_\theta}{Kc} = RT\left(\frac{\partial c}{\partial \pi}\right)_{p,T} P(q, c) \tag{3}$$

where K is a contrast factor which is differently defined in SLS and in SANS. π is the osmotic pressure and $RT\ (\partial c/\partial \pi)_{p,T}$ is the osmotic compressibility. This thermodynamic quantity occurs since it is related to the thermally induced concentration fluctuations which had to be averaged by a thermodynamic partition function. The scattering intensity is dominated by the magnitude of concentration fluctuations, and these fluctuations are increasingly suppressed by the osmotic pressure when locally the concentration is increased. The osmotic compressibility describes the interparticle interactions which in turn depend on the thermodynamic quality of the used solvent and have a significant concentration dependence. This fact has a large influence on the scattering data from the samples in the present study.

The absolute scattering intensity depends decisively on the contrast factor K. In light scattering this factor is

$$K = \frac{4\pi^2}{\lambda^4 N_A}\left(n_0 \frac{\partial n}{\partial c}\right)^2 \tag{4}$$

and requires separate measurement of the refractive index increment $\partial n/\partial c$, N_A is Avogadro's number. In SANS the scattering intensity is governed by the scattering length density which have distinct values for each atomic species. The corresponding equation for the contrast factor is given by King[26] and by Higgins and Benoit[25] and is defined by the equations

$$(\Delta\rho)^2 = (\rho_{pol} - \rho_{sol})^2 \tag{5}$$

$$\rho = \frac{\delta N_A}{M} \sum_i b_i \tag{6}$$

where δ is the bulk-density of the sample and N_A Avogadro's number, M is the molar mass of the particle and the b_i are the scattering lengths for the various atoms in the monomer repeat unit. We determined the contrast factor from eq 6. The SANS scattering intensities are calibrated by the known absolute value of water, and cross-checked with the results from polymer standards.[27] Still slight systematic errors are inevitable when measurements were made using different instruments. To get consistent results, we used the molar mass as determined by LS.

The scattering intensity has an angular dependence which arises from interferences of scattered rays originating from different scattering points in the particle. The influence of these interferences becomes markedly strong when the particle dimensions are at order of the wavelength. The angular dependent factor $P(q,c)$, also called formfactor, is the scattering intensity normalized at the angle $\theta = 0$ (or $q = 0$).

$$P_{app}(q, c) \equiv \frac{R_\theta(q, c)}{R_{\theta=0}} \tag{7}$$

It always approaches the value 1 at the forward scattering direction, i.e., at $\theta = 0$. The particle scattering factor is not solely an angular dependent function but also depends on the concentration. In two consecutive subsections, we will separately consider the thermodynamic contribution and the structure dependent angular distribution of the scattered light.

Molar Mass and Interparticle Interactions. Equation 3 requires the knowledge of the osmotic compressibility which is known in theory only for some special examples, e.g., hard spheres and to some extent also for cylindrical structures and now flexible coils in a good solvent.[28−30] However, in most cases, an analytical expression of concentration dependence is not required since only fairly diluted concentrations are applied. In such cases, the osmotic pressure can be expanded in a virial series. Inserting this virial series into eq 3 one obtains a rather inconvenient evaluation equation. Following a suggestion of Debye the reciprocal of eq 3 leads to the more convenient

$$\begin{aligned}\frac{1}{RT}\left(\frac{\partial \pi}{\partial c}\right)_{p,T} &= \frac{Kc}{R_{\theta=0}(c)} \\ &= \frac{1}{M_w} + 2A_2 c + 3A_3 c^2 + \ldots \\ &\equiv \frac{1}{M_{app}(c)}\end{aligned} \tag{3a}$$

which also defines the apparent molar mass $M_{app}(c)$ at finite concentration c. Thus

$$\begin{aligned}\frac{M_w}{M_{app}(c)} &= (1 + 2A_2 M_w + 3A_3 M_w c^2 + \ldots) \\ &= \frac{M_w}{RT}\left(\frac{\partial \pi}{\partial c}\right)_{p,T}\end{aligned} \tag{8}$$

includes all types of interparticle interactions though the analytic function is mostly not known. We wish to call attention to the notations $M_w = M_{app}(c = 0)$, and $M_{app}(c)$ is a measurable quantity (see eq 3a).

Correlation between the Particle Scattering Factor $P(q)$, the Radial Distance Distribution, and Fractal Behavior. The particle scattering factor is a function of q which has a dimension of 1/length. A return to r in space is achieved by the Fourier transform

$$4\pi \int_0^\infty P(q)\left\langle \frac{\sin(qr)}{qr} \right\rangle q^2\, dq = g(r) r^2\, dr \tag{9}$$

where free rotation of the particles is assumed. $g(r)$ is the radial distance correlation function. The angled bracket $\langle \ldots \rangle$ indicates the average over all distance fluctuations. The advantage of the radial distribution function becomes clear when excluded volume interactions between segments in a particle are taken into account. This may be elucidated by the familiar example of polydisperse random coils which was derived by Zimm[31]

$$P_{lincoil}(q) = \frac{1}{1 + q^2 R_g^2} \tag{10}$$

dx.doi.org/10.1021/ma300031g | Macromolecules 2012, 45, 3177−3187

The Fourier transform gives the radial distance distribution of

$$g_{lincoil}(r) = A\frac{\exp(-r/\xi)}{r} \tag{11}$$

in which ξ is a correlation length. This radial correlation function holds for structures with a fractal dimension of d_f =2 which is characteristic of linear random coils. De Gennes[32] expanded this correlation function to *fractals* with fractal dimensions between $1 < d_f < 3$

$$g_{d_f}(r) = A\frac{\exp(-r/\xi)}{r^{3-d_f}} \tag{12}$$

Sinha et al.[16] noticed that the Fourier transformation of this function can be performed analytically and obtained

$$P_{fractal}(q) = \frac{\sin[(d_f - 1)a\tan(q\xi)]}{q\xi(1 + q^2\xi^2)^{(d_f-1)/2}} \tag{13}$$

This function was shown to excellently describe the scattering behavior of polydisperse flexible chains as well as randomly branched clusters in good solvents. It also was successfully applied to aggregates with fractal dimension up to $d_f \approx 3$.[33,34] The correlation length ξ is related to the radius of gyration R_g which is

$$\xi^2 = \frac{2}{d_f(d_f + 1)}R_g^2 \tag{14}$$

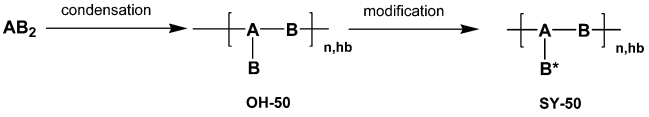
We will make use of eq 13 and 14 later in the discussion of our data.

EXPERIMENTAL SECTION

Sample Preparation. Two hyperbranched (hb) samples of about the same degree of polymerization (DP ≈ 90) were selected for a detailed SANS study, one with terminal OH-groups (denoted as OH-50), the other with *tert*-butyldimethylsilyl ether derivatized end groups (SY-50). The DP ≈ 90 was considered large enough to have reached the limiting degree of branching DB = 50% for a hb-polymer.[22] The hb polymers were polyesters and are based on monomer AB_2 repeat units of 4,4-bis(4′-hydroxyphenyl)pentanoic acid. The chemical structure is shown in Scheme 1.

The OH-terminated hb polyester OH-50 was synthesized by a procedure described in detail by Schallausky et al.[22] The modification of OH-50 resulting in SY-50 was described by Khalyavina et al.[4] The details of the synthesis will be not repeated here. Approximately a 100% modification was achieved. The corresponding polyreaction and modification are outlined in Scheme 2.

Scheme 2. Schematical Representation of the Synthesis of OH-50 and SY-50[4]



The molecular parameters of the two samples selected for SANS are given in Table 1. The molar mass was determined by size exclusion chromatography (SEC) in online combination with multiangle laser light scattering (MALLS) detection. Corresponding to the larger molar mass of the SY-50 repeat unit the M_w of the hb-sample is higher than that of the OH-50 sample, but the DP is about 10% lower. The lower DP of SY-50 originated from the required purification for the SY-sample. Table 1 also contains the data of the polymer densities, the chemical formula of the repeat units, the corresponding scattering lengths and the calculated contrast factor $(\Delta\rho)^2$ of the samples in THF-d_6 as solvent.[24]

Table 1. Molecular Parameters of the Hyper-Branched Samples OH-50 and SY-50 in THF-d_6

	OH-50	SY-50
M_w	25600 g/mol	29200 g/mol
R_g	87.5 Å	65.4 Å
A_2	7.87×10^{-4} mol cm^3/g^2	6.54×10^{-4} mol cm^3/g^2
A_3	9.90×10^{-3} mol cm^3/g^3	17.3×10^{-3} mol cm^3/g^3
c^*	49.6 mg/cm^3	52.4 mg/cm^3
M_{mono}[a]	268 g/mol	382 g/mL
chemical formula of the monomer	$C_{17}H_{18}O_4$	$C_{23}H_{30}O_3Si$
DP	96	85
scattering length density	175×10^{10} cm^{-2}	1.02×10^{10} cm^{-2}
density	1.103 g/cm^3	1.011 g/cm^3
contrast factor	35.05×10^{-4} cm^3 mol/g^2	47.02×10^{-4} cm^3 mol/g^2

[a] M_{mono} = 268 g/mol is based on the linear repeat unit in the polymer.

MD Simulation. The molecular dynamic simulations were performed applying the software package GROMACS, version 3.3.3.[35] The system type was chosen as an NpT ensemble with a constant pressure of 101.3 kPa and a constant temperature of 298 K as the thermodynamic standard state applying the Berendsen coupling method.[36] The used force field was G43B1, the cutoff radii for all the nonbonding interactions, i.e., the van der Waals and the Coulomb interactions was set to 1.8 nm and the dielectric constant ε_r to 1.0. The atomic charges of the solvent THF and the monomer unit were calculated by an ab initio quantum mechanical optimization method with the software package GAMESS[37] using the basis set 6-31G.

The monomer unit of 4,4-bis(4′-hydroxyphenyl)pentanoic acid (OH) was applied to build the model for the hyperbranched polymer OH-50 with DP = 35. Similar to the real synthetic procedure this model was modified by exchanging the protons of the L and T standing hydroxyl group by *tert*-butyl dimethyl silyl groups (Scheme 1). The corresponding two polymers OH-50 and SY-50 were dissolved in THF solvent in order to receive a dilute polymer solution system. These two systems were energetically minimized by a steepest descent method and relaxed to the thermodynamic standard state of 298 K and 1 atm afterward including a 1000 ps simulation time period for the evaluation of the time average ensemble of the relaxed state. The structure factor $P(q)$ was calculated by means of atomic coordinates taken from the last frame at the end of the simulation with respect to the atomic form factors.

SANS. Measurements were carried out at the D11-instrument of the ILL in Grenoble with a wavelength of 6 Å and at two detector distances of 8 and 1.2 m. The selected detector distances covered a broad q-range from 0.0083 to 0.0824 Å^{-1} (at 8 m) and 0.06−0.514 Å^{-1} (at 1.2 m) with a good overlap of the two q-regimes. Figure 1 shows the q-dependencies of the scattering intensities $I(q)$ from the two samples for five concentrations of approximately 1, 2, 3, 4, and 5% (the correct concentrations are given in the Table 2). The scattering intensities are normalized with a standard water measurement after the required transmission measurements have been carried out. The solvent THF-d_6 was separately measured, normalized and then subtracted from the solution data. The experimental errors were very small and are smaller than the size of the used symbols.[20a]

dx.doi.org/10.1021/ma300031g | Macromolecules 2012, 45, 3177−3187

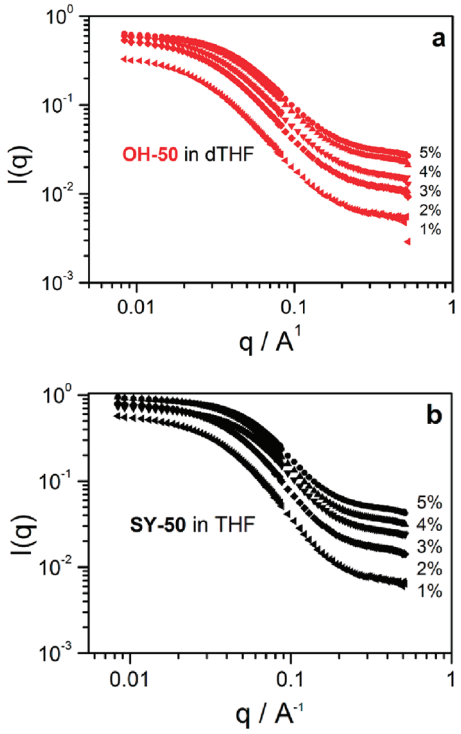


Figure 1. SANS intensity as a function of the momentum transfer q from 5 concentrations of the hyperbranched samples OH-50 (a) and SY-50 (b) of approximately the same degree of polymerization. The SY-50 sample is a silyl derivative of the OH-50 sample. The number 50 means a branching degree of 50%.

RESULTS

Basic structural parameters as the molar mass M_w, the radius of gyration R_g, and the second and third osmotic virial coefficients, A_2 and A_3 are evaluated from the Zimm equation[31]

$$\frac{Kc}{R_\theta(c)} = \frac{1}{M_w} + \frac{1}{3}\frac{\langle R_g^2(c)\rangle}{M_w}q^2 + 2A_2c + 3A_3c^2 + \ldots \quad (15)$$

Since the scattering angle is related to the magnitude of the q-vector one equally can write $R_\theta(c) = R_\theta(q,c)$. This makes the 2-fold dependence of the scattering function well apparent. The original Zimm equation is an approximation in which only the first term in the power representation of q^2 is taken into account. Mostly only the second virial coefficient is considered. Zimm suggested a special plot of the scattering data where $Kc/R(q,c)$ is plotted against $q^2 + kc$, with k is an arbitrarily chosen constant which shifts the various concentration curves to the right of the q^2 axis. This maneuver elucidates the special q^2 dependencies at the various concentrations. The limiting curve at $q^2 = 0$, obtained after extrapolation of $q^2 \to 0$, is of special interest as it represents the concentration dependence of the apparent reciprocal molar mass $1/M_{app}(c)$, see eq 8. It contains the influence of the second and third osmotic virial coefficients of the dissolved sample. Both, the q^2 and c dependencies are not linear, and the radius of gyration $\langle R_g^2\rangle^{1/2} \equiv R_g$ has to be found using the initial tangent to the curves. The scattering data often display an upturn curvature in the q^2 dependence, and in such cases Berry[38] suggested a plot of the root, $(Kc/R(q,c))^{1/2}$, against $q^2 + kc$, which often leads to a linear q^2 dependence. Figure 2a shows the Zimm plot for the OH-50 sample but a Berry plot for the SY-50 sample (Figure 2b). The data of M_w, $R_g(c)$ and the two virial coefficients A_2 and A_3 are collected in Table 1.

Interparticle Interaction. The magnitude of the second osmotic virial coefficient is mostly used as a measure of the solvent quality. Accordingly, the THF-d_6 would be a better solvent for OH-50 than for SY-50 and this holds true even when the slight difference in M_w is taken into account. A somewhat different aspect arises when the ratio $((M_w)/(M_{app}(c))) = ((M_w)/(RT))(\partial\pi/\partial c)_{p,T}$ is considered as a function of c/c^*, where $c^* = 1/A_2M_w$ is the overlap concentration. Now the SY-50 has the more pronounced concentration dependence and exerts a stronger repulsive interaction than the OH-50. The corresponding curves are shown in Figure 3, the SY-50 sample shows behavior of hard sphere whereas the OH-50 sample displays the expected behavior of partially swollen hb-polymers.[39−41]

Apparent and True Mean Square Radii of Gyration. We have no indication of association or decomposition in the chemically inert solvent. Still, the question remains whether the shape and structure is influenced by the osmotic pressure in the solution, for instance, by deformation of the shape or shrinking

Table 2. Concentration Dependence of the Reciprocal Apparent Molar Mass in 10^{-5} mol/g; the Apparent Radius of Gyration $R_{a,app}(c)$, the Interaction Function $(M_w/RT)(\partial\pi/\partial c)$ Represented by the Ratio $M_w/M_{app}(c)$, and the Resulting True Radius of Gyration at Concentration $R_g(c)$[a]

	c, mg/mL	c/c^*	$1/M_{app}(c)$, mol/g	$M_w/M_{app}(c)$	$R_{g,app}$, Å	$R_g(c)$, Å	$R_g(c)/R_g(c=0)$	error, %
	0	0	3.906	1.000	87.6	87.6	1.000	−1.3
	9.2	0.185	5.791	1.482	72.4	88.2	1.007	+1.6
OH-50	18.4	0.37	7.531	1.928	60.9	84.5	0.965	+0.3
	27.5	0.524	10.601	2.716	52.6	86.6	0.989	+4.6
	34.1	0.688	12.87	3.295	42.1	76.4	0.872	−6.0
	45.5	9.17	17.19	4.401	38.2	80.1	0.914	+1.6
	0	0	3.425	1.00	65.4	65.4	1.000	+3.4
	7.5	0.161	4.912	1.434	51.3	61.4	0.939	+0.1
SY-50	15.8	0.302	6.685	2.016	42.7	60.5	0.925	+1.9
	23.5	0.448	9.732	2.737	29.9	49.5	0.804	−13.8
	31.4	0.599	12.62	3.687	29.8	57.3	0.757	+3.2
	39.3	0.750	16.68	4.780	25.6	56.5	0.861	+5.66

[a]The ratio of $R_g(c)/R_g(c=0)$ represents the shrinking of the dimensions probably under the influence of the osmotic pressure. The column error refers to the deviation of the shrinking data from the linear fit $R_g(c)/R_g(c=0) = 0.995 - 0.147(c/c^*)$.

dx.doi.org/10.1021/ma300031g | Macromolecules 2012, 45, 3177−3187

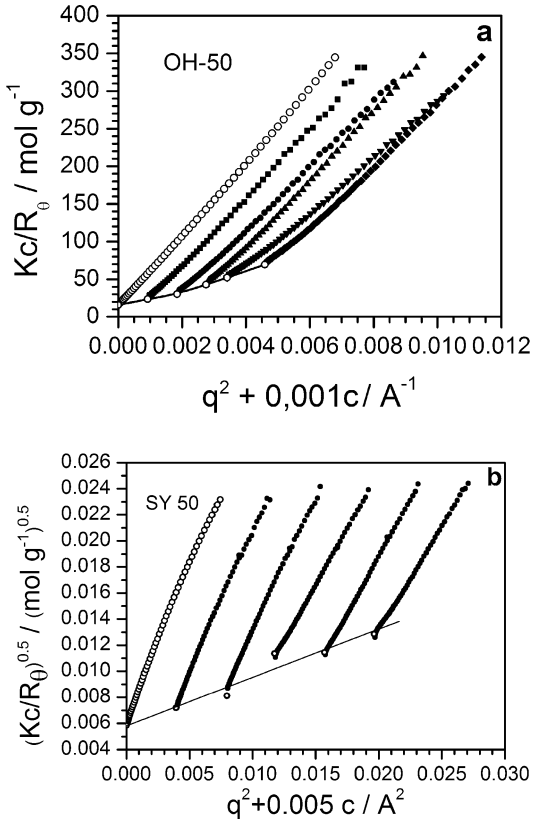


Figure 2. Zimm plot from OH-50 (a) and Berry plot from SY-50 (b) from SANS measurements in THF-d_6. Because of a fairly string concentration dependence the Berry plot was chosen for the SY-50 sample.

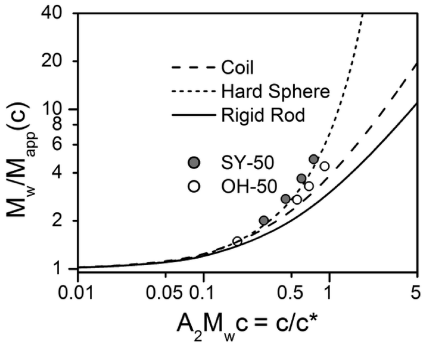


Figure 3. Variation of the interaction parameter $M_w/M_{app}(c)$ as a function of concentration and scaled concentration c/c^*, where $c^* \equiv 1/A_2M_w$ is the overlap concentration. The SY-50 sample shows behavior of spheres whereas the OH-50 sample displays the expected property of weakly swollen hb-polymers. The lines correspond to theories by Carnahan and Starling[39] (hard sphere), Ohta and Oono[40] (random coil), and Cotter and Martire[41] (rigid rod).

due to a screening of excluded volume interactions. This question can be answered with the help of eq 8, using the measured ratio $M_w/M_{app}(c)$. An apparent mean square radius of gyration may be defined by the following equation

$$\left\langle R_{g,app}{}^2(c) \right\rangle = 3 \times \frac{slope(q,\, c)}{intercept(q = 0,\, c)} = 3 \times slope(q,\, c) \times M_{app}(c) \qquad (16)$$

The slope in the Zimm equation is $slope(q,c) = R_g{}^2(c)/(3M_w)$ and the intercept is $1/M_{app}(c)$, and the combination with eq 16 yields

$$R_g{}^2(c) = R_{g,app}{}^2 \frac{M_w}{M_{app}(c)} \qquad (17)$$

where $R_g{}^2(c)$ and M_w are the *true* molecular parameters at finite concentration c. This relationship is actually nothing else than the solution of Zimm's eq 15 for the dimensions at finite concentration. Thus, the true radius of gyration at finite concentrations can be determined without knowing the actual values of the second and third virial coefficient, and no assumptions on a fractal dimension have to be made. Figure 4

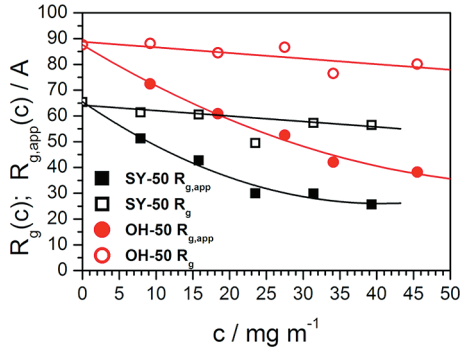


Figure 4. Concentration dependence of the apparent radius of gyration $R_{g,app}(c)$ and of the true radius of gyration $R_g(c)$ after correction for the interparticle interaction, by using the relationship $R_g{}^2(c) = R_{g,app}{}^2(c)(M_w/M_{app}(c))$.

shows the concentration dependences of $R_{g,app}(c)$ *and* $R_g(c)$, for the OH-50 and SY-50 samples. Only a weak decrease of $R_g(c)$ with the concentration can be detected, and this allows us to conclude that no significant deformation or other changes of the structure were obtained under influence of the osmotic pressure.

Apparent and True Particle Scattering Factors $P_{app}(q,c)$ and $P(q,c)$. Although the radius of gyration $R_g(c)$ remains unchanged in the moderately concentrated solutions the question still persists whether at large q values concentration dependent deviations occur in the particle scattering factor. Because in this large-q regime the segmental structure and not the global structure of the particles is probed. The apparent particle scattering factor $P_{app}(q,c)$ is defined in eq 7, and with this the Zimm eq 15 can be written in a somewhat different manner as

$$\frac{Kc}{R_\theta(c)} = \frac{1}{M_{app}(c)P_{app}(q,\, c)} = \frac{1}{M_wP(q,\, c)} + 2A_2c + 3A_3c^2 + \ldots \qquad (18)$$

with $P(q,c)$ a *true* particle scattering factor at finite concentration. Multiplying eq 18 by $M_{app}(c)$ and subtracting 1 on both sides one obtains

$$\frac{1}{P(q,\, c)} = 1 + \left(\frac{1}{P_{app}(q,\, c)} - 1 \right) \frac{M_w}{M_{app}(c)} \qquad (19)$$

Thus, $P(q,c)$ is obtained after taking into consideration the influence of interparticle interactions. Figure 5a shows the q

dx.doi.org/10.1021/ma300031g | Macromolecules 2012, 45, 3177−3187

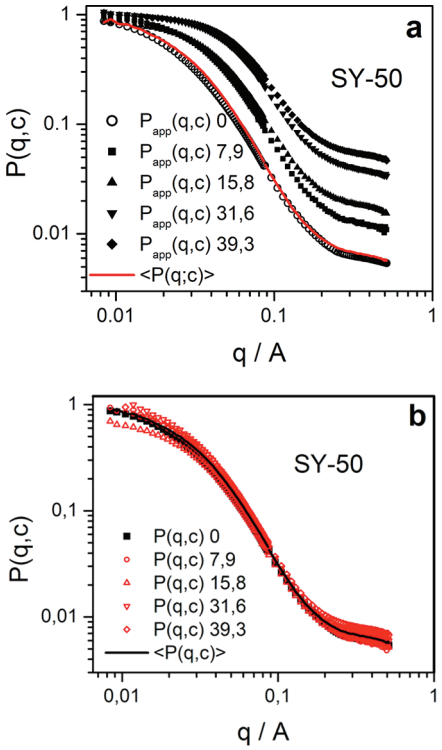


Figure 5. (a) Apparent particle scattering factors $P_{app}(q,c)$ at various concentrations of SY-50 (black curves) and the average particles scattering $\langle P(q,c)\rangle$ after removal of the influence of intermolecular interactions (line). (b) Particle scattering factor $P(q,c)$ of the individual concentration after removal of inter particle interaction (open data points) and the average over all concentrations (line). Note, the almost perfect agreement of $\langle P(q,c)\rangle$ with the scattering curve obtained by extrapolation of $P_{app}(q,c)$ to $c = 0$ (compare black data points with the full black symbols). See eq 19 and corresponding text.

dependencies of the apparent and *true* particle scattering factors as a function of q in a log–log presentation, and in Figure 5b, the effect on each concentration is explicitly shown (here only for the SY-50 sample). In both, the OH-50 and SY-50 examples, the pronounced concentration dependence of the apparent particle scattering factor reduces to the particle scattering factors at infinite dilution $P(q, c = 0)$, and this even in the large q-regime. This effect was not expected and actually may not be a general rule. The error is larger at small q but the average over all concentrations substantially gave the same curve.

Shape and Internal Structure of hb Polymers. The choice of two overlapping q-regimes for the measurements turned out to be not only a good option for getting optimum accuracy, but it presented a clear separation of probed distances into the small q-regime for large sizes compared to the monomer repeat unit (*global* structure). In the large q-regime the *local* structure; i.e., the short segments developed an unexpectedly significant effect. The results from both regimes are considered separately.

Global Structure. The molar mass averages M_w and M_n of the hb-polymers, (weight and number averages), were already predicted in 1953 by Flory[2] on the basis of probability theory. For the weight-average he found the now well-known function

$$DP_{w,hb} = \frac{1 - \alpha^2/2}{(1 - \alpha)^2} \tag{20}$$

where α is the extent of reaction of the focal functional group, which in other words is the probability that such a functional group has reacted. His result has been obtained in a somewhat more direct manner by the method of generating functions[42] and was first introduced with great success to randomly branched polymers by M. Gordon.[14,43] In 1970 Kajiwara, Burchard, and Gordon[44] published the first theory on the particle scattering factor from randomly branched chains with uncorrelated fluctuations of the individual segments (no excluded volume interaction) and in 1972 the theory was expanded to hb-polymers[12] which led to the prediction of $DP_w P(q, c = 0)$

$$DP_w P_z(q) = \frac{1 + \alpha\phi}{1 - \alpha\phi} + \frac{\alpha^2\phi^2/2}{(1 - \alpha\phi)^2} = \frac{1 - \alpha^2\phi^2/2}{(1 - \alpha\phi)^2} \tag{21}$$

with

$$\phi = \exp(-b^2q^2/6) \tag{22}$$

where $\phi(qb)$ represents the interference effect from the distance between two neighbored repeat units (bond length b). At $q = 0$, one has $\phi = 1$, and Flory's result for the DP_w (eq 20) is recovered. In the regime up to $q = 0.08$ Å^{-1} the probed length-sections are at least 20 times larger than the bond length b. Therefore, it is sufficient in this regime to consider only the linear term in the expansion of the exponential in eq 22 (Debye approximation). Applying this approximation $\phi = 1 - b^2q^2/6$ and introducing this in eq 21 one obtains

$$P(qR_g) = \frac{DP_{lin}}{DP_w}\frac{1}{1 + q^2R_{g,lin}{}^2/3} + \frac{DP_{br}}{DP_w}\frac{1}{(1 + q^2R_{g,br}{}^2/6)^2} \tag{23}$$

$$DP_w = \frac{1 - \alpha^2/2}{(1 - \alpha)^2}, \quad DP_{lin} = \frac{1 + \alpha}{1 - \alpha}, \quad DP_{br} = \frac{\alpha^2/2}{(1 - \alpha)^2}$$

$$R_{g,z}^2 = b^2\left(\frac{\alpha}{1 - \alpha} - \frac{\alpha^2/2}{1 - \alpha^2/2}\right), \quad R_{g,lin}{}^2 = b^2\frac{\alpha}{1 - \alpha^2}, \quad R_{g,br}{}^2 = b^2\frac{1}{1 - \alpha} \tag{24a–f}$$

With eq 24a, the probability α can be calculated from the measured DP_w. With this α-value DP_{lin} and DP_{br} can be calculated. The effective bond length is obtained from the measured mean square radius of gyration R_g and α. The two rations DP_{lin}/DP_w and DP_{br}/DP_w are important parameters for adapting the fractal approach to the present model, which is described below.

The derivation revealed a structurally heterogeneous hb-object that is built up from a contribution of linear chains and a branched structure contribution. This property was neglected

dx.doi.org/10.1021/ma300031g | *Macromolecules* 2012, 45, 3177–3187

in the original derivation,[12] and both contributions were added together (eq 21). For randomly distributed (i.e., independent) repeat units it makes no difference whether the two components are added or separately treated. The situation changes if a long-range *correlation* among the segments via excluded volume interactions is effective. For a long time there seemed to be no further progress in theory to deal with this issue, until recently.

Scientists recognized that disordered systems can often be represented by a fractal dimension d_f.[15b,45,46] For linear chains the fractal dimension can vary from d_f = 1.8−2.0, and for homogeneously branched samples from d_f = 2−2.5, where the low values refer to indifferent (Θ) solvents, the higher ones to thermodynamically good solvents (large positive second virial coefficients). In the analysis of SANS data the fractal dimension is derived from the negative slope of $\log(I(q))$ versus $\log(q)$. However, only in rare cases is a linear slope in the $\log(I(q))$ against $\log(q)$ found to extend over more than one decade in q. The initial part of the scattering curve cannot be described by a power-like behavior. As already mentioned in the theory section, a real progress was made by Sinha et al.[16] when he considered the Fourier transform of the scattering intensity to derive the radial distance correlation function $g(r)$ as it was given by de Gennes[32] (eq 12). The Fourier transform led Sinha et al. to $P(q)$ (see eq 13). This equation permitted an excellent description of the scattering behavior from topologically homogeneous structures, like from colloids[16] and randomly branched chains,[33,34] and it correctly included the initial part of the scattering curve.

We applied Sinha's procedure to the structurally heterogeneous hb-polymers and tried to fit the SANS measurements by fractal dimensions of d_f = 1.8 to 2.0 for the linear chain and d_f = 2.0 to 4.0 for the branched contributions. The result of a best fit is shown in Figure 6. In the very sensitive Kratky representation

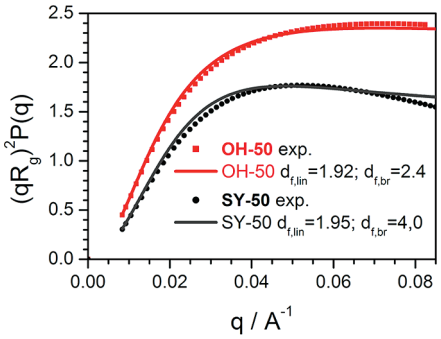


Figure 6. Kratky plot of the experimental data from the SY-50 and OH-50 samples and the corresponding fit curves with the fractal dimensions as indicated in the graph, see eqs 23 and 24 and comments in the text.

the fit for the SY-50 sample gave nearly perfect description with fractal dimensions of $d_{f,lin}$ = 1.95 and $d_{f,br} \approx$ 4.0 for the linear and branched parts. A different behavior was found with the OH-50 sample. Here the $d_{f,lin}$ = 1.92 and $d_{f,br}$ = 2.4 indicate marginally good solvent behavior, the latter is near the value d_f = 2.5 which was predicted for branched samples in a poor solvent. The SY-50 sample presents an unusual behavior and requires a special consideration that will be given in the Discussion.

Segmental and Local Structure. At q > 0.08 Å^{-1} Figure 6 displays deviations of the Sinha fractal approach from the experimental curves. In fact, the experimental curve at large q-values developed a very different appearance from that at small q-values as seen in the log−log presentation of Figure 7. The

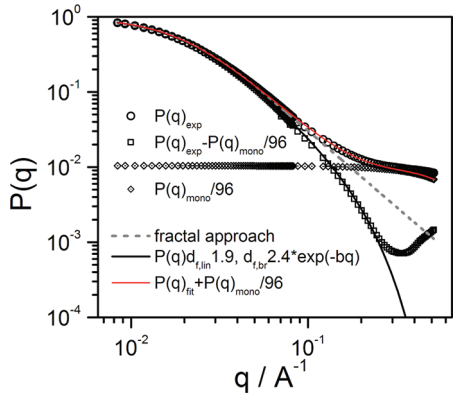


Figure 7. Particles scattering factor from experimental data of OH-50 in *d*-THF (black open circles). Experimental curve after subtraction of the monomer contribution (=1/DP $P_{mono}(q)$) (black squares). Attempt of fit by fractals of $d_{f,lin}$ = 1.9 and $d_{f,br}$ = 2 (dashed gray line); the fit curve after modification by the interference effect of a single bond length b (black line) and the resulting curve after adding the monomer contribution (red line). The sample degree of polymerization was DP = 96.

curves from the two samples at c = 0 intersect approximately at q = 0.08 Å^{-1}) (not shown) but the tangents at this point have different slopes of 2.45 for SY-50 and 1.86 for OH-50. However, the whole curves could not satisfactorily be described by only one fractal dimension. Moreover, in the large q > 0.2 Å^{-1} regime a slope of −0.245 was obtained for the OH-50 and −0.256 for the SY-50 sample. These slopes would correspond to fractal dimensions of $d_f \approx$ 0.25 which is below the lowest possible physical limit of d_f = 1. For uniform particles with a well developed surface a final decay with a power of −4 is predicted but an exponential decay for fringed surfaces with random segment lengths.[47] Expressed in terms of Porod's second invariant the integral over the function $\int_0^\infty q^2P(q)\,dq$ must necessarily remain finite. With our examples $q^2P(q)$ increases at large q with a power of about 1.75, and the integral diverges. Evidently, in the far q-regime another structure contributes to the scattering intensity. The probing q-range corresponds to lengths smaller than 2 Å, and this is in the range of the repeat unit. In fact, the structure of the repeat unit is not included in the fractal approach.

We measured SANS from the monomers and subtracted this monomer contribution from the corresponding intensity of OH-50 and SY-50. The effect is enormous and significantly changes the shape of the q-dependence that is shown in Figure 7 with the example of OH-50. A good fit of this curve with the two fractal dimensions for the linear and branched contributions was found to hold up to q < 0.08 Å^{-1}. Beyond this point the contribution from the bond length had to be taken into account. This was done by multiplying the scattering curve by $\phi_{bond} = \exp(-q^2R_{g,momo}{}^2/6)$) and now the fit described the curve up to q = 0.15 Å^{-1} (black line). After again adding the monomer contribution an almost perfect agreement with the experimental curve was obtained, the deviations were $\Delta < 5 \times 10^{-4}$, i.e., about 1.5% (red line). The SY-50 sample exhibited similar behavior.

dx.doi.org/10.1021/ma300031g | *Macromolecules* 2012, 45, 3177−3187

It may be recalled that the contribution of a finite bond length is not included in the fractal approach (which is represented by an integral, i.e., infinitely small bond lengths).

DISCUSSION

The SANS study with the present two hyper-branched samples revealed a few unexpected phenomena which need some explanation: (i) strong concentration dependence; (ii) deviation of the scattering data from single fractal behavior in the q-dependence; (iii) at large q values the local structure is probed; and finally, (iv) MD-simulations compared to experimental findings.

(i). Influence of Interparticle Interactions. The concentration dependence was not solely determined by the second virial coefficient, but at least a third virial coefficient had a significant influence. Zimm's derivation of the scattering behavior is exact for very dilute solutions and neglects the effect of higher concentrations. He argued that his derivation would remain a good approximation even when higher virial coefficients contribute. Benoit and Benmouna supported this view,[48] and in their theory they came to the conclusion that the Zimm approximation holds valid even beyond the overlap concentration. In such cases it is more appropriate to use the reciprocal osmotic compressibility (which actually is an osmotic modulus), since it includes higher virial coefficients than the third or a doubtful fourth virial coefficient. This osmotic modulus can be expressed by the experimentally accessible molar mass ratio $M/M_{app}(c)$. This fact facilitated a description of the influence of this thermodynamic parameter on the radius of gyration and the angular dependence of the scattered light at finite concentration. This effect follows immediately from Zimm's equation after a simple rearrangement which is given by eq 19. This equation also includes the already known relationship of $R_g^2(c) = R_{g,app}{}^2\mathrm{M/Mapp}(c)$.[49] As far as is known to us, this consequence from Zimm's equation has not been noticed before.

(ii). Influence of Excluded Volume on the Shape of the hb Macromolecules. The scattering behavior of unperturbed hb polymers was derived in 1972 by one of the present authors[12] being constructed of a linear and a branched contribution. Excluded volume interaction has significant influence.These effects are mostly described by a power law behavior, which should be observable in the log-plot of $I(q)$ versus q. A straight line asymptotically should occur with a negative slope of $-d_f$. Such clear behavior was found, but only in rare cases.[50,51] Mostly a bent curve is obtained. In such cases researchers try to draw tangents to more or less well-defined q-regimes, and the different slopes at different q-domains are interpreted as a change in fractal behavior when passing from large distances to smaller ones. A decisive improvement is achieved with Sinha et al.[16] who took de Gennes' radial distance distribution adapted to fractal behavior[32] and Fourier transformed this into the particles scattering factor. With this approach an excellent agreement with many examples was obtained. It also includes the correct behavior in the limit of small q-values.[16,34] Percolation simulations were predicted for branched samples in a good solvent a fractal dimenion of d_f = 2.5.[15] However, *no reasonable fit* could be achieved *with only one fractal dimension* in range of q = 0.008−0.08 Å^{-1}. This failure stands in agreement with earlier measurements by De Luca et al.,[17] Geladé et al.,[19] and Garamus et al.,[18] who obtained average d_f of 2.23−2.47 by force-fitting with one fractal dimension. Actually, a poor agreement with the experimental curves was obtained. In contrast, a very good fit was achieved for both of our samples, SY-50 and OH-50, if individual fractal dimensions were chosen for the linear part (outer chains) and the branched fraction. The fractal dimensions were those obtained from behavior in the small q-regime. The linear and branched fractals of the OH-50 sample indicate a weakly swollen structure in a marginally good solvent. A similar linear chain fractal was obtained also for the SY-50 sample, but for the branched component we found an apparent $d_f \approx 4$. Such a slope was predicted for *uniform* objects with a more or less well-defined surface (Porod law).[47] However, in the same article Porod pointed out that such q^{-4} behavior can never be observed with disordered systems consisting of irregularly fluctuating flexible chains. Such objects do not form a defined surface, and eventually the scattering intensity should decrease exponentially to zero. The observed d_f = 4 seems to be a physically senseless result. However, if we go back to de Gennes' radial pair distribution and insert d_f = 3 in eq 12, the Debye−Bueche[52] correlation function is obtained which after Fourier transformation gives the well-known asymptotic q^{-4} dependence for the scattering data (in the Kratky representation q^{-2}). Apparently, the influence of a large width in the molar mass distribution on the fractal behavior is not yet fully explored. Despite this uncertainty a densely packed branched structure (i.e., a d_f = 3) appears sensible to us, since the repeat units of SY-50 sample are fairly bulky, and, in addition, attractive forces may be effective among the SY-terminal groups and may cause a somewhat organized surface.

(iii). Influence of Local Structure. Both of our hb-polymers developed in the high q-regime a markedly different angular dependence, which does not fit the fractal conception and seems to arise from an additional component. We suspected that the monomer unit causes this effect, since the finite size of the monomer unit is not included when the scattering function is described by an integral. To obtain more confidence in our conjecture, we measured the monomers separately and subtracted their contributions from the polymer scattering curve. This manipulation led to a drastic change of the scattering curve, which now could be well fitted with the fractal dimensions as derived from the scattering curve at small q-values. Additionally, the interference effect from the finite bond length is taken into account. Finally, when adding back the monomer contribution a full agreement of the experimental curve with the fractal fit was obtained (Figure 7).

(iv). MD Simulations. A simulation work was started, parallel to the chemical preparation and the following characterization by static and dynamic light scattering, viscosity measurements and the present SANS study. The simulations gave the coordinates of the atoms in the macromolecule. Figure 8 shows a calotte-view of the obtained structure for OH-50. The corresponding pair distance distribution of atoms was derived from these coordinates. This distance distribution was then converted into the spherical-radial correlation function $g(r)$. Finally, numerical Fourier transformation led to the simulated particle scattering factor. These MD-simulations are not yet completed but the already obtained calotte structure for a DP 35 is shown in Figure 9.[53]

The drastic discrepancy to the experimental curve might be interpreted as a full failure, but at least the effect of the monomer contribution at large q is well confirmed. We have to recall that the *simulations refer to a uniform structure* whereas the samples have a rather broad molar mass distribution. We wondered whether the discrepancy between experimental and

dx.doi.org/10.1021/ma300031g | Macromolecules 2012, 45, 3177−3187

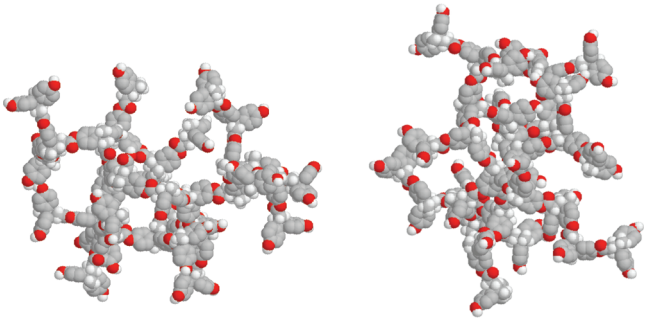


Figure 8. Two perspective views with different angles onto the same snapshot of a calotte model of OH-50 taken from a MD-simulation (500 ps) in THF, solvent not shown.

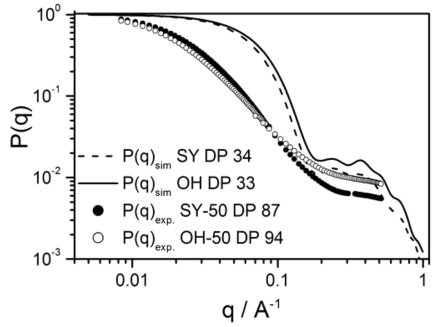


Figure 9. Experimental curves from SY-50 and OH-50 (DP ≈ 90) compared with the MD-simulated scattering curves (DP ≈ 35).

simulated curves might arise from this size distribution. We tried to mimic the polydispersity effect for a DP 90 by applying the following steps. (i) The simulated scattering curve of DP 35 could well be described by a Guinier approximation over the whole q-regime. (ii) Using Guinier's approximation $P_{Guinier}(q) \cong \exp(-q^2R_g^2/3)$ we calculated the particle scattering factor for each degree of polymerization, from DP 2 to DP 2000 and this for 45 different q values in the range of 0.005 to 1.00 Å^{-1}. These individual uniform particle scattering factors were multiplied by the Flory molar mass distribution.[2] *(iii)* Finally, the data for each q-value were summed over all DPs. The result is the average function $P_z(q) = \sum_{x=2}^{2000} xP(q,x)/x_w$, with x the degree of polymerization and x_w the weight-average of it.[54] The index z indicates the z-average that is measured in light and small angle neutron scattering. The resulting curve has a very different q-dependence from that with the z-average mean square radius of gyration inserted into the Guinier approximation. After adding the contribution of the monomer unit the result of Figure 10 was found. Within experimental errors a perfect agreement with the experimental curve was obtained. The agreement may be somewhat accidental. Nonetheless, the broadening of the scattering curve due to a broad molar mass distribution cannot be denied.

CONCLUSIONS

Concentration dependence: The strong concentration dependence found with the OH and SY terminal groups exerts a pronounced influence on the apparent radii of gyration and the q-dependence of scattering intensities. On the basis of Zimm's derivation this screening effect could be removed, and the true shape and size of the macromolecules at finite concentration became recognizable. The radius of gyration displayed only a weak shrinking under the influence of the osmotic pressure, but

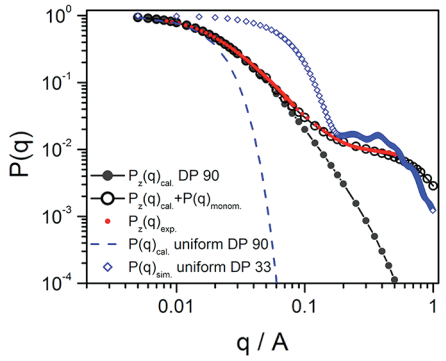


Figure 10. MD-simulated particles scattering factor (DP 35) (blue symbols) compared with the experimental points from OH-50 (DP 90) (red symbols) and with calculated $P_z(q)$ with (open black) and without (filled black) the contribution of the monomer, using Flory's size distribution. The blue dashed line corresponds to the uniform curve of DP 90 and the same radius of gyration but with the Guinier approximation for $P(q) = \exp(-(qR_{gz})^2/3)$. See text for details. Note the complete agreement of the calculated polydisperse curve (open black) with the experimental curve (red symbols).

the shape of the descreened particle scattering factor (including the q-range of the local structure) remained indistinguishable from that at infinite dilution. *Fractal behavior:* The particle scattering curve could be well fitted on the basis of Sinha's refinement of the fractal conception. Excellent fits were possible with two fractal dimension $d_{f,lin}$ and $d_{f,br}$ which take into account the structurally heterogeneous hb-polymers with their linear and branched contributions. *Simulations:* MD simulations for the hb-polymers of DP = 35 led to a particle scattering factor which grossly deviates from the experimental curve. The aggravating discrepancy proved to be caused by the broad molar mass distribution of hb polymers. Using Flory's equation of the molar mass distribution the effect of polydispersity could be taken into account. By this means we can modify the simulated monodisperse scattering curve. The resulting curve is virtually indistinguishable from the experimental curve. *Specific interaction of the terminal groups:* No specific interaction of the OH terminal groups (e.g., via hydrogen bonding) was observed, but the SY derivative gave indications for weak attractive interactions among the modified outer segments.

AUTHOR INFORMATION

Notes

The authors declare no competing financial interest.

REFERENCES

(1) Voit, B. I.; Lederer, A. *Chem. Rev.* **2009**, *109*, 5924−5973.
(2) Flory, P. J. *Principles of Polymer Chemistry*: Cornell University Press: Ithaca, 1953, Chapter 9
(3) Flory, P. J. *J. Am. Chem. Soc.* **1952**, *74*, 2718 See also ref 2..
(4) Khalyavina, A.; Schallausky, F.; Komber, H.; Al Samman, M.; Radke, W.; Lederer, A. *Macromolecules* **2010**, *43*, 3268.
(5) Meyer, K. H. *Natural and Synthetic Polymers*, 2nd ed.; Interscience Publishers: New York and London, 1950; p 453.
(6) Guilbot, A.; Mercier, C. Starch. In *The polysaccharides*; Aspinal, G. O., Ed.; Academic Press: Orlando, FL, 1985. Vol 3, Chapt. 3.
(7) Hawker, X. J.; Lee, R.; Frechet, J. M. *J. Am. Chem. Soc.* **1991**, *113*, 4583.
(8) Gao, C. D. Y. *Prog. Polym. Sci.* **2004**, *29*, 183.
(9) Froehling, P. J. *J. Polym. Sci., Part A: Polym. Chem.* **2004**, *42*, 3110.
(10) Mc Kee, M. G.; Unal, S.; Wlkes, G. L.; Long, T. E. *Prog. Polym. Sci.* **2005**, *30*, 507.

(11) Mori, H.; Müller, A. H. E.; Simon,P. F.-W. In *Macromolecular Engineering*; Matyjaszewski, K., Gnanou, Y., Leibler, L., Eds.; Wiley: Weinheim, Germany, 2007.
(12) Burchard, W. *Macromolecules* **1972**, *5*, 605.
(13) Kajiwara, K.; Burchard, W. *Polymer* **1981**, *12*, 57.
(14) Gordon, M. *Proc. R. Soc. London* **1962**, *A 268*, 240.
(15) (a) Stauffer., D.; Coniglio, A.; Adam, M. *Adv. Polym. Sci.* **1982**, *44*, 103. (b) Stauffer, D. *Introduction to Percolation Theory*: Taylor and Francis: London and Philadelphia, PA, 1985.
(16) (a) Sinha, S. K.; Feltoft,T.; Kjem, M. In *Kinetics of Aggregation and Gelation*; Family, F., Landau, D. P., Eds.; North-Holland: Amsterdam, 1984; p 87. (b) Feltoft, F.; Kjem, J.; Sinha, S. K. *Phys. Rev. B.* **1985**, *33*, 269.
(17) De Luca, E.; Richards, R. W.; Grillo, I.; King, S. M. *J. Polym. Sci., Part B: Polym. Phys.* **2003**, *41*, 1352.
(18) Garamus, V. M.; Maksimova, T. V.; Kautz, H.; Barriao, E.; Frey, H.; Schlotterbeck, U.; Mecking, S.; Richtering, W. *Macromolecules* **2004**, *37*, 8394.
(19) Geladé, E. T. F.; Goderis, B.; de Koster, C. G.; Meijerink, N.; van Benthem, R. A. T. M.; Fokkens, R.; Nibbering, N. M. M.; Mortensen, K. *Macromolecules* **2001**, *34*, 3552.
(20) (a) Lindner, P. In *Neutrons, X-Rays and Light Scattering Methods to Soft Condensed Matter*; Lindner, P.; Zemb, Th., Eds.; North-Holland-Elsevier: Amsterdam, 2002, Chapter 2. (b) Lieutnant, K.; Lindner, P.; Gähler, R. *J. Appl. Crystallogr.* **2007**, *40*, 1056.
(21) Prosa, T. J.; Bauer, B. J.; Amis, E. J.; Tomalia, D. A.; Scherrenberg, R. *J. Polym. Sci. Part B; Polym. Phys.* **1997**, *35*, 2913.
(22) Schallausky, F.; Erber, M.; Komber, H.; Lederer, A. *Macromol. Chem. Phys.* **2008**, *209*, 2331.
(23) Hölter, D.; Burgath, A.; Frey, H. *Acta Polym.* **1997**, *48*, 30.
(24) Khalyavina, A. Ph.D. Thesis, Technical University Dresden, 2011.
(25) Higgins, J. S.; Benoit, H. C. *Polymers and Neutron Scattering*; Oxford Science Publications, Clarendon Press: Oxford, England, 1994.
(26) King, S. M. In: *Modern Techniques for Polymer Characterization*; Pethrick, R. A.; Dawkins, J. V., Eds.; Wiley: Chichester, England, 1999; p 171.
(27) Lindner, P. *J. Appl. Crystallogr.* **2000**, *33*, 807.
(28) Carnahan, N. F.; Starling, K. E. *J. Chem. Phys.* **1969**, *51*, 635.
(29) Otha, T.; Oono, Y. *Phys. Lett.* **1982**, *79*, 839.
(30) Cotter, M. A.; Martiere, D. C. *J. Chem. Phys.* **1970**, *52*, 1909.
(31) Zimm, B. H. *J. Chem. Phys.* **1948**, *16*, 1099.
(32) De Gennes, P.-G. *Scaling Concepts in Polymer Physics*; Cornell University Press: Ithaca, NY, 1979.
(33) Burchard, W. *Macromolecules* **2004**, *37*, 3841.
(34) (a) Trappe, V.; Bauer, J.; Weissmüller, M.; Burchard, W. *Macromolecules* **1997**, *30*, 6966. (b) Trappe, V.; Burchard, W. In *Light Scattering and Photon Correlation Spectroscopy*; Pike, E. R., Abbiss, J. B., Eds.; Kluwer Academic Press: Dordrecht, The Netherlands, 1997; pp 141.
(35) van der Spoel, D.; Lindhal, E.; Hess, B.; Groenhof, G.; Mark, A. E.; Berendsen, H. J. C. *J. Comput. Chem.* **2005**, *26*, 1701.
(36) Berendsen, H. J. C.; Postma, J. P. M.; van Gunsteren, W. F.; DiNola, A.; Haak, J. R. *J. Chem. Phys.* **1984**, *8*, 3684.
(37) Schmidt, M. W.; Baldridge, K. K.; Boatz, J. A.; Elbert, S. T.; Gordon, M. S.; Jensen, J. H.; Koseki, S.; Matsunaga, N.; Nguyen, K. A.; Su, S.; Windus, T. L.; Dupuis, M.; Montgomery, J. A. *J. Comput. Chem.* **1993**, *14*, 1347.
(38) Berry, G. C. *J. Chem. Phys.* **1966**, *44*, 4550.
(39) Carnahan, N. F.; Starling, E. *J. Chem. Phys.* **1969**, *51*, 635.
(40) Ohta, T.; Oono, Y. *Phys. Lett.* **1983**, *79*, 839.
(41) Cotter, M. A.; Martire, D. C. *J. Chem. Phys.* **1970**, *52*, 1909.
(42) Feller, W., *An Introduction to Probability Theory and its Applications*; John Wiley: New York, 1968; Vol. *1*, Chapt. XII; Compound Distributions and Branching Process.
(43) (a) Gordon, M.; Scantleburry, G. R. *Trans. Farad. Soc.* **1964**, *60*, 604;(c) *Proc. Roy- Soc.* **1966**, *A292*, 380. (b) Dobson, G. R.; Gordon, M. *J. Chem. Phys.* **1964**, *41*, 2389;(d) **1966**, *43*, 705.
(44) Kajiwara, K.; Burchard, K. W.; Gordon, M. *Br. Polym. J.* **1970**, *2*, 110.
(45) Stanley, H.G., *Introduction to Phase Transition and Critical Phenomena*: ;Oxford Sience Publications, Oxford University Press: New York, 1970.
(46) Mandelbrot, B. B., *The Fractal Geometry in Nature*: Freeman and Co.: New York and San Francisco, CA, 1972 and 1983.
(47) Porod, G. In *Small Angle X-Ray Scattering*; Glatter, O., Kratky, O., Eds.; Academic Press: London, 1982 . Chapter 2, p 17.
(48) Benoit, H.; Benmouna, M. *Polymer* **1984**, *25*, 1059.
(49) (a) Aberle, T.; Burchard, W. *Starch/Stärke* **1997**, *49*, 215. (b) *Comp. Theor. Polym. Sci.* **1997**,*7*, 215. (c) Burchard, W. *Biomacromolecules* **2001**, *2*, 342. (d) Galinsky, G.; Burchard, W. *Macromolecules* **1997**, *30*, 4445.
(50) Schmidt, P.W. Use of Scattering to Determine the Fractal Dimension. In *The Fractal Approach to Heterogeneous Chemistry*; Avnir, D., Ed.; John Wiley: Chichester, England, 1992; Chapter 2.2, p 67.
(51) Daoud, M.; Martin, J. E. Fractal Properties of Polymers. In *The Fractal Approach to Heterogeneous Chemistry*; Avnir, D., Ed.; John Wiley: Chichester, England, 1992; Chapter 3.1.1, p 109.
(52) Debye, P.; Bueche, A. M. *J. Chem. Phys.* **1948**, *15*, 373.
(53) Friedel, P.; et al. Manuscript in preparation.
(54) The required relationship between the DP and R_g was established via a power law behavior, The exponent was varied until at the $DP_w = 90$ approximately the correct radius of gyration of $\langle R_g^2 \rangle_z = 84$ Å was obtained with the Flory hp-distribution. R_g at DP 2 was taken as $2R_g$ of the monomer.

Macromolecules

Article

pubs.acs.org/Macromolecules

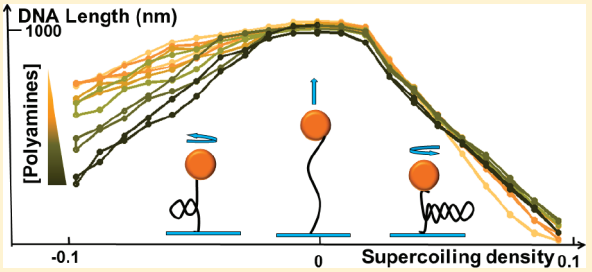
Physiological Levels of Salt and Polyamines Favor Writhe and Limit Twist in DNA

Qing Shao,[†] Sachin Goyal,[†] Laura Finzi,[†] and David Dunlap*[,‡]

[†]Departments of Physics and [‡]Cell Biology, Emory University, Atlanta, Georgia 30322, United States

Supporting Information

ABSTRACT: Quantitative analysis of single molecule experiments show that adding either of two natural polyamines, spermine or spermidine, produced more compact plectonemes in DNA in physiological concentrations of monovalent salt. They also promoted plectoneme formation at lower values of torsion in measurements of extension versus twist. Quantifying changes in the plectonemic DNA using some results from simple rod models suggested that exposure to polyamines reduced the radii and increased the densities of plectonemes. Thus, polyamines may limit the twist density by favoring writhe which maintains the B-form. Although polymerases may significantly stretch the double helix, denature DNA, and produce twist instead of writhe, natural polyamines stabilize base-pairing, limit twist to maintain the B-form, and promote supercoiling, which is conducive to replication and transcription and essential for DNA packaging.



INTRODUCTION

Polyamines are organic compounds having more than one amino group (NH_2). They are synthesized in living cells via highly regulated pathways and are known to regulate cell growth, gene transcription, and activation of DNA synthesis.[1] High levels of polyamines are associated with certain cancers.[2] Furthermore, increased polyamine levels can be diagnostic markers of drug resistance in oncological treatment.[3] How polyamines act in cellular metabolism to regulate normal or cancerous growth is not entirely understood nor are the structural changes in deoxyribonucleic acid (DNA) caused by polyamines in physiologically relevant conditions.

Inside living cells, DNA is compacted in hierarchical topological structures. Plectonemic, negative supercoils (extruded intertwined loops) form the basis of this compaction in live cells. Plectonemes are described by the topological parameters, writhe and twist, and play crucial roles in the regulation of DNA transcription and replication.[5] For instance, bacterial plasmids are negatively supercoiled,[4] which is known to favor local denaturation of DNA near replication origins and transcriptional promoters where polymerases must gain access to the coding strand within a double-stranded DNA molecule (dsDNA).[5] Positive supercoiling interferes with mRNA synthesis, arresting the progress of RNA polymerase complexes.[6] Clearly, DNA supercoiling and its regulation fundamentally impact cellular functions.

Not surprisingly, therefore, a family of enzymes, the topoisomerases, can regulate DNA supercoiling. For example, in bacteria, topoisomerase I relaxes negative supercoils by catalyzing torsion-driven rotation of one single DNA strand about the other in a dsDNA segment, and gyrase catalyzes passage of one dsDNA segment through another to introduce negative and relax positive supercoils.[5] Topoisomerases are prominent regulators of DNA supercoiling, but their activity might be strongly modulated by small molecules like polyamines that alter the mechanical properties of DNA.

Numerous experiments suggest that polyamines stabilize the right-handed, B-form double helix,[7] protect it from radiation and oxidation,[8,9] and compact and even aggregate DNA in low salt buffers.[10,11] The multiple positively charged amine groups can certainly interact electrostatically with the negatively charged phosphates of DNA. However, recent infrared spectroscopy data indicate that natural polyamines can bind in the major and minor grooves of DNA to interact with the DNA bases as well.[12] Spermidine, which has three amine groups, and spermine, which has four (see Figure 1), bind to

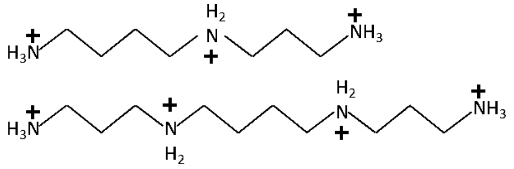


Figure 1. Structure of spermidine (top) and spermine (bottom). The basic amino (NH_2) groups attract protons at physiological pH to become positively charged.

the major and minor grooves of DNA[12,13] and are the two most important naturally occurring polyamines in mammals.[14] However, little is known about how these two polyamines

Received: January 29, 2012
Revised: March 20, 2012
Published: March 30, 2012

 © 2012 American Chemical Society

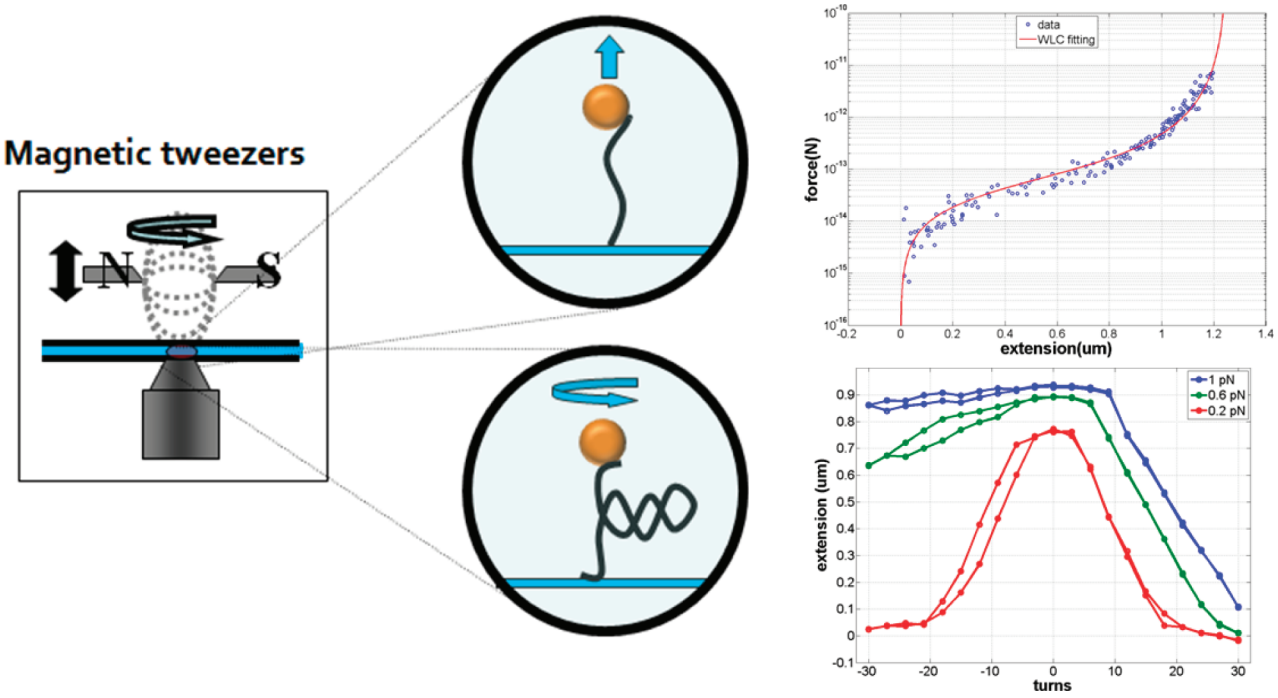


Figure 2. Stretching and twisting DNA with magnetic tweezers. Magnetic tweezers (left) can be used to stretch (upper middle) and twist (lower middle) single DNA molecules tethering paramagnetic beads to a glass surface. Systematically varying the separation between the magnets and the tethered bead generates a range of tensions as shown in a representative force vs extension curve for a single DNA molecule (upper right). The red curve is a wormlike-chain fit to the data. Rotating the magnets to twist the DNA tether produces extension vs twist curves for a DNA molecule at different tensions (lower right), from top to bottom: 1, 0.6, and 0.2 pN.

affect DNA supercoiling in physiological concentrations of monovalent salt.

It has been shown that the presence of spermine and spermidine can enhance the transcription rate despite high levels of positive supercoiling by changing the physical properties of supercoiled DNA.[15] Moreover, the presence of polyamines inhibited topoisomerase I-catalyzed relaxation of negative supercoils perhaps by stabilization of the DNA double helix.[15] Both the increase of positive supercoiling during transcription and the inhibition of topoisomerase I were observed with submillimolar spermine or millimolar spermidine concentrations, which are physiological.[14] Systematic regulation of the concentrations of polyamines[1] may be a primary mechanism by which a cell regulates DNA supercoiling and its related enzyme activities and cellular processes. Nevertheless, only qualitative explanations have been proposed for these effects,[15] and there are no quantitative measures of how polyamines alter DNA supercoils.

Previously, single-molecule experiments were performed to investigate DNA compaction as a function of tension[16] and twist[17] at various polyamine concentrations in buffers containing subphysiological concentrations of monovalent salt. More specifically, those experiments measured the tensions generated by compaction, which were found to be as high as 3 and 4 pN for spermidine and spermine, respectively. Those data were gathered by measuring the maximum level of tension at which single, torsionally constrained DNA molecules suddenly shortened (into compact forms). The compaction depended on polyamine concentrations, and free energies were reported to be −0.2 kT/base pair for spermidine and −0.33 kT/base pair for spermine.

At higher levels of monovalent salt, DNA molecules are less likely to compact. Indeed, high concentrations of KCl prevent DNA aggregation and catenation by enzymes.[18] The following data were recorded for single DNA molecules in 200 mM KCl to avoid compaction and allow analysis of the structure of plectonemic DNA over a low range of tensions. Magnetic tweezers were used to twist and stretch single DNA molecules at various physiological concentrations of the two polyamines. The observations suggest that polyamines stabilize the double-stranded, B-form of DNA and promote plectoneme formation. An analysis of the data using some key results from simple elastic rod theories indicated that both spermine and spermidine changed the form of the supercoiled DNA, producing more tightly wrapped plectonemes. An order of magnitude less tetravalent spermine produced the same degree of wrapping as the trivalent spermidine.

■ MATERIALS AND METHODS

Plasmid pDL2317[19] was used as a polymerase chain reaction (PCR) template to produce a linear, 3215 base-pair (bp) DNA fragment using the primer pair 5′-TAATACGACTCACTATAGGG and 5′-TATGCCCGAGAAGATGTT. The amplicon was digested with BamHI and XbaI to give a final 3096 bp fragment. Biotin- or digoxigenin-labeled fragments ∼1000 bp were created using PCR with the plasmid pDL1051 (D. A. Lewis, NIH) as a template and the primer pairs 5′-TGTATGGAACAACGCATAAC and 5′-TCCAAACTGGAACAACAC or 5′-AAGGTAACTGGCTTCAGC and 5′-TTATTGTCTCATGAGCGG to incorporate about 5% biotin- or digoxigenin-labeled dUTP. These fragments were digested with BamHI or XbaI to generate complementary ends for ligation to the main DNA fragment.[20] The ligated construct was attached at one end to the anti-digoxigenin-coated glass surface of a flow chamber and at the other end to a 2.8 μm streptavidin-coated, superparamagnetic bead (Invitrogen, Carlsbad, CA) (Figure 2). The DNA had multiple attachments at both ends to prevent torsional relaxation. Note that the biotin- and digoxigenin-labeled DNA ends form multiple attachments

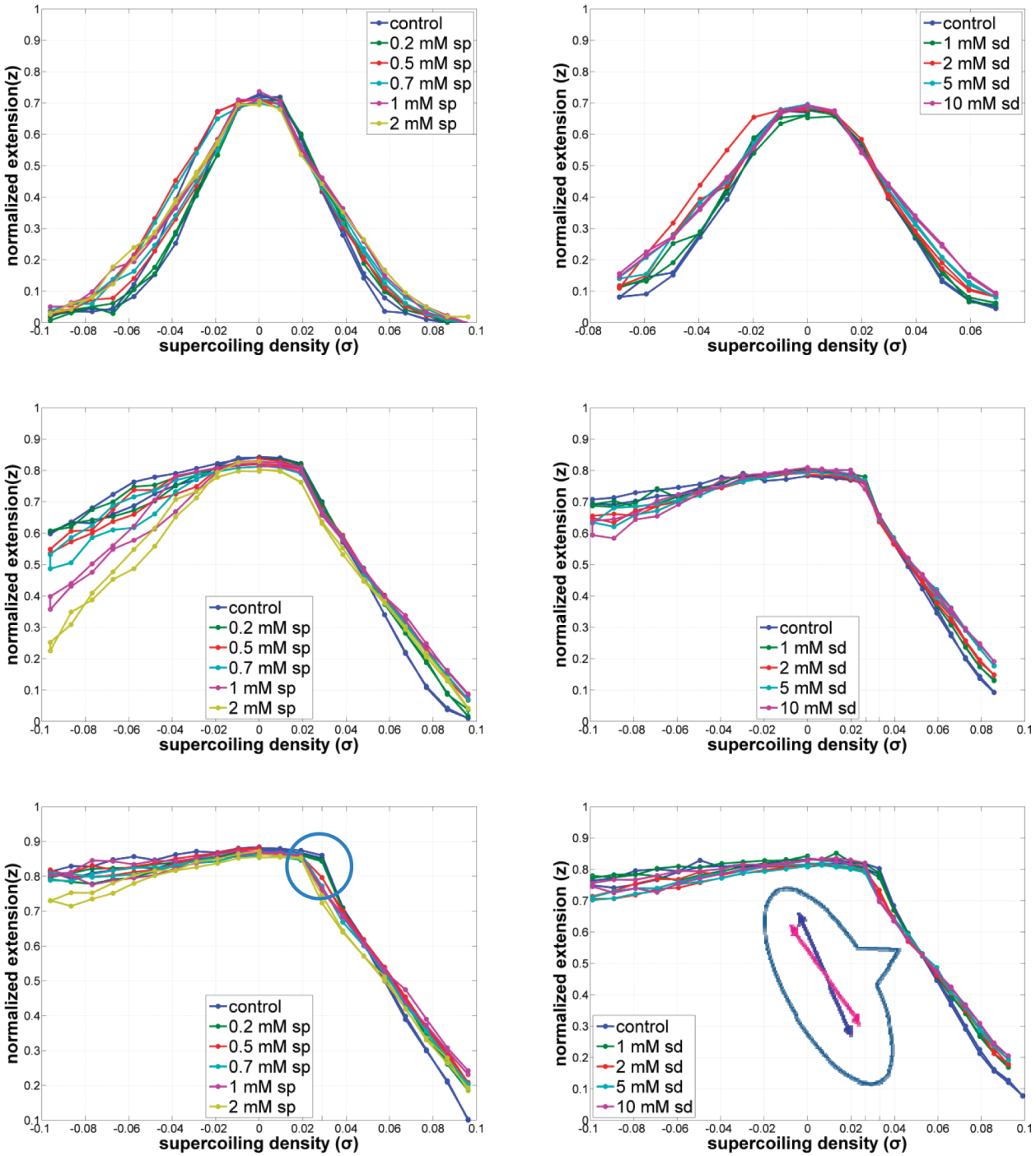


Figure 3. DNA extension vs supercoiling density as a function of spermine (left) or spermidine (right) concentrations at 0.2 (upper), 0.6 (middle), and 1 pN (lower) of tension. "Knee points" are encircled. The inset emphasizes the change in slope due to added spermidine. Typical measurement errors are shown in the Supporting Information on four of the curves for 0.6 pN with added spermine.

to the streptavidin-coated bead and anti-digoxigenin-coated glass, so that the free tether length is the unlabeled, 3096 bp main fragment.

The DNA was incubated in λ buffer, consisting of 10 mM Tis-HCl (pH 7.4), 200 mM KCl, 5% dimethyl sulfoxide (DMSO), 0.1 mM ethylenediaminetetraacetic acid (EDTA), and 0.2 mM dithiothreitol (DTT),[21] with the indicated concentrations of polyamines. Flow chambers of ~50 μL were assembled from slides using a continuous bead of silicon grease to form the walls of the chamber before sealing with a coverslip. Spermine was diluted in 200 μL of λ buffer to final concentrations of 0, 0.2, 0.5, 0.7, 1, and 2 mM and spermidine to final concentrations of 0, 1, 2, 5, and 10 mM. Working solutions containing high concentrations of spermine (>0.5 mM) and spermidine (>2 mM) were vortexed before use to dissolve fine particles.

At several polyamine concentrations, magnetic tweezers (MT) were used to stretch and twist the DNA tethers. Tension was varied by changing the separation between the DNA-tethered beads and a pair of neodymium magnets mounted above the microscope stage. Rotation of the magnets caused the oriented, paramagnetic beads to rotate and twist the attached DNA tethers (Figure 2). Extension versus twist data were recorded at tensions of 0.2, 0.6, and 1.0 pN for several concentrations of spermine and spermidine.

The contour length of tethered DNA under high tension (about 6 pN) agreed well with that predicted from the number of base pairs in

dx.doi.org/10.1021/ma300211t | *Macromolecules* 2012, 45, 3188−3196

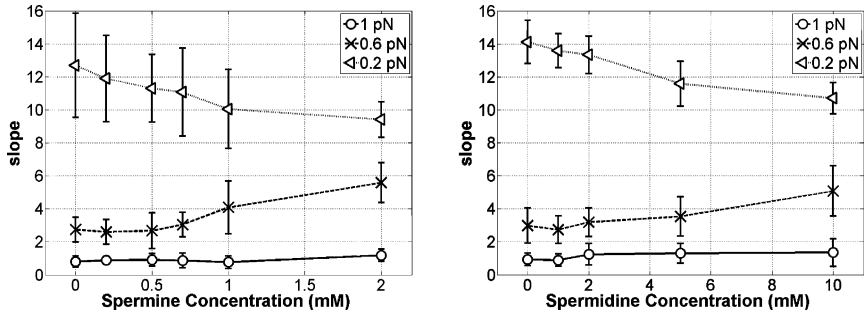


Figure 4. Average slope ($dz/d\sigma$, dimensionless) of the DNA extension vs twist in Figure 3 for underwound DNA as a function of spermine (left) or spermidine (right) concentrations at 0.2, 0.6, and 1 pN of tension. Error bars represent standard deviations.

the unlabeled fragment. Molecules were stretched and relaxed twice as the force varied from 0.02 to 4 pN, and their lengths were recorded. Also, DNA tethers under 0.2, 0.6, and 1 pN of tension were unwound to −10% supercoiling density (σ) (−30 turns for 3 kbp DNA), rewound to +10%, and unwound back to 0 in steps of 3 turns while recording the tether length.

Data were acquired at a rate of 20 frames/s and analyzed to determine the extension, $l = \langle z \rangle$, of the DNA molecule with an error of about 10 nm with 10 s averaging using video-rate, three-dimensional tracking of the bead.[22] Measuring the horizontal excursions of the bead $\langle \Delta x^2 \rangle$ allowed the tension in the molecule to be determined via the equipartition theorem, $F = kBTl/\langle \Delta x^2 \rangle$, with 10% accuracy. Mechanical drift in the data was eliminated using differential tracking of a second bead stuck on the surface. The data were analyzed to determine the probable dimensions of the plectonemes as described (see also Appendix I of the Supporting Information).

RESULTS AND ANALYSIS

Figure 3 shows the DNA extension, z, normalized by the contour length, L, versus twist for a representative DNA tether at various physiological concentrations of spermine (left panels) or spermidine (right panels). The twist has also been normalized and reported as the "supercoiling density", $\sigma = (Lk - Lk_0)/Lk_0 = n/Lk_0$, where Lk_0 is the number of the right-handed helical turns in the torsion-free, B-form dsDNA, and n is the number of mechanically added twists. The effects of polyamines on DNA extension versus twist were investigated at three different tensions (Figure 3): 0.2 (upper), 0.6 (middle), and 1.0 pN (lower). The blue curves represent the DNA without polyamine.

At all tensions, the extension of slightly overtwisted DNA changed very little initially but then contracted sharply beyond a threshold value of twist as the filament "buckled" and formed plectonemes at a critical value of twist, n_b. Such buckling has been observed previously in single-molecule experiments with DNA[23−25] and modeled and simulated using rod mechanics.[23,26] Beyond a threshold value of additional twist, the extension decreased linearly as more and more of the DNA shifted to the plectonemic form.

For 0.2 pN of tension, the extension decreased as a function of either positive or negative supercoiling for control DNA (blue in Figure 3, top panel) due to the formation of plectonemes. An intermediate tension of 0.6 pN hindered plectoneme formation in unwound molecules. This gentler decrease of the extension upon unwinding corresponded to partitioning between plectoneme formation and some other form of the DNA helix.[27] Indeed, at a tension of 1 pN, the extension remained constant for negative values of σ, indicating that perhaps plectonemes did not form at all. It is known that under high tension unwinding partially melts the double helix[28] or favors a transition to some other helical form.[29] However, well-defined models of DNA under these conditions are still under development. As a result, only plectonemes formed by positively twisted DNA will be analyzed quantitatively with rod theory in this paper.

Once a plectoneme nucleates in response to positive supercoiling and is sufficiently large, it has been shown from simple rod theories[30,31] that any additional twist is almost completely absorbed as writhe, keeping the torque constant. Thus, overtwisting drives a phase change to a plectonemic form, and a steadily increasing fraction of the DNA adopts the plectonemic phase at a constant torque. The slope of extension versus twist curve reveals the DNA length per writhe in the plectoneme, where more gradual slopes indicate shorter lengths of DNA per writhe, and hence plectonemes of smaller gyres.

Polyamines were found to alter the slope of the extension versus supercoiling density curves for positive σ and presumably the plectoneme structure. Three different effects of polyamines on DNA supercoiling behavior were observed and are described in the following sections.

Spermine and Spermidine Stabilize B-DNA Structure and Increase Plectoneme Formation for Negative Supercoiling. Spermine and spermidine stabilized the B-form as DNA was unwound at 0.6 pN of tension (middle panels of Figure 3). When a dsDNA tether is unwound, contraction of the molecule at low tension (0.2 pN) corresponds to the formation of plectoneme(s) as a fraction of the added linking number is absorbed as writhe. However, at higher tension, the torsional stress might disrupt B-DNA and induce the formation of a left-handed winding of unpaired filaments.[32] Increasing the spermine or spermidine concentration increased the extent of contraction versus unwinding at 0.6 pN, apparently stabilizing the B-form DNA and shifting this torsional equilibrium toward plectoneme formation.

Figure 4 quantitatively summarizes these results in plots of the average magnitude of the slope of the extension versus unwinding data for all the three tensions as a function of increasing concentrations up to 2 mM spermine (left) and 10 mM spermidine (right). At 1 pN, the near-zero slope does not change because the tension is high enough to oppose any plectoneme formation. Instead at 0.6 pN, increased polyamine concentrations increased the magnitude of the slope, indicating more extensive plectoneme formation. At lower tension (0.2 pN), the curves are symmetric even without polyamines. However, note that the slope of the extension versus unwinding curves decreases with increasing polyamine concentrations. This was interpreted as evidence of more compact plectonemes as described below for positive supercoiling.

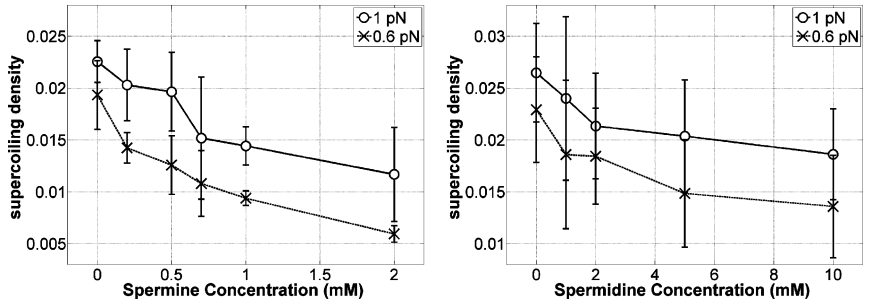


Figure 5. Twist values σ at which writhe first appeared in overtwisted DNA as a function of spermine (left) or spermidine (right) concentrations at 0.6 and 1 pN of tension. The σ values were defined using the linear extrapolation of extension vs σ curves.[33] Error bars represent standard deviations.

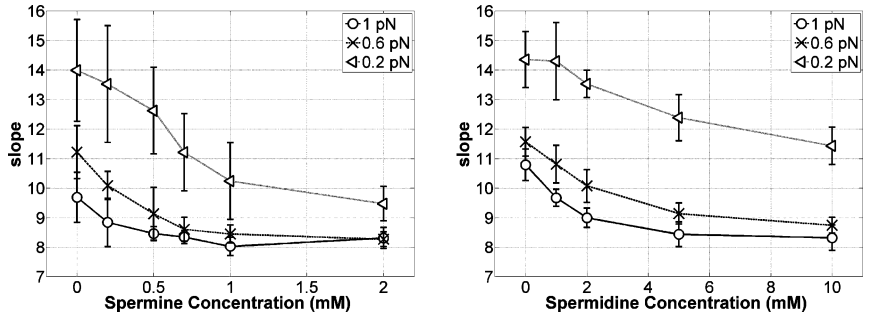


Figure 6. Average magnitude of the slope ($dz/d\sigma$, dimensionless) of DNA extension vs twist for positively supercoiled DNA as a function of spermine (left) or spermidine (right) concentrations at 0.2, 0.6, and 1 pN of tension. Error bars represent standard deviations.

Spermine and Spermidine Promote Plectoneme Formation for Positive Supercoiling. The two polyamines also promote the formation of plectonemes in overwound DNA molecules as shown in Figure 3, in which they began to form at lower levels of twist as the polyamine concentrations were increased.

This effect was particularly obvious at higher tensions, 0.6 and 1 pN, and the supercoiling density at which writhe initially reduced the extension of the DNA tether is shown as a function of increasing spermine and spermidine concentrations in Figure 5. Large fluctuations of the DNA extension obscured this effect at 0.2 pN of tension. A convenient framework with which to visualize this behavior is to contrast the torsional and flexural stiffness of two rods. If the rods have the same torsional but different flexural stiffness, the more flexible rod will exhibit more writhe at any level of tension to minimize conformational energy. Electrostatic softening of DNA by multivalent cations is well described for polyamine−DNA interactions, but these data indicate that polyamines differentially alter torsional and flexural characteristics of DNA.

Spermine and Spermidine Shrink Plectonemic Supercoils. Once overtwisted DNA begins to writhe, additional torque is absorbed as writhe and the extension decreases linearly as a function of twist as can be seen in Figure 3. Figure 6 shows the average magnitude of the slope of these extensions versus twist curves as a function of spermine or spermidine concentration. For all three values of tension, 0.2, 0.6, and 1 pN, the slope decreased with increasing polyamine concentration and somewhat asymptotically approached a constant value. Since the magnitude of the slope indicates the length of DNA consumed in each plectoneme, a lesser slope corresponds to smaller plectonemic gyres. Thus, polyamines appeared to promote tightly wrapped plectonemes.

In Figure 6, it is also clear that the size of plectonemes decreased as tension was increased. At all concentrations the slope of the extension versus twist curves varied inversely with tension. However, the more tightly wrapped plectonemes due to the polyamines were most pronounced at low tension. In order to analyze this plectonemic contraction quantitatively, the writhe density was derived from the slope as described below.

Quantitative Analysis of Plectonemes. In order to understand how spermine and spermidine affected the topological features of the plectonemic phase in overwound DNA, the writhe per helical turn was determined as a function of increasing polyamine concentrations at 0.6 and 1.0 pN tensions. The plectonemic phase was assumed to consist of two identical, intertwined duplexes with uniform radius, R, and uniform helical angle,[30,31] α, and the end loop was ignored.[30] Furthermore, externally applied twist was assumed to completely convert into writhe, W_r, leaving the torque on the molecule and the size of the plectonemes unchanged[24] as new ones were generated. With these assumptions, the writhe density in the plectonemic phase was derived (see Appendix 1 of Supporting Information) and found to be inversely proportional to the slope $|dz/d\sigma|$ as follows:

$$\left|\frac{Wr}{Lk_0(l_p/L)}\right| = \rho_{th}\left|\frac{dz}{d\sigma}\right|^{-1} \quad (1)$$

where z is the extension normalized by the contour length, L, of the DNA, σ is the number of turns, n, added to DNA normalized by the stress-free linking number Lk_0, l_p is the length of DNA absorbed into plectonemic phase, Wr is the writhe, and ρ_{th} is a contraction factor due to thermal fluctuations that were assumed to occur predominantly in the stretched phase of DNA. This contraction factor ρ_{th} was approximated using the Moroz and Nelson approximation for a

dx.doi.org/10.1021/ma300211t | Macromolecules 2012, 45, 3188−3196

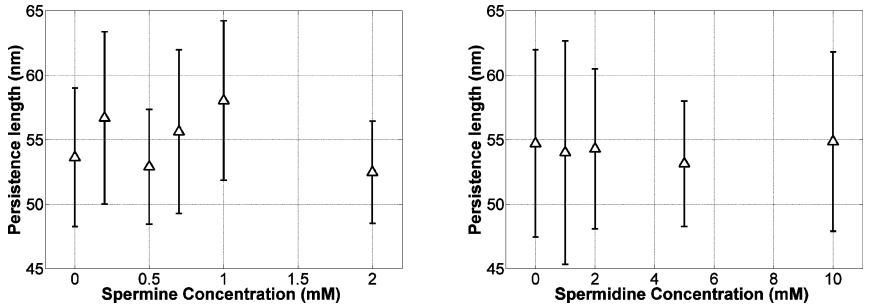


Figure 7. Average persistence length for eight DNA tethers at different spermine (left) or spermidine (right) concentrations. Polyamines did not significantly affect the bending stiffness of DNA. Error bars represent standard deviations.

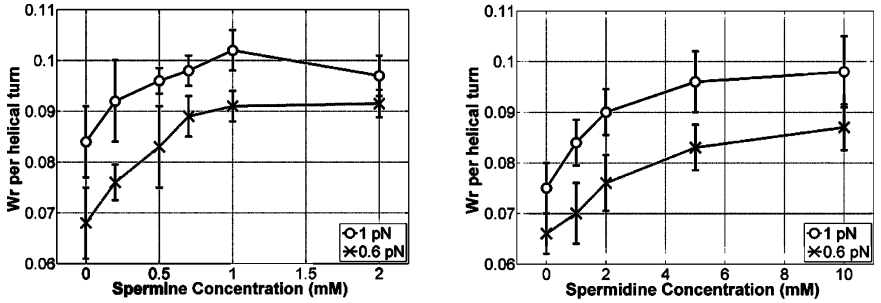


Figure 8. Effect of spermine (left) or spermidine (right) concentrations on the writhe density in the plectonemic phase at 0.6 and 1 pN of tension. The increase in writhe density is a quantitive measure of plectoneme shrinking. Error bars represent standard deviations. Note that the model is valid for small fluctuations at tensions above 0.5 pN.

twisted, fluctuating filament[34] under tensions greater than 0.5 pN as follows:

$$\rho_{th} \approx 1 - \frac{1}{2}\frac{1}{\sqrt{\frac{K_b F}{{k_B}^2 T^2} - \frac{{M^2}_{3(cr)}}{4{k_B}^2 T^2} - \frac{1}{32}}} + \frac{K_b k_B T}{L\left(K_b F - \frac{{M^2}_{3(cr)}}{4}\right)} \quad (2)$$

in which

$$M_{3(cr)} \approx \sqrt{2K_b F} \quad (3)$$

is the torque exerted by the twisted DNA on the bead, K_b is the bending stiffness, F is tension, k_B is the Boltzmann constant, and T is the absolute room temperature. Note that as plectonemes form, the torque, $M_{3(cr)}$, on the molecule remains constant at a value that depends only on the tension and the bending stiffness.

In order to complete the calculation of ρ_{th}, and hence of the writhe density, the bending stiffness was calculated using $K_b = k_B T P_l$, for which the bending persistence length, P_l, was determined by fitting the wormlike-chain expression[34−36] to extension versus force data for torsionally relaxed DNA.

$$\frac{F}{k_B T} = \frac{1}{P_l}\left[z + \frac{1}{4(1-z)^2} - \frac{1}{4}\right] \quad (4)$$

Figure 7 shows the persistence length, which is proportional to the effective bending stiffness, as a function of polyamine concentration. There were no significant changes in the bending persistence length as a function of polyamine concentration in 200 mM KCl. Such invariance is similar to that of persistence lengths previously reported for DNA in 100 mM NaCl which did not change significantly upon addition of 10 mM magnesium.[37] Both data sets differ from those of Bauman et al. in which millimolar concentrations of multivalent cations in ∼2 mM NaCl greatly reduced the persistence length of DNA.[10] The concentration of monovalent salt certainly changes the electrostatic screening environment, but in the case of polyamines, any potential increased flexibility due to charge neutralization by polyamines may also be opposed by polyamine linkages between the two phosphate backbones and the placement of exogenous amines in the minor groove that tend to structurally stiffen the DNA.[38,39] Solving eqs 1−4 allowed determinations of the writhe per helical turn as a function of polyamine concentration as shown in Figure 8.

DISCUSSION

Polyamines are thought to stabilize DNA duplexes, especially AT-rich regions, to prevent their denaturation in response to negative twist. The experiments described above clearly demonstrate that both spermine and spermidine promoted writhe in unwound DNA. Crystal structures and infrared spectra of polyamine−DNA complexes[12,40] show that spermine and spermidine molecules can form hydrogen bonds with bases from opposite strands of DNA duplex. This might reduce denaturation and produce writhe instead of unwinding DNA.

Alternatively to denaturation, negative twist can trigger a right- to left-hand helical transition. Increased unwinding is known to convert small GC repeat DNA insert (about 23 bp) to left-handed Z-DNA at high NaCl concentrations (>0.7 M).[41] Indeed, spermine and spermidine have been shown to induce Z-DNA formation not only in synthetic GC repeat DNA fragment[42,43] but also in calf thymus DNA.[44] However, investigations using torsionally constrained plasmids (σ = −0.033) without a synthetic GC repeat inset showed that

dx.doi.org/10.1021/ma300211t | Macromolecules 2012, 45, 3188−3196

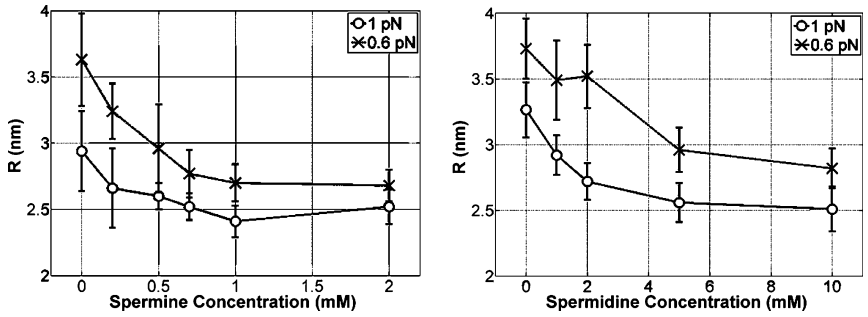


Figure 9. Radius of the helical plectoneme as a function of spermine (left) or spermidine (right) concentrations at 0.6 and 1 pN of tension. The radii of plectonemes decreased substantially as the polyamine concentration was increased, especially at low tension.

spermine and spermidine were unable to induce the B- to Z-DNA transition.[45] In the experiments described here, the low tension and degree of unwinding were unlikely to trigger the formation of left-handed DNA,[29] and the reduced extensions produced in slightly unwound (less than 1%) DNA were interpreted as plectonemes of right-handed duplexes. Raman and energy minimization studies indicate that spermine and spermidine bind along major and minor grooves of DNA duplex, respectively,[13,46] and therefore might stabilize the major and minor grooves of B-DNA to favor such writhing in the underwound DNA molecule (Figure 3).

The effect on overwound DNA appears to be more subtle. Spermine and spermidine promoted plectoneme formation at lower levels of twist. Once overwound DNA begins to form plectonemes, the torque and therefore twist per unit length remain constant.[24] Thereafter, plectonemes steadily grow to compensate for further increases in linking number. In the experiments reported here, polyamines increased the writhe density as much as 10% and promoted a commensurate decrease in twist density. A corollary to this idea is that by promoting the formation of compact plectonemes, polyamines tend to decrease the twist density in DNA. Such crowding of writhe to relax twist is a subtle but distinct variation of the conservation of linking number described by the Calugareanu–White–Fuller equation that might be tested as described in Appendix 2 of the Supporting Information.

To investigate further the shrinking of plectonemes, if the helical angle is known, one can calculate the radius, R, of the helical plectoneme from the writhe formula of a helix as follows:

$$R = \frac{\sin(2\alpha)}{4\pi}\left|\frac{Wr}{l_p}\right|^{-1} \quad (5)$$

The helical angle can be computed from the elastic rod models that account for electrostatic interactions. The computed helical angles are sensitive to the type of model for electrostatic screening.[31] However, we note that employing either the Ubbink and Odijk approximation of a Poisson–Boltzmann model[47] or the Ray and Manning approximation[48] of counterion condensation theory[49] in the simplistic rod model, the helical angle increases with the tension converging to approximately $\pi/6$ for tensions in the range of 0.6 pN and above.[33] Therefore, assuming a helical angle $\alpha \approx \pi/6$, eq 5 produces a rough estimate of how R may change as a function of the polyamine concentration. The trend is shown in Figure 9, and the radius was found to shrink substantially as polyamine concentrations increased. Plectoneme formation forces helices into proximity which will increase the binding constant of spermidine and spermine. Enough ions may bind to substantially decrease the repulsion at the distances estimated for the radius of the superhelix (Figure 9). The accuracy of these results relies on the formation of a uniform helix, which has been analyzed in a simplistic framework for a rod model and appears to be justified.[30,31]

While electrostatic neutralization of phosphate repulsions, which would promote more tightly wrapped plectonemes, is a widely accepted phenomenon, a constant helical angle in the plectonemic gyres was assumed for the estimates in Figure 9. Yet an increase of the helical angle above a threshold polyamine concentration due to repulsions between DNA-bound polyamines or a drop in the helical angle in response to increasing polyamine concentration due to phosphate charge neutralization is plausible. Nevertheless, since eq 5 indicates that the radius of the plectoneme is a direct function of the helical angle, and the radius decreases as polyamine concentration increases in Figure 9, the radius is likely to be a decreasing function of polyamine concentration.

A more robust description of plectonemic shape will require a model that can dynamically simulate the formation of plectonemes including electrostatic interaction[50] and non-homogeneity[51] along with accurate modeling of the stress–strain relationship that governs the bending and twisting deformations of DNA as discussed previously.[52] In general, nonlinear coupling between bending, twisting, and stretching may influence not only plectonemic shapes but also the buckling of DNA. While the effects of twist–stretch coupling on the buckling and nonuniform twist distribution have been explored,[53] this coupling and these models need to be systematically developed for application to magnetic tweezer data.

Broadly speaking, polyamines torsionally stiffened either under- or overwound DNA to promote the formation of plectonemes. The fact that polyamines attenuate distortions of helical DNA is likely to be very significant biologically. DNA motor enzymes can produce considerable topological stress in DNA molecules as a result of transcription, replication, and during packaging reactions.[54] Tuning polyamine levels could limit helical distortions to maintain the binding capacity of proteins that interact with DNA molecules in critical cellular processes. The fact that the levels of polyamines vary and are highly regulated, especially during the cell cycle, may reflect the importance of this regulatory mechanism in living organisms.[55]

CONCLUSION

In these experiments, both spermine and spermidine stabilized the right-handed, double-stranded B-form of DNA to promote

plectoneme formation in both under- and overwound molecules. Calculations quantitatively revealed increasingly tightly wrapped plectonemes formed by overwinding at physiological concentrations of the two polyamines which differed by a factor of 10. This likely derives from the electrostatic basis of their interactions with DNA and reflects the tetra- and trivalency of the spermine and spermidine cations, respectively. The data are consistent with the idea that these two natural polyamines "groom" DNA to limit the twist density and maintain the B-form, despite powerful enzymes that can distort the B-form double helix and produce large topological changes. This would preserve binding by DNA proteins that recognize the B-form and promote writhe which is critical for DNA packaging.

■ ASSOCIATED CONTENT

Supporting Information

Two appendices describing derivations and a copy of Figure 2b with added error bars. This material is available free of charge via the Internet at http://pubs.acs.org.

■ AUTHOR INFORMATION

Notes

The authors declare no competing financial interest.

■ ACKNOWLEDGMENTS

Discussions with Prof. Prashant Purohit, Dr. Sebastien Neukirch, and Dr Monica Fernandez were most helpful. This work was supported by National Institutes of Health (5R01GM084070-03 to L.F.), the Human Frontier Science Program (RGP0051/2009 to D.D.), and the University Research Council at Emory University (to D.D.).

■ REFERENCES

(1) Kusano, T.; Berberich, T.; Tateda, C.; Takahashi, Y. *Planta* **2008**, *228* (3), 367−81.
(2) Wallace, H. M.; Fraser, A. V.; Hughes, A. *Biochem. J.* **2003**, *376*, 1−14.
(3) Grandgirard, N.; Ly-Sunnaram, B.; Ferrant, D.; Gandemer, V.; Edan, C.; Le Gall, E.; Moulinoux, J. P.; Leray, E.; Goasguen, J. E. *Leuk. Res.* **2004**, *28* (5), 479−486.
(4) Mcclellan, J. A.; Boublikova, P.; Palecek, E.; Lilley, D. M. J. *Proc. Natl. Acad. Sci. U. S. A.* **1990**, *87* (21), 8373−8377.
(5) Wang, J. C. *Nat. Rev. Mol. Cell Biol.* **2002**, *3* (6), 430−440.
(6) Gartenberg, M. R.; Wang, J. C. *Proc. Natl. Acad. Sci. U. S. A.* **1992**, *89* (23), 11461−11465.
(7) Tabor, H. *Biochemistry* **1962**, *1* (3), 496−501.
(8) Ha, H. C.; Sirisoma, N. S.; Kuppusamy, P.; Zweier, J. L.; Woster, P. M.; Casero, R. A. *Proc. Natl. Acad. Sci. U. S. A.* **1998**, *95* (19), 11140−11145.
(9) Oh, T. J.; Kim, I. G. *Biotechnol. Tech.* **1998**, *12* (10), 755−758.
(10) Baumann, C. G.; Smith, S. B.; Bloomfield, V. A.; Bustamante, C. *Proc. Natl. Acad. Sci. U. S. A.* **1997**, *94* (12), 6185−90.
(11) Gosule, L. C.; Schellman, J. A. *Nature* **1976**, *259* (5541), 333−335.
(12) Ouameur, A. A.; Tajmir-Riahi, H. A. *J. Biol. Chem.* **2004**, *279* (40), 42041−42054.
(13) Feuerstein, B. G.; Pattabiraman, N.; Marton, L. J. *Nucleic Acids Res.* **1990**, *18* (5), 1271−1282.
(14) Davis, R. H.; Morris, D. R.; Coffino, P. *Microbiol. Rev.* **1992**, *56* (2), 280−290.
(15) Peng, H. F.; Jackson, V. *J. Biol. Chem.* **2000**, *275* (1), 657−668.
(16) Todd, B. A.; Rau, D. C. *Nucleic Acids Res.* **2008**, *36* (2), 501−510.
(17) Besteman, K.; Hage, S.; Dekker, N. H.; Lemay, S. G. *Phys. Rev. Lett.* **2007**, *98* (5), 058103.
(18) Krasnow, M. A.; Cozzarelli, N. R. *J. Biol. Chem.* **1982**, *257* (5), 2687−2693.
(19) Zurla, C.; Manzo, C.; Dunlap, D.; Lewis, D. E.; Adhya, S.; Finzi, L. *Nucleic Acids Res.* **2009**, *37* (9), 2789−95.
(20) Finzi, L.; Dunlap, D. *Methods Enzymol.* **2003**, *370*, 369−78.
(21) Nelson, P. C.; Zurla, C.; Brogioli, D.; Beausang, J. F.; Finzi, L.; Dunlap, D. *J. Phys. Chem. B* **2006**, *110* (34), 17260−17267.
(22) Strick, T. R.; Charvin, G.; Dekker, N. H.; Allemand, J. F.; Bensimon, D.; Croquette, V. *C. R. Phys.* **2002**, *3* (5), 595−618.
(23) Brutzer, H.; Luzzietti, N.; Klaue, D.; Seidel, R. *Biophys. J.* **2010**, *98* (7), 1267−1276.
(24) Forth, S.; Deufel, C.; Sheinin, M. Y.; Daniels, B.; Sethna, J. P.; Wang, M. D. *Phys. Rev. Lett.* **2008**, *100* (14), 148301.
(25) Strick, T. R.; Allemand, J. F.; Bensimon, D.; Bensimon, A.; Croquette, V. *Science* **1996**, *271* (5257), 1835−7.
(26) Goyal, S.; Perkins, N. C.; Lee, C. L. *Int. J. Nonlinear Mech.* **2008**, *43* (1), 65−73.
(27) Leger, J. F.; Romano, G.; Sarkar, A.; Robert, J.; Bourdieu, L.; Chatenay, D.; Marko, J. F. *Phys. Rev. Lett.* **1999**, *83* (5), 1066−1069.
(28) Strick, T. R.; Croquette, V.; Bensimon, D. *Proc. Natl. Acad. Sci. U. S. A.* **1998**, *95* (18), 10579−10583.
(29) Sheinin, M. Y.; Forth, S.; Marko, J. F.; Wang, M. D. *Phys. Rev. Lett.* **2011**, *107* (10), 108102.
(30) Neukirch, S.; Marko, J. F. *Phys. Rev. Lett.* **2011**, *106* (13), 138104.
(31) Purohit, P. K. In *Shape and Energetics of DNA Plectonemes*, IUTAM Symposium on Cell, Molecular and Tissue Dordrecht, 2010; Garikipati, K. A., Ellen, M., Eds.; Springer: Dordrecht, 2010.
(32) Sarkar, A.; Leger, J. F.; Chatenay, D.; Marko, J. F. *Phys. Rev. E: Stat., Nonlinear, Soft Matter Phys.* **2001**, *63* (5 Pt 1), 051903.
(33) Clauvelin, N.; Audoly, B.; Neukirch, S. *Biophys. J.* **2009**, *96* (9), 3716−3723.
(34) Moroz, J. D.; Nelson, P. *Macromolecules* **1998**, *31* (18), 6333−6347.
(35) Bustamante, C.; Marko, J. F.; Siggia, E. D.; Smith, S. *Science* **1994**, *265* (5178), 1599−1600.
(36) Kratky, O.; Porod, G. *Recl.: J. R. Neth. Chem. Soc.* **1949**, *68* (12), 1106−1122.
(37) Porschke, D. *Biophys. Chem.* **1991**, *40* (2), 169−179.
(38) Bailly, C.; Mollegaard, N. E.; Nielsen, P. E.; Waring, M. J. *EMBO J.* **1995**, *14* (9), 2121−31.
(39) Ouameur, A. A.; Tajmir-Riahi, H.-A. *J. Biol. Chem.* **2004**, *279* (40), 42041−42054.
(40) Jain, S.; Zon, G.; Sundaralingam, M. *Biochemistry* **1989**, *28* (6), 2360−2364.
(41) Lee, M.; Kim, S. H.; Hong, S. C. *Proc. Natl. Acad. Sci. U. S. A.* **2010**, *107* (11), 4985−4990.
(42) Behe, M.; Felsenfeld, G. *Proc. Natl. Acad. Sci. U. S. A.* **1981**, *78* (3), 1619−23.
(43) Tabor, C. W.; Tabor, H. *Annu. Rev. Biochem.* **1984**, *53*, 749−90.
(44) Hasan, R.; Alam, M. K.; Ali, R. *FEBS Lett.* **1995**, *368* (1), 27−30.
(45) Thomas, T. J.; Gunnia, U. B.; Thomas, T. *J. Biol. Chem.* **1991**, *266* (10), 6137−41.
(46) Ruiz-Chica, J.; Medina, M. A.; Sanchez-Jimenez, F.; Ramirez, F. J. *Biophys. J.* **2001**, *80* (1), 443−454.
(47) Ubbink, J.; Odijk, T. *Biophys. J.* **1999**, *76* (5), 2502−2519.
(48) Ray, J.; Manning, G. S. *Langmuir* **1994**, *10* (7), 2450−2461.
(49) Manning, G. S. *J. Chem. Phys.* **1969**, *51* (3), 924−&.
(50) Lillian, T. D.; Perkins, N. C. *Proceedings of ASME International Design Engineering Technical Conferences and Computers and Information in Engineering Conference*, Vol. 4, Parts A−C, 2010, pp 1447−1455, 2069.
(51) Goyal, S.; Perkins, N. C. *Int. J. Nonlinear Mech.* **2008**, *43* (10), 1121−1129.
(52) Palanthandalarn-Madapusi, H. J.; Goyal, S. *Automatica* **2011**, *47* (6), 1175−1182.

(53) Goyal, S.; Perkins, N. C.; Lee, C. L. *J. Comput. Phys.* **2005**, *209* (1), 371−389.
(54) Bustamante, C.; Bryant, Z.; Smith, S. B. *Nature* **2003**, *421* (6921), 423−7.
(55) Wallace, H. M.; Fraser, A. V.; Hughes, A. *Biochem. J.* **2003**, *376* (Pt 1), 1−14.

Macromolecules

Article

pubs.acs.org/Macromolecules

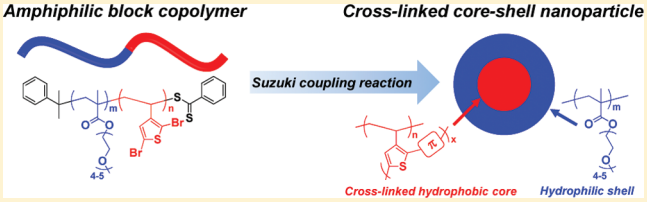
Cross-Linked Core–Shell Nanoparticles Based on Amphiphilic Block Copolymers by RAFT Polymerization and Palladium-Catalyzed Suzuki Coupling Reaction

Kazuhiro Nakabayashi, Hiroshi Oya, and Hideharu Mori*

Department of Polymer Science and Engineering, Graduate School of Science and Engineering, Yamagata University, 4-3-16, Jonan, Yonezawa 992-8510, Japan

Supporting Information

ABSTRACT: Well-defined amphiphilic block copolymers, poly[poly(ethylene glycol) methyl ether methacrylate]-*block*-poly(2,5-dibromo-3-vinylthiophene) poly(PEGMA)-*b*-poly(DB3VT), were synthesized by reversible addition–fragmentation chain transfer polymerization. A facile bottom-up modification was developed for preparing cross-linked core–shell nanoparticles from the amphiphilic block copolymers, in which an in situ Suzuki coupling reaction was carried out between 2,5-dibromide groups in the block copolymers and various diboronic acid compounds in the presence of a palladium catalyst after micelle formation in THF/H_2O solution. The stable and uniform core–shell structure was confirmed by scanning force microscopy and dynamic light scattering observations. Furthermore, the size of the cross-linked core–shell nanoparticles could be controlled by adjusting the compositions of each segment in the block copolymers and Suzuki coupling reaction conditions. The relationship between the optical properties and chemical structures of π-conjugated segments in the particles was clearly observed by changing the coupling agents (diboronic acid compounds). These results demonstrate that stable and uniform cross-linked core–shell nanoparticles were successfully prepared from well-defined amphiphilic block copolymers, and tuning of their optical properties could be accomplished as well.



INTRODUCTION

For several decades, there has been a great demand for the development of π-conjugated polymers for realizing various optoelectrical applications such as organic light-emitting diodes,[1] organic field effect transistors,[2] and organic photovoltaics.[3,4] Considering the applications based on π-conjugated polymers, it is noteworthy that highly ordered structures (i.e., high regioregularity, hierarchical structures derived from self-assembly, etc.) strongly affect their optoelectrical properties and can offer unique behaviors derived from highly ordered structure in some cases.[5−8] The synthesis of well-defined π-conjugated polymers and block copolymers with self-assembled capability is, thus, an interesting topic from the viewpoint of scientific research and industrial demands.[9−12] Among π-conjugated polymers, polythiophene and its derivatives are one of the most important classes for promising hole-transporting materials and a variety of applications have been also fabricated so far.[13,14] In 2005, the synthesis of poly(3-hexylthiophene) with the narrow polydispersity ($M_w/M_n \approx 1.10$) by the quasi-living Grignard metathesis method based on polycondensation was developed by Yokozawa[15] and McCullough.[16] Furthermore, the method has been expanded to the synthesis of polythiophene-based block copolymers[17,18] and other π-conjugated polymers,[19,20] thus contributing to the development of π-conjugated polymeric materials.

Controlled radical polymerization of vinyl thiophene derivatives offers a unique opportunity to provide a variety of well-defined polythiophene derivatives and block copolymers based on polythiophene segments in the field of chain polymerization. Free radical (co)polymerizations of various vinylthiophene derivatives, such as 2-vinylthiophene,[21,22] 3-vinylthiophene,[23−25] 4-bromo-2-vinylthiophene,[26] 5-alkyl-2-vinylthiophene,[27−29] 5-bromo-2-vinylthiophene,[30] 5-methoxy-2-vinylthiophene,[31] and 2,5-dimethyl-3-vinylthiophene,[32,33] have been established. Cationic polymerization[34,35] and electrochemical polymerization[36,37] of 2-vinylthiophene were also reported. Furthermore, polymerization of vinyl oligothiophenes (i.e., 3′-vinyl-2,2′:5′,2″-terthiophene,[38] 5-vinyl-2,2′:5′,2″-terthiophene,[39] and *N*-phenyl-2-(2′-thienyl)-5-(5″-vinyl-2″-thienyl)-pyrrole[40]) has been achieved so far. Controlled radical polymerization of these vinyl thiophene derivatives is, however, still a challenging issue because radicals having electron-donating moieties (e.g., thiophene, carbazole, etc.) are generally unstable (i.e., highly reactive). That is, the high reactivity of the radicals induces undesired chain-transfer and termination reactions, preventing controlled polymerization. In our previous work, we achieved the controlled synthesis of poly(vinylthiophene) derivatives from 2,5-dibromo-3-vinylthiophene (DB3VT) by reversible addition–fragmentation chain transfer (RAFT) polymerization using a dithiobenzoate-type

Received: February 2, 2012
Revised: March 12, 2012
Published: March 23, 2012

ACS Publications © 2012 American Chemical Society

Table 1. Synthesis of Poly(PEGMA)-*b*-poly(DB3VT) by RAFT Polymerization of DB3VT Using Poly(PEGMA) Macro-CTA[a]

run	[M]:[macro-CTA]	time (h)	conv. (%)[b]	M_n theory[c]	M_n NMR[b]	M_n SEC[d]	M_w/M_n[d]	*m*:*n*[b]
1	30:1	12	69	19000	19000	15000	1.24	65:35[e] (43:23)[f]
2	60:1	12	64	23000	26000	18000	1.29	48:52[e] (43:47)[f]
3	160:1	24	65	40000	43000	29000	1.33	28:72[e] (43:111)[f]
4	200:1	24	56	43000	50000	30000	1.26	24:76[e] (43:136)[f]

[a]Polymerization was carried out at [macro-CTA]/[AIBN] = 5/1 at 60 °C in 1,4-dioxane ([M] = 1.00 mol/L, $M_{n,NMR}$ and M_w/M_n of macro-CTA = 13 000 and 1.16). [b]Calculated by ^{1}H NMR in $CDCl_3$. [c]Theoretical molecular weight was calculated from [M]/[macro-CTA] × (M_w of monomer) × conv. + (M_w of macro-CTA). [d]Determined by SEC using polystyrene standards in THF. [e]Molar composition ratios. [f]Precise number of repeating units.

chain transfer agent (CTA).[41] Well-defined block copolymers composed of poly(methyl methacrylate) and poly(vinylthiophene) segments were successfully synthesized as well. To the best of our knowledge, this is the first report on the controlled synthesis of poly(vinylthiophene) derivatives by the radical polymerization, indicating that even the radical polymerization of vinyl monomers with electron-donating moieties can be controlled by RAFT polymerization using well-chosen CTAs. RAFT polymerization has been employed for the controlled synthesis of various optoelectronic polymers, mainly because of the compatibility with a wide range of functionalities in monomers, solvents, and impurities, and the absence of undesired metal species during the polymerization process, in addition to the feasibility of creating various complex architectures and supermolecular assemblies.[42]

In this Article, we synthesized novel well-defined amphiphilic block copolymers composed of poly(ethylene glycol) methyl ether methacrylate (PEGMA) and DB3VT segments by RAFT polymerization. The facile bottom-up modification for the preparation of cross-linked core−shell nanoparticles from amphiphilic block copolymers was developed, in which the in situ Suzuki coupling reaction was carried out between 2,5-dibromide groups in the block copolymers and various diboronic acid compounds in the presence of a palladium catalyst after the formation of the micelles in the THF/H_2O solution. The stable and uniform core−shell structure was confirmed by scanning force microscopy (SFM) and dynamic light scattering (DLS) observations. Furthermore, the size of the cross-linked core−shell nanoparticles could be controlled by adjusting the compositions of each segment in the block copolymers and Suzuki coupling reaction conditions. The relationship between the optical properties and chemical structures of π-conjugated segments in the particles was also investigated in detail.

EXPERIMENTAL SECTION

Materials. PEGMA (Aldrich, average $M_n \approx 300$) was purified with column chromatography (Aluminium oxide 90 standard). 2,2′-Azobisisobutyronitrile (AIBN, Kanto Chemical, 97%) was recrystallized with methanol. Other reagents and solvents were used as received unless otherwise stated. Cumyl dithiobenzoate used as a CTA[43,44] and 2,5-dibromo-3-vinyl thiophene (DB3VT)[41] were synthesized according to the previous literatures.

Synthesis of poly(PEGMA) macro-chain transfer agent (Macro-CTA). Typical procedure is as follows: PEGMA (3.0 g, 10 mmol), cumyl dithiobenzoate (63 mg, 0.25 mmol), AIBN (8.2 mg, 0.05 mmol), and dry 1,4-dioxane (10 mL) were placed in a dry glass ampule equipped with a magnetic stir bar, and then the solution was degassed by three freeze−evacuate−thaw cycles. After the ampule was flame-sealed under vacuum, the reaction was carried out at 60 °C for 12 h with stirring. Then, the reaction was stopped by rapid cooling with liquid nitrogen. After the reaction mixture was poured into hexane, the precipitate was collected with decantation and dried in vacuo at room temperature to yield pink viscous product (2.1 g, 70%). M_n = 8600 (M_w/M_n = 1.16), $M_{n,NMR}$ = 13 000, $M_{n,theory}$ = 9300. ^{1}H NMR ($CDCl_3$, δ): 4.2−3.9 (2H, bs), 3.8−3.3 (19H, bm), 2.0−1.5 (3H, bm), 1.1−0.7 (2H, bm).

Synthesis of Amphiphilic Block Copolymer. Typical procedure (Run 3 in Table 1) is as follows: Macro-CTA (0.29 g, 0.023 mmol, $M_{n,NMR}$ = 13 000, see Supporting Information), DB3VT (1.0 g, 3.7 mmol), AIBN (0.86 mg, 0.005 mmol), and dry 1,4-dioxane (3.7 mL) were placed in a dry glass ampule equipped with a magnetic stir bar, and then the solution was degassed by three freeze−evacuate−thaw cycles. After the ampule was flame-sealed under vacuum, the reaction was carried out at 60 °C for 24 h with stirring. Then, the reaction was stopped by rapid cooling with liquid nitrogen. After the reaction mixture was poured into hexane, the precipitate was collected with decantation and dried in vacuo at room temperature to yield light-red viscous product (65%, 0.84 g). M_n = 29 000 (M_w/M_n = 1.33), $M_{n,theory}$ = 40 000. ^{1}H NMR ($CDCl_3$, δ): 7.2−6.7 (1H, bm), 4.2−3.9 (2H, bs), 3.8−3.3 (19H, bm), 2.7−2.0 (1H, bm), 2.0−1.1 (5H, bm), 1.1−0.7 (2H, bm). The compositions of each segment (*m*:*n*) were estimated by the ^{1}H NMR spectra.

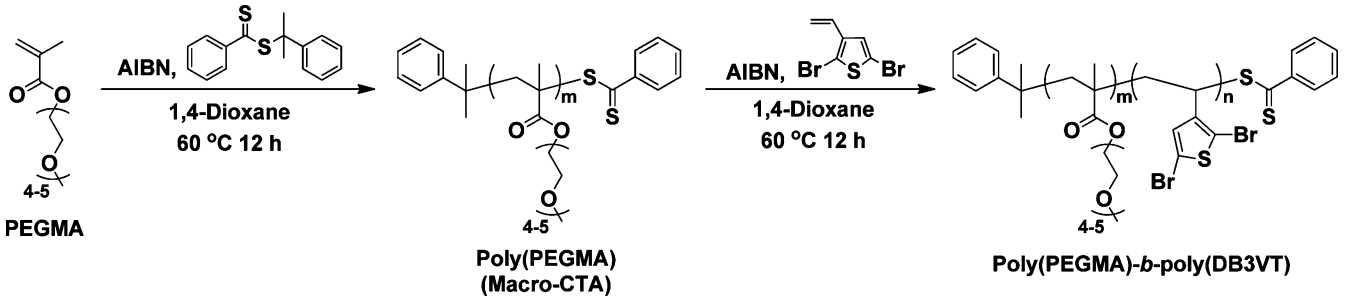
Table 2. Preparation of Cross-Linked Nanoparticles from Poly(PEGMA)-*b*-poly(DB3VT) by Suzuki Coupling Reaction[a]

run	comonomer composition PEGMA:DB3VT	THF:H_2O (vol %)	yield (%)[b]	D_h (nm)[c]
1	80:20	1:9	90	88
2		3:7	87	88
3		5:5	99	broad
4		7:3	99	bimodal
5		9:1	95	bimodal
6	68:32	3:7	94	110

[a]Reaction was carried out between the block copolymer and 2,5-thiophenediboronic acid at 70 °C for 24 h in THF/H_2O in the presence of Pd(dppf)Cl_2 (10 mol % for 2,5-thiophenediboronic acid). [b]After dialysis with water and THF. [c]Determined by DLS measurement in THF solution (conc. = 2.0 mg/mL) at 25 °C.

Preparation of Cross-Linked Core−Shell Nanoparticles by Suzuki Coupling Reaction. Typical procedure (Run 6 in Table 2) is as follows: The THF solution (15 mL) of poly(PEGMA)$_{68}$-*b*-poly(DB3VT)$_{32}$ (90 mg, 0.1 mmol based on the repeating unit), 2,5-thiophenediboronic acid (86 mg, 0.5 mmol), and $NaHCO_3$ (0.33 g, 4.0 mmol) was stirred at room temperature under an argon atmosphere. After the block copolymer was completely dissolved, Pd(dppf)Cl_2 (16.3 mg, 0.02 mmol) and water (35 mL) was added, and the reaction mixture was carried out at 70 °C for 24 h in the dark. After removing some amount of solvents, dialysis of the residue was carried out with water, followed by with THF. Then, the residue was

Scheme 1. Synthesis of Poly(PEGMA)-*b*-poly(DB3VT)



evaporated and dried in vacuo at room temperature to yield brown viscous product (94%, 85 mg). Unreacted diboronic acid compounds, $NaHCO_3$, and palladium catalyst were removed from the reaction mixture with dialysis. Therefore, the yield was determined by the amount of the product compared with the sum of the amounts of reacted boronic acid compound and block copolymer that has been cross-linked. ^{1}H NMR ($CDCl_3$, δ): 4.2−3.9 (2H, bs), 3.8−3.3 (19H, bm), 2.7−2.0 (1H, bm), 2.0−1.1 (5H, bm), 1.1−0.7 (2H, bm).

Instrumentation. ^{1}H NMR (400 MHz) spectrum was recorded JEOL JNM-ECX400. The UV−vis spectra were recorded with a on a JASCO V-630BIO UV−vis spectrophotometer. Fluorescence spectra were obtained from a JASCO FP-6100 spectrofluorophotometer. Elemental analysis was carried out on a Perkin-Elmer 2400 II CHNS/O analyzer. Number-average molecular weight (M_n) and molecular weight distribution (M_w/M_n) were estimated by GPC using a system consisting of a Tosoh DP-8020 pump and Viscotek. The column set was as follows: a guard column [TSK guard column HXL-H (4.0 cm) and four consecutive columns (Tosoh TSK-GELs (exclusion limited molecular weight): GMHXL (4×10^8), G4000HXL (4×10^5), G3000HXL (6×10^4), and G2500HXL (2×10^4), 30 cm each] eluted with THF at a flow rate of 1.0 mL/min. Polystyrene standards were employed for calibration. DLS measurement was performed by using an Sysmex Zatasizwer Nano with a He−Ne laser (λ_0 = 632.8 nm) and a scattering angle of 90°. Prior to the light scattering measurement, the polymer solutions were filtered using Millipore Teflon Filters with a pore size of 0.2 μm into a dust-free cylindrical cuvette. Tapping mode SFM observation was performed with an Agilent AFM 5500, using microfabricated cantilevers with a force constant of ~34 N/m. The sample was prepared as follows; The chloroform solution of the cross-linked nanoparticles (0.5 mg/L) was casted onto mica substrate and dried at room temperature.

RESULTS AND DICUSSION

Synthesis and Characterization of Amphiphilic Block Copolymers. Scheme 1 shows the synthetic route of amphiphilic block copolymers composed of PEGMA and DB3VT, poly(PEGMA)-*b*-poly(DB3VT). The synthetic approach by RAFT polymerization involves two steps. In the first step, poly(PEGMA) macro-CTAs with narrow polydispersities (1.16−1.26) were prepared from cumyl dithiobenzoate as a CTA and PEGMA. The dithiobenzoate-type CTA having tertiary leaving group, cumyl dithiobenzoate, used in our previous work[41] was chosen in consideration of the second step reaction, which was the polymerization of DB3VT from the methacrylate-type macro-CTA. It was reported that cumyl dithiobenzoate was effective to obtain well-defined poly(methyl methacrylate) macro-CTA, and chain extension from the macro-CTA to DB3VT could be well-controlled under suitable conditions to afford block copolymers having cross-linkable poly(DB3VT) segments.[41] In this study, the molecular weight of poly(PEGMA) macro-CTA was precisely controlled in the range of 8600 to 38 000. (See Table S1 and Figure S1 of the Supporting Information for details.) In the second step, poly(PEGMA)-*b*-poly(DB3VT) was synthesized by RAFT polymerization of DB3VT using poly(PEGMA) macro-CTA ($M_{n,NMR}$ = 13 000 and M_w/M_n = 1.16) under suitable conditions. The polymerization was carried out at 60 °C for 12−24 h with different ratios of [M]:[macro-CTA] (30:1 to 200:1), maintaining the ratio of [macro-CTA]:[AIBN] = 5:1. The results are summarized in Table 1. As expected, DB3VT was successfully polymerized from the dithiobenzoate-terminated macro-CTA to yield amphiphilic block copolymers with narrow polydispersities (M_w/M_n = 1.24 to 1.33). Furthermore, the comonomer compositions (*m*:*n*) of each segment in the block copolymers could be precisely controlled by adjusting the [M]:[macro-CTA] ratios. The size exclusion chromatography (SEC) profiles of the poly(PEGMA) macro-CTA and block copolymers show that the molecular weight clearly shifts to a lower elution time, which is consistent with increasing molecular weight (Figure 1). It should be noted that the

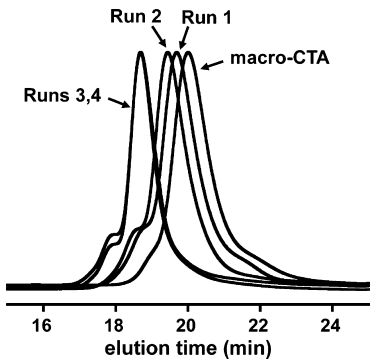


Figure 1. SEC profiles of poly(PEGMA)-*b*-poly(DB3VT) and poly(PEGMA) macro-CTA. See Table 1 for detailed polymerization procedure.

small shoulders at the lower elution time are due to byproduct formed by undesired bimolecular termination. In the ^{1}H NMR spectrum (Figure 2a), the peaks corresponding to both segments are clearly observed, indicating that the desired block copolymers were obtained. The block copolymers showed good solubility in THF, chloroform, and dichloromethane regardless of the comonomer composition. Additionally, the block copolymers with high poly(PEGMA) contents were soluble in methanol.

Preparation of Cross-Linked Nanoparticles by Suzuki Coupling Reaction. The preparation of cross-linked nanoparticles was carried out by the Suzuki coupling reaction between poly(PEGMA)-*b*-poly(DB3VT) and 2,5-thiophenediboronic acids in a THF/H_2O solution in the presence of the catalytic amount of Pd(dppf)Cl_2 at 70 °C for 24 h (Scheme 2).

dx.doi.org/10.1021/ma300239u | *Macromolecules* 2012, 45, 3197−3204

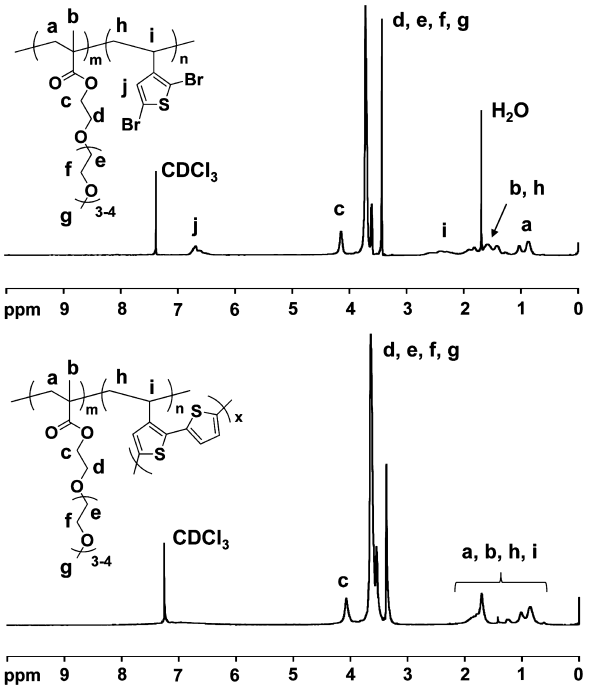


Figure 2. ^{1}H NMR spectra of poly(PEGMA)-*b*-poly(DB3VT) (top) and cross-linked nanoparticle (bottom) in $CDCl_3$.

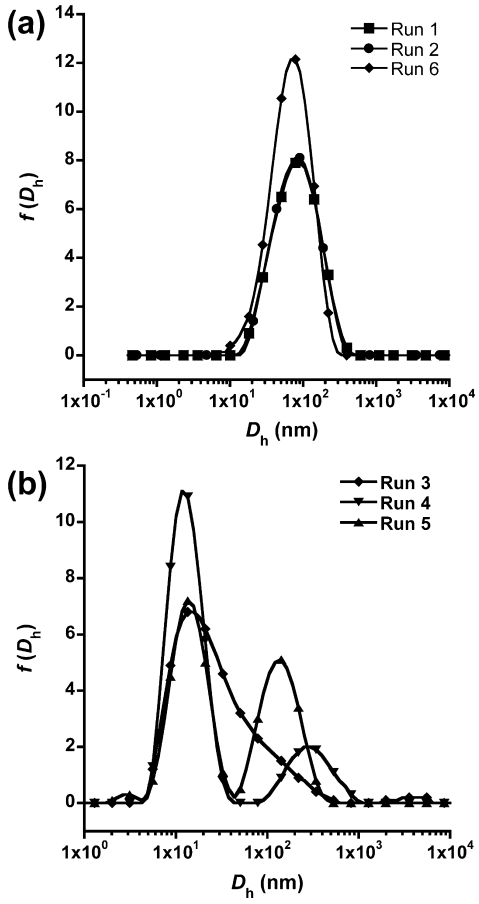
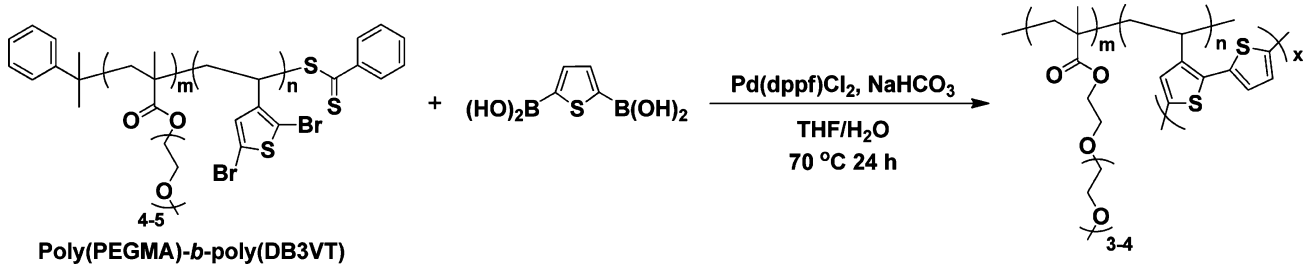


Figure 3. DLS profiles of cross-linked nanoparticles in THF solution (conc. = 2.0 mg/mL): (a) Runs 1, 2, and 6 and (b) Runs 3, 4, and 5 in Table 2.

In the THF/H_2O solution (1:9 and 3:7 vol %), poly(PEGMA)-*b*-poly(DB3VT) can form micelles consisting of a hydrophobic core of poly(DV3VT) covered with a hydrophilic shell of poly(PEGMA) segments. The inter- and intramolecular coupling reaction to form polythiophene segments within micelles (i.e., the formation of cross-linked core–shell nanoparticles) is, thus, likely to prospective under the Suzuki coupling reaction conditions described above. After the coupling reaction, purification was carried out by dialysis with water and then with THF to yield a brown viscous product. The obtained product is soluble in common organic solvents, such as THF, chloroform, and dichloromethane. In the ^{1}H NMR spectra (Figure 2), a broad peak corresponding to the DV3VT unit is clearly observed at 6.7 to 7.2 ppm in poly(PEGMA)-*b*-poly(DB3VT), whereas no peak corresponding to the poly(DV3VT) segment is detected in the product obtained after the Suzuki coupling reaction, implying the formation of the cross-linked core–shell nanoparticles with the polythiophene core. The solvent (i.e., volumes of THF and H_2O) is a dominant factor in the preparation of well-defined nanoparticles (Table 2). Except for THF/H_2O = 1:9 and 3:7 vol %, broad or bimodal hydrodynamic diameters are observed in DLS analysis (Figure 3), which is probably due to the fact that the micelles are not stable before the coupling reaction under such conditions. Comparison to the DLS profiles of the block copolymer before the cross-linking reaction (Figure S2 in the Supporting Information) suggested that the signal for small diameter (~30 nm) observed in Figure 3b (Runs 3–5) can be corresponding to that of free block copolymers. Sharp and unimodal DLS profiles are observed from nanoparticles prepared in THF/H_2O = 1:9 and 3:7 vol % (Runs 1, 2, and 6 in Table 2), and the size of nanoparticles could be precisely controlled by adjusting the compositions of each segment. The aforementioned conditions are particularly effective for preparing well-defined nanoparticles. Note that other factors, such as nature of the palladium catalyst, reaction temperature, and reaction procedure, were investigated in addition to the solvent conditions (see Tables S2–S4 in the Supporting

Scheme 2. Preparation of Cross-Linked Core-Shell Nanoparticle by Suzuki Coupling Reaction



Poly(PEGMA)-*b*-poly(DB3VT)

dx.doi.org/10.1021/ma300239u | *Macromolecules* 2012, 45, 3197–3204

Information for details), and these parameters had no significant effects on the size and distribution of the cross-linked nanoparticles.

Optical Properties of Cross-Linked Nanoparticles. The optical properties of the cross-linked nanoparticles in the solutions were investigated by absorption and fluorescence spectra (Figure 4). The absorption maximum peak corresponding to a thiophene ring is observed at around 250 nm in the absorption spectrum of the block copolymer before the coupling reaction. The cross-linked nanoparticles obtained after the coupling reaction show the red-shifted absorption maximum peaks at ~330 nm. These results indicate that the Suzuki coupling reaction was successfully achieved in the block copolymer, resulting in the red-shifted absorption derived from the expansion of π-conjugation lengths. In the fluorescence spectra, no emission peak is observed in the block copolymer, whereas the emission peaks derived from the polythiophene core are clearly observed at ~530 nm in the cross-linked nanoparticles. According to Rentsch and coworkers,[45] the absorption maximum peak at ~330 nm corresponded to that of terthiophene, and its Stokes shift was observed as ~70 nm (i.e., the emission maximum peak was observed at ~400 nm). Compared with these data, the emission peaks of the cross-linked nanoparticles are further red-shifted, which should be attributed to the strong interchain $\pi-\pi$ interaction. Given the ^{1}H NMR characterization and optical properties, the formation of the cross-linked dense polythiophene core is expected. (See the next section.)

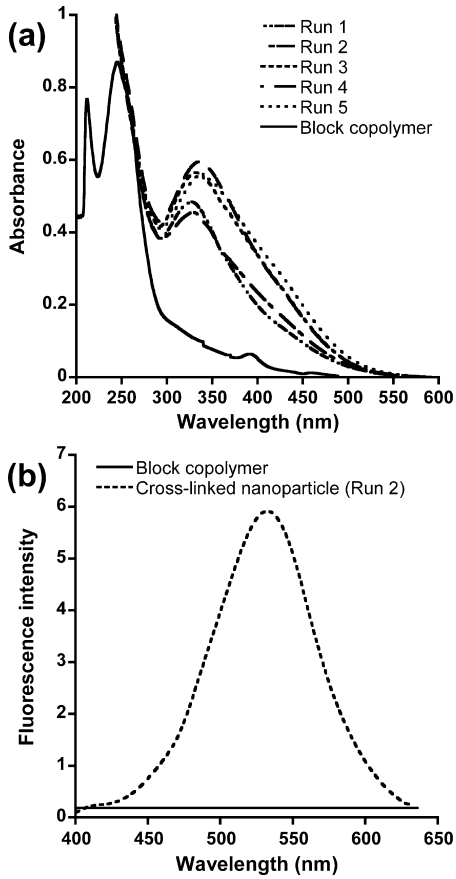


Figure 4. (a) Absorption and (b) fluorescence spectra of block copolymer and cross-linked nanoparticle in THF solution (conc. = 1.0 × 10^{-4} thiophene unit mol/L). See Table 2 for detailed sample information.

SFM Observation of Cross-Linked Nanoparticles. The tapping mode phase and height images of the cross-linked nanoparticles were recorded under ambient conditions on 2 × 2 μm^2 size scales (Figure 5). The sample was prepared from a diluted chloroform solution (0.5 mg/L) that would fully dissolve the block copolymer prior to cross-linking. Uniform nanoparticles are clearly observed in the phase and height images, indicating that the resulting nanoparticles are stable due to the cross-linking structure. The height and diameter of the nanoparticles on the mica substrate were determined to be about 10 and 150 nm, respectively. Furthermore, in the information of cross-sectional phase image, the difference of the hardness (i.e., positive and negative in the z-axis) corresponds to the cross-linked hard core derived from poly(DV3VT) and soft shell of the poly(PEGMA) segments, demonstrating the formation of the desired core–shell nanoparticles. These SFM data are consistent with the aforementioned ^{1}H NMR characterization and optical properties. The formation of the cross-linked nanoparticles is also supported by the DLS profiles of the block copolymer and cross-linked product in a good solvent for both components of the block copolymer (Figure S4, Supporting Information). The size of the block copolymer before cross-linking is apparently different from that of the cross-linked nanoparticles in the good solvent (e.g., THF and chloroform), suggesting that the block copolymers do not form the micelles under such conditions. In other words, this result indicates that the products visualized by SFM measurement correspond to the cross-linked nanoparticles, whereas the block copolymers do not provide similar SFM images in the good solvent.

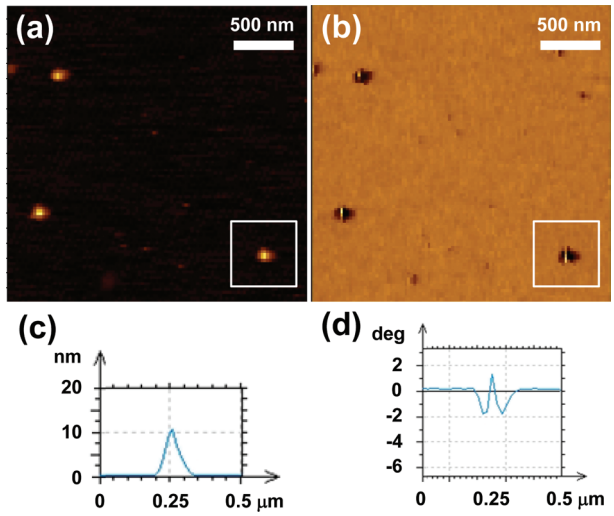
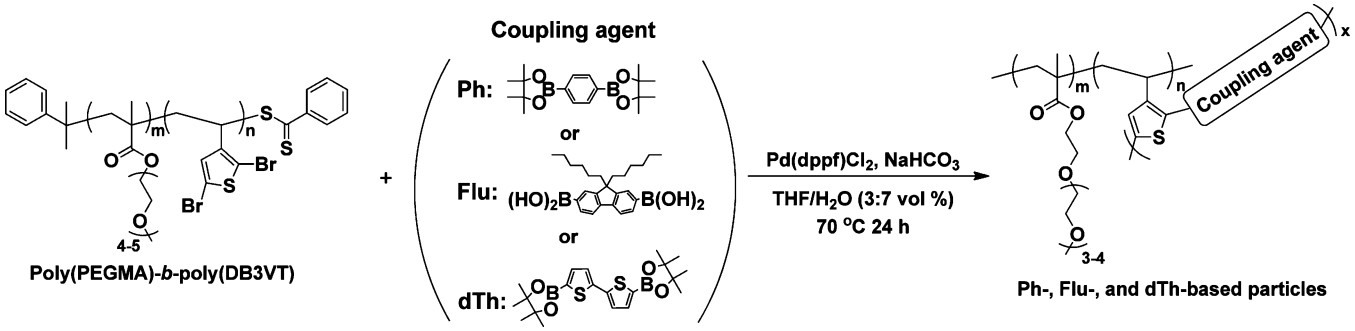


Figure 5. SFM images of the cross-linked nanoparticles (Run 2 in Table 2): (a) height image (z-range: 20 nm), (b) phase image (z-range: 10°), (c) cross-sectional height information in the square in panel a, and (d) cross-sectional phase information in the square in panel b.

In general, cross-linked micelles stay in their spherical shape with a height similar to the diameter (usually less because the shell is soft and flattens). In this study, the height of the products determined by SFM measurement is only 10 nm, which may be due to the fact that the poly(PEGMA) shell is very flexible owing to poly(ethylene glycol) side chain. Note

dx.doi.org/10.1021/ma300239u | Macromolecules 2012, 45, 3197–3204

Scheme 3. Preparation of Cross-Linked Core-Shell Nanoparticles with Various Coupling Agents



that the block copolymers having long poly(PEGMA) segments were employed for the preparation of the cross-linked nanoparticles, resulting in the formation of the core−shell nanoparticles having relatively thick poly(PEGMA) shell. Nevertheless, SFM measurements indicate that the size of all nanoparticles is uniform, in which the cross-linking structure may contribute to the uniformity of the nanoparticle. The advantages of cross-linked core−shell nanoparticles[46−50] are the uniformity and stability compared with stabilized nanoparticles (non-cross-linked nanoparticles).[51,52] In our system, cross-linked core−shell nanoparticles based on amphiphilic block copolymers were prepared by facile bottom-up modification (in situ cross-linking reaction after micellization). In contrast, the preparation of cross-linked core−shell nanoparticles is usually carried out by two-step modification (micellization, followed by the cross-linking reaction).[46,47] These results clearly demonstrate that our process is the efficient approach (i.e., one-step cross-linking) for preparing stable and uniform core−shell nanoparticles.

Preparation of Cross-Linked Nanoparticles with Various Coupling Agents. The tuning of optical properties in nanoparticles is an interesting topic.[53−55] The relationship between the optical properties and chemical structures of π-conjugated components in nanoparticles was thus investigated by changing coupling agents in the Suzuki coupling reaction. Using the method of preparing cross-linked core−shell nanoparticles with 2,5-thiophenediboronic acid, three nanoparticles, phenylene- (Ph-), fluorine- (Flu-), and dithiophene- (dTh-) based nanoparticles, were prepared with 1,4-benzenediboronic acid bis(pinacol) ester, 9,9-dihexylfluorene-2,7-diboronic acid, and 2,2-bithiophene-5,5-diboronic acid bis(pinacol) ester, respectively (Scheme 3). As can be seen in Table 3, cross-linked core−shell nanoparticles were successfully obtained in high yields (>90%). The obtained nanoparticles were soluble in common organic solvents such as THF, chloroform, and dichloromethane. In the absorption spectra, the Ph-, Flu-, and dTh-based nanoparticles show the absorption maximum peaks derived from the expansion of π-conjugated lengths at 332, 346, and 370 nm, respectively. In the fluorescence spectra, the emission maximum peaks of Ph-, Flu-, and dTh-based nanoparticles are observed at 467, 446, and 524 nm, respectively (Figure 6). Flu-based nanoparticles show much stronger emissions than Ph- and dTh-based nanoparticles due to the efficient fluorescence quantum yield of fluorine moieties. Furthermore, a smaller Stokes shift is

Table 3. Preparation of Cross-Linked Core-Shell Nanoparticles Using Various Coupling Agents[a]

sample	coupling agent[b]	yield (%)[c]	λ_{max}^{abs} (nm)[d]	λ_{max}^{em} (nm)[d]
Ph-based particle	Ph	93	332	467
Flu-based particle	Flu	91	346	446
dTh-based particle	dTh	91	370	524

[a]Reaction was carried out between poly(PEGMA)$_{85}$-*b*-poly(DB3VT)$_{15}$ and coupling agent at 70 °C for 24 h in THF/H_2O (3:7 vol %) in the presence of Pd(dppf)Cl_2 (10 mol % for the coupling agent). [b]Ph:1,4-benzenediboronic acid bis(pinacol) ester, Flu:9,9-dihexylfluorene-2,7-diboronic acid, and dTh:2,2-bithiophene-5,5-diboronic acid bis(pinacol) ester. [c]After dialysis with water and THF. [d]Measured in THF solution.

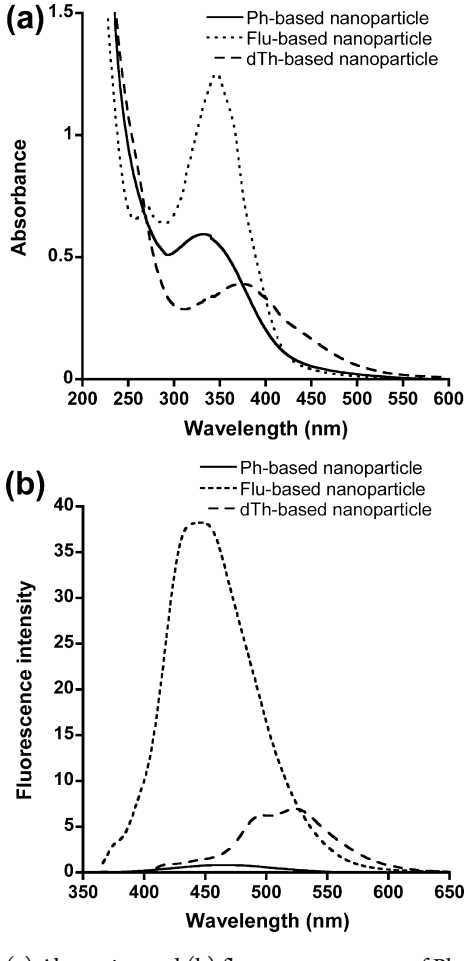


Figure 6. (a) Absorption and (b) fluorescence spectra of Ph-, Flu-, and dTh-based nanoparticles in THF solution (conc. = 1.0 × 10^{-4} thiophene unit mol/L).

dx.doi.org/10.1021/ma300239u | *Macromolecules* 2012, 45, 3197−3204

observed in Flu-based nanoparticles compared with Ph- and dTh-based nanoparticles, resulting from the weaker interchain $\pi-\pi$ interaction due to alkyl side chains in the fluorine moieties. These results demonstrate that cross-linked nanoparticles with various π-conjugated segments can be readily prepared by our facile bottom-up modification and the optical properties are tunable by adjusting the structures of the π-conjugated segments.

CONCLUSIONS

A well-defined amphiphilic block copolymer, poly(PEGMA)-*b*-poly(DB3VT), was successfully synthesized by RAFT polymerization. Cross-linked nanoparticles were then prepared by facile bottom-up modification, which was the formation of micelles in THF/H_2O solution, followed by the in situ Suzuki coupling reaction between 2,5-dibromide groups in the block copolymer and 2,5-thiophenediboronic acids in the presence of a palladium catalyst. The size of the cross-linked nanoparticles could be readily controlled by adjusting the composition of each segment in the block copolymers. Red-shifted absorption maximum peaks and appearance of emission peaks were observed after the cross-linking reaction, indicating the formation of a polythiophene core by the Suzuki coupling reaction. SFM observation revealed the formation of stable and uniform cross-linked nanoparticles. Three nanoparticles (Ph-, Flu-, and dTh-based nanoparticles) were also prepared with various coupling agents using the procedure described above, and the optical properties could be controlled by adjusting the structure of π-conjugated segments. Consequently, cross-linked core−shell nanoparticles were successfully prepared by the facile bottom-up modification using well-defined amphiphilic block copolymers having cross-linkable sites, and the tuning of their optical properties was also accomplished by adjusting the structure of the π-conjugated components.

ASSOCIATED CONTENT

Supporting Information

Figure showing SEC profiles of poly(PEGMA) macro-CTAs, DLS profiles of the block copolymer in different solvents, comparison of DLS profiles of the block copolymer before and after the cross-linking reaction, and tables summarizing results of synthesis of poly(PEGMA) macro-CTAs and preparation of cross-linked nanoparticles under various coupling reaction conditions. This material is available free of charge via the Internet at http://pubs.acs.org.

AUTHOR INFORMATION

Corresponding Author

*E-mail: h.mori@yz.yamagata-u.ac.jp.

Notes

The authors declare no competing financial interest.

REFERENCES

(1) Grimsdale, A. C.; Chan, K. L.; Martin, R. E.; Jokisz, P. G.; Holmes, A. B. *Chem. Rev.* **2009**, *103*, 897−1091.
(2) Facchetti, A. *Chem. Mater.* **2011**, *23*, 733−758.
(3) Boudreault, P.-L. T.; Najari, A.; Leclerc, M. *Chem. Mater.* **2011**, *23*, 456−469.
(4) Thompson, B. C.; Fréchet, J. M. *Angew. Chem., Int. Ed.* **2008**, *47*, 58−77.
(5) Kim, F. S.; Ren, G.; Jenekhe, S. A. *Chem. Mater.* **2011**, *23*, 682−732.
(6) Briseno, A. L.; Mannsfeld, S. C. B.; Jenekhe, S. A.; Bao, Z.; Xia, Y. *Mater. Today* **2008**, *11*, 39−47.
(7) Allard, S.; Forster, M.; Souharce, B.; Thiem, H.; Scherf, U. *Angew. Chem., Int. Ed.* **2008**, *47*, 4070−4098.
(8) Tajima, K.; Suzuki, Y.; Hashimoto, K. *J. Phys. Chem. C* **2008**, *112*, 8507−8510.
(9) Brabec, C. J.; Gowrisanker, S.; Halls, J. J. M.; Jia, S.; Williams, S. P. *Adv. Mater.* **2010**, *22*, 3839−3856.
(10) Helgesen, M.; Søndergaard, R.; Krebs, F. C. *J. Mater. Chem.* **2010**, *20*, 36−60.
(11) Sagalman, R. A.; McCulloch, B.; Kirmayer, S.; Urban, J. J. *Macromolecules* **2009**, *42*, 9206−9216.
(12) Cuendias, A. D.; Hiorns, R. C.; Cloutet, E.; Vignau, L.; Cramail, H. *Polym. Int.* **2010**, *59*, 1452−1476.
(13) Perepichka, I. F.; Perepichka, D. F.; Meng, H.; Wudl, F. *Adv. Mater.* **2005**, *17*, 2281−2305.
(14) Otsubo, T.; Aso, Y.; Takimiya, K. *J. Mater. Chem.* **2002**, *12*, 2565−2575.
(15) Miyakoshi, R.; Yokoyama, A.; Yokozawa, T. *J. Am. Chem. Soc.* **2005**, *127*, 17542−17547.
(16) Iovu, M. C.; Sheina, E. E.; Gil, R. R.; McCullough, R. D. *Macromolecules* **2005**, *38*, 8649−8656.
(17) Zhang, Y.; Tajima, K.; Hirota, K.; Hashimoto, K. *J. Am. Chem. Soc.* **2008**, *130*, 7812−7813.
(18) Ohshimizu, K.; Ueda, M. *Macromolecules* **2008**, *41*, 5289−5294.
(19) Miyakoshi, R.; Shimono, K.; Yokoyama, A.; Yokozawa, T. *J. Am. Chem. Soc.* **2006**, *128*, 16012−16013.
(20) Wu, S.; Sun, Y.; Huang, L.; Wang, J.; Zhou, Y.; Geng, Y.; Wang, F. *Macromolecules* **2010**, *43*, 4438−4440.
(21) Trumbo, D. L.; Suzuki, T.; Harwood, H. J. *Polym. Bull.* **1981**, *4*, 677−682.
(22) Trumbo, D. L. *Polym. Bull.* **1991**, *26*, 271−275.
(23) Trumbo, D. L. *J. Polym. Sci., Part A: Polym. Chem.* **1988**, *26*, 3127−3130.
(24) Trumbo, D. L. *J. Polym. Sci., Part A: Polym. Chem.* **1991**, *29*, 603−605.
(25) Trumbo, D. L.; Lin, F. T.; M., l. F.; Harwood, H. D. *Polym. Bull.* **1992**, *28*, 87−94.
(26) Trumbo, D. L. *Polym. Bull.* **1992**, *28*, 159−165.
(27) Trumbo, D. L. *Polym. Bull.* **1992**, *28*, 309−313.
(28) Trumbo, D. L. *Polym. Bull.* **1994**, *33*, 75−82.
(29) Trumbo, D. L. *Polym. Bull.* **1995**, *35*, 719−726.
(30) Trumbo, D. L. *Polym. Bull.* **1992**, *30*, 2063−2065.
(31) Trumbo, D. L. *Polym. Bull.* **1996**, *36*, 463−469.
(32) Trumbo, D. L. *Polym. Bull.* **1996**, *36*, 181−188.
(33) Trumbo, D. L. *Polym. Bull.* **1996**, *37*, 457−462.
(34) Hohne, S.; Seifert, A.; Friedrich, M.; Holze, R.; Spange, S. *Macromol. Chem. Phys.* **2004**, *205*, 1667−1676.
(35) Hohne, S.; Spange, S.; Schrepp, W. *Polym. Bull.* **2001**, *47*, 31−37.
(36) Randazzo, M. E.; Topparel, L.; Fernandez, J. E. *Macromolecules* **1994**, *27*, 5102−5106.
(37) Omalley, R. M.; Randazzo, M. E.; Weinzierl, J. E.; Fernandez, J. E.; Nuwaysir, L. M.; Castoro, J. A.; Wilkins, C. L. *Macromolecules* **1994**, *27*, 5107−5113.
(38) Kagan, J.; Liu, H. Q. *Synth. Met.* **1996**, *82*, 75−81.
(39) Naka, K.; Imae, I.; Noma, N.; Shirota, Y. *Macromolecules* **1995**, *28*, 723−729.
(40) Musick, K. Y.; Hu, Q.-S.; Pu, L. *Macromolecules* **1998**, *31*, 2933−2942.
(41) Mori, H.; Takano, K.; Endo, T. *Macromolecules* **2009**, *42*, 7342−7352.
(42) Moad, G.; Chen, M.; Häussler, M.; Postma, A.; Rizzardo, E.; Thang, S. H. *Polym. Chem.* **2011**, *2*, 492−519.
(43) Chiefari, J.; Chong, Y. K.; Ercole, F.; Krstina, J.; Jeffery, J.; Le, T. P. T; Mayadunne, R. T. A.; Meijs, G. F.; Moad, C. L.; Moad, G.; Rizzardo, E.; Thang, S. H. *Macromolecules* **1998**, *31*, 5559−5562.
(44) Perrier, S.; Barner-Kowollik, C.; Quinn, J. F.; Vana, P.; Davis, T. P. *Macromolecules* **2002**, *35*, 8300−8306.

(45) Grebner, D.; Helbig, M.; Rentsch, S. *J. Phys. Chem.* **1995**, *99*, 16991−16998.
(46) Iijima, M.; Nagasaki, Y.; Okada, T.; Kato, M.; Kataoka, K. *Macromolecules* **1999**, *32*, 1140−1146.
(47) Ievins, A. D.; Wang, X.; Moughton, A. O.; Skey, J.; O'Reilly, R. K. *Macromolecules* **2008**, *41*, 2998−3006.
(48) Piogé, S.; Nesterenko, A.; Brotons, G.; Pascual, S.; Fontaine, L.; Gaillard, C.; Nicol, E. *Macromolecules* **2011**, *44*, 594−603.
(49) Bronich, T. K.; Keifer, P. A.; Shlyakhttenko, L. S.; Kabanov, A. V. *J. Am. Chem. Soc.* **2005**, *127*, 8236−8237.
(50) Huang, H.; Hoogenboom, R.; Leenen, M. A. M.; Guillet, P.; Jonas, A. M.; Schubert, U. S.; Gohy, J.-F. *J. Am. Chem. Soc.* **2006**, *128*, 3784−3788.
(51) Hussain, H.; Tan, B. H.; Gudipati, C. S.; He, C. B.; Liu, Y.; Davis, T. P. *Langmuir* **2009**, *25*, 5557−5564.
(52) Cui, Q.; Wu, F.; Wang, E. *J. Phys. Chem. B* **2011**, *115*, 5913−5922.
(53) Fu, H.-B.; Yao, J.-N. *J. Am. Chem. Soc.* **2001**, *123*, 1434−1439.
(54) Verma, A.; Srivastava, S.; Rotello, V. M. *Chem. Mater.* **2005**, *17*, 6317−6322.
(55) Szymanski, C.; Wu, C.; Hooper, J.; Salazar, M. A.; Perdomo, A.; Dukes, A.; McNeill, J. *J. Phys. Chem. B* **2005**, *109*, 8543−8546.

Macromolecules

Article

pubs.acs.org/Macromolecules

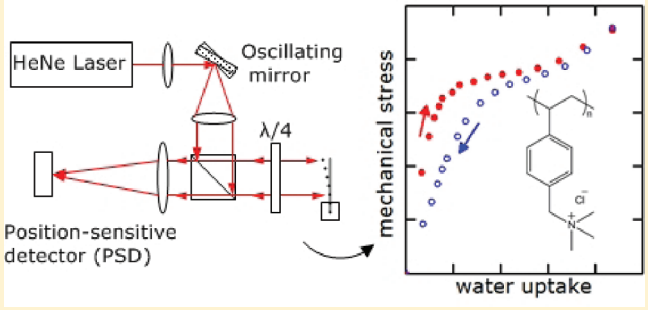
Absorption of Water and Mechanical Stress in Immobilized Poly(vinylbenzyltrialkylammonium chloride) Thin Films

James L. Langer,*[,†,‡] James Economy,[†] and David G. Cahill[†]

[†]Department of Materials Science and Engineering, The Center of Advanced Materials for the Purification of Water with Systems, University of Illinois at Urbana−Champaign, 1304 W Green St., Urbana, Illinois 61801, United States

[‡]Serionix Inc., 60 Hazelwood Dr., Champaign, Illinois 61820, United States

ABSTRACT: Absorption of water in cationic polyelectrolyte thin films is investigated by measuring mass uptake and mechanical stress using a quartz crystal microbalance and scanning optical laser apparatus, respectively. Thin layers of poly(vinylbenzyl chloride) and diazabicyclo[2.2.2]octane are spin-cast onto quartz crystal sensors or cover glasses. Films are subsequently cured and reacted by nucleophilic substitution with trimethylamine, triethylamine, tripropylamine, or tributylamine to give an immobilized poly(vinylbenzyltrialkylammonium chloride) matrix. Water absorption in these films depends strongly on both the amine modifier and counterion present in the matrix. Mass uptake ranges from 5.7% for a tributylamine-modified film in perchlorate form to 52% for a trimethylamine-modified film in fluoride form. This water uptake results in a maximum relative compressive biaxial stress of −33 and −113 MPa for these two films, respectively. Mass uptake and biaxial stress data give evidence of yielding upon hydration and dehydration. The yielding is attributed to elasto-viscoplastic deformation and influenced by a depression of the glass transition temperature via plasticizing. The Young's modulus (Y_f) of the unmodified film is measured from biaxial stress and ellipsometric thickness to be 3.9 GPa, consistent with structurally related polystyrene and slightly lower than Y_f = 5.0 GPa as measured acoustically. These results support the prevailing theory relating selectivity and diffusion in perchlorate-selective anion-exchange resins to hydrophilicity and water content and also suggest the mechanical properties of hydrophobic polycations may be effectively controlled through judicious selection of fixed ion and counterion.



INTRODUCTION

Polyelectrolyte films are used for a wide array of applications ranging from fuel cells[1−3] to electrodialysis membranes[4] to environmental sensors.[3,5,6] In bulk form, polyelectrolytes have also long found use as ion-exchange resins.[7,8] Entrained water plays a major role in dictating the physical and chemical properties of these materials.[7,8] For example, perchlorate selectivity and diffusion kinetics in anion exchange resins are strongly correlated with the relative hydrophilicity of their constitutive quaternary ammonium exchange sites.[9,10] Water absorption may lead to a reduction of the glass transition temperature (T_g),[11−13] which in turn affects the dynamics of water diffusion and stress formation and relaxation. Swelling forces due to water uptake and loss may be sufficient to cause delamination[14,15] or cracking,[16] while swelling gradients may lead to fracture in bulk polyelectrolytes such as ion-exchange beads.[7,8]

Many factors are known to affect the dry and swollen state properties of polyelectrolytes, including charge density, composition of the chemical backbone and side chains including ionogenic sites, cross-linking, and the nature of the counterions.[7,8,17,18] Understanding how polyelectrolytes of different composition interact with water is key to designing improved materials and processes. Outside of work on hydrophobically modified alkali-soluble emulsions (HASE), there is a dearth of information available regarding the interaction of hydrophobic polycations with water.[19−22]

In this study, polyelectrolyte films based on the quaternization of poly(vinylbenzyl chloride) (PVBCl) precursors were used to quantify swelling phenomena in hydrophobic polycations in response to changes in relative humidity (RH). Cationic quaternary ammonium *fixed ion* sites were affixed in the films by nucleophilic substitution with trimethylamine (TMA), triethylamine (TEA), tripropylamine (TPrA), and tributylamine (TBA). A scanning-laser apparatus was employed for measurement of mechanical stress in the films, while a quartz crystal microbalance (QCM) was used to measure mass uptake and mechanical loss. Composition of the films (i.e., cationic *fixed ions* and anionic counterions) was systematically varied, with each amine-modified matrix being studied in chloride (Cl^-) and perchlorate (ClO_4^-) counterion forms. The TMA-modified film was also studied in fluoride (F^-), iodide

Received: February 2, 2012
Revised: March 17, 2012
Published: March 28, 2012

 © 2012 American Chemical Society dx.doi.org/10.1021/ma300242j | *Macromolecules* 2012, 45, 3205−3212

(I^-), and nitrate (NO_3^-) forms, and the unmodified PVBCl film was examined as well.

We first present data for water uptake and mechanical stress for each of the films in chloride form as a function of RH. We then summarize the key findings regarding maximum stress, maximum water uptake, and the ratio of water molecules and ionogenic sites for every film composition. Next, we present the data as stress versus mass uptake in order to show the effect of water uptake on the mechanical properties of the films. We report a strong relationship between fixed ion and counterion composition and the resulting swelling and mechanical properties of the films. Hysteresis in the stress−moisture uptake curves is attributed to elasto-viscoplastic deformation. Lastly, we describe the interaction of water and films in greater detail. The specific volume of water in each film is determined from the ellipsometry and mass uptake measurements. At low water uptake, the specific volume of water (ν_w) is below its bulk value; at high water uptake ν_w increases to 90% of the bulk value. Water plasticizes the films, reducing their yield strengths and moduli as T_g approaches ambient temperature with higher water content. Water uptake as low as 5% provides sufficient plasiticizing to significantly reduce the film moduli and yield strength.

EXPERIMENTAL SECTION

Samples for measurements of water uptake were prepared by spin-coating. QCM sensors were first cleaned with acetone and 2-propanol, and a solution of PVBCl and diazabicyclo[2.2.2]octane (DABCO) in *N,N*-dimethylformamide (DMF) was subsequently filtered through a 0.2 μm polytetrafluoroethylene (PTFE) membrane and spin-coated (500 rpm s^{-1} ramp, 2000 rpm, 30 s) onto the surface.[23] The samples were cured in a 110 °C oven in air for a minimum of 48 h. The resulting immobilized PVBCl gel coatings were then reacted by nucleophilic substitution with tertiary amines including TMA, TEA, TPrA, and TBA under conditions described in Table 1 to give poly(vinylbenzyltrialkylammonium chloride) (PVBTC) films. After reaction, samples were rinsed using a combination of dioxane, ethanol, and DIW. See Scheme 1 for an overview of this synthetic process. Coatings thus prepared possessed dry thicknesses (h_0) of approximately 300−400 nm as measured by spectroscopic ellipsometry (Woolam VASE). Confinement effects are negligible at thickness >150 nm,[24−26] and therefore variations in thickness are not expected to affect the physical properties of these films.

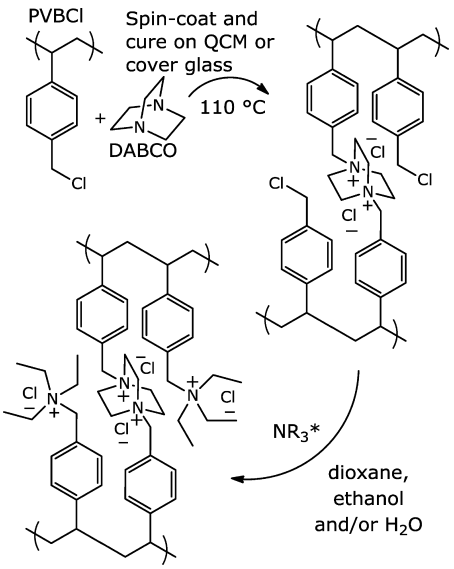
Table 1. Reaction Conditions for Quaternization of PVBCl Films

amine	solvent	temp (°C)	time (h)	Cl^- (mmol g^{-1})	% conv
TMA	DIW	20	3	2.7	43
TEA	ethanol, DIW	20	20	2.2	34
TPrA	dioxane, DIW	100	18	2.4	46
TBA	dioxane, DIW	100	24	2.1	44

Bulk PVBTC powders were prepared according to the same synthetic scheme as the QCM samples, using crushed, cured PVBCl−DABCO as a precursor. Inorganic chloride content of each material as determined by potentiometric titration with standard silver nitrate[27] is listed in Table 1. Additionally, the estimated yields are based on conversion of chloromethyl to quaternary ammonium groups. All four modifiers give roughly the same level of conversion (i.e., roughly 40% of available vinylbenzyl chloride groups react to form quaternary ammonium salts) under these conditions.

We prepared cantilevers for measurements of stress induced by absorption using a similar spin-coating procedure described for the QCMs. Microscope cover glasses (Gold Seal #1, 150 μm thick) were coated with 20 nm Cr and 50 nm Au on one side by electron beam evaporation to give a reflective surface. The cover glasses were then treated with a solution of H_2SO_4 and an ammonium peroxydisulfate oxidizer (NoChromix) for 10 min, rinsed with deionized water, air-dried, and functionalized by treatment with a 2% aminopropyltriethoxysilane (APTES) solution in $MgSO_4$-dried toluene for 60 min. APTES-coated samples were rinsed with acetone, placed in a sonication bath in acetone for 10 min, and cured in a 110 °C oven in air for 2 h. PVBCl and DABCO were spin-coated on the side opposite of the reflective coating. After the quaternization reaction, cantilevers approximately 25 mm × 1.5 mm were then cut from the cover glasses using a diamond-tipped pen. Thus, these samples meet the limitation of Stoney's equation of length being much greater than width and width much greater than thickness.[28,29]

Scheme 1. Synthesis of PVBTC-Coated QCMs and Cover Glass[a]



[a]Triethylamine is shown in this example (indicated by an asterisk).

Cantilevers and QCMs were metathesized to and from the virgin chloride form and other counterion forms by soaking in >0.5 M solutions of sodium chloride, fluoride, iodide, nitrate, or perchlorate.[27] Naming convention for all of the PVBTC films goes as "tertiary amine precursor" ("counterion"). For example, the trimethylamine-modified film in chloride form is referred to as TMA(Cl^-).

As described previously,[30,31] we used a 5 MHz QCM in combination with a frequency (f) counter (Stanford Research Systems QCM100 or QCM200 and BK Precision, respectively). Where the Sauerbrey equation is valid,[24,32] a frequency shift of +1 Hz corresponds to a mass change of −18 ng cm^{-2}, or ∼0.05% of the total film mass. Practically, f drifted on the order of 5−8 Hz over the course of a 36 h experiment. Drift is attributed to instability in the BK Precision timebase which is rated at ±1 ppm ± 1 count.

Moisture uptake generates a compressive mechanical stress in the PVBTC films; in conventional ion-exchange materials gradients in hygroscopic or swelling stress (σ_H) are sufficient to cause resin fracture.[8] For an isotropic film constrained to a flat, inert substrate, σ_H is given by eq 1

$$\sigma_H = \frac{Y_f}{3(1-\gamma_f)}\frac{\Delta V_w}{V_0} \quad (1)$$

where V_0 is the dry volume of the film and ΔV_w is the change in volume due to water uptake, and Y_f and γ_f are the Young's modulus and Poisson ratio of the film, respectively.[33−35] Note $Y_f/(1-\gamma_f)$ is the biaxial modulus of the film, and $\Delta V_w/3V_0$ is equivalent to strain (ε) in

the present geometry.[34,35] Mass fractional water uptake (ϕ) is defined in eq 2

$$\phi = \frac{\Delta m_w}{m_d} \tag{2}$$

where Δm_w is change in film mass due to absorbed water and m_d is the dry mass of the film. The the specific volume of water $\nu_s = \Delta V_w/\Delta m_w$, and therefore substituting the dry film density (ρ), ϕ, and ν_s into eq 1 gives eq 3.

$$\sigma_H = \frac{Y_f \phi \nu_s \rho}{3(1-\gamma_f)} \tag{3}$$

It is important to note neither Y_f nor γ_f is constant during a given experiment due to their dependence on ϕ: as ϕ increases, Y_f is generally expected to drop while γ_f should converge to 0.5 as the film approaches a rubbery state.

Solvent casting is known to leave films in a state of tensile stress due to deviation of the *current state* from the *stress-free state* the film would otherwise adopt if not constrained to a substrate.[35,36] Depending on the T_g, annealing may reduce or eliminate the initial σ_H but introduces thermal stress upon cooling due to mismatch in the coefficient of thermal expansion between the film and substrate.[35] Considering the complicated stress history in the PVBTC films, they may be in tension or compression in their dry state. While we were unable to measure the absolute biaxial stress state of these films because of uncertainty in the native curvature of the substrate, changes in stress were determined by monitoring changes in curvature of thin glass cantilevers.

Samples were mounted in a controlled-atmosphere cell using a PTFE clamp, and the curvature of the cantilevers was measured using a scanning-laser optical apparatus as shown in Figure 1. This apparatus is nearly identical to one described previously,[31] except that any signal due to initial curvature in the cantilevers was nulled solely by adjusting the position of lens f'. Changes in glass–film interfacial stress, Δg, are derived from the rms voltage output ΔV from the lock-in amplifier using eq 4

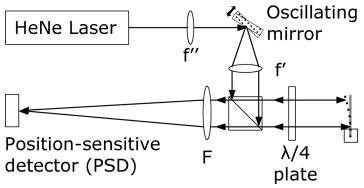


Figure 1. Diagram of the experimental setup used for measuring changes in biaxial stress in PVBTC films; stress is proportional to curvature, which in turn is proportional to the voltage output of the position sensitive detector (PSD) as monitored by a lock-in amplifier. Focal lengths of the lenses are 150 mm (f''), 50 mm (f'), and 500 mm (F). The cantilever at right is a cover glass coated with reflective Au/Cr on its left side and PVBTC on the right.

$$\Delta g = \frac{Y_s d^2}{6(1-\gamma_s)} \frac{\sqrt{2}\,\Delta V}{wF\beta} \tag{4}$$

where Y_s, γ_s, and d are the Young's modulus (75.9 GPa), Poisson ratio (0.22), and thickness (150 μm)of the glass cantilever substrate, respectively, β is the calibration constant of the PSD (2000 V m^{-1}), F is the primary lens focal length (m), and w is the laser scanning width on the cantilever. This expression is derived by consolidating Stoney's equation[30] and our measurement of curvature and assumes (i) PVBTC film thickness (h) is much less than d and (ii) the coating is in a uniform state of biaxial stress, as shear stress is only important within a few film widths from the edges.[28,35] Stress due to the glass–metal interface is assumed to be independent of changes in RH. Therefore, any changes in curvature are attributed solely to stress at the glass–PVBTC film interface.

Interfacial stress is equivalent to the in-plane biaxial stress integrated over h. We used profilometry (Sloan Dektak) and spectroscopic ellipsometry to measure h for the cantilevers and QCM sensors, respectively, under ambient conditions (40% RH). Since the ellipsometer was not attached to a RH-control apparatus, dry film thickness h_0 was measured using a cryostat sample holder at 0% RH (pressure below 10^{-5} Torr). Dividing Δg by h gives $\Delta\sigma_v$, the change in true biaxial stress. Since we lack h data for all but dry and 40% RH conditions, we report the change in engineering biaxial stress ($\Delta\sigma_e$) or equivalently $\Delta g/h_0$. Tensile stress is defined as positive. In light of the combined uncertainties of h, Y_s, γ_s, d, and w, accuracy of $\Delta\sigma_e$ is estimated at 10%.

Relative humidity of the sample cells containing both QCM and cantilever was controlled using three mass flow controllers in parallel delivering 2 L min^{-1} of nitrogen. Liquid nitrogen boil-off was passed through a 2 L column filled with desiccant prior to the flow controllers. One 0–2 L min^{-1} controller flowed directly to the sample cell while two controllers (one 0–2 L min^{-1} and a 0–0.2 L min^{-1}) flowed in parallel through water sparging columns to deliver nearly water-saturated nitrogen to the cell. Since controller accuracy is a percentage of full scale flow range, the controller with lower flow rate was used to improve RH accuracy and precision at levels <10%. Ambient temperature in the cell was measured with a thermistor. Dew point/frost point of the sample cell effluent was measured with a chilled-mirror hygrometer (CMH, Edgetech DewMaster) at an accuracy of ±0.2 °C. RH was calculated from the actual and saturated vapor pressure of water. Dynamic range of the CMH frost point was extended to −30 °C using an external thermoelectric chiller. This lower limit corresponds to a partial pressure of water of 38 Pa or approximately 1.5–2% RH at ambient laboratory temperature. A minimum value of 0.43% RH was measured independently using a capacitive probe (Picotech RH-02). While the dry nitrogen line is expected to be lower yet, it is possible off-gassing from surfaces such as Tygon tubing dictates the practical lower limit.[37] The dead volume of the cantilever sample cell and associated tubing was ~0.4 L, and the turnover rate of the system was 5 min^{-1}; the dead volume of the QCM flow cell in series with the cantilever cell was <20 mL, and thus the turnover rate of this cell was >100 min^{-1}.

Each experiment was performed by cycling RH in discrete steps from an initial high state (RH > 90%) down to low humidity and back up. The time interval (t_i) between changes in RH for the experiments was 60 min, with a few exceptions. In the case of three of the samples with the lowest ϕ_{max} (i.e., unmodified, TPrA(ClO_4^-), and TBA(Cl^-)) the previously mentioned QCM f drift of ±5–8 Hz led to an error of 10–15% during the 36 h experiment. For each of these films data from shorter intervals (t_i = 2–16 min) are reported in place of the 60 min intervals.

RESULTS AND DISCUSSION

The absolute value of the change in biaxial stress ($|\Delta\sigma_e|$) and ϕ in PVBTC films, relative to the dry state, are shown in Figure 2. The changes in stress are actually compressive. Each of the films show a similar trend of increasing ϕ over the range of RH, but their response differs widely in magnitude. Similarly, the films all display increasing $|\Delta\sigma_e|$ accompanying water uptake. Hysteresis observed in $|\Delta\sigma_e|$ is much larger than the hysteresis in the mass uptake (Figure 2) and is not entirely a kinetic effect as will be shown later. More likely, hysteresis is a result of elasto-viscoplastic deformation upon dehydration and hydration.[31,35,36] Notably, elastic behavior is suggested in the unmodified film by its lack of hysteresis in $|\Delta\sigma_e|$.

Figure 3a summarizes the effect of fixed ion composition on $|\Delta\sigma_e|_{max}$ and ϕ_{max}. Data are plotted against the log octanol–water partition coefficients (log K_{OW}) for analogous benzyltrialkylammonium chloride salts. KOWWIN[38] was used to calculate log K_{OW} values based on an atom/fragment

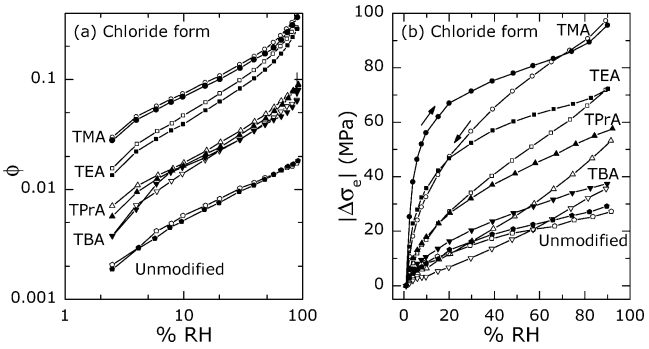


Figure 2. (a) Mass uptake (ϕ) and (b) and absolute changes in biaxial stress ($|\Delta\sigma_e|$) in PVBTC films in chloride form as a result of changes in relative humidity (RH). Filled and open symbols represent increasing and decreasing RH, respectively. Little hysteresis is observed in the mass uptake data. However, hysteresis is evident in the stress changes for all of the materials except the unmodified film. We attribute the hysteresis to elasto-viscoplastic deformation.[35,36]

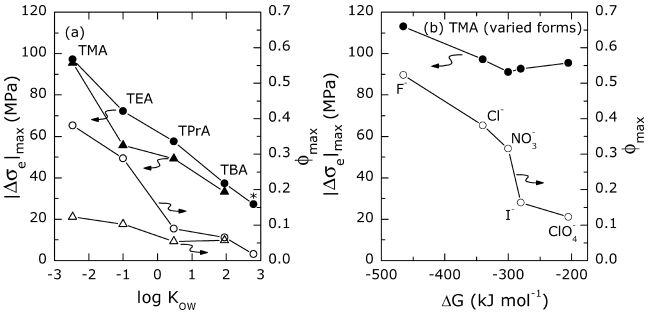


Figure 3. Maximum water uptake (ϕ_{max}) and absolute change in biaxial stress ($|\Delta\sigma_e|_{max}$) for PVBTC films: (a) each modified material in chloride (●, ○) and perchlorate (▲, △) form, where K_{OW} is the estimated octanol–water partition coefficient for the benzyltrialkylammonium chloride salt derived from each tertiary amine precursor (∗ refers to unmodified PVBCl) and (b) TMA-modified material in various forms plotted against ΔG, the free energy of hydration of the counterion derived from lattice energies. Fixed ion and counterion species both influence swelling and mechanical stress in PVBTC films.

contribution method;[39] the counterion is not considered in this calculation, but the general trend for relative hydrophilicity of PVBTC films should be reasonably accurate. Values for $|\Delta\sigma_e|_{max}$ range from 33 MPa for TBA(ClO_4^-) to 97 MPa for the TMA(Cl^-). Water uptake ranges from ϕ_{max} = 0.057 to 0.38 for the same materials, respectively. Despite having the same polymer backbone, the most and least hydrophobic materials span nearly an order of magnitude range in ϕ_{max}. By comparison, the unmodified PVBCl film has a $|\Delta\sigma_e|_{max}$ of 27 MPa and ϕ_{max} of 0.018. The film consisting of the most hydrophilic fixed ion and counterion (TMA(Cl^-)) exhibits the highest ϕ_{max}. As will be discussed further, the films appear to yield upon hydration in the range of ϕ = 0.05–0.1.

Systematic variations in the counterion form and their effect on $|\Delta\sigma_e|_{max}$ and ϕ_{max} are summarized in Figure 3b. ΔG is the free energy of hydration of each counterion derived from lattice energies;[40] ClO_4^- (ΔG = −205 kJ mol^{-1}) and F^- (ΔG = −465 kJ mol^{-1}) are the least and most hydrophilic counterions used in this study. Counterion form strongly affects the swelling of the films, with ϕ_{max} ranging from 0.12 to 0.52 for perchlorate and fluoride forms, respectively. This trend is consistent with counterion hydrophilicity as quantified by ΔG. Maximum changes in stress range from a plateau near 95 MPa for iodide, nitrate, and perchlorate forms to 113 MPa for the fluoride form. Thus, this 4-fold increase in ϕ_{max} results in an increase in $|\Delta\sigma_e|_{max}$ of only 20%. Three possible causes for this behavior include variation in ν_s, counterion-induced changes in T_g,[17] and incomplete drying of the more hydrophilic films.[41] See Figure 3c and discussion below for further description. This last possibility reemphasizes the general point that we are reporting changes in stress and water content since neither the absolute zero of stress (σ_0) nor m_d is known with certainty.

Maximum water uptake per fixed ion group (n_w/n_{ion}) is shown in Figure 4. These data again reinforce the extent to

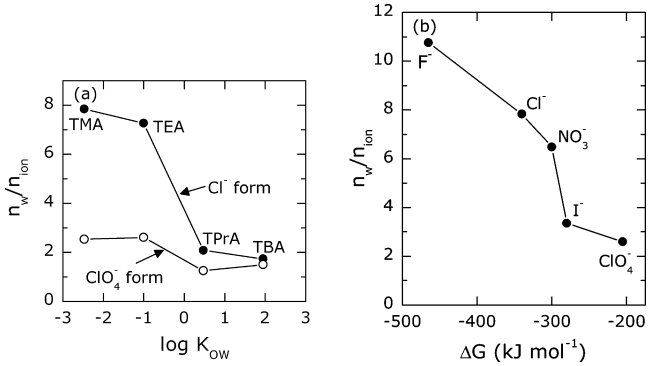


Figure 4. Maximum number of absorbed water molecules per fixed ion (n_w/n_{ion}): (a) for varied fixed ion composition plotted against log K_{OW} and (b) with varied counterion form plotted against ΔG. Maximal water uptake is consistent with relative hydrophilicity of both fixed ion and counterion.

which swelling is dictated by the specific composition of both the fixed ions and counterions in PVBTC matrices. The ratio in TMA(Cl^-) of approximately n_w/n_{ion} = 8 is slightly lower than a previous report of n_w/n_{ion} = 11 for a TMA-based anion exchange resin in chloride form.[41] Whereas the previous study involved absorption from liquid water, our system does not reach 100% RH and is expected to have lower n_w/n_{ion}. In the case of films in the Cl^- form, n_w/n_{ion} varies by a factor of 4 between the TBA- and TMA-modified films. Similarly, n_w/n_{ion} increases by roughly a factor of 4 between the perchlorate and fluoride forms of a TMA-modifed film.

Data for $|\Delta\sigma_e|$ plotted against ϕ in PVBTC films—both unmodified and amine-modified—are shown in Figure 5a. The modified films each display $|\Delta\sigma_e|$ quite close together over the entire range of ϕ, while the unmodified film exhibits roughly 50% greater stress for a given value of ϕ. Below ϕ = 0.05, $|\Delta\sigma_e|$ is roughly linear in response to ϕ as would be expected from eq 3, but deviation is observed for each of the materials absorbing higher levels of water. We attribute this deviation to the effects of reduction in Y_f and yield strength (σ_y) due to plasticizing by water. Polystyrene, by comparison, does not yield but has an ultimate strength (σ_u) of 38–55 MPa[11] and elongation-to-failure at 1–2.5%. Since the unmodified film exhibits $|\Delta\sigma_e|_{max}$ of only 27 MPa it is reasonable to expect elastic behavior. The TMA- and TEA-modified films experience the greatest deviation from linear response because they take up the most water. Figure 5b shows a similar result for each of the materials in perchlorate form. In both chloride and perchlorate form the TBA-modified film exhibits slightly lower $|\Delta\sigma_e|$ than the other films. TBA-modified films also exhibited the lowest values of ν_s, as shown below, which may partly contribute to the lower $|\Delta\sigma_e|$.

dx.doi.org/10.1021/ma300242j | Macromolecules 2012, 45, 3205–3212

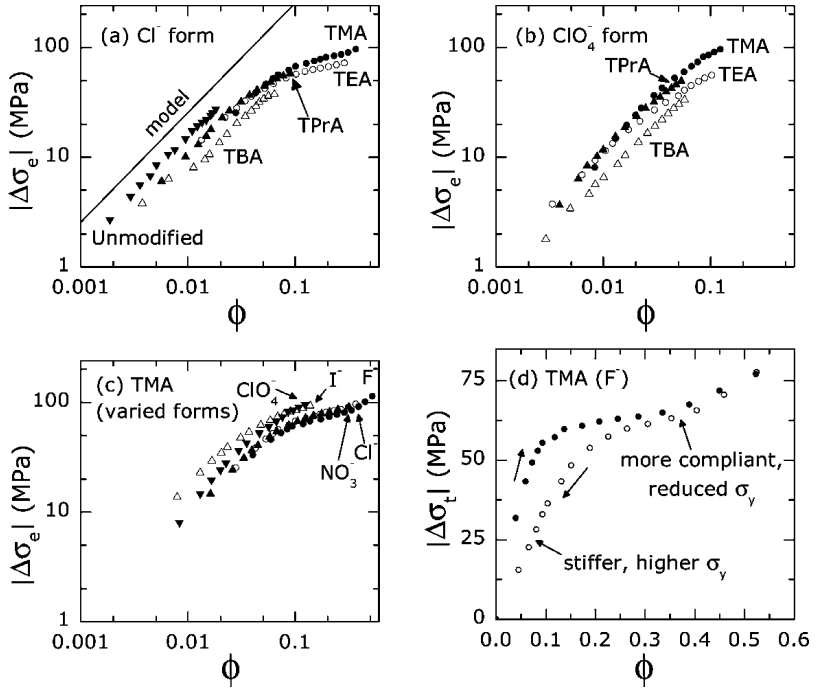


Figure 5. Absolute change in biaxial stress ($|\Delta\sigma_e|$) plotted against mass uptake (ϕ) for PVBTC films: (a) each modified material in chloride form; (b) each modified material in perchlorate form; (c) TMA-modified material in various forms; (d) absolute change in true biaxial stress ($|\Delta\sigma_t|$) of the TMA-modified film in fluoride form. The line in (a) refers to the response expected for a specific volume of water ν_s = 1 cm^3 g^{-1} and Young's modulus = 5.0 GPa as calculated from the longitudinal speed of sound in the unmodified film. Depressed ν_s and T_g both contribute to the lower-than-expected response in each film. Yielding is observed in (a) ϕ = 0.05−0.1. In (c) there is a pronounced effect of the counterion on the tendency to yield in this same range. $|\Delta\sigma_t|$ is plotted in (d) in place of $|\Delta\sigma_e|$ on a linear scale in order to more clearly show the magnitude of stress response to increasing and decreasing ϕ. Based on the stress history of the films, the absolute zero of stress is not obvious and may in fact be near the plateau at $|\Delta\sigma_t|$ = 60−65 MPa.

Additionally, the line in Figure 5a refers to the expected response on the basis of the following assumptions: (i) ν_s = 1 cm^3 g^{-1}, the bulk value; (ii) γ_f = 0.35, that of polystyrene;[42] (iii) and Y_f = 5.0 GPa, measured acoustically. The elastic moduli of the unmodified film was calculated from the longitudinal speed of sound (v_l = 2.63 nm ps^{-1}) determined using picosecond acoustics.[43] The elastic constant C_{11} and Y_f are given[44] by eqs 5 and 6:

$$C_{11} = \rho_f {v_l}^2 \tag{5}$$

$$Y_f = C_{11}\frac{(1 - 2\gamma_f)(1 + \gamma_f)}{1 - \gamma_f} \tag{6}$$

Again, assuming γ_f = 0.35, Y_f is approximately equal to 0.62C_{11} or 5.0 GPa. The deviation from the expected $|\Delta\sigma_e|$ in the unmodified film is relatively small, due in part to a depressed value of ν_s. According to eq 1, the $|\Delta\sigma_e|$ and change in thickness measured from 0% to 40% RH give Y_f = 3.9 GPa for the unmodified film. This value is close to the reported Y = 3.3−3.5 GPa for structurally related polystyrene.[26,42] Our assumption regarding γ_f may also contribute to the deviation because the calculation of Y_f from C_{11} depends strongly on γ_f (e.g., a 1% error in γ_f propagates into a 1.5% error in Y_f).

Counterions affect the stress response in TMA-modified PVBTC films, as shown in Figure 5c. In particular, the films containing the two most hydrophobic ions (i.e., I^- and ClO_4^-) exhibit nearly 50% greater stress at ϕ = 0.12 than the other forms. As mentioned previously, several factors such as depressed ν_s, dependence of T_g on ionic form,[17] and incomplete dehydration—and thus uncertainty in m_d and ϕ = 0—may affect the films' response to water uptake. Most likely, a combination of these factors is responsible. While the exact cause is unknown, it is clear that films containing more hydrophic counterions show a different mechanical response to water uptake.

Absolute value of the change in the true biaxial stress ($|\Delta\sigma_t|$)—calculated assuming ν_s = 1 cm^3 g^{-1}—is plotted against ϕ on a linear scale for TMA(F^-) in Figure 5d. The true change in biaxial stress is lower than the engineering stress shown in Figure 5c due to the large change in film thickness. At low ϕ the films sustain a greater amount of stress for a given change in ϕ. The response is not strictly elastic, as even at this low ϕ stress relaxation is observed similar to that shown in Figure 6b. Near ϕ = 0.1 the film appears to yield, owing to a decline in σ_y. From ϕ = 0.15−0.3 the films continue to deform elasto-viscoplastically, with the upturn in stress near ϕ = 0.35 consistent with stiffening seen in cross-linked materials at high extension.[11] For a linear plasticized polymer the stress would be expected to cease at a sufficiently high ϕ, but we do not expect to observe complete relaxation in PVBTC matrices as they are cross-linked.

Since the absolute zero of stress is unknown, our interpretation of the data is sensitive to the assignment of σ_0 = 0. For example, if the real zero of stress is near $|\Delta\sigma_t|$ = 60 MPa for TMA(F^-): (i) the plateau in that same region would correspond to a low modulus instead of plastic deformation, and (ii) plastic deformation would be occurring during hydration and dehydration at low ϕ. Future measurement of the absolute initial stress state—and thus determination of the real zero of stress—would be helpful for interpreting the data.

dx.doi.org/10.1021/ma300242j | Macromolecules 2012, 45, 3205−3212

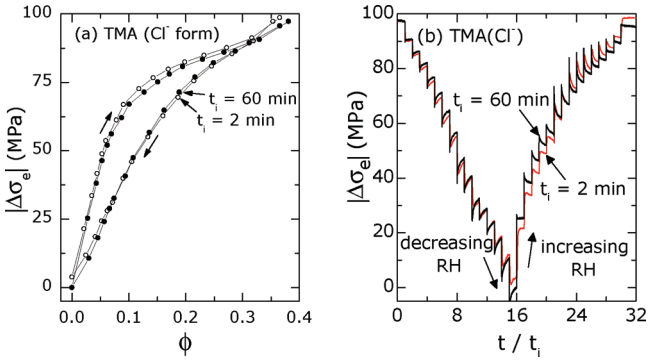


Figure 6. (a) Change in biaxial stress ($|\Delta\sigma_e|$) plotted against mass uptake (ϕ) in TMA-based PVBTC films in chloride form as a result of changes in RH. (b) $|\Delta\sigma_e|$ vs t/t_i where t_i is the time interval between RH steps. Hysteresis is evident at lower humidity levels, and is not simply a result of slow relaxation kinetics, as seen by comparing data for 2 and 60 min intervals. The hysteresis in stress is attributed to elasto-viscoplastic deformation in the film. Stress relaxation appears similar irrespective of the observation time, which suggests a log-normal distribution of viscoelastic or elasto-viscoplastic relaxation times.[47,48]

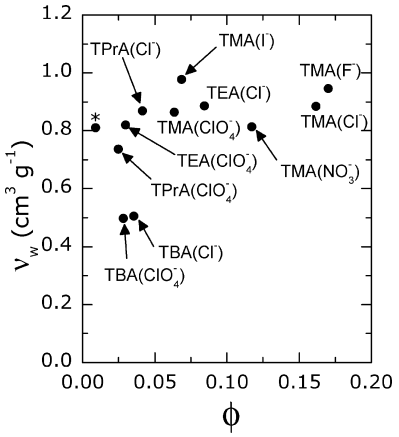


Figure 7. Specific volume of water (ν_s) in films calculated from change in thickness and mass uptake at 0 and 40% RH (or 27% for TMA(F-) and TEA(ClO_4^-)). ∗ refers to the unmodified film. With the exception of a couple of outliers, ν_s appears to trend from 0.8 to 0.9 cm^3 g^{-1} over the region studied; at higher ϕ, ν_s is expected to approach 1 cm^3 g^{-1}. Lower values of ν_s at lower ϕ are attributed to free volume in the matrix. The TBA-modified material exhibits the lowest ν_s, which may also be due to the extreme hydrophobicity of the fixed ions.

As mentioned previously, hysteresis is not solely a kinetic effect. Data collected using 2 and 60 min intervals are similar as shown in Figure 6a. More likely, hysteresis is a result of elasto-viscoplastic deformation.[31,36] As ϕ increases, σ_y is expected to drop along with T_g.[45] At sufficiently high ϕ, σ will exceed σ_y and yield. Conversely, the film undergoes the opposite process upon dehydration, consistent with behavior observed in previous studies.[36,46] Stress formation and relaxation over time (see Figure 6b) are consistent with prototypical elasto-viscoplastic deformation as described by Lei et al.[36] Moreover, relaxation kinetics appear similar independent of the observation time, suggesting a log-normal distribution of viscoelastic or elasto-viscoplastic relaxation times.[47,48] Khare[48] attributed a wide distribution of relaxation times in a cross-linked polyamide network to polydispersity in linear chain segments; in this context each segment of a specific length corresponds to a specific relaxation time. Elasto-viscoplastic deformation is reported elsewhere[35,36,46] for thin polymer films; hysteresis in swelling of polyelectrolyte multilayers has been observed previously as well.[49] Secondary rearrangements associated with the quaternary ammonium side groups may also contribute to hysteresis, especially in films containing bulky TPrA or TBA side groups. That the unmodified film exhibits almost no stress hysteresis supports this theory. However, we cannot distinguish the effect of side group rearrangements from ϕ-induced plastic deformation because the unmodified film also has the lowest ϕ_{max} and $|\Delta\sigma_e|_{max}$ and may behave elastically simply because of the low ε.

According to eq 3, depressed values of ν_s may lead to σ_H lower than expected. Indeed, Zhang et al.[31] report ν_s = 0.28 cm^3 g^{-1} for an aromatic polyamide and attribute the low value—compare to bulk ν_s = 1 cm^3 g^{-1}—to free volume. We calculated ν_s in PVBTC films by comparing h and m as measured at 0% and 40% RH. Figure 7 shows ν_s plotted against ϕ. Depressed values of ν_s at lower ϕ are attributed to free volume in the matrix; the exceptionally low ν_s observed in TBA films may be related to their extreme hydrophobicity. The data reveal depressed ν_s partly explains the deviation from predicted stress observed in Figure 5a. At a sufficiently high ϕ, ν_s must converge to its bulk value. However, over the range of observed ϕ there appears to be only a gradual increase to ν_s = 0.9 cm^3 g^{-1}.

In addition to the effect on σ_y, water uptake is expected to reduce T_g by acting as a plasticizer. Differential scanning calorimetry (DSC) showed a T_g onset of 68 °C for virgin PVBCl, while the cross-linked modified and unmodified PVBTC powders each displayed broader thermal transitions in the range of 85−105 °C. The Fox equation[11] is often used to describe the T_g of a mixture, with

$$\frac{1}{T_g} = \frac{w_1}{T_{g,1}} + \frac{w_2}{T_{g,2}} \tag{7}$$

where w_1 and w_2 are the mass fractions and $T_{g,1}$ and $T_{g,2}$ are the glass transition temperatures of the polymer and plasticizing agent, respectively. Water has a T_g of −137 °C;[50] therefore, T_g of a swollen film is expected to approach ambient temperature near ϕ = 0.1 on the basis of eq 7 and our assumption of $T_{g,1}$ and $T_{g,2}$. The equation applies generally across a wide variety of systems, although complications may arise such as in the case of phase separation[51] or specific interactions between plasticizer and polyelectrolytes.[12]

Measurements of shear loss compliance (J'') provide further evidence of changes in the mechanical properties of PVBTC films with water uptake. Figure 8 shows J'' for a TMA(Cl^-) film measured using the electromechanical resistance of the QCM and calculated from eq 8

$$J'' = \frac{3\pi Z \Delta R}{2L\omega^4\rho^2 h^3} \tag{8}$$

where Z, ΔR, L, and ω are the acoustic impedance (8.84 × 10^6 Pa s m^{-1}), change in electrical impedance, motional inductance (0.0402 H), and angular resonant frequency (i.e., $\omega = 2\pi f$) of the uncoated QCM sensor, respectively, and ρ and h are the film density and thickness.[32] Uncertainty in J'' is approximately 0.5 × 10^{-8} Pa^{-1}. The film becomes lossier at higher ϕ, ranging from 1 × 10^{-8} to 3 × 10^{-8} Pa^{-1} at dry and high humidity conditions, respectively. Smith[32,52] describes similar values for Decrolon vinyl toluene alkyd absorbing toluene vapor in a

dx.doi.org/10.1021/ma300242j | Macromolecules 2012, 45, 3205−3212

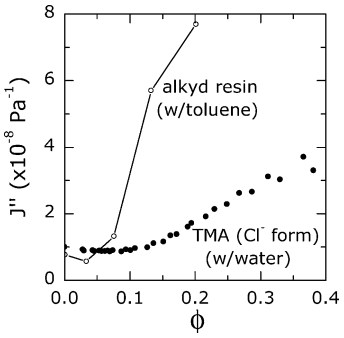


Figure 8. Shear loss compliance (J'') as a function of mass uptake (ϕ) for TMA(Cl^-) film. J'' is measured from the QCM sensor resistance in the TMA(Cl^-) film as a result of changes in RH. Data from Smith[52] for a Decrolon vinyl toluene alkyd resin absorbing toluene are included for comparison. The upturn in J'' near ϕ = 0.05−0.1 is attributed to plasticizing due to absorption of water or toluene. Greater mechanical loss at higher ϕ is consistent with a reduction in film modulus due to a depression of T_g.

nitrogen environment. As with Smith, we attribute the increase in J'' to the plasticizing effect of absorbed water.[12] Notably, plasticized polymers are known to exhibit relatively broad glass transitions;[51] the change in mechanical response of PVBTC matrices over the range of ϕ = 0.05−0.15 may have its origin in a broad glass transition region.

Our findings have important implications for the design of anion-exchange materials. Previous research has shown that ion-exchange resins with large and hydrophobic exchange sites, such as quaternary ammonium salts derived from TBA or trihexylamine (THxA), have exceptionally high selectivity for perchlorate and pertechnetate.[9,10,53] The high selectivity of these materials is attributed to strong affinity between hydrophobic matrices and ions with large ionic radii and low absolute free energies of hydration relative to other common anions.[9,40] Increasing resin hydrophobicity also leads to a substantial reduction of intraparticle diffusion kinetics and equilibration. Since the data for ϕ_{max} indicate strong dependence on fixed ion and counterion composition, it is reasonable to suggest the origins of selectivity lie in the preference for perchlorate *relative to other anions* to accept a partially dehydrated state. Additionally, since ion-exchange kinetics are known to depend strongly on resin water content,[8,7] the slow exchange kinetics in TBA- or THxA-modified materials are consistent with our observation of small ϕ_{max} for these materials.

CONCLUSIONS

Immobilized PVBCl thin films cast on QCMs and cover glass allow direct measurement of mass uptake and biaxial stress due to water absorption in polyelectrolytes. Altering counterion and fixed ion chemistry leads to widely different water uptake, with maximum mass uptake ranging from 5.7 to 52% and maximum stress ranging from 33 to 113 MPa. Elasto-viscoplastic deformation leads to hysteresis in stress upon cycling RH, with a noticeable drop in σ_y at ϕ > 0.05−0.1 attributed to the plasticizing effect of absorbed water. Thus, because of widely varying ϕ, films also varied widely in their stress response to increasing ϕ at high RH. Moreover, as diffusion rates in the materials are expected to be governed largely by water content,[8] the wide range of water uptake is consistent with previous research that showed a wide range of exchange kinetics of ion-exchange resins based on similar chemistries.[9,10] These results ultimately describe how, through judicious selection of fixed and counterion species, hydrophobic polycation films may be prepared with predictable and tunable mechanical response to water vapor.

AUTHOR INFORMATION

Corresponding Author

*E-mail: jlanger2@illinois.edu.

Notes

The authors declare no competing financial interest.

ACKNOWLEDGMENTS

This material is based upon work supported by the Center of Advanced Materials for the Purification of Water with Systems, a National Science Foundation Science and Technology Center, under Award No. CTS-0120978, and was carried out in part in the Frederick Seitz Materials Research Laboratory Central Facilities, University of Illinois. The authors thank Dr. Xijing Zhang for her assistance with the experimental setup.

NOMENCLATURE

C_{11}	elastic constant (GPa)
d	thickness of glass cantilever substrate (μm)
f	resonant frequency of the coated QCM sensor (Hz)
f_0	resonant frequency of the uncoated QCM sensor (Hz)
F	primary lens focal length (cm)
Δg	change in stress at glass-film interface (N m^{-1})
ΔG	free energy of hydration of counterion (kJ mol^{-1})
h	thickness of the film (nm)
h_0	dry thickness of the film (nm)
J''	shear loss compliance of the film (Pa^{-1})
K_{OW}	octanol−water partition coefficient
L	motional inductance of the QCM sensor (H)
Δm_w	change in areal mass due to absorbed water (μg cm^{-2})
m_d	areal mass of dry film (μg cm^{-2})
n_{ion}	number of ionogenic sites in film
n_w	number of absorbed water molecules
ΔR	change in electrical impedance of the QCM sensor (Ω)
T_g	glass transition temperature (°C)
ΔV	rms voltage from the lock-in amplifier (V)
v_l	longitudinal speed of sound in the film (nm ps^{-1})
V_f	film volume (cm^3)
V_0	dry film volume (cm^3)
ΔV_w	change in film volume due to absorbed water (cm^3)
w	scanning width of the laser beam (m)
Y_f	Young's modulus of the film (GPa)
Y_s	Young's modulus of the glass cantilever substrate (GPa)
Z	acoustic impedance of the QCM sensor (Pa s m^{-1})

Greek Letters

β	calibration constant of the position-sensitive detector (V m^{-1})
ε	strain
γ_f	Poisson ratio of the film
γ_s	Poisson ratio of the glass cantilever substrate
ν_s	specific volume of absorbed water (cm^3 g^{-1})
ϕ	mass fractional water uptake
ρ	density of the polyelectrolyte film (g cm^{-3})
$\Delta\sigma$	change in biaxial stress (MPa)
σ_e	engineering stress (MPa)
σ_H	hygroscopic stress (MPa)
σ_t	true stress (MPa)

σ_u ultimate strength (MPa)
σ_y yield strength (MPa)
ω angular frequency of the coated QCM sensor (Hz)

REFERENCES

(1) Jiang, S. P.; Liu, Z.; Tian, Z. Q. *Adv. Mater.* **2006**, *18*, 1068−1072.
(2) Smitha, B.; Sridhar, S.; Khan, A. A. *Macromolecules* **2004**, *37*, 2233−2239.
(3) Lutkenhaus, J. L.; Hammond, P. T. *Soft Matter* **2007**, *3*, 804−816.
(4) Sata, T.; Yang, W. *J. Membr. Sci.* **2002**, *206*, 31−60.
(5) Xu, Q.; An, L.; Yu, M.; Wang, S. *Macromol. Rapid Commun.* **2008**, *29*, 390−395.
(6) Loh, K. J.; Kim, J.; Lynch, J. P.; Kam, N. W. S.; Kotov, N. A. *Smart Mater. Struct.* **2007**, *16*, 429−438.
(7) Zagorodni, A. A. *Ion Exchange Materials: Properties and Applications*, 1st ed.; Elsevier: Amsterdam, 2007.
(8) Helfferich, F. G. *Ion Exchange*; McGraw-Hill Series in Advanced Chemistry; McGraw-Hill: New York, 1962.
(9) Gu, B.; Brown, G. M. In *Perchlorate Environmental Occurence, Interactions and Treatment*; Gu, B., Coates, J. D., Eds.; Springer: New York, 2006; pp 209−251.
(10) Bonnesen, P. V.; Brown, G. M.; Alexandratos, S. D.; Bavoux, L. B.; Presley, D. J.; Patel, V.; Ober, R.; Moyer, B. A. *Environ. Sci. Technol.* **2000**, *34*, 3761−3766.
(11) Fried, J. R. *Polymer Science and Technology*; Prentice Hall PTR: Upper Saddle River, NJ, 2003.
(12) Yeo, S. C.; Eisenberg, A. *J. Macromol. Sci., Part B: Phys.* **1977**, *13*, 441−484.
(13) Nolte, A. J.; Treat, N. D.; Cohen, R. E.; Rubner, M. F. *Macromolecules* **2008**, *41*, 5793−5798.
(14) Paddock, J. R.; Zudans, I.; Heineman, W. R.; Seliskar, C. J. *Appl. Spectrosc.* **2004**, *58*, 608−612.
(15) Croll, S. G. *J. Coat. Technol.* **1980**, *52*, 35−43.
(16) Thouless, M. D. *J. Vac. Sci. Technol., A* **1991**, *9*, 2510−2515.
(17) Weber, R. L.; Ye, Y. S.; Banik, S. M.; Elabd, Y. A.; Hickner, M. A.; Mahanthappa, M. K. *J. Polym. Sci., Part B: Polym. Phys.* **2011**, *49*, 1287−1296.
(18) Tiihonen, J.; Markkanen, I.; Laatikainen, M.; Paatero, E. *J. Appl. Polym. Sci.* **2001**, *82*, 1256−1264.
(19) Jenkins, R. D.; DeLong, L. M.; Bassett, D. R. In *Hydrophilic Polymers: Performance with Environmental Acceptance*; Glass, J. E., Ed.; Advances in Chemistry Series; American Chemical Society: Washington, DC, 1996; Vol. *248*, pp 425−447.
(20) Tam, K. C.; Ng, W. K.; Jenkins, R. D. *Polymer* **2005**, *46*, 4052−4059.
(21) Dai, S.; Tam, K. C.; Jenkins, R. D. *Macromol. Chem. Phys.* **2001**, *202*, 335−342.
(22) Knaebel, A.; Skouri, R.; Munch, J. P.; Candau, S. J. *J. Polym. Sci., Part B: Polym. Phys.* **2002**, *40*, 1985−1994.
(23) Pandey, A. K.; Goswami, A.; Sen, D.; Mazumder, S.; Childs, R. F. *J. Membr. Sci.* **2003**, *217*, 117−130.
(24) Vogt, B. D.; Lin, E. K.; Wu, W. L.; White, C. C. *J. Phys. Chem. B* **2004**, *108*, 12685−12690.
(25) Vogt, B. D.; Soles, C. L.; Lee, H. J.; Lin, E. K.; Wu, W. L. *Langmuir* **2004**, *20*, 1453−1458.
(26) Torres, J. M.; Stafford, C. M.; Vogt, B. D. *Polymer* **2010**, *51*, 4211−4217.
(27) Harland, C. E. *Ion-Exchange: Theory and Practice*, 2nd ed.; Royal Society of Chemistry: London, 1994.
(28) Evans, D. R.; Craig, V. S. J. *J. Phys. Chem. B* **2006**, *110*, 5450−5461.
(29) Sader, J. E. *J. Appl. Phys.* **2001**, *89*, 2911−2921.
(30) Zhang, X.; Cahill, D. G. *Langmuir* **2006**, *22*, 9062−9066.
(31) Zhang, X.; Cahill, D. G.; Coronell, O.; Marinas, B. J. *J. Membr. Sci.* **2009**, *331*, 143−151.
(32) Smith, A. L. In *Handbook of Thermal Analysis and Calorimetry: Recent Advaces, Techniques and Applications*; Brown, M. E., Gallagher, P. K., Eds.; Elsevier B.V.: Amsterdam, 2008; Vol. *5*, Chapter 5, pp 133−170.
(33) Perera, D. Y. *Prog. Org. Coat.* **1996**, *28*, 21−23.
(34) Berry, B. S.; Pritchet, W. C. *IBM J. Res. Dev.* **1984**, *28*, 662−667.
(35) Francis, L. F.; McCormick, A. V.; Vaessen, D. M.; Payne, J. A. *J. Mater. Sci.* **2002**, *37*, 4717−4731.
(36) Lei, H.; Payne, J. A.; McCormick, A. V.; Francis, L. F.; Gerberich, W. W.; Scriven, L. E. *J. Appl. Polym. Sci.* **2001**, *81*, 1000−1013.
(37) Wiederhold, P. R. *Water Vapor Measurement: Methods and Instrumentation*; Marcel Dekker, Inc.: New York, 1997.
(38) EPA, Estimation Programs Interface Suite for Microsoft Windows, 2011.
(39) Meylan, W. M.; Howard, P. H. *J. Pharm. Sci.* **1995**, *84*, 83−92.
(40) Moyer, B. A.; Bonnesen, P. V. In *Supramolecular Chemistry of Anions*; Bianchi, A., Bowman-James, K., García-España, E., Eds.; Wiley-VCH: New York, 1997; pp 1−44.
(41) Inczédy, J. *J. Therm. Anal.* **1978**, *13*, 257−261.
(42) Seitz, J. T. *J. Appl. Polym. Sci.* **1993**, *49*, 1331−1351.
(43) Antonelli, G. A.; Perrin, B.; Daly, B. C.; Cahill, D. G. *MRS Bull.* **2006**, *31*, 607−613.
(44) Levy, M.; Bass, H. E.; Stern, R. R. *Modern Acoustical Techniques for the Measurement of Mechanical Properties: Experimental Methods in the Physical Sciences*; Academic Press: San Diego, CA, 2001; Vol. *39*.
(45) Wypych, G. *Handbook of Plasticizers*; ChemTec Publishing: Norwich, 2004.
(46) Payne, J. A.; McCormick, A. V.; Francis, L. F. *J. Appl. Polym. Sci.* **1999**, *73*, 553−561.
(47) Nowick, A. S.; Berry, B. S. *IBM J. Res. Dev.* **1961**, *5*, 297−311.
(48) Khare, V. P.; Greenberg, A. R.; Krantz, W. B. *J. Appl. Polym. Sci.* **2004**, *94*, 558−568.
(49) Secrist, K. E.; Nolte, A. J. *Macromolecules* **2011**, *44*, 2859−2865.
(50) Capaccioli, S. *J. Chem. Phys.* **2011**, *135*, 104504.
(51) Boo, H.-K.; Shaw, M. T. *J. Vinyl Technol.* **1987**, *9*, 168−172.
(52) Smith, A. L. In *New Developments in Coatings Technology*; Zarras, P., Wood, T., Richey, B., Benicewicz, B. C., Eds.; ACS Symposium Series; American Chemical Society: Washington, DC, 2007; Vol. *962*, Chapter 17, pp 261−277.
(53) Gu, B. H.; Brown, G. M.; Bonnesen, P. V.; Liang, L. Y.; Moyer, B. A.; Ober, R.; Alexandratos, S. D. *Environ. Sci. Technol.* **2000**, *34*, 1075−1080.

Macromolecules

Article

pubs.acs.org/Macromolecules

Phototunable Response in Caged Polymer Brushes

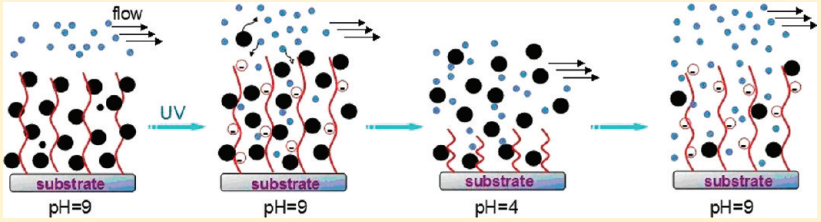
Jiaxi Cui,[†] Thi-Huong Nguyen,[†,§] Marcelo Ceolín,[‡] Rüdiger Berger,[†] Omar Azzaroni,[†,‡] and Aránzazu del Campo[†,*]

[†]Max-Planck-Institut für Polymerforschung, Ackermannweg 10, 55128 Mainz, Germany

[‡]Instituto de Investigaciones Fisicoquímicas Teóricas y Aplicadas (INIFTA) CONICET, Universidad Nacional de La Plata, CC 16 Suc. 4 (1900) La Plata, Argentina

[§]Institute of Pharmacy and Biochemistry, Johannes Gutenberg University Mainz, Mainz 55128, Germany

Supporting Information



ABSTRACT: A light-responsive brush was obtained by surface-initiated ATRP of a methacrylate monomer containing ionizable −COOH side groups caged with the photoremovable group 4,5-dimethoxy-2-nitrobenzyl (NVOC). In the caged form, the polymer brush (PNVOCMA) is neutral and hydrophobic due to the presence of the aromatic chromophore. Upon irradiation the NVOC group is removed and a polyanion (polymethacrylic acid, PMAA) chain is generated. The charged brush can swell and collapse depending on the pH and the exposure dose (i.e., uncaging degree). The behavior and properties of the brush layer for different photoconversion degrees were studied. On the basis of quartz crystal microbalance measurements, a threshold of 50% uncaging was identified in order to achieve significant swelling and pH response of the brush. Between 50 and 80% the photoconversion the response of the brush could be light-modulated. For photoconversions >80% only small changes in the response were detectable. X-ray reflectivity (XRR) and scanning force microscopy allowed us to measure thickness, roughness and swelling of the brushes at intermediate photoconversions. Combined XRR and grazing-incidence small-angle scattering experiments evidenced a change in the internal structure of the brush upon exposure and indicated the occurrence of domain segregation as a consequence of the coexistence of hydrophobic and charged groups in the brush structure.

INTRODUCTION

The use of photolabile protecting groups ("cages") for photoinducing changes in the macromolecular structure and resulting material properties has raised increasing interest in the past few years.[1] Light-triggered assembly and reorganization of caged block copolymers[2−4] and derived micelles,[5] disruption and swelling of nanoparticles containing drugs,[6] assembly and polymerization of supramolecular polymers[7] and hydrogels,[8,9] or the generation of surface patterns[10] are recent examples that demonstrate the variety of effects that can be achieved by including photolabile units in the structure of the polymer chain (either directly in the main chain or on functional side groups). Photolabile polymer brushes containing caged ionizable side groups have also been recently realized.[11−16] Light exposure triggers the generation of charged units along the brush and induces a pH-dependent conformational change between the extended and collapsed states,[15,16] Wettability,[11,12,16] and permeability[15] changes on surfaces and interfacial architectures (membranes) have been demonstrated with these systems.

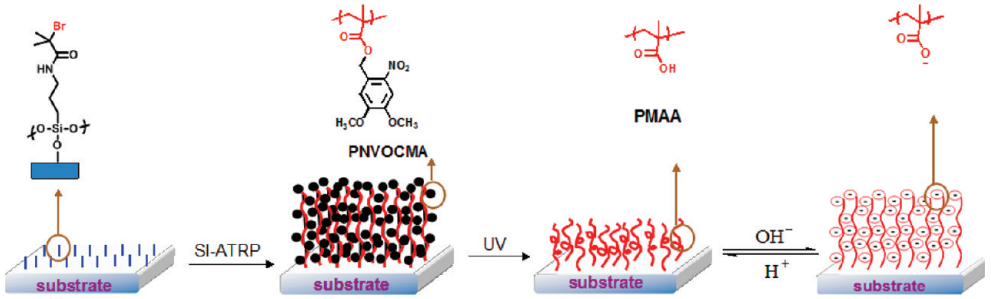
Most of the published studies on caged polymer systems concentrate in the initial (caged) and final (fully uncaged) states and derived properties. However, light allows precise dosage and modulation of the photocleavage reaction and, therefore, the generation of well-defined intermediate chemical states with light-tunable properties. Minimum thresholds or saturation levels for the light-response have not been investigated. Miscibility and compatibility issues at the nanoscale between uncaged caged units along the polymer chain may also well arise at intermediate conversions. All these effects merit careful investigation and might lead to unexpected responses and application fields.

In this context, this article studies the evolution of the response and the internal structure of a photolabile polymer brush during the photolytic process. The light-responsive brush is obtained by surface-initiated ATRP of a methacrylate monomer containing ionizable −COOH side groups caged with the photoremovable group 4,5-dimethoxy-2-nitrobenzyl (NVOC). NVOC was selected as caging group because its alcohol is commercially available as precursor for the synthesis and its photochemical properties are well-known. In the caged form, the polymer brush (PNVOCMA) is neutral and hydrophobic

Received: February 9, 2012
Revised: March 1, 2012
Published: March 20, 2012

 © 2012 American Chemical Society dx.doi.org/10.1021/ma300274b | *Macromolecules* 2012, 45, 3213−3220

Scheme 1. Schematic of the Formation, Photolysis, and Swelling of Photosensitive Polymer Brushes



due to the presence of the aromatic chromophore (Scheme 1). Upon irradiation the NVOC group is removed and a polyanion (polymethacrylic acid, PMAA) chain is generated. The charged brush can swell and collapse depending on the pH and the degree of uncaging. The exposure dose will be controlled in order to investigate the behavior and properties of the brush layer for different photoconversion degrees. The minimum illumination threshold and the saturation levels for light-modulated swelling and pH response will be identified using a quartz crystal microbalance with dissipation (QCM-D). X-ray reflectivity (XRR) will be used to determine the changes in the film thickness and swelling of the brush for different uncaging ratios under different conditions. These data will be complemented by scanning force microscopy (SFM) data. Combined XRR and grazing-incidence small-angle scattering (GISAXS) experiments will provide information about the evolution of the mesostructural order in the brush.

EXPERIMENTAL SECTION

Materials and Methods. 2-Isocyanatoethyl methacrylate (98%, Aldrich), 4,5-dimethoxy-2-nitrobenzyl alcohol (98%, Alfa), (3-aminopropyl)triethoxysilane (APTS, 99%, Aldrich), 2-bromisobutylryl bromide (BIB, 98%, Aldrich), *N,N,N′,N″,N″*-pentamethyldiethylenetriamine (PMDETA, 99%, Aldrich), copper(I) bromide (99.999%, Aldrich), and copper(II) bromide (99%, Aldrich), and poly(ethylene glycol) methyl ether (PEG, Aldrich, molecular weight ~550) were used as received. Methacrylic chloride (98%, Aldrich) was purified by distillation before use. All other reagents and solvents were used as obtained unless otherwise specified. Quartz slides (Suprasil 1) with a thickness of 1 mm were purchased from Heraeus Quarzglas (Hanau, Germany). Silicon wafers in (100) orientations were provided by Crystec (Berlin, Germany).

Solution ^{1}H and ^{13}C spectra were measured in $CDCl_3$ solution at 25 °C on Bruker Ultra Shield 250 MHz spectrometer. UV spectra were recorded on a Varian Cary 4000 UV−vis spectrometer (Varian Inc. Palo Alto, CA). Mass spectra were recorded on a Micromass Finnigan-MAT ZAB-HS mass spectrometer. Gel permeation chromatography (GPC) was performed with a polymer standard service (PSS) equipped with WinGPC. RI ERC 7512 (ERMA Inc.) and UV−Visible S-3702 (SOMA) were used as detectors. *N,N*-Dimethylformamide (DMF) was employed as eluent at a flow rate of 1.0 mL/min at 60 °C and columns SDV from PSS (100, 103, 104, and 106 Å porosity; 10 mm bead size; dimensions of 0.8 × 30 cm^2). GPC curves were calibrated against poly(methyl methacrylate) standards.

Synthesis. 4,5-Dimethoxy-2-nitrobenzyl methacrylate (NVOC-MA) was synthesized by reaction of 4,5-dimethoxy-2-nitrobenzyl alcohol and methacrylic chloride as previously reported[17] and purified via column chromatography (dichloromethane/ethyl acetate (10/1, v/v) as eluent) followed by recrystallization in ethanol before polymerization. PEG-based initiator (PEGBr) for performing ATRP in solution was synthesized by the reaction of poly(ethylene glycol) methyl ether and BIB in the presence of triethylamine following the conditions reported in the literature.[16] Polymer brushes were prepared by surface-initiated ATRP (SI-ATRP) on quartz or silicon wafers.[15,16] The substrates were first coated with the ATRP initiator (APTS + BIB), followed by immersion into a DMSO solution of the monomer, *N,N,N′,N″,N″*-pentamethyldiethylenetriamine, CuBr, and $CuBr_2$, in a molar ratio of 100:3:1:0.1 under continuous stream of nitrogen and at 90 °C and free initiator PEGBr (0.04 mol % of monomer).[15,16]

Light-Exposure and Photocleavage. Irradiation experiments were carried out using a PolychromeV lamp (TILL Photonics GmbH, Grafelfing, Germany) at 365 nm (4.7 $\mu W\ cm^{-2}$). After irradiation, substrates were washed with CH_2Cl_2 and Milli-Q water to remove the photocleaved chromophore. For the patterning experiments, a mask with 5 × 5 μm quartz squares separated by 5 μm gold spacers was placed on the substrate during exposure.

Quartz Crystal Microbalance with Dissipation (QCM-D) Measurements. were carried out in a Q-Sense E1 system (Sweden). A silica-coated crystal was used (Q-Sense, Sweden). The crystal was excited at its fundamental frequency (5 MHz), and measurements of the frequency and dissipation change (Δf, ΔD) were performed at the first, third, fifth, seventh, ninth, and 13th overtones, corresponding to 5, 15, 25, 35, 45, and 55 MHz. A 100 mM KCl aqueous solution was used as flow medium, and the pH value was adjusted with either KOH or HCl aqueous solution. A window cell that allowed in situ light exposure was used for the experiments.

X-ray Reflectivity (XRR) and Grazing-Incidence Small-Angle X-ray Scattering (GISAXS) Measurements. were performed at the D10A-XRD2 beamline of Laboratório Nacional de Luz Síncrotron (LNLS) (Campinas, Brazil) (λ = 1.608 Å). The sample-to-detector distance was kept to 550 mm, the outgoing photons were detected using a PILATUS 100 K detector (DECTRIS AG, Switzerland). Sample temperature was kept to 20 °C and sample humidity was controlled using a home-built chamber.

Scanning Force Microscopy (SFM) Measurement. The SFM (NanoWizard, JPK, Berlin, Germany) was operated in contact mode at lowest possible normal forces to keep overlapping trace and retrace scan lines. Au back-side coated silicon nitride cantilevers with a nominal spring constant of 0.12 N/m (NP, Olympus, Japan) were used. Before measurement, the sample was rinsed with water and mounted on a glass slide by using a double side adhesive tape. Then, the glass slide was installed on the SFM sample holder and buffer solution (100 mM KCl aqueous solution, HCl was used to adjust the pH to 4) was injected in the liquid cell. The setup was left for 6 h for stabilizing conformation of polymer brushes and thermal equilibration before measurement. For imaging a scan speed of 0.3 Hz per line was used with a normal force of ~0.2 nN at a scan length of 30 μm. After a series of measurements at pH 4 the buffer was removed from the liquid cell by a syringe and the sample was thoroughly rinsed with 1 mL water. Subsequently, one milliliter of buffer (100 mM KCl aqueous solution, KOH was used to adjust the pH to 9) was injected in the liquid cell and the sample was left again for another 6 h before imaging. Then, a second series of imaging of the sample surface at the same position was recorded. During one measurement, the sample typically remained for 7 h at pH 9, 15 min in water for rinsing and 7 more hours at pH 4. The pH switching cycle was repeated three times. The images were processed and analyzed using Gwyddion software. An average of 20 line profiles at the center of each pattern was analyzed to determine the height difference between UV-irradiated

dx.doi.org/10.1021/ma300274b | *Macromolecules* 2012, 45, 3213−3220

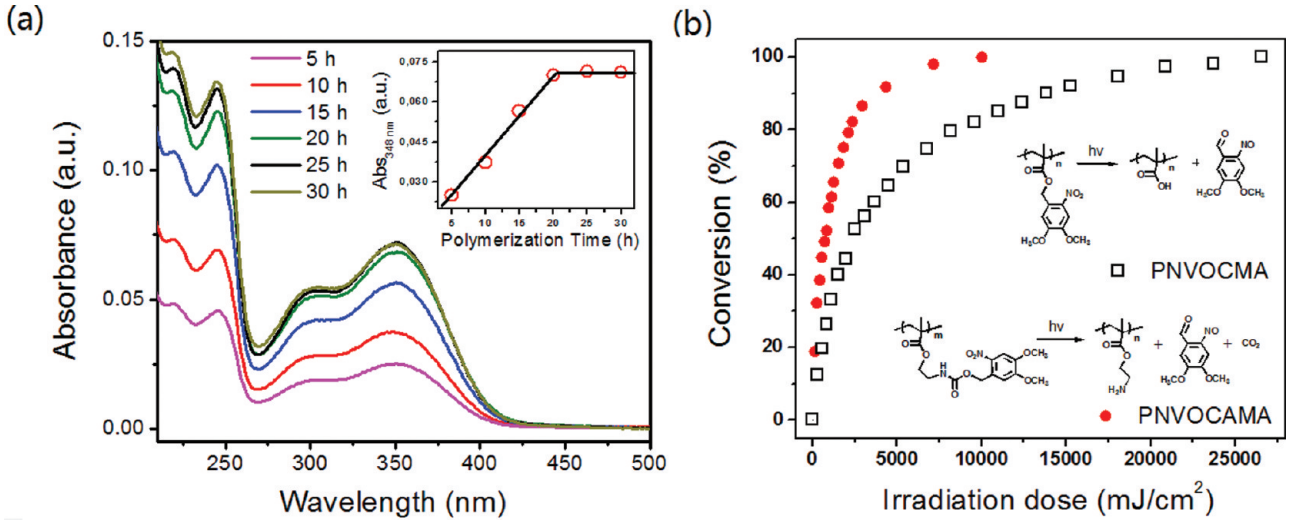


Figure 1. (a) UV spectra of PNVOCMA polymer brushes on quartz slides obtained with increasing polymerization times. The inset represents the linear increase in absorbance at 348 nm vs the polymerization time. (b) Conversion (%) for the photocleavage of PNVOCMA and PNVOCAMA brush at the surface upon irradiation at 365 nm. Data were calculated from the absorbance values at λ_{max} = 348 nm. Data of PNVOCAMA were extracted from ref 16.

and nonirradiated patterns. By comparing the height measured at the same position at pH 9 and pH 4, the swelling and deswelling of the polymer brushes at different pH was determined.

RESULTS AND DISCUSSION

Synthesis and Photochemical Properties of the Polymer Brush. The growth of the polymer brushes onto quartz substrates was followed by the increase in the UV absorbance. Figure 1 represents the UV−vis spectra of PNVOCMA brushes with increasing polymerization time. A linear increase in the absorbance was observed during the first 20 h of polymerization (inset in Figure 1), before polymer growth completely stopped. We hypothesized that the termination of the surface polymerization was due to the hydrolysis of the ester bond under our experimental conditions, rendering methacrylic acid that would poison the copper complex and stop chain growth.[18] ^{1}H NMR analysis of the polymerization reaction in solution showed the appearance of a signal at 4.78 ppm after 16 h reaction time that can be attributed to the methylene group of 4,5-dimethoxy-2-nitrobenzyl alcohol, confirming our hypothesis (Figure S1, Supporting Information). For this reason, we kept a polymerization time of 15 h for all substrates in order to obtain fully caged brushes.

Free initiator was added into the SI-ATRP solution and the obtained polymers in solution were isolated and characterized in order to estimate the molecular weight and distribution of the brushes.[16] The average molecular weight M_n was determined from the integrals of the ^{1}H NMR signals at 6.5−7.8 ppm for the aromatic proton and at 2.8−4.4 ppm for the methylene protons of the ethylene glycol chain (Figure S2, Supporting Information). The polydispersity index (PDI) was obtained by GPC. Values of M_n = 13300 g/mol and PDI = 1.48 were obtained after 15 h polymerization. Assuming that chains generated from free initiator in solution reach the same molecular weight as those from initiator at the surface,[19] the grafting density of the brush, Γ, can be estimated from the value of the degree of polymerization and the measured UV absorbance according to[20]

$$\Gamma = 1/2[A_\lambda \varepsilon_\lambda{}^{-1} n^{-1} N_A]$$

A_λ is the absorbance at a given wavelength, ε_λ is the molar extinction coefficient of the chromophore in solution at λ (ε_{348} = 6300 M^{-1} cm^{-1}), n is the average degree of polymerization and N_A is Avogadro's number. The factor $^1/_2$ refers to the fact that the quartz slides are modified on both sides. An average grafting density of 0.56 chains/nm^2 was obtained for PNVOCMA after 15 h polymerization.

Light exposure of quartz substrates modified with the polymer brushes cleaved the chromophore from the brush (Scheme 1) and the photolytic reaction was monitored by the decay of the UV absorbance of the substrates after exposure and a washing step (Figure S2, Supporting Information). Assuming that the detected absorbance is only associated with remaining chromophore on the brush, the conversion (%) of the photolytic reaction was calculated for the different exposure doses (Figure 1b). Following the photokinetic equation model for the special case of photolysis at surfaces,[21] a quantum yield (Φ_{365}) of 0.0071 was obtained for the photolysis of the surface attached chromophore. This value is close to the quantum yield reported for NVOC-caged phosphate esters in solution (0.003−0.009),[22] suggesting that the photolysis process and mechanism is similar in solution and on the surface. The quantum yield for the photolysis of nitrobenzyl derivatives is known to vary with the nature of the leaving group.[17,23] Figure 1b compares the conversion data of PNVOCMA (ester leaving group) with those of poly(2-[(4,5-dimethoxy-2-nitrobenzoxy)-carbonyl]aminoethyl) methacrylate, PNVOCAMA (carbamate leaving group) that we recently published.[16] PNVOCAMA was photocleaved more effectively than PNVOCMA at a given irradiation dose (i.e., 50% of PNVOCMA and 75% of PNVOCAMA were photocleaved at 2800 mJ/cm^2) and the Φ_{365} of PNVOCAMA was 0.026, significantly higher than that of PNVOCMA.

The photolytic reaction was also reflected in a change in the contact angle of the brush layers. In caged state, the advancing, static, and receding contact angles were 74°, 68°, and 37° respectively. After exposure the layers turned more hydrophilic and contact angles of 66°, 63°, and <5° were measured.

QCM Studies for in Situ Monitoring the Phototunable Uncaging and Swelling of the Brush. Quartz crystal

dx.doi.org/10.1021/ma300274b | Macromolecules 2012, 45, 3213−3220

microbalance (QCM) measurements were employed to follow the response of PNVOCMA brushes during light irradiation and pH cycling. The changes in the mass (associated with loss of the chromophore or uptake/release of water) were determined from the change in the resonant frequency (Δf). The ratio between the energy dissipated per cycle of oscillation and the total energy stored in the oscillating system was given by the D factor (ΔD).[24−26] We used a window-cell for the experiments that allowed direct illumination of the QCM crystal during measurement.

Figure 2a represents the Δf and ΔD of PNVOCMA under controlled light-exposure and pH changes. When the QCM crystal was modified with the caged brush (hydrophobic), it did not show any variation of Δf or ΔD at different pH, indicating no swelling of the brush in the buffer solutions (Figure S4, Supporting Information). The crystal was then irradiated at pH 8 with a dose corresponding to 40% photoconversion. During exposure, the frequency continuously decreased, indicating an increase in mass of the surface layer. In parallel, an increase in the dissipation values, associated with an increase in the viscoelasticity of the surface layer, was observed. During exposure, the chromophore is cleaved from the brush and it is expected to diffuse out of the surface layer (mass loss). At the same time, the brush becomes hydrophilic and, therefore, may uptake water (i.e., increase in mass and viscoelasticity). In our case, the swelling of the now COOH functionalized chains, negatively charged at pH 8, was dominant for the mass change, as reflected by the decrease in Δf. When the irradiation was switched off, the frequency remained constant, demonstrating the possibility of light-modulated swelling of the caged brushes.[27] As the pH was changed to 4, a significant Δf increase indicated the loss of water and collapse of the polymer brush due to the protonation of the carboxyl group. When the pH was returned to 8, the polymer brush swelled again. However, Δf did not return to the same value, indicating that additional mass was lost during the collapsing state. We hypothesized that the mass loss corresponded to photolytic byproduct that remained embedded in the surface layer during irradiation at pH 8, but was squeezed out of the brush during collapse at pH 4. This means that hydration of the brush after uncaging happens at much faster rate than diffusion of the photoproducts out of the brush. A model representing the uncaging and swelling processes at the different conditions is shown in Figure 2b.

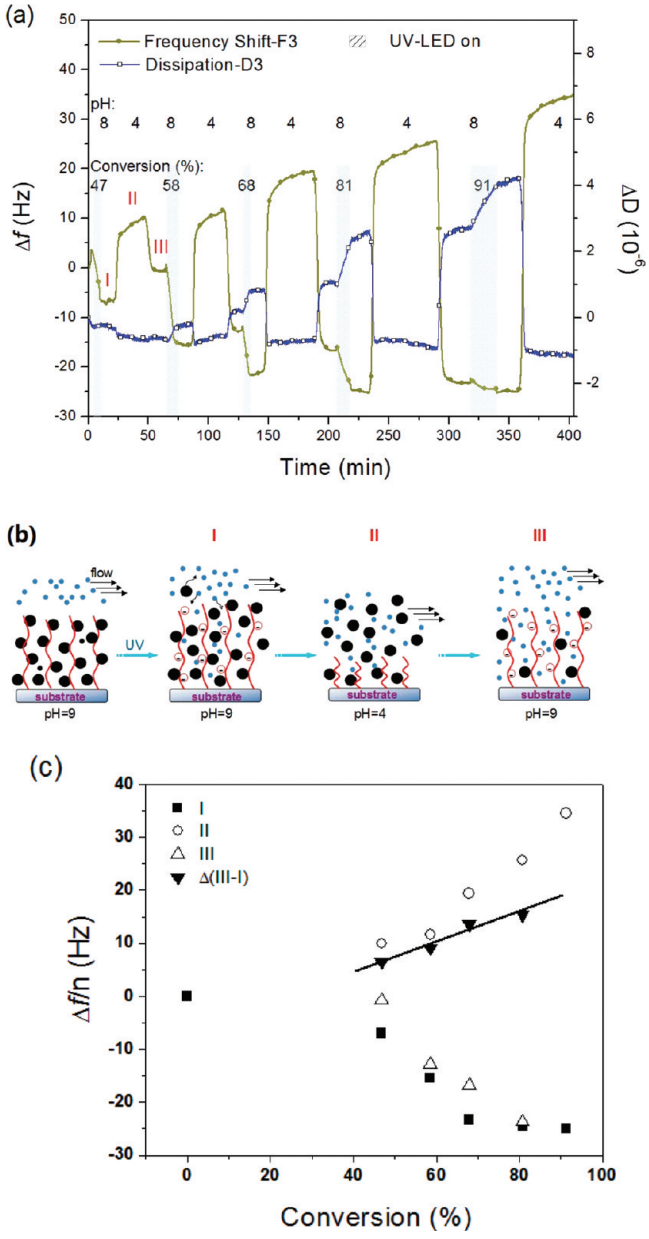


Figure 2. (a) Δf and ΔD of the third overtone of a SiO_2 QCM crystal coated with PNVOCMA brush under different conditions. (b) Representation of uncaging and swelling model. (c) $\Delta f/n(\Delta m)$ *vs* photolytic conversion plots.

Further irradiation steps and pH cycles were performed up to full conversion and were followed in the QCM. Figure 2c displays the frequency shift values of the different steps vs the photolytic conversion. On the basis of our model, Δf values of steps I and III reflect the water uptake with increasing uncaging ratio (i.e., generation of carboxylate groups along the polymer brush) with and without chromophore, respectively. The frequency difference between steps I and III corresponds to the mass of lost chromophore and, in fact, it correlates linearly with the conversion values. Δf values from step II reflect the water uptake of the (partially) uncaged brush in the collapsed state. It is interesting to note that water uptake did not linearly correlate with the photolytic conversion. In fact, small changes in frequency were observed for uncaging ratios below 50%, but drastic changes were observed for higher conversions. This result suggests that a threshold of ca. 50% uncaged groups in the chain are required to swell the initially hydrophobic PNVOCMA brush.

Figure 3 shows the pH-sensitivity of the fully uncaged PNVOCMA brush, i.e. the PMAA brush.[28−31] At pH > 9, the brush is highly charged and adopts an extending conformation, adsorbing the highest amount of water.[32] By lowering the pH, the brush becomes less charged and more hydrophobic and chains collapse. This leads to shrinking of the brush and less water uptake. The highest change in swelling occurs from pH 6.0 to 7.0, as expected from reported works on homo-PMAA brushes.[33] At acidic pH the carboxyl group is protonated, the brush is neutral and the chains collapse. When the pH was returned from 4 to 9, the Δf reverts to the initial negative value, implying that the brush is stable and the swelling is reversible. These results confirm that the uncaging reaction renders fully functional PMAA brushes with the expected pH response.

Evolution of the Thickness, Swelling, and Roughness of the Brush Layer upon Gradual Uncaging via XRR.

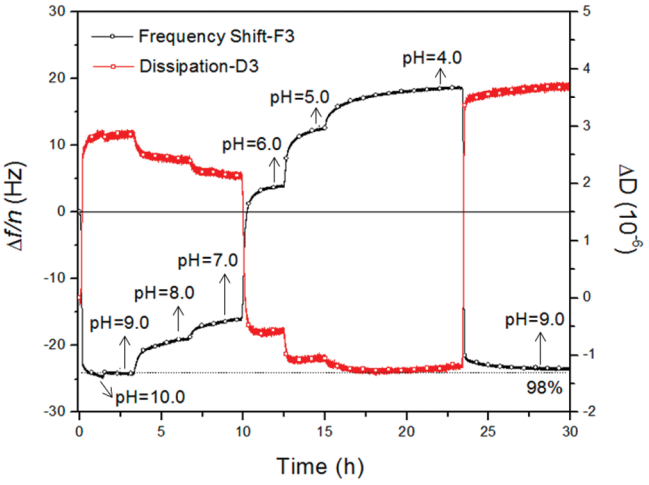


Figure 3. Δf and ΔD of the third overtone of a SiO_2 QCM crystal coated with PNVOCMA brushes after full exposure and the variation with the pH.

XRR measurements were performed to determine the changes in the film thickness of the brush upon controlled exposure. Figure 4 shows the X-ray reflectometry spectra of PNVOCMA brushes upon 0% (caged brush), 30% and 100% photolytic conversion. Measurements were performed under low (0% RH) and high (>90% RH) relative humidity conditions. The film thickness, *d*, was calculated from the difference in the scattering vector *q* from maximum to maximum of the Kiessig fringes (the interval between fringes), according to $d = 2\pi/\Delta q$. The corresponding values are collected in Table 1. Caged PNVOCMA brushes had a thickness of 6.7 nm in dry conditions that increased to 7.0 nm at 90% humidity (swelling ~4%).

Table 1. Thickness of the Brush Layer and Roughness Values of PNVOCMA Brushes As Determined by X-ray Reflectivity under Different Environmental Conditions

	relative humidity 0%		relative humidity 90%	
photoconversion (%)	thickness (nm)	roughness (nm)	thickness (nm)	roughness (nm)
0	6.7	0.67	7.0	0.68
30	6.1	0.83	6.4	0.87
100	5.2	0.72	5.8	0.74

Upon partial (30%) and full (100%) photocleavage, the thicknesses of dry films decreased to 6.1 and 5.2 nm, respectively. The photolyzed films also swelled in humid conditions to a thickness of 6.4 and 5.8 nm (swelling ~5 and 10% respectively). As expected and in agreement with the QCM data, the fully exposed PNVOCMA brush, *i.e.*: PMAA brush, showed higher affinity for water than the caged or the partially photolyzed brush.

The stochastic roughness of the brush layer was calculated from the Gaussian decay of the amplitude of the Kiessig fringes superimposed to the typical q^{-4} decay of the scattering pattern.[34] Upon light exposure, the Kiessig oscillations at higher *q*-values became less pronounced. The suppression of Kiessig oscillations is a hint for an increase in the film roughness and suggests that the removal of the chromophore induces detectable structural changes in the polymer brush. Table 1 depicts

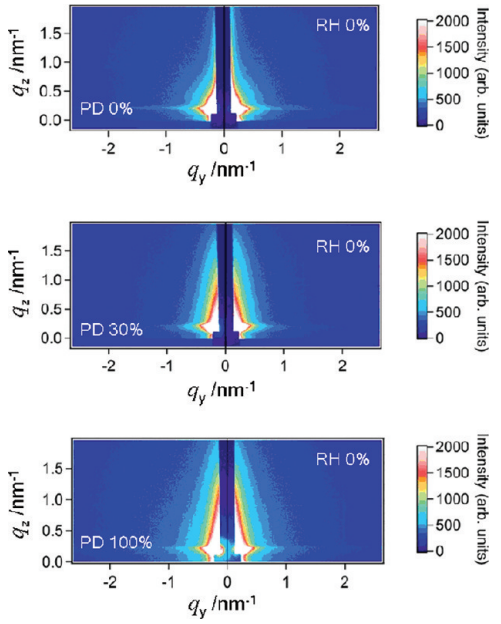


Figure 5. GISAXS patterns of PNVOCMA brushes with different photodeprotection degrees (PD): (top) 0%, (middle) 30%, and (bottom) 100%, obtained under dry conditions. The scattering vector q_y provides structural information on the lateral organization of polymer brush, whereas scattering features along q_z reveal changes normal to the surface of the thin film.

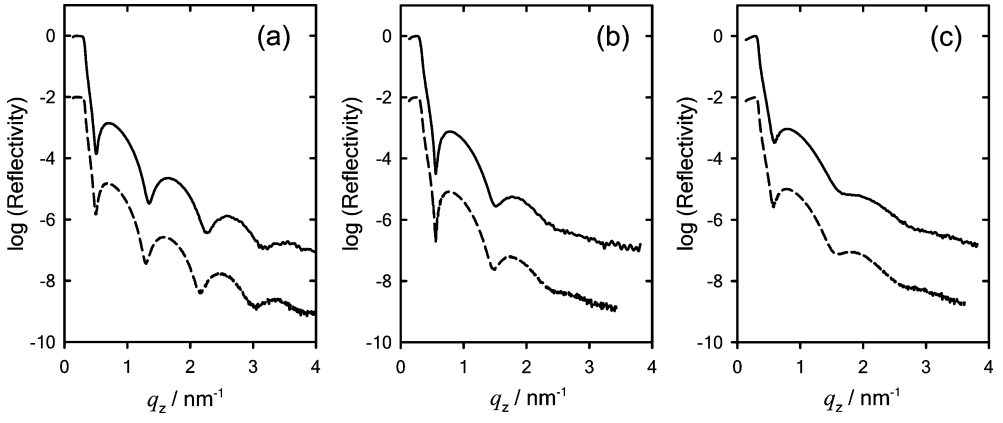


Figure 4. X-ray reflectivity data corresponding to PNVOCMA brushes after different degrees of photocleavage: (a) 0%, (b) 30%, and (c) 100%. Different traces correspond to experiments performed in dry (RH ~ 0%, dashed trace) and humid environments (RH ~ 90%, solid trace).

dx.doi.org/10.1021/ma300274b | *Macromolecules* 2012, 45, 3213–3220

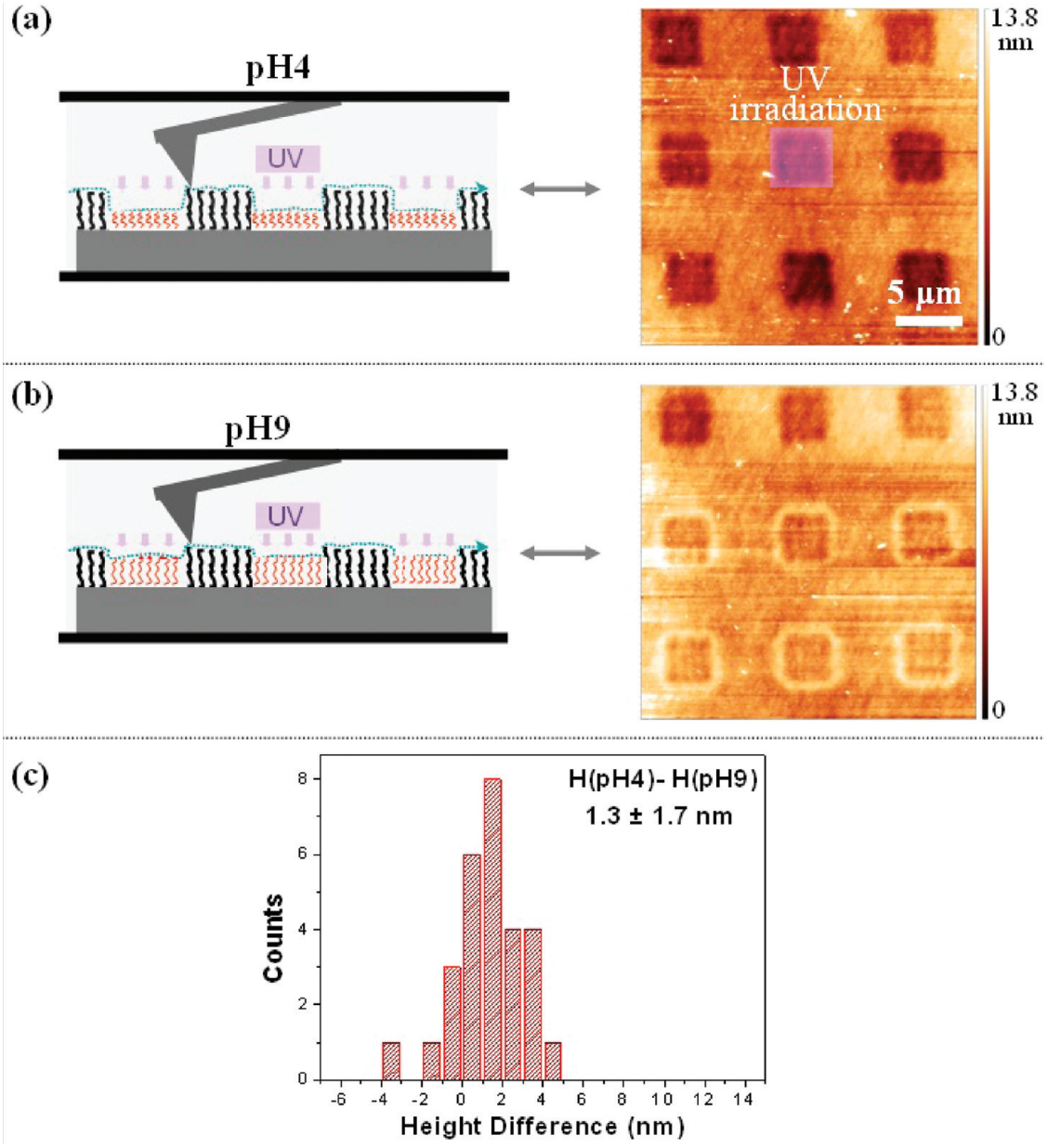


Figure 6. SFM contact mode imaging of masked-irradiated brush coated substrates at different pH. (a, b) Topography images taken at pH 4 (a) and pH 9 (b) with their corresponding sketches. (c) Histogram showing the distributions of different height collected from 3 measurements cycles and obtained from line profiles at ~30 different positions.

roughness values of caged and photolized brushes under different humidity conditions. We attribute the increase in roughness after partial photocleavage to a higher degree of heterogeneity in the brush layer due to the coexistence of hydrophilic and hydrophobic monomer units along the brushes. These could arrange into phase-segregated inner domains and lead to an increase in film roughness. The roughness in the fully exposed brush decreased again, reflecting the recovery of a brush with a homogeneous composition.

GISAXS Analysis of the Changes in the Internal Structure of the Brush upon Light Exposure. GISAXS measurements allowed us to investigate mesostructural order within the brush film.[35,36] The components of the scattering vector q_y and q_z enable discrimination between the scattering parallel and perpendicular to the sample surface and, therefore, they provide information about lateral and normal ordering within the thin film. Figure 5 and Figure S5 (Supporting Information) shows the GISAXS patterns of PNVOCMA brushes after controlled light exposure under dry and humid conditions. No significant changes in the GISAXS features between samples measured in humid or dry environments were observed. A comparative analysis of caged and irradiated samples revealed in both cases the absence of intensity maxima at finite scattering vectors which implies a broad distribution of domain sizes and/or that domain−domain correlation does not play a significant contribution to the scattering, i.e. the scattering is dominated by the form factor of the domains and not from the in-plane structure factor of the film. For the condition $q_z \rightarrow 0$, we observe a similar intensity distribution on the left and on the right of the vertical symmetry for protected and unprotected brushes. Analysis of the out-of-plane scans (Guinier plots at $q_z = 0.1$ nm^{-1}) indicated the presence domains with in-plane diameters ca. 36 nm.

dx.doi.org/10.1021/ma300274b | *Macromolecules* 2012, 45, 3213−3220

The scattering intensity in the direction perpendicular to the substrate (q_z) significantly changed upon light exposure, leading to a much smoother decay of scattering intensity toward larger q_z values (for $q_y \rightarrow 0$). The increase of scattering intensity at large q_z values suggests the creation of domains with smaller real-space dimensions stemming from the photocleavage process. In other words, the steeper decay of the intensity parallel to the sample surface rather than in the perpendicular direction means that the photogenerated hydrophilic domains distributed along the film thickness are flatter (or smaller in height) than the original "caged" hydrophobic domains.

Visualization of the Photoinduced Swelling on Photopatterned Brushes by SFM. Silica substrates modified with the PNVOCMA brushes were irradiated through a mask with 5 μm × 5 μm quartz squares separated by 5 μm gold spaces in order to generate surface patterns with caged and light-exposed brush areas. Scanning force microscopy (SFM) was used to probe the swelling and deswelling of the irradiated polymer brush at two different pH values (Figure 6). The SFM images recorded at pH 9 revealed the expected pattern geometry with 5 μm wide quadratic features. The light-exposed regions (that correspond to swollen PMAA brushes) appeared as recessed squares in the topography image. The depth of these areas (i.e., the height difference between caged brushes and uncaged brushes at pH 9) ranged from 1.5 to 5.0 nm depending on the exact position of the height measurement and the exposed area. This indicates that the thickness of the photocleaved brush layer after swelling was decreased compared to the original brush and, therefore, in agreement with the XRR measurements (Table 1). By changing the pH of the buffer in the liquid cell to 4, the difference between the height niveaus inside (PMAA) and outside (PNVOCMA) of the squares increased (in Figure 6 from b to a). A mean increase in the height difference of ∼1.3 nm was estimated reflecting the higher swelling degree of the brush in the deprotonated state, as seen in the QCM experiments.

CONCLUSIONS

Polymer brush layers containing photolabile caged COOH lateral groups have allowed us to build surfaces with a light-modulated response to humidity and pH. The cleavage of the chromophore from the brush layer upon exposure occurs with similar photophysical parameters and yield than in solution. The consequent generation of ionizable groups renders a more hydrophilic brush layer able to swell up to 10% after full deprotection. The diffusion of the chromophore out of the brush layer is slow and can be accelerated by collapsing the brush at acidic pH. A threshold of 50% uncaging was necessary in order to achieve significant swelling and pH response of the brush. Between 50 and 80% photoconversion, the response of the brush could be light-modulated. For photoconversions >80%, only small changes in the response were detectable.

The internal structure of the brush layer was changed upon light exposure. This was reflected in an increase in the surface roughness at intermediate conversions, where hydrophilic and hydrophobic groups are forced to coexist in the brush structure. We interpret these results as an indication for domain segregation.

ASSOCIATED CONTENT

Supporting Information

^{1}H NMR of polymers, UV−vis spectra, Δf and ΔD plots, and QCM-D image. This material is available free of charge via the Internet at http://pubs.acs.org/.

AUTHOR INFORMATION

Corresponding Author

*Telephone: +49 (0)6131 379563. Fax: +49 (0)6131 379271. E-mail: delcampo@mpip-mainz.mpg.de.

Notes

The authors declare no competing financial interest.

ACKNOWLEDGMENTS

A.d.C. acknowledges financial support from DFG, CA880/3-1. O.A. gratefully acknowledges financial support from Agencia Nacional de Promoción Científica y Tecnológica (ANPCyT) (PICT−PRH 163/08), Max-Planck- Gesellschaft (Max Planck Partner Group, MPIP/INIFTA), Consejo Nacional de Investigaciones Científicas y Técnicas (CONICET), Alexander von Humbolt Stiftung, Laboratório Nacional de Luz Síncrotron (LNLS) (XRD2—11639/10736). O.A and M.C. are CONICET fellows. T-H.N. acknowledges partial financial support from DFG (SFB 625) and IMPRS. We are also grateful to Uwe Rietzler, for his help with SFM measurements.

REFERENCES

(1) Zhao, H.; Sterner, E. S.; Bryan Coughlin, E.; Theato, P. *Macromolecules* **2012**, DOI: 10.1021/ma201924h.

(2) Schumers, J. M.; Bertrand, O.; Fustin, C. A.; Gohy, J. F. *J. Polym. Sci., Part A: Polym. Chem.* **2012**, *50* (3), 599−608.

(3) Schumers, J. M.; Fustin, C. A.; Gohy, J. F. *Macromol. Rapid Commun.* **2010**, *31* (18), 1588−1607.

(4) Schumers, J. M.; Gohy, J. F.; Fustin, C. A. *Polym. Chem.* **2010**, *1* (2), 161−163.

(5) Bertrand, O.; Schumers, J. M.; Kuppan, C.; Marchand-Brynaert, J.; Fustin, C. A.; Gohy, J. F. *Soft Matter* **2011**, *7* (15), 6891−6896.

(6) Klinger, D.; Landfester, K. *Macromolecules* **2011**, *44* (24), 9758−9772.

(7) Foster, E. J.; Berda, E. B.; Meijer, E. W. *J. Am. Chem. Soc.* **2009**, *131* (20), 6964−6966.

(8) Peng, K.; Tomatsu, I.; van den Broek, B.; Cui, C.; Korobko, A. V.; van Noort, J.; Meijer, A. H.; Spaink, H. P.; Kros, A. *Soft Matter* **2011**, *7* (10), 4881−4887.

(9) Kloxin, A. M.; Kasko, A. M.; Salinas, C. N.; Anseth, K. S. *Science* **2009**, *324* (5923), 59−63.

(10) Shafiq, Z.; Cui, J.; Pastor-Pérez, L.; San Miguel, V.; Gropeanu, R. A.; Serrano, C.; del Campo, A. *Angew. Chem., Int. Ed.* **2012**, inpress.

(11) Brown, A. A.; Azzaroni, O.; Fidalgo, L. M.; Huck, W. T. S. *Soft Matter* **2009**, *5*, 2738−2745.

(12) Brown, A. A.; Azzaroni, O.; Huck, W. T. S. *Langmuir* **2009**, *25*, 1744−1749.

(13) Fries, K.; Samanta, S.; Orski, S.; Locklin, J. *Chem. Commun.* **2008**, *47*, 6288−6290.

(14) Samanta, S.; Locklin, J. *Langmuir* **2008**, *24* (17), 9558−9565.

(15) Brunsen, A.; Cui, J.; Ceolín, M.; del Campo, A.; Soler-Illia, G. J. A. A.; Azzaroni, O. *Chem. Commun.* **2012**, *48*, 1422−1424.

(16) Cui, J.; Azzaroni, O.; Del Campo, A. *Macromol. Rapid Commun.* **2011**, *32* (21), 1699−1703.

(17) Brown, A. A.; Azzaroni, O.; Huck, W. T. S. *Langmuir* **2009**, *25* (3), 1744−1749.

(18) Matyjaszewski, K.; Patten, T. E.; Xia, J. *J. Am. Chem. Soc.* **1997**, *119* (4), 674−680.

(19) Ohno, K.; Kayama, Y.; Ladmiral, V.; Fukuda, T.; Tsujii, Y. *Macromolecules* **2010**, *43* (13), 5569−5574.

(20) Stegmaier, P.; Alonso, J. M.; del Campo, A. *Langmuir* **2008**, *24* (20), 11872−11879.

(21) Wöll, D.; Walbert, S.; Stengele, K.-P.; Albert, T. J.; Richmond, T.; Norton, J.; Singer, M.; Green, R. D.; Pfleiderer, W.; Steiner, U. E. *Helv. Chim. Acta* **2004**, *87* (1), 28−45.

(22) Goeldner, M.; Givens, R. *Dynamic Studies in Biology: Phototriggers, Photoswitches and Caged Biomolecules*; Wiley-VCH: Weinheim, Germany, 2005; p 159.
(23) Cameron, J. F.; Frechet, J. M. J. *J. Am. Chem. Soc.* **1991**, *113* (11), 4303−4313.
(24) Cheng, N.; Azzaroni, O.; Moya, S.; Huck, W. T. S. *Macromol. Rapid Commun.* **2006**, *27* (19), 1632−1636.
(25) Moya, S. E.; Brown, A. A.; Azzaroni, O.; Huck, W. T. S. *Macromol. Rapid Commun.* **2005**, *26* (14), 1117−1121.
(26) Notley, S. M.; Eriksson, M.; Wågberg, L. *J. Colloid Interface Sci.* **2005**, *292* (1), 29−37.
(27) Konradi, R.; Ruehe, J. *Macromolecules* **2005**, *38* (14), 6140−6151.
(28) Liu, G.; Zhang, G. *J. Phys. Chem. B* **2008**, *112* (33), 10137−10141.
(29) Santonicola, M. G.; de Groot, G. W.; Memesa, M.; Meszyńska, A.; Vancso, , G. J. *Langmuir* **2010**, *26* (22), 17513−17519.
(30) Rahane, S. B.; Floyd, J. A.; Metters, A. T.; Kilbey, S. M. II. *Adv. Funct. Mater.* **2008**, *18* (8), 1232−1240.
(31) Patil, V.; Malvankar, R. B.; Sastry, M. *Langmuir* **1999**, *15* (23), 8197−8206.
(32) Moya, S.; Azzaroni, O.; Farhan, T.; Osborne, V. L.; Huck, W. T. S. *Angew. Chem., Int. Ed.* **2005**, *44* (29), 4578−4581.
(33) Dong, R.; Lindau, M.; Ober, C. K. *Langmuir* **2009**, *25* (8), 4774−4779.
(34) Tolan, M. *X-Ray Scattering From Soft-Matter Thin Films*; Springer-Verlag: Heidelberg, Germany, 1999.
(35) Lazzari, R. *Lect. Notes Phys.* **2009**, *770*, 283−342.
(36) Buschbaum, P. In *Polymer Surfaces and Interfaces Characterization, Modification and Applications*; Stamm, M., Ed.; Springer-Verlag: Heidelberg, Germany, 2008; Chapter 2, pp 17−46.

Macromolecules

Article

pubs.acs.org/Macromolecules

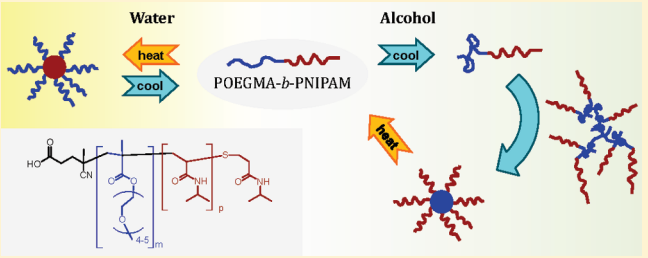
Comparison between the LCST and UCST Transitions of Double Thermoresponsive Diblock Copolymers: Insights into the Behavior of POEGMA in Alcohols

Peter J. Roth, Thomas P. Davis,* and Andrew B. Lowe*

Centre for Advanced Macromolecular Design (CAMD), School of Chemical Engineering, University of New South Wales, Kensington, Sydney, New South Wales 2052, Australia

Supporting Information

ABSTRACT: Doubly thermoresponsive polymers consisting of a poly[oligo(ethylene glycol) methyl ether methacrylate] (POEGMA) block displaying UCST behavior in alcohols and a block of poly(*N*-isopropylacrylamide) (PNIPAM) or poly(*N*,*N*-diethylacrylamide) (PDEAM), each of which has an LCST in water, were synthesized using RAFT polymerization followed by simultaneous activated ester/amine and nucleophilic thiol−ene postpolymerization conversions. Upon heating aqueous solutions of POEGMA-*b*-PNIPAM, ^{1}H NMR spectroscopy confirmed a sudden decrease of the PNIPAM signals at the LCST, indicating dehydration and chain collapse. Dynamic light scattering (DLS) and turbidity measurements observed the macroscopic phase separation of the PNIPAM block at the same temperature. In 2-propanol, ^{1}H NMR spectroscopy showed a gradual decrease of the POEGMA signals over a range of more than 30 °C during its UCST transition, indicating early stages of chain crumpling up to 20 °C above the macroscopic phase separation. The OEG side chains were found to collapse onto the backbone starting at the ester linkages, indicating the most unfavorable enthalpic polymer−solvent interactions occur adjacent to the ester group. Although the diblock copolymers displayed a strong concentration-dependent cloud point, ^{1}H NMR spectroscopy revealed a concentration-independent desolvation, indicating the potential for applications that are not based on phase separation but on changes of polymer conformation. The phase separation occurred within a narrow temperature range of ∼6 °C as evidenced by turbidity and DLS. This transition could be exploited to self-assemble POEGMA-*b*-PDEAM into micellar structures with POEGMA cores in 1-octanol. Cooling to ∼15 °C below the cloud point was necessary to produce compact structures. Upon heating, the aggregates remained compact until redissolving entirely within a range of 1 °C, making the UCST of POEGMA in alcohols a valuable tool for reversible self-assembly applications.



INTRODUCTION

Thermally responsive, smart materials have been receiving significant attention from various research fields including bioconjugate chemistry,[1] biomedicine,[2] sensors,[3−5] molecular actuators,[6] and separation technology.[7] The majority of these polymers display an LCST-type transition in aqueous solution; i.e., they phase separate upon heating. Prominent examples are poly(*N*-isopropylacrylamide) (PNIPAM, $LCST_{H_2O}$ ∼ 32 °C),[8] poly(*N*,*N*-diethylacrylamide) (PDEAM, $LCST_{H_2O}$ ∼ 33 °C),[9] and various (meth)acrylic poly(ethylene glycol) (PEG) analogues, such as poly[oligo(ethylene glycol) methyl ether methacrylate] ($M_{monomer}$ ∼ 300 g/mol) (POEGMA, $LCST_{H_2O}$ ∼ 64 °C).[10−13] The opposite, UCST-type behavior involving phase separation upon cooling is less common in polar solvents. Examples of polysulfobetaines[14,15] and certain amide functional polymers[16−19] display UCSTs in water, while poly(methyl methacrylate)[4,20] and some polyoxazolines[21,22] display UCSTs in water/alcohol mixtures. POEGMA was recently shown to undergo UCST transitions in aliphatic alcohols with the critical temperature increasing strongly with an increasing alcohol chain length.[23] Pioneered by Armes[24,25] and Laschewsky,[26,27] doubly thermoresponsive diblock copolymers consisting of an LCST-type and a UCST-type block have been employed for the temperature-controlled formation of micelles and inverted micelles.[21,28−33]

Although often considered direct opposites, LCST and UCST transitions have quite different theoretical foundations.[34] According to the solution theory by Flory and Huggins, a phase separation can only occur in a system featuring unfavorable enthalpic interactions between polymer segments and solvent molecules. In such a case the mixing entropy will still outbalance the positive enthalpy at low polymer concentrations. At thermodynamic equilibrium, a mixture of a very small amount of polymer in a very large amount of solvent will therefore consist of a single phase. For a given nonextreme concentration the type of phase transition (LCST or UCST) then depends on the temperature dependence of the mixing

Received: February 22, 2012
Revised: March 18, 2012
Published: April 2, 2012

ACS Publications © 2012 American Chemical Society

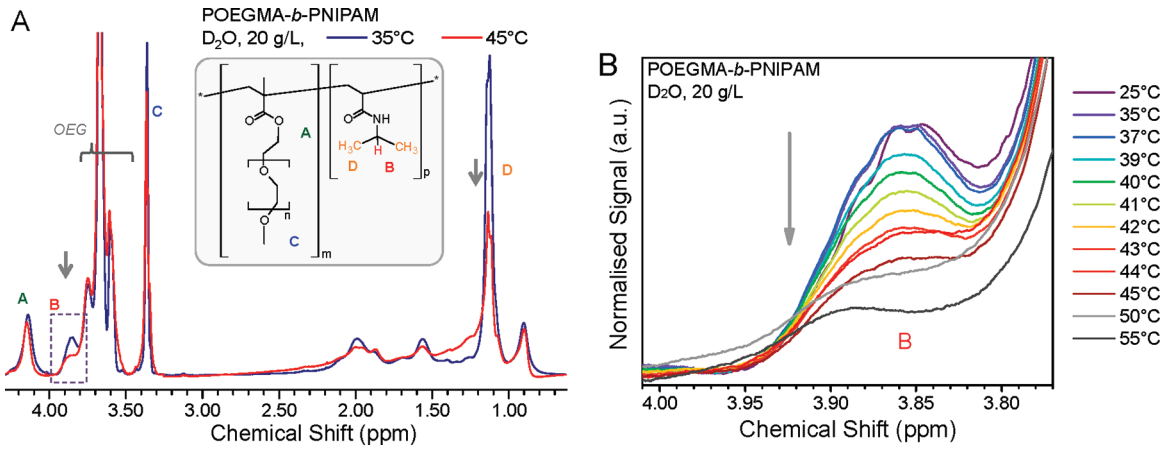


Figure 1. Variable temperature ^{1}H NMR measurements of POEGMA-*b*-PNIPAM in D_2O. (A) Overlay of NMR spectra at 35 and 45 °C showing the decrease and broadening of the PNIPAM signals above the critical temperature. (B) Section (dashed rectangle in part A) showing the decrease of the *N*-isopropylmethine proton with increasing temperature.

enthalpy or the associated interaction parameter χ. For an LCST transition, χ increases with temperature, making the polymer solvophobic above a critical temperature. The phase transition is driven by a gain of overall entropy when the dense, highly ordered solvation shell around the polymer is released into bulk water. LCST transitions usually occur sharply, and the critical temperatures of polymers such as PNIPAM[35] or POEGMA[13] in water have been shown to display very low concentration dependences. A UCST type transition, on the other hand, can occur when χ is positive and does not vary strongly with temperature. Upon cooling a solution, the entropic contribution favoring a mixing gradually decreases, allowing the unfavorable enthalpic term to dominate, which causes a phase separation. Pietsch, Hoogenboom, and Schubert recently exploited the gradual UCST transition of PMMA in ethanol/water for temperature sensing. The authors incorporated solvatochromic dyes into PMMA which allowed for a sensing regime of ∼30 °C while the PMMA chains gradually became insoluble upon cooling.[4]

As a PEG analogue, POEGMA is an interesting material not just because of its tunable LCST and UCST behaviors but also because of its well-established biocompatibility and nontoxicity.[11,12,36] The UCST behavior in alcohols presents a promising opportunity for directed self-assembly potentially leading to structures that might not be available easily through other techniques. However, apart from basic turbidity measurements, the solution properties of POEGMA in alcohols have not been further characterized. Whereas LCST-type polymers are frequently employed in thermally triggered self-assembly, the exploitation of the UCST of POEGMA in alcohols represents a complementary trigger for self-directed assembly that should be considered.

NMR spectroscopy is an expedient method for the observation of phase transitions of polymers and is routinely used to study LCST transitions of (co)polymers and mixtures thereof.[37−39] Through a broadening and disappearance of peaks, ^{1}H NMR spectroscopy gives direct information on the solvation of discrete structural units of (co)polymers. NMR spectroscopy has also been shown to be an alternative method to dynamic light scattering for verifying the self-assembly of pH responsive copolymers.[40]

Herein, we report on the synthesis of two diblock copolymers, POEGMA-*b*-PNIPAM and POEGMA-*b*-PDEAM, employing a combination of RAFT polymerization and the activated ester/amine and thiol−ene conjugation concepts. POEGMA is completely soluble in water during the LCST transitions of PNIPAM and PDEAM, while the latter two species remain soluble in 2-propanol in which POEGMA displays a UCST transition. Using these doubly thermoresponsive copolymers, we investigated the phase transitions in (deuterated) water and 2-propanol by ^{1}H NMR spectroscopy, turbidity, and DLS. In each case, the soluble blocks stabilized aggregates and served as an internal reference in the NMR experiments. Insights into the gradual desolvation of the POEGMA blocks during its UCST transition and a direct comparison with the prototypical smart polymer PNIPAM were possible on the same AB diblock copolymer. Concentration-dependent measurements showed that the phase transition cannot be observed by NMR spectroscopy and suggested that chain collapse and phase separation should be regarded separately for POEGMA in alcohols. Finally, implications of the gradual UCST transition and the potential for self-assembly were investigated in 1-octanol.

EXPERIMENTAL SECTION

Methods. Size exclusion chromatography (SEC) was performed on a Shimadzu system with four phenogel columns in THF operating at a flow rate of 1 mL/min. Chromatograms were analyzed by Cirrus SEC software version 3.0. The system was calibrated with a series of narrow molecular weight distribution polystyrene standards with molecular weights ranging from 0.58 to 1820 kg/mol.

Dynamic light scattering (DLS) measurements were performed on a Malvern Zetasizer Nano ZS at a scattering angle of 173° and analyzed by Malvern Zetasizer Software version 6.20. Measurements in alcohols were corrected for temperature-dependent viscosities for each temperature individually using the empirical relation η(2-propanol) = $10^{[-0.7009+841.50\times T^{-1}-6.068\times10^{-3}\times T+8.2964\times10^{-6}\times T^2]}$ [41] and η(1-octanol) = $9.653\times10^{-3}\times\exp[811.748\times T^{-1}+346920\times T^{-2}]$,[42] where η is the viscosity in cP and T is the temperature in K.

NMR spectroscopic measurements were performed on a Bruker DPX 300 instrument and evaluated using MestReC 4.7.0.0 software. For measurements in $CDCl_3$, the internal solvent signal was used as a standard (δ = 7.260 ppm). For measurements at variable temperatures in 2-propanol-d_8, the residual solvent signal of the methyl groups was set to 1.095 ppm. Samples were cooled and allowed to equilibrate at each temperature for at least 15 min prior to measurement. Curves at each temperature were normalized to the integral of the residual OH solvent signal. Integrals were evaluated in the following limits (see

dx.doi.org/10.1021/ma300374y | *Macromolecules* 2012, 45, 3221−3230

Figure 1 for assignment): oligo ethylene glycol (OEG) methylene (A) 4.265−4.060 ppm; $CHMe_2$ (B) 4.060−3.923 ppm; OEG 3.858−3.470 ppm, OEG methoxy (C) 3.470−3.278 ppm. Values were plotted relative to the integrals at 30 °C which were normalized to 100%. Measurements at variable temperatures in D_2O were performed by heating samples and allowing them to equilibrate for at least 15 min at each temperature prior to measurements. Because of the shifting of the internal HDO resonance signal with temperature the chemical shift of the OEG-methoxy group was used as a reference and set to 3.360 ppm at each temperature, in good agreement with the chemical shifts observed in $CDCl_3$ and 2-propanol-d_8. The curves were normalized to the integral of the OEG methyl group in the limits of 3.420−3.300 ppm, which therefore remained constant with temperature. The integral of the *N*-isopropylmethine group in the limits of 3.950−3.812 ppm was plotted relative to its value at 25 °C which was normalized to 100%.

Transmission electron microscopy (TEM) was performed on a Jeol 1400 instrument with an accelerating voltage of 100 kV. Samples in cold 1-octanol were prepared by cooling a solution (5.0 g/L) to 0 °C, dropping two drops onto a carbon-coated TEM grid on a tissue and letting it dry for 1 week in the fridge.

Turbidity measurements were performed on a Varian Cary 300 Scan spectrophotometer equipped with a Cary temperature controller and a Peltier heating element in quartz cuvettes of 10 mm path length at a wavelength of 520 nm. Heating rates were 1 °C/min for all measurements except for POEGMA-*b*-PNIPAM in D_2O at 20 g/L

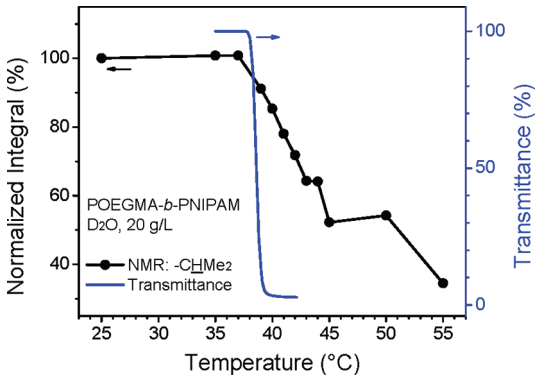


Figure 2. Relative decrease of the NMR integral of the *N*-isopropylmethine hydrogen in POEGMA-*b*-PNIPAM upon heating (black curve, left axis) and turbidity measurement (blue curve, right axis) showing the concomitant dehydration on a molecular level and clouding of the solution.

(Figure 2) which was heated at 0.1 °C/min to minimize a heating rate shift. For clear solutions (cold water; warm alcohol) the baseline was corrected to zero absorbance, *A*. Transmittance, $T = 10^{-A}$, was plotted against temperature, and cloud points were determined at 50% transmittance or at the average of maximal and minimal transmittance for samples of which the transmittance did not decrease to ∼0%.

Materials. All chemicals were purchased from Sigma-Aldrich at the highest available purity and used as received unless stated otherwise. Oligo(ethylene glycol) methyl ether methacrylate with an average M_n of 300 g/mol (OEGMA) was filtered through basic alumina to remove stabilizers. 2,2′-Azobis(isobutyronitrile) (AIBN) was recrystallized from methanol and stored at −25 °C until needed. 4-(4-Cyanopentanoic acid) dithiobenzoate (CPADB)[43] and pentafluorophenyl acrylate (PFPA)[44] were synthesized following literature procedures.

Synthesis of Poly[oligo(ethylene glycol) methyl ether methacrylate] (POEGMA). 2.25 g (7.5 mmol) of OEGMA, 8.2 mg (0.05 mmol) of AIBN, 83.7 mg of CPADB (0.3 mmol), and 3.0 mL of DMF were combined in a round-bottom flask which was capped with a rubber septum and nitrogen was bubbled through the solution for 20 min. The flask was then placed into a preheated oil bath at 80 °C and stirred overnight. POEGMA was isolated by precipitation into hexane. Yield 1.65 g (73%). M_n (SEC) = 6.3 kg/mol, PDI (SEC) = 1.18. ^{1}H NMR ($CDCl_3$) δ/ppm = 4.06 (bs, 2 H, −C(=O)OC$\underline{H}_2$−), 3.73−3.45 (m, ∼15 H, OEG), 3.36 (bs, 3 H, OEG-CH_3), 2.06−0.65 (m, 5 H, backbone).

Poly[oligo(ethylene glycol) methyl ether methacrylate]-*b*-poly(pentafluorophenyl acrylate) (POEGMA-*b*-PPFPA). POEGMA-*b*-PPFPA was prepared following a literature procedure.[45] Briefly, POEGMA was used as a macro-CTA for the polymerization of PFPA. The product POEGMA-*b*-PPFPA was isolated by precipitation into hexane. M_n (SEC) = 14.8 kg/mol, PDI (GPC) = 1.37. ^{1}H NMR ($CDCl_3$) δ/ppm = 4.08 (bs, 2 H, −C(=O)OC$\underline{H}_2$−), 3.81−3.50 (m, ∼15 H, OEG), 3.38 (bs, 3 H, OEG-CH_3), 2.93−0.65 (m, backbone). ^{19}F NMR ($CDCl_3$) δ/ppm = −153.6 (bs, 2 F, ortho), −157.1 (bs, 1 F, para), 162.6 (bs, 2 F, meta)

Conversion of POEGMA-*b*-PPFPMA into POEGMA-*b*-PNIPAM and POEGMA-*b*-PDEAM. 292 mg of POEGMA-*b*-PPFPA was dissolved in 5.0 mL of THF. 416 μL of isopropylamine or 560 μL of diethylamine (5.41 mmol) and 113 μL of triethylamine (0.81 mmol) were added, and the mixtures stirred at RT overnight. 200 μL of the reaction mixture was taken out and diluted with 450 μL of $CDCl_3$ for ^{19}F NMR analysis which showed the complete disappearance of the PFP ester peaks and instead the signals of free PFP−OH at δ/ppm = −170.4 (2 F, ortho), −171.5 (2 F, meta), and −189.1 (1 F, para). The NMR samples were recombined with the reaction mixtures and purified by dialysis against methanol in 3500 g/mol MWCO regenerated cellulose membranes for 3 days with solvent changes twice per day. The solvent was removed, a small amount of water was added, and the products were freeze-dried.

POEGMA-*b*-PNIPAM. Yield 184.8 mg (91%), M_n (SEC) = 12.3 kg/mol, PDI (GPC) = 1.22. ^{1}H NMR ($CDCl_3$) δ/ppm = 4.08 (bs, −C(=O)OC$\underline{H}_2$−), 3.98 (bs, −NHC$\underline{H}$(CH_3)$_2$), 3.81−3.47 (m, OEG), 3.37 (bs, OEG-CH_3), 3.00−0.65 (m, backbone), 1.12 (bs, −NHCH($C\underline{H}_3$)$_2$). ^{19}F NMR ($CDCl_3$): no signals.

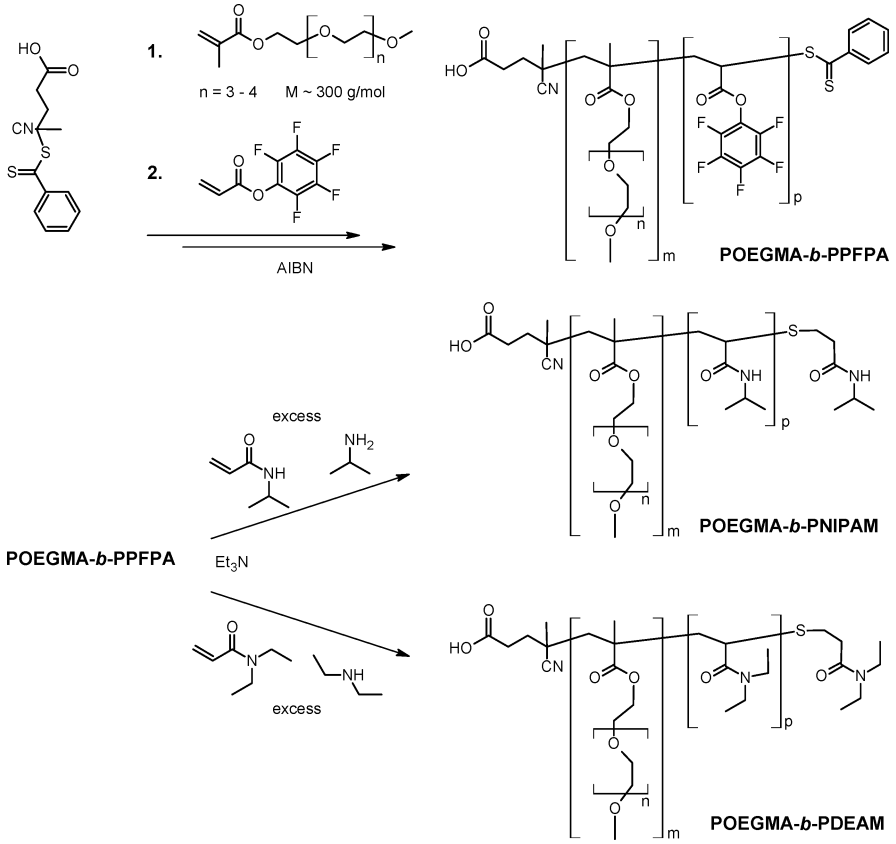
POEGMA-*b*-PDEAM. Yield 206.7 mg (92%), M_n (SEC) = 11.5 kg/mol, PDI (SEC) = 1.16. ^{1}H NMR ($CDCl_3$) δ/ppm = 4.08 (bs, −C(=O)OC$\underline{H}_2$−), 3.80−2.95 (m, OEG, −N($C\underline{H}_2CH_3$)$_2$), 2.95−0.65 (m, backbone), 1.07 (bs, −N($CH_2C\underline{H}_3$)$_2$). ^{19}F NMR ($CDCl_3$): no signals.

RESULTS AND DISCUSSION

Synthesis. An overview of the synthesis of the target diblock copolymers is given in Scheme 1. Reversible addition−fragmentation chain transfer (RAFT) polymerization of oligo(ethylene glycol methyl ether) methacrylate (OEGMA, monomer molecular weight = 300 g/mol) was employed to prepare a macro-RAFT agent with a molecular weight of 6.3 kg/mol and a PDI of 1.18. A sequential RAFT polymerization with pentafluorophenyl acrylate (PFPA) was used to prepare the diblock copolymer POEGMA-*b*-PPFPA with a molecular weight of 14.8 kg/mol and a PDI of 1.37. SEC showed a shift of the entire POEGMA peak toward higher molecular weight, as shown in Figure S1 of the Supporting Information, confirming successful block copolymer formation. In a subsequent postpolymerization modification, the activated PFP esters of the second block were converted into amides with either *N*-isopropylamine or *N*,*N*-diethylamine. Simultaneously, the dithioester end groups of the AB diblock copolymer were aminolyzed, and the resulting thiols were reacted in situ with *N*-isopropylacrylamide or *N*,*N*-diethylacrylamide in nucleophilic thiol−ene reactions.[46−48] This procedure avoided side reactions of the terminal thiols, e.g. oxidative coupling, and produced end groups that were chemically indistinct from the repeat units of the second block. The influence of end groups on the thermal behavior of the copolymers in water or alcohols could thus be neglected. The conversion of the PFP esters with amines to give amides was followed by ^{19}F NMR spectroscopy. The complete absence of fluorine signals confirmed the successful

dx.doi.org/10.1021/ma300374y | *Macromolecules* 2012, 45, 3221−3230

Scheme 1. Synthesis of POEGMA-*b*-PNIPAM and POEGMA-*b*-PDEAM by RAFT Polymerization and Subsequent Simultaneous Activated Ester/Nucleophilic Thiol−Ene Chemistry



aminolysis of the esters followed by a complete removal of the pentafluorophenol side product by dialysis (see Figure S2). The postpolymerization approach thus enabled the synthesis of two diblock copolymers with the same degrees of polymerization. POEGMA-*b*-PNIPAM was found to have a molecular weight of 12.3 kg/mol with a PDI of 1.22, while the sister polymer POEGMA-*b*-PDEAM had a molecular weight of 11.5 kg/mol and a PDI of 1.16. Both copolymers had similar weight ratios of each block. SEC traces, shown in Figure S1, showed monomodal size distributions and low PDIs, indicating that no disulfide coupling had taken place during aminolysis.

Solution Behavior in Water. The thermally triggered micellization of diblock copolymers consisting of a soluble block and an LCST-type block—especially PNIPAM—is a well-established technique.[49] Here, the solution behavior in water is briefly discussed to confirm the expected collapse of the PNIPAM block and to provide a direct comparison for the behavior of the diblock copolymers in alcohol. POEGMA-*b*-PNIPAM was analyzed by variable temperature ^{1}H NMR spectroscopic measurements at a concentration of 20 g/L in D_2O. Spectra measured at 35 and 45 °C are shown in Figure 1A. At 35 °C (blue spectrum) the PNIPAM block had not collapsed yet—seen from a comparison with a spectrum measured in $CDCl_3$ and from turbidity data discussed below. The increase of the phase transition temperature compared to the well-documented value of 32 °C, known for PNIPAM homopolymers,[8] was obviously caused by the hydrophilic POEGMA block.[49,50] In the spectrum measured at 45 °C (red spectrum) the characteristic signals of the POEGMA block had not changed. However, the signals attributed to the PNIPAM block, viz., the methine signal (denoted B) at 3.86 ppm and the methyl signal (D) at 1.10 ppm, had decreased and broadened due to dehydration. Additionally, the backbone signals from 2.20 to 1.20 ppm had flattened somewhat due to the PNIPAM backbone contribution to these peaks. The decrease of the methine proton signal (B) with temperature is shown in Figure 1B. The integrals of this peak, normalized to the value at 25 °C, are plotted in Figure 2 (black curve). During heating, the integral remains unchanged until it drops suddenly at 39 °C, where the chains lose hydration and collapse. A turbidity measurement was performed on the same solution in D_2O at a heating rate of 0.1 °C/min (blue curve in Figure 2), showing a sharp decrease of transmittance reaching 50% at 38.6 °C. It should be noted that the POEGMA block prevented a final precipitation of the phase-separated PNIPAM with the transmittance decreasing to ~2.8% at 42 °C. Most importantly, the molecular event observed by NMR, i.e. dehydration, and the macroscopic event observed by UV−vis, i.e. phase separation, occur at the same temperature. This is not unexpected;[49] PNIPAM has been receiving great attention for its sharp transition for decades,[8,35] and NMR spectroscopy has been shown to be a suitable method for monitoring such phase transitions.[38,39]

Solution Behavior in Alcohol. After the sharp PNIPAM LCST transition of POEGMA-*b*-PNIPAM had been confirmed in water, the solution behavior of POEGMA-*b*-PNIPAM and POEGMA-*b*-PDEAM in alcohols was investigated. First, the UCST transition of POEGMA was assessed by ^{1}H NMR and UV−vis spectroscopy and DLS on POEGMA-*b*-PNIPAM in (deuterated) 2-propanol. Differences in phase transition

dx.doi.org/10.1021/ma300374y | *Macromolecules* 2012, 45, 3221−3230

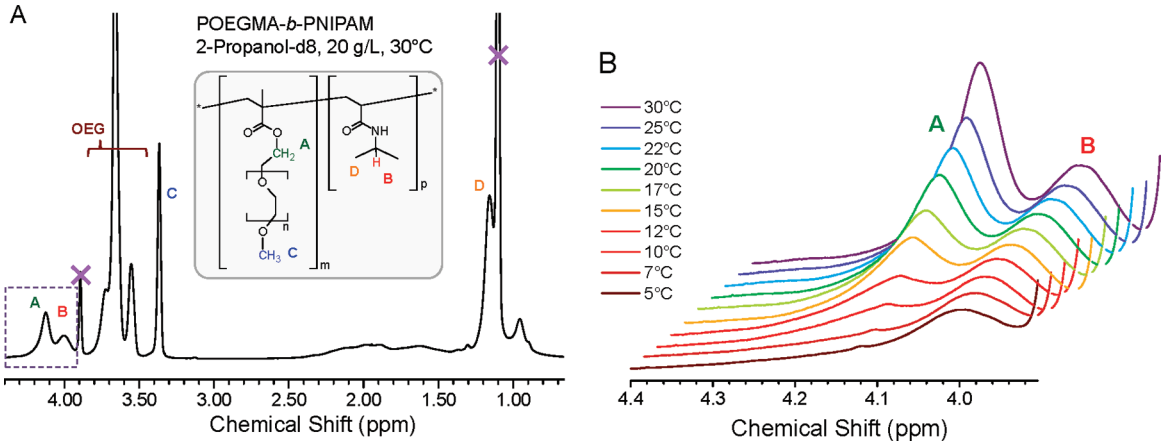


Figure 3. Variable temperature ^{1}H NMR measurements of POEGMA-*b*-PNIPAM in 2-propanol-d_8. (A) Spectrum at 30 °C with assigned peaks. Residual solvent signals are crossed out. (B) Sections of spectra (dashed rectangle in part A) showing the decrease of the peak corresponding to the OEG methylene group adjacent to the ester moiety during cooling.

behavior between deuterated and nondeuterated solvents have been shown to exist for the PNIPAM–H_2O/D_2O system.[51] However, these differences are small, and for 2-propanol, in which the mass percentage of H/D is greatly reduced compared to H_2O/D_2O, the isotope effect was neglected. Figure 3 shows ^{1}H NMR spectra measured on a 20 g/L sample. Apart from slightly shifted resonance frequencies, the spectrum at 30 °C, shown in Figure 3A, is in good agreement with the spectra measured in D_2O at 25 °C or in $CDCl_3$ at 25 °C, indicating that both blocks are molecularly dissolved and fully solvated. Upon cooling the solution, a decrease of most of the signals corresponding to the POEGMA block was observed, while the PNIPAM signals did not change until cooled well below the phase separation temperature of POEGMA (vide infra). Figure 3B shows the signals of the OEG methylene group closest to the backbone, denoted A, at 4.12 ppm, and the signal of the PNIPAM methine group, denoted B, at 4.01 ppm, at variable temperatures. It can clearly be seen that the signal arising from the POEGMA block decreases with temperature, indicating the loss of solvation during the UCST-type transition. In agreement with the solubility of PNIPAM in 2-propanol even at low temperatures, signal B does not change over the monitored temperature range.

In order to gain closer insights into the transition of POEGMA in alcohols, four NMR integrals were evaluated during the cooling of POEGMA-*b*-PNIPAM. Figure 4 shows

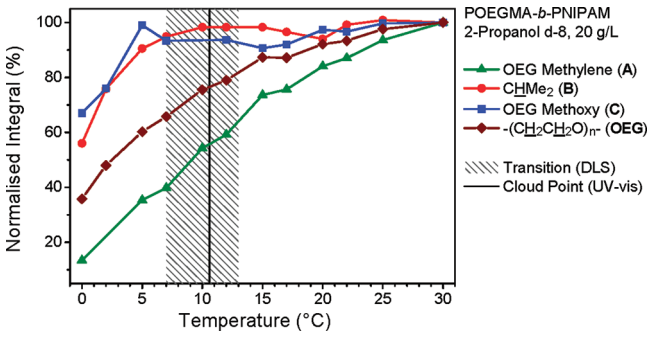


Figure 4. Normalized integrals of four NMR signals as assigned in Figure 3A in dependence of temperature; value of cloud point, and temperature regime in which a steep increase of average size was found by DLS.

the integrals, normalized to their values at 30 °C, of the signals A and B (mentioned above, green and red plot, respectively) and of the methoxy group located at the far end of the OEG side chains (denoted C, 3.36 ppm, blue plot) and of the multiplet in the range of 3.86–3.50 ppm, which corresponds to the OEG chain excluding groups A and C (denoted OEG, brown plot). Also shown in Figure 4 is the cloud point measured by UV–vis (10.6 °C, black vertical line). The turbidity measurement of the sample (shown in Figure S3 of the Supporting Information) showed a decrease of transmittance between 13 and 8 °C, indicating macroscopic phase separation and formation of aggregates. In agreement with this, DLS showed a (number-average) size increase from ~6 nm at 14 °C (unimers) to ~50 nm at 4 °C (micellar aggregates); this temperature region is shaded in Figure 4. In contrast to the PNIPAM signals in D_2O as described above, there is no sudden decrease of POEGMA integrals. From 30 °C downward, the integral of methylene group A decreases in an almost linear fashion (green curve), reaching 13% of its original value at 0 °C. Similarly, but less pronounced, the OEG integral (brown curve) also decreases gradually with decreasing temperatures with a slightly steeper slope at lower temperatures, dropping to 36% of its original value when the temperature is decreased to 0 °C. The results show the broad temperature range (spanning at least 30 °C) in which the solubility change of POEGMA takes place. This range is similar to the one observed for PMMA in ethanol/water.[4] Surprisingly, the OEG methoxy group (C, blue curve) does not undergo desolvation when the temperature is decreased, with its integral remaining above 92% over the entire temperature region from 30 to 5 °C. As mentioned above, the PNIPAM block remains soluble in cold alcohol, and its integral (B, red curve) does not decrease from its value at 30 °C until ~5 °C. Below 5 °C, the phase-separated POEGMA cores can be expected to collapse further, thus restricting the movements and increasing the relaxation times of the PNIPAM chains causing all integrals to drop. The striking feature is that there is no obvious connection between the phase transition observed by UV–vis and DLS and the molecular events observed by ^{1}H NMR spectroscopy. Phase separation occurred when the integral value of group A had reached ~54% of its original value. Apart from a decrease of all integrals well below the phase separation temperature, ^{1}H NMR spectroscopy gives no

dx.doi.org/10.1021/ma300374y | *Macromolecules* 2012, 45, 3221–3230

evidence that phase separation of the POEGMA blocks had occurred.

Similar results were obtained for the diblock copolymer POEGMA-*b*-PDEAM at a concentration of 20 g/L in (deuterated) 2-propanol (Figure 5). For this material, the

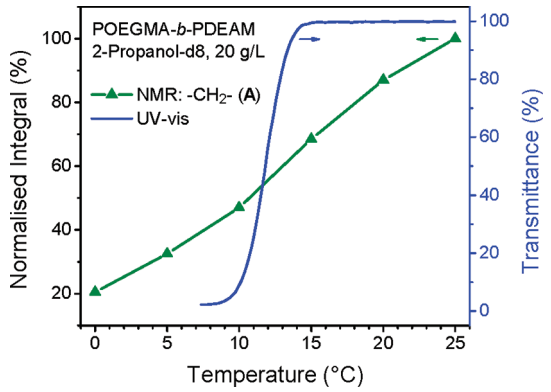


Figure 5. Cooling of POEGMA-*b*-PDEAM in 2-propanol: integral of NMR signal A (methylene group adjacent to ester linkage, green curve, left axis) and turbidity measurement (blue curve, right axis).

integral of group A also gradually decreased with decreasing temperature, unperturbed by the phase transition that was observed by turbidity at 11.8 °C. At this temperature, the integral of signal A had decreased to 55% of its value at 25 °C, showing that changing the second block did not have an impact on the solution behavior of POEGMA.

At high temperatures, where 2-propanol is a thermodynamically good solvent for POEGMA, this block can be expected to be in an expanded coil conformation with the OEG side chains extending like spokes from the backbone. The development of the integrals A, C, and OEG with decreasing temperature shows the gradual collapse of the OEG side chains onto the backbone, beginning at the ester linkage. This causes a solvation gradient along the OEG side chains which steepens with decreasing temperature as indicated by the steeper decrease of signal A compared to the OEG signal. A loss of solvent molecules in the immediate periphery of the backbone can also be expected to influence the conformation of the POEGMA chains. The theory of coil-to-globule collapse, followed by intrachain aggregation, of macromolecules in organic solvents has been extensively studied.[52−55] The process is generally considered to follow four stages: (1) intrachain crumpling, (2) knotting of individual chains, (3) intermolecular aggregation, and (4) interchain entanglement.[53] During the first two stages, the overall chain dimensions decrease only slightly.[55] The experimental observation of these events is challenging. Light scattering experiments on extremely dilute samples of high molecular weight (>1000 kg/mol) have been used to confirm a crumpled globular and a compact spherical globular state of single polymer chains in a polystyrene/cyclohexane system.[56−59] Assuming that POEGMA in 2-propanol undergoes a coil-to-globule collapse conforming with the general theory, the gradual desolvation starting ∼20 °C above the phase transition can be expected to reflect the crumpling stage of the POEGMA collapse. The knotting process (stage 2) is only observed for long polymers with a high degree of polymerization above a critical value and cannot be expected to occur for the present POEGMA block.[52,53,59] With the OEG side chains acting as a "sensor" for solvent being driven out of the surroundings of the backbone, qualitative information on the chain conformation and the early stage chain collapse can be obtained by NMR on a polymer several orders of magnitude too small, with respect to its molecular weight, for light scattering studies. A collapse starting at the ester linkage is in contrast to previous observations on PNIPAM, suggesting that chain collapse is initiated at the mobile chain ends.[60] For POEGMA in alcohol, the enthalpic interactions between solvent and OEG chains are obviously more unfavorable in closer proximity to the ester linkage. In this context it is noteworthy that a recent study by our group[61] has shown that the ester moiety in POEGMA also plays an important role in the dependence of the UCST on the value of *n* in the alcohol solvent $C_nH_{2n+1}OH$. While POEGMA displays UCST values that increase strongly with *n*, a formal replacement of the ester moieties with amide groups removes this dependence on *n*.

As mentioned in the Introduction, polymer concentration can have an enormous impact on the phase transition temperature. In Figure 6, the UCST-type cloud points of a

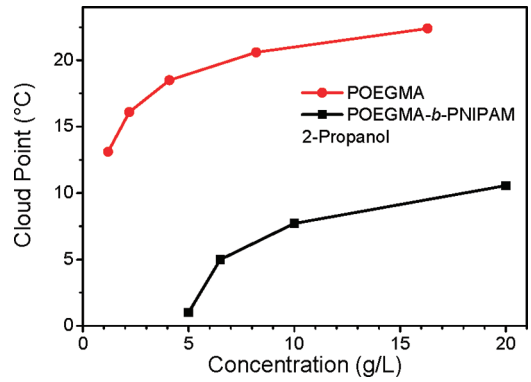


Figure 6. Concentration dependence of the phase separation of POEGMA and POEGMA-*b*-PNIPAM.

POEGMA sample, 8.7 kg/mol, taken from previous work[23] are plotted (red curve). As the concentration drops from 16.3 to 1.2 g/L, the cloud point decreases with an increasing slope, dropping by 9.3 °C from 22.4 to 13.1 °C. Also shown in Figure 6 are the cloud points measured for POEGMA-*b*-PNIPAM (black curve). The value for the 20 g/L sample, 10.6 °C, is indicated as a vertical line in Figure 4. The corresponding turbidity curves are shown in Figure S3 of the Supporting Information. It should be noted that the presence of the PNIPAM block prevented a precipitation and that the transmittance did not decrease to 0% due to the formation of large stabilized micellar aggregates. Same as homo POEGMA, POEGMA-*b*-PNIPAM displays a strong concentration-dependent UCST transition. However, the binodal is shifted toward higher concentrations with a large downward sloping occurring around 5 g/L. The presence of the PNIPAM block, enhancing the solubility and effectively diluting the POEGMA component in the solution is responsible for this difference.

The strong concentration dependence was also confirmed by DLS measurements. Figure 7 shows number-average size distributions of POEGMA-*b*-PNIPAM in 2-propanol at variable temperatures at 20 g/L (upper plot) and 5 g/L (lower plot). As mentioned above, the 20 g/L sample aggregates into micellar structures of ∼50 nm diameter in the temperature range of 13−7 °C, as is indicated by the shaded area in Figure 4. The DLS curves shown in Figure 7A show this size increase. As to be

dx.doi.org/10.1021/ma300374y | *Macromolecules* 2012, 45, 3221−3230

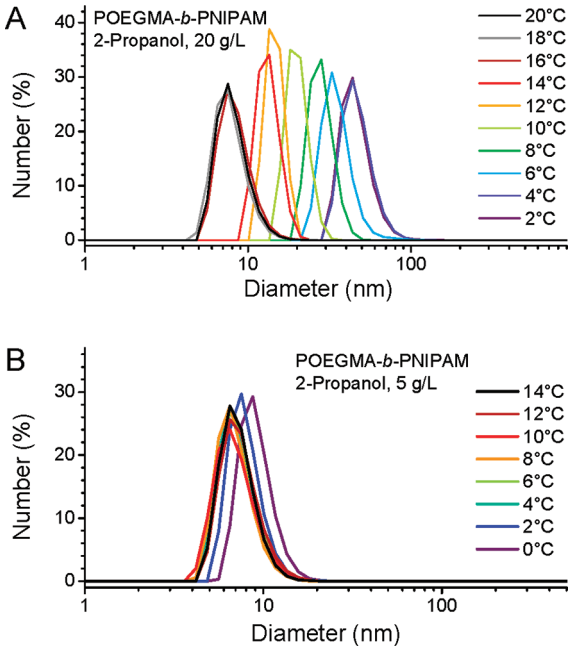


Figure 7. Number-average size distributions by DLS of POEGMA-*b*-PNIPAM in 2-propanol showing (A) a size increase due to phase separation and aggregation for a concentration of 20 g/L and (B) no formation of micellar aggregates above 0 °C for a concentration of 5 g/L.

expected for the 5 g/L sample with a much lower phase transition temperature, no such size increase was observed above 0 °C (the instrumental minimum temperature), with the size distribution indicating the presence of unimers of ∼7 nm diameter from 14 to 4 °C. At 2 and 0 °C, the average diameter increased to 8.0 and 9.2 nm, respectively. The cloud point of this sample of ∼1 °C is in reasonable agreement with the DLS data; differences in cooling rates or a certain temperature inaccuracy at the instrumental limit can be considered to cause the slight discrepancy.

Commonly, (co)polymers with a negligible concentration dependence on their stimulus responsive behavior are preferred—this being an important aspect in the success of PNIPAM and POEGMA in aqueous solution.[13] With ^{1}H NMR spectroscopy as a qualitative tool for monitoring the early stages of chain collapse of POEGMA in 2-propanol in hand, we next investigated the UCST transition of POEGMA-*b*-PNIPAM at 5 g/L. Recall that at 20 g/L the cloud point (i.e., the phase separation) occurred at 10.6 °C when integral A had decreased to 54% of its value at 30 °C. At a concentration of 5 g/L, the cloud point was 9.6 °C lower, at ∼1 °C. It might be expected that desolvation and the onset of the chain collapse would similarly be shifted to lower temperatures, causing interchain aggregation to occur at a similar percentage of remaining solvation than for the 20 g/L sample. Figure 8 compares the development of integrals A (green curves) and B (red curves) at a concentration of 20 g/L (light curves, open symbols) and 5 g/L (dark curves, solid symbols). All integrals were normalized to the values at 30 °C, at which temperature (apart from stronger residual solvent signals) the 5 g/L spectrum was virtually identical to the one measured at 20 g/L. Also indicated are the cloud points at 20 g/L (vertical gray line) and at 5 g/L (vertical black line). It can be seen that the concentration (within the observed range) does not impact the

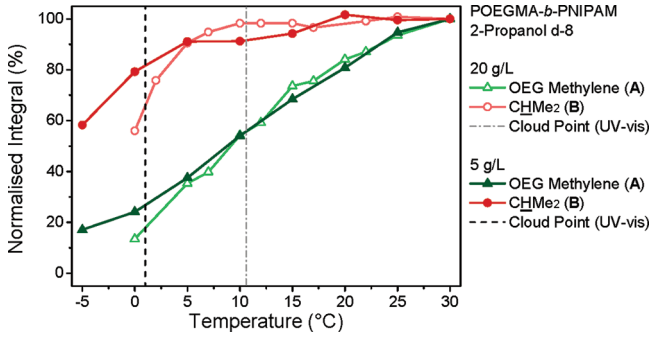


Figure 8. ^{1}H NMR Integrals of POEGMA methylene group (A) and PNIPAM methine group (B) in dependence of temperature at two concentrations.

gradual desolvation of the POEGMA blocks. The course of the integrals of group A is essentially identical for the two samples. At a concentration of 5 g/L, the macroscopic phase separation occurs when the ^{1}H NMR integral of the methylene groups adjacent to the ester linkages has decrease to ∼27% of its value at 30 °C. The collapse of the POEGMA blocks is thus further advanced than for the 20 g/L sample before intermolecular aggregation begins. Only at temperatures below the respective phase transitions was there a difference between the spectra at 20 and 5 g/L. As mentioned above, the interchain entanglement (stage 4 of the theory mentioned above) and globule compaction reduce the mobility of the entire diblock copolymer and thus also cause the ^{1}H NMR signals of the soluble PNIPAM block to decrease. It can be seen in Figure 8 that for the lower concentration sample this decrease occurs at lower temperatures than for the higher concentrated sample (red curves). Below 5 °C there is also a minimal difference between the two curves of signals A which can be attributed to the fact that at this temperature the 20 g/L sample had already undergone phase separation, causing a higher degree of overlapping of broadened NMR peaks.

These results suggest that desolvation (and implied chain collapse) is a material property and, as such, independent of concentration. The macroscopic phase separation, on the other hand, involving an interchain aggregation is strongly dependent on concentration and relies on the translational diffusion, collision of (partially collapsed) chains, and subsequent segmental diffusion.[53,62] For LCST-type transitions, complete chain collapse and phase transitions usually occur together within a narrow temperature range. Flowerlike micelles formed from telechelic hydrophobically modified PNIPAM have been shown to exhibit concentration independent dehydration temperatures above the strongly concentration-dependent cloud point temperatures.[63] Only on extremely dilute solutions have single chain collapses (without phase transitions) been observed.[35,51,64−66] With the smart materials arena being dominated by LCST-type systems such as PNIPAM or POEGMA in water, the elementary differences of UCST-type transitions in polar solvents should be noted. Although the cloud points of POEGMA in alcohol show a strong concentration dependence (and even more so in the diblock copolymer), a concentration-independent chain collapse is of importance for potential applications that do not rely on a macroscopic phase separation, but rather on the overall end-to-end distance of polymer chains. Examples include an end-to-end energy transfer[67,68] and the swelling of grafts on planar or spherical[69] surfaces or cross-linked networks.

dx.doi.org/10.1021/ma300374y | *Macromolecules* 2012, 45, 3221−3230

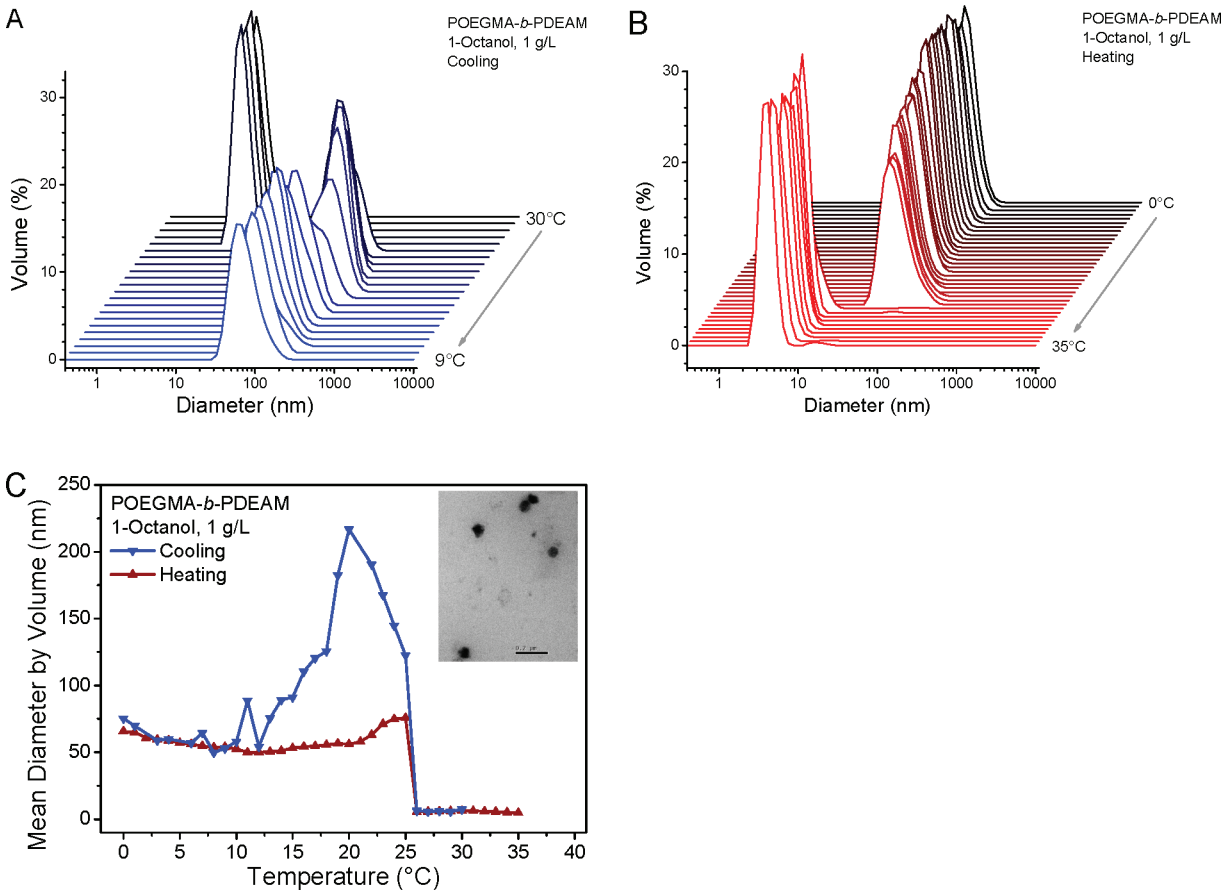


Figure 9. Self-assembly of POEGMA-*b*-PDEAM in 1-octanol monitored by DLS. Size distributions by volume during cooling (A), heating (B), and average diameters during cooling and heating in dependence of temperature (C) with a TEM image of a sample prepared at 0 °C (inset, scale bar 200 nm).

Self-Assembly. It is interesting to note that although ^{1}H NMR spectroscopy indicated that the gradual desolvation event for POEGMA occurs over a range of more than 30 °C, both DLS and UV−vis revealed a significantly narrow phase separation regime. This is a promising characteristic for potential self-assembly driven by a UCST phase separation. Commonly, concentrations lower than 20 g/L are used for the formation of well-defined micelles from AB diblock copolymers. For this reason, 1-octanol was used as solvent in which POEGMA has an increased UCST compared to 2-propanol. Therefore, at a lower concentration of 1 g/L, cloud points around RT could be exploited. The solubility of PNIPAM and PDEAM in 1-octanol at variable temperatures was confirmed by UV−vis and DLS (Figures S4 and S5 of the Supporting Information). Figure 9 shows the size evolution of POEGMA-*b*-PDEAM in 1-octanol during cooling (9A) and heating (9B). At 30 °C, the diblock copolymer is molecularly dissolved, and DLS shows unimers with a size of ∼6.0 nm (9A). At 25 °C, the diameter abruptly jumps to a value of more than 100 nm. There was no evidence of two populations at this phase transition temperature, suggesting that the majority of chains had aggregated. With further cooling, the (volume average) diameter further increased to a maximum of over 200 nm at 20 °C (Figure 9C). We attribute this to the formation of loosely aggregated clusters due to the fact that the POEGMA component is still solvated to a certain degree at this stage. In agreement with ^{1}H NMR measurements in 2-propanol-d_8 which suggested a further compaction of aggregates below the cloud point, DLS showed a diameter decrease upon further cooling to ∼12 °C, below which a diameter of ∼60 nm was observed (9A and 9C). This was attributed to the formation of micelles retaining a certain amount of solvent in their cores. Polydispersity indices (averaged from three DLS measurements at each temperature) ranged from 0.039 to 0.102 in the region of 0−10 °C, indicating micelles with a well-defined size distribution. TEM recorded of a sample dried at 0 °C (inset in Figure 9C) confirmed the presence of spherical aggregates of a similar diameter.

Upon heating, a different pathway was observed (9B). The diameter of the formed micelles stayed essentially constant, with a slight increase just before the dissolution into unimers at 25 °C. This suggests that a hysteresis similar to that found for LCST polymers[51,64] exists for POEGMA in alcohols. The POEGMA cores of the micelles stay intact and swell only slightly upon heating. Surprisingly, the disappearance and reformation of unimers occurred at 25 °C upon cooling and heating, respectively, showing no hysteresis of phase transition temperature. At 26 and 27 °C, a small population of micelles (less than 0.5 vol %) remained with the rest of the material being molecularly dissolved. These results show that defined micellar structures can indeed be obtained by exploiting the UCST transition of POEGMA in alcohols. However, due to the gradual transition from soluble to insoluble, cooling to a temperature ∼15 °C below the phase separation temperature was required to produce compact particles. These particles are

dx.doi.org/10.1021/ma300374y | *Macromolecules* 2012, 45, 3221−3230

then stable during heating, redissolving at a predetermined temperature.

CONCLUSION

The UCST transition of POEGMA in alcohols was investigated in detail by comparison of the solution behavior of the double thermoresponsive diblock copolymers POEGMA-*b*-PNIPAM and POEGMA-*b*-PDEAM in water and alcohols. In water, chain collapse and macroscopic phase separation of PNIPAM occurred together. In alcohol, the transition from soluble to insoluble for POEGMA during cooling occurred very gradually, with solvent being driven out of the periphery of the backbone over a range of ∼30 °C, indicating early stages of chain crumpling. The transition from soluble to insoluble was independent of concentration within a concentration range that strongly influences the macroscopic phase separation (cloud point). Below the phase separation, the ongoing desolvation caused a further compaction of aggregates, thus reducing overall polymer mobility and effecting aggregate diameters to decrease. During the heating of aggregates only a slight swelling was observed. The results suggest that for POEGMA in alcohol macroscopic phase separation and microscopic chain solvation and conformation should be treated separately. The narrow phase separation temperature and complete redissolution of aggregates are promising for the self-assembly of diblock copolymers leading to inverted structures with hydrophilic POEGMA cores.

ASSOCIATED CONTENT

Supporting Information

SEC traces of all polymers, ^{19}F NMR measurements, cloud point curves of POEGMA-*b*-PNIPAM in 2-propanol at varying concentration, DLS, and UV−vis measurements of PNIPAM and PDEAM in 1-octanol. This material is available free of charge via the Internet at http://pubs.acs.org.

AUTHOR INFORMATION

Corresponding Author

*E-mail: a.lowe@unsw.edu.au (A.B.L.); t.davis@unsw.edu.au (T.P.D.).

Notes

The authors declare no competing financial interest.

ACKNOWLEDGMENTS

P.J.R. kindly acknowledges Dr. Douglas Lawes of the Nuclear Magnetic Resonance Facility for help with variable temperature NMR measurements.

REFERENCES

(1) Gil, E. S.; Hudson, S. M. *Prog. Polym. Sci.* **2004**, *29*, 1173.
(2) Wei, H.; Cheng, S.-X.; Zhang, X.-Z.; Zhuo, R.-X. *Prog. Polym. Sci.* **2009**, *34*, 893.
(3) Uchiyama, S.; Kawai, N.; de Silva, A. P.; Iwai, K. *J. Am. Chem. Soc.* **2004**, *126*, 3032.
(4) Pietsch, C.; Hoogenboom, R.; Schubert, U. S. *Polym. Chem.* **2010**, *1*, 1005.
(5) Pietsch, C.; Hoogenboom, R.; Schubert, U. S. *Angew. Chem., Int. Ed.* **2009**, *48*, 5653.
(6) Li, C.; Gunari, N.; Fischer, K.; Janshoff, A.; Schmidt, M. *Angew. Chem., Int. Ed.* **2004**, *43*, 1101.
(7) Mori, T.; Umeno, D.; Maeda, M. *Biotechnol. Bioeng.* **2001**, *72*, 261.
(8) Schild, H. G. *Prog. Polym. Sci.* **1992**, *17*, 163.
(9) Idziak, I.; Avoce, D.; Lessard, D.; Gravel, D.; Zhu, X. X. *Macromolecules* **1999**, *32*, 1260.
(10) Hu, Z.; Cai, T.; Chi, C. *Soft Matter* **2010**, *6*, 2115.
(11) Lutz, J.-F. *Adv. Mater.* **2011**, *23*, 2237.
(12) Lutz, J.-F. *J. Polym. Sci., Part A: Polym. Chem.* **2008**, *46*, 3459.
(13) Lutz, J.-F.; Akdemir, Ö.; Hoth, A. *J. Am. Chem. Soc.* **2006**, *128*, 13046.
(14) Kudaibergenov, S.; Jaeger, W.; Laschewsky, A. In *Supramolecular Polymers Polymeric Betains Oligomers*; Springer: Berlin, 2006; Vol. *201*, p 157.
(15) Monroy Soto, V. M.; Galin, J. C. *Polymer* **1984**, *25*, 254.
(16) Nagaoka, H.; Ohnishi, N.; Eguchi, M. US Patent 7847047 B2, Chisso Corporation, Osaka, Japan, 2010.
(17) Ohnishi, N.; Furukawa, H.; Kataoka, K.; Katsuhiko, U. US Patent 7195925 B2, National Institute of Adanced Industrial Science and Technology, Chisso Corporation, 2007.
(18) Glatzel, S.; Laschewsky, A.; Lutz, J.-F. *Macromolecules* **2011**, *44*, 413.
(19) Seuring, J.; Bayer, F. M.; Huber, K.; Agarwal, S. *Macromolecules* **2011**, *45*, 374.
(20) Hoogenboom, R.; Rogers, S.; Can, A.; Becer, C. R.; Guerrero-Sanchez, C.; Wouters, D.; Hoeppener, S.; Schubert, U. S. *Chem. Commun.* **2009**, 5582.
(21) Hoogenboom, R.; Lambermont-Thijs, H. M. L.; Jochems, M. J. H. C.; Hoeppener, S.; Guerlain, C.; Fustin, C.-A.; Gohy, J.-F.; Schubert, U. S. *Soft Matter* **2009**, *5*, 3590.
(22) Hoogenboom, R.; Thijs, H. M. L.; Wouters, D.; Hoeppener, S.; Schubert, U. S. *Soft Matter* **2008**, *4*, 103.
(23) Roth, P. J.; Jochum, F. D.; Theato, P. *Soft Matter* **2011**, *7*, 2484.
(24) Weaver, J. V. M; Armes, S. P.; Bütün, V. *Chem. Commun.* **2002**, 2122.
(25) Bütün, V.; Liu, S.; Weaver, J. V. M; Bories-Azeau, X.; Cai, Y.; Armes, S. P. *React. Funct. Polym.* **2006**, *66*, 157.
(26) Arotcarena, M.; Heise, B.; Ishaya, S.; Laschewsky, A. *J. Am. Chem. Soc.* **2002**, *124*, 3787.
(27) Virtanen, J.; Arotcarena, M.; Heise, B.; Ishaya, S.; Laschewsky, A.; Tenhu, H. *Langmuir* **2002**, *18*, 5360.
(28) Maeda, Y.; Mochiduki, H.; Ikeda, I. *Macromol. Rapid Commun.* **2004**, *25*, 1330.
(29) Dimitrov, I.; Trzebicka, B.; Müller, A. H. E.; Dworak, A.; Tsvetanov, C. B. *Prog. Polym. Sci.* **2007**, *32*, 1275.
(30) Chang, Y.; Chen, W.-Y.; Yandi, W.; Shih, Y.-J.; Chu, W.-L.; Liu, Y.-L.; Chu, C.-W.; Ruaan, R.-C.; Higuchi, A. *Biomacromolecules* **2009**, *10*, 2092.
(31) Bai, Z.; He, Y.; Young, N. P.; Lodge, T. P. *Macromolecules* **2008**, *41*, 6615.
(32) Lee, H.-N.; Bai, Z.; Newell, N.; Lodge, T. P. *Macromolecules* **2010**, *43*, 9522.
(33) Boyer, C.; Stenzel, M. H.; Davis, T. P. *J. Polym. Sci., Part A: Polym. Chem.* **2011**, *49*, 551.
(34) Rubinstein, M.; Colby, R. E. *Polymer Physics*; Oxford University Press: New York, 2003; Chapter 4.
(35) Ding, Y.; Ye, X.; Zhang, G. *J. Phys. Chem. B* **2008**, *112*, 8496.
(36) Neugebauer, D. *Polym. Int.* **2007**, *56*, 1469.
(37) Starovoytova, L.; Spěváček, J.; Hanyková, L.; Ilavský, M. *Polymer* **2004**, *45*, 5905.
(38) Zeng, F.; Tong, Z.; Feng, H. *Polymer* **1997**, *38*, 5539.
(39) Deshmukh, M. V.; Vaidya, A. A.; Kulkarni, M. G.; Rajamohanan, P. R.; Ganapathy, S. *Polymer* **2000**, *41*, 7951.
(40) Vamvakaki, M.; Palioura, D.; Spyros, A.; Armes, S. P.; Anastasiadis, S. H. *Macromolecules* **2006**, *39*, 5106.
(41) Yaws, C. L. *Chemical Properties Handbook*; McGraw-Hill: New York, 1999; Chapter 22.
(42) Matsuo, S.; Makita, T. *Int. J. Thermophys.* **1989**, *10*, 833.
(43) Mitsukami, Y.; Donovan, M. S.; Lowe, A. B.; McCormick, C. L. *Macromolecules* **2001**, *34*, 2248.
(44) Eberhardt, M.; Mruk, R.; Zentel, R.; Théato, P. *Eur. Polym. J.* **2005**, *41*, 1569.

(45) Jochum, F. D.; Roth, P. J.; Kessler, D.; Theato, P. *Biomacromolecules* **2010**, *11*, 2432.
(46) Boyer, C.; Granville, A.; Davis, T. P.; Bulmus, V. *J. Polym. Sci., Part A: Polym. Chem.* **2009**, *47*, 3773.
(47) Hoyle, C. E.; Lowe, A. B.; Bowman, C. N. *Chem. Soc. Rev.* **2010**, *39*, 1355.
(48) Lowe, A. B. *Polym. Chem.* **2010**, *1*, 17.
(49) Zhang, W.; Shi, L.; Wu, K.; An, Y. *Macromolecules* **2005**, *38*, 5743.
(50) Roth, P. J.; Jochum, F. D.; Forst, F. R.; Zentel, R.; Theato, P. *Macromolecules* **2010**, *43*, 4638.
(51) Wang, X.; Wu, C. *Macromolecules* **1999**, *32*, 4299.
(52) Grosberg, A. Y.; Nechaev, S. K.; Shakhnovich, E. I. *J. Phys. (Paris)* **1988**, *49*, 2095.
(53) Grosberg, A. Y.; Kuznetsov, D. V. *Macromolecules* **1993**, *26*, 4249.
(54) Baysal, B. M.; Karasz, F. E. *Macromol. Theory Simul.* **2003**, *12*, 627.
(55) Halperin, A.; Goldbart, P. M. *Phys. Rev. E* **2000**, *61*, 565.
(56) Chu, B., Yu, J., Wang, Z., Ewen, B., Fischer, E., Fytas, G., Eds.; Springer: Berlin, 1993; Vol. *91*, p 142.
(57) Chu, B.; Ying, Q.; Grosberg, A. Y. *Macromolecules* **1995**, *28*, 180.
(58) Yu, J.; Wang, Z.; Chu, B. *Macromolecules* **1992**, *25*, 1618.
(59) Aseyev, V.; Tenhu, H.; Winnik, F.; Temperature Dependence of the Colloidal Stability of Neutral Amphiphilic Polymers in Water. In *Conformation-Dependent Design of Sequences in Copolymers II*; Khoklov, A. R., Ed.; Springer: Berlin, 2006; Vol. *196*, p 1.
(60) Chung, J. E.; Yokoyama, M.; Aoyagi, T.; Sakurai, Y.; Okano, T. *J. Control. Release* **1998**, *53*, 119.
(61) Chua, G. B. H.; Roth, P. J.; Duong, H. T. T.; Davis, T. P.; Lowe, A. B. *Macromolecules* **2012**, *45*, 1362.
(62) Piçarra, S.; Gomes, P. T.; Martinho, J. M. G. *Macromolecules* **2000**, *33*, 3947.
(63) Kujawa, P.; Segui, F.; Shaban, S.; Diab, C.; Okada, Y.; Tanaka, F.; Winnik, F. M. *Macromolecules* **2006**, *39*, 341.
(64) Wang, X.; Qiu, X.; Wu, C. *Macromolecules* **1998**, *31*, 2972.
(65) Wu, C.; Wang, X. *Phys. Rev. Lett.* **1998**, *80*, 4092.
(66) Xu, J.; Zhu, Z.; Luo, S.; Wu, C.; Liu, S. *Phys. Rev. Lett.* **2006**, *96*, 027802.
(67) Roth, P. J.; Haase, M.; Basche, T.; Theato, P.; Zentel, R. *Macromolecules* **2010**, *43*, 895.
(68) Hong, S. W.; Kim, D. Y.; Lee, J. U.; Jo, W. H. *Macromolecules* **2009**, *42*, 2756.
(69) Ieong, N. S.; Brebis, K.; Daniel, L. E.; O'Reilly, R. K.; Gibson, M. I. *Chem. Commun.* **2011**, *47*, 11627.

Macromolecules

Article

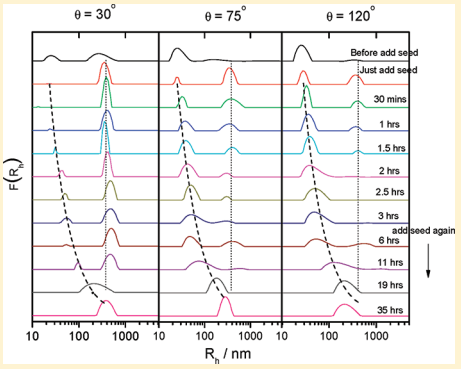
pubs.acs.org/Macromolecules

Mechanism of Narrowly Dispersed Latex Formation in a Surfactant-Free Emulsion Polymerization of Styrene in Acetone−Water Mixture

Zhiyong Li, He Cheng,* and Charles C. Han*

State Key Laboratory of Polymer Physics and Chemistry, Joint Laboratory of Polymer Science and Materials, Beijing National Laboratory for Molecular Sciences, Institute of Chemistry, Chinese Academy of Sciences, Beijing 100190, P. R. China

ABSTRACT: The mechanism of narrowly dispersed latex formation in a surfactant-free emulsion polymerization (SFEP) of styrene in acetone−water was studied by a combination of transmission electron microscopy (TEM) and dynamic light scattering (DLS). The critical nuclei were experimentally observed and the formation of narrowly dispersed PS latex is proved to be originated from competitive growth kinetics. Spherical nuclei were regenerated via a microphase inversion of PS oligomer in a 50% volume fraction acetone−water mixture at 70 °C. They followed a polydispersed log-normal distribution with $\bar{R}_s \sim 10.6$ nm and $\delta \sim 0.298$, and the smallest nucleus with $R_s \sim 1.1$ nm was similar to critical nuclei, with PS backbone (average chain length ∼6−7) repeat units) inside and sulfate groups to stabilize it at oligomer chain ends. Note that the spherical nuclei are not necessarily narrowly dispersed. Competitive growth kinetics makes smaller nuclei grow much faster than large nuclei in the subsequent polymerization process, resulting in narrowly dispersed PS latex. Time resolved dynamic light scattering (DLS) was used to verify this. Two kinds of PS seed particles which had already grown to the dimension of $\langle R_h \rangle \sim 300$ nm and ∼400 nm were added, separately, into two parallel surfactant-free emulsion polymerization batches of styrene in acetone−water mixture at 70 °C, when the average hydrodynamic radius of PS latex was about ∼20−30 nm. It was found that the size of ∼300 or 400 nm seed particles almost did not change, but the small size PS latex grew rapidly. Narrowly dispersed PS latex was finally obtained in the SFEP system, which supports the competitive growth mechanism proposed by Vanderhoff and co-workers.



1. INTRODUCTION

The mechanism of surfactant-free emulsion polymerization (SFEP) is a fundamental and classical problem in heterophase polymerization. The possibility of carrying out emulsion polymerization in the absence of emulsifiers stimulated the search for a general particle nucleation model beyond the assumption of micellar nucleation[1,2] for which no experimental proof exists. Harkins,[3−6] Priest,[7,8] and Goodwin[9,10] et al. have presented the homogeneous nucleation, coagulative nucleation and micellar nucleation model, which clearly indicated that the radical oligomers with hydrophobic chain backbone and charged end-groups precipitate or associate, absorb new radical oligomers and monomers to form primary particles, and aggregate until certain stability can be reached. In 1995, Tauer and Kuhn[11] proposed a completely different approach, that is, nucleation can be considered as multichain event and not as single chain event. At last, the SFEP process often leads to the formation of monodisperse latexes, which depends on the reaction recipe and conditions. However, two main puzzles remain, i.e., the critical dimension of nucleation was experimentally difficult to observe; and the origin of narrowly dispersed latex formation was not experimentally clarified either.

Although Vanderhoff et al.[12] predicted that the size of critical nuclei should be about 1.4 nm as early as 1985 (SFEP of styrene in water with potassium persulfate, KPS, as initiator), the experimental observation of critical nuclei is extremely difficult, if not impossible. On one hand,[13] microscopy in real space could not monitor the time dependent process of the emulsion polymerization; on the other hand, most of scattering techniques in reciprocal space failed to discriminate the generation of critical nuclei, as well. This is because that in the early stage of nucleation, monomer droplets (∼μm) and critical nuclei (∼nm) coexisted, the scattering from the former was overwhelming.

The origin of narrowly dispersed latex formation in surfactant-free emulsion polymerization is another puzzle. It was proposed in 1950 that if all particles are nucleated in a negligible short time, they can grow at the same rate, then narrowly dispsersed latex particles can be developed.[14] In fact, the nucleation process is not negligibly short. Although it was reported that the number of particles in SFEP gets a burst of $\sim 10^{13}$ mL^{-1} within a time gap of less than 1 s,[15] the data may be overestimated. There are two ways to calculate the particle number$\tilde{N}$. In the first approximation, the particle number$\tilde{N}$was calculated according to

$$\tilde{N} = C/\rho(\pi D^3/6) \quad (1)$$

Received: November 19, 2011
Revised: March 14, 2012
Published: March 28, 2012

 © 2012 American Chemical Society

where C is polymer concentration, ρ is polymer density, and D is diameter of particles measured from DLS or TEM. However, eqs 1 cannot be verified in the early stage of surfactant-free emulsion polymerization, because neither TEM nor DLS can measure the nuclei particle size, as demonstrated previously. In the second way[15]

$$\tau/\Delta\kappa = FD^4 \tag{2}$$

where τ is turbidity, scaling with $\tau \propto nD^6$ (n is the particle concentration, and D is the particle diameter), $\Delta\kappa$ is the difference between the calculated and experimental conductivity, and F is a complex constant that is fitted from off-line measured particle sizes which is only possible in the late stage of polymerization. Note that the error connected with the application of eqs 2 is greater in the early stage of SFEP (because of smaller τ). Therefore, both methods cannot accurately determine $\tilde{N}$ in the early stage of SFEP, and we cannot conclude that the small nuclei do not exist just because we cannot see them by DLS and TEM.

The present manuscript tries to contribute to better understanding of particle nucleation and growth in SFEP.

A microphase inversion (that is, PS oligomer was first dissolved in DMF, then added dropwise into an excess of acetone−water mixture, resulting in a transparent stable colloidal dispersion) of PS oligomer into 50% volume fraction of acetone−water mixture at 70 °C was used to generate spherical nuclei, experimentally. Wu and co-workers[16−18] have found that block copolymers or polymers with low amount and random distribution of charges along the chain (ionomers) can self-assemble in a selective solvent to form surfactant-free nanoparticles, which can be induced by chemical reaction, chain−chain complexation, and microphase inversion in addition to the normal controllable parameters (such as temperature and etc.). It was proved in these systems that the self-assembled structure is similar to its collapsed state in polymerization process.[19−21] Ganeva et al.[22] used amphiphilic RAFT (reversible addition−fragmentation chain transfer)-capped, acrylic acid and styrene block copolymers as stabilizers in emulsion polymerization. And they found that, further polymerization of these amphiphilic diblocks generates the final latex particles. These may suggest that it is possible to regenerate the nuclei formation process by directly self-assembly of oligomer in its polymerization environment.

On the other hand, narrowly dispersed PS latex may be grown from polydispersed PS nuclei via competitive growth kinetics which was pioneered by Vanderhoff and co-workers, with some further development by Morrison et al.[23−25] The volume growth of a particle is given by eq 3a, where K is assumed to be independent of particle size.

$$dV/dt = K\cdot R^x \text{ (a)}; \quad dR/dt = K'\cdot R^{x-2} \text{ (b)};$$
$$R^{3-x} - {R_0}^{3-x} = K''\cdot\Delta t \text{ (c)} \tag{3}$$

For the case that the size growth follows eqs 3b for spherical particles, it leads to the assumption that all Ks are independent of time (i.e., K, K', K'' only depend on polymerization conditions) after integration to eqs 3c. Note, the particle size is always the unswollen size; thus, using eqs 3a means the size dependence of the monomer concentration is neglected. D and D_0 are the sizes at the beginning and the end of polymerization with duration Δt, respectively. A closer inspection of eqs 3b and 3c reveals that if $x < 3$, smaller particles will grow faster and the particle size distribution is self-sharpening. Contrary to that, if $x > 3$, the distribution becomes broader as larger particles grow faster than smaller ones. However, if $x = 3$, particle growth does not depend on particle size.[23,24] So x should be a function of the particle radius (or volume). But for simplicity of discussion, x is often approximated as a volume independent parameter.

In this study, polydispersed spherical nuclei were observed experimentally after microphase inversion of styrene oligomer in 50% volume fraction of acetone−water mixture. They have a polydispersed log-normal distribution, and the smallest nucleus with a radius of ∼1.1 nm is similar to the critical nuclei size.[12] According to competitive growth kinetics, the polydispersed spherical nuclei can grow into monodispersed spherical PS latex after competing with one another for available monomer and radicals. In order to prove this, PS seed particles, with two different sizes (300 and 400 nm), were added into two parallel reaction batches of surfactant-free emulsion polymerization of styrene in 50% volume fraction of acetone−water mixture at 70 °C when the average hydrodynamic radius of growing latex is about 20−30 nm. Styrene monomers and KPS initiators were fed continuously afterward to support the competitive growth of these two different sized particles. It was found that the size distribution of such different-sized latexes grow to become narrowly distributed, eventually.

2. EXPERIMENTAL SECTION

2.1. Chemicals. In the present work, all chemicals were bought in analytical grade. Styrene monomer was purified by a standard procedure, that is, distilled at reduced pressure to remove stabilizers and stored in a refrigerator (−18 °C) before use. Potassium persulfate (KPS) was recrystallized from water, and stored at 4 °C. Analytical-grade acetone, and *N*,*N*-dimethylformamide (DMF) were used as received unless stated otherwise. Deionized water from a Millipore ultrapure water system with a resistivity of 18 MΩ·cm was used in all of the experiments. To obtain degassed water, oxygen was removed from water by bubbling high purity Argon (≥99.99%) through the liquids at ambient temperature.

2.2. Polymerization. The different procedures of surfactant-free emulsion polymerization are summarized in Table 1. The molar ratio of KPS and styrene ([KPS]/[St]) were listed for comparison and further discussions. PS-1 was used to measure the kinetics of surfactant-free emulsion polymerization of St in 50% volume fraction acetone−water mixture. PS-2 and PS-3 were used to prepare surface-

Table 1. Typical Procedures of SFEP through KPS Initiated Polymerization of Styrene in Water−Acetone Mixture (50% Volume Fraction of Acetone at 70°C)

sample	PS-1	PS-2	PS-3	PS-4[b]	PS-5[c]
c_{KPS}/g·L^{-1}	0.6	0.6	0.6	0.12	0.12
c_{St}/g·L^{-1}	5	1	2	10	10
[KPS]/[St]	0.12	0.6	0.3	0.012	0.012
$\langle j_{GPC}\rangle^a$	∼115	∼6	∼12	–	–
$\langle j_{MS}\rangle^a$	–	∼7	∼9	–	–
purpose	monitor the SFEP process	prepare PS oligomer		observe the competitive growth kinetics	

[a]The chain length of $\langle j_{GPC}\rangle$ and $\langle j_{MS}\rangle$ was obtained from the number-averaged molecular weight M_n measured by GPC and MALDI−TOF−MS techniques, respectively. Here, $\langle j_{GPC}\rangle$ was used for comparison with the critical chain length $\langle j_{cr}\rangle$ addressed in the model of Tauer and Kuhn.[11] [b]When $\langle R_{h,PSlatex}\rangle \sim$ 20−30 nm, seed particles with $\langle R_{h,seed}\rangle \sim$ 300 nm were added. The initial c_{St} was fixed at 10 g·L^{-1}. After 3 h of reaction, residual monomer was fed into the reacting system continuously at ∼5.0 g/(L·h). [c]When $\langle R_{h,PSlatex}\rangle \sim$ 20−30 nm, seed particles with $\langle R_{h,seed}\rangle \sim$ 400 nm were added.

dx.doi.org/10.1021/ma202535j | Macromolecules 2012, 45, 3231−3239

active oligomers. PS-4 and PS-5 were used to observe the competitive growth kinetics. In a typical SFEP, a four-neck flask was assembled inside the oven. The center neck was connected with a water reflux condenser with a coaxial glass stirrer. The other three necks were used for an argon inlet, an in situ sample drawing, and a monomer feeding head, respectively. The reaction mixture with a proper composition was weighted in the flask and was bubbled with argon for 30 min at room temperature. The flask was thermostated with silicone oil bath at 70 °C. After that, the reaction was started by injecting the corresponding stoichiometric amount of KPS initiator dissolved in degassed water. All polymerizations were carried out without the addition of surfactant.

2.3. Competitive Growth Experiments. Two parallel competitive growth kinetics experiments were carried out (PS-4 and PS-5). In a typical experiment, 100 μL of 10% mass fraction seed particles emulsion with monodispersed seed particles (the two batches of emulsion with 300 and 400 nm narrowly dispersed latex were prepared by SFEP in water with $c_{KPS} \sim 0.1$ g·L^{-1}, $c_{St} \sim 80$–100 g·L^{-1}) were added into the reacting system when the small particles grew to ~20–30 nm. Because the relative scattering intensity contribution from the seed particles is decreasing with the growth of small PS latex, DLS signal from seed particle will vanish after ~3 h.[26] Because the size of seed particles in the SFEP are still not changed much, a fixed amount of the large sized seeds emulsion (10 mL of a 10% mass fraction) were added into the reacting system again (we added two times of seed particles in each experiment) to make the seed particles remained measurable in DLS. The initial c_{St} was fixed at 10 g·L^{-1}. After 3 h, residual monomers were fed continuously at ~5.0 g/(L·hr) to maintain the growth of latex particles. During the SFEP, a small amount of the emulsion was sampled and diluted to do DLS experiments to determine the size distribution.

2.4. Oligomers Preparation and Characterization. A series of experiments were carried out with different procedures (PS-2 and PS-3). The reacting mixture was kept at 70 °C for 48 h. Then the solution was evaporated. The raw product was washed to remove salt, residual KPS and water-soluble oligomers, then the product was collected by centrifugation at 12000 rpm. After that, it was freeze-dried for 48 h. The apparent molecular weight of oligomers were measured by gel permeation chromatography (GPC), matrix-assisted laser desorption time-of-flight mass spectrometry (MALDI–TOF–MS), and dynamic light scattering (DLS). GPC was carried on Waters 1515 equipped with HR1, HR0.5 Waters Styragel columns, using tetrahydrofuran (THF) as eluant and PS as standard. All MALDI-TOF-MS were acquired on a Bruker Autoflex mass spectrometer (Bruker Daltonics, Bremen, Germany), equipped with a 355 nm nitrogen laser. The details of DLS will be introduced in the next section.

2.5. Latex Characterization. Latex samples were taken from the reacting system at different times and diluted for particle size distribution analysis by DLS and transmission electron microscopy (TEM). A commercial LS spectrometer (ALV/DLS/SLS-5022F) equipped with a cylindrical 22 mW He–Ne laser (Uniphase, at λ = 632.8 nm) was used. The spectrometer has a high coherence factor of $\beta \sim 0.95$ because of a novel single-mode fiber optics coupled with an efficient avalanche photodiode. The LS cell was held in a thermostat refractive index matching vat filled with purified and dust-free toluene. In static laser light scattering (SLS), the angular dependence of the excess time-averaged scattered intensity was acquired. In DLS, intensity–intensity correlation function $G^{(2)}(\tau,q)$ was acquired with an ALV-5000 multitau digital time correlator; a relaxation rate (Γ) distribution $f(\Gamma)$ was obtained by Laplace inversion.[27,28] For a pure diffusive relaxation, τ_i is related to the translational diffusion coefficient D_i by $\tau_i = 1/\Gamma_i$ and $D_i = \Gamma_i/q^2$ or to a hydrodynamic radius $R_h = k_BT/6\pi\eta D$ with k_B, T and η as the Boltzmann constant, the absolute temperature, and solvent viscosity, respectively. The details of LS instrumentation and theory can be found elsewhere.[29–34] TEM was performed using a Hitachi H-800 instrument (spatial resolution is ~0.5 nm), with an acceleration voltage of 100 kV. For TEM examination, the solution was diluted to the order of magnitude μL/L and then dropped on a copper grid which is covered by carbon membrane. Subsequently, the TEM grid was dried for at least 24 h to remove the solvent.

3. RESULTS AND DISCUSSION

3.1. Kinetics of Surfactant-Free Emulsion Polymerization. Fitch et al. first used SLS to investigate the kinetics of water-solvable monomers.[25,35–37] However, in a typical surfactant-free emulsion polymerization system of hydrophobic monomers with KPS as initiator, micrometer-size styrene droplets can only be stabilized in aqueous medium by mechanical stirring, which makes it very difficult to monitor the time-resolved kinetics evolution. Fortunately, Homola et al. and Okubo et al..[38,39] reported the surfactant-free emulsion polymerization of styrene in water with the addition of methanol or acetone. Wu and co-workers[30,40] further prepared uniform surfactant-free microlatex with the average radius down from 300 to 35 nm in a 50% volume fraction acetone–water mixture. Ngai et al.[40] explained that, the mixed solvent with equal amounts of acetone and water can reduce the surface tension of system, resulting in the formation of smaller particles.

All of the previous efforts made it possible to study the time-resolved kinetics in surfactant-free emulsion polymerization of styrene because styrene monomer droplets can stabilize themselves in a mixed solvent without mechanical stirring. Figure 1 is the time-resolved intensity–intensity time correlation function from the DLS and the corresponding hydrodynamic radius distribution of PS-1. At the very beginning (0 min), there is only one slow mode with a hydrodynamic radius ~300 nm existed, which corresponds to the styrene monomer droplet in the mixed solvent. Then KPS initiates the emulsion polymerization in acetone–water mixture phase, and PS radical oligomers with hydrophobic PS chain

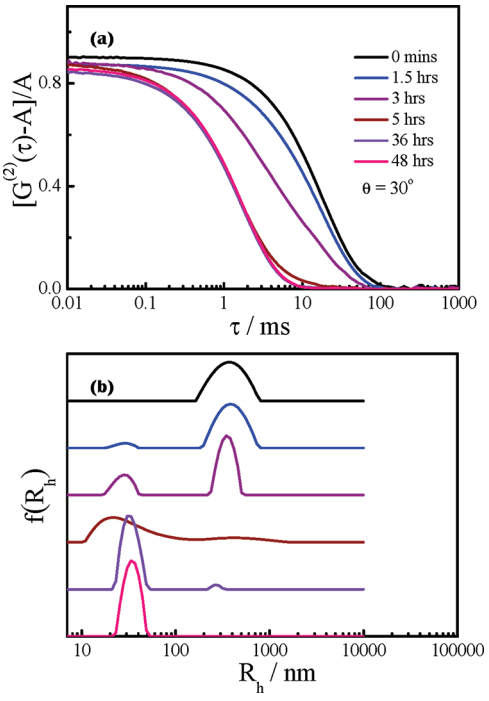


Figure 1. Evolution of (a) the intensity–intensity time correlation function ($G^{(2)}(q, \tau)$) and (b) the corresponding hydrodynamic radius distribution (the scattering angle θ = 30°) with time. Here the procedure corresponds to sample PS-1.

dx.doi.org/10.1021/ma202535j | Macromolecules 2012, 45, 3231–3239

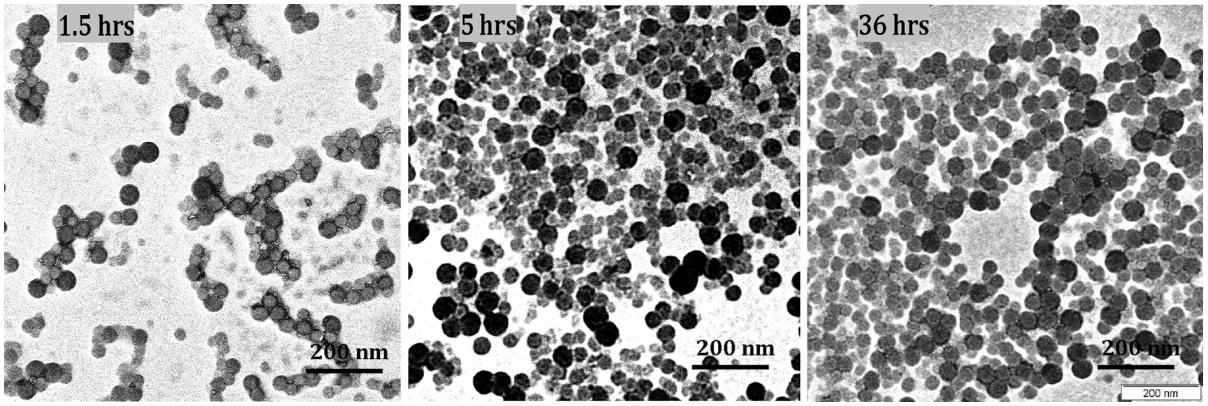


Figure 2. Typical TEM images of polystyrene latex obtained through surfactant-free emulsion polymerization of styrene in 50% volume fraction of acetone−water mixture (experiment PS-1).

backbone and sulfate end groups may form. The PS radical oligomer may propagate until a critical chain length is reached. They may then collapse and coagulate to form the critical nuclei. Unfortunately, the nucleation process cannot be observed by DLS, because the scattered light from critical nuclei is too small to be monitored due to the existence of the large monomer droplet, and there is only one slow mode of monomer droplet before 1.5 h in DLS. As we all know, the scattered light intensity comes from two parts, which is the summation from the critical nuclei and monomer droplet, respectively, i.e., $I \propto n_d M_d^2 + n_c M_c^2$, where n and M are number density and molar mass of monomer droplet and critical nuclei, respectively. If we assume that $\rho_d = \rho_c$ and $M = 4\pi\rho R^3/3$,

$$I_d/I_c = \frac{n_d M_d^2}{n_c M_c^2} = \frac{n_d R_d^6}{n_c R_c^6} \quad (4)$$

When critical nuclei are born, $R_d \sim 100R_c$, I_d is overwhelmingly larger, the generation of critical nuclei cannot be directly monitored. After the formation of nuclei, they will absorb new radical oligomers and monomers, aggregate and grow (polymerize) to form latex particles with certain stability. Both n_c and R_c grow simultaneously, when the scattering from latex particles and monomer droplets are comparable, a fast mode of ~27 nm appears. The amplitude and size of the fast mode increases, while the amplitude of the slow mode decreases with time, which means that the PS latex from the critical nuclei grow in size and consume styrene monomers from the styrene droplets. Finally, stable PS latex particles with $\langle R_h \rangle \sim 35$ nm form, which are stabilized by sulfate end groups. [KPS]/[St] is crucial for the formation of nanoscaled stable PS latex because it controls the average occupied surface area per sulfate groups on the PS nanoscaled latex periphery. Wu used LS to determine the surfactant interface thickness of spherical PS microlatices, and found the average occupied surface area per surfactant molecule on the surface of polymer core is a fundamental parameter for governing the final size of microlatices.[41] When [KPS]/[St] is very low, the growth of PS latex makes the averaged area occupied by each sulfate group on the latex periphery too large to stabilize itself. These latex will percolate and aggregate with each other, and only large PS latex can be obtained.[39] Therefore, a proper [KPS]/[St] ratio is necessary to make a nanoscaled PS latex polymerizable.[40] In PS-1, [KPS]/[St] ~ 0.12, the average area per sulfate end group is reasonable to stabilize the latex particle in the polymerization process, and collision cannot merge them together. We will discuss this in the next section again.

Figure 2 is the TEM images of polystyrene latex obtained through SFEP of styrene in 50% volume fraction of acetone−water mixture at different polymerization stages. At the very beginning, nothing can be observed because the size and population of nuclei are too small. After 1.5 h, nanoscaled PS latex can be observed. At 5 h (3.5 h later), lots of narrowly dispersed nanoscaled PS latex are generated. A longer reaction time makes essentially no difference on TEM image. Note that we cannot observe critical nuclei in real space, either, because their size may be too small or their number density is too low to be monitored in the early stage of emulsion polymerization. And the large 300 nm styrene droplets observed in the DLS (as the slow mode) cannot be observed (dried out) in the TEM image.

Therefore, eqs 1 cannot be verified by measuring particle numbers in the early stage of SFEP, because neither DLS nor TEM can observe the diameter of particles at that stage.

3.2.1. Microphase Inversion of PS Oligomer. *Synthesis of PS Oligomers.* In order to study the nucleation process in the early stage of surfactant-free emulsion polymerization, various methods have been used to prepare PS oligomers. Pohlein et al.[42] added water-soluble inhibitor in acrylic acid-styrene emulsion copolymerization systems, in order to obtain the critical oligomer size for particle entry in 1993. In 1994,[43] they further added chain transfer agent to the system and low molecular weight species were formed when water-born oligomeric radicals diffused to the surface of these seed particles. Tompson et al.[44] centrifuged the PMMA latex at 12 000 rpm and filtered the clear aqueous phase through a membrane (100 nm pore size) in a serum replacement cell to ensure removal of any debris present. The water-soluble MMA-based oligomers remaining were isolated and analyzed both as-produced and after hydrolysis. Yuan et al.[45] prepared water-soluble oligomers in the emulsion polymerization of styrene−butadiene-acrylic acid through ultracentrifugation (37 000 rpm for 36 h). Tauer et al.[15] summarized in their work in 1999 considering the isolation of oligomers from dispersion, that is, all efforts to obtain amounts of oligomers that is large enough can be handled have failed.

In this manuscript, we would like to present a new route, which is achieved by increasing [KPS]/[St] (batches PS-2 and PS-3 in Table 1), it can increase initiation and termination but decrease propagation in reacting process. A large amounts of

dx.doi.org/10.1021/ma202535j | Macromolecules 2012, 45, 3231−3239

radical oligomers are generated in the early stage of emulsion polymerization, which have hydrophobic chain backbone and charged end group and can form micelles after a critical concentration is reached,[10] or precipitate to form primary particles for chain length above a critical value j_{cr}.[46] The further polymerization of primary particles is constrained because no sufficient monomers are provided.[8] Because a large amount of initiator were added ([KPS]/[St] is large), it is expected that the double-end termination is dominating. However, in the preparation process of oligomers, we have washed the raw products with water to remove salt, those water-soluble oligomer, that is, one or two charged groups with shorter PS backbone have been removed. Therefore, it is reasonable to believe that our sample is mainly composed of short (slightly larger) oligomers with one end charged groups and longer oligomers with two end charged groups. It was expected that through such method, samples with chain length j, which is just equal to or above j_{cr}, dominates, where j_{cr} is the critical chain length.

3.2.2. Characterization of PS Oligomers. In light of these, PS oligomers were synthesized in 50% volume fraction acetone−water mixture with higher [KPS]/[St] ratio (PS-2 and PS-3 in Table 1). Figure 3 is the GPC results of these two

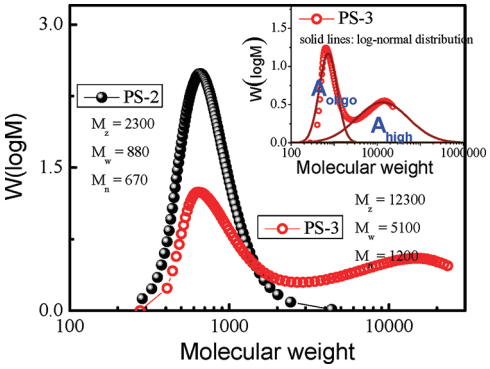


Figure 3. GPC results of two procedures of PS oligomer using THF as eluant: PS-2 and PS-3. The inset shows the log-normal distribution fitted curves of the two peaks of PS-3.

procedures of PS oligomer, PS-2 ([KPS]/[St] = 0.6) and PS-3 ([KPS]/[St] = 0.3), respectively. It was found that, bimodal molecular weight distribution appears when [KPS]/[St] increases to 0.3 in case of PS-3. Each peak has a log-normal distribution, as demonstrated in the inset in Figure 3. The further increase of [KPS]/[St] to ~0.6 (PS-2) leads to the formation of only one peak. With the increase of [KPS]/[St], it may switch from dispersion to solution, which is the origin of bimodal distribution in PS-3 and single log-normal distribution in PS-2. Figure 3 clearly shows that PS-2 oligomer has a log-normal distribution with M_w = 880 and M_w/M_n = 1.3. It will be better if we compare GPC results with DLS and MALDI-TOF mass spectrum results for PS-2 oligomer, as shown in Figure 4.

Figure 4a comes from the hydrodynamic radius distribution of PS-2 oligomer in DMF solution at room temperature. Adam and Delsanti studied the chain conformation of PS in good solvent by DLS and obtained the scaling law between hydrodynamic radius and z-averaged molecular weight, i.e., $R_h = A \cdot M_z^{\nu}$,[47,48] where $\nu \sim 0.55$, and $A \sim 0.15$. Thereby, the z-averaged molecular weight distribution of PS-2 oligomer in DMF can be directly transformed from its hydrodynamic radius distribution. Figure 4b demonstrates the number-averaged

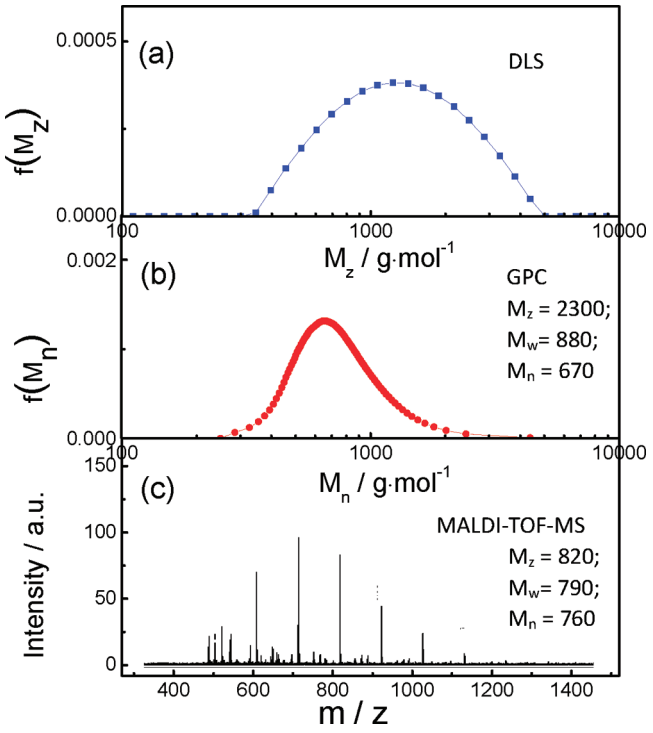


Figure 4. Comparisons of molecular weight distribution of PS-2 measured by (a) DLS, (b) GPC, and (c) MALDI−TOF mass spectrum.

molecular weight distribution of PS-2 oligomer in DMF solution by GPC. The result of $M_z \sim 2{,}300$ is consistent with DLS result. Figure 4c is the MALDI−TOF mass spectrum of PS-2. Mass resolved signals in Figure 4c allow the assignment of each peak to a specific oligomer which can be used to identify the structure of the oligomer and charged groups attached to the chain ends. The mass difference between the peaks is ~104 which is equal to the mass of one styrene monomer. Seven mass series are present in the mass spectrum in Figure 4c. The number-averaged molecular weight $M_n \sim 760$ and weight-averaged molecular weight $M_w \sim 790$. Both of them are reasonably consistent with GPC results ($M_n \sim 670$, $M_w \sim 880$).

In the persulfate-initiated polymerization system of styrene in water, the critical value of chain length $\langle j \rangle \sim$ (6 to 7) ($\langle j \rangle = (M_n - M_{SO_4^-})/M_{St}$); while the reported experimental results by Tauer and Kuhn is $j_{cr,exp} \sim 5$.[11] Fitch and Carro et al.[11,13,46] also suggested that during the early stage of emulsifier-free emulsion polymerization of styrene in water, oligomers with chain length from several to dozens of repeat units could be found for precursor particles. In this study, the addition of acetone into water enhances the solubility of styrene; with the combination of Figure 3 and Figure 4, we can show that the averaged chain length is $\langle j \rangle \sim 6$−7.

3.2.3. Microphase Inversion of PS Oligomers. The microphase inversion in our study is a redispersion process, namely, dissolving oligomer (oligomer prepared in PS-2 or PS-3) in a small amount of DMF to make a mother solution, with c_p = 20 mg/mL. Then the DMF mother solution is added dropwise to a large amount of 50% volume fraction acetone−water mixture under vigorous stirring at 70 °C for 12 h. As expected, DMF immediately mixed with acetone−water mixture, and PS oligomers self-assembled themselves, and should have the ionic sulfate chain end located on the periphery

dx.doi.org/10.1021/ma202535j | Macromolecules 2012, 45, 3231−3239

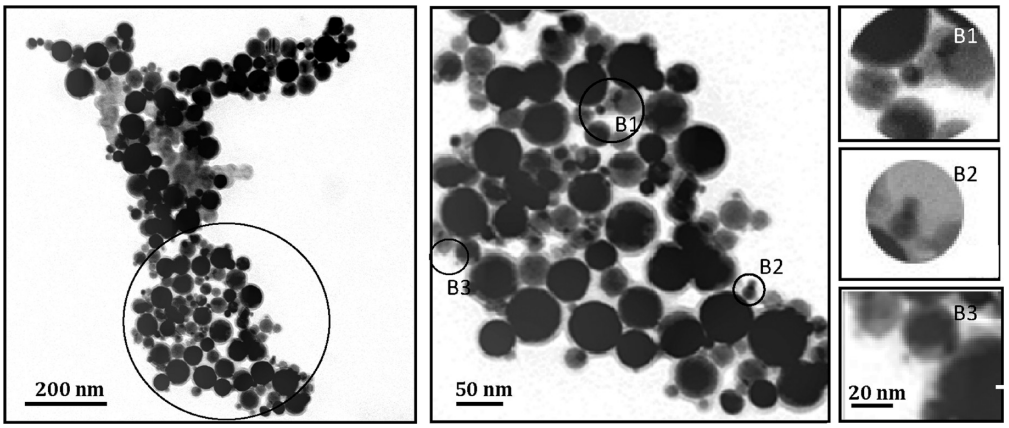


Figure 5. Typical TEM images of polystyrene latex obtained through the microphase inversion of PS-2 in 50% volume fraction acetone−water mixture. The temperature for self-assembly experiments is fixed at 70 °C. The pictures on the right (B1−B3) show the enlarged images of different regions from the middle image.

after the microphase inversion.[16] The self-assembled structure formed by oligomers during microphase inversion process may be similar (or comparable) to the nucleus at the early stage of SFEP. Figure 5 is the typical TEM images of polystyrene latex obtained through the microphase inversion of PS-2 in 50% volume fraction acetone−water mixture. Polydispersed PS nuclei can be vividly seen. These particles often show anomalous morphology, which can be attributed to the swelling of particles by monomers,[49−51] or hydrophilic regions inside latex particles in water.[21] In this study, there are no monomers in coexistence, and polydispersed homospheres are obtained. These polydispersed PS nuclei particles act as the "nanoreactor" in a real emulsion polymerization system. Monodispersed PS particles may be obtained after further reaction according to the competitive growth model by Vanderhoff and co-workers,[23,24] which we will discuss later.

The average size R_s and size distribution $f(R_s)$ can be obtained from the TEM result, as shown in Figure 6. As

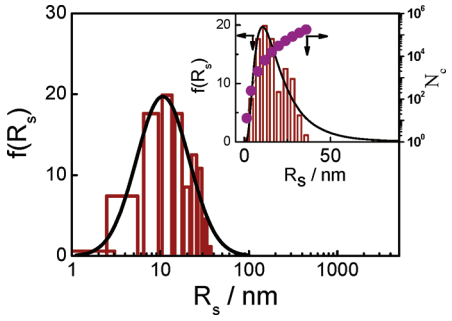


Figure 6. Size distribution $f(R_s)$ of spherical PS nuclei particles obtained from TEM image in Figure 5. The solid line showed the fitted results from the log-normal distribution function, and the inset showed the plot in linear axis and the number of oligomer chains (N_c) at the corresponding particle radius.

mentioned earlier, Tauer and Kuhn[11] have studied this problem of particle nucleation in emulsion polymerization. Their results indicated that at the number of oligomers $n_{olig} \sim 887$ and the average chain length $j_{cr} \sim 6$, particles can be self-assembled with a critical diameter of ~11.8 nm. The data in Figure 6 was obtained through counting and averaging of particles in Figure 5. A log-normal distribution with the mean value of radius $\bar{R}_s \sim$ 10.6 nm and the standard deviation $\delta \sim 0.298$ fits the size distribution of nuclei from microphase inversion quite well. Both $\bar{R}_s \sim 10.6$ nm and $\langle j_{cr} \rangle$ are consistent with the critical values in the calculation of Tauer and Kuhn.

Antonitti[52,53] and Wu[41] studied the structure of hydrophobic latex stabilized by charged groups on the surface. They all concluded that the average area occupied by each charged group is crucial to stabilize the latex. The sulfate groups packed inside hydrophobic styrene segments or inside the nuclei particle cannot contribute to stabilize the nuclei particle. So the nuclei with $\bar{R}_s \sim 10.6$ nm looks like certain grow-up structure from the original critical nuclei, and encloses lots of polystyrene chains inside. The smallest nucleus of ~1.1 nm (the smallest ones in the TEM picture, B3) in this study may be attributed to the critical nuclei, because these oligomers in self-assembled structure is similar to that in the parent collapsed globular state in which they were formed during polymerization.[20,54] The inset of Figure 6 also shows the number of oligomers inside each nucleus, N_c. And it was calculated as[40]

$$N_c = \frac{(4\pi {R_s}^3/3)\rho}{M_c/N_A} \tag{5}$$

Here, ρ is the density of bulk PS ($\rho \sim 1.05$ g/cm$_3$), M_c is the number-average molecular weight of oligomer from GPC measurement ($M_c \sim 670$ is used). When the size of particles is small, all the chain contribute end groups to the surface, hence, $N = N_c$, where N is the number of oligomers at the nuclei surface. When R_s increases from ~1.1 nm to ~35 nm, more oligomers aggregate, so N_c increase from ~13 to ~10^5. Note that in practice, some end groups are trapped inside the nuclei, that is, $N < N_c$, when oligomers begin to aggregate. The more end groups inside can come to the surface when aggregation continues until all end groups are consumed. In this study, the size of the critical nuclei, $R_s \sim 1.1$ nm, is about the end-to-end distance of critical oligomer, $\langle j \rangle \sim 6-7$.

3.3. Competitive Growth Kinetics. In order to test the model that the competitive growth kinetics is the origin of the narrow dispersed latex formation in surfactant-free emulsion polymerization, a small amount of ~300 nm PS seed particles were introduced to a SFEP in the early stage, and DLS was used to follow kinetics of particle size distribution variation, as shown in Figure 7 (PS-4). In DLS, an ill-defined Laplace transformation was used to obtain the hydrodynamic radius distributions of particles with different sizes. In order to

dx.doi.org/10.1021/ma202535j | Macromolecules 2012, 45, 3231−3239

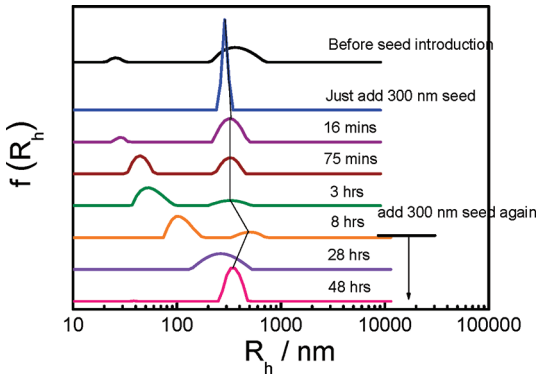


Figure 7. Evolution of the hydrodynamic radius distribution ($\theta = 30°$) in SFEP when seed particle was introduced in the early stage. 100 μL 10% mass fraction emulsion with $\langle R_h \rangle$ = 300 nm seed particles was added into the system (200 mL) when small latex particles grow to $\langle R_h \rangle \sim 20-30$ nm. After 3 h, 10 mL of 10% mass fraction large-size seeds emulsion was added again (in total, two batches of seeds were added in an experiment) to keep the scattering contribution from the slow mode "visible" by DLS.[26]

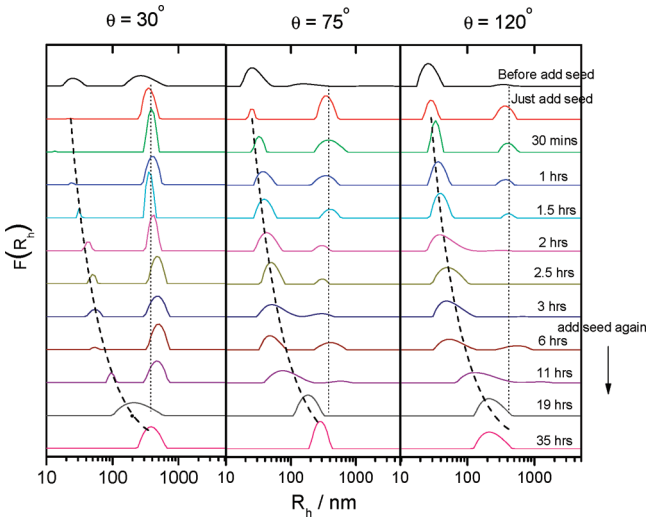


Figure 8. Evolution of the hydrodynamic radius distribution observed by DLS at three typical angles ($\theta = 30°, 75°, 120°$) in SFEP after seed particles were introduced. A small amount of 100 μL 10% mass fraction seed particles with $\langle R_h \rangle \sim 400$ nm in emulsion was added to a SFEP batch when the small latex particles grow to $\langle R_h \rangle \sim 20-30$ nm. After 3 h, another 10 mL of 10% mass fraction seeds emulsion was added again (in total, two batches of seeds were introduced in an experiment) to make the scattering contribution from the slow mode "visible" by DLS.[26]

discriminate the size differences between two, or more modes, they have to be within about one decade in size from each other. Figure 7 shows that at very beginning there are two modes from the DLS measurements before the introduction of seed particles, one is the monomer droplet, with $\langle R_h \rangle \sim 300$ nm; the other is the small PS latex, with $\langle R_h \rangle \sim 20-30$ nm. Because of this measurement constraint, the size of the seed particles prepared was also ~300−400 nm, which is similar to that of monomer droplets, in order to observe their competitive growth process by DLS. After the ~300 nm seed particles were added, they compete with the small ~20−30 nm latex for available monomer and initiator. However, after the addition of seed particles, there is only one narrowly ~300 nm seed peak at scattering angle of 30° in DLS as illustrated in Figure 7 (no distinguishable monomer droplets can be determined separately). It may be caused by the lower intensity contribution from the smaller amount of styrene droplets in the system (most styrene has been consumed or was dissolved in the acetone−water medium), or the ill-defined Laplace inversion technique cannot discriminate the contribution from monomer droplet and seed particles. So further investigation should be made, but it is not the focus of this manuscript. The time-resolved DLS measurement clearly proves the small ~20−30 nm PS latex grows much faster than the seed particles in Figure 7. After 28 h, these two peaks begin to merge into a broader one, and after 48 h, only a single narrowly dispersed, 350 nm PS latex peak remained in DLS measurement, which means that these two different sized particles grow to become the same size.

To clarify the result that the diminish of fast mode with $\langle R_h \rangle \sim 30$ nm in DLS at the scattering angle $\theta = 30°$ once a small amount of seed particles was added is caused by its relative small contribution to scattered light, a multiangle time-resolved DLS observation is essential.

Figure 8 shows the multiangle DLS observation of particle size evolution in a SFEP with a small amount of ~400 nm PS seed particles added at $\theta = 30°$, 75°, and 120°, respectively. Before adding seed, there are two modes in DLS. The fast mode, ~20−30 nm, corresponds to small latex particles, while the slow mode, ~300 nm should be attributed to styrene monomer droplets, which are all consistent with Figure 7. The larger the scattering angle, the larger contribution (relatively) from small particle to the scattering intensity. Therefore, the peak of small ~20−30 nm PS latex, which diminishes at $\theta = 30°$ after the large 400 nm seed particles were added, emerges at higher scattering angle (75 and 120°). And its peak area increases with scattering angle. The competitive growth begins after the introduction of seed particle. DLS data from different scattering angles demonstrate the same fact that the small particle grows much faster than the large one, their size difference becomes smaller with growth time. After 19 h, two peaks merged and became one single broad peak. Finally, a narrowly dispersed PS latex is obtained, and DLS cannot distinguish whether the final monodispersed particles were coming from the large seeds or the small particles. One of the reasons may be due to the fact that the final particle distribution is more narrowed; therefore, the constrained Laplace transformation cannot distinguish between the two original peaks anymore.

The phenomena above are easily understood, because the volume is a third power to the radius, $V \propto R^3$, while the mass increase is proportional to its surface area, that is, $\Delta m \propto R^2\,dR$, then $\Delta m/\Delta t$ should be scaled to $R^2(dR/dt)$. If both the small and large particles increase the same amount of mass, the small particle will of course grow much faster.[55] If there are two particles with different sizes in the system, and x in eqs 3 should be a size-dependent parameter in a particular competitive growth process. Vanderhoff et al. derived the following equation in 1956[23]

$$R_{large}/R_{small} = (R_{small}/R_{small,0})^{-1} \times [(R_{small}/R_{small,0})^{3-x} + (R_{large,0}/R_{small,0})^{3-x} - 1]^{1/(3-x)} \quad (6)$$

with the assumption that x is a constant. Here $R_{small,0}$ is the latex radius before the seed particles were added, $R_{large,0}$ is the original

dx.doi.org/10.1021/ma202535j | Macromolecules 2012, 45, 3231−3239

size of seed particles; R_{small} and R_{large} are the radius of small PS particles and large sized seeds as reaction continues, respectively.

Parts a and b of Figure 9 show the $R_{small}/R_{small,0}$ dependence of $_{large}/R_{small}$ corresponding to the procedure of PS-4 and PS-5

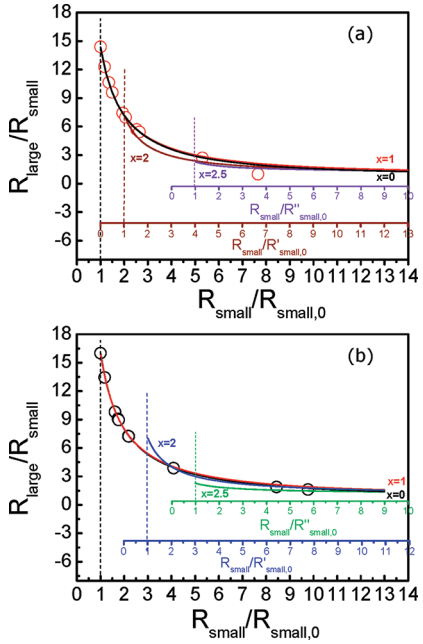


Figure 9. $R_{small}/R_{small,0}$ dependence of R_{large}/R_{small} in the procedure of (a) PS-4 and (b) PS-5 when the small latex particles grow to $\langle R_h \rangle \sim$ 20−30 nm, respectively. The lines are the theoretically calculated results according to eqs 6. Different x-axes indicate the starting points ($R_{small}/R_{small,0} = 1$, $R_{small}/R'_{small,0} = 1$, $R_{small}/R''_{small,0} = 1$) for different calculations. Here $R_{small,0}$, $R'_{small,0}$ and $R''_{small,0}$ are different particle sizes obtained after each time step as new initial sizes for the next growth step, and x is assumed to be a constant for a fixed $R_{large,0}/R_{small,0}$ in a fixed $R_{small}/R_{small,0}$ range.

(DLS data in Figure 7 and Figure 8) when the small latex particles grow to $\langle R_h \rangle \sim$ 20−30 nm. Theoretical calculations according to eqs 6 are shown for comparison, where x is the only variable, and is assumed to be constant for a fixed $R_{large,0}/R_{small,0}$ in a fixed $R_{small}/R_{small,0}$ range. Figure 9a shows that at the very beginning, $R_{small,0} \sim$ 20−30 nm, $R_{small}/R_{small,0} = 1$ and $R_{large,0}/R_{small,0} \sim 13.5$, when ~300 nm seed particles and small PS latex began to compete for available monomer and initiator resources. R_{large}/R_{small} decreases with $R_{small}/R_{small,0}$. All of the data are consistent with $0 < x < 1$ very well. Poehlein and Vanderhoff[24] also proposed that $0 < x < 1$ because of the poorer accuracy of the competitive-growth mechanism in the small particle-size range. Interestingly, if the particle sizes obtained after each time step are new initial sizes for the next growth step, different starting points with SFEP time is chosen, that is, $R'_{small,0} = 2R_{small,0}$ (medium x-axis) and $R''_{small,0} = 5R_{small,0}$ (upper x-axis), as shown in the inset bar in Figure 9 (a). Different x and different $R_{large,0}/R_{small,0}$ values are needed to analyze the kinetics at different growth step. It shows that the latex growth rate x increases to be 2.0 when $R_{large,0}/R'_{small,0} = 7$, and gets to be 2.5 when $R_{large,0}/R''_{small,0} = 3$. Vanderhoff and co-workers[23] also reported that for particle sizes larger than about 150 nm (e.g., initial sizes of 264 and 557 nm), the calculated value of $x = 2.5$ is consistent to the experimental data in a KPS initiated SFEP of styrene in water system.

Therefore, we can conclude that the size difference between the large seed and small latex becomes smaller with the growth of PS latex, then the growth rates of both particles also tend to be similar. But the small particle is always growing a little faster than the large particles because $x < 3$. Figure 9b further confirms the above assumption with the measurement of PS-5 series; that is, the competitive growth of latex particles of different sizes favors the smaller particles in the specific SFEP system. Thus, the initially polydispersed latexes in SFEP will decrease the polydispersity with particle growth when $x < 3$. Note that a necessary condition in competitive growth experiment is that the particle number does not change during the growth.[8,10,15,56] In the SFEP system, we assumed it is true because pure DLS cannot distinguish particle number variation from the increase of scattering light intensity.

4. SUMMARY

The manuscript is to reveal the structure of critical nuclei in SFEP, and demonstrate the origin of the narrowly dispersed latex formation. In a typical microphase inversion process of PS oligomer in 50% volume fraction of acetone−water mixture, polydispersed spherical nuclei with log-normal distribution were formed. The average nuclei size, ~10.6 nm, is too large for the average end-to-end distance of PS oligomer, so we proposed that the smallest nuclei, ~1.1 nm, might be the critical nuclei, which is stabilized by sulfate groups. Note the spherical nuclei are not necessarily narrowly dispersed. Competitive growth kinetics makes small nuclei grow much faster than large nuclei in the subsequent polymerization process, resulting in a narrowly dispersed PS latex distribution. Time-resolved DLS was used to verify this mechanism. Large seeds with $\langle R_h \rangle \sim$ 300 or 400 nm were added into two different reacting systems, when the average hydrodynamic radius of PS latex is ~20−30 nm at 70 °C. It was found that the size of 300 nm seed particles only changed a little, but the small $\langle R_h \rangle \sim$ 20−30 nm PS latex grows rapidly in size. At last, a narrowly dispersed PS latex is obtained. This is rationalized according to the treatments of Vanderhoff and co-workers. The results suggest that even when the size distribution of particles at early stage is broad, the resultant latex can be narrowly distributed. This study provides us with better understanding of the formation of narrowly distributed ultrafine particles in emulsifier-free emulsion polymerization.

AUTHOR INFORMATION

Corresponding Author

*Telephone: +86 010 82618089. Fax +86 010 62521519. E-mail: (C.C.H) c.c.han@iccas.ac.cn; (H.C.) chenghe@iccas.ac.cn.

Notes

The authors declare no competing financial interest.

ACKNOWLEDGMENTS

The authors appreciate the financial support of the National Basic Research Program of China (973 Program, 2012CB821500), and National Natural Scientific Foundation of China (No. 21174152, and Young Scientists Fund No. 20804052).

REFERENCES

(1) Smith, W. V. *J. Am. Chem. Soc.* **1948**, *70*, 3695−3702.
(2) Smith, W. V.; Ewart, R. H. *J. Chem. Phys.* **1948**, *16*, 592−599.

(3) Harkins, W. D. *J. Chem. Phys.* **1945**, *13*, 381−382.
(4) Harkins, W. D. *J. Am. Chem. Soc.* **1947**, *69*, 1428−1444.
(5) Harkins, W. D. *J. Polym. Sci.* **1950**, *5*, 217−251.
(6) Fitch, R. M. *Polymer Colloids*; Plenum Press: New York, 1971.
(7) Priest, W. J. *J. Phys. Chem.* **1952**, *56*, 1077−1082.
(8) Feeney, P. J.; Napper, D. H.; Gilbert, R. G. *Macromolecules* **1987**, *20*, 2922−2930.
(9) Goodwin, J. W.; Hearn, J.; Hoe, C. C.; Ottewill, R. H. *Br. Polym. J.* **1973**, *5*, 341−362.
(10) Goodall, A. R.; Wilkinson, M. C.; Hearn, J. *J. Polym. Sci.: Polym. Chem.* **1977**, *15*, 2193−2218.
(11) Tauer, K.; Kuhn, I. *Macromolecules* **1995**, *28*, 2236−2239.
(12) Vanderhoff, J. W. *J. Polym. Sci.: Polym. Sym.* **1985**, *72*, 161−198.
(13) Carro, S.; Herrera-Ordonez, J. *Macromol. Rapid Commun.* **2006**, *27*, 274−278.
(14) Lamer, V. K.; Dinega, R. H. *J. Am. Chem. Sci.* **1950**, *72*, 4847−4854.
(15) Tauer, K.; Deckwer, R.; Kuhn, I.; Schellenberg, C. *Colloid Polym. Sci.* **1999**, *277*, 607−626.
(16) Zhang, G. Z.; Niu, A. Z.; Peng, S. F.; Jiang, M.; Tu, Y. F.; Li, M.; Wu, C. *Acc. Chem. Res.* **2001**, *34*, 249−256.
(17) Zhang, G. Z.; Liu, L.; Zhao, Y.; Ning, F. L.; Jiang, M.; Wu, C. *Macromolecules* **2000**, *33*, 6340−6343.
(18) Hao, J. K.; Li, Z. Y.; Cheng, H.; Wu, C.; Han, C. C. *Macromolecules* **2010**, *43*, 9534−9540.
(19) Siu, M. H.; Cheng, H.; Wu, C. *Macromolecules* **2003**, *36*, 6588−6592.
(20) Zhang, G. Z.; Wu, C. *Adv. Polym. Sci.* **2006**, *195*, 101−176.
(21) Tauer, K. *Macromolecules* **2006**, *39*, 2007−2009.
(22) Ganeva, D. E.; Sprong, E.; de Bruyn, H.; Warr, G. G.; Such, C. H.; Hawkett, B. S. *Macromolecules* **2007**, *40*, 6181−6189.
(23) Vanderhoff, J. W.; Vitkuske, J. F.; Bradford, E. B. Jr.; T., A. *J. Polym. Sci.* **1956**, *20*, 225−234.
(24) Poehlein, G. W.; Vanderhoff, J. W. *J. Polym. Sci.: Polym. Chem.* **1973**, *11*, 447−452.
(25) Morrison, B. R.; Maxwell, I. A.; Gilbert, R. G.; Napper, D. H. In *Polymer Latexes*; American Chemical Society: 1992; Vol. *492*, pp 28−44.
(26) According to Eqs 4, the ratio of scattering intensity from seed and smaller PS latex can be expressed as $I_{seed}/I_{latex} = (n_{seed}M_{seed}^2)/(n_{seed}M_{latex}^2) = (n_{seed}R_{latex}^2)/(n_{seed}R_{latex}^6)$. When the seed particles ($\langle R_{h,seed}\rangle \sim 300$ nm) is introduced to the SFEP system ($\langle R_{h,latex}\rangle \sim 25$ nm), it is reasonable to suppose $I_{seed}/I_{latex} \sim 10$, because both peaks can be seen in DLS. Then $n_{seed}/n_{latex} \sim 10/10^6$; when $\langle R_{h,latex}\rangle$ grows to be 70 nm, $\langle R_{h,seed}\rangle$ almost does not change, $I_{seed}/I_{latex} \sim 0.02$ if we suppose n_{seed}/n_{latex} is fixed. So we will not see a signal from seed particles after several hours in DLS if we do not add more seeds into the SFEP system (note that we will not see the signals from small PS latex if we add more seeds at the beginning).
(27) Provencher, S. W. *Comput. Phys. Commun.* **1982**, *27*, 229−242.
(28) Provencher, S. W. *Comput. Phys. Commun.* **1982**, *27*, 213−227.
(29) Li, Z. Y.; Cheng, H.; Li, J. Y.; Hao, J. K.; Zhang, L.; Hammouda, B.; Han, C. C. *J. Phys. Chem. B* **2011**, *115*, 7887−7895.
(30) Zhang, W. M.; Gao, J.; Wu, C. *Macromolecules* **1996**, *30*, 6388−6390.
(31) Chu, B. *Laser light scattering*; Academic Press: New York, 1974.
(32) Berne, B.; Pecora, R. *Dynamic Light Scattering*; Plenum Press: New York, 1976.
(33) Han, C. C.; Akcasu, A. Z. *Scattering and Dynamics of Polymers: Seeking Order in Disordered Systems*; John Wiley & Sons (Asia) Pte Ltd.: Singapore, 2011.
(34) Cong, R. J.; Temyanko, E.; Russo, P. S.; Edwin, N.; Uppu, R. M. *Macromolecules* **2006**, *39*, 731−739.
(35) Fitch, R. M.; Palmgren, T. H.; Aoyagi, T.; Zuikov, A. *Angew. Makrom. Chem.* **1984**, *123*, 261−283.
(36) Fitch, R. M.; Palmgren, T. H.; Aoyagi, T.; Zuikov, A. *J. Polym. Sci.: Polym. Sym.* **1985**, *72*, 221−224.
(37) Fitch, R. M. In *Emulsion Polymers and Emulsion Polymerization*; Bassett, D. R., Hamielec, A. E., Eds.; Amercian Chemical Society: Washington, DC, 1981; Vol. *165*, pp 1−29.
(38) Homola, A. M.; Inoue, M.; Robertson, A. A. *J. Appl. Polym. Sci.* **1975**, *19*, 3077−3086.
(39) Okubo, M.; Yamada, A.; Shibao, S.; Nakamae, K.; Matsumoto, T. *J. Appl. Polym. Sci.* **1981**, *26*, 1675−1679.
(40) Ngai, T.; Wu, C. *Langmuir* **2005**, *21*, 8520−8525.
(41) Wu, C. *Macromolecules* **1994**, *27*, 298−299.
(42) Wang, S.-T.; Poehlein, G. W. *J. Appl. Polym. Sci.* **1993**, *49*, 91−1001.
(43) Wang, S.-T.; Poehlein, G. W. *J. Appl. Polym. Sci.* **1994**, *51*, 593−604.
(44) Thomson, B.; Wang, Z.; Paine, A.; Lajoie, C.; Rubin, A. *J. Polym. Sci.: Polym. Chem.* **1995**, *33*, 2297−2304.
(45) Yuan, X.-y.; Dimonie, V. L.; Sudol, E. D.; El-Aasser, M. S. *Macromolecules* **2002**, *35*, 8346−8355.
(46) Fitch, R. M. *Br. Polym. J.* **1973**, *5*, 461−483.
(47) Adam, M.; Delsanti, M. *J. Phys.* **1976**, *9*, 1045−1049.
(48) Han, C. C.; McCrackin, F. L. *Polymer* **1979**, *20*, 427−432.
(49) Williams, D. J.; Bobalek, E. G. *J. Polym. Sci.: Part A-1* **1966**, *4*, 3065−3079.
(50) Grancio, R.; Williams, D. J. *J. Polym. Sci., Part A: Polym. Chem.* **1970**, *8*, 2617−2629.
(51) Tauer, K.; Hernandez, H.; Kozempel, S.; Lazareva, O.; Nazaran, P. *Colloid Polym. Sci.* **2008**, *286*, 499−515.
(52) Antonietti, M.; Bremser, W.; Muschenborn, D.; Rosenauer, C.; Schupp, B.; Schmidt, M. *Macromolecules* **1991**, *24*, 6636−6643.
(53) Antonietti, M.; Lohmann, S.; Niel, C. V. *Macromolecules* **1992**, *25*, 1139−1143.
(54) Khokhlov, A. R.; Khalatur, P. G. *Phys. Rev. Lett.* **1999**, *82*, 3456.
(55) Gilbert, R. G. *Emulsion polymerization, a mechanistic approach*; Academic Press: London, 1995.
(56) Kuhn, I.; Tauer, K. *Macromolecules* **1995**, *28*, 8122−8128.

Macromolecules

Article

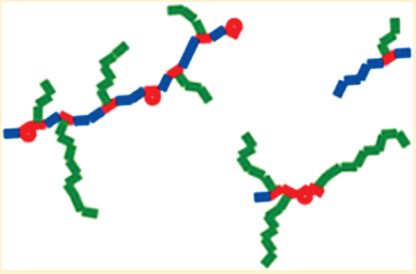
pubs.acs.org/Macromolecules

Nonuniformities of Distributions of Molecular Weights of Grafted Polymers

Karel Dušek,* Miloš Netopilík, and Pavel Kratochvíl

Institute of Macromolecular Chemistry, Academy of Sciences of the Czech Republic, 162 06 Prague, Czech Republics

ABSTRACT: The nonuniformities of graft (co)polymers have been analyzed using the probability generating functions and their moments. The nonuniformity is described by ratios of averages of molecular weights of the graft (co)polymers. The general feature of the nonuniformity of graft (co)polymers is that, with increasing degree of grafting and degree of polymerization of the backbone, the nonuniformity of a graft (co)polymer passes through a maximum and approaches more or less closely the nonuniformity of the backbone (co)polymer. The nonuniformities of graft (co)polymer are a function of the number- and weight-average degrees of polymerization of the backbone and grafts and are independent of the type of the degree-of-polymerization distribution. The nonuniformity depends markedly on the disparity in the molecular weights of monomer units of the backbone copolymer and the grafts if the graft copolymer has a small number of grafts per backbone, but the disparity effect gets smaller with increasing degree of polymerization of the backbone and fraction of graftable units.



INTRODUCTION

Grafting and graft polymers play an important role in materials science and macromolecular and supramolecular chemistry. In materials technology, graft (co)polymers are widely used as polymer blend compatibilizers.[1] Grafting of biological motifs on synthetic polymer backbones to make hydrophilic polymers or gels suitable for targeted drug delivery[2−4] (especially with molecular recognition) or preparation of polymer brushes for switching and sensing can serve as examples. The number of grafts and their distribution are of utmost importance for proper functions. This information is usually not available experimentally, and one has to rely on simulation.

Chemists often strive to obtain products with the highest accessible degree of uniformity. Those that are positively tuned trust that, when working with extreme preciosity, they can obtain a tailored polymer in which all macromolecules are virtually identical.[5]

Unfortunately, this is far from being true due to the statistical nature of reactions that are used in polymer tailoring.[6] The situation is particularly involved with graft (co)polymers. This is illustrated by model calculations simulating synthesis of a graft polymer with a particular number of grafts on a backbone targeted to reach desired properties in solution.[7] The present-day analytical methods do not allow finding such subtle details as the distributions of the degree of polymerization (DP) of graft chains in a molecule. For this reason, theoretical methods have to be used, the statistical ones being the most suitable for the majority of cases. The distributions of graft polymers were modeled by a number of authors[8−16] and a suitable choice of parameters was found satisfying the experimentally determined distributions.[8−11] In addition to purely statistical treatments, grafting was modeled kinetically and formulated by sets of kinetic differential equations or by Monte Carlo sampling. Nie et al.[12] considered systems of differential equations for mutual grafting of polyfunctional chains leading to gelation. Dušek and Somvársky considered cross-linking of primary chains generated kinetically as mutual grafting of backbones with a distribution of graftable sites. In both cases, the distributions of DP were obtained in the form of generating functions.[13] For more complex multistep free-radical cross-linking (co)polymerization, the moment method was used to generate primary chains which were mutually grafted to generate branched molecules and a network.[14] Also, a kinetic treatment of formation of a graft polymer formed by copolymerization of macromonomers with simple monomers was offered by Tobita.[15] The kinetic approach to generation of distributions in various polymer systems was developed by Galina and Lechowicz.[16] The Monte Carlo approach was used for modeling of polymer grafting based on the (co)polymerization kinetics[17] and for coupling of branched molecules when group reactivities depended on molecule sizes and the moment method could not be applied.[18]

In this paper, we shall develop relations between the distribution of the DP of backbone chains, the grafting efficiency and the distribution of DP of grafts as input information. The averages of molecular weights or degrees of polymerization of the graft polymer have been selected as the output information. The backbone chain is considered as a copolymer composed of graftable and nongraftable monomer units. The consideration of grafting of (co)polymers of graftable and nongraftable units is extremely important for bioactive polymers and gels because the bioactive group (often a polypeptide) must have sufficient space for its placement and action. Also, when the hydrophilic backbone is to act as osmotic engine, there must be available

Received: January 6, 2012
Revised: March 1, 2012
Published: March 22, 2012

 © 2012 American Chemical Society dx.doi.org/10.1021/ma3000187 | *Macromolecules* 2012, 45, 3240−3246

sufficient amount of work-performing nongraftable units relative to the stimulus sensitive grafts. The frequent usage of experimentally determined invariance or change of nonuniformity as a measure of success or failure of the grafting step has often a very weak theoretical foundation. To get a guidance in the expected and observed changes of nonuniformity was one of our motivations for this work.

In our derivation, the distributions are described by the formalism of probability generating functions (pgf). This formalism allows for easy transformation of various distributions and extraction of moments and average values of DP and molecular weight. Moreover, if the resulting graft polymer participates in further structure build-up by self-assembly or cross-linking, the corresponding pgf can directly be used as input (cf., e.g., ref 19).

DESCRIPTION OF THE SYSTEMS

The systems studied are graft (co)polymers, composed of backbone (co)polymers to which graft homopolymer chains are attached. The composition of the systems is schematically illustrated by Figure 1.

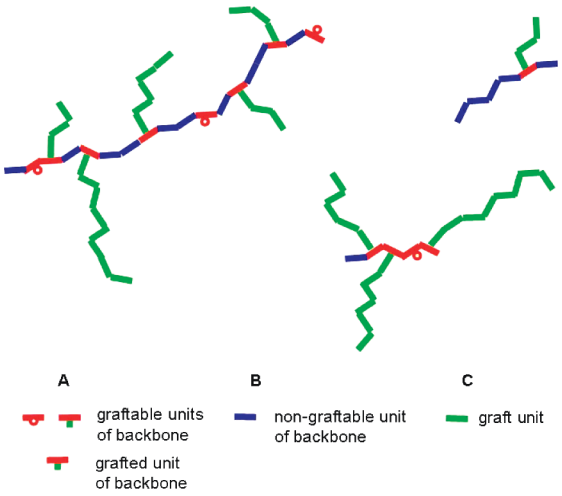


Figure 1. Description of components of a grafted copolymer.

The backbone copolymer AB is a copolymer of monomers A and B, of which units A are graftable, i.e., a chain of graft units C can be attached to them, the B units are nongraftable, and they cannot bear a graft. In the grafted (co)polymers, some of the graftable A units are already grafted − they bear a graft which is a chain of graft units C. The backbone chain is characterized by degree-of-polymerization distribution and compositional distribution, the graft chains only by degree-of-polymerization distribution. The following distributions and averages will be defined for certain types of degree-of-polymerization distribution and compositional distribution:

- Number of grafts per backbone chain of a particular degree of polymerization
- Mass fraction of grafts per backbone chain of a particular degree of polymerization
- Molecular-weight averages of the grafted (co)polymer

THEORY

In a probability generating function (pgf) denoted as $F(Z)$

$$F(Z) \equiv \sum_i a_i Z^i \tag{1}$$

a_i is the set of probabilities of the events characterized by the variable i within the defined probability space, so that $\sum_i a_i = 1, F(Z = 1) \equiv F(1) = 1$. In what follows, the exponents will be assigned to numbers of units or molecular weights of these units, or numbers of units of a certain type per selected base unit, e.g., a backbone chain or molecular weight of these units. Z in eq 1 is the auxiliary variable which after transformation (e. g., differentiation or integration) of pgf is put equal to 1 or 0. It is well-known that the average value of i, $\overline{i}$, can be obtained by differentiation

$$\frac{\partial F(Z)}{\partial Z} = \sum_i i a_i Z^{i-1} \tag{2}$$

$$\left[\frac{\partial F(Z)}{\partial Z}\right]_{Z=1} = \sum_i i a_i = \overline{i} \tag{3}$$

Higher moments of the distribution can be obtained;[20] e.g.; the second moment

$$\left[\frac{\partial\left(Z\frac{\partial F(Z)}{\partial Z}\right)}{\partial Z}\right]_{Z=1} = \sum_i i^2 a_i = \overline{i^2} \tag{4}$$

For systems composed of various kinds of units described by vectors of variables $\mathbf{Z} = (Z_A, Z_B, Z_C,)$, we will be using the following shorthand notation for the values of derivatives

$$\left[\frac{\partial F(\mathbf{Z})}{\partial Z_X}\right]_{\mathbf{Z=1}} \equiv F^X; \quad \left[\frac{\partial^2 F(\mathbf{Z})}{\partial Z_{XY}}\right]_{\mathbf{Z=1}} \equiv F^{XY}; \quad \left[\frac{\partial^2 F(\mathbf{Z})}{\partial {Z_X}^2}\right]_{\mathbf{Z=1}} \equiv F^{XX} \tag{5}$$

Table 1. Number Distribution n_i and Their Generating Functions $N(Z)$

distribution	n_i	parameter	$N(Z)$	P_n	Pw
most probable	$(1-q)q^{i-1}$	$q = 1 - 1/P_n$	$[(1-q)Z]/[1-qZ]$	$1/(1-q)$	$(1+q)/(1-q)$
SCMP[a]	$(i-1)(1-q)^2 q^{i-21}$	$q = 1 - 2/P_n$	$(1-q)^2Z^2/(1-qZ)^2$	$2/(1-q)$	$(2+q)/(1-q)$
Schulz–Zimm	$(P_w - P_n)^{[P_n/(P_w-P_n)]}.i^{[2(P_w-P_n)/(P_w-P_n)]}$ $\exp[-i/(P_w - P_n)]$	P_n, P_w	$(1/[1-(P_w-P_n)\ln Z])^{P_n/[P_w-P_n]}$	P_n	P_W
Poisson	$\lambda^{i-1}/(i-1)!\exp(-\lambda)$	$\lambda + 1 = P_n$	$Z\exp[\lambda(Z-1)]$	$\lambda + 1$	$[\lambda^2 + 3\lambda + 1]/[\lambda + 1]$

[a]Self-convoluted most probable distribution.

dx.doi.org/10.1021/ma3000187 | Macromolecules 2012, 45, 3240−3246

DEFINITION OF DISTRIBUTIONS CONSIDERED

The number-fraction pgf for degree of polymerization distribution is defined as

$$N(Z) \equiv \sum_{i=1}^{\infty} n_i Z^i \tag{6}$$

where n_i is the number fraction of molecules composed of i monomer units and Z is the auxiliary variable. Such pgf can be formulated explicitly for the backbone as well as for the grafts. Examples of n_i and $N(Z)$ for some common distributions and the correrspponding pgfs were summarized by Kajiwara and Gordon[21] and are presented in Table 1 after a small correction of n_i for SCMP.

The derivatives of $N(Z)$ have the following values

$$\left(\frac{\partial N(Z)}{\partial Z}\right)_{Z=1} \equiv N^Z = \sum_{i=1}^{\infty} i n_i = P_n;$$
$$\left(\frac{\partial^2 N(Z)}{\partial Z^2}\right)_{Z=1} \equiv N^{ZZ} = \sum_{i=1}^{\infty} i(i-1) n_i = P_n(P_w - 1) \tag{7}$$

The following pgfs are defined:

1. The number-fraction pgf for the backbone:

$$N_{AB}(Z) \equiv \sum_{i=1}^{\infty} n_{ABi} Z_{AB}^i \tag{8}$$

2. Compositional pgf: The backbone is considered as a copolymer of graftable and nongraftable units. For a binary copolymer, the compositional distribution is considered here as random, i.e., the probability of occurrence of component unit is given by its molar fraction independent of the nature of the adjacent units (absence of the neighbor effect). The pgf variable Z_{AB} becomes itself a pgf of variables Z_A and Z_B:

$$Z_{AB}(Z_A, Z_B) = x_A Z_A + x_B Z_B \tag{9}$$

where x_A and x_B are the molar fractions of the components A and B, respectively, ($x_B = 1 - x_A$) and Z_A and Z_B are the auxiliary variables associated with numbers of units A and B.

If the distribution of the composition is not random, it can be approximated by the Markov-chain statistics. This will affect the distribution $N_{AB}(Z)$ as well. For the first−order Markovian statistics, the distribution can be constructed from transition probabilities p_{AA}, p_{AB}($p_{AA} + p_{AB} = 1$) and p_{BA}, p_{BB}($p_{BA} + p_{BB} = 1$) which are related to the fraction of dyads n_{AA}, n_{AB}, n_{BB}, ($n_{AA} + n_{AB} + n_{BB} = 1$). These fractions can be obtained by solution of the respective kinetic differential equations.

3. The probability generating function for the number and molecular weight of units bearing grafts: The graftable unit has the additional property that it can bear a graft, and the probability of that connection is expressed by a bond related variable z_{AC} (a bond extending from A to C)

$$Z_{AB}(Z_A, Z_B, z_{AC}) = x_A Z_A z_{AC} + x_B Z_B \tag{10}$$

Once the backbone chain has been constructed, grafts are being grafted to graftable units A. The fraction of grafted units A is denoted by α. If the reactivity of the graftable unit A is independent of the nature of the neighbors, i.e., whether the neighbors are A or B units and whether the A unit has reacted or not, the probability that any A unit is grafted is equal to α and that it is not grafted is equal to $1 - \alpha$. Thus,

$$z_{AC}(Z_C) = 1 - \alpha + \alpha N_C(Z_C) \tag{11}$$

where $N_C(Z_C)$ describes the distribution of the number of units C per graft.

Two other scenarios can be considered:

- The grafts are composed of monomer units C; they are either preformed or they grow simultaneously. In either case, the distribution of their degrees of polymerization depends on the relative rates of formation of A-C and C−C bonds and the initial molar ratio of [C]:[A]. The distribution can be obtained kinetically similarly as in ref 14.
- The preformed C chains are grafted to A units but the reactivity of A depends on the nature and state of neighbors, i.e., the adjacent-unit effect is operative. This dependence can be respected by defining triads (the considered A unit is in the center of triad) and the kinetic differential equations for evolution of triad fractions are formulated and solved. The adjacent unit effect can greatly influence the time dependence of the number of grafts. In the case of buildup of grafts from monomer units C, also their degree-of-polymerization distribution will be affected.

Distributions and Averages Related to the Grafted (Co)polymer. Usually, not the degree-of-polymerization distribution and averages but instead the molecular-weight distribution and averages are the quantities that are compared with the results of characterization of grafted polymers. The passage from contributions by numbers of units to mass increments of units can be simply effectuated by substituting

$$n_i Z^i \rightarrow n_i Z^{iM_X}$$

which means replacement of the variable Z for Z^{M_X}. Upon differentiation, the weighting by n_i is changed from i to iM_X.

Thus, $Z_{AB}(Z_A,Z_B,z_{AC})$ of eq 10 is changed to

$$\zeta(Z_A, Z_B, Z_C) = x_A Z_A^{M_A}(1 - \alpha + \alpha N_C(\psi)) + x_B Z_B^{M_B};\ \psi = Z_C^{M_C} \tag{12}$$

The basic pgf $N_g(\mathbf{Z})$ for obtaining various averages of the grafted copolymer or its substructures under assumptions discussed in the preceding section reads

$$N_g(\mathbf{Z}) \equiv N_{AB}(\zeta(Z_A, Z_B, Z_C)) \tag{13}$$

where $N_{AB}(\zeta)$ is the number fraction pgf for the number of units of backbone copolymer AB irrespective of type of units, and the pgf$N_C(\psi)$describes the distribution of the number of C units per graft. The expanded form of $N_g(\mathbf{Z})$ reads

$$N_g(\mathbf{Z}) = \sum_{\substack{i,j,k=0 \\ i+j+k\geq 1}}^{\infty} n_{ijk} Z_A^{iM_A} Z_B^{jM_B} Z_C^{kM_C} \tag{14}$$

where n_{ijk} is the number fraction of molecules composed of i units A, j units B, and k units C having molecular weights M_A, M_B, and M_C, respectively.

All averages of molecular weights are obtained by manipulation with the pgf (eq 13). For $M_A = M_B = M_C = 1$, we get the degree-of-polymerization distribution of the grafted polymer. For $Z_C = 1$, the distribution refers to the backbone. If we are interested in the distribution of the number of grafts per backbone, $N_C(\psi)=\psi$ and $Z_A=Z_B = 1$ (the variable ψ then counts grafts). Alternatively, putting $M_C = 1$ and $Z_A=Z_B = 1$, the distribution of number of C

dx.doi.org/10.1021/ma3000187 | Macromolecules 2012, 45, 3240−3246

units per backbone is obtained. Various other means can be calculated if needed.

The presentation of the distribution in the form of eqs 12 and 13 makes it possible to get the average molecular weight of the grafted copolymer without regard to the specific form of distributions $N_{AB}(\zeta)$ and $N_C(\psi)$, even for arbitrary distributions made artificially by blending fractions. This finding can be explained by random distribution of grafts among randomly distributed grafted monomer units of the backbone. Thus, the number-average molecular weight of the grafted copolymer, $M_{g,n}$, is obtained by differentiation and putting the variable Z equal to 1

$$M_{g,n} = N_g^A + N_g^B + N_g^C = N_{AB}^{\zeta}\zeta^A + N_{AB}^{\zeta}\zeta^B + N_{AB}^{\zeta}\zeta^{N_C}N_C^{\psi}M_C \quad (15)$$

For the particular form of ζ, eq 15 gives

$$M_{g,n} = P_{AB,n}(x_A M_A + x_B M_B + x_A \alpha P_{C,n} M_C) \quad (16)$$

weight−fraction generating function $W_g(\mathbf{Z})$ which is derived from $N_g(\mathbf{Z})$ by differentiation

$$W_g(\mathbf{Z}) = W_g(Z_A, Z_B, Z_C) = \left(Z_A\frac{\partial N_g(\mathbf{Z})}{\partial Z_A} + Z_B\frac{\partial N_g(\mathbf{Z})}{\partial Z_B} + Z_C\frac{\partial N_g(\mathbf{Z})}{\partial Z_C}\right)/M_{g,n} \quad (17)$$

and

$$M_{g,w} = \left[\frac{\partial W_g(\mathbf{Z})}{\partial Z_A}\right]_{\mathbf{Z}=\mathbf{1}} + \left[\frac{\partial W_g(\mathbf{Z})}{\partial Z_B}\right]_{\mathbf{Z}=\mathbf{1}} + \left[\frac{\partial W_g(\mathbf{Z})}{\partial Z_C}\right]_{\mathbf{Z}=\mathbf{1}} \equiv W_g^A + W_g^B + W_g^C \quad (18)$$

The effect of these operations can be more easily understood by inspection of the expanded form of the pgf $N_g(\mathbf{Z})$ (eq 14)

$$\frac{\partial N_g(\mathbf{Z})}{\partial Z_A} + \frac{\partial N_g(\mathbf{Z})}{\partial Z_B} + \frac{\partial N_g(\mathbf{Z})}{\partial Z_C} = \sum_{\substack{i,j,k=0\\ i+j+k\geq 1}}^{\infty} (iM_A + jM_B + kM_C) n_{ijk} Z_A^{iM_A-1} Z_B^{jM_B-1} Z_C^{kM_C-1}$$

$$Z_A\frac{\partial N_g(\mathbf{Z})}{\partial Z_A} + Z_B\frac{\partial N_g(\mathbf{Z})}{\partial Z_B} + Z_C\frac{\partial N_g(\mathbf{Z})}{\partial Z_C} = \sum_{\substack{i,j,k=0\\ i+j+k\geq 1}}^{\infty} (iM_A + jM_B + kM_C) n_{ijk} Z_A^{iM_A} Z_B^{jM_B} Z_C^{kM_C} = W_g(\mathbf{Z}) M_{g,n}$$

$$\frac{\partial W_g(\mathbf{Z})}{\partial Z_A} + \frac{\partial W_g(\mathbf{Z})}{\partial Z_B} + \frac{\partial W_g(\mathbf{Z})}{\partial Z_C} = \frac{\sum_{\substack{i,j,k=0\\ i+j+k\geq 1}}^{\infty} (iM_A + jM_B + kM_C)^2 n_{ijk} Z_A^{iM_A-1} Z_B^{jM_B-1} Z_C^{kM_C-1}}{\sum_{\substack{i,j,k=0\\ i+j+k\geq 1}}^{\infty} (iM_A + jM_B + kM_C) n_{ijk}} \quad (19)$$

$W_g(\mathbf{Z})$ is a function of $N_g(\mathbf{Z})$ which is a function of pgfs N_{AB}, N_C, and ψ. The weight-average molecular weight of the graft polymer is thus composed of values of derivatives of the pgfs for the backbone and grafts, so that these distributions affect the number- and weight-average molecular weights of the graft polymer only through their number and weight averages. It is easy to see that for higher averages (e.g., the z-average) of molecular weight also higher averages of the distributions N_{AB} and N_C are necessary.

A detailed listing of values of derivatives from which $M_{g,w}$ is composed is given in Table 2. The superscripts at values of derivatives mean the variable with respect to which the differentiation has been performed. Thus,

$$F^X \equiv \left(\frac{\partial F(\mathbf{Z})}{\partial Z_X}\right)_{\mathbf{Z}=\mathbf{1}}, \quad F^{XY} \equiv \left(\frac{\partial F^2(\mathbf{Z})}{\partial Z_X \partial Z_Y}\right)_{\mathbf{Z}=\mathbf{1}}$$

$$F^{\zeta} \equiv \left(\frac{\partial F(\zeta(\mathbf{Z}))}{\partial \zeta}\right)_{\mathbf{Z}=\mathbf{1}}, \quad F^{\zeta\zeta} \equiv \left(\frac{\partial F^2(\zeta(\mathbf{Z}))}{\partial \zeta^2}\right)_{\mathbf{Z}=\mathbf{1}}$$

The independence of averages of the form of distributions has resulted from the absence of interdependence of the distributions of backbone and grafts. The mathematical reason for that is the fact that differentiation of a composite function results in product of derivatives of its components.

RESULTS AND DISCUSSION

The method for calculation of molecular-weight averages described in the preceding section can be used for any type of distribution of degrees of polymerization. If one wants to use a specific degree-of-polymerization distribution, the corresponding pgf for some of the most frequently used ones (most-probable, self-convoluted most-probable, and Poisson) and the corresponding degree-of-polymerization averages are displayed in Table 1. However, the number- and weight-average molecular weights of the graft copolymer given by eqs 15 and 17 are independent of any particular type of distribution of backbonce and grafts. This is apparently due to statistical independence of backbone and graft distributions because of random distribution of the number of grafts (grafted sites) grafted to the backbone. Although not shown here, it is not difficult to extend the method to an expression for z-average molecular weight

$$M_{g,z} = \frac{\sum_{\substack{i,j,k=0\\ i+j+k\geq 1}}^{\infty} (iM_A + jM_B + kM_C)^3 n_{ijk}}{\sum_{\substack{i,j,k=0\\ i+j+k\geq 1}}^{\infty} (iM_A + jM_B + kM_C)^2 n_{ijk}}$$

dx.doi.org/10.1021/ma3000187 | Macromolecules 2012, 45, 3240−3246

Table 2. Listing of Values of Derivatives of pgfs for Degree-of-Polymerization Distribution of Backbone and Grafts Necessary for Calculation of Molecular Weight Averages of the Grafted Copolymer According to Eqs 15 − 17

$$M_w = W_g^A + W_g^B + W_g^C$$

$$W_g^A = (N_g^A + N_g^{AA} + N_g^{BA} + N_g^{CA})/M_n$$

$$W_g^B = (N_g^B + N_g^{AB} + N_g^{BB} + N_g^{CB})/M_n$$

$$W_g^C = (N_g^C + N_g^{AC} + N_g^{BC} + N_g^{CC})/M_n$$

$$\zeta^{AA} = x_A M_A (M_A - 1)$$

$$\zeta^{BA} = \zeta^{AB} = 0$$

$$\zeta^{CA} = \zeta^{AC} = x_A M_A \alpha M_C P_{C,n},$$

$$\zeta^{BB} = x_B M_B (M_B - 1)$$

$$\zeta^{BC} = \zeta^{CB} = 0$$

$$\zeta^{CC} = x_A \alpha (M_C (M_C - 1) P_{C,n} + P_{C,n}(P_{C,w} - 1) M_C^2)$$

$$N_g^{XY} = N_g^{YX} = N_{\tilde{AB}}^{\zeta\zeta} \zeta^X \zeta^Y + N_{\tilde{AB}}^{\zeta} \zeta^{XY}$$

$$N_g^{AA} = N_{\tilde{AB}}^{\zeta\zeta} (\zeta^A)^2 + N_{\tilde{AB}}^{\zeta} \zeta^{AA}$$

$$N_g^{BB} = N_{\tilde{AB}}^{\zeta\zeta} (\zeta^B)^2 + N_{\tilde{AB}}^{\zeta} \zeta^{BB}$$

$$N_g^{CC} = N_{\tilde{AB}}^{\zeta\zeta} (\zeta^C)^2 + N_{\tilde{AB}}^{\zeta} \zeta^{CC}$$

$$N_g^{AB} = N_g^{BA} = N_{\tilde{AB}}^{\zeta\zeta} \zeta^A \zeta^B$$

$$N_g^{BC} = N_g^{CB} = N_{\tilde{AB}}^{\zeta\zeta} \zeta^B \zeta^C$$

$$N_g^{AC} = N_g^{CA} = N_{\tilde{AB}}^{\zeta\zeta} \zeta^A \zeta^C + N_{\tilde{AB}}^{\zeta} \zeta^{AC}$$

$$N_{\tilde{AB}}^{\zeta} = P_{AB,n}$$

$$N_{\tilde{AB}}^{\zeta\zeta} = P_{AB,n}(P_{AB,w} - 1)$$

$$N_g^A = N_{\tilde{AB}}^{\zeta} \zeta^A, \quad N_g^B = N_{\tilde{AB}}^{\zeta} \zeta^B, \quad N_g^C = N_{\tilde{AB}}^{\zeta} \zeta^C$$

$$\zeta^A = x_A M_A$$

$$\zeta^B = x_B M_B$$

$$\zeta^C = x_A \alpha M_C P_{C,n}$$

by calculating the values of the third derivatives of $N_g(\mathbf{Z})$. One also should remember that the number- and weight-fraction distributions remain stored in the pgfs and it is only a technical problem how to recover the distributions explicitly.

We shall discuss in terms of nonuniformities M_w/M_n the dependence of molecular-weight distribution on various parameters characterizing graft copolymers. The relevant parameters are number- and weight-average degrees of polymerization of backbone and grafts, $P_{AB,n}$, $P_{AB,w}$, $P_{C,n}$, $P_{C,w}$, respectively, molar fractions of monomer units A and B of the backbone copolymer x_A, x_B, molecular weights of monomer units A, B, and C, M_A, M_B, M_C, respectively, and fraction of units A that are grafted, α. Almost in all cases, the dependence of the nonuniformity M_w/M_n on the degree of grafting α has a characteristic shape: Starting from M_w/M_n of the backbone, the nonuniformity increases and passes through a maximum and then decreases reaching at $\alpha = 1$ a value more or less higher than is the value of M_w/M_n for the backbone (Figures 2−7).

In some special cases, M_w/M_n may asymptotically reach the nonuniformity of the backbone (cf., examples in Figures 2 and 4). The nonuniformity is larger at lower content of A-units in the backbone copolymer, x_A, or lower degree of grafting α. If the backbone is short, e. g., $P_{AB,n} = 10$, the maximum is found at higher values of α and the dependence M_w/M_n vs α is more flat (Figures 4 and 5). The increasing nonuniformity of backbones and grafts does not change the general shape of dependences of M_w/M_n on α; only the scales are changed (cf. Figures 4 and 5).

If one puts $M_A = M_B = M_C = 1$, one can find some other regularities related, for example, to the value of nonuniformity increments at maximum M_w/M_n. However, since the differences (disparities) in the molecular weights of monomer units A, B, and C have a large effect on the value of M_w/M_n, these interrelations are of little practical use. In real life, the chemist cannot preselect the molecular weights of reactants; they are determined by chemistry, the desired function, and their availability. The effect of disparity of molecular weight of monomer units deserves a special comment. If we are thinking of

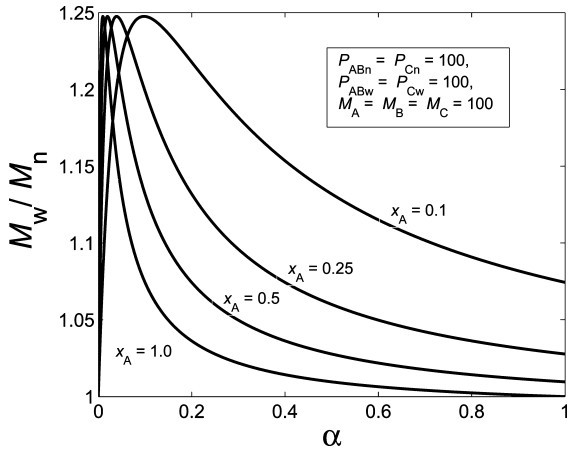


Figure 2. Nonuniformity as M_w/M_n of the graft copolymers with uniform backbone and grafts having different fractions of graftable monomer units, x_A, in dependence on the degree of grafting α; P_{ABn} and P_{ABw} are number- and weight-average degrees of polymerization of the backbone copolymer, P_{Cn} and P_{Cw} number- and weight-average degrees of polymerization per one graft; M_A, M_B, M_C are molecular weights of monomer units A, B, and C, respectively.

uniformity and nonuniformity, we are inclined to think in terms of numbers of units−degrees of polymerization. In practice, the instruments sense more weights or volumes rather than pieces. Two examples illustrate the effect of disparities of units and differences between nonuniformities expressed as P_w/P_n or M_w/M_n. Figure 6 illustrates the disparity between monomer units A and B of the backbone, while Figure 7 shows the effect of disparity of units C relative to units of the backbone.

The disparity is important whenever the number of grafts per backbone is small. For graft polymers characterized by larger x_A and α the effect of disparity of monomer units gets unimportant. It may seem that such systems with a few large grafts are not encountered in practical life. However, some polymer constructs used for drug delivery and molecular

dx.doi.org/10.1021/ma3000187 | Macromolecules 2012, 45, 3240−3246

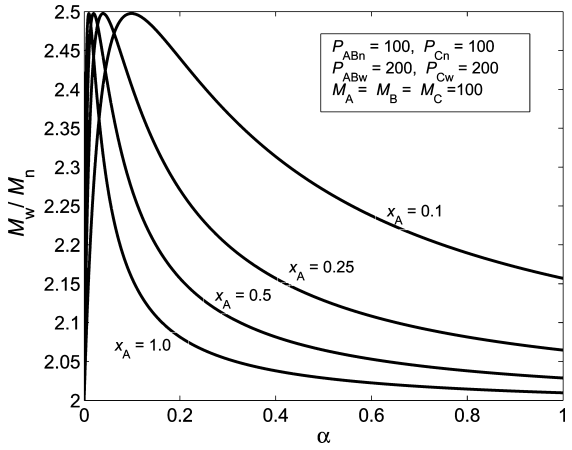


Figure 3. Nonuniformity as M_w/M_n of a graft copolymer with nonuniform backbone and grafts having different fractions of graftable monomer units, x_A, in dependence on the degree of grafting α.

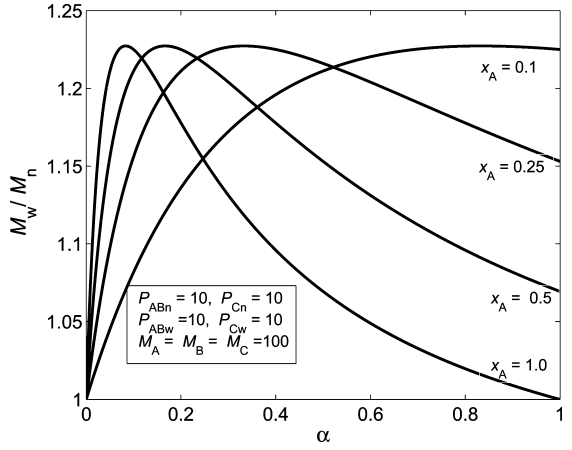


Figure 4. Nonuniformity as M_w/M_n of a graft copolymer with short uniform backbone and grafts, the backbone having different fractions of graftable monomer units, x_A, in dependence on the degree of grafting α.

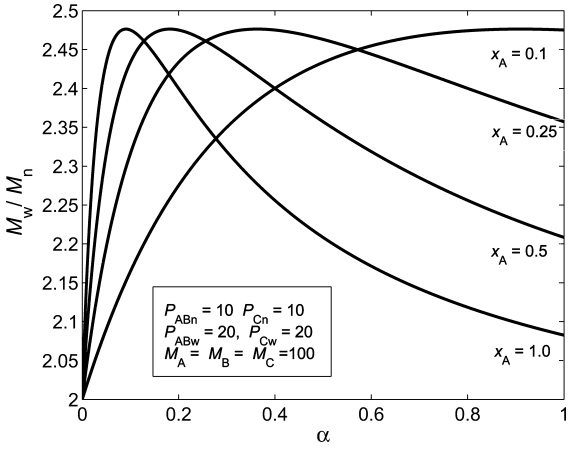


Figure 5. Nonuniformity as M_w/M_n of a graft copolymer with short nonuniform backbone and grafts, the backbone having different fractions of graftable monomer units, x_A, in dependence on the degree of grafting α.

recognition where a few biopolymer motifs of high molecular weight are grafted to synthetic hydrophilic copolymer backbones fall in this category. A broadening of molecular weight distribution after grafting should not be considered as a sign of

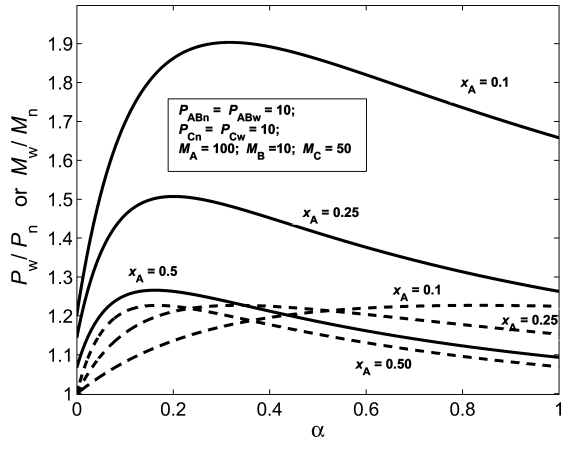


Figure 6. Nonuniformity as M_w/M_n and P_w/P_n of graft copolymers with short uniform backbone and grafts and disparity in molecular weights of backbone units A and B having different fractions of graftable monomer units, x_A, in dependence on the degree of grafting α. Full lines M_w/M_n, dashed lines P_w/P_n.

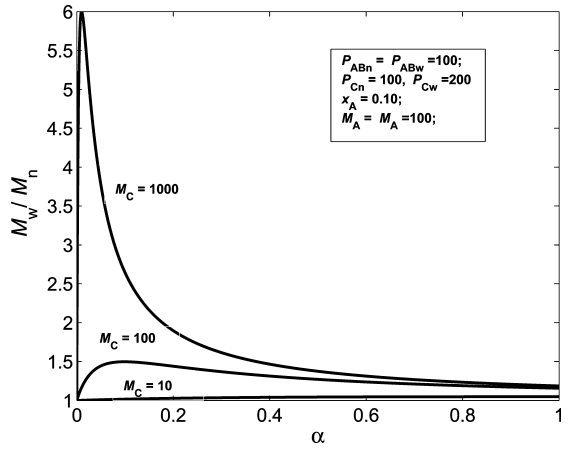


Figure 7. Nonuniformity as M_w/M_n of graft copolymers with uniform backbone and nonuniform grafts and disparity in molecular weights of backbone units and graft units C for the fraction of graftable units x_A = 0.1, in dependence on the degree of grafting α.

less success in bonding the grafts to the backbone, it just follows from the statistical nature of polymer chemistry.

The general shape of the dependence of M_w/M_n on α – passage through a maximum and subsequent decrease – can be explained as follows: The introduction of the first few grafts increases the nonuniformity of the graft copolymer, because larger backbone molecules have on average more graftable units A than the shorter ones. After a maximum, grafting of more chains has a "homogenization" effect and M_w/M_n decreases. The molecular weight distribution of the grafts gets less important. Mathematically, this effect can be related to the fact that a k-fold convolution of a distribution is narrower than the $(k-1)$-fold convolution; i.e., $D((N(\psi))^k) < D((N(\psi))^{k-1})$, $D \equiv M_w/M_n$ (see proof in Appendix). That is why also grafted copolymers with lower fraction of graftable units A, x_A, are more non-uniform. In any case, the non-uniformity of the backbone seems to be dominant over the non-uniformity of the grafts.

■ CONCLUSIONS

The generating function formalism has proved itself very efficient and economical in treatment of distributions of degrees

dx.doi.org/10.1021/ma3000187 | Macromolecules 2012, 45, 3240–3246

of polymerization and molecular weights of graft (co)polymers especially if the nonuniformities are expressed in terms of moments of distribution. It was found that for random grafting of graftable sites of a (co)polymer, the nonuniformities are a function of number- and weight-average degrees of polymerization of backbone and grafts and are independent of the type of degree-of-polymerization distribution. The general feature of the nonuniformity of graft (co)polymers is that, with increasing degree of grafting and degree of polymerization of the backbone, the nonuniformity of a graft (co)polymer passes through a maximum and approaches more or less closely the nonuniformity of the backbone (co)polymer. The disparity in the molecular weights of monomer units of the backbone copolymer and the grafts can have a large effect on the nonuniformity of the graft (co)polymer especially when the number of grafts per backbone is small. The disparity is unimportant in the case of a large degree of polymerization of the backbone and fraction of graftable units.

While grafted polymers of large molecular weight are typical of the area of supramolecular chemistry, the shorter ones of oligomeric nature and bearing functional groups find a wide application as precursors of polymer networks used especially as binders in protective coatings. Numerous examples can be found in the patent literature. In this case, the basic eq 10 can be slightly modified by introduction of a variable related to the reactive group (usually fixed to the graft) able to form bonds with a cross-linker. The modified eq 13 in its pgf form can serve as input information for the branching theory.

APPENDIX: NONUNIFORMITIES OF DISTRIBUTIONS OBTAINED BY CONVOLUTION OF DISTRIBUTIONS

For the number-fraction generating function $N(Z)$

$$N(Z) \equiv \sum_{i=1}^{k} n_i Z^i$$

the nonuniformity D_0 in terms of values of first and second derivatives of N reads

$$D_0 \equiv \frac{P_w^0}{P_n^0} = \frac{N''(1) + N'(1)}{(N'(1))^2} \tag{A-1}$$

Consider now a distribution obtained by convolution of k distributions $N(Z)$

$$\begin{aligned} C(Z) &\equiv (N(Z))^k \\ C'(Z) &= k(N(Z))^{k-1}N'(Z) \\ C''(Z) &= k(k-1)(N(Z))^{k-2}(N'(Z))^2 + k(N(Z))^{k-1}N''(Z) \end{aligned} \tag{A-2}$$

This gives the nonuniformity

$$\begin{aligned} D &\equiv \frac{P_w}{P_n} \\ &= \frac{C''(1) + C'(1)}{(C'(1))^2} \\ &= \frac{k(k-1)(N'(1))^2 + kN''(1) + kN'(1)}{k^2(N'(1))^2} \\ &= 1 - \frac{1}{k} + \frac{1}{k}\frac{N''(1)}{(N'(1))^2} + \frac{1}{kN'(1)} \\ &= 1 + \frac{1}{k}(D_0 - 1) \end{aligned} \tag{A-3}$$

Let us consider the ratio of nonuniformities

$$\frac{D}{D_0} = \frac{D_0 + k - 1}{kD_0} \tag{A-4}$$

For $k = 1$, $D = D_0$; for $D_0 = 1$, $D = D_0 = 1$; for $D_0 > 1$, and $k > 1$, it always holds that $D < D_0$, and $D(k+1) < D(k)$. Also, $\lim_{k\to\infty}(D/D_0) = 1$ holds.

AUTHOR INFORMATION

Notes

The authors declare no competing financial interest.

ACKNOWLEDGMENTS

M.N. acknowledges with thanks the financial support of the Grant Agency of the Czech Republic (Project P205/11/J043). K.D. acknowledges participation in the EC FP7 PITN-GA-2009-238700 NANOPOLY project.

REFERENCES

(1) Vainio, T.; Hu, C. H.; Lambla, M.; Seppälä, J. V. *J. Appl. Polym. Sci.* **1996**, *61*, 843−852.
(2) Kopeček, J.; Kopečková, P. *Adv. Drug Delivery Rev.* **2010**, *62*, 122−149.
(3) Radu-Wu, L. C.; Yang, J.; Wu, K.; Kopeček, J. *Biomacromolecules* **2009**, *10*, 2319−2327.
(4) Kopeček, J.; Yang, J. *Acta Biomater.* **2009**, *5*, 805−816.
(5) Gauthier, M.; Möller, M. *Macromolecules* **1991**, *24*, 4548−4553.
(6) Inoue, Y.; Matsugi, T.; Kashiwa, N.; Matyjaszewski, K. *Macromolecules* **2004**, *37*, 3651−3658.
(7) Štěpánek, M.; Košovan, P.; Procházka, K.; Janata, M.; Netopilík, M .; Pleštil, J.; Šlouf, M. *Langmuir* **2010**, *26*, 9289−9296.
(8) Tung, L. H.; Wiley, R. M. *J. Polym. Sci., Part B, Polym. Phys* **1973**, *11*, 1413−1421.
(9) Vorlíček, J.; Kratochvíl, P. *J. Polym. Sci., Part B: Polym. Phys* **1973**, *11*, 1251−1262.
(10) Ikada, Y.; Horii, F. *Macromol. Chem* **1974**, *175*, 227−236.
(11) Zhu, S. *Macromolecules* **1998**, *31*, 7519−7527.
(12) Nie, L.; Narayan, N.; Grulke, E. A. *Polymer* **1995**, *36*, 2227−2235.
(13) Dušek, K.; Šomvársky, J. *Polym. Bull.* **1985**, *13*, 313−319.
(14) Dušek, K.; Šomvársky, J. *Polym. Int.* **1997**, *44*, 225−236.
(15) Tobita, H. *Polymer* **1999**, *40*, 3565−3573.
(16) Galina, H.; Lechowicz, J. *Adv. Polym. Sci.* **1998**, *13*, 135−181.
(17) Liang, H.; Li, F.; He, X.; Jiang, W. *Eur. Polym. J.* **2000**, *36*, 1613−1617.
(18) Šomvársky, J.; Dušek, K.; Smrčková, M. *Comput. Theor. Polym. Sci.* **1998**, *8*, 201−208.
(19) Dušek, K.; Dušková-Smrčková, M.; Huybrechts, J. *J. Nanostruct. Polym. Mat* **2005**, *1*, 45−53.
(20) Gordon, M. *Proc. R. Soc. London, Ser. A, Math. Phys. Sci* **1962**, *268*, 240−256.
(21) Kajiwara, K.; Gordon, M. *J. Chem. Phys.* **1973**, *59*, 3623−3632.

Macromolecules

Article

pubs.acs.org/Macromolecules

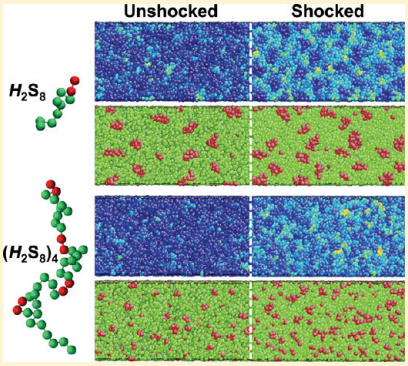
Viscoelastic Properties and Shock Response of Coarse-Grained Models of Multiblock versus Diblock Copolymers: Insights into Dissipative Properties of Polyurea

Bedri Arman, A. Srinivas Reddy, and Gaurav Arya*

Department of NanoEngineering, University of California, San Diego, 9500 Gilman Drive, Mail Code 0448, La Jolla, California 92093, United States

Supporting Information

ABSTRACT: We compare and contrast the microstructure, viscoelastic properties, and shock response of coarse-grained models of multiblock copolymer and diblock copolymers using molecular dynamics simulations. This study is motivated by the excellent dissipative and shock-mitigating properties of polyurea, speculated to arise from its multiblock chain architecture. Our microstructural analyses reveal that the multiblock copolymer microphase-separates into small, interconnected, rod-shaped, hard domains surrounded by a soft matrix, whereas the diblock copolymer forms larger, unconnected, hard domains. Our viscoelastic analyses indicate that compared with the diblock copolymer, the multiblock copolymer is not only more elastic but also more dissipative, as signified by its larger storage and loss modulus at low to intermediate frequencies. Our shock simulations and slip analyses reveal that shock waves propagate slower in the multiblock copolymer in comparison with the diblock copolymer, most likely due to the more deformable hard domains in the former system. These results suggest that the multiblock architecture of polyurea might impart polyurea with smaller, more deformable, and interconnected hard domains that lead to improved energy dissipation and lower shock speeds.



1. INTRODUCTION

Polyurea is a polymer formed by the reaction of a difunctional amine ($H_2N-R-NH_2$) and a difunctional isocyanate (OCN−R′−NCO). In general, R is a linear hydrocarbon chain and R′ an aromatic moiety, which make polyurea a multiblock polymer with alternating soft (R) and hard (R′) segments along its backbone (Figure 1a). Hydrogen bonding across distinct urea linkages (−HN−CO−NH−) along with possible Π-stacking interactions between aromatic rings cause the rigid segments to self-assemble and form high-T_g (glass-transition temperature), rod-shaped hard domains dispersed within a low-T_g soft matrix composed of the linear hydrocarbon chains.[1] At room temperature, the soft domains are above their T_g and impart polyurea its elastomeric properties, whereas the hard domains are below their T_g and impart polyurea its mechanical toughness and compressive stiffness, allowing polyurea to be used in a wide range of coating applications.[2,3] More recently, polyurea has been found to possess good dissipative properties and thus has been used as a shock-resistant material, especially to prevent the traumatic brain injury resulting from impacts and blasts.[4−6]

Whereas some ideas along the lines of a rubbery-to-glassy phase transformation within polyurea,[4] resonance of hard domains at high frequencies,[7] and breakage of hydrogen bonds across urea linkage[8] accompanying an impact have been proposed, a clear understanding of the mechanisms responsible for the superior energy dissipation properties of polyurea is still lacking. The dissipative nature of polyurea could arise from its "multiblock" architecture—repeating units of hard and soft segments. Interestingly, such a chain structure allows for the microphase-separated hard domains to remain covalently linked to each other via the soft segments, as the hard segments in one chain could conceivably participate in more than one hard domain. Such connectivity between the hard domains would not be achievable in a "diblock" version of polyurea possessing only a single hard and soft segment. In addition, because of the larger number of restrictions imposed on the multiblock copolymer chains compared with its diblock equivalent, the hard domains in multiblock polyurea are expected to be smaller and less stable than those of a diblock polyurea. These restrictions include entropy loss and bending penalty on the soft segments to permit the intervening or flanking hard segments to participate in a hard domain. How the multiblock chain architecture of polyurea, or any polymer for that matter, might enhance its energy dissipation and shock-mitigation properties clearly calls for a more detailed examination.

Here we take the first step toward addressing this question by carrying out a detailed comparison of the microstructure, viscoelastic properties, and shock response of a polyurea-like multiblock copolymer, a diblock copolymer, and two homopolymers. Our approach is computational, involving the use of idealized coarse-grained models to treat the four

Received: January 25, 2012
Revised: March 19, 2012
Published: March 28, 2012

 © 2012 American Chemical Society

polymers and the use of molecular dynamics (MD) simulations to compute their bulk properties. Because the study is motivated by polyurea, the composition of the hard and soft segments in our multiblock copolymer and their segregation strength are chosen to be roughly compatible with that of polyurea. However, no attempts have been made to rigorously map our multiblock copolymer chains onto polyurea to keep the model sufficiently generic and applicable to other multiblock copolymer systems that microphase-separate into well-segregated hard and soft domains. The diblock copolymer used for comparison is taken to be a shortened version of the multiblock copolymer, possessing a single hard and soft segment, and the homopolymers are taken to be of similar molecular weight as the two block copolymers but possess only the soft segments. Not only would the results from this study be relevant to the design of next-generation elastomeric materials for blast mitigation but also they would be of general interest to the polymers community, as this study represents to the best of our knowledge the first detailed computational investigation of the viscoelastic and shock response of block copolymers.

The rest of this Article is organized as follows. In Section 2, we describe coarse-grained modeling of the four polymer systems and the computation of their microstructure, viscoelastic properties, and shock response via MD simulations. In Section 3, we compare the polymeric systems in terms of chain configurations, monomer distributions, domain morphology, dynamic shear modulus, loss and storage modulus, shock velocities, and slip profiles. In Section 4, we discuss how these results provide useful insight into the superior dissipative properties of polyurea and suggest possible future extensions.

2. METHODS

Coarse-Grained Modeling of Polymers. We examine four polymeric systems in this study: a polyurea-like multiblock copolymer composed of hard and soft segments, a diblock version of the multiblock copolymer, and two homopolymers of soft segments with the same chain lengths as the multiblock and diblock copolymers. We employ the coarse-grained, bead-chain model of Kremer and Grest[9] to treat the four types of polymer chains. In this model, segments of the polymer are treated as coarse-grained beads of size σ and mass m. Two different types of beads denoted by H and S are employed to treat the hard and soft segments in the block copolymer chains, respectively. The number of beads of each type and their size are assigned according to the polyurea chain shown in Figure 1a, which is synthesized from the reaction of a diphenylmethane diisocyanate (hard segment) and a poly(tetramethylene oxide)-diaminobenzoate (soft segment) and is extensively used for blast mitigation.[10−12] Specifically, two H beads with σ = 11.2 Å and m = 150.6 amu are used to represent the hard segment of polyurea, and eight S beads of the same size as the H beads are used to represent the soft segment. The *diblock* version of polyurea thus comprises of a total of 10 beads and is denoted by H_2S_8 (Figure 1b). The *multiblock* chain is composed of four repeating units of the diblock copolymer (i.e., total of 40 beads) and is denoted by $(H_2S_8)_4$ (Figure 1c). Note that the degree of polymerization of experimental polyurea chains is much larger, but computational limitations preclude us from simulating chains longer than 40 beads. The *homopolymer* versions of the diblock and multiblock copolymers are composed of 10 and 40 soft beads and are denoted by S_{10} and S_{40}, respectively.

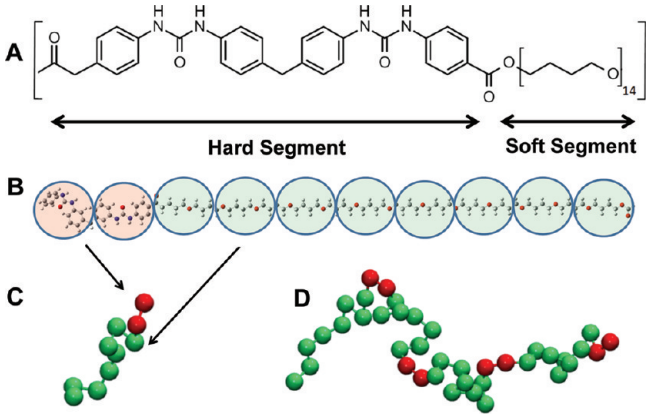


Figure 1. (a) Chemical structure of polyurea and (b) its mapping onto a coarse-grained bead−spring model. The hard segment is represented by two H beads (red), and the soft segment is represented by eight S beads (green). This mapping yields the (c) H_2S_8 and (d) $(H_2S_8)_4$ models of the diblock and multiblock copolymer.

The adjacent beads in all four polymer chains—$(H_2S_8)_4$, H_2S_8, S_{40}, and S_{10}—are connected via a strong finitely extensible nonlinear elastic (FENE) potential

$$U_{\mathrm{FENE}} = -\frac{k}{2}R_0^2 \ln[1 - (r/R_0)^2] \quad (1)$$

where r is the distance between bonded beads, $R_0 = 1.5\sigma$ is the maximum possible length of the spring, and $k = 30\varepsilon/\sigma^2$ is the spring constant. The parameter ε sets the energy scale (see below).

All $S-S$ and $H-S$ nonbonded interactions are treated using a short-range purely repulsive potential, also known as the Weeks−Chandler−Anderson (WCA) potential[13]

$$U_{\mathrm{rep}} = \begin{cases} 4\varepsilon[(\sigma/r)^{12} - (\sigma/r)^6 + 1/4] & r < 2^{1/6}\sigma \\ 0 & r \geq 2^{1/6}\sigma \end{cases} \quad (2)$$

All $H-H$ nonbonded interactions are treated using a short-range potential that includes both repulsive and attractive components[14,15]

$$U_{\mathrm{att}} = \begin{cases} 4\varepsilon[(\sigma/r)^{12} - (\sigma/r)^6 + 1/4] - \Phi & r < 2^{1/6}\sigma \\ \frac{1}{2}\Phi[\cos(\alpha r^2 + \beta) - 1] & 2^{1/6}\sigma \leq r < 1.5\sigma \\ 0 & r \geq 1.5\sigma \end{cases} \quad (3)$$

In U_{att}, the constants α = 3.17307 and β = −0.85623 are chosen so that the potential is continuous and approaches smoothly to zero at the cutoff distance and Φ represents the attractive well depth of this potential and is responsible for promoting microphase separation in our two block copolymers.

The parameter Φ represents the "effective" attraction between the $H-H$ segments and is given by $E_{HH} + E_{SS} - 2E_{HS}$, where E_{ij} are the "actual" attraction energies for the three pairs of interactions. According to previous studies,[16,17] we choose $\Phi = 2.5\varepsilon$ and $\varepsilon = k_BT$, which are known to yield strongly segregated microphases. Moreover, rough calculations show that the chosen value of Φ yields a dimensionless Flory−Huggins parameter χ_{HS} close to a previously reported value for polyurea. Specifically, χ_{HS} for our system can be computed

dx.doi.org/10.1021/ma3001934 | Macromolecules 2012, 45, 3247−3255

using the standard relation $\chi_{HS} = z\Delta w/k_BT$, where z is the average coordination number of the polymer segments (beads) and Δw is an energy parameter that is a function of the individual pairwise contact energies of the hard and soft beads: $\Delta w = w_{HS} - 1/2(w_{HH} + w_{SS})$.[18] Using $z \approx 5$, as estimated from Cahoon's chart,[19] $w_{HS} = w_{SS} = 0$, and $w_{HH}/k_BT = -\Phi$, we obtain $\chi_{HS} \approx 6.25$, which is close to the value of 5.42 reported by Grujicic et al.[20]

For convenience, we report our results in reduced units of bead mass m, size σ, and energy ε. These quantities in reduced units, identified by asterisks, can be converted to real units, without asterisks, as follows: time $t^* = t(\varepsilon/m\sigma^2)^{1/2}$, frequency $\omega^* = \omega(m\sigma^2/\varepsilon)^{1/2}$, length $l^* = l/\sigma$, temperature $T^* = k_BT/\varepsilon$, energy $E^* = E/\varepsilon$, pressure $P^* = P\sigma^3/\varepsilon$, viscosity $\eta^* = \eta\sigma^2/(m\varepsilon)^{1/2}$, speed $u^* = u(m/\varepsilon)^{1/2}$, moduli $G^* = G\sigma^3/\varepsilon$, and number density $\rho^* = \rho\sigma^3$. From this point onward, we report only reduced values but omit the asterisks for convenience, unless otherwise noted.

Calculation of Polymer Properties. The microstructure and viscoelastic properties of the four polymer systems previously introduced are computed using equilibrium MD simulations performed in the canonical (NVT) ensemble. In our simulations, we set the temperature T to a value of 1 using a Nosé–Hoover thermostat.[21] A standard velocity-Verlet algorithm is used to integrate the equations of motion with a time step of $\Delta t = 0.012$ similar to previous studies.[22,23] The initial configurations are generated by placing linear chains in a large simulation box implementing periodic boundary conditions (PBCs). The simulation box is then gradually compressed until the bead density ρ reaches a value of 0.85. At the chosen density and temperature, the soft segments are above their T_g and exist in a melt state,[9] the hard segments are below their T_g and display a solid state,[17] and the entire system is below the order–disorder transition temperature.[17] During this compression step, only the repulsive pair interactions (eq 2) are implemented. In the two block copolymer systems, the attractive interactions are turned on after the relaxation of the chains at the same density. We utilize system sizes composed of $n = 20\,000$ and $80\,000$ total beads for determining the viscoelastic properties and microstructure, respectively. The simulations are run for 2×10^7 and 4×10^7 time steps for the homopolymers and block copolymers, respectively. Assuming ε to be on the order of k_BT at room temperature, the time step is ~0.1 ps and the simulations span ~2–4 μs of real time.

The time-dependent shear modulus $G(t)$ is computed from the stress autocorrelation function (SACF)

$$G(t) = \frac{V}{k_BT}\langle \sigma_{\alpha\beta}(t)\sigma_{\alpha\beta}(0)\rangle \tag{4}$$

and the Newtonian shear viscosity η is computed using the Green–Kubo formulation

$$\eta = \int_0^\infty G(t)\, dt \tag{5}$$

where V is the system volume, T is the temperature, k_B is the Boltzmann constant, and $\langle\cdots\rangle$ denotes ensemble average. The stress $\sigma_{\alpha\beta}$ is calculated via the virial theorem

$$\sigma_{\alpha\beta} = \frac{1}{V}\left[\sum_{i=1}^{n} m_i v_{i\alpha} v_{i\beta} + \sum_{i=1}^{n-1}\sum_{j=i+1}^{n} r_{ij\alpha} F_{ij\beta}\right] \tag{6}$$

Here m_i, $v_{i\alpha}$, and $v_{i\beta}$ are the mass and α- and β-component velocities of bead i, respectively; and $r_{ij\alpha}$ and $F_{ij\beta}$ are the α-component separation distance and β-component force acting between beads i and j, respectively. The first term specifies the kinetic energy contribution, and the second term specifies the bonded and nonbonded energy contributions. Note that the three off-diagonal elements of the stress tensor σ_{xy}, σ_{xz}, and σ_{yz} are equivalent, as expected for an isotropic system. We therefore use the average of the three stresses to obtain smoother estimates of the SACF. Furthermore, the stresses are computed each time step to obtain accurate results, as done in previous studies.[24]

The storage modulus $G'(\omega)$ and the loss modulus $G''(\omega)$ are computed by converting $G(t)$ into its frequency (ω)-dependent complex form $G^*(\omega)$

$$G^*(\omega) = i\omega \int_0^\infty e^{-i\omega t} G_{xy}(t)\, dt \tag{7}$$

where $G'(\omega)$ and $G''(\omega)$ represent the real and complex portions of $G^*(\omega)$, respectively

$$G'(\omega) = \omega \int_0^\infty G_{xy}(t)\sin(\omega t)\, dt \tag{8}$$

$$G''(\omega) = \omega \int_0^\infty G_{xy}(t)\cos(\omega t)\, dt \tag{9}$$

In shock simulations, a sufficiently long simulation box along the direction of wave propagation is required. To this end, the simulation box used for computing viscoelastic properties is replicated ×12 along the chosen direction for shock propagation (z-axis), yielding a box of sides 28.7 × 28.7 × 338 containing 240 000 beads. The PBCs are implemented only along the two directions orthogonal to the shock direction and equilibrated to a pressure $P \approx 0$ in an NPT ensemble, which is nominal for shock simulations. The resulting configuration is then used as the starting point for the shock simulations. The shock runs are performed by adopting the projectile-wall geometry and a microcanonical (NVE) ensemble to mimic adiabatic conditions.[25−27] In this approach, the desired "particle" velocity u_p pointing in the $+z$ direction is added to the thermal velocity of each polymer bead. The simulation box dimensions are fixed along the x and y directions such that a 1D strain loading mimicking the experiments is generated. Upon the impact of polymer beads with the wall located at the $+z$ end of the simulation box, a shock wave is generated that travels away from the wall in the direction opposite to u_p. The energetic interaction between the wall particles and the polymer beads are treated using a 12–6 Lennard-Jones potential.[27]

To characterize atomic-level deformations of the polymer in the shocked and unshocked regions, we compute the slip vector s_i, which is defined as the maximum relative displacement[27,28] of bead i with respect to its j neighbors

$$\mathbf{s}_i \equiv \max(\mathbf{x}_{ij} - \mathbf{X}_{ij}) \tag{10}$$

where $\mathbf{x}_{ij}$ and $\mathbf{X}_{ij}$ represent the interbead vector in the current and reference configurations, respectively.[29] The reference configurations are taken as the preshock structures, and the scalar slip $s_i = |\mathbf{s}_i|$ is used in our analysis. Although the slip vector approach was originally developed for crystalline materials,[29] it has proven to be a valuable tool for probing plastic deformation in amorphous materials.[27,30] Shock profiles of particle velocity u_p and slip magnitudes s along the z

dx.doi.org/10.1021/ma3001934 | Macromolecules 2012, 45, 3247–3255

direction are obtained via 1D binning procedure (averaging over beads residing within equal-sized "bins" along the shock direction[26,31]).

All MD simulations in this study are performed using the large-scale atomic/molecular massively parallel simulator (LAMMPS) package, developed by Sandia National Laboratories.[32]

3. RESULTS

Polymer Microstructure. Figure 2a,b shows representative configurations of the block copolymers H_2S_8 (diblock) and

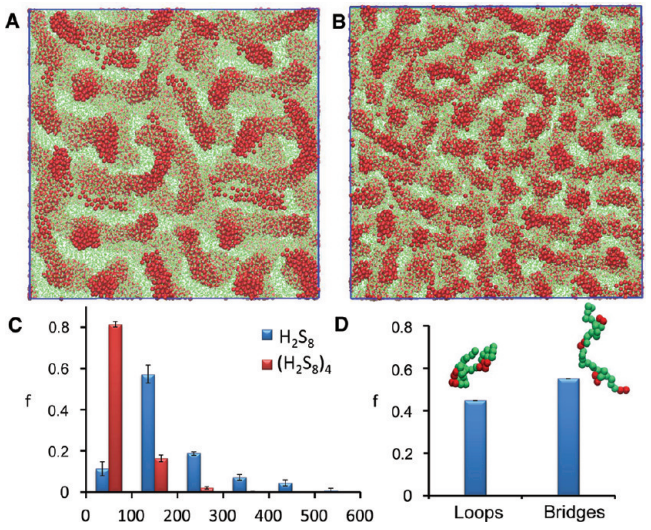


Figure 2. (a,b) Snapshot of the simulation box (of size 45.49σ) illustrating microphase separation of H_2S_8 and $(H_2S_8)_4$ into hard and soft domains. For visualization purposes, the H beads are represented by red spheres and the S beads by green points. (c) Size distribution of hard domains in H_2S_8 and $(H_2S_8)_4$ in terms of fraction of domains with sizes 0−100, 100−200 beads, and so on. (d) Fraction of soft segments in $(H_2S_8)_4$ that form loops and bridges.

$(H_2S_8)_4$ (multiblock) taken from our MD simulations following extensive equilibration. Both block copolymers undergo microphase separation into rod-shaped hard domains composed of H beads surrounded by a soft domain composed of S beads. However, the two block copolymers show distinct differences in their morphology. Whereas H_2S_8 displays thick, long, and strongly segregated hard domains, $(H_2S_8)_4$ displays thinner, shorter, and less strongly segregated hard domains. The diameters of the rod-like hard domains fall in the range $5-8\sigma$ (6−10 nm) for H_2S_8 and $4-7\sigma$ (5−8 nm) for $(H_2S_8)_4$. These sizes agree well with the reported diameters of 5−10 nm for poly(urethane urea) hard domains obtained via AFM tapping measurements.[33] To explore these differences further, we have computed the size distribution of the hard domains for both block copolymers (Figure 2c). H_2S_8 exhibits a broad size distribution of hard domains containing 76−540 H beads with ∼57% of the domains containing 100−200 beads. $(H_2S_8)_4$ exhibits a narrower size distribution of hard domains containing 25−280 H beads with ∼80% of the domains containing 0−100 beads. Because the number of hard segments is the same in both systems, H_2S_8 segregates into a smaller number of hard domains (∼85) compared with $(H_2S_8)_4$ (∼211). The fact that $(H_2S_8)_4$ yields smaller hard domains than H_2S_8 can be explained based on the connectivity restraint between the hard segments of a chain, which imposes a large entropic and energetic penalty for the hard segments from the same or different chains to participate in the formation of hard domains. Stronger entanglements effects in the case of the longer $(H_2S_8)_4$ chains further hinder the formation of large hard domains.

The hard segments of a single multiblock copolymer chain can be involved in more than one hard domain, allowing for hard domains to be connected to each other via intervening soft segments. To investigate the degree of connectivity between hard domains, we have computed the fraction of soft segments that "bridge" across distinct hard domains, as denoted by f_{bridge}, and the fraction that "loop" to allow two hard segments to participate in a common hard domain, as denoted by $f_{loop} \approx 1 - f_{bridge}$. Therefore, f_{bridge} quantifies the degree of connectivity between the hard domains while f_{loop} quantifies their independence. The results of such an analysis are shown in Figure 2d, indicating that the hard domains are well-connected to each other. In fact, more than half of the soft segments (f_{bridge} = 0.56) are involved in connections between hard domains.

Figure 3 presents the radial distribution functions $g(r)$ for the three pairwise interactions $H-H$, $S-S$, and $H-S$ in the H_2S_8

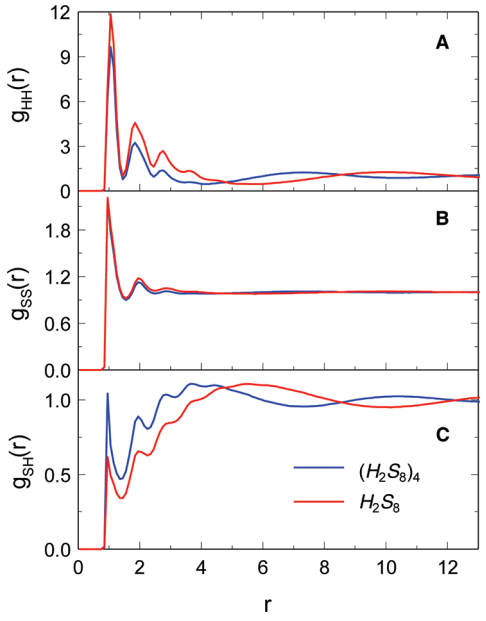


Figure 3. Radial distribution functions of (a) $H-H$, (b) $S-S$, and (c) $S-H$ beads compared for H_2S_8 (red lines) and $(H_2S_8)_4$ (blue lines).

and $(H_2S_8)_4$, where r is the separation distance between the polymer beads. The distributions reveal key structural differences between the hard and soft domains as well as differences between the domain morphology of the diblock and multiblock copolymers. First, the shallow, long-range peak in g_{HH} (Figure 3a), which corresponds to the average separation between hard domains, indicates that the interdomain distances are larger ($\sim 10\sigma$) in H_2S_8 compared with $(H_2S_8)_4$ ($\sim 7\sigma$). This result is expected given the smaller number of larger-sized hard domains in the diblock copolymer compared with the multiblock copolymer. Second, the considerably higher short-range peak in g_{HH} (Figure 3a) compared with g_{SS} (Figure 3b) reflects a near-crystalline solid structure of the hard domains compared with the more fluid-like structure of the soft domains, in agreement with the expected morphology of polyurea. Third, this g_{HH} peak is somewhat lower in $(H_2S_8)_4$ compared with

dx.doi.org/10.1021/ma3001934 | Macromolecules 2012, 45, 3247−3255

H_2S_8, indicating less compact and segregated hard domains in the former system. Fourth, the higher short-range peaks in the g_{SH} of $(H_2S_8)_4$ (Figure 3c) are reflective of the larger number of bonded $H-S$ segments.

Viscoelastic Properties. The Newtonian shear viscosity η of the diblock and multiblock copolymers and of the corresponding homopolymers has been obtained using eqs 4−6. As expected, $(H_2S_8)_4$ with $\eta = 2232 \pm 312$ is more viscous than H_2S_8 with $\eta = 498 \pm 122$ because of the longer chains and the network-like connectivity of the hard domains previously discussed. Also, as expected, the two copolymers exhibit a significantly higher viscosity than their corresponding homopolymers S_{40} and S_{10}, with $\eta = 33.7 \pm 3.2$ and 10.2 ± 1.3, respectively. The viscosities of the two homopolymers are in good agreement with previously computed values.[34]

The dynamic shear modulus $G(t)$ of the two block copolymers and of the two homopolymers are plotted in Figure 4. To reduce the large noise present in $G(t)$ at longer

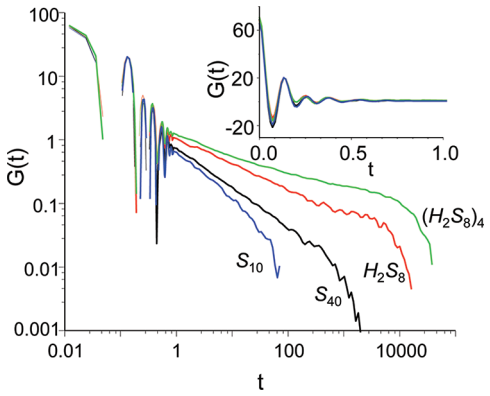


Figure 4. Dynamic shear modulus $G(t)$ for S_{10} (blue), S_{40} (black), H_2S_8 (red), and $(H_2S_8)_4$ (green) in log−log scale. The inset shows the short-time behavior of $G(t)$ in regular scale.

times, we report running averages from $0.9t$ to $1.1t$ for each time, t, as suggested by a previous study.[34] At short times $t = 0$ to 1.0, the primary mechanism for stress relaxation is the rearrangement of bond lengths and is independent of the microstructure. Therefore, the $G(t)$ values for the four polymeric systems are similar at short times (Figure 4 inset). At intermediate times, the reorientation of chain segments becomes more dominant for relaxing polymer conformations and the $G(t)$ values for the four systems begin to differ. Because we do not expect any significant entanglement effects in homopolymers of lengths 10 and 40 beads,[34] their $G(t)$ roughly follow the Rouse scaling $t^{-1/2}$. Significant "slowing down" and deviations from the Rouse scaling are observed in the case of the two block copolymers. We also observe a hint of a plateau in the $G(t)$ of the block copolymers, which is more apparent in $(H_2S_8)_4$ than H_2S_8. Such plateauing is indicative of a solid-like response stemming from the immobilization of hard segments within the hard domains. The network-like connectivity of hard domains also likely contributes to this effect in the case of multiblock copolymers. A similar looking but more prominent plateau was recently observed in the $G(t)$ of polymer nanocomposites[35,36] that was attributed to the lower mobility of polymer segments near particle surfaces. Therefore, the block copolymers' response are intermediate to that of homopolymer melts and polymer nanocomposites. At even longer times, all $G(t)$ drop precipitously in an exponential manner with a time constant given by the longest relaxation mode in the system.[34] The fact that we observe such a drop suggests that the MD simulations are sufficiently long to capture the mechanisms responsible for stress relaxation and that the plateauing effect might be real and not an artifact of the time-limitation of MD simulations.

The storage $G'(\omega)$ and loss $G''(\omega)$ moduli of the four polymers, as computed via eqs 8 and 9, are plotted in Figure 5.

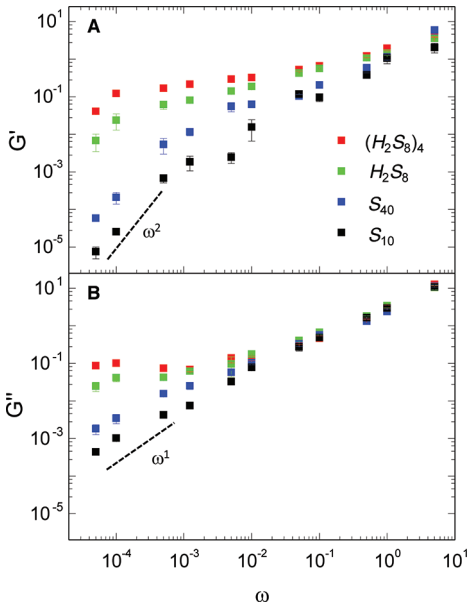


Figure 5. Storage G' and loss G'' moduli as a function of frequency ω for S_{10} (blue), S_{40} (black), H_2S_8 (red), and $(H_2S_8)_4$ (green). The dashed lines in the G' and G'' representing ω^2 and ω^1 scalings are included as guides.

The viscoelastic response at low frequencies is strongly indicative of the state of the material.[18] The homopolymers show liquid-like terminal behavior at low frequencies, that is, $G' \approx \omega^2$ and $G'' \approx \omega^1$. In contrast, the diblock and multiblock copolymer show departure from the above scalings in the same frequency range with $G' \approx \omega^\nu$ and $G'' \approx \omega^\mu$, where $\nu < 2$ and $\mu < 1$. This nonterminal behavior indicates that the two block copolymer systems behave as an intermediate to a Newtonian fluid ($G'' \approx \omega^1$) and a solid ($G'' \approx \omega^0$), as expected for block copolymers below their order−disorder temperature.[18,37] This loss of terminal liquid-like behavior in both $G'(\omega)$ and $G''(\omega)$ is more prominent in $(H_2S_8)_4$ than H_2S_8. Interestingly, $(H_2S_8)_4$ exhibits the largest storage and loss modulus across the entire frequency range, followed by H_2S_8, then S_{40} and S_{10}. The higher $G'(\omega)$ in $(H_2S_8)_4$ is expected given its higher elasticity arising from the more networked, hard domains, but the fact that the networked structure of $(H_2S_8)_4$ also yields a higher loss modulus is not so obvious. How exactly the connectivity between hard domains leads to higher dissipation is not clear but could arise from concerted motions of the interconnected hard domains. A similar result has been observed experimentally in block copolymers possessing hard A (diamide) and soft B (poly(tetramethylene oxide)) segments, where multiblock polymers $(AB)_4$ exhibit higher overall modulus than triblock ABA_7 and diblock copolymers AB_3.[38]

The general shapes of the computed $G'(\omega)$ and $G''(\omega)$ for the two block copolymers agree well with those measured experimentally for cubic and bicontinuous microphase-forming

dx.doi.org/10.1021/ma3001934 | Macromolecules 2012, 45, 3247−3255

block copolymers.[39,40] At low frequencies, $G'(\omega) < G''(\omega)$ and the material is more dissipative than elastic. At intermediate frequencies, a crossover occurs and the material becomes more elastic, that is, $G'(\omega) > G''(\omega)$. At the onset of this regime, the $G'(\omega)$ and $G''(\omega)$ exhibit a plateau and a dip, respectively, which are typically indicative of entanglement effects. Note that the block copolymers studied here are too short to exhibit true chain entanglements. Hence, the observed plateauing effect most likely arises from the immobilization of the H segments of the polymer chains within the hard domains. At higher frequencies, $G''(\omega)$ and $G'(\omega)$ both rise monotonically in a manner similar to homopolymers until $G'(\omega) < G''(\omega)$ again. This ω-dependent modulation in the "dissipativeness" of the two block copolymers may also be gleaned from calculations of $\tan \delta$ $[= G''(\omega)/G'(\omega)]$ provided in the Supporting Information, Figure S1.

In general, the sensitivity of $G'(\omega)$ and $G''(\omega)$ to the microstructure diminishes above a critical frequency ω_c roughly given by $0.1\tau^{-1}$, where τ is the single-chain terminal relaxation time estimated from the frequency at which $G'(\omega)$ and $G''(\omega)$ cross.[37] For our polymer systems, one can obtain $\omega_c \approx 0.01$ from Figure 5. Therefore, according to the above argument, the $G'(\omega)$ and $G''(\omega)$ curves are supposed to become similar for all systems for $\omega > \omega_c$. Whereas $G''(\omega)$ curves follow this rule, as noted by their rapid convergence for $\omega > \omega_c$, the $G'(\omega)$ curves converge much slower. In particular, the distinction between all four polymers remains until $\omega \approx 0.5$, even though the diblock and multiblock copolymer $G'(\omega)$ seems to have converged by $\omega \approx \omega_c$. Such lower sensitivity of $G''(\omega)$ compared with $G'(\omega)$ has also been observed in experiments and theoretical models.[37,41]

Shock Response. The two block copolymers and the S_{40} homopolymer were subjected to shock loading with a particle velocity u_p in the range 0.25 to 3.0. Figure 6a,b shows representative shocked-state configurations of $(H_2S_8)_4$ and H_2S_8 for $u_p = 2$, illustrating the differences in the polymer microstructure across the shock-unshocked interface. The corresponding u_p–z profiles for the two systems recorded at equivalent time intervals after shock initiation are shown in Figure 6c; here z specifies position along the shock direction and u_p is the measured particle velocity. The above profiles demonstrate the existence of well-supported shocks and also illustrate differences in the shock velocities developed within the two systems.

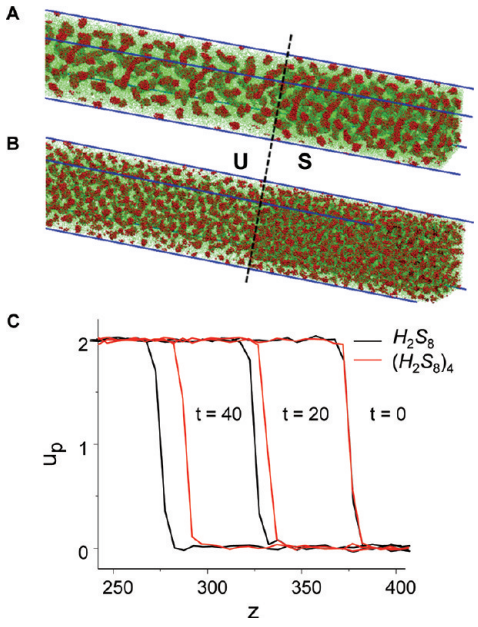


Figure 6. (a,b) Representative configurations of H_2S_8 (a) and $(H_2S_8)_4$ (b) captured from shock simulation illustrating the shock front (dotted line) separating the unshocked region (U) from the shocked (S) regions. The H beads are shown as red spheres and the S beads as green dots. (c) Particle velocity $u_p(x)$ profiles for H_2S_8 (black) and $(H_2S_8)_4$ (red).

In Figure 7, we have plotted the shock velocity u_s as a function of particle velocity u_p, commonly referred to as the u_s–u_p Hugoniot, for the three systems investigated here. The shock velocities have been computed from the rate of propagation of the shock front with time. A linear dependence between u_s and u_p across the investigated range of particle velocities is observed. A similar linear relationship has also seen in the experimental shock response of polyurea-1000.[42] More importantly, we find $(H_2S_8)_4$ consistently exhibits a lower u_s than H_2S_8, and the difference between the two becomes more pronounced at $u_p > 1.0$. This difference in shock speeds can also be gleaned from the shock profiles shown in Figure 6c. Overall, $(H_2S_8)_4$ shows shock velocities comparable to the homopolymer S_{40}.

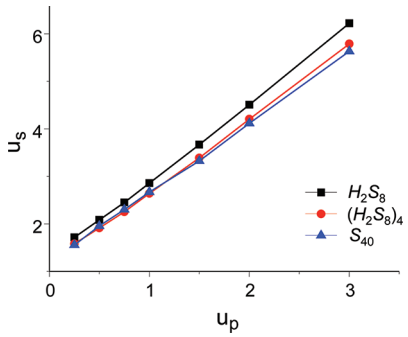


Figure 7. Computed u_s–u_p Hugoniot for the H_2S_8 (black squares), $(H_2S_8)_4$ (red circles), and S_{40} (blue triangles).

To investigate the molecular origin of the lower shock velocity in the multiblock copolymer as compared to the diblock copolymer, we have computed the magnitudes s of the slip vector for each polymer bead in the two block copolymers according to eq 10. The difference between the slip magnitude s of shocked and unshocked material roughly quantifies the amount of plastic deformations associated with shock propagation. Figure 8a,c shows representative snapshots of the diblock and multiblock copolymer configurations, shock-loaded at $u_p = 2$, in which each polymer bead has been color-coded according to the magnitude of the slip vector s. To match the computed s with the bead type (H or S), we have also included another representation in which polymer beads are now colored according to their type (Figure 8b,d). We have also computed the overall slip magnitudes s and the individual slip values of the H and S segments across the shock front as a function of position z along the shock direction (Figure 9a,b).

Figures 8 and 9 show that for both block copolymers the unshocked regions exhibit a finite slip as a result of thermal fluctuations and that the slip increases nearly two-fold in the shocked regions. More importantly, the slip profiles $s(z)$ in Figure 9a reveal that whereas H_2S_8 exhibits a larger slip ($s \approx 3.2$) than $(H_2S_8)_4$ ($s \approx 2.8$) in the unshocked regions, both

dx.doi.org/10.1021/ma3001934 | Macromolecules 2012, 45, 3247–3255

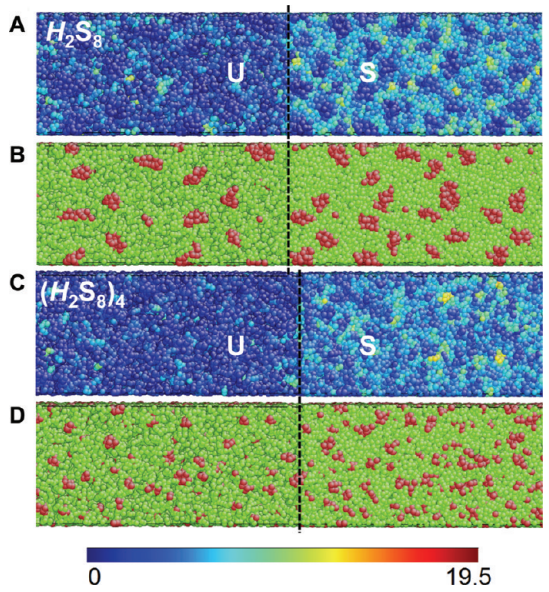


Figure 8. Slip magnitude s of H_2S_8 (a) $(H_2S_8)_4$ (c) beads according to the included color scheme. The corresponding color representations according to bead type are shown in (b) and (d), respectively. The H and S beads are shown as red spheres and green dots, respectively. The labels U and S indicate unshocked and shocked regions, which are separated the dotten line. The visualization is created via AtomEye.[49]

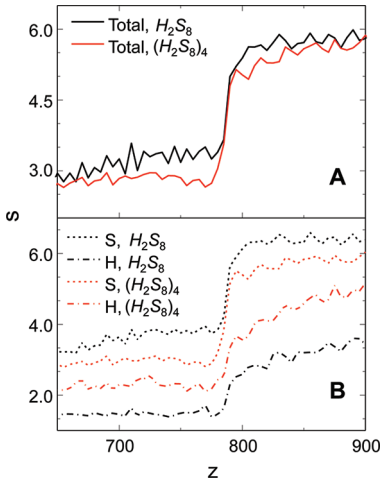


Figure 9. (a) Total slip s profiles along the z direction (solid lines) and (b) contributions from H (dotted-dashed lines) and S (dotted lines) beads for H_2S_8 (black lines) and $(H_2S_8)_4$ (red lines) at $u_p = 2$.

copolymers exhibit higher and more comparable slips in the shocked region with $s \approx 5.9$ for H_2S_8 and $s \approx 5.7$ for $(H_2S_8)_4$. The difference in s between the shocked (S) and unshocked (U) regions, $\Delta s \equiv s_S - s_U$, suggests that $(H_2S_8)_4$ undergoes an overall larger deformation ($\Delta s = 2.9$) upon shock than H_2S_8 ($\Delta s = 2.7$). The individual slip profiles $s(z)$ in Figure 9b reveal that the H beads undergo larger jumps in the slip Δs across the shock front in $(H_2S_8)_4$ ($\Delta s \approx 2.7$) as compared with H_2S_8 ($\Delta s \approx 2.0$). The S beads exhibit similar jumps $\Delta s \approx 2.9$ in both $(H_2S_8)_4$ and H_2S_8. The lower jump Δs of the H beads for H_2S_8 reflects a higher conservation of hard domains in H_2S_8 under shock loading as compared with $(H_2S_8)_4$. This difference between the two block copolymers can also be observed from the greater conservation of the dark blue regions (corresponding to the hard domains) across the shock front in the slip representation of H_2S_8 (Figure 8a) compared with that of $(H_2S_8)_4$ (Figure 8c). Therefore, the hard domains in the diblock copolymer essentially behave as rigid bodies with high shock impedance resulting in increased u_s, similar to recent studies on carbon nanotube composites.[27,43] Multiblock copolymers show an overall more homogeneous s distribution for both hard and soft segments in the shocked state, indicating that the H beads are possibly more open to deformation upon shock loading. In other words, whereas the soft segments carry most of the plastic deformation in H_2S_8, both the soft and hard segments are equally involved in carrying plastic deformations in $(H_2S_8)_4$. The above analyses thus suggest that the stronger dissipation and lower shock speeds observed in the multiblock copolymer in relation to diblock copolymers might arise from the larger deformability of the hard domains of the multiblock copolymer.

Our slip analyses reveals several additional insights. First, the S segments contribute the most slip in both block copolymers (Figure 9b). These strongly slipping S beads can be seen as the light blue colored beads in Figure 8a,c. The higher s of the S beads is understandable given their higher mobility compared with the H beads, which are trapped within hard domains. A similar reasoning explains why the S beads of H_2S_8 chains exhibit higher s and are more mobile than those of $(H_2S_8)_4$ chains; that is, only one end of the S segment is trapped in the hard domains of diblock copolymers, whereas both of its ends are trapped in multiblock copolymers. Second, as expected, the H segments (red beads) in both copolymers are more densely packed in the shocked state compared with the unshocked region (Figure 8). Because of the higher deformability of the multiblock copolymer compared with the diblock copolymer, one expects the multiblock copolymer to exhibit a higher relative increase in density ρ_S/ρ_U across the shock front. Given the well-known relationship between the shock and particle speeds $u_s = u_p/(1 - \rho_S/\rho_U)$ arising from mass balance,[44] one can conclude that the more deformable multiblock copolymer should naturally exhibit lower shock speeds. Third, the shock front in Figure 9b shows critical differences between the H and S beads. The s values of the S beads in both copolymers exhibit a sharp jump at the shock front and also approach a steady value quickly. The s values for the H beads, in contrast, display a more gradual transition to the shocked state, yielding a broader shock front. The more gradual shock front in the H beads might result from their higher viscosity (compared with S beads) because there exists an inverse relationship between effective viscosity and steepness of the shock front.[43,45]

4. DISCUSSION

We have used a computational approach to provide insight into how the multiblock chain architecture of polyurea, composed of repeating units of "hard" and "soft" segments, might endow it with structural and dynamical properties suitable for energy dissipation. Specifically, we have carried out MD simulations to compute and compare the microstructure, viscoelastic properties, and shock response of a polyurea-like multiblock copolymer, its diblock copolymer counterpart, and two homopolymers of similar molecular weights composed of only soft segments.

Our equilibrium simulations demonstrate that the multiblock copolymer microphase-separates into rod-shaped hard domains dispersed within a soft matrix. Because of the strong restraints on chain conformations in multiblock copolymer limiting its microphase separation, the hard domains are smaller and more

dx.doi.org/10.1021/ma3001934 | Macromolecules 2012, 45, 3247−3255

uniformly sized compared with those of the diblock copolymer. Examination of chain conformations reveals that about half of the soft segments in the multiblock copolymer are involved in bridging interactions across hard domains, whereas the remaining half yield loops connected to the same hard domain. The radial distribution functions for the interactions between the hard segments reveal a more strongly segregated, crystalline structure of the hard domains in the diblock copolymer compared with the multiblock copolymer. A comparison of the viscoelastic properties of the polymers reveals that the multiblock copolymer possesses a higher storage and loss modulus relative to the diblock copolymer and the homopolymers. We have also investigated the dynamic response of the polymers under shock loadings. Our shock simulations reveal that the shock wave propagates slower in the multiblock copolymer relative to its diblock counterpart. Deformation analysis based on slip vector calculation reveals that the hard segments undergo larger deformations across the shock front in multiblock copolymer in comparison with those in the diblock copolymer.

The observed differences between the properties of multiblock and diblock copolymers provide important insight into how the multiblock chain architecture of polyurea might endow it with superior dissipative properties. First, the networked structure observed in multiblock copolymers, where the hard domains are linked to each other via soft segments, allows hard domain motions to be coupled. Such coupling might enhance energy dissipation in polyurea through concerted, resonant motions of the hard domains,[7] which help trap the energy of a pressure/shock wave. The trapped energy can then be dissipated through the soft segments. The superior dissipative properties of the multiblock copolymer are evident from its larger loss modulus and lower shock velocities relative to those of the diblock copolymer. Second, our microstructure analyses suggest that the multiblock architecture of polyurea likely prevents its microphase segregation into large, strongly segregated hard domains. The resulting hard domains that are smaller and more weakly segregated are therefore easier to deform or dissociate when a shock or pressure wave passes through the material. Indeed, our shock simulations capture the stronger deformation of the multiblock copolymer hard domains compared with those of the diblock copolymer. Such deformations in the hard domains, along with their possible dissociation, have the potential to absorb large amounts of energy, thereby enhancing dissipation.

In conclusion, the current study lays the groundwork for future computational studies on the structure−function relationship of polyurea with the ultimate goal of enhancing its dissipative properties by tuning its molecular architecture. One possible direction is to examine how other parameters linked to block copolymers,[37] such as the chain length, the ratio of the hard and soft segments, and the degree of segregation (Φ) affect the viscoelastic properties and shock response of multiblock copolymers. Another direction is the development of higher resolution, coarse-grained models of polyurea through approaches like force-matching[46] and iterative Boltzmann inversion[47] that treat more accurately the specific and directional interactions in polyurea. A third future direction is examining how the energy from shock waves could be scattered or redirected through control over the alignment of anisotropic hard domains, which will aid ongoing experimental work in this area.[48]

■ ASSOCIATED CONTENT

Ⓢ Supporting Information

Plot of tan δ versus ω for the four polymeric systems investigated here. This material is available free of charge via the Internet at http://pubs.acs.org.

■ AUTHOR INFORMATION

Corresponding Author

*E-mail: garya@ucsd.edu. Phone: 858-822-5542. Fax: 858-534-9553.

Notes

The authors declare no competing financial interest.

■ ACKNOWLEDGMENTS

We thank Dr. Roshdy Barsoum, Prof. Sia Nemat-Nasser, Dr. Alireza Amirkhizi, Dr. Jay Oswald, Dr. Davide Hill, and Darren Yang for useful discussions. This work has been partially supported through ONR under grant no. N00014-09-1-1126 to the University of California, San Diego. Computations were performed at the Northwestern University Supercomputing Facility.

■ REFERENCES

(1) Das, S.; Cox, D. F.; Wilkes, G. L.; Klinedinst, D. B.; Yilgor, I.; Yilgor, E.; Beyer, F. L. *J. Macromol. Sci., Part B* **2007**, *46*, 853.
(2) Chattopadhyay, D. K.; Raju, K. V. S. N. *Prog. Polym. Sci.* **2007**, *32*, 352.
(3) http://www.polyurea.com/ (accessed Jan 15, 2012).
(4) Bogoslovov, R. B.; Roland, C. M.; Gamache, R. M. *Appl. Phys. Lett.* **2007**, *90*, 221910.
(5) Xue, L.; Mock, W. Jr.; Belytschko, T. *Mech. Mater.* **2010**, *42*, 981.
(6) Grujicic, M.; Pandurangan, B.; He, T.; Cheeseman, B. A.; Yen, C. F.; Randow, C. L. *Mater. Sci. Eng., A* **2010**, *527*, 7741.
(7) Qiao, J.; Amirkhizi, A. V.; Schaaf, K.; Nemat-Nasser, S.; Wu, G. *Mech. Mater.* **2011**, *43*, 598.
(8) Grujicic, M.; Pandurangan, B.; Bell, W. C.; Cheeseman, B. A.; Yen, C. F.; Randow, C. L. *Mater. Sci. Eng., A* **2011**, *528*, 3799.
(9) Kremer, K.; Grest, G. *J. Chem. Phys.* **1990**, *92*, 5057.
(10) Tekalur, S. A.; Shukla, A.; Shivakumar, K. *Compos. Struct.* **2008**, *84*, 271.
(11) Gardner, N.; Wang, E.; Kumar, P.; Shukla, A. *Exp. Mech.* **2012**, *52*, 119.
(12) Amirkhizi, A. V.; Isaacs, J.; McGee, J.; Nemat-Nasser, S. *Philos. Mag.* **2006**, *86*, 5847.
(13) Weeks, J.; Chandler, D.; Andersen, H. *J. Chem. Phys.* **1971**, *54*, 5237.
(14) Soddemann, T.; Dunweg, B.; Kremer, K. *Eur. Phys. J. E* **2001**, *6*, 409.
(15) Guo, H.; Kremer, K. *J. Chem. Phys.* **2003**, *118*, 7714.
(16) Arya, G.; Rottler, J.; Panagiotopoulos, A.; Srolovitz, D.; Chaikin, P. *Langmuir* **2005**, *21*, 11518.
(17) Arya, G.; Panagiotopoulos, A. *Phys. Rev. Lett.* **2005**, *95*, 188301.
(18) Larson, R. G. *The Structure and Rheology of Complex Fluids*; Oxford University Press: New York, 1999.
(19) Cahoon, J. R. *Can. J. Phys.* **2004**, *82*, 291.
(20) Grujicic, M.; Pandurangan, B.; King, A. E.; Runt, J.; Tarter, J.; Dillon, G. *J. Mater. Sci.* **2011**, *46*, 1767.
(21) Nose, S. *Prog. Theor. Phys. Suppl.* **1991**, *103*, 1.
(22) Auhl, R.; Everaers, R.; Grest, G. S.; Kremer, K.; Plimpton, S. J. *J. Chem. Phys.* **2003**, *119*, 12718.
(23) Sukumaran, S. K.; Likhtman, A. E. *Macromolecules* **2009**, *42*, 4300.
(24) Likhtman, A. E.; Sukumaran, S. K.; Ramirez, J. *Macromolecules* **2007**, *40*, 6748.
(25) Holian, B. L. *Shock Waves* **1995**, *5*, 149.

(26) Luo, S. N.; Han, L.-B.; Xie, Y.; An, Q.; Zheng, L. Q.; Xia, K. *J. Appl. Phys.* **2008**, *103*, 093530.
(27) Arman, B.; An, Q.; Luo, S. N.; Desai, T. G.; Tonks, D. L.; Cagin, T.; Goddard, W. A. III. *J. Appl. Phys.* **2006**, *109*, 13503.
(28) Brandl, C. Ph.D. Thesis No. 4591, Ecole Polytechnique Fédérale de Lausanne, 2009.
(29) Zimmerman, J. A.; Kelchner, C. L.; Klein, P. A.; Hamilton, J. C.; Foiles, S. M. *Phys. Rev. Lett.* **2001**, *87*, 165507.
(30) Lee, W.-J.; Ju, S.-P.; Cheng, C.-H. *Langmuir* **2008**, *24*, 13440.
(31) Arman, B.; Luo, S.-N.; Germann, T. C.; Cagin, T. *Phys. Rev. B* **2010**, *81*, 144201.
(32) http://lammps.sandia.gov (accessed Jan 15, 2012).
(33) Garrett, J. T.; Siedlecki, C. A.; Runt, J. *Macromolecules* **2001**, *34*, 7066.
(34) Sen, S.; Kumar, S.; Keblinski, P. *Macromolecules* **2005**, *38*, 650.
(35) Thomin, J. D.; Keblinski, P.; Kumar, S. K. *Macromolecules* **2008**, *41*, 5988.
(36) Smith, G.; Bedrov, D.; Li, L.; Byutner, O. *J. Chem. Phys.* **2002**, *117*, 9478.
(37) Fredrickson, G.; Bates, F. *Annu. Rev. Mater. Sci.* **1996**, *26*, 501.
(38) Arun, A.; Dullaert, K.; Gaymans, R. J. *Polym. Eng. Sci.* **2010**, *50*, 756.
(39) Zhao, J.; Majumdar, B.; Schulz, M. F.; Bates, F. S.; Almdal, K.; Mortensen, K.; Hajduk, D. A.; Gruner, S. M. *Macromolecules* **1996**, *29*, 1204.
(40) Sebastian, J. M.; Graessley, W. W.; Register, R. A. *J. Rheol.* **2002**, *46*, 863.
(41) Zhang, Z.; Zhang, H.; Yang, Y.; Vinckier, I.; Laun, H. *Macromolecules* **2001**, *34*, 1416.
(42) Mock, W.; Bartyczak, S.; Lee, G.; Fedderly, J.; Jordan, K. Dynamic Properties of Polyurea 1000. In *Shock Compression of Condensed Matter*; American Institute for Physics: Melville, NY, 2009; Vol. *1195*.
(43) Makeev, M. A.; Sundaresh, S.; Srivastava, D. *J. Appl. Phys.* **2009**, *106*, 014311.
(44) Holian, B. L.; Hoover, W. G.; Moran, B.; Straub, G. K. *Phys. Rev. A* **1980**, *22*, 2798.
(45) Hoover, W. G. *Phys. Rev. Lett.* **1979**, *42*, 1531.
(46) Ercolessi, F.; Adams, J. B. *Europhys. Lett.* **1994**, *26*, 583.
(47) Reith, D.; Putz, M.; Muller-Plathe, F. *J. Comput. Chem.* **2003**, *24*, 1624.
(48) Amirkhizi, A. V.; Tehranian, A.; Nemat-Nasser, S. *Wave Motion* **2010**, *47*, 519.
(49) Li, J. *Modell. Simul. Mater. Sci. Eng.* **2003**, *11*, 173.

Macromolecules

Article

pubs.acs.org/Macromolecules

Intrachain Ordering and Segregation of Polymers under Confinement

Youngkyun Jung,*[,†] Juin Kim,[‡] Suckjoon Jun,[§] and Bae-Yeun Ha*[,∥]

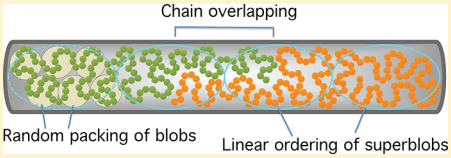
[†]Supercomputing Center, Korea Institute of Science and Technology Information, Daejeon 305-806, Korea

[‡]Department of Physics, Korea Advanced Institute of Science and Technology, Daejeon 305-701, Korea

[§]FAS Center for Systems Biology, Harvard University, Cambridge, Massachusetts 02138, United States

[∥]Department of Physics and Astronomy, University of Waterloo, Waterloo, Ontario, Canada N2L 3G1

ABSTRACT: We study the relationship between intrachain ordering and segregation tendency of two polymers confined in a cylindrical space. We find the chains segregate spontaneously even outside de Gennes' linear-ordering scaling regime, in which each chain is a linear array of blobs. When the chains are weakly compressed against each other, linear ordering is well preserved and the chains remain segregated. On the other hand, for moderate compression, new chain-ordering units emerge at intermediate length scales, within which blobs are randomly packed; yet these units (termed "superblobs") are linearly ordered, and the chains still segregate in the confined space. As the chains continue to be compressed, the linear regime disappears, but the chains can resist mixing effectively, more so in a more asymmetric space. We conclude that the linearly ordered *E. coli* chromosome is in the segregation regime.



I. INTRODUCTION

Considerable effort has been made recently to understand how chromosomes are spatially organized in cells.[1−8] In particular, the entropic mechanism highlights the interplay between chain entropy and confinement:[3−8] under the right conditions, two chromosomes partition or segregate spontaneously mainly driven by their chain entropy, especially in an elongated bacterial cell. Qualitatively speaking, under cylindrical confinement, chain molecules become more compactly space-filling and thus constrain each other better[9] (see refs 10 and 11 for a polymer solution trapped in a cylindrical pore). This explains how entropic forces are brought about when individual chains experience anisotropic confinement. This entropic picture has offered quantitative insights into chromosome segregation, especially in rod-shaped *E. coli* cells,[3−6] and challenged the conventional view that requires dedicated segregation machinery as in eukaryotes.[12,13] It is worth emphasizing that the entropic picture is rather generic and largely independent of molecular details.[6] It remains relevant under a variety of physical constraints (e.g., ring chain topology and chain cross-linking).[3,6] A recent study even points out that various DNA binding proteins cooperate with the process of entropic segregation.[3]

However, confined polymers have been much better understood at the single-chain level, whether they are flexible or stiff.[14−20] For instance, (open) cylindrical confinement induces linear chain ordering[6−21] and stiffen them.[6,18,19] This polymer picture is consistent with the recent observation that the *E. coli* chromosome is linearly organized with high precision along the long axis,[22,23] which would otherwise remain disordered (see refs 6 and 15 for theoretical explanations). Confinement not only reshapes individual chains[21] but also has a nontrivial impact on how they interact (see ref 6 for some primitive discussion). Despite its significance in further exploiting the entropic mechanism, the relationship between intrachain organization and segregation remains to be explored. Is linear ordering required for chain segregation, as often assumed in the literature?[3,5,10]

Here, we study the relationship between intrachain ordering and segregation tendency of two self-avoiding chains confined in a closed cylindrical space (i.e., a cylinder capped at both ends), using molecular dynamics (MD) simulations as well as a phenomenological free energy approach; see the illustration in Figure 1. In particular, we consider the "internal distance" of each chain, R_{ij}, i.e., the direct distance between two monomers i and j on the same chain, as a function of $|i - j|$. We then relate it to the way the confined chains interact. Even though our study is limited to linear chains, its applicability goes beyond the linear case, since the effect of ring topology is shown to be mimicked in the linear case by appropriately reducing cylinder diameters.[6]

When the chains are weakly compressed against each other, we find that their linear ordering is well preserved beyond $\xi \approx D$, as in an open cylinder, and they remain segregated.[3−6] Here, ξ is the blob size or a length scale at which the crossover from the self-avoiding walk (SAW) to linear regime occurs and D the diameter of the cylinder.[21] For moderate compression, however, new ordering units emerge at some length scale $\zeta_{\|}$ ($>D$) in the longitudinal direction, each consisting of several randomly packed blobs. Similarly to blobs in an open cylinder or in the weakly compressed case, these units are linearly ordered and are referred to as "superblobs". As a result, the

Received: November 25, 2011
Revised: March 6, 2012
Published: March 26, 2012

 © 2012 American Chemical Society

chains segregate up to 80−90%. As the chains continue to be compressed, linear ordering is eventually lost, but the chains can resist mixing effectively and remain segregated up to 70−80%, more so in a more asymmetric space. While the chains do not mix, if linearly ordered, linear ordering is not a requirement for segregation.

Our results suggest that the linearly ordered *E. coli* chromosome[22,23] is in the spontaneous segregation regime. However, we do not attempt to resolve any discrepancy between the competing (active vs entropic) segregation mechanisms but content ourselves with general principles that are common to interacting chain molecules under confinement.

The article is organized as follows. The simulation procedure is outlined in Sec. II. Sec. III is mainly devoted to the analysis and interpretation of simulation results. In particular, the interrelationship between chain ordering and segregation is discussed in detail. Also, a free energy basis of chain segregation is presented. The entropic segregation of *E. coli* chromosomes is reconsidered in view of the interrelationship and the relevance of our polymer model is discussed.

II. MOLECULAR DYNAMICS SIMULATIONS

In our MD simulations, we use the bead−spring model of a polymer, which is characterized by two distinct interactions. (See subsection III.C for its relevance for the study of chromosome organization.) First, beads (among themselves and with the confining walls) interact via the fully repulsive Weeks−Chandler−Andersen (WCA) potential:[24]

$$U_{\mathrm{WCA}}(r) = \begin{cases} 4\varepsilon\left[\left(\frac{\sigma}{r}\right)^{12} - \left(\frac{\sigma}{r}\right)^{6} + \frac{1}{4}\right] & \text{for } r < 2^{1/6}\sigma \\ 0 & \text{otherwise} \end{cases} \quad (1)$$

Here ε and σ represent the strength and range of the WCA potential, respectively; r denotes the center-to-center distance between two beads, or the distance of the bead center from the confining cylinder minus σ. As a result, the monomer size $a \approx \sigma$.

In addition, two neighboring beads are joined together through the finitely extensible nonlinear elastic (FENE) potential of the form

$$U_{\mathrm{FENE}}(r) = -\frac{1}{2}kr_0^2 \ln\left[1 - \left(\frac{r}{r_0}\right)^2\right] \quad (2)$$

where the molecular spring constant $k = 30\varepsilon/\sigma^2$ and the maximum bond length $r_0 = 1.5\sigma$.[25] This interaction ensures chain connectivity.

We integrated Newton's equations of motion using the velocity Verlet algorithm with an integration time step $\delta t = 0.01\tau$, where $\tau = \sigma(m/\varepsilon)^{1/2}$ is the characteristic time scale with bead mass $m = 1$. A Langevin thermostat with the damping constant $0.1\tau^{-1}$ was used to keep the system at the fixed temperature $T = 1.0\varepsilon/k_{\mathrm{B}}$, where k_{B} is the Boltzmann constant (see ref 19 for details). To obtain reliable chain statistics, we carried out 200 independent simulations corresponding to different initial chain conformations. We first performed 10^8 integration steps in order for the chain to equilibrate for a given initial conformation; after equilibration, we ran additional 10^8 integration steps and obtained a data point every 10^4 steps.

III. RESULTS

A. Chain Ordering and Segregation. First, we have examined chain structures under a varying degree of confinement and longitudinal compression. In this work, the chain structure is quantified in terms of the internal distance $R_{ij} = [\langle \mathbf{R}^2(|i-j|)\rangle]^{1/2}$, the direct distance between two monomers i and j on the same chain, as a function of $|i-j|$, i.e., the contour length in units of a, where $\langle ...\rangle$ is an ensemble average or an average over simulations (see section II for details). Figure 1 shows our simulation results for R_{ij} for $D = 14$ (a) and $D = 20$ (b). Here and below, all lengths are measured in units of a, unless otherwise stated. Different colors are used to represent a varying degree of longitudinal compression (see the legend) or a range of the volume fraction of monomers denoted as ϕ. This consideration allows us to probe internal chain statistics under various conditions. Here, we relate single-chain properties such as R_{ij} to interchain organization. The main advantage is that our results will not be complicated by partial overlapping, which would make each chain inhomogeneous, as illustrated in the inset in Figure 1. To this end, we first trap each chain in a closed cylinder of length L and calculate R_{ij}. In our analysis of interchain organization, two chains are confined in a cylinder of length $2L$ and the overlap distance λ is measured, where λ is the distance between the two farthermost monomers on different chains as described in the inset of Figure 1 (also see Figure 2a for an alternative interpretation).

A few distinct regimes are identified and labeled: the self-avoiding walk (SAW) at length scales $<\xi$, random walk (RW) at intermediate length scales, and linear regimes outside the RW regime, which are depicted by dashed lines with different slopes 3/5, 1/2, and 1, respectively.[26] In addition to the representative dashed line, we have included a thin dashed line to highlight the RW regime for some parameter choices in Figure 1a,b—its emergence is clear. For sufficiently small L [e.g., the blue curve with symbols in (a)], however, the RW regime is not clearly shown. This can be attributed to closed-confinement effects, which tend to make R_{ij} saturated beyond a special value of $|i-j|$.

For moderate compression, as illustrated in the top panel, all the three regimes are realized (e.g., the light blue curve in (a) and the dark yellow curve in (b), both with symbols). For weak compression (the first five curves in (a) and the first two curves in (b), from the top), the RW regime is missing, while for strong compression, the linear regime disappears (the curves with filled symbols). The length scale ξ at which the crossover from the SAW to RW or linear regime occurs naturally defines structural units known as "blobs" and is smaller for larger ϕ (the semidilute scaling law $\xi \approx \phi^{-3/4}$ will apply to the confined chain case as long as $\xi < D$);[21] a few blobs are highlighted in the top panel. Chain segments within a blob are not perturbed by confinement or other segments outside the blob.[21] In other words, self-avoidance is unscreened.

The physical picture emerging from our results in Figure 1 is as follows: for weak compression, linear ordering is well preserved beyond $\xi \approx D$, in the sense that the RW regime is not realized, as in an open cylinder.[21] As a result, $\xi \approx D$ is the only crossover length scale that characterizes the chain conformation. The appearance of the RW regime for moderate compression is a natural consequence of breakage of each blob into smaller ones, as ϕ increases[20] (also see ref 27 for a

dx.doi.org/10.1021/ma2025732 | Macromolecules 2012, 45, 3256−3262

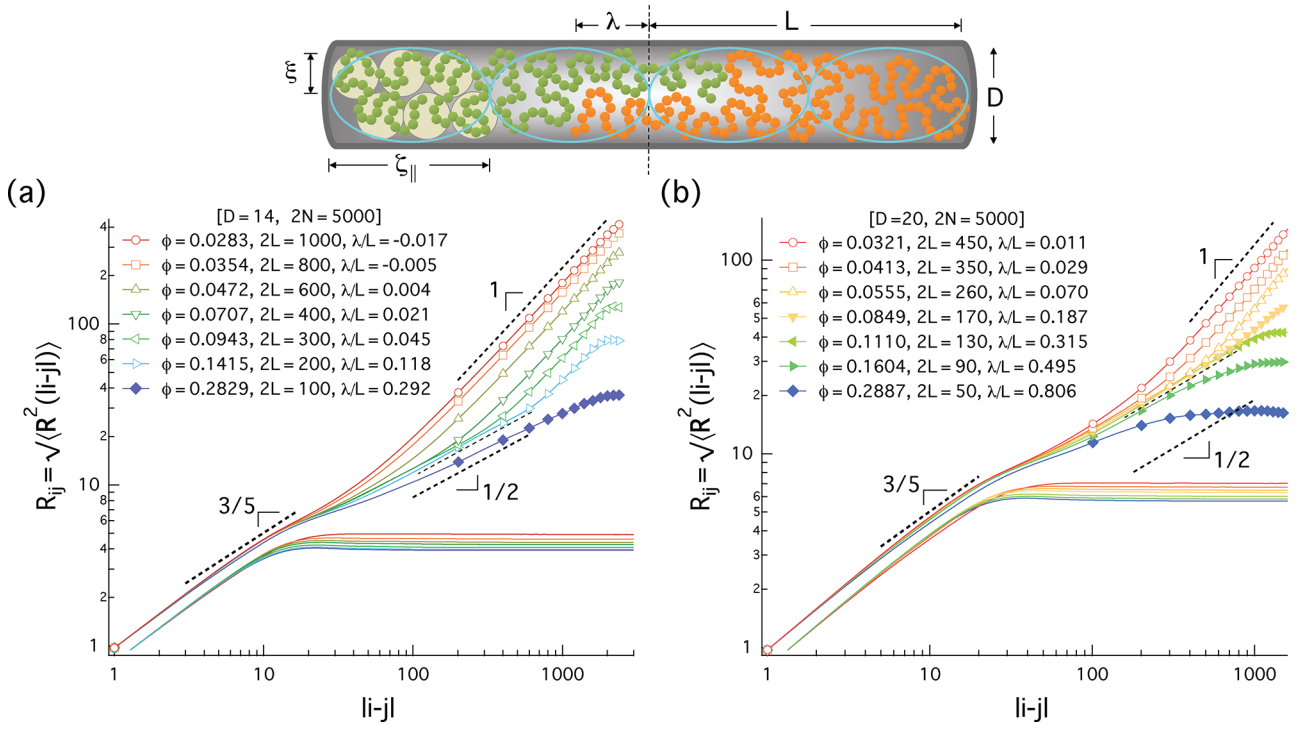


Figure 1. Internal distance of a confined chain $R_{ij} = [\langle \mathbf{R}^2(|i - j|)\rangle]^{1/2}$ (solid lines with symbols) and its relationship with λ/L, the fractional overlap distance between two chains (specified in the legend) for $D = 14$ in (a) and $D = 20$ in (b) in units of a. The dashed lines, with the slopes 3/5, 1/2, and 1, depict the self-avoiding walk (SAW) within ξ, random walk (RW) at intermediate lengths,[26] and linear regimes, respectively. If the confined chain is weakly compressed longitudinally, it is linearly ordered beyond the blob size $\xi \approx D$, as in an open cylinder, and the RW regime is missing. For intermediate compression, as illustrated in the top panel, "superblobs" emerge as ordering units at some length scale denoted as $\zeta_\parallel$, within which blobs are randomly packed (a few blobs are highlighted). For strong compression, the linear regime is suppressed (i.e., $\zeta_\parallel \approx L$). For the entire range shown, the RW regime is not clearly seen in the transverse component $R_{ij}^{\perp} = [\langle \mathbf{R}_\perp^2(|i - j|)\rangle]^{1/2}$ (the bottom lines without symbols). In all cases that display the linear regime (solid lines unfilled symbols), the chains are (almost) completely segregated. Even when linear ordering is lost, they segregate up to 70−80%, more so in a more asymmetrical space. Under anisotropic confinement, chain segregation in the RW regime is sensitive to the aspect ratio $k = D/2L$.

similar issue under spherical confinement). Compression diminishes chain ordering in the sense that it makes "slower" the crossover to the linear regime at some length scale denoted as $\zeta_\parallel$ ($>D$). The crossover length $\zeta_\parallel$ defines new chain-ordering units, referred to as "superblobs", each consisting of randomly packed blobs, as illustrated in Figure 1. Note the asymmetrical shape of the superblob, which is elongated in the longitudinal direction. In this case, linear ordering is preserved for length scales $> \zeta_\parallel > D$. As the chains continue to be compressed, $\zeta_\parallel$ increases and becomes comparable to the chain size eventually. The linear regime then disappears.

The unique anisotropy of cylindrical confinement is responsible for the crossover from the RW to linear regime at the length scale $\zeta_\parallel$, which is missing under spherical confinement.[27] This necessitates the introduction of new ordering units (called superblobs in this work). To capture the anisotropy better, it proves useful to consider the internal distance in the transverse direction $R_{ij}^{\perp} = [\langle \mathbf{R}_\perp^2(|i - j|)\rangle]^{1/2}$, where $\mathbf{R}_\perp(|i - j|)$ is the transverse component of $\mathbf{R}(|i - j|)$. For the entire parameter range shown in Figure 1, the RW regime is not seen clearly in the transverse component (see the bottom curves without symbols). Even in the RW regime, the confine chain is transversely restricted.

Also included in the legend is the fractional overlap distance λ/L, which describes interchain organization or "effective" chain miscibility[28] (recall that λ is the distance between the two farthermost monomers on different chains). In all cases that display the linear regime (curves with open symbols), the chains are segregated completely (for weak compression) or up to 80−90% (for moderate compression). However, the emergence of the linear regime is not a requirement for entropic segregation, as postulated in the literature.[3,5,10] In fact, the chains resist mixing effectively, even when the linear regime is completely lost, as indicated by the bottom curve with symbols in (a) or the fifth one in (b); chain miscibility is still low around 30%. This observation is analogous to the recent finding that two polymers in a melt can segregate in a cylindrical box.[29] (In the melt, $\xi \approx a$ and the SAW regime is suppressed.) Similarly, it was shown earlier that ring polymers in a melt segregate.[30] This is understandable in light of the recent finding that under cylindrical confinement ring polymers segregate better than the corresponding linear chains.[6]

As the chains continue to be compressed against each other, their linear regime will diminish in size and they mix or overlap better. The free energy basis for the crossover from the mixed to segregated state has been illusive. (See refs 10 and 20 for the difficulty with a free energy approach and subsection B for our attempt.) Crudely speaking, the free energy cost for chain backfolding inside a superblob becomes comparable to that for chain overlapping (also see ref 6 for relevant discussion). This will enhance (effective) chain miscibility.

Finally, compare (a) and (b) for the sensitivity of interchain organization to D, especially for $\phi \approx 0.29$ (the bottom curves with symbols in both cases). In both cases, each chain is a RW

dx.doi.org/10.1021/ma2025732 | Macromolecules 2012, 45, 3256−3262

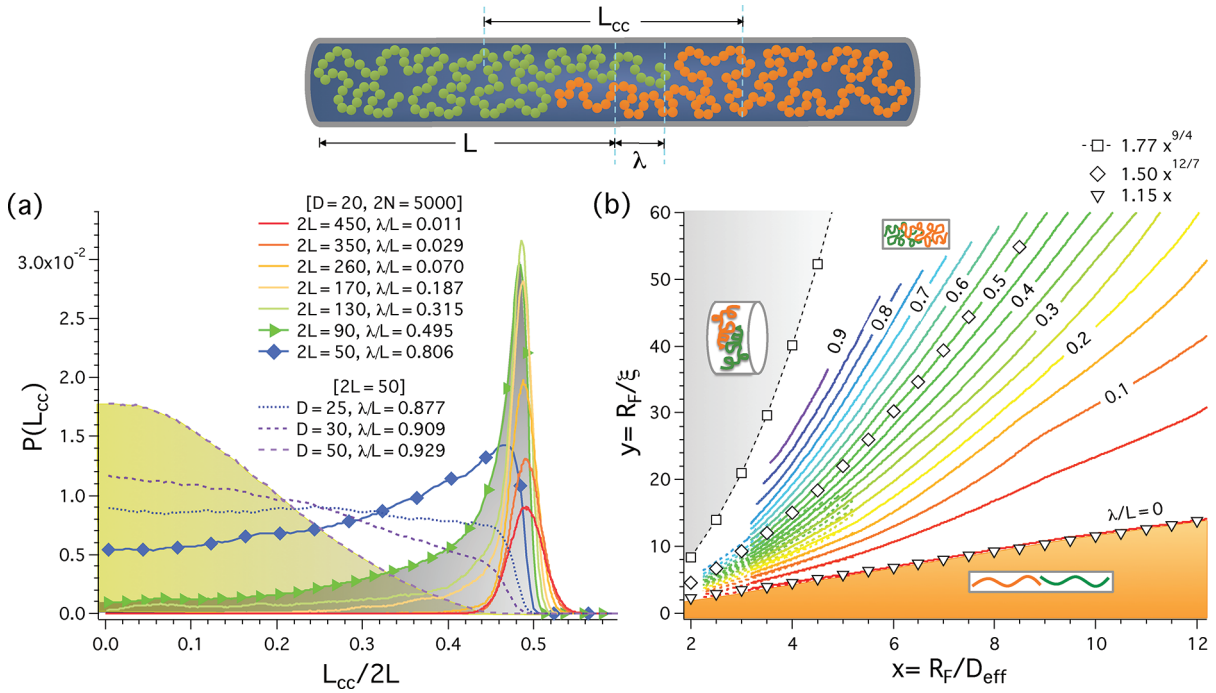


Figure 2. (a) Distribution of the center-to-center distance L_{cc} of two confined chains $P(L_{cc})$ (a) and chain miscibility (b). (The miscibility diagram is reproduced from ref 6 with modifications by permission of the Royal Society of Chemistry.) The color scheme in these plots is comparable to that used in Figure 1b. For the well-segregated cases (solid lines without symbols), $P(L_{cc})$ has a narrow peak at $L_{cc}/2L \approx 0.5$. On the other hand, $P(L_{cc})$ for the much mixed cases (lines with filled diamonds) is broader. In the most miscible case $k = D/2L = 1$ (the dashed line in purple); $P(L_{cc})$ is a Gaussian distribution centered at $L_{cc} = 0$. In the diagram in (b), $D_{eff} = D$ for linear chains (solid lines), while for ring polymers, $D_{eff} = D/\sqrt{2}$ (dashed lines).[6] The dotted line with open squares describes the symmetrical case of $k = D/2L = 1$ for which $y = 1.77x^{9/4}$. Beyond this, the confined space resembles a closed "slit". We have also included the theoretical prediction of the boundary curve $y = 1.50x^{12/7}$ between the segregated and mixed regimes[3,10] (see open "diamonds"). The prefactor has been chosen so that the boundary curve collapses on one of the contours. It best fits the line describing $\lambda/L = 0.5$. In addition, we note that the $\lambda/L = 0$ line is best fit by $y = 1.15x$ (open inverted triangles).

beyond $\xi \approx \phi^{-3/4}$, which is roughly the same for both curves, up to the entire contour length in the longitudinal direction. However, λ/L is significantly different between the two cases. If the chains are much segregated in (a), they are almost completely mixed in (b). Thus, the smaller D case in (a), more constrained in the transverse direction, shows a stronger segregation tendency. Even for RW chains, segregation can be sensitive to the aspect ratio of the confined space.

Our results in Figure 1 are statistical averages over many realizations of chain conformations. To understand chain miscibility beyond the average behavior, we have plotted in Figure 2a the distribution of the center-to-center distance L_{cc} for $D = 20$, denoted as $P(L_{cc})$, as a function of $L_{cc}/2L$. This is normalized so that $\int_0^{2L} P(L_{cc})\, dL_{cc} = 1$. Here we have employed the same color scheme used in Figure 1b to represent various cases. Also note that the curves describing $\lambda/L \approx 0.5$ (green with symbols) and $2L = D$ (purple dashed) are highlighted with a shade, since they represent special boundaries in the diagram in (b). As shown in the figure, for the much segregated case (curves without symbols in this plot), $P(L_{cc})$ has a peak at $L_{cc}/2L \approx 0.5$ or $L_{cc} \approx L$, meaning that the two chains are well segregated, consistent with our corresponding results for λ/L; also, the width of the peak is narrow and is about 10% of the cylinder length. Similarly, we have shown that $P(L_{cc})$ for $D = 14$ has a peak at $L_{cc} \approx L$ for the parameters used in Figure 1a (the data not shown here).

In contrast, $P(L_{cc})$ for the much mixed case (the solid lines with filled symbols) is broader. Nevertheless, the most probable state corresponding to the peak of $P(L_{cc})$ is still in the segregated regime, i.e., $L_{cc}/2L \approx 0.5$, even when $\lambda/L > 0.5$. However, there is no contradiction between the two pictures. In the overlapping region, each chain is better aligned than in the homogeneous region. This means that the farthermost monomer in green can reach deeper into the right-half space than indicated by $P(L_{cc})$. Furthermore, $\lambda/L = 0.5$ has special meaning in chain miscibility. It separates between the segregated and mixed regimes, as shown below. This seems to be consistent with the miscibility picture based on λ/L (and even with the picture $P(L_{cc})$ presents, as long as it is interpreted correctly).

The three dotted or dashed lines in Figure 2a show how $P(L_{cc})$ evolves as the confined space becomes symmetrical or as the aspect ratio $k = 2L/D$ approaches one. In our simulations, we increased D from $D = 20$ up to 50, while keeping $2L = 50$. For $D = 25$, $P(L_{cc})$ is almost flat, meaning that the free energy cost is comparable for random packing and for chain overlapping. As $k \to 1$, chain directionality is lost and $P(L_{cc})$ becomes a Gaussian function centered at the origin (the purple curve with a shade). The confined chains are most miscible for $k = 1$, as supported by our miscibility diagram in Figure 2b (also see below). However, this has to be understood with some caution, since the distribution is broad. In this case, the most probable state corresponding to $L_{cc} = 0$ (i.e., completely mixed) does not necessarily coincide with what we expect from chain miscibility on average. Nevertheless, the two chains under isotropic confinement are well mixed, i.e., more than 90%.

Displayed in Figure 2b is an effective miscibility diagram in the plane of $x = R_F/D_{eff}$ and $y = R_F/\xi$, where the fractional

dx.doi.org/10.1021/ma2025732 | Macromolecules 2012, 45, 3256−3262

overlap distance λ/L is specified. Here, R_F = constant × $N^{3/5}$ (constant = 1.1 for linear and 0.87 for ring chains); $D_{eff} = D$ for linear chains (solid lines), while for ring polymers, $D_{eff} = D/\sqrt{2}$ (dashed lines).[6] The agreement between the linear and ring chain means that ring-topology-enhanced segregation can be mimicked in the linear case by reducing D as $D \rightarrow D/\sqrt{2}$ (see ref 6 for details). The color schemes used in Figure 2a,b and in Figure 1b are comparable to each other; for instance, the red line represents $\lambda/L = 0$ and the blue line $\lambda/L = 0.8$. In earlier scaling approaches,[3,10] the mixed and segregated regimes are separated by the curve $y = x^{12/7}$. To test this, we have plotted the curve $y = 1.50x^{12/7}$ (see unfilled diamonds). The prefactor has been chosen so that the boundary curve collapses onto one of the contours. Our analysis indicates that the curve best fits the line describing $\lambda/L = 0.5$. See the green curve with a shade in Figure 2a for the corresponding $P(L_{cc})$. In view of this, this fitting curve describes the crossover boundary between the segregated and mixed regimes. According to our results in Figure 1b, linear ordering is completely lost on this curve.

In addition, we note that the $\lambda/L = 0$ line is best fit by $y = 1.15x$ (inverted triangles). The prefactor in this relation (>1) is consistent with the observation that the confined chains resist mixing, even when they are weakly compressed against each other, and thus ξ is somewhat smaller than D. Finally, we have included the curve $y = 1.77x^{9/4}$ (the dotted line with squares) that represents the isotropic case of $D = 2L$, for which the chains are most miscible [recall $P(L_{cc})$ is Gaussian centered at $L_{cc} = 0$]. For $k \approx 1$, however, the notion of the overlap distance becomes obscure, since the distinction between longitudinal and transverse directions becomes arbitrary. Nevertheless, our results in Figure 2a,b clearly indicate that the confined chains are well mixed. Beyond this curve, however, the confined space resembles a closed slit, as illustrated by a cartoon on the left in Figure 2b.

B. Scaling Approach to Chain Segregation. Our results for R_{ij} in Figure 1 indicate that compressed chains resist mixing as long as they are overall linearly ordered, i.e., $\zeta_{\parallel} \ll L$. However, this finding is not as obvious to interpret as it may seem, especially on a free energy basis. The main difficulty is that a free energy approach (at the mean-field level) is not always reliable and often leads to incorrect results.[10,21] Even for the case of a single confined chain, there has been some confusion and the correct free energy approach, known as a renormalized Flory approach, has only recently been obtained (see ref 20 and references therein). Here we extend this approach as a free energy basis for segregation in the linear regime. To this end, we compare the two limiting cases: "segregated" and "mixed," as illustrated in Figures 3a and 3b, respectively.

First, recall that the free energy of a single chain in an open cylinder is given by

$$\frac{\mathcal{F}(L)}{k_B T} = A\frac{L^2}{(N/g)D^2} + B\frac{D(N/g)^2}{L} \qquad (3)$$

where A and B are (nonuniversal) constants of order 1 and $g \approx D^{5/3}$ is the number of monomer per blob.[21] Recall all lengths are estimated in units of a. Here L should be interpreted as the longitudinal size of the confined chain, which coincides with the cylinder length. The free energy in eq 3 leads to correct chain sizes, and confinement free energy, and effective spring constants. This approach is based on the assumption that the confined chain is in the linear regime and remains valid unless the chain is too much compressed longitudinally. Reference 20 suggests that it is valid for $0.5L_0 < L < 1.2L_0$.[20]

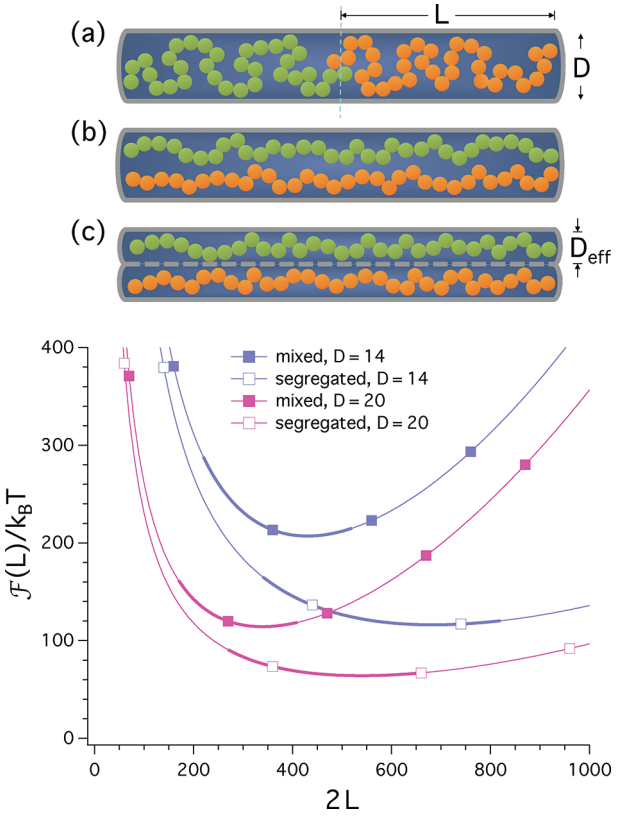


Figure 3. Free energy basis for chain miscibility in the linear regime (i.e., $\zeta_{\parallel} \ll L$); for visual clarity, the weakly compressed case ($\zeta_{\parallel} \approx \xi$) is illustrated in the top panel. We compare the Flory free energy $\mathcal{F}(L)$ of a segregated state (a) with that of a mixed state (b), as a function of L, for D = 14 and 20; in both cases, N = 2500. To this end, we map (b) onto (c) for which $D_{eff} = D/\sqrt{2}$ is the effective diameter of an imaginary tube enclosing each chain. As shown in this figure (the bottom panel), mixing is disfavored by free energy. As L decreases, the difference is diminished, and the chains are more miscible for smaller L. Our Flory approach is known to be accurate for $0.5L_0 < L < 1.2L_0$,[20] where $L_0 \sim ND^{-2/3}$ is the unperturbed chain size in the equivalent open cylinder case.[21]

To understand the applicability of $\mathcal{F}(L)$ in eq 3 for $0.5L_0 < L < 1.2L_0$, note that at the lower bound, i.e., $L_{lower} = 0.5L_0$, $\xi \approx 0.6D$, if we take $\xi = D$ for $L = L_0$, as assumed in de Gennes' scaling approach.[21] The RW regime is not realized for this range of L, i.e., the range $0.5L_0 < L < 1.2L_0$ represents weak compression, consistent with the illustrations in the top panel in Figure 3. As L decreases, blobs will break into smaller ones, but only for sufficiently small L, the RW regime will emerge, as described in Figure 1. In this case, our free energy approach is less accurate quantitatively. This is, however, a general feature of a Flory-type approach, which is formulated in terms of a single-order parameter, i.e., L in our case. Here, we argue that this limitation will not invalidate our free energy comparison between the segregated (a) and mixed states (b), since it will influence both cases similarly.

By requiring that the free energy of segregated chains is extensive with the number of chains for given ϕ, we can readily

dx.doi.org/10.1021/ma2025732 | Macromolecules 2012, 45, 3256–3262

write down the free energy of the two chain system in (a), each occupying a half space of length L, as

$$\mathcal{F}_{\mathrm{seg}}(L) \approx 2\mathcal{F}_{\mathrm{linear}}(L) \tag{4}$$

On the other hand, a recent study suggests that under cylindrical confinement a ring polymer can map onto a "parallel connection" of two linear chains, each occupying an imaginary cylinder of reduced diameter $D_{\mathrm{eff}} = D/\sqrt{2}$, as illustrated in (c). On the basis of this, we argue that the free energy of two mixed chains in (b) is well approximated by that in (c). For visual clarity, the chains in de Gennes' linearly ordered scaling regime are illustrated in the top panel.

Following ref 6, we have

$$\frac{\mathcal{F}_{\mathrm{mix}}(L)}{k_{\mathrm{B}}T} \approx \hat{A}\frac{L^2}{(N/g)D^2} + \hat{B}\frac{D(N/g)^2}{L} \tag{5}$$

where $\hat{A} = 2^{13/6}A$ and $\hat{B} = 2^{13/6}B$. Here, the parameters g, N, and D in the second term on the right-hand side are for the corresponding linear case.

In Figure 3 (the bottom panel), we compare the segregated (a) and mixed states (b) as a function of $2L$ the cylinder length using two choices of D: $D = 14$ and 20. Also, we have chosen $A = B = 1$ as well as $2N = 5000$. Even though we are mostly interested in the compressed case $L < L_0$, we include the stretched case as well ($L > L_0$). The bold line represents the aforementioned L-range, $0.5L_0 < L < 1.2L_0$. As shown in this figure, segregation is favored by free energy. This is consistent with our earlier finding that chains in the linear regime remain segregated. As L decreases, the difference between the mixed and segregated cases becomes smaller. Our results in Figure 3 are, however, less accurate for $L < 0.5L_0$. Nevertheless, they suggest that the chains become more miscible as $2L \rightarrow D$.

C. Bacterial Chromosomes and Confined Polymers. How much do chromosomes resemble polymer chains discussed in this work? When measured by fluorescence correlation spectroscopy,[31] an isolated *E. coli* chromosome appears to consist of "structural units", each containing supercoiled plectonemes.[31,32] Because of their topological structure, they should repel one another and can be considered as effective monomers;[6] each monomer contains DNA segments and bound proteins. This mapping is based on the view that the action of DNA-binding proteins is local,[3] and its effect can thus be subsumed into monomers.[6] (See ref 33 for various DNA-binding proteins such as MukB.) The global properties of such chain molecules such as their interchain organization will not depend sensitively on this simplification, owing to chain connectivity.[21] (See ref 34 for a similar coarse-grained, polymer model of eukaryotic chromosomes and ref 35 for coarse-graining in a more general context.)

If we use typical *E. coli* parameters such as the nucleoid diameter $D \approx 5$ and length $L \approx 28$,[36] and the number of units $N \approx 200$ (see also refs 3, 6, 31, and 32), we find $\xi \approx 3$; here all the lengths are given in units of the size of the structural unit (≈70 nm). The *E. coli* chromosome is indeed in de Gennes' linear ordering regime; i.e., it is weakly compressed or $\zeta_{\parallel} \approx \xi \approx D$ with its degree of ordering similar to that illustrated in Figure 3 (see also Figure 5 in ref 6, which shows how ring topology enhances linear ordering). *E. coli* chromosomes in a dividing cell can segregate spontaneously. This is driven by physical effects chain molecules experience under anisotropic confinement. It is thus expected to play a nontrivial role in the global organization of chromosomes, largely independent of their local properties.

IV. DISCUSSION

In conclusion, we have presented a physical picture of how interchain organization is related to intrachain ordering under cylindrical confinement, which has been illusive in the literature. Our simulations presented here suggest that while linear ordering ensures complete or almost complete segregation, it is not required for segregation. Even when each chain consists of randomly packed blobs along its entire length, the chain is still restricted in the transverse direction (see Figure 1). This anisotropy is responsible for chain segregation up to 70−80%, outside de Gennes' linear-ordering regime.

Earlier studies indicate that the *E. coli* chromosome is linearly ordered.[23] In light of our results reported here, it is clear that *E. coli* chromosomes in a dividing cell are in the entropic segregation regime. Note that this conclusion is largely independent of such molecular details as ring topology and local packing of the chromosome. While the former effect can be accurately mimicked in the linear case by adjusting cylinder diameters,[6] the latter can be subsumed into monomers in our polymer model, since we are interested in much large-scale properties.[21,35]

Technical advances now allow one to isolate, confine, and manipulate single chromosomes in narrow channels.[37,38] The interrelationship between intrachain ordering and interchain organization described in this work will be useful for further exploiting the entropic mechanism[3−8] and can serve as a model for comparison with future experiments.

AUTHOR INFORMATION

Corresponding Author

*E-mail: yjung@kisti.re.kr (Y.J.); byha@uwaterloo.ca (B.-Y.H.).

Notes

The authors declare no competing financial interest.

ACKNOWLEDGMENTS

B.-Y.H. acknowledges the financial support of NSERC (Canada). We thank C. Jeon for helpful discussions. This work was in part supported by the NRF of Korea funded by the MEST (No. 2011-0028908) (J.K.).

REFERENCES

(1) Kleckner, N.; Zickler, D.; Jones, G. H.; Dekker, J.; Padmore, R.; Henle, J.; Hutchinson, J. A mechanical basis for chromosome function. *Proc. Natl. Acad. Sci. U. S. A.* **2004**, *101*, 12592−12597.

(2) Bloom, K.; Joglekar, A. Towards building a chromosome segregation machine. *Nature* **2010**, *463*, 446−456.

(3) Jun, S.; Wright, A. Entropy as the driver of chromosome segregation. *Nature* **2010**, *6*, 600−607.

(4) Jun, S.; Mulder, B. Entropy-driven spatial organization of highly confined polymers: Lessons for the bacterial chromosome. *Proc. Natl. Acad. Sci. U. S. A.* **2006**, *103*, 12388−12393.

(5) Jung, Y.; Ha, B.-Y. Overlapping two self-avoiding polymers in a closed cylindrical pore: Implications for chromosome segregation in a bacterial cell. *Phys. Rev. E* **2010**, *82*, 051926−1−051926−5.

(6) Jung, Y.; Jeon, C.; Kim, J.; Jeong, H.; Jun, S.; Ha, B.-Y. Ring polymers as model bacterial chromosomes: confinement, chain topology, single chain statistics, and how they interact. *Soft Matter* **2012**, *8*, 2095−2102.

(7) Cook, P. R.; Marenduzzo, D. Entropic organization of interphase chromosomes. *J. Cell Biol.* **2009**, *186*, 825−834.

(8) Dorier, J.; Stasiak, A. Topological origins of chromosomal territories. *Nucleic Acids Res.* **2009**, *37*, 6316−6322.
(9) Similar effects can be induced by chain topology such as ring or branchlike structure (see for instance refs 6−8). In particular, the recent theoretical and numerical studies suggest that under cylindrical confinement the miscibility of ring polymers can map onto that of an appropriately chosen linear chain case.
(10) Daoud, M.; de Gennes, P. G. Statistics of Macromolecular Solutions Trapped in Small Pores. *J. Phys. (Paris)* **1977**, *38*, 85−93.
(11) Teraoka, I.; Wang, Y. Computer simulation studies on overlapping polymer chains confined in narrow channels. *Polymer* **2004**, *45*, 3835−3843.
(12) Ptacin, J. L.; Lee, S. F.; Garner, E. C.; Toro, E.; Eckart, M.; Comolli, L. R.; Moerner, W. E.; Shapiro., L. A spindle-like apparatus guides bacterial chromosome segregation. *Nat. Cell Biol.* **2010**, *12*, 791−798.
(13) Toro, E.; Shapiro, L. Bacterial Chromosome Organization and Segregation. *Cold Spring Harb. Perspect. Biol.* **2010**, *2*, a000349−1−a000349−15.
(14) Su, T.; Das, S. K.; Xiao, M.; Purohit, P. K. Transition between Two Regimes Describing Internal Fluctuation of DNA in a Nanochannel. *PLoS One* **2011**, *6*, e16890−1−e16890−9.
(15) Buenemann, M.; Lenz, P. Geometrical Model for DNA Organization in Bacteria. *PLoS One* **2010**, *5*, e138061−e13806−13.
(16) Wang, Y.; Tree, D. R.; Dorfman, K. D. Simulation of DNA Extension in Nanochannels. *Macromolecules* **2011**, *44*, 6594−6604.
(17) Milchev, A. Single-polymer dynamics under constraints: scaling theory and computer experiment. *J. Phys.: Condens. Matter* **2011**, *23*, 1031011−1031011−24.
(18) Arnold, A.; Bozorgui, B.; Frenkel, D.; Ha, B.-Y.; Jun, S. Unexpected relaxation dynamics of a self-avoiding polymer in cylindrical confinement. *J. Chem. Phys.* **2007**, *127*, 164903−1−164903−9.
(19) Jung, Y.; Jun, S.; Ha, B.-Y. Self-avoiding polymer trapped inside a cylindrical pore: Flory free energy and unexpected dynamics. *Phys. Rev. E* **2009**, *79*, 061912−1−061912−8.
(20) Jun, S.; Thirumalai, D.; Ha, B.-Y. Compression and Stretching of a Self-Avoiding Chain in Cylindrical Nanopores. *Phys. Rev. Lett.* **2008**, *101*, 138101−1−138101−4.
(21) de Gennes, P.-G. *Scaling Concepts in Polymer Physics*; Cornell University Press: Ithaca, NY, 1979.
(22) Nielsen, H. J.; Li, Y.; Youngren, B.; Hansen, F. G.; Austin, S. Progressive segregation of the Escherichia coli chromosome. *Mol. Microbiol.* **2006**, *61*, 383−393.
(23) Wiggins, P. A.; Cheveralls, K. C.; Martin, J. S.; Lintner, R.; Kondev, J. Strong intranucleoid interactions organize the Escherichia coli chromosome into a nucleoid filament. *Proc. Natl. Acad. Sci. U. S. A.* **2010**, *107*, 4991−4995.
(24) Weeks, J. D.; Chandler, D.; Andersen, H. C. Role of Repulsive Forces in Determining the Equilibrium Structure of Simple Liquids. *J. Chem. Phys.* **1971**, *54*, 5237−5247.
(25) Kremer, K.; Grest, G. S. Dynamics of entangled linear polymer melts: A molecular-dynamics simulation. *J. Chem. Phys.* **1990**, *92*, 5057−5086.
(26) Our date fitting analysis indicates that the slope of the RW regime is slightly smaller than 1/2. Earlier it was shown that polymer conformations in a melt deviate from what we expect from the Flory's ideality hypothesis (see: Wittmer, J. P.; et al. *Europhys. Lett.* **2007**, *77*, 56003−1−56003−5). As a result, chain segments repel each other, at short length scales. This is not seen in our results, possibly because of confinement effects and the essential difference between the melt-chain and confined-chain cases. In the latter case, the chain maps onto an equivalent semidilute solution[27].
(27) Jun, S.; Arnold, A.; Ha, B.-Y. Confined Space and Effective Interactions of Multiple Self-Avoiding Chains. *Phys. Rev. Lett.* **2007**, *98*, 128303−1−128303−4.
(28) By themselves, two chains in a good or athermal solvent repel each other and are not miscible if in free space. Under confinement, this repulsion competes against compression, which tends to mix the chains. The resulting effective interaction dictates the effective miscibility measured in terms of λ/L. For our convenience, we use "effective miscibility" and "miscibility" interchangeably.
(29) Jacobsen, J. L. Demixing of compact polymer chains in three dimensions. *Phys. Rev. E* **2010**, *82*, 051802−1−051802−6.
(30) Vettorel, T.; Grosberg, A. Y.; Kremer, K. Statistics of polymer rings in the melt: a numerical simulation study. *Phys. Biol.* **2009**, *6*, 025013−1−025013−10.
(31) Romantsov, T.; Fishov, I.; Krichevsky, O. Internal Structure and Dynamics of Isolated Escherichia coli Nucleoids Assessed by Fluorescence Correlation Spectroscopy. *Biophys. J.* **2007**, *92*, 2875−2884.
(32) Woldringh, C. L.; Odijk, T. Structure of DNA within the Bacterial Cell: Physics and Physiology. In *Organization of the Prokaryotic Genome*; Charlebois, R. L., Ed.; ASM Press: Washington, DC, 1999.
(33) Hirano, T. At the heart of the chromosome: SMC proteins in action. *Nat. Rev. Mol. Cell Biol.* **2006**, *7*, 311−322.
(34) Marko, J. F.; Siggia, E. D. Polymer Models of Meiotic and Mitotic Chromosomes. *Mol. Biol. Cell* **1997**, *8*, 2217−2231.
(35) Hyeon, C.; Thirumalai, D. Capturing the essence of folding and functions of biomolecules using coarse-grained models. *Nat. Commun.* **2011**, *2*, 487−1−487−11, DOI: 10.1038/ncomms1481.
(36) The values refer to the nucleoid, i.e., the space inside which the chromosome is confined dominantly by molecular crowding.[3,6,32]
(37) Rasmussen, K. H.; Marie, R.; Lange, J. M.; Svendsen, W. E.; Kristensena, A.; Mir, K. U. A device for extraction, manipulation and stretching of DNA from single human chromosomes. *Lab Chip* **2011**, *11*, 1431−1433.
(38) Prinz, C.; Tegenfeldt, J.; Austin, R.; Cox, E.; Sturm, J. Bacterial chromosome extraction and isolation. *Lab Chip* **2002**, *2*, 207−212.

Macromolecules

Article

pubs.acs.org/Macromolecules

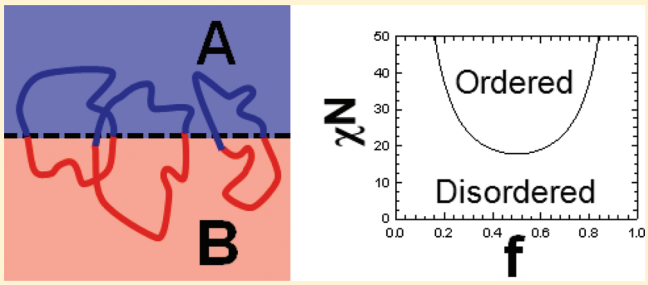
Self-Consistent Field Theory of Gaussian Ring Polymers

Jaeup U. Kim,*[,†] Yong-Biao Yang,[†] and Won Bo Lee*[,‡]

[†]School of Mechanical and Advanced Materials Engineering, Ulsan National Institute of Science and Technology (UNIST), Ulsan 689-798, Korea

[‡]Department of Chemical and Biomolecular Engineering, Sogang University, Seoul 121-742, Korea

ABSTRACT: We present a self-consistent field theory (SCFT) formalism of topologically unconstrained ring polymers for the first time. The resulting static properties of homogeneous and inhomogeneous ring polymers are compared with the random phase approximation (RPA) results. For ring homopolymer mixture, as χN increases, the interfacial width and segment profile converge to those of the linear polymer mixture. The critical point for the ring homopolymer system is exactly the same as the linear polymer case, $(\chi N)_c = 2$, since the critical point does not depend on the local structure of polymers. The critical point for ring diblock copolymer melts is $(\chi N)_c = 17.795$, which is ~1.7 times that of linear diblock copolymer melts, $(\chi N)_c = 10.495$. The difference results from the ring structure constraint.



INTRODUCTION

Ring polymers, being free from chain ends, have fundamental difference from linear chain systems in understanding their statics and dynamics since the static/dynamic properties of linear polymers are strongly influenced by the chain end effects.[1] The topological constraints of ring polymers make the problem nontrivial, which results in limited success in the analytical or semianalytical formulation of ring polymer theory.[2−6] In addition, due to difficulties in their synthesis and purification, experimental studies on ring polymers have progressed slowly.[7−14] This is one of the reasons why the subject has attracted numerous experimentalists as well as theorists.

Most of the computational studies on ring homopolymer melts are performed through molecular dynamics (MD) and Monte Carlo (MC) simulations.[15−24] However, preparation of equilibrium ring polymer melts (nonconcatenated) and investigation of the static and dynamic properties require enormous computation power as well as time as molecular weight increases. Recently, massive computer MD simulations were done and provided insights into evolutions of individual polymer structures in ring homopolymer melts.[18,19]

However, regarding inhomogeneous ring polymer properties such as phase transitions, there have been only a few researches,[25−28] at least to the best of our knowledge. This is mainly because the relaxation time for formation of microstructures is too long to be simulated with particle-based techniques (MD or MC) even by the state-of-art computers. In addition, Marko[27] presented RPA results of Gaussian ring diblock copolymer melts, which is correct in the limit of weak segregation. To overcome the difficulties for investigating inhomogeneity of ring polymer melts, SCFT is a prominent tool since it is a powerful and efficient method for studying inhomogeneous polymer systems[29−32] beyond the weak segregation regime. It has produced many successful applications such as multiblock copolymer melts, supramolecular polymers, lipid/water mixtures, etc.[31,33−42]

In this report, we present SCFT and also random phase approximation (RPA) calculations of Gaussian ring polymer melts and their applications to ring homopolymer blends and ring diblock copolymer melts. The paper is organized as follows. SCFT theory for Gaussian ring polymer melts is presented in section II. In sections III and IV, numerical methods for solving SCFT equations and simulation results are presented, respectively. In addition, in section IV, RPA results for Gaussian ring polymer melts are also discussed. Conclusion is presented in section V.

SCFT FORMALISM

In this section, we briefly review the standard SCFT method for linear polymers (see refs 32 and 43 and references therein for more details) and discuss how we can construct a ring polymer SCFT. The coarse-grained trajectory of a flexible polymer chain is specified by a space curve, $\mathbf{r}_\alpha(s)$, where the integer subscript α labels each chain ($1 \le \alpha \le n$, n is the total number of chains), and its monomer positions are represented by the parameter s which runs along the backbone of the polymer ($0 \le s \le 1$). Once the trajectory is given, a dimensionless segment concentration can be defined as

$$\hat{\phi}_\alpha(\mathbf{r}) = \frac{N}{\rho_0}\int_0^1 ds\, \delta(\mathbf{r} - \mathbf{r}_\alpha(s)) \quad (1)$$

Received: November 28, 2011
Revised: March 12, 2012
Published: March 20, 2012

 © 2012 American Chemical Society

where ρ_0^{-1} is the segment volume and N is the polymerization index.

The free energy of a segment in the interval, $s_1 \le s \le s_2$, of a polymer chain, $\mathbf{r}_\alpha(s)$, is given as a functional of its path

$$E[\mathbf{r}_\alpha;\, s_1,\, s_2] = \int_{s_1}^{s_2} \mathrm{d}s \left(\frac{3}{2a^2 N} \left| \frac{\partial \mathbf{r}_\alpha(s)}{\partial s} \right|^2 + w(\mathbf{r}_\alpha(s)) \right) \tag{2}$$

where a is the statistical segment length. The first term accounts for the Gaussian probability, and the second term is the energy contribution due to the field $w(\mathbf{r})$ acting on the polymer segment. For the case of AB block copolymers with A fraction, f, we need two different fields, $w_A(\mathbf{r})$ and $w_B(\mathbf{r})$, which are used for $0 \le s \le f$ and $f \le s \le 1$, respectively.

The major goal of most SCFT works is to calculate the ensemble average concentration, $\phi(\mathbf{r}) = \langle \sum_\alpha \hat{\phi}_\alpha(\mathbf{r}) \rangle$, and the free energy of the system. For a polymer segment of length sN with its two ends fixed at $\mathbf{r}_0$ and $\mathbf{r}$, respectively, its partition function is formally defined as

$$q(\mathbf{r},\, \mathbf{r}_0,\, s) \propto \int \mathcal{D}\mathbf{r}_\alpha \exp\left(-\frac{E[\mathbf{r}_\alpha;\, 0,\, s]}{k_B T} \right) \delta(\mathbf{r}_\alpha(0) - \mathbf{r}_0)\delta(\mathbf{r}_\alpha(s) - \mathbf{r}) \tag{3}$$

where a proportional constant has no effect on the polymer statistics. This is a functional integral over all possible polymer configurations, $\mathbf{r}_\alpha(s)$, whose weight is given by the Boltzmann factor, and the two end positions are fixed by the delta functions. Direct calculation of the partial partition function requires a heavy computational work, and it is customary to calculate it by solving the following modified diffusion equation:

$$\frac{\partial}{\partial s} q(\mathbf{r},\, \mathbf{r}_0,\, s) = \left[\frac{a^2 N}{6} \nabla^2 - w(\mathbf{r}) \right] q(\mathbf{r},\, \mathbf{r}_0,\, s) \tag{4}$$

with an initial condition

$$q(\mathbf{r},\, \mathbf{r}_0,\, 0) = (a^2 N)^{3/2} \delta(\mathbf{r} - \mathbf{r}_0) \tag{5}$$

The theoretical development so far is independent of the type of polymers (linear homopolymers, block copolymers, ring polymers, etc.). For most SCFT works which model linear polymers, the next algebraic step is to integrate out the initial position $\mathbf{r}_0$ to define $q(\mathbf{r},s) \equiv \int \mathrm{d}\mathbf{r}_0\, q(\mathbf{r},\mathbf{r}_0,s)/(a^2N)^{3/2}$. This new partial partition function is a function of s and one spatial coordinate $\mathbf{r}$, and it is the partition function one obtains numerically by solving the modified diffusion equation. In this way, we not only remove the numerically troublesome delta functions but also reduce the number of spatial variables.

For the linear polymer SCFT, one also needs the conjugate partial partition function, $q^\dagger(\mathbf{r},\mathbf{r}_1,s)$, with an initial condition, $q^\dagger(\mathbf{r},\mathbf{r}_1,1) = (a^2N)^{3/2}\, \delta(\mathbf{r} - \mathbf{r}_1)$. It represents the probability of a length $(1 - s)N$ segment whose ends are fixed at $\mathbf{r}$ and $\mathbf{r}_1$. Again, for most linear polymer SCFT works, one uses $q^\dagger(\mathbf{r},s) \equiv \int \mathrm{d}\mathbf{r}_1\, q^\dagger(\mathbf{r},\mathbf{r}_1,s)/(a^2N)^{3/2}$, obtained by integrating out $\mathbf{r}_1$ dependence. Using these two partial partition functions, the total partition function of the linear chain is calculated as

$$Q^{\mathrm{linear}}[w] = \int \mathrm{d}\mathbf{r}\, q(\mathbf{r},\, s) q^\dagger(\mathbf{r},\, s) \propto \int D\mathbf{r}_\alpha \exp\left(-\frac{E[\mathbf{r}_\alpha;\, 0,\, 1]}{k_B T} \right) \tag{6}$$

The latter expression makes it clear that it counts all the possible chain paths, weighted by the appropriate Boltzmann factors. For the completion of the SCFT formalism, one needs to calculate the segment density using the partition functions, and iterations continue until self-consistency is achieved.

Unfortunately, the same type of SCFT does not exist for the ring polymers. Partition functions analogous to $q(\mathbf{r},s)$ and $q^\dagger(\mathbf{r},s)$ of linear chains cannot be defined due to the absence of chain ends whose dependences must be integrated out. Nonetheless, as described below, we have developed an algebra which allows one to perform meaningful calculations in the SCFT framework.

For a ring polymer, by arbitrarily selecting one segment of the chain as $s = 0$ point, we can define a space curve, $\mathbf{r}_\alpha(s)$, with an implicit restriction that $\mathbf{r}_\alpha(0) = \mathbf{r}_\alpha(1)$. In other words, we regard a ring polymer as a linear polymer with its two ends residing at the same position. Now, most of the above equations are still valid, and there is no problem in defining the two point partial partition function $q(\mathbf{r},\mathbf{r}_0,s)$ which satisfies the modified diffusion equation (eq 4). One must be careful that the conjugate partial partition function must be written as $q^\dagger(\mathbf{r},\mathbf{r}_0,s)$, because the two end points must meet at $\mathbf{r}_0$. Unfortunately, $\mathbf{r}_0$ can be anywhere, and it makes the problem more difficult. Let us fix the position $\mathbf{r}_0$ for the time being and evaluate the total partition function of ring polymers with both $\mathbf{r}_\alpha(0)$ and $\mathbf{r}_\alpha(1)$ residing at $\mathbf{r}_0$:

$$Q[w,\, \mathbf{r}_0] \equiv \frac{1}{(a^2N)^{3/2}} \int \mathrm{d}\mathbf{r}\, q(\mathbf{r},\, \mathbf{r}_0,\, s) q^\dagger(\mathbf{r},\, \mathbf{r}_0,\, s) \propto \int \mathcal{D}\mathbf{r}_\alpha \exp\left(-\frac{E[\mathbf{r}_\alpha;\, 0,\, 1]}{k_B T} \right) \delta(\mathbf{r}_\alpha(0) - \mathbf{r}_0)\delta(\mathbf{r}_\alpha(1) - \mathbf{r}_0) \tag{7}$$

The latter expression indicates that we consider all possible chains with $s = 0$ and $s = 1$ points fixed at $\mathbf{r}_0$. It is therefore a ring polymer total partition function with $s = 0$ point fixed at $\mathbf{r}_0$. The total partition function without such a restriction must account for all possible $\mathbf{r}_0$ positions:

$$Q[w] \equiv \int \mathrm{d}\mathbf{r}_0\, Q[w,\, \mathbf{r}_0] \propto \int \mathcal{D}\mathbf{r}_\alpha \exp\left(-\frac{E[\mathbf{r}_\alpha;\, 0,\, 1]}{k_B T} \right) \delta(\mathbf{r}_\alpha(0) - \mathbf{r}_\alpha(1)) \tag{8}$$

This expression is similar to the partition function for linear chains, eq 6, except an additional delta function to guarantee that the chain has a ring geometry.

For the complete polymer statistics calculation, both $q(\mathbf{r},\mathbf{r}_0,s)$ and $q^\dagger(\mathbf{r},\mathbf{r}_0,s)$ must be evaluated by solving the modified diffusion equation for all possible $\mathbf{r}_0$ values. Even though it is computationally costly, the numerical implementation is straightforward, and solutions in low-dimensional systems can

dx.doi.org/10.1021/ma202583y | Macromolecules 2012, 45, 3263−3269

be obtained in a reasonable time. The segment concentration of the ring polymers is calculated as

$$\begin{aligned}\phi(\mathbf{r}) &= \langle n\hat{\phi}_\alpha(\mathbf{r})\rangle \\ &= \frac{n}{Q[w]}\int \mathcal{D}\mathbf{r}_\alpha \hat{\phi}_\alpha(\mathbf{r})\exp\left(-\frac{E[\mathbf{r}_\alpha;\,0,\,1]}{k_BT}\right) \\ &\quad \delta(\mathbf{r}_\alpha(0)-\mathbf{r}_\alpha(1)) \\ &= \frac{nN}{\rho_0 Q[w]}\int_0^1 ds\int \mathcal{D}\mathbf{r}_\alpha \delta(\mathbf{r}-\mathbf{r}_\alpha(s)) \\ &\quad \exp\left(-\frac{E[\mathbf{r}_\alpha;\,0,\,1]}{k_BT}\right)\delta(\mathbf{r}_\alpha(0)-\mathbf{r}_\alpha(1)) \\ &= \frac{V}{Q[w]}\int_0^1 ds\left[\frac{1}{(a^2N)^{3/2}}\int d\mathbf{r}_0\, q(\mathbf{r},\mathbf{r}_0,s)q^\dagger(\mathbf{r},\mathbf{r}_0,s)\right]\end{aligned} \tag{9}$$

where $V \equiv nN/\rho_0$ is the total polymer volume. This expression is already complete, but it would be convenient to introduce a new variable, $\phi(\mathbf{r};\mathbf{r}_0)$, which represents the segment density contribution of ring polymers with $s = 0$ point fixed at $\mathbf{r}_0$:

$$\begin{aligned}\phi(\mathbf{r}) &= \frac{1}{(a^2N)^{3/2}}\int d\mathbf{r}_0\,\phi(\mathbf{r};\,\mathbf{r}_0) \\ \phi(\mathbf{r};\,\mathbf{r}_0) &= \frac{V}{Q[w]}\int_0^1 ds\, q(\mathbf{r},\mathbf{r}_0,s)q^\dagger(\mathbf{r},\mathbf{r}_0,s)\end{aligned} \tag{10}$$

The generic ring polymer SCFT stops here. The complete SCFT formalism requires the relation between the input fields and output concentrations, and the details of the system must be specified: melts or in solvents, one component system or mixture, homopolymers or block copolymers, etc. For most cases, the equations for the linear polymer theory are acceptable with the modifications presented above. In this report, we test two heterogeneous systems: (i) melts of A ring and B ring mixture with equal chain length and (ii) symmetric AB ring block copolymers, as shown in Figure 1. For both cases, the self-consistency equations to be satisfied are

$$\begin{aligned}w_A(\mathbf{r}) &= \chi N\phi_B(\mathbf{r}) + \xi(\mathbf{r}) \\ w_B(\mathbf{r}) &= \chi N\phi_A(\mathbf{r}) + \xi(\mathbf{r})\end{aligned} \tag{11}$$

where χ is the interaction parameter between A and B segments and $\xi(\mathbf{r})$ is the pressure field enforcing incompressibility. After the self-consistency is satisfied, the free energy per chain of the ring mixture is

$$\begin{aligned}\frac{F}{nk_BT} &= -\frac{V_A}{V}\log\left(\frac{Q_A[w]}{V_A}\right) - \frac{V_B}{V}\log\left(\frac{Q_B[w]}{V_B}\right) \\ &\quad + \frac{1}{V}\int d\mathbf{r}\,(\chi N\phi_A(\mathbf{r})\phi_B(\mathbf{r}) - w_A(\mathbf{r})\phi_A(\mathbf{r}) \\ &\quad - w_B(\mathbf{r})\phi_B(\mathbf{r}))\end{aligned} \tag{12}$$

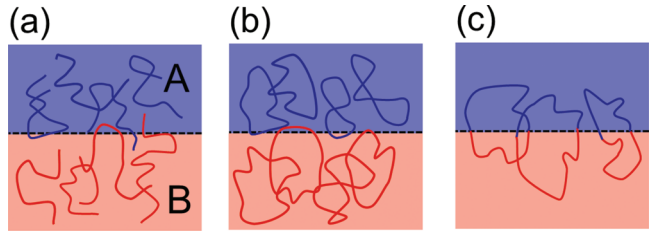


Figure 1. Schematic diagram of (a) A and B linear polymer mixture, (b) A and B ring polymer mixture, and (c) AB ring diblock copolymers.

where V_i and Q_i are the volume and total partition function of i species (i = A or B), respectively. For the second system, the free energy per chain of AB ring block copolymers is

$$\begin{aligned}\frac{F}{nk_BT} &= -\log\left(\frac{Q[w]}{V}\right) + \frac{1}{V}\int d\mathbf{r}\,(\chi N\phi_A(\mathbf{r})\phi_B(\mathbf{r}) \\ &\quad - w_A(\mathbf{r})\phi_A(\mathbf{r}) - w_B(\mathbf{r})\phi_B(\mathbf{r}))\end{aligned} \tag{13}$$

NUMERICAL METHODS

As we briefly mentioned in the previous section, this methodology imposes heavy computational demands because the partition function we solve is now a function of $\mathbf{r}_0$. In other words, the modified diffusion equation must be solved for all possible $\mathbf{r}_0$ values. A spatially three-dimensional system has to use a seven-dimensional partition function, six for the two spatial coordinates, $\mathbf{r}$ and $\mathbf{r}_0$, and one for s. In this report, our major goal is to demonstrate the validity of our methodology, and thus we mostly discuss a one-dimensional system which can be calculated in a relatively short time with high accuracy. Even with this restriction, the results shown in the next section present many interesting features.

Apart from the $\mathbf{r}_0$ integral, the required calculation is essentially unchanged from the linear chain SCFT. The most important task is still to solve the modified diffusion equation, but this time with a delta function initial condition. Various methods have been developed for the fast and accurate evaluation of the partition functions, and we can categorize them as spectral method,[33,43] pseudospectral method,[44,45] and real space method.[46−49] In this report, we solve the modified diffusion equation in one-dimensional real space using Crank−Nicolson method.[50] This simple treatment allows us to use large number of spatial grid M, up to 2000 for ring mixture and 500 for ring diblock copolymers. For both model systems, the number of discretized points in s direction, N, is 500.

For many linear polymer systems, the smallest possible unit cell is obtained by imposing the Neumann boundary condition. However, for the ring polymers, it is not a recommendable strategy even when the segment density has a reflecting symmetry. This problem is well demonstrated in Figure 2a. Our SCFT evaluates the partition function for each fixed point $\mathbf{r}_0$, which acts as starting (s = 0) and ending (s = 1) points of the chain. When Neumann boundary condition is used, a linear chain with its two ends equally distanced from a reflecting plane in opposite directions is wrongly recognized as a valid ring polymer configuration as shown in Figure 2a.

We avoid this problem by using the periodic boundary condition. For the periodic boundary case, one may still construct a similar unphysical configuration as shown in Figure 2b. If the distance between the starting and ending points is an

dx.doi.org/10.1021/ma202583y | Macromolecules 2012, 45, 3263−3269

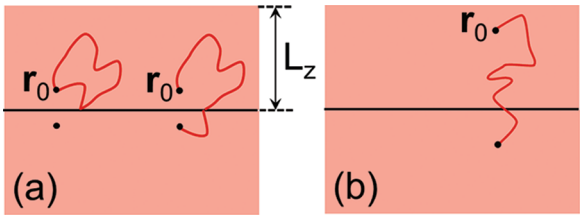


Figure 2. (a) Two chain configurations indistinguishable under Neumann boundary condition. The left one is a valid ring polymer, while the right one is a linear chain. The upper half is the physical world, and the lower half is its mirror image. (b) A linear chain configuration contributing to the ring chain partition function under periodic boundary condition. Now, the lower half is the periodic repetition of the physical world.

integer multiple of the system size, L_z, it will be wrongly recognized as a valid ring polymer configuration. However, unlike the Neumann boundary case, such a probability decays exponentially as the system size increases. In this work, by using system sizes exceeding $4aN^{1/2}$, we have successfully removed contributions from such unphysical configurations. Note that the use of periodic boundary with large box size inevitably slows down the calculation, making higher dimensional calculation more time-consuming.

The use of periodic boundary gives us another challenge. When using the simplest three point Laplacian expression and Neumann boundary, the implicit part of the Crank–Nicolson method includes a matrix equation $\mathbf{Ax} = \mathbf{b}$, where $\mathbf{A}$ is a known $M \times M$ tridiagonal matrix, and $\mathbf{x}$ and $\mathbf{b}$ are unknown and known column vectors of length M, respectively. Even though $\mathbf{A}$ matrix shape slightly deviates from the tridiagonal one due to the periodic boundary condition, we managed to solve the nearly tridiagonal matrix equation in $O(M)$ time complexity by adopting a new algorithm.[51]

One last thing to comment is the choice of $s = 0$ point and the evaluation of $q^\dagger(\mathbf{r},\mathbf{r}_0,s)$. For the homogeneous ring polymers, we may start from any point to evaluate $q(\mathbf{r},\mathbf{r}_0,s)$. Because of the symmetry, $q^\dagger(r,r_0,s)$ is always equal to $q(\mathbf{r},\mathbf{r}_0,1-s)$, and we do not need to calculate it separately. One needs to be more careful for the AB ring block copolymers. Only when we choose $s = 0$ point at the exact center of one block, say A, such a symmetry can be utilized. For polymers without such inversion symmetry, such as ABC ring block copolymers, separate calculation of the two partition functions is inevitable.

SCFT RESULTS AND DISCUSSION

We can easily confirm that this theoretical framework reproduces many known properties of ideal Gaussian chains in the absence of field, for which the partial partition function can be analytically evaluated as[43]

$$q(\mathbf{r},\mathbf{r}_0,s) = \left(\frac{3}{2\pi s}\right)^{3/2} \exp\left(\frac{-3(\mathbf{r}-\mathbf{r}_0)^2}{2sa^2N}\right) \tag{14}$$

and the conjugate partial partition function is $q^\dagger(\mathbf{r},\mathbf{r}_0,s) = q(\mathbf{r},\mathbf{r}_0,1-s)$. Then, the mean-square distance between two segments at $s' = 0$ and $s' = s$ is calculated as follows:

$$\langle R^2(s)\rangle = \frac{\int d\mathbf{r}\, \mathbf{r}^2 q(\mathbf{r},\mathbf{r}_0,s) q^\dagger(\mathbf{r},\mathbf{r}_0,s)}{\int d\mathbf{r}\, q(\mathbf{r},\mathbf{r}_0,s) q^\dagger(\mathbf{r},\mathbf{r}_0,s)} = s(1-s)a^2N \tag{15}$$

At $s = 1/2$, it reproduces the well-known result for the ring diameter of ideal Gaussian chains, $\langle R_e^2\rangle = a^2N/4$. The radius of gyration is also calculated as

$$\langle R_g^2\rangle = \frac{1}{2}\int_0^1 ds\, s(1-s)a^2N = \frac{1}{12}a^2N \tag{16}$$

where the 1/2 factor is introduced to compensate double counting of segment pairs.

The simplest heterogeneous polymer system we can imagine is the mixture of two different homopolymers. As an example, we have tested the mixture of two types of ring homopolymers, A and B, with the same statistical segment length a, segment volume ρ_0^{-1}, and polymerization index N. As expected, macroscopic phase separation occurs at large enough χN, and the segment density profile for various χN values is plotted in Figure 3a. A conventional definition for the width of interfacial region is[43]

$$w_I \equiv \frac{\phi_A(\infty) - \phi_A(-\infty)}{\phi'_A(0)} \tag{17}$$

When the length is normalized by this interfacial width, the segment profile converges to the following universal function (see Figure 3b) as χN increases:

$$\phi_A^{SST}(z) \equiv \frac{1}{2}\left[1 + \tanh\left(\frac{2z}{w_I}\right)\right] \tag{18}$$

Note that the above result is originally derived for the linear polymer mixture for which the corresponding profiles are shown in Figure 3c,d (see ref 43 and references therein). It is not trivial whether the strong-segregation theory (SST) of linear polymer is still valid for the ring polymers, but here is a simple argument why the result is the same. As the chain length increases, the density contribution from chain end penetration becomes negligible, and the contribution from loop shaped penetration becomes dominant. It means that the profile of the ring mixture, which only allows loop shaped penetration, must converge to the same function, eq 18. It also justifies why the ring polymer profile converges to this function faster than that of the linear polymers. The SST also predicts that the interfacial width converges to an analytic function $w_I^{SST} = 2a/(6\chi)^{1/2}$. Figure 3e shows that this prediction also works much better for ring polymers than it does for linear polymers.

Another important parameter is the effective interfacial tension γ_I which is defined as the excess free energy per unit area of interface. It is well known that the SST predicts its asymptotic behavior as $\gamma_I^{SST} = k_BTa\rho_0(\chi/6)^{1/2}$. Interestingly, Figure 3f shows that the ring polymer data convergence is worse for this case. For the quantitative explanation, it is required to develop linear and ring polymer SST while maintaining the leading order error terms, which is beyond the scope of this paper.

The difference between the linear and ring polymers is more pronounced at smaller χN where the chain end effect is more

dx.doi.org/10.1021/ma202583y | Macromolecules 2012, 45, 3263–3269

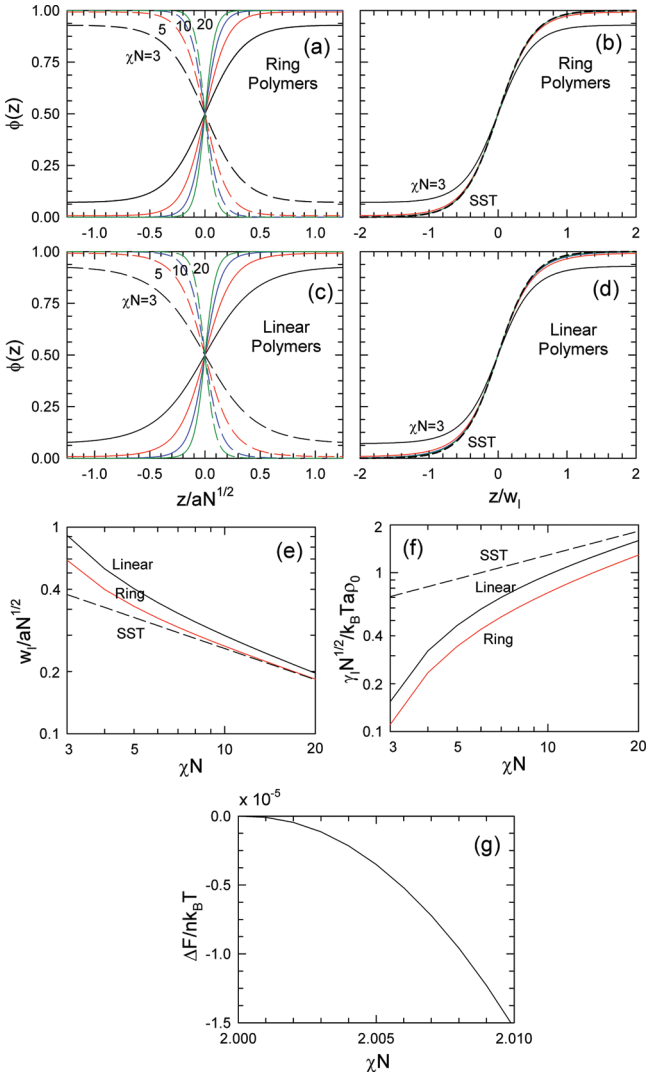


Figure 3. (a) Density profile of A ring (real line) and B ring (dashed line) mixture with χN = 3, 5, 10, and 20, calculated by SCFT. (b) Density profile rescaled by the interfacial width, w_I. The dashed line denotes the prediction of strong-segregation theory (SST). (c, d) Density profile of A and B linear polymer mixture at the same parameters. (e) Interfacial width, w_I, plotted logarithmically as a function of segregation, χN. The dashed line denotes the SST prediction. (f) Interfacial tension, γ_I, plotted logarithmically as a function of segregation. The dashed line denotes the SST prediction. (g) Energy difference between segregated and mixed states of ring mixture. The slope becoming zero at $\Delta F = 0$ shows the characteristic of a second-order phase transform, occurring exactly at $\chi N = 2$.

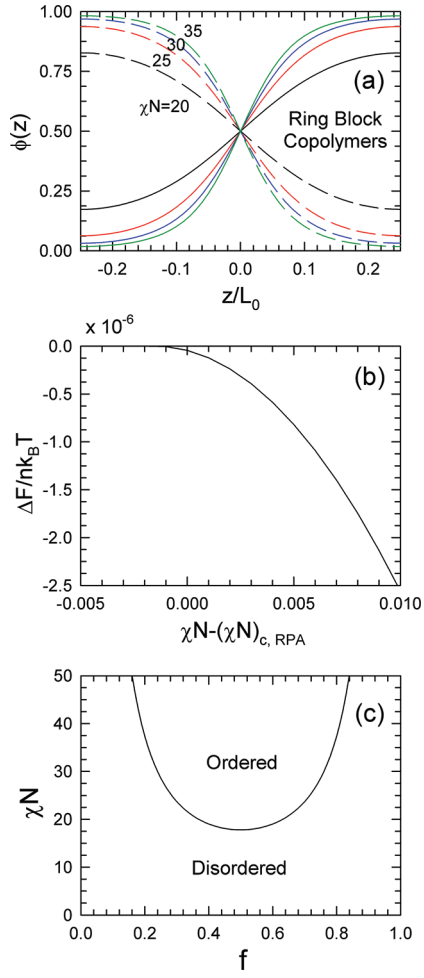


Figure 4. (a) Density profile of symmertic (f = 0.5) AB ring block copolymers with χN = 20, 25, 30, and 35. (b) Energy difference between segregated and mixed states of ring diblock copolymers, calculated by SCFT. The predicted critical point is within 0.001 of the RPA prediction, $(\chi N)_{c,RPA}$ = 17.795. (c) Phase diagram predicted by an RPA calculation.

significant. Nonetheless, the critical point for the ring polymer system is $(\chi N)_c = 2$, exactly the same as the linear polymer case. Here is a simple but convincing argument. As the system approaches to the critical point, the wavelength of the dominant fluctuation increases, and the density gradient becomes smaller. In this limit, a chain with finite length can be viewed as a point particle with an effective interaction parameter, χN. It suggests that the critical point does not depend on the local structure of the polymers as long as the mean-field picture remains valid. As shown in Figure 3g, SCFT calculation confirms this prediction with an error less than 1×10^{-3}.

We have also employed an RPA method[1,27,52] to investigate the critical points of ring polymer systems. The RPA analysis bases on the following fact: the coefficient at the quadratic order turns out to be the inverse structure factor of a system when the free energy functional is expanded in terms of an order parameter, i.e., the density of one component. Divergence of the structure factor at a specific wavenumber points out an instability of the system, which leads to the zero value of the inverse structure factor. The core part of this analysis is calculating the structure factor which may be done by evaluating density−density pair correlation functions for ideal ring chains, with a Gaussian ring chain model.[1,27,52−54] They are listed in the Appendix. For A/B ring homopolymer mixture, the critical point turns out to be exactly the same as the linear polymer case, $(\chi N)_c = 2$, since a critical point does not depend on local structures of polymers as discussed above.

Unlike the ring homopolymer mixture, the situation is not so trivial for the ring diblock copolymers whose segment density profile at various χN values is shown in Figure 4a. In this case, even at the critical point, i.e., the order−disorder transition, the dominant fluctuation wavelength is finite; therefore, the detailed structure of the polymers is important, and we expect a critical point higher than that of the linear diblock copolymers, $(\chi N)_c$ = 10.495. A crude estimation is to regard a ring diblock copolymer as the collection of two half-length

dx.doi.org/10.1021/ma202583y | Macromolecules 2012, 45, 3263−3269

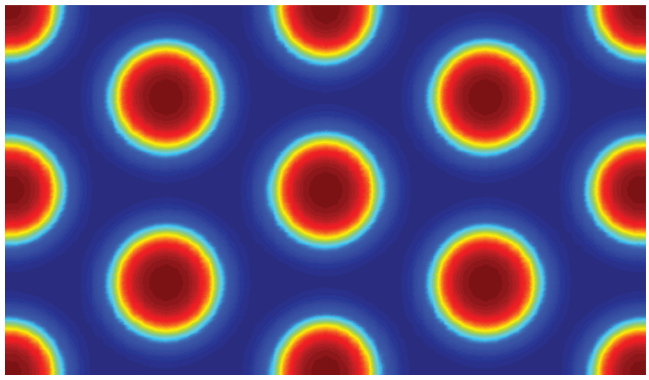


Figure 5. Hexagonally packed cylindrical morphology of AB ring block copolymers with $\chi N = 40$ and $f = 0.3$ (A in red and B in blue colors). Two-dimensional SCFT calculation is performed in a box of $4.31aN^{1/2} \times 2.49aN^{1/2}$.

linear diblock copolymers joined at both ends. Such an argument suggests a doubled value of critical point, $(\chi N)_c = 20.990$.

Our RPA calculation for the ring diblock copolymer melts predicts a somewhat lower critical point, $(\chi N)_c = 17.795$, which is ~1.7 times of the linear diblock copolymer case, as pointed out by Marko.[27] The fact that its order−disorder transition and spinodal points are higher than that of linear diblock copolymer melts suggests that ring melts preserve homogeneity better than the linear melts. This is explained by the structural constraint of ring polymers which causes suppression of density inhomogeneity, which is also seen in density profiles of linear and ring homopolymer melts at the same strength of segregation (see Figure 3a,c).

We have also performed an SCFT calculation for the ring diblock copolymer critical point. Near the critical point, the energy depends very weakly on the domain period, and thus we adopt the exact period predicted by RPA, $L_0 = 0.891aN^{1/2}$. In order to remove the finite box size effect discussed in the previous section, we use a box size, $L_z = 4.455aN^{1/2}$, which corresponds to 5 periods. Despite these efforts, the calculated critical point shown in Figure 4b, $(\chi N)_c = 17.794$, lies ~0.001 below the RPA prediction.

We do not think this small difference is meaningful. In the limit of infinite grid points, the critical points obtained by the two methods, SCFT and RPA, must be identical. Note that eq 13 allows us to analytically calculate the exact mixed state free energy per chain, $F_{mixed}/nk_BT = -0.5 \log(3/2\pi) + 0.25\chi N$. The difference between this analytical prediction and the numerical SCFT result is 3 orders of magnitude larger than the segregation energy gain calculated at $\chi N = 17.795$; therefore, the errors mentioned above are likely due to numerical errors in the discretized calculation.

Until now, we have discussed one-dimensional fine calculation of ring polymer SCFT. In order to demonstrate that this methodology is valid in higher dimension, we have performed a two-dimensional SCFT calculation for a system with $\chi N = 40$ and $f = 0.3$. We solve the two-dimensional modified diffusion equation using Crank−Nicolson finite-difference scheme with the alternate directions implicit (ADI) method.[47] Now the number of spatial grid is 60 × 60, and 60 points are used in s direction. The equilibrium morphology is, not surprisingly, hexagonally packed cylinders with cylinder-to-cylinder distance $L_0 = 1.245aN^{1/2}$. We have confirmed that the hexagonal packing has lower free energy than the square packing at the given parameters. Note that, in order to reduce the effect of nonphysical chain configurations demonstrated in Figure 2, two periods of minimal unit cell are used in both vertical and horizontal directions. Considering the remaining effect of the nonphysical configurations, we expect that the true cylinder-to-cylinder distance at equilibrium can be slightly larger than the above L_0.

■ CONCLUSIONS

In the paper, we developed an SCFT framework of Gaussian ring polymers for the first time. The framework can predict equilibrium nanostructures of topologically unconstrained ring polymer system. The formalism was applied to two model systems—ring homopolymer mixture and ring diblock copolymer melts—and we successfully found segregated phases of the model systems. In addition, RPA calculation for the ring polymers were performed, and the results matched very well with the SCFT predictions.

It should be noted that topological constraints result in nontrivial effects, which is ignored in the SCFT framework. In many experiments and simulations, the chains are prepared in nonconcatenated and unknotted state. The topology is kept afterward, and the ring polymers are known to collapse due to the effective repulsion between chains. There have been debates on the ultimate exponent, but the radius of gyration seems to scale as $\sim N^{1/3}$ for long enough ring chains.[18,24] The mean-field formalism presented here cannot capture such effects in its current shape.

The general problem solving strategy introduced in this paper is applicable for many other problems, such as the morphology of cyclic block copolymers and polymers with ring-included complex geometry. On the basis of this work, we hope to develop efficient numerical algorithms and present studies of challenging inhomogeneous ring polymer systems in the near future.

■ APPENDIX. RING POLYMER RPA

The density−density pair correlation functions, S_{ij}, are as follows:

For the Gaussian ring homopolymer blend

$$S_{AA} = \phi_{Ah} N g_{D,ringh}(x) \tag{19}$$

$$S_{BB} = \phi_{Bh} N g_{D,ringh}(x) \tag{20}$$

where $g_{D,ringh}(x)$ is the Debye function for a ring homopolymer with $x = q^2a^2N/6$. The ring homopolymer Debye function is $2f_{Dawson}[(x)^{1/2}/2]/(x)^{1/2}$, where $f_{Dawson}(x) = \exp(-x^2) \int_0^x \exp(-y^2)\, dy$.

For the Gaussian ring diblock copolymer melt

$$S_{AA} = N g_{D,ring}(x, f) \tag{21}$$

$$S_{BB} = N g_{D,ring}(x, 1 - f) \tag{22}$$

$$S_{AB} = \frac{1}{2} N (g_{D,ring}(x, 1) - g_{D,ring}(x, f) - g_{D,ring}(x, 1 - f)) \tag{23}$$

dx.doi.org/10.1021/ma202583y | Macromolecules 2012, 45, 3263−3269

where

$$g_{D,ring}(x,f) = \frac{e^{-x/4}}{2x}[2(e^{x/4} - e^{(1-2f)^2 x/4}) - (1-2f)\sqrt{\pi x}(\mathrm{erfi}(\sqrt{x}/2) - \mathrm{erfi}((1-2f)\sqrt{x}/2))] \quad (24)$$

is the Debye function for a ring diblock copolymer with $x = q^2a^2N/6$. The function erfi(z) represents the imaginary error function defined as erf(iz)/i where erf(z) is the error function.

AUTHOR INFORMATION

Corresponding Author

*E-mail: jukim@unist.ac.kr (J.U.K.); wblee92@sogang.ac.kr (W.B.L.).

Notes

The authors declare no competing financial interest.

ACKNOWLEDGMENTS

We are grateful to Mark Matsen for useful discussions. This work was supported by the National Research Foundation of Korea (NRF) grant funded by the Korea government (MEST) (No. 2011-0027260 and 2011-0005403), by the year of 2009 Research Fund of the UNIST (Ulsan National Institute of Science and Technology), and by the PLSI supercomputing resources of KISTI. W.B.L. acknowledges the support by the Human Resources Development Program of KETEP grant (No. 20114010203090).

REFERENCES

(1) de Gennes, P. G. *Scaling Concept in Polymer Physics*; Cornell University Press: Ithaca, NY, 1979.
(2) Cates, M. E.; Deutsch, J. M. *J. Phys. (Paris)* **1986**, *47*, 2121−2128.
(3) Khokhlov, A.; Nechaev, S. *Phys. Lett. A* **1985**, *112*, 156−160.
(4) Rubinstein, M. *Phys. Rev. Lett.* **1986**, *57*, 3023−3026.
(5) Nechaev, S. K.; Semenov, A. N.; Koleva, M. K. *Physica A* **1987**, *140*, 506−520.
(6) Obukhov, S. P.; Rubinstein, M.; Duke, T. *Phys. Rev. Lett.* **1994**, *73*, 1263−1266.
(7) Hild, G.; Strazielle, C.; Rempp, P. *Eur. Polym. J.* **1983**, *19*, 721−727.
(8) Roovers, J.; Toporowski, P. M. *Macromolecules* **1983**, *16*, 843−849.
(9) McKenna, G. B.; Hadziioannou, G.; Lutz, P.; Hild, G.; Strazielle, C.; Straupe, C.; Rempp, P. *Macromolecules* **1987**, *20*, 498−512.
(10) Roovers, J.; Toporowski, P. M. *J. Polym. Sci., Part B* **1988**, *26*, 1251−1259.
(11) Lee, H. C.; Lee, H.; Lee, W.; Chang, T.; Roovers, J. *Macromolecules* **2000**, *33*, 8119−8121.
(12) Takano, A.; Kadoi, O.; Hirahara, K.; Kawahara, S.; Isono, Y.; Suzuki, J.; Matsushita, Y. *Macromolecules* **2003**, *36*, 3045−3050.
(13) Matsushita, Y.; Iwata, H.; Asari, T.; Uchida, T.; ten Brinke, G.; Takano, A. *J. Chem. Phys.* **2004**, *121*, 1129−1132.
(14) Kapnistos, M.; Lang, M.; Vlassopoulos, D.; Pyckhou-Hintzen, W.; Richter, D.; Cho, D.; Chang, T.; Rubinstein, M. *Nat. Mater.* **2008**, *7*, 997−1002.
(15) Müller, M.; Wittmer, J. P.; Cates, M. E. *Phys. Rev. E* **1996**, *53*, 5063−5074.
(16) Müller, M.; Wittmer, J. P.; Barrat, J.-L. *Europhys. Lett.* **2000**, *52*, 406−412.
(17) Müller, M.; Wittmer, J. P.; Cates, M. E. *Phys. Rev. E* **2000**, *61*, 4078−4089.
(18) Halverson, J. D.; Lee, W. B.; Grest, G. S.; Grosberg, A. Y.; Kremer, K. *J. Chem. Phys.* **2011**, *134*, 204904.
(19) Halverson, J. D.; Lee, W. B.; Grest, G. S.; Grosberg, A. Y.; Kremer, K. *J. Chem. Phys.* **2011**, *134*, 204905.
(20) Brown, S.; Szamel, G. *J. Chem. Phys.* **1998**, *108*, 4705−4708.
(21) Brown, S.; Szamel, G. *J. Chem. Phys.* **1998**, *109*, 6184−6192.
(22) Brown, S.; Lenczycki, T.; Szamel, G. *Phys. Rev. E* **2001**, *63*, 052801.
(23) Suzuki, J.; Takano, A.; Deguchi, T.; Matsushita, Y. *J. Chem. Phys.* **2008**, *129*, 034903.
(24) Suzuki, J.; Takano, A.; Deguchi, T.; Matsushita, Y. *J. Chem. Phys.* **2009**, *131*, 144902.
(25) Schwahn, D.; Mortensen, K.; Yee-Madeira, H. *Phys. Rev. Lett.* **1987**, *58*, 1544−1546.
(26) Bates, F. S.; Rosedale, J. H.; Stepanek, P.; Lodge, T. P.; Wiltzius, P.; Fredrickson, G. H.; Hjelm, J. R. P. *Phys. Rev. Lett.* **1990**, *65*, 1893−1896.
(27) Marko, J. F. *Macromolecules* **1993**, *26*, 1442−1444.
(28) Aksimentiev, A.; Holyst, R. *Prog. Polym. Sci.* **1999**, *24*, 1045−1093.
(29) Fredrickson, G. H.; Ganesan, V.; Drolet, F. *Macromolecules* **2002**, *35*, 16−39.
(30) Fredrickson, G. H. *The Equilibrium Theory of Inhomogeneous Polymers*; Oxford University Press: New York, 2006.
(31) Matsen, M. W.; Schick, M. *Curr. Opin. Colloid Interface Sci.* **1996**, *1*, 329−336.
(32) Matsen, M. *J. Phys.: Condens. Matter* **2002**, *14*, R21−R47.
(33) Matsen, M. W.; Schick, M. *Phys. Rev. Lett.* **1994**, *72*, 2660−2663.
(34) Matsen, M. W. *Phys. Rev. Lett.* **1995**, *74*, 4225−4228.
(35) Matsen, M. W. *Macromolecules* **1995**, *28*, 5765−5773.
(36) Cochran, E. W.; Garcia-Cervera, C. J.; Fredrickson, G. H. *Macromolecules* **2006**, *39*, 2449−2451.
(37) Feng, E. H.; Lee, W. B.; Fredrickson, G. H. *Macromolecules* **2007**, *40*, 693−702.
(38) Lee, W. B.; Mezzenga, R.; Fredrickson, G. H. *Phys. Rev. Lett.* **2007**, *99*, 187801.
(39) Lee, W. B.; Elliot, R.; Katsov, K.; Fredrickson, G. H. *Macromolecules* **2007**, *40*, 8445−8454.
(40) Elliott, R.; Fredrickson, G. H. *J. Chem. Phys.* **2009**, *131*, 144906.
(41) Guo, Z.; Zhang, G.; Qiu, F.; Zhang, H.; Yang, Y.; Shi, A. C. *Phys. Rev. Lett.* **2008**, *101*, 028301.
(42) Li, W.; Xu, Y.; Zhang, G.; Qiu, F.; Yang, Y.; Shi, A. C. *J. Chem. Phys.* **2010**, *133*, 064904.
(43) Matsen, M. W. In *Soft Matter: Volume 1: Polymer Melts and Mixtures*; Gompper, G., Schick, M., Eds.; Wiley-VCH: Weinheim, 2006.
(44) Tzeremes, G.; Rasmussen, K. O.; Lookman, T.; Saxena, A. *Phys. Rev. E* **2002**, *65*, 041806.
(45) Stasiak, P.; Matsen, M. W. *Eur. Phy. J. E* **2011**, *34*, 110.
(46) Drolet, F.; Fredrickson, G. H. *Phys. Rev. Lett.* **1999**, *83*, 4317−4320.
(47) Kim, J. U.; Matsen, M. W. *Macromolecules* **2008**, *41*, 246−252.
(48) Kim, J. U.; Matsen, M. W. *Phys. Rev. Lett.* **2009**, *102*, 078303.
(49) Kim, J. U.; Matsen, M. W. *Soft Matter* **2009**, *5*, 2889−2895.
(50) Press, W. H.; Teukolsky, S. A.; Vetterling, W. T. *Numerical Recipes in C: the Art of Scientific Computing*; Cambridge University Press: Cambridge, 1993.
(51) Boisvert, R. F. *SIAM J. Sci. Stat. Comput.* **1991**, *12*, 423−442.
(52) Leibler, L. *Macromolecules* **1980**, *13*, 1602−1617.
(53) Yamakawa, H. *Modern Theory of Polymer Solutions*; Harper and Row Inc.: New York, 1971.
(54) Hammouda, B. *J. Chem. Phys.* **1993**, *99*, 9182−9187.

Macromolecules

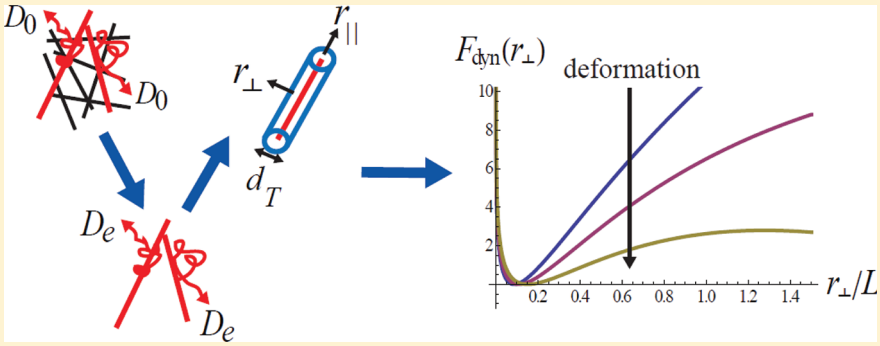
Article

pubs.acs.org/Macromolecules

Microscopic Theory of Quiescent and Deformed Topologically Entangled Rod Solutions: General Formulation and Relaxation after Nonlinear Step Strain

Daniel M. Sussman[†] and Kenneth S. Schweizer*[,‡,§]

[†]Department of Physics, [‡]Department of Materials Science, and [§]Frederick Seitz Materials Research Laboratory, University of Illinois, 1304 W. Green Street, Urbana, Illinois 61801, United States



ABSTRACT: We describe in detail a new self-consistent microscopic theory for the transverse tube confinement potential and the slow dynamics of topologically entangled rod polymer solutions under quiescent (equilibrium) and stressed conditions. Building on this advance, a theory is formulated for the nonlinear relaxation of stress and orientational order after an instantaneous step-strain deformation. The theory accounts for a time- and deformation-dependent (dilated) tube diameter, a maximum confinement force, and a transverse entropic barrier. These aspects result in competing (and coupled) time-dependent relaxation mechanisms under stress: reptative rotational motion and activated transverse barrier hopping. We predict an acceleration of the terminal rotational relaxation due to tube dilation and at sufficiently high deformations the emergence of a competitive transverse hopping (tube breaking) relaxation process. Both of these effects are a consequence of the predicted anharmonic form of the dynamic tube confinement potential and the finite strength of the entanglement force experienced by a tagged rod. After a large enough strain the entanglement network is predicted to break down, and the tube is destroyed in a manner akin to a microscopic yielding event. This results in a regime of ultrafast relaxation of stress and orientation on a time scale much shorter than the terminal relaxation time, and additional dynamical features at intermediate times not present under equilibrium conditions. As stress relaxes, the entanglement constraints and confining tube re-emerge, resulting in a return to an unperturbed reptative relaxation process at long times. The approach to this state is characterized by apparent power-law healing kinetics of the tube diameter, maximum confinement force, and rotational relaxation time. An important consequence of the dynamical evolution of the transverse confinement field is the prediction of a different damping function compared to the classic tube model.

I. INTRODUCTION

This article presents a detailed description of our new theoretical approach for microscopically constructing the dynamic confining tube potential in both equilibrium ("quiescent") and stressed entangled liquids of rigid macromolecules and its extension to treat the fundamental rheological deformation, nonlinear step-strain. The Introduction contains the key motivation and background required to place our work in context.

A. Quiescent Entangled Liquids. Achieving a first-principles theoretical understanding of the spectacular viscoelasticity of strongly entangled synthetic and biological polymer liquids is a very challenging problem in time-dependent statistical mechanics.[1] The key concept is the emergence of "topological constraints": the dynamical consequence of polymer connectivity and uncrossability in liquids of interpenetrating macromolecules that are sufficiently large and/or concentrated. For many decades the primary theoretical approach for linear entangled polymer solutions and melts has been the phenomenological reptation-tube model.[1,2] Its central postulate is that the dynamical effect of many surrounding macromolecules on single-polymer motion can be represented as an effectively static confining potential that strictly prohibits motion transverse to the polymer backbone beyond a mesoscopic length scale, the tube diameter. At zeroth order, this single material parameter is assumed to fully quantify the

Received: January 2, 2012
Revised: March 2, 2012
Published: March 26, 2012

 © 2012 American Chemical Society

lateral dynamical constraints and consequences of intermolecular forces. For random-coil chains, long-time transport proceeds via anisotropic one-dimensional curvilinear diffusion, and scaling laws close, but not equal, to experimental observations are predicted. In practice, many competing nonreptative processes are of high importance (e.g., contour-length fluctuations, dynamic dilution, and constraint release), all of which reduce motional anisotropy and are required to understand experiment.[3]

The reptation-tube approach has been undeniably very useful for polymers of diverse architecture. However, the confining tube concept is a bold ansatz that is not deduced from the statistical mechanics of the fundamental interpolymer interactions in a first-principles, self-consistent manner. Recent perspective and opinion articles[4,5] emphasize that the tube model lacks a microscopic foundation, and a "bottom up" conceptual breakthrough on the crucial tube diameter length scale is needed to address open questions such as the following: (i) What is the nature of an entanglement and of the tube confinement field, and can it be derived theoretically? (ii) What is the microscopic basis of constraint release? (iii) Can the connection between polymer chemistry, concentration, and the tube diameter be understood from first principles? (iv) How does the branch point in a star polymer diffuse subject to the tube constraint?

Several recent experimental and simulation studies have challenged the commonly postulated one-parameter harmonic approximation for the tube confinement field. Particularly relevant for our work are experiments and complementary theoretical work on entangled solutions of the semiflexible biopolymer F-actin,[6,7] and simulations of F-actin[8] and rigid rod[9] model polymers. By studying displacement distributions at intermediate times, or averaging mean-square displacements over many trajectories, these studies have revealed an effective transverse confining potential that is significantly softer than harmonic. Evidence of strong anharmonic softening has also been observed in DNA solutions[10] and in primitive-path simulations of entangled flexible chain melts.[11,12] Hybrid Monte Carlo/primitive-path simulations of polyethylene melts have found highly non-Gaussian distributions of effective tube diameters,[13] which could be indicative of an underlying softer-than-harmonic confining potential. We note that some alternative simulation methods of extracting probability distributions of the radial displacement of a monomer from its mean position in a flexible polymer melt appear to find an effectively harmonic confinement potential over the (limited) displacement range studied,[14] but the bulk of the evidence points toward ubiquitous anharmonicities. The latter are relevant for a deeper understanding of quiescent nonreptative motions involving lateral motion and even more importantly can have qualitative consequences for large-deformation response.

B. Nonlinear Rheology. Extending the reptation-tube model to treat nonlinear rheology and polymer relaxation requires additional uncontrolled approximations that are difficult to directly test. For step-shear strain experiments on entangled chain liquids, a notable early success of Doi–Edwards (DE) theory was the qualitative form of the nonlinear relaxation modulus, $G(t,\gamma) = \sigma(t,\gamma)/\gamma$, where σ is the shear stress and γ is the applied strain.[1] Agreement between the theory and some (not all) experimental data was found for the so-called "damping function", $h(\gamma) = G(t > \tau_x, \gamma)/G(t > \tau_x, \gamma_0 \ll 1)$, where τ_x is a crossover time often cited as of order the longest Rouse relaxation time. The DE theory for the nonlinear rheology of entangled rod solutions has many of the same qualitative features that are predicted for flexible coils as a consequence of assuming a rapid Rouse-like retraction of stretched chains.[1,15]

Motivated by a perceived analogy between temporary physical entanglements in molten polymers and chemical cross-links in a rubber network, Doi and Edwards assumed for simplicity that stress does not modify the tube diameter.[1] Subsequent work by others argued for the other two postulates: stress increases[3,16] or decreases (for extensional deformation)[17] the tube diameter. This issue remains unresolved within the phenomenological tube-model framework, but recent simulations have found evidence for stress-induced tube widening ("dilation") or the reduction of entanglement upon extensional[18] or shear[19] deformation. A perhaps related issue is the original tube-model prediction of a nonmonotonic steady-state flow curve exhibiting unphysical shear thinning.[1] This apparent failure led to the proposal of a many-chain "convective constraint release" (CCR) mechanism whereby fast flows effectively tear apart the entanglement network on time scales much shorter than quiescent reptation.[3] Various implementations of CCR (with adjustable parameter(s)) qualitatively improve agreement with experiment, but their microscopic basis at the level of forces remains unclear.

In addition to the questions raised in the equilibrium quiescent regime, recent perspective articles[4,5] have emphasized the need for conceptual advances under nonlinear deformation conditions. For example, (v) what is the microscopic foundation of CCR, and (vi) how are entanglements and tubes modified under large deformations? Combined rheology/microscopy experiments on entangled chain solutions and melts have suggested that stress can induce an "entanglement–disentanglement transition" and that the tube can be strongly weakened or completely destroyed in analogy with a microscopic "yielding" process.[20] Recent step-strain experiments have been interpreted as evidence that the entanglement network can break down, resulting in "elastic yielding".[21] Such effects are strictly forbidden by existing phenomenological tube models. The key point underlying these (contentious) issues is the assumption that even under high stress or strain conditions (in the absence of CCR) the dynamical effect of the surrounding chains on a tagged polymer can continued to be modeled by infinitely strong tube constraints prohibiting large transverse motion. The "infinitely strong" aspect cannot be literally true for physical entanglements, but the question is whether it is an acceptable approximation under experimental conditions. This issue touches directly on whether the tube confinement field is anharmonic, which would necessarily result in stress-induced weakening of lateral confinement and the possibility of a complete destruction of the tube.

C. Microscopic Approach to Topologically Entangled Dynamics. In two short Letters we have very recently proposed a new microscopic approach for the quiescent and stressed dynamics of entangled, nonrotating rigid rod fluids.[22,23] Its centerpiece is the self-consistent construction of an anharmonic transverse confinement (tube) field based solely on topological entanglements. Under quiescent equilibrium conditions, the theory is consistent with the DE model for how the tube diameter and rotational/transverse center-of-mass (CM) diffusion constants vary with rod density. It also predicts a strongly anharmonic confinement field with key features in quantitative accord with highly entangled F-actin experi-

dx.doi.org/10.1021/ma300006s | Macromolecules 2012, 45, 3270–3284

ments[6,22] and qualitatively consistent with chain melt simulations[11] and DNA solution measurements.[10] The single most important feature of our theory is that the dynamic entanglement force localizing a polymer in a tube is of finite strength, which results in multiple novel consequences for the role of applied stress on the tube diameter, diffusion, and relaxation[23] that are not anticipated by existing reptation-tube models.

The goal of this article is twofold. First, a detailed exposition of our theory is presented that, to date, has only been sketched in two short Letters. Questions (i)−(vi) are addressed, except for (iv) which was partially treated based on fluctuation-driven activated hopping of the center-of-mass of topologically entangled 3D crosses, a potential analogue for the branch-point motion of rigid six-arm stars.[24] Our aim is a unified presentation of the new ideas with ample physical discussion, but not all the mathematical analysis (which is well documented[22−26]). The second goal is to formulate and apply the first extension of our approach to describe stress relaxation after a large amplitude step-strain. We propose a generalized Maxwell model with deformation-modified reptation and stress-assisted transverse barrier hopping as two competing parallel relaxation channels, both of which are self-consistently coupled with the tube confinement potential, macroscopic stress, and rod orientational order. Quantitative and qualitative deviations from the predictions of Doi−Edwards theory are found.

Section II presents the key theoretical aspects for both quiescent and stressed conditions (self-diffusion constant, tube diameter, dynamic confinement potential, incorporation of stress and orientation, concept and definition of "microscopic yielding"), including a full exposition of various analytically derivable results and a new analysis of entanglement onset. Section III briefly discusses the initial consequences of stress and orientation immediately after an instantaneous step-shear strain, including how the tube dilates and is possibly destroyed. Section IV presents calculations of the two competing relaxation times from knowledge of the dynamic confinement potential as a function of degree of entanglement and strain amplitude. Our theory for the time evolution of stress and rod orientation under nonlinear step-strain deformations is given in section V, along with numerical calculations. We conclude in section VI with a summary and discussion. We emphasize that our treatment of nonlinear rheology is carried out under the assumption of homogeneous deformation, which ignores the possibility of constitutive instabilities (such as strain localization or shear banding) and macroscopically nonquiescent relaxation.

II. THEORY FUNDAMENTALS

In this section we review the advances and theoretical techniques we used to derive the various microscopic features of the entangled needle system in equilibrium and when subjected to an applied shear stress. Sections IIA and IIB describe some of the more technical aspects of the prior work we build on, deriving expressions for the long-time diffusion constant and a characteristic localization length for a needle in a tube, respectively. These first two sections also comment on the limitations of approximations used and present a new analysis of the critical entanglement density. Nevertheless, a reader not interested in these theoretical details may skip these two sections and proceed to section IIC and its discussion of the tube confinement potential. Section IID generalizes the confinement potential to treat shear deformation, and section IIE allows for the confinement potential to be modified by an anisotropic distribution of needle orientations.

A. Quiescent Diffusion. Our starting point is the self-consistent dynamic mean-field theory of Szamel, which describes a solution of infinitely thin, nonrotating rigid rods or needles of length L.[25,26] The rod fluid has ideal-gas structure and thermodynamics, so its dynamics are determined solely by topological constraints. For heavily entangled rods that are allowed to rotate the long-time rotational diffusion constant is proportional to its transverse CM diffusion analogue ($D_\perp$) and is inversely related to the terminal rotational relaxation time;[26] thus, knowledge of $D_\perp$ captures all long-time dynamics.[25,26] Polymer connectivity and uncrossability are exactly enforced at the two-rod-collision level. This is in contrast to the usual mode coupling theories (MCT) which do not rigorously forbid polymer backbone crossing at any level due to a factorization of multipoint dynamic correlations.[27] In both Szamel's and our approach, beyond-two-body effects are described via a self-consistent renormalization. A schematic illustrating the spirit of the approach is presented in Figure 1.

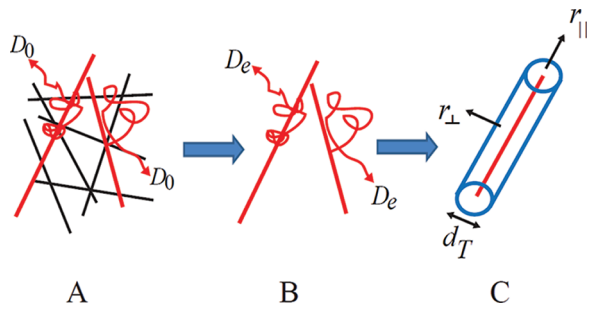


Figure 1. (a) Uncrossable rods diffusing with bare dynamics in between impulsive hard-core collisions. (b) Self-consistent renormalization of many-body effects into an effective diffusion tensor at the two-rod-dynamics level. (c) Analysis of the short-time structure of $\vec{\vec{D}}_e$ determines the full transverse dynamic tube confinement potential.

The Szamel theory is formulated in terms of coupled equations for reduced distribution functions, ρ_i, derived from the N-particle generalized Smoluchowski equation, the first two of which are[25]

$$\frac{\partial \rho_1}{\partial t} = \nabla_1 \cdot (\vec{\vec{D}}_0(\vec{u}_1) \cdot \nabla_1 \rho_1 - \vec{\vec{D}}_0(\vec{u}_1) \cdot \int \mathrm{d}2\ \mathbf{T}(12)\rho_2) \tag{1}$$

$$\frac{\partial \rho_2}{\partial t} = (\nabla_1 \cdot \vec{\vec{D}}_0(\vec{u}_1) \cdot [\nabla_1 - \mathbf{T}(12)] + \nabla_2 \cdot \vec{\vec{D}}_0(\vec{u}_2) \cdot [\nabla_2 - \mathbf{T}(21)])\rho_2 - \sum_{i=1}^{2} \nabla_i \cdot \vec{\vec{D}}_0(\vec{u}_i) \cdot \int \mathrm{d}3\ \mathbf{T}(i3)\rho_3 \tag{2}$$

where the arguments of the reduced distribution functions have been suppressed, the variables of integration are denoted as $\mathrm{d}l = (4\pi)^{-1}\ \mathrm{d}\vec{r}_l\ \mathrm{d}\vec{u}_l$, and $\vec{u}_l$ is the orientation of rod l. Here $\vec{\vec{D}}_0$ is the bare diffusion tensor in the limit of zero concentration describing Brownian short-time motion in an implicit solvent, which in terms of the longitudinal and transverse components can be written as $\vec{\vec{D}}_0(\vec{u}_1) = D_{\|,0}\vec{u}_1^T\vec{u}_1 + D_{\perp,0}(\vec{\vec{I}} - \vec{u}_1^T\vec{u}_1)$. The key features are the T-operators, which exactly describe binary collisions and rigorously enforce rod uncrossability at all times. They correspond to an impulsive "entanglement force"

dx.doi.org/10.1021/ma300006s | Macromolecules 2012, 45, 3270−3284

perpendicular to the plane formed by the orientations of the two colliding rods. For hard, infinitely thin rods of length L the T-operator is[28]

$$\mathbf{T}(12) = \hat{w}_{12}T(12) = \hat{w}_{12}\lim_{b\to 0^+}\delta(\vec{w}_{12} - b)\Theta(L/2 - |\alpha|)\Theta(L/2 - |\beta|) \tag{3}$$

where $b \to 0$ is the rod radius, $\vec{w}$ is the component of the relative CM separation of the two rods, $\vec{r}$, along the vector $\vec{u}_1 \times \vec{u}_2$, and

$$\alpha = \frac{\vec{r}\cdot\vec{u}_1 - (\vec{r}\cdot\vec{u}_2)(\vec{u}_1\cdot\vec{u}_2)}{1 - (\vec{u}_1\cdot\vec{u}_2)^2}, \quad \beta = \frac{\vec{r}\cdot\vec{u}_2 - (\vec{r}\cdot\vec{u}_1)(\vec{u}_1\cdot\vec{u}_2)}{1 - (\vec{u}_1\cdot\vec{u}_2)^2} \tag{4}$$

The infinite dynamic hierarchy is closed by writing a self-consistent equation for $\vec{\vec{D}}_e$, a nonlocal in space and time effective diffusion tensor. This is achieved by dropping the integral over the three-body term in eq 2 and replacing the bare diffusion tensor with this same effective self-diffusion tensor. By comparing the definition of the test-rod current with a derived expression, one obtains in Fourier−Laplace space the self-consistent equation:[26]

$$\vec{\vec{D}}_e^{\,-1}(\vec{u}_1; z) = \vec{\vec{D}}_0^{\,-1}(\vec{u}_1) + \frac{\rho}{4\pi}\int d\vec{u}_2\, d\vec{r}\; g(\vec{r}, \vec{u}_1, \vec{u}_2)\mathbf{T}(12)\frac{1}{z - \Omega_e^\dagger(z)}\mathbf{T}(12) \tag{5}$$

Here z is the reciprocal time variable, $g(\vec{r}, \vec{u}_1, \vec{u}_2)$ is the 2-rod equilibrium pair correlation function (equal to unity almost everywhere for an isotropic solution of infinitely thin needles), and the effective adjoint Smoluchowski operator is given by

$$\Omega_e^\dagger(z) = ([\nabla_{\vec{r}} + \mathbf{T}(12)]\cdot[\vec{\vec{D}}_e(\vec{u}_1; z) + \vec{\vec{D}}_e(\vec{u}_2; z)]\cdot\nabla_{\vec{r}}) \tag{6}$$

Two main approximations have been used to derive this expression: (i) neglect of the $\vec{k}$ dependence of the effective diffusion tensor, $\vec{\vec{D}}_e(\vec{k}, \vec{u}_1; z) \approx \vec{\vec{D}}_e(\vec{k} = 0, \vec{u}_1; z)$, and (ii) use of the same effective diffusion tensor to capture the effect of the surroundings on both the tagged and the untagged rod. Together these approximations can be thought of as replacing the wavevector-dependent collective diffusion tensor by an effective self-diffusion tensor,[26] reminiscent of a Vineyard-like approximation successfully employed in glassy-dynamics contexts.[29,30] Szamel's theory has been shown to be related to a sophisticated version of a MCT-like approach that avoids factorizing four-point correlation functions into products of two-point correlations,[27] the crucial feature required to capture dynamical polymer backbone uncrossability.

Equations 5 and 6 are infinite order in the effective diffusion constant and T-operator. Hence, an infinite sequence of correlated collisions of a tagged rod with its surroundings is approximately taken into account. If the effective diffusion constant in eq 6 is replaced by its dilute solution value, then an independent binary collision (IBC) theory[31] is recovered, akin to dynamic second-order perturbation theory. The IBC description can describe the initial consequences of inter-rod collisions, but cannot predict tube localization, a non-perturbative phenomenon.

The self-consistent dynamic mean-field theory makes several notable predictions. The most elementary, presented here for the first time, comes from asking what happens if one assumes that rods diffuse isotropically. By ignoring the distinction between transverse and longitudinal motion, and employing the same mathematical methods discussed previously,[24,26] we find $D/D_0 = 1 - (\rho/\rho_{c,iso})$, corresponding to a nonergodicity transition at $\rho_{c,iso}L^3 \approx 18.2$. This quenching of isotropic motion, or formation of a "topological glass", occurs at an eminently reasonable density in the sense that it requires $(18.2/L^3)(\pi L^3/6) \approx 10$ interpenetrating rods to occupy a sphere of diameter L. Of course, such an isotropic glass is not expected to be realized if the system is allowed to exploit anisotropic modes of transport.

Carrying out the full anisotropic calculation, wherein $D_\parallel = D_{\parallel,0}$ (longitudinal reptation) and $D_\perp$ is self-consistently computed,[25] agreement with the asymptotic high-density scaling law of the static tube-reptation theory is obtained, $D_\perp/D_0 \propto (\rho L^3)^{-2}$. A full numerical analysis from the IBC to the reptative scaling regime yields a dynamical crossover at $\rho_e L^3 \approx 10.1$.[22] Recall that the underlying physics controlling long-time transverse center-of-mass and rotational diffusion is qualitatively identical: each proceeds via a small lateral displacement or a rotation when a rod reptates out of its local tube.[26] The practical estimate of the entanglement crossover above agrees quite well with what is predicted if reptation as a mode of motion is removed by hand. Doing so (i.e., setting $D_{\parallel,0} = 0$), one finds $D_\perp/D_0 = 1 - (\rho/\rho_c{}^*)$, corresponding to strict transverse localization at $\rho_c{}^*L^3 = 9.29$.[26] Recent numerical calculations have also shown[22] that after rescaling ρ by its crossover value the theory agrees quantitatively with simulations for both the rotational and transverse translational diffusion constants over the entire density range.[32,33]

B. Transverse Localization and the Dynamic Tube Diameter. The possibility of tube localization can be addressed by taking the low-frequency limit of the effective self-diffusion tensor, $D_e(z \to 0)$, and assuming Gaussian localization characterized by a mean harmonic localization radius, r_l. A self-consistent expression for the transverse localization length (half of the mean tube diameter) can thus be derived:[26]

$$\frac{4}{r_l^2} = \frac{-\rho}{8\pi}(\vec{\vec{I}} - \vec{u}_1^T\vec{u}_1): \int d\vec{r}\; d\vec{u}_2\; \mathbf{T}(12)(\Omega_{loc}^\dagger)^{-1}\mathbf{T}(12) \tag{7}$$

where the colon denotes a double contraction of tensorial indices, and

$$\Omega_{loc}^\dagger = -1 + \frac{r_l^2}{4}[\nabla_{\vec{r}} + \mathbf{T}(12)]\cdot(2\vec{\vec{I}} - \vec{u}_1^T\vec{u}_1 - \vec{u}_2^T\vec{u}_2)\cdot\nabla_{\vec{r}} \tag{8}$$

Equation 7 is derived by analyzing a system where the longitudinal (reptative) motion of all rods is quenched. Conceptually, this is similar to how simulations perform primitive path analyses to deduce the tube diameter.[34] We re-emphasize that *no* equilibrium structural-correlation information enters eqs 7 and 8, since thermodynamically the rods are an ideal gas. Note that since r_l and the T-operators enter the adjoint "localized" Smoluchowski operator, eq 7 corresponds to an infinite-order resummation of the multiple correlated collisions which are the microscopic origin of tube localization.

With a particular choice of boundary conditions for a Helmholtz differential equation used to solve eq 7 for r_l,

transverse localization is found to emerge at a critical density $\rho_c L^3 = 3\sqrt{2}$.[24] The numerical discrepancy between this critical density and the entanglement crossover for the long-time diffusion constant discussed above is partly a result of the technical mathematical approximations used to solve the Helmholtz equation and partly a result of the inaccuracy of the theory at very large displacements.[24] Specifically, at ρ_c the theory predicts that the inverse localization length increases continuously from zero, and $r_l^{-1} \ll L^{-1}$ is precisely the regime in which the Vineyard-like replacement of the collective-diffusion tensor with a k-independent self-diffusion tensor is expected to be least accurate. However, we emphasize that the theory predicts sensible localization lengths ($r_l < L$) at all rod densities greater than $2.3\rho_c \approx \rho_e$. Our focus here is $\rho \gg \rho_c$, where the theory is not sensitive to the approximations discussed above. In the heavily entangled limit one finds[25] $d_T \equiv 2r_l = 16\sqrt{2}/(\pi\rho L^2)$. This is in agreement with the DE scaling law for the tube diameter[1] and is quantitatively close to the result found in simulations of rotating and translating needles at high density,[9] $d_T \approx 5/\rho L^2$.

C. Quiescent Transverse Confinement Potential. Starting from the microscopic dynamics of a fluid of entangled needles of length L, the previous sections derive results for the long-time longitudinal and transverse diffusion constants of a tagged needle and a localization length that characterizes the spatial extent of fluctuations transverse to the needle when it is inside the confining tube (i.e., a tube diameter). The theory predicts the distinctive connection between the transverse localization length and long-time transport, $D_\perp/D_{\|,0} \propto (\rho L^3)^{-2} \propto (d_T/L)^2$, which is also the result of the real space reptation-tube ansatz for entangled rod solutions. The key result for our purposes here is eq 7, which is a self-consistent equation for the localization length r_l assuming purely *Gaussian* fluctuations. The above approach has been qualitatively extended[22] to create a microscopic theory of the full dynamic transverse confinement potential as a function of the instantaneous CM transverse displacement, $r_\perp$, that goes beyond a Gaussian description. We start by rewriting the explicit form of eq 7 as a force balance:

$$f(r_l) = \frac{2k_BT}{r_l} - 2r_l K_\perp(r_l) = 0 \tag{9}$$

$$K_\perp(r_l) = \frac{\pi\rho L k_BT}{8\sqrt{2}}(L/r_l - I_1(2L/r_l) + \mathbf{L}_1(2L/r_l)) \equiv \frac{\pi\rho L k_BT}{8\sqrt{2}} g(L/r_l) \tag{10}$$

where $\mathbf{L}_1$ (I_1) is the first Struve function (modified Bessel function of the first kind). Equation 9 suggests interpreting the derived tube localization result as a competition between a delocalizing entropic driving force and a localizing entanglement force. The fact that the entanglement force takes the form of a highly nonlinear spring with the displacement-dependent coefficient $K_\perp(r_l)$ is an early hint that the confining tube is more complicated than a simple harmonic potential, and our previous work showed that these anharmonicities are crucial to understanding experimental data even in quiescent, heavily entangled systems.[22] The basis for reinterpreting the localization length equation as a force balance stems from recent theoretical work in glass physics, where a self-consistent localization result of the form of eq 7 emerges from a dynamical-Gaussian-approximation treatment of kinetic vitrification within an amorphous solid model.[30] It is well-known for structural glasses that such strict-localization results are an artifact of the Gaussian approximations used (common to both ideal MCT and the Szamel approach), which only address the stability of kinetic arrest to small-amplitude fluctuations and ignore large-amplitude, ergodicity-restoring, barrier-hopping events. We thus use some of the microscopic methods and concepts developed in the glass physics community for describing such large-amplitude events to probe the stability of the confining tube to non-Gaussian fluctuations.

One such highly developed microscopic approach to treat activated dynamics at the single-particle level is the nonlinear Langevin equation (NLE) theory.[30,35] Its key insight is to interpret eq 9 as a force balance at the instantaneous tagged-particle-displacement level, coupled with a nonensemble-averaged version of the local equilibrium concept, so that the tagged needle stochastically samples transverse displacements in a way consistent with the forces prescribed by eq 9. Predicting tagged particle trajectories requires additional noise and short-time friction terms, and in the overdamped limit this leads to the stochastic NLE for the transverse rod center-of-mass displacement

$$-\zeta_s \frac{dr_\perp}{dt} - \frac{\partial}{\partial r_\perp} F_{dyn}(r_\perp) + \delta f_s = 0 \tag{11}$$

where ζ_s is the short-time friction constant, δf_s the corresponding white noise random force, and

$$F_{dyn}(r_\perp) = \int_{r_l}^{r_\perp} f(r)\, dr \tag{12}$$

is a "dynamic free energy". This corresponds to the transverse tube potential that captures the effects of entanglement forces, including an exact accounting of two-rod uncrossability. Unlike in the phenomenological tube theory, the resulting confinement field is not a static, geometrically determined object, but is rather the consequence of dynamic intermolecular correlations.[35] The NLE theory goes beyond eq 7 in the sense that in the absence of noise eq 11 reduces to eq 7 at long times.

We note that the NLE framework has been derived from microscopic statistical mechanics for sphere fluids and can describe activated relaxation via highly non-Gaussian trajectory fluctuations.[35] The underlying physical ideas are not tied to the precise nature of the Gaussian self-consistent theory that serves as its starting point (here, eq 7) and thus can be applied to topologically entangled liquids. For numerical convenience, in subsequent calculations $g(x)$ in eq 10 is replaced with a Pade approximation that correctly recovers its asymptotic behavior:

$$\frac{r^2}{2L^2} g\left(\frac{L}{r}\right) \approx \frac{r\left(a + 48\pi\frac{r}{L}\right)}{2L\left(a + 48\pi\frac{r}{L} + 18\pi^2\frac{r^2}{L^2}\right)} \simeq \begin{cases} \frac{r}{2L}, & r \ll L \\ \frac{4}{3\pi} - \frac{L}{4r}, & r \gg L \end{cases} \tag{13}$$

where $a = 128 - 9\pi^2$.

There are many interesting features of the dynamic tube confinement potential (see Figure 2 for examples). In qualitative contrast with particle glasses where activation barriers are finite,[30,35] for all densities $\rho > \rho_c$ the topological

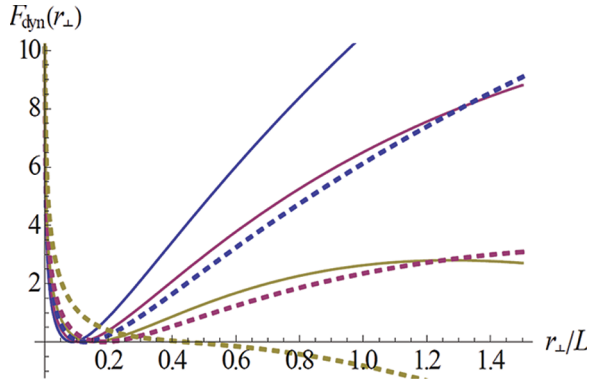


Figure 2. Transverse tube confinement potential (in units of the thermal energy) as a function of the dimensionless rod center-of-mass transverse displacement at fixed reduced density, $\rho/\rho_c = 10$. From top to bottom the solid curves correspond to $S = 0$ and $\sigma/\sigma_y = 0,1/3, 2/3$. From top to bottom the dashed curves correspond to $S = 1/2$ and $\sigma/\sigma_y = 0,1/3, 2/3$.

confinement potential is predicted to be infinitely deep. This would seem to provide some justification for the most basic aspect of the reptation-tube ansatz, that is, the quenching of unbounded lateral motion or the idea that polymers must reptatively "diffuse around" entanglement constraints. However, in contrast to phenomenological harmonic tube models (e.g., spring or slip-link models[36]) which typically postulate a confinement field characterized by a single parameter, the tube diameter, the dynamic free energy is only parabolic up to $\sim k_B T$ above its minimum. It then crosses over to a weaker quasi-linear regime out to displacements of order the rod length and finally grows logarithmically for very large displacements. The predicted harmonic and quasi-linear regimes are in very good accord with experiments on heavily entangled F-actin solutions, which observe long exponential tails in the rod displacement distribution on time scales short compared to the reptation time.[6]

The large-displacement form of the tube potential follows from eqs 10 and 12 as

$$F_{dyn}(r_\perp \gg L) \sim (\rho/\rho_c - 2)\log(r_\perp/L) \tag{14}$$

We caution that this logarithmic growth, and hence our prediction that the transverse barrier is infinitely high, is a technically subtle result that we believe is sensitive to the Vineyard-like and local-equilibrium approximations of the theory. One might have physically expected a large, but finite, entropic barrier at $r_\perp \approx L$. However, the very-large-displacement form of the transverse tube confinement potential is not relevant in practice. The reason is that in strongly entangled systems its height at $r_\perp \approx L$ (before the crossover to logarithmic growth) is already enormous relative to the thermal energy, and thus a tagged rod reptates out of the local tube by longitudinal motion long before its transverse displacement ever approaches the logarithmic regime.

We emphasize that the key to our previously demonstrated quantitative agreement with F-actin experiments[6] (and, qualitatively, the consistency of our approach with DNA experiments[10] and the entangled-chain-melt primitive-path simulations[11,12]) is the harmonic and quasi-linear part of the dynamic tube potential (Figure 2) and the concomitant prediction of a maximum entanglement restoring force. Such confinement softening emerges from a self-consistent treatment of nonlinear feedback between lateral polymer displacements and the transverse dynamic localization constraints. As a speculative comment, this feature can perhaps be qualitatively viewed as a microscopic realization of local constraint release or a "double reptation"-like process in the language of the classic tube model.[3] Szamel previously showed that the needle theory captures some constraint-release-like effects at the CM self-diffusion level,[26] and we here propose that our theory for the dynamic confinement potential similarly self-consistently captures some matrix-mobility effects. That is, as the tagged rod displaces, the dynamical constraints it experiences are also relaxed via the motion of the other polymers entangled with it (since $\vec{\vec{D}}_e$ is responsible for the dynamic evolution of both the one- and two-body density distributions), resulting in a dynamical softening of the tube constraint. Note this is certainly not the textbook global constraint release mechanism tied to the reptative motion of a matrix rod end past a tagged polymer;[1] it is fundamentally more general since it exists when reptation is quenched. A generalized constraint release motion not tied to reptation has also been suggested based on primitive path simulations of chain melts.[11]

Indirect, but we believe significant, evidence for the anharmonic nature of the tube confinement field for thin, rigid macromolecules can also be found in recent Brownian simulation studies of heavily entangled semiflexible chains constructed to mimic F-actin[8] and rigid needles.[9] These studies investigated the lateral mean-square displacement (MSD) of the center of a polymer defined in a way that ignored contributions from the longitudinal motion. The classic tube idea predicts that this MSD would saturate at quite early times after a displacement of order d_T^2. However, even at very high degrees of entanglement this was not found, neither for stiff semiflexible chains[8] nor rigid rods.[9] Instead a slow, seemingly unbounded increase (at lower densities) or steadily upward creep (at high densities) of the lateral MSD was detected, and significant lateral displacements beyond the putative mean tube diameter occurred on time scales less than the reptation-controlled rotational relaxation time. Moreover, by varying the longitudinal friction, the simulations determined that this "tube leakage" is not due to a simple constraint-release effect of one polymer reptating past a local entanglement[9] and that it can be eliminated if all polymers surrounding the tagged one are frozen, per a network. Hence, these tube-leakage phenomena appear to be an intrinsic, *many-polymer* property of lateral dynamical constraints, and their essence seems qualitatively consistent with our prediction of an anharmonic confinement potential.

In the heavily entangled regime, the displacement at which a rod feels the maximum confining force, r_m, is much less than L. A series expansion of eq 10 in inverse density can be carried out to obtain

$$\begin{aligned} f_{max} &\simeq \frac{k_B T}{L}\left(\frac{\pi\rho L^3}{4\sqrt{2}} - 2\sqrt{\rho L^3/\sqrt{2}} + \ldots\right) \\ &= 2k_B T\left(\frac{1}{r_l} + \frac{-2\sqrt{2}}{\sqrt{\pi r_l}} + \ldots\right) \\ &= 2k_B T(r_l^{-1} - 2r_m^{-1}) \end{aligned} \tag{15}$$

dx.doi.org/10.1021/ma300006s | *Macromolecules* 2012, 45, 3270−3284

where in the second equality the high-density approximation for the localization length is used. The displacement at which the maximum force occurs is

$$r_m^{-1} \simeq \sqrt{\rho L/(4\sqrt{2})} \ll r_l^{-1} \simeq \pi\rho L^2/(8\sqrt{2}) \quad (16)$$

At high densities r_m is small compared to L, and hence is unaffected by the long-range logarithmic growth of the confinement potential, but is large compared to the localization length. In the heavily entangled limit we obtain $f_{max} = 2k_BT/r_l$, a direct connection between the maximum entanglement force and the tube diameter. Although we derive this result only for rigid needles, it perhaps provides a theoretical basis for a speculative argument by Wang et al. based on dimensional analysis concerning the finite strength of tube localization for entangled flexible chain liquids.[20]

D. Effect of Applied Stress on the Confinement Potential and Microscopic Yielding. To include the effect of applied deformation at the single-polymer level in the framework of NLE theory, a stress-based microrheology approach is employed as previously formulated for finite-excluded-volume complex liquids that interact via conservative forces.[37,38] This treatment is significantly less microscopically rigorous than our theory for quiescent dynamics, but the stress-generalized NLE theory has been successfully applied to quantitatively understand many aspects of nonlinear activated relaxation and mechanics in colloidal and polymer glasses.[37,38] The appropriate stress-generalization of the NLE is expected to depend on the particular deformation of interest, and here we focus specifically on shear stresses. For both simplicity (and consistency with the scalar localization length derived above) we neglect the tensorial nature of the deformation and formulate a theory in terms of a scalar stress, σ. The key physical idea is that the macroscopic stress results in a constant effective force on the CM of a particle, molecule, or polymer (a microrheological-like perspective). This external force weakens the dynamical constraints encoded in F_{dyn}, which thus acquires a mechanical-work-like contribution that is linear in both stress and instantaneous transverse displacement:

$$F_{dyn}(r_\perp, \sigma) = F_{dyn}(r_\perp, \sigma = 0) - \pi L^2 \sigma r_\perp/4 \quad (17)$$

Since the theory treats the ensemble-averaged confinement potential, we neglect the fact that the transverse displacement of any given tagged rod may not be in the direction of the stress plane; that is, eq 17 conceptually represents the effect of constructing the confinement potential and averaging it over (an isotropic distribution of) all rod orientations. Breaking the assumption of isotropy and treating orientational ordering effects will be presented in the following section.

The relevant cross-sectional area, A, for converting macroscopic stress to microscopic force is taken to be a circle of diameter L. For spheres the relevant area seems obvious, i.e., proportional to the square of the particle diameter.[37] For needles the choice is less obvious, but since L is the only intrapolymer length scale $A \sim L^2$ seems a natural and inevitable choice. The only plausible alternative would be to employ an area determined by the localization length (tube diameter). This is an emergent length scale that in some way quantifies how the surrounding interpenetrating polymers transmit stress (and hence applied force) to the tagged rod. However, for this needle system we find that such a choice leads to seemingly unphysical or counterintuitive predictions, e.g., the ability of the fluid to support arbitrarily large strains at high density (cf. eqs 21 and 22).

A general consequence of our theory, also true for glasses and gels within the NLE framework,[37,38] is the existence of an "absolute yield" stress at which the transverse entropic barrier first vanishes and hence tube localization is destroyed, $\sigma_y \equiv f_{max}/A$. One can think of it as the onset of an imbalance between the larger applied force experienced by a tagged macromolecule and the intrinsic entanglement force that keeps it in a tube. Beyond this critical stress, lateral motion occurs spontaneously in a barrier-free manner.

We note that our subsequent numerical results are quantitatively sensitive to the choice of A, but qualitatively depend only on adopting $A \propto L^2$. We also point out that stress directly effects only the transverse motion. However, in section IV we couple stress to rotational relaxation, which is controlled by longitudinal diffusion insofar as it triggers rotation and transverse displacement via small steps on the scale of the tube diameter each time a local tube is exited via reptation.[26] So far, deformation is assumed not to modify the (isotropic) rod orientation distribution; this restriction is relaxed in section IIE.

In general, the stress dependence of key features of the tube confinement potential must be determined numerically. A critical general finding is that any nonzero value of σ destroys the infinitely deep nature of the lateral confining field, resulting in a stress-induced finite entropic barrier. This is a direct consequence of the fragile logarithmic localization predicted for large displacements in the quiescent theory. The two extreme limits for the entropic barrier can be analytically analyzed. For relatively low values of stress the barrier is given by

$$F_B \approx 2(1 - \rho/\rho_c) \log \tilde{\sigma} \quad (18)$$

where $\tilde{\sigma} \equiv \sigma L^3/k_BT$. In the opposite extreme where the stress is close to its absolute yield value (defined microscopically here as when the localization well and entropic barrier first vanish), the dynamic confinement potential exhibits a "fold catastrophe" form with

$$F_B \propto (1 - \sigma/\sigma_y)^{3/2} \quad (19)$$

This result can be derived in the limit of large density using eqs 15 and 16 and the small-displacement approximation for F_{dyn} obtained from eqs 9−13. However, we find that the practical relevance of these two limiting results is small, for different physical reasons, as will be discussed in section IV.

Figure 2 shows that the transient localization length (confinement-potential minimum) grows monotonically with stress, corresponding to deformation-induced tube dilation. The ratio of the tube radius just before absolute yield to its unperturbed value monotonically grows with degree of entanglement as

$$r_{l,yield}/r_l \sim \sqrt{\rho L^3}, \quad \text{for } \rho \gg \rho_c \quad (20)$$

The explicit expression for the absolute yield stress at very high densities follows from eq 15 (keeping only the dominant term) as

$$\sigma_y = \frac{4f_{max}}{\pi L^2} \simeq \frac{\rho k_BT}{\sqrt{2}} = \frac{5}{3\sqrt{2}} G_e \quad (21)$$

where $G_e = 3\rho k_B T/5$ is the needle-fluid shear modulus.[1] Adopting an elastic solid perspective of the entanglement network, one estimates a corresponding absolute yield strain as

$$\gamma_y = \frac{\sigma_y}{G_e} \simeq \frac{5}{3\sqrt{2}} \approx 1.18, \quad \rho \gg \rho_c \tag{22}$$

Although the precise numerical results are sensitive to our choice of cross-sectional area, a yield strain of order unity seems to be at least qualitatively consistent with recent experiments on entangled microtubulin (rigid rod) networks.[39] Intriguingly, yield strains of order unity have also been reported in entangled flexible chain liquids.[20,21,40]

E. Effect of Rod Orientation on the Dynamic Confinement Potential. Since we consider zero-excluded-volume rods, spontaneous nematic ordering cannot occur. However, the dynamical consequences of externally induced rod alignment can still be treated as long as the distribution of rod centers of mass remains random, since in that case all the technical approximations employed for the isotropic fluid are still valid.[22] Specifically, the effect of rod alignment on entanglement dynamics for both the Szamel and NLE theories can be captured by modifying the pair correlation function in eq 5 with an Onsager-like distribution[1] for the relative orientation of two rods: $f(\mu,\alpha) = \alpha \cosh(\mu\alpha)/4\pi \sinh \alpha$, where α parametrizes the degree of orientation relative to some axis and $\mu = \vec{u}_1 \cdot \vec{u}_2$. Expressing our results in terms of the nematic order parameter, $S = \langle (3 \cos^2 \theta - 1)/2 \rangle$, we find[22]

$$D_\perp(S)/D_\perp(0) \approx (1 - S)^{-1} \tag{23}$$

$$r_l(S)/r_l(0) \approx (1 - S)^{-1/2} \tag{24}$$

Orientation reduces inter-rod collisions, thereby enhancing lateral and rotational diffusion. A reduction of collisions also results in the tube diameter increasing with orientation (see Figure 2). The predicted rod-alignment effects are qualitatively similar to the Doi–Edwards calculation for rod densities beyond the purely topological regime, where non-zero-excluded-volume physics enters.[1] We also find that the predicted tube-model scaling of $D_\perp \propto (r_l/L)^2$ continues to hold in the presence of rod orientation. Moreover, all features of the tube confinement potential, including the maximum entanglement force, soften with orientation and stress (Figure 2).

The above results suggest, and we have numerically verified, that to a very good approximation the effect of orientational order can be thought of as modifying the effective fluid density as $\rho \to \rho(1 - S)^{1/2}$, and hence

$$F_{dyn}(r_\perp, \rho, \sigma, S) = F_{dyn}(r_\perp, \rho\sqrt{1 - S}, \sigma = 0) - \pi L^2 \sigma r_\perp/4 \tag{25}$$

This expression succinctly captures how the consequences of macroscopic stress and orientation are microscopically included at the tagged-rod level. The approach is self-consistent in the sense that stress modifies the tube confinement potential and hence polymer dynamics, but polymer displacement weakens the confining force and also determines stress relaxation. The effects of stress and orientation on r_l follow from this dynamic tube potential. For example, one can derive the high-density result

$$\left(\frac{r_l(\rho, 0, 0)}{r_l(\rho, S, \sigma)}\right)^2 \approx (\sqrt{1 - S} - \tilde{\sigma}/3(\rho/\rho_c))^2 \tag{26}$$

an expression valid as long as the localization length is finite (i.e., for stresses not too high). This result follows by expanding eq 25 in powers of inverse density, and combining eqs 9–12 to write the quiescent dynamic confining potential in limit when the localization length is small, $r_l \ll L$. Then, employing the full stress- and orientation-dependent F_{dyn}, differentiating, and solving for the minimum yields eq 26. At the highest density considered in this paper ($\rho/\rho_c = 1000$), we find eq 26 is reasonably accurate all the way up to the absolute yield stress. However, for only modestly entangled systems (e.g., $\rho/\rho_c = 10$), this expression grossly underestimates tube dilation. Combining eqs 15 and 26, the reduction of the maximum entanglement force by rod alignment in the heavily entangled regime is

$$f_{max} \simeq \frac{2k_B T}{r_l(\rho, 0, 0)}\sqrt{1 - S} \tag{27}$$

This implies the absolute yield stress (and strain) decrease with increasing rod alignment.

Figure 2 shows sample dynamic tube confinement potentials computed numerically at fixed density and various levels of applied stress and orientational order. Both can massively weaken the entropic barrier to transverse motion. Note that all the effects of stress and orientation on the tube potential, and the dynamical consequences discussed above and in subsequent sections, are absent by assumption in the Doi–Edwards theory of purely topologically entangled rods.[1]

III. STEP STRAIN DEFORMATION: INITIAL STATE

Besides their relevance to liquid crystals, rod orientation effects are critical for entangled polymers subjected to an external deformation. An applied stress or strain results in both an effective force on the polymer CM and an external torque that orients rods. For a step strain, the initial induced stress and orientation are treated via the standard assumption of affine deformation: an instantaneous shear strain of dimensionless amplitude γ results in a stress[1]

$$\sigma(t = 0^+) = \frac{3\rho k_B T \gamma}{5 + \gamma^2} = G_e \gamma h(\gamma) \tag{28}$$

where an approximate, but accurate, analytic form of the DE damping function, $h(\gamma)$, is utilized. The Lodge–Meissner relation is then used to relate the alignment angle to shear and normal stresses,[1] resulting in an initial orientational order of

$$S(t = 0^+) = \frac{2}{-1 + 3\sqrt{1 + 4\gamma^{-2}}} \tag{29}$$

Given eqs 28 and 29, the combined effects of stress and orientation on the dynamic confinement potential can be determined as a function of applied strain.

dx.doi.org/10.1021/ma300006s | Macromolecules 2012, 45, 3270–3284

Using eqs 21, 22, and 27, the absolute yield strain corresponding to tube destruction then becomes a self-consistent equation which in the heavily entangled limit is

$$\gamma_y = \frac{\sigma_y(S(\gamma_y))}{G_e} \simeq \frac{5}{3\sqrt{2}}\sqrt{1 - S(\gamma_y)} \tag{30}$$

Employing eq 29 in eq 30, one finds $\gamma_y \approx 0.96$, which is modestly smaller than the result in eq 22 due to rod-alignment-induced weakening of the maximum tube confinement force. We note this precise value is subject to small errors owing to the approximations that enter the calculation of σ_y (cf. yield strain numbers below).

Figure 3 plots calculations of the initial change ($t = 0^+$) in the normalized localization length as a function of strain. The tube

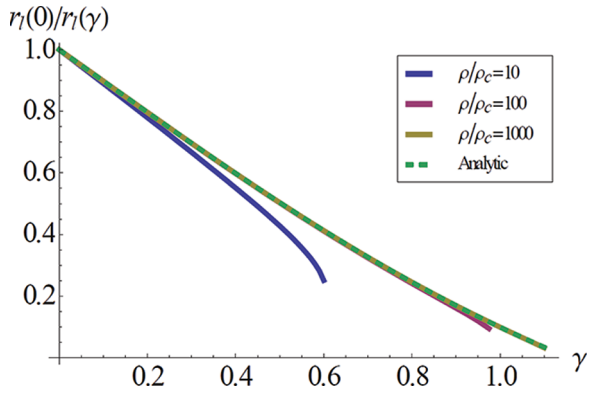


Figure 3. Inverse localization length (normalized by its quiescent value) at $t = 0^+$ after an instantaneous step strain of amplitude γ. From left to right the curves correspond to calculations at ρ/ρ_c = 10, 100, and 1000, and the dashed curve (indistinguishable on the scale of this plot with the ρ/ρ_c = 1000 calculation) is the approximate prediction based on eqs 26, 28, and 29.

diameter is monotonically widened (dilated) by deformation due to the combined effect of applied stress and rod alignment. The inverse tube diameter decreases roughly linearly with strain over an extended range, until the absolute yield strain is approached, beyond which the tube no longer exists. For a relatively modest degree of entanglement ($\rho/\rho_c = 10$), the tube is stable up $\gamma_y \sim 0.6$, and at higher degrees of entanglement ($\rho/\rho_c = 1000$) it is stable up to $\gamma_y \approx 1.12$, comparable to the estimate in section IID based on an elastic solid model. The normalized initial tube radius can be analytically estimated from eqs 26, 28, and 29. The result is shown as the uppermost curve in Figure 3 and is an increasingly good approximation as rod density increases. The analytic form predicts a density-independent yield strain of $\gamma_y = 1.16$, quite close to the estimate in section IID.

IV. PARALLEL RELAXATION MECHANISMS

Recall that the Doi–Edwards tube model assumes that for a step strain deformation of any amplitude, affinely oriented rods relax via *unperturbed quiescent* reptation. As described below, our theory agrees with this picture for very low strain amplitudes. However, as the strain amplitude grows the initial stress and rod orientation increase, which we predict triggers tube dilation and thus speeds up reptation-driven rotational relaxation. In addition, the transverse entropic barrier is decreased, effectively "turning on" a competing activated hopping process where the lateral tube confinement can be dynamically surmounted. Moreover, the entire transverse confinement potential evolves in time in a manner that depends on the degree of entanglement and strain.

A. Stress-Accelerated Reptation. Knowledge of the confinement potential allows microscopic predictions to be made for the two longest relaxation times as a function of density, stress, and orientational order, the critical information required to describe nonlinear stress relaxation after a step-strain in our theory. In the quiescent heavily entangled state the terminal rotational relaxation time is inversely proportional to the transverse diffusion constant[22,26] $D_\perp/D_{\perp,0} \propto D_{rot}/D_{rot,0}$, and in the absence of stress one has

$$\tau_{rot}(\rho) = \frac{\tau_0}{36}\frac{D_{\perp,0}}{D_\perp(\rho)} \tag{31}$$

where $\tau_0 = L^2/D_{\parallel,0}$ is proportional to the fast (dilute-solution-like for rods[1]) CM longitudinal "reptation time".

Including stress in the full dynamical calculation of the long-time transverse diffusion constant is a daunting task. For simplicity, we exploit the connection between τ_{rot}, $D_\perp$, and r_l to express the reptation-controlled rotational relaxation time in terms of the localization length, $\tau_{rot} \propto r_l^{-2}$.The effects of stress and orientation on r_l are then obtained from the confinement potential and related back to τ_{rot}. Since the tube dilates with increasing stress, the terminal rotational relaxation time is reduced as

$$\frac{\tau_{rot}(\rho, S, \sigma)}{\tau_{rot}(\rho, 0, 0)} = \left(\frac{r_l(\rho, 0, 0)}{r_l(\rho, S, \sigma)}\right)^2 \approx (\sqrt{1 - S} - \tilde{\sigma}/3(\rho/\rho_c))^2 \tag{32}$$

where the limitations of the final approximate equality are discussed in section IIE. The stress and orientation dependence of the tube potential can have dramatic consequences for the long-time dynamics because the transient localization length grows with S and σ. Specifically, since $D_{rot} \propto D_\perp \propto \tau_{rot}^{-1} \propto (r_l/L)^2$, tube dilation can significantly accelerate reptative rotational relaxation and transverse diffusion, especially for heavily entangled solutions near the absolute yield stress, σ_y.

Sample rotational relaxation times immediately after an instantaneous step-strain are plotted in Figure 4 for three

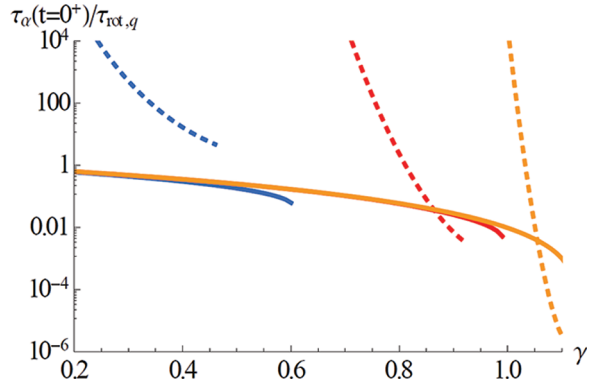


Figure 4. Log–linear plot of the initial mean transverse hopping (dashed) and terminal relaxation (solid) times normalized by the quiescent terminal relaxation time given by eq 31. From left to right the curves correspond to calculations at ρ/ρ_c = 10, 100, and 1000. The yield strains at these rod densities are γ_y = 0.6, 1.0, and 1.12, respectively.

dx.doi.org/10.1021/ma300006s | *Macromolecules* 2012, 45, 3270–3284

different degrees of entanglement. The amount of stress acceleration is heavily density-dependent, since $r_l(\rho,\sigma_y)/r_l(\rho,0) \sim (\rho L^3)^{1/2}$ at $\rho \gg \rho_c$, and hence the maximum enhancement of τ_{rot} increases linearly with ρ. As the absolute yield strain is approached, the rotational relaxation time is predicted to accelerate by over 2 orders of magnitude for the most heavily entangled system. Figure 4 also shows the quantitative increase of the absolute yield strain with degree of entanglement, which ultimately saturates as $\rho/\rho_c \to \infty$.

B. Activated Transverse Barrier Hopping. We also predict the emergence of a qualitatively new relaxation channel due to stress-reduction of the transverse entropic barrier. The characteristic rate of lateral barrier hopping can be computed from Kramers' result for the mean first-passage time:[41]

$$\frac{\tau_{\perp,hop}(\rho, S, \sigma)}{\tau_0} = \frac{2\pi}{\sqrt{K_0 K_B}} e^{\beta F_B(\rho,S,\sigma)} \quad (33)$$

where K_0 and K_B are the absolute magnitudes of the dimensionless local curvatures at the confinement potential minimum and barrier location, respectively. We find that lateral hopping times become comparable to the reptation-controlled terminal relaxation process only when the barrier is relatively small. In these cases, the relevant part of the quiescent tube potential is not the large-displacement logarithmic part, but rather the well-validated[22] quasi-linear regime. Nevertheless, analytic analysis of the low-stress regime is straightforward and yields important insight.

Recall that as a consequence of eq 14, for relatively low stresses the barrier is given by eq 18. Hence, for $\sigma \ll \sigma_y$ the hopping time decreases as a power law with an exponent determined by the degree of entanglement:

$$\tau_{\perp,hop} \propto (\sigma/\sigma_y)^{-\theta} \quad (34)$$

where $\theta = 2(\rho/\rho_c - 1)$. Thus, while the lateral hopping time is astronomically long for low stress and high density, it decreases with stress at an enormously faster rate than the acceleration of τ_{rot}. Sample calculations of the hopping time as a function of strain amplitude are shown in Figure 4.

Physically, as the strain approaches it absolute yield value, entanglements and tube localization are destroyed, $F_B \to 0$, and the transverse hopping time must smoothly recover its "bare" value,[42] $\tau_{\perp,hop} \to \tau_0$. In practice, as is well-known, eq 33 is a poor approximation as the barrier height approaches the thermal energy, and thus in Figure 4 curves are shown only for $F_B \geq 1.5\ k_BT$. In the calculations below, when an activated hopping time is required under conditions where the barrier is lower than this threshold, as a practical numerical approach we fix S and use a simple linear interpolation between the hopping time at the stress value that gives a barrier of 2 k_BT and the bare time τ_0 relevant at $\sigma = \sigma_y(S)$.

C. Stress-Modified Relaxation: Reptation versus Transverse Barrier Hopping. Figure 4 compares the mean initial transverse barrier hopping (a tube-breaking event) and terminal reptative rotational relaxation times after a step strain of variable amplitude, each normalized by the quiescent relaxation time, $\tau_{rot}(\rho)$, given by eq 31. The massive reduction of $\tau_{\perp,hop}$ relative to the comparatively weak tube-dilation effect on the rotational relaxation time is evident. Even for $\rho/\rho_c \sim$ 100−1000, very high degrees of entanglement relevant to synthetic rods or stiff biopolymers (e.g., long PBLG synthetic rods and F-actin[6−9]), entropic barriers can become sufficiently low that transverse hopping becomes faster than (tube-dilated) reptation at strains of order unity, which is below the classic "over-orientation" stress maximum[1] at $\gamma = \sqrt{5}$.

Because of the strain-dependent competition between tube-dilated reptation and activated transverse hopping, three distinct dynamical regimes are predicted. (i) For γ/γ_y sufficiently less than unity, the hopping time is astronomically long relative to τ_{rot}, the transverse confinement is dynamically stable, and hence the quiescent reptation-tube picture remains essentially unchanged in accord with the Doi−Edwards theory. (ii) In the opposite limit of $\gamma > \gamma_y$, a microscopic-instability-like, or "absolute yielding", phenomenon is predicted, defined by the complete destruction of the transverse barrier and hence the tube constraints. (iii) A third dynamical regime emerges at high-enough densities over an intermediate range of strains, in which the entropic barrier still exists but it is small enough that $\tau_{\perp,hop} < \tau_{rot}$. This regime occurs when, on average, the strain causes the entanglement network to collapse via transverse barrier hopping before reptative relaxation is completed. In the context of structural glasses and gels, this behavior is often called "dynamic yielding", corresponding to achieving irreversible motion and flow via thermally induced activation on the experimental time scale.[37,38] These latter two regimes have no analogue in classic tube theories.

V. GENERALIZED MAXWELL MODEL FOR INSTANTANEOUS STEP STRAIN

A. Coupled Evolution Equations. We now consider the coupled nonlinear stress and orientational relaxation following an instantaneous shear strain. A minimalist generalized Maxwell model is adopted in which relaxation can proceed in parallel via reptation-controlled terminal rotational motion and transverse barrier hopping. Thus, at any moment we take the effective relaxation rate to be

$$\tau_{eff}^{-1}(t) = \tau_{rot}^{-1}(\rho, S(t), \sigma(t)) + \tau_{hop}^{-1}(\rho, S(t), \sigma(t)) \quad (35)$$

The coupling between the relaxation time and the system stress and orientational order renders the nonlocal-in-time integral representation of evolution equations unwieldy. Hence, we employ a time-local differential formulation. The evolution equations are formally first order in time, but highly nonlinear in stress and orientation due to the coupling via τ_{eff}:

$$\frac{d\sigma}{dt} = \frac{-\sigma(t)}{\tau_{eff}(t)} \quad (36)$$

$$\frac{dS}{dt} = \frac{-S(t)}{\tau_{eff}(t)} \quad (37)$$

Equations 35−37 assume a $1/e$ increment of stress and orientational relaxation associated with each type of dynamical event. While one can image countless variations on this assumption, as a first approximation it should correctly capture the qualitative implications of having two competing terminal relaxation processes. Equations 36 and 37 imply the logarithmic derivatives of the time-dependent stress and orientation are equal, and hence $d(\log(\sigma/S))/dt = 0$. Thus, stress and S are proportional at all times, a type of stress-optical relation.[1]

The key input to the evolution equations is the time evolution of the tube diameter, rotational reptation time, and transverse barrier-hopping time, which are all nonlinear functions of strain (their detailed properties are discussed in section IV). Extensive calculations of all aspects of the dynamic tube confinement potential and stress and orientational

dx.doi.org/10.1021/ma300006s | Macromolecules 2012, 45, 3270−3284

relaxation after step-strains have been performed over a wide range of strain amplitudes and degrees of entanglement. Results will be presented for ρ/ρ_c = 10, 100, and 1000. The essential new physics emerges from the self-consistent, microscopically computed connection between time-dependent stress, orientational order parameter, and characteristic single-rod relaxation times. The latter are directly connected to the dynamic confinement potential, most notably the tube diameter and entropic barrier height.

B. Nonequilibrium Relaxation of the Dynamic Confinement Potential. Figure 5 shows the time dependence

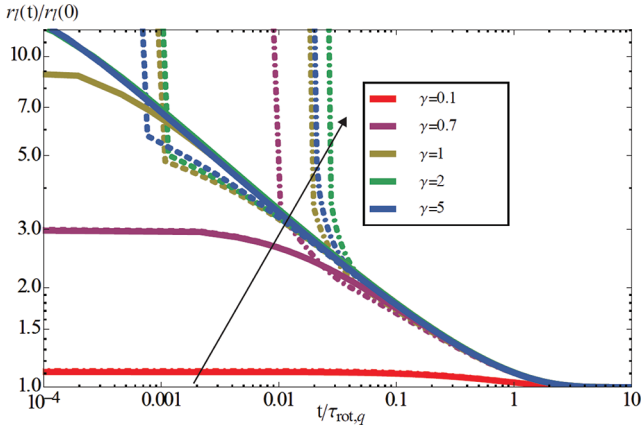


Figure 5. Time evolution of the normalized localization length or tube diameter for various initial strain amplitudes. Solid curves correspond to ρ/ρ_c = 1000, dashed curves to ρ/ρ_c = 100, and dash-dotted curves to ρ/ρ_c = 10. Read in the direction of the arrow, strain amplitudes are γ = 0.1, 0.7, 1, 5, and 2.

of the tube diameter after various step strains, both above and below the absolute yield strain. For very low strain amplitudes the tube diameter remains essentially unperturbed. At intermediate strain amplitudes below absolute yield there is a period of nearly constant tube dilation at short times, followed by a decrease to its quiescent value at long times. For large deformations the tube is completely destroyed initially (i.e., there is no lateral confinement force), and this state persists for some finite period of time. The tube then eventually re-emerges and slowly grows back in ("heals") with increasing time, with the localization length monotonically approaching the quiescent value from above. Similarly, since the terminal rotational time is linked to the tube diameter, $\tau_{rot} \sim r_l^{-2}$, it is initially much smaller than its quiescent value, which it approaches from below at long times. Since the rotational relaxation time and tube diameter are directly related, the former is plotted only for the highest degree of entanglement in Figure 6a; for the other cases, τ_{rot} can be inferred from the behavior of the tube diameter. In contrast, the mean transverse barrier hopping time is initially very fast for large enough strains. Indeed, Figure 6b shows that if the barrier initially vanishes after a large step strain, the hopping time approaches the bare time but then grows to astronomical values rather quickly as stress and rod orientation decay and entanglements are restored over short time scales. Note that Figure 6b contains only two representative curves, both above the yield strain; the mean hopping time for lower strains is far off the scale of this plot (cf. Figure 4).

Intriguingly, when the tube is initially either strongly dilated or destroyed, the temporal manner in which the tube diameter

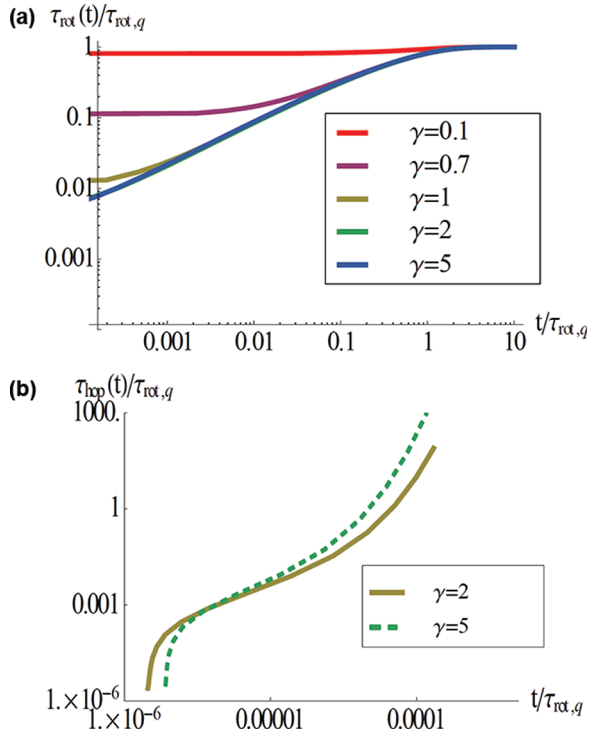


Figure 6. (A) Time evolution of the terminal rotational relaxation time (nondimensionalized by the quiescent terminal relaxation time) with increasing strain (top to bottom) at ρ/ρ_c = 1000. (B) Time evolution of normalized transverse hopping time for γ = 2 (solid curve) and γ = 5 (dashed curve) at ρ/ρ_c = 1000.

approaches its equilibrium value has an apparent power-law behavior, roughly independent of strain amplitude and degree of entanglement, over an intermediate time window (Figure 5). The scaling is roughly $r_l \sim t^{-0.3}$, with higher densities supporting this behavior over an ever-larger time regime. This behavior implies a regime of power-law growth of the terminal reptative rotational relaxation time ($\tau_{rot} \sim t^{0.6}$) as the entanglement network reforms, as seen in Figure 6a.

In those cases where the initial deformation is sufficient to destroy the entanglement network ("microscopic yielding"), the transverse hopping relaxation channel, which now proceeds on the short time scale of the bare relaxation time (Figure 6b), rapidly relaxes both stress and orientation and allows the entanglement network to re-form. The time t^* at which a tube first re-emerges when $\gamma > \gamma_y$ is plotted in Figure 7. This time is a nonmonotonic function of strain that reflects the nonmonotonicity of the initial stress, $\sigma(t = 0^+)$. However, in all cases tube reformation occurs at a short time of order τ_0. The radius of the newly reformed tube at t^* can be implicitly read off from Figure 5. The main trends are that $r_l(t^*)$ becomes much larger with increasing rod density since (as discussed in section IID) at higher degrees of entanglement the tube can grow to a larger radius before being destroyed, i.e., $r_l(\rho,\sigma_y)/r_l(\rho,0) \sim (\rho L^3)^{1/2}$. Above the absolute yield strain there is a comparatively modest variation in $r_l(t^*)$ with increasing γ.

Entanglement-constraint healing can also be characterized by the growing back in of the maximum lateral confinement force after the tube has been initially destroyed by a large step strain. Even though the relation $f_{max} \sim k_BT/r_l$ in eq 21 was derived under equilibrium conditions, we find that it continues to be

dx.doi.org/10.1021/ma300006s | Macromolecules 2012, 45, 3270−3284

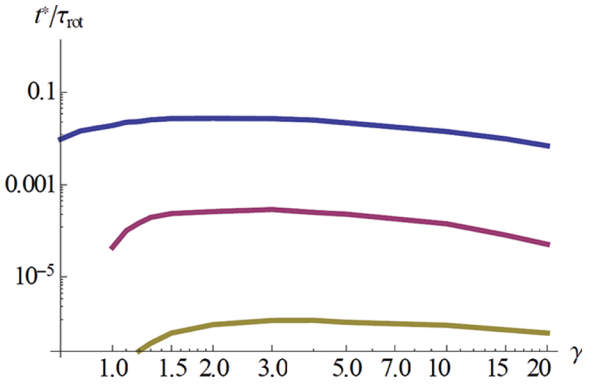


Figure 7. Normalized time at which the tube constraints first re-emerge for deformations $\gamma > \gamma_y$. From top to bottom the curves correspond ρ/ρ_c = 10, 100, and 1000.

reasonably accurate numerically at high densities under large deformation conditions:

$$f_{max}(\rho \gg \rho_c, S(t), \sigma(t)) \sim r_l(\rho, S(t), \sigma(t))^{-1} \quad (38)$$

Thus, the maximum transverse force also exhibits intermediate-time power-law healing kinetics, $f_{max} \sim t^{0.3}$, until enough time elapses for it to approach its quiescent value.

C. Nonlinear Stress and Orientation Relaxation. Figure 8 presents calculations of orientational relaxation, and Figure 9

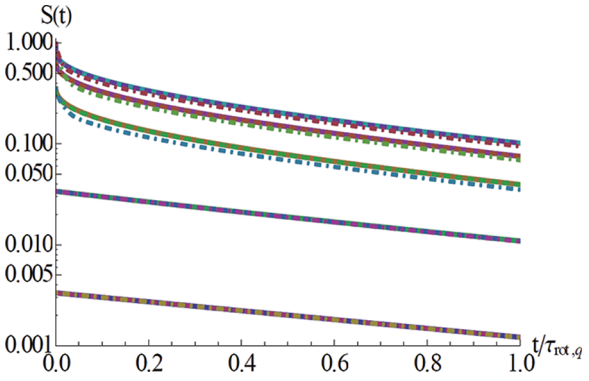


Figure 8. Log−linear plot of the decay of orientational order parameter after step strains of (top to bottom) γ = 10, 5, 1, 0.5, 0.1, and 0.01. Dash-dotted, dashed, and solid curves correspond to ρ/ρ_c = 10, 100, and 1000, respectively.

shows the dynamic nonlinear relaxation modulus, for three degrees of entanglement. Given that a stress-optical-like relation is obeyed by our theory, these two quantities are directly connected. Thus, we plot the orientational order in a log−linear fashion to highlight the return to single-exponential decay with time and the modulus in a log−log plot to highlight the ultrafast, short-time relaxation at high strains. Several trends are evident.

For low dimensionless strains ($\gamma \ll 1$), the effective relaxation time is only very weakly perturbed from its equilibrium reptation value, resulting in essentially unmodified exponential decay of both $S(t)$ and $G(t)$. Note that if the time scale is nondimensionalized by the quiescent relaxation time, there is only a very weak dependence on degree of entanglement, most readily seen in Figure 8. This corresponds to the Doi−Edwards scenario. However, we predict this behavior eventually breaks down due to modification of the tube potential by the imposed deformation.

At intermediate strains (but still $\gamma < \gamma_y$), acceleration of the terminal reptative rotational time is the first observable correction to quiescent relaxation, and at even higher strains much more dramatic effects emerge. In the latter case, a significant amount of stress and orientation relax on the bare time scale, τ_0, since the large deformation temporarily removes the transverse barrier and thereby allows very rapid relaxation until stress and orientation decrease sufficiently for the tube to re-form. The separation in time scales between the quiescent terminal and bare times is greatest for larger degrees of entanglement, thereby allowing a clear short-time plateau in the relaxation modulus to be observed (Figure 9a). This feature emerges due to an ultrafast relaxation of stress, that then necessitates much slower rotational (or transverse diffusive) motions for further relaxation to continue as the entanglement constraints are re-established (cf. the very rapid growth of τ_{hop} in Figure 6b). For weaker degrees of entanglement (Figure 9b,c) stress plateaus are less well developed. Note that the apparent nonmonotonicity of the height of the stress plateau as a function of strain for the two highest strain values in Figure 9 is the result of our choice to normalize the curves by the strain-dependent $G(t=0)$ instead of the entanglement modulus G_e. Thus, in the results for the damping function discussed below no such nonmonotonicity is present. In any event, in all cases of nonperturbative strain amplitude, Figure 9 demonstrates that the relaxation of stress and orientation is strongly modified from the quiescent reptation behavior, in contrast to the Doi−Edwards model. Moreover, stress and orientation relaxation are highly nonexponential in time for two physical reasons: the tube constraints are time-dependent, and there are two competing relaxation mechanisms.

D. Damping Function. Regardless of the strain amplitude or rod density, at long times both stress and orientation relax to low enough values that the tube reforms and a purely exponential decay of stress and S occurs, characterized by the quiescent terminal relaxation time (inset of Figure 10). This allows an apparent damping function to be defined via superposition at long times as

$$h(\gamma) = G(t \to \infty, \gamma)/G(t \to \infty, \gamma_0) \quad (39)$$

where we have used $\gamma_0 = 10^{-3}$, and "$t \to \infty$" indicates a long enough time that superposition can be achieved. As seen in Figure 10, since there are additional fast relaxation processes, qualitative departures from the classic DE damping function appear.[1] In particular, our damping function is not well-described as a Lorentzian and decays with strain amplitude much faster due to stress- and orientation-induced dynamical softening of the tube potential. As a secondary effect, there is a very weak dependence of the damping function on density.

To more thoroughly understand the physical origin of our predicted deviations from the Doi−Edwards theory, the calculations were repeated with modified input but still within an effective tube model framework. Specifically, in the original DE theory of entangled rods a tube dilation effect can arise from orientational considerations in the more concentrated nematic-liquid-crystal regime.[1] This effect does not enter in the pure topologically entangled "semidilute" regime,[15] but we can adopt this orientational-tube-dilation effect to take into account transient, deformation-induced orientational order as discussed above. We have performed numerical calculations of a modified classic tube model analogous to the calculations in section V.A,

dx.doi.org/10.1021/ma300006s | Macromolecules 2012, 45, 3270−3284

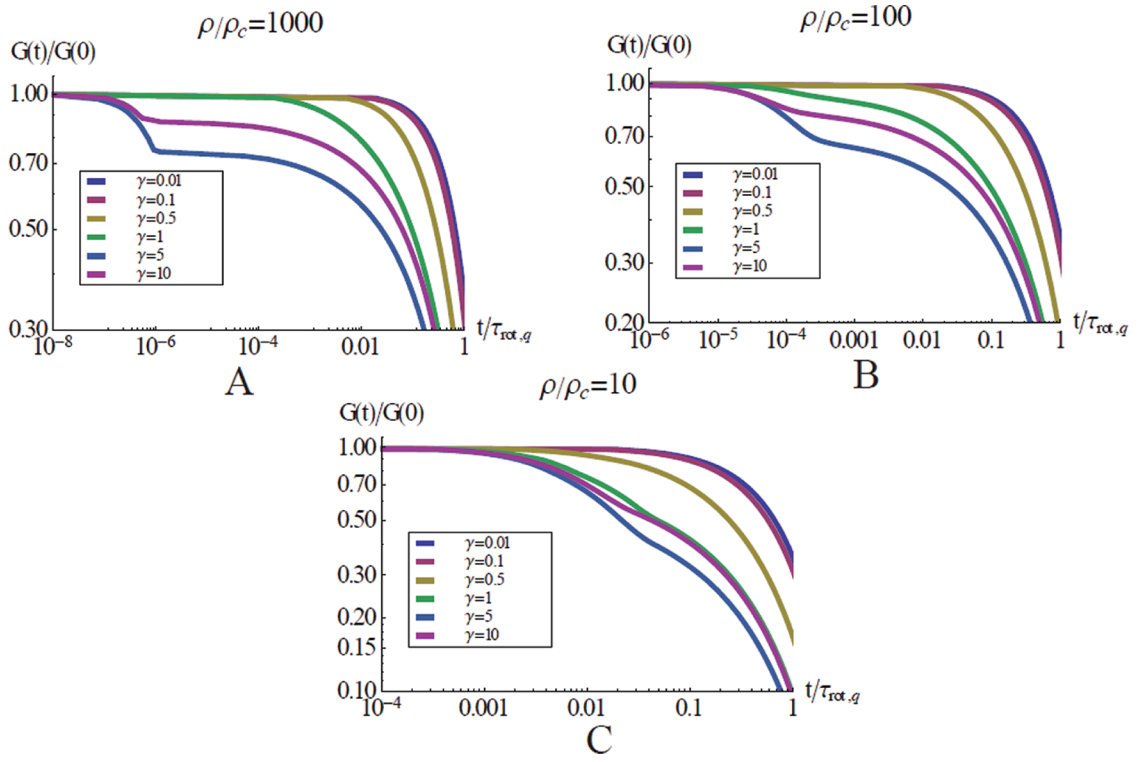


Figure 9. (A) Log–log plot of normalized stress relaxation modulus as a function of time at six strain amplitudes for (A) ρ/ρ_c = 1000, (B) ρ/ρ_c = 100, and (C) ρ/ρ_c = 10.

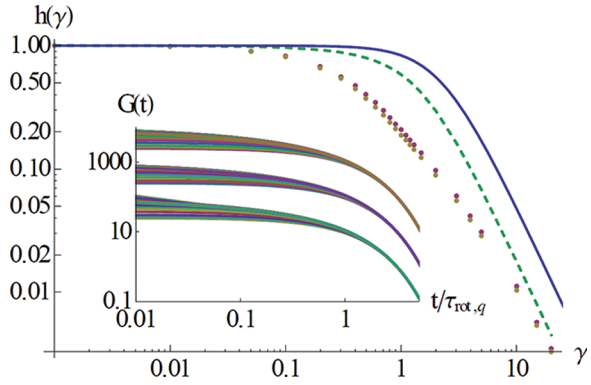


Figure 10. Log–log plot of the damping function (eq 39) at ρ/ρ_c = 10, 100, and 1000 (points). The solid curve is the original DE $h = 5/(5 + \gamma^2)$, and the dashed curve corresponds to the modified classic tube model that includes an orientation-dependent tube diameter (see text). Inset: log–log superposition plot of the nonlinear relaxation modulus from which the damping function is determined.

where (a) transverse activated barrier hopping was turned off by hand ($\tau_{hop} \rightarrow \infty$), but (b) the terminal rotational time was modified by orientation-dependent tube dilation. We emphasize that in the context of our NLE theory, point (b) is equivalent to assuming that orientation modifies the tube confinement potential but stress does not. The damping function that results is shown in Figure 10 as the dashed curve. While it differs from the classic DE prediction, functionally it is very similar in the sense that it is again well-described by a Lorentzian, $h(\gamma) \approx 2/(2 + \gamma^2)$. The corresponding time evolution of stress is also more like the original DE model than our full theory since the nonlinear relaxation modulus never develops a plateau at short times. This is a consequence of τ_{rot} being accelerated via orientation but not including tube-breaking, transverse hopping events.

Given the above analysis, we can unambiguously conclude that the most dramatic new effects predicted by our theory of nonlinear stress relaxation are the direct result of the explicit and self-consistent coupling of the tube confinement field to stress, which results in both strongly accelerated reptative rotational relaxation and barrier-free lateral motion for deformations beyond the absolute yield strain. It is interesting to note that this explicit coupling of stress and confinement potential also underlies distinctive aspects of nonlinear relaxation and mechanical response in polymer and colloidal glasses within the NLE theory framework.[37,38]

VI. SUMMARY AND CONCLUSION

We have presented a unified exposition of our self-consistent microscopic theory for the transverse tube confinement potential and dynamics of topologically entangled needle solutions under both equilibrium quiescent and nonequilibrium stressed conditions. In essence, we have attempted to statistically describe at the level of (impulsive) forces what an entanglement is and where a confining tube comes from. The key physics of polymer connectivity and uncrossability is exactly taken into account at the 2-rod level, with three- and higher-body dynamical effects renormalizing the 2-rod entanglement problem in a self-consistent manner via single polymer diffusive motion.[25,26] An explicit accounting of dynamical uncrossability at the 2-rod level is the minimum level of description required to discuss entanglement and is already beyond the single-chain reptation model where tube localization is postulated, not deduced.

Under quiescent conditions, the theory predicts with quantitative accuracy (i) a very sensible value of the number

dx.doi.org/10.1021/ma300006s | Macromolecules 2012, 45, 3270–3284

of interpenetrating rods required for the onset of entanglements and tube localization, (ii) perpendicular and rotational diffusion over the full range of rod densities[22] including agreement with the Doi–Edwards asymptotic scaling laws[1] and several computer simulations,[32,33] and (iii) key anharmonic features of the confinement field[22] observed in recent experiments on heavily entangled F-actin solutions[6] and more qualitatively in both DNA experiments[10] and primitive-path simulations of chain melts.[11] The anharmonicity of the confinement field is an emergent, not assumed, feature of our NLE approach which predicts that lateral tube constraints continuously weaken as a tagged polymer and its neighbors move.

The anharmonic nature of the transverse dynamical confinement potential has the very large qualitative implication that there is a maximum restoring force keeping a tagged rod in its tube due to topological interactions with its surroundings; i.e., physical entanglements cannot always be literally treated as chemical cross-links in rubber networks. In this sense, the theory might be viewed as having some features in common with venerable "transient network" models.[43−45] The consequences of a finite entanglement force are especially dramatic under applied deformation, leading to phenomena such as stress- and orientation-driven tube dilation, transverse entropic barrier reduction, and ultimately tube destruction beyond a critical level of stress or strain when the external force on a tagged rod exceeds the intrinsic entanglement force localizing the polymer in a tube. This last feature may be akin to empirical attempts to describe stress-dependent cross-links in transient network models,[45,46] and recent experimentally motivated physical ideas about force imbalance in entangled chain liquids.[20,40]

By building on the above advances, we formulated a minimalist, generalized Maxwell model theory for stress and orientational relaxation after an instantaneous (and homogeneous) step-strain deformation. The richness of this theory arises from taking into account nonlinear couplings to a time- and deformation-dependent tube diameter, a maximum confinement force, and an entropic barrier. As a consequence, time- and deformation-dependent reptative rotational relaxation and transverse activated barrier hopping processes emerge as competing relaxation mechanisms. We predict both the acceleration of the terminal rotational time due to stress- and orientation-dependent tube dilation and the emergence at sufficiently high deformations of a transverse barrier-hopping (tube breaking) relaxation process as a consequence of the highly anharmonic form of the dynamic confinement potential. These features result in an extended regime of strongly nonexponential stress relaxation after a step strain of sufficient magnitude. All these aspects are not present in classic reptation-tube models of topologically entangled rods.

An important finding is that beyond a large enough step strain the tube is destroyed in a manner that can be thought of as an elastic instability or microscopic yielding event.[20] This results in a regime of ultrafast relaxation of stress and orientation on a time scale much shorter than the (reptation-controlled) terminal relaxation time. After this initially very fast relaxation we predict that, as a consequence of the reduced levels of stress and orientation, the entanglement constraints re-emerge, resulting in the slower, reptative relaxation process again becoming dominant at long times. The approach to this state of quiescent reptation-tube dynamics is characterized by intriguing apparent power-law evolution, or healing kinetics, of the tube diameter, maximum entanglement force, and rotational relaxation time toward their quiescent values. An important consequence of including the stress-assisted transverse hopping process is the prediction of a qualitatively different damping function compared to the Doi–Edwards model.

For entangled chain solutions and melts, there has been a long ongoing debate about whether the tube diameter should couple to deformation.[3] Some researchers argue that in a step-strain deformation the competition between tube dilation and contraction should cancel and leave the tube diameter unchanged,[47] the original simplifying assumption of Doi and Edwards.[1] Clearly, for rods we do not have the processes thought to govern one side of that competition—chain retraction dilating the tube. Other workers have proposed either tube dilation or contraction, which might depend on deformation type for flexible chains (e.g., shear versus extension), based on qualitatively different ansatzes.[3,17] Our microscopic theory for rigid rods always predicts tube dilation under applied shear stress or strain as a direct consequence of the anharmonic nature of the quiescent dynamic tube potential. This result, and others we have obtained, suggests it is essential to self-consistently couple stress to the microscopic construction of the tube field, in analogy with the situation for colloid and polymer glasses.[37,38,48]

Unfortunately, there is a dearth of experimental data on the nonlinear rheological response (especially for step strains) of high-aspect-ratio rod solutions in the isotropic state which could serve to test our theory. This presumably is in part due to the difficulty of studying such systems while avoiding the liquid crystalline regime. Nevertheless, this problem seems experimentally addressable based on synthetic or biological (e.g., microtubules) rigid rod polymers that interact via short-range repulsive forces, and we encourage new measurements to be undertaken.

There is also very little computer simulation data for Brownian solutions of entangled rigid needles that can be used to incisively test our ideas, especially under nonlinear step strain conditions. For the quiescent topologically entangled needle system, there is a tentative study long ago by Doi[15] and a more recent work by Ramanathan and Morse.[9] This is surely a tractable problem for simulation, including the application of primitive path analysis under both quiescent[11] and highly deformed[19] conditions. We suggest that new simulations of the topologically entangled needle system be performed to critically test the key features of our quiescent tube confinement potential and its response to prescribed applied stress and imposed rod orientation. Our many predicted consequences of the latter on entanglement dynamics are also testable, such as how the terminal rotational relaxation time and tube diameter respond to stress and rod orientation and the detailed time dependence of stress relaxation and various dynamical properties after a nonlinear step strain. Perhaps the most penetrating test would be to determine whether the tube can be completely destroyed beyond a critical strain (microscopic yielding), and, if so, the nature of its re-formation kinetics.

We note that some of our results seem intriguingly similar to the physical interpretations given by Wang and co-workers of recent rheology/microscopy studies of step-strain, startup shear, and creep nonlinear response of heavily entangled chain polymer liquids.[20,21,40] Specifically, the concept of a tube or entanglement network that has a finite strength related to the tube diameter (including the functional dependence of f_{max}

on d_T) and the possibility of stress- or strain-induced microscopic yielding.[20] Of course, the nonlinear rheology of such systems is presumably influenced by processes not present in rigid rods, most notably chain stretch and retraction. However, it is interesting to recall that Doi and Edwards, in their seminal work, emphasized that most of the nonlinear rheological response predicted by their tube model is essentially the same for rods and chains based on the assumed rapid equilibration of chain stretch via fast Rouse dynamics.[1,15] Efforts are underway to generalize our theory to apply to entangled flexible chains, although this is a theoretically formidable task. We are also extending the entangled rod solution theory to study other deformations, and our investigations concerning continuous startup shear, including stress overshoots, shear thinning, and the steady state flow curve, will be reported soon.

AUTHOR INFORMATION

Corresponding Author

*E-mail: kschweiz@illinois.edu.

Notes

The authors declare no competing financial interest.

ACKNOWLEDGMENTS

This work was supported by the Nanoscale Science and Engineering Initiative of the National Science Foundation under NSF Award DMR-0642573. We thank Venkat Ganesan, Hiroshi Watanabe, and especially Shi-Qing Wang for stimulating and informative discussions and/or correspondence.

REFERENCES

(1) Doi, M.; Edwards, S. F. *The Theory of Polymer Dynamics*; Oxford University Press: Oxford, UK, 1986.
(2) de Gennes, P. G. *J. Chem. Phys.* **1971**, *55*, 572.
(3) McLeish, T. C. B. *Adv. Phys.* **2002**, *51*, 13709.
(4) Larson, R. G. *J. Polym. Sci., Part B: Polym. Phys.* **2007**, *45*, 3240.
(5) Likhtman, A. E. *J. Non-Newtonian Fluid Mech.* **2009**, *157*, 158.
(6) Wang, B.; Guan, J.; Anthony, S. M.; Bae, S. C.; Schweizer, K. S.; Granick, S. *Phys. Rev. Lett.* **2010**, *104*, 118301.
(7) Glaser, J.; Chakraborty, D.; Kroy, K.; Lauter, I.; Kirchgeßner, N.; Hoffmann, B.; Merkel, R.; Giesen, M. *Phys. Rev. Lett.* **2010**, *105*, 037801.
(8) Ramanathan, S.; Morse, D. C. *Phys. Rev. E* **2007**, *76*, 010501.
(9) Ramanathan, S. Ph.D. Thesis, University of Minnesota, 2006.
(10) Robertson, R. M.; Smith, D. E. *Phys. Rev. Lett.* **2007**, *99*, 126001.
(11) Zhou, Q.; Larson, R. G. *Macromolecules* **2006**, *39*, 6737.
(12) Tzoumanekas, C.; Theodorou, D. N. *Macromolecules* **2006**, *39*, 4592.
(13) Foteinopoulou, K.; Karayiannis, N. C.; Mavrantzas, V. G.; Kröger, M. *Macromolecules* **2006**, *39*, 4207. Foteinopoulou, K.; Karayiannis, N. C.; Laso, M.; Kröger, M. *J. Phys. Chem. B* **2009**, *113*, 442.
(14) Bisbee, W.; Qin, J.; Milner, S. T. *Macromolecules* **2011**, *44*, 8972.
(15) Kuzuu, N.; Doi, M. *Polym. J.* **1980**, *12*, 883.
(16) Deutsch, J. M.; Madden, T. L. *J. Chem. Phys.* **1989**, *91*, 3252.
(17) Wagner, M. H. *J. Rheol.* **1994**, *38*, 655.
(18) Kushwaha, A.; Shaqfeh, E. S. G. *J. Rheol.* **2011**, *55*, 463.
(19) Baig, C.; Mavrantzas, V. G.; Kröger, M. *Macromolecules* **2010**, *43*, 6886.
(20) Wang, S. Q.; Ravindranath, S.; Wang, Y.; Boukany, P. *J. Chem. Phys.* **2007**, *127*, 064903 and references cited therein.
(21) Boukany, P. E.; Wang, S. Q.; Wang, X. *Macromolecules* **2009**, *42*, 6261.
(22) Sussman, D. M.; Schweizer, K. S. *Phys. Rev. Lett.* **2011**, *107*, 078102.
(23) Sussman, D. M.; Schweizer, K. S. *J. Chem. Phys.* **2011**, *135*, 131104.
(24) Sussman, D. M.; Schweizer, K. S. *Phys. Rev. E* **2011**, *83*, 061501.
(25) Szamel, G. *Phys. Rev. Lett.* **1993**, *70*, 3744.
(26) Szamel, G.; Schweizer, K. S. *J. Chem. Phys.* **1994**, *100*, 3127.
(27) Miyazaki, K.; Yethiraj, A. *J. Chem. Phys.* **2002**, *117*, 10448.
(28) Cichocki, B. *Z. Phys. B: Condens. Matter* **1987**, *66*, 537.
(29) Kirkpatrick, T. R.; Wolynes, P. G. *Phys. Rev. A* **1987**, *35*, 3072.
(30) Schweizer, K. S.; Saltzman, E. J. *J. Chem. Phys.* **2003**, *119*, 1181.
(31) Hansen, J. P.; McDonald, I. R. *Theory of Simple Liquids*; Academic Press: London, 1986.
(32) Doi, M.; Yamamoto, I.; Kano, F. *J. Phys. Soc. Jpn.* **1984**, *53*, 3000.
(33) Bitsanis, I.; Davis, H. T.; Tirrell, M. *Macromolecules* **1990**, *23*, 1157.
(34) Everaers, R.; Sukumaran, S. K.; Grest, G. S.; Svaneborg, C.; Sivasubramanian, A.; Kremer, K. *Science* **2004**, *303*, 823.
(35) Schweizer, K. S. *J. Chem. Phys.* **2005**, *123*, 244501.
(36) Likhtman, A. E. *Macromolecules* **2005**, *38*, 612.
(37) Kobelev, V.; Schweizer, K. S. *Phys. Rev. E* **2005**, *71*, 021401; *J. Chem. Phys.* **2005**, *123*, 164902.
(38) Chen, K.; Schweizer, K. S. *Europhys. Lett.* **2007**, *79*, 26006. Chen, K.; Saltzman, E. J.; Schweizer, K. S. *Ann. Rev. Condens. Matter Phys.* **2010**, *1*, 277.
(39) Lin, Y.-C.; Koenderink, G. H.; MacKintosh, F. C.; Weitz, D. A. *Macromolecules* **2007**, *40*, 7714.
(40) Wang, Y.; Wang, S. Q. *J. Rheol.* **2009**, *53*, 1389.
(41) Hänggi, P.; Talkner, P.; Borkovec, M. *Rev. Mod. Phys.* **1990**, *62*, 251.
(42) Saltzman, E. J.; Schweizer, K. S. *J. Chem. Phys.* **2006**, *125*, 044509.
(43) Lodge, A. S. *Elastic Liquids*; Academic Press: London, 1964.
(44) Green, M. S.; Tobolsky, A. V. *J. Chem. Phys.* **1946**, *14*, 80.
(45) Lodge, A. S. *Ind. Eng. Chem. Res.* **1995**, *34*, 3355.
(46) Lodge, A. S.; Meissner, J. *Rheol. Acta* **1973**, *12*, 41.
(47) Marrucci, G. *J. Non-Newtownian Fluid Mech.* **1996**, *62*, 279.
(48) Chen, K.; Schweizer, K. S. *Phys. Rev. E* **2010**, *82*, 041804; *Macromolecules* **2011**, *44*, 3988.

Macromolecules

Note

pubs.acs.org/Macromolecules

Bisnitrone: New Starting Material for Heterocyclic Poly(1,2,4-oxadiazolidin-5-one) via Polycycloaddition with Diisocyanate and Urethane Prepolymer

Marcus Dickmeis, Hakan Cinar, and Helmut Ritter*

Institut für Organische Chemie und Makromolekulare Chemie II, Heinrich-Heine-Universität Düsseldorf, Universitätsstrasse 1, 40225 Düsseldorf, Germany

Supporting Information

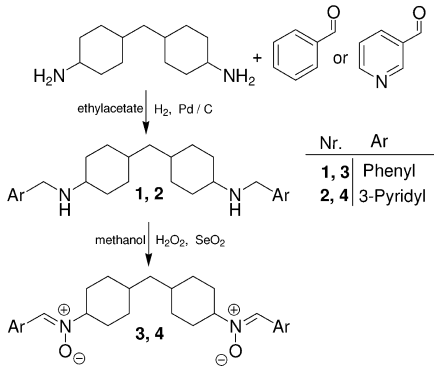
INTRODUCTION

Nitrones are typical 1,3-dipoles involving 4π-electrons which readily undergo cycloaddition with a variety of suitable unsaturated compounds.[1−3] The cycloaddition of mononitrones with monoisocyanates was first described by Goldschmidt and Beckmann in 1890.[4−6] The structure of the nitrone isocyanate adducts were later established as 1,2,4-oxadiazolidin-5-ones,[7−9] a motif found in alkaloids.[10,11] 1,2,4-oxadiazolidin-5-one derivates are potential candidates for the development of pharmaceutical and other biologically relevant substances, because they are configurationally stable heterocycles, which combine structural features of barbituric acid and hydantoin derivates, compounds with broad medical applications.[12,13] Isocyanates like 4,4′-methylene diphenyl diisocyanate (MDI) and toluene diisocyanate (TDI) are commonly used in industrial polyurethane production.[14,15] However, diisocyanates have not been used in 1,3-dipolar polycycloaddition with bisnitrones so far. Beside the wide range of described low molecular weight five-membered heterocyclic ring systems that have been synthesized via nitrone cycloaddition,[1−3] nitrones have been applied in polymer chemistry in recent years.[16] We have investigated the synthesis of polymeric nitrones,[17,18] the cross-linking of polynitrones[19,20] and the poly(isoxazolidine) synthesis via polycycloaddition of bisnitrones with bismaleimides.[21] Despite the wide range of known nitrone synthesis,[1−3] all bisnitrones, which were used in literature as monomers for poly(isoxazolidine)s with either bismaleimides or bisacrylates,[21−24] were prepared simply by condensation of dialdehydes with *N*-substituted hydroxylamines. However, although this is the most common synthesis, it is limited by the accessibility of the suitable hydroxylamines.[25] Therefore, we synthesized bisnitrones in a broad manner via oxidation of bis(secondary amine)s with hydrogen peroxide. According to best of our knowledge, the use of nitrone isocyanate reactions in polymer chemistry has not been described yet. The 1,3-dipolar polycycloaddition of bisnitrones with diisocyanates is the topic of the present paper. Additionally, the copolymer synthesis using a urethane prepolymer with isocyanate end groups is described.

RESULTS AND DISCUSSION

Two new bisnitrones bis(4-benzylideneaminocyclohexyl)-methane-*N*,*N*′-dioxide (**3**) and bis[4-(3-pyridylmethylene)-aminocyclohexyl]methane-*N*,*N*′-dioxide (**4**) were prepared from technical 4,4′-methylene-bis(cyclohexylamine), which consists of a mixture of three stereo isomers.[26,27] NMR spectroscopy showed that the composition mainly consists of 1,4-*trans*,1′,4′-*trans*- and 1,4-*cis*,1′,4′-*trans*-isomer, whereas the corresponding 1,4-*cis*,1′,4′-*cis*-isomer is barely there. Initially, bis(4-benzylamino-cyclohexyl)methane (**1**) and bis[4-(3-pyridylmethyl)amino-cyclohexyl]methane (**2**) were synthesized from 4,4′-methylene-bis(cyclohexylamine) through a reductive amination process. Then **1** and **2** were oxidized to the desired bisnitrones **3** and **4** according to an oxidation method described in literature (Scheme 1).[28,29] This method concerns the use of hydrogen peroxide and selenium dioxide as catalyst in methanol at 0 °C. The bisamines **1** and **2** and bisnitrones **3** and **4** were identified by ^{1}H NMR, ^{13}C NMR, mass, and IR spectra. The CH═N-proton of the bisnitrones **3** and **4** showed a singlet at 7.37 and 7.44 ppm, respectively. Moreover the IR spectra of the bisnitrones **3** and **4** exhibit a strong absorption band ν_{N-O} at about 1150 cm^{-1}.

Scheme 1. Synthesis of Bisnitrones 3 and 4

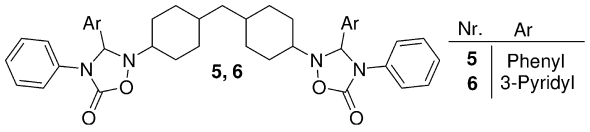


In order to estimate the possibility of polymer chain formation by cycloaddition of **3** and **4** with 4,4′-methylene diphenyl diisocyanate (MDI) and 2,4-toluene diisocyanate (2,4-TDI), respectively, **3** and **4** were reacted with phenylisocyanate in toluene under reflux without any catalyst. Dibutyltin dilaurate (DBTL), a standard catalyst for polyurethane formation, has no catalyzing effect in this system. In accordance to literature[7] the cycloaddition reactions lead to formation of 1,2,4-oxadiazolidin-5-ones (Chart 1). The obtained cycloadducts are

Received: January 24, 2012
Revised: March 12, 2012
Published: March 28, 2012

ACS Publications © 2012 American Chemical Society

Chart 1. Structures of Bis(1,2,4-oxadiazolidin-5-one)s 5 and 6



bis[4-(3,4-diphenyl-5-oxo-1,2,4-oxadiazolidin-2-yl)cyclohexyl]-methane (**5**) and bis{4-[3-(3-pyridyl)-4-phenyl-5-oxo-1,2,4-oxadiazolidin-2-yl]cyclohexyl}methane (**6**), respectively.

The bis(1,2,4-oxadiazolidin-5-one)s **5** and **6** were isolated as colorless solids and characterized by elemental analysis, mass spectrometry, ^{1}H, ^{13}C NMR and IR spectroscopy. To illustrate the cycloaddition, a section of ^{1}H NMR spectrum of **3** in $CDCl_3$ is compared with the corresponding section of ^{1}H NMR spectrum of **5** in Figure 1. The CH═N-proton of the former

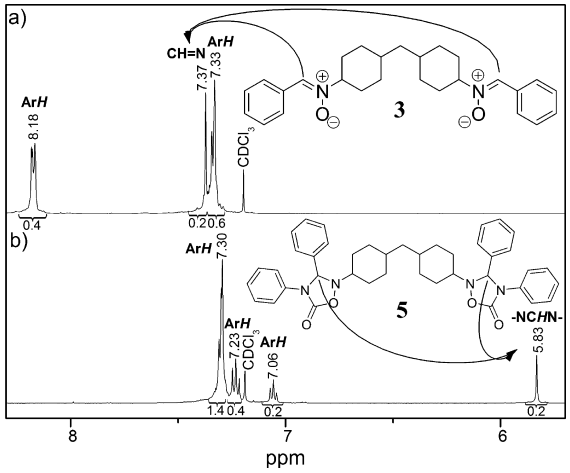
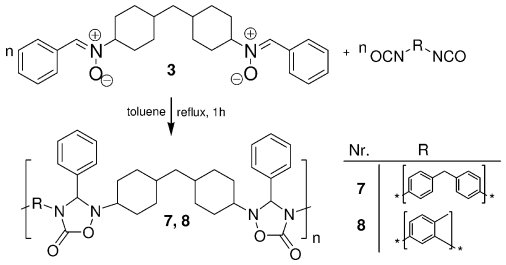


Figure 1. ^{1}H NMR spectra of **3** and corresponding cycloadduct **5**.

nitrone functionality at 7.37 ppm appears after 1,3-dipolaric cycloaddition as singlet of 1,2,4-oxadiazolidin-5-one unit at 5.83 ppm.

Scheme 2. Poly(1,2,4-oxadiazolidin-5-one)s 7 and 8



In the IR spectra the signal at around 1150 cm^{-1} of the N−O vibration of the former binistrones **3** and **4** vanished and a strong broad signal at 1738 cm^{-1} of the C═O vibration of the bis(1,2,4-oxadiazolidin-5-one)s **5** and **6** appeared. We discovered that the reaction strongly depends on the electronic properties of the substituent next to the carbon atom of the nitrone. According to ^{1}H NMR measurements, we showed that the reaction of bisnitrone **3** with phenylisocyanate was faster than the cycloaddition of electron poor bisnitrone **4** and lead to a quantitative conversion into the corresponding bis(1,2,4-oxadiazolidin-5-one) **5** within 30 minutes. Thus, the electron withdrawing group obviously makes the oxygen atom of the nitrone less nucleophilic and reduces the tendency of the nitrone oxygen attack toward the electron poor isocyanate group.

We focused on the polycycloaddition of **3** with MDI and 2,4-TDI to obtain linear poly(1,2,4-oxadiazolidin-5-one)s **7** and **8**, because of the observed higher reactivity of **3** toward isocyanate functions in comparison to **4**. These reactions were performed using the same method as described for the bis-(1,2,4-oxadiazolidin-5-one)s **5** and **6** (Scheme 2).

The structures of the new polymer products **7** and **8** were proven by IR and NMR spectroscopy. The repeating units of 1,2,4-oxadiazolidin-5-one were identified by the broad signal in the ^{1}H NMR spectra of **7** and **8** at about 6.50 ppm in DMSO-d_6 (about 5.80 ppm in $CDCl_3$). Figure 2 illustrates it for polycycloadduct **7**. Moreover, a strong C═O vibration at about 1750 cm^{-1} in the IR spectra confirmed five-membered 1,2,4-oxadiazolidin-5-one structure (Figure 3).

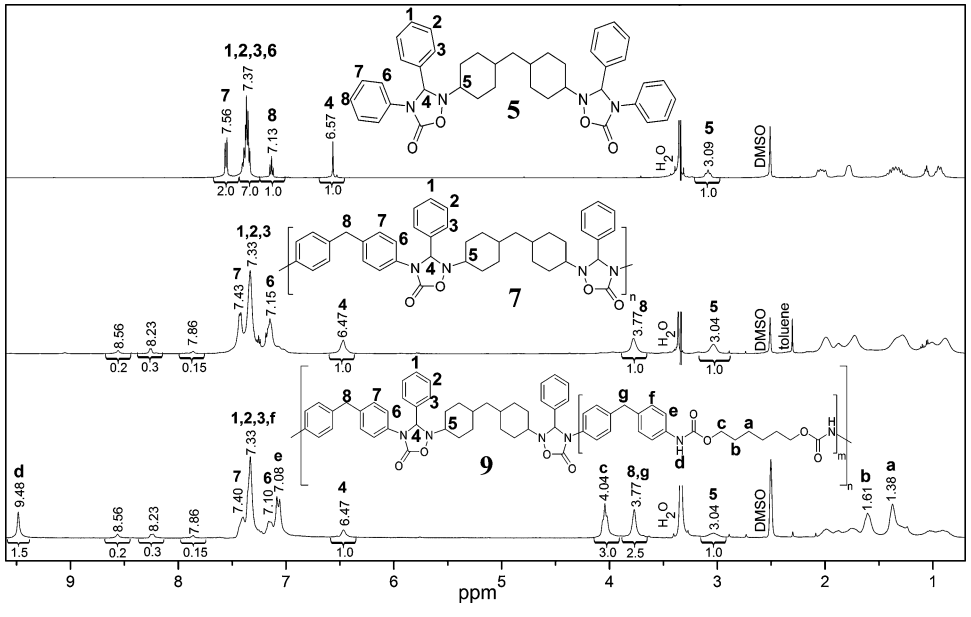


Figure 2. ^{1}H NMR spectra of bis(1,2,4-oxadiazolidin-5-one) **5** and polycyloadducts **7** and **9** (DMSO-d_6).

dx.doi.org/10.1021/ma300181g | *Macromolecules* 2012, 45, 3285−3288

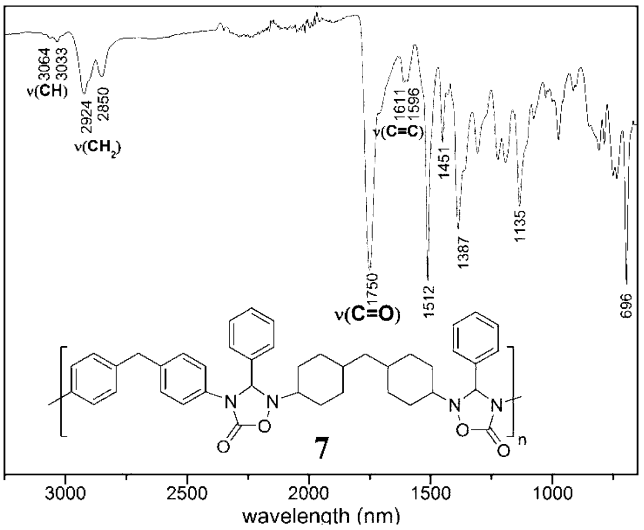
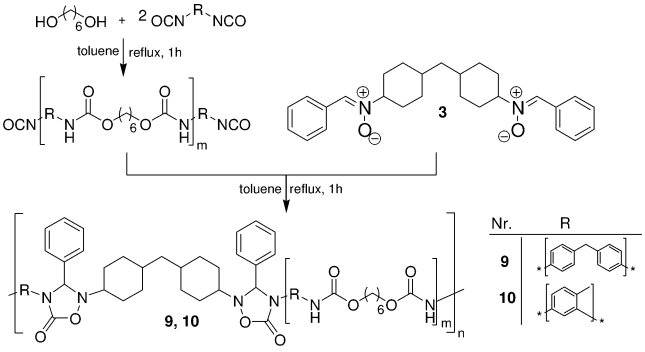


Figure 3. IR spectrum of poly(1,2,4-oxadiazolidin-5-one) **7**.

Gel permeation chromatography (GPC) indicated the formation of MDI bisnitrone **3** polycycloadducts **7** (M_w = 10400 g/mol, M_n = 4500 g/mol) and 2,4-TDI bisnitrone **3** polycycloadducts **8** (M_w = 19000 g/mol, M_n = 6400 g/mol). Free standing films of poly(1,2,4-oxadiazolidin-5-one)s **7** and **8** could be obtained from chloroform on a glass surface.

To achieve higher molecular weights with desirable properties, the strategy adopted here was to incorporate a urethane prepolymer as chain extender in the poly(1,2,4-oxadiazolidin-5-one) synthesis. Therefore, we refluxed 1,6-hexanediol and MDI or 2,4-TDI in toluene and incorporated bisnitrone **3** in the second stage of the two-step process to obtain the poly(urethane-*co*-1,2,4-oxadiazolidin-5-one)s **9** and **10** (Scheme 3).

Scheme 3. Poly(urethane-*co*-1,2,4-oxadiazolidin-5-one)s 9 and 10



The presence of 1,2,4-oxadiazolidin-5-one and urethane in the copolymers **9** and **10** could be elucidated by IR spectroscopy. IR spectra showed vibration bands of the 1,2,4-oxadiazolidin-5-one C═O at about 1750 cm^{-1}, the urethane C═O at about 1720 cm^{-1} and the NH stretching of secondary amide at about 3300 cm^{-1}. The original diisocyanate (−N═C═O) at about 2300 cm^{-1} was fully absent in the spectra, indicating a complete conversion.

The chemical structures of the copolymers **9** and **10** were also analyzed by ^{1}H NMR spectroscopy and compared with the nonpolymeric cycloadduct **5** and the poly(1,2,4-oxadiazolidin-5-one)s **7** and **8**. This is illustrated in Figure 2. The signal at 6.47 ppm was attributed to the proton of 1,2,4-oxadiazolidin-5-one units. The urethane linkage was verified through the signals at 4.04 and 9.48 ppm, which were assigned to −OCH_2− and −NH− protons. A urethane/1,2,4-oxadiazolidin-5-one ratio of 3:2 for copolymer **9** was determined by analysis of the integrations of the key resonances. The same ratio was found for copolymer **10**. The side signals in ^{1}H NMR spectrum at 8.23 and 7.86 ppm belong to remaining nitrone functions.

Molecular weight of the poly(urethane-*co*-1,2,4-oxadiazolidin-5-one)s **9** (M_w = 20000 g/mol, M_n = 7200 g/mol) and **10** (M_w = 29600 g/mol, M_n = 7100 g/mol) were determined by GPC. Compared to the poly(1,2,4-oxadiazolidin-5-one)s **7** and **8**, the poly(urethane-*co*-1,2,4-oxadiazolidin-5-one)s **9** and **10** have a higher number and weight-average molar mass, as expected from the use of prepolymers. The formation of urethane copolymers **9** and **10** increased significantly the mass of the MDI prepolymer (M_w = 4382 g/mol, M_n = 939 g/mol) and the 2,4-TDI prepolymer (M_w = 1017 g/mol, M_n = 703 g/mol). This is illustrated in Figure 4.

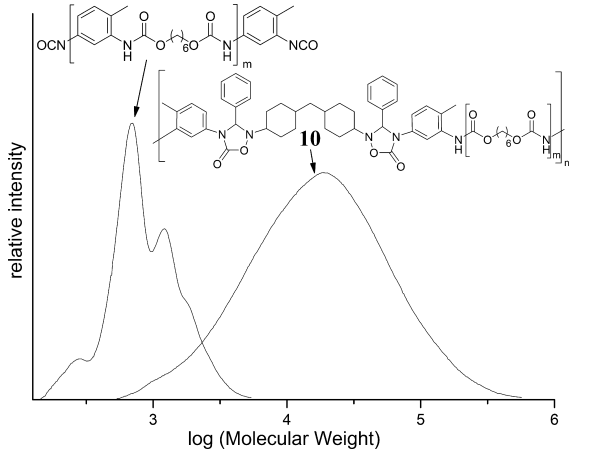


Figure 4. GPC curves of 2,4-TDI prepolymer and urethane copolymer **10**.

Thermal properties of the poly(1,2,4-oxadiazolidin-5-one)s **7** and **8** and the poly(urethane-*co*-1,2,4-oxadiazolidin-5-one)s **9** and **10** were performed using differential scanning calorimetry (DSC) measurements. Glass transition temperatures (T_g) could not been detected. However, after a weak melting point all polymers exhibit a sharp exothermic peak above 180 °C which can be attributed to thermal decomposition. The missing IR absorption of C═O (1750 cm^{-1}) after heating above 180 °C in DSC oven verified the decomposition, which probably takes place via evolution of CO_2.

CONCLUSION

In conclusion, polycycloaddition reactions of bisnitrones with diisocyanates yield linear polymer chains. As proof, bisnitrone **3** builds poly(1,2,4-oxadiazolidin-5-one)s **7** and **8** with MDI and 2,4-TDI, respectively. Moreover, poly(urethane-*co*-1,2,4-oxadiazolidin-5-one)s **9** and **10** were synthesized via incorporation of a urethane prepolymer as chain extender. 1,2,4-oxadiazolidin-5-one structures in the main chain of **7**−**10** were identified by IR and NMR spectroscopy. Studies on model reaction between bisnitrones **3** and **4** with phenyliscocyanate showed that the reaction depends on the nitrone structure and is positively enhanced by electron donating groups at the nitrone carbon atom. To best of our knowledge, the use of bisnitrones for

dx.doi.org/10.1021/ma300181g | *Macromolecules* 2012, 45, 3285−3288

synthesis of 1,2,4-oxadiazolidin-5-one ring containing polymers has not been described in literature so far. Thus, this opens up a new field for further investigations.

■ ASSOCIATED CONTENT

Supporting Information

Description of the organic synthesis and a characterization of the obtained compounds. This material is available free of charge via the Internet at http://pubs.acs.org.

■ AUTHOR INFORMATION

Corresponding Author

*Fax: (+49)211-8115-840. E-mail: h.ritter@uni-duesseldorf.de.

Notes

The authors declare no competing financial interest.

■ REFERENCES

(1) Hamer, J.; Macaluso, A. *Chem. Rev.* **1964**, *64* (4), 473−495.
(2) Merino, P. *Science of Synthesis*; George-Thieme Verlag: Stuttgart, Germany, 2004, Vol. *27*, pp 511−580.
(3) Merino, P. *Science of Synthesis Knowledge Updates 2010/4*; George-Thieme Verlag: Stuttgart, Germany, 2011; pp 325−403.
(4) Goldschmidt, H. *Ber. Dtsch. Chem. Ges.* **1890**, *23* (2), 2746−2749.
(5) Beckmann, E. *Ber. Dtsch. Chem. Ges.* **1890**, *23* (2), 3331−3341.
(6) Beckmann, E. *Ber. Dtsch. Chem. Ges.* **1894**, *27* (2), 1957−1959.
(7) Seidl, H.; Huisgen, R.; Grashey, R. *Chem. Ber.* **1969**, *102* (3), 926−930.
(8) Bell, A. M. T.; Bridges, J.; Cross, R.; Falshaw, C. P.; Taylor, B. F.; Taylor, G. A.; Whittaker, I. C. *J. Chem. Soc. Perkin Trans. I* **1987**, 2593−2596.
(9) Karabiyik, H.; Aygün, M.; Coçkun, N.; Kazak, C. *J. Chem. Crystallogr.* **2005**, *35* (8), 577−582.
(10) Takayama, H.; Katakawa, K.; Kitajima, M.; Seki, H.; Yamaguchi, K.; Aimi, N. *Org. Lett.* **2001**, *3* (26), 4165−4167.
(11) Elliot, M. C.; Paine, J. S. *Org. Biomol. Chem.* **2009**, *7* (17), 3455−3462.
(12) Ritter, T.; Carreira, E. M. *Angew. Chem., Int. Ed.* **2005**, *44* (6), 936−938.
(13) Safir, S. R.; Lopresti, R. J. *J. Am. Chem. Soc.* **1958**, *80* (18), 4921−4923.
(14) Bayer, O.; Rinke, H.; Siefken, W.; Orthner, L.; Schild, H. (I.G. Farben), DRP 728 981, 1937.
(15) Arpe, H.-J. *Industrielle Organische Chemie*, 6. überarb. Aufl., Wiley-VCH: Weinheim, Germany, 2007; pp 420−426.
(16) Wong, E. H. H.; Junkers, T.; Barner-Kowollik, C. *Polym. Chem.* **2011**, *2*, 1008−1017.
(17) Heinenberg, M.; Ritter, H. *Macromol. Chem. Phys.* **1999**, *200* (7), 1792−1805.
(18) Heinenberg, M.; Menges, B.; Mittler, S.; Ritter, H. *Macromolecules* **2002**, *35* (9), 3448−3455.
(19) Cinar, H.; Tabatabai, M.; Ritter, H. *Polym. Int.* **2012**, DOI: 10.1002/pi.4133.
(20) Tabatabai, M.; Garska, B.; Moszner, N.; Utterodt, A.; Ritter, H. *Polym. Int.* **2011**, *60* (7), 995−1000.
(21) Vretik, L.; Ritter, H. *Macromolecules* **2003**, *36* (17), 6340−6345.
(22) Manecke, G.; Klawitter, J. *Makromol. Chem.* **1967**, *108* (1), 292−295.
(23) Manecke, G.; Klawitter, J. *Makromol. Chem.* **1971**, *142* (1), 253−257.
(24) Goodall, G. W.; Cosstick, K.; Richards, S. C.; Hayes, W. *Eur. Polym. J.* **2008**, *44* (6), 1881−1890.
(25) Cardona, F.; Bonanni, M.; Soldaini, G.; Goti, A. *ChemSusChem* **2008**, *1* (4), 327−332.
(26) Barkdoll, A. E.; Gray, H. W.; Kirk, W. *J. Am. Chem. Soc.* **1951**, *73* (2), 741−746.
(27) Richter, R.; Temme, G. H. *J. Org. Chem.* **1978**, *43* (9), 1825−1827.
(28) Murahashi, S.-I.; Shiota, T. *Tetrahedron Lett.* **1987**, *28* (21), 2383−2386.
(29) Ballini, R.; Marcantoni, E.; Petrini, M. *J. Org. Chem.* **1992**, *57* (4), 1316−1318.